

AWARD NUMBER: W81XWH-10-1-0823

TITLE: Determine the Role of Canonical Wnt Signaling in Ovarian Tumorigenesis

PRINCIPAL INVESTIGATOR: Rugang Zhang, Ph.D.

CONTRACTING ORGANIZATION: The Wistar Institute  
Philadelphia, PA 19104

REPORT DATE: December 2015

TYPE OF REPORT: Final Report

PREPARED FOR: U.S. Army Medical Research and Materiel Command  
Fort Detrick, Maryland 21702-5012

DISTRIBUTION STATEMENT: Approved for Public Release;  
Distribution Unlimited

The views, opinions and/or findings contained in this report are those of the author(s) and should not be construed as an official Department of the Army position, policy or decision unless so designated by other documentation.

|  |                         |                                |   |  |   |
|--|-------------------------|--------------------------------|---|--|---|
| <b>REPORT DOCUMENTATION PAGE</b>   |                         |                                |   | <i>Form Approved</i><br><b>OMB No. 0704-0188</b>         |   |
| <small>Public reporting burden for this collection of information is estimated to average 1 hour per response, including the time for reviewing instructions, searching existing data sources, gathering and maintaining the data needed, and completing and reviewing this collection of information. Send comments regarding this burden estimate or any other aspect of this collection of information, including suggestions for reducing this burden to Department of Defense, Washington Headquarters Services, Directorate for Information Operations and Reports (0704-0188), 1215 Jefferson Davis Highway, Suite 1204, Arlington, VA 22202-4302. Respondents should be aware that notwithstanding any other provision of law, no person shall be subject to any penalty for failing to comply with a collection of information if it does not display a currently valid OMB control number. <b>PLEASE DO NOT RETURN YOUR FORM TO THE ABOVE ADDRESS.</b></small>   |                         |                                |   |  |   |
| <b>1. REPORT DATE</b><br>December 2015   |                         | <b>2. REPORT TYPE</b><br>Final |   | <b>3. DATES COVERED</b><br>15 Sept. 2010 – 14 Sept. 2015 |   |
| <b>4. TITLE AND SUBTITLE</b><br><br>Determine the Role of Canonical Wnt Signaling in Ovarian Tumorigenesis   |                         |                                |   | <b>5a. CONTRACT NUMBER</b>                               |   |
|  |                         |                                |   | <b>5b. GRANT NUMBER</b><br>W81XWH-10-1-0823              |   |
|  |                         |                                |   | <b>5c. PROGRAM ELEMENT NUMBER</b>                        |   |
| <b>6. AUTHOR(S)</b><br><br>Rugang Zhang, Ph.D.<br><br>E-Mail: <a href="mailto:rzhang@wistar.org">rzhang@wistar.org</a>   |                         |                                |   | <b>5d. PROJECT NUMBER</b>                                |   |
|  |                         |                                |   | <b>5e. TASK NUMBER</b>                                   |   |
|  |                         |                                |   | <b>5f. WORK UNIT NUMBER</b>                              |   |
| <b>7. PERFORMING ORGANIZATION NAME(S) AND ADDRESS(ES)</b><br><br>The Wistar Institute<br>Philadelphia, PA 19104  |                         |                                |   | <b>8. PERFORMING ORGANIZATION REPORT NUMBER</b>          |   |
| <b>9. SPONSORING / MONITORING AGENCY NAME(S) AND ADDRESS(ES)</b><br>U.S. Army Medical Research and Materiel Command<br>Fort Detrick, Maryland 21702-5012   |                         |                                |   | <b>10. SPONSOR/MONITOR'S ACRONYM(S)</b>                  |   |
|  |                         |                                |   | <b>11. SPONSOR/MONITOR'S REPORT NUMBER(S)</b>            |   |
| <b>12. DISTRIBUTION / AVAILABILITY STATEMENT</b><br>Approved for Public Release; Distribution Unlimited  |                         |                                |   |  |   |
| <b>13. SUPPLEMENTARY NOTES</b>   |                         |                                |   |  |   |
| <b>14. ABSTRACT</b><br>Ovarian cancer ranks first as the cause of death for gynecological cancers. Obviously, there is an urgent need to develop novel treatment methods for ovarian cancer. To do this, we must better understand key events associated with ovarian cancer development. In order to combat cancer, a normal cell's typical response to a tumor-promoting genetic alteration is irreversible growth arrest, consequently preventing the normal human cell from progressing towards becoming a cancer cell. This process is termed senescence. When this process fails, those cells containing tumor-promoting genetic alterations can grow without control and become a tumor. The potential use of cellular senescence for cancer therapy would rely on reactivation of this process in cancer cells. We have previously discovered a pathway that opposes the beneficial process of senescence. This pathway is referred to as the canonical Wnt signaling pathway. Therefore, we hypothesize that canonical Wnt signaling pathway contributes to the development of ovarian cancer through bypassing senescence. The proposed studies may lead to development of strategies for ovarian cancer treatment using reactivation of cellular senescence as a novel mechanism by targeting ovarian cancer promoting canonical Wnt signaling. |                         |                                |   |  |   |
| <b>15. SUBJECT TERMS</b><br>Ovarian Cancer, Cellular Senescence, Wnt Signaling   |                         |                                |   |  |   |
| <b>16. SECURITY CLASSIFICATION OF:</b>   |                         |                                | <b>17. LIMITATION OF ABSTRACT</b><br><br>UU | <b>18. NUMBER OF PAGES</b><br><br>343                    | <b>19a. NAME OF RESPONSIBLE PERSON</b><br>USAMRMC |
| <b>a. REPORT</b><br>U  | <b>b. ABSTRACT</b><br>U | <b>c. THIS PAGE</b><br>U       |   |  | <b>19b. TELEPHONE NUMBER</b> (include area code)  |

# Table of Contents

|                                   |    |
|-----------------------------------|----|
| Introduction.....                 | 4  |
| Body.....                         | 4  |
| Key Research Accomplishments..... | 18 |
| Reportable Outcomes.....          | 19 |
| Conclusions.....                  | 22 |
| References.....                   | 22 |
| Appendices.....                   | 24 |

## **Introduction:**

The role of Wnt signaling in epithelial ovarian cancer (EOC) development remains largely elusive. We have evidence to suggest that canonical Wnt signaling is activated through downregulation of Wnt5a in EOC. Wnt5a is a non-canonical Wntligand that acts as an antagonist of canonical Wnt signaling. Furthermore, inhibition of canonical Wnt signaling or restoration of Wnt5a expression inhibits the growth of EOC cells. The overall hypothesis of this proposal is that canonical Wnt signaling activated by loss of Wnt5a contributes to EOC development by abrogation of OIS. The objectives of the proposed studies are to determine the role of canonical Wnt signaling in regulating OIS of ovarian epithelial cells during progression of benign ovarian tumors into invasive EOCs, and to investigate the effects of inhibition of the canonical Wnt signaling on malignant behavior of EOC cells. The specific aims are: 1): Elucidate the mechanisms by which inhibition of canonical Wnt signaling inhibits the growth of EOC cells; 2): Determine whether loss of Wnt5a contributes to EOC development by abrogation of OIS; 3): Investigate the effects of inhibition of canonical Wnt signaling on malignant behavior of EOC cells in immunodeficient mice.

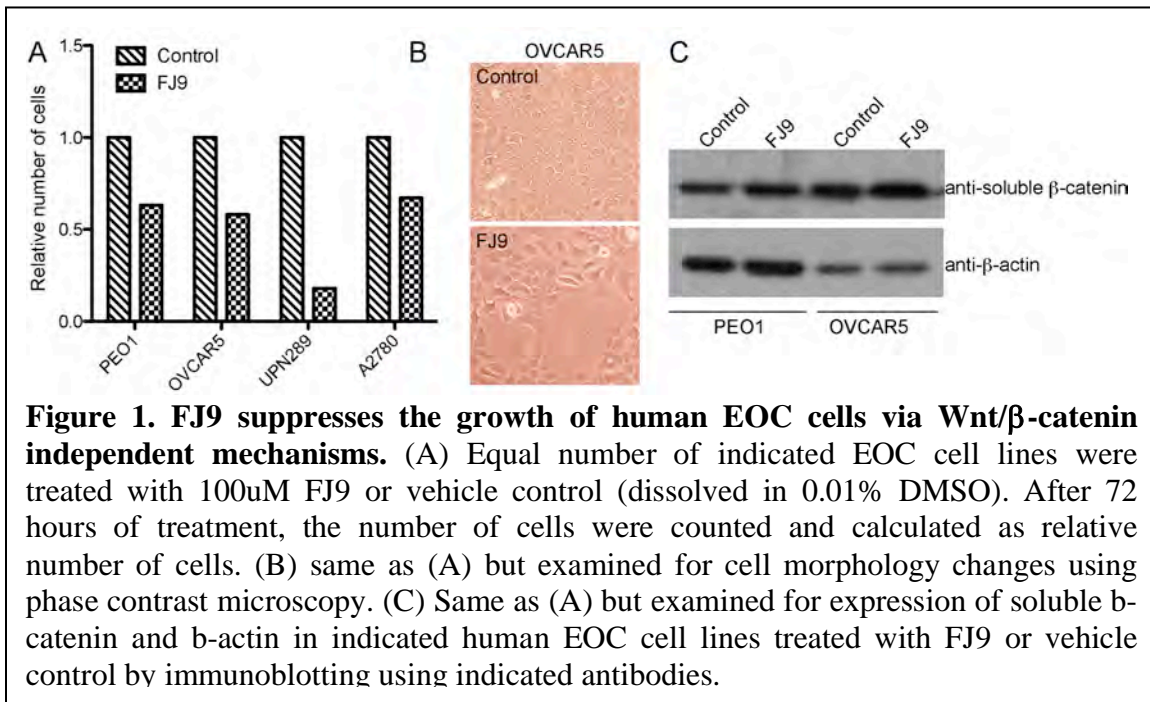
## **Body:**

1. Research accomplishments associated with each task outlined in the approved Statement of Work.

### **Task 1. Determine whether inhibition of canonical Wnt signaling inhibits the growth of EOC cells through inducing cell senescence. (Months 1-12)**

Specifically, we will determine whether inhibition of canonical Wnt signaling induces the expression of markers of senescence in human EOC cells.





**Progress report:** FJ9 has previously been demonstrated as an inhibitor of canonical Wnt signaling [1]. We showed that FJ9 inhibits the growth of human EOC cells in a panel of human EOC cell lines (Figure 1A). Consistent with the idea that this is due to senescence induction, cells treated with FJ9 demonstrated features of senescence such as a large flat cell morphology (Figure 1B). However, examination of markers of canonical Wnt signaling in FJ9 treated or control cells showed that there is no evidence to suggest the observed effects are due to inhibition of canonical Wnt/β-catenin pathway. For example, the levels of soluble β-catenin, a marker of active canonical Wnt/β-catenin pathway were not decreased by FJ9 treatment (Figure 1C). This result suggests that FJ9 inhibits the growth of human EOC cells via canonical Wnt signaling independent mechanisms.

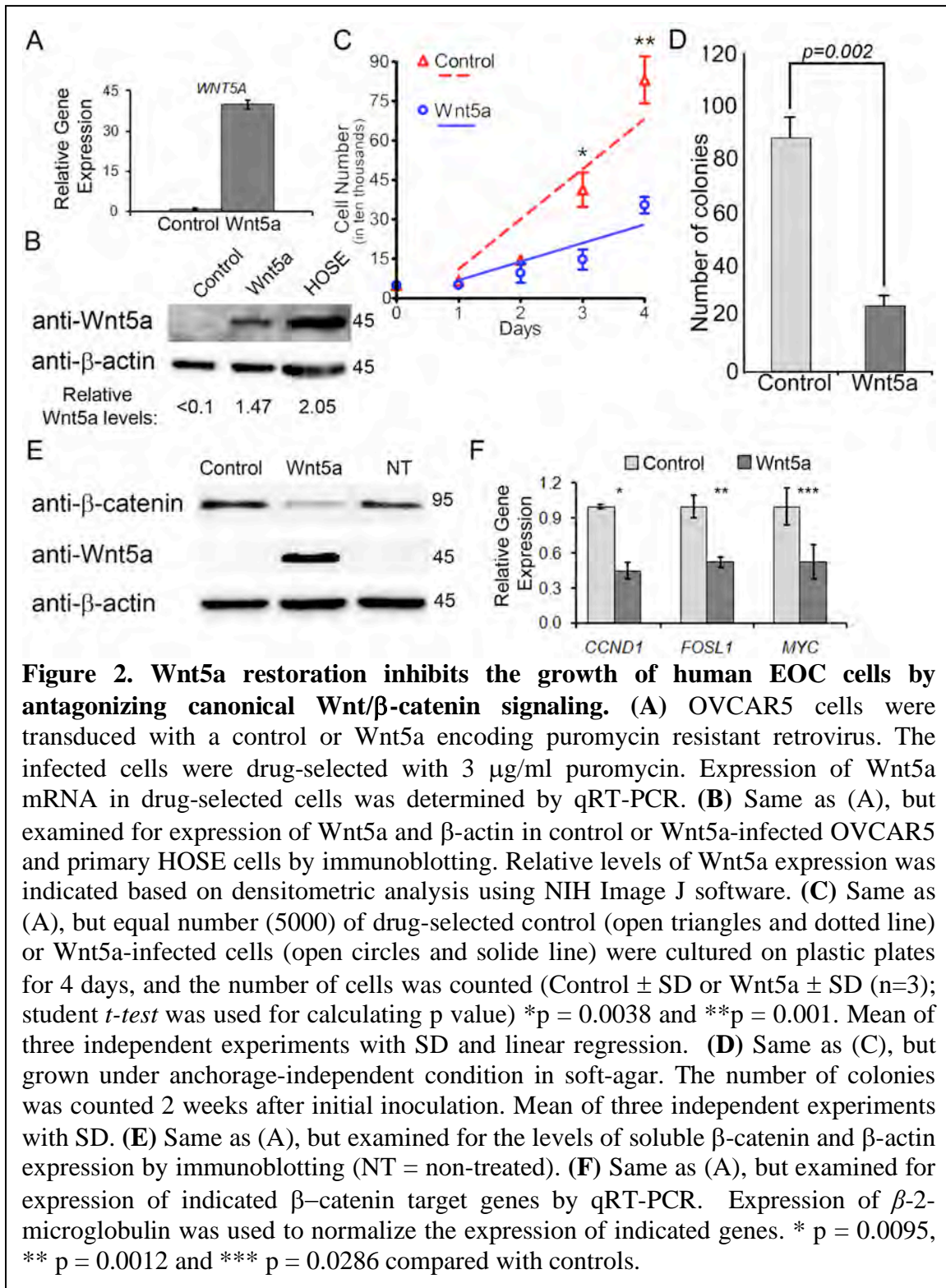
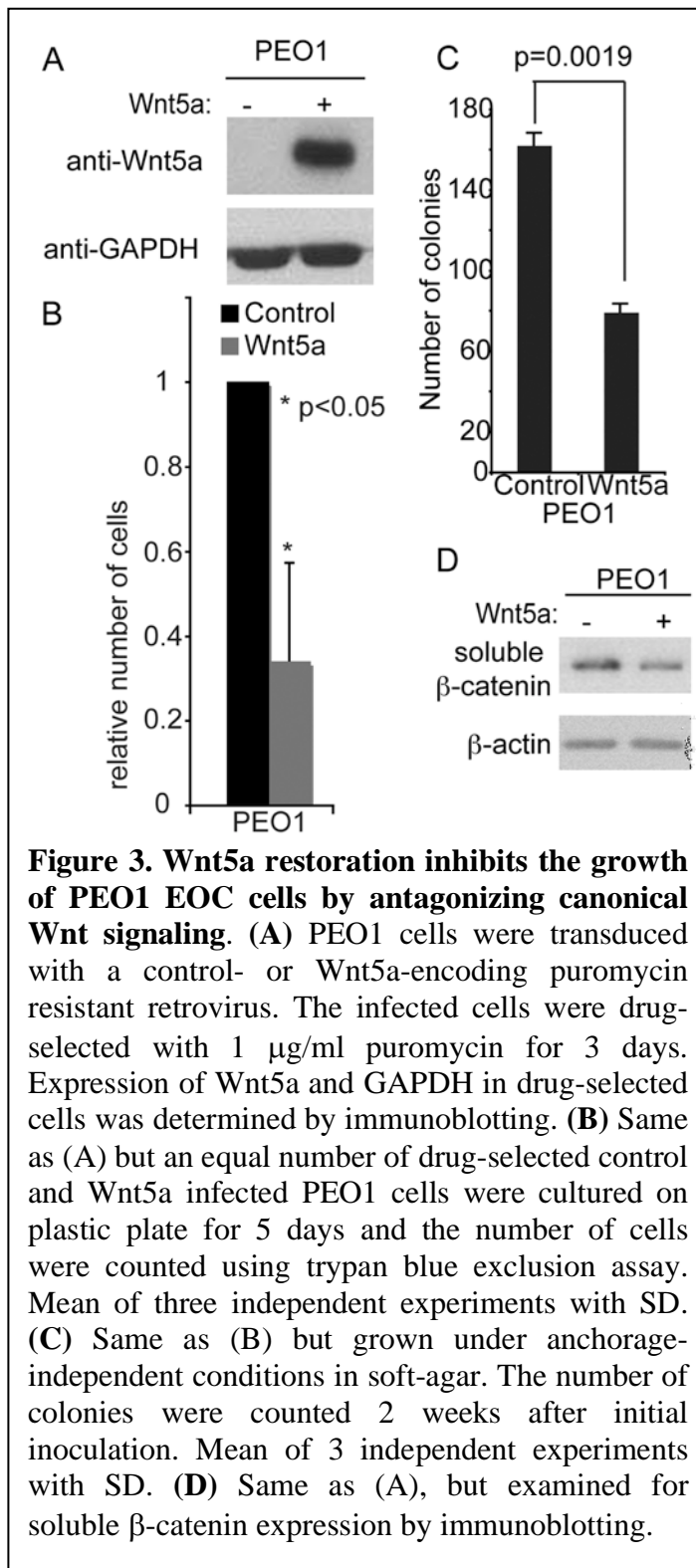


**Figure 2. Wnt5a restoration inhibits the growth of human EOC cells by antagonizing canonical Wnt/β-catenin signaling.** (A) OVCAR5 cells were transduced with a control or Wnt5a encoding puromycin resistant retrovirus. The infected cells were drug-selected with 3 μg/ml puromycin. Expression of Wnt5a mRNA in drug-selected cells was determined by qRT-PCR. (B) Same as (A), but examined for expression of Wnt5a and β-actin in control or Wnt5a-infected OVCAR5 and primary HOSE cells by immunoblotting. Relative levels of Wnt5a expression was indicated based on densitometric analysis using NIH Image J software. (C) Same as (A), but equal number (5000) of drug-selected control (open triangles and dotted line) or Wnt5a-infected cells (open circles and solid line) were cultured on plastic plates for 4 days, and the number of cells was counted (Control ± SD or Wnt5a ± SD (n=3); student *t*-test was used for calculating p value) \*p = 0.0038 and \*\*p = 0.001. Mean of three independent experiments with SD and linear regression. (D) Same as (C), but grown under anchorage-independent condition in soft-agar. The number of colonies was counted 2 weeks after initial inoculation. Mean of three independent experiments with SD. (E) Same as (A), but examined for the levels of soluble β-catenin and β-actin expression by immunoblotting (NT = non-treated). (F) Same as (A), but examined for expression of indicated β-catenin target genes by qRT-PCR. Expression of β-2-microglobulin was used to normalize the expression of indicated genes. \* p = 0.0095, \*\* p = 0.0012 and \*\*\* p = 0.0286 compared with controls.

We sought to determine the effects of Wnt5a reconstitution in human EOC cells. Wnt5a expression was reconstituted in the OVCAR5 EOC cell line via retroviral transduction. Ectopically expressed Wnt5a was confirmed by both qRT-PCR and immunoblotting in

OVCAR5 cells stably expressing Wnt5a or a vector control (Figure 2A-B). Of note, the levels of ectopically expressed Wnt5a in OVCAR5 cells are comparable to the levels observed in primary HOSE cells (Figure 2B). Interestingly, Wnt5a reconstitution in

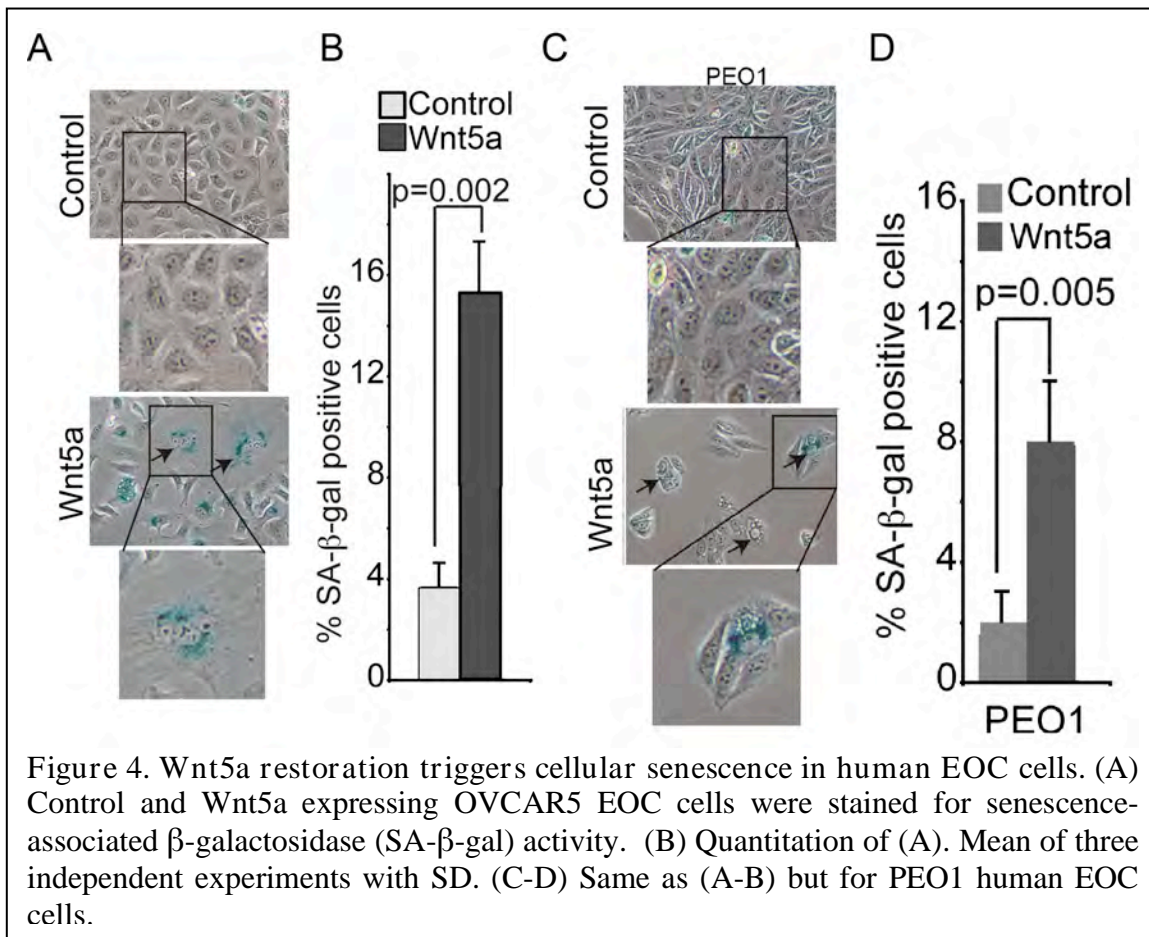


OVCAR5 human EOC cells significantly inhibited both anchorage-dependent and anchorage-independent growth in soft-agar compared with vector controls (Figure 2C-D). In addition, similar growth inhibition by Wnt5a reconstitution was also observed in the PEO1 human EOC cell line (Figure 3A-C), suggesting that this effect is not cell line specific. Based on these results, we conclude that Wnt5a reconstitution inhibits the growth of human EOC cells in vitro.

Canonical Wnt signaling promotes cell proliferation and Wnt5a has been demonstrated to antagonize the canonical Wnt/ $\beta$ -catenin signaling in certain cell contexts [2-5]. We hypothesized that Wnt5a would suppress the growth of human EOC cells by antagonizing canonical Wnt/ $\beta$ -catenin signaling. To test our hypothesis, we examined the effect of Wnt5a reconstitution on expression of markers of active Wnt/ $\beta$ -catenin signaling in human EOC cells, namely the levels of “active” soluble  $\beta$ -catenin[6-8] and expression of  $\beta$ -catenin target genes such as CCND1, c-MYC and FOSL1 [9, 10]. Indeed, we observed a decrease in soluble  $\beta$ -catenin in Wnt5a reconstituted OVCAR5 cells compared with vector controls (Figure 2E). Consistently, we also observed a

significant decrease in the levels of  $\beta$ -catenin target genes in these cells, namely CCND1 ( $p = 0.0095$ ), FOSL1 ( $p = 0.0012$ ) and c-MYC ( $p = 0.0286$ ) (Figure 2F). Similar effects of Wnt5a reconstitution on expression of markers of active Wnt/ $\beta$ -catenin signaling (such as decreased levels of soluble  $\beta$ -catenin) were also observed in PEO1 human EOC cells (Figure 3D), suggesting that this is not cell line specific. Based on these results, we conclude that Wnt5a suppresses the growth of human EOC cells by antagonizing canonical Wnt/ $\beta$ -catenin signaling in human EOC cells.

Next, we sought to determine the cellular mechanism whereby Wnt5a inhibits the growth of human EOC cells. We sought to determine whether Wnt5a restoration might induce senescence in human EOC cells. To do so, we determined whether Wnt5a restoration induces SA- $\beta$ -gal activity, a universal marker of cellular senescence [11]. Indeed, SA- $\beta$ -gal activity was notably induced by Wnt5a reconstitution in both OVCAR5 and PEO1 human EOC cells compared with controls (Figure 4).

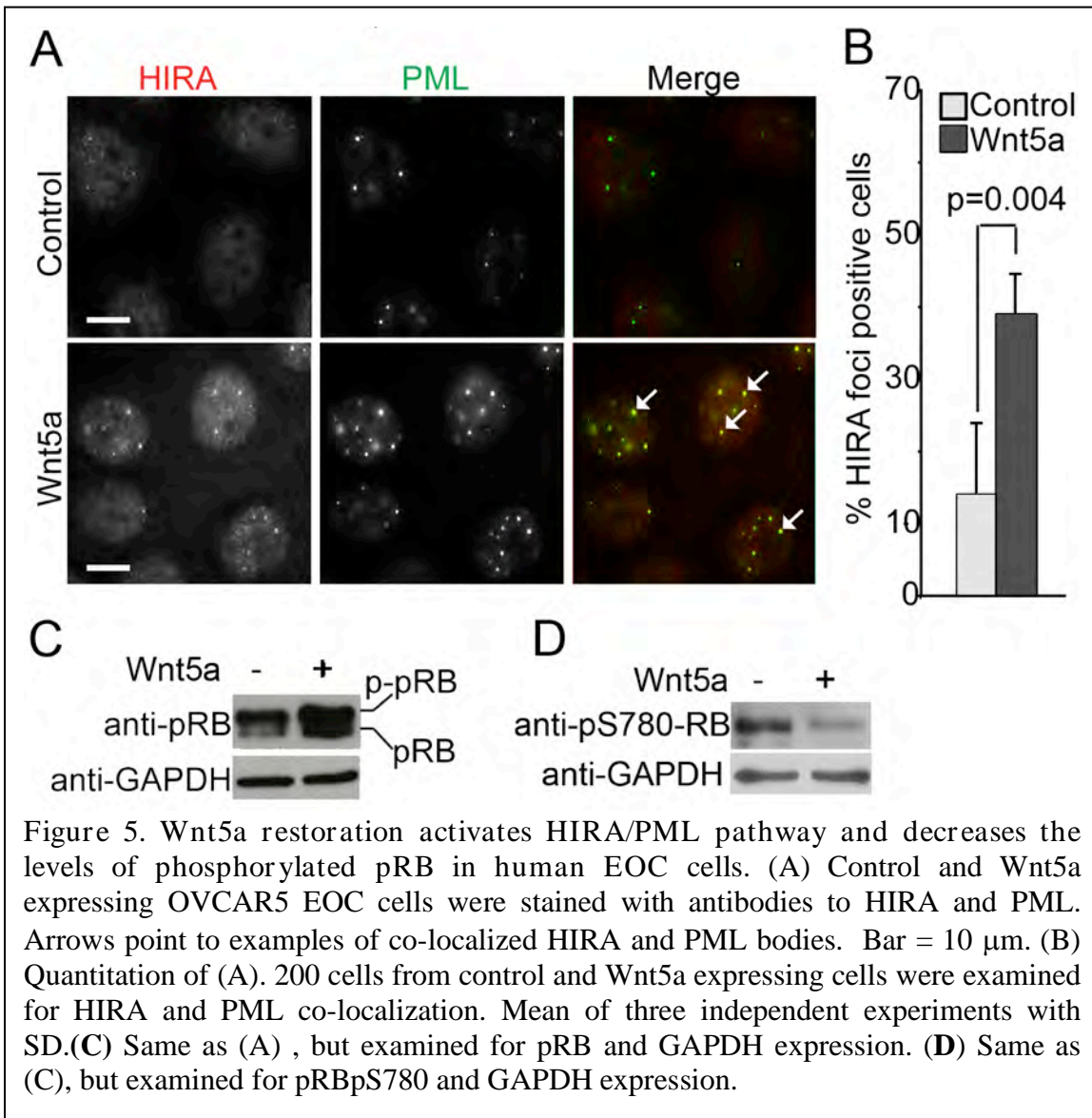


**Task 2. Determine the effects of inhibition of Wnt/ $\beta$ -catenin signaling on key senescence-regulating pathways in human EOC cells. (Month 13-24)**

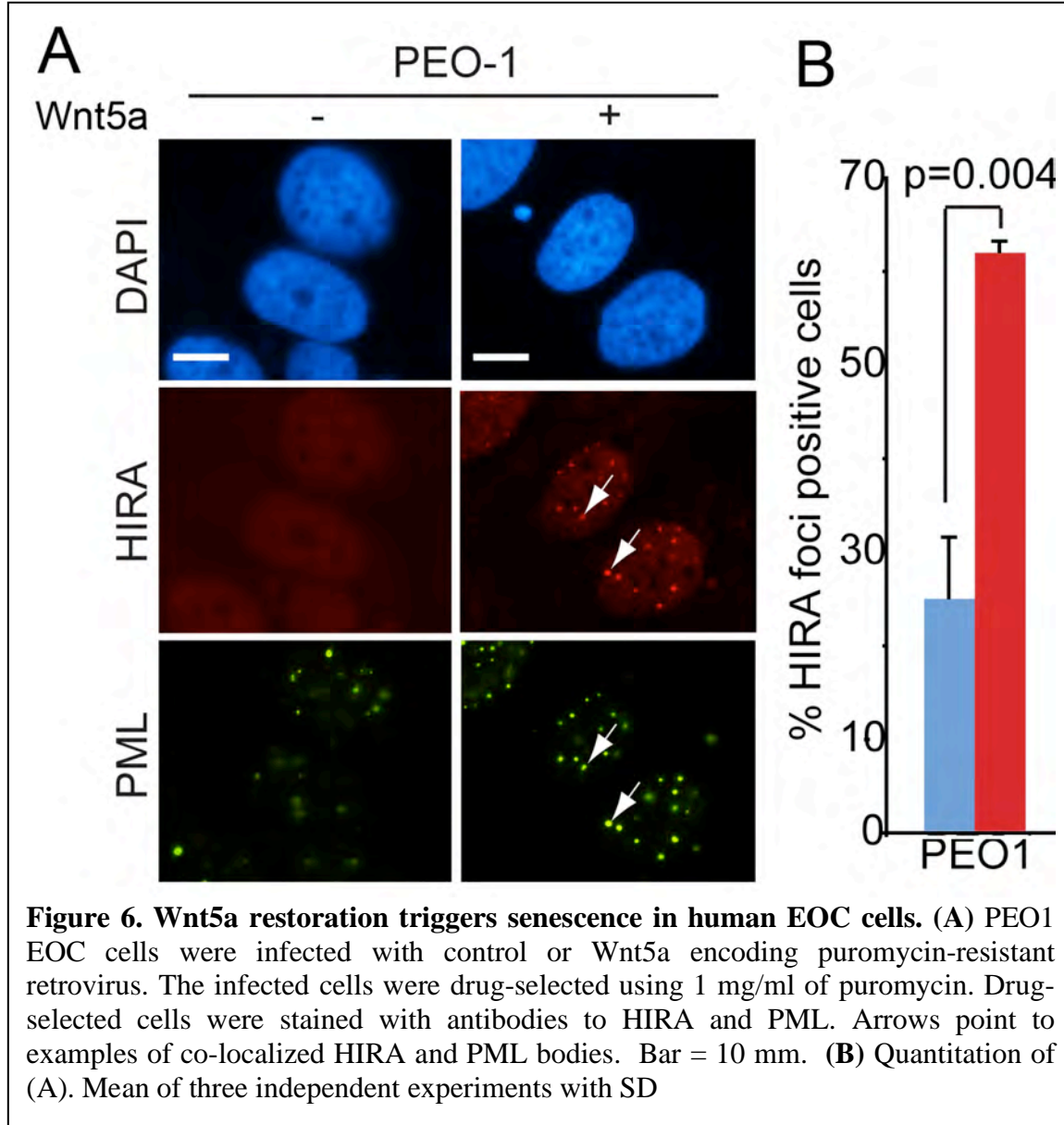
Specifically, we will determine the effects of inhibition of Wnt/ $\beta$ -catenin signaling by FJ9 treatment or enforced Wnt5a expression on status of p53, pRB and HIRA/PML pathways.



*Progress report:* Since FJ9 failed to inhibit canonical Wnt signaling (Figure 1C), we focused on our study on using Wnt5a restoration as a way to inhibit canonical Wnt signaling (Figure 2 and 3). We have previously shown that suppression of canonical Wnt signaling promotes cellular senescence in primary human fibroblasts by activating the senescence-promoting histone repressor A (HIRA)/ promyelocytic leukemia (PML) pathway [8]. PML bodies are 20-30 dot-like structures in the nucleus of virtually all human cells. PML bodies are sites of poorly defined tumor suppressor activity, and are disrupted in acute promyelocytic leukemia [12]. PML has been implicated in regulating cellular senescence. For example, the foci number and size of PML bodies increase during senescence [12, 13] and inactivation of PML suppresses senescence [14]. Activation of the HIRA/PML pathway is reflected by the recruitment of HIRA into PML bodies [15].



As Wnt5a antagonizes canonical Wnt signaling in human EOC cells (Figure 2E-F), we sought to determine whether Wnt5a restoration might activate the senescence-promoting HIRA/PML pathway in human EOC cells. Towards this goal, we examined the localization of HIRA in OVCAR5 EOC cells reconstituted with Wnt5a or vector



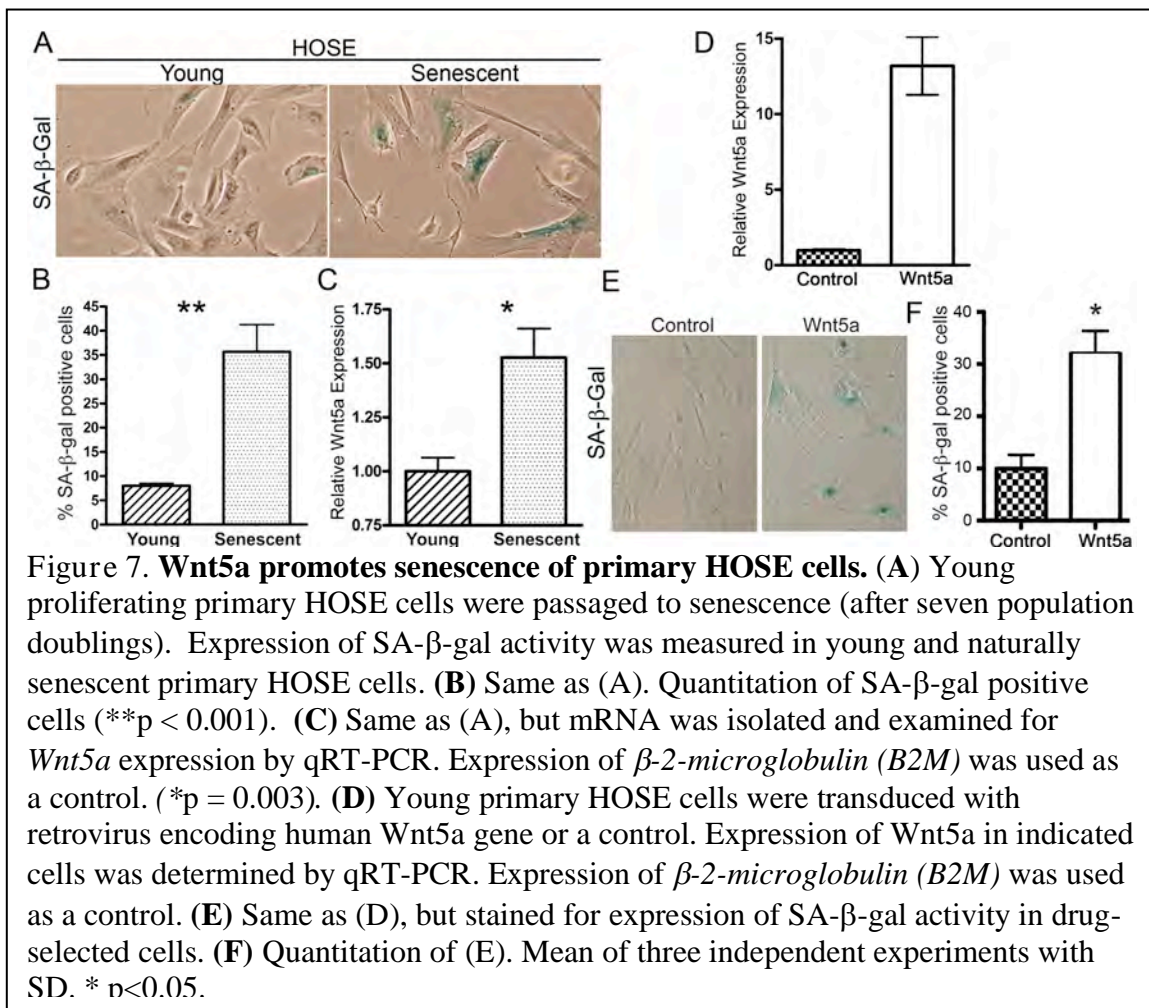
control. Notably, there was a significant increase in the percentage of cells with HIRA localized to PML bodies in Wnt5a restored human EOC cells compared with controls (Figure 5A-B,  $p = 0.004$ ). In addition, we also observed an increase in the number and size of PML bodies in the Wnt5a restored OVCAR5 EOC cells (Figure 5A), which are also established markers of cellular senescence [14, 16].

The p53 and pRB tumor suppressor pathways play a key role in regulating senescence [11]. Thus, we sought to determine the effects of Wnt5a on the p53 and pRB

pathways. Interestingly, p16<sup>INK4a</sup>, the upstream repressor of pRB, is deleted in OVCAR5 human EOC cell line [17]. In addition, the levels of total phosphorylated pRB were not decreased by Wnt5a, while the levels of cyclin D1/CKD4-mediated Serine 780 phosphorylation on pRB (pRBpS780) were decreased by Wnt5a [18] (Figure 4C-D). Further, p53 is null in OVCAR5 cells [19]. We conclude that cellular senescence induced by Wnt5a restoration is independent of both p53 and p16<sup>INK4a</sup>.

Similarly, we observed activation of the HIRA/PML pathway by Wnt5a restoration in PEO1 human EOC cells (Figure 6A-B), suggesting that the observed effects are not cell line specific. Together, we conclude that Wnt5a reconstitution activates the HIRA/PML senescence pathway.

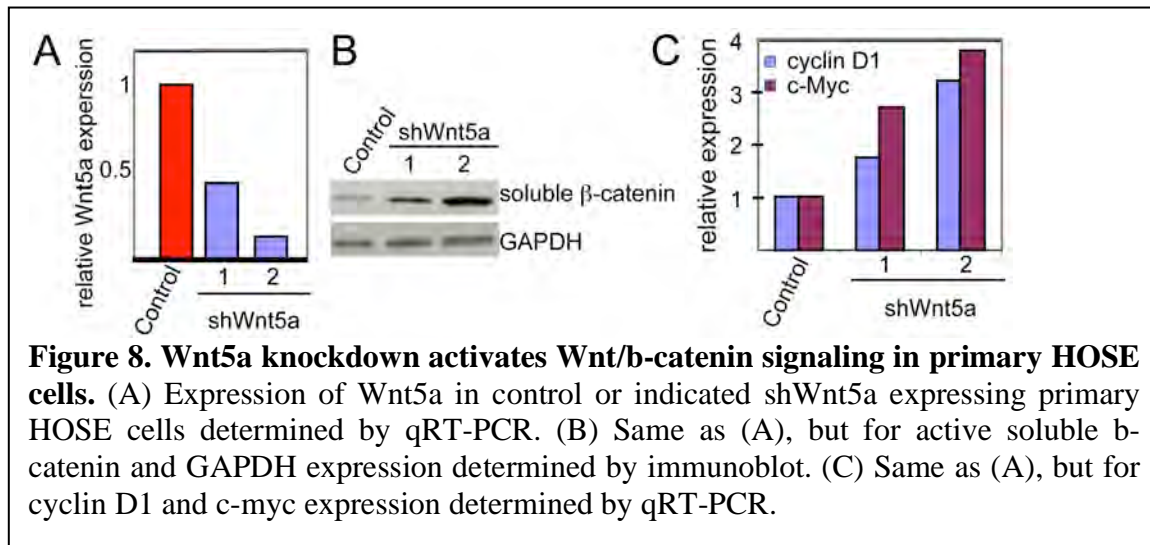
Based on these results, we concluded that Wnt5a restoration induced senescence of human EOC cells by activating the HIRA/PML senescence pathway.



**Specific Aim 2. Determine whether loss of Wnt5a contributes to ovarian cancer development by abrogation of oncogene-induced senescence (OIS) (Months 25-48).**

**Task 3. Determine whether loss of Wnt5a activates canonical Wnt signaling, delays OIS and facilitates activated oncogene initiated transformation of primary HOSE cells. (Months 25-36)**

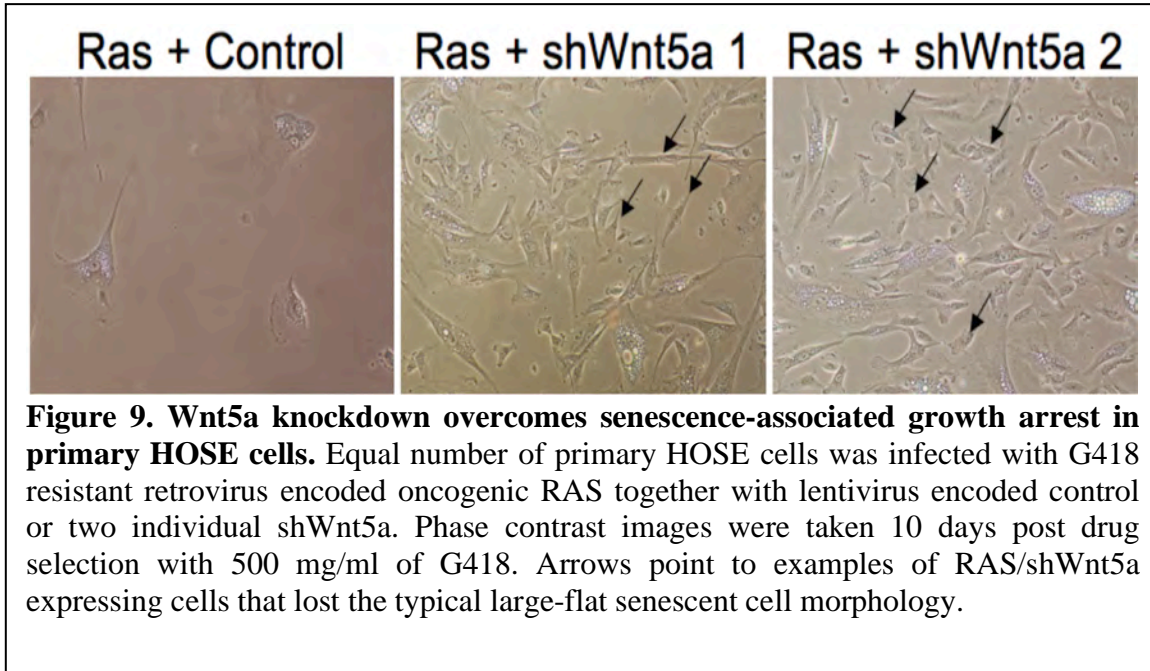
*Progress report:* We next asked whether Wnt5a expression is regulated during natural senescence of primary HOSE cells. Indeed, we observed an increase in the levels of Wnt5a mRNA in senescent primary HOSE cells compared with young cells (Figure 7A-C). In addition, we found that ectopic Wnt5a induces senescence of primary HOSE cells (Figure 7D-F). Together, we conclude that Wnt5a plays a role in regulating senescence of primary HOSE cells.



We next asked whether downregulation of Wnt5a activates canonical Wnt signaling in primary HOSE cells. To knockdown Wnt5a in primary HOSE, two lentivirus-encoded individual shRNAs to human Wnt5a gene were generated. The knockdown efficacy of shWnt5a was confirmed by qRT-PCR (Figure 8A). We found that Wnt5a knockdown led to increased expression of soluble b-catenin and its target genes c-Myc and cyclin D1 in primary HOSE cells (Figure 8B-C)



We next determined whether canonical Wnt signaling induced by shWnt5a suppresses OIS of primary HOSE cells. Compared with control, two individual shWnt5as that efficiently knockdown this gene also abolish senescence-associated cell growth arrest in primary HOSE cells induced by the RAS oncogene (Figures 8A and 9). Thus, our preliminary data suggest that canonical Wnt signaling can overcome OIS of primary



HOSE cells. This is consistent with the notion that loss of Wnt5a activates canonical Wnt signaling, delays OIS and facilitates activated oncogene initiated transformation of primary HOSE cells by suppressing senescence.

**Task 4. Determine whether downregulation of Wnt5a correlates with loss of markers of senescence and activation of canonical Wnt signaling during progression of benign ovarian tumors into invasive ovarian carcinomas. (Months 37-48)**

*Progress report:* We examined Wnt5a expression in 130 cases of primary human EOC specimens and 31 cases of normal human ovary with surface epithelium by immunohistochemistry (IHC) using an antibody against Wnt5a (Table 1). Additionally, there is recent evidence to suggest that a proportion of high-grade serous EOC may arise from distant fallopian tube epithelium [20]. Thus, we also included 28 cases of normal human fallopian tube specimens in our IHC analysis (Table 1)

As shown in Figure 10A, in normal human ovarian surface epithelial cells and fallopian tube epithelial cells, both cytoplasm and cell membrane were positive for Wnt5a IHC staining (black arrows, Figure 10A). In contrast, Wnt5a staining in EOC cells was dramatically decreased (Figure 10A). We scored expression of Wnt5a as high (H-score  $\geq 30$ ) or low (H-score  $< 30$ ) based on a histological score (H-score) [21], which considers both intensity of staining and percentage of positively stained cells, as previously described [22]. Wnt5a expression was scored as high in 58.1% (18/31) cases

of normal human ovarian surface epithelium and 82.1% (23/28) cases of normal human fallopian tube epithelium (Table 1). In contrast, Wnt5a expression was scored as high in 37.7% (49/130) cases of primary human EOCs (Table 1). Statistical analysis revealed that Wnt5a was expressed at significantly lower levels in primary human EOCs compared with either normal human ovarian surface epithelium ( $p = 0.039$ ) or normal human fallopian tube epithelium ( $p < 0.001$ ) (Table 1). On the basis of these studies, we conclude that Wnt5a is expressed at significantly lower levels in primary human EOCs compared with either normal human ovarian surface epithelium or fallopian tube epithelium.

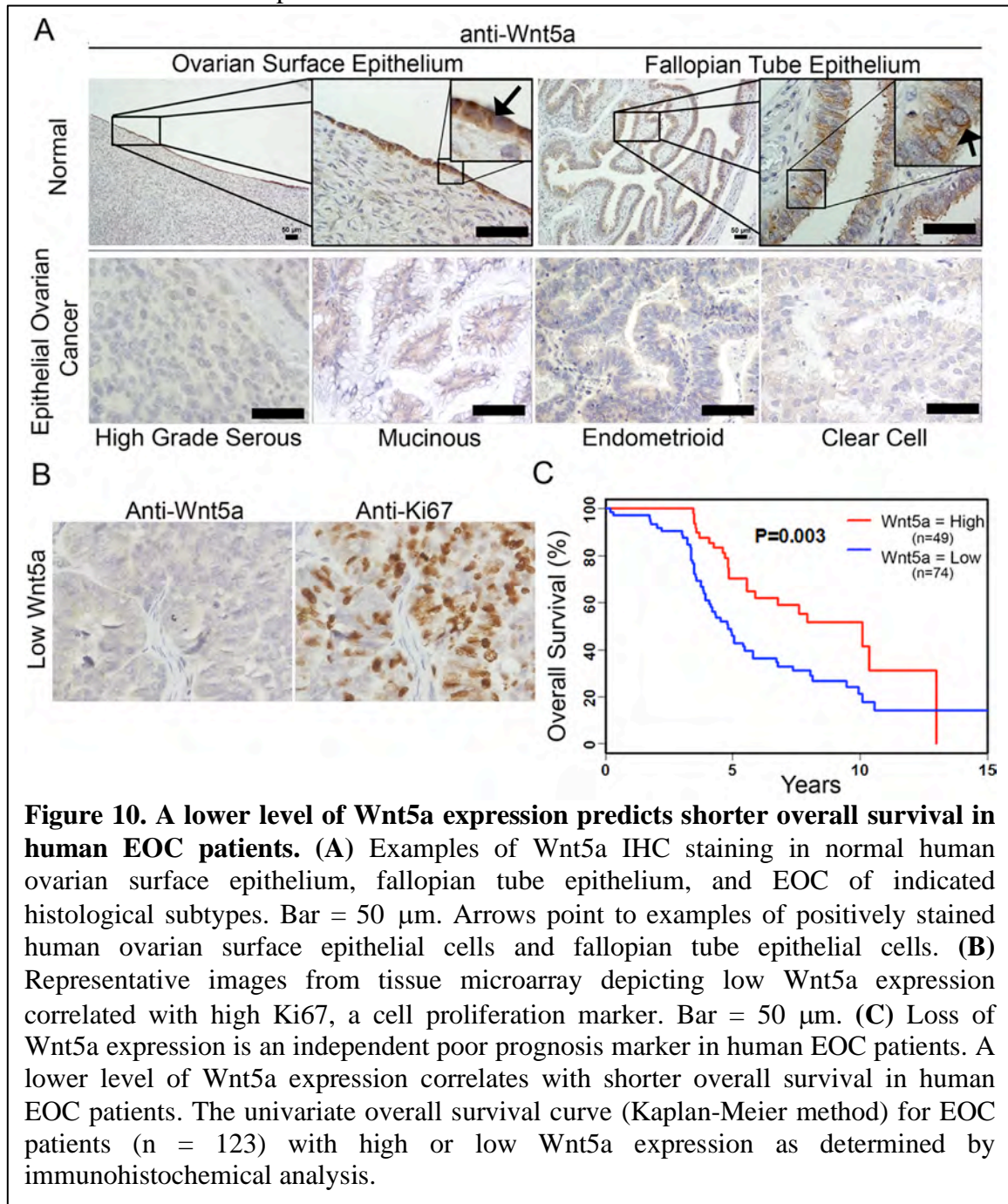
| Patient characteristics      | Wnt5a Protein Expression |          |           |          | p                  |
|------------------------------|--------------------------|----------|-----------|----------|--------------------|
|                              | Low (n)                  | High (n) | Total (n) | High (%) |                    |
| Age (23-85yrs, mean 59.2yrs) |                          |          |           |          |                    |
| ≤55                          | 24                       | 16       | 40        | 40.0%    | 0.900              |
| >55                          | 52                       | 33       | 85        | 38.8%    |                    |
| Unknown                      | 5                        | 0        | 5         |          |                    |
| Laterality                   |                          |          |           |          |                    |
| Left                         | 22                       | 14       | 36        | 38.9%    | 0.957              |
| Right                        | 12                       | 9        | 21        | 42.9%    |                    |
| Bilaterality                 | 35                       | 24       | 59        | 40.7%    |                    |
| Undetermined                 | 12                       | 2        | 14        |          |                    |
| Histotype                    |                          |          |           |          |                    |
| Epithelial ovarian cancer    | 81                       | 49       | 130       | 37.7%    | 0.005 <sup>#</sup> |
| Type I                       | 16                       | 21       | 37        | 56.8%    |                    |
| Low Grade Serous             | 1                        | 1        | 2         | 50.0%    |                    |
| Endometrioid                 | 4                        | 9        | 13        | 69.2%    |                    |
| Mucinous                     | 2                        | 3        | 5         | 60.0%    |                    |
| Clear Cell                   | 5                        | 4        | 9         | 44.4%    |                    |
| Others                       | 4                        | 4        | 8         | 50.0%    |                    |
| Type II                      |                          |          |           |          |                    |
| High Grade Serous            | 65                       | 28       | 93        | 30.1%    |                    |
| Normal epithelium            |                          |          |           |          |                    |
| Ovarian Surface              | 13                       | 18       | 31        | 58.1%    | 0.039 *            |
| Fallopian Tube               | 5                        | 23       | 28        | 82.1%    | <0.001 *           |
| Ki67                         |                          |          |           |          |                    |
| Low                          | 22                       | 23       | 44        | 52.3%    | 0.038              |
| High                         | 51                       | 24       | 75        | 32.0%    |                    |
| Undetermined                 | 7                        | 3        | 11        |          |                    |
| Tumor grade                  |                          |          |           |          |                    |
| 1                            | 3                        | 7        | 10        | 70.0%    |                    |
| 2                            | 12                       | 8        | 20        | 40.0%    |                    |
| 3                            | 64                       | 31       | 95        | 32.6%    |                    |
| Undetermined                 | 2                        | 3        | 5         |          |                    |
| Tumor stage                  |                          |          |           |          |                    |
| Stage 1/2                    | 12                       | 18       | 30        | 60.0%    | 0.003 **           |
| Stage 3/4                    | 67                       | 29       | 96        | 30.2%    |                    |
| Undetermined                 | 2                        | 2        | 4         |          |                    |

<sup>#</sup> Compared with Type I epithelial ovarian cancer  
\* Compared with epithelial ovarian cancer; \*\* compared with Stage 1/2

Table 1. Wnt5a expression in primary human EOCs and correlation of its expression with clinicopathological variables.

We next examined the correlation between Wnt5a expression and clinical and pathological features of human EOCs. Significantly, there was a negative correlation between Wnt5a expression and tumor stage ( $p = 0.003$ ) (Table 1). Notably, the majority of examined cases are high-grade serous subtypes that are usually of stage 3/4. In addition, we examined the correlation between expression of Wnt5a and a marker of cell

proliferation, Ki67 [23] (Figure 10B). There was a significant negative correlation between Wnt5a expression and Ki67 ( $p = 0.038$ ) (Table 1). This is consistent with the idea that Wnt5a loss promotes senescence bypass. We next assessed whether Wnt5a expression based on H-score might predict prognosis of EOC patients (High, H-score  $\geq 30$ ; Low, H-score  $< 30$ ) ( $n = 123$ ), for which long-term follow-up data were available. Significantly, lower Wnt5a expression correlated with shorter overall survival in the examined EOC patients ( $p = 0.003$ ) (Figure 10C). Together, we conclude that a lower level of Wnt5a expression correlates with tumor stage and predicts shorter overall survival in human EOC patients.



**Specific Aim 3: Investigate the effects of inhibition of canonical Wnt signaling on malignant behavior of human EOC cells in immunodeficient mice. (Months 48-60)**

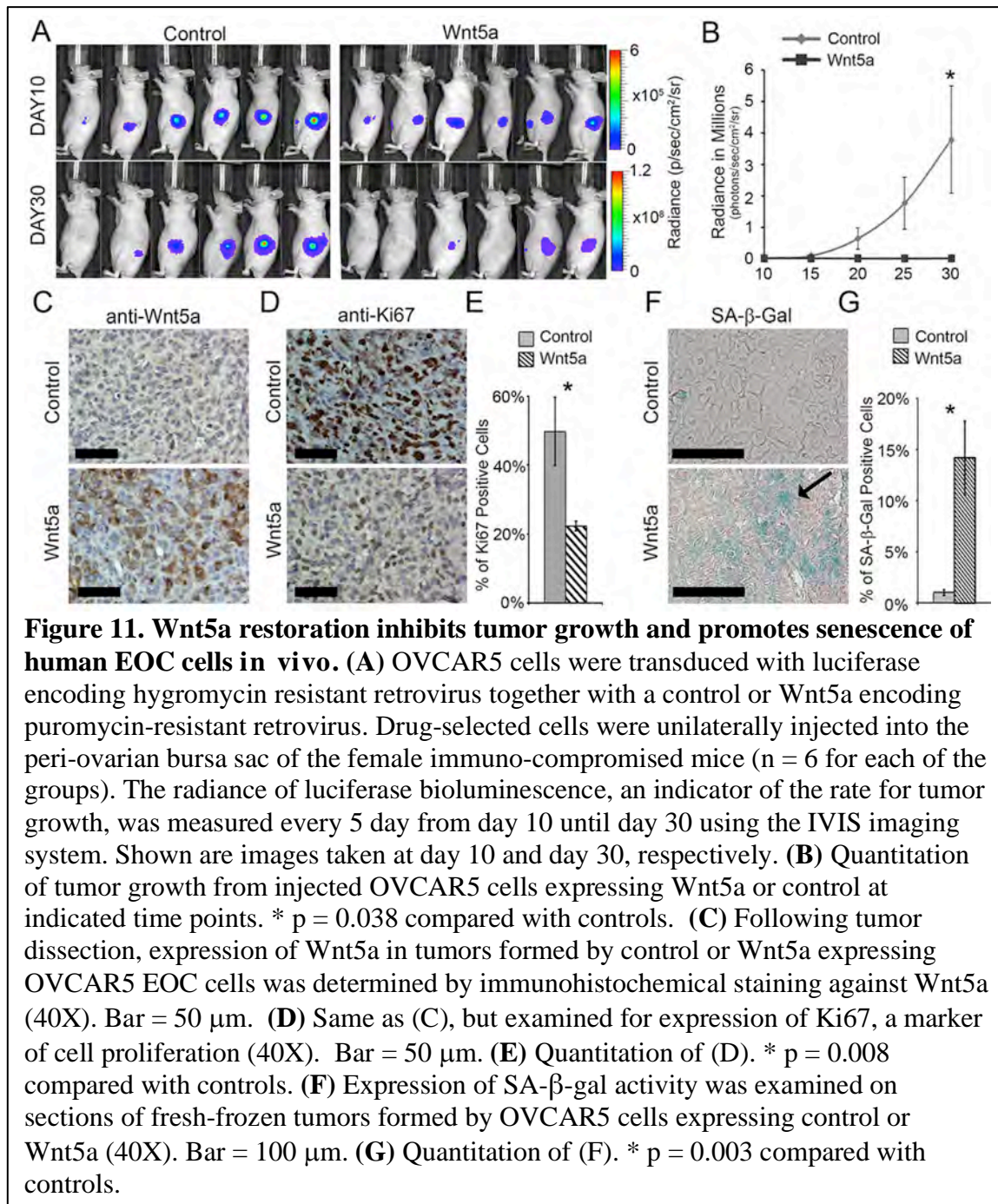
**Task 5. Determine whether inhibition of canonical Wnt signaling in engrafted human EOC cells through ectopic Wnt5a expression induces senescence of engrafted EOC cells, and consequently blocks the further growth of human EOC cells in immunodeficient mice. (Months 48-60)**

*Progress report:* We next sought to determine whether Wnt5a would mediate growth inhibition and induce senescence *in vivo* in an orthotopic EOC model in immuno-compromised mice. A luciferase gene was retrovirally transduced into control or Wnt5a reconstituted OVCAR5 cells to monitor the cell growth *in vivo* via non-invasive imaging. These cells were injected unilaterally into the bursa sac covering the ovary in female immuno-compromised mice (n = 6 for each of the groups). Tumor growth was monitored every 5 days starting at day 10 post-injection by measuring luciferase activity, and the growth of the tumor was followed for a total of 30 days (Figure 11A). Wnt5a significantly suppressed the growth of xenografted OVCAR5 human EOC cells compared with controls (Figure 11B,  $p < 0.03$ ). Consistently, following general pathological examination during surgical dissection at day 30, we observed that tumor sizes were notably smaller from mice injected with Wnt5a reconstituted OVCAR5 cells compared with controls. The expression of ectopic Wnt5a was confirmed by IHC staining in sections from dissected tumors (Figure 11C).

We next sought to determine whether cell proliferation was suppressed by Wnt5a reconstitution in dissected tumors. Towards this goal, we examined the expression of Ki67 by IHC. We observed there was a significant decrease in the number of Ki67 positive cells in tumors formed by Wnt5a reconstituted OVCAR5 cells compared with controls (Figure 11D-E). In addition, intensity of Ki67 staining was also notably weaker in Ki67 positive Wnt5A reconstituted OVCAR5 cells compared with control Ki67 positive cells (Figure 11D). On the basis of these results, we conclude that Wnt5a reconstitution inhibits the proliferation of human EOC cells *in vivo* in an orthotopic xenograft EOC model.

We next investigated whether the growth inhibition observed by Wnt5a reconstitution *in vivo* was due to induction of cellular senescence. Towards this goal, we examined the expression of SA- $\beta$ -gal activity in fresh sections of dissected tumors formed by OVCAR5 cells reconstituted with Wnt5a or control cells. Indeed, we observed a significant increase in the number of cells positive for SA- $\beta$ -gal activity in OVCAR5 cells reconstituted with Wnt5a compared with control tumors (Figure 11F-G;  $p = 0.003$ ). Together, we conclude that Wnt5a reconstitution inhibits the growth of human EOC cells *in vivo* by inducing cellular senescence.





### Key Research Accomplishments:

- FJ9 suppresses the growth of human EOC cells but likely through canonical Wntsignaling independent mechanisms.
- Wnt5a suppresses the growth of human EOC cells.

- Wnt5a inhibits canonical Wnt signaling.
- Wnt5a induces cellular senescence.
- Cellular senescence induced by Wnt5a restoration is independent of both p53 and p16.
- Cellular senescence induced by Wnt5a restoration correlates with activation of the HIRA/PML senescence-promoting pathway.
- Cellular senescence induced by Wnt5a restoration correlates with a decreased level of serine 780 phosphorylated pRB.
- Wnt5a plays a role in regulating senescence of primary HOSE cells.
- Wnt5a loss may contribute to transformation of HOSE cells by suppressing oncogene-induced senescence.
- A lower level of Wnt5a expression correlates with tumor stage and predicts shorter overall survival in human EOC patients.
- Wnt5a restoration inhibits tumor growth and promotes senescence of human EOC cells *in vivo*.

## Reportable Outcomes:

### *Manuscripts:*

1. Aird KM, Worth AJ, Snyder NW, Lee JV, Sivanand S, Liu Q, Blair IA, Wellen KE, **Zhang R** \*. ATM couples replication stress and metabolic reprogramming during cellular senescence. Cell Rep. 11:893-901, 2015.
2. Zhao B, Zhang WD, Duan YL, Lu YQ, Cun YX, Li CH, Guo K, Nie WH, Li L, **Zhang R**, Zheng P. Filia Is an ESC-Specific Regulator of DNA Damage Response and Safeguards Genomic Stability. Cell Stem Cell. 16:684-698, 2015.
3. Zhu H, Ren S, Bitler BG, Aird KM, Tu Z, Skordalakes E, Zhu Y, Yan J, Sun Y, **Zhang R** \*. SPOP E3 Ubiquitin Ligase Adaptor Promotes Cellular Senescence by Degrading the SENP7 deSUMOylase. Cell Rep. 13:1183-1193, 2015.
4. Wang Z, Deng Z, Dahmane N, Tsai K, Wang P, Williams DR, Kossenkov AV, Showe LC, **Zhang R**, Huang Q, Conejo-Garcia JR, Lieberman PM. Telomeric repeat-containing RNA (TERRA) constitutes a nucleoprotein component of extracellular inflammatory exosomes. Proc Natl Acad Sci U S A. 112: E6293-E6300, 2015.

5. Aird KM, **Zhang R** \*. ATM in senescence. *Oncotarget*. 6:14729-14730, 2015.
6. Bengsch F, Tu Z, Tang HY, Zhu H, Speicher DW, **Zhang R** \*. Comprehensive analysis of the ubiquitinome during oncogene-induced senescence in human fibroblasts. *Cell Cycle*. 14:1540-1547, 2015.
7. Bitler BG, Aird KM, Garipov A, Li H, Amatangelo M, Kossenkov AV, Schultz DC, Liu Q, Shih Ie M, Conejo-Garcia JR, Speicher DW, **Zhang R** \*. Synthetic lethality by targeting EZH2 methyltransferase activity in ARID1A-mutated cancers. *Nat Med*. 21:231-238, 2015.
8. Bitler BG, Fatkhutdinov N, **Zhang R** \*. Potential therapeutic targets in ARID1A-mutated cancers. *Expert Opin Ther Targets*. 19:1419-1422, 2015.
9. Bitler BG, Aird KM, **Zhang R** \*. An epigenetic synthetic lethality in ovarian clear cell carcinoma: EZH2 and ARID1A mutations. *Mol Cell Oncol*, DOI: 10.1080/23723556.2015.1032476, 2015.
10. Caino MC, Ghosh JC, Chae YC, Vaira V, Rivadeneira DB, Favarsani A, Rampini P, Kossenkov AV, Aird KM, **Zhang R**, Webster MR, Weeraratna AT, Bosari S, Languino LR, Altieri DC. PI3K therapy reprograms mitochondrial trafficking to fuel tumor cell invasion. *Proc Natl Acad Sci U S A*. 112:8638-8643, 2015.
11. Rutkowski MR, Stephen TL, Svoronos N, Allegrezza MJ, Tesone AJ, Perales-Puchalt A, Brencicova E, Escovar-Fadul X, Nguyen JM, Cadungog MG, **Zhang R**, Salatino M, Tchou J, Rabinovich GA, Conejo-Garcia JR. Microbially driven TLR5-dependent signaling governs distal malignant progression through tumor-promoting inflammation. *Cancer Cell*. 27:27-40, 2015.
12. Yokoyama Y, Zhu H, **Zhang R**, Noma K. A novel role for the condensin II complex in cellular senescence. *Cell Cycle*. 14:2160-2170, 2015.
13. Zeppernick F, Ardighieri L, Hannibal CG, Vang R, Junge J, Kjaer SK, **Zhang R**, Kurman RJ, Shih Ie M. BRAF mutation is associated with a specific cell type with features suggestive of senescence in ovarian serous borderline (atypical proliferative) tumors. *Am J Surg Pathol*. 38:1603-1611, 2014.
14. Aird K.M., **Zhang R** \*. Metabolic basis of oncogene-induced senescence, *Molecular and Cellular Oncology*, 1:3, e963481, 2014.
15. Aird KM, **Zhang R**. Nucleotide metabolism, oncogene-induced senescence and cancer. *Cancer Lett*. 356:204-210, 2015.

16. Aird K.M., Li H., Xin F., Konstantinopoulos P.A., **Zhang R \***. Identification of ribonucleotide reductase M2 as a potential target for pro-senescence therapy in epithelial ovarian cancer. *Cell Cycle* 13: 199-207, 2014.
17. Tu Z., Aird K.M., **Zhang R \***. Chromatin remodeling, BRCA1, SAHF and senescence. *Cell Cycle*, 12: 1653-1654, **2013**.
18. Li H., **Zhang R \***. Role of EZH2 in epithelial ovarian cancer: from biological insights to therapeutic target. *Front Oncol.* 3: 47 doi: 10.3389/fontc.2013.00047, **2013**.
19. Bitler B, Fink L, Wei Z, Peterson JR, **Zhang R \***. A high-content screening assay for small molecule modulators of oncogene-induced senescence. *J Biomol. Screening*, 18: 1054-1061, **2013**.
20. Tang H.Y., Beer L.A., Tanyi J.L., **Zhang R.**, Liu Q., Speicher D.W. Protein isoform-specific validation defines multiple chloride intracellular channel and tropomyosin isoforms as serological biomarkers of ovarian cancer. *J. Proteomics*, 89: 165-178, **2013**.
21. Amatangelo M., Garipov A., Li H., Conejo-Garcia J., Speicher D.W., **Zhang R \***. Three-dimensional culture sensitizes ovarian cancer cells to EZH2 inhibition. *Cell Cycle*, 12: 2113-2119, **2013**.
22. Aird KM, Zhang G, Li H, Tu Z, Bitler BG, Garipov A, Wu H, Wei Z, Wagner SN, Herlyn M, **Zhang R \***. Suppression of nucleotide metabolism underlies the establishment and maintenance of oncogene-induced senescence. *Cell Reports*, 3: 1252-1265, **2013**.
23. Tu Z, Zhuang X, Yao YG, **Zhang R \***. BRG1 is required for formation of senescence-associated heterochromatin foci induced by oncogenic RAS or BRCA1 loss. *Mol. Cell. Biol.*, 33: 1819-1829, **2013**.
24. Garipov A., Li H., Thapa R.J., Balachandran S., **Zhang R \***. NF-YA underlies EZH2 upregulation and is essential for proliferation of human epithelial ovarian cancer cells. *Mol. Cancer Res.* 11: 360-369, **2013**.
25. Beer, L.A., Wang, H., Tang, H.Y., Cao, Z., Chang-Wong, T., Tanyi, J.L., **Zhang, R.**, Liu, Q., Speicher, D.W. Identification of multiple novel protein biomarkers shed by human serous ovarian tumors into the blood of immunocompromised mice and verified in patient sera. *Plos One*, 8: e60129, **2013**.
26. Aird K.M., **Zhang R \***. Detection of senescence-associated heterochromatin foci. *Methods Mol. Biol.* 965: 185-196, **2013**.
27. Li H., Cai Q., Wu H., Li T., Hua X., Sanchez-Beato M., **Zhang R \***. SUZ12 promotes human epithelial ovarian cancer by suppressing apoptosis via silencing HRK. *Mol. Cancer Res.* 10: 1462- 1472, **2012**.



28. Tu Z., Aird K.M. and **Zhang R \***. RAS, cellular senescence and transformation: the BRCA1 DNA repair pathway at the crossroads. *Small GTPases* 3: 162-167, **2012**.
29. Li H., Bitler B.G., Maradeo M.E., Slifker M., Vathipadiekal V., Careasy C., Tummino P., Cairns P., Birrer M.J., **Zhang R \***. ALDH1A1 is a novel EZH2 target gene in epithelial ovarian cancer identified by genome-wide approaches. *Cancer Prev Res.* 5: 484-91, **2012**.
30. Tu Z., Nicodemus J., Beehary N., Xia B., Yen T. and **Zhang R \***. Oncogenic Ras regulates BRIP1 expression to induce dissociation of BRCA1 from chromatin, inhibit DNA repair, and promote senescence. *Dev. Cell* 21: 1077-91, **2011**.
31. Bitler B.G., Nicodemus J.P., Li H., Cai Q., Wu H., Hua X., Li T., Birrer M.J., Godwin A.K., Cairns P., **Zhang R \***. Wnt5a suppresses epithelial ovarian cancer by promoting cellular senescence. *Cancer Res.* 71:6184-94, **2011**.
32. Li H., Cai Q., Godwin A.K. and **Zhang R \***. Enhancer of zeste homology 2 promotes the proliferation and invasion of human epithelial cells. *Mol. Cancer Res.* 8: 1610-1618, **2010**.

**Abstracts:**

An abstract based on this study has been published by American Association of Cancer Research.

An abstract based on this study has been published by the 3<sup>rd</sup> International Symposium on Ovarian Cancer

**Presentations:**

A poster has been presented at 2011 AACR annual meeting.

A talk has been presented at the 3<sup>rd</sup> International Symposium on Ovarian Cancer

**Patents:**

A patent has been filed based on the funded studies.

U.S. Patent Application Serial Number: 61/445, 145.

**Conclusions:**

Wnt5a promotes senescence of human EOC cells by suppressing the proliferation promoting canonical Wnt/ $\beta$ -catenin pathway. We suggest that strategies to drive senescence in EOC cells by reconstituting Wnt5a signaling may offer an effective new strategy for EOC therapy

**References:**

1. Fujii, N., et al., *An antagonist of dishevelled protein-protein interaction suppresses beta-catenin-dependent tumor cell growth*. Cancer Res, 2007. **67**(2): p. 573-9.
2. Liang, H., et al., *Wnt5a inhibits B cell proliferation and functions as a tumor suppressor in hematopoietic tissue*. Cancer Cell, 2003. **4**(5): p. 349-60.
3. Mikels, A.J. and R. Nusse, *Purified Wnt5a protein activates or inhibits beta-catenin-TCF signaling depending on receptor context*. PLoS Biol, 2006. **4**(4): p. e115.
4. Topol, L., et al., *Wnt-5a inhibits the canonical Wnt pathway by promoting GSK-3-independent beta-catenin degradation*. J Cell Biol, 2003. **162**(5): p. 899-908.
5. McDonald, S.L. and A. Silver, *The opposing roles of Wnt-5a in cancer*. Br J Cancer, 2009. **101**(2): p. 209-14.
6. Cheyette, B.N., et al., *Dapper, a Dishevelled-associated antagonist of beta-catenin and JNK signaling, is required for notochord formation*. Dev Cell, 2002. **2**(4): p. 449-61.
7. Reya, T. and H. Clevers, *Wnt signalling in stem cells and cancer*. Nature, 2005. **434**(7035): p. 843-50.
8. Ye, X., et al., *Downregulation of Wnt signaling is a trigger for formation of facultative heterochromatin and onset of cell senescence in primary human cells*. Mol Cell, 2007. **27**(2): p. 183-96.
9. Katoh, M., *WNT signaling pathway and stem cell signaling network*. Clin Cancer Res, 2007. **13**(14): p. 4042-5.
10. Mann, B., et al., *Target genes of beta-catenin-T cell-factor/lymphoid-enhancer-factor signaling in human colorectal carcinomas*. Proc Natl Acad Sci U S A, 1999. **96**(4): p. 1603-8.
11. Kuilman, T., et al., *The essence of senescence*. Genes Dev, 2010. **24**(22): p. 2463-79.
12. Bernardi, R. and P.P. Pandolfi, *Structure, dynamics and functions of promyelocytic leukaemia nuclear bodies*. Nat Rev Mol Cell Biol, 2007. **8**(12): p. 1006-16.
13. Mallette, F.A., et al., *Human fibroblasts require the Rb family of tumor suppressors, but not p53, for PML-induced senescence*. Oncogene, 2004. **23**(1): p. 91-9.
14. Ferbeyre, G., et al., *PML is induced by oncogenic ras and promotes premature senescence*. Genes Dev, 2000. **14**(16): p. 2015-27.
15. Salomoni, P. and P.P. Pandolfi, *The role of PML in tumor suppression*. Cell, 2002. **108**(2): p. 165-70.
16. Pearson, M., et al., *PML regulates p53 acetylation and premature senescence induced by oncogenic Ras*. Nature, 2000. **406**(6792): p. 207-10.
17. Watson, J.E., et al., *Identification and characterization of a homozygous deletion found in ovarian ascites by representational difference analysis*. Genome Res, 1999. **9**(3): p. 226-33.
18. Lundberg, A.S. and R.A. Weinberg, *Functional inactivation of the retinoblastoma protein requires sequential modification by at least two distinct cyclin-cdk complexes*. Mol Cell Biol, 1998. **18**(2): p. 753-61.

19. Yaginuma, Y. and H. Westphal, *Abnormal structure and expression of the p53 gene in human ovarian carcinoma cell lines*. Cancer Res, 1992. **52**(15): p. 4196-9.
20. Kurman, R.J. and M. Shih Ie, *The origin and pathogenesis of epithelial ovarian cancer: a proposed unifying theory*. Am J Surg Pathol, 2010. **34**(3): p. 433-43.
21. McCarty, K.S., Jr., et al., *Use of a monoclonal anti-estrogen receptor antibody in the immunohistochemical evaluation of human tumors*. Cancer Res, 1986. **46**(8 Suppl): p. 4244s-4248s.
22. Li, H., et al., *Enhancer of zeste homolog 2 promotes the proliferation and invasion of epithelial ovarian cancer cells*. Mol Cancer Res, 2010. **8**(12): p. 1610-8.
23. Gerdes, J., et al., *Cell cycle analysis of a cell proliferation-associated human nuclear antigen defined by the monoclonal antibody Ki-67*. J Immunol, 1984. **133**(4): p. 1710-5.

## Appendices:

### Manuscripts:

1. Aird KM, Worth AJ, Snyder NW, Lee JV, Sivanand S, Liu Q, Blair IA, Wellen KE, **Zhang R** \*. ATM couples replication stress and metabolic reprogramming during cellular senescence. Cell Rep. 11:893-901, 2015.
2. Zhao B, Zhang WD, Duan YL, Lu YQ, Cun YX, Li CH, Guo K, Nie WH, Li L, **Zhang R**, Zheng P. Filia Is an ESC-Specific Regulator of DNA Damage Response and Safeguards Genomic Stability. Cell Stem Cell. 16:684-698, 2015.
3. Zhu H, Ren S, Bitler BG, Aird KM, Tu Z, Skordalakes E, Zhu Y, Yan J, Sun Y, **Zhang R** \*. SPOP E3 Ubiquitin Ligase Adaptor Promotes Cellular Senescence by Degrading the SENP7 deSUMOylase. Cell Rep. 13:1183-1193, 2015.
4. Wang Z, Deng Z, Dahmane N, Tsai K, Wang P, Williams DR, Kossenkov AV, Showe LC, **Zhang R**, Huang Q, Conejo-Garcia JR, Lieberman PM. Telomeric repeat-containing RNA (TERRA) constitutes a nucleoprotein component of extracellular inflammatory exosomes. Proc Natl Acad Sci U S A. 112: E6293-E6300, 2015.
5. Aird KM, **Zhang R** \*. ATM in senescence. Oncotarget. 6:14729-14730, 2015.
6. Bengsch F, Tu Z, Tang HY, Zhu H, Speicher DW, **Zhang R** \*. Comprehensive analysis of the ubiquitinome during oncogene-induced senescence in human fibroblasts. Cell Cycle. 14:1540-1547, 2015.
7. Bitler BG, Aird KM, Garipov A, Li H, Amatangelo M, Kossenkov AV, Schultz DC, Liu Q, Shih Ie M, Conejo-Garcia JR, Speicher DW, **Zhang R** \*. Synthetic lethality by targeting EZH2 methyltransferase activity in ARID1A-mutated cancers. Nat Med. 21:231-238, 2015.

8. Bitler BG, Fatkhutdinov N, **Zhang R \***. Potential therapeutic targets in ARID1A-mutated cancers. *Expert Opin Ther Targets*. 19:1419-1422, 2015.
9. Bitler BG, Aird KM, **Zhang R \***. An epigenetic synthetic lethality in ovarian clear cell carcinoma: EZH2 and ARID1A mutations. *Mol Cell Oncol*, DOI: 10.1080/23723556.2015.1032476, 2015.
10. Caino MC, Ghosh JC, Chae YC, Vaira V, Rivadeneira DB, Favarsani A, Rampini P, Kossenkova AV, Aird KM, **Zhang R**, Webster MR, Weeraratna AT, Bosari S, Languino LR, Altieri DC. PI3K therapy reprograms mitochondrial trafficking to fuel tumor cell invasion. *Proc Natl Acad Sci U S A*. 112:8638-8643, 2015.
11. Rutkowski MR, Stephen TL, Svoronos N, Allegrezza MJ, Tesone AJ, Perales-Puchalt A, Brencicova E, Escovar-Fadul X, Nguyen JM, Cadungog MG, **Zhang R**, Salatino M, Tchou J, Rabinovich GA, Conejo-Garcia JR. Microbially driven TLR5-dependent signaling governs distal malignant progression through tumor-promoting inflammation. *Cancer Cell*. 27:27-40, 2015.
12. Yokoyama Y, Zhu H, **Zhang R**, Noma K. A novel role for the condensin II complex in cellular senescence. *Cell Cycle*. 14:2160-2170, 2015.
13. Zeppernick F, Ardighieri L, Hannibal CG, Vang R, Junge J, Kjaer SK, **Zhang R**, Kurman RJ, Shih Ie M. BRAF mutation is associated with a specific cell type with features suggestive of senescence in ovarian serous borderline (atypical proliferative) tumors. *Am J Surg Pathol*. 38:1603-1611, 2014.
14. Aird K.M., **Zhang R \***. Metabolic basis of oncogene-induced senescence, *Molecular and Cellular Oncology*, 1:3, e963481, 2014.
15. Aird KM, Zhang R. Nucleotide metabolism and oncogene-induced senescence. *Cancer Letters*, pii: S0304-3835(14)00053-6. [Epub ahead of print], 2014.
16. Aird KM, Li H, Xin F, Konstantinopoulos PA, Zhang R. Identification of ribonucleotide reductase M2 as a potential target for pro-senescence therapy in epithelial ovarian cancer. *Cell Cycle* 13: 199-207, 2014.
17. Tu Z., Aird K.M., **Zhang R**. Chromatin remodeling, BRCA1, SAHF and senescence. *Cell Cycle*, 12: 1653-1654, 2013.
18. Li H., **Zhang R**. Role of EZH2 in epithelial ovarian cancer: from biological insights to therapeutic target. *Front Oncol*. 3: 47 doi: 10.3389/fonc.2013.00047, 2013.
19. Bitler B, Fink L, Wei Z, Peterson JR, **Zhang R \***. A high-content screening assay for small molecule modulators of oncogene-induced senescence. *J Biomol. Screening*, 18: 1054-1061, 2013.

20. Tang H.Y., Beer L.A., Tanyi J.L., **Zhang R.**, Liu Q., Speicher D.W. Protein isoform-specific validation defines multiple chloride intracellular channel and tropomyosin isoforms as serological biomarkers of ovarian cancer. *J. Proteomics*, 89: 165-178, **2013**.
21. Amatangelo M., Garipov A., Li H., Conejo-Garcia J., Speicher D.W., **Zhang R \***. Three-dimensional culture sensitizes ovarian cancer cells to EZH2 inhibition. *Cell Cycle*, 12: 2113-2119, **2013**.
22. Aird KM, Zhang G, Li H, Tu Z, Bitler BG, Garipov A, Wu H, Wei Z, Wagner SN, Herlyn M, **Zhang R \***. Suppression of nucleotide metabolism underlies the establishment and maintenance of oncogene-induced senescence. *Cell Reports*, 3: 1252-1265, **2013**.
23. Tu Z, Zhuang X, Yao YG, **Zhang R \***. BRG1 is required for formation of senescence-associated heterochromatin foci induced by oncogenic RAS or BRCA1 loss. *Mol. Cell. Biol.*, 33: 1819-1829, **2013**.
24. Garipov A., Li H., Thapa R.J., Balachandran S., **Zhang R.\*** NF-YA underlies EZH2 upregulation and is essential for proliferation of human epithelial ovarian cancer cells. *Mol. Cancer Res.* 11: 360-369, **2013**.
25. Beer, L.A., Wang, H., Tang, H.Y., Cao, Z., Chang-Wong, T., Tanyi, J.L., **Zhang, R.**, Liu, Q., Speicher, D.W. Identification of multiple novel protein biomarkers shed by human serous ovarian tumors into the blood of immunocompromised mice and verified in patient sera. *Plos One*, 8: e60129, **2013**.
26. Aird K.M., **Zhang R.\*** Detection of senescence-associated heterochromatin foci. *Methods Mol. Biol.* 965: 185-196, **2013**.
27. Li H., Cai Q., Wu H., Li T., Hua X., Sanchez-Beato M., **Zhang R.\*** SUZ12 promotes human epithelial ovarian cancer by suppressing apoptosis via silencing HRK. *Mol. Cancer Res.* 10: 1462- 1472, **2012**.
28. Tu Z., Aird K.M. and **Zhang R.\*** RAS, cellular senescence and transformation: the BRCA1 DNA repair pathway at the crossroads. *Small GTPases* 3: 162-167, **2012**.
29. Li H., Bitler B.G., Maradeo M.E., Slifker M., Vathipadiekal V., Careasy C., Tummino P., Cairns P., Birrer M.J., **Zhang R.\*** ALDH1A1 is a novel EZH2 target gene in epithelial ovarian cancer identified by genome-wide approaches. *Cancer Prev Res.* 5: 484-91, **2012**.
30. Tu Z., Nicodemus J., Beehary N., Xia B., Yen T. and **Zhang R.\*** Oncogenic Ras regulates BRIP1 expression to induce dissociation of BRCA1 from chromatin, inhibit DNA repair, and promote senescence. *Dev. Cell* 21: 1077-91, **2011**.

31. Bitler B.G., Nicodemus J.P., Li H., Cai Q., Wu H., Hua X., Li T., Birrer M.J., Godwin A.K., Cairns P., **Zhang R.\*** Wnt5a suppresses epithelial ovarian cancer by promoting cellular senescence. ***Cancer Res.*** 71:6184-94, **2011**.
32. Li H., Cai Q., Godwin A.K. and **Zhang R\***. Enhancer of zeste homology 2 promotes the proliferation and invasion of human epithelial cells. ***Mol. Cancer Res.*** 8: 1610-1618, **2010**.

***Abstracts:***

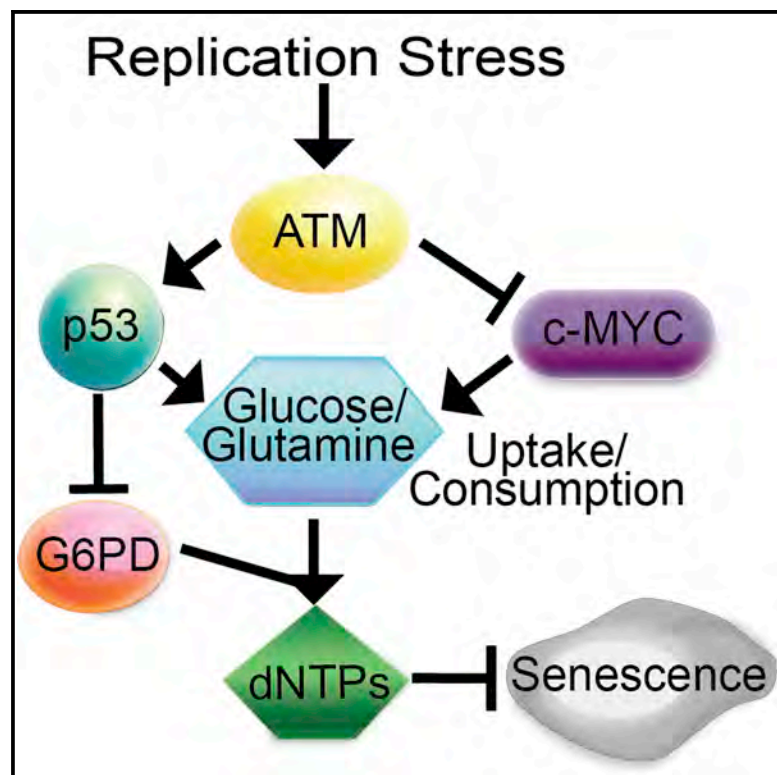
An abstract based on this study has been published by American Association of Cancer Research.

An abstract based on this study has been published by the 3<sup>rd</sup> International Symposium on Ovarian Cancer

# Cell Reports

## ATM Couples Replication Stress and Metabolic Reprogramming during Cellular Senescence

### Graphical Abstract



### Authors

Katherine M. Aird, Andrew J. Worth, ..., Kathryn E. Wellen, Rugang Zhang

### Correspondence

rzhang@wistar.org

### In Brief

Replication stress and metabolic reprogramming are hallmarks of cancer. Aird et al. demonstrate that ATM couples replication stress and metabolic reprogramming during senescence. ATM thus inhibits the cancer-associated metabolic program to promote senescence in response to replication stress.

### Highlights

- ATM knockdown rescues dNTP levels to bypass replication-stress-induced senescence
- ATM knockdown enhances glucose and glutamine consumption for dNTP biosynthesis
- Rescue of dNTP levels correlates with an increase in G6PD activity by ATM knockdown
- ATM knockdown coordinately suppresses p53 and upregulates c-MYC to shift metabolism



# ATM Couples Replication Stress and Metabolic Reprogramming during Cellular Senescence

Katherine M. Aird,<sup>1</sup> Andrew J. Worth,<sup>2</sup> Nathaniel W. Snyder,<sup>2</sup> Joyce V. Lee,<sup>3</sup> Sharanya Sivanand,<sup>3</sup> Qin Liu,<sup>4</sup> Ian A. Blair,<sup>2</sup> Kathryn E. Wellen,<sup>3</sup> and Rugang Zhang<sup>1,\*</sup>

<sup>1</sup>Gene Expression and Regulation Program, The Wistar Institute, Philadelphia, PA 19104, USA

<sup>2</sup>Department of Pharmacology, University of Pennsylvania, Philadelphia, PA 19104, USA

<sup>3</sup>Department of Cancer Biology, University of Pennsylvania, Philadelphia, PA 19104, USA

<sup>4</sup>Molecular and Cellular Oncogenesis Program, The Wistar Institute, Philadelphia, PA 19104, USA

\*Correspondence: [rzhang@wistar.org](mailto:rzhang@wistar.org)

<http://dx.doi.org/10.1016/j.celrep.2015.04.014>

This is an open access article under the CC BY license (<http://creativecommons.org/licenses/by/4.0/>).

## SUMMARY

Replication stress induced by nucleotide deficiency plays an important role in cancer initiation. Replication stress in primary cells typically activates the cellular senescence tumor-suppression mechanism. Senescence bypass correlates with development of cancer, a disease characterized by metabolic reprogramming. However, the role of metabolic reprogramming in the cellular response to replication stress has been little explored. Here, we report that ataxia telangiectasia mutated (ATM) plays a central role in regulating the cellular response to replication stress by shifting cellular metabolism. ATM inactivation bypasses senescence induced by replication stress triggered by nucleotide deficiency. This was due to restoration of deoxyribonucleotide triphosphate (dNTP) levels through both upregulation of the pentose phosphate pathway via increased glucose-6-phosphate dehydrogenase (G6PD) activity and enhanced glucose and glutamine consumption. These phenotypes were mediated by a coordinated suppression of p53 and upregulation of c-MYC downstream of ATM inactivation. Our data indicate that ATM status couples replication stress and metabolic reprogramming during senescence.

## INTRODUCTION

Replication stress induced by deficiency in cellular deoxyribonucleotide triphosphate (dNTP) levels is an important early event during cancer initiation (Bester et al., 2011), while its bypass correlates with cancer progression (Bester et al., 2011; Zeman and Cimprich, 2014). Replication stress causes DNA damage accumulation and genomic instability (Bester et al., 2011; Burhans and Weinberger, 2007; Zeman and Cimprich, 2014), which is a hallmark of cancer (Negrini et al., 2010). Notably, activation of oncogenes is known to decrease dNTP levels and consequently triggers replication stress (Aird et al., 2013; Bartkova et al., 2006;

Di Micco et al., 2006; Mannava et al., 2013). In normal diploid cells, activation of oncogenes, and the subsequent replication stress, causes a tumor-suppressive, stable cell-growth arrest termed cellular senescence (Yaswen and Campisi, 2007). Indeed, oncogene-induced suppression of nucleotide metabolism via suppression of ribonucleotide reductase M2 (RRM2) underlies the observed replication stress and the associated DNA damage response (DDR) during senescence (Aird et al., 2013). Therefore, senescence suppresses tumors initiated by replication stress (Bester et al., 2011; Zeman and Cimprich, 2014). dNTP biosynthesis relies on glucose and glutamine consumption, which are at the heart of cancer metabolism (Ward and Thompson, 2012). However, the role of metabolic reprogramming in response to replication stress is unknown. Here, we report that ataxia telangiectasia mutated (ATM) status couples replication stress and metabolic reprogramming during senescence.

## RESULTS

### Knockdown of ATM Bypasses Replication-Stress-Induced Senescence

Suppression of RRM2, which depletes the levels of all four dNTPs, underlies replication stress observed during oncogene-induced senescence (Aird et al., 2013). This induces a robust DDR and ultimately a stable senescence-associated cell growth arrest. The replication stress sensors ataxia telangiectasia and Rad3-related protein (ATR) and ATM are activated by oncogenes during senescence (Di Micco et al., 2006). We sought to determine whether ATM and/or ATR are regulated during senescence induced by short-hairpin-mediated RRM2 knockdown (shRRM2). shRRM2 significantly activated both ATM and ATR, as demonstrated by immunofluorescence using phospho-specific antibodies (Figures 1A, 1B, and S1A). Next, we examined whether these proteins are necessary for the observed senescence. We knocked down ATM or ATR in combination with RRM2 knockdown with two independent short hairpin RNAs (shRNAs) for ATM (shATM) or ATR (shATR). shATM in combination with shRRM2 suppressed senescence markers such as p21 expression (Figure 1C) and senescence-associated  $\beta$ -galactosidase (SA- $\beta$ -gal) activity (Figures 1D and 1E). This correlated with



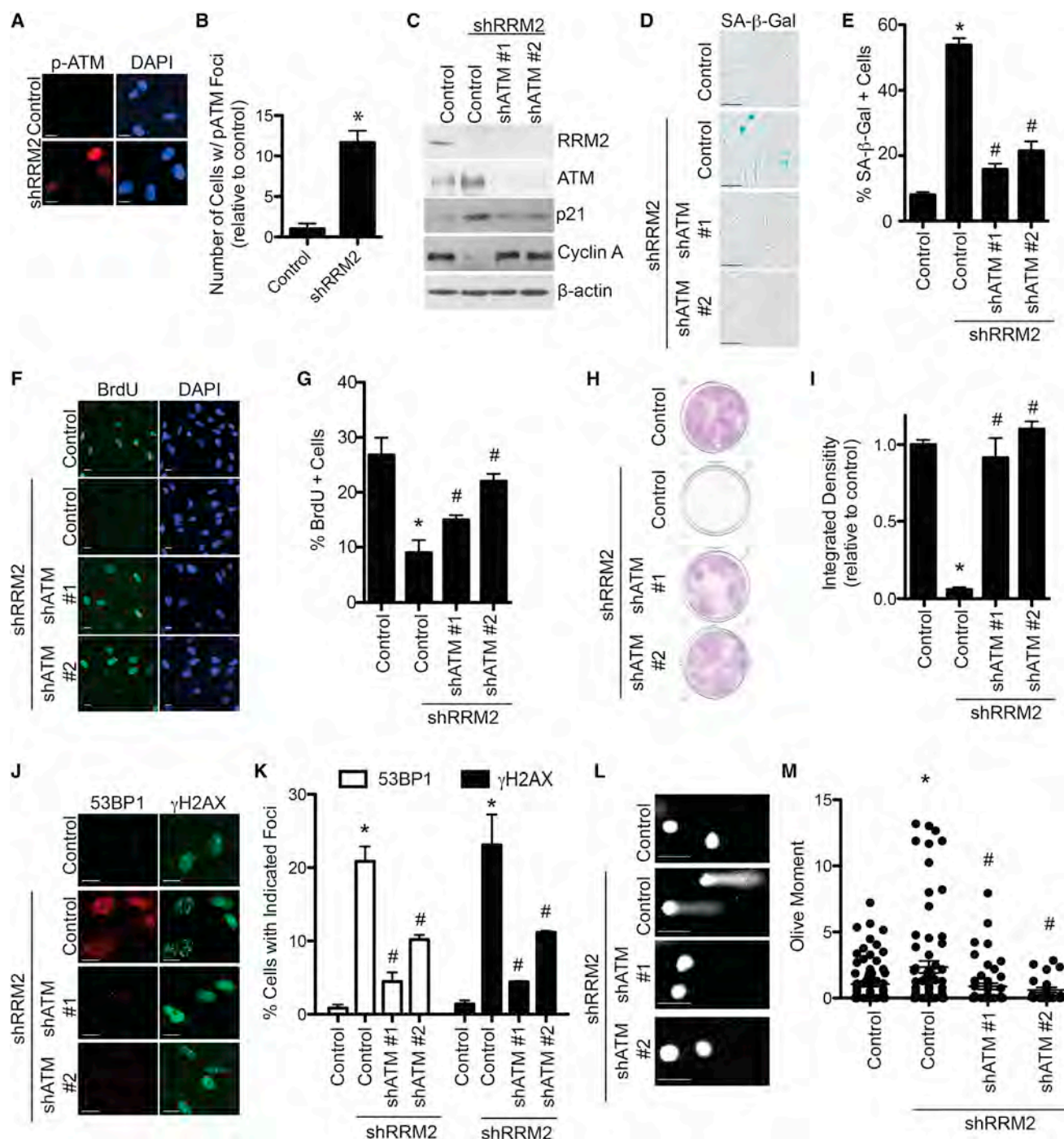


**Figure 1. Knockdown of ATM Bypasses Senescence and Suppresses DNA Damage Induced by RRM2 Knockdown**

(A) Primary human IMR90 cells were infected with a lentivirus encoding shRRM2 or control. Cells were stained for p-ATM (Ser1981) by immunofluorescence. DAPI staining was used to visualize nuclei.

(B) Quantification of (A). 200 cells from each of the indicated groups were quantified for p-ATM foci-positive cells (n = 3).

(C) Primary human IMR90 cells were infected with a lentivirus encoding shRRM2 alone or in combination with lentivirus encoding two independent shATMs. Cells were examined for expression of RRM2, ATM, p21, and β-actin by immunoblotting.

(D) Same as (C) but stained for SA-β-gal activity.

(E) Quantification of (D). 100 cells from each of the indicated groups were quantified for SA-β-gal positivity (n = 3).

(F) Same as (C), but cells were labeled with BrdU for 1 hr and BrdU incorporation was visualized by immunofluorescence. DAPI staining was used to visualize nuclei.

(legend continued on next page)

an increase in cell proliferation markers such as cyclin A expression (Figure 1C), bromodeoxyuridine (BrdU) incorporation (Figures 1F and 1G), and apparent cell growth as determined by focus-formation assays (Figures 1H and 1I). Similar results were observed when ATM was inhibited by the specific inhibitor KU55933 (Figures S1B and S1C). shATM suppressed DDR induced by shRRM2 as determined by a decrease in  $\gamma$ H2AX and 53BP1 foci formation (Figures 1J and 1K). Notably, this is in contrast to its positive role in DNA repair but consistent with the idea that DDR contributes to senescence induced by replication stress. ATM phosphorylates H2AX during foci formation, although other kinases can also phosphorylate H2AX (Yuan et al., 2010). To confirm that the observed decrease in  $\gamma$ H2AX foci formation was due to decreased DDR instead of a dependence of its phosphorylation by ATM, we directly measured the extent of DNA damage in these cells by comet assay. shATM significantly decreased the extent of DNA damage induced by shRRM2 (Figures 1L and 1M). In contrast, neither two independent shATRs nor the ATR inhibitor VE822 was able to suppress senescence and its associated DDR induced by shRRM2 (Figures S1D–S1P). Interestingly, shRRM2/shATR cells had an even more robust senescent phenotype than shRRM2 alone as indicated by higher SA- $\beta$ -gal activity and lower focus-formation ability (e.g., Figures S1F and S1J). Likewise, shRRM2 failed to induce senescence in primary patient fibroblasts with mutated ATM (Figures S1Q–S1S), but not ATR (Figures S1T–S1V). Similar to previous reports (Bartkova et al., 2006; Di Micco et al., 2006), RAS-induced senescence was suppressed by shATM (Figures S1W and S1X). These results demonstrate that loss of ATM, but not ATR, bypasses senescence induced by replication stress, which correlates with the suppression of DDR. In this context, loss of ATM suppresses DDR induced by replication stress, a function different from its canonical, positive role in DNA repair.

### Knockdown of ATM Rescues dNTP Levels and Aberrant DNA Replication

We next sought to determine the effect of knockdown of ATM on cellular dNTP levels. shATM significantly rescued the dNTPs compared with shRRM2 alone (Figure 2A). This correlated with a significant rescue of aberrant replication dynamics induced by shRRM2 as determined by DNA combing analysis (Figure 2B). Collapsed replication forks are characterized by co-localization of pulse-labeled BrdU and  $\gamma$ H2AX (Groth et al., 2010). shATM significantly reduced the co-localized BrdU and  $\gamma$ H2AX induced by shRRM2 (Figures 2C and 2D). shATR did not affect aberrant replication dynamics induced by shRRM2 (Figure S2), which correlated with the inability of shATR to suppress senescence (Figures S1D–S1N). These results demonstrate that knockdown

of ATM rescues dNTPs, which correlates with the suppression of aberrant replication dynamics and DDR.

### Knockdown of ATM Increases Substrate Availability for dNTP Biosynthesis through Enhanced Glutamine and Glucose Uptake and Metabolism

We next sought to determine the mechanism whereby loss of ATM increases dNTPs. Ribonucleotide reductase (RNR) is involved in de novo dNTP synthesis (Figure S3A) (Nordlund and Reichard, 2006; Reichard, 1988). We first sought to determine whether the increase in dNTPs was due to the salvage pathway, which does not rely on RNR (Blakley and Vitols, 1968; Murray, 1971; Reichard, 1988). We used 3-AP, which inhibits de novo dNTP synthesis by inhibiting both RRM2 and RRM2B, two enzymes necessary for de novo dNTP synthesis (Finch et al., 2000; Finch et al., 1999). Suppression of the de novo pathway reversed the ability of shATM to bypass senescence (Figures S3B and S3C). We next sought to determine whether the rescue of dNTP levels is due to a compensation of shRRM2 by an increase in RRM2B expression. shATM did not increase RRM2B expression in shRRM2 cells (Figure S3D). These results suggest that de novo dNTP synthesis and RRM2B activity are necessary for the observed senescence bypass.

Substrates for dNTP synthesis are derived from consumption of glucose and glutamine (Figure S3A). Since ATM is a tumor suppressor, we hypothesized that knockdown of ATM may increase glucose and glutamine consumption, a hallmark of cancer metabolism, which increases substrate availability for dNTP synthesis. We used 2NBDG, a fluorescent glucose analog, to determine whether shATM increased glucose uptake in shRRM2 cells. shATM in combination with shRRM2 significantly increased glucose uptake (Figure 3A). Metabolite profiling also showed a significant increase in glucose consumption (Figure 3B). Lactate levels were significantly increased in the media, suggesting glucose utilization (Figure 3B). Both glutamine consumption and utilization (glutamate secretion) were also significantly increased (Figure 3C). Similar results were also observed using KU55933, an ATM inhibitor (Figures S3E and S3F). Likewise, shATM also increased glucose and glutamine consumption and utilization in RAS-expressing cells (Figures S3G–S3I). These results were observed in multiple cell types (Figures S3J–S3M). Thus, knockdown of ATM increases substrate availability for dNTP biosynthesis by enhancing glucose and glutamine uptake and metabolism.

### Knockdown of ATM Increases PPP Activity through p53-Mediated Regulation of G6PD Activity

Glucose is metabolized and shunted into different metabolic pathways (Vander Heiden et al., 2009). We used liquid

(G) Quantification of (F). 200 cells from each of the indicated groups were quantified for BrdU positivity ( $n = 3$ ).

(H) Same as (C), but an equal number of cells were seeded in six-well plates and focus formation was determined by crystal violet staining 14 days later.

(I) Quantification of (H). The intensity of foci formed was quantified using NIH ImageJ software ( $n = 3$ ).

(J) Same as (C), but cells were examined for 53BP1 and  $\gamma$ H2AX foci formation. Scale bars, 5  $\mu$ m.

(K) Quantification of (J). 200 cells from each of the indicated groups were quantified for 53BP1 and  $\gamma$ H2AX foci positivity ( $n = 3$ ).

(L) Same as (C), but comet assay was performed.

(M) Quantification of (L). The extent of DNA damage was quantified as Olive Moment using CometScore software ( $n = 100$ ).

\* $p < 0.05$  shRRM2 versus control; # $p < 0.05$  shRRM2/shATM versus shRRM2. Error bars represent SEM. Scale bars represent 10  $\mu$ m unless otherwise specified. See also Figure S1.

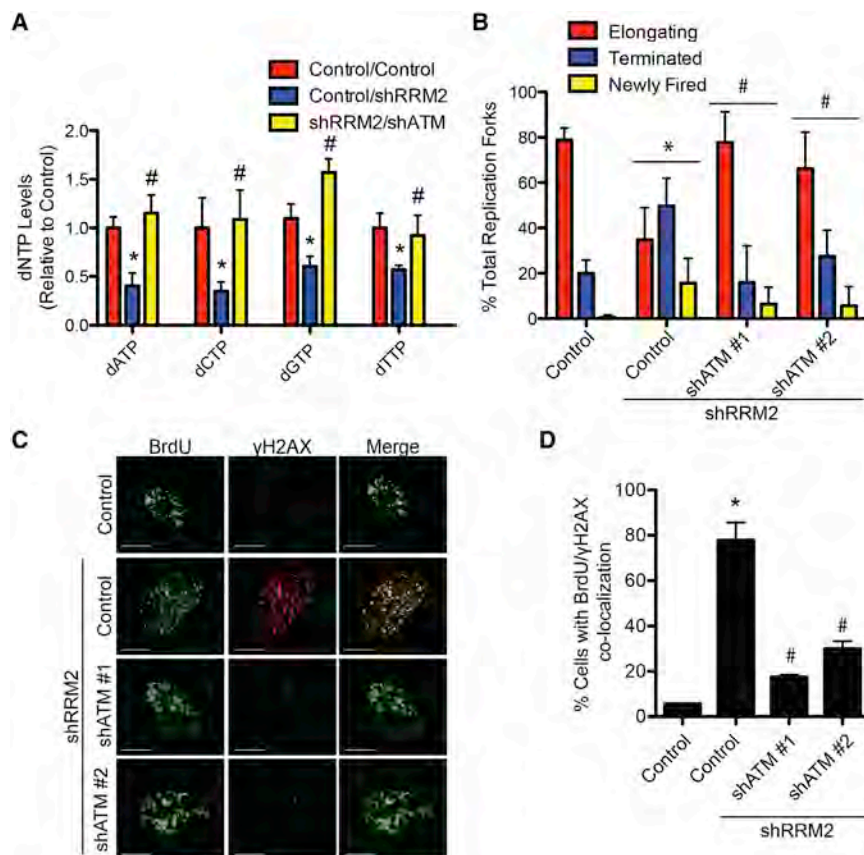


**Figure 2. Knockdown of ATM Rescues Replication Stress by Restoring Cellular dNTP Levels**

(A) Primary IMR90 cells were infected with an shRRM2-expressing lentivirus alone or in combination with a shATM (#1)-expressing lentivirus. dNTP levels were quantified day 1 post-drug selection (n = 3).

(B) Same as (A). DNA fiber analysis was conducted to observe replication fork dynamics in the indicated cells at day 1 post-drug selection. The percentage of elongating, terminated, or newly fired replication forks was quantified in the indicated cells (n = 3).

(C) Same as (B), but cells were labeled with BrdU for 15 min and the collapsed replication forks were visualized by co-localized BrdU and γH2AX as determined by immunofluorescence using a confocal microscope. Scale bars, 5 μm.

(D) Quantification of (C). 200 cells from each of the indicated groups were quantified for BrdU and γH2AX co-localization-positive cells (n = 3). Note that more than ten/nuclei of co-localized BrdU and γH2AX foci was considered positive.

\*p < 0.05 shRRM2 versus control; #p < 0.05 shRRM2/shATM versus shRRM2. Error bars represent SEM. See also Figure S2.

chromatography (LC) tandem mass spectrometry (MS/MS) to determine changes in metabolites of multiple metabolic pathways downstream of glucose. There was a significant decrease in the pentose phosphate pathway (PPP) metabolite 6-phosphogluconate (6-PG) in shRRM2/shATM cells (Figure 3D), suggesting that PPP metabolites are being consumed to a greater extent in these cells. To determine whether glucose is being utilized by the PPP, we performed stable isotope tracer analysis using [<sup>13</sup>C<sub>6</sub>]-glucose. There was an increase in the fractional proportion of <sup>13</sup>C-labeled 6-PG in shRRM2/shATM cells (Figure 3E). These findings suggest that the observed increase in glucose uptake was at least in part utilized by the PPP in these cells for dNTP biosynthesis.

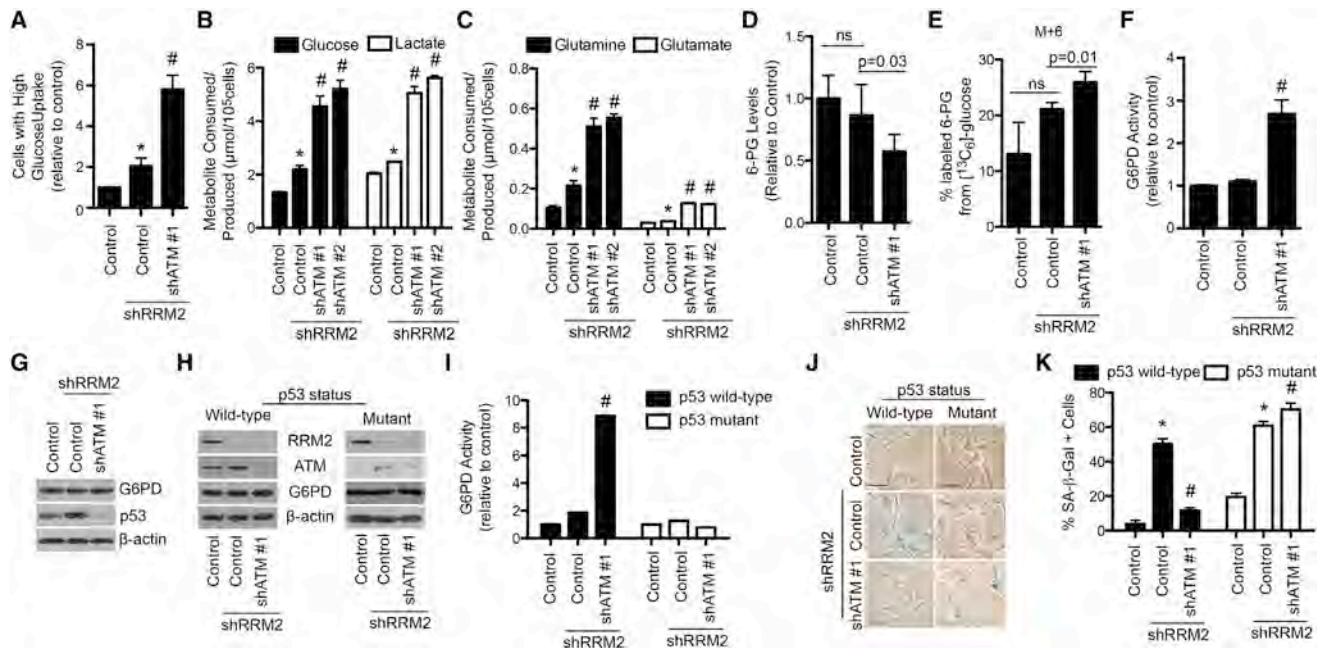
Glucose-6-phosphate dehydrogenase (G6PD) is the rate-limiting enzyme in the PPP, and its activity metabolizes glucose-6-phosphate (G6P) into 6-PG for dNTP synthesis (Figure S3A) (Patra and Hay, 2014). We sought to determine whether G6PD is regulated by ATM knockdown in shRRM2 cells. G6PD activity was significantly increased in shATM/shRRM2 cells compared to shRRM2 alone (Figure 3F). Similar results were observed using KU55933, an ATM inhibitor (Figure S3N), or in RAS/shATM cells (Figure S3O). There was no change in G6PD protein expression (Figure 3G). Notably, wild-type p53 has been shown to negatively regulate G6PD activity (Jiang et al., 2011), and knockdown of ATM significantly decreased p53 levels in shRRM2 cells (Figure 3G). Therefore, we sought to determine

whether p53 levels contributed to G6PD activity in the context of shATM-mediated senescence bypass. We used melanoma cell lines with known p53 mutational status. Knockdown of ATM (Figure 3H)

significantly increased G6PD activity in shRRM2-expressing p53 wild-type, but not mutant, melanoma cells (Figure 3I). Knockdown of p53 (shp53) in combination with shRRM2 in wild-type melanoma cells increased G6PD activity compared to shRRM2 alone (Figure S3P). p53 status, and therefore G6PD activity, correlated with the ability of shATM to bypass senescence in melanoma cells induced by shRRM2 (Figures 3J and 3K). These results were observed in multiple p53 wild-type and mutant cell lines (Figures S3Q–S3T), demonstrating this is not a cell-line-specific effect. Notably, shRRM2 alone did not decrease G6PD activity (Figure 3F), even though we observed an increase in p53 expression (Figure 3G). This suggests that G6PD activity is also regulated by another p53-independent mechanism in shRRM2-expressing cells. Indeed, G6PD activity is known to be positively regulated by ATM-mediated phosphorylation of HSP27 (pHSP27) (Cosentino et al., 2011). Consistently, pHSP27 was increased in shRRM2 cells (Figure S3U), which correlates with activation of ATM by shRRM2 (Figures 1A and 1B). These data support that G6PD activity is regulated in a context-dependent manner through a balance between p53 and HSP27, and when ATM is inhibited, downregulation of p53 correlates with an increase in G6PD activity. We conclude that loss of ATM leads to an increase in G6PD activity through abrogation of p53-mediated suppression.

Suppression of p53 is known to affect metabolism (Cairns et al., 2011; Schwartzberg-Bar-Yoseph et al., 2004). Indeed,





shp53 in combination with shRRM2 increased glucose uptake (Figure 4A) and glucose and glutamine consumption compared to shRRM2 alone (Figures S4A and S4B). Therefore, we sought to determine whether shp53 phenocopies shATM. shp53 (Figure 4B) only partially suppressed senescence phenotypes, such as causing a decrease in SA- $\beta$ -gal activity (Figures 4C and 4D). However, shp53 did not fully bypass the senescence-associated cell-growth arrest, as demonstrated by BrdU incorporation (Figures 4E and 4F) and focus-formation assays (Figures 4G and 4H). This correlated with the inability of shp53 to reduce markers of DNA damage (Figures 4I and 4J). These results suggest that p53 suppression is necessary, but not sufficient, for bypassing senescence induced by replication stress.

### Knockdown of ATM Cooperatively Regulates p53 and c-MYC to Increase Substrate Availability

shp53 in combination with shRRM2 increased glucose uptake but to a lesser extent compared to that of shATM (Figure 4A). This suggests that an additional pathway is implicated in the

observed shift in cellular metabolism induced by shATM. c-MYC plays a major role in cellular metabolism (Dang et al., 2009). c-MYC is a known regulator of RAS-induced senescence (Land et al., 1983; Sinn et al., 1987). Thus, we examined c-MYC protein levels. shATM in combination with shRRM2 significantly increased c-MYC protein expression compared to shRRM2 alone (Figure 4K). This was observed in multiple cell lines (Figure S4D).

Next, we determined the mechanism underlying the observed c-MYC upregulation by shATM. No change in c-MYC mRNA expression was observed in senescence-bypassed cells (Figure S4E). p27 has been implicated in negatively regulating c-MYC protein stability post-translationally (Maclean et al., 2007). Bypass of senescence by shATM correlated with downregulation of p27 (Figure S4F). This correlated with an increase in c-MYC protein stability (Figures S4G and S4H). To further demonstrate the role of c-MYC upregulation in the observed senescence bypass, we simultaneously knocked down ATM,

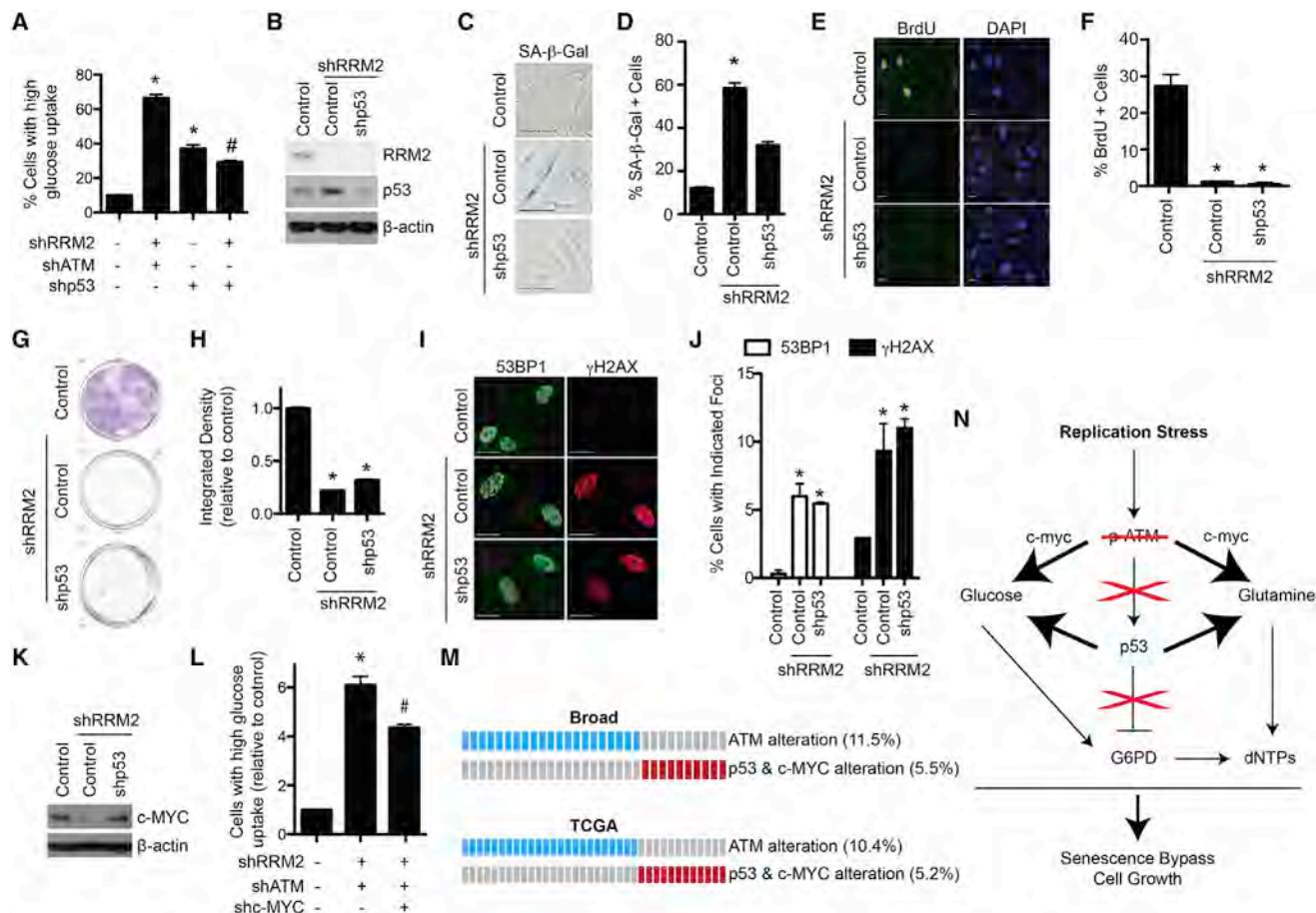


**Figure 4. ATM Knockdown Cooperatively Inhibits p53 and Upregulates c-MYC in Senescence-Bypassed Cells**

(A) Primary IMR90 cells were infected with lentivirus expressing the indicated shRNAs. Glucose uptake was determined by incubating cells with a fluorescent glucose analog (2NBDG) followed by flow cytometry. Cells were gated for high glucose uptake based on fluorescence (n = 3).

(B) Primary IMR90 cells were infected with a shRRM2-expressing lentivirus alone or in combination with a shp53-expressing lentivirus, and RRM2, p53, and β-actin protein expression was determined by immunoblotting.

(C) Same as (B), but SA-β-gal activity was determined.

(D) Quantification of (C). 100 cells from each of the indicated groups were quantified for SA-β-gal positivity (n = 3).

(E) Same as (B), but cells were labeled with BrdU for 1 hr and BrdU incorporation was determined by immunofluorescence. DAPI staining was used to visualize nuclei.

(F) Quantification of (E). 200 cells from each of the indicated groups were quantified for BrdU positivity (n = 3).

(G) Same as (B), but an equal number of cells were seeded in six-well plates and focus formation was determined by crystal violet staining 14 days later.

(H) Quantification of (G). The intensity of foci was quantified using NIH ImageJ software (n = 3).

(I) Same as (B) but 53BP1 and γH2AX foci were observed by immunofluorescence.

(J) Quantification of (I). 200 cells from each of the indicated groups were quantified for 53BP1 and γH2AX foci-positive cells (n = 3).

(K) Primary IMR90 cells were infected with an shRRM2-expressing lentivirus alone or in combination with a shATM-expressing lentivirus, and c-MYC and β-actin protein expression was determined by immunoblotting.

(L) Same as (K), but cells were also infected with a shc-MYC expressing lentivirus and glucose uptake was determined by incubating cells with a fluorescent glucose analog (2NBDG), followed by flow cytometry (n = 3). Cells were gated for high glucose uptake based on fluorescence.

(M) Publicly available lung adenocarcinoma databases from cBioPortal were analyzed for ATM, p53, and c-MYC status. Blue boxes indicate patients with ATM mutation or deletion. Red boxes indicate patients with p53 mutation/deletion and c-MYC amplification.

(N) Schematic of senescence bypass induced by shATM. Replication stress induced by nucleotide deficiency activates ATM. If ATM is inhibited, p53 is not activated, which abrogates its inhibition of G6PD. Additionally, c-MYC expression is increased, which along with lower p53 expression leads to increased glucose and glutamine consumption. The convergence of increased substrates and increased G6PD activity leads to increased dNTP levels, which allows for DNA replication and proliferation.

\*p < 0.05 versus control; #p < 0.05 versus shRRM2/shATM. Error bars represent SEM. Scale bars, 10 μm. See also Figure S4 and Table S1.

RRM2, and c-MYC (Figure S4I). These cells showed decreased glucose uptake and glutamine consumption compared to senescence-bypassed shATM/shRRM2 cells (Figures 4L and S4J).

These results support that increased c-MYC expression cooperates with decreased p53 to induce metabolic reprogramming to allow the senescence bypass by shATM.

Our results indicate that ATM converges on the p53 and c-MYC pathways to regulate senescence. We found that ATM mutation/deletion is mutually exclusive from p53 mutation/deletion and c-MYC amplification in multiple tumor types (Figure 4M; Table S1). These data support the notion that ATM functions in the same pathway as p53 and c-MYC in cancers. Overall, our data support a model whereby loss of ATM affects both p53 and c-MYC to bypass the senescence-associated cell-growth arrest to drive cell proliferation (Figure 4N).

## DISCUSSION

Senescence induced by oncogenes is characterized by increased glucose consumption that is shunted toward the tricarboxylic acid cycle and away from aerobic glycolysis and presumably the PPP (Kaplon et al., 2013; Li et al., 2013; Mazurek et al., 2001). Consistently, we observed increased glucose and glutamine consumption in cells undergoing senescence induced by shRRM2 (Figures 3A–3C and S3), suggesting that replication stress itself may cause changes in cellular metabolic pathways similar to those induced by oncogenes. Knockdown of ATM in combination with shRRM2 further increased both glucose and glutamine consumption. These data are consistent with the idea that ATM inactivation further drives senescence-associated metabolic reprogramming over a threshold that is necessary to support the proliferation of senescence-bypassed cells in cancer. Our data support the notion that the increased glucose was shunted into the PPP, because we observed an increase in  $^{13}\text{C}$ -labeling of the PPP metabolite 6-PG after incubation with [ $^{13}\text{C}_6$ ]-glucose (Figure 3E). In this context, ATM functions as a tumor suppressor by inhibiting cancer-associated metabolic reprogramming.

In addition to an increase in metabolic substrates for dNTP synthesis, ATM knockdown also increased activity of the PPP pathway rate-limiting enzyme G6PD. Increased G6PD activity correlated with decreased p53 expression (Figures 3F and 3G). p53 downregulation is known to shift cellular metabolism (Cairns et al., 2011). Knockdown of ATM decreased p53 (Figure 3G), which correlated with increased glucose and glutamine consumption (Figures 3B and 3C). Knockdown of p53 did not increase glucose uptake to the same extent as ATM knockdown (Figure 4A). Indeed, knockdown of p53 was not sufficient to fully overcome senescence (Figure 4). Consistently, there was also an increase in c-MYC expression induced by ATM knockdown (Figure 4K). c-MYC is among genes that are upregulated in ATM-knockout mice (Yan et al., 2006). In the present study, the observed increase in c-MYC expression was post-transcriptional and correlated with a decrease in p27 expression, a known negative regulator of c-MYC protein stability (Figure S4F). Indeed, c-MYC stability was increased in cells with knockdown of both RRM2 and ATM compared to knockdown of RRM2 alone (Figures S4G and S4H). These data support a model whereby downregulation of p53 and upregulation of c-MYC cooperate to enhance glucose and glutamine consumption, which accounts for the observed increase in substrate availability for the dNTP biosynthesis induced by ATM knockdown (Figure 4N).

Our data show that ATM plays a central role in coupling replication stress and metabolic reprogramming. ATM suppresses

cancer-associated metabolic reprogramming to prevent bypass of the senescence tumor-suppression mechanism, where its inactivation suppresses DDR induced by replication stress. This is different from its classical role in DNA repair, where its activation suppresses cancer by preventing genomic instability. Replication stress induced by nucleotide deficiency plays an important role in the early stages of cancer development; therefore, this mechanistic insight will have broad implications for understanding replication stress and metabolic reprogramming in cancer.

## EXPERIMENTAL PROCEDURES

### Cells and Culture Conditions

IMR90 human fibroblasts were cultured according to the ATCC in low oxygen (2%) as previously described (Tu et al., 2011). Experiments were performed on IMR90 between population doubling #25–35. Human melanoma cell lines (a kind gift from Dr. Meenhard Herlyn) were cultured as previously described (Satyamoorthy et al., 1997).

### Reagents, Plasmids, and Antibodies

All chemicals and reagents were purchased from Sigma-Aldrich. pLKO.1-shRNA plasmids were obtained from Open Biosystems. The mature sense sequences are shRRM2: 5'-CGGAGGAGAGAGTAAGAGAAA-3'; shATM #1: 5'-CGTGTCTTAATGAGACTACAA-3'; shATM #2: 5'-TGATGGTCTTAAGGAA CATCT-3'; shp53: 5'-GAGGGATGTTGGGAGATGTA-3'; and shc-MYC: 5'-CCTGAGACAGATCAGCAACAA-3. The following antibodies were obtained from the indicated suppliers: mouse anti-phospho-ATM (Rockland), goat anti-ATM (Bethyl), goat anti-RRM2 (Santa Cruz Biotechnology), mouse anti-cyclin A (Novocastra), mouse anti- $\gamma$ H2AX (Millipore), rabbit anti-53BP1 (Bethyl), mouse anti-BrdU fluorescein isothiocyanate (BD Biosciences), mouse anti-p53 (Calbiochem), rabbit anti-G6PD (Sigma-Aldrich), rabbit anti-p21 (Abcam), rabbit anti-c-MYC (Cell Signaling), and mouse anti- $\beta$ -actin (Sigma-Aldrich).

### Lentivirus Infections

Lentivirus was packaged using the Virapower Kit from Invitrogen following the manufacturer's instructions as described previously (Li et al., 2010; Tu et al., 2011). Cells infected with viruses encoding the puromycin-resistance gene were selected in 1  $\mu\text{g}/\text{ml}$  puromycin.

### Immunofluorescence, BrdU Labeling, Single-Cell Gel

#### Electrophoresis, also known as Comet Assay, and SA- $\beta$ -Gal Staining

Immunofluorescence staining, BrdU labeling, and single-cell gel electrophoresis (comet assay) for cultured cells was performed as described previously using the antibodies described above (Tu et al., 2011). Confocal microscopy was used for co-localization of BrdU and  $\gamma$ H2AX using a Leica TCS SP1 scanning confocal microscope. The comet assay was analyzed using CometScore software (TriTek). SA- $\beta$ -gal staining was performed as previously described (Dimri et al., 1995).

### Focus-Formation Assay

For focus formation, an equal number of cells (3,000 cells/well) were inoculated in six-well plates and cultured for an additional 2 weeks. Focus formation was visualized by staining the plates with 0.05% crystal violet as previously described (Tu et al., 2011). Integrated density was determined using NIH ImageJ software.

### DNA Combing Analysis

DNA combing was performed as previously described (Aird et al., 2013). DNA replication forks were scored as elongating, terminated, or newly fired as previously described (Aird et al., 2013; Bartkova et al., 2006).

### Measurement of dNTP Concentrations in Cells

Samples were harvested and dNTP levels were measured as previously described (Aird et al., 2013; Wilson et al., 2011).



### Flow Cytometry for Glucose Uptake

Cells were incubated with 5  $\mu$ M 2NBDG (Invitrogen) for 2 hr. After rinsing with PBS, 2NBDG-positive cells were run on a LSRII (14-color; Becton Dickinson), and data were analyzed with FlowJo Software.

### YSI Metabolite Measurements

Glucose and glutamine consumption and lactate and glutamate production were measured using a YSI 7100 Bioanalyzer. Briefly, the same number of cells was seeded in 12-well plates, and 24 hr later, the media was changed. The media was harvested 24 hr later, and cells were counted to normalize for proliferation.

### $C^{13}$ -Glucose Labeling and LC-MS Analysis

To extract metabolites, media was aspirated and cells were quenched by the direct addition of 1 ml  $-80^{\circ}\text{C}$  4:1 methanol:water (v/v). Plates were placed at  $-80^{\circ}\text{C}$  for 20 min then scraped and transferred into tubes. Samples were pulse sonicated on ice for 30 s at a rate of 1 pulse/s prior to centrifugation at  $16,000 \times g$  at  $4^{\circ}\text{C}$  for 10 min. The supernatants were transferred to clean glass tubes and evaporated to dryness under nitrogen. Dried residues were resuspended in 100  $\mu$ l of mobile phase A for LC-MS analysis. For labeling studies, cells were grown in media omitting glucose supplemented with 1 mg/mL  $[^{13}\text{C}_6]$ -glucose.

For liquid chromatography-mass spectrometry, separations were performed using an Agilent 1200 series high-performance liquid chromatography pump and autosampler (Agilent Technologies). Analytes were separated by reverse-phase ion-pairing chromatography using a Phenomenex Kinetex Luna C18 column (250  $\times$  2.1 mm I.D., 3  $\mu$ m). N,N-diisopropylethylamine (DIPEA) was used as the ion-pairing reagent. Solvent A was 400 mM 1,1,1,3,3,3-hexafluoro-2-propanol (HFIP) and 10 mM DIPEA in water, and solvent B was 300 mM HFIP and 10 mM DIPEA in methanol. The linear gradient conditions were as follows: 2% B at 0 min, 2% B at 3 min, 10%B at 32 min, 95% B at 38 min, and 2% B at 39 min, followed by a 6-min equilibration. Analyses were conducted using an Agilent Technologies 6460 triple-quadrupole mass spectrometer with a JetStream electrospray ionization source, in the negative mode. The samples were maintained at  $4^{\circ}\text{C}$ , and injections of 10  $\mu$ l were made for all runs. The column effluent was diverted to waste for the first 5 min and the last 10 min of the analyses. The Agilent 6460 operating conditions were as follows: gas temperature was set at  $275^{\circ}\text{C}$ , and the gas flow was set to 8 l/min. Sheath gas temperature was  $400^{\circ}\text{C}$ , and the sheath gas flow was set to 10 l/min. The capillary voltage was set to 3,500 V. The nozzle voltage was set to 1,000 V.

### G6PD Activity Assay

Cells were harvested by trypsinization and resuspended in cold PBS. Cells were sonicated and then centrifuged at 16,000 rpm for 10 min at  $4^{\circ}\text{C}$ . The supernatant was transferred to new tubes, and the combined activity of G6PD and 6-phosphogluconate dehydrogenase (6PGD) was measured by the rate of conversion of  $\text{NADP}^{+}$  to NADPH in the presence of G6P. The activity of 6PGD alone was then measured by the conversion of  $\text{NADP}^{+}$  to NADPH in the presence of 6-PG. G6PD activity was calculated as the difference of these two activities. Cell lysates were added to the reaction buffer containing 50 mM Tris and 1 mM  $\text{MgCl}_2$  (pH 8.1),  $\text{NADP}^{+}$  (100  $\mu$ M), and G6P (200  $\mu$ M) or 6-PG (200  $\mu$ M). The absorbance at 341nm was read 10 min later. Enzyme activities were normalized to protein concentration.

### Statistical Analysis

GraphPad Prism version 5.0 was used to perform statistical analyses. The Student's t test was used to determine p values of raw data. A p value  $< 0.05$  was considered significant.

### SUPPLEMENTAL INFORMATION

Supplemental Information includes Supplemental Experimental Procedures, four figures, and one table and can be found with this article online at <http://dx.doi.org/10.1016/j.celrep.2015.04.014>.

### AUTHOR CONTRIBUTIONS

K.M.A. designed experiments. K.M.A., A.J.W., N.W.S., J.V.L., and S.S. conducted experiments. K.M.A., A.J.W., N.W.S., K.E.W., and R.Z. analyzed data. Q.L. performed statistical analysis. I.A.B. and K.E.W. also designed and supervised experiments. R.Z. conceived and supervised the study. K.M.A., K.E.W., and R.Z. wrote the manuscript.

### ACKNOWLEDGMENTS

This work was supported by grants from the NIH/NCI (R01CA160331 and P50CA174523 to R.Z. and T32CA9171-35 and K99CA194309 to K.M.A.), a DoD award (OC093420 to R.Z.), and NIH/NIEHS (P30ES013508 to A.J.W. and I.A.B. and T32ES019851 to A.J.W.). Support of Core Facilities used in this study was provided by Cancer Center Support Grant (CCSG) CA010815 to The Wistar Institute.

Received: January 28, 2015

Revised: March 23, 2015

Accepted: April 5, 2015

Published: April 30, 2015

### REFERENCES

- Aird, K.M., Zhang, G., Li, H., Tu, Z., Bitler, B.G., Garipov, A., Wu, H., Wei, Z., Wagner, S.N., Herlyn, M., and Zhang, R. (2013). Suppression of nucleotide metabolism underlies the establishment and maintenance of oncogene-induced senescence. *Cell Rep.* 3, 1252–1265.
- Bartkova, J., Rezaei, N., Liontos, M., Karakaidos, P., Kleitas, D., Issaeva, N., Vassiliou, L.V., Kolettas, E., Niforou, K., Zoumpouris, V.C., et al. (2006). Oncogene-induced senescence is part of the tumorigenesis barrier imposed by DNA damage checkpoints. *Nature* 444, 633–637.
- Bester, A.C., Roniger, M., Oren, Y.S., Im, M.M., Sami, D., Chaoat, M., Bensimon, A., Zamir, G., Shewach, D.S., and Kerem, B. (2011). Nucleotide deficiency promotes genomic instability in early stages of cancer development. *Cell* 145, 435–446.
- Blakley, R.L., and Vitols, E. (1968). The control of nucleotide biosynthesis. *Annu. Rev. Biochem.* 37, 201–224.
- Burhans, W.C., and Weinberger, M. (2007). DNA replication stress, genome instability and aging. *Nucleic Acids Res.* 35, 7545–7556.
- Cairns, R.A., Harris, I.S., and Mak, T.W. (2011). Regulation of cancer cell metabolism. *Nat. Rev. Cancer* 11, 85–95.
- Cosentino, C., Grieco, D., and Costanzo, V. (2011). ATM activates the pentose phosphate pathway promoting anti-oxidant defence and DNA repair. *EMBO J.* 30, 546–555.
- Dang, C.V., Le, A., and Gao, P. (2009). MYC-induced cancer cell energy metabolism and therapeutic opportunities. *Clin. Cancer Res.* 15, 6479–6483.
- Di Micco, R., Fumagalli, M., Cicalese, A., Piccinin, S., Gasparini, P., Luise, C., Schurra, C., Garre', M., Nuciforo, P.G., Bensimon, A., et al. (2006). Oncogene-induced senescence is a DNA damage response triggered by DNA hyper-replication. *Nature* 444, 638–642.
- Dimri, G.P., Lee, X., Basile, G., Acosta, M., Scott, G., Roskelley, C., Medrano, E.E., Linskens, M., Rubelj, I., Pereira-Smith, O., et al. (1995). A biomarker that identifies senescent human cells in culture and in aging skin in vivo. *Proc. Natl. Acad. Sci. USA* 92, 9363–9367.
- Finch, R.A., Liu, M.C., Cory, A.H., Cory, J.G., and Sartorelli, A.C. (1999). Triapine (3-aminopyridine-2-carboxaldehyde thiosemicarbazone; 3-AP): an inhibitor of ribonucleotide reductase with antineoplastic activity. *Adv. Enzyme Regul.* 39, 3–12.
- Finch, R.A., Liu, M., Grill, S.P., Rose, W.C., Loomis, R., Vasquez, K.M., Cheng, Y., and Sartorelli, A.C. (2000). Triapine (3-aminopyridine-2-carboxaldehyde-thiosemicarbazone): A potent inhibitor of ribonucleotide reductase activity with broad spectrum antitumor activity. *Biochem. Pharmacol.* 59, 983–991.



- Groth, P., Ausländer, S., Majumder, M.M., Schultz, N., Johansson, F., Petermann, E., and Hellday, T. (2010). Methylated DNA causes a physical block to replication forks independently of damage signalling, O(6)-methylguanine or DNA single-strand breaks and results in DNA damage. *J. Mol. Biol.* **402**, 70–82.
- Jiang, P., Du, W., Wang, X., Mancuso, A., Gao, X., Wu, M., and Yang, X. (2011). p53 regulates biosynthesis through direct inactivation of glucose-6-phosphate dehydrogenase. *Nat. Cell Biol.* **13**, 310–316.
- Kaplon, J., Zheng, L., Meissl, K., Chaneton, B., Selivanov, V.A., Mackay, G., van der Burg, S.H., Verdegaaal, E.M., Cascante, M., Shlomi, T., et al. (2013). A key role for mitochondrial gatekeeper pyruvate dehydrogenase in oncogene-induced senescence. *Nature* **498**, 109–112.
- Land, H., Parada, L.F., and Weinberg, R.A. (1983). Tumorigenic conversion of primary embryo fibroblasts requires at least two cooperating oncogenes. *Nature* **304**, 596–602.
- Li, H., Cai, Q., Godwin, A.K., and Zhang, R. (2010). Enhancer of zeste homolog 2 promotes the proliferation and invasion of epithelial ovarian cancer cells. *Mol. Cancer Res.* **8**, 1610–1618.
- Li, M., Durbin, K.R., Sweet, S.M., Tipton, J.D., Zheng, Y., and Kelleher, N.L. (2013). Oncogene-induced cellular senescence elicits an anti-Warburg effect. *Proteomics* **13**, 2585–2596.
- Maclean, K.H., Kastan, M.B., and Cleveland, J.L. (2007). Atm deficiency affects both apoptosis and proliferation to augment Myc-induced lymphomagenesis. *Mol. Cancer Res.* **5**, 705–711.
- Mannava, S., Moparthy, K.C., Wheeler, L.J., Natarajan, V., Zucker, S.N., Fink, E.E., Im, M., Flanagan, S., Burhans, W.C., Zeitouni, N.C., et al. (2013). Depletion of deoxyribonucleotide pools is an endogenous source of DNA damage in cells undergoing oncogene-induced senescence. *Am. J. Pathol.* **182**, 142–151.
- Mazurek, S., Zwerschke, W., Jansen-Dürr, P., and Eigenbrodt, E. (2001). Metabolic cooperation between different oncogenes during cell transformation: interaction between activated ras and HPV-16 E7. *Oncogene* **20**, 6891–6898.
- Murray, A.W. (1971). The biological significance of purine salvage. *Annu. Rev. Biochem.* **40**, 811–826.
- Negrini, S., Gorgoulis, V.G., and Halazonetis, T.D. (2010). Genomic instability—an evolving hallmark of cancer. *Nat. Rev. Mol. Cell Biol.* **11**, 220–228.
- Nordlund, P., and Reichard, P. (2006). Ribonucleotide reductases. *Annu. Rev. Biochem.* **75**, 681–706.
- Patra, K.C., and Hay, N. (2014). The pentose phosphate pathway and cancer. *Trends Biochem. Sci.* **39**, 347–354.
- Reichard, P. (1988). Interactions between deoxyribonucleotide and DNA synthesis. *Annu. Rev. Biochem.* **57**, 349–374.
- Satyamoorthy, K., DeJesus, E., Linnenbach, A.J., Kraj, B., Kornreich, D.L., Rendle, S., Elder, D.E., and Herlyn, M. (1997). Melanoma cell lines from different stages of progression and their biological and molecular analyses. *Melanoma Res.* **7** (2), S35–S42.
- Schwartzberg-Bar-Yoseph, F., Armoni, M., and Karnieli, E. (2004). The tumor suppressor p53 down-regulates glucose transporters GLUT1 and GLUT4 gene expression. *Cancer Res.* **64**, 2627–2633.
- Sinn, E., Muller, W., Pattengale, P., Tepler, I., Wallace, R., and Leder, P. (1987). Coexpression of MMTV/v-Ha-ras and MMTV/c-myc genes in transgenic mice: synergistic action of oncogenes in vivo. *Cell* **49**, 465–475.
- Tu, Z., Aird, K.M., Bitler, B.G., Nicodemus, J.P., Beeharry, N., Xia, B., Yen, T.J., and Zhang, R. (2011). Oncogenic RAS regulates BRIP1 expression to induce dissociation of BRCA1 from chromatin, inhibit DNA repair, and promote senescence. *Dev. Cell* **21**, 1077–1091.
- Vander Heiden, M.G., Cantley, L.C., and Thompson, C.B. (2009). Understanding the Warburg effect: the metabolic requirements of cell proliferation. *Science* **324**, 1029–1033.
- Ward, P.S., and Thompson, C.B. (2012). Metabolic reprogramming: a cancer hallmark even warburg did not anticipate. *Cancer Cell* **21**, 297–308.
- Wilson, P.M., Labonte, M.J., Russell, J., Louie, S., Ghobrial, A.A., and Ladner, R.D. (2011). A novel fluorescence-based assay for the rapid detection and quantification of cellular deoxyribonucleoside triphosphates. *Nucleic Acids Res.* **39**, e112.
- Yan, M., Zhu, C., Liu, N., Jiang, Y., Scofield, V.L., Riggs, P.K., Qiang, W., Lynn, W.S., and Wong, P.K. (2006). ATM controls c-Myc and DNA synthesis during postnatal thymocyte development through regulation of redox state. *Free Radic. Biol. Med.* **41**, 640–648.
- Yaswen, P., and Campisi, J. (2007). Oncogene-induced senescence pathways weave an intricate tapestry. *Cell* **128**, 233–234.
- Yuan, J., Adamski, R., and Chen, J. (2010). Focus on histone variant H2AX: to be or not to be. *FEBS Lett.* **584**, 3717–3724.
- Zeman, M.K., and Cimprich, K.A. (2014). Causes and consequences of replication stress. *Nat. Cell Biol.* **16**, 2–9.



## A novel role for the condensin II complex in cellular senescence

Yuhki Yokoyama, Hengrui Zhu, Rugang Zhang & Ken-ichi Noma

**To cite this article:** Yuhki Yokoyama, Hengrui Zhu, Rugang Zhang & Ken-ichi Noma (2015) A novel role for the condensin II complex in cellular senescence, *Cell Cycle*, 14:13, 2160-2170, DOI: [10.1080/15384101.2015.1049778](https://doi.org/10.1080/15384101.2015.1049778)

**To link to this article:** <http://dx.doi.org/10.1080/15384101.2015.1049778>



View supplementary material [↗](#)



Accepted author version posted online: 27 May 2015.



Submit your article to this journal [↗](#)



Article views: 278



View related articles [↗](#)



View Crossmark data [↗](#)



Citing articles: 1 View citing articles [↗](#)

# A novel role for the condensin II complex in cellular senescence

Yuhki Yokoyama, Hengrui Zhu, Rugang Zhang, and Ken-ichi Noma\*

The Wistar Institute; Philadelphia, PA USA

**Keywords:** cellular senescence, condensin, genome organization, human, nuclear architecture, oncogene-induced senescence, SAHF

**Abbreviations:** SAHF, senescence-associated heterochromatic foci; SADS, senescence-associated distension of satellites; SMC, structural maintenance of chromosomes; hCAP-H2, human chromosome-associated protein H2; *NCAPH2*, non-SMC chromosome-associated protein H2 gene; RPE-1, hTERT-immortalized retinal pigment epithelial cell line; hTERT, human telomerase reverse transcriptase; uORF, upstream open reading frame; BrdU, bromodeoxyuridine; SA- $\beta$ -gal, senescence-associated  $\beta$ -galactosidase; Rb, retinoblastoma protein; CDK, cyclin dependent kinase; DAPI, 4,6-diamidino-2-phenylindole; shRNA, short-hairpin RNA.

Although cellular senescence is accompanied by global alterations in genome architecture, how the genome is restructured during the senescent processes is not well understood. Here, we show that the hCAP-H2 subunit of the condensin II complex exists as either a full-length protein or an N-terminus truncated variant ( $\Delta$ N). While the full-length hCAP-H2 associates with mitotic chromosomes, the  $\Delta$ N variant exists as an insoluble nuclear structure. When overexpressed, both hCAP-H2 isoforms assemble this nuclear architecture and induce senescence-associated heterochromatic foci (SAHF). The hCAP-H2 $\Delta$ N protein accumulates as cells approach senescence, and hCAP-H2 knockdown inhibits oncogene-induced senescence. This study identifies a novel mechanism whereby condensin drives senescence via nuclear/genomic reorganization.

## Introduction

Protein complexes consisting of structural maintenance of chromosomes (SMC) proteins are essential for the faithful segregation of chromosomes. Two of the best-studied SMC complexes are condensin and cohesin, which are required for mitotic chromosome assembly and for holding sister chromatids together, respectively.<sup>1–3</sup> These SMC complexes function as connectors between 2 chromatin fibers.<sup>4</sup> Recent studies have revealed that cohesin can mediate interactions between gene promoters and enhancers.<sup>5</sup> Condensin is also known to function in higher-order genome organization in yeast and is involved in the gene regulation in *Caenorhabditis elegans*.<sup>6–9</sup> Condensin I and II complexes exist in humans, where the condensin II complex binds to promoters and enhancers, and participates in gene regulation.<sup>10,11</sup> Therefore, condensin likely regulates gene expression in a variety of organisms through its role in higher-order genome organization.

Cellular senescence was originally defined by Hayflick, who demonstrated that normal human fibroblasts could not proliferate indefinitely, but reach their “Hayflick limit” and senesce.<sup>12</sup> Currently, cellular senescence is defined as the state of stable cell-cycle arrest caused by exhausting the capacity of DNA replication or by various cellular stresses including DNA damage, chemotherapeutic drug treatment, and excessive growth stimulus by

overexpression of oncogenic Ras.<sup>13,14</sup> It is accompanied by diverse changes in gene expression and is associated with significant alterations in the global genome architecture.<sup>15,16</sup> Senescence-associated heterochromatic foci (SAHF) and senescence-associated distension of satellites (SADS) are characteristic of senescent cells.<sup>17–19</sup>

Several chromatin factors including a histone H2A variant (macroH2A), histone chaperons (ASF1 and HIRA), and the High-Mobility Group A (HMGA) proteins are involved in SAHF formation during cellular senescence.<sup>20,21</sup> Lamin B1, a structural component of the nuclear lamina, has also been implicated in the senescent processes.<sup>22</sup> Since heterochromatic histone modifications such as H3 lysine 9 and 27 tri-methylation are dispensable for SAHF formation, heterochromatic histone marks are not entirely responsible for SAHF formation.<sup>23</sup> Senescence appears to be a cellular event orchestrated by numerous cellular factors, but how SAHF are assembled during senescence and contribute to the senescent processes remains unclear.

In this study, we have shown that 2 hCAP-H2 isoforms of the condensin II subunit exist in human cells. The relative expression of these hCAP-H2 isoforms is regulated during the cell cycle and upon starvation. We find that the small upstream open reading frame (uORF) plays a role in regulating the translation of the hCAP-H2 isoforms and that the N-terminus truncated variant, hCAP-H2 $\Delta$ N, accumulates in

\*Correspondence to: Ken-ichi Noma; Email: noma@wistar.org

Submitted: 12/22/2014; Revised: 04/30/2015; Accepted: 05/06/2015

<http://dx.doi.org/10.1080/15384101.2015.1049778>

## Results

### Identification of 2 isoforms of hCAP-H2 condensin II subunit

To understand how condensin expression is regulated in human cells, we investigated several components of the condensin I and II complexes in 3 cancer cell lines (HeLa, HCT116, and U2OS) and RPE-1 (hTERT-immortalized retinal pigment epithelial) cells, which exhibit a stable diploid karyotype and are therefore often used for chromosome research. We observed that SMC4 (SMC subunit) and hCAP-H (kleisin subunit of condensin I) proteins were less abundant in HCT116 cells (Fig. S1A). Unexpectedly, 2 different sizes of proteins (84 and 91 kDa) were detected by the hCAP-H2 antibody in RPE-1 cells, but not in the cancer cell lines (top panels in Fig. 1A). These two proteins were both depleted by the short-hairpin RNA (shRNA) directed against *NCAPH2* transcripts, indicating that both proteins are derived from the *NCAPH2* gene (Fig. S1B). Based on the protein sizes, the top and bottom bands represent the full-length hCAP-H2 and a smaller variant, respectively. Since the 3 cancer cell lines expressed only the full-length hCAP-H2, we investigated whether this is a common feature of cancer cells. While the 2 hCAP-H2 isoforms were detected in primary human ovarian surface epithelial cells (HOSE4), both were also detected in the ovarian cancer cell lines (PEO-1, OVCAR5, and SKOV3), suggesting that the absence of the bottom

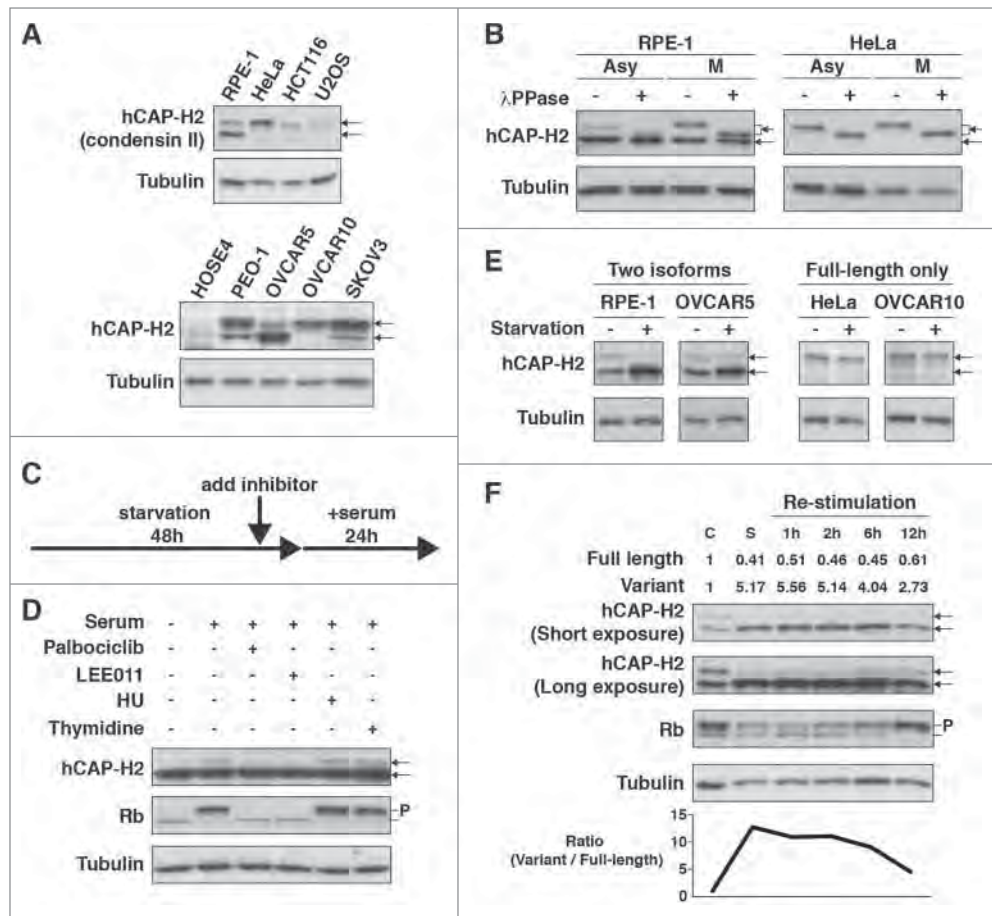


**Figure 1.** Full-length hCAP-H2 and its variant detected in human cell lines. (A) hCAP-H2 proteins in RPE-1, HeLa (cervical cancer), HCT116 (colon cancer), U2OS (osteosarcoma), HOSE4, and ovarian cancer cell lines (PEO-1, OVCAR5, OVCAR10, and SKOV3) were assessed by immunoblot analysis. Arrows indicate the full-length hCAP-H2 and its smaller variant. Tubulin serves as a loading control. (B) Asynchronous (Asy) and mitotic (M) RPE-1 and HeLa cells were subjected to Western blot analysis to detect hCAP-H2 proteins. Mitotic cells were prepared by mitotic shake-off. Cell lysates were treated with lambda protein phosphatase ( $\lambda$ PPase). (C) Schematic protocol for the inhibitor treatments employed in panel D. (D) RPE-1 cells grown in normal medium were subsequently cultured for 48 hours in starvation medium, which consists of 20 times less fetal bovine serum (FBS) than normal. CDK4/6 inhibitors (Palbociclib and LEE011), DNA replication inhibitors (HU and Thymidine), or DMSO (control) were added to starvation medium 2 hours before serum re-stimulation. Cells were further cultured for 24 hours in normal medium (serum +) containing the inhibitors, and lysates were subjected to immunoblot analysis. P indicates phosphorylated Rb proteins. (E) The indicated cell lines were cultured for 2 days in normal medium (starvation –) or phosphorylation medium (starvation +), followed by Western blot analysis. (F) RPE-1 cells grown in normal medium (C, control) were subsequently cultured for 2 days in starvation medium (S, Starvation). After the starvation treatment, cells were further cultured in normal medium for the indicated periods of time (Re-stimulation). Cell lysates derived from the respective culturing steps were subjected to immunoblot analysis. Band intensities (top) and expression ratio (bottom) of the hCAP-H2 isoforms are shown.

quiescent and senescent cells. We show that hCAP-H2 $\Delta$ N exists as a part of the insoluble nuclear architecture, while the full-length protein associates with mitotic chromosomes. Overexpression of this single condensin subunit, hCAP-H2, is sufficient to induce the formation of the condensin-mediated nuclear architecture and SAHF. This study demonstrates that the condensin II complex facilitates a nuclear/genomic reorganization leading to cellular senescence.

band is not necessarily indicative of cancer cells or their proliferative potential (bottom panels in Fig. 1A). For instance, the OVCAR5 and OVCAR10 cell lines had the different expression patterns of the hCAP-H2 isoforms, but showed similar rates of BrdU incorporation (Fig. 1A; Fig. S1C). Moreover, retinoblastoma (Rb) tumor suppressor proteins were predominantly phosphorylated in both the RPE-1 and cancer cell lines (except for HeLa cells, where Rb was absent), indicating that the expression



pattern of the 2 hCAP-H2 isoforms does not directly reflect cell proliferation (Fig. S1D and E).

#### Cell cycle-dependent regulation of hCAP-H2 isoforms

Next, we examined how expression of the hCAP-H2 isoforms is regulated during the cell cycle. We found that the full-length hCAP-H2 became more abundant in RPE-1 cells during mitosis compared to asynchronous cells, while the smaller hCAP-H2 variant was relatively decreased in mitotic cells (Fig. 1B). In contrast, expression levels were similar between mitotic and asynchronous HeLa cells, where only the full-length hCAP-H2 was present. We also found that  $\lambda$ PPase treatment converted the full-length hCAP-H2 from both asynchronous and mitotic cells to faster migrating bands (Fig. 1B). Moreover, the full-length hCAP-H2 bands from mitotic RPE-1 and HeLa cells were located slightly above those from asynchronous cells (Fig. 1B). These results indicate that hCAP-H2 is phosphorylated during interphase and additionally phosphorylated during mitosis (Fig. 1B). Phosphorylation of hCAP-H2 during mitosis was previously reported.<sup>24,25</sup> A similar band shift was not detected for the smaller variant, indicating that the phosphorylation is specific to the full-length hCAP-H2 (Fig. 1B).

We next performed serum re-stimulation assays with the CDK4/6 and DNA replication inhibitors (Fig. 1C). Starvation treatment arrests the cell cycle during G1/G0 phase, and serum re-stimulation with the CDK4/6 and DNA replication inhibitors allows the cell cycle to synchronously progress until midG1 and S phases, respectively. In RPE-1 cells treated by the CDK4/6 inhibitors, the full-length hCAP-H2 was not detected, while it was detected in cells treated by the DNA replication inhibitors (Fig. 1D). Furthermore, when the full-length hCAP-H2 was detected, Rb proteins were predominantly phosphorylated. These results suggest that the full-length hCAP-H2 accumulates between the midG1 and S phase, and that phosphorylation of Rb and accumulation of the full-length hCAP-H2 might be coordinated. Since the full-length hCAP-H2 is enriched during mitosis (Fig. 1B), our current hypothesis is that full-length proteins translated around the midG1-S phase are likely sustained until mitosis. Alternatively, it is also possible that the stability of hCAP-H2 proteins is regulated during the cell cycle. Together, these results indicate that protein levels of the hCAP-H2 isoforms are regulated during the cell cycle.

#### Regulation of hCAP-H2 isoforms upon starvation

We observed that the hCAP-H2 variant was increased in RPE-1 and OVCAR5 cells after serum starvation, while the full-length protein was decreased (Fig. 1E). In contrast, the full-length hCAP-H2 was not affected by the starvation treatment in the HeLa and OVCAR10 cell lines, which contained only the full-length protein (Fig. 1E). In addition, re-stimulation of cell growth after the starvation treatment gradually increased and decreased the full-length hCAP-H2 and its variant, respectively, and an increase in Rb phosphorylation was evident (Fig. 1F). These results suggest that when both of the hCAP-H2 isoforms are present, cell proliferation is associated with an increase of the full-length hCAP-H2 and a reduction of the variant, although

the basal expression pattern of the isoforms does not directly represent cell proliferation and is dependent upon cell lines (Fig. 1A). We also observed that *NCAPH2* gene transcription was not affected by the starvation treatment in RPE-1 cells (Fig. S1F). These results indicate that expression of the hCAP-H2 isoforms is regulated upon starvation in a post-transcriptional manner, and that the variant accumulates in quiescent cells induced by starvation.

#### Regulatory role of the uORF in translation of hCAP-H2 isoforms

The mouse *Ncapdh2* gene is known to produce splicing variants.<sup>26</sup> Therefore, we hypothesized that alternative splicing might be responsible for the synthesis of the hCAP-H2 protein isoforms. However, we did not observe splicing variants of *NCAPH2* in RPE-1 and HeLa cells, indicating that the hCAP-H2 variant protein is not derived from alternative splicing (Fig. S2A).

Small upstream open reading frames (uORFs) have been identified in about half of human transcripts and are known to control the translation of downstream ORFs.<sup>27,28</sup> A uORF is present in the *NCAPH2* mRNA and is conserved among mammalian species (Fig. 2A).<sup>26</sup> NetStart software predicts that hCAP-H2 translation initiates from the first (AUG1) and second (AUG2) start codons (Fig. 2B).<sup>29</sup> We hypothesized that the uORF might regulate translational initiation from the 2 start codons. To test this hypothesis, we made several constructs and observed that the wild-type construct expressed the 2 hCAP-H2 isoforms (Fig. 2C and D). The size difference between these 2 proteins was 7 kDa, which is exactly the same as for the endogenous hCAP-H2 isoforms (Fig. 1A). In contrast, the  $\Delta u$ AUG mutation that prevents translation of the uORF inhibited the production of the smaller protein. The  $\Delta$ AUG1 mutation, which removes the first start codon, resulted in the expression of only the smaller protein. The  $\Delta$ AUG2 mutation prevented the production of the smaller protein, and it resulted in the expression of an additional, even smaller protein, suggesting that there is an additional potential translational start site downstream of the second start codon. These results indicate that the translation of the larger and smaller proteins are initiated from the AUG1 and AUG2 codons, respectively, and that the uORF is required for efficient translational initiation from the AUG2 start codon. Small uORFs are known to modulate translation of the downstream ORFs through a reinitiation mechanism.<sup>30</sup> It has recently been shown that the *NIPBL* gene encoding a cohesin loading factor has an uORF, which regulates NIPBL translation in a cell cycle-dependent manner.<sup>31</sup> Therefore, it is possible that the uORF in the *NCAPH2* gene might contribute to the observed regulation of the hCAP-H2 isoforms during the cell cycle (Fig. 1B and D).

We next expressed non-tagged full-length hCAP-H2 and  $\Delta$ N proteins from plasmids in RPE-1 cells and compared the sizes of these proteins to the endogenous hCAP-H2 isoforms (Fig. 2E). In this system, the translation of the exogenous full-length hCAP-H2 and  $\Delta$ N variant is initiated from the AUG1 and AUG2 start codons, respectively. We observed that the size of the exogenous full-length hCAP-H2 was similar to the endogenous

Since DAPI-dense foci are reminiscent of senescence-associated heterochromatic foci (SAHF), we asked whether DAPI-dense foci we observed have the same characteristics as SAHF.

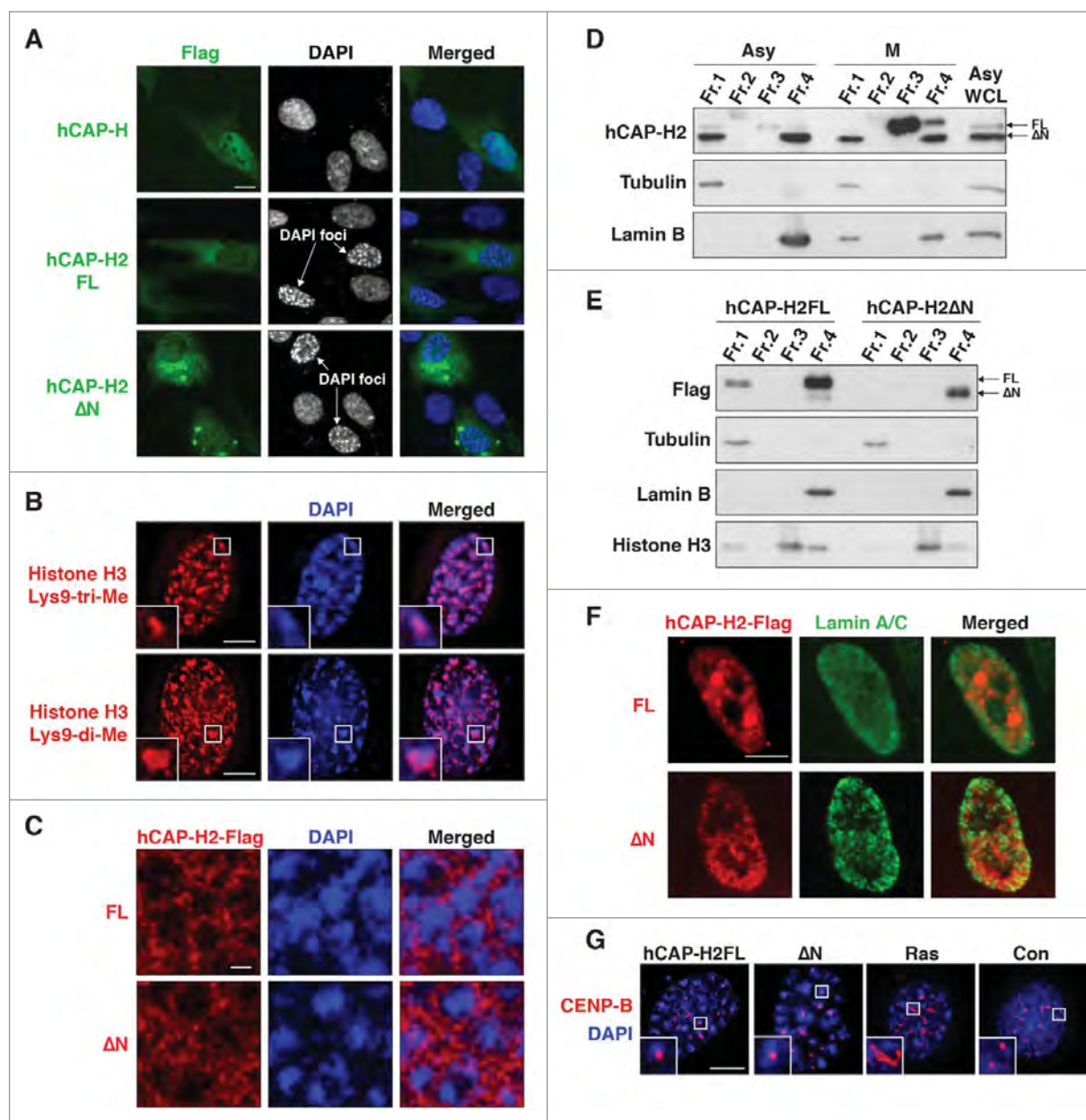


**Figure 3.** Overexpression of hCAP-H2 induces formation of DAPI-dense chromatin foci. **(A)** hCAP-H and hCAP-H2 (FL and ΔN) proteins fused to the Flag epitope were expressed in RPE-1 cells for 2 days and visualized by IF analysis. Scale bar indicates 10  $\mu$ m. **(B)** Histone H3 di- and tri-methylated Lys9 were visualized by IF in RPE-1 cells expressing the full-length hCAP-H2. Inset shows enlarged views. Scale bar indicates 5  $\mu$ m. **(C)** hCAP-H2 (FL and ΔN) proteins fused to the Flag epitope were expressed in RPE-1 cells and visualized by IF. These microscopic images, at a relatively high resolution, were captured by a Leica SP5 II laser scanning confocal microscope. Scale bar indicates 1  $\mu$ m. **(D)** Chromatin-unbound (Fr. 1), DNase-extractable (Fr. 2), high salt-extractable (Fr. 3), and high salt-resistant (Fr. 4) fractions were prepared from asynchronous (Asy) and mitotic (M) RPE-1 cells (See Materials and Methods) and subjected to Western blotting. WCL indicates whole cell lysate. **(E and F)** The same fractionation was performed using RPE-1 cells expressing Flag-tagged hCAP-H2 proteins (FL and ΔN). The fractions were subjected to immuno blotting (E). The high salt-resistant fraction was further applied for IF analysis to co-visualize hCAP-H2 and lamin A/C proteins (F). Scale bar indicates 5  $\mu$ m. **(G)** RPE-1 cells were transfected with plasmids encoding EYFP-tagged hCAP-H2 proteins (FL and ΔN) and culture for 2 days. Cells were subjected to IF analysis to stain CENP-B proteins, which bind to centromeric satellites. RPE-1 cells were infected with a retrovirus encoding H-RasV12 (Ras) or a control virus without H-RasV12 (Con) and subjected to IF analysis 8 days after the infection. Scale bar indicates 5  $\mu$ m.

We observed that DAPI-dense foci associated with histone H3 di- and tri-methylated Lys9, which are heterochromatic epigenetic marks (Fig. 3B). As previously reported, H3 tri-methylated Lys9 was located at the center of SAHF, while di-methylated

Lys9 was more enriched near the surface of SAHF (Fig. 3B). Histone H3 tri-methylated Lys9 was more scattered in the nuclei without DAPI-dense foci (Fig. S3B).<sup>23</sup> In contrast, histone H3 di/tri-methylated Lys4 (euchromatic mark) was present outside



of the DAPI-dense foci, consistent with the previous observation (Fig. S3C).<sup>17</sup> These results indicate that DAPI-dense chromatin foci induced by expression of the hCAP-H2 isoforms have characteristics of SAHF.

#### hCAP-H2 $\Delta$ N exists as a part of the insoluble nuclear architecture

To begin to understand the roles of the hCAP-H2 isoforms in the formation of DAPI-dense foci, we visualized these proteins and found that they were localized to the intervening region surrounding DAPI-dense foci (Fig. 3C). To further characterize hCAP-H2 localization, we performed cellular fractionation analysis (See Materials and Methods) and found that endogenous hCAP-H2 $\Delta$ N proteins were enriched in the insoluble fraction (fraction 4) in both asynchronous and mitotic cells (Fig. 3D). This insoluble fraction is also referred to as a nuclear matrix. The full-length hCAP-H2, but not the  $\Delta$ N variant, was found in the high salt-extractable fraction (fraction 3) during mitosis. Proteins tightly bound to DNA are mainly enriched in fraction 3. This result indicates that the condensin II complex containing the full-length hCAP-H2 preferentially interacts with mitotic chromosomes to mediate chromosome compaction,<sup>36,37</sup> while the complex with the  $\Delta$ N variant exists as a part of the insoluble nuclear architecture. As a control, we observed that tubulin was enriched in the chromatin-unbound soluble fraction 1, while lamin B was detected in fraction 4. Since this fractionation analysis monitors hCAP-H2 proteins without overexpression, it is likely that the endogenous hCAP-H2 isoforms have distinct functions in chromosome compaction and the nuclear architecture.

Exogenous full-length hCAP-H2 and  $\Delta$ N proteins highly expressed from plasmids as well as endogenous lamin B proteins were enriched in fraction 4, while histone H3 proteins were mainly detected in fraction 3 (Fig. 3E). When fraction 4 was subjected to IF analysis to visualize the hCAP-H2 isoforms, we observed that these proteins and lamin A/C were associated with the nucleus (Fig. 3F). These results demonstrate that, when overexpressed, both the hCAP-H2 isoforms exist as a part of the nuclear architecture. This is consistent with previous observations that several components of the condensin II complex are present in the nuclear matrix.<sup>38</sup>

Since senescence-associated distension of satellites (SADS), which occurs during the senescence process, is a more consistent phenomenon in human and mouse cells than SAHF,<sup>18</sup> we investigated whether the expression of the hCAP-H2 isoforms triggers SADS. To visualize SADS, we performed CENP-B staining, which specifically visualizes centromeric satellites and has previously been used for detection of SADS.<sup>18</sup> Consistent with the previous finding, 45% of RPE-1 cells showed SADS at the late senescent phase (day 8) when oncogenic Ras was expressed (Fig. 3G). On the other hand, expression of the hCAP-H2 isoforms induced DAPI-dense chromatin foci 2 days after transfection, but 0% of the cells showed SADS at the same time point (Fig. 3G). This result suggests that overexpression of the hCAP-H2 isoforms can cause the formation of DAPI-dense chromatin foci, likely SAHF, without SADS. Together, these results suggest

that overexpressed hCAP-H2 proteins facilitate the formation of the condensin-associated insoluble nuclear architecture and SAHF.

#### hCAP-H2 functions in cellular senescence

To investigate whether hCAP-H2 plays a role in cellular senescence, we expressed the hCAP-H2 isoforms in IMR90 human fibroblasts, which are commonly used for senescence research. Overexpression of the full-length hCAP-H2 and  $\Delta$ N variant induced senescence, as indicated by decrease in BrdU incorporation (cell cycle/growth marker), senescence-associated  $\beta$ -galactosidase (SA- $\beta$ -gal) staining, and SAHF formation, all of which were statistically significant ( $P < 0.001$ ; Fig. 4D). We also observed that hCAP-H2 $\Delta$ N expression was increased during senescence induced by oncogenic Ras (Fig. 4E). Moreover, Ras-induced senescence was significantly impaired by hCAP-H2 knockdown using shH2#1, as indicated by the reduced percentages of cells positive for SA- $\beta$ -gal activity and SAHF formation ( $P < 0.001$ ; Fig. 4F). hCAP-H2 knockdown using 2 different shRNAs (shH2#2 and #3) also inhibited Ras-induced senescence (Fig. S3D and E). These results collectively indicate that the condensin II complex functions during oncogene-induced senescence, and that the complex with the  $\Delta$ N variant likely participates in the senescent process.

## Discussion

While there are the 2 hCAP-H2 isoforms present in the non-cancerous cell lines (RPE-1 and HOSE4), some cancer cell lines contain only the full-length protein, suggesting that the presence of the 2 isoforms is likely the normal situation for growing cells. We show that expression of the 2 hCAP-H2 isoforms is modulated during the cell cycle and upon starvation, and that the uORF plays a regulatory role in the translation of the hCAP-H2 isoforms. We also find that the condensin II complex containing the full-length hCAP-H2 preferentially associates with mitotic chromosomes to mediate chromosome compaction, while the complex with the  $\Delta$ N variant exists as a component of the insoluble nuclear architecture (Fig. 3D). Only the hCAP-H2 $\Delta$ N variant is accumulated in quiescent and senescent cells induced by starvation and oncogenic Ras, respectively (Figs. 1E and 4E). This makes sense because these cells do not progress through mitosis and thus do not need the full-length isoform to induce chromosome compaction. Therefore, non-growing cells express the  $\Delta$ N variant, which contributes to the formation of a nuclear environment favorable for growth arrest.

When overexpressed, both of the hCAP-H2 isoforms associate with the specific nuclear architecture and induce DAPI-dense chromatin foci (Fig. 3). We also show that the protein level of the endogenous hCAP-H2 $\Delta$ N variant is increased as cells approach senescence, and that hCAP-H2 knockdown inhibits SAHF formation and oncogene-induced senescence (Fig. 4E and F). Taken all together, our current hypothesis is that the specific nuclear architecture built by the condensin II complex containing the  $\Delta$ N variant promotes SAHF formation,

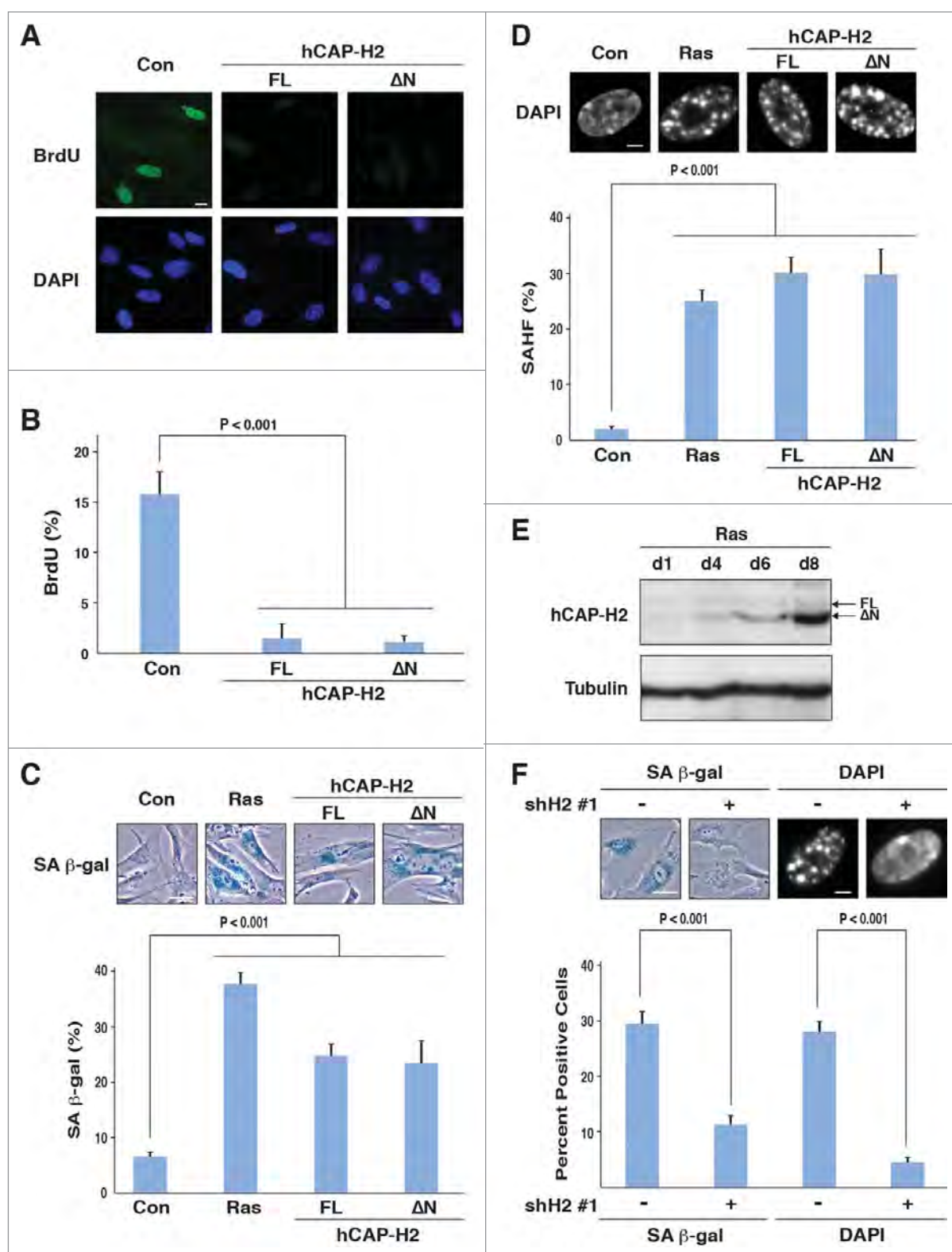


**Figure 4.** hCAP-H2 facilitates cellular senescence. (A and B) IMR90 cells were infected with retroviruses encoding the full-length hCAP-H2 or ΔN variant, or a control virus without encoding these proteins. BrdU incorporation and visualization were performed 8 days after the infection (A). Scale bar indicates 10 μm. Percentages of IMR90 cells showing BrdU staining were scored 8 days after retrovirus infection (B). (C and D) IMR90 cells were infected by retroviruses encoding the H-RasV12, full-length hCAP-H2, or ΔN variant, or a control virus, and subjected to SA-β-gal staining 8 days after the infection (C). Infected cells were stained by DAPI to assess SAHF formation (D). Scale bars in panels C and D indicate 50 μm and 5 μm, respectively. (E) hCAP-H2 levels were monitored from day 1 (d1) to day 8 (d8), after IMR90 cells were infected with a retrovirus encoding H-RasV12. Tubulin serves as a loading control. (F) IMR90 cells were infected with a retrovirus encoding H-RasV12 as well as a lentivirus encoding shRNA against *NCAPH2* mRNA (shH2#1), and assessed for SA-β-gal activity and SAHF formation 8 days after the infection. Scale bars indicate 50 (left) and 5 μm (right).

which in turn facilitates senescence. It has recently been shown that lamin B1 knockdown induces dissociation of heterochromatin from the nuclear periphery and SAHF formation.<sup>39</sup> Therefore, the lamina and the condensin-mediated nuclear architectures likely play opposing roles in SAHF formation. Consequently, overexpression of hCAP-H2 might be necessary to induce SAHF in the presence of the nuclear lamina. In case of senescence induced by oncogenic Ras, lamin B1 is down-regulated, and hCAP-H2 $\Delta$ N expression is enhanced (Fig. 4E).<sup>22</sup>

We also found that the Rb tumor suppressor associates with the nuclear architecture assembled by the condensin II complex (Fig. S3F). Interestingly, Rb foci were almost always detected at the surface of the condensin architecture and outside of DAPI-dense signals. It has previously been shown that Rb interacts with the hCAP-D3 subunit of the condensin II complex in human cells.<sup>40</sup> Therefore, Rb associates with the condensin II nuclear architecture likely through the interaction between Rb and hCAP-D3. Consistent with this interpretation, Rb is known to be present in the insoluble nuclear fraction.<sup>41</sup> It has also been shown that Rb binds to and represses E2F-target genes, thereby contributing to cellular senescence.<sup>17</sup> Based on these results, we speculate that Rb associates the E2F-target genes with the condensin II nuclear architecture, which might play a role in the gene repression for the E2F-target genes. As a similar example, SATB1 forms a nuclear architecture in mouse cells and regulates many genes by tethering those genes to the SATB1 nuclear architecture.<sup>42</sup> Since senescence is accompanied by altered expression of many genes,<sup>15,16</sup> the condensin-mediated nuclear architecture might contribute to the gene expression program during senescence processes.

## Materials and Methods

### Cell culture

RPE-1 cells (ATCC) were cultured in DMEM/F12 medium (Life Technologies, 11330032) supplemented with 10% tet-system approved fetal bovine serum (FBS; Clontech Laboratories, 631106), 100 U/ml penicillin, 100  $\mu$ g/ml streptomycin, and 0.01 mg/ml hygromycin B. HeLa, HCT116, and U2OS cells were cultured in DMEM medium (Mediatech, MT10-013-CV) supplemented with 10% FBS, 100 U/ml penicillin, and 100  $\mu$ g/ml streptomycin. PEO-1, OVCAR5, OVCAR10, and SKOV3 cells were cultured in RPMI1640 medium (Life Technologies, 22400089) supplemented with 10% FBS, 100 U/ml penicillin, and 100  $\mu$ g/ml streptomycin. HOSE4 cells were cultured as previously described.<sup>43</sup> IMR90 cells were cultured in DMEM medium supplemented with 10% FBS, 100 U/ml penicillin, 100  $\mu$ g/ml streptomycin, 0.15% sodium bicarbonate, 2 mM L-glutamine, 1 mM sodium pyruvate, and 1  $\times$  MEM non-essential amino acids (Life Technologies, 11120052).

### Expression of hCAP-H2 and its variants

*NCAPH2* cDNA in pCMV6-Entry vector (OriGene) was used to generate the *NCAPH2* $\Delta$ N and  $\Delta$ C genes by a PCR-based method. hCAP-H2 (full length,  $\Delta$ N, and  $\Delta$ C) proteins

fused to the Flag epitope were expressed from either pCMV6-Entry or pTRE3G plasmids (Clontech Laboratories). For co-immunoprecipitation (co-IP) assay, pTRE3G plasmids carrying *NCAPH2* (full length,  $\Delta$ N, or  $\Delta$ C) and pCMV-Tet3G were co-transfected into cells, and *NCAPH2* expression was induced by 1  $\mu$ g/ml doxycycline for 48 hours. hCAP-H2 (full length and  $\Delta$ N) proteins fused to EYFP were expressed from pEYFP-N1 plasmids (Clontech Laboratories). Cells were transfected with plasmids using the Fugene HD reagent (Promega, E2311).

### Retrovirus and lentivirus infections

DNA fragments encoding hCAP-H2 (full length and  $\Delta$ N) fused to the Flag epitope were inserted into pBABE-neo vector.<sup>20</sup> pBABE-neo plasmids carrying either H-rasV12, *NCAPH2*, or *NCAPH2* $\Delta$ N were used for retrovirus packaging, and virus infection was performed as described previously.<sup>20</sup> Cells were cultured with selection medium containing 500  $\mu$ g/ml G418. pTRIPZ plasmid containing *NCAPH2* shRNA (Thermo Scientific Open Biosystems) was used for lentivirus production. Doxycycline (1  $\mu$ g/ml) was added to culture medium every 48 hours for shRNA expression. Cells were cultured in medium containing 3  $\mu$ g/ml puromycin.

### Senescence-associated $\beta$ -galactosidase (SA- $\beta$ -gal) and BrdU assays

SA- $\beta$ -gal staining was performed as described previously.<sup>44</sup> For BrdU incorporation experiments, cells were plated on coverslips and labeled with 100  $\mu$ g/ml 5-Bromo-2'-deoxyuridine (BrdU, Sigma-Aldrich, B5002) for 30 minutes. The cells were fixed by 4% paraformaldehyde (pFA) for 15 minutes and permeabilized by PBS buffer containing 0.2% Triton X-100. The cells were further fixed for 30 minutes by 1% pFA in PBS buffer containing 0.01% Tween-20 and treated with 5 units of RQ1 RNase-free DNase I (Promega, M6101) or 2 N HCl. The cells were then incubated with 1:10-diluted FITC-labeled mouse monoclonal anti-BrdU (BD Biosciences, 556028) for 30 minutes. Nuclei were stained with 1  $\mu$ g/ml 4,6-diamidino-2-phenylindole (DAPI) solution for 5 minutes.

### Fractionation analysis

Fractionation analysis was performed as previously described with slight modifications.<sup>45</sup> Cells were lysed at 4°C for 30 minutes with 400  $\mu$ l CSK buffer [10 mM PIPES (pH 6.8), 100 mM NaCl, 300 mM sucrose, 3 mM MgCl<sub>2</sub>, 1 mM EGTA, 1 mM DTT, 0.25 mM PMSF, 10 mM NaF, 0.1 mM ATP, and Complete protease inhibitor cocktail (Roche, 11836170001)] containing 0.3% Triton X-100. Soluble fraction (fraction 1, chromatin-unbound fraction) and insoluble fraction were separated by centrifugation at 2,300  $\times$  g for 10 minutes. The insoluble fraction was incubated with 100 units of RQ1 RNase-free DNase I at room temperature for 30 minutes. After centrifugation at 16,000  $\times$  g for 10 minutes, the supernatant was recovered as fraction 2 (DNase-extractable fraction). The pellet was then suspended in 200  $\mu$ l CSK buffer containing 0.3% Triton X-100 and 2 M NaCl, and the suspension was rotated at 4°C for 30 minutes. After centrifugation at 16,000  $\times$  g for



10 minutes, the supernatant was recovered as fraction 3 (high salt-extractable fraction), and the pellet was boiled with 50  $\mu$ l Laemmli sample buffer (fraction 4, high salt-resistant fraction).

### Western blotting

Cells were suspended with Laemmli sample buffer (Bio-Rad Laboratories, 1610737) and boiled at 100°C for 5 minutes. Primary antibodies used in this study were the following: 1:1000-diluted rabbit polyclonal anti-SMC4 (Abcam, ab17958), 1:2000-diluted rabbit polyclonal anti-hCAP-H (Sigma-Aldrich, HPA003008), 1:500-diluted rabbit polyclonal anti-hCAP-H2 (Abgent, AP1973A), 1:200-diluted mouse monoclonal anti-hCAP-D2 (Santa Cruz Biotechnology, sc-166878), 1:1000-diluted rabbit polyclonal anti-hCAP-D3 (Abcam, ab70349), 1:2000-diluted mouse monoclonal anti-hCAP-G (Novus Biologicals, H00064151-M01), 1:1000-diluted mouse monoclonal anti-Rb (Cell Signaling Technology, #9309), 1:500-diluted goat polyclonal anti-Lamin B (Santa Cruz Biotechnology, sc-6217), 1:20000-diluted mouse monoclonal anti- $\alpha$ -tubulin (Sigma-Aldrich, T6199), 1:1000-diluted mouse monoclonal anti-Flag (Sigma-Aldrich, F1804), and 1:2000-diluted rabbit monoclonal anti-histone H3 (Cell Signaling Technology, #4499). Secondary antibodies, such as horseradish peroxidase (HRP)-conjugated sheep anti-mouse IgG, HRP-conjugated donkey anti-rabbit IgG (GE Healthcare, NA931, NA934), and HRP-conjugated rabbit anti-goat IgG (Kirkegaard & Perry Laboratories, 14-13-06), were used for detection of target proteins by ECL or ECL plus kits (GE Healthcare, RPN2109, RPN2133).

### Immunoprecipitation

Cells were suspended in 1 ml IP buffer [50 mM HEPES (pH 7.6), 75 mM KCl, 0.1% NP-40, 20% Glycerol, 1 mM EDTA, 10 mM NaF, 10 mM  $\beta$ -glycerophosphate, and Complete protease inhibitor cocktail]. Cell lysate was mixed with  $\text{MgCl}_2$  (final 5 mM) and 50 units of RQ1 RNase-free DNase I were added. DNase I reaction was performed at 37°C for 30 minutes and terminated by adding EDTA (final 10 mM). Soluble fraction of the cell lysate was incubated with anti-Flag M2 magnetic beads (Sigma-Aldrich, M8823). The beads were washed with 400  $\mu$ l of IP buffer 5 times and boiled with 20  $\mu$ l Laemmli sample buffer to elute proteins.

### Immunofluorescence microscopy

Cells plated on coverslips were fixed with 2% pFA for 15 minutes. Fixed cells were permeabilized with PBS containing 0.5% Triton X-100 for 5 minutes and incubated with TBST (Tris-buffered saline plus 0.1% Tween-20) containing 1% BSA for 1 hour. Cells were then incubated for 1 hour with primary antibodies: 1:200-diluted mouse or rat monoclonal anti-Flag (Agilent Technologies, 200471, 200473), 1:500-diluted mouse monoclonal anti-histone H3 di-methyl Lys9 (Abcam, ab1220), 1:1000-diluted rabbit polyclonal anti-histone H3 tri-methyl Lys9 (Abcam, ab8898), 1:200-diluted mouse monoclonal anti-histone H3 di/tri-methyl Lys4 (Abcam, ab6000), 1:1000-diluted rabbit polyclonal anti-CENPB (Abcam, ab25734), 1:200-diluted rabbit polyclonal anti-lamin A/C (Cell Signaling Technology,

#2032), and 1:200-diluted mouse monoclonal anti-Rb (Cell Signaling Technology). Cells were subsequently incubated for 1 hour with secondary antibodies, such as 1:500-diluted Alexa Flour 488-conjugated anti-mouse IgG, 1:400-diluted Alexa Flour 594-conjugated anti-mouse IgG, 1:400-diluted Alexa Flour 594-conjugated anti-rat IgG, 1:400-diluted Alexa Flour 488-conjugated anti-rabbit IgG, 1:400-diluted Alexa Flour 594-conjugated anti-rabbit IgG, and 1:4000-diluted Cy3-conjugated anti-rabbit IgG. Nuclei were stained with 1  $\mu$ g/ml DAPI solution for 5 minutes. Immunofluorescent (IF) images were captured by a Zeiss Axioimager Z1 fluorescence microscope with an oil immersion objective lens (Plan Apochromat, 63 $\times$ , NA 1.4, Zeiss), unless otherwise indicated. The images were acquired at 0.2  $\mu$ m intervals in the z-axis controlled by Axiovision 4.6.3 software (Zeiss). To visualize hCAP-H2 and lamin A/C proteins in fraction 4, cells attached to coverslips were treated by CSK buffer, DNase I, and 2 M NaCl, as described in the fractionation procedure. The cells were then fixed by 2% pFA, followed by the same IF procedure.

### RT-PCR and qRT-PCR

RNA was extracted from human cells using RNeasy Plus Mini Kit (Qiagen, 74134). RNA samples were subjected to RT-PCR using onestep RT-PCR kit (Qiagen, 210212) or SYBR green one-step kit (Bio-Rad, 172-5151). Alternatively, RNA samples were subjected to cDNA synthesis using high-capacity cDNA reverse transcription kit (Life Technologies, 4368814), followed by qPCR analysis using SYBR green qPCR kit (Sigma-Aldrich, KCQS00). Primer sequences are indicated in Table S1.

### Disclosure of Potential Conflicts of Interest

No potential conflicts of interest were disclosed.

### Acknowledgments

We would like to thank Meenhard Herlyn, Kazuko Nishikura, Ashani Weeraratna, and Susan Janicki for experimental materials; the Wistar Institute Molecular Screening Facility for lentivirus preparation; and the Imaging Facility for microscopic analysis. We also thank Maureen Murphy, Michael Showe, and Louise Showe for critically reading the manuscript and Sylvie Shaffer for editorial assistance.

### Funding

This work was supported by the National Institutes of Health (NIH) grant CA010815, the W. W. Smith Charitable Trust, the V Foundation, the Edward Mallinckrodt, Jr. Foundation, and the Wistar Pilot Project Funds to KN.

### Supplemental Material

Supplemental data for this article can be accessed on the publisher's website.

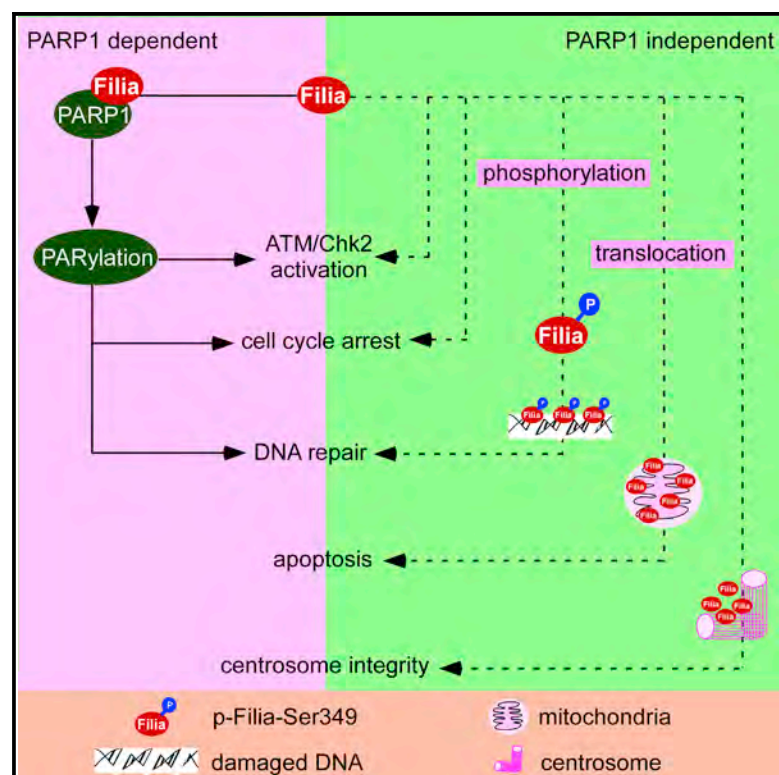
## References

- Koshland D, Strunnikov A. Mitotic chromosome condensation. *Annu Rev Cell Dev Biol* 1996; 12:305-33; PMID:8970729; <http://dx.doi.org/10.1146/annurev.cellbio.12.1.305>
- Hirano T. Chromosome cohesion, condensation, and separation. *Annu Rev Biochem* 2000; 69:115-44; PMID:10966455; <http://dx.doi.org/10.1146/annurev.biochem.69.1.115>
- Nasmyth K, Haering CH. The structure and function of SMC and kleisin complexes. *Annu Rev Biochem* 2005; 74:595-648; PMID:15952899; <http://dx.doi.org/10.1146/annurev.biochem.74.082803.133219>
- Hirano T. At the heart of the chromosome: SMC proteins in action. *Nat Rev Mol Cell Biol* 2006; 7:311-22; PMID:16633335; <http://dx.doi.org/10.1038/nrm1909>
- Kagey MH, Newman JJ, Bilodeau S, Zhan Y, Orlando DA, van Berkum NL, Ebmeier CC, Goossens J, Rahl PB, Levine SS, et al. Mediator and cohesin connect gene expression and chromatin architecture. *Nature* 2010; 467:430-5; PMID:20720539; <http://dx.doi.org/10.1038/nature09380>
- Chuang PT, Albertson DG, Meyer BJ. DPY-27: A chromosome condensation protein homolog that regulates *C. elegans* dosage compensation through association with the X chromosome. *Cell* 1994; 79:459-74; PMID:7954812; [http://dx.doi.org/10.1016/0092-8674\(94\)90255-0](http://dx.doi.org/10.1016/0092-8674(94)90255-0)
- Haeussler RA, Pratt-Hyatt M, Good PD, Gipson TA, Engelke DR. Clustering of yeast tRNA genes is mediated by specific association of condensin with tRNA gene transcription complexes. *Genes Dev* 2008; 22:2204-14; PMID:18708579; <http://dx.doi.org/10.1101/gad.1675908>
- Iwasaki O, Tanaka A, Tanizawa H, Grewal SIS, Noma KI. Centromeric localization of dispersed Pol III genes in fission yeast. *Mol Biol Cell* 2010; 21:254-65; PMID:19910488; <http://dx.doi.org/10.1091/mbc.E09-09-0790>
- Tanaka A, Tanizawa H, Sriswasdi S, Iwasaki O, Chatterjee AG, Speicher DW, Levin HL, Noguchi E, Noma KI. Epigenetic regulation of condensin-mediated genome organization during the cell cycle and upon DNA damage through histone H3 lysine 56 acetylation. *Mol Cell* 2012; 48:532-46; PMID:23084836; <http://dx.doi.org/10.1016/j.molcel.2012.09.011>
- Ono T, Losada A, Hirano M, Myers MP, Neuwald AF, Hirano T. Differential contributions of condensin I and condensin II to mitotic chromosome architecture in vertebrate cells. *Cell* 2003; 115:109-21; PMID:14532007; [http://dx.doi.org/10.1016/S0092-8674\(03\)00724-4](http://dx.doi.org/10.1016/S0092-8674(03)00724-4)
- Dowen JM, Bilodeau S, Orlando DA, Hübner MR, Abraham BJ, Spector DL, Young RA. Multiple structural maintenance of chromosome complexes at transcriptional regulatory elements. *Stem Cell Reports* 2013; 1:371-8; PMID:24286025; <http://dx.doi.org/10.1016/j.stemcr.2013.09.002>
- Hayflick L. The limited in vitro lifetime of human diploid cell strains. *Exp Cell Res* 1965; 37:614-36; PMID:14315085; [http://dx.doi.org/10.1016/0014-4827\(65\)90211-9](http://dx.doi.org/10.1016/0014-4827(65)90211-9)
- Campisi J. Aging, cellular senescence, and cancer. *Annu Rev Physiol* 2013; 75:685-705; PMID:23140366; <http://dx.doi.org/10.1146/annurev-physiol-030212-183653>
- Salama R, Sadaie M, Hoare M, Narita M. Cellular senescence and its effector programs. *Genes Dev* 2014; 28:99-114; PMID:24449267; <http://dx.doi.org/10.1101/gad.235184.113>
- Shelton DN, Chang E, Whittier PS, Choi D, Funk WD. Microarray analysis of replicative senescence. *Curr Biol* 1999; 9:939-45; PMID:10508581; [http://dx.doi.org/10.1016/S0960-9822\(99\)80420-5](http://dx.doi.org/10.1016/S0960-9822(99)80420-5)
- Debacq-Chainiaux F, Pascal T, Boilan E, Bastin C, Bauwens E, Toussaint O. Screening of senescence-associated genes with specific DNA array reveals the role of IGFBP-3 in premature senescence of human diploid fibroblasts. *Free Radic Biol Med* 2008; 44:1817-32; PMID:18329388; <http://dx.doi.org/10.1016/j.freeradbiomed.2008.02.001>
- Narita M, Núñez S, Heard E, Narita M, Lin AW, Hearn SA, Spector DL, Hannon GJ, Lowe SW. Rb-mediated heterochromatin formation and silencing of E2F target genes during cellular senescence. *Cell* 2003; 113:703-16; PMID:12809602; [http://dx.doi.org/10.1016/S0092-8674\(03\)00401-X](http://dx.doi.org/10.1016/S0092-8674(03)00401-X)
- Swanson EC, Manning B, Zhang H, Lawrence JB. Higher-order unfolding of satellite heterochromatin is a consistent and early event in cell senescence. *J Cell Biol* 2013; 203:929-42; PMID:24344186; <http://dx.doi.org/10.1083/jcb.201306073>
- De Cecco M, Criscione SW, Peckham EJ, Hillenmeyer S, Hamm EA, Manivannan J, Peterson AL, Kreiling JA, Neretti N, Sedivy JM. Genomes of replicatively senescent cells undergo global epigenetic changes leading to gene silencing and activation of transposable elements. *Aging Cell* 2013; 12:247-56; PMID:23360310; <http://dx.doi.org/10.1111/acel.12047>
- Zhang R, Poustovoitov MV, Ye X, Santos HA, Chen W, Daganzo SM, Erzberger JP, Serebriiskii IG, Canutescu AA, Dunbrack RL, et al. Formation of MacroH2A-containing senescence-associated heterochromatin foci and senescence driven by ASF1a and HIRA. *Dev Cell* 2005; 8:19-30; PMID:15621527; <http://dx.doi.org/10.1016/j.devcel.2004.10.019>
- Narita M, Narita M, Krizhanovsky V, Núñez S, Chicas A, Hearn SA, Myers MP, Lowe SW. A novel role for high-mobility group a proteins in cellular senescence and heterochromatin formation. *Cell* 2006; 126:503-14; PMID:16901784; <http://dx.doi.org/10.1016/j.cell.2006.05.052>
- Shimi T, Butin-Israeli V, Adam SA, Hamaana RB, Goldman AE, Lucas CA, Shumaker DK, Kosak ST, Chandan NS, Goldman RD. The role of nuclear lamin B1 in cell proliferation and senescence. *Genes Dev* 2011; 25:2579-93; PMID:22155925; <http://dx.doi.org/10.1101/gad.179515.111>
- Chandra T, Kirschner K, Thuret JY, Pope BD, Ryba T, Newman S, Ahmed K, Samarajiva SA, Salama R, Carroll T, et al. Independence of repressive histone marks and chromatin compaction during senescent heterochromatic layer formation. *Mol Cell* 2012; 47:203-14; PMID:22795131; <http://dx.doi.org/10.1016/j.molcel.2012.06.010>
- Olsen JV, Vermeulen M, Santamaria A, Kumar C, Miller ML, Jensen LJ, Gnäd F, Cox J, Jensen TS, Nigg EA, et al. Quantitative phosphoproteomics reveals widespread full phosphorylation site occupancy during mitosis. *Sci Signal* 2010; 3:ra3; PMID:20068231; <http://dx.doi.org/10.1126/scisignal.2000475>
- Abe S, Nagasaka K, Hirayama Y, Kozuka-Hata H, Oyama M, Aoyagi Y, Obuse C, Hirota T. The initial phase of chromosome condensation requires Cdk1-mediated phosphorylation of the CAP-D3 subunit of condensin II. *Genes Dev* 2011; 25:863-74; PMID:21498573; <http://dx.doi.org/10.1101/gad.2016411>
- Theodoratos A, Wilson LOW, Gosling KM, Fahrner AM. Splice variants of the condensin II gene Ncapd2 include alternative reading frame translations of exon 1. *FEBS J* 2012; 279:1422-32; PMID:22331518; <http://dx.doi.org/10.1111/j.1742-4658.2012.08530.x>
- Calvo SE, Pagliarini DJ, Mootha VK. Upstream open reading frames cause widespread reduction of protein expression and are polymorphic among humans. *Proc Natl Acad Sci U S A* 2009; 106:7507-12; PMID:19372376; <http://dx.doi.org/10.1073/pnas.0810916106>
- Wethmar K, Smink JJ, Leutz A. Upstream open reading frames: molecular switches in (patho)physiology. *Bioessays* 2010; 32:885-93; PMID:20726009; <http://dx.doi.org/10.1002/bies.201000037>
- Pedersen AG, Nielsen H. Neural network prediction of translation initiation sites in eukaryotes: perspectives for EST and genome analysis. *Proc Int Conf Intell Syst Mol Biol* 1997; 5:226-33; PMID:9322041.
- Kozak M. Pushing the limits of the scanning mechanism for initiation of translation. *Gene* 2002; 299:1-34; PMID:12459250; [http://dx.doi.org/10.1016/S0378-1119\(02\)01056-9](http://dx.doi.org/10.1016/S0378-1119(02)01056-9)
- Stumpf C, Moreno M, Olshen A, Taylor B, Ruggero D. The translational landscape of the mammalian cell cycle. *Mol Cell* 2013; 52:574-82; PMID:24120665; <http://dx.doi.org/10.1016/j.molcel.2013.09.018>
- Schleiffer A, Kaita S, Maurer-Stroh S, Glotzer M, Nasmyth K, Eisenhaber F. Kleisins: A superfamily of bacterial and eukaryotic SMC protein partners. *Mol Cell* 2003; 11:571-5; PMID:12667442; [http://dx.doi.org/10.1016/S1097-2765\(03\)00108-4](http://dx.doi.org/10.1016/S1097-2765(03)00108-4)
- Fennell-Fezzie R, Gradia SD, Akey D, Berger JM. The MukF subunit of *Escherichia coli* condensin: architecture and functional relationship to kleisins. *EMBO J* 2005; 24:1921-30; PMID:15902272; <http://dx.doi.org/10.1038/sj.emboj.7600680>
- Onn I, Aono N, Hirano M, Hirano T. Reconstitution and subunit geometry of human condensin complexes. *EMBO J* 2007; 26:1024-34; PMID:17268547; <http://dx.doi.org/10.1038/sj.emboj.7601562>
- Haering CH, Schoffnegger D, Nishino T, Helmhart W, Nasmyth K, Löwe J. Structure and stability of cohesin's Smc1-kleisin interaction. *Mol Cell* 2004; 15:951-64; PMID:15383284; <http://dx.doi.org/10.1016/j.molcel.2004.08.030>
- Ono T, Fang Y, Spector DL, Hirano T. Spatial and temporal regulation of Condensins I and II in mitotic chromosome assembly in human cells. *Mol Biol Cell* 2004; 15:3296-308; PMID:15146063; <http://dx.doi.org/10.1091/mbc.E04-03-0242>
- Hirota T, Gerlich D, Koch B, Ellenberg J, Peters JM. Distinct functions of condensin I and II in mitotic chromosome assembly. *J Cell Sci* 2004; 117:6435-45; PMID:15572404; <http://dx.doi.org/10.1242/jcs.01604>
- Takata H, Nishijima H, Ogura SI, Sakaguchi T, Bubulya PA, Mochizuki T, Shibahara KI. Proteome analysis of human nuclear insoluble fractions. *Genes Cell* 2009; 14:975-90; PMID:19695025; <http://dx.doi.org/10.1111/j.1365-2443.2009.01324.x>
- Sadaie M, Salama R, Carroll T, Tomimatsu K, Chandra T, Young ARJ, Narita M, Pérez-Mancera P, Bennett DC, Chong H, et al. Redistribution of the Lamin B1 genomic binding profile affects rearrangement of heterochromatic domains and SAHF formation during senescence. *Genes Dev* 2013; 27:1800-8; PMID:23964094; <http://dx.doi.org/10.1101/gad.217281.113>
- Longworth MS, Herr A, Ji JY, Dyson NJ. RBF1 promotes chromatin condensation through a conserved interaction with the Condensin II protein dCAP-D3. *Genes Dev* 2008; 22:1011-24; PMID:18367646; <http://dx.doi.org/10.1101/gad.1631508>
- Reyes JC, Muchardt C, Yaniv M. Components of the human SWI/SNF complex are enriched in active chromatin and are associated with the nuclear matrix. *J Cell Biol* 1997; 137:263-74; PMID:9128241; <http://dx.doi.org/10.1083/jcb.137.2.263>
- Cai S, Han HJ, Kohwi-Shigematsu T. Tissue-specific nuclear architecture and gene expression regulated by SATB1. *Nat Genet* 2003; 34:42-51; PMID:12692553; <http://dx.doi.org/10.1038/ng1146>
- Bellacosa A, Godwin AK, Peri S, Devarajan K, Caretti E, Vanderveer L, Bove B, Slater C, Zhou Y, Daly M, et al. Altered gene expression in morphologically normal epithelial cells from heterozygous carriers of

- BRCA1 or BRCA2 mutations. *Cancer Prev Res (Phila)* 2010; 3:48-61; PMID:20051372; <http://dx.doi.org/10.1158/1940-6207.CAPR-09-0078>
44. Dimri GP, Lee X, Basile G, Acosta M, Scott G, Roskelley C, Medrano EE, Linskens M, Rubelj I, Pereira-Smith O, et al. A biomarker that identifies senescent human cells in culture and in aging skin in vivo. *Proc Natl Acad Sci U S A* 1995; 92: 9363-7; PMID:7568133; <http://dx.doi.org/10.1073/pnas.92.20.9363>
45. Takemoto A, Kimura K, Yokoyama S, Hanaoka F. Cell cycle-dependent phosphorylation, nuclear localization, and activation of human condensin. *J Biol Chem* 2004; 279:4551-9; PMID:14607834; <http://dx.doi.org/10.1074/jbc.M310925200>

# Filia Is an ESC-Specific Regulator of DNA Damage Response and Safeguards Genomic Stability

## Graphical Abstract



## Authors

Bo Zhao, Wei-dao Zhang, ..., Rugang Zhang, Ping Zheng

## Correspondence

zhengp@mail.kiz.ac.cn

## In Brief

Zhao et al. identify Filia as an ESC-specific regulator of genomic stability that is induced by genotoxic stress. Functional characterization highlights dynamic subcellular translocation and roles in governing multiple DNA damage response pathways, including stimulation of PARP1 enzymatic activity.

## Highlights

- Loss of Filia promotes genomic instability and transformation in ESCs
- Filia is induced by genotoxic stress and regulates repair responses
- Filia is regulated by post-translational modification and sub-cellular translocation
- Filia interacts with PARP1 and stimulates its enzymatic activity





# Filia Is an ESC-Specific Regulator of DNA Damage Response and Safeguards Genomic Stability

Bo Zhao,<sup>1,2</sup> Wei-dao Zhang,<sup>1,2,3</sup> Ying-liang Duan,<sup>1,2</sup> Yong-qing Lu,<sup>1,2</sup> Yi-xian Cun,<sup>1,2</sup> Chao-hui Li,<sup>1,2,3</sup> Kun Guo,<sup>1,2,3</sup> Wen-hui Nie,<sup>1</sup> Lei Li,<sup>4</sup> Rugang Zhang,<sup>5</sup> and Ping Zheng<sup>1,2,\*</sup>

<sup>1</sup>State Key Laboratory of Genetic Resources and Evolution, Kunming Institute of Zoology, Chinese Academy of Sciences, Kunming, Yunnan 650223, China

<sup>2</sup>Yunnan Key Laboratory of Animal Reproduction, Kunming Institute of Zoology, Chinese Academy of Sciences, Kunming, Yunnan 650223, China

<sup>3</sup>Kunming College of Life Science, University of Chinese Academy of Sciences, Kunming 650204, China

<sup>4</sup>State Key Laboratory of Reproductive Biology, Institute of Zoology, Chinese Academy of Sciences, Beijing, 100101, China

<sup>5</sup>Gene Expression and Regulation Program, The Wistar Institute Cancer Center, The Wistar Institute, Philadelphia, PA 19104, USA

\*Correspondence: [zhengp@mail.kiz.ac.cn](mailto:zhengp@mail.kiz.ac.cn)

<http://dx.doi.org/10.1016/j.stem.2015.03.017>

## SUMMARY

Pluripotent stem cells (PSCs) hold great promise in cell-based therapy, but the genomic instability seen in culture hampers their full application. A greater understanding of the factors that regulate genomic stability in PSCs could help address this issue. Here we describe the identification of Filia as a specific regulator of genomic stability in mouse embryonic stem cells (ESCs). Filia expression is induced by genotoxic stress. Filia promotes centrosome integrity and regulates the DNA damage response (DDR) through multiple pathways, including DDR signaling, cell-cycle checkpoints and damage repair, ESC differentiation, and apoptosis. Filia depletion causes ESC genomic instability, induces resistance to apoptosis, and promotes malignant transformation. As part of its role in DDR, Filia interacts with PARP1 and stimulates its enzymatic activity. Filia also constitutively resides on centrosomes and translocates to DNA damage sites and mitochondria, consistent with its multifaceted roles in regulating centrosome integrity, damage repair, and apoptosis.

## INTRODUCTION

Pluripotent stem cells (PSCs) hold great potential for cell-based regenerative medicine. However, genomic instability and tumorigenicity limit their full applications. Understanding the mechanisms that regulate their genome stability is critical to address this issue. These mechanistic insights are also important to understand how pluripotent cells (e.g., germ cells and early embryos) sustain their genome integrity to ensure the successful development of an organism. Pluripotent cells are capable of developing into all cell types, whereas somatic cells are cell fate-restricted. Accordingly, pluripotent cells possess a higher competence than somatic cells to protect their genetic integrity.

DNA damage response (DDR) is a fundamental and evolutionarily conserved mechanism to preserve the genomic integrity of cells (Behrens et al., 2014; Jackson and Bartek, 2009). Upon DNA damage triggered by endogenous or exogenous insults, cells elicit complicated and highly coordinated response networks, including damage sensing and signal transduction, which trigger cell-cycle arrest and DNA repair. When the extent of DNA damage is beyond repairable, cells undergo apoptosis or senescence to prevent the passage of the mutations to descendent cell populations. These responses are coordinated at multiple levels of gene regulation, including at the transcriptional, post-transcriptional, translational, and post-translational levels. Recent advances have further extended our understanding of the DDR by documenting cytoplasmic Golgi dispersal as a novel component of the DDR network (Farber-Katz et al., 2014). Because of the importance of DDR in genomic stability, its dysfunction is closely associated with genetic diseases, tumorigenicity, and tissue aging (Bartkova et al., 2005; Liang et al., 2009; Rass et al., 2007). DDR has been studied intensively in somatic cells, and many key players have been identified. Compared with somatic cells, very few studies have been conducted in pluripotent cells regarding their DDR network components. Limited reports have suggested that PSCs employed distinct strategies to cope with DNA damage (Wyles et al., 2014). For instance, mouse embryonic stem cells (ESCs) bypass the G1/S cell-cycle checkpoint because of an extremely short G1 phase (van der Laan et al., 2013). Instead, intra-S and G2 cell-cycle checkpoints are critical for ESCs (Momčilović et al., 2011). PSCs predominantly employ error-free homolog recombination (HR) rather than the error-prone non-homologous end joining (NHEJ) pathway to repair DNA double-strand break (DSB) (Tichy et al., 2010). Moreover, PSCs utilize high mitochondrial priming and retention of constitutively active Bax at the Golgi to sensitize them to DNA damage (Dumitru et al., 2012; Liu et al., 2013). Although it is appreciated that DDR regulation in PSCs is distinct from that in somatic cells, the key players and their functional mechanisms remain unknown. In particular, PSC-specific DDR factors have never been identified.

*Filia* (official name, KH domain containing 3; also known as *Ecat1*) was first identified in mouse embryonic stem cells

(mESCs) (Mitsui et al., 2003). Its expression is restricted to undifferentiated ESCs. Later studies reported its expression in growing oocytes and identified two transcriptional isoforms. The long isoform (~1.6 kb) encodes a ~70 kDa protein and is predominantly expressed in ESCs, while the short isoform (~1.2 kb), encoding a ~50 kDa protein, is primarily detected in growing oocytes (Ohsugi et al., 2008). Functional analysis revealed that *Filia* is not essential for ESC self-renewal (Mitsui et al., 2003), whereas depletion of maternal *Filia* protein in oocytes led to severe aneuploidy in cleavage stage embryos (Zheng and Dean, 2009). Here we report *Filia* acts as a mESC-specific regulator of DDR and safeguards genomic stability.

## RESULTS

### Loss of *Filia* Causes Genomic Instability and Promotes Malignant Transformation of mESCs

To investigate the role of *Filia* in regulating genomic stability of mESCs, we derived three *Filia*<sup>-/-</sup> ESC lines—FK(I), FK(II), and FK(III)—and two wild-type (WT) counterparts from *Filia*-targeted mutant mice (Zheng and Dean, 2009). The success rates of ESC derivation did not differ between mutant and WT blastocysts (33.3%, [2 of 6] in WT versus 25% [3 of 12] in the *Filia* mutant), indicating that *Filia* is not required for the derivation of ESCs. Consistent with previous studies (Mitsui et al., 2003), loss of *Filia* did not impair the self-renewal of ESCs. FK ESCs displayed a comparable morphology, expression of pluripotency markers, alkaline phosphatase staining, formation of embryonic bodies, cell-cycle profiles, and growth competition ability compared with WT cells (Figures S1A–S1C). No overt morphological abnormality was observed in FK ESCs after 100 passages.

However, cytogenetic analysis of chromosome metaphase spreads revealed that FK ESCs exhibited severe chromosome abnormalities, including chromosome breaks (Figures 1A and 1B), fusion of chromosome ends (Figures 1A, 1C, and 1D), and sister chromatid exchange (SCE) (Figure 1E). Consistently, FK ESCs displayed a higher rate of chromosomal anaphase bridges (Figures 1B and 1F) and an increase in DNA damage markers such as  $\gamma$ H2AX accumulation and focus formation (Figures 1G and 1H). The increase in DNA damage in FK ESCs was further validated by comet assay, a method that measures the extent of DNA damage on a single-cell basis (Figure 1I). Moreover, FK ESCs had high incidences of abnormal centrosomes, spindle assembly (Figure 1J), and aneuploidy (Figures S1D and S1E). These phenotypes were reproducibly observed in another ESC line with a distinct genetic background in which *Filia* expression was knocked down by an inducible short hairpin RNA (shRNA) (Figures S2A–S2E), indicating they are not genetic background-specific.

Genomic instability is known to promote cell transformation and tumorigenesis. Accordingly, we assessed the tumorigenicity of FK ESCs by injecting the unlabeled FK and GFP-labeled WT ESCs into the right or left testis of the same non-obese diabetic (NOD)/severe combined immunodeficiency (SCID) mouse. Teratomas formed by FK ESCs (GFP<sup>-</sup>) weighed more than those formed by WT ESCs (GFP<sup>+</sup>) (Figures 1K–1M). Furthermore, aggressive tumors lacking GFP expression were detected in the pancreas (Figure 1N), suggesting that they were formed by FK ESCs. Consistently, FK ESCs showed a delay in differen-

tiation (Figure S1F). Therefore, we conclude that loss of *Filia* causes genomic instability and promotes tumorigenesis.

### *Filia* Is Induced by Genotoxic Insults and Is Required for Activation of ATM and Chk2

Because FK ESCs displayed a severe DNA damage phenotype under normal culture conditions, we sought to determine whether *Filia* regulates DDR. Toward this goal, we investigated whether *Filia* expression is regulated by genotoxic insults. Indeed, the 70-kDa *Filia* was upregulated by DNA-damaging agents such as UV light, etoposide, doxorubicin, camptothecin, and hydroxyl urea (Nagy and Soutoglou, 2009; Figure 2A). The 50-kDa isoform was not detected in ESCs (Figure S3A). The expression and upregulation of *Filia* was specific to ESCs; mouse embryonic fibroblasts (MEFs) and mesenchymal stem cells (MSCs) did not express *Filia* in either the untreated or treated condition (Figure S3B).

We then systematically investigated the effects of *Filia* loss on major DDR signaling components, including  $\gamma$ H2AX, ATM, ATR, Chk1, Chk2, and p53. Upon etoposide treatment,  $\gamma$ H2AX, p-ATM, p-ATR, p-Chk1, and p-Chk2 were induced and sustained for at least 12 hr in WT ESCs (Figure 2B). In contrast,  $\gamma$ H2AX and p-ATM were initially induced at comparable levels in FK and WT ESCs but failed to sustain in FK cells (Figure 2B; Figure S3C). Strikingly, Chk2, one of the key substrates of ATM, was not phosphorylated at all in FK ESCs (Figure 2B). This suggests that *Filia* participates in the Chk2 activation via mechanisms independent of ATM. Unlike the ATM-Chk2 signaling axis, ATR and Chk1 kinases were not significantly affected by *Filia* loss (Figure 2B; Figure S3D). ATM/Chk2 regulates p53 activity. Consistently, phosphorylation of p53 at its S15 and S20 was impaired in FK ESCs compared with WT ESCs (Figure 2B). To further define the domain necessary for regulating the signal transduction, we stably expressed full-length *Filia*, a *Filia* fragment containing amino acids (aas) 1–340, or hnRNP K homology (KH) domain (atypical RNA-binding domain) containing aas 1–125, in FK ESCs (FK-*Filia*, FK-340, and FK-KH rescue cells, respectively) (Figures S3A, S3E, and S3F). The induction of  $\gamma$ H2AX, p-ATM, p-Chk2, and p-p53 were restored in FK-*Filia* and FK-340 (Figure 2B) but not in FK-KH cells (Figure S3G). These data revealed that the C terminus of *Filia* (aas 341–440) was dispensable for DDR signaling. Moreover, these functions were independent of the genetic background based on shRNA knockdown ESCs, as described above (Figure S2A).

In somatic cells, ATM and Chk2 activation exhibited pulsatile dynamics in response to DNA damage. Recurrent initiation of ATM/Chk2 activation is an important mechanism to sustain DDR (Batchelor et al., 2008). To better understand the dynamics of ATM/Chk2 activation in ESCs and the influence of *Filia* loss on ATM and Chk2 activation, we conducted a detailed time course analysis. WT ESCs displayed two waves of ATM activation. *Filia* loss did not affect the initial ATM activation between 1–4 hr post-damage but completely abolished ATM activity thereafter (Figure 2C). This suggests that distinct mechanisms regulate two phases of ATM activation, with the second phase relying on *Filia*. Unlike ATM, Chk2 activation did not exhibit discrete phases in ESCs. Moreover, *Filia* loss completely blocked Chk2 activation (Figure 2C), implying that *Filia* is necessary for Chk2 activation.

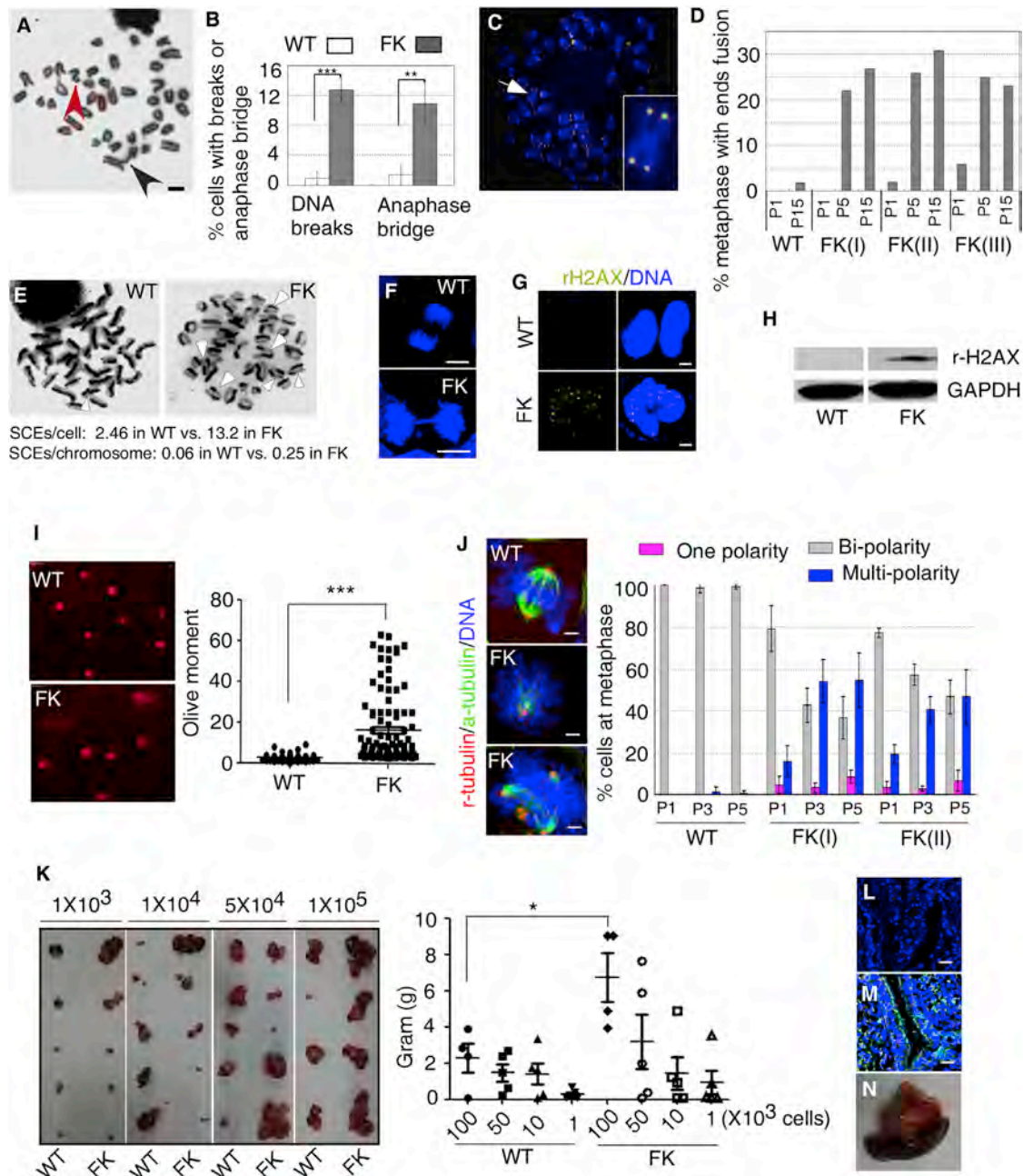


**Figure 1. Fila Maintains Genomic Stability and Prevents Malignant Transformation of ESCs**

(A) Metaphase chromosome spread of FK ESCs. Arrowheads indicate chromosome breaks (red) and chromosome end fusion (black).  
 (B) Frequencies of chromosome breaks and anaphase bridges in WT and FK ESCs. More than 200 cells were examined in each sample.  
 (C) Chromosome end fusion detected by T-FISH.  
 (D) Frequencies of metaphase with chromosome end fusion in WT and FK ESCs. More than 100 metaphase spreads were examined in each sample. P, passage.  
 (E) SCE (arrowheads) in WT and FK ESCs. 50 cells were examined in each group.  
 (F) Anaphase bridges in FK ESCs.  
 (G)  $\gamma$ H2AX foci in WT and FK ESCs.  
 (H)  $\gamma$ H2AX accumulation in WT and FK cells detected by immunoblotting.  
 (I) Comet assay showing that FK ESCs had severe DNA damage.  
 (J) Centrosomes in FK and WT ESCs at P3 and P5. More than 200 cells were examined in each of the indicated groups.  
 (K) Teratomas formed from FK ESCs were bigger and weighed more than those from WT ESCs injected at different concentrations.  
 (L) Teratoma tissue formed by FK ESCs that were GFP-negative.  
 (M) Teratoma tissue formed by GFP-labeled WT ESCs.  
 (N) FK ESC formed tumors in the pancreas.

Data are represented as mean  $\pm$  SEM. Scale bars, 10  $\mu$ m. \* $p$  < 0.05, \*\* $p$  < 0.01, \*\*\* $p$  < 0.001. See also Figures S1 and S2.



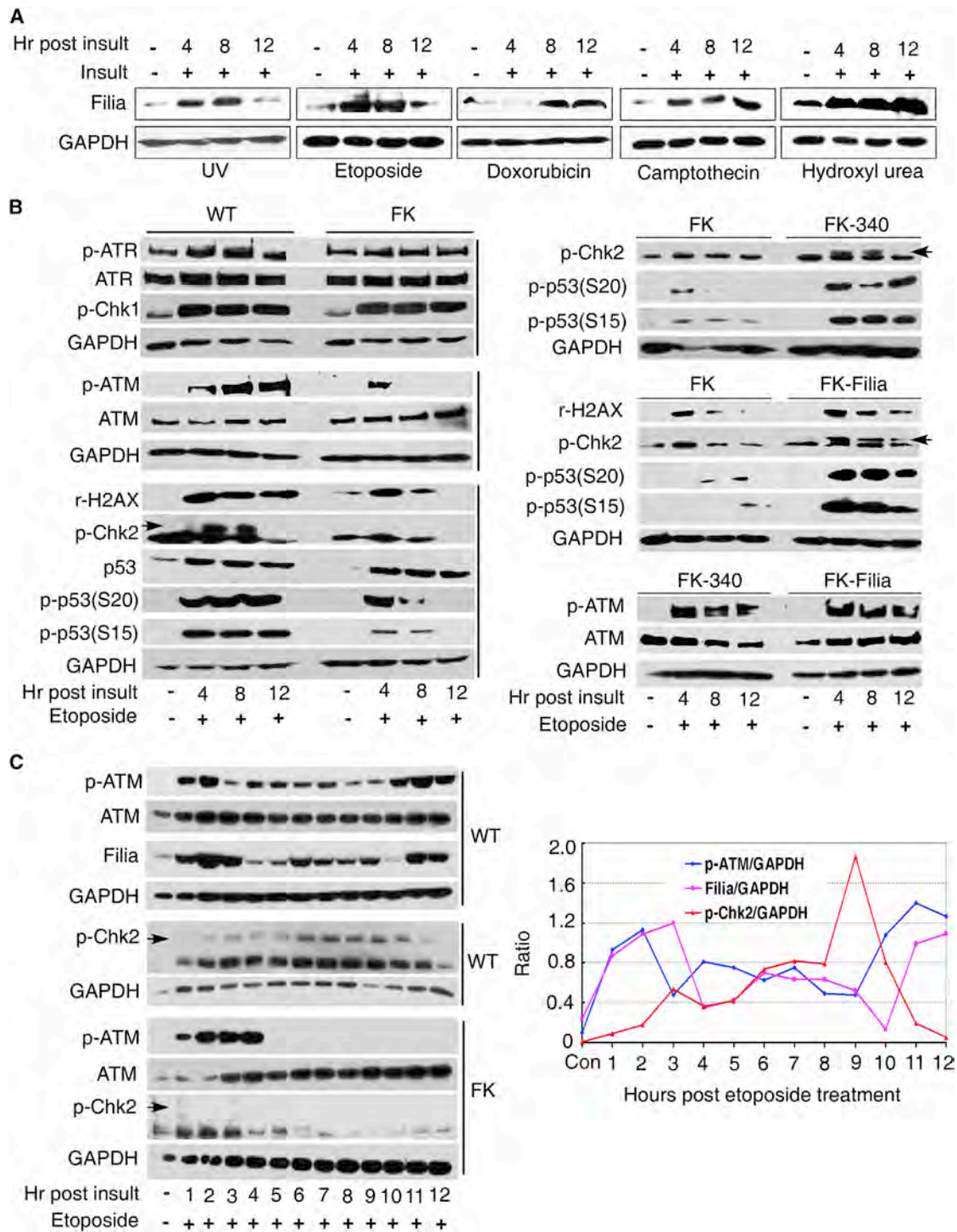


**Figure 2. Filia Regulates DNA Damage Signaling**

(A) Filia protein expression was upregulated by genotoxic insults.

(B) The induction of  $\gamma$ H2AX, p-ATM, p-Chk2, and p-p53 was compromised in FK ESCs, whereas p-ATR or p-Chk1 was not affected. Re-expression of Filia or Filia340 successfully rescued the defects.

(C) Detailed time course analysis of p-ATM, p-Chk2, and Filia expression in WT and FK ESCs treated with etoposide. Arrows indicate p-Chk2.

See also Figures S2 and S3.

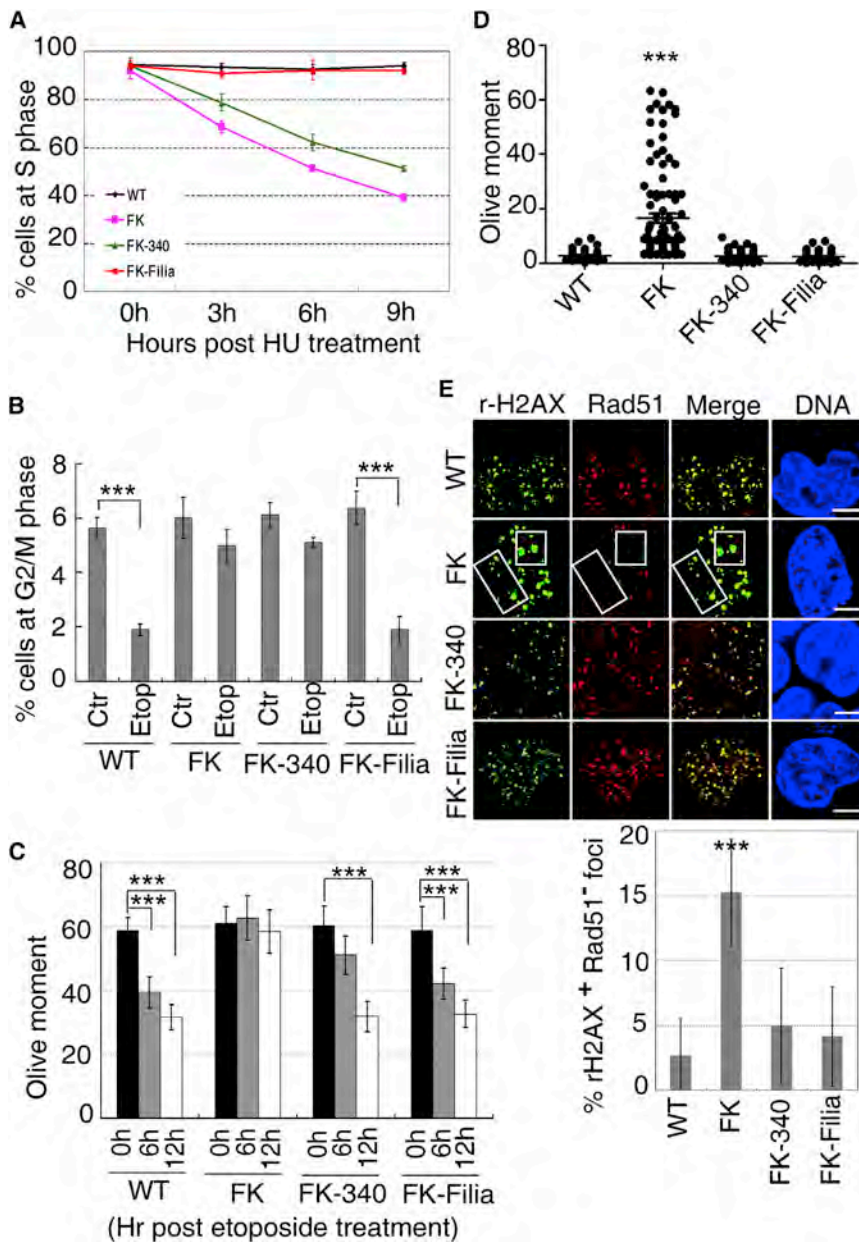


**Figure 3. Fila Is Necessary for Cell Cycle Checkpoints and DNA Damage Repair**

(A) The S phase checkpoint was functional in WT and FK-Filia rescue ESCs but failed in FK and FK-340 cells. HU, hydroxyl urea.

(B) Similarly, FK ESCs lost the G2 checkpoint, which was restored in FK-Filia but not FK-340 ESCs. Ctr, control. Etop, etoposide.

(C) WT, FK-Filia, and FK-340 ESCs could repair DNA damage induced by etoposide treatment whereas FK ESCs could not.

(D) DNA integrity assessment of WT, FK, FK-340, and FK-Filia ESCs by comet assay showed persistent DNA breaks in FK ESCs.

(E) Rad51 was recruited to DSB sites in WT, FK-340, and FK-Filia ESCs upon DNA damage. However, its recruitment was compromised in FK ESCs. Squares indicate examples of  $\gamma$ H2AX<sup>+</sup> Rad51<sup>+</sup> foci. 50 cells were examined in each sample.

Data are represented as mean  $\pm$  SEM. Scale bars, 10  $\mu$ m. \*\*\* $p$  < 0.001. See also Figure S3.

et al., 2000). ATM is critical for both G2/M checkpoint and DNA repair in ESCs (Momcilović et al., 2009; Yamamoto et al., 2012). Cell-cycle analysis revealed that the S and G2/M checkpoints were impaired in FK ESCs, which could be rescued by Fila (Figures 3A and 3B). Intriguingly, expression of Fila340 failed to restore cell-cycle checkpoints despite its ability to rescue DDR signaling (Figures 3A and 3B). Therefore, cell-cycle checkpoint defects in FK ESCs were not simply a consequence of DDR signaling failure. Rather, Fila itself participated in the regulation of cell-cycle checkpoints, and this function required its C terminus (aas 341–440).

ATM activation is essential for DNA damage repair (Yamamoto et al., 2012). To investigate whether Fila loss impairs DNA damage repair, we performed a comet assay to evaluate the repair

competence in WT, FK, FK-Filia, and FK-340 rescue ESCs. ESCs were treated with etoposide, and the extent of DNA damage was evaluated after 0 hr, 6 hr and 12 hr of recovery. Notably, WT, FK-Filia, and FK-340 cells displayed a similar competence in DNA damage repair, whereas FK cells exhibited an impairment in damage repair (Figure 3C). Although Fila340 was less efficient than Fila at 6 hr, this difference disappeared at 12 hr post-recovery (Figure 3C). Consistently, FK-Filia and FK-340 ESCs showed similarly mild DNA damage compared with WT cells (Figure 3D), supporting the notion that re-introduction of Fila or Fila340 into FK ESCs is sufficient to restore DNA damage repair. Rad51 is a key protein involved in HR-mediated DSB repair. In WT as well as in FK-Filia and FK-340 rescue ESCs treated with etoposide, most  $\gamma$ H2AX foci were co-localized with the Rad51 foci when examined 12 hr post-damage (Figure 3E). However, in FK

Of interest, Fila expression exhibited a similar oscillation pattern as ATM activation in WT ESCs (Figure 2C). To further explore the relationships among Fila, ATM, and Chk2, we inhibited ATM kinase activity using a specific ATM inhibitor, KU55933, and examined Fila expression and Chk2 activation. Inhibition of ATM activity did not affect Fila expression but impaired Chk2 activation (Figure S3H). These data suggest that Fila functions upstream of ATM in DDR.

### Fila Regulates Cell Cycle Checkpoints and DNA Damage Repair

Cell-cycle checkpoint and DNA repair rely on DDR signaling (Branzei and Foiani, 2008). For instance, Chk1 is required for initiation of the G2/M checkpoint in mESCs (Liu et al., 2000), and Chk2 is required for the maintenance of G2/M arrest (Hirao

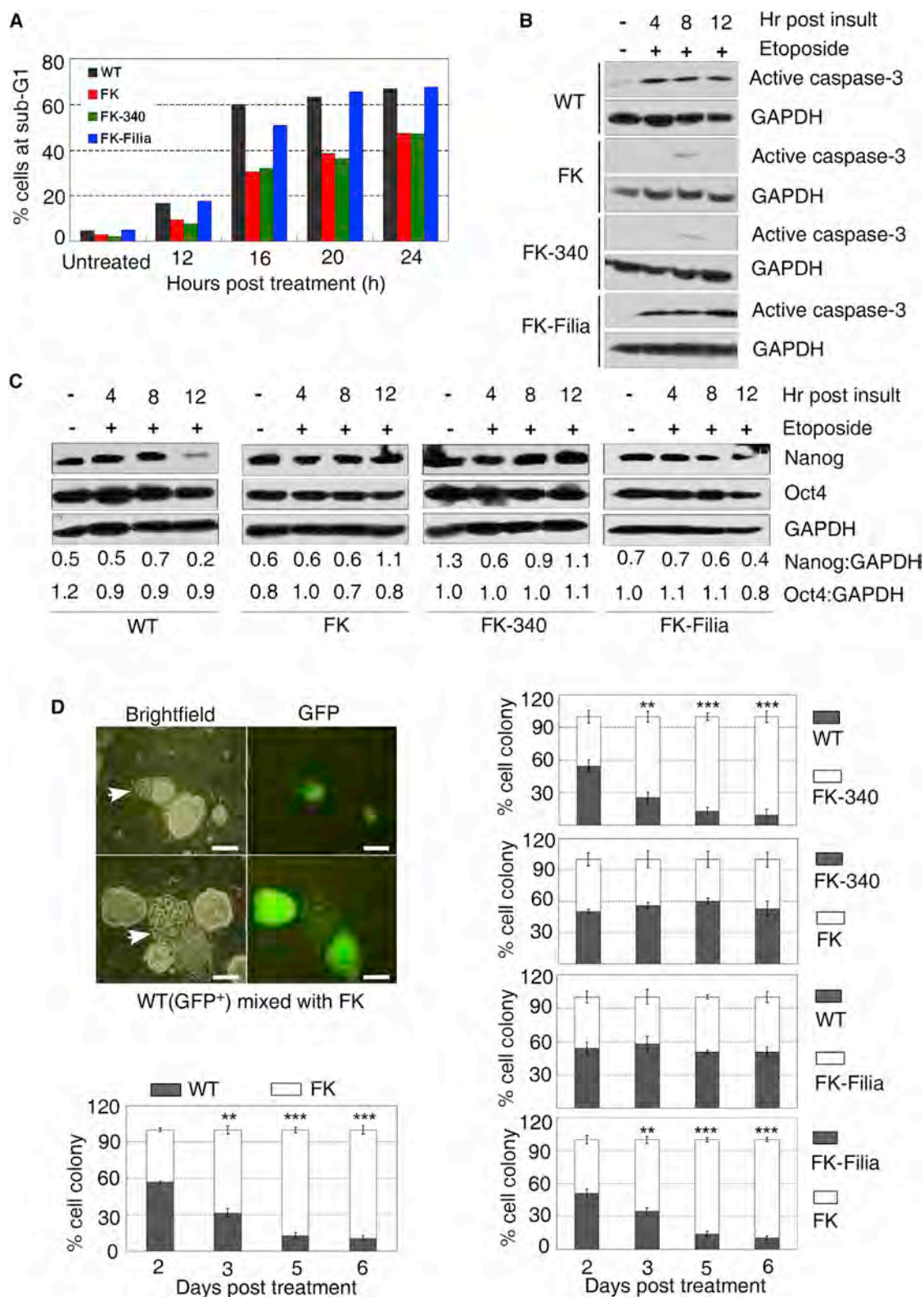


**Figure 4. Filia Is Required for ESCs to Undergo Differentiation and Apoptosis in Response to DNA Damage**

(A) FACS analysis showed that a higher proportion of WT and FK-Filia ESCs were at sub-G1 phase, indicative of cell death after etoposide treatment.

(B) WT and FK-Filia ESCs expressed more active caspase-3 than FK and FK-340 ESCs in response to etoposide treatment.

(legend continued on next page)



ESCs, the number and size of Rad51 foci decreased, and there were a significant number of  $\gamma$ H2AX foci lacking co-localized Rad51 (Figure 3E). Notably, the recruitment of active DNA-PKcs to DNA damage sites, a marker of NHEJ-mediated DSB repair (Davis et al., 2014), was not affected by Filia loss (Figure S3I). This suggests that Filia depletion preferentially impairs HR-mediated DSB repair. Rad51 protein was expressed at comparable levels in WT, FK, FK-340 or FK-Filia ESCs (Figure S3J), implying that Filia facilitates the efficient recruitment of Rad51 to the damage sites. It is intriguing that Filia340-rescued cells are capable of repairing DNA damage despite the lack of cell-cycle checkpoints. This suggests that cell-cycle arrest is not a prerequisite for DNA damage repair and that the two processes are regulated independently.

### Filia Regulates Differentiation and Apoptosis of ESCs in Response to DNA Damage

Elimination of cells with irreparable DNA damage is the last and most critical safeguarding event in DDR. Stem cells display hypersensitivity to DNA damage (Dumitru et al., 2012; Liu et al., 2013) and are primed to undergo rapid differentiation and apoptosis to ensure genome stability (Inomata et al., 2009; Lin et al., 2005). FK ESCs did not encounter culture crisis despite accumulated spontaneous DNA damage, suggesting that hypersensitivity to DNA damage is impaired in these cells. To test this hypothesis, we treated the ESCs with etoposide and investigated the dynamics of differentiation and apoptosis. Sub-G1 apoptotic cell analysis revealed that FK ESCs were more resistant to cell death than WT ESCs (Figure 4A). Consistently, there was a decrease of cleaved caspase-3, a critical executioner and marker of apoptosis, in FK compared with WT ESCs (Figure 4B). This phenotype was rescued by Filia but not Filia340 (Figures 4A and 4B). This result indicates that the C terminus of Filia (aas 341–440) was necessary for this function. ESC differentiation is triggered by transactivation of p53 that binds to the enhancer region of *Nanog* to suppress its expression (Li et al., 2012; Lin et al., 2005). Consistently, *Nanog*, but not *Oct4*, displayed significant downregulation 12 hr after damage in WT and FK-Filia ESCs but not in FK or FK-340 cells (Figure 4C).

To more comprehensively evaluate the functional outcome of Filia loss on cell survival in response to DNA damage, we performed a clonal competition assay in which same numbers of two types of ESCs were mixed, exposed to DNA damage, and co-cultured for 6 days. To distinguish the two mixed cell types, one was labeled with GFP expression. Compared with WT ESCs, FK cells showed a higher survival rate (Figure 4D). Furthermore, WT, but not FK ESCs, displayed a flattened morphology indicative of ESC differentiation (Figure 4D). Consistently, expression of Filia, but not Filia340, in FK ESCs restored their hypersensitivity to DNA damage (Figure 4D). Therefore, Filia plays a critical role in ensuring ESCs' hypersensitivity to DNA damage, and this depends on its C terminus.

### Phosphorylation of Serine 349 Is Required for Filia Function in DNA Damage Repair

Our data suggest that Filia, akin to p53 in somatic cells, functions in two opposite aspects of DDR in ESCs. It is required for DNA repair, which enables cells to survive the damage. It is also essential for damaged cells to undergo differentiation and apoptosis. Phosphorylation often correlates with a change in protein functions. There is evidence to suggest that the S349 residue on Filia is subjected to phosphorylation in response to DNA damage (Pines et al., 2011). Therefore, we investigated whether S349 was indeed phosphorylated and whether this modification played a role in modulating Filia's functions. Accordingly, we mutated S349 into alanine (S349A) that can no longer be phosphorylated and stably expressed this mutant in FK ESCs (FK-S349A) (Figure S4A). FiliaS349A protein rescued the observed defects in DDR signaling (Figure S4B) and intra-S and G2/M cell-cycle checkpoints in FK ESCs (Figures S4C and S4D). However, it failed to restore DNA repair, as demonstrated by the comet assay under normal and etoposide-treated conditions (Figures 5A and 5B). Consistently, FiliaS349A failed to rescue Rad51 recruitment to damage sites (Figure S4E). As a result, FK-S349A ESCs were more sensitive to DNA damage and prone to undergo apoptosis compared with WT ESCs (Figures 5C–5E). Consequently, these cells could not be maintained in culture for more than 12 passages. To further validate the phosphorylation of S349, we generated a polyclonal antibody that specifically recognizes the phosphorylated Filia at S349 (p-Filia(S349)). Immunoblotting revealed a specific, ~70-kDa band that displayed increasing intensity in response to DNA damage in WT but not FK-S349A ESCs (Figure 5F). Together, these data indicate that the S349 residue of Filia is phosphorylated in response to DNA damage and that this modification is essential for Filia's function in DNA damage repair. Moreover, S349 is not a substrate of ATM; suppressing ATM kinase activity with KU55933 does not affect S349 phosphorylation (Figure S3H).

To further explore the biological significance of S349 phosphorylation, we substituted serine with aspartic acid to mimic its phosphorylation and stably expressed FiliaS349D in FK ESCs (FK-S349D rescue cells; Figure S4A). FiliaS349D restored DDR signaling (Figure S4B) and cell-cycle checkpoints (Figures S4C and S4D) but failed to rescue the damage repair (Figures 5A and 5B; Figure S4E). Surprisingly, S349D severely impaired Filia's ability in regulating apoptosis, which correlates with a hyper-tolerance of FK-S349D cells to DNA damage compared with either WT or FK ESCs (Figures 5D, 5G, and 5H). Together, these data support the notion that S349 phosphorylation is required for DNA repair, whereas the non-phosphorylation status might be critical for Filia's pro-apoptotic function.

### Filia Dynamically Translocates to Different Sub-Cellular Sites in Response to DNA Damage

We next examined Filia's sub-cellular localization under normal and DNA damage conditions. 3xFLAG-tagged Filia, Filia340,

(C) *Nanog* was downregulated in WT and FK-Filia but not in FK or FK-340 ESCs after DNA damage.

(D) Clonal competition assay revealed that FK ESCs were less sensitive to DNA damage than WT ESCs. Re-expression of Filia, but not Filia340, restored their sensitivity to DNA damage. Shown are representative images of mixtures of WT (GFP<sup>+</sup>) and FK ESC clones. Note that WT ESC clones (white arrow) initiated differentiation. Data are represented as mean  $\pm$  SEM. \*\*p < 0.01, \*\*\*p < 0.001.



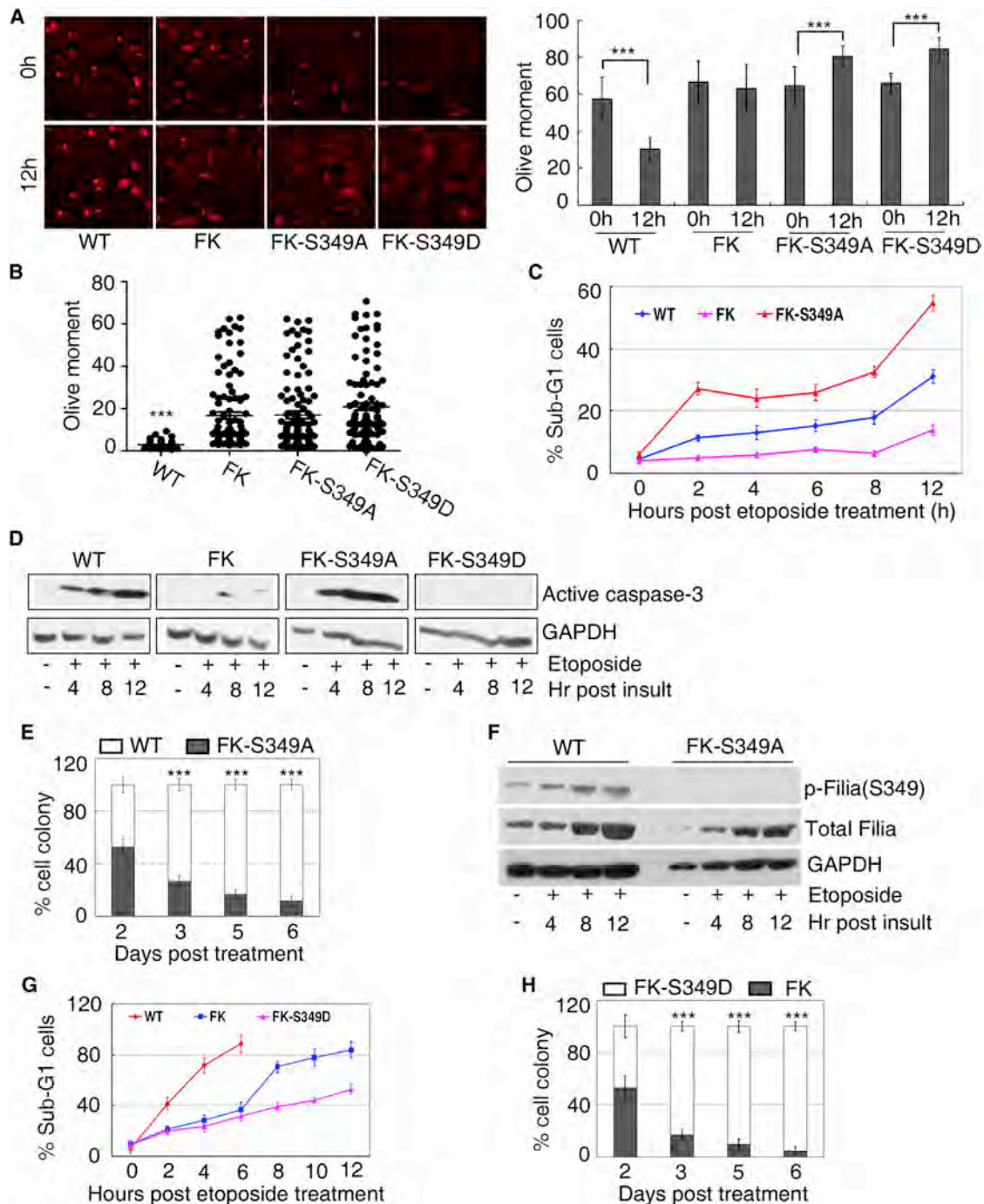


**Figure 5. S349 Is Phosphorylated to Modulate Filia's Role in DNA Damage Repair**

(A) After etoposide treatment, WT ESCs were more efficient to repair DNA damage than FK, FK-S349A, and FK-S349D ESCs.

(B) Consistently, untreated FK, FK-S349A, and FK-S349D ESCs had severe DNA damage compared with WT ESCs.

(C) Higher proportion of FK-S349A ESCs were dead compared with WT and FK ESCs after etoposide treatment.

(D) Consistently, FK-S349A ESCs expressed more active caspase-3 than WT, FK, and FK-S349D ESCs.

(E) A clonal competition assay confirmed that FK-S349A ESCs had superior sensitivity to DNA damage than WT cells.

(F) Immunoblotting with antibody specifically recognizing phosphorylated S349 in Filia validated this phosphorylation modification. Note that the phosphorylation level was upregulated by DNA damage.

(G) Sub-G1 analysis indicated that FK-S349D ESCs were more resistant to apoptosis.

(H) A clonal competition analysis further confirmed the higher tolerance of FK-S349D ESCs to DNA damage than FK ESCs.

Data are represented as mean  $\pm$  SEM. \*\*\* $p$  < 0.001. See also Figures S3 and S4.

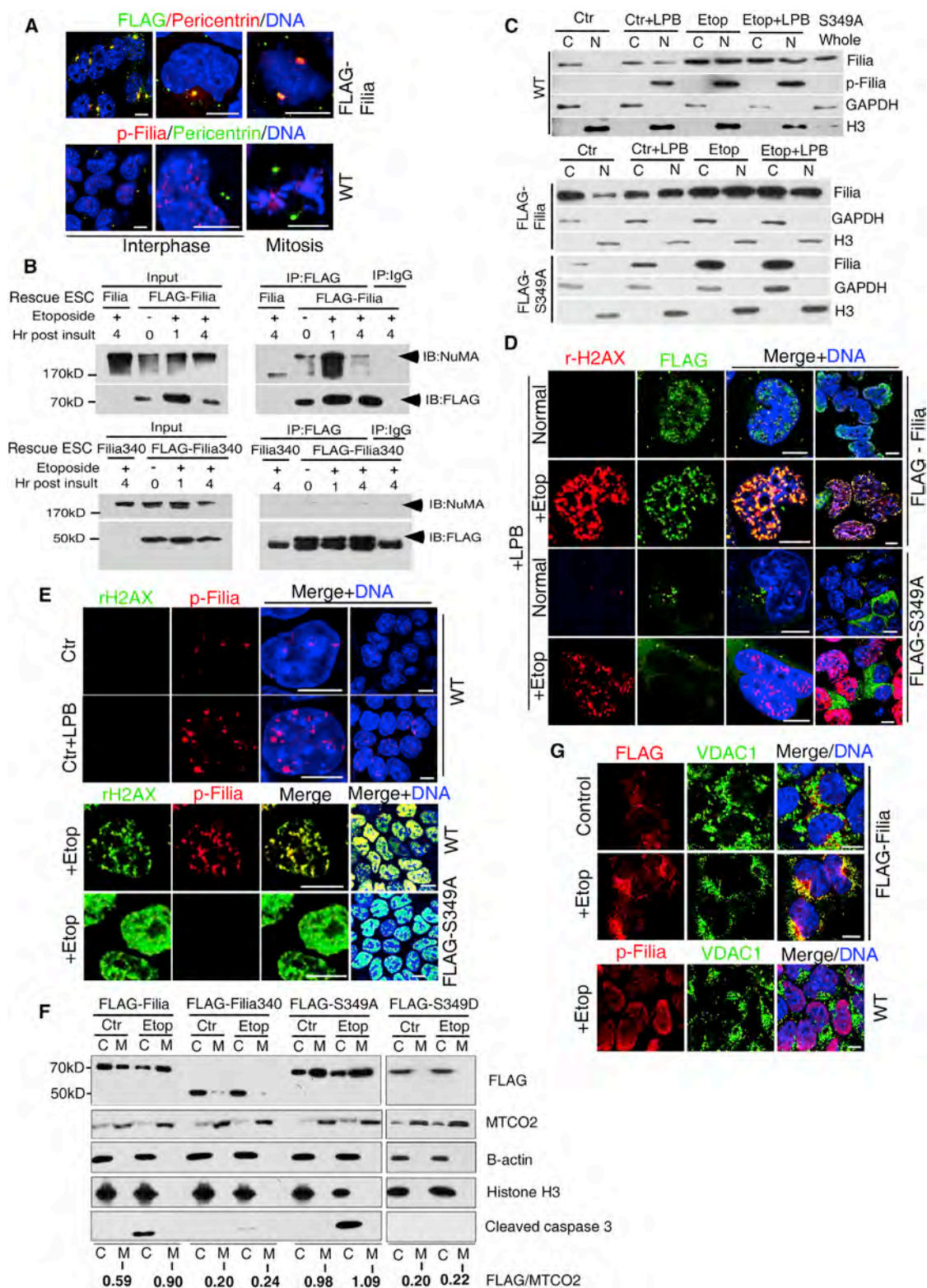


**Figure 6. Filia Constitutively Localizes on Centrosomes and DNA Damage Stimulates Its Translocation to Damage Sites or Mitochondria**  
(A) Constitutive localization of Filia, but not p-Filia(S349), on centrosomes labeled by pericentrin.  
(B) Immunoprecipitation (IP) combined with immunoblotting (IB) confirmed the interaction of Filia or Filia340 with Numa.

(legend continued on next page)

FiliaS349A, or FiliaS349D were stably expressed in FK ESCs. Immunostaining revealed that Filia is primarily located in cytoplasm regardless of cell-cycle or genotoxic damage (Figure S5A). Centrosomes are considered as command centers for cellular control and are known to integrate cell-cycle regulation and DNA repair (Doxsey et al., 2005; Löffler et al., 2006; Shimada and Komatsu, 2009). To examine whether Filia is localized on centrosomes, we extracted free cytosolic Filia and co-stained FLAG-tagged Filia with pericentrin and  $\gamma$ -tubulin, two integral components of pericentriolar material. Filia accumulated on centrosomes at interphase and mitotic phase (Figure 6A; Figure S5B) under normal conditions. DNA damage did not enhance the centrosomal accumulation of Filia (Figure S5B), suggesting that this localization was constitutive. Centrosomal localization was also observed for Filia340, FiliaS349A, and FiliaS349D (Figure S5C). However, p-Filia(S349) did not localize to the centrosome (Figure 6A). Interestingly, Chk2 resides on centrosomes of mESCs (Hong and Stambrook, 2004). p-ATM was also detected on centrosomes of WT and rescue ESCs but not FK cells (Figure S5D). These findings suggest that centrosome-localized Filia may play a role in regulating ATM, Chk2, and cell-cycle checkpoints.

The constitutive centrosomal localization of Filia implied a role in regulating centrosome integrity. Centrosomes in FK ESCs were abnormal (Figure 1J). This could be a consequence of DNA damage (Bourke et al., 2007; Löffler et al., 2013). To exclude this possibility, we examined the centrosome integrity of FK-Filia, FK-Filia340, FK-S349A, and FK-S349D rescue ESCs. Notably, all examined ESCs displayed grossly normal centrosomes and spindle assemblies (Figure S5E), despite the fact that sustained DNA damage was observed in FK-S349A and FK-S349D ESCs (Figure 5B). This observation excluded the causal relationship of DNA damage and centrosome defects observed in FK ESCs. Rather, it suggests that Filia itself plays a direct role in maintaining centrosome integrity. Indeed, co-immunoprecipitation combined with mass spectrometry identified Numa, a critical regulator of spindle pore integrity (Silk et al., 2009; Zeng, 2000), as an interacting protein of Filia on the centrosome (Figure 6B). The C terminus of Filia (aas 341–440) contributes to this interaction because there was an impairment of interaction between Numa and Filia340 compared with full-length Filia (Figure 6B).

In addition to the cytoplasmic distribution, there was a small amount of Filia in nuclei, as determined by immunostaining and nucleus fractionation (Figure S5A; Figure 6C). To confirm the presence of nuclear Filia, we treated the WT and FLAG-Filia rescue ESCs with leptomycin B (LPB) to inhibit nuclear protein export (Alpatov et al., 2014; Tamanini et al., 1999). Nuclear local-

ization of Filia was clearly visible after LPB treatment (Figure 6D). Under normal conditions, Filia was diffused in the nucleus. DNA damage evoked an increase in both the abundance of nuclear Filia and its translocation to the damage sites, as labeled by  $\gamma$ H2AX (Figures 6C and 6D). Intriguingly, S-to-A mutation (FLAG-S349A cells) prevented the entry of Filia into nuclei regardless of DNA damage (Figures 6C and 6D), indicating that Filia S349 phosphorylation is required for its nuclear localization. Consistently, p-Filia(S349) was exclusively stained for nuclei of WT ESCs under normal conditions and co-localized with  $\gamma$ H2AX upon DNA damage (Figures 6C and 6E). Filia340 showed a similar nuclear distribution as full Filia (Figures S6A and S6B), which correlates with its ability to restore DNA repair. Intriguingly, FiliaS349D protein exhibited proper nuclear localization (Figures S6A and S6B) despite its inability to repair DNA damage.

We next determined whether Filia translocated to mitochondria upon apoptosis induction. Under normal conditions, a basal level of Filia was detected in mitochondria, as assayed by immunostaining and mitochondrial fractionation. Apoptosis induction with etoposide triggered a robust translocation of Filia into mitochondria (Figures 6F and 6G). Filia localization to mitochondria was compromised in Filia340 and FiliaS349D, whereas it was enhanced in FiliaS349A (Figure 6F; Figure S6C). These results support the notion that localization of Filia in mitochondria is necessary for its apoptosis-promoting role. They also implied that mitochondrial translocation of Filia requires its C terminus and S349 at the non-phosphorylated status. Consistently, p-Filia(S349) was not detected in mitochondria (Figure 6G).

### Filia Interacts with PARP1 and Stimulates Its Enzymatic Activity in DDR

To further explore the mechanistic basis by which Filia regulates DDR, we performed co-immunoprecipitation combined with mass spectrometry analysis. We identified PARP1 as one of Filia's interaction proteins (Figure 7A). PARP1 catalyzes the poly(ADP-ribosylation) (PARylation) of its target proteins and plays a key role in early DDR (De Vos et al., 2012; Krishnakumar and Kraus, 2010). The interaction between PARP1 and Filia was validated in NIH/3T3 cells ectopically expressing Filia (Figure 7B). The interaction between PARP1 and Filia is regulated, and it was enhanced by DNA damage (Figure 7A). Moreover, the interaction did not require the C terminus of Filia because Filia340 pulled down PARP1 efficiently (Figure 7A). Although these two proteins interact, there was no obvious co-localization between them. PARP1 was predominantly distributed in nuclei (Figure S7A), whereas the majority of Filia

(C) Nucleus fractionation documented the presence of Filia in the cytoplasm (C) and nucleus (N) of WT and FLAG-Filia rescued ESCs. However, FiliaS349A and p-Filia(S349) were exclusively detected in the cytoplasm and nucleus, respectively. LPB as well as etoposide treatment increased the nuclear accumulation of Filia and p-Filia. Whole lysates of FK-S349A ESCs were used as a control. Ctr, control. Etop, etoposide.

(D) Immunostaining revealed the nuclear localization of Filia but not FiliaS349A proteins. Etoposide treatment stimulated the recruitment of Filia to DNA damage sites labeled with  $\gamma$ H2AX.

(E) In WT ESCs, p-Filia(S349) was detected in the nucleus under normal and DNA damage conditions. Etoposide treatment increased the accumulation of p-Filia(S349) on DNA damage sites. FK-S349A cells served as a negative control.

(F) Mitochondria fractionation revealed the localization of Filia and FiliaS349A on mitochondria (M) marked by MTCO2. Apoptosis induction by etoposide treatment evoked their accumulation on mitochondria. However, little Filia340 or FiliaS349D protein was detected on mitochondria under normal or DNA damage conditions. C represents the fraction of whole-cell lysates depleted of mitochondria.

(G) Immunostaining confirmed the localization of Filia but not p-Filia(S349) on mitochondria marked with VDAC1.

Scale bars, 10  $\mu$ m. See also Figures S5 and S6.



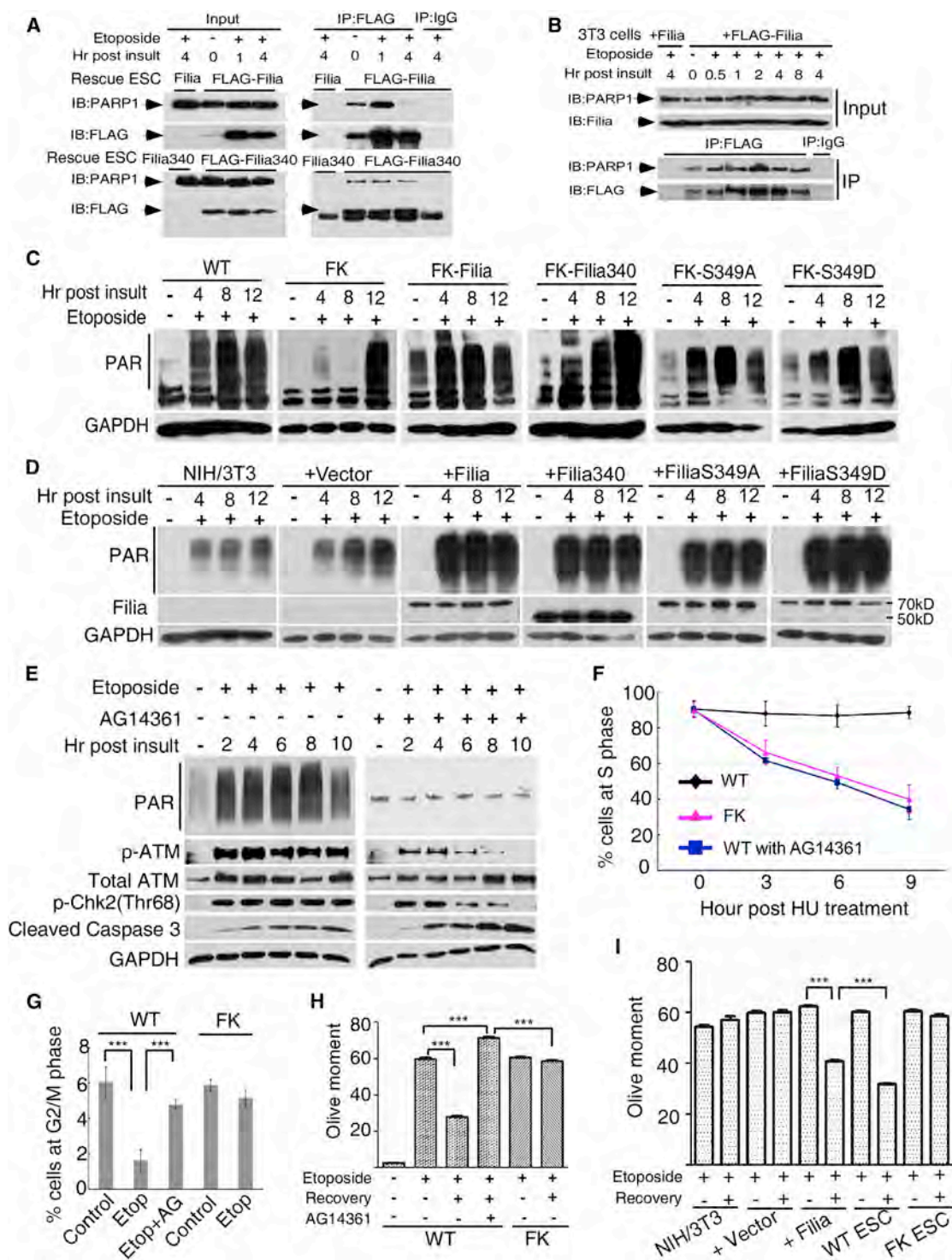


**Figure 7. Fila Interacts with PARP1 and Stimulates Its Enzymatic Activity Which Amplify Fila's Roles in DDR**

(A) Immunoprecipitation combined with immunoblotting confirmed the interaction of Fila or Fila340 with PARP1 in ESCs under normal or DNA damage conditions.

(B) Fila interacts with PARP1 in NIH/3T3 cells ectopically expressing Fila under normal or DNA damage conditions.

(C) FK ESCs had a much lower PAR level than WT ESCs. However, re-expression of Fila or its variants restored the PAR level.

(D) Similarly, ectopic expression of Fila or its variants in NIH/3T3 cells significantly increased the PAR level in response to DNA damage.

(E) Inhibition of PARP1 activity by AG14361 significantly attenuated ATM and Chk2 activation. Consequently, cells with deficient PARP1 activity were prone to undergo apoptosis.

(legend continued on next page)

was detected in the cytoplasm (Figure S5A). Unlike Filia (Figure 6D), PARP1 nuclear foci were typically not co-localized with  $\gamma$ H2AX foci induced by DNA damage (Figure S7A). These observations support the notion that the interaction between Filia and PARP1 is transient.

To determine whether PARP1 is responsible for PARylation in ESCs, we inhibited PARP1 enzymatic activity using a specific inhibitor, AG14361 (Calabrese et al., 2004; Figure S7B). Time course analysis revealed that inhibition of PARP1 completely abolished PARylation (Figure S7C), indicating that PARP1 plays a major role in regulating PARylation in ESCs. We next examined whether Filia regulates PARP1 activity by comparing PAR levels between WT and FK ESCs. In WT ESCs, PAR levels increased after etoposide treatment, whereas significantly less PAR was detected in untreated or etoposide-treated FK cells examined at 4 and 8 hr (Figure 7C). Therefore, Filia is necessary for robust PARP1 activation in response to DNA damage. Intriguingly, PARP1-dependent but Filia-independent PAR was elevated at 12 hr in FK cells (Figure 7C; Figure S7C). The Filia-independent PAR displayed abnormal accumulation at the nucleolus (Figure S7D), which is known as a storage site for PAR in DDR (Mortusewicz et al., 2007). Re-expression of Filia, Filia340, FiliaS349A, or FiliaS349D in FK ESCs efficiently restored PARP1 activity and PAR levels (Figure 7C). Importantly, differentiating ESCs and somatic cells have much less PAR compared with undifferentiated ESCs (Figures S7E and S7F). Ectopic expression of Filia and its variants in NIH/3T3 cells significantly increased PAR levels (Figure 7D). The majority of PAR was detected in nuclei of ESCs expressing Filia, Filia340, and FiliaS349D, whereas PAR was predominantly accumulated in the cytoplasm of FK-S349A rescue cells (Figure S7G). This is consistent with the cytoplasmic distribution of FiliaS349A. Notably, localization of Filia to DNA damage site did not rely on PAR modification (Figure S7H).

To determine whether PARP1 plays a role in mediating Filia function in DDR, we inhibited PARP1 activity using AG14361 and examined its effects on ATM and Chk2 activation, cell-cycle checkpoints, DNA damage repair, and apoptosis. Inhibition of PARP1 significantly attenuated, but did not completely block, ATM and Chk2 activation (Figure 7E). Notably, PARP1 inhibition caused the same extent of defects in cell-cycle checkpoints and DNA damage repair as Filia knockout (Figures 7F–7H). Consistently, ectopic expression of Filia in NIH/3T3 cells not only increased PAR levels (Figure 7D) but also enhanced DNA damage repair in these cells (Figure 7I). However, DNA damage-induced apoptosis was not impaired by PARP1 inhibition (Figure 7E). This suggests that PARP1 activity is not necessary for apoptosis induction. Together, these data support the notion that Filia interacts with PARP1 and activates its enzymatic activity in response to DNA damage, which contributes to the observed roles of Filia in regulating DDR signaling, cell-cycle checkpoints, and DNA damage repair.

## DISCUSSION

Compared with somatic cells, PSCs have superior competence and unique strategies to cope with DNA damage to maintain genomic integrity. In addition to using common proteins found in somatic cells with alternative strategies (Dumitru et al., 2012), PSCs possess unique proteins to safeguard their genome integrity (Zalzman et al., 2010). However, little is known regarding the PSC-specific factors in regulating genomic stability. Here we identify an ESC-specific protein, Filia, as a powerful regulator of genomic stability. Through its coordinated cytoplasmic and nuclear functions, Filia regulates centrosome integrity and DDR at multiple levels. These include DDR signal transduction, cell-cycle checkpoints, DNA damage repair, and apoptosis. Therefore, Filia depletion not only causes robust genomic instability but also impedes the elimination of damaged cells by ESC differentiation or apoptosis. This, in turn, increases the risk of transformation and tumorigenesis in ESCs. In somatic cells, p53 plays similar dual regulatory roles in DDR (Green and Kroemer, 2009). However, these well established roles of p53 are not evident in mESCs (Zhao and Xu, 2010). We hypothesize that PSCs utilize specific factors such as Filia to safeguard their genome integrity. Of note, reprogramming somatic cells into induced PSCs (iPSCs) is characterized by large variation in *Filia* (*Ecat1*) expression (Aoi et al., 2008; Kaji et al., 2009; Takahashi and Yamanaka, 2006). This suggests that *Filia* expression is a potential molecular marker that correlates with iPSC quality.

Filia carries out its multiple functions through different mechanisms. On one hand, Filia is dynamically translocated to centrosomes, DNA damage sites, and mitochondria to execute its regulation on DDR independent of PARP1. On the other hand, Filia physically interacts with PARP1 and stimulates PARP1's enzymatic activity to regulate DDR. PARP1 plays a key role in regulating DDR and genomic integrity (Krishnakumar and Kraus, 2010; Luo and Kraus, 2012). For instance, PARP1- or PAR-deficient cells are compromised in ATM activation, DNA damage signaling, cell-cycle checkpoints, and DNA repair (Aguilar-Quesada et al., 2007; Haince et al., 2007; Min et al., 2013). Knockout mice for *Parp1* or *Parp2* are hypersensitive to DNA-damaging agents and display increased genomic instability after genotoxic stress (Hassa et al., 2006). More than 100 PARylation targets were identified in DDR, including PARP1 itself, histones, CDK2, kinases, and damage repair proteins (Jungmichel et al., 2013). Filia is uniquely expressed in ESCs, which correlates with high PAR levels and a superior ability to maintain genomic stability in these cells. Therefore, these findings support a model in which activation of PARP1 by Filia contributes to the observed phenotypes in ATM and Chk2 activation, cell-cycle checkpoints, and DNA damage repair in FK ESCs.

Filia and PARP1 do not apparently co-localize. In addition, FiliaS349A is able to stimulate PARP1 activity despite its restrictive cytoplasmic distribution. These findings suggest

(F–H) Inhibition of PARP1 activity in ESCs abolished S phase (F) and G2/M (G) cell-cycle checkpoints and compromised DNA damage repair (H).

(I) Ectopic expression of Filia in NIH/3T3 cells significantly enhanced their DNA damage repair ability. NIH/3T3 cells, NIH/3T3 cells transfected with vectors, WT ESCs, and FK ESCs were used as controls.

In (H) and (I), cells were recovered for 12 hr.

Data are represented as mean  $\pm$  SEM. \*\*\* $p < 0.001$ . See also Figure S7.



that the dynamic interaction between PARP1 and Filia and activation of PARP1 by Filia occur in both the cytoplasm and nuclei. PAR regulates the protein's sub-cellular redistribution, and this provides a possible explanation for the presence of PAR and p-ATM in the nuclei of FiliaS349A-rescued ESCs.

Compared with Filia knockout, PARP1 inhibition caused a less obvious defect in ATM and Chk2 activation in response to DNA damage. Filia340 failed to rescue the defects in cell-cycle checkpoints despite its ability to activate PARP1. These findings suggest that Filia also regulates ATM-Chk2 activation and cell-cycle checkpoints in a PARP1-independent manner. ATM activation exhibits two phases, and the first phase is not overtly affected by Filia knockout. This might be due to the presence of basal levels of PAR in Filia knockout cells, which accounts for the first phase of ATM activation. Centrosomes are known to integrate many regulatory factors that control cell-cycle progression and DDR. Cell-cycle regulators such as the Cdk-cyclin complex (Bailey et al., 1992; Hinchcliffe et al., 1999), Chk1 (Krämer et al., 2004; Zhang et al., 2007), and Chk2 (Golan et al., 2010; Hong and Stambrook, 2004; Zhang et al., 2007) are present on centrosomes. Furthermore, DDR regulators such as ATM, ATR, and DNA-PK have also been shown to reside on centrosomes (Zhang et al., 2007). Consistently, we observed the localization of p-ATM on centrosomes of ESCs. However, p-ATM was absent from centrosomes when Filia was depleted. Re-expression of Filia340, FiliaS349A, or FiliaS349D, all of which localize on centrosomes, restored a second wave of ATM activation. Therefore, the centrosomally localized Filia may coordinate the control of DDR signaling, cell-cycle checkpoints, and centrosome integrity.

FiliaS349A- or FiliaS349D-rescued ESCs fail to repair DNA damage despite the PARP1 activity and PAR levels being normal. This is consistent with the idea that Filia also regulates DNA damage repair in a PARP1-independent manner. The phosphorylation of S349 at the C terminus is necessary for Filia's nuclear localization. However, without the C terminus, Filia340 is localized to nuclei (Figure S6B). Notably, bioinformatics analysis indicates that Filia340 (aas 1–340) contains a potential nuclear localization signal (NLS). Therefore, it is possible that the phosphorylation of S349 regulates NLS function. Specifically, non-phosphorylated S349 suppresses NLS function, whereas phosphorylation of S349 or simply removing the C terminus activates NLS function. Upon LPB treatment, nuclear Filia is diffusive in the absence of DNA damage. DNA damage triggers the translocation of Filia to DNA damage sites, indicating that Filia's entry into nuclei and its translocation to DNA damage sites are regulated separately. PARylation plays a critical role in recruiting DNA repair proteins to damage sites (Krishnakumar and Kraus, 2010; Tallis et al., 2014). However, localization of Filia into DNA damage sites is regulated neither by PARylation nor by interaction with PARP1.

In summary, our data demonstrate that Filia functions as the first of its kind ESC-specific regulator of genome integrity. These data support the notion that ESCs employ distinct mechanisms and utilize specific factors, such as Filia, to safeguard their genomic integrity. They also suggest that the Filia expression level is a potential biomarker for the quality of iPSCs with regard to genomic stability and transformation potential.

## EXPERIMENTAL PROCEDURES

### Derivation and Culture of Mouse ESCs

All experimental procedures and animal care were performed according to the protocols approved by the Ethics Committee of the Kunming Institute of Zoology, Chinese Academy of Sciences. MEF preparation, ESC derivation, and culture were performed in standard ways (Evans and Kaufman, 1981). ESC genotyping was performed as described previously (Zheng and Dean, 2009).

### Cytogenetic Analysis and T-FISH

Metaphase chromosome spreads were prepared and stained with Giemsa solution or DAPI. For telomere fluorescent in situ hybridization (T-FISH), metaphase spreads were prepared. DNA was denatured and hybridized with peptide-nucleic acid (PNA) telomere probes (Tel G-Alexa 488, PANAGENE, F1010-5) (Lansdorp et al., 1996). DNA was counterstained with 4',6-diamidino-2-phenylindole, dihydrochloride (DAPI).

### Immunoblotting and Immunofluorescent Staining

Immunoblotting and immunofluorescent staining were performed according to standard procedures (Närvä et al., 2012). The primary antibodies are listed in Table S1. Rabbit polyclonal antibodies against Filia and p-Filia(S349) were generated by Abmart.

### Cell-Cycle Checkpoint Analysis

ESCs were treated with hydroxyl urea to induce replication stress, and S-phase arrest was evaluated by 5-ethynyl-2'-deoxyuridine (EdU) pulse-chase incorporation assay (Buck et al., 2008). The G2/M checkpoint was examined by standard methods after treating ESCs with etoposide (Greer Card et al., 2010).

### Alkaline Comet Assay and Clonal Competition Assay

An alkaline comet assay was performed according to the standard procedure (Tice et al., 2000). Comets were analyzed using CASP comet assay analysis software (Andor Technology), and 100 cells were calculated in each sample. The same numbers of two types of ESCs, of which one was labeled with GFP expression, were mixed. The mixed ESCs were subjected to the same genotoxic stress and co-culture. Colony growth was monitored daily, and 200 clones were examined at each time point.

## SUPPLEMENTAL INFORMATION

Supplemental Information includes Supplemental Experimental Procedures, seven figures, and one table and can be found with this article online at <http://dx.doi.org/10.1016/j.stem.2015.03.017>.

## ACKNOWLEDGMENTS

We thank Dr. Jurrien Dean at the NIH for providing *Filia* mutant mice; Wei-jian Sang, Rui Bi, and Zhengyuan Xie for technical support in making lentiviral expression vectors; the Protein Mass Spectrometry Center at the Shanghai Institute of Materia Medica, CAS, for performing the mass spectrometry analysis; and Dr. Jurrien Dean at the NIH and Dr. Jiali Li at the Kunming Institute of Zoology, CAS, for carefully reading and editing the paper. This work was supported by the Chinese NSFC grant 31171424 (to P.Z.), by CAS Strategic Priority Research Program Grant XDA01010203, and by a talent grant from Yunnan Province. R.Z. is supported by NIH/NCI Grant R01CA160331 and Cancer Center Core Grant CA010815.

Received: September 3, 2014

Revised: February 16, 2015

Accepted: March 22, 2015

Published: April 30, 2015

## REFERENCES

Aguilar-Quesada, R., Muñoz-Gámez, J.A., Martín-Oliva, D., Peralta, A., Valenzuela, M.T., Matínez-Romero, R., Quiles-Pérez, R., Menissier-de

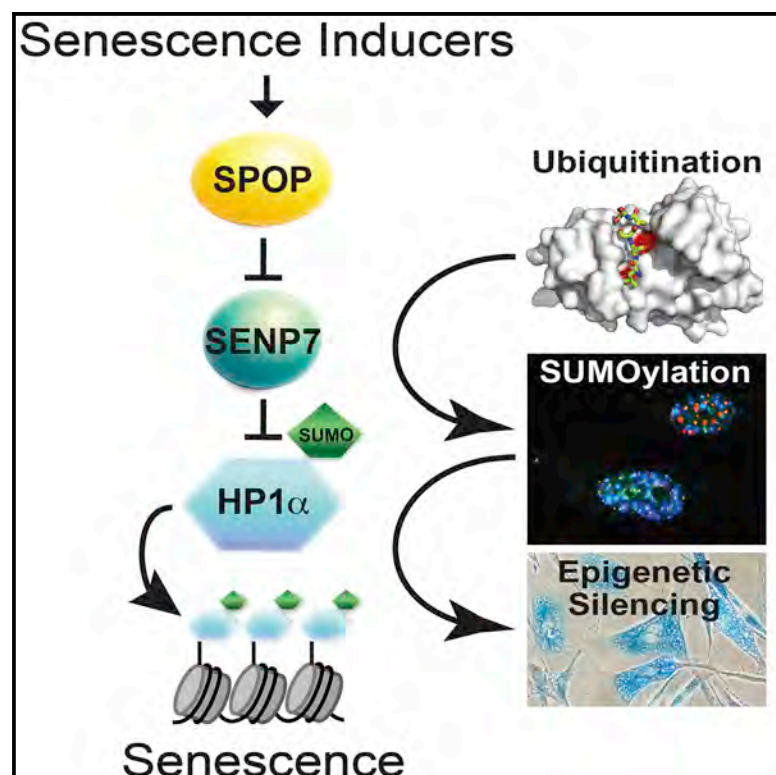
- Murcia, J., de Murcia, G., Ruiz de Almodóvar, M., and Oliver, F.J. (2007). Interaction between ATM and PARP-1 in response to DNA damage and sensitization of ATM deficient cells through PARP inhibition. *BMC Mol. Biol.* 8, 29.
- Alpatov, R., Lesch, B.J., Nakamoto-Kinoshita, M., Blanco, A., Chen, S., Stützer, A., Armache, K.J., Simon, M.D., Xu, C., Ali, M., et al. (2014). A chromatin-dependent role of the fragile X mental retardation protein FMRP in the DNA damage response. *Cell* 157, 869–881.
- Aoi, T., Yae, K., Nakagawa, M., Ichisaka, T., Okita, K., Takahashi, K., Chiba, T., and Yamanaka, S. (2008). Generation of pluripotent stem cells from adult mouse liver and stomach cells. *Science* 321, 699–702.
- Bailly, E., Pines, J., Hunter, T., and Bornens, M. (1992). Cytoplasmic accumulation of cyclin B1 in human cells: association with a detergent-resistant compartment and with the centrosome. *J. Cell Sci.* 101, 529–545.
- Bartkova, J., Horejsi, Z., Koed, K., Krämer, A., Tort, F., Zieger, K., Guldberg, P., Sehested, M., Nesland, J.M., Lukas, C., et al. (2005). DNA damage response as a candidate anti-cancer barrier in early human tumorigenesis. *Nature* 434, 864–870.
- Batchelor, E., Mock, C.S., Bhan, I., Loewer, A., and Lahav, G. (2008). Recurrent initiation: a mechanism for triggering p53 pulses in response to DNA damage. *Mol. Cell* 30, 277–289.
- Behrens, A., van Deursen, J.M., Rudolph, K.L., and Schumacher, B. (2014). Impact of genomic damage and ageing on stem cell function. *Nat. Cell Biol.* 16, 201–207.
- Bourke, E., Dodson, H., Merdes, A., Cuffe, L., Zachos, G., Walker, M., Gillespie, D., and Morrison, C.G. (2007). DNA damage induces Chk1-dependent centrosome amplification. *EMBO Rep.* 8, 603–609.
- Branzei, D., and Foiani, M. (2008). Regulation of DNA repair throughout the cell cycle. *Nat. Rev. Mol. Cell Biol.* 9, 297–308.
- Buck, S.B., Bradford, J., Gee, K.R., Agnew, B.J., Clarke, S.T., and Salic, A. (2008). Detection of S-phase cell cycle progression using 5-ethynyl-2'-deoxyuridine incorporation with click chemistry, an alternative to using 5-bromo-2'-deoxyuridine antibodies. *Biotechniques* 44, 927–929.
- Calabrese, C.R., Almassy, R., Barton, S., Batey, M.A., Calvert, A.H., Canan-Koch, S., Durkacz, B.W., Hostomsky, Z., Kumpf, R.A., Kyle, S., et al. (2004). Anticancer chemosensitization and radiosensitization by the novel poly(ADP-ribose) polymerase-1 inhibitor AG14361. *J. Natl. Cancer Inst.* 96, 56–67.
- Davis, A.J., Chen, B.P., and Chen, D.J. (2014). DNA-PK: a dynamic enzyme in a versatile DSB repair pathway. *DNA Repair (Amst.)* 17, 21–29.
- De Vos, M., Schreiber, V., and Dantzer, F. (2012). The diverse roles and clinical relevance of PARPs in DNA damage repair: current state of the art. *Biochem. Pharmacol.* 84, 137–146.
- Doxsey, S., Zimmerman, W., and Mikule, K. (2005). Centrosome control of the cell cycle. *Trends Cell Biol.* 15, 303–311.
- Dumitru, R., Gama, V., Fagan, B.M., Bower, J.J., Swahari, V., Pevny, L.H., and Deshmukh, M. (2012). Human embryonic stem cells have constitutively active Bax at the Golgi and are primed to undergo rapid apoptosis. *Mol. Cell* 46, 573–583.
- Evans, M.J., and Kaufman, M.H. (1981). Establishment in culture of pluripotent cells from mouse embryos. *Nature* 292, 154–156.
- Farber-Katz, S.E., Dippold, H.C., Buschman, M.D., Peterman, M.C., Xing, M., Noakes, C.J., Tat, J., Ng, M.M., Rahajeng, J., Cowan, D.M., et al. (2014). DNA damage triggers Golgi dispersal via DNA-PK and GOLPH3. *Cell* 156, 413–427.
- Golan, A., Pick, E., Tsvetkov, L., Nadler, Y., Kluger, H., and Stern, D.F. (2010). Centrosomal Chk2 in DNA damage responses and cell cycle progression. *Cell Cycle* 9, 2647–2656.
- Green, D.R., and Kroemer, G. (2009). Cytoplasmic functions of the tumour suppressor p53. *Nature* 458, 1127–1130.
- Greer Card, D.A., Sierant, M.L., and Davey, S. (2010). Rad9A is required for G2 decatenation checkpoint and to prevent endoreduplication in response to topoisomerase II inhibition. *J. Biol. Chem.* 285, 15653–15661.
- Haince, J.F., Kozlov, S., Dawson, V.L., Dawson, T.M., Hendzel, M.J., Lavin, M.F., and Poirier, G.G. (2007). Ataxia telangiectasia mutated (ATM) signaling network is modulated by a novel poly(ADP-ribose)-dependent pathway in the early response to DNA-damaging agents. *J. Biol. Chem.* 282, 16441–16453.
- Hassa, P.O., Haenni, S.S., Elser, M., and Hottiger, M.O. (2006). Nuclear ADP-ribosylation reactions in mammalian cells: where are we today and where are we going? *Microbiol. Mol. Biol. Rev.* 70, 789–829.
- Hinchcliffe, E.H., Li, C., Thompson, E.A., Maller, J.L., and Sluder, G. (1999). Requirement of Cdk2-cyclin E activity for repeated centrosome reproduction in *Xenopus* egg extracts. *Science* 283, 851–854.
- Hirao, A., Kong, Y.Y., Matsuoka, S., Wakeham, A., Ruland, J., Yoshida, H., Liu, D., Elledge, S.J., and Mak, T.W. (2000). DNA damage-induced activation of p53 by the checkpoint kinase Chk2. *Science* 287, 1824–1827.
- Hong, Y., and Stambrook, P.J. (2004). Restoration of an absent G1 arrest and protection from apoptosis in embryonic stem cells after ionizing radiation. *Proc. Natl. Acad. Sci. USA* 101, 14443–14448.
- Inomata, K., Aoto, T., Binh, N.T., Okamoto, N., Tanimura, S., Wakayama, T., Iseki, S., Hara, E., Masunaga, T., Shimizu, H., and Nishimura, E.K. (2009). Genotoxic stress abrogates renewal of melanocyte stem cells by triggering their differentiation. *Cell* 137, 1088–1099.
- Jackson, S.P., and Bartek, J. (2009). The DNA-damage response in human biology and disease. *Nature* 461, 1071–1078.
- Jungmichel, S., Rosenthal, F., Altmeyer, M., Lukas, J., Hottiger, M.O., and Nielsen, M.L. (2013). Proteome-wide identification of poly(ADP-Ribosylation) targets in different genotoxic stress responses. *Mol. Cell* 52, 272–285.
- Kaji, K., Norrby, K., Paca, A., Mileikovsky, M., Mohseni, P., and Woltjen, K. (2009). Virus-free induction of pluripotency and subsequent excision of reprogramming factors. *Nature* 458, 771–775.
- Krämer, A., Mailand, N., Lukas, C., Syljuåsen, R.G., Wilkinson, C.J., Nigg, E.A., Bartek, J., and Lukas, J. (2004). Centrosome-associated Chk1 prevents premature activation of cyclin-B-Cdk1 kinase. *Nat. Cell Biol.* 6, 884–891.
- Krishnakumar, R., and Kraus, W.L. (2010). The PARP side of the nucleus: molecular actions, physiological outcomes, and clinical targets. *Mol. Cell* 39, 8–24.
- Lansdorp, P.M., Verwoerd, N.P., van de Rijke, F.M., Dragowska, V., Little, M.T., Dirks, R.W., Raap, A.K., and Tanke, H.J. (1996). Heterogeneity in telomere length of human chromosomes. *Hum. Mol. Genet.* 5, 685–691.
- Li, M., He, Y., Dubois, W., Wu, X., Shi, J., and Huang, J. (2012). Distinct regulatory mechanisms and functions for p53-activated and p53-repressed DNA damage response genes in embryonic stem cells. *Mol. Cell* 46, 30–42.
- Liang, Y., Lin, S.Y., Brunicardi, F.C., Goss, J., and Li, K. (2009). DNA damage response pathways in tumor suppression and cancer treatment. *World J. Surg.* 33, 661–666.
- Lin, T., Chao, C., Saito, S., Mazur, S.J., Murphy, M.E., Appella, E., and Xu, Y. (2005). p53 induces differentiation of mouse embryonic stem cells by suppressing Nanog expression. *Nat. Cell Biol.* 7, 165–171.
- Liu, Q., Guntuku, S., Cui, X.S., Matsuoka, S., Cortez, D., Tamai, K., Luo, G., Carattini-Rivera, S., DeMayo, F., Bradley, A., et al. (2000). Chk1 is an essential kinase that is regulated by Atr and required for the G(2)/M DNA damage checkpoint. *Genes Dev.* 14, 1448–1459.
- Liu, J.C., Guan, X., Ryan, J.A., Rivera, A.G., Mock, C., Agrawal, V., Letai, A., Lerou, P.H., and Lahav, G. (2013). High mitochondrial priming sensitizes hESCs to DNA-damage-induced apoptosis. *Cell Stem Cell* 13, 483–491.
- Löffler, H., Lukas, J., Bartek, J., and Krämer, A. (2006). Structure meets function—centrosomes, genome maintenance and the DNA damage response. *Exp. Cell Res.* 312, 2633–2640.
- Löffler, H., Fechter, A., Liu, F.Y., Poppelreuther, S., and Krämer, A. (2013). DNA damage-induced centrosome amplification occurs via excessive formation of centriolar satellites. *Oncogene* 32, 2963–2972.
- Luo, X., and Kraus, W.L. (2012). On PAR with PARP: cellular stress signaling through poly(ADP-ribose) and PARP-1. *Genes Dev.* 26, 417–432.
- Min, W., Bruhn, C., Grigaravicius, P., Zhou, Z.W., Li, F., Krüger, A., Siddeek, B., Greulich, K.O., Popp, O., Meisezahl, C., et al. (2013). Poly(ADP-ribose) binding to Chk1 at stalled replication forks is required for S-phase checkpoint activation. *Nat. Commun.* 4, 2993.

- Mitsui, K., Tokuzawa, Y., Itoh, H., Segawa, K., Murakami, M., Takahashi, K., Maruyama, M., Maeda, M., and Yamanaka, S. (2003). The homeoprotein Nanog is required for maintenance of pluripotency in mouse epiblast and ES cells. *Cell* 113, 631–642.
- Momčilović, O., Choi, S., Varum, S., Bakkenist, C., Schatten, G., and Navara, C. (2009). Ionizing radiation induces ataxia telangiectasia mutated-dependent checkpoint signaling and G(2) but not G(1) cell cycle arrest in pluripotent human embryonic stem cells. *Stem Cells* 27, 1822–1835.
- Momčilović, O., Navara, C., and Schatten, G. (2011). Cell cycle adaptations and maintenance of genomic integrity in embryonic stem cells and induced pluripotent stem cells. *Results Probl. Cell Differ.* 53, 415–458.
- Mortusewicz, O., Amé, J.C., Schreiber, V., and Leonhardt, H. (2007). Feedback-regulated poly(ADP-ribosylation) by PARP-1 is required for rapid response to DNA damage in living cells. *Nucleic Acids Res.* 35, 7665–7675.
- Nagy, Z., and Soutoglou, E. (2009). DNA repair: easy to visualize, difficult to elucidate. *Trends Cell Biol.* 19, 617–629.
- Närvä, E., Rahkonen, N., Emani, M.R., Lund, R., Pursiheimo, J.P., Nästi, J., Autio, R., Rasool, O., Denessiouk, K., Lähdesmäki, H., et al. (2012). RNA-binding protein LITD1 interacts with LIN28 via RNA and is required for human embryonic stem cell self-renewal and cancer cell proliferation. *Stem Cells* 30, 452–460.
- Ohsugi, M., Zheng, P., Baibakov, B., Li, L., and Dean, J. (2008). Maternally derived FILIA-MATER complex localizes asymmetrically in cleavage-stage mouse embryos. *Development* 135, 259–269.
- Pines, A., Kelstrup, C.D., Vrouwe, M.G., Puigvert, J.C., Typas, D., Misovic, B., de Groot, A., von Stechow, L., van de Water, B., Danen, E.H., et al. (2011). Global phosphoproteome profiling reveals unanticipated networks responsive to cisplatin treatment of embryonic stem cells. *Mol. Cell. Biol.* 31, 4964–4977.
- Rass, U., Ahel, I., and West, S.C. (2007). Defective DNA repair and neurodegenerative disease. *Cell* 130, 991–1004.
- Shimada, M., and Komatsu, K. (2009). Emerging connection between centrosome and DNA repair machinery. *J. Radiat. Res. (Tokyo)* 50, 295–301.
- Silk, A.D., Holland, A.J., and Cleveland, D.W. (2009). Requirements for NuMA in maintenance and establishment of mammalian spindle poles. *J. Cell Biol.* 184, 677–690.
- Takahashi, K., and Yamanaka, S. (2006). Induction of pluripotent stem cells from mouse embryonic and adult fibroblast cultures by defined factors. *Cell* 126, 663–676.
- Tallis, M., Morra, R., Barkauskaite, E., and Ahel, I. (2014). Poly(ADP-ribosylation) in regulation of chromatin structure and the DNA damage response. *Chromosoma* 123, 79–90.
- Tamanini, F., Bontekoe, C., Bakker, C.E., van Unen, L., Anar, B., Willemsen, R., Yoshida, M., Galjaard, H., Oostra, B.A., and Hoogeveen, A.T. (1999). Different targets for the fragile X-related proteins revealed by their distinct nuclear localizations. *Hum. Mol. Genet.* 8, 863–869.
- Tice, R.R., Agurell, E., Anderson, D., Burlinson, B., Hartmann, A., Kobayashi, H., Miyamae, Y., Rojas, E., Ryu, J.C., and Sasaki, Y.F. (2000). Single cell gel/comet assay: guidelines for in vitro and in vivo genetic toxicology testing. *Environ. Mol. Mutagen.* 35, 206–221.
- Tichy, E.D., Pillai, R., Deng, L., Liang, L., Tischfield, J., Schwemberger, S.J., Babcock, G.F., and Stambrook, P.J. (2010). Mouse embryonic stem cells, but not somatic cells, predominantly use homologous recombination to repair double-strand DNA breaks. *Stem Cells Dev.* 19, 1699–1711.
- van der Laan, S., Tsanov, N., Crozet, C., and Maiorano, D. (2013). High Dub3 expression in mouse ESCs couples the G1/S checkpoint to pluripotency. *Mol. Cell* 52, 366–379.
- Wyles, S.P., Brandt, E.B., and Nelson, T.J. (2014). Stem cells: the pursuit of genomic stability. *Int. J. Mol. Sci.* 15, 20948–20967.
- Yamamoto, K., Wang, Y., Jiang, W., Liu, X., Dubois, R.L., Lin, C.S., Ludwig, T., Bakkenist, C.J., and Zha, S. (2012). Kinase-dead ATM protein causes genomic instability and early embryonic lethality in mice. *J. Cell Biol.* 198, 305–313.
- Zalzman, M., Falco, G., Sharova, L.V., Nishiyama, A., Thomas, M., Lee, S.L., Stagg, C.A., Hoang, H.G., Yang, H.T., Indig, F.E., et al. (2010). Zscan4 regulates telomere elongation and genomic stability in ES cells. *Nature* 464, 858–863.
- Zeng, C. (2000). NuMA: a nuclear protein involved in mitotic centrosome function. *Microsc. Res. Tech.* 49, 467–477.
- Zhang, S., Hemmerich, P., and Grosse, F. (2007). Centrosomal localization of DNA damage checkpoint proteins. *J. Cell. Biochem.* 101, 451–465.
- Zhao, T., and Xu, Y. (2010). p53 and stem cells: new developments and new concerns. *Trends Cell Biol.* 20, 170–175.
- Zheng, P., and Dean, J. (2009). Role of Filia, a maternal effect gene, in maintaining euploidy during cleavage-stage mouse embryogenesis. *Proc. Natl. Acad. Sci. USA* 106, 7473–7478.

# Cell Reports

## SPOP E3 Ubiquitin Ligase Adaptor Promotes Cellular Senescence by Degrading the SENP7 deSUMOylase

### Graphical Abstract



### Authors

Hengrui Zhu, Shancheng Ren, Benjamin G. Bitler, ..., Jun Yan, Yinghao Sun, Rugang Zhang

### Correspondence

sunyh@medmail.com.cn (Y.S.),  
rzhang@wistar.org (R.Z.)

### In Brief

The *SPOP* gene, which encodes an E3 ubiquitin ligase adaptor, is mutated in a number of cancer types. Zhu et al. show that SPOP promotes senescence, a tumor suppression mechanism, by degrading the SENP7 deSUMOylase. This correlates with HP1 $\alpha$ -associated epigenetic gene silencing through a relay of ubiquitination and sumoylation post-transcriptional modifications.

### Highlights

- SPOP upregulation promotes senescence by degrading SENP7
- Cancer-associated SPOP mutants fail to induce senescence and degrade SENP7
- Senescence induced by SPOP correlates with HP1 $\alpha$ -mediated epigenetic gene silencing
- SENP7 is expressed at higher levels in SPOP-mutated prostate tumors





# SPOP E3 Ubiquitin Ligase Adaptor Promotes Cellular Senescence by Degrading the SENP7 deSUMOylase

Hengrui Zhu,<sup>1,4</sup> Shancheng Ren,<sup>2,4</sup> Benjamin G. Bitler,<sup>1</sup> Katherine M. Aird,<sup>1</sup> Zhigang Tu,<sup>1</sup> Emmanuel Skordalakes,<sup>1</sup> Yasheng Zhu,<sup>2</sup> Jun Yan,<sup>3</sup> Yinghao Sun,<sup>2,\*</sup> and Rugang Zhang<sup>1,\*</sup>

<sup>1</sup>Gene Expression and Regulation Program, The Wistar Institute, Philadelphia, PA 19104, USA

<sup>2</sup>Department of Urology, Shanghai Changhai Hospital, Second Military Medical University, Shanghai 200433, People's Republic of China

<sup>3</sup>MOE Key Laboratory of Model Animal for Disease Study, Model Animal Research Center, Nanjing University, Nanjing, Jiangsu 210061, People's Republic of China

<sup>4</sup>Co-first author

\*Correspondence: [sunyh@medmail.com.cn](mailto:sunyh@medmail.com.cn) (Y.S.), [rzhang@wistar.org](mailto:rzhang@wistar.org) (R.Z.)

<http://dx.doi.org/10.1016/j.celrep.2015.09.083>

This is an open access article under the CC BY-NC-ND license (<http://creativecommons.org/licenses/by-nc-nd/4.0/>).

## SUMMARY

The *SPOP* gene, which encodes an E3 ubiquitin ligase adaptor, is frequently mutated in a number of cancer types. However, the mechanisms by which *SPOP* functions as a tumor suppressor remain poorly understood. Here, we show that *SPOP* promotes senescence, an important tumor suppression mechanism, by targeting the SENP7 deSUMOylase for degradation. *SPOP* is upregulated during senescence. This correlates with ubiquitin-mediated degradation of SENP7, which promotes senescence by increasing HP1 $\alpha$  sumoylation and the associated epigenetic gene silencing. Ectopic wild-type *SPOP*, but not its cancer-associated mutants, drives senescence. Conversely, *SPOP* knockdown overcomes senescence. These phenotypes correlate with ubiquitination and degradation of SENP7 and HP1 $\alpha$  sumoylation, subcellular re-localization, and its associated gene silencing. Furthermore, SENP7 is expressed at higher levels in prostate tumor specimens with *SPOP* mutation ( $n = 13$ ) compared to those with wild-type *SPOP* ( $n = 80$ ). In summary, *SPOP* acts as a tumor suppressor by promoting senescence through degrading SENP7.

## INTRODUCTION

Speckle-type POZ protein (*SPOP*) is a bric-a-brac-tramtrack-broad/poxvirus and zinc finger (BTB/POZ) domain protein that functions as an adaptor for the E3 ubiquitin ligase cullin 3. Recent genome-wide next-generation sequencing studies have revealed that *SPOP* is frequently mutated in a number of cancer types such as prostate and endometrial (Barbieri et al., 2012; Berger et al., 2011; Le Gallo et al., 2012). These findings suggest that *SPOP* is a putative tumor suppressor. *SPOP* binds to its

substrates via its N-terminal meprin and traf homology (MATH) domain (Zhuang et al., 2009), whereas it interacts with cullin 3 through the BTB domain at its C terminus (Pintard et al., 2003; Xu et al., 2003). *SPOP* mutations observed in human cancers are clustered in its substrate binding MATH domain (Barbieri et al., 2012; Berger et al., 2011), suggesting that *SPOP* mutations may promote cancer via altering the function of its substrates. Indeed, *SPOP* mutations correlate with changes in the ubiquitin landscape in prostate cancer (Theurillat et al., 2014). Despite the fact that a number of *SPOP* substrates have been described (such as C/Gli, macroH2A, Daxx, SRC3, AR, and DEK; An et al., 2014; Hernández-Muñoz et al., 2005; Kwon et al., 2006; Li et al., 2014; Theurillat et al., 2014; Zhang et al., 2006), the mechanistic basis by which *SPOP* functions as a tumor suppressor remains poorly understood.

Cellular senescence is a state of stable cell growth arrest (Pérez-Mancera et al., 2014). It is an important tumor suppression mechanism by halting the progression of cancer progenitor cells harboring the initial oncogenic hits. Oncogenic signaling triggers senescence via mechanisms such as formation of senescence-associated heterochromatin foci (SAHF), which are specialized domains of facultative heterochromatin that contribute to senescence by helping silence proliferation-promoting genes (such as the E2F target genes; Narita et al., 2003). Heterochromatin markers such as heterochromatin protein 1 (HP1) proteins are components of SAHF and are associated with the promoters of the proliferation-promoting genes in senescent cells (Narita et al., 2003). Activation of these signaling pathways cultivates the expression of markers of senescence such as an increased senescence-associated  $\beta$ -galactosidase (SA- $\beta$ -gal) activity (Dimri et al., 1995).

Small ubiquitin-like modifiers (SUMO) is a dynamic post-translational protein modification that regulates the function and subcellular localization of its target proteins (Cubéñas-Potts and Matunis, 2013). SUMO has been implicated in regulating senescence (Bischof et al., 2006; Li et al., 2006; Yates et al., 2008). SUMO is conjugated to its targets by SUMO-conjugating machinery, whereas removal of SUMO is performed by a class of enzymes called sentrin/SUMO-specific proteases (SENP)



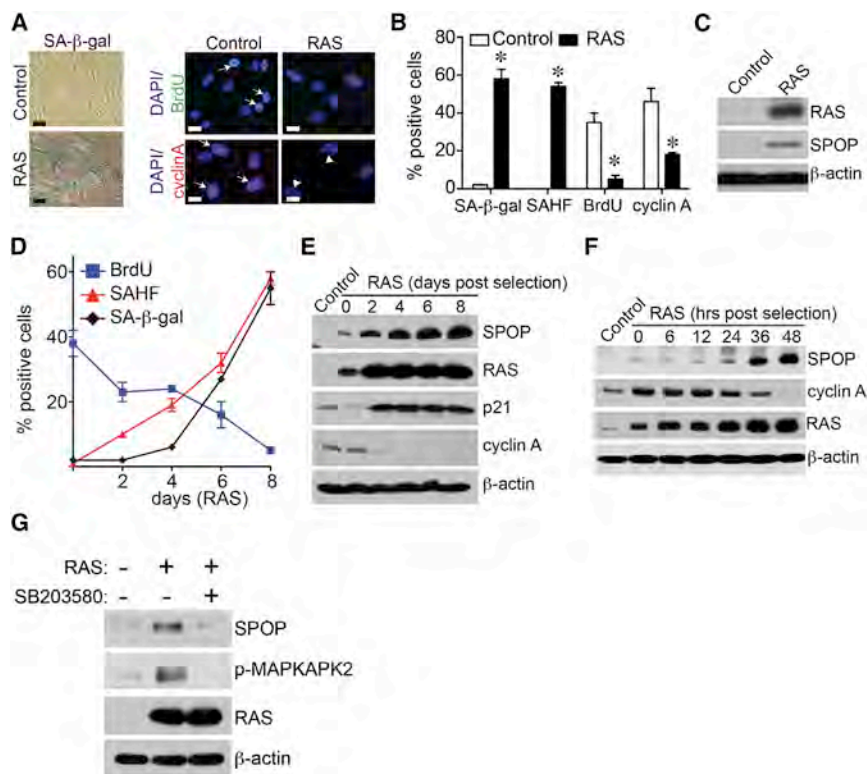


**Figure 1. SPOP Is Upregulated during Senescence**

(A) IMR90 primary human fibroblasts were infected with retrovirus encoding control or RAS to induce senescence. Drug-selected cells were stained for SA-β-gal activity, labeled with BrdU for 30 min, or stained for cyclin A expression at day 8. Arrows point to examples of positive cells for the indicated markers. The scale bar represents 10 μm.

(B) Same as (A) but quantified for SA-β-gal staining, SAHF, BrdU, and cyclin A-positive cells in control and RAS-infected cells. A total of 200 cells were examined for each of the indicated groups. Error bars represent mean of three independent experiments with SD. \**p* < 0.01.

(C) Same as (A) but examined for expression of SPOP, RAS, and β-actin by immunoblotting.

(D) Time course for senescence markers such as SA-β-gal activity and SAHF formation and the cell proliferation marker BrdU incorporation in control and RAS-infected IMR90 cells. Mean of three independent experiments with SD is shown.

(E and F) Same as (D) but examined for expression of SPOP, RAS, p21, cyclin A, and β-actin by immunoblotting at the indicated time points.

(G) Same as (A), but the RAS-infected cells were treated with or without 5 μM p38 inhibitor SB203580 for 24 hr before harvesting cells for immunoblotting. The expression of SPOP, RAS, and phospho-MAP-kinase-activated protein kinase 2 (p-MAPKAPK2), a direct target of p38 kinase, in the indicated cells was examined by immunoblotting. β-actin expression was used as a loading control.

through their isopeptidase activity (Mukhopadhyay and Dasso, 2007). Here, we report that SPOP epigenetically promotes senescence by ubiquitin-mediated degradation of SENP7, which facilitates HP1α-associated gene silencing via its sumoylation. Our studies indicate that SPOP acts a tumor suppressor by promoting cellular senescence.

## RESULTS

### SPOP Is Upregulated during Senescence

To determine whether SPOP is regulated during senescence, IMR90 primary human fibroblasts were induced to undergo senescence by oncogenic RAS, a well-established model for studying senescence in normal human cells in vitro (Figure S1A). The senescence status was confirmed by markers such as SA-β-gal activity and formation of SAHF (Figures 1A and 1B). Consistently, cell proliferation markers such as BrdU incorporation and cyclin A expression were decreased by RAS infection (Figures 1A and 1B). Interestingly, SPOP was upregulated in senescent cells (Figure 1C). Next, we performed a detailed time course study for SPOP upregulation and expression of markers of senescence (such as SA-β-gal activity, SAHF formation, and upregulation of p21) and cell proliferation markers (including BrdU incorporation and cyclin A expression). Indeed, SPOP upregulation was accompanied by induction of markers of senescence and senescence-associated cell-cycle exit (Figures 1D–1F). SPOP upregulation was also observed during senescence induced by knockdown of the tumor suppressor PTEN

or extended cell passing, but not by DNA damage agent doxorubicin (Figures S1B–S1J). Similar observation was also made in BJ primary human fibroblasts (Figures S1K–S1M). Together, we conclude that SPOP is upregulated during senescence.

We next determined the mechanism by which SPOP is upregulated during senescence. Notably, there was no increase in SPOP mRNA levels in senescent cells (Figure S1N). This suggests that SPOP upregulation occurs at the post-transcriptional level. Notably, there is evidence to suggest that p38 regulates SPOP protein stability (Bunce et al., 2008). Thus, we sought to determine whether SPOP upregulation is dependent upon p38 activity. Toward this goal, we suppressed the p38 activity using a small molecular inhibitor SB203580. Indeed, SB203580 treatment significantly decreased the levels of SPOP in treated cells (Figure 1G). Together, we conclude that SPOP is upregulated at the post-transcriptional level in a p38-dependent manner during senescence.

### Ectopic Expression of Wild-Type SPOP, but Not Its Cancer-Associated Mutants, Drives Senescence

Because we observed an upregulation of SPOP during senescence (Figure 1), we determined whether ectopic expression of wild-type SPOP is sufficient to drive senescence. We ectopically expressed wild-type SPOP in IMR90 cells (Figure 2A). Indeed, ectopic SPOP expression induced expression of markers of senescence such as SA-β-gal activity and upregulation of p53 and p21, whereas it suppressed cell proliferation markers such as BrdU incorporation, serine 10 phosphorylated histone H3

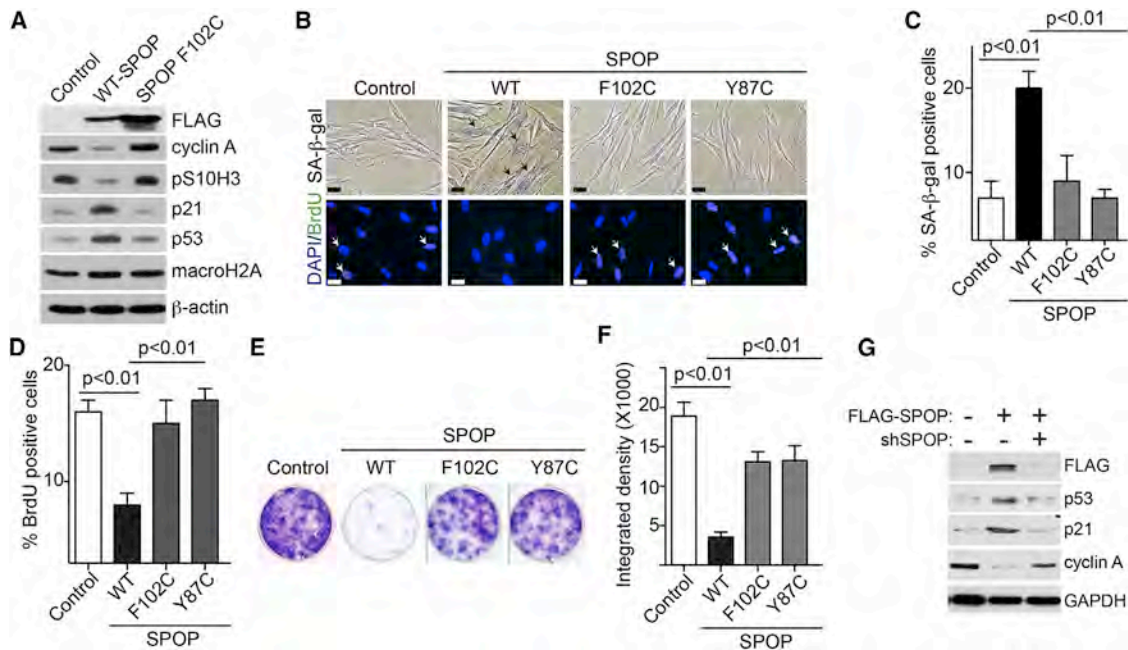


**Figure 2. Ectopic Expression of Wild-Type SPOP, but Not Cancer-Associated SPOP Mutants, Induces Senescence and the Associated Cell Growth Arrest**

(A) IMR90 cells were infected with retrovirus encoding wild-type or the indicated cancer-associated mutant SPOP. Six days post-drug selection, the indicated cells were examined for expression of the indicated proteins by immunoblotting.  
(B) Same as (A) but stained for SA-β-gal activity or examined for BrdU incorporation. Arrows point to examples of SA-β-gal- and BrdU-positive cells. The scale bar represents 10 μm.  
(C and D) Quantification of (B). Two hundred cells from each of the indicated groups were examined for expression of SA-β-gal activity (C) or BrdU positivity (D). Mean of three independents with SD is shown.  
(E and F) Same as (A), but 3,000 of each of the indicated cells were seeded into 6-well plates for focus formation assays. Cells were fixed and stained with 0.05% crystal violet after growing for an additional 10 days (E). The integrated density was quantified using NIH ImageJ software (F).  
(G) IMR90 cells were infected with a control retrovirus or one encoding wild-type SPOP together with an shRNA that targets the open reading frame of SPOP or controls. The cells were examined for expression of the indicated proteins by immunoblotting 6 days post-drug selection.

(pS10H3), and cyclin A expression (Figures 2A–2D). Notably, DNA damage markers such as γH2AX expression and foci formation were not activated during senescence induced by SPOP (Figures S2A–S2C). Expression of the known SPOP substrate macroH2A that is implicated in senescence (Zhang et al., 2005) was not affected by SPOP expression (Figure 2A). This suggests that senescence induced by SPOP is mediated by previously unidentified substrates. Consistently, SPOP induced an apparent cell growth inhibition as determined by focus formation (Figures 2E and 2F). The observed effects were specifically due to SPOP overexpression because knockdown of the ectopic SPOP suppressed the senescence phenotype in these cells (Figure 2G; data not shown). The p53 and pRB pathways play critical roles in senescence (Pérez-Mancera et al., 2014). Consistently, knockdown of either p53 or pRB impaired senescence induced by SPOP (Figures S2D–S2G). We conclude that ectopic expression of wild-type SPOP induces senescence.

We next determined whether SPOP mutants observed in prostate cancers are impaired in senescence induction. We ectopically expressed two MATH-domain-mutated SPOPs (F102C and Y87C) that are frequently observed in prostate cancers (Barbieri et al., 2012; Berger et al., 2011; Jones et al., 2014; Le Gallo

et al., 2012). Compared with wild-type SPOP, the SPOP mutants were impaired in senescence induction as determined by a significant decrease in SA-β-gal activity and p53 and p21 expression (Figures 2A–2C and S2H). Consistently, there was an increase in cell proliferation markers such as BrdU incorporation and expression of pS10H3 and cyclin A in cells expressing SPOP mutants compared with wild-type SPOP (Figures 2A–2D). Indeed, SPOP-induced growth inhibition was also significantly impaired by the cancer-associated mutants as determined by focus formation (Figures 2E and 2F). We conclude that wild-type SPOP drives senescence, whereas its cancer-associated mutants are impaired in senescence induction.

### SPOP Knockdown Suppresses Senescence

Next, we determined whether SPOP knockdown suppresses senescence. IMR90 cells were induced to undergo senescence with oncogenic RAS together with an shRNA to the human SPOP gene (shSPOP) or control. Indeed, SPOP knockdown suppressed the expression of senescence markers such as SA-β-gal activity, SAHF formation, and upregulation of p53 and p21 (Figures 3A–3C). In contrast, cell proliferation markers such as cyclin A expression and BrdU incorporation were significantly increased in shSPOP/RAS cells compared with

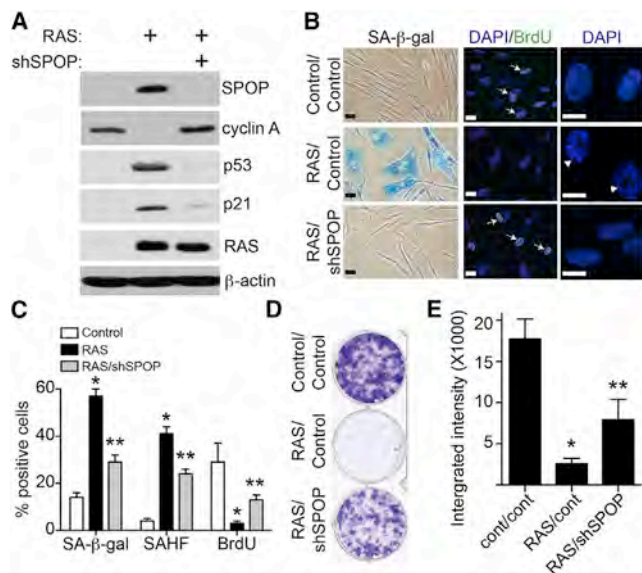


**Figure 3. SPOP Knockdown Suppresses Senescence**

(A) IMR90 cells were infected with a retrovirus encoding oncogenic RAS together with a lentivirus encoding shSPOP or control. Eight days post-drug selection, the indicated cells were examined for expression of SPOP, cyclin A, p53, p21, RAS, and  $\beta$ -actin by immunoblotting.

(B) Same as (A) but examined for SA- $\beta$ -gal activity, BrdU incorporation, or SAHF formation by DAPI staining for the punctate pattern in cell nuclei. Arrows point to examples of cells positive for the indicated markers. Arrowheads indicate SAHF-positive cells. The scale bar represents 10  $\mu$ m.

(C) Quantitation of (B). Two-hundred cells from each of the indicated groups were examined for the expression of the indicated markers. Mean of three independent experiments with SD is shown. \* $p < 0.01$  compared with controls and \*\* $p < 0.01$  compared with RAS infected only.

(D) Same as (A). Six days post-drug selection, 3,000 cells from each of the indicated groups were seeded in 6-well plates for focus formation assays. Cells were fixed and stained with 0.05% crystal violet after growing for an additional 12 days.

(E) Quantification of (D). The integrated intensity of foci from the indicated cells was quantified by using the NIH ImageJ software. Mean of three independent experiments with SD is shown. \* $p < 0.01$  compared with controls and \*\* $p < 0.01$  compared with RAS infected only.

RAS-expressing cells (Figures 3A–3C). Consistently, shSPOP significantly rescued growth inhibition induced by oncogenic RAS as determined by focus formation (Figures 3D and 3E). We conclude that SPOP knockdown suppresses RAS-induced senescence.

### SEN7 Is a SPOP Substrate that Is Degraded during Senescence

Next, we determined the mechanism by which SPOP regulates senescence. We performed an *in silico* analysis of proteins that are putative SPOP substrates based on the SPOP-binding recognition motif  $\Phi$ - $\pi$ -S-S/T-S/T ( $\Phi$ , non-polar residue;  $\pi$ , polar residue; Zhuang et al., 2009). This analysis revealed that the deSUMOylase SEN7 contains two SPOP-binding motifs (Figure 4A). These motifs are unique to SEN7 as the other six members of the SENPs (SEN1–3, SEN5–6, and SEN8) do not contain SPOP-binding motifs (Figures S3A and S3B). In addition, SEN7 has two isoforms, namely SEN7L and SEN7S (Bawa-

Khalife et al., 2012). Notably, only SEN7L, but not SEN7S, contains the SPOP-binding motif (Figure S3C). To validate this analysis, we performed co-immunoprecipitation analysis in 293T cells ectopically expressing GFP-SPOP and FLAG-SEN7. Indeed, ectopic SPOP and SEN7 co-immunoprecipitated with each other (Figure 4B). In addition, we treated senescent IMR90 cells, in which SPOP expression is induced, with the proteasome inhibitor MG132 to prevent potential degradation of SEN7 by the up-regulated SPOP. Co-immunoprecipitation analysis revealed that endogenous SPOP co-immunoprecipitated with endogenous SEN7 (Figure 4C). As a negative control, there was no co-immunoprecipitation between SPOP and SENP1 (Figure 4C).

Next, we determined whether SEN7 is subject to SPOP-mediated degradation. We co-expressed SEN7 with a titrated amount of SPOP. Indeed, there was a SPOP dose-dependent decrease in SEN7 expression (Figure 4D), suggesting that SPOP promotes SEN7 degradation. The observed decrease in SEN7 protein levels by SPOP was inhibited by the proteasome inhibitor MG132 (Figure 4D). This supports our hypothesis that SPOP promotes ubiquitin-mediated SEN7 degradation. To directly determine the effects of SPOP on SEN7 ubiquitination, we examined the ubiquitinated levels of SEN7 in cells expressing a HA-tagged ubiquitin treated with MG132 to prevent the proteasome-dependent degradation of ubiquitinated SEN7. Indeed, there was a dose-dependent increase in ubiquitinated SEN7 in SPOP-expressing cells (Figure 4E).

Consistent with the hypothesis that SEN7 is a substrate for SPOP-mediated degradation during senescence, we observed a decrease in SEN7 expression in senescent IMR90 cells (Figure 4F). And SPOP knockdown was sufficient to restore SEN7 expression in these cells (Figure 4G), further supporting the idea that SPOP mediates SEN7 degradation during senescence.

Next, we determined whether SPOP mutants observed in prostate cancer are impaired in their ability to degrade SEN7. Indeed, compared with wild-type SPOP that degrades SEN7 efficiently, cancer-associated SPOP mutants were impaired in SEN7 degradation (Figure 4H). Similar observations were also made in prostate cancer cell lines (Figure S4). Consistently, compared with wild-type SPOP, cancer-associated SPOP mutants were impaired in their ability to ubiquitinate SEN7 (Figure 4I). This correlated with an impaired interaction between the cancer-associated mutant SPOP and SEN7 (Figure 4J).

Finally, we determined the correlation of SEN7 protein with SPOP mutational status in prostate tumor specimens. We performed immunohistochemical staining of SEN7 in a series of 80 SPOP wild-type and 13 SPOP-mutated prostate tumor specimens (Figure 4K). SEN7 staining was scored as negative (0), weak (1), intermediate (2), or strong (3). Statistical analysis revealed that SEN7 is expressed at significantly ( $p < 0.0001$ ) higher levels in prostate tumors with SPOP mutations compared to those with wild-type SPOP (Figure 4L; Table S1). This further supports the notion that SEN7 is a substrate of SPOP-mediated degradation.

### SEN7 Binds to SPOP via Its First SPOP-Binding Motif, and the Ubiquitination of SEN7 by SPOP Depends upon Its Interaction with SPOP

Because there are two SPOP-binding motifs on SEN7 (Figure 4A), we determined whether the binding between SEN7



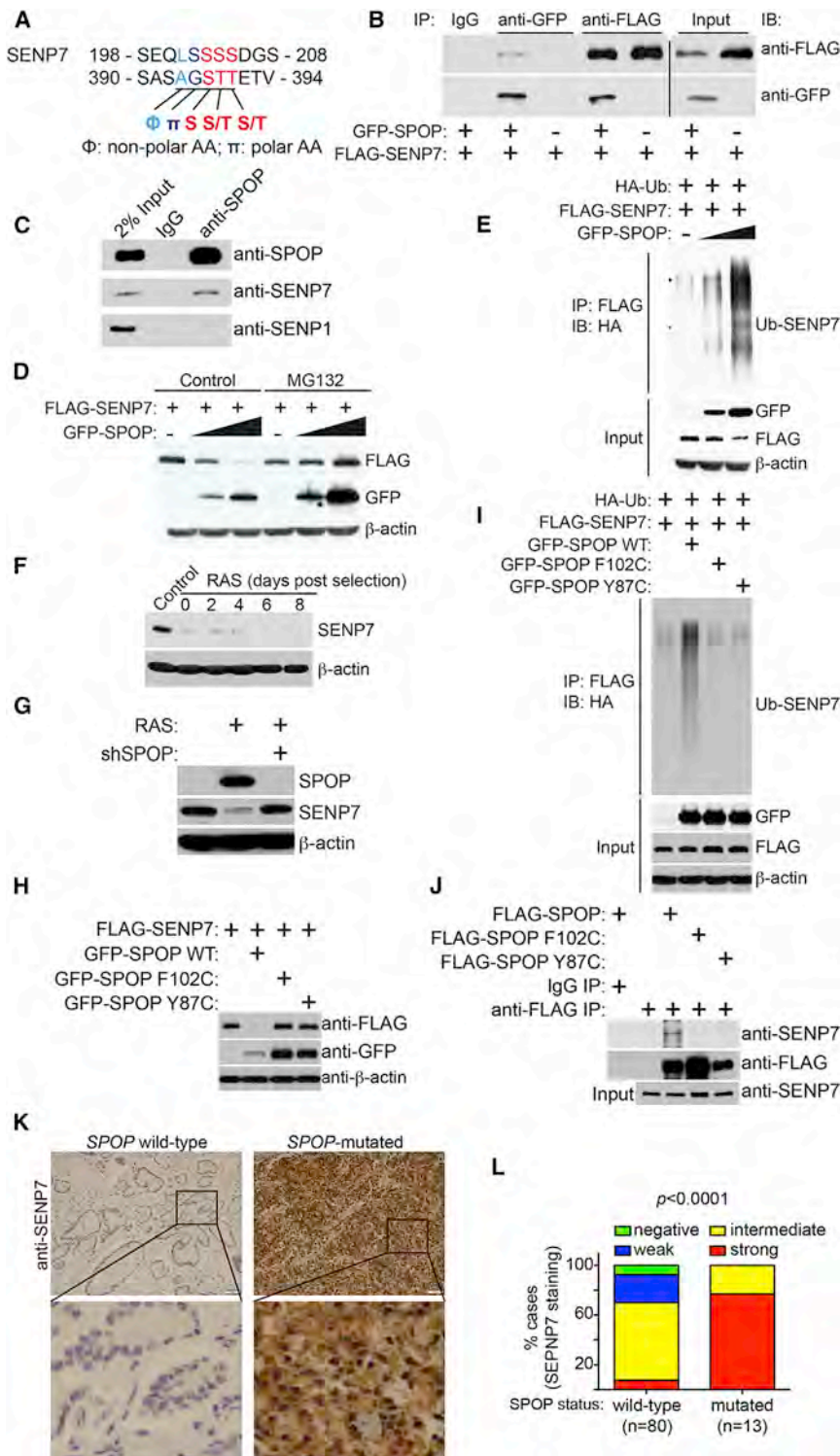


**Figure 4. SENP7 is a SPOP-Binding Substrate that Is Subjected to SPOP-Adaptor-Mediated Degradation**

(A) SENP7 has two putative SPOP-binding consensus motifs.

(B) Ectopic SPOP and SENP7 interact with each other. 293T cells were transfected with the indicated GFP-SPOP and/or FLAG-SENP7 plasmids, and 16 hr post-transfection, cells were treated with 20  $\mu$ M MG132 for 8 hr and subjected to co-immunoprecipitation analysis using the indicated antibodies or IgG controls. The co-immunoprecipitation was analyzed by immunoblotting using anti-FLAG or anti-GFP antibodies.

(C) Endogenous SPOP interacts with SENP7 in RAS-infected IMR90 cells. IMR90 cells were infected with a retrovirus encoding oncogenic RAS to induce SPOP expression. Drug-selected cells were treated with 20  $\mu$ M MG132 for 8 hr, and the cells were subjected to co-immunoprecipitation analysis using an anti-SPOP antibody or an isotype-matched IgG control. The IP'd product was analyzed by immunoblotting using the indicated antibodies.

(D) SPOP degrades SENP7 expression in a proteasome-dependent manner. 293T cells were transfected with 100 ng FLAG-SENP7 together with 0, 500, or 1,000 ng GFP-SPOP plasmids. Sixteen hours post-transfection, cells were treated with control or 20  $\mu$ M MG132 for 8 hr and subjected to immunoblotting analysis using the indicated antibodies.

(E) SPOP promotes polyubiquitination of SENP7. 293T cells were transfected with the indicated plasmids, and 16 hr post-transfection, cells were treated with 20  $\mu$ M MG132 for 8 hr and subjected to immunoprecipitation with an anti-FLAG antibody for SENP7. The ubiquitination level of SENP7 was analyzed by immunoblotting using an anti-HA antibody for ubiquitin.

(F) Time course analysis for SENP7 expression during senescence of IMR90 cells induced by oncogenic RAS. Expression of SENP7 and  $\beta$ -actin was examined at the indicated time points by immunoblotting.

(G) IMR90 cells were co-infected with a retrovirus encoding for oncogenic RAS together with a lentivirus encoding shSPOP or control. Eight days post-drug selection, cells were examined for expression of SPOP, SENP7, and  $\beta$ -actin by immunoblotting.

(H) Cancer-associated SPOP mutants lack the ability to degrade SENP7. 293T cells were transfected with FLAG-SENP7 together with GFP-tagged wild-type SPOP or the indicated SPOP mutants. Sixteen hours post-transfection, cells were subjected to immunoblotting analysis using the indicated antibodies.

(I) SPOP-induced polyubiquitination of SENP7 is impaired by cancer-associated SPOP mutants. 293T cells were transfected with the indicated plasmids, and 16 hr post-transfection, the indicated cells were treated with 20  $\mu$ M MG132 for 8 hr and subjected to immunoprecipitation with an

anti-FLAG antibody for SENP7. The ubiquitination level of SENP7 was analyzed by immunoblotting using an anti-HA antibody for ubiquitin.

(J) The cancer-associated SPOP mutants are impaired in SENP7 interaction. IMR90 cells were infected with a retrovirus encoding the indicated FLAG-tagged wild-type or cancer-associated mutant SPOP or control. Drug-selected cells were treated with 20  $\mu$ M MG132 for 8 hr, and the cells were subjected to co-immunoprecipitation analysis using an anti-FLAG antibody or an isotype-matched IgG control. The IP'd product was analyzed by immunoblotting using the indicated antibodies.

(K) Examples of SENP7 immunohistochemical staining in SPOP-mutated or wild-type prostate tumor specimens. The scale bar represents 50  $\mu$ m.

(L) Quantification of SENP7 expression levels in 80 cases of SPOP wild-type and 13 cases of SPOP-mutated prostate tumor specimens.

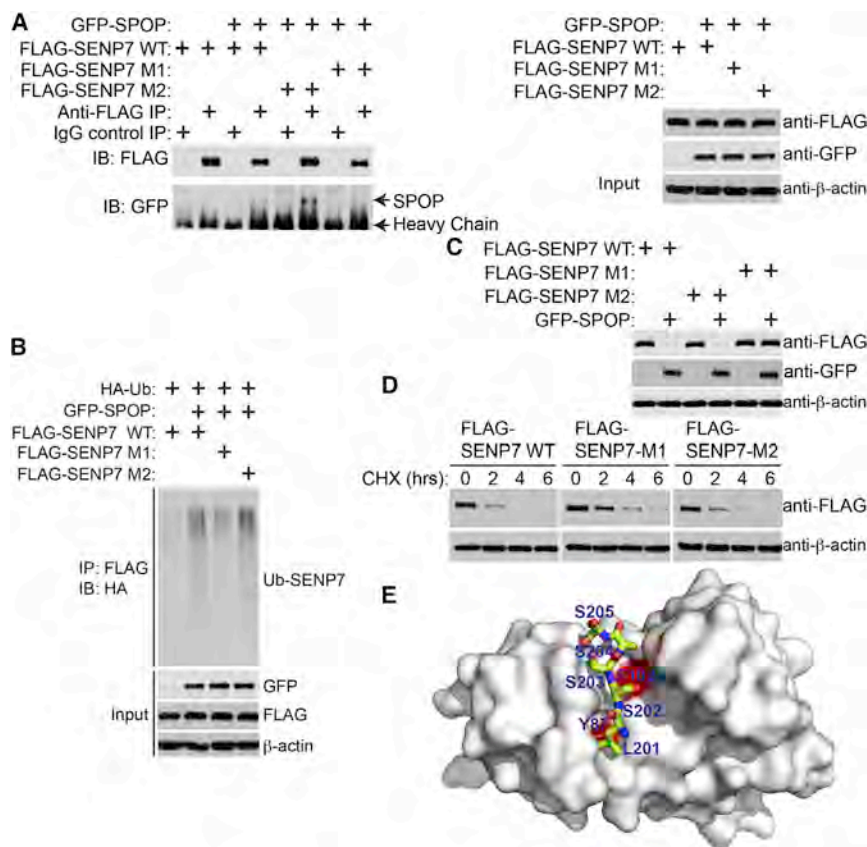


**Figure 5. Degradation of SENP7 Depends upon Its Interaction with SPOP via the First SPOP-Binding Motif in SENP7**

(A) The first SPOP-binding motif in SENP7 is required for its binding to SPOP. 293T cells were transfected with the indicated plasmids expressing GFP-SPOP, FLAG-SEN7 wild-type (WT), first SPOP-binding motif mutated SENP7 (SEN7 M1) that SENP7 aas 201–205 LSSSS was mutated into LAAAS, or second SPOP-binding motif deleted SENP7 (SEN7 M2) that deleted SENP7 aas 393–397 AGSTT (393–397). Sixteen hours post-transfection, cells were treated with 20  $\mu$ M MG132 for 8 hr and subjected to co-immunoprecipitation analysis using the indicated antibodies. (B) The first SPOP-binding motif in SENP7 is required for its ubiquitination by SPOP. 293T cells were transfected with indicated plasmids, and 16 hr post-transfection, cells were treated with 20  $\mu$ M MG132 and subjected to immunoprecipitation with an anti-FLAG antibody for SENP7. The ubiquitination level of SENP7 was analyzed by immunoblotting using an anti-HA antibody for ubiquitin. (C) The first SPOP-binding motif in SENP7 is required for its degradation by SPOP. 293T cells were transfected with the indicated plasmids. Sixteen hours post-transfection, cells were subjected to immunoblotting analysis using the indicated antibodies. (D) Protein abundance of SENP7 wild-type and the indicated mutants determined by cycloheximide chase assay. Equal amounts of the indicated SENP7 wild-type or mutants were transfected into 293T cells, and cells were treated with 50  $\mu$ g/ml

cycloheximide (CHX) 16 hr post-transfection. Expression of transfected wild-type or the indicated SENP7 indicated time points after CHX treatment. (E) The first SPOP-binding motif of SENP7 peptide (aas 201–205 LSSSS; shown in green sticks) bound to SPOP substrate-binding MATH domain (shown in gray surface representation) is modeled based on two published X-ray crystal structures of substrate bound to the SPOP MATH domain (RCSB ID 3HQM and 3HQL).

and SPOP requires one or both binding motifs. Accordingly, we mutated the two SPOP-binding motifs in SENP7 individually and ectopically expressed the FLAG-tagged wild-type, binding-site-1-mutated (M1), or binding-site-2-mutated (M2) SENP7 together with a GFP-tagged SPOP. Co-immunoprecipitation analysis revealed that both wild-type and SENP7 M2 co-immunoprecipitated with SPOP, whereas the SENP7 M1 mutant was impaired in its interaction with SPOP (Figure 5A). Indeed, ubiquitin analysis showed that both wild-type and M2 mutant SENP7 were ubiquitinated by ectopic SPOP at comparable levels, whereas the SENP7 M1 mutant was impaired in its ubiquitination by SPOP (Figure 5B). Consistently, the expression levels of both wild-type and SENP7 M2 were reduced by SPOP, whereas the degradation of SENP7 M1 was impaired (Figure 5C). Finally, to directly determine the stability of SENP7 wild-type and mutants, we treated cells with the gene translation inhibitor cycloheximide (CHX) and chased the levels of wild-type or mutant SENP7 levels over 6 hr. Compared with wild-type SENP7 and SENP7 M2, which have comparable degradation rates, there was an increase in protein stability of the SENP7 M1 mutant (Figure 5D). Further, structure modeling indicated that the SPOP-binding motif SENP7 peptide fits nicely into the binding pocket of the SPOP MATH domain (Fig-

ure 5E). We conclude that the first SPOP-binding motif on SENP7 is required for its binding, ubiquitination, and degradation by SPOP.

### Downregulation of SENP7 Promotes Senescence, which Correlates with an Increase in HP1 $\alpha$ Sumoylation and Its Subcellular Re-localization and the Associated Gene Silencing

Next, we determined whether SENP7 downregulation drives senescence of primary IMR90 cells. We knocked down SENP7 expression using an shSEN7 in IMR90 cells. Indeed, SENP7 knockdown induced the expression of markers of senescence such as SA- $\beta$ -gal activity, SAHF formation, and upregulation of p21 and p53 (Figures 6A–6C). Consistently, cell proliferation markers such as cyclin A expression and BrdU incorporation were suppressed by SENP7 knockdown (Figures 6A–6C). Likewise, cell growth was inhibited by SENP7 knockdown as determined by focus formation (Figures 6D and 6E). Similar observations were also made in prostate cancer cells (Figure S5). Knockdown of either p53 or pRB impaired senescence induced by SENP7 knockdown as evidenced by a decrease in the SA- $\beta$ -gal-positive cells (Figures S5F–S5H). Furthermore, ectopic SENP7 suppressed senescence induced by SPOP



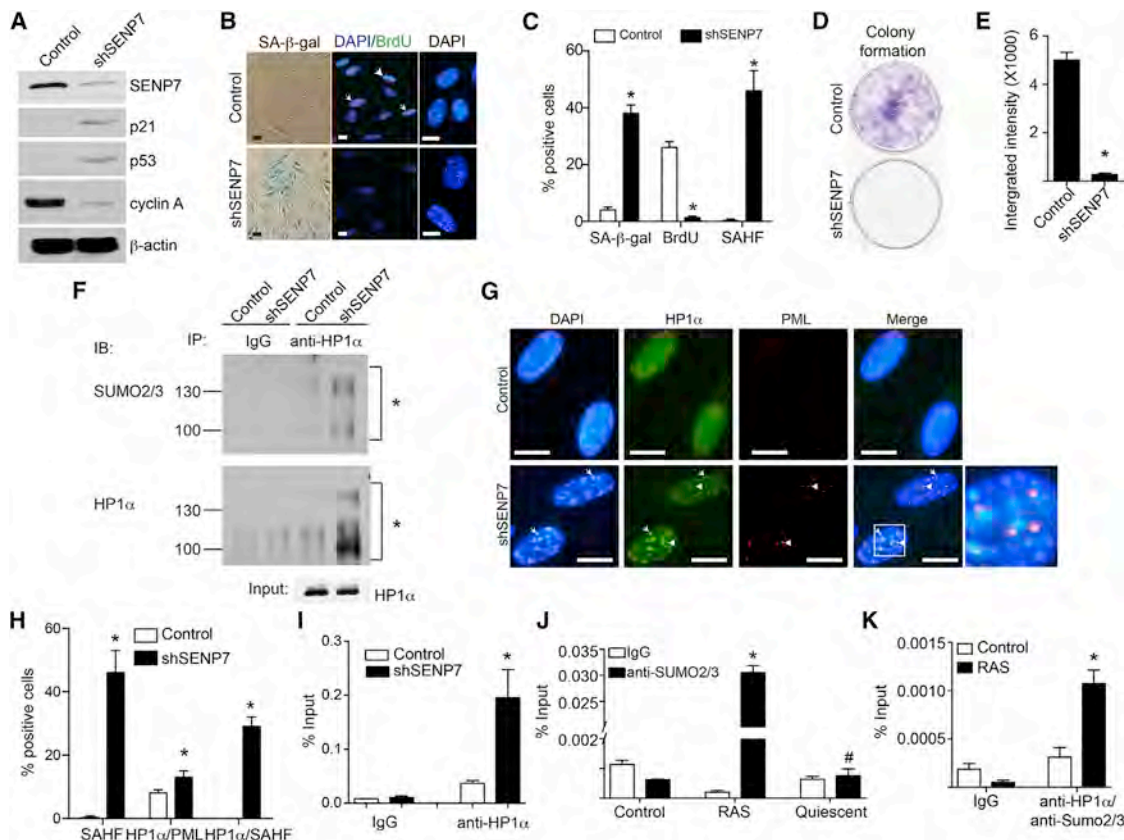


**Figure 6. SENP7 Knockdown Induces Senescence, which Correlates with an Increase in HP1 $\alpha$  Sumoylation and Its Associated Gene Silencing**

(A) IMR90 cells were infected with a lentivirus encoding shSENP7 or control. Day 8 after drug selection, the expression of SENP7, p21, p53, and cyclin A was examined by immunoblotting.  $\beta$ -actin expression was used as loading control.

(B) Same as (A) but stained for SA- $\beta$ -gal activity, examined for BrdU incorporation, or stained with DAPI to visualize SAHF. Arrows point to examples of BrdU-positive cells. The scale bar represents 10  $\mu$ m.

(C) Quantification of (B). Two hundred cells from each of the indicated groups were examined for SA- $\beta$ -gal activity or BrdU- or SAHF-positive cells. Mean of three independent experiments with SD is shown. \* $p < 0.01$ .

(D) Same as (A) but examined for focus formation. Three thousand of the indicated cells were seeded in 6-well plates, and cells were fixed and stained with 0.05% crystal violet after growing for an additional 12 days.

(E) Quantitation of (D). The integrated intensity of foci formed by the indicated cells was measured using the NIH ImageJ software. Mean of three independent experiments with SD is shown. \* $p < 0.001$ .

(F) Same as (A) but examined for HP1 $\alpha$  sumoylation. The indicated cells were subjected to immunoprecipitation with an anti-HP1 $\alpha$  antibody or an isotype-matched IgG control using buffers with NEM, an inhibitor of SUMO protease (please see [Experimental Procedures](#) for details). The immunoprecipitated samples were subjected to immunoblotting using an anti-HP1 $\alpha$  or anti-SUMO2/3 antibody to detect the sumoylation of HP1 $\alpha$ . Asterisks indicated sumoylated HP1 $\alpha$ .

(G) SENP7 knockdown promotes SAHF formation and HP1 $\alpha$ 's localization into SAHF. Shown is same as (A) but stained for HP1 $\alpha$ , PML bodies, and DAPI to visualize SAHF. Arrows point to the co-localized HP1 $\alpha$  and SAHF. Arrowheads indicate the co-localized HP1 $\alpha$  and PML bodies. The scale bar represents 10  $\mu$ m.

(H) Quantification of (F). One hundred cells from each of the indicated groups were examined for SAHF formation, co-localization of HP1 $\alpha$  with PML, and co-localization of HP1 $\alpha$  with SAHF. Mean of three independent experiments with SD is shown. \* $p < 0.05$  compared with controls.

(I) SENP7 knockdown enhances HP1 $\alpha$ 's association with the CCNA2 gene promoter. Same as (A), but the cells were subjected to chromatin immunoprecipitation (ChIP) analysis using an anti-HP1 $\alpha$  antibody or an isotype-matched IgG control for the CCNA2 promoter. \* $p < 0.01$  compared with controls.

(J) The enhanced association of Sumo2/3 with the CCNA2 gene promoter in cells undergoing senescence, but not quiescence. IMR90 cells were infected with RAS for 48 hr to induce senescence or made quiescent by contacting inhibition and serum starvation (0.1% serum). The indicated cells were subjected to ChIP analysis using an anti-SUMO2/3 antibody or an isotype-matched IgG control for the CCNA2 gene promoter. Mean of three independent experiments with SD is shown. \* $p < 0.01$  and # $p > 0.05$  compared with controls.

(K) Same as (J), but control or RAS-infected cells (48 hr post-infection) were subjected to sequential ChIP analysis using an anti-HP1 $\alpha$  antibody followed by an anti-SUMO2/3 antibody for the CCNA2 gene promoter. Mean of three independent experiments with SD is shown. \* $p < 0.01$  compared with controls.

overexpression as indicated by a decrease in the SA- $\beta$ -gal-positive cells (Figures S5I–S5K). We conclude that SENP7 downregulation promotes senescence.

Next, we determined the mechanism by which SENP7 downregulation promotes senescence. It has previously been demonstrated that SENP7 binds to HP1 $\alpha$  and regulates HP1 $\alpha$ 's

localization to pericentromeric heterochromatin via its sumoylation (Maison et al., 2012). SENP7 is a SUMO2/3 chain removal deSUMOylase (Shen et al., 2009). Because SENP7 knockdown induces SAHF formation (Figures 6B and 6C), we examined the effects of SENP7 knockdown on SUMO2/3-modified HP1 $\alpha$  levels. Indeed, compared with controls, there was an increase in SUMO2/3-modified HP1 $\alpha$  in SENP7 knockdown cells (Figure 6F). Sumoylation is known to regulate target protein subcellular localization including their PML body localization (Cubéñas-Potts and Matunis, 2013). In addition, localization of HP1 $\alpha$  into PML bodies is known to facilitate its deposition into SAHF (Zhang et al., 2005). Thus, we examined the changes in distribution of HP1 $\alpha$  in SENP7 knockdown cells compared with controls. We observed a significant increase in the localization of HP1 $\alpha$  into SAHF and a significant but mild increase of 1.5-fold in its localization into PML bodies (Figures 6G and 6H), thus arguing that HP1 $\alpha$ -sumoylation is only weakly participating to PML localization. This suggests that SENP7 downregulation promotes SAHF formation by increasing HP1 $\alpha$ -sumoylation to facilitate its deposition into SAHF. Consistently, both SPOP ectopic expression and SENP7 knockdown significantly suppressed the E2F reporter activity (Figure S5L). Finally, we sought to determine whether this correlates with the recruitment of HP1 $\alpha$  onto the promoters of proliferation-promoting genes such as the E2F target gene *CCNA2* (encoding for cyclin A), whose expression is suppressed by SENP7 knockdown (Figure 6A) and is a known target of HP1 $\alpha$  and SAHF-mediated gene silencing (Narita et al., 2003). We performed chromatin immunoprecipitation (ChIP) analysis for the *CCNA2* gene promoter using antibodies to HP1 $\alpha$  or an IgG control. Indeed, there was a significant increase in the association of HP1 $\alpha$  with the *CCNA2* gene promoter in SENP7 knockdown cells compared with controls (Figure 6I). Notably, ChIP analysis revealed that there was a significant increase in the association of SUMO2/3 with the *CCNA2* promoter during senescence (Figure 6J). However, there is no enrichment of SUMO2/3 in the *CCNA2* promoter in quiescent cells (Figure 6J). Consistently, sequential ChIP using an anti-HP1 $\alpha$  followed by an anti-SUMO2/3 antibody showed a significant enrichment of SUMO2/3-HP1 $\alpha$  in the *CCNA2* promoter, but not in the negative control *ACTB* promoter, compared with controls (Figures 6K and S5M). In contrast, there is no enrichment of SUMO2/3-HP1 $\alpha$  in the *CCNA2* promoter in quiescent cells (Figure S5N). We conclude that SENP7 knockdown promotes senescence, which correlates with an increase in HP1 $\alpha$  sumoylation, subcellular re-localization to SAHF, and its associated silencing of certain proliferation-promoting genes.

#### **The Effects of SPOP on Senescence Correlate with Changes in HP1 $\alpha$ Sumoylation, HP1 $\alpha$ 's SAHF Localization, and Its Associated Gene Silencing**

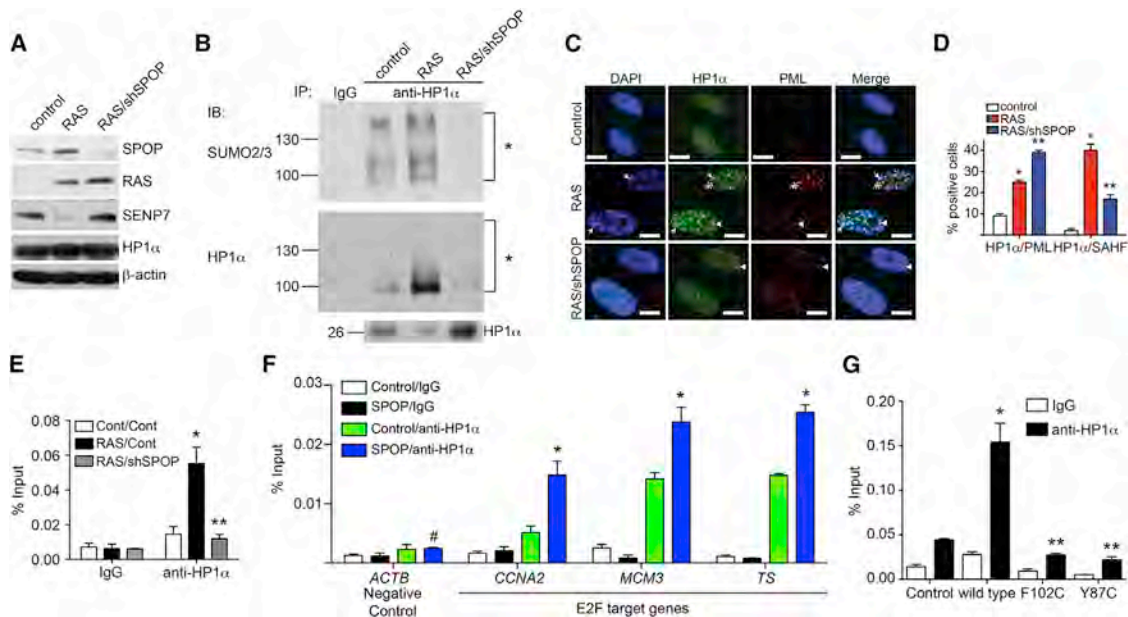
SPOP knockdown suppressed senescence (Figure 3), which correlated with an increase in its substrate SENP7 expression (Figure 7A). Thus, we determined the effects of SPOP knockdown on HP1 $\alpha$  sumoylation, subcellular localization, and its association with the *CCNA2* gene promoter. Compared with controls, there was an increase in sumoylated HP1 $\alpha$  in RAS-infected cells, which correlated with its SAHF localization and its recruitment on the promoter of the *CCNA2* gene (Figures 7B–

7E). SPOP knockdown caused a decrease in the levels of sumoylated HP1 $\alpha$  in senescent cells (Figure 7B). This correlated with a decrease in the localization of HP1 $\alpha$  to SAHF and its association with the *CCNA2* gene promoter (Figures 7C–7E). SPOP knockdown increased HP1 $\alpha$ 's localization into PML bodies (Figures 7C and 7D). Because SPOP knockdown decreased HP1 $\alpha$  sumoylation due to an increase in SENP7 (Figures 7A and 7B), this suggests that HP1 $\alpha$  sumoylation is important for translocation of HP1 $\alpha$  from PML bodies to SAHF (Zhang et al., 2005). Notably, HP1 $\alpha$ 's association with the promoters of the E2F target genes such as *CCNA2*, *MCM3*, and *thymidylate synthase* (*TS*), but not with a negative control *ACTB* gene promoter, was enhanced by wild-type SPOP (Figure 7F). Compared with wild-type SPOP, cancer-associated SPOP mutants were impaired in recruitment of HP1 $\alpha$  to the *CCNA2* gene promoter (Figure 7G). This correlated with the ability of wild-type, but not mutant, SPOP in degrading SENP7 and inducing senescence (Figures 2 and 5). Together, these data support a model whereby upregulation of SPOP promotes senescence by degrading SENP7 deSUMOylase, which in turn leads to an increase in the physical presence of sumoylated HP1 $\alpha$  at certain proliferation-promoting genes concomitant with their silencing.

## **DISCUSSION**

Our data support the hypothesis that SPOP functions as a tumor suppressor by promoting cellular senescence. This is consistent with the findings from recent genome-wide deep-sequencing studies that *SPOP* is mutated in a number of cancer types (Barbieri et al., 2012; Berger et al., 2011; Le Gallo et al., 2012). Counterintuitively, SPOP is also overexpressed in other cancer types such as clear cell renal cell carcinoma (Liu et al., 2009), where it acts as a tumorigenic hub (Li et al., 2014). The molecular basis for the observed functional differences in different cancer types remains unclear. It is possible that overcoming SPOP-induced senescence promotes tumorigenesis in cancers where SPOP is overexpressed. In this context, SPOP's role in cancer is akin to that of oncogenes, where oncogene activation induces senescence, whereas bypass of senescence induced by oncogenes contributes to cancer progression. In cancers with *SPOP* mutations, cells harboring *SPOP* mutations are impaired in the senescence tumor suppression mechanism. This contributes to the development of *SPOP*-mutated cancers. Thus, SPOP's role in cancer is likely context and tumor type dependent.

Our findings demonstrate that SPOP promotes senescence, which correlates with HP1 $\alpha$ -associated gene silencing. This is due to its ability to degrade SENP7 deSUMOylase, a SPOP substrate identified in the current study. Consequently, SENP7 downregulation leads to an increase in sumoylation levels of HP1 $\alpha$ . This has previously been linked to pericentromeric localization of HP1 $\alpha$  (Maison et al., 2012). In addition, SENP7 has been shown to promote chromatin relaxation for homologous recombination DNA repair (Garvin et al., 2013), which is consistent with the notion that its degradation promotes heterochromatin formation. The ability of SPOP wild-type and its cancer-associated mutants to induce senescence correlates with HP1 $\alpha$ -associated silencing of certain proliferation-promoting genes. Together, these data support the notion



that epigenetic gene silencing contributes to senescence induced by SPOP.

SENP7 knockdown induces formation of microscopically evident SAHF in addition to an increase in HP1 $\alpha$  sumoylation and its localization to proliferation-promoting genes such as *CCNA2* (Figure 6). Despite the fact that we observed an enhanced interaction between HP1 $\alpha$  and the *CCNA2* gene promoter, we did not observe formation of microscopically evident SAHF in SPOP overexpressing cells (data not shown). This is likely due to the fact that SENP7 acts downstream of SPOP, thus driving a more-pronounced phenotype as reflected by visible SAHF formation. Regardless, both SPOP overexpression and SENP7 knockdown decreases cyclin A expression, which correlates with HP1 $\alpha$ 's recruitment to the *CCNA2* gene promoter. Consistently, it has recently been demonstrated that SENP7 loss induces senescence of breast cancer cells, where

SENP7 was first linked to HP1 $\alpha$  sumoylation-mediated silencing of E2F target genes (Bawa-Khalife et al., 2012). These findings support the hypothesis that SPOP and SENP7 function in the same pathway at the molecular level.

SPOP is mutated in a number of cancer types and, most notably, in prostate cancer (up to 13%; Barbieri et al., 2012; Berger et al., 2011). Primary prostate tumors with SPOP mutations typically lack other genetic changes such as *PTEN* and *PIK3CA* alterations, *ETS* fusions, or *TP53* mutations (Barbieri et al., 2012). Thus, SPOP mutations represent a distinct subtype of prostate cancer. Our findings show that SENP7 knockdown drives senescence of prostate cancer cell lines (Figure S5). Silencing of proliferation-promoting E2F target genes induces senescence regardless of p53 and pRB status (Maehara et al., 2005; Narita et al., 2003). Our data indicate that SENP7 knockdown is sufficient to directly silence E2F target genes (such as



CCNA2), which correlates with gene promoter recruitment of HP1 $\alpha$  (Figure 6). There are no established cancer cell lines that carry mutations in *SPOP* (based on cBioportal analysis), which prevented us from testing the effects of SENP7 knockdown in *SPOP*-mutated cells. Regardless, our results suggest that SENP7 inhibition may be an intervention strategy for *SPOP*-mutated cancers. In addition, because SENP7 knockdown induces senescence of *SPOP* wild-type prostate cancer cell lines (Figure S5), this suggests that SENP7 inhibition may synergize with other targeted therapies in prostate cancer. Finally, these findings also suggest that patients harboring *SPOP* mutation might be less sensitive to treatments that are known to induce senescence.

In summary, we showed that *SPOP* promotes cellular senescence, an important tumor suppression mechanism, by degrading SENP7 deSUMOylase, a *SPOP*-binding substrate. This correlates with HP1 $\alpha$ -associated epigenetic gene silencing during senescence through a relay of ubiquitination and sumoylation post-transcriptional modifications. These findings establish that *SPOP* functions as a tumor suppressor in the context of cellular senescence and the associated cell growth arrest.

## EXPERIMENTAL PROCEDURES

### ChIP and Ubiquitinated Protein Analysis

ChIP was performed as previously described (Tu et al., 2013) using rabbit anti-HP1 $\alpha$  antibody (Novus), anti-SUMO2/3 antibody (Abcam), or an isotype-matched IgG control. Immunoprecipitated DNA was analyzed using SYBR Green qPCR (SABiosciences) against the indicated gene promoters using primers as detailed in the Supplemental Information.

For ubiquitinated protein analysis, cells were treated with 20  $\mu$ M MG132, a protease inhibitor, for 8 hr to prevent degradation of the ubiquitinated proteins prior to harvest. For co-immunoprecipitation, cells were harvested with cold buffer A (10 mM HEPES-KOH [pH 8.0], 10 mM KCl, 1.5 mM MgCl<sub>2</sub>, 0.34 M sucrose, 10% glycerol, and 0.5% Triton X-100 [pH 7.5]) supplemented with Complete Protease inhibitor cocktail (Roche) and 1 mM PMSF for 5 min on ice and centrifuged at 3,000 rpm at 4°C for 5 min to collect the nucleus pellets. The pellets were then resuspended in lysis buffer (50 mM Tris-HCl [pH 8.0], 1 mM EDTA, 0.5% NP-40, 300 mM NaCl, 10 mM NaF, protease inhibitor cocktail, and 1 mM PMSF) and rotated at 4°C for 20 min. The lysate was then centrifuged at 12,000 g at 4°C for 10 min, and the supernatant was used for co-immunoprecipitation. The supernatant was incubated with anti-*SPOP*, anti-GFP, anti-FLAG antibody, or an IgG control for 3 hr at 4°C and subsequently with Protein G Dynabeads (Life Technologies) for 1 hr. The beads were washed with NETN buffer three times, boiled in Laemmli sample buffer, and subjected to immunoblotting.

### Structure Modeling

A model of the *SPOP* MATH domain bound to the first *SPOP*-binding motif of SENP7 peptide (aas 201–205; LSSSS) was generated using the X-ray crystal structure of *SPOP*-substrate complexes RCSB ID 3HQM and 3HQL. The two crystal structures were overlaid in Coot (Emsley et al., 2010), and the peptide residues were mutated to the corresponding LSSSS peptide using sequence alignment as a guide. The figure was prepared in PyMOL (The PyMOL Molecular Graphics System; Version 1.5.0.5 Schrödinger).

### Prostate Tumor Specimens and IHC

Prostate tumor specimens were obtained from Shanghai Changhai Hospital. Use of these specimens was approved by the Institute Review Board of Shanghai Changhai Hospital. *SPOP* mutation status in prostate tumors was determined as previously described (Blattner et al., 2014) based on an initial pre-PCR amplification step to enrich the *SPOP* exons 6 and 7 followed by a

high-resolution melting screen and Sanger sequencing. Paraformaldehyde-fixed paraffin-embedded tumor samples were deparaffinized, rehydrated, and subjected to heat-mediated antigen retrieval. For immunohistochemistry (IHC) analysis, we used UltraSensitive S-P(Rabbit) IHC Kit (KIT-9706; Fuzhou Maixin Biotech), following the manufacturer's instructions with minor modification. Briefly, the sections were incubated with 3% H<sub>2</sub>O<sub>2</sub> for 15 min at room temperature to quench endogenous peroxidase activity. After incubating in normal goat serum for 1 hr, sections were treated with primary antibody at 4°C overnight. IHC analysis of tumor samples was performed using primary antibodies against SENP7 (dilution 1:200; Novus Biologicals; catalog number: NB100-92106). The sections were then washed three times in PBS and treated for 30 min with biotinylated goat-anti-rabbit IgG secondary antibodies (Fuzhou Maixin Biotech). After washing three times in PBS, sections were incubated with streptavidin-conjugated HRP (Fuzhou Maixin Biotech). After washing three times in PBS for 5 min each, specific detection was developed with 3,3'-diaminobenzidine (DAB-2031; Fuzhou Maixin Biotech). Images were taken by using an Olympus camera and matched software.

### Statistical Analysis

GraphPad Prism Version 5.0 was used to perform for statistical analyses. The Student's *t* test was used to determine *p* values of raw data. *p* value < 0.05 was considered as significant.

## SUPPLEMENTAL INFORMATION

Supplemental Information includes Supplemental Experimental Procedures, five figures, and one table and can be found with this article online at <http://dx.doi.org/10.1016/j.celrep.2015.09.083>.

## AUTHOR CONTRIBUTIONS

H.Z. and R.Z. designed experiments. H.Z., B.G.B., K.M.A., and Z.T. conducted experiments and analyzed the data. S.R., Y.Z., and Y.S. conducted experiments and analyzed the data related to Figures 4K and 4L and Table S1. E.S. contributed to Figure 5E. J.Y. contributed key reagents. H.Z. and R.Z. wrote the manuscript.

## ACKNOWLEDGMENTS

We thank Drs. Dario Altieri and Maureen Murphy for critical comments. This work was supported by NIH/NCI grants (R01CA160331 and R01CA163377 to R.Z.) and a DOD award (OC140632P1 to R.Z.). B.G.B. is supported by a NIH/NCI grant (K99CA194318). K.M.A. is supported by NIH/NCI grants (K99CA194309 and T32CA9171-35). J.Y. is supported by National Natural Science Foundation (81172009). Support of Core Facilities used in this study was provided by Cancer Center Support Grant (CCSG) CA010815 to the Wistar Institute.

Received: May 4, 2015

Revised: August 12, 2015

Accepted: September 29, 2015

Published: October 29, 2015

## REFERENCES

- An, J., Wang, C., Deng, Y., Yu, L., and Huang, H. (2014). Destruction of full-length androgen receptor by wild-type *SPOP*, but not prostate-cancer-associated mutants. *Cell Rep.* 6, 657–669.
- Barbieri, C.E., Baca, S.C., Lawrence, M.S., Demichelis, F., Blattner, M., Theurillat, J.P., White, T.A., Stojanov, P., Van Allen, E., Stransky, N., et al. (2012). Exome sequencing identifies recurrent *SPOP*, *FOXA1* and *MED12* mutations in prostate cancer. *Nat. Genet.* 44, 685–689.
- Bawa-Khalfe, T., Lu, L.S., Zuo, Y., Huang, C., Dere, R., Lin, F.M., and Yeh, E.T. (2012). Differential expression of SUMO-specific protease 7 variants regulates epithelial-mesenchymal transition. *Proc. Natl. Acad. Sci. USA* 109, 17466–17471.



- Berger, M.F., Lawrence, M.S., Demichelis, F., Drier, Y., Cibulskis, K., Sivachenko, A.Y., Sboner, A., Esquivela, R., Pflueger, D., Sougnez, C., et al. (2011). The genomic complexity of primary human prostate cancer. *Nature* 470, 214–220.
- Bischof, O., Schwamborn, K., Martin, N., Werner, A., Sustmann, C., Groschedl, R., and Dejean, A. (2006). The E3 SUMO ligase PIASy is a regulator of cellular senescence and apoptosis. *Mol. Cell* 22, 783–794.
- Blattner, M., Lee, D.J., O'Reilly, C., Park, K., MacDonald, T.Y., Khani, F., Turner, K.R., Chiu, Y.L., Wild, P.J., Dolgalev, I., et al. (2014). SPOP mutations in prostate cancer across demographically diverse patient cohorts. *Neoplasia* 16, 14–20.
- Bunce, M.W., Boronenkov, I.V., and Anderson, R.A. (2008). Coordinated activation of the nuclear ubiquitin ligase Cul3-SPOP by the generation of phosphatidylinositol 5-phosphate. *J. Biol. Chem.* 283, 8678–8686.
- Cubeñas-Potts, C., and Matunis, M.J. (2013). SUMO: a multifaceted modifier of chromatin structure and function. *Dev. Cell* 24, 1–12.
- Dimri, G.P., Lee, X., Basile, G., Acosta, M., Scott, G., Roskelley, C., Medrano, E.E., Linskens, M., Rubelj, I., Pereira-Smith, O., et al. (1995). A biomarker that identifies senescent human cells in culture and in aging skin in vivo. *Proc. Natl. Acad. Sci. USA* 92, 9363–9367.
- Emsley, P., Lohkamp, B., Scott, W.G., and Cowtan, K. (2010). Features and development of Coot. *Acta Crystallogr. D Biol. Crystallogr.* 66, 486–501.
- Garvin, A.J., Densham, R.M., Blair-Reid, S.A., Pratt, K.M., Stone, H.R., Weekes, D., Lawrence, K.J., and Morris, J.R. (2013). The deSUMOylase SENP7 promotes chromatin relaxation for homologous recombination DNA repair. *EMBO Rep.* 14, 975–983.
- Hernández-Muñoz, I., Lund, A.H., van der Stoop, P., Boutsma, E., Muijers, I., Verhoeven, E., Nusinow, D.A., Panning, B., Marahrens, Y., and van Lohuizen, M. (2005). Stable X chromosome inactivation involves the PRC1 Polycomb complex and requires histone MACROH2A1 and the CULLIN3/SPOP ubiquitin E3 ligase. *Proc. Natl. Acad. Sci. USA* 102, 7635–7640.
- Jones, S., Stransky, N., McCord, C.L., Cerami, E., Lagowski, J., Kelly, D., Angiuoli, S.V., Sausen, M., Kann, L., Shukla, M., et al. (2014). Genomic analyses of gynaecologic carcinosarcomas reveal frequent mutations in chromatin remodelling genes. *Nat. Commun.* 5, 5006.
- Kwon, J.E., La, M., Oh, K.H., Oh, Y.M., Kim, G.R., Seol, J.H., Baek, S.H., Chiba, T., Tanaka, K., Bang, O.S., et al. (2006). BTB domain-containing speckle-type POZ protein (SPOP) serves as an adaptor of Daxx for ubiquitination by Cul3-based ubiquitin ligase. *J. Biol. Chem.* 281, 12664–12672.
- Le Gallo, M., O'Hara, A.J., Rudd, M.L., Urlick, M.E., Hansen, N.F., O'Neil, N.J., Price, J.C., Zhang, S., England, B.M., Godwin, A.K., et al.; NIH Intramural Sequencing Center (NISC) Comparative Sequencing Program (2012). Exome sequencing of serous endometrial tumors identifies recurrent somatic mutations in chromatin-remodeling and ubiquitin ligase complex genes. *Nat. Genet.* 44, 1310–1315.
- Li, T., Santockyte, R., Shen, R.F., Tekle, E., Wang, G., Yang, D.C., and Chock, P.B. (2006). Expression of SUMO-2/3 induced senescence through p53- and pRB-mediated pathways. *J. Biol. Chem.* 281, 36221–36227.
- Li, G., Ci, W., Karmakar, S., Chen, K., Dhar, R., Fan, Z., Guo, Z., Zhang, J., Ke, Y., Wang, L., et al. (2014). SPOP promotes tumorigenesis by acting as a key regulatory hub in kidney cancer. *Cancer Cell* 25, 455–468.
- Liu, J., Ghanim, M., Xue, L., Brown, C.D., Iossifov, I., Angeletti, C., Hua, S., Nègre, N., Ludwig, M., Stricker, T., et al. (2009). Analysis of Drosophila segmentation network identifies a JNK pathway factor overexpressed in kidney cancer. *Science* 323, 1218–1222.
- Maehara, K., Yamakoshi, K., Ohtani, N., Kubo, Y., Takahashi, A., Arase, S., Jones, N., and Hara, E. (2005). Reduction of total E2F/DP activity induces senescence-like cell cycle arrest in cancer cells lacking functional pRB and p53. *J. Cell Biol.* 168, 553–560.
- Maison, C., Romeo, K., Bailly, D., Dubarry, M., Quivy, J.P., and Almouzni, G. (2012). The SUMO protease SENP7 is a critical component to ensure HP1 enrichment at pericentric heterochromatin. *Nat. Struct. Mol. Biol.* 19, 458–460.
- Mukhopadhyay, D., and Dasso, M. (2007). Modification in reverse: the SUMO proteases. *Trends Biochem. Sci.* 32, 286–295.
- Narita, M., Nunez, S., Heard, E., Narita, M., Lin, A.W., Hearn, S.A., Spector, D.L., Hannon, G.J., and Lowe, S.W. (2003). Rb-mediated heterochromatin formation and silencing of E2F target genes during cellular senescence. *Cell* 113, 703–716.
- Pérez-Mancera, P.A., Young, A.R., and Narita, M. (2014). Inside and out: the activities of senescence in cancer. *Nat. Rev. Cancer* 14, 547–558.
- Pintard, L., Willis, J.H., Willems, A., Johnson, J.L., Srayko, M., Kurz, T., Glaser, S., Mains, P.E., Tyers, M., Bowerman, B., and Peter, M. (2003). The BTB protein MEL-26 is a substrate-specific adaptor of the CUL-3 ubiquitin-ligase. *Nature* 425, 311–316.
- Shen, L.N., Geoffroy, M.C., Jaffray, E.G., and Hay, R.T. (2009). Characterization of SENP7, a SUMO-2/3-specific isopeptidase. *Biochem. J.* 421, 223–230.
- Theurillat, J.P., Udeshi, N.D., Errington, W.J., Svinkina, T., Baca, S.C., Pop, M., Wild, P.J., Blattner, M., Groner, A.C., Rubin, M.A., et al. (2014). Prostate cancer. Ubiquitylome analysis identifies dysregulation of effector substrates in SPOP-mutant prostate cancer. *Science* 346, 85–89.
- Tu, Z., Zhuang, X., Yao, Y.G., and Zhang, R. (2013). BRG1 is required for formation of senescence-associated2d heterochromatin foci induced by oncogenic RAS or BRCA1 loss. *Mol. Cell. Biol.* 33, 1819–1829.
- Xu, L., Wei, Y., Reboul, J., Vaglio, P., Shin, T.H., Vidal, M., Elledge, S.J., and Harper, J.W. (2003). BTB proteins are substrate-specific adaptors in an SCF-like modular ubiquitin ligase containing CUL-3. *Nature* 425, 316–321.
- Yates, K.E., Korb, G.A., Shtutman, M., Roninson, I.B., and DiMaio, D. (2008). Repression of the SUMO-specific protease Senp1 induces p53-dependent premature senescence in normal human fibroblasts. *Aging Cell* 7, 609–621.
- Zhang, R., Poustovoitov, M.V., Ye, X., Santos, H.A., Chen, W., Daganzo, S.M., Erzberger, J.P., Serebriiskii, I.G., Canutescu, A.A., Dunbrack, R.L., et al. (2005). Formation of MacroH2A-containing senescence-associated heterochromatin foci and senescence driven by ASF1a and HIRA. *Dev. Cell* 8, 19–30.
- Zhang, Q., Zhang, L., Wang, B., Ou, C.Y., Chien, C.T., and Jiang, J. (2006). A hedgehog-induced BTB protein modulates hedgehog signaling by degrading Ci/Gli transcription factor. *Dev. Cell* 10, 719–729.
- Zhuang, M., Calabrese, M.F., Liu, J., Waddell, M.B., Nourse, A., Hammel, M., Miller, D.J., Walden, H., Duda, D.M., Seyedin, S.N., et al. (2009). Structures of SPOP-substrate complexes: insights into molecular architectures of BTB-Cul3 ubiquitin ligases. *Mol. Cell* 36, 39–50.

# Telomeric repeat-containing RNA (TERRA) constitutes a nucleoprotein component of extracellular inflammatory exosomes

Zhuo Wang<sup>a,b</sup>, Zhong Deng<sup>a</sup>, Nadia Dahmane<sup>c</sup>, Kevin Tsai<sup>a</sup>, Pu Wang<sup>a</sup>, Dewight R. Williams<sup>d</sup>, Andrew V. Kossenkov<sup>a</sup>, Louise C. Showe<sup>a</sup>, Rugang Zhang<sup>a</sup>, Qihong Huang<sup>a</sup>, José R. Conejo-García<sup>a</sup>, and Paul M. Lieberman<sup>a,1</sup>

<sup>a</sup>Gene Expression and Regulation Program, The Wistar Institute, Philadelphia, PA 19104; <sup>b</sup>Cancer Biology Program, University of the Sciences in Philadelphia, Philadelphia, PA 19104; <sup>c</sup>Department of Neurosurgery, University of Pennsylvania, Philadelphia, PA 19104; and <sup>d</sup>Department of Biochemistry and Biophysics, University of Pennsylvania, Philadelphia, PA 19104

Edited by Vishva M. Dixit, Genentech, San Francisco, CA, and approved October 5, 2015 (received for review March 25, 2015)

Telomeric repeat-containing RNA (TERRA) has been identified as a telomere-associated regulator of chromosome end protection. Here, we report that TERRA can also be found in extracellular fractions that stimulate innate immune signaling. We identified extracellular forms of TERRA in mouse tumor and embryonic brain tissue, as well as in human tissue culture cell lines using RNA in situ hybridization. RNA-seq analyses revealed TERRA to be among the most highly represented transcripts in extracellular fractions derived from both normal and cancer patient blood plasma. Cell-free TERRA (cfTERRA) could be isolated from the exosome fractions derived from human lymphoblastoid cell line (LCL) culture media. cfTERRA is a shorter form (~200 nt) of cellular TERRA and copurifies with CD63- and CD83-positive exosome vesicles that could be visualized by cryo-electron microscopy. These fractions were also enriched for histone proteins that physically associate with TERRA in extracellular ChIP assays. Incubation of cfTERRA-containing exosomes with peripheral blood mononuclear cells stimulated transcription of several inflammatory cytokine genes, including *TNFα*, *IL6*, and C-X-C chemokine 10 (*CXCL10*). Exosomes engineered with elevated TERRA or liposomes with synthetic TERRA further stimulated inflammatory cytokines, suggesting that exosome-associated TERRA augments innate immune signaling. These findings imply a previously unidentified extrinsic function for TERRA and a mechanism of communication between telomeres and innate immune signals in tissue and tumor microenvironments.

TERRA | telomere | exosome | innate immunity | cytokine

**T**elomeres are the repetitive and dynamic DNA structures that play a critical role in controlling cellular replicative capacity and cancer suppression (1, 2). Human telomeric DNA contains 4- to 15-kb double-stranded DNA with a sequence of TTAGGG repeats that are bound by a telomere-specific protein complex, referred to as shelterin (3). Telomere repeats are lost by attrition during DNA replication due to the end-replication problem, and critically short telomeres elicit a DNA damage-associated cell cycle arrest and replicative senescence (3, 4). Telomere repeat loss is thought to be part of a somatic cell senescence program that restricts cellular proliferation and regulates tissue homeostasis. Specialized telomere elongation mechanisms, including activation of the reverse transcriptase telomerase or alternative lengthening of telomeres (ALTs) through recombination, can overcome telomere repeat loss-induced cellular senescence. Telomere dysfunction occurs when abnormally short telomeres fail to induce senescence and is an early hallmark of human cancer. Cells with telomere dysfunction are also known to secrete distinct types of inflammatory cytokines (5, 6), but how telomeres are linked to this phenotype is not well characterized.

Telomere repeat DNA can be transcribed in response to developmental changes and cellular stress conditions (7, 8). Telomeric repeat-containing RNA (TERRA) has been implicated in telomere length regulation and DNA damage signaling (9, 10). TERRA can be found in complexes containing nuclear

proteins, including hnRNP1, Pot1, RPA, and HP1 (11, 12) and forms stable RNA-DNA hybrids at telomere DNA repeats (13, 14). TERRA may also form foci in cells that can colocalize with the inactive X chromosome (15, 16) or form aggregates in some cancer cells and tissues (17). TERRA can also form highly stable G-quadruplex structures (18), and these structures have been implicated in telomere length regulation (19). Whether TERRA has additional functions distinct from telomere end regulation is not yet known.

Structured nucleic acids, like TERRA, can have potent effects on innate immune sensing pathways (20). Extracellular forms of repetitive DNA fragments, including telomeric DNA, have been shown to modulate inflammatory cytokine production (21). Furthermore, cell-free nucleic acids can be used as a biomarkers for various diseases, including autoimmunity and cancer (22). Cell-free nucleic acid has been identified in stable protein complexes, as well as encapsulated in microvesicles and exosomes (23–25). Exosomes are small (50–100 nm) vesicles that carry a unique composition of proteins (26), lipids (27), mRNA (28), and miRNA (29). Exosomes form in the endosomal multivesicular bodies of the cytoplasm of various cell types and are secreted into body fluids, including blood plasma (30). Depending on their cellular origin and conditions, exosomes exhibit differential enrichment of components, allowing for specialized functions (23).

## Significance

**Loss of telomere repeats leads to cellular senescence and the secretion of inflammatory cytokines. How telomere dysfunction is linked to this inflammatory phenotype and its role in aging and cancer is not yet understood. We show here that noncoding telomere RNA transcripts [telomeric repeat-containing RNA (TERRA)] are secreted into the extracellular environment in exosome vesicle fractions. This cell-free TERRA (cfTERRA) is shorter and more stable than intracellular TERRA, is associated with histone proteins, and can induce inflammatory cytokines in responsive cells. These findings suggest that TERRA can have a cell extrinsic function and provide a mechanism through which telomere dysfunction can lead to the activation of inflammatory cytokine signals in the tissue microenvironment through the signaling capacity of cfTERRA.**

Author contributions: Z.W., Z.D., N.D., J.R.C.-G., and P.M.L. designed research; Z.W., Z.D., N.D., K.T., P.W., D.R.W., A.V.K., and Q.H. performed research; Z.W., N.D., A.V.K., L.C.S., R.Z., Q.H., and J.R.C.-G. contributed new reagents/analytic tools; Z.W., Z.D., N.D., K.T., P.W., D.R.W., A.V.K., L.C.S., R.Z., Q.H., J.R.C.-G., and P.M.L. analyzed data; and Z.W. and P.M.L. wrote the paper.

The authors declare no conflict of interest.

This article is a PNAS Direct Submission.

Freely available online through the PNAS open access option.

<sup>1</sup>To whom correspondence should be addressed. Email: [lieberman@wistar.org](mailto:lieberman@wistar.org).

This article contains supporting information online at [www.pnas.org/lookup/suppl/doi:10.1073/pnas.1505962112/-DCSupplemental](http://www.pnas.org/lookup/suppl/doi:10.1073/pnas.1505962112/-DCSupplemental).

Exosomes have been implicated in regulation of the immune response (31), gene expression by transmission of miRNA (32), and pathogen spreading (33). Tumor-derived exosomes promote tumor progression at many levels, either by suppressing antitumor immune responses (34) or by incorporating oncogenic materials (35). Whether telomeres and their derived RNA are involved in intercellular communication through exosome transport has not been studied.

Here, we report the identification of a previously unidentified, small form of TERRA found in the cell-free environment of mouse normal and tumor tissue, human blood plasma, and cell culture medium. This cell-free TERRA (cfTERRA) was highly enriched in exosome fractions that also induced transcription of inflammatory cytokines. These findings reveal a previously unrecognized extracellular localization of TERRA and provide a molecular mechanism through which telomere dysfunction may impact the tissue microenvironment.

## Results

**Identification of cfTERRA in the Fraction of Exosomes.** In a previous study (17) we observed that TERRA formed discrete foci in the nuclear compartment of highly proliferating cells in mouse embryonic cerebellum and brain tumors. We now report that a significant number of TERRA foci localize outside of the nuclear and cellular compartments in tissue sections of a mouse model of medulloblastoma (Fig. 1*A, Left*), as well as in developing embryonic brain (Fig. 1*A, Right*). Many of these foci were sensitive to RNase treatment, indicating they are mostly telomeric RNA and not DNA fragments (Fig. 1*A, Lower*). We also observed TERRA foci forming outside of nuclear compartments in human tissue culture cells, especially in serum-starved human lymphoblastoid cell lines (LCLs) (Fig. 1*B*). Consistent with this, we found that serum-starved LCLs produced higher levels of a shorter form of TERRA (Fig. S1*A and B*). We next asked whether TERRA RNA could be detected in RNA-seq analyses from cell-free RNA derived from plasma samples of normal or cancer patients (Fig. 1*C*). TERRA RNA, as defined by a least six telomere repeats, was detected at relatively high abundance in all samples. RNA with 2 or 3 UUAGGG-repeats were found at much lower read counts, suggesting that most TERRA RNA was derived from longer repeat transcripts (Table S1). While no significant differences between cancer and normal patients were found, read counts for TERRA ranked in the top 20 most frequent transcripts for all RNA-seq reads of extracellular RNA (Fig. 1*C*). These findings indicate that extracellular TERRA is a relatively abundant component of the cell free RNA from human blood plasma.

To investigate the possibility that TERRA was exported to the extracellular compartment, we isolated the microvesicle and exosomal fractions from LCL culture media using differential centrifugation (Fig. 1*D*). We then assayed the total cellular RNA, cellular debris, microvesicle fraction, and exosome fractions for TERRA RNA by Northern blot (Fig. 1*E*). We found that a smaller form of TERRA migrating at ~200 nt was highly enriched in the exosome fraction. Identical forms of TERRA were identified when exosomes were isolate by ultrafiltration or exosome precipitation reagent (Fig. S1*C and D*). Quantitative RT-PCR (qRT-PCR) with primers situated close (<300 nt) to the subtelomere–telomere junction showed enrichment in exosome fractions relative to total cellular TERRA (Fig. S1*E*). Similar forms of TERRA could be isolated from different cell types, although LCLs produced the highest amounts among the cells tested (Fig. S2*A*). TERRA production correlated with higher levels of fast migrating CD63-positive exosomes (Fig. S2*B*) and did not correlate with cell death or apoptosis (Fig. S2*C*). This form of TERRA (referred to as cfTERRA) was partly resistant to RNase A treatment, forming a diffuse and slower migrating signal on Northern blot (Fig. 1*D*). We did not detect any antisense TERRA, sug-

gesting that this is mostly G-rich single-stranded RNA. The control 18S probe identified 18S RNA in cellular debris and microvesicles, but not in the exosome fraction. These results indicate that cfTERRA is enriched in exosome-like fractions from human LCLs.

## cfTERRA Was Protected by a Structure with Similar Density as Exosomes.

To better characterize cfTERRA, we fractionated extracellular vesicles on sucrose gradients using tetraspanin CD63 as a marker for exosomes (36) (Fig. 2). We observed that cfTERRA cofractionated with the faster migrating form of CD63<sup>+</sup> through the sucrose gradient centrifugation (Fig. 2*A and B*). We examined these fractions by electron cryo-microscopy and observed that most of the spherical exosomes (red arrows) comigrated with cfTERRA and fast migrating CD63 in fraction 9 (density, 1.15 g/mL), along with some other membrane vesicles (green arrows). Although fraction 3 contained the slower mobility (and presumably glycosylated) form of CD63 typically associated with exosomes, there were few exosome structures and many large macromolecular complexes presumably of protein composition (blue arrows) in this fraction. To investigate whether cfTERRA was within exosomes, we compared the RNase sensitivity of cellular TERRA with exosome fraction of cfTERRA (Fig. 2*D*). Although cellular TERRA was efficiently degraded by RNase mixture treatment, cfTERRA was protected from RNase activity when the exosome structure was intact. In contrast, purified cfTERRA from denatured exosomes were mostly degraded by RNase mixture treatment (Fig. 2*D*). Exosome fractions did not contain detectable amounts of control 18S RNA. These findings indicate that cfTERRA cofractionates with the nonglycosylated CD63<sup>+</sup> exosome fraction where it remains resistant to RNase treatment either by encapsulation within the exosome or its association with other factors that copurify with exosomes.

**cfTERRA Is Bound by Histones in Exosome Fraction.** Sucrose gradient fractions enriched in TERRA (fraction 9) and CD63 were analyzed by silver staining of SDS/PAGE and then by liquid chromatography–tandem mass spectrometry (LC-MS/MS) to identify the protein composition (Fig. 3*A and B*, Fig. S3, and Dataset S1). MS revealed histones and ribosomal proteins, as well as many known exosome components (Fig. S3), including CD81, CD20, and annexin A1 (Fig. 3*B*) (37). Western blot confirmed the enriched levels of histone H3 and H4, as well as CD81, CD63, and LMP1 in the sucrose fractions containing TERRA (Fig. 3*B*). To determine whether cfTERRA is associated with any of the protein components of the exosome fraction, we performed immunoprecipitation assays on these exosomes (Fig. 3*D–F*). We found exosome-associated TERRA could be immunopurified with antibodies to exosome membrane constituents CD81 and to a lesser extent with CD63. TERRA could also be detected in immunoprecipitation (IP) with H3 antibody, suggesting some cfTERRA may associate with chromatin components outside of exosomes (Fig. 3*E and F*). Exosome-associated TERRA was detected at higher levels than 18S RNA relative to total cellular amounts, suggesting that TERRA is selectively enriched in exosomes in LCLs.

To determine whether TERRA was physically associated with any protein constituents found in exosome fractions, we performed extracellular ChIP (Exo RNA-ChIP) assays using formaldehyde cross-linking before exosome lysis (Fig. 4*A*). We found that TERRA was significantly enriched in histone H3 Exo RNA-ChIP and to a much lesser extent with TRF2 (Fig. 4*B and C*). In contrast, 18S RNA was enriched with S6 and H3 cellular RNA-ChIP, but not detectable in Exo RNA-ChIP. We also performed Exo DNA-ChIP on total extracellular fractions (Fig. S4). We found that telomere repeat DNA (both sense and antisense) could be detected in both H3 and TRF2 Exo DNA-ChIPs, whereas  $\alpha$ -satellite DNA was enriched only in the H3 ChIP (Fig. S4*B and C*). These findings indicate that chromatin-associated



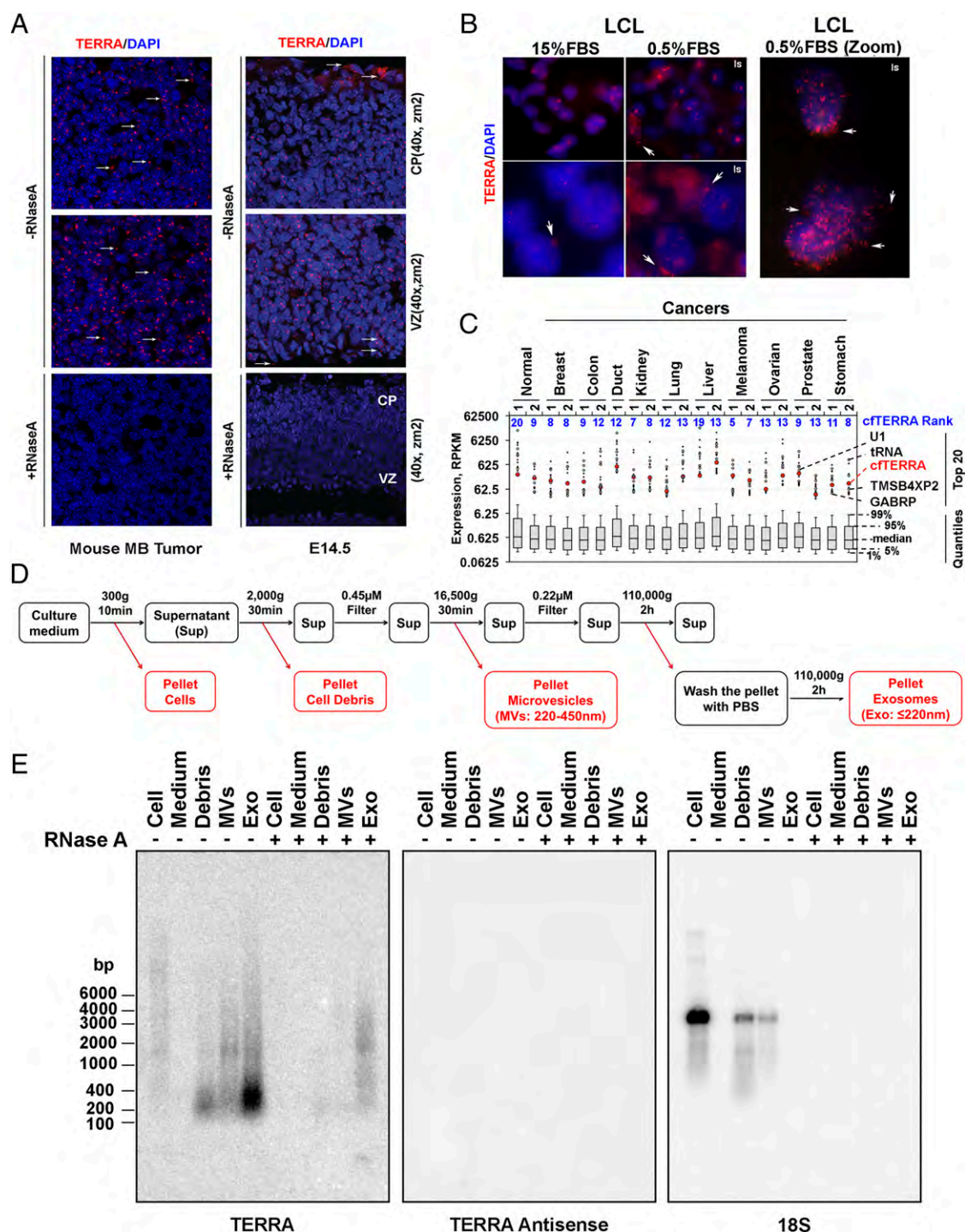


**Fig. 1.** Identification of cfTERRA in exosome fractions. (A) RNA-FISH analysis of TERRA expression on mouse medulloblastoma tumor (Left) and embryonic E14.5 brain tissue sections by confocal microscopy. TERRA was stained with (CCCTAA)<sub>3</sub> PNA probe in red, and nuclei were counterstained with DAPI in blue on mouse medulloblastoma tissue (Left) or cerebral cortex section of E14.5 WT mouse embryo (Right). Cortical plate (CP) and ventricular Zone (VZ) are indicated. RNase A treatment eliminates all signals of TERRA (Lower). Arrows indicate TERRA signals found outside of nuclei. Images were taken with 40× lens at zoom 2. (B) TERRA foci were found outside of nuclei in human lymphoblastoid cell lines grown under normal serum (15%) or serum starved (0.5%) conditions for 24 h before fixation. (Right) Zoom image of the same LCL samples. (C) RNA-seq analysis of cell-free DNA from various normal and cancer blood plasma samples. TERRA (as defined by six tandem UUAGGG repeats) and its ranks in read counts relative to all other genes. Whisker plots demonstrate distribution of gene expression levels that had at least 10 aligned RNA-seq reads. Dots represent RPKM values for the top 20 expressed genes. Among those, highlighted are cfTERRA and 6 other known genes that appear in the top 20 genes across all samples the most. (D) Flowchart for fractionation of culture medium by differential centrifugation. The conditions of each centrifugation or filtering are indicated above the black arrows. Pellets highlighted in red are used for analysis of RNA or proteins. (E) Northern blot analysis of TERRA levels in extracellular fractions from LCL culture medium. RNA was isolated from pellets of the differential centrifugation as shown in C. Equal mass amounts of RNA (1 μg) were either mock treated (–) or treated with RNase A (100 μg/mL) for 30 min at 37 °C before Northern blot analysis. The blot is hybridized with <sup>32</sup>P-labeled probes for TERRA, antisense TERRA, or 18S RNA, or indicated under the blot. Numbers on the left show the position of RNA markers in base pairs.



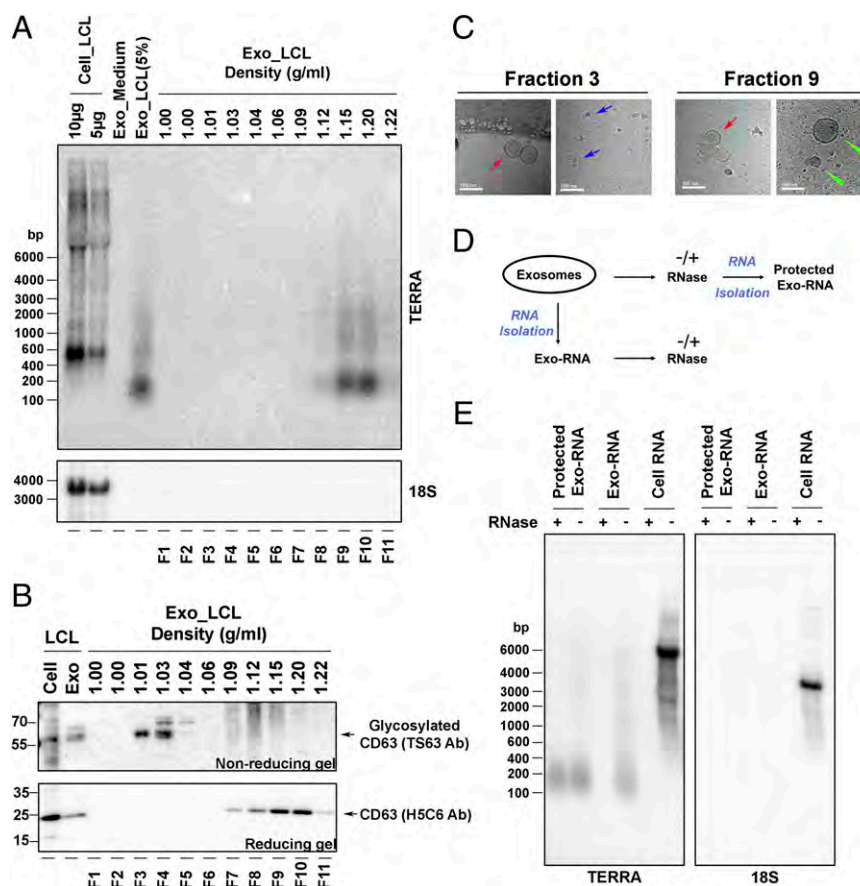


**Fig. 2.** cTERRA copurifies with exosomes. (A) Northern blot analysis of total cellular RNA (10 and 5  $\mu$ g) or RNA isolated from total exosome fractions from either fresh media or LCL extracellular media or exosomes that were fractionated on a continuous sucrose gradient (fractions 1–11) were probed for TERRA (*Upper*) or 18S RNA (*Lower*). (B) Western blot analysis of sucrose fractions (as shown in A) with CD63 antibody using nonreducing (*Upper*) or reducing (*Lower*) SDS/PAGE. The unmodified and glycosylated CD63 mobilities are shown as indicated. (C) Electron cryo-microscopy analysis of sucrose fractions 3 and 9. Exosomes are indicated with red arrows, whereas other vesicle structures are indicated with green arrows. The blue arrows indicate a presumed protein macromolecular complexes found in fraction 3. (Scale bars, 100 nm.) (D) Schematic of RNase protection assay used in E. Exosomes were treated with or without RNase mixture (Protected Exo-RNA) or exosome RNA was first isolated and then treated with or without RNase mixture (Exo-RNA). (E) Northern blot of RNA isolated from LCLs or LCL-derived exosomes. Exosomes were pretreated without (–) or with (+) RNase mixture before RNA isolation (Protected Exo-RNA) or treated after RNA isolation (Exo-RNA) and cellular RNA. The isolated RNA was analyzed by Northern blotting and hybridized with  $^{32}$ P-labeled probes for TERRA or 18S RNA as indicated.

DNA fragments enriched with telomeric and  $\alpha$ -satellite DNA fragments can be found in extracellular fractions.

**cfTERRA Modulates the Transcription of Inflammatory Cytokines in Recipient Cells.** Exosomes have been implicated in various types of intercellular communications, including the modulation of inflammatory cytokines and the innate immune signaling (38). We therefore tested whether exosomes from LCLs enriched with cfTERRA could induce transcription for various cytokines and chemokines. We found that cfTERRA-enriched exosome fractions efficiently induced transcription of several cytokines, including *IL6*, *TNF $\alpha$* , GM-CSF, and C-X-C chemokine 10 (*CXCL10*) (Fig. 5 *A* and *B* and Fig. S5*A*). To determine whether cfTERRA levels in exosomes correlated with cytokine activation, we isolated exosomes from cells engineered to produce elevated TERRA levels (Fig. 5*C*). Exosomes were isolated from HCT116 cells transduced with ectopic TRF1( $\Delta$ N) or TRF1( $\Delta$ N) fused to the transcription activation domain of VP16 [VP16-TRF1( $\Delta$ N)]. We validated by Northern blot that VP16-TRF1( $\Delta$ N) induced high levels of cellular and exosome-associated TERRA relative to vector and TRF1 $\Delta$ N only (Fig. 5*D*), suggesting TERRA was induced by the VP16 domain instead of ectopic expression of TRF1( $\Delta$ N). Although some 18S RNA was detected in exosomes from vector control samples, no 18S was detected in TRF1( $\Delta$ N)

or VP16-TRF1( $\Delta$ N), and U1 RNA was not detected in any exosome fraction (Fig. 5D). Protein levels of cellular TRF1 and exosomal CD63 were monitored by Western blot (Fig. 5E). Exosomes normalized by CD63 expression levels were then incubated with peripheral blood mononuclear cells (PBMCs) and assayed for cytokine induction (Fig. 5F). We found that exosomes from VP16-TRF1( $\Delta$ N) containing the highest levels of cfTERRA induced the highest levels of cytokine mRNA, including *IL6*, *TNF $\alpha$* , and *CXCL10* while having no significant effect on control *GUSB* mRNA levels (Fig. 5F and Fig. S5B). To determine whether TERRA alone is capable of stimulating inflammatory cytokine transcription on recipient cells, we expressed and purified sense or antisense TERRA-containing RNA transcripts, as well as equimolar U6 transcripts, and delivered these in liposomes to either PBMCs (Fig. S6A) or IMR90 fibroblasts (Fig. 5G and H). We found that synthetic TERRA-containing liposomes selectively stimulated *IL6*, *CXCL10*, and *TNF $\alpha$*  in IMR90 cells (Fig. 5H) and to a lesser extent in PBMCs (Fig. S6A). We also found that short synthetic oligonucleotides (36 bp) containing TERRA could partially induce some cytokine production, although not fully recapitulating endogenous exosomes (Fig. S6B). Taken together, these findings suggest that exosome-associated cfTERRA may function to modulate cytokine production in recipient cells.

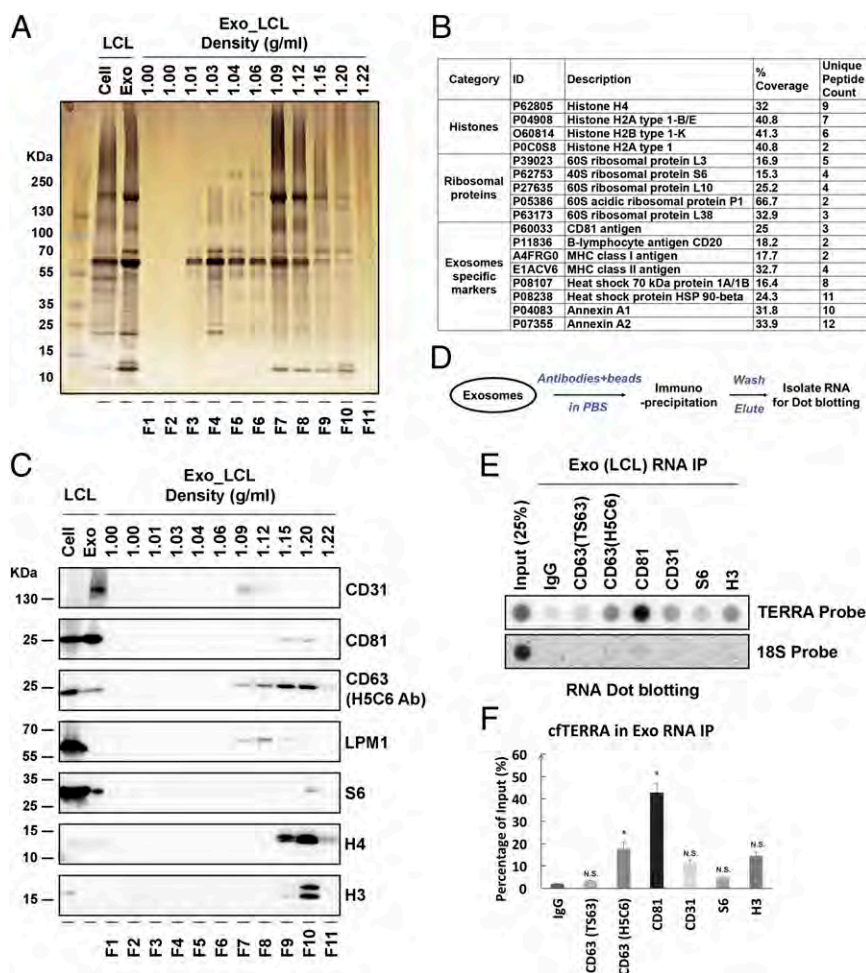


**Fig. 3.** cfTERRA is associated with exosomes. (A) Sucrose fractions collected in Fig. 2 were assayed by SDS/PAGE and visualized by silver staining. Molecular weight of the marker was indicated on the left in kilodaltons. (B) Summary of LC/MS/MS data from sucrose fractions F8 and F9. Proteins identified by MS from the major categories of histone, ribosomal protein, or exosome component are shown. Percent coverage and unique peptide counts are indicated. Full list of MS identified peptides is provided in Table S2. (C) Western blotting of sucrose fractions using antibodies specific for CD31, CD81, CD63, LMP1, S6, histone H4, and H3 antibodies. (D) Schema of exosome immunoprecipitation and RNA isolation method used in D and E. (E) Exo RNA IP using antibodies to CD63 (TS63), CD63 (H5C6), CD81, CD31, S6, H3, or control IgG. Isolated RNA was then assayed by dot blotting with TERRA or 18S-specific probes. (F) Quantification of three independent replicates of Exo RNA IP as represented in E. Error bars, SD.

## Discussion

Telomeres have been implicated in the cell intrinsic regulation of senescence (39), as well as in more complex functions, including tissue homeostasis (40) and organismal aging (41). Telomere-associated changes are known to occur in cancerous and precancerous lesions (42), and many of these lesions are known to have a senescence-associated secretory phenotype (SASP) that can drive carcinogenesis (43). Cells with short telomeres produce a distinct pattern of cytokines that has been referred to as a telomere-associated secretory phenotype (TASP), which is distinct from SASP (5, 44). The mechanism through which telomere dysfunction produces extracellular signals relevant to tissue microenvironment, inflammation, and cancer is not completely understood.

Here, we demonstrate that TERRA-derived RNA fragments can be found in the extracellular fraction of mouse tumor and normal embryonic tissue, human blood plasma, and human cell lines in culture. cfTERRA from human LCLs copurified with CD63<sup>+</sup> and CD81<sup>+</sup> exosome fractions and coprecipitated with histone H3, suggesting that cfTERRA forms a chromosomal-like ribonucleoprotein particle within or associated with exosomes. We showed that exosome fractions enriched in cfTERRA induced inflammatory cytokines from human PBMCs. We also

found that synthetic TERRA could induce a similar inflammatory response in human fibroblasts. We conclude that cfTERRA is a component of exosome fractions that can modulate the inflammatory response.

**TERRA Is Deregulated in Cancer and Stress Response.** TERRA expression can be regulated by developmental and stress-related signals, including DNA damage and viral infection (7, 45–47). Telomere shortening may also increase TERRA expression (48), but it is not clear that senescent cells show a global increase in TERRA levels. We found that TERRA can be enriched in some cancer tissues (17) and is highly induced in cells after infection by herpes simplex virus 1 (HSV1) (47). TERRA has been shown to have several functions at telomeres, including recruitment of telomerase (48), inhibition of telomerase (49), assembly of DNA damage repair proteins (50), and maintenance of telomeric heterochromatin (12). However, TERRA has not yet been implicated in TASP or other related telomere-extrinsic functions.

**Telomeres and Immunological Response.** Several lines of evidence suggest that telomeric events can impact the innate immune response and tissue microenvironment. Although telomere shortening

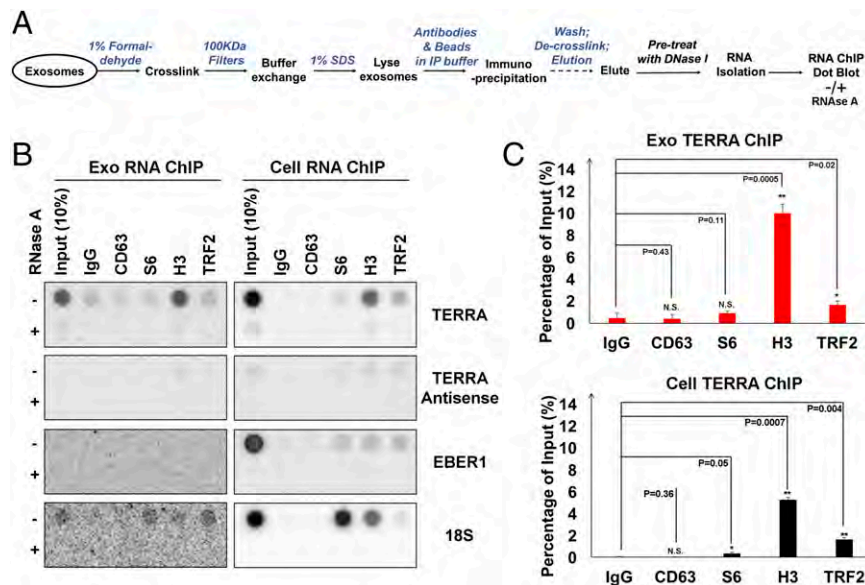


**Fig. 4.** cfTERRA is associated with histones. (A) Schema of Exo RNA ChIP assay. (B) RNA ChIP assays were performed with exosomes (Exo) or cellular (Cell) LCLs using antibodies specific for CD63, S6, H3, TRF2, or control IgG. Isolated RNA was treated with either mock (–) or RNase A and then assayed by hybridization with probes for TERRA, TERRA-antisense, EBER1, or 18S, as indicated. (C) Quantification of at least three independent TERRA RNA ChIP assays, a representative shown in B. Bar graphs represent mean values with SDs. P values were calculated by two-tailed Student t test: \*P < 0.05, \*\*P < 0.01.

and dysfunction can limit immunological function by restricting proliferation of immune cells, telomere shortening appears to also increase systemic inflammation, including that associated with lupus erythematosus, rheumatoid arthritis, and granulomatous diseases (51). Individuals with short telomeres in leukocytes were found to have elevated biomarkers for systemic inflammation (52). TERC<sup>−/−</sup> mice with shortened telomeres undergo immune inflammatory response in bone marrow macrophages due to a TLR4-dependent activation of IL6 and TNFα (53). Perhaps related is the finding that telomere shortening in aged human macrophages resulted in impaired STAT5 signaling (54). Telomere uncapping was found to be associated with cellular senescence and inflammation in human arteries (55). Furthermore, malignant cells with elevated TRF2 levels had a decrease in natural killer (NK) cell infiltration in the tumor microenvironment (56). These findings suggest that telomeres contribute directly or indirectly to inflammatory signaling.

**Immunological Effects of Telomere Repeat DNA.** Synthetic oligonucleotides containing CpG-DNA are known to be potent agonists of innate immunity through activation of Toll-like receptors (TLRs) (57). This activity is thought to reflect the innate immune response to foreign viral and bacterial DNA. Interestingly, synthetic telomere repeat DNA was found to suppress the production of cytokines induced by CpG DNA, as well as by other TLR agonists, including lipopolysaccharides (LPSs) (58) and various polyclonal activators (21, 59). Molecular targets for TTAGGG-repeat oligonucleotides have included STAT1 and STAT4 (60) and the lupus autoantigen Ku (61). Additionally, native DNA from telomerase-deficient mice had reduced capacity to inhibit inflammation compared to that of the control DNA (62), supporting the hypothesis that telomere-rich DNA is immunomodulatory. There have been fewer studies on the immunological effects of telomeric RNAs. However, a recent report showed that telomere RNA forming G-quadruplex structures can induce global changes in gene expression, including suppression of innate immune sensing genes (63).

**Components of the Exosome Code.** The complex combination of factors that comprise exosomes and the type of recipient cells that sense the exosomes may determine the nature of the signal

and response. Specific signaling through exosomes depends on the cell source of the exosomes, as well as the recipient cell receptors. Exosome coding information is provided by the lipid, protein, and nucleic acid composition. Although we did not detect full-length TERRA molecules in exosomes, the smaller processed forms of TERRA are highly enriched in exosomes from various cell types, especially LCLs (Fig. S2). This smaller, processed form of TERRA was also found to be associated with histones, which were also a major protein component of the inflammatory exosome fraction from human LCLs. Although exosomes containing higher levels of TERRA elicited greater cytokine response and purified TERRA molecules can stimulate cytokines, it is not yet clear whether the endogenous cfTERRA in exosomes is the primary immunomodulator in these microvesicles. Nevertheless, we propose that processed cfTERRA associated with histones constitutes an important telomere-derived component of inflammatory exosomes with potential to modulate signaling capacity. Thus, cfTERRA may constitute an important component of a complex, yet incompletely understood exosome code.

## Materials and Methods

**Plasmids for TERRA Induction.** TRF1ΔN (44–439) was cloned from pBSK-hTRF1 (a gift from T. de Lange, Rockefeller University, New York) and inserted either in control Lentivirus vector pLU-CMV-Flag (Protein Expression Facility, Wistar Institute) or Vp16 domain-containing vector pLU-CMV-Flag-Vp16.

**Culture Medium Fractionation and Exosome Isolation.** The supernatant of the LCL culture was fractionated and prepared for exosomes isolation by differential centrifugation as previously described (64), with some modifications (SI Materials and Methods).

**ChIP Assays.** Cellular ChIP assays were performed as previously described (65).

**PBMC Isolation and Cytokine Stimulation.** PBMCs were isolated from fresh donated human blood by density gradient centrifugation with Lymphoprep in SepMate-50 tubes (Stemcell Technologies). Liposomes were prepared by incorporating RNA from in vitro transcription or synthesized oligos (IDT) into Lipofectamine 2000 as previously described (66).

Additional methods are included in SI Materials and Methods.



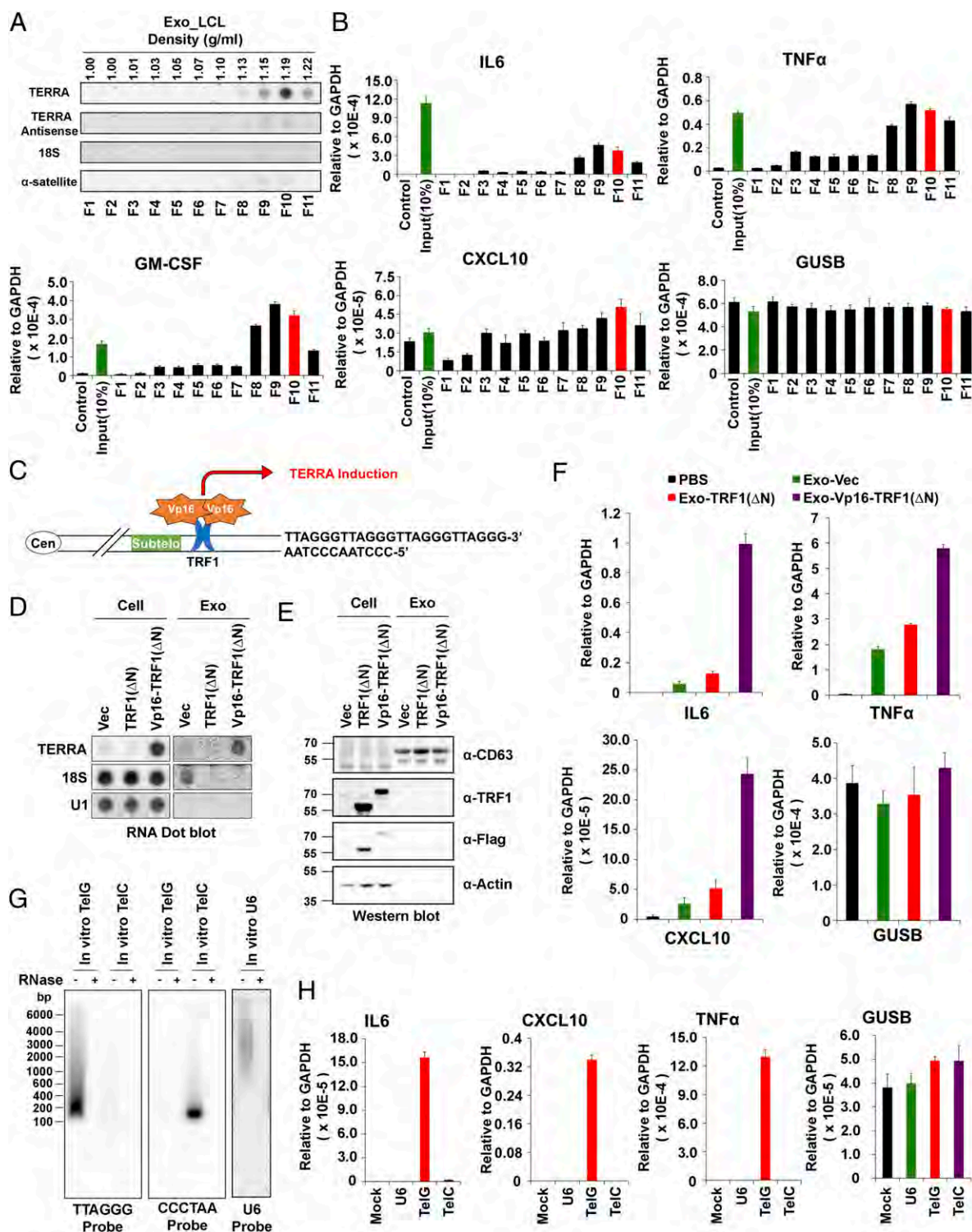


**Fig. 5.** Exosome-associated TERRA stimulates inflammatory cytokines. (A) RNA dot blot analysis of sucrose gradient fractionation of LCL-derived exosomes probed for TERRA (Upper), TERRA antisense, 18S rRNA, or alpha-satellite RNA (Lower). (B) Total exosomes (input) or sucrose gradient fractions were incubated with PBMCs for 3 h and then assayed by qRT-PCR for expression of *IL6*, *TNF $\alpha$* , *GM-CSF*, *CXCL10*, or control *GUSB* mRNA. Bar graphs represent qRT-PCR values relative to *gaphd* mRNA (mean  $\pm$  SD) from three independent experiments. (C) Schema of VP16-TRF1( $\Delta$ N) activation of TERRA. (D) RNA dot blot for TERRA, 18S, or U1 RNA from HCT116 cells (Left) or exosomes (Right) transduced with vector, TRF1( $\Delta$ N), or VP16-TRF1( $\Delta$ N). (E) HCT116 cells transduced as in D were assayed by Western blot for CD63, TRF1, FLAG, and Actin. (F) qRT-PCR for expression of *IL6*, *TNF $\alpha$* , *CXCL10*, or control *GUSB* mRNA for PBMCs treated with exosomes derived from HCT116 cells transduced with vector control (green), TRF1( $\Delta$ N) (red), VP16-TRF1( $\Delta$ N) (purple), or PBS control (black). (G) Northern blot of in vitro transcribed TelG, TelC, or U6 RNA treated with control or RNaseA and probed for TERRA (Left), TERRA antisense (Center), or U6 (Right). (H) IMR90 cells were treated with liposomes containing TelG or TelC RNA for 24 h and then assayed by qRT-PCR for *IL6*, *TNF $\alpha$* , *CXCL10*, or control *GUSB* mRNA. Bar graphs represent qRT-PCR values relative to *gaphd* mRNA (mean  $\pm$  SD) from three independent experiments.



**ACKNOWLEDGMENTS.** We thank Andreas Wiedmer for technical assistance, Harold C. Riethman for plasmids, and the Wistar Cancer Center Cores for Genomics and Proteomics. This work was supported by funding from National

Institutes of Health, National Cancer Institute (NCI) Grant CA RO1CA140652 (to P.M.L.), NCI Cancer Center Core Grant P30 CA10815, and the Commonwealth Universal Research Enhancement Program, PA Department of Health.

- Blackburn EH, Greider CW, Szostak JW (2006) Telomeres and telomerase: The path from maize, Tetrahymena and yeast to human cancer and aging. *Nat Med* 12(10):1133–1138.
- Cech TR (2004) Beginning to understand the end of the chromosome. *Cell* 116(2):273–279.
- Palm W, de Lange T (2008) How shelterin protects mammalian telomeres. *Annu Rev Genet* 42:301–334.
- O'Sullivan RJ, Karlseder J (2010) Telomeres: Protecting chromosomes against genome instability. *Nat Rev Mol Cell Biol* 11(3):171–181.
- Braig M, et al. (2014) A 'telomere-associated secretory phenotype' cooperates with BCR-ABL to drive malignant proliferation of leukemic cells. *Leukemia* 28(10):2028–2039.
- Fumagalli M, et al. (2012) Telomeric DNA damage is irreparable and causes persistent DNA-damage-response activation. *Nat Cell Biol* 14(4):355–365.
- Schoeftner S, Blasco MA (2008) Developmentally regulated transcription of mammalian telomeres by DNA-dependent RNA polymerase II. *Nat Cell Biol* 10(2):228–236.
- Azzalin CM, Reichenbach P, Khoraiuli L, Giulotto E, Lingner J (2007) Telomeric repeat containing RNA and RNA surveillance factors at mammalian chromosome ends. *Science* 318(5851):798–801.
- Azzalin CM, Lingner J (2015) Telomere functions grounding on TERRA firma. *Trends Cell Biol* 25(1):29–36.
- Maicher A, Lockhart A, Luke B (2014) Breaking new ground: Digging into TERRA function. *Biochim Biophys Acta* 1839(5):387–394.
- Flynn RL, et al. (2011) TERRA and hnRNP A1 orchestrate an RPA-to-POT1 switch on telomeric single-stranded DNA. *Nature* 471(7339):532–536.
- Deng Z, Nourse J, Wiedmer A, Riethman H, Lieberman PM (2009) TERRA RNA binding to TRF2 facilitates heterochromatin formation and ORC recruitment at telomeres. *Mol Cell* 35(4):403–413.
- Arora R, et al. (2014) RNaseH1 regulates TERRA-telomeric DNA hybrids and telomere maintenance in ALT tumour cells. *Nat Commun* 5:5220.
- Balk B, et al. (2013) Telomeric RNA-DNA hybrids affect telomere-length dynamics and senescence. *Nat Struct Mol Biol* 20(10):1199–1205.
- Schoeftner S, et al. (2009) Telomere shortening relaxes X chromosome inactivation and forces global transcriptome alterations. *Proc Natl Acad Sci USA* 106(46):19393–19398.
- Zhang LF, et al. (2009) Telomeric RNAs mark sex chromosomes in stem cells. *Genetics* 182(3):685–698.
- Deng Z, et al. (2012) Formation of telomeric repeat-containing RNA (TERRA) foci in highly proliferating mouse cerebellar neuronal progenitors and medulloblastoma. *J Cell Sci* 125(Pt 18):4383–4394.
- Xu Y, Komiyama M (2012) Structure, function and targeting of human telomere RNA. *Methods* 57(1):100–105.
- Takahama K, et al. (2013) Regulation of telomere length by G-quadruplex telomere DNA- and TERRA-binding protein TLS/FUS. *Chem Biol* 20(3):341–350.
- Babalat R, Ewald SE, Mouchess ML, Barton GM (2011) Nucleic acid recognition by the innate immune system. *Annu Rev Immunol* 29:185–214.
- Gursel I, et al. (2003) Repetitive elements in mammalian telomeres suppress bacterial DNA-induced immune activation. *J Immunol* 171(3):1393–1400.
- Mansour H (2014) Cell-free nucleic acids as noninvasive biomarkers for colorectal cancer detection. *Front Genet* 5:182.
- Théry C, Zitvogel L, Amigorena S (2002) Exosomes: Composition, biogenesis and function. *Nat Rev Immunol* 2(8):569–579.
- Robbins PD, Morelli AE (2014) Regulation of immune responses by extracellular vesicles. *Nat Rev Immunol* 14(3):195–208.
- Théry C (2011) Exosomes: Secreted vesicles and intercellular communications. *F1000 Biol Rep* 3:15.
- Ji H, et al. (2013) Proteome profiling of exosomes derived from human primary and metastatic colorectal cancer cells reveal differential expression of key metastatic factors and signal transduction components. *Proteomics* 13(10-11):1672–1686.
- Laulagnier K, et al. (2004) Mast cell- and dendritic cell-derived exosomes display a specific lipid composition and an unusual membrane organization. *Biochem J* 380(Pt 1):161–171.
- Tomasoni S, et al. (2013) Transfer of growth factor receptor mRNA via exosomes unravels the regenerative effect of mesenchymal stem cells. *Stem Cells Dev* 22(5):772–780.
- Valadi H, et al. (2007) Exosome-mediated transfer of mRNAs and microRNAs is a novel mechanism of genetic exchange between cells. *Nat Cell Biol* 9(6):654–659.
- Denzer K, Kleijmeer MJ, Heijnen HF, Stoorvogel W, Geuze HJ (2000) Exosome: From internal vesicle of the multivesicular body to intercellular signaling device. *J Cell Sci* 113(Pt 19):3365–3374.
- Théry C, Ostrowski M, Segura E (2009) Membrane vesicles as conveyors of immune responses. *Nat Rev Immunol* 9(8):581–593.
- Umez U, Ohayashiki K, Kuroda M, Ohayashiki JH (2013) Leukemia cell to endothelial cell communication via exosomal miRNAs. *Oncogene* 32(22):2747–2755.
- Dreux M, et al. (2012) Short-range exosomal transfer of viral RNA from infected cells to plasmacytoid dendritic cells triggers innate immunity. *Cell Host Microbe* 12(4):558–570.
- Lundholm M, et al. (2014) Prostate tumor-derived exosomes down-regulate NKG2D expression on natural killer cells and CD8+ T cells: Mechanism of immune evasion. *PLoS One* 9(9):e108925.
- Atay S, et al. (2014) Oncogenic KIT-containing exosomes increase gastrointestinal stromal tumor cell invasion. *Proc Natl Acad Sci USA* 111(2):711–716.
- Caby MP, Lankar D, Vincendeau-Scherrer C, Raposo G, Bonnerot C (2005) Exosomal-like vesicles are present in human blood plasma. *Int Immunol* 17(7):879–887.
- Verweij FJ, et al. (2011) LMP1 association with CD63 in endosomes and secretion via exosomes limits constitutive NF- $\kappa$ B activation. *EMBO J* 30(11):2115–2129.
- Beninson LA, Fleschner M (2014) Exosomes: An emerging factor in stress-induced immunomodulation. *Semin Immunol* 26(5):394–401.
- Suram A, Herbig U (2014) The replicometer is broken: Telomeres activate cellular senescence in response to genotoxic stresses. *Aging Cell* 13(5):780–786.
- Armanios M, Blackburn EH (2012) The telomere syndromes. *Nat Rev Genet* 13(10):693–704.
- Falandry C, Bonnefoy M, Freyer G, Gilson E (2014) Biology of cancer and aging: A complex association with cellular senescence. *J Clin Oncol* 32(24):2604–2610.
- Reddel RR (2014) Telomere maintenance mechanisms in cancer: Clinical implications. *Curr Pharm Des* 20(41):6361–6374.
- Velarde MC, Demaria M, Campisi J (2013) Senescent cells and their secretory phenotype as targets for cancer therapy. *Interdiscip Top Gerontol* 38:17–27.
- Coppé JP, et al. (2008) Senescence-associated secretory phenotypes reveal cell-non-autonomous functions of oncogenic RAS and the p53 tumor suppressor. *PLoS Biol* 6(12):2853–2868.
- Porro A, et al. (2014) Functional characterization of the TERRA transcriptome at damaged telomeres. *Nat Commun* 5:5379.
- Caslini C, Connelly JA, Serna A, Broccoli D, Hess JL (2009) MLL associates with telomeres and regulates telomeric repeat-containing RNA transcription. *Mol Cell Biol* 29(16):4519–4526.
- Deng Z, et al. (2014) HSV-1 remodels host telomeres to facilitate viral replication. *Cell Reports* 9(6):2263–2278.
- Cusanelli E, Romero CA, Chartrand P (2013) Telomeric noncoding RNA TERRA is induced by telomere shortening to nucleate telomerase molecules at short telomeres. *Mol Cell* 51(6):780–791.
- Schoeftner S, Blasco MA (2010) Chromatin regulation and non-coding RNAs at mammalian telomeres. *Semin Cell Dev Biol* 21(2):186–193.
- Porro A, Feuerhahn S, Lingner J (2014) TERRA-reinforced association of LSD1 with MRE11 promotes processing of uncapped telomeres. *Cell Reports* 6(4):765–776.
- Georj-Lavialle S, et al. (2010) The telomere/telomerase system in autoimmune and systemic immune-mediated diseases. *Autoimmun Rev* 9(10):646–651.
- Wong JY, De Vivo I, Lin X, Fang SC, Christiani DC (2014) The relationship between inflammatory biomarkers and telomere length in an occupational prospective cohort study. *PLoS One* 9(1):e87348.
- Bhattacharjee RN, Banerjee B, Akira S, Hande MP (2010) Telomere-mediated chromosomal instability triggers TLR4 induced inflammation and death in mice. *PLoS One* 5(7):e11873.
- Sebastián C, et al. (2009) Telomere shortening and oxidative stress in aged macrophages results in impaired STAT5a phosphorylation. *J Immunol* 183(4):2356–2364.
- Morgan RG, et al. (2013) Age-related telomere uncapping is associated with cellular senescence and inflammation independent of telomere shortening in human arteries. *Am J Physiol Heart Circ Physiol* 305(2):H251–H258.
- Biorcio A, et al. (2013) TRF2 inhibits a cell-extrinsic pathway through which natural killer cells eliminate cancer cells. *Nat Cell Biol* 15(7):818–828.
- Ishii KJ, Akira S (2006) Innate immune recognition of, and regulation by, DNA. *Trends Immunol* 27(11):525–532.
- Yagci FC, et al. (2010) Mammalian telomeric DNA suppresses endotoxin-induced uveitis. *J Biol Chem* 285(37):28806–28811.
- Lenert PS (2010) Classification, mechanisms of action, and therapeutic applications of inhibitory oligonucleotides for Toll-like receptors (TLR) 7 and 9. *Mediators Inflamm* 2010:986596.
- Shirota H, Gursel M, Klinman DM (2004) Suppressive oligodeoxynucleotides inhibit Th1 differentiation by blocking IFN- $\gamma$ - and IL-12-mediated signaling. *J Immunol* 173(8):5002–5007.
- Bianchi A, de Lange T (1999) Ku binds telomeric DNA in vitro. *J Biol Chem* 274(30):21223–21227.
- Klinman DM, Tross D, Klaschik S, Shirota H, Sato T (2009) Therapeutic applications and mechanisms underlying the activity of immunosuppressive oligonucleotides. *Ann N Y Acad Sci* 1175:80–88.
- Hirashima K, Seimiya H (2015) Telomeric repeat-containing RNA/G-quadruplex-forming sequences cause genome-wide alteration of gene expression in human cancer cells in vivo. *Nucleic Acids Res* 43(4):2022–2032.
- Théry C, Amigorena S, Raposo G, Clayton A (2006) Isolation and characterization of exosomes from cell culture supernatants and biological fluids. *Current Protocols in Cell Biology*, ed Bonifacino JS (John Wiley & Sons, Somerset, NJ), Chap 3.
- Deng Z, et al. (2012) A role for CTCF and cohesin in subtelomere chromatin organization, TERRA transcription, and telomere end protection. *EMBO J* 31(21):4165–4178.
- Rigby RE, et al. (2014) RNA:DNA hybrids are a novel molecular pattern sensed by TLR9. *EMBO J* 33(6):542–558.
- Dahl JA, Collas P (2009) MicroChIP: Chromatin immunoprecipitation for small cell numbers. *Methods Mol Biol* 567:59–74.

## ATM in senescence

Katherine M. Aird and Rugang Zhang

Senescence is a state of stable cell growth arrest that can be triggered by multiple stressors, including oncogene activation [1]. In normal diploid mammalian cells, activation of oncogenes such as oncogenic RAS or BRAF decreases dNTP levels, which leads to replication stress and ultimately senescence [2]. In this context, oncogene-induced senescence (OIS) is considered to be an important tumor suppressor mechanism [1]. Overcoming OIS is necessary for cell transformation, which may ultimately lead to cancer development [3]. Therefore, understanding the basic mechanisms whereby cells bypass OIS is important for understanding the earliest events in tumorigenesis. Additionally, knowledge of the pathways that can overcome replication stress-induced senescence may allow for targeting of these specific pathways for cancer therapy or prevention.

We previously found that during OIS, downregulation of ribonucleotide reductase M2 (RRM2), the rate-limiting enzyme in dNTP biosynthesis, underlies the observed replication stress [2]. This correlates with a significant decrease in dNTP levels and the associated DNA damage response (DDR). This leads to the establishment and maintenance of the stable senescence-associated cell growth arrest observed during OIS. Ectopic RRM2 or supplementation of cells with exogenous nucleosides is sufficient to overcome OIS, demonstrating the importance of nucleotide metabolism to OIS and the associated stable cell growth arrest.

A question that arises from our previous study is how can cells overcome replication stress-induced senescence? To address this important question, we examined the effects of inhibition of ATM and ATR, two major players in the DDR that are activated during replication stress induced by RRM2 suppression [4]. Notably, inactivation of ATM, but not ATR, was able to overcome senescence induced by replication stress. Consistently, loss or mutations in ATM, but not ATR, increases cancer risk [5]. Senescence bypass induced by ATM inactivation correlates with an increase in cellular dNTP levels, further highlighting the importance of dNTP levels in the replication stress observed during senescence. This was neither due to compensation by other nucleotide metabolic pathway enzymes nor increased dNTP salvage. Instead, restoration of cellular dNTP levels by ATM inactivation in the context of replication stress is accompanied by metabolic reprogramming.

It has recently become clear that changes in metabolism occur during OIS, which often oppose the

cancer-associated Warburg Effect [6]. We found that in the context of replication stress, loss of ATM increased glucose and glutamine consumption and utilization, similar to what is observed in cancer cells [3]. This suggests that reprogramming of cellular metabolism is sufficient to switch cells from a tumor suppressive to a tumor promoting phenotype. The observed metabolic reprogramming induced by ATM inactivation occurs through a coordinated downregulation of p53 activity and upregulation of c-MYC stability. Wild-type p53, but not its cancer-associated mutants, is known to suppress the activity of glucose-6-phosphate dehydrogenase (G6PD), the rate-limiting enzyme in the pentose phosphate pathway (PPP). The PPP is necessary for production of ribose-5-phosphate, which is the sugar base of all nucleosides. Consistently, ATM inactivation increased G6PD activity in a p53 mutational status-dependent manner. Therefore,

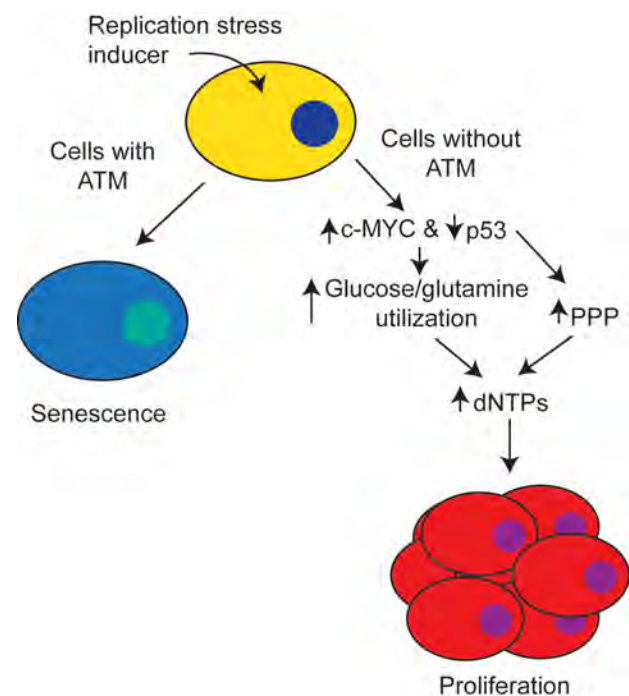


**Figure 1: ATM inactivation overcomes replication stress-induced senescence.** In cells with functional ATM, replication stress induces senescence. In cells without ATM, there is a coordinated upregulation of c-MYC and downregulation of p53 to increase glucose and glutamine utilization. Additionally, decreased p53 increases activity of the pentose phosphate pathway (PPP). This reprogramming in cellular metabolism increases dNTPs, which allows for cells to overcome the senescence-associated cell growth arrest to proliferate.

ATM inactivation suppresses replication stress and the associated senescence by restoring cellular dNTP levels through a coordinated increase in nutrient substrates and activity of the PPP for dNTP biosynthesis (Figure 1).

Our results demonstrate that in addition to its classical tumor suppressive role in the DDR, ATM functions as a tumor suppressor by suppressing cancer-associated metabolism to promote senescence and the associated stable cell growth arrest. In our report, we found that inactivation of ATM coordinately suppressed p53 and activated c-MYC. Analysis of The Cancer Genome Atlas (TCGA) datasets indicates a mutual exclusivity between ATM inactivation and p53 mutation/inactivation/c-MYC amplification. This further supports our central hypothesis that these alterations function in the same pathway (where ATM is upstream of p53 and c-MYC) and either ATM inactivation or p53 inactivation together with c-MYC upregulation can induce the observed metabolic reprogramming.

Our results have potential implications for developing cancer therapeutic strategies. There has been continuous interest in developing ATM inhibitors for utilization as a cancer therapy. However, based on our study, inhibition of ATM may lead to metabolic reprogramming that could enhance the cancer-associated Warburg Effect. This will need to be evaluated with caution to determine the impact on long-term changes in the malignant behavior of cancer cells given that metabolic pathways affect many aspects of cancer biology. Additionally, it is possible that patients with inactivated

ATM will be more sensitive to therapeutic intervention using metabolic inhibitors. Further studies are warranted to determine the metabolic weaknesses exposed by ATM inactivation in order to target them with metabolic inhibitors.

In conclusion, we found that ATM inactivation reprograms cellular metabolism to overcome replication stress-induced senescence. Understanding how cells overcome the tumor suppressive metabolism observed during senescence may lead to ways to prevent transformation of these cells or new ways to target these pathways in order to develop new cancer therapeutic strategies.

Katherine M. Aird: Gene Expression and Regulation, The Wistar Institute, Philadelphia, PA, USA

**Correspondence to:** Katherine M. Aird, **email** [kaird@wistar.org](mailto:kaird@wistar.org)

**Received:** May 28, 2015

**Published:** June 10, 2015

## REFERENCES

1. Campisi J, et al. *Nat Rev Mol Cell Biol.* 2007; 8:729-740.
2. Aird KM, et al. *Cell Rep.* 2013; 3:1252-1265.
3. Hanahan D, et al. *Cell.* 2011; 144:646-674.
4. Aird KM, et al. *Cell Rep.* 2015; 11:893-901.
5. McKinnon PJ *Annu Rev Pathol.* 2012; 7:303-321.
6. Aird KM, et al. *Molecular & Cellular Oncology.* 2014; 1.



# Comprehensive analysis of the ubiquitinome during oncogene-induced senescence in human fibroblasts

Fee Bengsch, Zhigang Tu, Hsin-Yao Tang, Hengrui Zhu, David W Speicher & Rugang Zhang

To cite this article: Fee Bengsch, Zhigang Tu, Hsin-Yao Tang, Hengrui Zhu, David W Speicher & Rugang Zhang (2015) Comprehensive analysis of the ubiquitinome during oncogene-induced senescence in human fibroblasts, Cell Cycle, 14:10, 1540-1547, DOI: [10.1080/15384101.2015.1026492](https://doi.org/10.1080/15384101.2015.1026492)

To link to this article: <http://dx.doi.org/10.1080/15384101.2015.1026492>



View supplementary material [↗](#)



Accepted author version posted online: 18 Mar 2015.



Submit your article to this journal [↗](#)



Article views: 253



View related articles [↗](#)



View Crossmark data [↗](#)



# Comprehensive analysis of the ubiquitinome during oncogene-induced senescence in human fibroblasts

Fee Bengsch<sup>1,†</sup>, Zhigang Tu<sup>1,4,†</sup>, Hsin-Yao Tang<sup>2</sup>, Hengrui Zhu<sup>1</sup>, David W Speicher<sup>3,\*</sup>, and Rugang Zhang<sup>1,\*</sup>

<sup>1</sup>Gene Expression and Regulation Program; The Wistar Institute Cancer Center; The Wistar Institute; Philadelphia, PA USA; <sup>2</sup>Proteomics Facility; The Wistar Institute; Philadelphia, PA USA; <sup>3</sup>Molecular and Cellular Oncogenesis Program and Center for Systems and Computational Biology; The Wistar Institute; Philadelphia, PA USA; <sup>4</sup>Current address: Institute of Life Sciences; Jiangsu University; China

<sup>†</sup>These authors equally contributed to this work.

**Keywords:** oncogene-induced senescence, proteomics, mass spectrometry, protein translation, protein synthesis, ubiquitination

Oncogene-induced senescence (OIS) is an important tumor suppression mechanism preventing uncontrolled proliferation in response to aberrant oncogenic signaling. The profound functional and morphological remodelling of the senescent cell involves extensive changes. In particular, alterations in protein ubiquitination during senescence have not been systematically analyzed previously. Here, we report the first global ubiquitination profile of primary human cells undergoing senescence. We employed a well-characterized *in vitro* model of OIS, primary human fibroblasts expressing oncogenic RAS. To compare the ubiquitinome of RAS-induced OIS and controls, ubiquitinated peptides were enriched by immune affinity purification and subjected to liquid chromatography tandem mass spectrometry (LC-MS/MS). We identified 4,472 ubiquitination sites, with 397 sites significantly changed (>3 standard deviations) in senescent cells. In addition, we performed mass spectrometry analysis of total proteins in OIS and control cells to account for parallel changes in both protein abundance and ubiquitin levels that did not affect the percentage of ubiquitination of a given protein. Pathway analysis revealed that the OIS-induced ubiquitinome alterations mainly affected 3 signaling networks: eIF2 signaling, eIF4/p70S6K signaling, and mTOR signaling. Interestingly, the majority of the changed ubiquitinated proteins in these pathways belong to the translation machinery. This includes several translation initiation factors (eIF2C2, eIF2B4, eIF3I, eIF3L, eIF4A1) and elongation factors (eEF1G, eEF1A) as well as 40S (RPS4X, RPS7, RPS11 and RPS20) and 60S ribosomal subunits (RPL10, RPL11, RPL18 and RPL35a). In addition, we observed enriched ubiquitination of aminoacyl-tRNA ligases (isoleucyl-, glutamine-, and tyrosine-tRNA ligase), which provide the amino acid-loaded tRNAs for protein synthesis. These results suggest that ubiquitination affects key components of the translation machinery to regulate protein synthesis during OIS. Our results thus point toward ubiquitination as a hitherto unappreciated regulatory mechanism during OIS.

## Introduction

Cellular senescence is a state of stable cell growth arrest.<sup>1</sup> In primary mammalian cells, activation of oncogenes such as RAS typically induces senescence.<sup>2,3</sup> Oncogene-induced senescence (OIS) prevents primary cells from uncontrolled proliferation and malignant transformation.<sup>4</sup> During OIS, cells undergo a diverse array of phenotypic changes. For example, chromatin in senescent cells reorganizes to form senescence-associated heterochromatin foci (SAHF) that contributes to senescence-associated cell growth arrest by silencing the proliferation-promoting genes.<sup>5,6</sup> In addition, senescent cells display an increase in senescence-associated  $\beta$ -galactosidase (SA- $\beta$ -Gal) activity.<sup>7</sup> It has been well established that p16/pRB and p53/p21 tumor suppressor pathways play a key role in senescence-associated cell growth arrest.<sup>8</sup> The extensive functional and structural remodelling of the cell

during OIS is reflected by profound changes in the proteome.<sup>9</sup> This suggests that regulation of protein synthesis and/or degradation might play a role in OIS.

Ubiquitination is an effective regulatory mechanism to induce proteome alterations. It is a common post-translational modification (PTM) where one (monoubiquitination) or a chain of several ubiquitin molecules (polyubiquitination) are covalently attached to a substrate protein. Different states of ubiquitination determine the fate of a protein: polyubiquitination usually marks a protein for degradation in 26S proteasome-dependent manner,<sup>10</sup> while monoubiquitination can alter protein function.<sup>11</sup> Ubiquitination is carried out by 3 types of enzymes, E1, E2, and E3 ligases, which consecutively activate, transfer and covalently link ubiquitin to lysine residues in a substrate protein.<sup>12</sup> In contrast, ubiquitin can be removed from proteins by deubiquitinating enzymes (DUBs).<sup>13</sup> Thus, ubiquitination is a dynamic

\*Correspondence to: Rugang Zhang; Email: rzhang@wistar.org; David W. Speicher; Email: speicher@wistar.org

Submitted: 12/19/2014; Revised: 02/20/2015; Accepted: 02/28/2015

<http://dx.doi.org/10.1080/15384101.2015.1026492>

cellular process that can quickly affect cellular protein levels and function. Despite studies of alterations in gene expression profiles and proteomes in OIS,<sup>9,14</sup> changes in ubiquitinated proteins (ubiquitinome) during senescence have never been profiled. Here, we systematically analyzed OIS-related changes of the ubiquitinome in primary human fibroblasts.

## Results

We set out to identify OIS-associated changes in the ubiquitinome in primary human cells by LC-MS/MS. First we sought to determine the time needed for RAS-infected primary human cells to undergo senescence. Toward this goal, we infected primary human fibroblasts IMR90 cells with a retrovirus encoding oncogenic H-RAS<sup>G12V</sup> to induce senescence. Consistent with previous studies,<sup>15</sup> RAS-infected cells exhibited a significant increase in SA- $\beta$ -gal activity (Fig. 1A and B) 6 d after infection. Next, we sought to examine senescence-associated cell cycle exit by BrdU incorporation. Indeed, there was a significant decrease in BrdU positive cells in RAS-infected cells compared with controls (Fig. 1C and D). Consistently, the expression of cell proliferation marker cyclin A was reduced in RAS-infected cells, while the expression of senescence marker p16 was upregulated in these cells compared with controls (Fig. 1E). Likewise, there was an apparent cell growth inhibition in RAS-expressing cells compared with controls as determined by colony formation assay (Fig. S1). Together, we conclude that 6 d post infection, there is a significant increase in the expression of markers of senescence and a decrease in cell proliferation markers in RAS-infected cells compared with control. Thus, we chose to perform our ubiquitinome and global proteome analyses at 6 d post RAS-infection.

For ubiquitinome analysis, stable isotope labeling with amino acids in cell culture (SILAC)<sup>16</sup> was performed in primary IMR90 fibroblasts starting at population doubling 20 (PD20). Cells were passaged in culture medium labeled with heavy <sup>13</sup>C<sub>6</sub>-lysine and <sup>13</sup>C<sub>6</sub>-arginine for 5 passages to ensure that all proteins in these cells were isotope labeled. Next, these cells were infected with a retrovirus encoding oncogenic H-RAS<sup>G12V</sup> (Fig. 2A). In parallel, control retrovirus-infected cells at the same passage were cultured in regular culture medium with light labeled <sup>12</sup>C<sub>6</sub>-lysine and <sup>12</sup>C<sub>6</sub>-arginine. The control and RAS-infected cells were harvested at day 6 post-infection. Before cell harvest, cells were treated with the proteasome inhibitor MG132 (5  $\mu$ M) for 5 hours to prevent ubiquitin-dependent protein degradation. For comparison, protein lysates of heavy isotope labeled RAS-infected and control cells cultured in light isotopes were mixed in a 1:1 ratio. As a quality control, a 1:1 mixture of protein lysates from heavy and light labeled controls was included for comparison. Tryptic digest of the protein lysates generated peptides with  $\epsilon$ -G-G residues at ubiquitination sites, since the C-terminal sequence of ubiquitin is KESTLHLVLRGG, which is cleaved after Arg (R).<sup>17</sup> Prior to LC-MS/MS, ubiquitinated peptides were enriched by immune affinity purification using an anti- $\epsilon$ -G-G peptide antibody (Fig. 2B). A global proteome analysis was also performed on non-enriched combined lysates of RAS-

infected heavy labeled and control light labeled cells to determine the general protein level changes.

The ubiquitinome analysis of RAS-infected and control cells identified 4,472 ubiquitinated peptides (at a false discovery rate of 1%), of which 397 (8.8%) showed a significantly changed abundance ( $>3$  Standard Deviations relative to biological replicate control). The biological replicate control using equal amounts of light and heavy labeled protein lysates from control fibroblast showed only 85 peptides with significant change out of 5,135 identified ubiquitinated peptides (1.6%) (Fig. 3A). This demonstrates a good signal (8.8%) to noise (1.6%) ratio. One example of a ubiquitinated peptide with significant change in OIS compared to control fibroblasts was VHIDK(gl)AQQNN-VEHK representing the ribosomal protein RPS7 with a Heavy/Light fold change of 2.7 (Fig. 3B). The 397 significantly changed ubiquitinated peptides belonged to 253 proteins. Some proteins (such as RPS11 and EIF4A1) were ubiquitinated at multiple sites. In most cases where multiple ubiquitinated peptides were identified in a single protein (multiubiquitination), the ubiquitination sites showed very similar OIS-induced abundance changes. The global proteome analysis of RAS-infected and control fibroblasts identified 5,195 proteins. Fold changes detected in the global proteome analysis were used to adjust the fold changes in the ubiquitinome dataset. Not all proteins with changed ubiquitination were identified in the global proteomics analysis and the associated ubiquitinated sites were not included in the final data set of modified sites. In addition, correction for changes in protein level reduced some ubiquitination site changes to less than 1.5-fold and these sites were removed from the final dataset. Therefore, the final data set of significantly changed ubiquitinated proteins used for further analyses was reduced to 201 proteins (Fig. 3C).

Ingenuity pathway analysis (IPA) was performed on the global proteome data of RAS-infected and control fibroblasts. The analysis revealed major OIS-induced changes in regulatory networks including: dermatological diseases, cancer, cellular assembly, and DNA replication (Table S1). Alterations in these protein networks reflect cellular and functional alterations that occur during OIS, such as changes in fibroblast marker proteins, enhanced oncogenic signaling, structural changes, and induction of replication shutdown. Further analysis identified the most affected canonical pathways: adherens junction signaling ( $-\log p = 7.00$ ), cell cycle control of chromosomal replication ( $-\log p = 6.79$ ), hepatic fibrosis ( $-\log p = 6.76$ ), including several cytokines typically secreted during senescence (IL8, IL1 $\alpha$ , and IL1 $\beta$ ) (Table S2). The pathways identified from analyzing our dataset are consistent with previously published OIS-dependent proteome changes.<sup>9</sup>

Next, we sought to analyze the OIS-associated changes in the ubiquitinome. For our analysis of the ubiquitinome data set we used the 201 proteins that exhibited significant fold changes of at least 1.5-fold after correcting for any changes in the total levels of individual proteins. IPA on the processed dataset revealed that the molecular networks most affected in the OIS ubiquitinome included: 1 (hereditary disorder, carbohydrate metabolism, 2) developmental disorder, muscular and skeletal disorder, protein

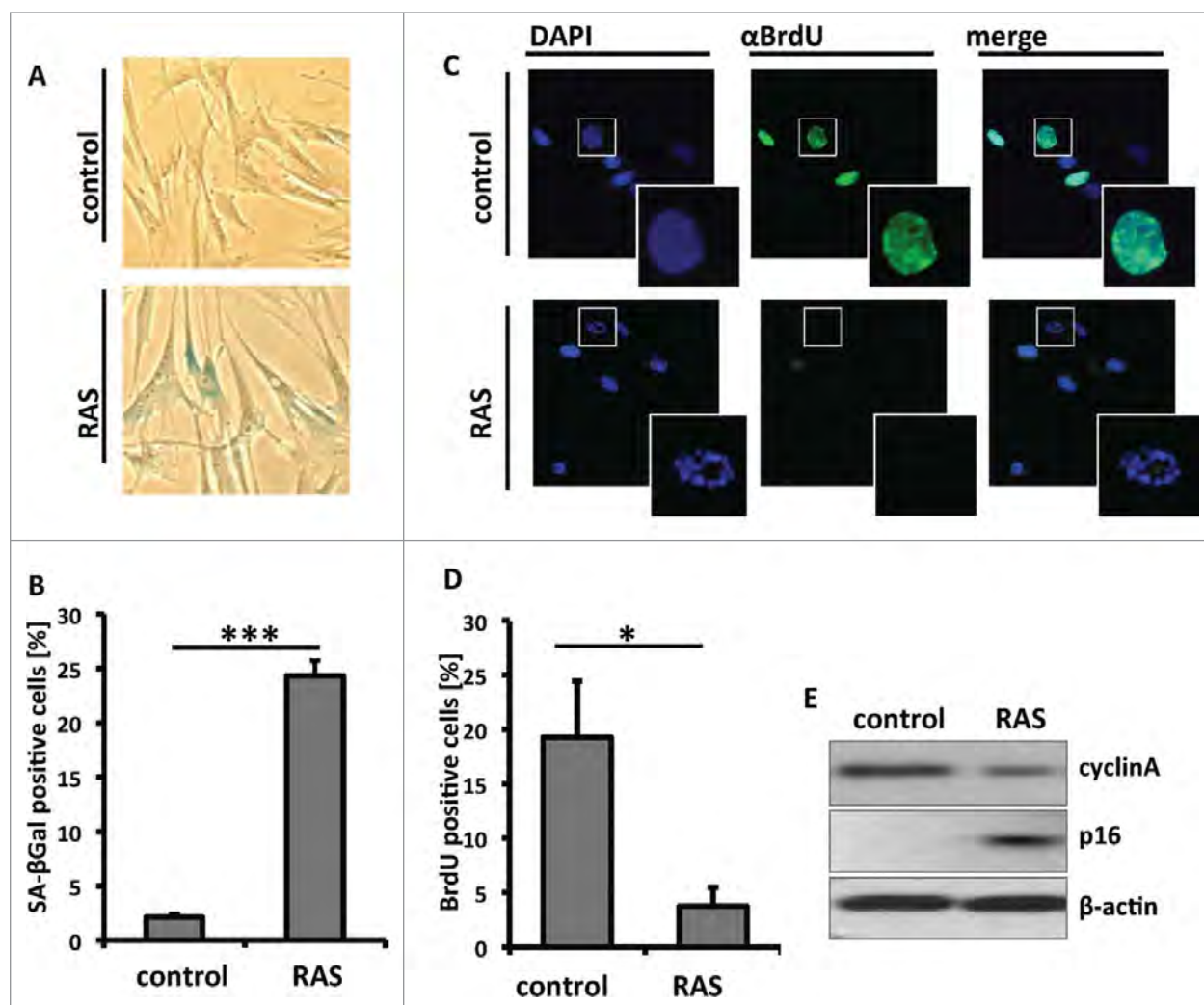


**Figure 1.** Senescence-induction by overexpression of oncogenic RAS. (A) Primary human fibroblasts (IMR90) were infected with a retrovirus encoding for oncogenic H-RAS<sup>G12V</sup> or control. At day 6 post infection, drug-selected cells were assayed for Senescence-associated β-galactosidase (SA-β-gal) activity. (B) Quantitation of A. Mean of 3 independent experiments (error bars = SEM). \*\*\**P* < 0.001. (C) Same as A, but labeled with BrdU for 1 hour to visualize replicating cells. (D) Quantitation of C. Mean of 3 independent experiments (error bars = SEM). \**P* < 0.05. (E) At day 6 post infection, drug-selected cells were examined for the expression of cyclin A and p16 by immunoblotting.

synthesis, 3) cancer, cardiovascular disease (Fig. 4A). Notably, ubiquitin (UBC) represents the central node of the network with the highest score “hereditary disorder, carbohydrate metabolism,” supporting a mechanistic link (Fig. 4B).

The main canonical pathways affected in the ubiquitinome of senescent cells were eIF2 signaling (−log<sub>10</sub> = 9.90), eIF4 and p70S6K signaling (−log<sub>10</sub> = 8.00), and mTOR signaling (−log<sub>10</sub> = 5.02) (Fig. 5A). These identified pathways transmit mitogenic signals to induce cell growth and proliferation. The mTOR pathway controls cell metabolism and proliferation in response to hormones, growth factors and mitogens.<sup>18</sup> It is also activated by oncogenic RAS signaling.<sup>19</sup> Downstream of mTOR, S6Kinase activates ribosome biogenesis and protein synthesis.<sup>20</sup> eIF2 is a regulator of translation initiation, the rate-limiting step of protein synthesis.<sup>21,22</sup> The 3 affected canonical pathways converge on their effector molecules, which are ribosomal proteins and

translation factors (Fig. 5). The translation initiation factors eIF-2B4, eIF3L, and eIF4A1 were enriched (3.4-fold, 2.4-fold, 2.7-fold) in the OIS-associated ubiquitinome (Fig. 5B; Table S3). They are involved in formation of the ternary complex and initiation complex to start mRNA translation. Apart from that, several translation elongation factors were changed as well (Table S3). The most striking difference (9.2-fold) was observed for eEF1G, a subunit of the elongation factor-1 complex, which is responsible for the delivery of aminoacyl-tRNAs to the ribosome (Table S3). The 40S ribosomal subunits RPS4X, and RPS7 were enriched (2.3-fold and 2.7-fold respectively), whereas RPS20 was decreased (−3.7-fold). The 60S ribosomal subunits RPL10, RPL11, and RPL35a were also increased (2.1-fold, 2.8-fold and 2.7-fold, respectively), while RPL18 was decreased (−8.6-fold) in the OIS ubiquitinome (Fig. 5B; Tables S3 and S4). In addition, we observed enriched ubiquitination of isoleucyl-,

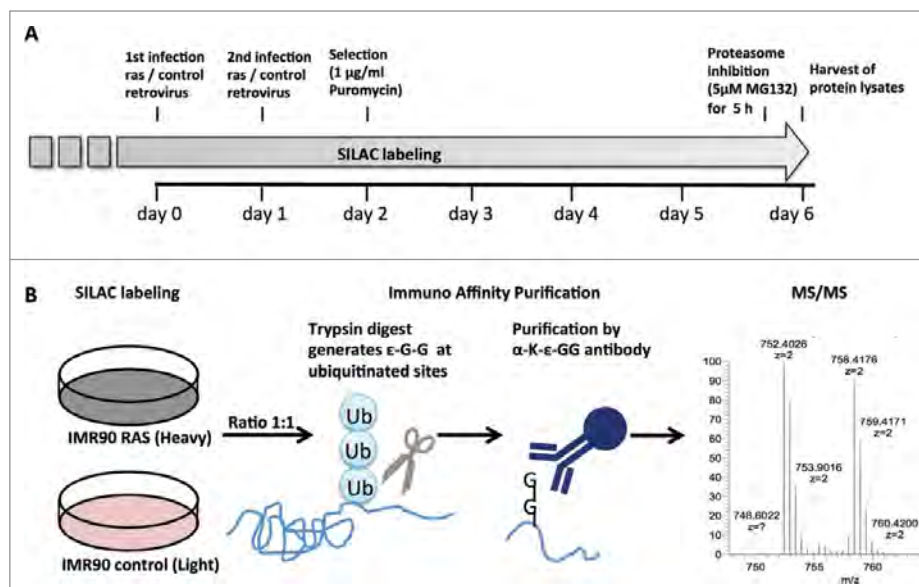


**Figure 2.** Experimental setup for analysis of the OIS-associated ubiquitinome. **(A)** time course of RAS-induced OIS experiment. SILAC labeling of primary fibroblast (IMR90) was initiated at population doubling 20 and maintained for the duration of the experiment. Cells were infected twice with H-RAS<sup>G12V</sup> or control retrovirus and selected by puromycin (1  $\mu$ g/ml). Samples for mass spectrometry were collected at day 6 after a 5 h treatment with the proteasome inhibitor MG132 (5  $\mu$ M). **(B)** Schematic of ubiquitination site identification by mass spectrometry. RAS and control fibroblasts labeled with heavy or light SILAC, respectively, cell lysates were harvested and mixed in a 1:1 ratio. Trypsin digest generated  $\epsilon$ -G-G residues at ubiquitination site and these peptides were enriched by immune affinity purification prior to MS/MS.

glutamine-, and tyrosine-tRNA-ligase, (65-fold, 5.3-fold, and 3.0-fold respectively), which synthesize amino acid-loaded tRNAs for protein synthesis (Table S3). These identified changes cumulatively indicate an effect on ribosome biogenesis and translation in OIS. Taken together, the OIS-associated changes in ubiquitination of many functionally different components of the translation machinery might indicate a general effect on protein synthesis (Fig. 6).

## Discussion

OIS is a cellular process that involves dramatic functional and morphologic changes inducing a stable cell growth arrest. This is reflected by alterations in the proteome.<sup>9</sup> Our study reveals that ubiquitination is implicated in OIS-associated remodelling of the proteome. Global proteome comparison of RAS-induced senescent and control fibroblasts showed significant changes in fibroblast proteins, oncogenic signaling, structure molecules, and replication. In addition, typical OIS-related changes were observed in cell cycle control, DNA replication and in cytokines typically secreted in senescence. Our analysis of the OIS-associated ubiquitinome showed significant changes in 397 ubiquitination sites. Correcting the fold changes of the ubiquitinated peptides by protein level changes (indicated by the global proteome analysis), as we have done here, may result in the loss a few biologically meaningful changes from the data set. However, it

filters out cases where the protein abundance level has changed but the stoichiometry of ubiquitin modification has not changed. This should make the ubiquitinome data more reliable as changes in ubiquitin stoichiometry are more likely to affect the biological phenotype. IPA analysis revealed that the molecular networks most affected in the OIS ubiquitinome were hereditary disorder and carbohydrate metabolism, developmental disorder, muscular and skeletal disorders, protein synthesis, and cancer. A role of carbohydrate metabolism for the maintenance of senescence has been established before.<sup>23,24</sup> The main signaling pathways affected were eIF2, S6Kinase and mTOR signaling. All of these pathways regulate cell growth and proliferation.<sup>25</sup> They also share common downstream effector proteins: translation initiation and elongation factors and ribosomal subunits. These effectors control protein synthesis by regulating cap-dependent translation of mRNAs, ribosome biogenesis and tRNA loading.<sup>20,26,27</sup> Since K- $\epsilon$ -G-G MS/MS does not discriminate between poly- and monoubiquitinated sites,<sup>17</sup> detection of an enhanced ubiquitination

implies either increased degradation of the target protein or changes in protein function. Our findings suggest that mRNA translation may be altered in OIS as a consequence of ubiquitination changes in several components of the translation machinery.

There is evidence for ubiquitination of ribosomal proteins in response to mitogenic signals.<sup>28</sup> Continuous mitogenic/oncogenic signaling, as in OIS, causes ribosomal stress that affects translation initiation.<sup>29</sup> Importantly, translation is not completely shut down in senescent cells, since they remain metabolically active and protein synthesis is a prerequisite for the induction of the senescence associated secretory phenotype (SASP). Inhibiting protein synthesis by cycloheximide treatment prevents fibroblasts from RAS-induced senescence.<sup>9</sup> It is therefore likely that protein synthesis is differentially regulated by ubiquitination in a way that decreases general mRNA translation while enhancing translation of mRNAs encoding for OIS-relevant proteins such as SASP factors. Regulation of mRNA translation could be an important means to alter the proteome and enforce the OIS phenotype. Compared with changes in transcription, changes in translation induced by ubiquitination may represent a fast and efficient way to drive OIS-associated phenotypes. Together, our data suggest that ubiquitination represents an important regulatory mechanism during OIS.

Cellular senescence is an important tumor suppression mechanism and has been suggested as an alternative to apoptosis induction for developing cancer therapeutics.<sup>30</sup> Our findings indicate that ubiquitination affects key components of the translation



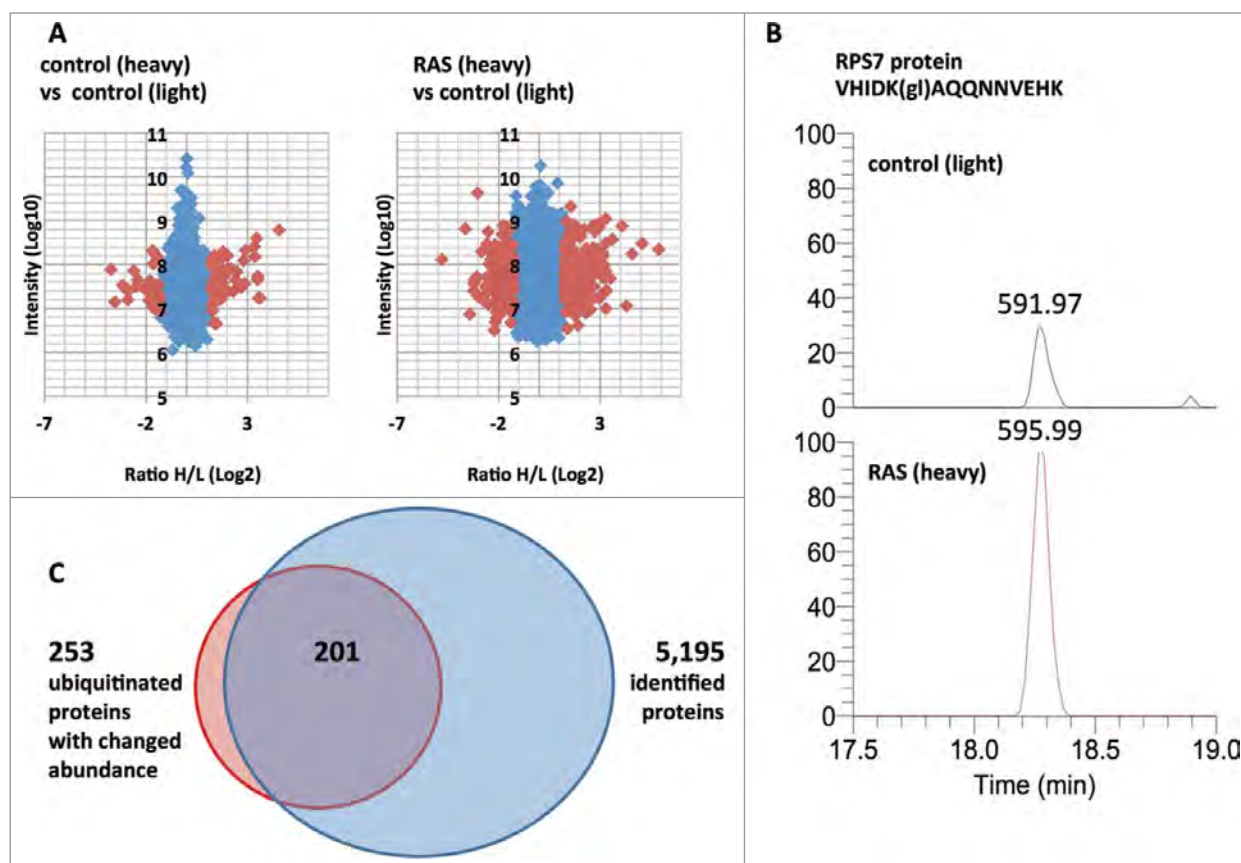


**Figure 3.** Representation of ubiquitin site proteomics and global proteomics data. (A) Ratio Heavy/Light versus intensity plots of ubiquitinated sites identified in control and experimental samples. Identifications with significantly changed ubiquitinated peptides ( $>3$  Standard Deviations) are indicated in red. (B) Extracted ion chromatograms of a SILAC pair (591.97 m/z, 595.99 m/z) corresponding to the triple charged ubiquitinated peptide VHIDK(gl)AQQNNVEHK of the protein RPS7. The maximum intensity for both plots are fixed at  $1E6$ . (gl) indicates diglycine remnant. (C) Venn diagram of proteins identified as significantly changed in ubiquitin site proteomics vs. proteins identified by global proteomics.

machinery to regulate protein synthesis during oncogene-induced senescence. These findings suggest that targeting aspects of the ubiquitination system with small molecules or biological reagents<sup>31</sup> to regulate translation machinery may represent new strategies for inducing cancer cells to undergo senescence.

## Materials and Methods

### Cells and culture conditions

Human primary IMR90 fibroblasts were obtained from ATCC and cultured according to ATCC and in DMEM, 10% FCS, 1% L-glutamine, 1% non-essential amino acids, 1%  $\text{NaHCO}_3$ , 1% Penicillin/Streptomycin. Experiments were performed on IMR90 cells between population doubling #25–30. The plasmid pBabe-neo-H-RAS<sup>G12V</sup><sup>5</sup> was used to generate retrovirus for RAS overexpression in IMR90 fibroblasts. Retrovirus production and transduction were performed as described previously using Phoenix cells to package the infection viruses.<sup>32</sup> An empty pBabe vector plasmid was used as a control. IMR90 fibroblasts were infected twice and selected with 1  $\mu\text{g}/\text{ml}$  puromycin (Sigma #P8833).

### Western blot, $\beta$ -Galactosidase staining, and BrdU labeling

Cell lysates for Western blot were collected in RIPA buffer supplemented with complete protease inhibitor cocktail (Roche #1183617001). SA- $\beta$ -galactosidase staining and BrdU labeling was performed as described earlier.<sup>5,7</sup>

### SILAC labeling

SILAC (Invitrogen #MS10030) labeling of IMR90 fibroblasts with heavy  $^{13}\text{C}_6$ -lysine and  $^{13}\text{C}_6$ -arginine or control light  $^{12}\text{C}_6$ -lysine and  $^{12}\text{C}_6$ -arginine SILAC medium was performed for 5 passages prior to induction of senescence and maintained in the respective medium during the experimental period. To prevent degradation of ubiquitinated proteins, cells were treated with MG132 (5  $\mu\text{M}$ ) (Sigma #C2211) for 5 h before cell harvest.

### Sample preparation

Cells were lysed with 8 M urea, 50 mM Tris-Cl (pH8), 1 mM EDTA, 1 mM  $\text{Na}_3\text{VO}_4$ , 2.5 mM sodium pyrophosphate. Protein concentration was measured by BCA protein assay (Thermo Scientific #PI-23227). For immune affinity enrichment, 5.4 mg of experimental sample was created by mixing equal amounts of lysates (2.7 mg each) from IMR90 cells

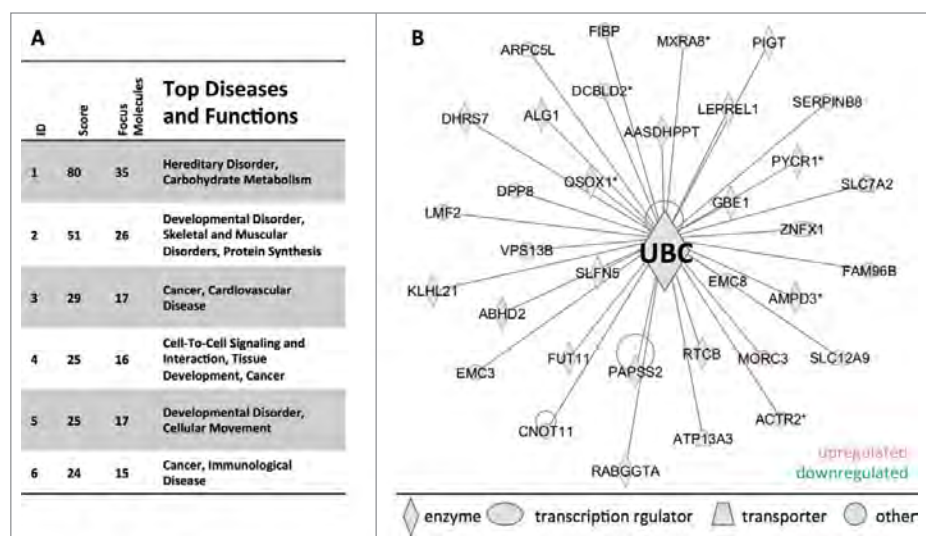


**Figure 4.** Disease and function networks affected by ubiquitinome alterations in RAS-induced OIS. (A) Ingenuity network analysis of proteins with OIS-associated significant fold changes ( $>3$  SD) at ubiquitination sites. Fold changes in ubiquitination sites were adjusted by changes on the protein level. The cut-off for observations included in the analysis was set to a 1.5-fold change. (B) Ubiquitin (UBC) is the central knot of the network "hereditary disorder, carbohydrate metabolism".

expressing oncogenic RAS (heavy SILAC labeled) or controls transfected with empty vector (light SILAC labeled). To evaluate technical and biological reproducibility of the proteome analysis

teome analysis without immune affinity enrichment, 18  $\mu$ g of the experimental sample was separated on a SDS-PAGE gel. The gel lane was sliced into 11 equal fractions, digested with trypsin and analyzed by LC-MS/MS.

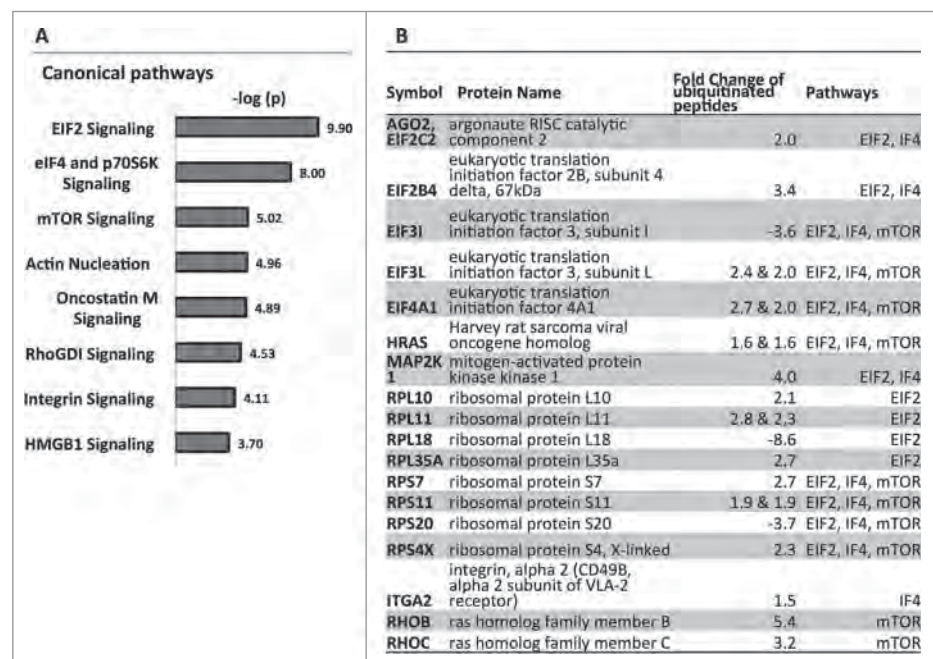


**Figure 5.** Canonical pathways affected by ubiquitinome alterations in RAS-induced OIS. (A) Ingenuity pathway analysis of proteins with OIS-associated significant fold changes ( $>3$  SD) at ubiquitination sites. Fold changes in ubiquitination sites were adjusted by changes on the protein level. The cut-off for observations included in the analysis was set to a 1.5-fold change. (B) Focus molecules of the affected pathways with respective fold changes at ubiquitination sites.

pipeline, equal amount of lysates from control cells grown in light and heavy SILAC medium were mixed at 1:1 ratio. All combined heavy/light samples were reduced with 5 mM DTT, pH 8, 37°C, 45 min, alkylated with 10 mM Iodoacetamide, pH 8, 37°C, 30 min and quenched with 10 mM cysteine, pH 8, 37°C, 30 min. The samples were then digested with modified trypsin (Promega; enzyme:protein = 1:100) for 4 h at a final urea concentration of 4 M, followed by overnight digestion at a final urea concentration of 2 M after adding another aliquot of trypsin. Tryptic peptides were desalted using Sep-Pak C18 (Waters Corporation, Milford, MA, USA), and ubiquitinated peptides were enriched using an antibody against the ubiquitin remnant motif (K- $\epsilon$ -GG) (Cell Signaling, Cambridge, UK) according to the manufacturer's protocol and subjected to LC-MS/MS analysis. For global proteome analysis without immune affinity enrichment, 18  $\mu$ g of the experimental sample was separated on a SDS-PAGE gel. The gel lane was sliced into 11 equal fractions, digested with trypsin and analyzed by LC-MS/MS.

## LC-MS/MS

Liquid chromatography tandem mass spectrometry (LC-MS/MS) analysis was performed on a Q Exactive mass spectrometer (Thermo Scientific) coupled with a Nano-ACQUITY UPLC system (Waters). Samples were injected onto a UPLC Symmetry trap column (180  $\mu$ m i.d.  $\times$  2 cm packed with 5  $\mu$ m C18 resin; Waters), and tryptic peptides were separated by RP-HPLC on a BEH C18 nanocapillary analytical column (75  $\mu$ m i.d.  $\times$  25 cm, 1.7  $\mu$ m particle size; Waters) using a gradient formed by solvent A (0.1% formic acid in water) and solvent B (0.1% formic acid in acetonitrile). For ubiquitin remnant enriched samples, the gradient used was: 5–28% B over 42 min, 28–50% B over 25.5 min, 50–80% B over 5 min, and constant 80% B over 7.5 min. For global proteome analysis, the gradient used was: 5–28% B over 170 min, 28–50% B over 50 min, 50–80% B over 10 min, and constant 80% B over 10 min. A 30-min blank gradient was run between sample injections to

minimize carryover. Eluted peptides were analyzed by the mass spectrometer set to repetitively scan  $m/z$  from 400 to 2000. The full MS scan was collected at 70,000 resolution followed by data-dependent MS/MS scans at 17,500 resolution on the 20 most abundant ions exceeding a minimum threshold of 8,300. Peptide match was set as preferred, exclude isotopes option and charge-state screening were enabled to reject singly and unassigned charged ions.

### MS data analysis

Mass spectrometry data were analyzed with MaxQuant 1.3.0.5 software.<sup>33</sup> MS/MS data were searched against the human UniRef 100 protein database (March 2013, Protein Information Resource, Georgetown University) using full trypsin specificity with up to 2 missed cleavages, static carboxamidomethylation of Cys, and variable oxidation of Met, protein N-terminal acetylation and diglycine addition to Lys. Consensus identification lists were generated with false discovery rates of 1% at protein, peptide and site levels. Reverse hits, contaminants, and identifications without any H/L ratio were removed from all datasets. Ubiquitinated sites were determined from the GlyGly (K)Sites.txt table. Fold changes were calculated from the normalized Heavy/Light ratio. A 3 standard deviation (SD) cut-off was determined from the control heavy/light labeled sample, and was used to identify sites displaying significant change in the experimental sample. For global proteome analysis, protein identifications were obtained from the proteinGroups.txt table, and were required to have at least 2 razor+unique peptides and a minimum ratio count of 2. Fold changes of ubiquitinated sites were adjusted by the observed fold change of the respective protein in the global proteome comparison.

### Ingenuity pathway analysis

QIAGEN's Ingenuity® Pathway Analysis (IPA®, QIAGEN Redwood City, www.qiagen.com/ingenuity) was employed to analyze the data. The cut-off for observations included in the analysis was set to a minimum of 1.5-fold change. Specialized tissue functions were included in disease and function analysis. Affected disease networks and canonical pathways were identified by significant abundance changes in their focus molecules.

### References

- Hayflick L, Moorhead PS. The serial cultivation of human diploid cell strains. *Exp Cell Res* 1961; 25: 585–621; PMID:13905658; [http://dx.doi.org/10.1016/0014-4827\(61\)90192-6](http://dx.doi.org/10.1016/0014-4827(61)90192-6)
- Yaswen P, Campisi J. Oncogene-induced senescence pathways weave an intricate tapestry. *Cell* 2007; 128: 233–4; PMID:17254959; <http://dx.doi.org/10.1016/j.cell.2007.01.005>
- Serrano M, Lin AW, McCurrach ME, Beach D, Lowe SW. Oncogenic ras provokes premature cell senescence associated with accumulation of p53 and p16INK4a. *Cell* 1997; 88: 593–602; PMID:9054499; [http://dx.doi.org/10.1016/S0092-8674\(00\)81902-9](http://dx.doi.org/10.1016/S0092-8674(00)81902-9)
- Rodier F, Campisi J. Four faces of cellular senescence. *J Cell Biol* 2011; 192: 547–56; PMID:21321098; <http://dx.doi.org/10.1083/jcb.201009094>
- Zhang R, Chen W, Adams PD. Molecular dissection of formation of senescence-associated heterochromatin

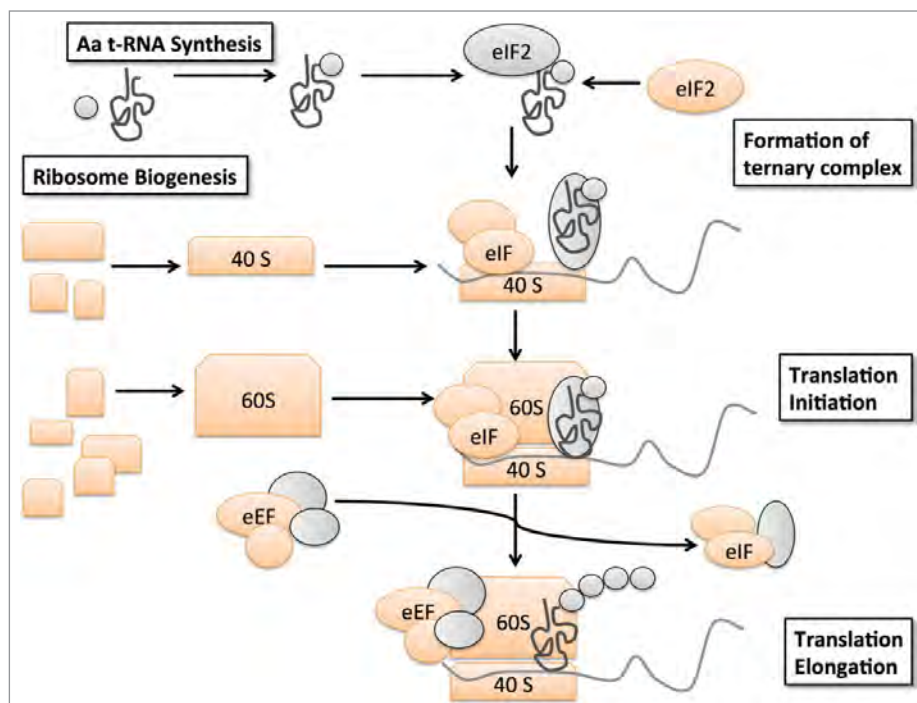


**Figure 6.** Schematic representation of translation machinery components affected by OIS-associated changes in ubiquitination. OIS-associated ubiquitination changes occur in amino acyl-tRNA-ligases, eukaryotic translation initiation factors, elongation factors, small and large ribosomal subunits (depicted in orange).

### Disclosure of Potential Conflicts of Interest

No potential conflicts of interest were disclosed.

### Acknowledgments

We thank Dr. Benjamin Bitler for critical reading of the manuscript, the Wistar Proteomics Facility for assistance with the proteome analyses, and the Wistar Bioinformatics Facility for assistance with data analysis.

### Funding

This work was supported in part by NIH/NCI grants R01CA160331 to R.Z., R01CA131582 to D.W.S., and an institutional grant to The Wistar Institute (NCI Cancer Core Grant CA010815).

### Supplemental Material

Supplemental data for this article can be accessed on the publisher's website.



- foci. *Mol Cell Biol* 2007; 27: 2343–58; PMID:17242207; <http://dx.doi.org/10.1128/MCB.02019-06>
6. Narita M, Nunez S, Heard E, Narita M, Lin AW, Hearn SA, Spector DL, Hannon GJ, Lowe SW. Rb-mediated heterochromatin formation and silencing of E2F target genes during cellular senescence. *Cell* 2003; 113: 703–16; PMID:12809602; [http://dx.doi.org/10.1016/S0092-8674\(03\)00401-X](http://dx.doi.org/10.1016/S0092-8674(03)00401-X)
7. Dimri GP, Lee X, Basile G, Acosta M, Scott G, Roskelley C, Medrano EE, Linskens M, Rubelj I, Pereira-Smith O, et al. A biomarker that identifies senescent human cells in culture and in aging skin in vivo. *Proc Natl Acad Sci U S A* 1995; 92: 9363–7.
8. Salama R, Sadaie M, Hoare M, Narita M. Cellular senescence and its effector programs. *Genes Dev* 2014; 28: 99–114; PMID:24449267; <http://dx.doi.org/10.1101/gad.235184.113>
9. Li M, Durbin KR, Sweet SM, Tipton JD, Zheng Y, Kelleher NL. Oncogene-induced cellular senescence elicits an anti-Warburg effect. *Proteomics* 2013; 13: 2585–96; PMID:23798001; <http://dx.doi.org/10.1002/pmic.201200298>
10. Chau V, Tobias JW, Bachmair A, Marriott D, Ecker DJ, Gonda DK, Varshavsky A. A multiubiquitin chain is confined to specific lysine in a targeted short-lived protein. *Science* 1989; 243: 1576–83; PMID:2538923; <http://dx.doi.org/10.1126/science.2538923>
11. Mittal R, McMahon HT. Arrestins as adaptors for ubiquitination in endocytosis and sorting. *EMBO Rep* 2009; 10: 41–3; PMID:19057574; <http://dx.doi.org/10.1038/embor.2008.240>
12. Neutzner M, Neutzner A. Enzymes of ubiquitination and deubiquitination. *Essays Biochem* 2012; 52: 37–50; PMID:22708562; <http://dx.doi.org/10.1042/bse0520037>
13. Singhal S, Taylor MC, Baker RT. Deubiquitylating enzymes and disease. *BMC Biochem* 2008; 9 Suppl 1: S3; PMID:19007433; <http://dx.doi.org/10.1186/1471-2091-9-S1-S3>
14. Young AR, Narita M, Narita M. Spatio-temporal association between mTOR and autophagy during cellular senescence. *Autophagy* 2011; 7: 1387–8; PMID:21799306; <http://dx.doi.org/10.4161/auto.7.11.17348>
15. Tu Z, Aird KM, Bitler BG, Nicodemus JP, Beechary N, Xia B, Yen TJ, Zhang R. Oncogenic RAS regulates BRIP1 expression to induce dissociation of BRCA1 from chromatin, inhibit DNA repair, and promote senescence. *Dev Cell* 2011; 21: 1077–91; PMID:22137763; <http://dx.doi.org/10.1016/j.devcel.2011.10.010>
16. Ong SE, Blagoev B, Kratchmarova I, Kristensen DB, Steen H, Pandey A, Mann M. Stable isotope labeling by amino acids in cell culture, SILAC, as a simple and accurate approach to expression proteomics. *Mol Cell Proteomics* 2002; 1: 376–86; PMID:12118079; <http://dx.doi.org/10.1074/mcp.M200025-MCP200>
17. Xu G, Paige JS, Jaffrey SR. Global analysis of lysine ubiquitination by ubiquitin remnant immunoaffinity profiling. *Nat Biotechnol* 2010; 28: 868–73; PMID:20639865; <http://dx.doi.org/10.1038/nbt.1654>
18. Laplante M, Sabatini DM. mTOR signaling in growth control and disease. *Cell* 2012; 149: 274–93; PMID:22500797; <http://dx.doi.org/10.1016/j.cell.2012.03.017>
19. Mendoza MC, Er EE, Blenis J. The Ras-ERK and PI3K-mTOR pathways: cross-talk and compensation. *Trends Biochem Sci* 2011; 36: 320–8; PMID:21531565; <http://dx.doi.org/10.1016/j.tibs.2011.03.006>
20. Fonseca BD, Smith EM, Yelle N, Alain T, Bushell M, Pause A. The ever-evolving role of mTOR in translation. *Semin Cell Dev Biol* 2014; 36: 102–12; PMID:25263010; <http://dx.doi.org/10.1016/j.semcdb.2014.09.014>
21. Baird TD, Wek RC. Eukaryotic initiation factor 2 phosphorylation and translational control in metabolism. *Adv Nutr* 2012; 3: 307–21; PMID:22585904; <http://dx.doi.org/10.3945/an.112.002113>
22. Mohammad-Qureshi SS, Jennings MD, Pavitt GD. Clues to the mechanism of action of eIF2B, the guanine-nucleotide-exchange factor for translation initiation. *Biochem Soc Trans* 2008; 36: 658–64; PMID:18631136; <http://dx.doi.org/10.1042/BST0360658>
23. Aird KM, Li H, Xin F, Konstantinopoulos PA, Zhang R. Identification of ribonucleotide reductase M2 as a potential target for pro-senescence therapy in epithelial ovarian cancer. *Cell Cycle* 2014; 13: 199–207; PMID:24200970; <http://dx.doi.org/10.4161/cc.26953>
24. Aird KM, Zhang R. Nucleotide metabolism, oncogene-induced senescence and cancer. *Cancer Lett* 2014; 356: 204–10; PMID:24486217; <http://dx.doi.org/10.1016/j.canlet.2014.01.017>
25. Magnuson B, Ekim B, Fingar DC. Regulation and function of ribosomal protein S6 kinase (S6K) within mTOR signalling networks. *Biochem J* 2012; 441: 1–21; PMID:22168436; <http://dx.doi.org/10.1042/BJ20110892>
26. Iadevaia V, Liu R, Proud CG. mTORC1 signaling controls multiple steps in ribosome biogenesis. *Semin Cell Dev Biol* 2014; 36: 113–20; PMID:25148809; <http://dx.doi.org/10.1016/j.semcdb.2014.08.004>
27. Laplante M, Sabatini DM. mTOR Signaling. *Cold Spring Harbor Perspect Biol* 2012; 4; PMID:22129599; <http://dx.doi.org/10.1101/cshperspect.a011593>; <http://www.ncbi.nlm.nih.gov/pubmed/22129599>
28. Sun XX, DeVine T, Challagundla KB, Dai MS. Interplay between ribosomal protein S27a and MDM2 protein in p53 activation in response to ribosomal stress. *J Biol Chem* 2011; 286: 22730–41; PMID:21561866; <http://dx.doi.org/10.1074/jbc.M111.223651>
29. Das S, Fregoso OI, Krainer AR. A new path to oncogene-induced senescence: at the crossroads of splicing and translation. *Cell Cycle* 2013; 12: 1477–9; PMID:23624837; <http://dx.doi.org/10.4161/cc.24749>
30. Perez-Mancera PA, Young AR, Narita M. Inside and out: the activities of senescence in cancer. *Nat Rev Cancer* 2014; 14: 547–58; PMID:25030953; <http://dx.doi.org/10.1038/nrc3773>
31. Popovic D, Vucic D, Dikic I. Ubiquitination in disease pathogenesis and treatment. *Nat Med* 2014; 20: 1242–53; PMID:25375928; <http://dx.doi.org/10.1038/nm.3739>
32. Zhang R, Poustovoitov MV, Ye X, Santos HA, Chen W, Daganzo SM, Erzberger JP, Serebriiskii IG, Canutescu AA, Dunbrack RL, et al. Formation of Mac-roH2A-containing senescence-associated heterochromatin foci and senescence driven by ASF1a and HIRA. *Dev Cell* 2005; 8: 19–30; PMID:15621527; <http://dx.doi.org/10.1016/j.devcel.2004.10.019>
33. Cox J, Mann M. MaxQuant enables high peptide identification rates, individualized p.p.b.-range mass accuracies and proteome-wide protein quantification. *Nat Biotechnol* 2008; 26: 1367–72; PMID:19029910; <http://dx.doi.org/10.1038/nbt.1511>



# Synthetic lethality by targeting EZH2 methyltransferase activity in *ARID1A*-mutated cancers

Benjamin G Bitler<sup>1</sup>, Katherine M Aird<sup>1</sup>, Azat Garipov<sup>1</sup>, Hua Li<sup>1</sup>, Michael Amatangelo<sup>1</sup>, Andrew V Kossenkov<sup>2</sup>, David C Schultz<sup>3</sup>, Qin Liu<sup>4</sup>, Je-Ming Shih<sup>5</sup>, Jose R Conejo-Garcia<sup>6</sup>, David W Speicher<sup>2,4</sup> & Rugang Zhang<sup>1</sup>

The gene encoding *ARID1A*, a chromatin remodeler, shows one of the highest mutation rates across many cancer types. Notably, *ARID1A* is mutated in over 50% of ovarian clear cell carcinomas, which currently have no effective therapy. To date, clinically applicable targeted cancer therapy based on *ARID1A* mutational status has not been described. Here we show that inhibition of the EZH2 methyltransferase acts in a synthetic lethal manner in *ARID1A*-mutated ovarian cancer cells and that *ARID1A* mutational status correlated with response to the EZH2 inhibitor. We identified *PIK3IP1* as a direct target of *ARID1A* and EZH2 that is upregulated by EZH2 inhibition and contributed to the observed synthetic lethality by inhibiting PI3K–AKT signaling. Importantly, EZH2 inhibition caused regression of *ARID1A*-mutated ovarian tumors *in vivo*. To our knowledge, this is the first data set to demonstrate a synthetic lethality between *ARID1A* mutation and EZH2 inhibition. Our data indicate that pharmacological inhibition of EZH2 represents a novel treatment strategy for cancers involving *ARID1A* mutations.

A major discovery of recent cancer genome-wide sequencing studies has been the identification of significant alterations in genes responsible for modifying chromatin structure<sup>1</sup>. *ARID1A*, which encodes a component of the SWI/SNF chromatin-remodeling complex, is among the genes that show the highest mutation rates across multiple cancer types<sup>2</sup>. The SWI/SNF complex remodels nucleosomes to modulate transcription, and its inactivation is thought to drive tumorigenesis by altering gene expression<sup>3</sup>. Notably, *ARID1A* is mutated in ~57% of ovarian clear cell carcinomas (OCCCs)<sup>4,5</sup>. *ARID1A*-mutated OCCCs are typically characterized by a lack of genomic instability<sup>4,6</sup>. It has been suggested that perturbations in the regulation of epigenetic chromatin remodeling may be able to substitute for genomic instability<sup>3</sup>. These findings suggest that epigenetic mechanisms play a critical role in OCCC. Despite the prevalence of genetic mutations of *ARID1A*, a rational therapeutic approach to target cancers with *ARID1A* mutations has not yet been explored.

EZH2, the catalytic subunit of polycomb repressive complex 2, silences gene expression through generation of the lysine 27 trimethylation mark on histone H3 (H3K27Me3) by its catalytic SET domain<sup>7</sup>. EZH2 is often overexpressed in OCCCs<sup>8</sup>, and *EZH2* gain-of-function mutations occur in hematopoietic malignancies such as diffuse large B cell lymphoma (DLBCL). Highly specific small molecule EZH2 inhibitors have been developed, and the response to EZH2 inhibitors often correlates with gain-of-function mutations in *EZH2* (refs. 9–11). EZH2 inhibitors have entered clinical trials for the diseases mentioned above. Here we show that inhibition of EZH2 methyltransferase activity acts in a synthetic lethal manner in *ARID1A*-mutated cells. Our findings

establish a new approach for targeting *ARID1A* mutation in cancer by using pharmacological inhibition of EZH2 methyltransferase activity.

## RESULTS

### EZH2 inhibitor is selective against *ARID1A* inactivation

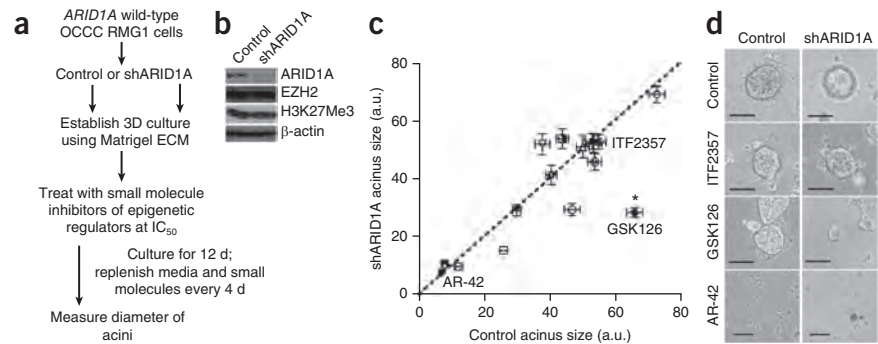
As epigenetic mechanisms may play a critical role in *ARID1A*-mutated OCCCs, we evaluated a panel of 15 commercially available small molecule inhibitors known to target epigenetic regulators to identify ‘hits’ that selectively inhibit the growth of *ARID1A*-inactivated cells (Supplementary Table 1). More than 90% of the *ARID1A* mutations observed in OCCCs are frame-shift or nonsense mutations that result in a loss of *ARID1A* protein expression<sup>4,5,12</sup>. To mimic the loss of *ARID1A* protein expression caused by the vast majority of *ARID1A* mutations<sup>4</sup> and ensure the same genetic background, we performed the screen using *ARID1A* wild-type OCCC RMG1 cells with or without shRNA-mediated *ARID1A* knockdown (Fig. 1a,b and Supplementary Fig. 1a). Following drug selection, cells were plated onto Matrigel and treated with one of 15 individual small molecules or vehicle control using the half-maximal inhibitory concentration (IC<sub>50</sub>) (Supplementary Table 2). We performed the screen in 3D cultures using Matrigel to more closely mimic the tumor microenvironment<sup>13</sup>. Notably, *ARID1A* knockdown itself did not significantly affect the growth of RMG1 cells in 3D culture (Supplementary Fig. 1b). We based the dose of each small molecule on the previously established IC<sub>50</sub> value (Supplementary Table 2). Diameters of acini formed in 3D culture were measured as a surrogate for cell growth (Fig. 1c). We identified three small molecule inhibitors that significantly

<sup>1</sup>Gene Expression and Regulation Program, The Wistar Institute, Philadelphia, Pennsylvania, USA. <sup>2</sup>Center for Systems and Computational Biology, The Wistar Institute, Philadelphia, Pennsylvania, USA. <sup>3</sup>Center for Chemical Biology and Translational Medicine, The Wistar Institute, Philadelphia, Pennsylvania, USA.

<sup>4</sup>Molecular and Cellular Oncogenesis Program, The Wistar Institute, Philadelphia, Pennsylvania, USA. <sup>5</sup>Department of Pathology, Oncology, and Gynecology and Obstetrics, Johns Hopkins Medical Institutions, Baltimore, Maryland, USA. <sup>6</sup>Tumor Microenvironment and Metastasis Program, The Wistar Institute, Philadelphia, Pennsylvania, USA. Correspondence should be addressed to R.Z. (rzhang@wistar.org).

Received 27 August 2014; accepted 5 January 2015; published online 16 February 2015; doi:10.1038/nm.3799

**Figure 1** GSK126, an EZH2 inhibitor, is selective against ARID1A-knockdown cells compared with controls. (a) Flow diagram of the evaluation for a panel of epigenetic inhibitors. ECM, extracellular matrix. (b) Immunoblot of ARID1A, EZH2, H3K27Me3 and loading control  $\beta$ -actin in the indicated *ARID1A* wild-type RMG1 cells. (c) Quantification of the average acinus diameter (each symbol represents a small molecule) graphed as a scatter plot. The x-axis indicates the size of acini formed by treated control *ARID1A* wild-type RMG1 cells, and the y-axis indicates the size of acini formed by shARID1A-expressing RMG1 cells treated with the same small molecule. \* $P < 0.0001$  calculated via two-tailed *t*-test using GraphPad Prism 5 software. The number of acini (*n*) for each of the small molecules used for analysis is listed in **Supplementary Table 1**. Error bars represent sem. (d) Representative images from screen of acini from indicated small molecules. Scale bars denote 75 measurable units (a.u.) in NIH Image J software. GSK126 (100 nM) represents a screening hit that selectively inhibited the growth of ARID1A-knockdown cells compared with controls. ITF2357 and AR-42 represent small molecule inhibitors that showed no significant effects on growth inhibition and significantly suppressed cell growth, regardless of ARID1A status.



( $P \leq 0.0001$ ) and selectively inhibited the growth of ARID1A-knockdown cells compared to controls (**Supplementary Table 1**). GSK126 was the hit with the highest selectivity against ARID1A-knockdown cells (**Fig. 1c,d** and **Supplementary Table 1**).

We observed a decrease in the size of acini with GSK126 using two individual shRNAs against *ARID1A* (shARID1As) (**Supplementary Fig. 1c–e**). GSK126 is a highly selective and potent small molecule inhibitor of EZH2 methyltransferase activity<sup>9</sup>. Notably, ARID1A knockdown did not alter the expression levels of EZH2 or H3K27Me3 (**Fig. 1b**).

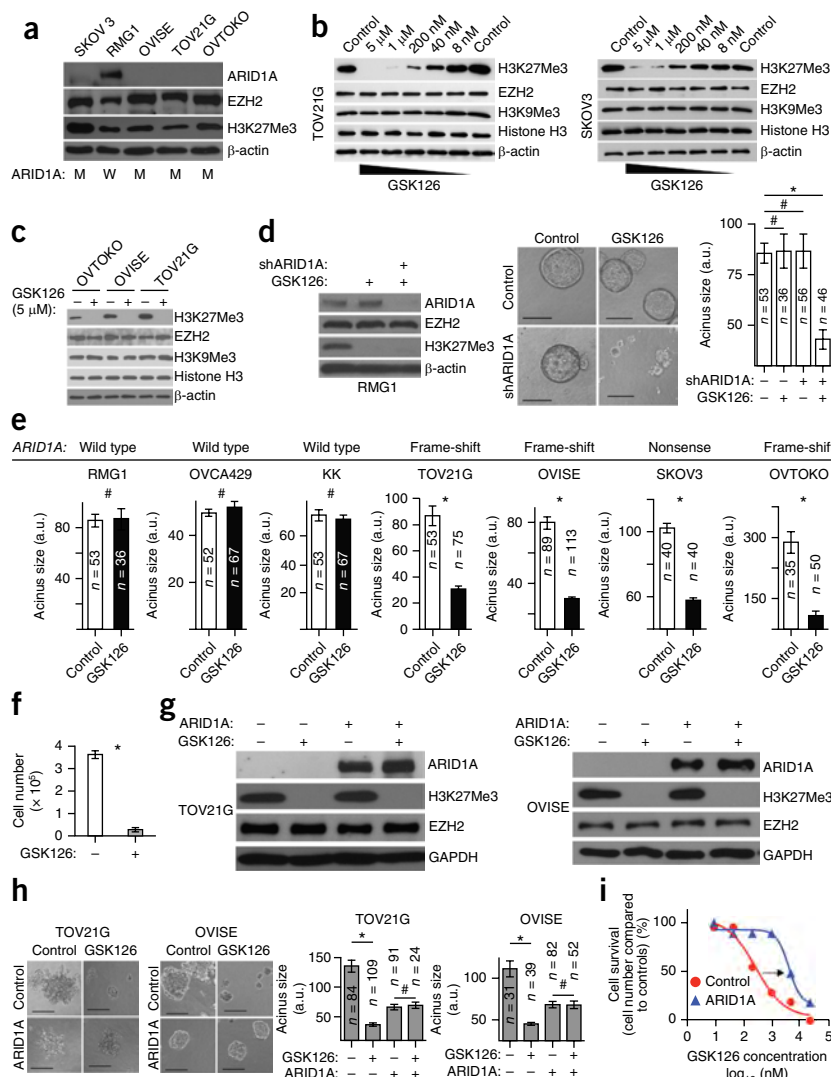
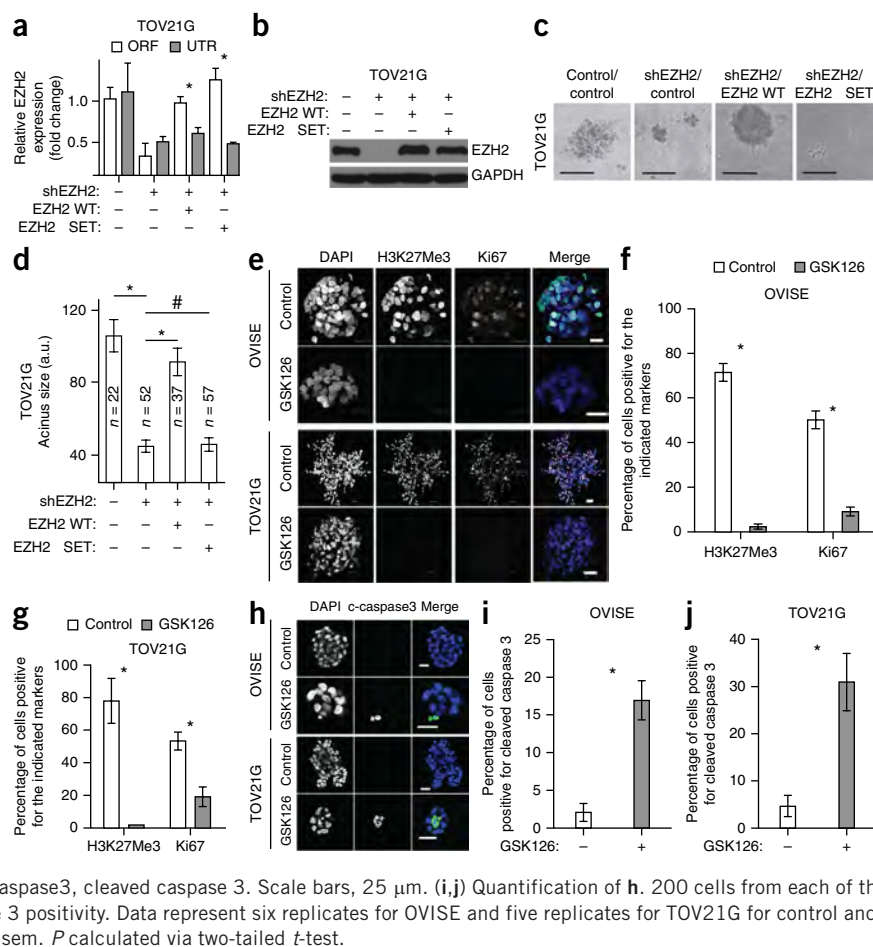


**Figure 2** Response to EZH2 inhibitor is dependent on ARID1A status. (a) Immunoblot of ARID1A, EZH2, H3K27Me3 and loading control  $\beta$ -actin in the indicated cell lines. *ARID1A* mutation status is indicated as mutated (M) or wild type (W). (b,c) Immunoblots of the indicated proteins following treatment with GSK126 for 72 h. (d) From left to right: immunoblot of the indicated proteins in RMG1 cells expressing shARID1A or control treated with or without 5  $\mu$ M GSK126. Representative images of formed acini from three replicates; scale bars, 75 a.u. in NIH ImageJ software. Bar graph presents the measured diameters of acini. \* $P < 0.0001$ , # $P > 0.05$ . (e) Quantification of the diameter of acini formed by the indicated cells with or without 5  $\mu$ M GSK126 treatment in 3D culture for 12 d. # $P = 0.914$ , \* $P < 0.0001$ . *ARID1A* mutation status is indicated above each graph. (f) Quantification of cell numbers for the *ARID1A*-mutated OVISE cells. Data represent six replicates. \* $P < 0.0001$ . (g) Immunoblots of the indicated proteins in *ARID1A*-mutated OVISE and TOV21G cells with or without wild-type ARID1A restoration treated with or without 5  $\mu$ M GSK126. (h) Acinus formation was examined after 12 d in 3D culture, and the diameters of acini were measured. # $P > 0.05$ , \* $P < 0.0001$ . Scale bars, 75 a.u. in NIH ImageJ software. (i) Dose-response curves for *ARID1A*-mutated TOV21G cells with or without wild-type ARID1A restoration treated with the indicated doses of GSK126 for 12 d in 3D culture. The arrow indicates the shift in  $IC_{50}$  induced by wild-type ARID1A restoration. The number of acini (*n*) is indicated on the graphs as representative of three experimental repeats. Error bars represent sem. *P* calculated via two-tailed *t*-test.

**Figure 3** EZH2 inhibitor triggers apoptosis of *ARID1A*-mutated cells. **(a)** Quantitative RT-PCR analysis of *EZH2* untranslated region (UTR) and open reading frame (ORF) in TOV21G cells expressing a UTR targeting shRNA against *EZH2* (shEZH2) together with a wild-type (WT) *EZH2* or a SET domain-deleted *EZH2* mutant (*EZH2*  $\Delta$ SET). Data represent three replicates; \* $P < 0.01$ . **(b)** Immunoblot of *EZH2* and GAPDH in the indicated cells. **(c)** Images of acini formed after 12 d in 3D culture. Scale bars, 75  $\mu$ m in NIH ImageJ software. **(d)** Quantification of acini in **c**. The number of acini ( $n$ ) is indicated on the graphs as representative of three experimental repeats. \* $P < 0.01$ , # $P > 0.05$ . **(e)** Immunofluorescence staining of Ki67 (red), H3K27Me3 (green) and DAPI (blue) for acini formed by *ARID1A*-mutated OVISe and TOV21G cells cultured in 3D and treated with 5  $\mu$ M GSK126 or vehicle control for 12 d. Scale bars, 25  $\mu$ m; note that images are at different magnifications in different panels because of growth suppression by GSK126 treatment (also in **h**). **(f,g)** Quantification of **e**. 200 cells from each of the indicated groups were examined for expression of Ki67 and H3K27Me3. Data represent three replicates for H3K27Me3 and four replicates for Ki67 for control and GSK126 treatment in OVISe cells; data represent five replicates for H3K27Me3 and four replicates for Ki67 for control and GSK126 treatment in TOV21G cells; \* $P < 0.01$ . **(h)** Same as in **e**, but stained for cleaved caspase 3 (green) and DAPI (blue) after 8 d of GSK126 treatment. c-caspase3, cleaved caspase 3. Scale bars, 25  $\mu$ m. **(i,j)** Quantification of **h**. 200 cells from each of the indicated groups were examined for cleaved caspase 3 positivity. Data represent six replicates for OVISe and five replicates for TOV21G for control and GSK126 treatment. \* $P < 0.01$ . Error bars represent sem.  $P$  calculated via two-tailed  $t$ -test.



### *ARID1A* mutation correlates with response to EZH2 inhibitor

To validate the initial findings, we used four different ovarian cancer cell lines (TOV21G, OVISe, OVTOKO and SKOV3) with known *ARID1A* mutations<sup>4,6</sup>. We observed a loss of *ARID1A* protein expression in these *ARID1A*-mutated cell lines (Fig. 2a). There was a dose-dependent decrease in H3K27Me3 levels in *ARID1A*-mutated cells treated with GSK126 (Fig. 2b); a >95% reduction in H3K27Me3 levels was achieved with 5  $\mu$ M GSK126 (Fig. 2b,c). H3K9Me3, which is generated by different histone methyltransferases such as SUV39H1 and SETDB1 (ref. 14), was not affected by GSK126 (Fig. 2b,c and Supplementary Fig. 1f–h). GSK126 had no appreciable effect on *EZH2* expression (Fig. 2b,c)<sup>9</sup>. *ARID1A* knockdown did not alter the dose-dependent reduction of H3K27Me3 levels by GSK126 (Supplementary Fig. 1h).

Similar to what was observed in RMG1 cells, GSK126 treatment resulted in a significant decrease in 3D growth in *ARID1A*-knockdown KK and OVCA429 cells, two additional *ARID1A* wild-type OCCC cell lines (Fig. 2d and Supplementary Fig. 1i–l)<sup>15</sup>. Furthermore, GSK126 significantly reduced the size of acini in all tested cell lines with *ARID1A* mutation, whereas the effects of GSK126 on the growth of *ARID1A* wild-type cell lines were not significant (Fig. 2e). This was not due to the inability of GSK126 to inhibit *EZH2* activity in *ARID1A* wild-type cells, as GSK126 was equally effective at decreasing H3K27Me3 levels in these cells (Supplementary Fig. 1j). GSK126 treatment led to a significant reduction in cell number in *ARID1A*-mutated cells, but not in wild-type cells (Fig. 2f and Supplementary Fig. 1m). Similar growth inhibition by GSK126

was observed in conventional 2D cultures as determined by cell counting (Supplementary Fig. 1n). Growth inhibition of *ARID1A*-mutated cells also was observed with UNC1999 (ref. 16), another *EZH2* inhibitor with less selectivity than GSK126 (Supplementary Fig. 1o–q).

To determine whether reintroducing wild-type *ARID1A* in *ARID1A*-mutated cells affects sensitivity to GSK126, we ectopically expressed wild-type *ARID1A* in *ARID1A*-mutated OVISe and TOV21G OCCC cells. As reported<sup>15</sup>, *ARID1A* restoration suppressed the growth of OCCC cells with *ARID1A* mutation (Fig. 2g,h). GSK126 did not further reduce the size of acini in *ARID1A*-restored cells (Fig. 2h). The IC<sub>50</sub> of GSK126 in *ARID1A*-mutated cells was ~267 nM (Fig. 2i), which is comparable to what was previously observed in DLBCL with gain-of-function *EZH2* mutation<sup>9</sup>. Restoration of wild-type *ARID1A* caused an ~16-fold increase in the IC<sub>50</sub> of GSK126 compared to controls (Fig. 2i).

To establish that the observed effects were specifically due to inhibition of *EZH2* activity, we knocked down *EZH2* expression in *ARID1A*-mutated cells in combination with GSK126 treatment. Knockdown of *EZH2* mimicked the growth inhibition induced by GSK126 treatment (Supplementary Fig. 2a–f). GSK126 did not have any substantial further effects on the growth of *EZH2*-knockdown *ARID1A*-mutated cells (Supplementary Fig. 2d–f). The observed growth inhibition caused by *EZH2* knockdown was rescued by wild-type *EZH2* but not by an enzymatically inactive SET domain-deleted *EZH2* mutant (Fig. 3a–d)<sup>7</sup>. This supports the notion that the observed growth inhibition depends upon *EZH2* methyltransferase activity.



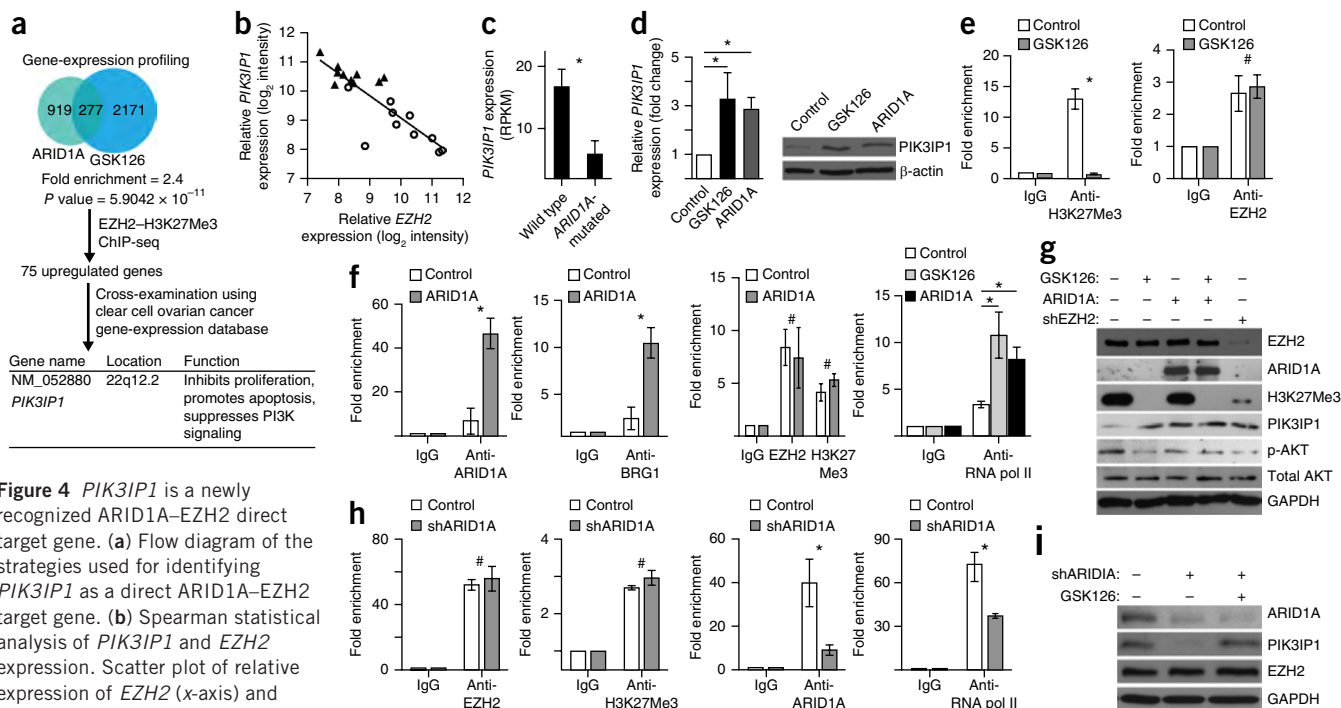


**Figure 4** *PIK3IP1* is a newly recognized ARID1A-EZH2 direct target gene. (a) Flow diagram of the strategies used for identifying *PIK3IP1* as a direct ARID1A-EZH2 target gene. (b) Spearman statistical analysis of *PIK3IP1* and *EZH2* expression. Scatter plot of relative expression of *EZH2* (x-axis) and *PIK3IP1* (y-axis) from laser-capture and microdissected normal ovarian epithelial cells ( $n = 10$ ; triangles) and OCCC cells ( $n = 10$ ; circles). Spearman correlation  $r = -0.8211$ ;  $P < 0.0001$ . (c) Relative *PIK3IP1* mRNA expression in ARID1A-mutated ( $n = 4$  cases) and wild-type ( $n = 5$  cases) OCCC cells.  $*P = 0.0207$ . RPKM, reads per kilobase of transcript per million mapped reads. (d) Quantitative RT-PCR analysis of *PIK3IP1* ( $n = 4$  replicates;  $*P < 0.01$ ) and immunoblot of PIK3IP1 and  $\beta$ -actin in the indicated ARID1A-mutated OVISE cells. (e) ChIP analysis of OVISE cells treated with vehicle control or 5  $\mu$ M GSK126 using antibodies against H3K27Me3 or EZH2 for the *PIK3IP1* gene promoter ( $n = 3$  replicates,  $*P < 0.001$ ,  $\#P = 0.9405$ ). (f) ChIP analysis of ARID1A-mutated OVISE cells with or without ARID1A restoration using the indicated antibodies or IgG control for the *PIK3IP1* gene promoter ( $n = 3$  replicates,  $\#P > 0.05$ ,  $*P < 0.05$ ). (g) Immunoblot of the indicated proteins in ARID1A-mutated TOV21G cells with or without ARID1A restoration treated with or without GSK126 (5  $\mu$ M) or expressing shEZH2. (h) ChIP analysis of ARID1A wild-type RMG1 cells expressing control or shARID1A using the indicated antibodies or IgG control for the *PIK3IP1* gene promoter ( $n = 3$  replicates,  $\#P > 0.05$ ,  $*P < 0.01$ ). (i) Immunoblot of the indicated proteins in ARID1A wild-type RMG1 cells expressing control or shARID1A treated with or without 5  $\mu$ M GSK126. Error bars represent sem.  $P$  calculated via two-tailed  $t$ -test, except in a, where we used Spearman's test.

### EZH2 inhibition triggers apoptosis in ARID1A-mutated cells

We stained acini for H3K27Me3 and the cell proliferation marker Ki67. GSK126 treatment significantly decreased amounts of H3K27Me3 and the percentage of Ki67-positive cells compared to controls (Fig. 3e–g). GSK126 is known to induce apoptosis in DLBCL with gain-of-function *EZH2* mutations<sup>9</sup>. To determine whether GSK126 triggers apoptosis in OCCC cells, we stained the acini for cleaved caspase 3, an apoptotic marker. Compared with controls, there was a significant increase in the percentage of cells positive for cleaved caspase 3 in GSK126-treated ARID1A-mutated cells (Fig. 3h–j). Other apoptotic markers such as annexin V were also induced by GSK126 (Supplementary Fig. 3).

### PIK3IP1 contributes to the observed synthetic lethality

ARID1A and EZH2 belong to the SWI/SNF and polycomb complexes, respectively. The antagonistic roles of SWI/SNF and polycomb proteins in gene transcription were initially suggested on the basis of genetic studies in *Drosophila*<sup>17</sup>. We sought to determine whether the observed phenotypes are due to changes in gene expression. Microarray analysis of ARID1A-mutated OVISE cells treated with GSK126 or restored with wild-type ARID1A revealed a significant overlap in differentially regulated genes (2.4-fold enrichment,  $P = 5.9042 \times 10^{-11}$  for overlap in genes regulated by wild-type ARID1A restoration and GSK126 treatment) (Fig. 4a). Known ARID1A target

genes such as *CDKN1A*<sup>15</sup> were upregulated only by ARID1A restoration. Conversely, known EZH2 target genes such as *TNSF10* (ref. 18) were upregulated only by GSK126 treatment. This suggests that the observed effects in EZH2 methyltransferase-inhibited ARID1A-mutated cells are mediated by a previously undefined set of genes that are commonly regulated by both ARID1A and EZH2.

To identify direct EZH2 and H3K27Me3 target genes in ARID1A-mutated cells, we cross-examined genes that were commonly upregulated by ARID1A restoration or GSK126 treatment with published data from chromatin immunoprecipitation followed by next-generation sequencing (ChIP-seq) of EZH2 and H3K27Me3 using ARID1A-mutated ovarian cancer cells<sup>18</sup> (Fig. 4a). To identify biologically relevant genes, we cross-referenced the genes that were commonly upregulated by ARID1A restoration and GSK126 treatment with a publicly available OCCC gene expression database (Fig. 4a) that compares laser-capture microdissected (LCM) OCCC specimens with normal human ovarian surface epithelial (HOSE) cells<sup>19</sup>. H3K27Me3 silences gene expression<sup>7</sup>; therefore, we focused on genes that were commonly upregulated by both GSK126 treatment and wild-type ARID1A restoration but downregulated in the LCM OCCC specimens compared to normal HOSE cells (Fig. 4a and Supplementary Table 3).

We chose the PI3K-interacting protein 1 gene (*PIK3IP1*) for validation for the following reasons: (1) *PIK3IP1* negatively regulates



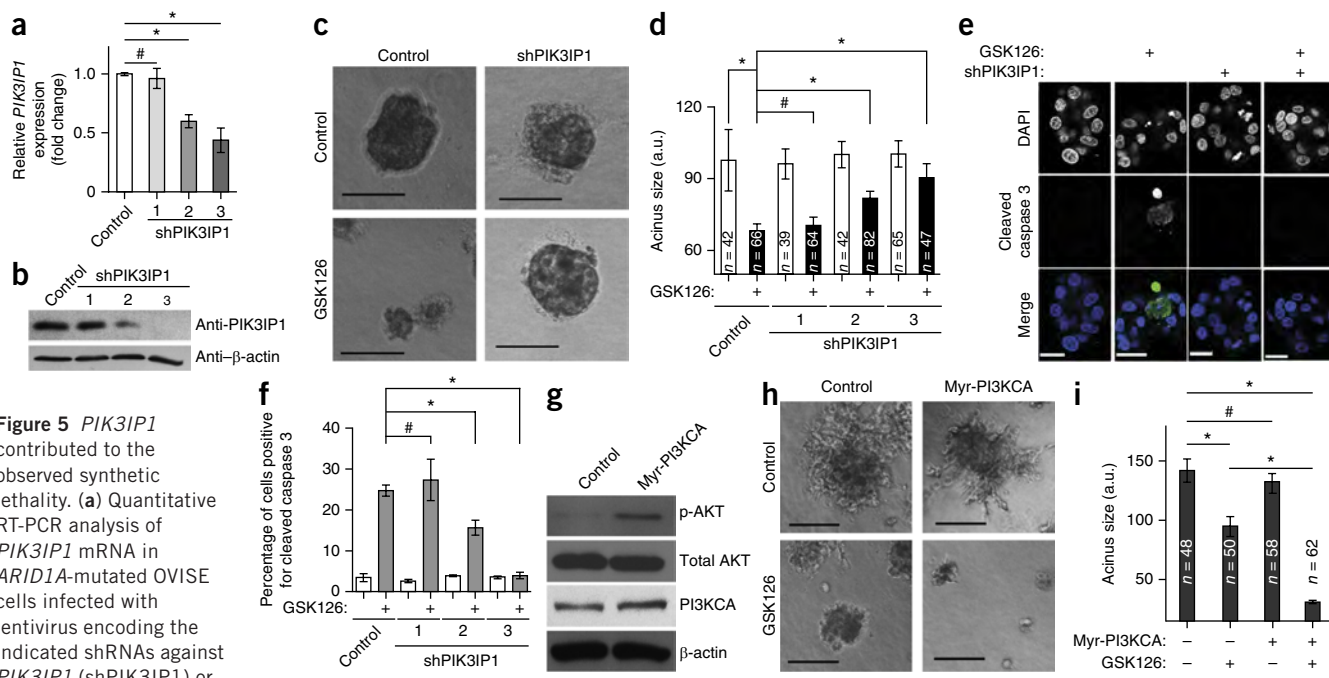


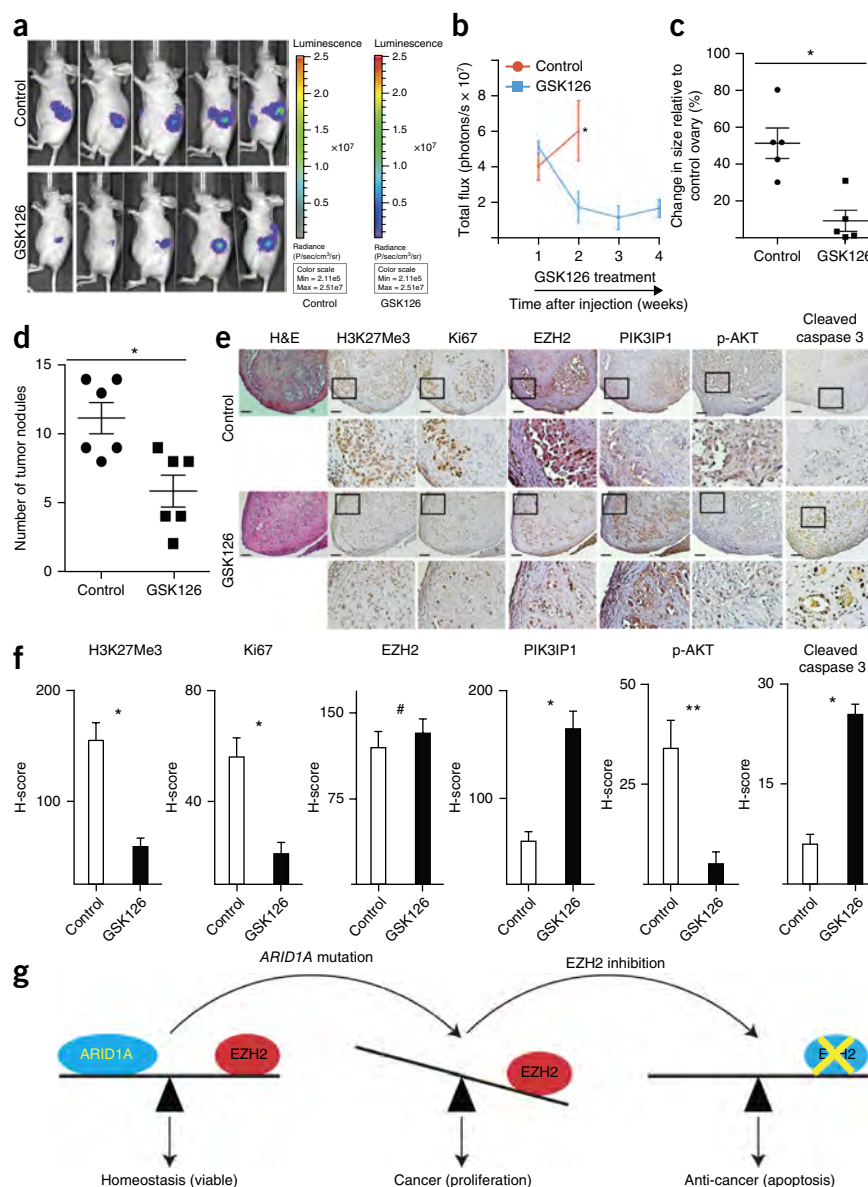
**Figure 5** *PIK3IP1* contributed to the observed synthetic lethality. **(a)** Quantitative RT-PCR analysis of *PIK3IP1* mRNA in *ARID1A*-mutated OVISE cells infected with lentivirus encoding the indicated shRNAs against *PIK3IP1* (shPIK3IP1) or controls (data represent three replicates;  $\#P = 0.8149$ ,  $*P < 0.001$ ). **(b)** Immunoblot of *PIK3IP1* and  $\beta$ -actin in the indicated OVISE cells. **(c)** Phase-contrast images of control or shPIK3IP1 3-expressing OVISE cells treated with or without 5  $\mu$ M GSK126 for 12 d in 3D culture. **(d)** Quantification of **c**. Data represent three replicates;  $\#P = 0.628$ ,  $*P < 0.01$ . **(e)** Immunofluorescence staining for the apoptotic marker cleaved caspase 3 (green) in the acini formed by the indicated cells at day 8. Shown is shPIK3IP1 3. Scale bars, 25  $\mu$ m. **(f)** Quantification of **e**. Data represent three replicates;  $\#P = 0.642$ ,  $*P < 0.05$ . **(g)** Immunoblot of phospho-AKT (p-AKT) and the indicated proteins in *ARID1A*-mutated, *PI3KCA* wild-type OVTOKO cells expressing a constitutively active myristoylated *PI3KCA* (I143V) mutant (Myr-PI3KCA) or controls. **(h)** Phase-contrast images of the indicated cells treated with or without 5  $\mu$ M GSK126 for 12 d in 3D culture. **(i)** Quantification of **h**. Data represent three replicates;  $\#P > 0.05$ ,  $*P < 0.001$ . The number of acini ( $n$ ) is indicated on the graphs in **d** and **i** as representative of three experimental repeats. Error bars represent sem.  $P$  calculated with two-tailed  $t$  test.

PI3K-AKT signaling<sup>20,21</sup>; (2) *PI3KCA* is often mutated in OCCC, and mutations in *PI3KCA* and *ARID1A* often coexist in OCCC<sup>22,23</sup>; and (3) *PIK3IP1* negatively regulates cell proliferation and promotes apoptosis<sup>20</sup>, the phenotypes observed in GSK126-treated *ARID1A*-mutated cells. There was a significant negative correlation between expression of *EZH2* and *PIK3IP1* in the microarray analysis of LCM specimens (Fig. 4b)<sup>19</sup>. Notably, *PIK3IP1* was expressed at significantly lower levels in *ARID1A*-mutated than in wild-type OCCC cells<sup>4</sup> (Fig. 4c). Thus, we ectopically overexpressed *PIK3IP1* and confirmed that *PIK3IP1* inhibited PI3K-AKT signaling, suppressed cell growth and induced apoptosis in *ARID1A*-mutated cells (Supplementary Fig. 4a–d). *PIK3IP1* expression was significantly upregulated by both wild-type *ARID1A* restoration and GSK126 treatment in *ARID1A*-mutated cells (Fig. 4d and Supplementary Fig. 4e). Supporting the notion that the observed upregulation of *PIK3IP1* is due to inhibition of *EZH2* methyltransferase activity by GSK126, *PIK3IP1* upregulation induced by *EZH2* knockdown in *ARID1A*-mutated cells was rescued by wild-type *EZH2* but not by an enzymatically inactive SET domain-deleted *EZH2* mutant (Supplementary Fig. 4f). *PIK3IP1* expression was not upregulated by GSK126 in *ARID1A* wild-type RMG1 cells (Supplementary Fig. 4g), which correlated with the observation that GSK126 did not affect RMG1 cell growth (Fig. 2d).

ChIP analysis revealed a significant decrease in the association of H3K27Me3 with the *PIK3IP1* gene promoter in GSK126-treated *ARID1A*-mutated cells compared with vehicle-treated controls (Fig. 4e). In addition, *ARID1A* restoration caused a significant increase in the association of *ARID1A* with the *PIK3IP1* gene promoter (Fig. 4f). The association of core histone H3 with the *PIK3IP1* gene

promoter, assessed as a control, was not affected by either GSK126 treatment or *ARID1A* restoration (Supplementary Fig. 4h). Association of BRG1, the catalytic subunit of the *ARID1A*-containing chromatin-remodeling complex, with the *PIK3IP1* gene promoter was significantly enhanced by *ARID1A* restoration (Fig. 4f). Consistent with this, there is evidence to suggest that *ARID1A* recruits the remodeling complex to its target genes<sup>15,24</sup>. Interestingly, the association of *EZH2* with the *PIK3IP1* gene promoter was not decreased by either *ARID1A* restoration or GSK126 treatment (Fig. 4e,f). Likewise, the association of H3K27Me3 with the *PIK3IP1* gene promoter was not significantly decreased by *ARID1A* restoration (Fig. 4f). The induction of *PIK3IP1* by *ARID1A* restoration correlated with RNA polymerase II recruitment to its promoter (Fig. 4f). Although *EZH2* and H3K27Me3 are predominantly associated with silenced genes, they also localize to active genes<sup>25</sup>. However, these active genes are typically not regulated by *EZH2* or H3K27Me3 (ref. 25). Together, these data support a model whereby when both *ARID1A* and *EZH2* are present at the *PIK3IP1* gene promoter, *ARID1A* dominates over *EZH2* and drives *PIK3IP1* expression (Supplementary Fig. 4i). Indeed, *ARID1A* restoration induced *PIK3IP1* expression in *ARID1A*-mutated cells (Fig. 4d), and the *EZH2* inhibitor did not affect *PIK3IP1* expression in *ARID1A* wild-type cells (Supplementary Fig. 4g). When *ARID1A* was absent, *EZH2* silenced *PIK3IP1* expression, and when *EZH2* methyltransferase activity was subsequently suppressed, *PIK3IP1* was expressed (Supplementary Fig. 4i). Consistent with this, there was no additional increase in *PIK3IP1* expression in *ARID1A*-mutated cells treated with a combination of GSK126 and wild-type *ARID1A* restoration (Fig. 4g).

**Figure 6** EZH2 inhibitor caused the regression and reduced the number of tumor nodules of *ARID1A*-mutated OCCC tumors. (a) Mice with established tumors were imaged every 7 d after treatment with vehicle control or GSK126; shown are images taken at day 14. (b) Quantification of tumor growth.  $n = 5$  mice per group,  $*P = 0.0026$ . (c) Size of the dissected tumors relative to control.  $n = 5$  mice per group,  $*P = 0.003$ . (d) Number of tumor nodules in intraperitoneal cavity on day 30 of treatment with GSK126 or vehicle control.  $n = 6$  mice per group,  $*P = 0.008$ . (e) Immunohistochemical staining using the indicated antibodies for tumors dissected from GSK126-treated or control mice (magnification for each set:  $\times 10$  (top) and  $\times 40$  (bottom)). Scale bars, 50  $\mu\text{m}$ . Representative images of consecutive sections of a tumor with six mice in each group. (f) H-score quantification of e.  $n = 13$  different fields from five different tumors.  $*P = 0.0001$ ,  $**P = 0.012$ ,  $\#P = 0.547$ . (g) A proposed model for the observed synthetic lethality between *ARID1A* mutation and inhibition of EZH2 methyltransferase activity. Error bars represent sem.  $P$  calculated via two-tailed  $t$ -test.



ChIP analysis in *ARID1A* wild-type cells revealed that both *ARID1A* and *EZH2* are associated with the *PIK3IP1* gene promoter (Fig. 4h). *ARID1A* knockdown in *ARID1A* wild-type cells decreased the association of *ARID1A* with the *PIK3IP1* gene promoter (Fig. 4h), which correlated with a decrease in RNA polymerase II's association with the *PIK3IP1* gene promoter (Fig. 4h) and suppression of *PIK3IP1* expression (Fig. 4i and Supplementary Fig. 4j). There was no decrease in the association of either *EZH2* or *H3K27Me3* with the *PIK3IP1* gene promoter after *ARID1A* knockdown (Fig. 4h). Indeed, treatment of *ARID1A*-knockdown cells with GSK126 led to the restoration of *PIK3IP1* expression in *ARID1A* wild-type cells (Fig. 4i).

To determine whether genetic knockdown of *PIK3IP1* rescues the growth inhibition observed in GSK126-treated *ARID1A*-mutated cells, we used two individual shRNAs against *PIK3IP1* that knocked down its expression. Knockdown of *PIK3IP1* significantly rescued the growth suppression induced by GSK126 in *ARID1A*-mutated cells (Fig. 5a–d and Supplementary Fig. 5a,b). Upregulation of cleaved caspase 3 induced by GSK126 in *ARID1A*-mutated cells was also significantly suppressed by *PIK3IP1* knockdown (Fig. 5e,f and Supplementary Fig. 5c,d).

As *PIK3IP1* suppresses *PI3K*–*AKT* signaling (Supplementary Fig. 4a) and contributed to the observed effects of GSK126 in *ARID1A*-mutated cells (Fig. 5), we sought to determine whether *PI3K*–*AKT* signaling affects the sensitivity of *ARID1A*-mutated cells to GSK126. We ectopically expressed a constitutively active myristoylated *PI3KCA* mutant (myr*PI3KCA*) in an *ARID1A*-mutated OVTOKO cell line that does not have mutated *PI3KCA* to increase *PI3K*–*AKT* signaling (Fig. 5g). Indeed, the *PI3KCA* mutant further enhanced the observed growth inhibition by GSK126 (Fig. 5h,i). This supports the notion

that the effects of *EZH2* inhibition in *ARID1A*-mutated cells are due to increased expression of *PIK3IP1*, an inhibitor of *PI3K* activity. Consequently, increased *PI3K* activity results in increased sensitivity to *EZH2* inhibition, which results in more growth inhibition.

### EZH2 inhibitor causes regression of *ARID1A*-mutated tumors

GSK126 is a specific *EZH2* inhibitor that is well tolerated in immunocompromised mice<sup>9</sup>. We orthotopically injected luciferase-expressing *ARID1A*-mutated OVISE cells into the bursa sac covering the ovary in immunocompromised female mice. The injected cells were allowed to grow for 1 week to establish tumors. We randomly assigned mice into two groups ( $n = 5$  mice per group) and treated mice daily with vehicle control or GSK126 (50 mg/kg) by intraperitoneal injection for an additional 3 weeks<sup>9</sup>. GSK126 treatment caused regression of the orthotopically transplanted *ARID1A*-mutated OVISE cells (Fig. 6a,b). At necropsy, we measured the tumor size and found that GSK126 treatment significantly decreased the size of the orthotopically xenografted tumors compared with controls (Fig. 6c). Similarly,

GSK126 treatment (50 mg/kg daily for 2 weeks) caused regression of orthotopically xenografted *ARID1A*-mutated TOV21G tumors that had been established over 4 weeks (Supplementary Fig. 6a). In contrast, GSK126 treatment did not significantly affect the size of orthotopically xenografted *ARID1A* wild-type RMG1 tumors (Supplementary Fig. 6b).

We sought to determine the effects of GSK126 on another clinical feature of ovarian cancer<sup>26</sup>, the dissemination of *ARID1A*-mutated OCCC cells, in an intraperitoneal xenograft model. We injected *ARID1A*-mutated OVISe cells into the mouse intraperitoneal cavity. The injected tumor cells were allowed to grow for 4 d, and the mice were then randomized into two groups ( $n = 6$  mice per group). Mice were treated daily with GSK126 (50 mg/kg) or vehicle control via intraperitoneal injection. Compared with controls, GSK126 significantly reduced the number of tumor nodules within the peritoneal cavity after 3 weeks of treatment (Fig. 6d and Supplementary Fig. 6c).

Immunohistochemical analysis of *ARID1A*-mutated tumors treated with GSK126 or vehicle controls revealed that H3K27Me3 staining was decreased by GSK126, whereas GSK126 did not weaken EZH2 staining (Fig. 6e,f). Furthermore, GSK126 treatment decreased the expression of Ki67 (Fig. 6e,f). There was an increase in PIK3IP1 staining and a decrease in phospho-AKT staining in GSK126-treated tumors (Fig. 6e,f). Consistent with this, the apoptotic marker cleaved caspase 3 was induced by GSK126 (Fig. 6e,f). In *ARID1A* wild-type tumors, although GSK126 decreased H3K27Me3 staining (Supplementary Fig. 6d), it did not affect the expression of Ki67, PIK3IP1, phospho-AKT or cleaved caspase 3 (Supplementary Fig. 6d).

## DISCUSSION

The EZH2 inhibitor selectively suppressed the growth of *ARID1A*-mutated cells. This was not due to either changes in EZH2 expression or an inability of the EZH2 inhibitor to suppress the enzymatic activity of EZH2 in *ARID1A* wild-type cells, as GSK126 was consistently effective in decreasing H3K27Me3 levels regardless of *ARID1A* mutation status (Fig. 2). Similarly, in DLBCL, the response to EZH2 inhibitors often correlates with gain-of-function mutations in *EZH2* (refs. 9–11), despite the fact that EZH2 inhibitors are equally effective at reducing H3K27Me3 levels in cells with wild-type *EZH2*. A recent study shows that ARID1B is a specific vulnerability in *ARID1A*-mutated cancers<sup>27</sup>, further highlighting the potential of synthetic lethal strategies for *ARID1A* mutation in cancer.

ARID1A and EZH2 are antagonistic in regulating *PIK3IP1* expression (Fig. 4). We were unable to perform ARID1A ChIP-seq analysis because of the lack of a suitable anti-ARID1A antibody; regardless, we successfully identified *PIK3IP1* as the ARID1A–EZH2 target gene contributing to the observed synthetic lethality (Fig. 5). In rhabdoid tumors, a loss of SNF5, a core subunit of SWI/SNF, directly upregulates EZH2 (ref. 28). The survival of SNF5-deficient cancer cells depends on the upregulated EZH2, and these cancer cells are sensitive to EZH2 inhibition<sup>28,29</sup>. Here, ARID1A knockdown did not affect EZH2 expression, but it did sensitize cells to EZH2 inhibition (Figs. 1b,c and 2d and Supplementary Fig. 1i–l). Conversely, the restoration of wild-type ARID1A in *ARID1A*-mutated cells conferred resistance to the EZH2 inhibitor, also without changing EZH2 expression (Fig. 2g). Thus, the antagonism between EZH2 and ARID1A occurs at a functional level (Fig. 6g and Supplementary Fig. 4i).

Our studies demonstrate that targeting EZH2 methyltransferase activity through the use of EZH2 inhibitors in *ARID1A*-mutated cells represents a novel synthetic lethal therapeutic strategy. Given that mutation and loss of expression of *ARID1A* and genetic alterations in

other subunits of ATP-dependent chromatin remodeling complexes are observed at a high frequency in many cancer types<sup>1,30</sup>, we expect our finding to have far-reaching implications for future epigenetic therapeutic strategies.

## METHODS

Methods and any associated references are available in the online version of the paper.

**Accession codes.** GEO: GSE54979.

*Note:* Any Supplementary Information and Source Data files are available in the online version of the paper.

## ACKNOWLEDGMENTS

We thank D. Altieri, M. Murphy and R. Shiekhattar for critical comments and X. Hua and Y. Park for technical assistance. This work was supported by grants from the US National Institutes of Health/National Cancer Institute (R01CA160331 and R01CA163377 to R.Z.), a US Department of Defense Ovarian Cancer Academy award (OC093420 to R.Z.) and an Ovarian Cancer Research Fund Program project (to R.Z.). R.Z. is an Ovarian Cancer Research Fund Liz Tilberis Scholar. B.G.B. is supported by an American Cancer Society postdoctoral fellowship (PF-13-058-01-TBE). K.M.A. is supported by a training grant from the US National Institutes of Health/National Cancer Institute (T32CA9171-35). Support of Core Facilities was provided by Cancer Center Support grant CA010815 to the Wistar Institute.

## AUTHOR CONTRIBUTIONS

B.G.B. designed and performed all the experiments, analyzed data and wrote the manuscript. K.M.A. contributed to Figure 5g–i and manuscript writing. A.G. contributed to Figure 2b,c. H.L. contributed to Supplementary Figure 4g. M.A. contributed to Supplementary Figure 2c,f. A.V.K. performed the analysis presented in Figure 4a,c. D.C.S. contributed to the epigenetic-set construction. Q.L. contributed to statistical design and analysis. I.-M.S. contributed key reagents. J.R.C.-G. and D.W.S. participated in the experimental design. R.Z. conceived the study and wrote the manuscript.

## COMPETING FINANCIAL INTERESTS

The authors declare no competing financial interests.

Reprints and permissions information is available online at <http://www.nature.com/reprints/index.html>.

- Garraway, L.A. & Lander, E.S. Lessons from the cancer genome. *Cell* **153**, 17–37 (2013).
- Lawrence, M.S. *et al.* Discovery and saturation analysis of cancer genes across 21 tumour types. *Nature* **505**, 495–501 (2014).
- Wilson, B.G. & Roberts, C.W. SWI/SNF nucleosome remodellers and cancer. *Nat. Rev. Cancer* **11**, 481–492 (2011).
- Wiegand, K.C. *et al.* ARID1A mutations in endometriosis-associated ovarian carcinomas. *N. Engl. J. Med.* **363**, 1532–1543 (2010).
- Jones, S. *et al.* Frequent mutations of chromatin remodeling gene ARID1A in ovarian clear cell carcinoma. *Science* **330**, 228–231 (2010).
- Anglesio, M.S. *et al.* Type-specific cell line models for type-specific ovarian cancer research. *PLoS ONE* **8**, e72162 (2013).
- Cao, R. & Zhang, Y. The functions of E(Z)/EZH2-mediated methylation of lysine 27 in histone H3. *Curr. Opin. Genet. Dev.* **14**, 155–164 (2004).
- Li, H., Cai, Q., Godwin, A.K. & Zhang, R. Enhancer of zeste homolog 2 promotes the proliferation and invasion of epithelial ovarian cancer cells. *Mol. Cancer Res.* **8**, 1610–1618 (2010).
- McCabe, M.T. *et al.* EZH2 inhibition as a therapeutic strategy for lymphoma with EZH2-activating mutations. *Nature* **492**, 108–112 (2012).
- Knutson, S.K. *et al.* A selective inhibitor of EZH2 blocks H3K27 methylation and kills mutant lymphoma cells. *Nat. Chem. Biol.* **8**, 890–896 (2012).
- Qi, W. *et al.* Selective inhibition of EZH2 by a small molecule inhibitor blocks tumor cells proliferation. *Proc. Natl. Acad. Sci. USA* **109**, 21360–21365 (2012).
- Guan, B., Gao, M., Wu, C.H., Wang, T.L. & Shih Ie, M. Functional analysis of in-frame indel ARID1A mutations reveals new regulatory mechanisms of its tumor suppressor functions. *Neoplasia* **14**, 986–993 (2012).
- Yamada, K.M. & Cukierman, E. Modeling tissue morphogenesis and cancer in 3D. *Cell* **130**, 601–610 (2007).
- Jenuwein, T. The epigenetic magic of histone lysine methylation. *FEBS J.* **273**, 3121–3135 (2006).
- Guan, B., Wang, T.L. & Shih Ie, M. ARID1A, a factor that promotes formation of SWI/SNF-mediated chromatin remodeling, is a tumor suppressor in gynecologic cancers. *Cancer Res.* **71**, 6718–6727 (2011).



16. Konze, K.D. *et al.* An orally bioavailable chemical probe of the lysine methyltransferases EZH2 and EZH1. *ACS Chem. Biol.* **8**, 1324–1334 (2013).
17. Kennison, J.A. & Tamkun, J.W. Dosage-dependent modifiers of polycomb and antennapedia mutations in *Drosophila*. *Proc. Natl. Acad. Sci. USA* **85**, 8136–8140 (1988).
18. Li, H. *et al.* ALDH1A1 is a novel EZH2 target gene in epithelial ovarian cancer identified by genome-wide approaches. *Cancer Prev. Res. (Phila.)* **5**, 484–491 (2012).
19. Stany, M.P. *et al.* Identification of novel therapeutic targets in microdissected clear cell ovarian cancers. *PLoS ONE* **6**, e21121 (2011).
20. He, X. *et al.* PIK3IP1, a negative regulator of PI3K, suppresses the development of hepatocellular carcinoma. *Cancer Res.* **68**, 5591–5598 (2008).
21. Zhu, Z. *et al.* PI3K is negatively regulated by PIK3IP1, a novel p110 interacting protein. *Biochem. Biophys. Res. Commun.* **358**, 66–72 (2007).
22. Yamamoto, S., Tsuda, H., Takano, M., Tamai, S. & Matsubara, O. Loss of ARID1A protein expression occurs as an early event in ovarian clear-cell carcinoma development and frequently coexists with PIK3CA mutations. *Mod. Pathol.* **25**, 615–624 (2012).
23. Samartzis, E.P., Noske, A., Dedes, K.J., Fink, D. & Imesch, P. ARID1A mutations and PI3K/AKT pathway alterations in endometriosis and endometriosis-associated ovarian carcinomas. *Int. J. Mol. Sci.* **14**, 18824–18849 (2013).
24. Chandler, R.L. *et al.* ARID1a-DNA interactions are required for promoter occupancy by SWI/SNF. *Mol. Cell. Biol.* **33**, 265–280 (2013).
25. Davidovich, C., Zheng, L., Goodrich, K.J. & Cech, T.R. Promiscuous RNA binding by polycomb repressive complex 2. *Nat. Struct. Mol. Biol.* **20**, 1250–1257 (2013).
26. Cho, K.R. & Shih, M. Ovarian cancer. *Annu. Rev. Pathol.* **4**, 287–313 (2009).
27. Helming, K.C. *et al.* ARID1B is a specific vulnerability in ARID1A-mutant cancers. *Nat. Med.* **20**, 251–254 (2014).
28. Wilson, B.G. *et al.* Epigenetic antagonism between polycomb and SWI/SNF complexes during oncogenic transformation. *Cancer Cell* **18**, 316–328 (2010).
29. Knutson, S.K. *et al.* Durable tumor regression in genetically altered malignant rhabdoid tumors by inhibition of methyltransferase EZH2. *Proc. Natl. Acad. Sci. USA* **110**, 7922–7927 (2013).
30. Hargreaves, D.C. & Crabtree, G.R. ATP-dependent chromatin remodeling: genetics, genomics and mechanisms. *Cell Res.* **21**, 396–420 (2011).



## ONLINE METHODS

**Cell lines and 3D culture conditions.** OVISe, TOV21G, RMG1 and OVtoko cell lines were all obtained from the Japanese Collection of Research Bioresources. The SKOV3 cell line was obtained from the American Type Culture Collection. OVCA429 and KK cell lines were obtained from I.-M. Shih. All cell lines were cultured according to instructions and in 3D conditions using Matrigel, unless otherwise specified. All cell lines were used within 6 months of culture after they were received, but they were not tested. The 3D culture procedure was adapted from previously published methods<sup>31</sup> and used growth-factor-reduced Matrigel (BD Biosciences). In the 3D culture models, GSK126 treatment was started at the time of assay setup. Briefly, a single cell suspension was plated in eight-well chambers covered with Matrigel. Matrigel media with either vehicle control (DMSO) or drug was changed every 4 d, and cells were grown for 12 d. Each of the experiments was performed in duplicate in three independent experimental repeats.

**Reagents and antibodies.** Small molecules used in the screen were all obtained from the Molecular Screening Facility at the Wistar Institute. GSK126 was obtained from Xcess Biosciences and Active Biochem. UNC1999 was obtained from Selleckchem. The following antibodies from the indicated suppliers were used: anti-EZH2 (BD Bioscience, cat. no. 612666, 1:1,000), anti-EZH2 (Cell Signaling, cat. no. 5246, 1:100), anti-ARID1A (Sigma, cat. no. HPA005456, 1:1,000), anti-H3K27Me3 (Cell Signaling, cat. no. 9733, 1:1,000), anti- $\beta$ -actin (Sigma, cat. no. A5441, 1:10,000), anti-ARID1A (Santa Cruz, cat. no. sc-32761, 1:500), anti-Ki67 (Cell Signaling, cat. no. 9449, 1:1,000), anti-PIK3IP1 (Santa Cruz, cat. no. sc-86785, 1:500), anti-histone H3 (Millipore, cat. no. 06-755, 1:1,000), anti-GAPDH (Millipore, cat. no. MAB374, 1:10,000), anti-cleaved caspase 3 (Cell Signaling, cat. no. 9661, 1:10,000), anti-PI3K (p110alpha) (Cell Signaling, cat. no. 4255, 1:1,000), anti-pAKT (T308, Cell Signaling, cat. no. 13038, 1:1,000), anti-AKT (Cell Signaling, cat. no. 9272, 1:1,000) and anti-H3K9me3 (Abcam, cat. no. ab8898, 1:1,000). pBabe-Myr-PIK3CA143V plasmid was obtained from Addgene. pBabe-EZH2, pBabe-EZH2  $\Delta$ SET and pQCXIP-PIK3IP1 plasmids were generated via standard molecular cloning protocols, and details are available upon request.

**Lentivirus infection.** pLenti-CMV-Puro-Luciferase was obtained from Addgene. pLKO.1-shARID1As (TRCN0000059090 and TRCN0000059089), pLKO.1-shEZH2 (TRCN0000040073), and pLKO.1-shPIK3IP1 (1, TRCN0000133982; 2, TRCN0000135363; and 3, TRCN0000138560) were obtained from the Molecular Screening Facility at the Wistar Institute. Lentivirus was packaged using the Virapower Kit from Invitrogen according to the manufacturer's instructions as described previously<sup>8,32,33</sup>.

**Microarray, database and bioinformatics.** ARID1A-mutated OVISe cells expressing inducible wild-type ARID1A<sup>15</sup> were plated on Matrigel and treated with DMSO, 1  $\mu$ M doxycycline to induce wild-type ARID1A expression, or with 5  $\mu$ M GSK126. Cells were recovered from 3D culture, and RNA was extracted with Trizol (Invitrogen) and subsequently cleaned and DNase-treated using RNeasy columns (Qiagen). Eukaryote total RNA nano Bioanalyzer (Agilent) assay was used to confirm the quality of the RNA, and all RNA used for subsequent steps had an RNA integrity number >8.6. cDNA made from the RNA was hybridized to Illumina Bead Array HumanHT-12 v4 by the Wistar Genomics Facility (whole human genome). Images were analyzed and expression changes were evaluated in Illumina GenomeStudio. Illumina GenomeStudio was also used to export expression levels and detect *P* values for each probe of each sample. Signal-intensity data were quantile normalized, and probes that showed an insignificant detection *P* value (*P* > 0.05) in all samples were removed from further analysis. Pair-wise group comparisons were done using paired SAM test<sup>34</sup>, and correction for multiple testing to estimate the false discovery rate (FDR) was done with the procedure described by Storey and Tibshirani<sup>35</sup>. Differentially expressed genes in the ARID1A-restored sample were overlapped with differentially expressed genes in the GSK126 sample, and the significance of the overlap was calculated using the hypergeometric test. We used statistical methods for defining significantly changed genes with an FDR of 10% as a cutoff plus *P* < 0.05 for overlap. All microarray data can be found at the Gene Expression Omnibus (GEO) database (GEO accession number: GSE54979).

Gene-expression microarray data sets for 10 cases of laser-capture and microdissected ovarian clear cell carcinomas and 10 individual isolations of normal human ovarian surface epithelial cells were obtained from GEO (<http://www.ncbi.nlm.nih.gov/geo/>) (GEO accession number: GSE29450)<sup>19</sup>. EZH2-H3K27Me3 ChIP-seq in ARID1A-mutated ovarian cancer SKOV3 cells was obtained through published data<sup>18</sup>. RNA-seq data for ARID1A wild-type or mutated OCCC specimens were obtained from the European Genome-Phenome Archive<sup>4</sup>. Only samples with comparable 50-bp length-read data were analyzed. Sample CCC66 was not considered for analysis because of the low number of reads (<50% of the median number of reads across all samples). Bowtie2 (ref. 36) was used for alignment against the hg19 version of the human genome, and TopHat2 (ref. 37) was used to estimate RPKM expression values for each gene transcript in each sample using transcript information from the UCSC database. ARID1A-positive samples without mutation were assigned to the ARID1A wild-type group (*n* = 5: CCC67, CCC69, CCC71, CCC72 and CCC73), and ARID1A-negative samples with mutation were assigned to the ARID1A-mutated group (*n* = 4: CCC02, CCC04, CCC14 and CCC14). A two-tailed unpaired *t*-test was used to compare the two groups.

**Annexin V staining for detecting apoptotic cells (Guava assay).** Phosphatidylserine externalization was detected using an annexin V staining kit (Millipore) according to the manufacturer's instructions. Annexin V-positive cells were detected using the Guava System and analyzed with the Guava Nexin software module (Millipore).

**Reverse-transcriptase quantitative PCR.** RNA was extracted from cells with Trizol (Life Technologies) and DNase-treated using RNeasy columns (Qiagen). The expression of mRNA levels for PIK3IP1 (forward, 5'-GCTAGGAGGAAGTACCACTTTG-3'; reverse, 5'-GATGGACAAGGAGC ACTGTTA-3'), EZH2 ORF (forward, 5'-GACGGCTTCCCAATAACAGTA-3'; reverse, 5'-AGTGCCAATGAGGACTCTAAA-3') and EZH2 3'UTR (forward, 5'-AATCCCTTGACCTCTGAAAC-3'; reverse, 5'-ACTGGTA CAAAACACTTTGC-3') was determined using SYBR green iScript (Bio-Rad) master mix on a Bio-Rad Chromo4 machine.  $\beta$ -2-microglobulin was used as an internal control.

**Immunofluorescence and immunohistochemical staining.** Immunofluorescence was performed on day 8 or 12 as indicated in Figs. 3e, 3h and 5e by fixing samples in 2% paraformaldehyde and permeabilizing in 2% paraformaldehyde with 0.5% Triton-X. Samples were incubated with primary antibodies for 2 h at room temperature and with highly cross-absorbed secondary antibodies (Invitrogen) for 1 h at room temperature and mounted with ProLong antifade reagent (Invitrogen). Immunostained acini were then imaged using a Leica confocal microscope. Immunohistochemical staining was performed as described previously<sup>38</sup> on consecutive sections from xenografted tumors dissected from control or GSK126-treated immunocompromised nude female mice.

**Intraperitoneal and intrabursal orthotopic xenograft models *in vivo*.** The protocols were approved by the Institutional Animal Care and Use Committee of the Wistar Institute. For the intraperitoneal model,  $3 \times 10^6$  OVISe cells were injected intraperitoneally into 6–8-week-old female immunocompromised nude mice. On day 4 after injection, mice were randomized into vehicle control (capsitol) and GSK126 treatment groups at 50 mg/kg daily for an additional 26 d (*n* = 6 mice per group). At the end of experiments (day 30), mice were killed, and the formation of tumor nodules in the peritoneal cavity was examined. Intrabursal orthotopic xenograft was performed as described previously<sup>38,39</sup>. Briefly,  $1 \times 10^6$  luciferase-expressing ARID1A-mutated OVISe cells were unilaterally injected into the ovarian bursa sac of 6–8-week-old female immunocompromised nude mice (*n* = 5 per group). For *in vivo* experiments, the sample size of five mice per group was determined on the basis of data from *in vitro* experiments. The observed effect size (defined as the difference of means divided by the sd) was as large as 2.9 in our *in vitro* data. To be conservative, for *in vivo* experiments, we expected to see an effect size of at least 2.0. In order to have more than 80% power to detect an effect size of 2.0 or larger at a two-sided statistical significance level, five mice per group would be required.

The *in vivo* experimental data reflect an effect size of 2.7, which is consistent with our hypothesis. One week after injection of OVISe cells, we visualized tumors by injecting luciferin (IP; 4 mg per mouse) resuspended in PBS and imaged them with an IVIS Spectrum imaging system. The mice were then randomized into two groups based on luciferase activity and treated with vehicle control (captisol) or GSK126 at 50 mg/kg daily for an additional 3 weeks, during which time they were imaged weekly for luciferase activity. Images were analyzed using Live Imaging 4.0 software. Imaging analysis was performed blindly but not randomly. At the end of the experiments (day 30), tumors were surgically dissected, and the sizes of ovaries from both the injected side and the contralateral side were measured. We calculated the tumor size by subtracting the size of the control-side ovary from that of ovary on the side injected with tumor cell to limit variations among different mice. For intrabursal orthotopic xenografts using *ARID1A*-mutated TOV21G or *ARID1A* wild-type RMG1 cells, the same procedure was used, except tumors were established for 4 weeks before the randomized mice were treated with vehicle control (captisol) or GSK126 at 50 mg/kg daily for an additional 2 weeks.

**Chromatin immunoprecipitation.** ChIP was performed as previously described<sup>33</sup>. The following antibodies were used to perform ChIP: anti-H3K27Me3 (Cell Signaling, cat. no. 9733), anti-ARID1A (Santa Cruz, cat. no. sc-32761), anti-BRG1 (Santa Cruz, cat. no. sc-10768), anti-RNA polymerase II (Santa Cruz, cat. no. sc-899) and anti-EZH2 (Cell Signaling, cat. no. 5246). Isotype-matched immunoglobulin G was used as a negative control. ChIP DNA was analyzed by quantitative PCR against the promoter of the human *PIK3IP1* gene using the

following primers: forward, 5'-CACATTGA-GCTGGTGTGTTGTT-3'; and reverse, 5'-CCATTGCCACTTCAAAGAGTTT-3'.

**Statistical analysis.** Statistical analyses were performed using GraphPad Prism 5 (GraphPad) for Mac. Quantitative data are expressed as mean  $\pm$  sem unless otherwise stated. Spearman's test was used to measure statistical correlation. For all statistical analyses, the level of significance was set at 0.05.

31. Debnath, J., Muthuswamy, S.K. & Brugge, J.S. Morphogenesis and oncogenesis of MCF-10A mammary epithelial acini grown in three-dimensional basement membrane cultures. *Methods* **30**, 256–268 (2003).
32. Ye, X. *et al.* Downregulation of Wnt signaling is a trigger for formation of facultative heterochromatin and onset of cell senescence in primary human cells. *Mol. Cell* **27**, 183–196 (2007).
33. Tu, Z. *et al.* Oncogenic RAS regulates BRIP1 expression to induce dissociation of BRCA1 from chromatin, inhibit DNA repair, and promote senescence. *Dev. Cell* **21**, 1077–1091 (2011).
34. Zhang, S. A comprehensive evaluation of SAM, the SAM R-package and a simple modification to improve its performance. *BMC Bioinformatics* **8**, 230 (2007).
35. Storey, J.D. & Tibshirani, R. Statistical significance for genomewide studies. *Proc. Natl. Acad. Sci. USA* **100**, 9440–9445 (2003).
36. Langmead, B. & Salzberg, S.L. Fast gapped-read alignment with Bowtie 2. *Nat. Methods* **9**, 357–359 (2012).
37. Kim, D. *et al.* TopHat2: accurate alignment of transcriptomes in the presence of insertions, deletions and gene fusions. *Genome Biol.* **14**, R36 (2013).
38. Bitler, B.G. *et al.* Wnt5a suppresses epithelial ovarian cancer by promoting cellular senescence. *Cancer Res.* **71**, 6184–6194 (2011).
39. Li, H. *et al.* SUZ12 promotes human epithelial ovarian cancer by suppressing apoptosis via silencing HRK. *Mol. Cancer Res.* **10**, 1462–1472 (2012).



## Potential therapeutic targets in ARID1A-mutated cancers

Benjamin G Bitler, Nail Fatkhutdinov & Rugang Zhang PhD

**To cite this article:** Benjamin G Bitler, Nail Fatkhutdinov & Rugang Zhang PhD (2015) Potential therapeutic targets in ARID1A-mutated cancers, Expert Opinion on Therapeutic Targets, 19:11, 1419-1422, DOI: [10.1517/14728222.2015.1062879](https://doi.org/10.1517/14728222.2015.1062879)

**To link to this article:** <http://dx.doi.org/10.1517/14728222.2015.1062879>



Published online: 30 Jun 2015.



Submit your article to this journal [↗](#)



Article views: 597



View related articles [↗](#)



View Crossmark data [↗](#)

# EXPERT OPINION

1. Introduction
2. Epigenetic synthetic lethality by targeting EZH2 in *ARID1A*-mutated cancers
3. Targeting residual SWI/SNF complex as a specific vulnerability in *ARID1A*-mutated cancers
4. Targeting mutual exclusivity between *TP53* and *ARID1A* mutation
5. Targeting PI3K/AKT signaling in *ARID1A*-mutated cancers
6. Targeting the SWI/SNF-dependent DNA damage response in *ARID1A*-mutated cancers
7. Targeting tumor microenvironment in *ARID1A*-mutated cancers
8. Conclusion
9. Expert opinion



Taylor & Francis  
Taylor & Francis Group

## Potential therapeutic targets in *ARID1A*-mutated cancers

Benjamin G Bitler, Nail Fatkhutdinov & Rugang Zhang<sup>†</sup>

<sup>†</sup>The Wistar Institute, Gene Expression and Regulation Program, Philadelphia PA, USA

*ARID1A* is a subunit of the Switch/Sucrose Non-Fermentable (SWI/SNF) chromatin-remodeling complex that regulates gene expression by controlling gene accessibility. *ARID1A* shows one of the highest mutation rates across different human cancer types. For example, *ARID1A* is mutated in ~ 50% of ovarian clear cell carcinoma (OCCC). There is considerable interest in developing cancer therapeutics that correlate with *ARID1A* mutational status. A recent study demonstrated a synthetic lethality by targeting EZH2 histone methyltransferase activity in *ARID1A*-mutated OCCC using a clinically applicable small-molecule inhibitor. The observed synthetic lethality correlated with inhibition of PI3K/AKT signaling. In addition, there is evidence indicating that *ARID1A*-mutated cancer may also be subjected to therapeutic intervention by targeting residual SWI/SNF activity, the PI3K/AKT pathway, the DNA damage response, the tumor immunological microenvironment and stabilizing wild-type p53. In summary, we propose EZH2 inhibitor-based combinatorial strategies for targeting *ARID1A*-mutated cancers.

**Keywords:** *ARID1A*, EZH2, ovarian cancer, synthetic lethality

*Expert Opin. Ther. Targets* (2015) **19**(11): 1419-1422

### 1. Introduction

The Switch/Sucrose Non-Fermentable (SWI/SNF) complex regulates gene transcription through its ATP-dependent chromatin-remodeling activity. Consistent with its role in gene transcription, the SWI/SNF complex is involved in essential cellular processes such as transformation, development, DNA damage repair and cell cycle regulation. The SWI/SNF complex has garnered substantial attention because subunits of the complex are collectively mutated in > 20% of human cancers [1]. Among the SWI/SNF subunits, *ARID1A* has the highest mutation rate in human cancers. *ARID1A* is mutated in ~ 50% of ovarian clear cell carcinoma (OCCC) [2,3]. *ARID1A* mutations are typically nonsense or frame-shift, which cause loss of *ARID1A* protein expression. Further highlighting the importance of the SWI/SNF complex in human cancer, several studies have found correlations between the mutational and/or expressional status of SWI/SNF complex subunits and tumor progression, prognosis and response to chemotherapy. These findings have raised considerable interest in developing targeted therapies that take advantage of *ARID1A* mutations.

Here we will highlight advances in identifying therapeutic targets for *ARID1A*-mutated cancers and discuss additional therapeutic targets based on newly gained mechanistic insights into *ARID1A*'s role in cancer.

### 2. Epigenetic synthetic lethality by targeting EZH2 in *ARID1A*-mutated cancers

A recent study examined epigenetic inhibitors that selectively suppress the growth of *ARID1A*-deficient compared with proficient OCCC cells. The authors identified an inhibitor of EZH2, a histone methyltransferase, which selectively promotes



apoptosis in *ARID1A*-mutated OCCC cells [4]. EZH2, a subunit of the polycomb complex, represses gene transcription. Mechanistically, the observed synthetic lethality is due to the antagonistic roles played by ARID1A and EZH2 in regulating the expression of ARID1A/EZH2 target genes. Similar epigenetic antagonism exists between EZH2 and SNF5, a core subunit of the SWI/SNF complex that is often deleted in childhood rhabdoid tumors [5]. Consistently, inhibition of EZH2 causes regression of SNF5-deleted rhabdoid tumors [5]. In addition, mutations of *SMARCA4*, the gene encoding the ATPase SWI/SNF subunit BRG1, in non-small cell lung cancer increase sensitivity to a combinatorial EZH2 and topoisomerase inhibition [6].

EZH2 inhibitors are in clinical development for hematopoietic malignancies such as diffuse large B cell lymphoma. These recent findings indicate that targeting EZH2 using a clinically applicable EZH2 inhibitor represents a strategy for cancers with mutations in subunits of the SWI/SNF complex. Further studies are warranted to determine whether EZH2 inhibition displays a similar selectivity in cancers with genetic inactivation of other SWI/SNF subunits and whether the selectivity of EZH2 inhibition in *ARID1A*-mutated cancer cells is tissue- and/or genetic context-dependent.

### 3. Targeting residual SWI/SNF complex as a specific vulnerability in *ARID1A*-mutated cancers

The observation that knockdown of SWI/SNF's catalytic subunit, BRG1, inhibits the growth of SNF5-deficient rhabdoid tumors suggests that the survival of SNF5-deficient tumors depends upon the residual SWI/SNF complex activity [7]. Residual SWI/SNF complex dependence was further validated by examining mutually exclusive SWI/SNF subunits. Specifically, ARID1A and ARID1B are mutually exclusive in their association with the SWI/SNF complex. The survival of *ARID1A*-mutated cancer cells depends upon the presence of ARID1B in the residual SWI/SNF complex [8]. Likewise, BRG1 and BRM1 (encoded by the *SMARCA2* gene) are mutually exclusive subunits of the SWI/SNF complex and survival of *SMARCA2*-mutated cells depends upon the residual BRG1-containing complex [9]. Conversely, knockdown of BRM1 selectively suppresses the growth of BRG1-deficient cells. Collectively, these findings raise the possibility of targeting the residual SWI/SNF complex based on mutual exclusivity of different subunits. The challenge of this potential approach lies in the development of a subunit-specific inhibitor given the structure and functional similarities.

### 4. Targeting mutual exclusivity between *TP53* and *ARID1A* mutation

Genetic profiling of *ARID1A*-mutated ovarian cancer reveals enrichment of wild-type *TP53* in these tumors [10].

Functional characterization reveals that ARID1A and p53 function in the same pathway to regulate the expression of p53 target genes [10]. It is therefore possible that stabilization of wild-type p53 might be sufficient to overcome the effects of ARID1A loss and reactivate p53 target tumor suppressor genes. Notably, Nutlin 3, a p53 stabilizer, suppresses the growth of *ARID1A*-mutated A2780 ovarian cancer cells [11]. Clinically applicable p53-stabilizers have been developed [12]. Although it is unlikely that a p53-stabilizer itself will have substantial clinical activity, it provides a target for combinational therapies.

### 5. Targeting PI3K/AKT signaling in *ARID1A*-mutated cancers

*ARID1A* mutation often co-exists with genetic alterations that lead to activation of the PI3K/AKT pathway. These include gain-of-function mutations in the *PIK3CA* oncogene in OCCC or inactivation of the tumor suppressor *PTEN* in ovarian endometrioid carcinoma (OEC). In an immunohistochemical analysis of OCCC tumors, loss of nuclear ARID1A expression correlated to an increase in AKT phosphorylation [13]. Combination of conditional inactivation of *ARID1A* with activation of *PIK3CA* or inactivation of *PTEN* drives the development of OCCC and OEC, respectively [14]. PIK3IP1, an inhibitor of PI3K/AKT, plays a major role in the observed synthetic lethality between *ARID1A* mutation and EZH2 inhibition [4]. *ARID1A*-mutated cells are more sensitive to PI3K/AKT inhibitors compared with *ARID1A* wild-type cells [4,15]. Notably, inhibitors of mTOR, the downstream effector activated by PI3K/AKT signaling, such as temsirolimus and everolimus, are now in clinical trials for OCCC. The single-agent inhibition of PI3K/AKT is likely not sufficient to eradicate the disease. Consistently, in an ARID1A/PIK3CA mouse model of OCCC, an inhibitor of PI3K only increased survival by 3.5 weeks [14].

### 6. Targeting the SWI/SNF-dependent DNA damage response in *ARID1A*-mutated cancers

In addition to modulating signaling through gene regulation, the SWI/SNF complex is implicated in DNA damage repair. SWI/SNF complexes often localize to sites of DNA double-strand breaks and facilitate phosphorylation of histone H2AX via ATM/ATR [16]. Thus, SWI/SNF mutated cancers could be sensitive to DNA damage-inducing chemotherapeutics. Counter intuitively, *ARID1A*-mutated OCCC typically lacks genomic instability, and OCCC tumors are less responsive to DNA damage inducing platinum-based chemotherapy. This suggests that the role of the SWI/SNF complex in DNA damage might be subunit- and/or tissue dependent.

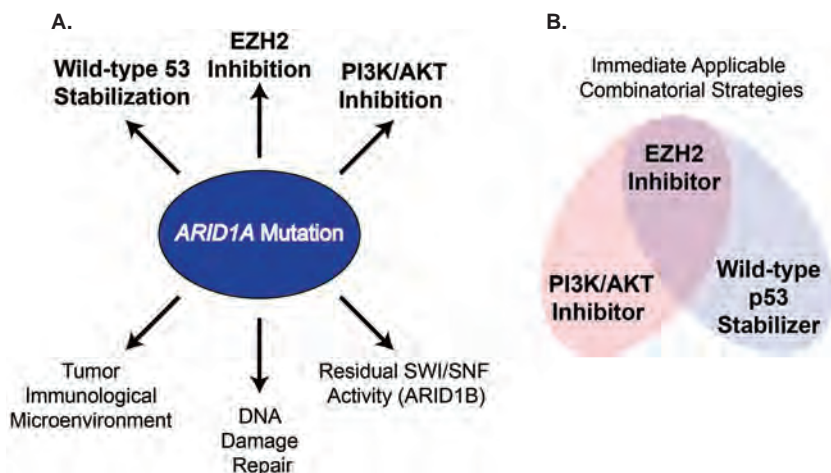


**Figure 1. Potential therapeutic targets in *ARID1A*-mutated cancer.** *ARID1A*-containing SWI/SNF chromatin remodeling-complex regulates multiple biological processes related to tumor suppression. **A)** *ARID1A* mutation and/or loss of expression leads to atypical signaling and cellular functions. In *ARID1A*-mutated cancers, the indicated pathways are potential targets that are selective against *ARID1A* mutation. **B)** To achieve a sustained clinical response, combinatorial therapies will be necessary. An EZH2 inhibitor-based approach presents a unique opportunity for combinatorial strategies.

SWI/SNF: Switch/Sucrose non-fermentable

## 7. Targeting tumor microenvironment in *ARID1A*-mutated cancers

The link between chronic inflammation and carcinogenesis is well-characterized and is a hallmark of cancer. Chronic inflammation and expression of pro-inflammatory cytokines (e.g. IL6) are important for escape from anti-tumor immune responses. Recent evidence suggests that *ARID1A* protects against inflammation-driven tumorigenesis [14]. In a mouse model, *ARID1A* loss and *PIK3CA* mutation cooperate to promote OCCC through sustained IL6 production. Subsequently, IL6 knockdown resulted in significantly smaller tumors, indicating the potential for anti-IL6 therapies in *ARID1A*-mutated cancers. Given the recent success in targeting immune checkpoints, it will be interesting to evaluate the impact of *ARID1A* mutation on anti-tumor immunity and whether *ARID1A*-mutated cancers are sensitive to reactivation of anti-tumor immunity.

## 8. Conclusion

Recent genome-wide sequencing studies have revealed frequent *ARID1A* mutations in a variety of cancer types. Clinical and pathological studies suggest a great need to develop precision therapy that correlates with *ARID1A* mutational status. In this review, we discussed literature on therapeutic targets with the potential of specifically and selectively targeting *ARID1A*-mutated cancers (Figure 1A). They include EZH2, residual SWI/SNF activity, the PI3K/AKT pathway, the DNA damage response, the tumor immunological microenvironment and stabilizing wild-type p53. The

synthetic lethality between EZH2 inhibition and *ARID1A* mutation presents a unique opportunity for developing novel combination therapeutic strategies that correlate with *ARID1A* mutation, the very definition of precision medicine.

## 9. Expert opinion

EZH2 inhibition is synthetic lethal with *ARID1A* mutation and causes the regression of established *ARID1A*-mutated OCCC *in vivo*. These findings indicate that the newly discovered synthetic lethality between *ARID1A* mutation and EZH2 inhibition could be developed as an urgently needed therapeutic for *ARID1A*-mutated OCCC. It will be important to investigate whether this approach can be extended into other cancers with *ARID1A* mutation. As EZH2 inhibition has also been shown to inhibit the growth of SNF5-deficient rhabdoid tumors, it will be interesting to determine whether EZH2 inhibition-based synthetic lethality extends to mutations in other SWI/SNF complex subunits.

Despite the well-described advantages of selectivity and limited toxicity of targeted cancer therapy, clinical trials have extensively demonstrated that targeted therapy, including synthetic lethality-based therapy, often leads to the development of resistance and is not sufficient to eradicate cancer. Combinatorial therapeutic strategies offer a solution for this major clinical challenge. Clinically applicable drugs that target EZH2, stabilize wild-type p53 or inhibit PI3K/AKT signaling have already been developed. Based on the genetic makeup of *ARID1A*-mutated cancers such as OCCC, an EZH2 inhibitor in combination with a PI3K/AKT signaling inhibitor or wild-type p53 stabilizer may represent a therapeutic strategy that conveys a sustained clinical response (Figure 1B). Further studies are



warranted to investigate potential side effects and pharmacodynamics of these proposed combinatorial approaches. In the long term, given the recent evidence that ARID1A suppresses tumor-promoting inflammation, it will be interesting to explore EZH2 inhibition in combination with reagents that target the tumor immunological microenvironment.

## Declaration of interest

R Zhang was supported by US National Institutes of Health/ National Cancer Institute grants (R01CA160331 and

R01CA163377), a US Department of Defense ovarian cancer academy award (OC093420) and an Ovarian Cancer Research Fund program project (to R Zhang). BG Bitler is supported by an American Cancer Society postdoctoral fellowship (PF-13-058-01-TBE). Support of Core Facilities was provided by Cancer Center Support Grant (CCSG) CA010815 to The Wistar Institute. The authors have no other relevant affiliations or financial involvement with any organization or entity with a financial interest in or financial conflict with the subject matter or materials discussed in the manuscript apart from those disclosed.

## Bibliography

Papers of special note have been highlighted as either of interest (●) or of considerable interest (●●) to readers.

1. Kadoch C, Hargreaves DC, Hodges C, et al. Proteomic and bioinformatic analysis of mammalian SWI/SNF complexes identifies extensive roles in human malignancy. *Nat Genet* 2013;45(6):592-601
2. Jones S, Wang TL, Shih Ie M, et al. Frequent mutations of chromatin remodeling gene ARID1A in ovarian clear cell carcinoma. *Science* 2010;330(6001):228-31
3. Wiegand KC, Shah SP, Al-Agha OM, et al. ARID1A mutations in endometriosis-associated ovarian carcinomas. *N Engl J Med* 2010;363(16):1532-43
- **References 2 and 3 are the first studies showing that ARID1A is mutated in ovarian clear cell carcinoma.**
4. Bitler BG, Aird KM, Garipov A, et al. Synthetic lethality by targeting EZH2 methyltransferase activity in ARID1A-mutated cancers. *Nat Med* 2015;21(3):231-8
- **This is the first study showing the synthetic lethality between EZH2 inhibition and ARID1A mutation in ovarian clear cell carcinoma.**
5. Wilson BG, Wang X, Shen X, et al. Epigenetic antagonism between polycomb and SWI/SNF complexes during oncogenic transformation. *Cancer Cell* 2010;18(4):316-28
6. Fillmore CM, Xu C, Desai PT, et al. EZH2 inhibition sensitizes BRG1 and EGFR mutant lung tumours to TopoII inhibitors. *Nature* 2015;520(7546):239-42
7. Wang X, Sansam CG, Thom CS, et al. Oncogenesis caused by loss of the SNF5 tumor suppressor is dependent on activity of BRG1, the ATPase of the SWI/SNF chromatin remodeling complex. *Cancer Res* 2009;69(20):8094-101
8. Helming KC, Wang X, Wilson BG, et al. ARID1B is a specific vulnerability in ARID1A-mutant cancers. *Nat Med* 2014;20(3):251-4
9. Oike T, Ogiwara H, Tominaga Y, et al. A synthetic lethality-based strategy to treat cancers harboring a genetic deficiency in the chromatin remodeling factor BRG1. *Cancer Res* 2013;73(17):5508-18
10. Guan B, Wang TL, Shih Ie M. ARID1A, a factor that promotes formation of SWI/SNF-mediated chromatin remodeling, is a tumor suppressor in gynecologic cancers. *Cancer Res* 2011;71(21):6718-27
- **This is the first study showing the enrichment of wild-type TP53 in ARID1A-mutated ovarian clear cell carcinoma.**
11. Meijer A, Kruyt FA, van der Zee AG, et al. Nutlin-3 preferentially sensitises wild-type p53-expressing cancer cells to DR5-selective TRAIL over rhTRAIL. *Br J Cancer* 2013;109(10):2685-95
12. Vassilev LT, Vu BT, Graves B, et al. In vivo activation of the p53 pathway by small-molecule antagonists of MDM2. *Science* 2004;303(5659):844-8
13. Wiegand KC, Hennessey BT, Leung S, et al. A functional proteogenomic analysis of endometrioid and clear cell carcinomas using reverse phase protein array and mutation analysis: protein expression is histotype-specific and loss of ARID1A/BAF250a is associated with AKT phosphorylation. *BMC Cancer* 2014;14:120
14. Chandler RL, Damrauer JS, Raab JR, et al. Coexistent ARID1A-PIK3CA mutations promote ovarian clear-cell tumorigenesis through pro-tumorigenic inflammatory cytokine signalling. *Nat Commun* 2015;6:6118
15. Samartzis EP, Gutsche K, Dedes KJ, et al. Loss of ARID1A expression sensitizes cancer cells to PI3K- and AKT-inhibition. *Oncotarget* 2014;5(14):5295-303
16. Park JH, Park EJ, Lee HS, et al. Mammalian SWI/SNF complexes facilitate DNA double-strand break repair by promoting gamma-H2AX induction. *EMBO J* 2006;25(17):3986-97

## Affiliation

Benjamin G Bitler<sup>1</sup>, Nail Fatkhutdinov<sup>1,2</sup> & Rugang Zhang<sup>†1</sup> PhD

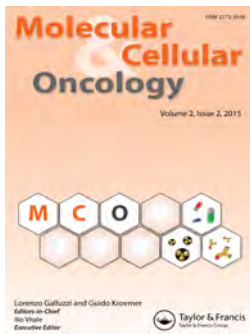
<sup>†</sup>Author for correspondence

<sup>1</sup>The Wistar Institute, Gene Expression and Regulation Program, Room 312, Philadelphia, PA 19104, USA

Tel: +1 215 495 6840;

E-mail: rzhang@wistar.org

<sup>2</sup>Kazan Federal University, Kazan, Russia



## Epigenetic synthetic lethality in ovarian clear cell carcinoma: EZH2 and ARID1A mutations

Benjamin G Bitler, Katherine M Aird & Rugang Zhang

**To cite this article:** Benjamin G Bitler, Katherine M Aird & Rugang Zhang (2016) Epigenetic synthetic lethality in ovarian clear cell carcinoma: EZH2 and ARID1A mutations, *Molecular & Cellular Oncology*, 3:1, e1032476, DOI: [10.1080/23723556.2015.1032476](https://doi.org/10.1080/23723556.2015.1032476)

**To link to this article:** <http://dx.doi.org/10.1080/23723556.2015.1032476>



Accepted author version posted online: 14 Apr 2015.



Submit your article to this journal [↗](#)



Article views: 121



View related articles [↗](#)



View Crossmark data [↗](#)



# Epigenetic synthetic lethality in ovarian clear cell carcinoma: EZH2 and *ARID1A* mutations

Benjamin G Bitler\*, Katherine M Aird, and Rugang Zhang\*

Gene Expression and Regulation; The Wistar Institute; Philadelphia, PA USA

**Keywords:** ARID1A, EZH2, ovarian cancer, SWI/SNF chromatin-remodeling complex, synthetic lethality

The components of the Switch/Sucrose non-fermentable (SWI/SNF) complex are mutated in approximately 20% of human cancers. The A/T-rich interacting domain 1A (ARID1A) subunit has one of the highest mutation rates. Most notably, *ARID1A* is mutated in over 50% of ovarian clear cell carcinomas (OCCCs). We reported that inhibition of enhancer of zeste homology 2 (EZH2) is synthetically lethal in *ARID1A*-mutated OCCC.

Genes encoding subunits of the ATP-dependent chromatin-remodeling complex are mutated in many cancer types.<sup>1</sup> Most notably, the A/T-rich interacting domain 1A (*ARID1A*) gene, which encodes a subunit of the Switch/Sucrose non-fermentable (SWI/SNF) chromatin-remodeling complex, is mutated in up to 57% of ovarian clear cell carcinomas (OCCCs).<sup>2,3</sup> Indeed, *ARID1A* is among the genes that show the highest mutation rates across multiple cancer types,<sup>1</sup> including up to 27% of gastric carcinomas, 13% of hepatocellular carcinomas, 13% of bladder carcinomas, 15% of esophageal adenocarcinomas, and 17% of Burkitt lymphomas. In addition to mutation, loss of ARID1A expression has been reported in several cancer types, most frequently in breast and kidney cancers.<sup>4</sup> However, despite the prevalence of *ARID1A* mutations in many cancer types, a rational therapeutic approach to target cancers with *ARID1A* mutations has not yet been explored.

Epithelial ovarian cancer remains the most lethal gynecologic malignancy in the developed world. OCCC ranks second as a cause of death from epithelial ovarian cancer and is associated with a poor prognosis compared to other histologic subtypes. OCCC typically has a low initial response rate to platinum-based standard care, and there is currently no effective therapy for the disease. More than 90% of the *ARID1A* mutations observed in

OCCC are frame-shift or nonsense mutations that result in loss of ARID1A protein expression.<sup>3</sup> Notably, loss of ARID1A expression in OCCC significantly correlates with a shorter progression-free survival and is associated with a worse response to chemotherapy compared with ARID1A-positive OCCC. Thus, there is an even greater need for targeted therapy that is selective for *ARID1A*-mutated OCCC. Similarly, *ARID1A* mutation and/or loss of expression have been reported to be a marker of poor prognosis in a number of other cancer types. Thus, new therapeutics based on *ARID1A* mutational status is of high clinical impact.

Cancer mutations that cause a loss of function are not directly druggable with conventional targeted approaches such as antibodies. Synthetic lethality is a phenomenon in which only the simultaneous perturbation of 2 factors results in cell death.<sup>5</sup> Our recent study demonstrates that inhibition of enhancer of zeste homology 2 (EZH2) activity selectively suppresses the growth of *ARID1A*-mutated OCCC cells in a synthetic lethal manner.<sup>6</sup> EZH2 is an epigenetic regulator that silences the expression of its target genes. Notably, EZH2 is often overexpressed in OCCC. Highly specific EZH2 inhibitors (such as GSK126) have been developed, and are now in clinical trials for hematopoietic malignancies.<sup>7</sup> Significantly, the EZH2 inhibitor GSK126

caused the regression of established *ARID1A*-mutated OCCC and decreased the number of disseminated tumor nodules in xenograft models.<sup>6</sup>

Given the recent success in targeting chromatin regulators in cancer, our study has substantial translational potential for the management of *ARID1A*-mutated OCCC. In this context, *ARID1A* mutation status, determined by genome sequence in the upcoming era of precision medicine, or loss of ARID1A protein expression could serve as biomarkers to predict therapeutic efficacy to EZH2 inhibitors. Future studies are warranted to determine whether the observed synthetic lethality between EZH2 inhibition and *ARID1A* mutation extends beyond *ARID1A*-mutated OCCC. Moreover, genetic alterations in components of the SWI/SNF complex are a well-recognized feature of many cancer types. For example, in rhabdoid tumors, a rare childhood cancer, loss of expression of sucrose nonfermenting 5 (SNF5), a non-catalytic core subunit of SWI/SNF, directly upregulates EZH2 expression.<sup>8</sup> Survival of SNF5-deficient cancer cells depends upon the upregulated EZH2.<sup>9</sup> Therefore, it will be critical to determine whether the observed synthetic lethality also applies to mutations in other components of the SWI/SNF complex and to develop companion predictive markers for response to EZH2 inhibitors in these contexts.

\*Correspondence to: Benjamin G Bitler; Email: bbitler@wistar.org; Rugang Zhang; Email: rzhang@wistar.org  
Submitted: 03/13/2015; Revised: 03/16/2015; Accepted: 03/17/2015  
<http://dx.doi.org/10.1080/23723556.2015.1032476>

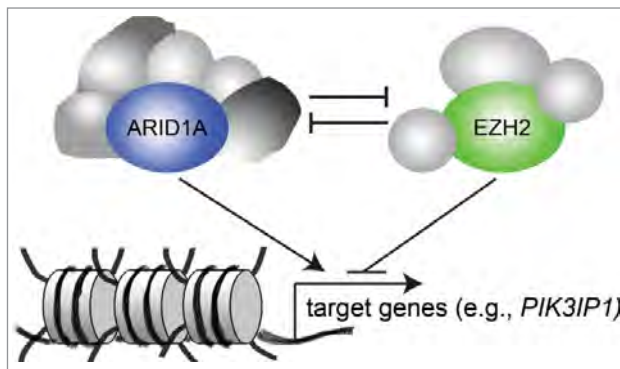


**Figure 1.** Antagonism between A/T-rich interacting domain 1A (ARID1A) and enhancer of zeste homology 2 (EZH2) underlies the observed synthetic lethality between EZH2 inhibition and *ARID1A* mutations. ARID1A and EZH2 are antagonistic in regulating the expression of the same set of target genes (such as *phosphoinositide 3-kinase interacting protein 1* [*PIK3IP1*]) and ARID1A dominates over EZH2 in determining the expression pattern of these genes.

To elucidate the mechanism underlying the observed synthetic lethality, we profiled changes in gene expression induced by restoration of wild type *ARID1A* or GSK126 treatment in *ARID1A*-mutated cells. This analysis revealed antagonistic roles of ARID1A and EZH2 in regulating a significant number of overlapping genes (Fig. 1). Notably, the antagonistic roles of SWI/SNF and polycomb proteins, which include ARID1A and EZH2 respectively, were initially suggested in genetic studies using *Drosophila*. The most interesting novel ARID1A/EZH2 target gene that we identified was *phosphoinositide 3-kinase interacting protein 1* (*PIK3IP1*). Functionally, we demonstrated that *PIK3IP1* contributes to the observed synthetic lethality in *ARID1A*-mutated cells treated with EZH2 inhibitor. At the chromatin level, our data indicate that ARID1A dominates in the expression of the ARID1A/EZH2 target genes when both ARID1A and EZH2 are present. In contrast, in the

absence of ARID1A, the balance is tipped toward EZH2-dependent silencing of these genes. Consequently, inhibition of EZH2 activity in the absence of functional ARID1A leads to reactivation of target genes such as *PIK3IP1* to trigger apoptosis. As such, EZH2 inhibitors selectively suppress the growth of *ARID1A*-mutated, but not wild type, cells.

In addition to *ARID1A* mutation, the phosphoinositide 3-kinase (PI3K)/protein kinase B (best known as AKT), pathway is often activated in OCCC as a result of gain-of-function mutations in *PIK3CA*, the gene encoding the catalytic subunit of PI3K. Indeed, conditional *Arid1a* knock-out together with activation of *phosphatidylinositol 4,5-bisphosphate 3-kinase catalytic subunit  $\alpha$  isoform* (*Pik3ca*) leads to the development of OCCC in genetic mouse models.<sup>10</sup> Interestingly, the validated ARID1A/EZH2 target gene *PIK3IP1* is a negative regulator of PI3K. These findings suggest that *ARID1A* mutation cooperates with PI3K/AKT

signaling to drive OCCC. Thus, a combination of the EZH2 inhibitor together with inhibition of the PI3K/AKT pathway may carry an even greater clinical benefit.

In summary, our recent studies demonstrate that targeting EZH2 activity using clinically applicable small molecule EZH2 inhibitors represents a novel synthetically lethal therapeutic strategy in *ARID1A*-mutated OCCC. Given that mutation and loss of expression of *ARID1A* and genetic alterations in other subunits of the ATP-dependent chromatin remodeling complex are observed at a high frequency in many cancer types, these findings will have far-reaching implications for the future development of epigenetic therapeutic strategies.

#### Disclosure of Potential Conflicts of Interest

No potential conflicts of interest were disclosed.

#### Funding

This work was supported by grants from the US National Institutes of Health/National Cancer Institute (R01CA160331 and R01CA163377 to R. Z. and Cancer Center Support grant CA010815 to the Wistar Institute), a US Department of Defense Ovarian Cancer Academy award (OC093420 to R.Z.), and an Ovarian Cancer Research Fund Program project (to R.Z.). R.Z. is an Ovarian Cancer Research Fund Liz Tilberis Scholar. B.G.B. is supported by an American Cancer Society postdoctoral fellowship (PF-13-058-01-TBE). K.M.A. is supported by a training grant from the US National Institutes of Health/National Cancer Institute (T32CA9171-35).

#### References

- Lawrence MS, Stojanov P, Mermel CH, Robinson JT, Garraway LA, Golub TR, Meyerson M, Gabriel SB, Lander ES, Getz G., Discovery and saturation analysis of cancer genes across 21 tumour types. *Nature* 2014; 505(7484):495-501; PMID:24390350; <http://dx.doi.org/10.1038/nature12912>
- Jones S, Wang TL, Shih Ie M, Mao TL, Nakayama K, Roden R, Glas R, Slamon D, Diaz LA, Vogelstein B Jr. et al., Frequent mutations of chromatin remodeling gene ARID1A in ovarian clear cell carcinoma. *Science* 2010; 330(6001):228-31; PMID:20826764; <http://dx.doi.org/10.1126/science.1196333>
- Wiegand KC, Shah SP, Al-Agha OM, Zhao Y, Tse K, Zeng T, Senz J, McConechy MK, Anglesio MS, Kallinger SE, et al., ARID1A mutations in endometriosis-associated ovarian carcinomas. *N Engl J Med* 2010; 363(16):1532-43; PMID:20942669; <http://dx.doi.org/10.1056/NEJMoa1008433>
- Wang X, Nagl NG, Flowers S Jr., Zweitzig D, Dallas PB, Moran E. Expression of p270 (ARID1A), a component of human SWI/SNF complexes, in human tumors. *Int J Cancer* 2004; 112(4):636; PMID:15382044; <http://dx.doi.org/10.1002/ijc.20450>
- Kaelin WG, Jr. The concept of synthetic lethality in the context of anticancer therapy. *Nat Rev Cancer* 2005; 5(9):689-98; PMID:16110319; <http://dx.doi.org/10.1038/nrc1691>
- Bitler BG, Aird KM, Garipov A, Li H, Amatangelo M, Kossenkova AV, Schultz DC, Liu Q, Shih IM, Conejo-Garcia JR, et al., Synthetic lethality by targeting EZH2 methyltransferase activity in ARID1A-mutated cancers. *Nat Med* 2015; 21(3):231-8; PMID:25686104; <http://dx.doi.org/10.1038/nm.3799>
- McCabe MT, Ott HM, Ganji G, Korenchuk S, Thompson C, Van Aller GS, Liu Y, Graves AP, Della Pietra A 3rd, Diaz E, et al., EZH2 inhibition as a therapeutic strategy for lymphoma with EZH2-activating mutations. *Nature* 2012; 492(7427):108-12; PMID:23051747; <http://dx.doi.org/10.1038/nature11606>
- Wilson, BG, Wang X, Shen X, McKenna ES, Lemieux ME, Cho YJ, Koellhoffer EC, Pomeroy SL, Orkin SH, Roberts CW. Epigenetic antagonism between polycomb and SWI/SNF complexes during oncogenic transformation. *Cancer Cell* 2010; 18(4):316-28; PMID:20951942; <http://dx.doi.org/10.1016/j.ccr.2010.09.006>

9. Knutson SK, Warholc NM, Wigle TJ, Klaus CR, Allain CJ, Raimondi A, Porter Scott M, Chesworth R, Moyer MP, Copeland RA, et al., Durable tumor regression in genetically altered malignant rhabdoid tumors by inhibition of methyltransferase EZH2. *Proc Natl Acad Sci U S A* 2013; 110(19): 7922-7; PMID:23620515; <http://dx.doi.org/10.1073/pnas.1303800110>
10. Chandler RL, Damrauer JS, Raab JR, Schisler JC, Wilkerson MD, Didion JP, Starmer J, Serber D, Yee D, Xiong J, et al., Coexistent ARID1A-PIK3CA mutations promote ovarian clear-cell tumorigenesis through pro-tumorigenic inflammatory cytokine signalling. *Nat Commun* 2015; 6:6118; PMID:25625625; <http://dx.doi.org/10.1038/ncomms7118>

# PI3K therapy reprograms mitochondrial trafficking to fuel tumor cell invasion

M. Cecilia Caino<sup>a,b</sup>, Jagadish C. Ghosh<sup>a,b</sup>, Young Chan Chae<sup>a,b</sup>, Valentina Vaira<sup>c,d</sup>, Dayana B. Rivadeneira<sup>a,b</sup>, Alice Favarsani<sup>d</sup>, Paolo Rampini<sup>e</sup>, Andrew V. Kossenkov<sup>f</sup>, Katherine M. Aird<sup>g</sup>, Rugang Zhang<sup>g</sup>, Marie R. Webster<sup>b</sup>, Ashani T. Weeraratna<sup>b</sup>, Silvano Bosari<sup>d,h</sup>, Lucia R. Languino<sup>a,i</sup>, and Dario C. Altieri<sup>a,b,†</sup>

<sup>a</sup>Prostate Cancer Discovery and Development Program, The Wistar Institute, Philadelphia, PA 19104; <sup>b</sup>Tumor Microenvironment and Metastasis Program, The Wistar Institute, Philadelphia, PA 19104; <sup>c</sup>Istituto Nazionale Genetica Molecolare "Romeo ed Enrica Invernizzi," Milan 20122, Italy; <sup>d</sup>Division of Pathology, Fondazione Istituto di Ricovero e Cura a Carattere Scientifico (IRCCS) Ca' Granda Ospedale Maggiore Policlinico, Milan 20122, Italy; <sup>e</sup>Division of Neurosurgery, Fondazione IRCCS Ca' Granda Ospedale Maggiore Policlinico, Milan 20122, Italy; <sup>f</sup>Center for Systems and Computational Biology, The Wistar Institute, Philadelphia, PA 19104; <sup>g</sup>Gene Expression and Regulation Program, The Wistar Institute, Philadelphia, PA 19104; <sup>h</sup>Department of Pathophysiology and Organ Transplant, University of Milan, Milan 20122, Italy; and <sup>i</sup>Department of Cancer Biology, Kimmel Cancer Center, Thomas Jefferson University, Philadelphia, PA 19107

Edited by Vincent T. Marchesi, Yale University School of Medicine, New Haven, CT, and approved May 26, 2015 (received for review January 13, 2015)

**Molecular therapies are hallmarks of "personalized" medicine, but how tumors adapt to these agents is not well-understood. Here we show that small-molecule inhibitors of phosphatidylinositol 3-kinase (PI3K) currently in the clinic induce global transcriptional reprogramming in tumors, with activation of growth factor receptors, (re)phosphorylation of Akt and mammalian target of rapamycin (mTOR), and increased tumor cell motility and invasion. This response involves redistribution of energetically active mitochondria to the cortical cytoskeleton, where they support membrane dynamics, turnover of focal adhesion complexes, and random cell motility. Blocking oxidative phosphorylation prevents adaptive mitochondrial trafficking, impairs membrane dynamics, and suppresses tumor cell invasion. Therefore, "spatiotemporal" mitochondrial respiration adaptively induced by PI3K therapy fuels tumor cell invasion, and may provide an important antimetastatic target.**

mitochondria | molecular therapy | cytoskeleton | PI3K | cell invasion

The phosphatidylinositol 3-kinase (PI3K) is a universal tumor driver (1) that integrates growth factor signaling with downstream circuitries of cell proliferation, metabolism, and survival (2). Exploited in nearly every human tumor, including through acquisition of activating mutations (3), PI3K signaling is an important therapeutic target, and several small-molecule antagonists of this pathway have entered clinical testing (4). However, the patient response to these agents has been inferior to expectations (5), dampened by drug resistance (6) and potentially other mechanisms of adaptation by the tumor (7).

In this context, there is evidence that therapeutic targeting of PI3K promotes tumor adaptation, paradoxically reactivating protein kinase B (PKB/Akt) in treated cells (8) and reprogramming mitochondrial functions in bioenergetics and apoptosis resistance (9). How these changes affect tumor traits, however, is unclear. Against the backdrop of a ubiquitous "Warburg effect" (10), where tumors switch from cellular respiration to aerobic glycolysis, a role of mitochondria in cancer has not been clearly defined (11) and at times has been proposed as that of a tumor suppressor (12).

In this study, we examined the impact of mitochondrial reprogramming induced by PI3K therapy on mechanisms of tumor progression.

## Results

**PI3K Therapy Reactivates Akt and Mammalian Target of Rapamycin Signaling.** Treatment of patient-derived glioblastoma (GBM) organotypic cultures (13) with PX-866, an irreversible pan-PI3K antagonist currently in the clinic (4), caused transcriptional up-regulation of multiple growth factor receptor pathways (Fig. 1*A*). This was associated with widespread phosphorylation, namely activation of the GBM kinome in primary organotypic cultures

(Fig. 1*B* and Table S1) as well as GBM LN229 cells (Fig. S1*A*). Consistent with previous observations (8), structurally diverse small-molecule PI3K antagonists induced robust (re)phosphorylation of Akt1 (S473) and Akt2 (S474) in tumor cells (Fig. 1*C* and Fig. S1*B*), as well as phosphorylation of downstream mammalian target of rapamycin (mTOR) and its effectors, 70S6K and 4EBP1 (Fig. 1*D* and Fig. S1*C*). Similar results were obtained in primary 3D GBM neurospheres, where PI3K therapy strongly induced Akt (Fig. 1*E*) and mTOR (Fig. 1*F*) phosphorylation. By transcriptome analysis, PI3K antagonists up-regulated two main gene networks of protection from apoptosis (9) and increased cell motility (Fig. 1*G*) in treated tumors.

**Increased Tumor Cell Motility Mediated by PI3K Therapy.** Consistent with these data, PI3K inhibitors vigorously stimulated tumor cell invasion across Matrigel-coated Transwell inserts (Fig. 2*A* and *B* and Fig. S1*D* and *E*) and in 3D tumor spheroids (Fig. 2*A* and *B*). Tumor cell proliferation was not significantly affected (Fig. S1*F*) (9). In addition, PI3K therapy dose-dependently increased the number and size of 3D GBM neurospheres (Fig. 2*C* and Fig. S1*G* and *H*).

## Significance

Despite the promise of personalized cancer medicine, most molecular therapies produce only modest and short-lived patient gains. In addition to drug resistance, it is also possible that tumors adaptively reprogram their signaling pathways to evade therapy-induced "stress" and, in the process, acquire more aggressive disease traits. We show here that small-molecule inhibitors of PI3K, a cancer node and important therapeutic target, induce transcriptional and signaling reprogramming in tumors. This involves the trafficking of energetically active mitochondria to subcellular sites of cell motility, where they provide a potent, "regional" energy source to support tumor cell invasion. Although this response may paradoxically increase the risk of metastasis during PI3K therapy, targeting mitochondrial reprogramming is feasible, and could provide a novel therapeutic strategy.

Author contributions: M.C.C. and D.C.A. designed research; M.C.C., J.C.G., Y.C.C., V.V., D.B.R., A.F., K.M.A., R.Z., M.R.W., and A.T.W. performed research; P.R. contributed new reagents/analytic tools; P.R. provided primary, patient-derived glioblastoma samples; K.M.A. and R.Z. performed and analyzed quiescence studies in tumor cells; M.R.W. and A.T.W. performed and analyzed 3D cell invasion assays; M.C.C., A.V.K., S.B., L.R.L., and D.C.A. analyzed data; and M.C.C., J.C.G., and D.C.A. wrote the paper.

The authors declare no conflict of interest.

This article is a PNAS Direct Submission.

<sup>†</sup>To whom correspondence should be addressed. Email: daltieri@wistar.org.

This article contains supporting information online at [www.pnas.org/lookup/suppl/doi:10.1073/pnas.1500722112/-DCSupplemental](http://www.pnas.org/lookup/suppl/doi:10.1073/pnas.1500722112/-DCSupplemental).





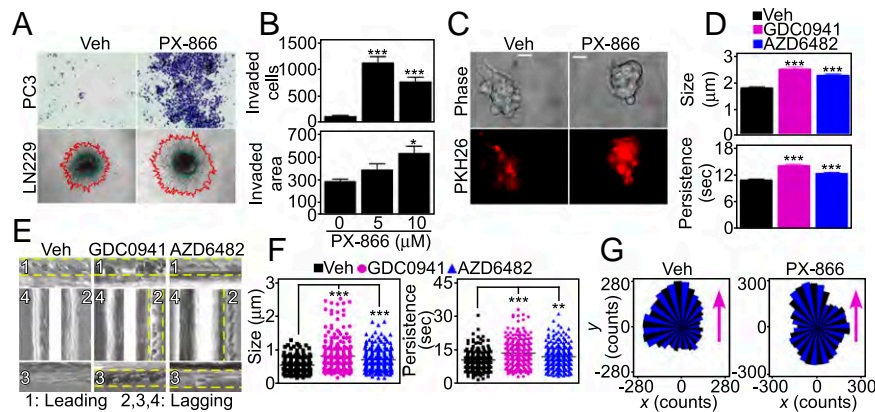


**Fig. 2.** PI3K therapy induces adaptive tumor cell motility and invasion. (A) Tumor cells treated with vehicle or 10  $\mu$ M PX-866 for 48 h were analyzed for invasion across Matrigel-coated Transwell inserts (Top) or in 3D spheroids (Bottom). Red, invasive edge; green, core. Representative images. Magnification, 10 $\times$ . (B) PC3 (Top) or LN229 (Bottom) cells were treated with the indicated increasing concentrations of PX-866 and quantified for invasion across Matrigel (Top) or in 3D spheroids (Bottom). The distance between the core and edge of 3D spheroids was determined. Mean  $\pm$  SEM of replicates from a representative experiment. \* $P$  = 0.02; \*\*\* $P$  < 0.0001. (C) Patient-derived GBM spheroids were treated with vehicle or PX-866 (0–10  $\mu$ M) for 48 h and analyzed by phase-contrast (Top) or fluorescence microscopy (Bottom). The vital dye PKH26 was used to counterstain live GBM neurospheres. (Scale bar, 20  $\mu$ m.) (D) Membrane ruffling was quantified in PC3 cells treated with vehicle or PI3K inhibitors for 48 h by SACED microscopy. Average values from at least 330 ruffles per treatment are shown for ruffle size (Top) and time of ruffle persistence (Bottom). Mean  $\pm$  SEM ( $n$  = 15). \*\*\* $P$  < 0.0001. (E) Representative stroboscopic images from time-lapse video microscopy of PC3 cells treated with vehicle or PI3K inhibitors. Four SACED regions corresponding to the top (1), right (2), bottom (3), and left (4) of each cell are shown. The ruffling activity (broken yellow lines) is restricted to one main region (1) on the vehicle cell but is distributed equally between three regions (1–3) on cells treated with PI3K inhibitors. See also Movie S1. (F) PC3 cells were treated with vehicle or PI3K inhibitors, and membrane dynamics at lagging areas were quantified. Ruffle size (Left) or time of ruffle persistence (Right) from at least 205 individual lagging ruffles are shown. Mean  $\pm$  SEM ( $n$  = 15). \*\* $P$  = 0.0047; \*\*\* $P$  < 0.0001. (G) PC3 cells were treated with vehicle or PX-866 for 48 h and quantified for directional versus random cell migration by time-lapse video microscopy (8 h). Rose plots show the distribution of cells migrating along each position interval (range interval 10 $^\circ$ , internal angle 60 $^\circ$ ). Arrows indicate the direction of chemotactic gradient.

therapy profoundly affected FA dynamics (Fig. 3H and Movie S2), increasing both the assembly and decay of FA complexes (Fig. S5D) and their turnover rate (Fig. S5E). In contrast, PI3K inhibition reduced the number of stable FA complexes (Fig. S5F).

Mitochondria are a primary source of reactive oxygen species (ROS), and these moieties have been implicated in tumor cell motility. PI3K antagonists increased the production of mitochondrial superoxide in tumor cells compared with untreated cultures (Fig. S6A and B), and this response was abolished by a mitochondrial-targeted ROS scavenger, mitoTEMPO (Fig. S6C). In contrast, ROS scavenging with mitoTEMPO did not affect mitochondrial repositioning to the cortical cytoskeleton (Fig. 4A and Fig. S6D and E) or tumor cell invasion (Fig. 4B) mediated by PI3K inhibitors. Increasing concentrations of the pan-antioxidant *N*-acetyl cysteine (NAC) had no effect on PI3K therapy-mediated tumor cell invasion (Fig. S6F). The increase in basal cell motility in the presence of antioxidants may reflect release of ROS-regulated inhibitory mechanisms of mitochondrial trafficking.

**Role of Bioenergetics in Mitochondrial Trafficking and Tumor Cell Invasion.** Next, we asked whether mitochondrial bioenergetics was important for this pathway, and generated LN229 cells devoid of oxidative phosphorylation ( $\rho$ 0 cells). Chemoattractant stimulation of respiration-competent LN229 cells induced repositioning of mitochondria to the cortical cytoskeleton (Fig. S7A) that colocalized with paxillin<sup>+</sup> FA complexes (Fig. S7B). In contrast, respiration-deficient LN229  $\rho$ 0 cells failed to reposition mitochondria to the cortical cytoskeleton (Fig. 4C). This absence of mitochondria proximal to FA complexes (Fig. 4D) was associated with loss of FA dynamics (Fig. S7C and D and Movie S3) and suppression of tumor cell invasion across Matrigel-containing inserts (Fig. 4E and Fig. S7E).

As an independent approach, we treated tumor cells with Gamitrinib, a mitochondrial-targeted small-molecule Hsp90 inhibitor that induces misfolding and degradation of the oxidative phosphorylation complex II subunit SDHB (19). Nontoxic

concentrations of Gamitrinib abolished the trafficking of mitochondria to pFAK-containing FA complexes in response to PI3K antagonists (Fig. 4F and G) and preserved a polarized and perinuclear mitochondrial distribution (Fig. S8A). Consistent with these findings, Gamitrinib abolished the increase in tumor cell invasion (Fig. 4H) and the expansion of primary GBM neurospheres (Fig. S8B and C) mediated by PI3K antagonists. To validate these findings, we next silenced the expression of TRAP-1 (Fig. S8D), a mitochondrial Hsp90-like chaperone targeted by Gamitrinib and implicated in complex II stability (19). TRAP-1 silencing in vehicle-treated cells did not affect mitochondrial localization (Fig. S8E, Left). In contrast, knockdown of TRAP-1 abolished mitochondrial trafficking to the cortical cytoskeleton in the presence of PI3K antagonists, increasing the fraction of polarized and perinuclear organelles in these cells (Fig. S8E, Right). Finally, treatment with small-molecule inhibitors of mitochondrial complex I (Rotenone), complex III (Antimycin A), or complex V (Oligomycin) or a mitochondrial uncoupler (carbonyl cyanide *m*-chlorophenyl hydrazine; CCCP) inhibited mitochondrial repositioning to the cortical cytoskeleton (Fig. S8F) and tumor cell invasion (Fig. 4I) in the presence of PI3K therapy.

To begin elucidating the signaling requirements of adaptive mitochondrial trafficking and tumor cell invasion, we next targeted the PI3K–Akt–mTOR axis, which becomes reactivated in response to PI3K therapy (8, 9). Knockdown of Akt1 or Akt2 (Fig. S9A), mTOR (Fig. S9B), or FAK (Fig. S9C) independently prevented the repositioning of mitochondria to the cortical cytoskeleton (Fig. 4J and K and Fig. S9D) and suppressed tumor cell invasion (Fig. 4L and Fig. S9G) induced by PI3K antagonists. In contrast, knockdown of these molecules in the absence of PI3K inhibition had no effect on mitochondrial trafficking (Fig. S9E) or organelle morphology (Fig. S9F).

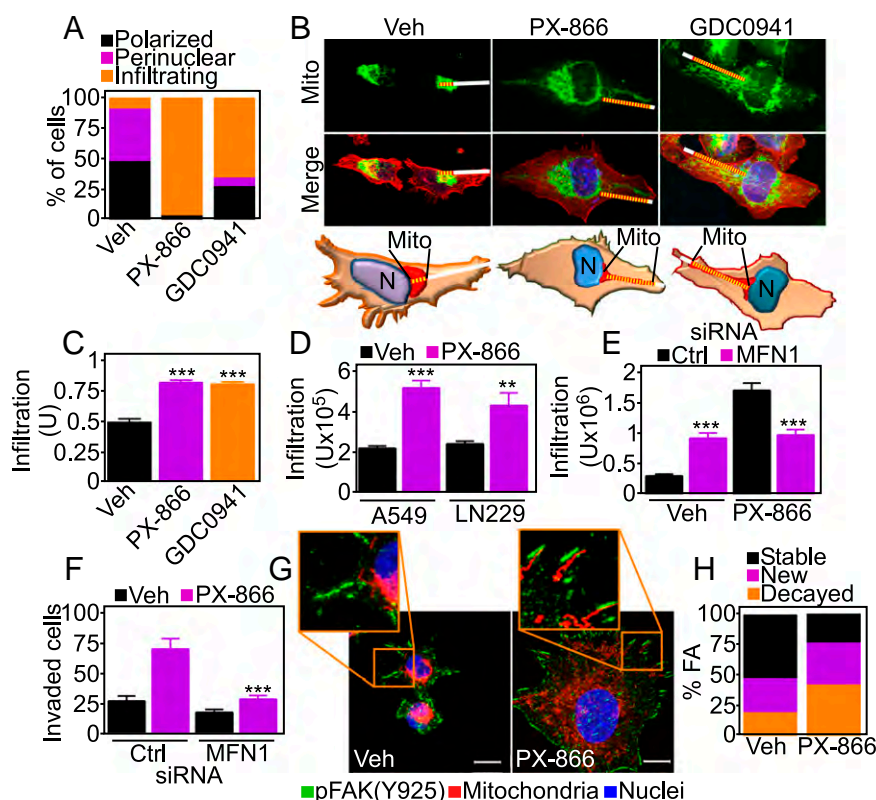


**Fig. 3.** Mitochondria fuel focal adhesion dynamics. (A) PC3 cells treated with vehicle or PI3K inhibitors for 48 h were stained with MitoTracker Red, phalloidin Alexa488, and DAPI, and full cell stacks were used to generate 3D max projection images that were scored for mitochondrial morphology (polarized, perinuclear, infiltrating). (B) Representative confocal 3D max projection images of PC3 cells treated with vehicle or the indicated PI3K inhibitors and stained as in A. (Bottom) Models for quantification of mitochondrial trafficking. Mito, mitochondria. White lines indicate the distance from nuclei to the cell border. Yellow lines indicate the length of mitochondrial infiltration into membrane lamellipodia. Magnification, 63 $\times$ . (C) PC3 cells treated with vehicle or the indicated PI3K inhibitors were labeled as in A and quantified for mitochondrial infiltration into lamellipodia. At least 18 cells were analyzed at two independent lamellipodia, and data were normalized to total lamellipodia length. Mean  $\pm$  SEM ( $n = 36$ ). \*\*\* $P < 0.0001$ . (D) Lung adenocarcinoma A549 or glioblastoma LN229 cells were labeled as in A and scored for mitochondrial infiltration into membrane lamellipodia by fluorescence microscopy. Mean  $\pm$  SEM. \*\*\* $P = 0.0056$ ; \*\*\* $P < 0.0001$ . (E) PC3 cells were transfected with control (Ctrl) or MFN1-directed siRNA, labeled as in A, and quantified for mitochondrial infiltration in the cortical cytoskeleton in the presence of vehicle or PX-866. Mean  $\pm$  SEM. \*\*\* $P < 0.0001$ . (F) PC3 cells transfected with control or MFN1-directed siRNA were treated with vehicle or PX-866 and analyzed for Matrigel invasion after 48 h. Mean  $\pm$  SEM. \*\*\* $P = 0.0002$ . (G) PC3 cells treated with vehicle or PI3K inhibitors for 48 h were replated onto fibronectin-coated slides for 5 h and labeled with an antibody to phosphorylated FAK (pY925) Alexa488, MitoTracker Red, and DAPI. Representative 1- $\mu$ m extended-focus confocal images with localization of mitochondria near FA complexes are shown. Magnification, 63 $\times$ . (Scale bar, 10  $\mu$ m.) (H) PC3 cells expressing Talin-GFP to label FA were treated as indicated and quantified for decay, formation, and stability of FA complexes per cell over 78 min;  $n = 631$ . See also Movie S2.

## Discussion

In this study, we have shown that small-molecule PI3K inhibitors currently in the clinic induce global reprogramming of transcriptional and signaling pathways in tumor cells, paradoxically resulting in increased tumor cell motility and invasion. Mechanistically, this involves the trafficking of energetically active mitochondria to the cortical cytoskeleton of tumor cells, where they support membrane lamellipodia dynamics, turnover of FA complexes, and random cell migration and invasion. Conversely, interference with this spatiotemporal control of mitochondrial bioenergetics abolishes tumor cell invasion.

Although associated with important tumor traits, including “stemness” (20), malignant regrowth (21), and drug resistance (22), a general role of mitochondria in cancer has been difficult to determine (11). Whether these organelles play a role in tumor cell invasion and, therefore, metastatic competency has been equally controversial, with evidence that mitochondrial respiration is important (23), not important (24), or must be dysfunctional (25) to affect cell movements. Here disabling cellular respiration with depletion of mitochondrial DNA (26) or targeting an oxidative phosphorylation complex(es) (19) prevented

mitochondrial trafficking to the cortical cytoskeleton, abolished membrane dynamics of cell motility, and suppressed cell invasion. Conversely, scavenging of mitochondrial ROS, which are increased in response to PI3K therapy, did not affect organelle dynamics and tumor cell invasion. Together, these data suggest that oxidative phosphorylation contributes to cancer metabolism and provides a “regional” and potent ATP source to fuel highly energy-demanding processes of cell movements and invasion (27).

This “spatiotemporal” model of mitochondrial bioenergetics is reminiscent of the accumulation of mitochondria at subcellular sites of energy-intensive processes in neurons (28), including synapses, active growth cones, and branches (29). Whether the cytoskeletal machinery that transports mitochondria along the microtubule network in neurons (30) is also exploited in cancer (this study) is currently unknown. However, there is evidence that comparable mechanisms of organelle dynamics (31) support mitochondrial redistribution in lymphocytes (32) and may contribute to directional migration of tumor cells (33). Consistent with this model (31), interference with the mitochondrial fusion machinery, namely mitofusins, suppressed mitochondrial



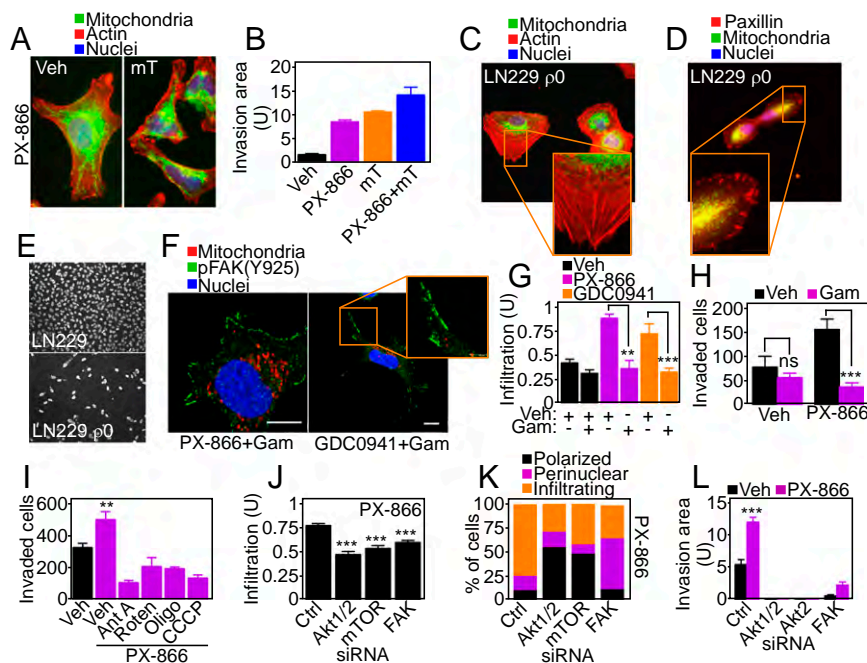


**Fig. 4.** Control of tumor cell invasion by spatiotemporal mitochondrial bioenergetics. (A) PC3 cells were labeled with MitoTracker Red, phalloidin Alexa488, and DAPI, treated with PX-866, and analyzed for mitochondrial infiltration into the peripheral cytoskeleton in the presence of vehicle or the mitochondrial-targeted ROS scavenger mitoTEMPO (mT; 50  $\mu$ M). (B) PC3 cells were incubated with the indicated agents alone or in combination (PX-866+mT) and analyzed for tumor cell invasion across Matrigel. Mean  $\pm$  SEM.  $P$  (ANOVA)  $< 0.0001$ . (C and D) Mitochondrial (mt)DNA-depleted LN229 ( $\rho 0$ ) cells were stimulated with NIH 3T3 conditioned media for 2 h, labeled with MitoTracker Red, DAPI, and either phalloidin Alexa488 (C) or an antibody to FA-associated paxillin (D), and analyzed by fluorescence microscopy. Representative pseudocolored images are shown. Magnification, 60 $\times$ . (E) WT or  $\rho 0$  LN229 cells were analyzed for invasion across Matrigel-coated Transwell inserts. Representative images of invasive cells stained with DAPI are shown. Magnification, 20 $\times$ . (F) PC3 cells treated with vehicle or PI3K inhibitors in combination with the mitochondrial-targeted small-molecule Hsp90 inhibitor Gamitrinib (Gam) were labeled with anti-pY925-FAK Alexa488 followed by fluorescence microscopy. Representative 1- $\mu$ m extended-focus confocal images are shown. Magnification, 63 $\times$ . (Scale bar, 10  $\mu$ m.) (G) PC3 cells treated with vehicle or PI3K inhibitors with or without Gamitrinib (1  $\mu$ M) were labeled with MitoTracker Red, phalloidin Alexa488, and DAPI and quantified after 48 h for mitochondrial infiltration into lamellipodia by fluorescence microscopy;  $n = 48$ . Mean  $\pm$  SEM.  $^{**}P = 0.0044$ ;  $^{***}P < 0.0009$ . (H) PC3 cells were treated with vehicle or PX-866 (5  $\mu$ M) with or without Gamitrinib and quantified for invasion across Matrigel. Mean  $\pm$  SEM of replicates ( $n = 2$ ).  $^{***}P < 0.0001$ . ns, not significant. (I) PC3 cells were incubated with vehicle or PX-866 alone or in combination with the various mitochondrial respiratory chain inhibitors and analyzed for Matrigel invasion. Ant A, Antimycin A; Oligo, Oligomycin; Roten, Rotenone. Mean  $\pm$  SEM.  $^{**}P = 0.006$ . (J) PC3 cells transfected with control siRNA or siRNA to Akt1/2, mTOR, or FAK were labeled as in C, treated with PX-866, and quantified for mitochondrial infiltration into lamellipodia;  $n = 44$ . Mean  $\pm$  SEM.  $^{***}P < 0.0001$ . (K) siRNA-transfected PC3 cells labeled as in C were treated with PX-866 (5  $\mu$ M) and analyzed for mitochondrial morphology (polarized, perinuclear, infiltrating) by fluorescence microscopy;  $n = 21$ . (L) PC3 cells transfected with the indicated siRNAs were quantified for invasion across Matrigel in the presence of vehicle or PX-866. Mean  $\pm$  SEM ( $n = 4$ ).  $^{***}P < 0.0001$ .

repositioning to the cortical cytoskeleton and tumor cell invasion mediated by PI3K therapy.

In addition to oxidative phosphorylation, Akt/mTOR signaling was identified here as a key regulator of mitochondrial trafficking and tumor cell invasion. This is consistent with a pivotal role of PI3K in directional cell movements (34), supporting chemotaxis at the leading edge of migration (35) and Rac1 activation (36). A third signaling requirement of this pathway involved FAK activity (18), which has also been implicated in cytoskeletal dynamics (37).

Despite hopes for “personalized” medicine (4), small-molecule PI3K inhibitors have produced modest and short-lived patient responses in the clinic (5). Our data suggest that these agents potently activate global adaptive mechanisms in tumors (7), unexpectedly centered on mitochondrial reprogramming in cell survival/bioenergetics (9) and subcellular trafficking (this study). In this context, the increased tumor cell motility and invasion stimulated by PI3K inhibitors may create an “escape” mechanism for tumor cells to elude therapy-induced environmental stress, reminiscent of the heightened metastatic propensity associated with other unfavorable conditions of hypoxia (38), acidosis (39), and antiangiogenic therapy (40, 41). Although this adaptive response to PI3K therapy may paradoxically promote more aggressive tumor traits and further compromise clinical

outcomes, disabling mitochondrial adaptation is feasible (19) and may provide a viable strategy to increase the anticancer efficacy of PI3K antagonists in the clinic.

## Methods

**Two-Dimensional Chemotaxis.** Cells were treated with PI3K inhibitors for 48 h and seeded in 2D chemotaxis chambers (Ibidi) in 10% (vol/vol) FBS medium. After a 6-h attachment, cells were washed and the reservoirs were filled with 0.1% BSA/RPMI, followed by gradient setup by addition of NIH 3T3 conditioned medium. Video microscopy was performed over 8 h, with a time-lapse interval of 10 min. At least 30 cells were tracked using the WimTaxis module (Wimasis), and the tracking data were exported into Chemotaxis and Migration Tool v2.0 (Ibidi) for graphing and statistical testing. Experiments were repeated twice ( $n = 3$ ).

**FA Dynamics.** Cells growing in high-optical-quality 96-well  $\mu$ -plates (Ibidi) were transduced with Talin-GFP BacMam virus (50 particles per cell) for 18 h and imaged with a 40 $\times$  objective on a Nikon TE300 inverted time-lapse microscope equipped with a video system containing an Evolution QEi camera and a time-lapse video cassette recorder. The atmosphere was equilibrated to 37  $^{\circ}$ C and 5% CO $_2$  in an incubation chamber. Time-lapse fluorescence microscopy was carried out for the indicated times at 1 min per frame. Sequences were aligned in Image-Pro Plus 7 (Media Cybernetics) and imported into ImageJ (NIH) for further analysis. The initial and final frames were duplicated and assembled as composite images. FA complexes were manually counted and classified according to presence in some or all of the



time frames: decaying, newly formed, stable sliding (FA moves to a different position over time), and stable mature (merged areas). The rate of decay and assembly of FA complexes was calculated for each cell as the number of FA complexes changing per h. At least 400 FA complexes from 10 cells were analyzed from 5 independent time lapses per condition.

**Tumor Cell Invasion.** Experiments were carried out essentially as described (42). Briefly, 8- $\mu$ m PET Transwell migration chambers (Corning) were coated with 150  $\mu$ L 80  $\mu$ g/mL Matrigel (Becton Dickinson). Tumor cells were seeded in duplicates onto the coated Transwell filters at a density of  $1.25 \times 10^5$  cells per well in media containing 2% (vol/vol) FCS (FCIII; HyClone), and media containing 20% (vol/vol) FCS were placed in the lower chamber as chemo-attractant. Cells were allowed to invade and adhere to the bottom of the plate, stained in 0.5% crystal violet/methanol for 10 min, rinsed in tap water, and analyzed by bright-field microscopy. Digital images were batch-imported into ImageJ, thresholded, and analyzed with the Analyze Particles function. For analysis of tumor cell invasion in 3D spheroids, tissue culture-treated 96-well plates were coated with 50  $\mu$ L 1% Difco Agar Noble (Becton Dickinson). LN229 cells were seeded at 5,000 cells per well and allowed to form spheroids over 72 h. Spheroids were harvested, treated with PX-866 (0–10  $\mu$ M), and placed in a collagen plug containing Eagle's minimum essential medium (EMEM), FBS, L-glutamine, sodium bicarbonate, and collagen type I (Gibco; 1.5 mg/mL). The collagen plug was allowed to set and 1 mL DMEM with 5% (vol/vol) FBS was added to the top of the plug. Cell invasion was analyzed every 24 h and quantified using Image-Pro Plus 7, as described (42).

**Patient Samples.** For studies using human samples, informed consent was obtained from all patients enrolled, and the study was approved by an Institutional Review Board of the Fondazione IRCCS Ca' Granda. The clinicopathological features of GBM patients used in this study are summarized in Table S1.

**Statistical Analysis.** Data were analyzed using either two-sided unpaired *t* test (for two-group comparisons) or one-way ANOVA test with Dunnett's multiple comparison posttest (for more than two-group comparisons) using a GraphPad software package (Prism 6.0) for Windows. Data are expressed as mean  $\pm$  SD or mean  $\pm$  SEM of multiple independent experiments. A *P* value of  $<0.05$  was considered statistically significant.

**ACKNOWLEDGMENTS.** We thank James Hayden and Frederick Keeney of the Wistar Imaging Facility for outstanding help with time-lapse imaging. This work was supported by National Institutes of Health Grants P01 CA140043 (to D.C.A. and L.R.L.), R01 CA78810 and CA190027 (to D.C.A.), F32 CA177018 (to M.C.C.), and R01 CA089720 (to L.R.L.), the Office of the Assistant Secretary of Defense for Health Affairs through the Prostate Cancer Research Program under Award W81XWH-13-1-0193 (to D.C.A.), and a Joint Grant in Molecular Medicine 2013 from Fondazione IRCCS Ca' Granda and Istituto Nazionale Genetica Molecolare (to V.V.). Support for the core facilities used in this study was provided by Cancer Center Support Grant CA010815 to The Wistar Institute.

- Engelman JA, Luo J, Cantley LC (2006) The evolution of phosphatidylinositol 3-kinases as regulators of growth and metabolism. *Nat Rev Genet* 7(8):606–619.
- Manning BD, Cantley LC (2007) AKT/PKB signaling: Navigating downstream. *Cell* 129(7):1261–1274.
- Vivanco I, Sawyers CL (2002) The phosphatidylinositol 3-kinase AKT pathway in human cancer. *Nat Rev Cancer* 2(7):489–501.
- Rodon J, Dienstmann R, Serra V, Tabernero J (2013) Development of PI3K inhibitors: Lessons learned from early clinical trials. *Nat Rev Clin Oncol* 10(3):143–153.
- Fruman DA, Rommel C (2014) PI3K and cancer: Lessons, challenges and opportunities. *Nat Rev Drug Discov* 13(2):140–156.
- Jänne PA, Gray N, Settleman J (2009) Factors underlying sensitivity of cancers to small-molecule kinase inhibitors. *Nat Rev Drug Discov* 8(9):709–723.
- Cohen AA, et al. (2008) Dynamic proteomics of individual cancer cells in response to a drug. *Science* 322(5907):1511–1516.
- Chakrabarty A, Sánchez V, Kuba MG, Rinehart C, Arteaga CL (2012) Feedback upregulation of HER3 (ErbB3) expression and activity attenuates antitumor effect of PI3K inhibitors. *Proc Natl Acad Sci USA* 109(8):2718–2723.
- Ghosh JC, et al. (2015) Adaptive mitochondrial reprogramming and resistance to PI3K therapy. *J Natl Cancer Inst* 107(3):djv502.
- Ward PS, Thompson CB (2012) Metabolic reprogramming: A cancer hallmark even Warburg did not anticipate. *Cancer Cell* 21(3):297–308.
- Wallace DC (2012) Mitochondria and cancer. *Nat Rev Cancer* 12(10):685–698.
- Frezza C, et al. (2011) Haem oxygenase is synthetically lethal with the tumour suppressor fumarate hydratase. *Nature* 477(7363):225–228.
- Vaira V, et al. (2010) Preclinical model of organotypic culture for pharmacodynamic profiling of human tumors. *Proc Natl Acad Sci USA* 107(18):8352–8356.
- Roussos ET, Condeelis JS, Patsialou A (2011) Chemotaxis in cancer. *Nat Rev Cancer* 11(8):573–587.
- Hinz B, Alt W, Johnen C, Herzog V, Kaiser H-W (1999) Quantifying lamella dynamics of cultured cells by SACED, a new computer-assisted motion analysis. *Exp Cell Res* 251(1):234–243.
- Petrie RJ, Doyle AD, Yamada KM (2009) Random versus directionally persistent cell migration. *Nat Rev Mol Cell Biol* 10(8):538–549.
- Youle RJ, van der Blik AM (2012) Mitochondrial fission, fusion, and stress. *Science* 337(6098):1062–1065.
- Sulzmaier FJ, Jean C, Schlaepfer DD (2014) FAK in cancer: Mechanistic findings and clinical applications. *Nat Rev Cancer* 14(9):598–610.
- Chae YC, et al. (2013) Landscape of the mitochondrial Hsp90 metabolome in tumours. *Nat Commun* 4:2139.
- Janiszewska M, et al. (2012) Imp2 controls oxidative phosphorylation and is crucial for preserving glioblastoma cancer stem cells. *Genes Dev* 26(17):1926–1944.
- Viale A, et al. (2014) Oncogene ablation-resistant pancreatic cancer cells depend on mitochondrial function. *Nature* 514(7524):628–632.
- Haq R, et al. (2013) Oncogenic BRAF regulates oxidative metabolism via PGC1 $\alpha$  and MITF. *Cancer Cell* 23(3):302–315.
- LeBleu VS, et al. (2014) PGC-1 $\alpha$  mediates mitochondrial biogenesis and oxidative phosphorylation in cancer cells to promote metastasis. *Nat Cell Biol* 16(10):992–1003.
- Shiraishi T, et al. (2015) Glycolysis is the primary bioenergetic pathway for cell motility and cytoskeletal remodeling in human prostate and breast cancer cells. *Oncotarget* 6(1):130–143.
- Porporato PE, et al. (2014) A mitochondrial switch promotes tumor metastasis. *Cell Reports* 8(3):754–766.
- Olgun A, Akman S (2007) Mitochondrial DNA-deficient models and aging. *Ann N Y Acad Sci* 1100:241–245.
- De Bock K, et al. (2013) Role of PFKFB3-driven glycolysis in vessel sprouting. *Cell* 154(3):651–663.
- Lee CW, Peng HB (2006) Mitochondrial clustering at the vertebrate neuromuscular junction during presynaptic differentiation. *J Neurobiol* 66(6):522–536.
- Saxton WM, Hollenbeck PJ (2012) The axonal transport of mitochondria. *J Cell Sci* 125(Pt 9):2095–2104.
- Birsa N, Norkett R, Higgs N, Lopez-Domench G, Kittler JT (2013) Mitochondrial trafficking in neurons and the role of the Miro family of GTPase proteins. *Biochem Soc Trans* 41(6):1525–1531.
- Zhao J, et al. (2013) Mitochondrial dynamics regulates migration and invasion of breast cancer cells. *Oncogene* 32(40):4814–4824.
- Morlino G, et al. (2014) Miro-1 links mitochondria and microtubule dynein motors to control lymphocyte migration and polarity. *Mol Cell Biol* 34(8):1412–1426.
- Desai SP, Bhatia SN, Toner M, Irimia D (2013) Mitochondrial localization and the persistent migration of epithelial cancer cells. *Biophys J* 104(9):2077–2088.
- Kölsch V, Charest PG, Firtel RA (2008) The regulation of cell motility and chemotaxis by phospholipid signaling. *J Cell Sci* 121(Pt 5):551–559.
- Weiger MC, et al. (2009) Spontaneous phosphoinositide 3-kinase signaling dynamics drive spreading and random migration of fibroblasts. *J Cell Sci* 122(Pt 3):313–323.
- Kraynov VS, et al. (2000) Localized Rac activation dynamics visualized in living cells. *Science* 290(5490):333–337.
- Fabry B, Klemm AH, Kienle S, Schäffer TE, Goldmann WH (2011) Focal adhesion kinase stabilizes the cytoskeleton. *Biophys J* 101(9):2131–2138.
- Pennacchietti S, et al. (2003) Hypoxia promotes invasive growth by transcriptional activation of the met protooncogene. *Cancer Cell* 3(4):347–361.
- Gatenby RA, Gillies RJ (2004) Why do cancers have high aerobic glycolysis? *Nat Rev Cancer* 4(11):891–899.
- Ebos JM, et al. (2009) Accelerated metastasis after short-term treatment with a potent inhibitor of tumor angiogenesis. *Cancer Cell* 15(3):232–239.
- Páez-Ribes M, et al. (2009) Antiangiogenic therapy elicits malignant progression of tumors to increased local invasion and distant metastasis. *Cancer Cell* 15(3):220–231.
- Caino MC, et al. (2013) Metabolic stress regulates cytoskeletal dynamics and metastasis of cancer cells. *J Clin Invest* 123(7):2907–2920.
- Kang BH, et al. (2009) Combinatorial drug design targeting multiple cancer signaling networks controlled by mitochondrial Hsp90. *J Clin Invest* 119(3):454–464.
- Ortensi B, et al. (2012) Rai is a new regulator of neural progenitor migration and glioblastoma invasion. *Stem Cells* 30(5):817–832.
- Vaira V, et al. (2012) miR-296 regulation of a cell polarity-cell plasticity module controls tumor progression. *Oncogene* 31(1):27–38.
- Livak KJ, Schmittgen TD (2001) Analysis of relative gene expression data using real-time quantitative PCR and the 2- $\Delta\Delta$ CT method. *Methods* 25(4):402–408.
- Benjamini Y, Hochberg Y (1995) Controlling the false discovery rate: A practical and powerful approach to multiple testing. *J R Stat Soc Series B Stat Methodol* 57(1):289–300.
- Louis DN, et al. (2007) The 2007 WHO classification of tumors of the central nervous system. *Acta Neuropathol* 114(2):97–109.

# Microbially Driven TLR5-Dependent Signaling Governs Distal Malignant Progression through Tumor-Promoting Inflammation

Melanie R. Rutkowski,<sup>1</sup> Tom L. Stephen,<sup>1</sup> Nikolaos Svoronos,<sup>1</sup> Michael J. Allegrezza,<sup>1</sup> Amelia J. Tesone,<sup>1</sup> Alfredo Perales-Puchalt,<sup>1</sup> Eva Brencicova,<sup>1</sup> Ximena Escovar-Fadul,<sup>1</sup> Jenny M. Nguyen,<sup>1</sup> Mark G. Cadungog,<sup>2</sup> Rugang Zhang,<sup>3</sup> Mariana Salatino,<sup>4</sup> Julia Tchou,<sup>4,5,6</sup> Gabriel A. Rabinovich,<sup>7</sup> and Jose R. Conejo-Garcia<sup>1,\*</sup>

<sup>1</sup>Tumor Microenvironment and Metastasis Program, The Wistar Institute, Philadelphia, PA 19104, USA

<sup>2</sup>Helen F. Graham Cancer Center, Christiana Care Health System, 4701 Ogletown-Stanton Road, Newark, DE 19713, USA

<sup>3</sup>Gene Expression and Regulation Program, The Wistar Institute, Philadelphia, PA 19104, USA

<sup>4</sup>Division of Endocrine and Oncologic Surgery, Department of Surgery

<sup>5</sup>Rena Rowan Breast Center

<sup>6</sup>Abramson Cancer Center, Perelman School of Medicine  
University of Pennsylvania, Philadelphia, PA 19104-1693, USA

<sup>7</sup>Laboratorio de Inmunopatología, Instituto de Biología y Medicina Experimental (IBYME-CONICET), Buenos Aires, Argentina

\*Correspondence: [jrconejo@wistar.org](mailto:jrconejo@wistar.org)

<http://dx.doi.org/10.1016/j.ccell.2014.11.009>

## SUMMARY

The dominant *TLR5*<sup>R392X</sup> polymorphism abrogates flagellin responses in >7% of humans. We report that TLR5-dependent commensal bacteria drive malignant progression at extramucosal locations by increasing systemic IL-6, which drives mobilization of myeloid-derived suppressor cells (MDSCs). Mechanistically, expanded granulocytic MDSCs cause  $\gamma\delta$  lymphocytes in TLR5-responsive tumors to secrete galectin-1, dampening antitumor immunity and accelerating malignant progression. In contrast, IL-17 is consistently upregulated in TLR5-unresponsive tumor-bearing mice but only accelerates malignant progression in IL-6-unresponsive tumors. Importantly, depletion of commensal bacteria abrogates TLR5-dependent differences in tumor growth. Contrasting differences in inflammatory cytokines and malignant evolution are recapitulated in TLR5-responsive/unresponsive ovarian and breast cancer patients. Therefore, inflammation, antitumor immunity, and the clinical outcome of cancer patients are influenced by a common *TLR5* polymorphism.

## INTRODUCTION

A rapidly growing paradigm is that commensal microorganisms are required to maintain immune homeostasis of mucosal surfaces such as the intestine (Mazmanian et al., 2008) while facilitating the shaping of immune responses against pathogens in the periphery (Abt et al., 2012; Clarke et al., 2010). Most recently, interactions between microbiota and mucosal surfaces have

been demonstrated to have a crucial role in therapeutic responses for tumors occurring outside of the intestinal tract (Iida et al., 2013; Viaud et al., 2013). Although the mechanisms of distal immune regulation by the microbiota are poorly understood, their importance is illustrated by the lack of cellular immune responses and a very narrow T cell repertoire in germ-free mice.

Pattern recognition receptors recognize pathogen-associated molecular patterns, including those contained in commensal

### Significance

7.5% of the general population harbor a single dominant nucleotide polymorphism in *TLR5*, resulting in up to an 80% reduction in signaling. We perform a survival analysis of TCGA data sets for individuals with this polymorphism and show that TLR5 signaling affects the malignant progression of ovarian and breast cancer differently. In both TLR5-responsive and nonresponsive mice, depletion of commensal bacteria abrogates differences in tumor progression. We also show that TLR5 recognition of commensal bacteria results in elevated IL-6 levels during tumor progression, whereas, in TLR5 nonresponsive, tumor-bearing mice, there is an increased systemic production of IL-17. Mechanistically, we demonstrate that TLR5 signaling is driving differential tumor-promoting inflammation and that the balance of IL-6 and IL-17 influences the outcome of malignant progression.

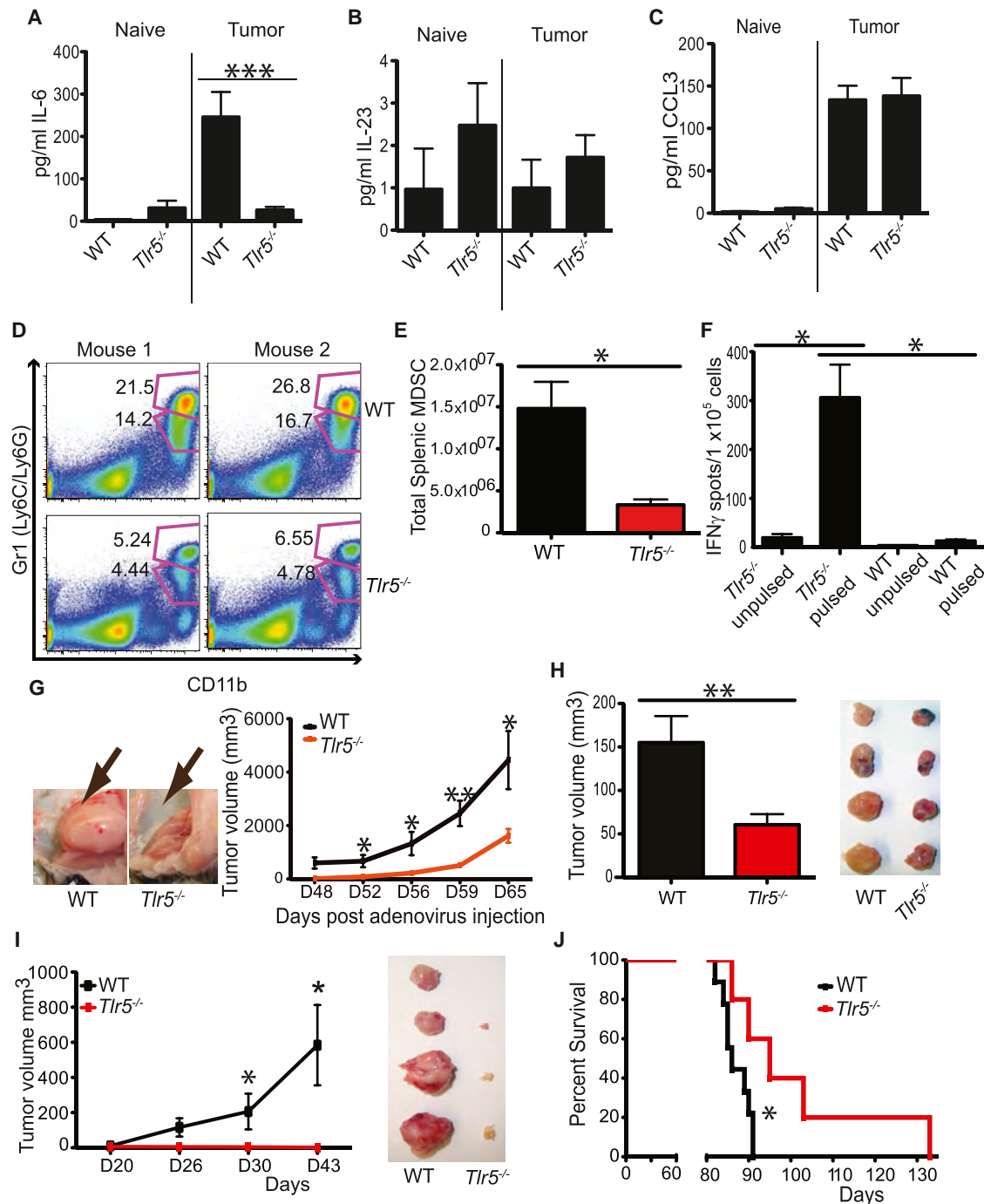


**Figure 1. Tumor-Promoting Inflammation Is Driven by TLR5-Dependent Signaling**

(A–C) Serum levels of IL-6 (A), IL-23 (B), and CCL3 (C) in TLR5-responsive (WT) and TLR5-deficient (*Tlr5*<sup>-/-</sup>) mice with advanced (days 64–75) flank sarcomas (Tumor, n  $\geq 15$ /group) or naive littermate controls, as detected by ELISA.

(D and E) Proportions (D) and total numbers (E) of MDSC infiltrating into the spleens of WT or *Tlr5*<sup>-/-</sup> mice bearing equally sized tumors. Shown is one representative of two independent experiments with five to eight animals per group.

(F) IFN $\gamma$  enzyme-linked Immunospot of sorted antigen-specific CD8 T cells from the draining lymph node (inguinal) of mice bearing day 64 hind flank sarcomas incubated with tumor-lysed, pulsed BMDCs (pulsed) or BMDCs only (unpulsed). Data are representative of two experiments with at least three mice per group.

(G) Representative images of tumors and growth curve of *Tlr5*<sup>-/-</sup> or WT transgenic mice administered subcutaneous adenovirus-Cre into the hind flank. Data are representative of five individual experiments with at least six to ten mice per group.

(H) Representative final tumor volume and resected ID8-Vegf-Defb29 tumors 27 days after injection into the axillary flank. Data are representative of two individual experiments with at least five to eight mice per group.

(legend continued on next page)

microbiota. At least 23% of individuals in the general population are carriers of functional polymorphisms in Toll-like receptor (TLR) genes (Casanova et al., 2011), but their effect on immunosurveillance against extraintestinal tumors remains poorly understood. One of the most frequent polymorphisms is found in *TLR5*. Approximately 7.5% of the general population harbor a single dominant nucleotide polymorphism in *TLR5* (1174 C > T), encoding a stop codon in place of an arginine at codon 392 (*TLR5*<sup>R392X</sup>) (Hawn et al., 2003; Misch and Hawn, 2008). This polymorphism results in truncating the transmembrane signaling domain of TLR5 (the specific receptor of flagellin), abrogating signaling by 50%–80%, even for individuals who are heterozygous for this allele. Although the relative frequency of heterozygous carriers within the general population indicates compatibility with a healthy lifestyle, this polymorphism has immunological consequences because heterozygous carriers have an enhanced susceptibility to Legionnaires disease (Hawn et al., 2003), urinary tract infections (Hawn et al., 2009), and bronchopulmonary dysplasia (Sampath et al., 2012). However, virtually nothing is known about the systemic consequences of microbially induced TLR5-dependant signaling, and malignant progression of tumors occurring outside of the intestines.

Here we dissected the role of TLR5 signaling at mucosal surfaces on tumor progression at extramucosal locations through systemic inflammation.

## RESULTS

### TLR5 Signaling Results in Tumor-Promoting Systemic Inflammatory Responses during Malignant Progression

To determine whether TLR5 signaling influences the malignant progression of extraintestinal tumors, we generated B6 mice with latent mutations in p53 and K-ras (*Trp53*<sup>flx/flx</sup>; *LSL-Kras*<sup>G12D/+</sup>) (Jackson et al., 2001; Jonkers et al., 2001; Scarlett et al., 2012) on a TLR5-deficient (*Tlr5*<sup>−/−</sup>) or TLR5-responsive (wild-type [WT]) background. No evidence of metabolic syndrome or colitis in *Tlr5*<sup>−/−</sup> mice was observed in our facilities (Figures S1A–S1C available online). Subcutaneous delivery of adenoviruses expressing Cre-recombinase into the hind flank led to concurrent ablation of p53 and activation of oncogenic K-ras, resulting in palpable tumors with histological features of sarcoma. Notably, tumor-bearing (but not naive) WT mice exhibited significantly greater serum levels of IL-6 compared with *Tlr5*<sup>−/−</sup> littermates bearing similarly sized tumors (Figure 1A; Figure S1D), whereas other inflammatory cytokines were increased at similar levels or remained unchanged in both groups (Figures 1B and 1C; Figures S1E and S1F).

Consistent with IL-6-mediated systemic inflammation, we found increased mobilization of myeloid-derived suppressor cells (MDSCs) (Figures 1D and 1E)—both Ly6C<sup>+</sup> and Ly6G<sup>+</sup> (Figure S1G)—in TLR5-responsive mice compared with *Tlr5*<sup>−/−</sup> littermates with an equivalent tumor burden. As expected, no TLR5-dependent differences were found in tumor-free mice

(Figure S1H). Reconstitution with IL-6-deficient bone marrow (Figure S1I) and antibody-mediated neutralization of IL-6 (Figure S1J) resulted in significant decreases in the mobilization of MDSCs in tumor-bearing WT hosts. Accordingly, tumor-specific effector CD8 T cell responses were significantly impaired in WT animals (Figure 1F) but were restored in tumor-bearing WT animals reconstituted with IL-6-deficient bone marrow (Figure S1K). Correspondingly, tumor growth was increased in TLR5-competent hosts (Figure 1G).

Accelerated malignant progression in TLR5-responsive mice was not driven by TLR5-dependent responses in the tumor cells (e.g., in response to bacterial translocation), as the same tumor cells, or syngeneic p53/K-ras ovarian tumor-derived cells (Scarlett et al., 2012) injected into the axillary flank also progressed significantly faster in TLR5-responsive mice, compared to TLR5-deficient littermates (Figures 1H and 1I). Differences in tumor progression (Figure 1J) and antitumor immunity (Figure S1L) were also recapitulated when ovarian tumor cells were administered intraperitoneally.

No endotoxin could be detected in the serum or tumor ascites (data not shown). More importantly, the background PCR signals for bacterial ribosomal 16S detected in the serum, tumor, draining lymph nodes, or ascites from WT or *Tlr5*<sup>−/−</sup> mice were similar to those found in matching control samples from healthy WT mice (Figure S1M).

Taken together, these data indicate that TLR5 signaling is sufficient to drive systemic tumor-promoting inflammation associated with impaired antitumor immunity and accelerated malignant progression and without obvious dysbiosis in TLR5-deficient hosts.

### TLR5-Dependent Accelerated Extraintestinal Tumor Growth Is Mediated through Interactions with Commensal Microbiota

Notably, although the composition of the microbiota in TLR5-deficient and TLR5-competent mice was more similar than when compared individually with WT syngeneic mice from a different facility within the campus of the University of Pennsylvania, microbiome-wide differences remained between WT and *Tlr5*<sup>−/−</sup> mice after cohousing them in the same cage for 4 weeks (Figures 2A and 2B). Significant differences were found in the genera of *Allobaculum*, *Bacteroides*, and *Lactobacillus*, although not in other species associated with inflammation, such as *Candidatus* *Arthromitus* or *Clostridia*. In addition, cohoused WT and *Tlr5*<sup>−/−</sup> mice retained differences in the progression of both ovarian tumors and transplantable sarcomas generated from p53/K-ras autochthonous tumors (termed MPKAS; Figures 2C–2F). Because mice are naturally coprophagic, differences in the composition of the microbiota after cohousing suggest that the absence of TLR5 activity contributes to forge a dissimilar repertoire of commensal bacteria under similar environmental conditions. To test the influence of TLR5-dependent commensal microorganisms on the progression of extramucosal tumors, we first confirmed significantly elevated serum levels of IL-6

(I) Growth curve and representative resected UPK10 (p53/K-ras-dependent ovarian) tumors 43 days after challenge in the axillary flank. Data are representative of two individual experiments with at least four to six mice per group.

(J) Survival proportions of *Tlr5*<sup>−/−</sup> and WT mice bearing syngeneic ID8 ovarian tumor cells (≥ 5/group with two repetitions).

All data represent the mean ± SEM. \*p < 0.05, \*\*\*p < 0.001 *Tlr5*<sup>−/−</sup> compared with WT using Mann-Whitney test and log rank test for survival. See also Figure S1.



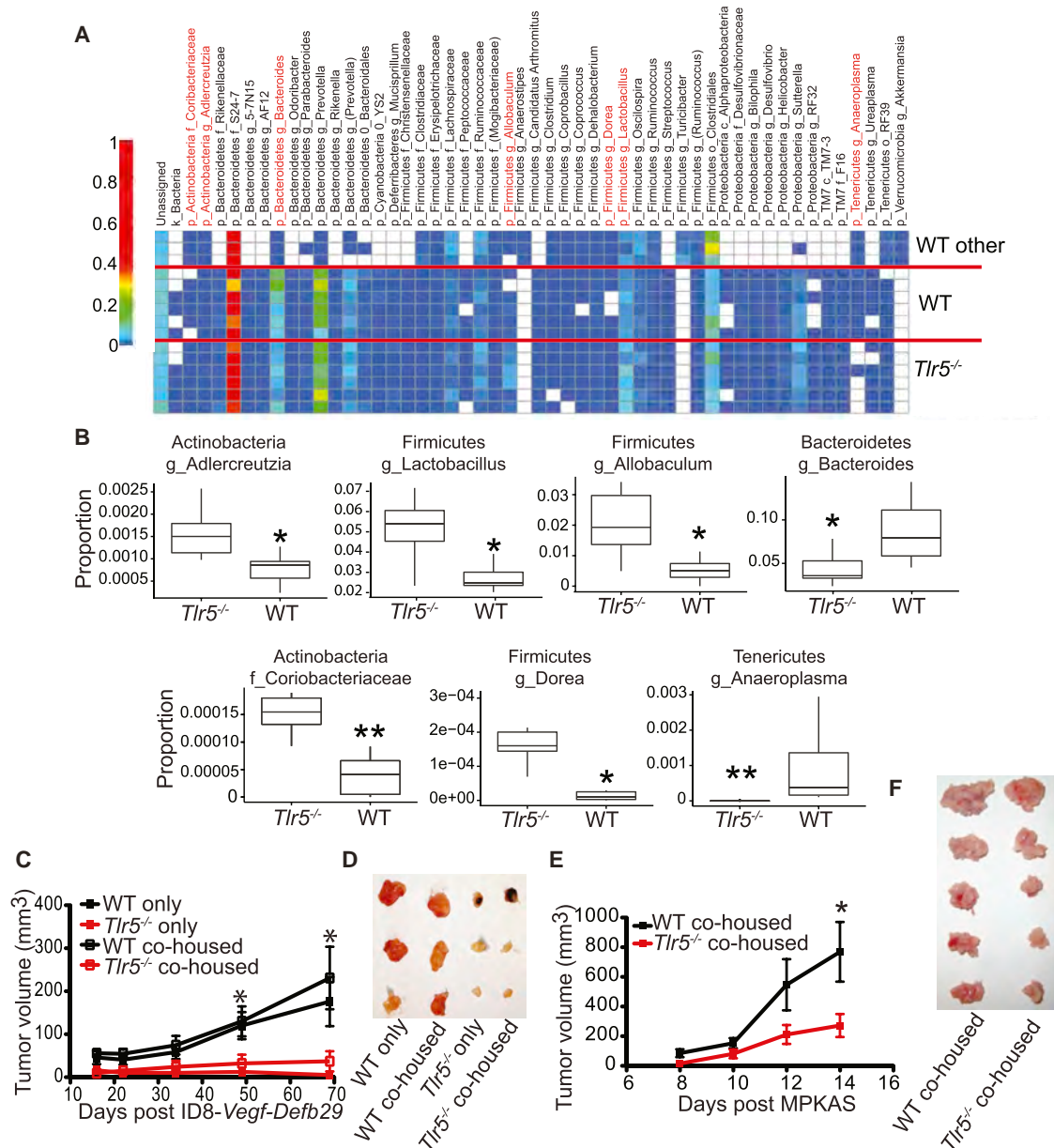


**Figure 2. The Absence of TLR5 Signaling Results in a Divergent Microbial Composition and Reduced Tumor Progression**

(A) Heatmap of operational taxonomic units of commensal bacterial phyla from WT or *Tlr5*<sup>-/-</sup> mice cohoused for 4 weeks compared with naive WT mice housed in a different animal facility (WT other).

(B) Proportions of the indicated bacterial phyla in cohoused WT and *Tlr5*<sup>-/-</sup> mice. Boxes represent the interquartile range (bottom, 25<sup>th</sup> percentile; top, 75<sup>th</sup> percentile), and the line inside represents the median. Whiskers denote the lowest and highest values within 1.5× the interquartile range. Kruskal-Wallis one-way ANOVA was used to calculate significance.

(C) Tumor growth kinetics of ID8-Vegf-Defb29 injected into the axillary flank of WT and *Tlr5*<sup>-/-</sup> mice cohoused for 4 weeks prior to the injection. Data are representative of one experiment with at least five mice per group.

(D) Tumors from cohoused mice in (C) resected after 69 days.

(E) Growth kinetics of MPKAS sarcomas injected in the axillary flank of WT and *Tlr5*<sup>-/-</sup> mice cohoused for 3 weeks prior to the injection. Data are representative of one experiment with at least five mice per group.

(F) Resected tumors from cohoused mice in (C) 14 days after injection.

All data represent the mean ± SEM. \*p < 0.05, \*\*p < 0.01, \*\*\*p < 0.001. Unless stated otherwise, Mann-Whitney test was used.

(Figure 3A) and accelerated tumor growth (Figure 3B) in WT mice challenged with transplantable MPKAS sarcomas. Depletion of commensal microbiota in both TLR5-responsive and deficient

mice by oral administration of antibiotics (ABX) resulted in enlarged ceca and a reduction in the burden of bacteria in the intestines, as evidenced by 16 s quantification of the bacterial

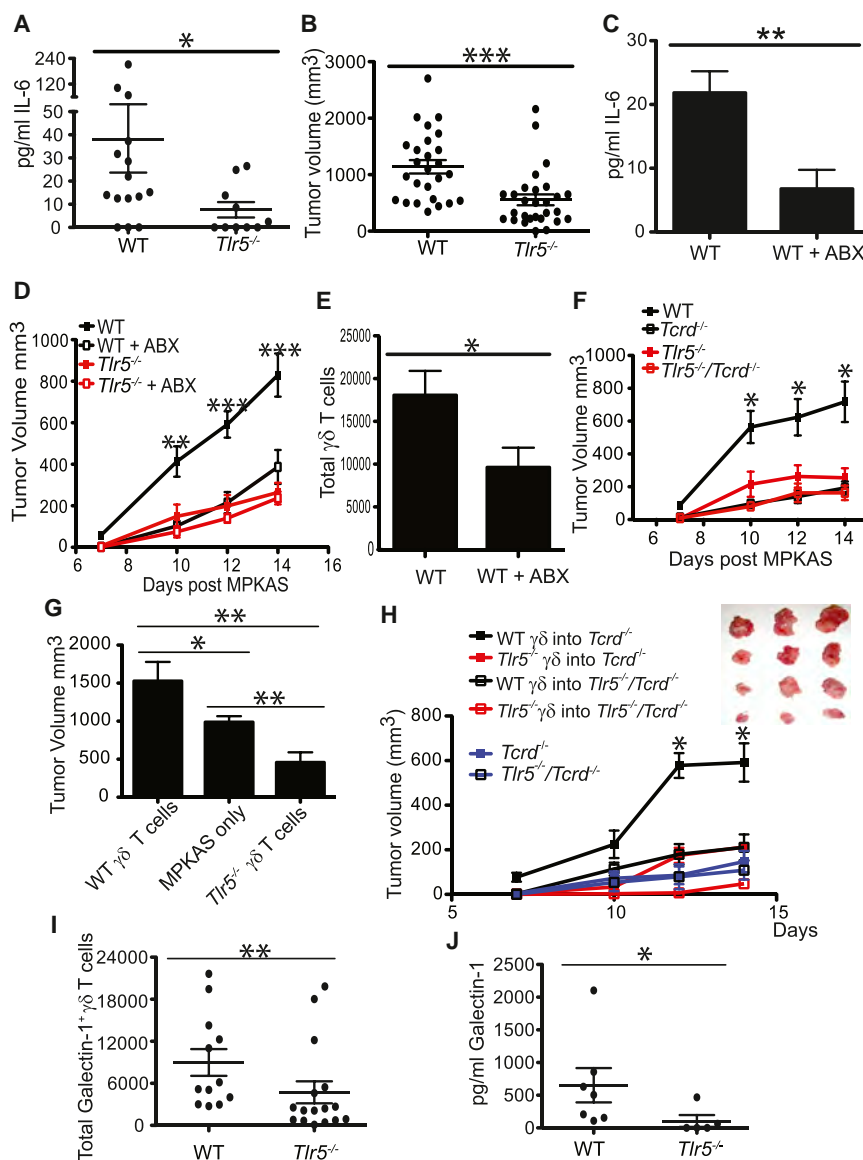


**Figure 3. Commensal Microbiota Modulate TLR5-Dependent Tumor Growth through Increased IL-6 and  $\gamma\delta$  T Cells**

(A) IL-6 serum levels of WT or *Tlr5*<sup>-/-</sup> mice 14 days after being transplanted with the MPKAS sarcoma cell line.

(B) Tumor volume of MPKAS in *Tlr5*<sup>-/-</sup> or WT mice at day 14 ( $n \geq 26$ /group).

(C–E) WT and *Tlr5*<sup>-/-</sup> mice were gavaged daily for 2 weeks with an antibiotic cocktail (ABX) to eliminate the commensal microbiota or with autoclaved H<sub>2</sub>O prior to the initiation of MPKAS tumors, and antibiotic depletion was continued throughout the course of tumor progression. IL-6 serum levels in mice 14 days after initiation of MPKAS tumors (C), tumor growth kinetics (D), and total  $\gamma\delta$  T cells in the draining axillary and brachial lymph node in mice 14 days after initiation of MPKAS tumors (E) are shown. Data are representative of at least three experiments with five mice per group.

(F) Growth kinetics of MPKAS tumors in *Tcrd*<sup>-/-</sup> or *Tlr5*<sup>-/-</sup>/*Tcrd*<sup>-/-</sup> mice compared with the appropriate WT and *Tlr5*<sup>-/-</sup> littermate controls. Data are representative of two individual experiments with at least five to eight mice per group.

(G) Volume of tumors 14 days after transplantation of MPKAS tumor cells alone or together with WT or *Tlr5*<sup>-/-</sup> tumor-associated  $\gamma\delta$  T cells into the axillary flank of naive WT mice.

(H) Tumor growth curve of MPKAS cells admixed with tumor-associated  $\gamma\delta$  T cells sorted from WT or *Tlr5*<sup>-/-</sup> tumor-bearing mice injected into the axillary flank of *Tcrd*<sup>-/-</sup> or *Tlr5*<sup>-/-</sup>/*Tcrd*<sup>-/-</sup> mice and representative resected tumors 14 days after the implantation.

(I) Total Galectin-1<sup>+</sup>  $\gamma\delta$  T cells from tumor-draining lymph nodes of WT or *Tlr5*<sup>-/-</sup> mice with advanced autochthonous sarcomas.

(J)  $\gamma\delta$  T cells were sorted from the draining lymph nodes of WT or *Tlr5*<sup>-/-</sup> mice bearing advanced autochthonous sarcomas and cultured for 6 hr with phorbol 12-myristate 13-acetate/ionomycin. Supernatants were collected and assayed for galectin-1 levels.

All data represent the mean  $\pm$  SEM. \* $p < 0.05$ , \*\* $p < 0.01$ , \*\*\* $p < 0.001$  using Mann-Whitney test. See also Figure S2.

load from fecal pellets of treated and untreated mice (Figures S2A and S2B). Most importantly, differences in systemic IL-6 levels (Figure 3C), mobilization of MDSCs (Figure S2C), and tumor growth (Figure 3D; Figure S2D) were all completely abrogated when commensal bacteria were eliminated from tumor-challenged WT and *Tlr5*<sup>-/-</sup> mice as a result of significantly delayed tumor progression in WT mice. Correspondingly, bacterial depletion was associated with an increased accumulation of interferon  $\gamma$  (IFN $\gamma$ )-producing effector CD8 T cells (Figure S2E). Decreased tumor growth could not be attributed to nonspecific antitumor activity of the (oral) antibiotic cocktail because there was no effect on tumor cell proliferation (Figure S2F).

#### $\gamma\delta$ T Cells Promote Tumor Growth through Galectin-1 Secretion in a TLR5-Dependent Manner

Unexpectedly, bacterial depletion resulted in a significant and selective decrease in the number of  $\gamma\delta$  T cells in the tumor

microenvironment (TME) in TLR5-responsive hosts (Figure 3E; Figure S2G).  $\gamma\delta$  lymphocytes preferentially accumulate at mucosal surfaces, linking innate and adaptive immunity through the secretion of cytokines and chemokines, providing help for adaptive responses, lysing target cells, or directly presenting antigens.

To understand the role of  $\gamma\delta$  T cells infiltrating into tumors that grow more aggressively in the presence of TLR5 signaling, WT and *Tlr5*<sup>-/-</sup> littermates deficient of  $\gamma\delta$  T cells were challenged with syngeneic MPKAS sarcomas. Tumors progressed significantly more slowly in WT mice lacking  $\gamma\delta$  T cells, whereas tumor growth in *Tlr5*<sup>-/-</sup>  $\gamma\delta$ -deficient mice was unchanged (Figure 3F). To verify that tumor-derived  $\gamma\delta$  T cells were sufficient to accelerate malignant growth only in the presence of TLR5 signaling,  $\gamma\delta$  T cells were sorted from the draining lymph nodes of WT and *Tlr5*<sup>-/-</sup> mice with advanced autochthonous p53/K-ras flank sarcomas and admixed with MPKAS tumor cells for injection

into naive WT recipients. Compared with tumor cells administered alone and together with tumor-derived  $\gamma\delta$  T cells from *Tlr5*<sup>-/-</sup> mice,  $\gamma\delta$  T cells from WT mice significantly accelerated tumor growth (Figure 3G). Correspondingly, administration of tumor-associated  $\gamma\delta$  T cells from TLR5-responsive mice (but not from *Tlr5*<sup>-/-</sup> mice) enhanced tumor growth in  $\gamma\delta$  T cell-deficient mice (Figure 3H). However, accelerated malignant progression only occurred in TLR5-responsive hosts, suggesting that intrinsic TLR5-dependent mechanisms regulate the tumor-promoting activity of  $\gamma\delta$  T cells.

An exhaustive phenotypic analysis of  $\gamma\delta$  T cells sorted from tumors and draining lymph nodes of WT and *Tlr5*<sup>-/-</sup> mice did not reveal significant differences in the levels of NKG2D, CD39/CD73, and PD-1 or in the production of IL-10, IFN $\gamma$ , PGE2, perforin, and IL-2 (Figures S2H–S2K). In contrast, as detectable by intracellular flow cytometry (Figure 3I) and ELISA (Figure 3J), tumor-associated  $\gamma\delta$  T cells from WT mice produced significantly more immunosuppressive galectin-1. Additionally, antibiotic treatment of mice also resulted in a significant reduction in galectin-1-producing  $\gamma\delta$  T cells (Figure S2L). Galectin-1 is a pleiotropic molecule that binds to surface glycoconjugates that contain *N*-acetylglucosamine sequences, promoting their crosslinking. Because of the dissimilar glycosylation pattern of different subsets of T helper and effector cells, galectin-1 exerts apoptosis and unresponsiveness on Th1, Th17, and CD8 effector T cells but enhances regulatory T cell activity (Dalotto-Moreno et al., 2013; Rubinstein et al., 2004; Toscano et al., 2007).

Interestingly, exposure of  $\gamma\delta$  T cells to granulocytic Ly6C<sup>low</sup>Ly6G<sup>+</sup> MDSCs sorted from both WT and *Tlr5*<sup>-/-</sup> tumor-bearing hosts induced a significant upregulation of galectin-1 to a greater extent than monocytic Ly6C<sup>+</sup>Ly6G<sup>-</sup> MDSCs sorted from the same hosts or Gr1<sup>+</sup>CD11b<sup>+</sup> myeloid cells sorted from the spleens of tumor-free mice, whereas control bone marrow-derived dendritic cells (BMDCs) had negligible effects (Figures 4A–4C). Transwell experiments demonstrated that this was attributable to soluble mediators (Figures 4A and 4B) that were not upregulated by IL-6 or flagellin signaling (Figure S3A). Notably, incubation of naive  $\gamma\delta$  T cells with different agonists of adenosine, generated at higher levels by granulocytic (compared with monocytic) MDSCs (Ryzhov et al., 2011) increased the proportion of galectin-1<sup>+</sup> lymphocytes, whereas IL-6, PGE2, or transforming growth factor  $\beta$  alone had no significant effect (Figure S3B). Consequently, depletion of MDSCs in sarcoma-bearing mice resulted in a significant decrease in  $\gamma\delta$  T cell-derived galectin-1 (Figure 4D), reducing the differences in the growth of tumors between *Tlr5*<sup>-/-</sup> and WT mice (Figure 4E). Together, these data indicate that MDSCs preferentially mobilized in response to TLR5-dependent, microbiota-driven inflammation and induce  $\gamma\delta$  T cells in the TME to produce immunosuppressive galectin-1 through soluble factors, including adenosine, causing accelerated tumor growth.

#### Galectin-1 Secretion Specifically by Immunosuppressive $\gamma\delta$ T Cells Is Sufficient to Accelerate Tumor Growth

As expected, tumors grew more slowly in galectin-1-deficient (*Lgals1*<sup>-/-</sup>) mice (Figures S3C and S3D). Other tumor-infiltrating cells, including MDSCs, also produced galectin-1, although

at lower levels (Figure S3E). To define whether galectin-1 specifically produced by  $\gamma\delta$  T cells contributed significantly to differential tumor growth, we generated chimeras with  $\gamma\delta$ - and galectin-1-deficient mixed bone marrow in p53/K-Ras mice, which were subsequently challenged with adenovirus-Cre to induce tumor formation. As shown in Figure 4F, tumors progressed significantly more slowly when the only  $\gamma\delta$  T cells in the host were galectin-1-deficient, without defects in the reconstitution of the  $\gamma\delta$  T cell compartment (Figure S3F). Furthermore, MPKAS tumor cells admixed with galectin-1-deficient  $\gamma\delta$  T cells from tumor-draining lymph nodes grew significantly slower than MPKAS cells admixed with galectin-1<sup>+</sup>  $\gamma\delta$  T cells derived from tumors of identical size or even MPKAS tumors alone (Figures S3G and S3H).

To determine whether galectin-1-producing, tumor-derived  $\gamma\delta$  T cells inhibit antigen-specific T cell responses,  $\gamma\delta$  T cells were again sorted from tumor-bearing hosts. As shown in Figure 4G, the antigen-specific proliferation of endogenous tumor-reactive T cells in response to BMDCs pulsed with UV light- and  $\gamma$ -irradiated (immunogenic) tumor cells was impaired significantly in the presence of  $\gamma\delta$  T cells from syngeneic and autochthonous tumor-bearing, TLR5-responsive mice, whereas  $\gamma\delta$  T cells from tumor-bearing *Tlr5*<sup>-/-</sup> hosts did not significantly inhibit proliferation. Most importantly,  $\gamma\delta$  T cells from WT tumor-bearing hosts impaired the strong proliferation of ovalbumin-specific T cells, whereas their counterparts in galectin-1-deficient mice had no suppressive effect (Figure 4H). Taken together, these data indicate that  $\gamma\delta$  T cells in TLR5-responsive, but not TLR5-deficient, tumor-bearing hosts are capable of suppressing T cell responses by secreting galectin-1, significantly contributing to malignant progression.

#### Accelerated Malignant Progression in TLR5-Competent Hosts Depends on Tumor-Derived IL-6

Our results so far indicated that TLR5 signaling at places of bacterial colonization in tumor-bearing hosts induced tumor-promoting systemic inflammation, resulting in the mobilization of MDSCs and immunosuppressive  $\gamma\delta$  T cells. To define the general applicability of these findings, WT and *Tlr5*<sup>-/-</sup> mice were challenged with multiple tumor models, and the growth was compared. TC-1 cells and ovarian cancer cell lines generated from a p53/K-ras model (Scarlett et al., 2012) grew significantly faster in TLR5-competent syngeneic mice (Figure 1I and data not shown). Unexpectedly, syngeneic A7C11 mammary tumor cells, derived from autochthonous p53/K-ras-dependent mammary carcinomas (Rutkowski et al., 2014), progressed faster in TLR5-deficient mice in multiple independent experiments (Figure 5A). Serum levels of IL-6 in this system were much lower than in tumors that progressed more rapidly in WT mice and were independent of tumor burden or TLR5 signaling (Figure 5B). Comparable results were obtained with different clones derived from autochthonous mammary tumors concurrently carrying myristoylated (constitutively activated) p110 $\alpha$  (termed BRPKP110 cells; Figure S4A). Notably, exogenous IL-6 had negligible effects on the upregulation of IL-6 in A7C11 cells (Figure 5C), although STAT3 was effectively activated (Figure S4B), and tumor cells expressed the IL-17 receptor, IL-6, receptor and gp300 (Figures S4C and S4D). In contrast, tumors that induced TLR5-dependent systemic IL-6 upregulation

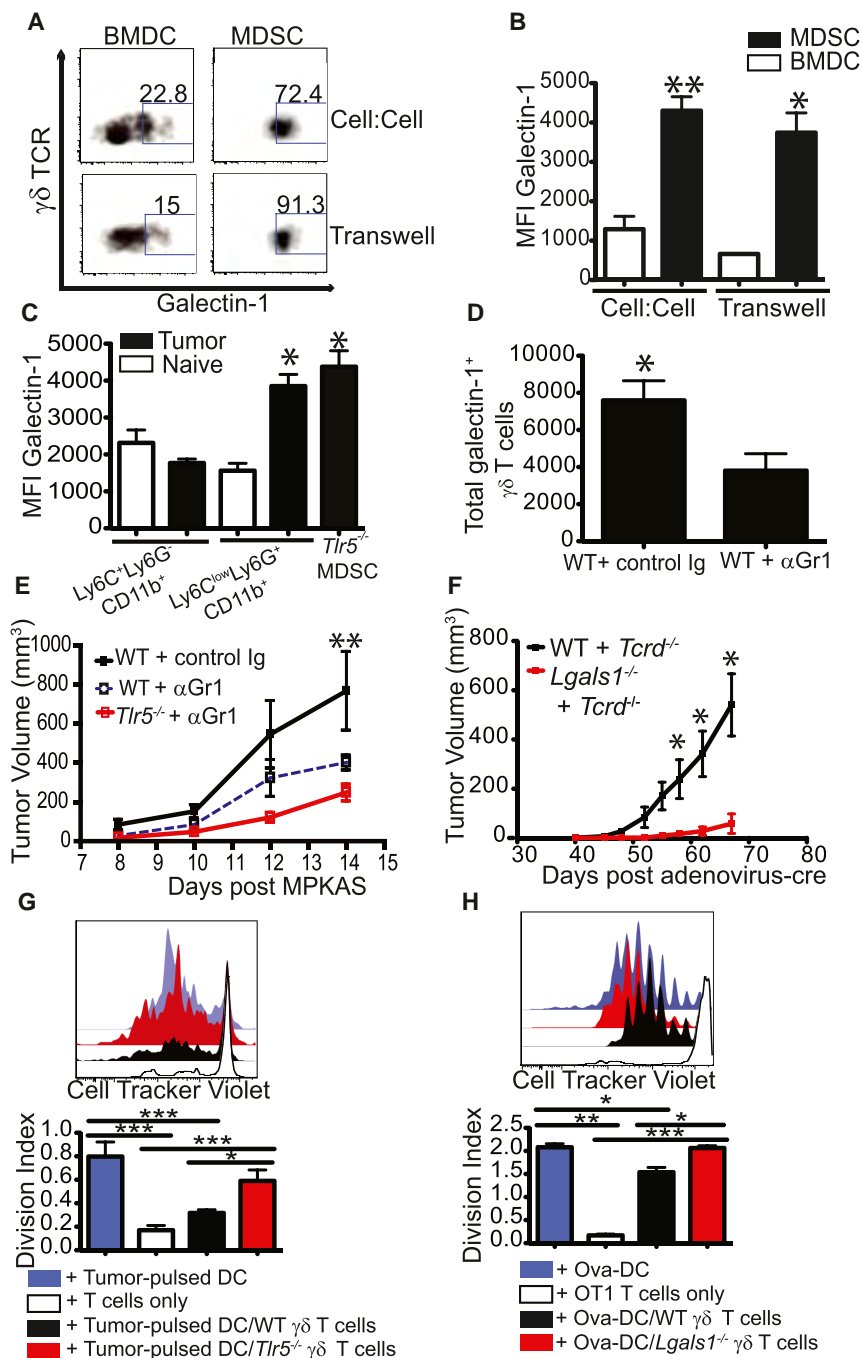


**Figure 4. Galectin-1-Producing  $\gamma\delta$  T Cells Are Sufficient to Promote Accelerated TLR5-Mediated Malignant Progression**

(A and B) Scatter plots (A) and median fluorescence intensity (MFI) (B) of intracellular galectin-1 expression of naive  $\gamma\delta$  T cells sorted from pooled axillary and inguinal lymph nodes of WT mice and incubated directly (Cell:Cell) or separated by a transwell insert (Transwell) for 5 days with MDSCs sorted from the spleens of WT mice carrying advanced autochthonous sarcomas or with bone marrow-derived dendritic cells from naive WT mice (BMDC).

(C) MFI of intracellular galectin-1 expression from naive  $\gamma\delta$  T cells cocultured with monocytic (Ly6C<sup>+</sup>Ly6G<sup>+</sup>) and granulocytic (Ly6C<sup>low</sup>Ly6G<sup>+</sup>) MDSCs from tumor-bearing WT mice or with total MDSCs from tumor-bearing *Tlr5*<sup>-/-</sup> mice. Polymorphonuclear leukocytes and monocytes were sorted from the spleens of naive WT mice as controls.

(D) Total galectin-1<sup>+</sup>  $\gamma\delta$  T cells in the draining lymph nodes of WT MPKAS tumor-bearing mice depleted of MDSCs ( $\alpha$ Gr1). Ig, immunoglobulin. (E) Representative MPKAS tumor growth curve in WT mice depleted of MDSCs.

(F) Representative tumor growth curve after reconstitution of *Trp53*<sup>flx/flx</sup>:*LSL-Kras*<sup>G12D/+</sup> mice with bone marrow from WT or *Lgals1*<sup>-/-</sup> mice admixed (1:1) with *Tcrd*<sup>-/-</sup> bone marrow, followed by tumor initiation with adenovirus-Cre.

(G and H)  $\gamma\delta$  T cells sorted from the draining lymph nodes of WT or *Tlr5*<sup>-/-</sup> mice bearing advanced autochthonous sarcomas or D14 MPKAS tumors and incubated at a 10:10:1 ratio with CellTracker Violet-labeled endogenous tumor-reactive T cells sorted from advanced sarcoma-bearing mice incubated with MPKAS-pulsed dendritic cells (G) or OT-1 T cells and BMDCs pulsed with full-length ovalbumin (Ova) (H). Proliferation of tumor-reactive T cells was measured by flow cytometric analysis five days later.

Data are representative of two independent experiments (five mice total). All data represent the mean  $\pm$  SEM. \*p < 0.05, \*\*p < 0.01, \*\*\*p < 0.001 (Mann-Whitney test). See also Figure S3.

responded to exogenous IL-6 by producing high levels of the same cytokine (Figure 5C).

Confirming the contribution of TLR5-dependent, tumor-derived IL-6 to accelerated malignant growth, silencing IL-6 secretion in MPKAS tumor cells with two different constructs resulted in significantly reduced growth of tumors in vivo, whereas no differences were observed in vitro (Figure 5D; Figures S4E–S4G). Notably, mice growing IL-6-silenced sarcomas induced significantly reduced serum IL-6 levels compared with scrambled small hairpin RNA (shRNA)-expressing controls

MDSCs (Figure S4H). As a result, a significant increase in the accumulation of IFN $\gamma$ -producing CD8 T cells was observed in these tumors (Figure 5H; Figure S4I). Leukocyte-derived IL-6 also contributed to the systemic overexpression of IL-6 because reconstitution of mice with IL-6-deficient bone marrow resulted in a dramatic decrease in tumor growth (Figure 5I) and was associated with decreased galectin-1<sup>+</sup>  $\gamma\delta$  T cells (Figure S4J). Correspondingly, accelerated malignant progression in TLR5-responsive hosts was completely abrogated upon IL-6 neutralization (Figure 5J). Together, these results demonstrate that



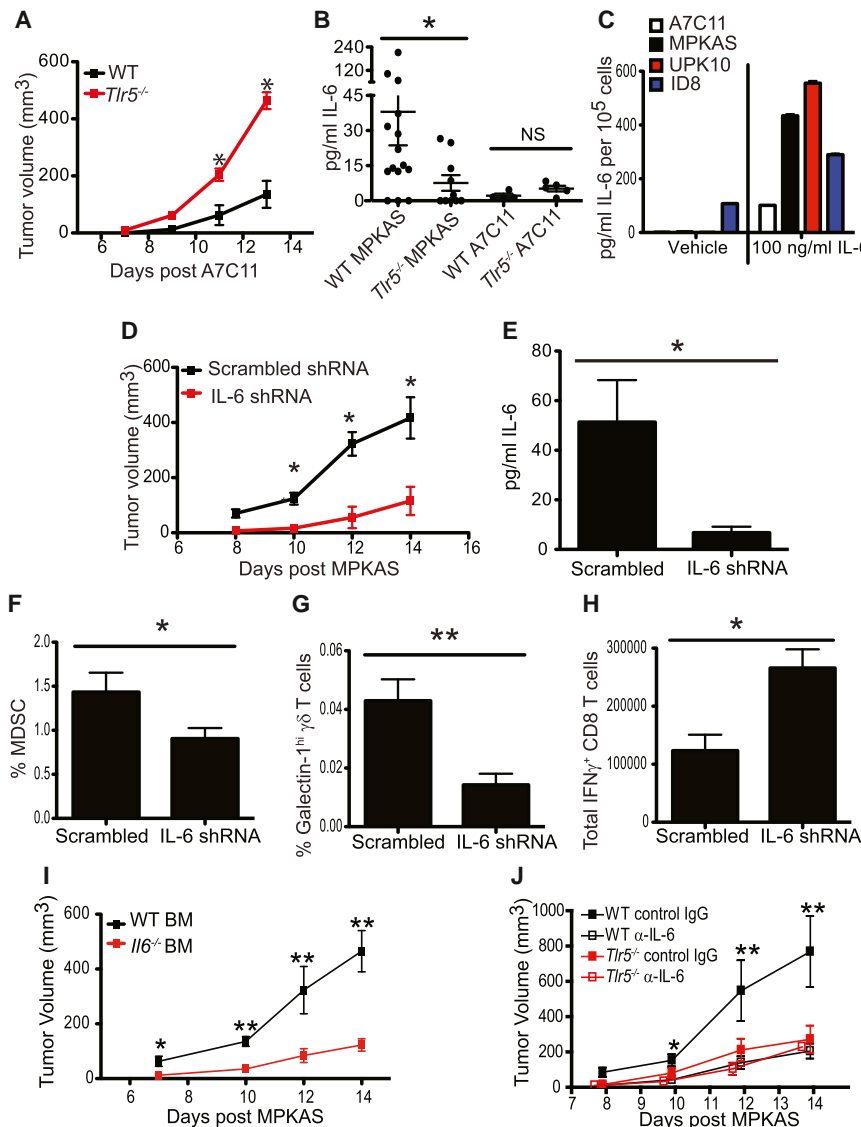


**Figure 5. Tumor- and Leukocyte-Derived IL-6 Drives Tumor Growth in TLR5-Responsive Mice**

(A) Growth kinetics of the mammary tumor cell line A7C11 in WT or *Tlr5*<sup>-/-</sup> mice.

(B) Serum IL-6 level of WT or *Tlr5*<sup>-/-</sup> mice bearing advanced A7C11 (days 14–16) tumors.

(C) ELISA quantification of IL-6 production by the indicated tumor cell lines 72 hr after overnight incubation with 100 ng/ml recombinant mouse IL-6 followed by washing of wells and the addition of fresh media.

(D) Growth kinetics of MPKAS expressing IL-6 shRNA or scrambled shRNA in WT mice.

(E) Serum levels of IL-6 in WT mice 14 days after injection with MPKAS expressing IL-6 shRNA or scrambled control. Shown is one representative of two independent experiments (eight mice per group total).

(F–H) Proportions of tumor-associated Gr1<sup>+</sup> CD11b<sup>+</sup> MDSCs (F), galectin-1-producing  $\gamma\delta$  T cells (G), and IFN $\gamma$ -producing CD8 T cells (H) from dissociated tumors (F) and tumor-draining lymph-nodes (G and H) 14 days after injection of WT mice with MPKAS tumor cell lines expressing IL-6 shRNA or scrambled shRNA.

(I) Tumor kinetics of WT mice reconstituted with IL-6-deficient (*Il6*<sup>-/-</sup>) or WT bone marrow (BM) followed by challenge with the MPKAS tumor cell line.

(J) Tumor kinetics of WT or *Tlr5*<sup>-/-</sup> mice administered IL-6 neutralizing antibody ( $\alpha$ -IL-6) or isotype control IgG challenged with MPKAS tumors.

All data represent the mean  $\pm$  SEM. \**p* < 0.05, \*\**p* < 0.01, \*\*\**p* < 0.001, NS, not significant (Mann Whitney test). See also Figure S4.

both tumor- and leukocyte-derived IL-6 contribute to accelerate the progression of IL-6-responsive tumors in TLR5-sufficient hosts.

#### IL-17 Secreted through Interactions with Commensal Bacteria Accelerates Malignant Progression Only in IL-6-Unresponsive Tumors

These results suggest that only IL-6-responsive tumors undergo TLR5-dependent accelerated growth, whereas IL-6-unresponsive tumors rely on other signals. Supporting this proposition, TLR5-deficient mice with advanced A7C11 tumors had significantly higher serum levels of IL-17 compared with WT tumor-bearing mice (Figure 6A). Increased systemic IL-17 was also observed in TLR5-deficient mice growing orthotopic ovarian cancer (Figure S5A) and MPKAS and autochthonous p53/K-ras-dependent flank tumors (Figures 6B and 6C). Despite increased systemic levels of IL-17 in *Tlr5*<sup>-/-</sup> tumor-bearing mice, we found only minor differences in the ratio of tumor-infil-

trating IL-17<sup>+</sup> cells, which included CD4 and  $\gamma\delta$  T cells in similar proportions (Figures S5B and S5C).

To define the contribution of IL-17 to accelerated tumor progression in TLR5-deficient hosts, we neutralized IL-17 in A7C11 tumor-challenged *Tlr5*<sup>-/-</sup> and WT littermates. Blockade of IL-17 abrogated differences in the progression of these tumors in WT versus *Tlr5*<sup>-/-</sup> hosts, resulting in a significant reduction of tumor burden and growth kinetics in *Tlr5*<sup>-/-</sup> mice (Figure 6D; Figure S5D). In contrast, IL-17 neutralization had no effect in the progression of IL-6-dependent MPKAS tumors (Figure 6E; Figure S5E). Remarkably, silencing IL-6 production in the same tumor cells was sufficient to render sarcomas sensitive to the tumor-promoting activity of IL-17 because IL-17 blockade reduced malignant progression in otherwise identical tumors transduced with IL-6-shRNA (Figure 6F). Consistent with the elevation of systemic IL-17 in all *Tlr5*<sup>-/-</sup> tumor-bearing mice, IL-6 silencing in MPKAS sarcomas was sufficient to reverse the effects of TLR5 signaling on malignant evolution because the same tumors that previously grew faster in WT hosts started progressing more rapidly in *Tlr5*<sup>-/-</sup> mice when IL-6 was silenced (Figure 6G). Therefore, although IL-6 is systemically upregulated in IL-6-responsive tumors through TLR5 signaling and typically

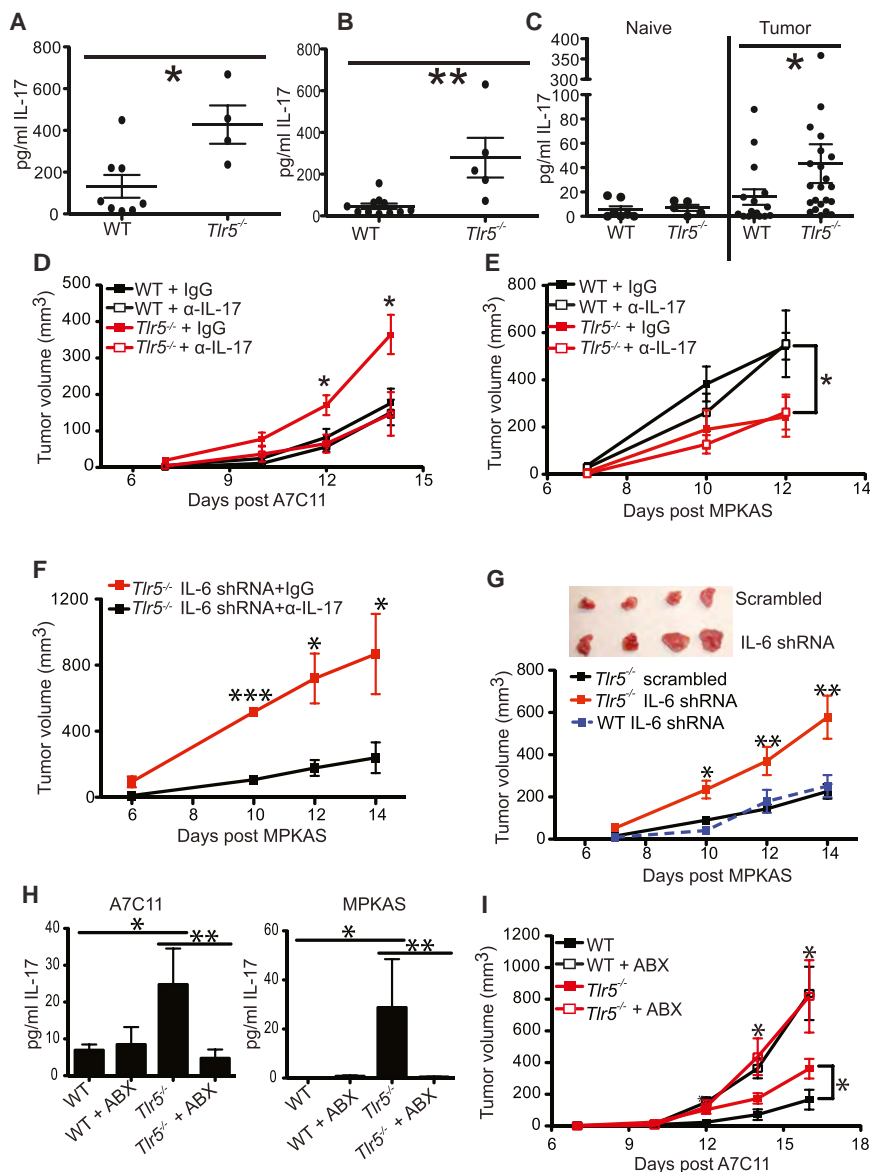


**Figure 6. Tumor Growth for IL-6-Unresponsive Tumors Is Mediated by IL-17 Induced by Interactions with Commensal Microbiota**

(A–C) Serum levels of IL-17 from WT or *Tlr5*<sup>-/-</sup> mice bearing advanced A7C11 mammary tumors (A), advanced MPKAS tumors (B), or advanced autochthonous sarcomas from naive controls (C). (D) A7C11 growth kinetics in WT and *Tlr5*<sup>-/-</sup> mice administered IL-17 neutralizing antibody ( $\alpha$ -IL-17) or IgG control (IgG).

(E) MPKAS tumor kinetics in WT or *Tlr5*<sup>-/-</sup> mice treated with  $\alpha$ -IL-17 or IgG.

(F) Growth kinetics of MPKAS tumors expressing IL-6 shRNA or scrambled shRNA in *Tlr5*<sup>-/-</sup> mice administered  $\alpha$ -IL-17 or IgG.

(G) Growth kinetics of MPKAS expressing IL-6 shRNA or scrambled shRNA in *Tlr5*<sup>-/-</sup> and WT mice and representative resected tumors from *Tlr5*<sup>-/-</sup> mice.

(H) Serum levels of IL-17 in ABX or vehicle-treated MPKAS or A7C11 tumor-bearing mice 14 days (MPKAS) or 16 days (A7C11) after tumor initiation. (I) Growth kinetics of A7C11 tumors from WT and *Tlr5*<sup>-/-</sup> mice treated with ABX or vehicle.

All data are representative of at least two repetitions with at least four animals per group. All data represent the mean  $\pm$  SEM. \**p* < 0.05, \*\**p* < 0.01, \*\*\**p* < 0.001 using Mann-Whitney test. See also Figure S5.

macro- and microenvironments are controlled by the commensal microbiota and influence malignant progression.

### TLR5-Deficient Breast Cancer Patients Show Accelerated Malignant Progression and Upregulation of IL-17 in the TME

To substantiate the relevance of our mechanistic observations, we first confirmed that CD45<sup>+</sup>CD14<sup>+</sup> myeloid leukocytes sorted from freshly dissociated human ovarian tumors of three *TLR5*<sup>R392X</sup> heterozygous carriers showed negligible

dominates tumor-promoting inflammation in TLR5-competent hosts, IL-17 accelerates malignant progression in IL-6-unresponsive tumors. Because IL-17 is systemically higher in TLR5-deficient, tumor-bearing hosts, the progression of tumors associated with relatively low levels of IL-6 is accelerated.

Notably, antibiotic depletion of commensal bacteria also induced a significant decrease in serum IL-17 levels and, correspondingly, reduced IL-17 producing cells in the draining lymph nodes of *Tlr5*<sup>-/-</sup> tumor-bearing mice (Figure 6H; Figure S5F), resulting in the complete abrogation of differences in tumor progression between *Tlr5*<sup>-/-</sup> and WT littermates (Figure 6I; Figure S5G). Together, these results indicate that the balance of IL-6 and IL-17 influence the outcome of malignant progression. Because IL-17 is overproduced in TLR5-deficient, tumor-bearing individuals, in the absence of IL-6, this cytokine predominately drives tumor-promoting inflammation. These results demonstrate that both IL-6- and IL-17-driven inflammatory

induction of IL-8 transcript levels in response to flagellin compared with the same cell population sorted from three patients homozygous for the ancestral allele (Figure 7A). These results corroborate previous reports demonstrating that *TLR5*<sup>R392X</sup> carriers are functionally unable to respond to bacterial flagellin (Gewirtz et al., 2006; Hawn et al., 2003). Most importantly, a survival analysis performed from fully or partially sequenced samples of estrogen receptor-positive (ER<sup>+</sup>) breast cancer patients from The Cancer Genome Atlas (TCGA) data sets identified a significantly poorer outcome for carriers of the *TLR5*<sup>R392X</sup> allele compared with patients homozygous for the ancestral *TLR5* allele (Figure 7B).

Supporting the relevance of our observations in murine tumor models, IL-17A transcript levels in our ER<sup>+</sup> breast cancer and ovarian carcinoma specimens were also significantly higher in *TLR5*<sup>R392X</sup> carriers compared with control patients homozygous for the ancestral allele (Figure 7C). Both  $\gamma\delta$  and  $\alpha\beta$  (CD3<sup>+</sup> $\gamma\delta$  TCR<sup>+</sup>)

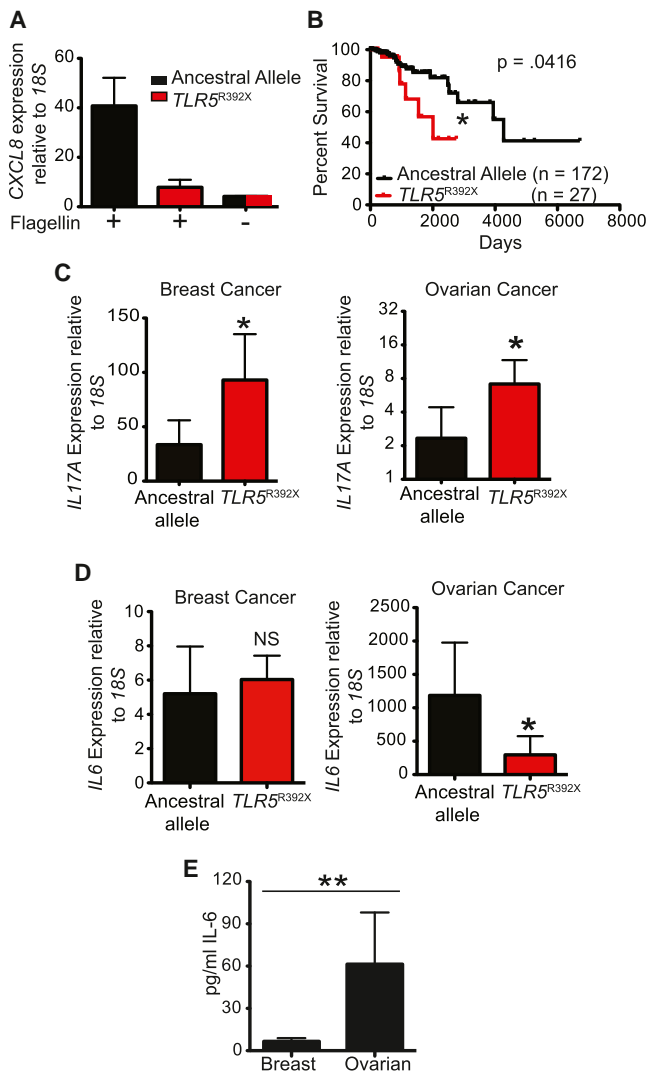


**Figure 7. TLR5-Deficient Patients Diagnosed with Breast Cancer Have Accelerated Malignant Progression and Increased Intratumoral IL-17 Levels**

(A) CXCL8 transcript levels in CD14<sup>+</sup>CD45<sup>+</sup> myeloid cells sorted from three heterozygous *TLR5<sup>R392X</sup>* or three TLR5-responsive advanced ovarian tumors and incubated with 500 ng/ml of flagellin for 72 hr. CXCL8 transcript levels were calculated relative to 18S expression.

(B) Survival analysis of TCGA data sets for ER<sup>+</sup> breast cancer. Differences in overall survival were calculated with log rank.

(C and D) Quantification of *IL17A* (C) or *IL6* (D) transcripts relative to 18S expression in nine frozen ER<sup>+</sup> breast tumor specimens from *TLR5<sup>R392X</sup>* carriers,  $\geq 10$  randomly selected ER<sup>+</sup> breast tumors from patients homozygous for the ancestral allele, five to six stage III/IV ovarian carcinoma specimens from *TLR5<sup>R392X</sup>* carriers, and  $\geq 15$  randomly selected ovarian carcinoma specimens homozygous for the ancestral allele.

(E) Serum IL-6 levels in patients homozygous for the ancestral allele of *TLR5* diagnosed with ER<sup>+</sup> breast carcinoma versus ovarian carcinoma.

All data represent the mean  $\pm$  SEM. \*p < 0.05, \*\*p < 0.01, \*\*\*p < 0.001 (Mann-Whitney test). See also Figure S6.

T cells contributed to IL-17 production in breast and ovarian tumors (Figures S6A and S6B). However, significant differences in IL-6 transcript levels were only observed between TLR5-

responsive and nonresponsive ovarian tumor specimens but not between TLR5-responsive and nonresponsive ER<sup>+</sup> breast tumor specimens (Figure 7D), further supporting the contribution of tumor-derived IL-6 to differences in overall tumor-promoting inflammation. Additionally, we found much lower levels of circulating IL-6 in 20 available serum samples from ER<sup>+</sup> breast cancer patients compared with sera from 12 available ovarian cancer patients (all of them TLR5-responsive; Figure 7E). These data further support the fact that, in hosts where TLR5-dependent IL-6 does not dominate systemic tumor-promoting inflammatory responses through dramatic systemic upregulation, tumors grow faster in the presence of IL-17 overexpression, which is higher in the absence of TLR5 signaling. Together, these studies demonstrate that a common genetic polymorphism, present in >7% of individuals in the general population (Hawn et al., 2003), influences systemic inflammatory responses and determines the outcome of breast cancer patients.

#### Higher Proportions of Long-Term Survivors among TLR5-Defective Ovarian Cancer Patients

To further investigate the link between IL-6 upregulation and accelerated tumor progression in the presence of TLR5 signaling, we next analyzed ovarian cancer TCGA data sets. A total number of 25 *TLR5<sup>R392X</sup>* patients with outcome and deep sequencing information was insufficient to identify significant differences in overall survival compared with homozygous carriers of the ancestral allele. However, the proportion of long-term survivors ( $\geq 6$  years after the ovarian cancer diagnosis) was significantly higher among *TLR5<sup>R392X</sup>* carriers (but not carriers of other nonfunctional polymorphisms; Figures 8A and 8B), indicating that, as in our orthotopic ovarian preclinical model, TLR5 signaling drives accelerated malignant progression in ovarian cancer.

As in our murine models, the expression of immunosuppressive galectin-1 was significantly higher in TLR5-responsive ovarian cancer patients from our tumor bank, at both transcript and protein levels (Figures 8C and 8D). Furthermore, we found that, in multiple samples, CD3<sup>+</sup>CD4<sup>+</sup>CD8<sup>+</sup>  $\gamma\delta$  T cells outnumbered Foxp3<sup>+</sup> regulatory T cells in the ovarian cancer microenvironment, representing up to ~6% of tumor-infiltrating lymphocytes, as detected by histology (Figure 8E and data not shown) and flow cytometry (Figure 8F). At least 20% of ovarian cancer-infiltrating  $\gamma\delta$  T cells, which predominantly represent peripheral blood-derived V $\gamma$ 9<sup>+</sup> lymphocytes, produced significant levels of galectin-1 (Figure 8F). Further supporting the relevance of our observations on the mechanistic role of  $\gamma\delta$  T cells in the TME, tumors from patients carrying *TLR5<sup>R392X</sup>* contained a significantly lower number of galectin-1-producing  $\gamma\delta$  T cells (Figure 8G) compared with patients homozygous for the ancestral allele. In addition,  $\gamma\delta$  T cells in tumors from TLR5-responsive patients had significantly higher levels of intracellular galectin-1 on a per-cell basis (Figure 8H) and at significantly higher levels than in tumor-associated MDSCs (Figures S7A and S7B). Nevertheless, higher proportions of galectin-1<sup>+</sup> myeloid leukocytes were also found in dissociated tumors from patients with the ancestral TLR5 allele (Figure S7C). Therefore, supporting the relevance of our preclinical models, these findings reveal that a frequent polymorphism abrogating TLR5 responses to flagellin profoundly

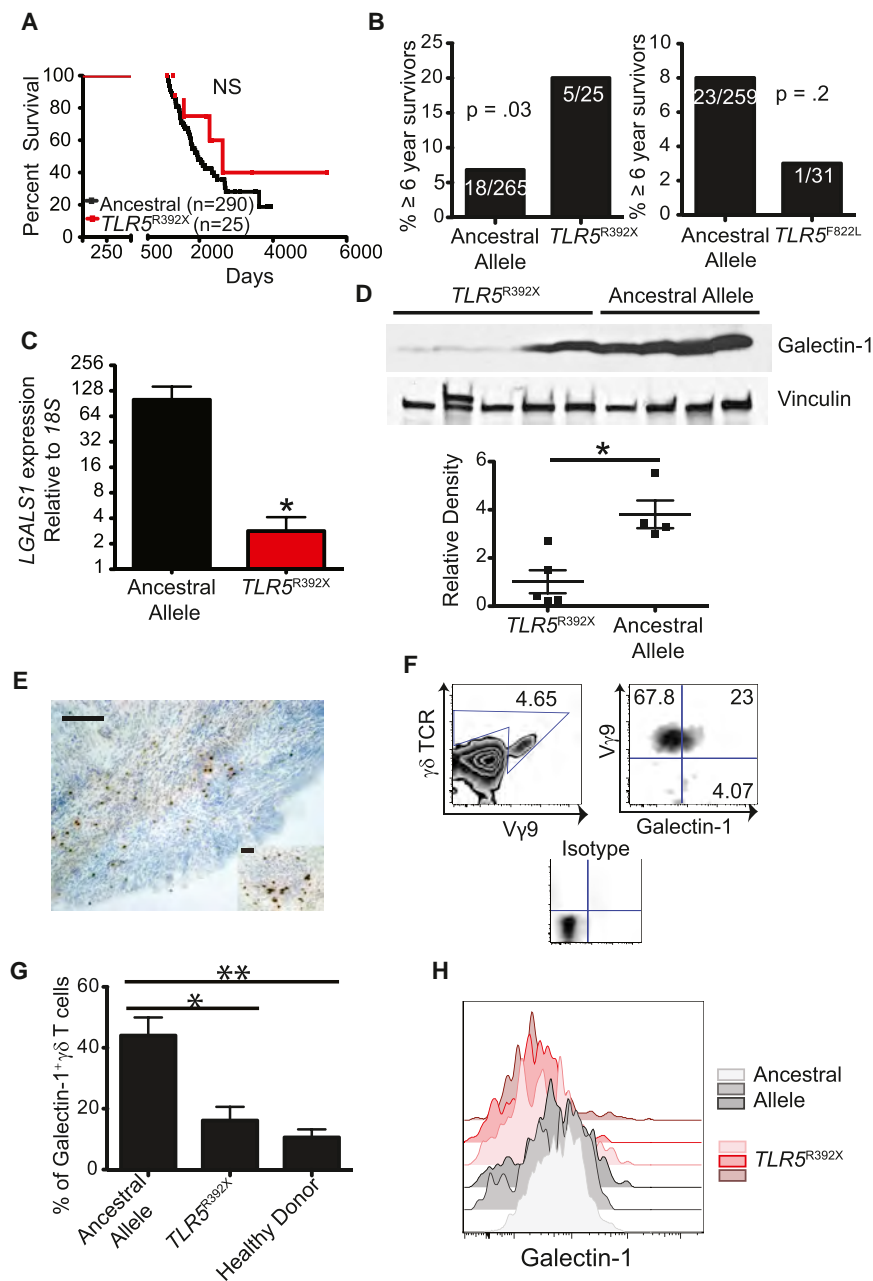


**Figure 8. Higher Proportions of Long-Term Survivors and Decreased Galectin-1 Expression Are Found in TLR5-Deficient Patients Diagnosed with Ovarian Cancer**

(A) Survival analysis of TCGA data sets for ovarian cancer. The difference was calculated with log rank.

(B) Fisher's exact test of the proportions of ovarian cancer patients surviving longer than or equal to 6 years after initial diagnosis with or without the *TLR5*<sup>R392X</sup> polymorphism or with or without the nondeleterious *TLR5*<sup>F822L</sup> polymorphism.

(C) Transcript levels of *LGALS1* relative to *18S* levels from six ovarian tumor samples with *TLR5*<sup>R392X</sup> and 91 randomly selected ovarian tumor samples homozygous for the ancestral allele of *TLR5*.

(D) Galectin-1 protein expression of 5 *TLR5*<sup>R392X</sup> ovarian tumor samples and four randomly selected ovarian tumor samples from patients homozygous for the ancestral allele of *TLR5*. Shown is a corresponding densitometric analysis of band intensities for galectin-1 normalized to vinculin.

(E)  $\gamma\delta$  T cell immunohistochemistry from a frozen ovarian tumor specimen homozygous for the *TLR5* ancestral allele. Scale bars, 100  $\mu$ m.

(F) Representative gating strategy for flow cytometric analysis of galectin-1-expressing, tumor-infiltrating  $\gamma\delta$  T cells. Numbers represent the proportions of live cells gated from CD45<sup>+</sup>CD3<sup>+</sup> $\gamma\delta$  TCR<sup>+</sup> tumor-associated microenvironmental leukocytes compared with the isotype control.

(G) Frequency of galectin-1-producing  $\gamma\delta$  T cells in the ovarian cancer microenvironment from three ovarian tumors from *TLR5*<sup>R392X</sup> carriers, PBMCs from four healthy donors, and 12 randomly selected ovarian tumor samples from patients homozygous for the ancestral allele.

(H) Histogram of galectin-1 expression from tumor-associated  $\gamma\delta$  T cells from the three available disassociated ovarian tumor samples from *TLR5*<sup>R392X</sup> carriers and three randomly selected ovarian tumor samples from patients homozygous for the ancestral allele of *TLR5*.

All data represent the mean  $\pm$  SEM. \*p < 0.05, \*\*p < 0.01, \*\*\*p < 0.001 (Mann-Whitney test). See also Figure S7.

influences the inflammation orchestrated by extraintestinal tumors and, subsequently, their clinical progression.

## DISCUSSION

Our study demonstrates that TLR5 recognition of commensal microbiota regulates systemic tumor-promoting inflammation and, subsequently, extramucosal malignant progression. In some tumors, TLR5 signaling drives the systemic upregulation of IL-6, promoting MDSC mobilization, induction of suppressive galectin-1-producing  $\gamma\delta$  T cells and, subsequently, accelerated tumor growth. Accordingly, most tumors tested progressed significantly more slowly in TLR5-deficient individuals. In

contrast, IL-17 is commonly upregulated in TLR5-deficient, tumor-bearing hosts but only drives accelerated tumor growth in systems where tumor cells are poorly responsive to IL-6. Any differences in malignant evolution are completely abrogated following depletion of commensal bacteria.

Interestingly, TLR5-dependent increased systemic IL-6 is triggered during tumor initiation because it does not occur in tumor-free hosts. TLR5-dependent tumor growth appears to require IL-6 production by both hematopoietic and tumor cells because only IL-6-responsive tumor models are able to induce IL-6-driven MDSC mobilization and subsequent accelerated tumor progression compared with TLR5-nonresponsive animals. Accordingly, knockdown of IL-6 in IL-6-responsive tumor cell



lines significantly diminishes *in vivo* tumor growth in TLR5-responsive mice, which is associated with decreased serum IL-6 and, subsequently, reduced mobilization of MDSCs and diminished production of galectin-1 by  $\gamma\delta$  T cells. Supporting the crucial role of IL-6 in tumor-promoting inflammation, in luminal (although not in triple-negative) breast tumors, where systemic IL-6 is significantly lower (e.g., compared with ovarian cancer patients) (Casanova et al., 2011), tumors grow faster in TLR5-defective individuals because IL-17 overexpressed in the TME drives tumor-promoting inflammation. The role of IL-17 during tumor progression remains controversial because it has a clear protective role during ovarian cancer progression but is associated with malignant promotion in other tumors, such as breast cancer (Kryczek et al., 2009; Wang et al., 2009). In our preclinical models, IL-17 neutralization delayed tumor growth only when IL-6 was systemically low but had no effect on tumors that progress faster in TLR5-responsive individuals in an IL-6-dependent manner. Of note, silencing IL-6 was sufficient to transform IL-6-dependent, IL-17-insensitive tumors that grow faster in TLR5-responsive hosts into tumors that become sensitive to IL-17 neutralization and progress faster in TLR5-deficient individuals. The effects of other inflammatory cytokines, therefore, add another layer of complexity to the role of IL-17 in cancer and provide an understanding for its conflicting activities. Most importantly, all differences in tumor-promoting inflammation and malignant progression are eliminated upon depletion of the microbiota. We identified TLR5-dependent microbiome-wide differences in the repertoire of commensal bacteria that persisted after cohousing mice in the same cage. The composition of the microbiota is therefore different in the absence of TLR5 signaling, and this influences tumor-promoting inflammation.

Our results also underscore the contribution of  $\gamma\delta$  T cells to immunosuppression in multiple tumors, including ovarian cancer. Although the regulatory activity of  $\gamma\delta$  T cells in breast cancer has been reported (Peng et al., 2007), the mediators of effector T cell suppression remained elusive. We demonstrate that bulk populations of galectin-1-secreting  $\gamma\delta$  T cells suppress T cell responses to potent antigens *in vitro* and that galectin-1 specifically produced by tumor-derived  $\gamma\delta$  T cells is sufficient to accelerate tumor growth *in vivo*. Galectin-1 has emerged as a crucial driver of immunosuppression in multiple tumors (Rabinovich and Croci, 2012). Secreted galectin-1 crosslinks cell surface glycoconjugates bearing multiple units of the *N*-acetyllactosamine (Gal $\beta$ 1-4-NAcGlc) disaccharide and selectively blunts Th1, Th17, and CD8 effector T cell responses (Rubinstein et al., 2004). Our study identifies  $\gamma\delta$  T cells as a relevant source of this tolerogenic factor in the TME.

Finally, the most significant conclusion of our study is that frequent polymorphisms that abrogate TLR5 activity are associated with the outcomes of cancer patients. TLR5-dependent differences in survival are particularly striking for ER<sup>+</sup> patients, for whom a TLR5 deficiency is associated with accelerated malignant progression. In contrast, in ovarian cancer patients who have higher serum IL-6, TLR5 signaling has a negative effect on the proportion of long-term survivors. Because at least 30% of individuals in the general population are carriers of a limited set of polymorphisms in multiple pattern recognition receptor genes that could also influence tumor-promoting inflammation

(Casanova et al., 2011; Hugot et al., 2007), our study opens avenues for understanding how differential inflammatory responses and, subsequently, dissimilar malignant progression takes place in many cancer patients. Our work also provides a rationale for manipulating the microbiota through antibiotic treatment to modulate tumor-promoting inflammation.

## EXPERIMENTAL PROCEDURES

### Mice

Transgenic *Kras*<sup>tm4Tyj</sup> and *Trp53*<sup>tm1Brn</sup> mice (Jackson et al., 2001; Jonkers et al., 2001) were obtained from the National Cancer Institute (NCI) Mouse Models of Human Cancers Consortium, brought to a full C57BL/6 background (Scarlett et al., 2012), and bred to TLR5-deficient (*Tlr5*<sup>-/-</sup>) mice (B6.129S1-*Tlr5*<sup>tm1Flv/J</sup>) (Cubillos-Ruiz et al., 2009). Galectin-1-deficient (*Lgals1*<sup>-/-</sup>) mice were provided by G.A. Rabinovich at the Instituto de Biología y Medicina Experimental (IBYME-CONICET) Argentina and were originally generated by F. Poirier (Jacques Monod Institut).  $\gamma\delta$  T cell-deficient mice *Tcrd*<sup>-/-</sup> mice (B6.129P2-*Tcrd*<sup>tm1Mom/J</sup>) were obtained from The Jackson Laboratory and bred to *Tlr5*<sup>-/-</sup> mice. WT C57BL/6 mice were obtained from the NCI. OT1 C57BL/6-Tg (*Tcr* $\alpha$ *Tcrb*)1100Mjb/J and IL-6-deficient (B6.129S2-*Il6*<sup>tm1kop/J</sup>) transgenic mice were obtained from The Jackson Laboratory. All animals were maintained in pathogen-free barrier facilities. All experiments were conducted according to the approval of the Institutional Animal Care and Use Committee of the Wistar Institute.

### Genetic Tumor Models and Cell Lines

Autochthonous p53/*Kras* flank sarcomas were initiated by subcutaneous delivery of  $2.5 \times 10^8$  plaque-forming units of adenovirus-cre (Gene Transfer Vector Core, University of Iowa) into transgenic mice. For the mixed bone marrow chimeras, transgenic mice were irradiated for two consecutive days with 650 rads, followed by reconstitution with WT or *Lgals1*<sup>-/-</sup> bone marrow mixed at a 1:1 ratio with *Tcrd*<sup>-/-</sup> bone marrow. Flank tumors were initiated in reconstituted animals 6 weeks following engraftment. ID8 cells were provided by K. Roby (Department of Anatomy and Cell Biology, University of Kansas) and retrovirally transduced to express *Defb29* and *Vegf-a* (Conejo-Garcia et al., 2004). MPKAS cells were generated from passaging sorted tumor cells (CD45-negative) derived from mechanically dissociated autochthonous p53/*Kras* axillary sarcomas. Mouse ovarian tumor UPK10 cells were generated by culturing a mechanically dissociated p53/*Kras* primary ovarian tumor mass (Scarlett et al., 2012). The A7C11 and BRPKP110 primary mammary tumor cell lines were generated by passaging sorted tumor cells from mechanically dissociated p53/*Kras* (A7C11) or p53/*Kras*/myristoylated p110 $\alpha$  (BRPKP110) mammary carcinomas (Rutkowski et al., 2014). Flank tumors with MPKAS- or MPKAS shRNA-expressing clones ( $1 \times 10^5$  cells), UPK10, and ID8-*Vegf-Defb29* ( $10^6$ ) were admixed at a 1:1 ratio with growth factor-reduced Matrigel (BD Biosciences) and injected into the axillary flank. A7C11 tumors were initiated by injecting  $2 \times 10^4$  cells into the axillary flank. Intraperitoneal ID8-*Vegf-Defb29* tumors were initiated by intraperitoneal injection of  $2 \times 10^6$  cells. The tumor volume was calculated as:  $0.5 \times (L \times W^2)$ , where L is length, and W is width.

### Human Specimens

Human ovarian carcinoma tissues were procured under a protocol approved by the Committee for the Protection of Human Subjects at Dartmouth-Hitchcock Medical Center (#17702) and under a protocol approved by the Institutional Review Board at Christiana Care Health System (#32214) and the Institutional Review Board of The Wistar Institute (#21212263). Human breast tumor tissues and sera were obtained under a protocol approved by the Institutional Review Board of the University of Pennsylvania (#805139) and the Institutional Review Board of The Wistar Institute (#21204259). Informed consent was obtained from all subjects.

### ACCESSION NUMBERS

Deep sequencing analysis of the microbiota is available in the Sequence Read Archive (SRA) database (<http://www.ncbi.nlm.nih.gov/sra>) under the accession number SRP045910.

## SUPPLEMENTAL INFORMATION

Supplemental Information includes Supplemental Experimental Procedures and seven figures and can be found with this article online at <http://dx.doi.org/10.1016/j.ccell.2014.11.009>.

## AUTHOR CONTRIBUTIONS

M.R.R. designed, performed, and analyzed most experiments and cowrote the manuscript. T.L.S. provided intellectual and technical support and characterized clinical specimens. N.S. performed immunohistochemistry and contributed to the design of in vitro experiments. M.J.A., A.P.P., E.B., and A.J.T. contributed to the design of in vivo experiments and performed in vitro experiments. X.E.F. performed the identification of R392X carriers. J.N. processed and stored clinical specimens. M.G.C. and J.T. provided clinical specimens and expertise. R.Z. provided intellectual support and helped to interpret experimental results. G.A.R. and M.S. provided expertise in the biology of galectin-1 and the KO model and helped with writing the manuscript and interpreting experiments. J.R.C.G. oversaw and designed the study and experiments, analyzed data, and cowrote the manuscript.

## ACKNOWLEDGMENTS

Support for shared resources was provided by Cancer Center Support Grant CA010815 (to The Wistar Institute). We thank P. Wickramasinghe for outstanding bioinformatical analysis, C. Huangci for technical support, and Dr. F. Bushman and A. Bailey (UPenn Viral/Molecular Core) for the analysis of microbiota. This study was supported by Grants R01CA157664, R01CA124515, R01CA178687, U54CA151662, and P30CA10815 and by Breast Cancer Alliance and Ovarian Cancer Research Fund Program Project Development awards. M.J.A. and N.S. were supported by Grant T32CA009171. A.P.P. was supported by the Fundación Alfonso Martín Escudero. A.J.T. was a nested Teal Scholar in Department of Defense Grant OC100059.

Received: April 25, 2014

Revised: August 29, 2014

Accepted: November 8, 2014

Published: December 18, 2014

## REFERENCES

- Abt, M.C., Osborne, L.C., Monticelli, L.A., Doering, T.A., Alenghat, T., Sonnenberg, G.F., Paley, M.A., Antenus, M., Williams, K.L., Erikson, J., et al. (2012). Commensal bacteria calibrate the activation threshold of innate antiviral immunity. *Immunity* 37, 158–170.
- Casanova, J.L., Abel, L., and Quintana-Murci, L. (2011). Human TLRs and IL-1Rs in host defense: natural insights from evolutionary, epidemiological, and clinical genetics. *Annu. Rev. Immunol.* 29, 447–491.
- Clarke, T.B., Davis, K.M., Lysenko, E.S., Zhou, A.Y., Yu, Y., and Weiser, J.N. (2010). Recognition of peptidoglycan from the microbiota by Nod1 enhances systemic innate immunity. *Nat. Med.* 16, 228–231.
- Conejo-Garcia, J.R., Benencia, F., Courreges, M.C., Kang, E., Mohamed-Hadley, A., Buckanovich, R.J., Holtz, D.O., Jenkins, A., Na, H., Zhang, L., et al. (2004). Tumor-infiltrating dendritic cell precursors recruited by a beta-defensin contribute to vasculogenesis under the influence of Vegf-A. *Nat. Med.* 10, 950–958.
- Cubillos-Ruiz, J.R., Engle, X., Scarlett, U.K., Martinez, D., Barber, A., Elgueta, R., Wang, L., Nesbeth, Y., Durant, Y., Gewirtz, A.T., et al. (2009). Polyethylenimine-based siRNA nanocomplexes reprogram tumor-associated dendritic cells via TLR5 to elicit therapeutic antitumor immunity. *J. Clin. Invest.* 119, 2231–2244.
- Dalotto-Moreno, T., Croci, D.O., Cerliani, J.P., Martinez-Allo, V.C., Dergan-Dylon, S., Méndez-Huergo, S.P., Stupirski, J.C., Mazal, D., Osinaga, E., Toscano, M.A., et al. (2013). Targeting galectin-1 overcomes breast cancer-associated immunosuppression and prevents metastatic disease. *Cancer Res.* 73, 1107–1117.
- Gewirtz, A.T., Vijay-Kumar, M., Brant, S.R., Duerr, R.H., Nicolae, D.L., and Cho, J.H. (2006). Dominant-negative TLR5 polymorphism reduces adaptive immune response to flagellin and negatively associates with Crohn's disease. *Am. J. Physiol. Gastrointest. Liver Physiol.* 290, G1157–G1163.
- Hawn, T.R., Verbon, A., Lettinga, K.D., Zhao, L.P., Li, S.S., Laws, R.J., Skerrett, S.J., Beutler, B., Schroeder, L., Nachman, A., et al. (2003). A common dominant TLR5 stop codon polymorphism abolishes flagellin signaling and is associated with susceptibility to legionnaires' disease. *J. Exp. Med.* 198, 1563–1572.
- Hawn, T.R., Scholes, D., Li, S.S., Wang, H., Yang, Y., Roberts, P.L., Stapleton, A.E., Janer, M., Aderem, A., Stamm, W.E., et al. (2009). Toll-like receptor polymorphisms and susceptibility to urinary tract infections in adult women. *PLoS ONE* 4, e5990.
- Hugot, J.P., Zaccaria, I., Cavanaugh, J., Yang, H., Vermeire, S., Lappalainen, M., Schreiber, S., Annese, V., Jewell, D.P., Fowler, E.V., et al.; IBD International Genetics Consortium (2007). Prevalence of CARD15/NOD2 mutations in Caucasian healthy people. *Am. J. Gastroenterol.* 102, 1259–1267.
- Iida, N., Dzutsev, A., Stewart, C.A., Smith, L., Bouladoux, N., Weingarten, R.A., Molina, D.A., Salcedo, R., Back, T., Cramer, S., et al. (2013). Commensal bacteria control cancer response to therapy by modulating the tumor micro-environment. *Science* 342, 967–970.
- Jackson, E.L., Willis, N., Mercer, K., Bronson, R.T., Crowley, D., Montoya, R., Jacks, T., and Tuveson, D.A. (2001). Analysis of lung tumor initiation and progression using conditional expression of oncogenic K-ras. *Genes Dev.* 15, 3243–3248.
- Jonkers, J., Meuwissen, R., van der Gulden, H., Peterse, H., van der Valk, M., and Berns, A. (2001). Synergistic tumor suppressor activity of BRCA2 and p53 in a conditional mouse model for breast cancer. *Nat. Genet.* 29, 418–425.
- Kryczek, I., Banerjee, M., Cheng, P., Vatan, L., Szeliga, W., Wei, S., Huang, E., Finlayson, E., Simeone, D., Welling, T.H., et al. (2009). Phenotype, distribution, generation, and functional and clinical relevance of Th17 cells in the human tumor environments. *Blood* 114, 1141–1149.
- Mazmanian, S.K., Round, J.L., and Kasper, D.L. (2008). A microbial symbiosis factor prevents intestinal inflammatory disease. *Nature* 453, 620–625.
- Misch, E., and Hawn, T. (2008). Toll-like receptor polymorphisms and susceptibility to human disease. *Clinical science (London, England: 1979)* 114, 347–360.
- Peng, G., Wang, H.Y., Peng, W., Kiniwa, Y., Seo, K.H., and Wang, R.F. (2007). Tumor-infiltrating gammadelta T cells suppress T and dendritic cell function via mechanisms controlled by a unique toll-like receptor signaling pathway. *Immunity* 27, 334–348.
- Rabinovich, G.A., and Croci, D.O. (2012). Regulatory circuits mediated by lectin-glycan interactions in autoimmunity and cancer. *Immunity* 36, 322–335.
- Rubinstein, N., Alvarez, M., Zwirner, N.W., Toscano, M.A., Ilarregui, J.M., Bravo, A., Mordoh, J., Fainboim, L., Podhajcer, O.L., and Rabinovich, G.A. (2004). Targeted inhibition of galectin-1 gene expression in tumor cells results in heightened T cell-mediated rejection; A potential mechanism of tumor-immune privilege. *Cancer Cell* 5, 241–251.
- Rutkowski, M.R., Allegrezza, M.J., Svoronos, N., Tesone, A.J., Stephen, T.L., Perales-Puchalt, A., Nguyen, J., Zhang, P.J., Fiering, S.N., Tchou, J., and Conejo-Garcia, J.R. (2014). Initiation of metastatic breast carcinoma by targeting of the ductal epithelium with adenovirus-cre: a novel transgenic mouse model of breast cancer. *J. Vis. Exp.* 26.
- Ryzhov, S., Novitskiy, S.V., Goldstein, A.E., Biktasova, A., Blackburn, M.R., Biaggioni, I., Dikov, M.M., and Feoktistov, I. (2011). Adenosinergic regulation of the expansion and immunosuppressive activity of CD11b+Gr1+ cells. *J. Immunol.* 187, 6120–6129.
- Sampath, V., Garland, J.S., Le, M., Patel, A.L., Konduri, G.G., Cohen, J.D., Simpson, P.M., and Hines, R.N. (2012). A TLR5 (g.1174C > T) variant that encodes a stop codon (R392X) is associated with bronchopulmonary dysplasia. *Pediatr. Pulmonol.* 47, 460–468.
- Scarlett, U.K., Rutkowski, M.R., Rauwerdink, A.M., Fields, J., Escovar-Fadul, X., Baird, J., Cubillos-Ruiz, J.R., Jacobs, A.C., Gonzalez, J.L., Weaver, J., et al.

- (2012). Ovarian cancer progression is controlled by phenotypic changes in dendritic cells. *J. Exp. Med.* **209**, 495–506.
- Toscano, M.A., Bianco, G.A., Ilarregui, J.M., Croci, D.O., Correale, J., Hernandez, J.D., Zwirner, N.W., Poirier, F., Riley, E.M., Baum, L.G., and Rabinovich, G.A. (2007). Differential glycosylation of TH1, TH2 and TH-17 effector cells selectively regulates susceptibility to cell death. *Nat. Immunol.* **8**, 825–834.
- Viaud, S., Saccheri, F., Mignot, G., Yamazaki, T., Daillère, R., Hannani, D., Enot, D.P., Pfirschke, C., Engblom, C., Pittet, M.L., et al. (2013). The intestinal microbiota modulates the anticancer immune effects of cyclophosphamide. *Science* **342**, 971–976.
- Wang, L., Yi, T., Kortylewski, M., Pardoll, D.M., Zeng, D., and Yu, H. (2009). IL-17 can promote tumor growth through an IL-6-Stat3 signaling pathway. *J. Exp. Med.* **206**, 1457–1464.



## A novel role for the condensin II complex in cellular senescence

Yuhki Yokoyama, Hengrui Zhu, Rugang Zhang & Ken-ichi Noma

**To cite this article:** Yuhki Yokoyama, Hengrui Zhu, Rugang Zhang & Ken-ichi Noma (2015) A novel role for the condensin II complex in cellular senescence, *Cell Cycle*, 14:13, 2160-2170, DOI: [10.1080/15384101.2015.1049778](https://doi.org/10.1080/15384101.2015.1049778)

**To link to this article:** <http://dx.doi.org/10.1080/15384101.2015.1049778>



View supplementary material [↗](#)



Accepted author version posted online: 27 May 2015.



Submit your article to this journal [↗](#)



Article views: 278



View related articles [↗](#)



View Crossmark data [↗](#)



Citing articles: 1 View citing articles [↗](#)



# A novel role for the condensin II complex in cellular senescence

Yuhki Yokoyama, Hengrui Zhu, Rugang Zhang, and Ken-ichi Noma\*

The Wistar Institute; Philadelphia, PA USA

**Keywords:** cellular senescence, condensin, genome organization, human, nuclear architecture, oncogene-induced senescence, SAHF

**Abbreviations:** SAHF, senescence-associated heterochromatic foci; SADS, senescence-associated distension of satellites; SMC, structural maintenance of chromosomes; hCAP-H2, human chromosome-associated protein H2; *NCAPH2*, non-SMC chromosome-associated protein H2 gene; RPE-1, hTERT-immortalized retinal pigment epithelial cell line; hTERT, human telomerase reverse transcriptase; uORF, upstream open reading frame; BrdU, bromodeoxyuridine; SA- $\beta$ -gal, senescence-associated  $\beta$ -galactosidase; Rb, retinoblastoma protein; CDK, cyclin dependent kinase; DAPI, 4,6-diamidino-2-phenylindole; shRNA, short-hairpin RNA.

Although cellular senescence is accompanied by global alterations in genome architecture, how the genome is restructured during the senescent processes is not well understood. Here, we show that the hCAP-H2 subunit of the condensin II complex exists as either a full-length protein or an N-terminus truncated variant ( $\Delta$ N). While the full-length hCAP-H2 associates with mitotic chromosomes, the  $\Delta$ N variant exists as an insoluble nuclear structure. When overexpressed, both hCAP-H2 isoforms assemble this nuclear architecture and induce senescence-associated heterochromatic foci (SAHF). The hCAP-H2 $\Delta$ N protein accumulates as cells approach senescence, and hCAP-H2 knockdown inhibits oncogene-induced senescence. This study identifies a novel mechanism whereby condensin drives senescence via nuclear/genomic reorganization.

## Introduction

Protein complexes consisting of structural maintenance of chromosomes (SMC) proteins are essential for the faithful segregation of chromosomes. Two of the best-studied SMC complexes are condensin and cohesin, which are required for mitotic chromosome assembly and for holding sister chromatids together, respectively.<sup>1–3</sup> These SMC complexes function as connectors between 2 chromatin fibers.<sup>4</sup> Recent studies have revealed that cohesin can mediate interactions between gene promoters and enhancers.<sup>5</sup> Condensin is also known to function in higher-order genome organization in yeast and is involved in the gene regulation in *Caenorhabditis elegans*.<sup>6–9</sup> Condensin I and II complexes exist in humans, where the condensin II complex binds to promoters and enhancers, and participates in gene regulation.<sup>10,11</sup> Therefore, condensin likely regulates gene expression in a variety of organisms through its role in higher-order genome organization.

Cellular senescence was originally defined by Hayflick, who demonstrated that normal human fibroblasts could not proliferate indefinitely, but reach their “Hayflick limit” and senesce.<sup>12</sup> Currently, cellular senescence is defined as the state of stable cell-cycle arrest caused by exhausting the capacity of DNA replication or by various cellular stresses including DNA damage, chemotherapeutic drug treatment, and excessive growth stimulus by

overexpression of oncogenic Ras.<sup>13,14</sup> It is accompanied by diverse changes in gene expression and is associated with significant alterations in the global genome architecture.<sup>15,16</sup> Senescence-associated heterochromatic foci (SAHF) and senescence-associated distension of satellites (SADS) are characteristic of senescent cells.<sup>17–19</sup>

Several chromatin factors including a histone H2A variant (macroH2A), histone chaperons (ASF1 and HIRA), and the High-Mobility Group A (HMGA) proteins are involved in SAHF formation during cellular senescence.<sup>20,21</sup> Lamin B1, a structural component of the nuclear lamina, has also been implicated in the senescent processes.<sup>22</sup> Since heterochromatic histone modifications such as H3 lysine 9 and 27 tri-methylation are dispensable for SAHF formation, heterochromatic histone marks are not entirely responsible for SAHF formation.<sup>23</sup> Senescence appears to be a cellular event orchestrated by numerous cellular factors, but how SAHF are assembled during senescence and contribute to the senescent processes remains unclear.

In this study, we have shown that 2 hCAP-H2 isoforms of the condensin II subunit exist in human cells. The relative expression of these hCAP-H2 isoforms is regulated during the cell cycle and upon starvation. We find that the small upstream open reading frame (uORF) plays a role in regulating the translation of the hCAP-H2 isoforms and that the N-terminus truncated variant, hCAP-H2 $\Delta$ N, accumulates in

\*Correspondence to: Ken-ichi Noma; Email: noma@wistar.org

Submitted: 12/22/2014; Revised: 04/30/2015; Accepted: 05/06/2015

<http://dx.doi.org/10.1080/15384101.2015.1049778>

## Results

### Identification of 2 isoforms of hCAP-H2 condensin II subunit

To understand how condensin expression is regulated in human cells, we investigated several components of the condensin I and II complexes in 3 cancer cell lines (HeLa, HCT116, and U2OS) and RPE-1 (hTERT-immortalized retinal pigment epithelial) cells, which exhibit a stable diploid karyotype and are therefore often used for chromosome research. We observed that SMC4 (SMC subunit) and hCAP-H (kleisin subunit of condensin I) proteins were less abundant in HCT116 cells (Fig. S1A). Unexpectedly, 2 different sizes of proteins (84 and 91 kDa) were detected by the hCAP-H2 antibody in RPE-1 cells, but not in the cancer cell lines (top panels in Fig. 1A). These two proteins were both depleted by the short-hairpin RNA (shRNA) directed against *NCAPH2* transcripts, indicating that both proteins are derived from the *NCAPH2* gene (Fig. S1B). Based on the protein sizes, the top and bottom bands represent the full-length hCAP-H2 and a smaller variant, respectively. Since the 3 cancer cell lines expressed only the full-length hCAP-H2, we investigated whether this is a common feature of cancer cells. While the 2 hCAP-H2 isoforms were detected in primary human ovarian surface epithelial cells (HOSE4), both were also detected in the ovarian cancer cell lines (PEO-1, OVCAR5, and SKOV3), suggesting that the absence of the bottom

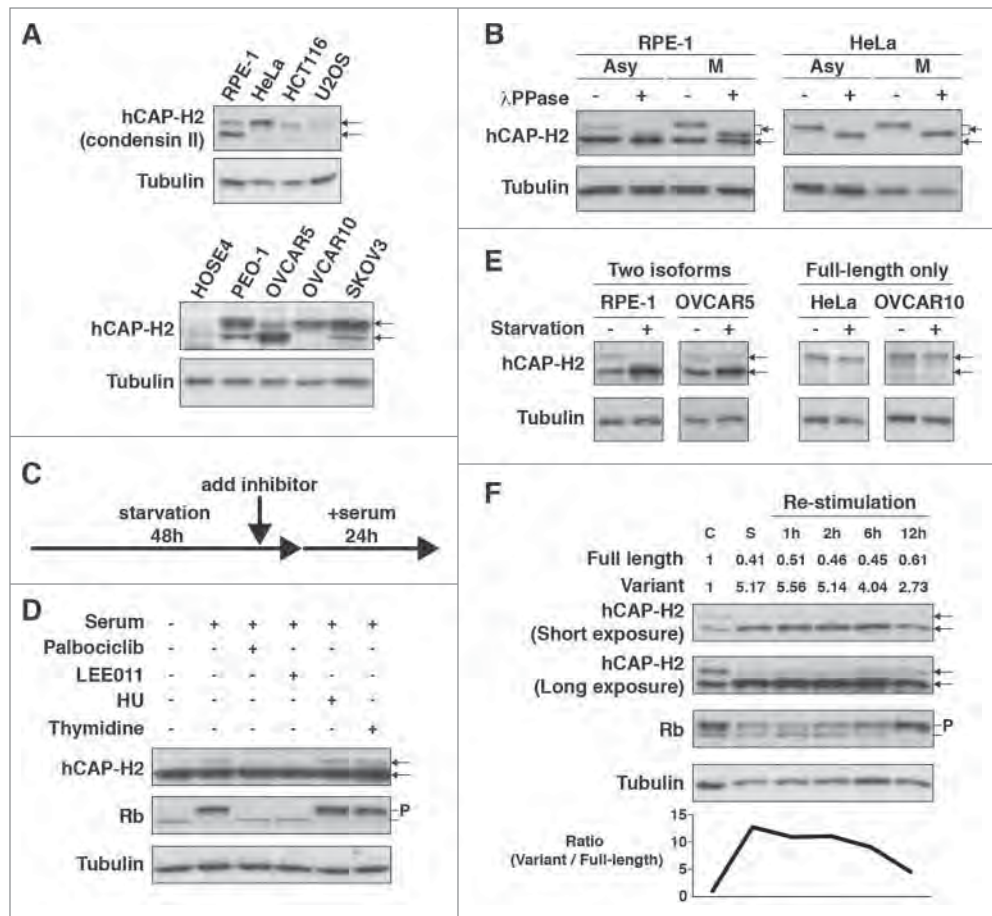


**Figure 1.** Full-length hCAP-H2 and its variant detected in human cell lines. (A) hCAP-H2 proteins in RPE-1, HeLa (cervical cancer), HCT116 (colon cancer), U2OS (osteosarcoma), HOSE4, and ovarian cancer cell lines (PEO-1, OVCAR5, OVCAR10, and SKOV3) were assessed by immunoblot analysis. Arrows indicate the full-length hCAP-H2 and its smaller variant. Tubulin serves as a loading control. (B) Asynchronous (Asy) and mitotic (M) RPE-1 and HeLa cells were subjected to Western blot analysis to detect hCAP-H2 proteins. Mitotic cells were prepared by mitotic shake-off. Cell lysates were treated with lambda protein phosphatase ( $\lambda$ PPase). (C) Schematic protocol for the inhibitor treatments employed in panel D. (D) RPE-1 cells grown in normal medium were subsequently cultured for 48 hours in starvation medium, which consists of 20 times less fetal bovine serum (FBS) than normal. CDK4/6 inhibitors (Palbociclib and LEE011), DNA replication inhibitors (HU and Thymidine), or DMSO (control) were added to starvation medium 2 hours before serum re-stimulation. Cells were further cultured for 24 hours in normal medium (serum +) containing the inhibitors, and lysates were subjected to immunoblot analysis. P indicates phosphorylated Rb proteins. (E) The indicated cell lines were cultured for 2 days in normal medium (starvation –) or phosphorylation medium (starvation +), followed by Western blot analysis. (F) RPE-1 cells grown in normal medium (C, control) were subsequently cultured for 2 days in starvation medium (S, Starvation). After the starvation treatment, cells were further cultured in normal medium for the indicated periods of time (Re-stimulation). Cell lysates derived from the respective culturing steps were subjected to immunoblot analysis. Band intensities (top) and expression ratio (bottom) of the hCAP-H2 isoforms are shown.

quiescent and senescent cells. We show that hCAP-H2 $\Delta$ N exists as a part of the insoluble nuclear architecture, while the full-length protein associates with mitotic chromosomes. Overexpression of this single condensin subunit, hCAP-H2, is sufficient to induce the formation of the condensin-mediated nuclear architecture and SAHF. This study demonstrates that the condensin II complex facilitates a nuclear/genomic reorganization leading to cellular senescence.

band is not necessarily indicative of cancer cells or their proliferative potential (bottom panels in Fig. 1A). For instance, the OVCAR5 and OVCAR10 cell lines had the different expression patterns of the hCAP-H2 isoforms, but showed similar rates of BrdU incorporation (Fig. 1A; Fig. S1C). Moreover, retinoblastoma (Rb) tumor suppressor proteins were predominantly phosphorylated in both the RPE-1 and cancer cell lines (except for HeLa cells, where Rb was absent), indicating that the expression

pattern of the 2 hCAP-H2 isoforms does not directly reflect cell proliferation (Fig. S1D and E).

#### Cell cycle-dependent regulation of hCAP-H2 isoforms

Next, we examined how expression of the hCAP-H2 isoforms is regulated during the cell cycle. We found that the full-length hCAP-H2 became more abundant in RPE-1 cells during mitosis compared to asynchronous cells, while the smaller hCAP-H2 variant was relatively decreased in mitotic cells (Fig. 1B). In contrast, expression levels were similar between mitotic and asynchronous HeLa cells, where only the full-length hCAP-H2 was present. We also found that  $\lambda$ PPase treatment converted the full-length hCAP-H2 from both asynchronous and mitotic cells to faster migrating bands (Fig. 1B). Moreover, the full-length hCAP-H2 bands from mitotic RPE-1 and HeLa cells were located slightly above those from asynchronous cells (Fig. 1B). These results indicate that hCAP-H2 is phosphorylated during interphase and additionally phosphorylated during mitosis (Fig. 1B). Phosphorylation of hCAP-H2 during mitosis was previously reported.<sup>24,25</sup> A similar band shift was not detected for the smaller variant, indicating that the phosphorylation is specific to the full-length hCAP-H2 (Fig. 1B).

We next performed serum re-stimulation assays with the CDK4/6 and DNA replication inhibitors (Fig. 1C). Starvation treatment arrests the cell cycle during G1/G0 phase, and serum re-stimulation with the CDK4/6 and DNA replication inhibitors allows the cell cycle to synchronously progress until midG1 and S phases, respectively. In RPE-1 cells treated by the CDK4/6 inhibitors, the full-length hCAP-H2 was not detected, while it was detected in cells treated by the DNA replication inhibitors (Fig. 1D). Furthermore, when the full-length hCAP-H2 was detected, Rb proteins were predominantly phosphorylated. These results suggest that the full-length hCAP-H2 accumulates between the midG1 and S phase, and that phosphorylation of Rb and accumulation of the full-length hCAP-H2 might be coordinated. Since the full-length hCAP-H2 is enriched during mitosis (Fig. 1B), our current hypothesis is that full-length proteins translated around the midG1-S phase are likely sustained until mitosis. Alternatively, it is also possible that the stability of hCAP-H2 proteins is regulated during the cell cycle. Together, these results indicate that protein levels of the hCAP-H2 isoforms are regulated during the cell cycle.

#### Regulation of hCAP-H2 isoforms upon starvation

We observed that the hCAP-H2 variant was increased in RPE-1 and OVCAR5 cells after serum starvation, while the full-length protein was decreased (Fig. 1E). In contrast, the full-length hCAP-H2 was not affected by the starvation treatment in the HeLa and OVCAR10 cell lines, which contained only the full-length protein (Fig. 1E). In addition, re-stimulation of cell growth after the starvation treatment gradually increased and decreased the full-length hCAP-H2 and its variant, respectively, and an increase in Rb phosphorylation was evident (Fig. 1F). These results suggest that when both of the hCAP-H2 isoforms are present, cell proliferation is associated with an increase of the full-length hCAP-H2 and a reduction of the variant, although

the basal expression pattern of the isoforms does not directly represent cell proliferation and is dependent upon cell lines (Fig. 1A). We also observed that *NCAPH2* gene transcription was not affected by the starvation treatment in RPE-1 cells (Fig. S1F). These results indicate that expression of the hCAP-H2 isoforms is regulated upon starvation in a post-transcriptional manner, and that the variant accumulates in quiescent cells induced by starvation.

#### Regulatory role of the uORF in translation of hCAP-H2 isoforms

The mouse *Ncapdh2* gene is known to produce splicing variants.<sup>26</sup> Therefore, we hypothesized that alternative splicing might be responsible for the synthesis of the hCAP-H2 protein isoforms. However, we did not observe splicing variants of *NCAPH2* in RPE-1 and HeLa cells, indicating that the hCAP-H2 variant protein is not derived from alternative splicing (Fig. S2A).

Small upstream open reading frames (uORFs) have been identified in about half of human transcripts and are known to control the translation of downstream ORFs.<sup>27,28</sup> A uORF is present in the *NCAPH2* mRNA and is conserved among mammalian species (Fig. 2A).<sup>26</sup> NetStart software predicts that hCAP-H2 translation initiates from the first (AUG1) and second (AUG2) start codons (Fig. 2B).<sup>29</sup> We hypothesized that the uORF might regulate translational initiation from the 2 start codons. To test this hypothesis, we made several constructs and observed that the wild-type construct expressed the 2 hCAP-H2 isoforms (Fig. 2C and D). The size difference between these 2 proteins was 7 kDa, which is exactly the same as for the endogenous hCAP-H2 isoforms (Fig. 1A). In contrast, the  $\Delta$ uAUG mutation that prevents translation of the uORF inhibited the production of the smaller protein. The  $\Delta$ AUG1 mutation, which removes the first start codon, resulted in the expression of only the smaller protein. The  $\Delta$ AUG2 mutation prevented the production of the smaller protein, and it resulted in the expression of an additional, even smaller protein, suggesting that there is an additional potential translational start site downstream of the second start codon. These results indicate that the translation of the larger and smaller proteins are initiated from the AUG1 and AUG2 codons, respectively, and that the uORF is required for efficient translational initiation from the AUG2 start codon. Small uORFs are known to modulate translation of the downstream ORFs through a reinitiation mechanism.<sup>30</sup> It has recently been shown that the *NIPBL* gene encoding a cohesin loading factor has an uORF, which regulates NIPBL translation in a cell cycle-dependent manner.<sup>31</sup> Therefore, it is possible that the uORF in the *NCAPH2* gene might contribute to the observed regulation of the hCAP-H2 isoforms during the cell cycle (Fig. 1B and D).

We next expressed non-tagged full-length hCAP-H2 and  $\Delta$ N proteins from plasmids in RPE-1 cells and compared the sizes of these proteins to the endogenous hCAP-H2 isoforms (Fig. 2E). In this system, the translation of the exogenous full-length hCAP-H2 and  $\Delta$ N variant is initiated from the AUG1 and AUG2 start codons, respectively. We observed that the size of the exogenous full-length hCAP-H2 was similar to the endogenous



Since DAPI-dense foci are reminiscent of senescence-associated heterochromatic foci (SAHF), we asked whether DAPI-dense foci we observed have the same characteristics as SAHF.



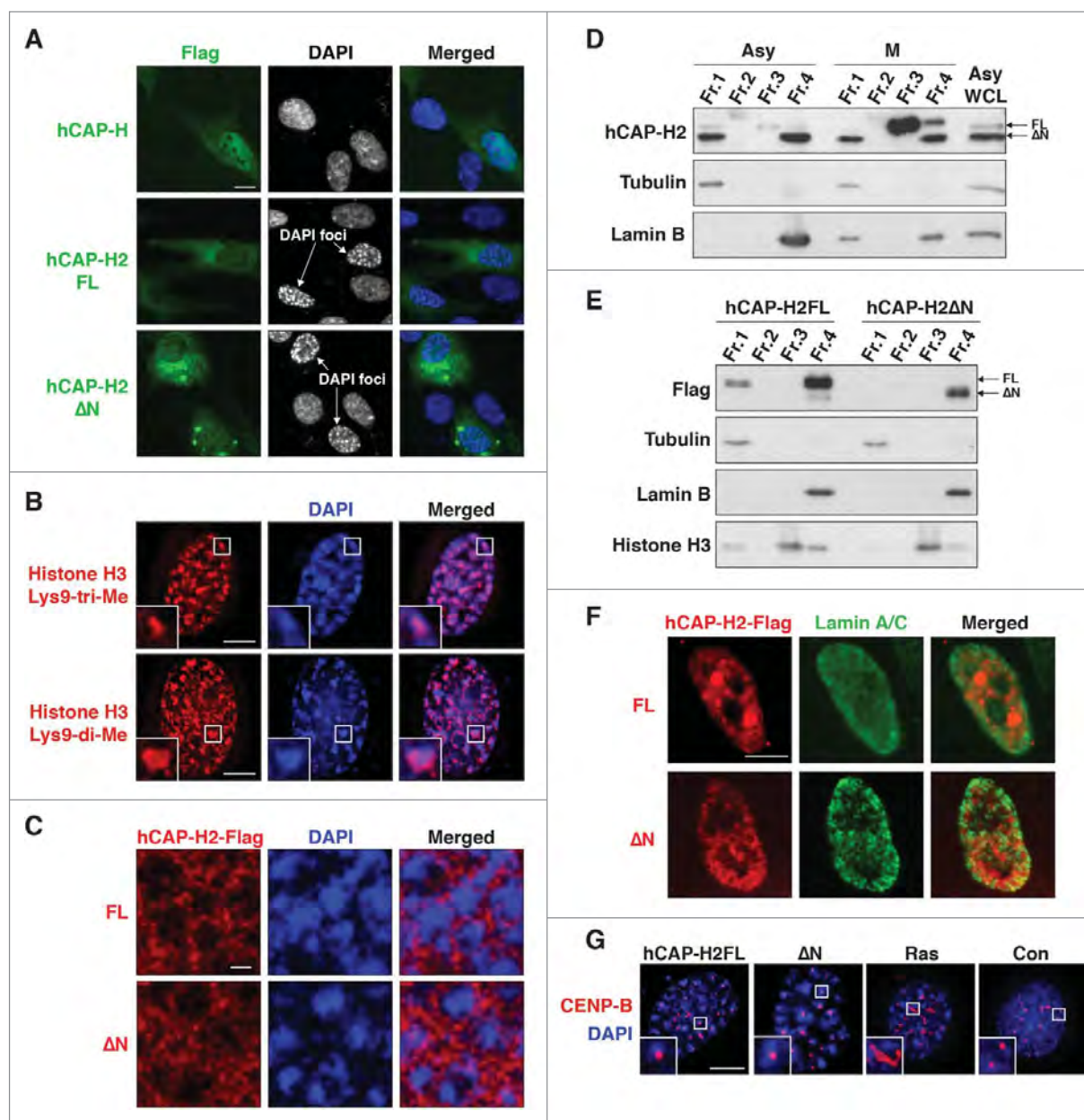


**Figure 3.** Overexpression of hCAP-H2 induces formation of DAPI-dense chromatin foci. **(A)** hCAP-H and hCAP-H2 (FL and ΔN) proteins fused to the Flag epitope were expressed in RPE-1 cells for 2 days and visualized by IF analysis. Scale bar indicates 10  $\mu$ m. **(B)** Histone H3 di- and tri-methylated Lys9 were visualized by IF in RPE-1 cells expressing the full-length hCAP-H2. Inset shows enlarged views. Scale bar indicates 5  $\mu$ m. **(C)** hCAP-H2 (FL and ΔN) proteins fused to the Flag epitope were expressed in RPE-1 cells and visualized by IF. These microscopic images, at a relatively high resolution, were captured by a Leica SP5 II laser scanning confocal microscope. Scale bar indicates 1  $\mu$ m. **(D)** Chromatin-unbound (Fr. 1), DNase-extractable (Fr. 2), high salt-extractable (Fr. 3), and high salt-resistant (Fr. 4) fractions were prepared from asynchronous (Asy) and mitotic (M) RPE-1 cells (See Materials and Methods) and subjected to Western blotting. WCL indicates whole cell lysate. **(E and F)** The same fractionation was performed using RPE-1 cells expressing Flag-tagged hCAP-H2 proteins (FL and ΔN). The fractions were subjected to immuno blotting (E). The high salt-resistant fraction was further applied for IF analysis to co-visualize hCAP-H2 and lamin A/C proteins (F). Scale bar indicates 5  $\mu$ m. **(G)** RPE-1 cells were transfected with plasmids encoding EYFP-tagged hCAP-H2 proteins (FL and ΔN) and culture for 2 days. Cells were subjected to IF analysis to stain CENP-B proteins, which bind to centromeric satellites. RPE-1 cells were infected with a retrovirus encoding H-RasV12 (Ras) or a control virus without H-RasV12 (Con) and subjected to IF analysis 8 days after the infection. Scale bar indicates 5  $\mu$ m.

We observed that DAPI-dense foci associated with histone H3 di- and tri-methylated Lys9, which are heterochromatic epigenetic marks (Fig. 3B). As previously reported, H3 tri-methylated Lys9 was located at the center of SAHF, while di-methylated

Lys9 was more enriched near the surface of SAHF (Fig. 3B). Histone H3 tri-methylated Lys9 was more scattered in the nuclei without DAPI-dense foci (Fig. S3B).<sup>23</sup> In contrast, histone H3 di/tri-methylated Lys4 (euchromatic mark) was present outside

of the DAPI-dense foci, consistent with the previous observation (Fig. S3C).<sup>17</sup> These results indicate that DAPI-dense chromatin foci induced by expression of the hCAP-H2 isoforms have characteristics of SAHF.

#### hCAP-H2 $\Delta$ N exists as a part of the insoluble nuclear architecture

To begin to understand the roles of the hCAP-H2 isoforms in the formation of DAPI-dense foci, we visualized these proteins and found that they were localized to the intervening region surrounding DAPI-dense foci (Fig. 3C). To further characterize hCAP-H2 localization, we performed cellular fractionation analysis (See Materials and Methods) and found that endogenous hCAP-H2 $\Delta$ N proteins were enriched in the insoluble fraction (fraction 4) in both asynchronous and mitotic cells (Fig. 3D). This insoluble fraction is also referred to as a nuclear matrix. The full-length hCAP-H2, but not the  $\Delta$ N variant, was found in the high salt-extractable fraction (fraction 3) during mitosis. Proteins tightly bound to DNA are mainly enriched in fraction 3. This result indicates that the condensin II complex containing the full-length hCAP-H2 preferentially interacts with mitotic chromosomes to mediate chromosome compaction,<sup>36,37</sup> while the complex with the  $\Delta$ N variant exists as a part of the insoluble nuclear architecture. As a control, we observed that tubulin was enriched in the chromatin-unbound soluble fraction 1, while lamin B was detected in fraction 4. Since this fractionation analysis monitors hCAP-H2 proteins without overexpression, it is likely that the endogenous hCAP-H2 isoforms have distinct functions in chromosome compaction and the nuclear architecture.

Exogenous full-length hCAP-H2 and  $\Delta$ N proteins highly expressed from plasmids as well as endogenous lamin B proteins were enriched in fraction 4, while histone H3 proteins were mainly detected in fraction 3 (Fig. 3E). When fraction 4 was subjected to IF analysis to visualize the hCAP-H2 isoforms, we observed that these proteins and lamin A/C were associated with the nucleus (Fig. 3F). These results demonstrate that, when overexpressed, both the hCAP-H2 isoforms exist as a part of the nuclear architecture. This is consistent with previous observations that several components of the condensin II complex are present in the nuclear matrix.<sup>38</sup>

Since senescence-associated distension of satellites (SADS), which occurs during the senescence process, is a more consistent phenomenon in human and mouse cells than SAHF,<sup>18</sup> we investigated whether the expression of the hCAP-H2 isoforms triggers SADS. To visualize SADS, we performed CENP-B staining, which specifically visualizes centromeric satellites and has previously been used for detection of SADS.<sup>18</sup> Consistent with the previous finding, 45% of RPE-1 cells showed SADS at the late senescent phase (day 8) when oncogenic Ras was expressed (Fig. 3G). On the other hand, expression of the hCAP-H2 isoforms induced DAPI-dense chromatin foci 2 days after transfection, but 0% of the cells showed SADS at the same time point (Fig. 3G). This result suggests that overexpression of the hCAP-H2 isoforms can cause the formation of DAPI-dense chromatin foci, likely SAHF, without SADS. Together, these results suggest

that overexpressed hCAP-H2 proteins facilitate the formation of the condensin-associated insoluble nuclear architecture and SAHF.

#### hCAP-H2 functions in cellular senescence

To investigate whether hCAP-H2 plays a role in cellular senescence, we expressed the hCAP-H2 isoforms in IMR90 human fibroblasts, which are commonly used for senescence research. Overexpression of the full-length hCAP-H2 and  $\Delta$ N variant induced senescence, as indicated by decrease in BrdU incorporation (cell cycle/growth marker), senescence-associated  $\beta$ -galactosidase (SA- $\beta$ -gal) staining, and SAHF formation, all of which were statistically significant ( $P < 0.001$ ; Fig. 4D). We also observed that hCAP-H2 $\Delta$ N expression was increased during senescence induced by oncogenic Ras (Fig. 4E). Moreover, Ras-induced senescence was significantly impaired by hCAP-H2 knockdown using shH2#1, as indicated by the reduced percentages of cells positive for SA- $\beta$ -gal activity and SAHF formation ( $P < 0.001$ ; Fig. 4F). hCAP-H2 knockdown using 2 different shRNAs (shH2#2 and #3) also inhibited Ras-induced senescence (Fig. S3D and E). These results collectively indicate that the condensin II complex functions during oncogene-induced senescence, and that the complex with the  $\Delta$ N variant likely participates in the senescent process.

## Discussion

While there are the 2 hCAP-H2 isoforms present in the non-cancerous cell lines (RPE-1 and HOSE4), some cancer cell lines contain only the full-length protein, suggesting that the presence of the 2 isoforms is likely the normal situation for growing cells. We show that expression of the 2 hCAP-H2 isoforms is modulated during the cell cycle and upon starvation, and that the uORF plays a regulatory role in the translation of the hCAP-H2 isoforms. We also find that the condensin II complex containing the full-length hCAP-H2 preferentially associates with mitotic chromosomes to mediate chromosome compaction, while the complex with the  $\Delta$ N variant exists as a component of the insoluble nuclear architecture (Fig. 3D). Only the hCAP-H2 $\Delta$ N variant is accumulated in quiescent and senescent cells induced by starvation and oncogenic Ras, respectively (Figs. 1E and 4E). This makes sense because these cells do not progress through mitosis and thus do not need the full-length isoform to induce chromosome compaction. Therefore, non-growing cells express the  $\Delta$ N variant, which contributes to the formation of a nuclear environment favorable for growth arrest.

When overexpressed, both of the hCAP-H2 isoforms associate with the specific nuclear architecture and induce DAPI-dense chromatin foci (Fig. 3). We also show that the protein level of the endogenous hCAP-H2 $\Delta$ N variant is increased as cells approach senescence, and that hCAP-H2 knockdown inhibits SAHF formation and oncogene-induced senescence (Fig. 4E and F). Taken all together, our current hypothesis is that the specific nuclear architecture built by the condensin II complex containing the  $\Delta$ N variant promotes SAHF formation,

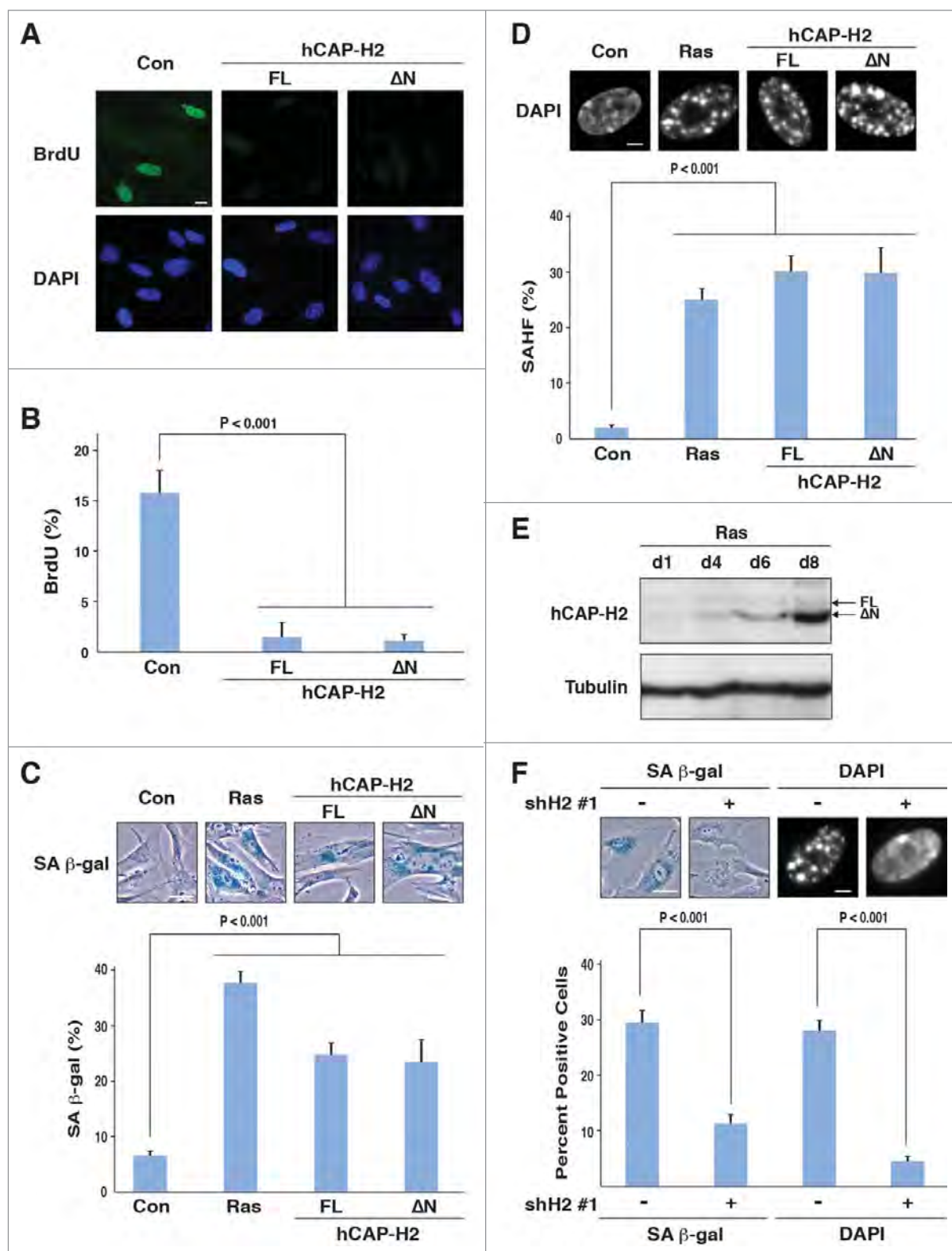


**Figure 4.** hCAP-H2 facilitates cellular senescence. (A and B) IMR90 cells were infected with retroviruses encoding the full-length hCAP-H2 or ΔN variant, or a control virus without encoding these proteins. BrdU incorporation and visualization were performed 8 days after the infection (A). Scale bar indicates 10 μm. Percentages of IMR90 cells showing BrdU staining were scored 8 days after retrovirus infection (B). (C and D) IMR90 cells were infected by retroviruses encoding the H-RasV12, full-length hCAP-H2, or ΔN variant, or a control virus, and subjected to SA-β-gal staining 8 days after the infection (C). Infected cells were stained by DAPI to assess SAHF formation (D). Scale bars in panels C and D indicate 50 μm and 5 μm, respectively. (E) hCAP-H2 levels were monitored from day 1 (d1) to day 8 (d8), after IMR90 cells were infected with a retrovirus encoding H-RasV12. Tubulin serves as a loading control. (F) IMR90 cells were infected with a retrovirus encoding H-RasV12 as well as a lentivirus encoding shRNA against *NCAPH2* mRNA (shH2#1), and assessed for SA-β-gal activity and SAHF formation 8 days after the infection. Scale bars indicate 50 (left) and 5 μm (right).



which in turn facilitates senescence. It has recently been shown that lamin B1 knockdown induces dissociation of heterochromatin from the nuclear periphery and SAHF formation.<sup>39</sup> Therefore, the lamina and the condensin-mediated nuclear architectures likely play opposing roles in SAHF formation. Consequently, overexpression of hCAP-H2 might be necessary to induce SAHF in the presence of the nuclear lamina. In case of senescence induced by oncogenic Ras, lamin B1 is down-regulated, and hCAP-H2 $\Delta$ N expression is enhanced (Fig. 4E).<sup>22</sup>

We also found that the Rb tumor suppressor associates with the nuclear architecture assembled by the condensin II complex (Fig. S3F). Interestingly, Rb foci were almost always detected at the surface of the condensin architecture and outside of DAPI-dense signals. It has previously been shown that Rb interacts with the hCAP-D3 subunit of the condensin II complex in human cells.<sup>40</sup> Therefore, Rb associates with the condensin II nuclear architecture likely through the interaction between Rb and hCAP-D3. Consistent with this interpretation, Rb is known to be present in the insoluble nuclear fraction.<sup>41</sup> It has also been shown that Rb binds to and represses E2F-target genes, thereby contributing to cellular senescence.<sup>17</sup> Based on these results, we speculate that Rb associates the E2F-target genes with the condensin II nuclear architecture, which might play a role in the gene repression for the E2F-target genes. As a similar example, SATB1 forms a nuclear architecture in mouse cells and regulates many genes by tethering those genes to the SATB1 nuclear architecture.<sup>42</sup> Since senescence is accompanied by altered expression of many genes,<sup>15,16</sup> the condensin-mediated nuclear architecture might contribute to the gene expression program during senescence processes.

## Materials and Methods

### Cell culture

RPE-1 cells (ATCC) were cultured in DMEM/F12 medium (Life Technologies, 11330032) supplemented with 10% tet-system approved fetal bovine serum (FBS; Clontech Laboratories, 631106), 100 U/ml penicillin, 100  $\mu$ g/ml streptomycin, and 0.01 mg/ml hygromycin B. HeLa, HCT116, and U2OS cells were cultured in DMEM medium (Mediatech, MT10-013-CV) supplemented with 10% FBS, 100 U/ml penicillin, and 100  $\mu$ g/ml streptomycin. PEO-1, OVCAR5, OVCAR10, and SKOV3 cells were cultured in RPMI1640 medium (Life Technologies, 22400089) supplemented with 10% FBS, 100 U/ml penicillin, and 100  $\mu$ g/ml streptomycin. HOSE4 cells were cultured as previously described.<sup>43</sup> IMR90 cells were cultured in DMEM medium supplemented with 10% FBS, 100 U/ml penicillin, 100  $\mu$ g/ml streptomycin, 0.15% sodium bicarbonate, 2 mM L-glutamine, 1 mM sodium pyruvate, and 1  $\times$  MEM non-essential amino acids (Life Technologies, 11120052).

### Expression of hCAP-H2 and its variants

*NCAPH2* cDNA in pCMV6-Entry vector (OriGene) was used to generate the *NCAPH2* $\Delta$ N and  $\Delta$ C genes by a PCR-based method. hCAP-H2 (full length,  $\Delta$ N, and  $\Delta$ C) proteins

fused to the Flag epitope were expressed from either pCMV6-Entry or pTRE3G plasmids (Clontech Laboratories). For co-immunoprecipitation (co-IP) assay, pTRE3G plasmids carrying *NCAPH2* (full length,  $\Delta$ N, or  $\Delta$ C) and pCMV-Tet3G were co-transfected into cells, and *NCAPH2* expression was induced by 1  $\mu$ g/ml doxycycline for 48 hours. hCAP-H2 (full length and  $\Delta$ N) proteins fused to EYFP were expressed from pEYFP-N1 plasmids (Clontech Laboratories). Cells were transfected with plasmids using the Fugene HD reagent (Promega, E2311).

### Retrovirus and lentivirus infections

DNA fragments encoding hCAP-H2 (full length and  $\Delta$ N) fused to the Flag epitope were inserted into pBABE-neo vector.<sup>20</sup> pBABE-neo plasmids carrying either H-rasV12, *NCAPH2*, or *NCAPH2* $\Delta$ N were used for retrovirus packaging, and virus infection was performed as described previously.<sup>20</sup> Cells were cultured with selection medium containing 500  $\mu$ g/ml G418. pTRIPZ plasmid containing *NCAPH2* shRNA (Thermo Scientific Open Biosystems) was used for lentivirus production. Doxycycline (1  $\mu$ g/ml) was added to culture medium every 48 hours for shRNA expression. Cells were cultured in medium containing 3  $\mu$ g/ml puromycin.

### Senescence-associated $\beta$ -galactosidase (SA- $\beta$ -gal) and BrdU assays

SA- $\beta$ -gal staining was performed as described previously.<sup>44</sup> For BrdU incorporation experiments, cells were plated on coverslips and labeled with 100  $\mu$ g/ml 5-Bromo-2'-deoxyuridine (BrdU, Sigma-Aldrich, B5002) for 30 minutes. The cells were fixed by 4% paraformaldehyde (pFA) for 15 minutes and permeabilized by PBS buffer containing 0.2% Triton X-100. The cells were further fixed for 30 minutes by 1% pFA in PBS buffer containing 0.01% Tween-20 and treated with 5 units of RQ1 RNase-free DNase I (Promega, M6101) or 2 N HCl. The cells were then incubated with 1:10-diluted FITC-labeled mouse monoclonal anti-BrdU (BD Biosciences, 556028) for 30 minutes. Nuclei were stained with 1  $\mu$ g/ml 4,6-diamidino-2-phenylindole (DAPI) solution for 5 minutes.

### Fractionation analysis

Fractionation analysis was performed as previously described with slight modifications.<sup>45</sup> Cells were lysed at 4°C for 30 minutes with 400  $\mu$ l CSK buffer [10 mM PIPES (pH 6.8), 100 mM NaCl, 300 mM sucrose, 3 mM MgCl<sub>2</sub>, 1 mM EGTA, 1 mM DTT, 0.25 mM PMSF, 10 mM NaF, 0.1 mM ATP, and Complete protease inhibitor cocktail (Roche, 11836170001)] containing 0.3% Triton X-100. Soluble fraction (fraction 1, chromatin-unbound fraction) and insoluble fraction were separated by centrifugation at 2,300  $\times$  g for 10 minutes. The insoluble fraction was incubated with 100 units of RQ1 RNase-free DNase I at room temperature for 30 minutes. After centrifugation at 16,000  $\times$  g for 10 minutes, the supernatant was recovered as fraction 2 (DNase-extractable fraction). The pellet was then suspended in 200  $\mu$ l CSK buffer containing 0.3% Triton X-100 and 2 M NaCl, and the suspension was rotated at 4°C for 30 minutes. After centrifugation at 16,000  $\times$  g for



10 minutes, the supernatant was recovered as fraction 3 (high salt-extractable fraction), and the pellet was boiled with 50  $\mu$ l Laemmli sample buffer (fraction 4, high salt-resistant fraction).

### Western blotting

Cells were suspended with Laemmli sample buffer (Bio-Rad Laboratories, 1610737) and boiled at 100°C for 5 minutes. Primary antibodies used in this study were the following: 1:1000-diluted rabbit polyclonal anti-SMC4 (Abcam, ab17958), 1:2000-diluted rabbit polyclonal anti-hCAP-H (Sigma-Aldrich, HPA003008), 1:500-diluted rabbit polyclonal anti-hCAP-H2 (Abgent, AP1973A), 1:200-diluted mouse monoclonal anti-hCAP-D2 (Santa Cruz Biotechnology, sc-166878), 1:1000-diluted rabbit polyclonal anti-hCAP-D3 (Abcam, ab70349), 1:2000-diluted mouse monoclonal anti-hCAP-G (Novus Biologicals, H00064151-M01), 1:1000-diluted mouse monoclonal anti-Rb (Cell Signaling Technology, #9309), 1:500-diluted goat polyclonal anti-Lamin B (Santa Cruz Biotechnology, sc-6217), 1:20000-diluted mouse monoclonal anti- $\alpha$ -tubulin (Sigma-Aldrich, T6199), 1:1000-diluted mouse monoclonal anti-Flag (Sigma-Aldrich, F1804), and 1:2000-diluted rabbit monoclonal anti-histone H3 (Cell Signaling Technology, #4499). Secondary antibodies, such as horseradish peroxidase (HRP)-conjugated sheep anti-mouse IgG, HRP-conjugated donkey anti-rabbit IgG (GE Healthcare, NA931, NA934), and HRP-conjugated rabbit anti-goat IgG (Kirkegaard & Perry Laboratories, 14-13-06), were used for detection of target proteins by ECL or ECL plus kits (GE Healthcare, RPN2109, RPN2133).

### Immunoprecipitation

Cells were suspended in 1 ml IP buffer [50 mM HEPES (pH 7.6), 75 mM KCl, 0.1% NP-40, 20% Glycerol, 1 mM EDTA, 10 mM NaF, 10 mM  $\beta$ -glycerophosphate, and Complete protease inhibitor cocktail]. Cell lysate was mixed with  $\text{MgCl}_2$  (final 5 mM) and 50 units of RQ1 RNase-free DNase I were added. DNase I reaction was performed at 37°C for 30 minutes and terminated by adding EDTA (final 10 mM). Soluble fraction of the cell lysate was incubated with anti-Flag M2 magnetic beads (Sigma-Aldrich, M8823). The beads were washed with 400  $\mu$ l of IP buffer 5 times and boiled with 20  $\mu$ l Laemmli sample buffer to elute proteins.

### Immunofluorescence microscopy

Cells plated on coverslips were fixed with 2% pFA for 15 minutes. Fixed cells were permeabilized with PBS containing 0.5% Triton X-100 for 5 minutes and incubated with TBST (Tris-buffered saline plus 0.1% Tween-20) containing 1% BSA for 1 hour. Cells were then incubated for 1 hour with primary antibodies: 1:200-diluted mouse or rat monoclonal anti-Flag (Agilent Technologies, 200471, 200473), 1:500-diluted mouse monoclonal anti-histone H3 di-methyl Lys9 (Abcam, ab1220), 1:1000-diluted rabbit polyclonal anti-histone H3 tri-methyl Lys9 (Abcam, ab8898), 1:200-diluted mouse monoclonal anti-histone H3 di/tri-methyl Lys4 (Abcam, ab6000), 1:1000-diluted rabbit polyclonal anti-CENPB (Abcam, ab25734), 1:200-diluted rabbit polyclonal anti-lamin A/C (Cell Signaling Technology,

#2032), and 1:200-diluted mouse monoclonal anti-Rb (Cell Signaling Technology). Cells were subsequently incubated for 1 hour with secondary antibodies, such as 1:500-diluted Alexa Flour 488-conjugated anti-mouse IgG, 1:400-diluted Alexa Flour 594-conjugated anti-mouse IgG, 1:400-diluted Alexa Flour 594-conjugated anti-rat IgG, 1:400-diluted Alexa Flour 488-conjugated anti-rabbit IgG, 1:400-diluted Alexa Flour 594-conjugated anti-rabbit IgG, and 1:4000-diluted Cy3-conjugated anti-rabbit IgG. Nuclei were stained with 1  $\mu$ g/ml DAPI solution for 5 minutes. Immunofluorescent (IF) images were captured by a Zeiss Axioimager Z1 fluorescence microscope with an oil immersion objective lens (Plan Apochromat, 63 $\times$ , NA 1.4, Zeiss), unless otherwise indicated. The images were acquired at 0.2  $\mu$ m intervals in the z-axis controlled by Axiovision 4.6.3 software (Zeiss). To visualize hCAP-H2 and lamin A/C proteins in fraction 4, cells attached to coverslips were treated by CSK buffer, DNase I, and 2 M NaCl, as described in the fractionation procedure. The cells were then fixed by 2% pFA, followed by the same IF procedure.

### RT-PCR and qRT-PCR

RNA was extracted from human cells using RNeasy Plus Mini Kit (Qiagen, 74134). RNA samples were subjected to RT-PCR using onestep RT-PCR kit (Qiagen, 210212) or SYBR green one-step kit (Bio-Rad, 172-5151). Alternatively, RNA samples were subjected to cDNA synthesis using high-capacity cDNA reverse transcription kit (Life Technologies, 4368814), followed by qPCR analysis using SYBR green qPCR kit (Sigma-Aldrich, KCQS00). Primer sequences are indicated in Table S1.

### Disclosure of Potential Conflicts of Interest

No potential conflicts of interest were disclosed.

### Acknowledgments

We would like to thank Meenhard Herlyn, Kazuko Nishikura, Ashani Weeraratna, and Susan Janicki for experimental materials; the Wistar Institute Molecular Screening Facility for lentivirus preparation; and the Imaging Facility for microscopic analysis. We also thank Maureen Murphy, Michael Showe, and Louise Showe for critically reading the manuscript and Sylvie Shaffer for editorial assistance.

### Funding

This work was supported by the National Institutes of Health (NIH) grant CA010815, the W. W. Smith Charitable Trust, the V Foundation, the Edward Mallinckrodt, Jr. Foundation, and the Wistar Pilot Project Funds to KN.

### Supplemental Material

Supplemental data for this article can be accessed on the publisher's website.

## References

- Koshland D, Strunnikov A. Mitotic chromosome condensation. *Annu Rev Cell Dev Biol* 1996; 12:305-33; PMID:8970729; <http://dx.doi.org/10.1146/annurev.cellbio.12.1.305>
- Hirano T. Chromosome cohesion, condensation, and separation. *Annu Rev Biochem* 2000; 69:115-44; PMID:10966455; <http://dx.doi.org/10.1146/annurev.biochem.69.1.115>
- Nasmyth K, Haering CH. The structure and function of SMC and kleisin complexes. *Annu Rev Biochem* 2005; 74:595-648; PMID:15952899; <http://dx.doi.org/10.1146/annurev.biochem.74.082803.133219>
- Hirano T. At the heart of the chromosome: SMC proteins in action. *Nat Rev Mol Cell Biol* 2006; 7:311-22; PMID:16633335; <http://dx.doi.org/10.1038/nrm1909>
- Kagey MH, Newman JJ, Bilodeau S, Zhan Y, Orlando DA, van Berkum NL, Ebmeier CC, Goossens J, Rahl PB, Levine SS, et al. Mediator and cohesin connect gene expression and chromatin architecture. *Nature* 2010; 467:430-5; PMID:20720539; <http://dx.doi.org/10.1038/nature09380>
- Chuang PT, Albertson DG, Meyer BJ. DPY-27: A chromosome condensation protein homolog that regulates *C. elegans* dosage compensation through association with the X chromosome. *Cell* 1994; 79:459-74; PMID:7954812; [http://dx.doi.org/10.1016/0092-8674\(94\)90255-0](http://dx.doi.org/10.1016/0092-8674(94)90255-0)
- Haeussler RA, Pratt-Hyatt M, Good PD, Gipson TA, Engelke DR. Clustering of yeast tRNA genes is mediated by specific association of condensin with tRNA gene transcription complexes. *Genes Dev* 2008; 22:2204-14; PMID:18708579; <http://dx.doi.org/10.1101/gad.1675908>
- Iwasaki O, Tanaka A, Tanizawa H, Grewal SIS, Noma KI. Centromeric localization of dispersed Pol III genes in fission yeast. *Mol Biol Cell* 2010; 21:254-65; PMID:19910488; <http://dx.doi.org/10.1091/mbc.E09-09-0790>
- Tanaka A, Tanizawa H, Sriswasdi S, Iwasaki O, Chatterjee AG, Speicher DW, Levin HL, Noguchi E, Noma KI. Epigenetic regulation of condensin-mediated genome organization during the cell cycle and upon DNA damage through histone H3 lysine 56 acetylation. *Mol Cell* 2012; 48:532-46; PMID:23084836; <http://dx.doi.org/10.1016/j.molcel.2012.09.011>
- Ono T, Losada A, Hirano M, Myers MP, Neuwald AF, Hirano T. Differential contributions of condensin I and condensin II to mitotic chromosome architecture in vertebrate cells. *Cell* 2003; 115:109-21; PMID:14532007; [http://dx.doi.org/10.1016/S0092-8674\(03\)00724-4](http://dx.doi.org/10.1016/S0092-8674(03)00724-4)
- Dowen JM, Bilodeau S, Orlando DA, Hübner MR, Abraham BJ, Spector DL, Young RA. Multiple structural maintenance of chromosome complexes at transcriptional regulatory elements. *Stem Cell Reports* 2013; 1:371-8; PMID:24286025; <http://dx.doi.org/10.1016/j.stemcr.2013.09.002>
- Hayflick L. The limited in vitro lifetime of human diploid cell strains. *Exp Cell Res* 1965; 37:614-36; PMID:14315085; [http://dx.doi.org/10.1016/0014-4827\(65\)90211-9](http://dx.doi.org/10.1016/0014-4827(65)90211-9)
- Campisi J. Aging, cellular senescence, and cancer. *Annu Rev Physiol* 2013; 75:685-705; PMID:23140366; <http://dx.doi.org/10.1146/annurev-physiol-030212-183653>
- Salama R, Sadaie M, Hoare M, Narita M. Cellular senescence and its effector programs. *Genes Dev* 2014; 28:99-114; PMID:24449267; <http://dx.doi.org/10.1101/gad.235184.113>
- Shelton DN, Chang E, Whittier PS, Choi D, Funk WD. Microarray analysis of replicative senescence. *Curr Biol* 1999; 9:939-45; PMID:10508581; [http://dx.doi.org/10.1016/S0960-9822\(99\)80420-5](http://dx.doi.org/10.1016/S0960-9822(99)80420-5)
- Debacq-Chainiaux F, Pascal T, Boilan E, Bastin C, Bauwens E, Toussaint O. Screening of senescence-associated genes with specific DNA array reveals the role of IGFBP-3 in premature senescence of human diploid fibroblasts. *Free Radic Biol Med* 2008; 44:1817-32; PMID:18329388; <http://dx.doi.org/10.1016/j.freeradbiomed.2008.02.001>
- Narita M, Núñez S, Heard E, Narita M, Lin AW, Hearn SA, Spector DL, Hannon GJ, Lowe SW. Rb-mediated heterochromatin formation and silencing of E2F target genes during cellular senescence. *Cell* 2003; 113:703-16; PMID:12809602; [http://dx.doi.org/10.1016/S0092-8674\(03\)00401-X](http://dx.doi.org/10.1016/S0092-8674(03)00401-X)
- Swanson EC, Manning B, Zhang H, Lawrence JB. Higher-order unfolding of satellite heterochromatin is a consistent and early event in cell senescence. *J Cell Biol* 2013; 203:929-42; PMID:24344186; <http://dx.doi.org/10.1083/jcb.201306073>
- De Cecco M, Criscione SW, Peckham EJ, Hillenmeyer S, Hamm EA, Manivannan J, Peterson AL, Kreiling JA, Neretti N, Sedivy JM. Genomes of replicatively senescent cells undergo global epigenetic changes leading to gene silencing and activation of transposable elements. *Aging Cell* 2013; 12:247-56; PMID:23360310; <http://dx.doi.org/10.1111/acel.12047>
- Zhang R, Poustovoitov MV, Ye X, Santos HA, Chen W, Daganzo SM, Erzberger JP, Serebriiskii IG, Canutescu AA, Dunbrack RL, et al. Formation of MacroH2A-containing senescence-associated heterochromatin foci and senescence driven by ASF1a and HIRA. *Dev Cell* 2005; 8:19-30; PMID:15621527; <http://dx.doi.org/10.1016/j.devcel.2004.10.019>
- Narita M, Narita M, Krizhanovsky V, Núñez S, Chicas A, Hearn SA, Myers MP, Lowe SW. A novel role for high-mobility group a proteins in cellular senescence and heterochromatin formation. *Cell* 2006; 126:503-14; PMID:16901784; <http://dx.doi.org/10.1016/j.cell.2006.05.052>
- Shimi T, Butin-Israeli V, Adam SA, Hamaana RB, Goldman AE, Lucas CA, Shumaker DK, Kosak ST, Chandan NS, Goldman RD. The role of nuclear lamin B1 in cell proliferation and senescence. *Genes Dev* 2011; 25:2579-93; PMID:22155925; <http://dx.doi.org/10.1101/gad.179515.111>
- Chandra T, Kirschner K, Thuret JY, Pope BD, Ryba T, Newman S, Ahmed K, Samarajiva SA, Salama R, Carroll T, et al. Independence of repressive histone marks and chromatin compaction during senescent heterochromatic layer formation. *Mol Cell* 2012; 47:203-14; PMID:22795131; <http://dx.doi.org/10.1016/j.molcel.2012.06.010>
- Olsen JV, Vermeulen M, Santamaria A, Kumar C, Miller ML, Jensen LJ, Gnäd F, Cox J, Jensen TS, Nigg EA, et al. Quantitative phosphoproteomics reveals widespread full phosphorylation site occupancy during mitosis. *Sci Signal* 2010; 3:ra3; PMID:20068231; <http://dx.doi.org/10.1126/scisignal.2000475>
- Abe S, Nagasaka K, Hirayama Y, Kozuka-Hata H, Oyama M, Aoyagi Y, Obuse C, Hirota T. The initial phase of chromosome condensation requires Cdk1-mediated phosphorylation of the CAP-D3 subunit of condensin II. *Genes Dev* 2011; 25:863-74; PMID:21498573; <http://dx.doi.org/10.1101/gad.2016411>
- Theodoratos A, Wilson LOW, Gosling KM, Fahrner AM. Splice variants of the condensin II gene Ncapd2 include alternative reading frame translations of exon 1. *FEBS J* 2012; 279:1422-32; PMID:2233158; <http://dx.doi.org/10.1111/j.1742-4658.2012.08530.x>
- Calvo SE, Pagliarini DJ, Mootha VK. Upstream open reading frames cause widespread reduction of protein expression and are polymorphic among humans. *Proc Natl Acad Sci U S A* 2009; 106:7507-12; PMID:19372376; <http://dx.doi.org/10.1073/pnas.0810916106>
- Wethmar K, Smink JJ, Leutz A. Upstream open reading frames: molecular switches in (patho)physiology. *Bioessays* 2010; 32:885-93; PMID:20726009; <http://dx.doi.org/10.1002/bies.201000037>
- Pedersen AG, Nielsen H. Neural network prediction of translation initiation sites in eukaryotes: perspectives for EST and genome analysis. *Proc Int Conf Intell Syst Mol Biol* 1997; 5:226-33; PMID:9322041.
- Kozak M. Pushing the limits of the scanning mechanism for initiation of translation. *Gene* 2002; 299:1-34; PMID:12459250; [http://dx.doi.org/10.1016/S0378-1119\(02\)01056-9](http://dx.doi.org/10.1016/S0378-1119(02)01056-9)
- Stumpf C, Moreno M, Olshen A, Taylor B, Ruggero D. The translational landscape of the mammalian cell cycle. *Mol Cell* 2013; 52:574-82; PMID:24120665; <http://dx.doi.org/10.1016/j.molcel.2013.09.018>
- Schleiffer A, Kaitna S, Maurer-Stroh S, Glotzer M, Nasmyth K, Eisenhaber F. Kleisins: A superfamily of bacterial and eukaryotic SMC protein partners. *Mol Cell* 2003; 11:571-5; PMID:12667442; [http://dx.doi.org/10.1016/S1097-2765\(03\)00108-4](http://dx.doi.org/10.1016/S1097-2765(03)00108-4)
- Fennell-Fezzie R, Gracia SD, Akey D, Berger JM. The MukF subunit of *Escherichia coli* condensin: architecture and functional relationship to kleisins. *EMBO J* 2005; 24:1921-30; PMID:15902272; <http://dx.doi.org/10.1038/sj.emboj.7600680>
- Onn I, Aono N, Hirano M, Hirano T. Reconstitution and subunit geometry of human condensin complexes. *EMBO J* 2007; 26:1024-34; PMID:17268547; <http://dx.doi.org/10.1038/sj.emboj.7601562>
- Haering CH, Schoffnegger D, Nishino T, Helmhart W, Nasmyth K, Löwe J. Structure and stability of cohesin's Smc1-kleisin interaction. *Mol Cell* 2004; 15:951-64; PMID:15383284; <http://dx.doi.org/10.1016/j.molcel.2004.08.030>
- Ono T, Fang Y, Spector DL, Hirano T. Spatial and temporal regulation of Condensins I and II in mitotic chromosome assembly in human cells. *Mol Biol Cell* 2004; 15:3296-308; PMID:15146063; <http://dx.doi.org/10.1091/mbc.E04-03-0242>
- Hirota T, Gerlich D, Koch B, Ellenberg J, Peters JM. Distinct functions of condensin I and II in mitotic chromosome assembly. *J Cell Sci* 2004; 117:6435-45; PMID:15572404; <http://dx.doi.org/10.1242/jcs.01604>
- Takata H, Nishijima H, Ogura SI, Sakaguchi T, Bubulya PA, Mochizuki T, Shibahara KI. Proteome analysis of human nuclear insoluble fractions. *Genes Cell* 2009; 14:975-90; PMID:19695025; <http://dx.doi.org/10.1111/j.1365-2443.2009.01324.x>
- Sadaie M, Salama R, Carroll T, Tomimatsu K, Chandra T, Young ARJ, Narita M, Pérez-Mancera P, Bennett DC, Chong H, et al. Redistribution of the Lamin B1 genomic binding profile affects rearrangement of heterochromatic domains and SAHF formation during senescence. *Genes Dev* 2013; 27:1800-8; PMID:23964094; <http://dx.doi.org/10.1101/gad.217281.113>
- Longworth MS, Herr A, Ji JY, Dyson NJ. RBF1 promotes chromatin condensation through a conserved interaction with the Condensin II protein dCAP-D3. *Genes Dev* 2008; 22:1011-24; PMID:18367646; <http://dx.doi.org/10.1101/gad.1631508>
- Reyes JC, Muchardt C, Yaniv M. Components of the human SWI/SNF complex are enriched in active chromatin and are associated with the nuclear matrix. *J Cell Biol* 1997; 137:263-74; PMID:9128241; <http://dx.doi.org/10.1083/jcb.137.2.263>
- Cai S, Han HJ, Kohwi-Shigematsu T. Tissue-specific nuclear architecture and gene expression regulated by SATB1. *Nat Genet* 2003; 34:42-51; PMID:12692553; <http://dx.doi.org/10.1038/ng1146>
- Bellacosa A, Godwin AK, Peri S, Devarajan K, Caretti E, Vanderveer L, Bove B, Slater C, Zhou Y, Daly M, et al. Altered gene expression in morphologically normal epithelial cells from heterozygous carriers of

- BRCA1 or BRCA2 mutations. *Cancer Prev Res (Phila)* 2010; 3:48-61; PMID:20051372; <http://dx.doi.org/10.1158/1940-6207.CAPR-09-0078>
44. Dimri GP, Lee X, Basile G, Acosta M, Scott G, Roskelley C, Medrano EE, Linskens M, Rubelj I, Pereira-Smith O, et al. A biomarker that identifies senescent human cells in culture and in aging skin in vivo. *Proc Natl Acad Sci U S A* 1995; 92: 9363-7; PMID:7568133; <http://dx.doi.org/10.1073/pnas.92.20.9363>
45. Takemoto A, Kimura K, Yokoyama S, Hanaoka F. Cell cycle-dependent phosphorylation, nuclear localization, and activation of human condensin. *J Biol Chem* 2004; 279:4551-9; PMID:14607834; <http://dx.doi.org/10.1074/jbc.M310925200>

# BRAF Mutation Is Associated With a Specific Cell Type With Features Suggestive of Senescence in Ovarian Serous Borderline (Atypical Proliferative) Tumors

Felix Zeppernick, MD,\*† Laura Ardighieri, MD,\* Charlotte G. Hannibal, MSc,‡  
Russell Vang, MD,\* Jette Junge, MD,§ Susanne K. Kjaer, MD,‡|| Rugang Zhang, PhD,¶  
Robert J. Kurman, MD,\*# and Ie-Ming Shih, MD, PhD\*#

**Abstract:** Serous borderline tumor also known as atypical proliferative serous tumor (APST) is the precursor of ovarian low-grade serous carcinoma (LGSC). In this study, we correlated the morphologic and immunohistochemical phenotypes of 71 APSTs and 18 LGSCs with the mutational status of *KRAS* and *BRAF*, the most common molecular genetic changes in these neoplasms. A subset of cells characterized by abundant eosinophilic cytoplasm (EC), discrete cell borders, and bland nuclei was identified in all (100%) 25 *BRAF*-mutated APSTs but in only 5 (10%) of 46 APSTs without *BRAF* mutations ( $P < 0.0001$ ). Among the 18 LGSCs, EC cells were found in only 2, and both contained *BRAF* mutations. The EC cells were present admixed with cuboidal and columnar cells lining the papillae and appeared to be budding from the surface, resulting in individual cells and clusters of detached cells “floating” above the papillae. Immunohistochemistry showed that the EC cells always expressed p16, a senescence-associated marker, and had a significantly lower Ki-67 labeling index than adjacent cuboidal and columnar cells ( $P = 0.02$ ). In vitro studies supported the interpretation that these cells were undergoing senescence, as the same morphologic features could be reproduced in cultured epithelial cells by ectopic expression of *BRAF*<sup>V600E</sup>. Senescence was further established by markers such

as SA- $\beta$ -gal staining, expression of p16 and p21, and reduction in DNA synthesis. In conclusion, this study sheds light on the pathogenesis of this unique group of ovarian tumors by showing that *BRAF* mutation is associated with cellular senescence and the presence of a specific cell type characterized by abundant EC. This “oncogene-induced senescence” phenotype may represent a mechanism that impedes progression of APSTs to LGSC.

**Key Words:** serous borderline tumors, low-grade serous carcinoma, ovarian neoplasm, *BRAF* mutation, senescence

(*Am J Surg Pathol* 2014;38:1603–1611)

Serous carcinoma, the most common and lethal ovarian cancer, is composed of 2 types, low-grade serous carcinoma (LGSC) and high-grade serous carcinoma (HGSC), which are characterized by distinctly different clinicopathologic and molecular features.<sup>1–5</sup> It has been proposed that the immediate precursor of many HGSCs is an intraepithelial carcinoma in the fallopian tube, so-called “serous tubal intraepithelial carcinoma,” whereas the immediate precursor of most LGSCs is a noninvasive ovarian LGSC, also termed “serous borderline tumor, micro-papillary variant.” The latter develops from a serous borderline tumor (SBT) also known as “atypical proliferative serous tumor (APST).” Although the majority of SBTs behave in a benign manner, approximately 5% progress to LGSC, which has a poor outcome for those with measurable disease after cytoreductive surgery.<sup>6</sup> At present, there are no markers that reliably predict progression to LGSC, and some pathologists, therefore, prefer the designation SBT to draw attention to this possibility, whereas other pathologists prefer the designation APST to emphasize the benign nature of most of these tumors recognizing that some benign tumors have the potential to progress to malignant neoplasms. The recent World Health Organization Classification of Tumors of the Female Reproductive Organs considers both terms synonymous.<sup>7</sup> In this manuscript the term APST is used.

In view of the uncertainty regarding the behavior of APSTs, patients and their physicians face a difficult dilemma in planning subsequent management, particularly for those women who present with advanced-stage

From the Departments of \*Pathology and Gynecology and Obstetrics; #Oncology, Johns Hopkins Medical Institutions, Baltimore, MD; ¶The Wistar Institute, Philadelphia, PA; †Department of Gynecology and Obstetrics, University Hospital Aachen, Aachen, Germany; ‡Unit of Virus, Lifestyle and Genes, Danish Cancer Society Research Center; ||Juliane Marie Centre, Rigshospitalet, University of Copenhagen, Copenhagen; and §Department of Pathology, Hvidovre Hospital, Denmark Gynecologic Clinic, Hvidovre, Denmark.

Conflicts of Interest and Source of Funding: Supported by a research grant, RO1CA116184, from NIH/NCI. F.Z. was supported by the Rotation Program of the Medical Faculty RWTH Aachen, Germany, Katie Oppo Research Fund and Colleen’s Dream Foundation. L.A. was supported by Fondazione Beretta (Brescia, Italy) and by the International Society of Gynecologic Pathologists Hernando Salazar Fellowship Award 2011. R.Z. is supported by NIH/NCI grants: R01CA160331 and R01CA163377. The authors have disclosed that they have no significant relationships with, or financial interest in, any commercial companies pertaining to this article.

Correspondence: Ie-Ming Shih, MD, PhD, Departments of Pathology and Gynecology and Obstetrics, Johns Hopkins University School of Medicine, 1550 Orleans Street, CRB-II, Room 306, Baltimore, MD (e-mail: shihie@yahoo.com).

Copyright © 2014 by Lippincott Williams & Wilkins



disease, as even the majority of these tumors do not progress to LGSC. The options are adjuvant chemotherapy, with its attendant potential complications, versus observation. In either case the anxiety associated with the uncertainty of the behavior of this tumor takes a significant emotional toll on the patient and her family. Accordingly, identification of a marker that reliably predicts outcome would be highly beneficial.

APST and LGSC are characterized by very low levels of DNA copy number changes as compared with other gynecologic tumors, reflecting relative genomic stability during tumor evolution.<sup>8,9</sup> The most prominent molecular alterations so far described are somatic activating mutations of *KRAS* and *BRAF*, leading to their constitutive kinase activation. Approximately two thirds of APSTs contain either mutant *KRAS* or *BRAF*, as the mutations are mutually exclusive.<sup>10–12</sup> As *KRAS* and *BRAF* are involved in the MEK signaling pathway, it is believed that aberrant signaling activity of MEK, due to activating mutations in either *KRAS* or *BRAF*, plays a major role in the development of most APSTs.<sup>13</sup>

We have previously identified a population of cells in APSTs with abundant eosinophilic cytoplasm (EC) that showed a significant decrease in steroid hormone receptors (ER and PR), WT1, and Ki-67 proliferation index compared with neighboring cuboidal and columnar cells lacking abundant EC, suggesting that the EC cells were senescent.<sup>12,14</sup> The current study presents immunohistochemical and molecular genetic evidence showing that the EC cells occur preferentially in tumors harboring mutant *BRAF*. Moreover, *in vitro* studies demonstrated that ectopic expression of *BRAF*<sup>V600E</sup> in epithelial cells induces cellular senescence, thereby providing compelling evidence that APSTs with mutant *BRAF* are undergoing senescence and that EC cells are a useful morphologic marker.

## MATERIALS AND METHODS

### Identification and Selection of Cases

The study group consists of 89 cases of APSTs (n = 71) and LGSC (n = 18) derived from 2 study sets. Most APSTs (n = 49) were selected from the files of the nationwide Danish Pathology Data Bank as previously described.<sup>12</sup> The study was approved by the Danish Data Protection Agency and the Danish Scientific Ethical Committee. The remaining cases (22 cases of APST and 18 LGSCs) were obtained from the pathology files of the Johns Hopkins Hospital. Acquisition of tissue specimens was approved by Institutional Review Board at the Johns Hopkins Hospital, Baltimore, MD. In addition to the primary ovarian tumor, sufficient tumor tissue was available from implants or metastatic lesions for 40 APSTs and 4 LGSCs. Bilateral APSTs were analyzed in 11 cases. This resulted in a total of 160 tumor lesions that were examined. Of the 71 APSTs, 56 were advanced stage (FIGO II to IV), 6 were FIGO stage I, and for 9 cases the information about FIGO stage was not accessible.

### Morphologic Evaluation and Immunohistochemistry Analysis

Sections of all 160 lesions were reviewed independently by 2 investigators (I.-M.S., F.Z.) who were blinded to the clinical and mutational data. The number of cells with abundant EC (as previously described<sup>12,14</sup>) was semiquantitatively scored as a percentage of the total number of epithelial cells in a specimen as follows: not detectable, <1%, 1% to 25%, and >25% of epithelial tumor cells. Only cases with a sufficient amount of tumor cells (at least 400 tumor cells) were included. A subset of cases was selected for further immunohistochemical analysis. Sections were stained with anti-Ki-67 antibody (Ventana Medical Systems, Tucson, AZ; prediluted) and an anti-p16 antibody (Ventana Medical Systems; prediluted) and counterstained with either hematoxylin or eosin. The Ki-67 proliferation index was scored in a similar semiquantitative manner by counting at least 400 cells and determining the percentage of positive cells. The EC and cuboidal/columnar cell populations were counted separately. p16 immunoreactivity in EC cells was reported as positive (both nuclear and cytoplasmic) or negative. Immunostaining with the mouse monoclonal VE1 antibody was used to detect mutant *BRAF* protein (V600E) as described previously (Spring Bioscience, Pleasanton, CA; 1:250).<sup>12</sup> It has been shown that APSTs with *BRAF* V600E mutations were all positive for VE1 immunoreactivity, whereas none of the wild-type *BRAF* specimens was positive for VE1.<sup>12</sup> VE1 immunohistochemistry was applied to determine the *BRAF* mutation status in 6 cases of which the mutational analysis was unsuccessful.

### Mutational Analysis

Mutational analysis was performed using the conventional Sanger sequencing technique in *KRAS* at exon 2 including codons 12–13 and *BRAF* at exon 15 including codon 600 as previously described.<sup>11</sup> Polymerase chain reaction amplification was performed using genomic DNA from microdissected formalin-fixed, paraffin-embedded tissue with the following primers for exon 15 of *BRAF*: forward 5'-TGCTTGCTCTGATAGGAAAATGA-3' and reverse 5'-CCACAAAATGGATCCAGACAAC-3'; for exon 2–3 of *KRAS*: forward 5'-TAAGGCCTGCTGAAAATGACTG-3' and *KRAS* reverse 5'-TGGTCCTGCACCAGTAATATGC-3'. Amplified polymerase chain reaction products were sequenced at the Beckman Coulter Inc., (Danvers, MA) and analyzed with the Mutation Surveyor DNA Variant Analysis Software. Mutational analysis was successful in 83 cases. In addition 6 APSTs, which could not be analyzed for their mutational status, positive *BRAF* VE1 staining was used as a surrogate for *BRAF*<sup>V600E</sup> mutation.

### Cell Culture and Transduction

Primary human ovarian surface epithelial (HOSE) cells were prepared from ovaries obtained during prophylactic oophorectomies as described previously.<sup>15</sup> The cells were cultured in medium 199 and MCDB-105 (1:1) supplemented with 4% fetal bovine serum and 0.2 U/mL

of insulin.<sup>16</sup> pBABE-puro and pBABE-puro-BRAF<sup>V600E</sup> were obtained from Addgene (Cambridge, MA). Retrovirus production and transduction were performed as described,<sup>17</sup> using Phoenix cells to package the viruses (a gift from Dr Gary Nolan, Stanford University). Cells infected with viruses encoding drug-resistant gene to puromycin were selected in 1 µg/mL. FG12-CMV-Lenti-GFP and FG12-CMV-Lenti-GFP-BRAF<sup>V600E</sup> were kindly provided by Dr Daniel Peeper. Lentivirus was packaged using Virapower Kit from Invitrogen following manufacturer's instruction as described previously.<sup>18</sup>

Immunofluorescence, BrdU Labeling, and SA-β-Gal Staining

The following antibodies were obtained from indicated suppliers: mouse anti-BrdU FITC (BD Bioscience), mouse anti-p21 (Santa Cruz), mouse anti-BRAF

TABLE 1. Summary of APST Cases Showing Cells With Abundant EC

| Mutational Status | EC Cells Present | EC Cells Absent | Total |
|-------------------|------------------|-----------------|-------|
| BRAF-mut*†        | 25               | 0               | 25    |
| BRAF-wt*          | 5                | 41              | 46    |
| KRAS-mut          | (4)              | (25)            | (29)  |
| BRAF/KRAS-wt      | (1)              | (16)            | (17)  |

\*P < 0.0001, Fisher's exact test, 2-tailed.  
†For 6 APSTs, BRAF mutation was assumed after mutational analysis failed, but VE1 immunohistochemistry stained positive.  
mut indicates mutant; wt, wild-type.

(Santa Cruz), mouse anti-β-actin (Abcam),<sup>19</sup> and mouse anti-p16 was a gift from Dr Greg Enders. Immunofluorescence staining and BrdU labeling for cultured cells were performed as previously described using the

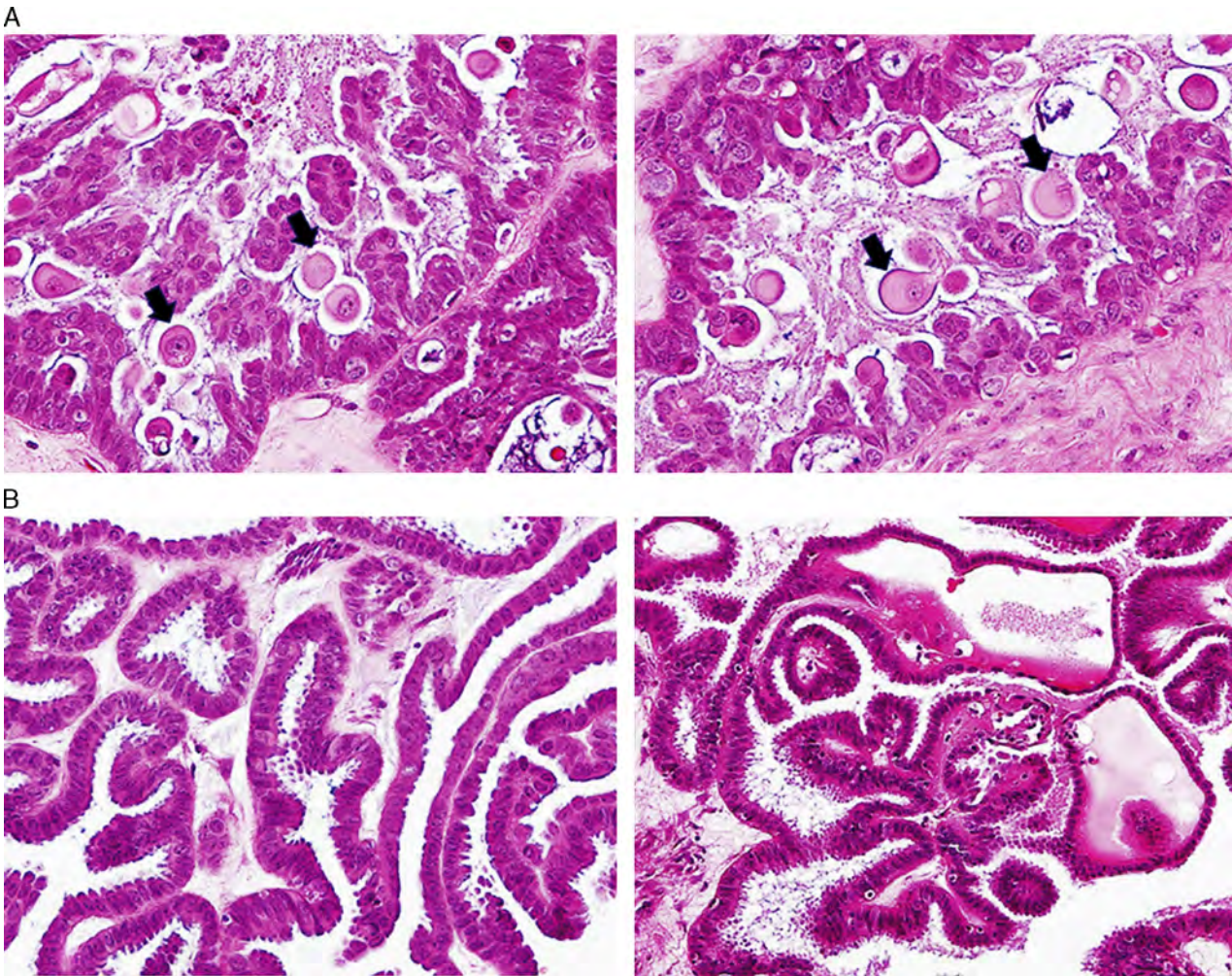


FIGURE 1. A, Eosinophilic cells (EC) in an APST with mutant BRAF<sup>V600E</sup> are present on the surface of papillae along with cuboidal and columnar cells. Many EC cells are detached (arrows), floating above the surface of papillae. They are characterized by abundant EC and discrete cell borders. The nuclei are mostly round with a smooth nuclear membrane and contain faintly staining chromatin. EC cells appear to bud from cuboidal/columnar epithelial cells on the surface of the papillae. B, Another APST without BRAF mutation does not demonstrate any EC cells.



**TABLE 2.** Mutational Status and FIGO Stage of APST (n=71)

| FIGO Stage | BRAF-Mut | KRAS-Mut | WT |
|------------|----------|----------|----|
| NA         | 7        | 1        | 1  |
| I          | 6        | —        | —  |
| II         | 5        | 12       | 5  |
| III        | 6        | 16       | 11 |
| IV         | 1        | —        | —  |

NA indicates not accessible; Mut, somatic mutation; WT, wild-type KRAS and BRAF.

antibodies listed above.<sup>16,18</sup> SA-β-Gal staining was performed as previously described.<sup>20</sup>

Statistical Analysis

All calculations were done using the statistical software environment R, version 3.1.0 and Graph Pad

Prism Version 5.0. Statistical significance was set at the level of 0.05.

RESULTS

Morphologic examination of 71 APSTs including 25 with *BRAF* mutations, 29 with *KRAS* mutations, and 17 with wild-type *BRAF* and *KRAS* revealed a population of epithelial cells containing abundant EC and discrete cell borders. The nuclei tended to be round with a smooth nuclear membrane and contained faintly staining chromatin. Mitotic figures were not observed in these cells. These cells were adjacent to cuboidal and columnar cells with round to oval nuclei in which the nuclear chromatin was more distinct and coarser and which were devoid of abundant EC. The EC cells appeared to bud from the overlying epithelial layer of the APST (Fig. 1). They were often detached from the epithelium, floating freely above

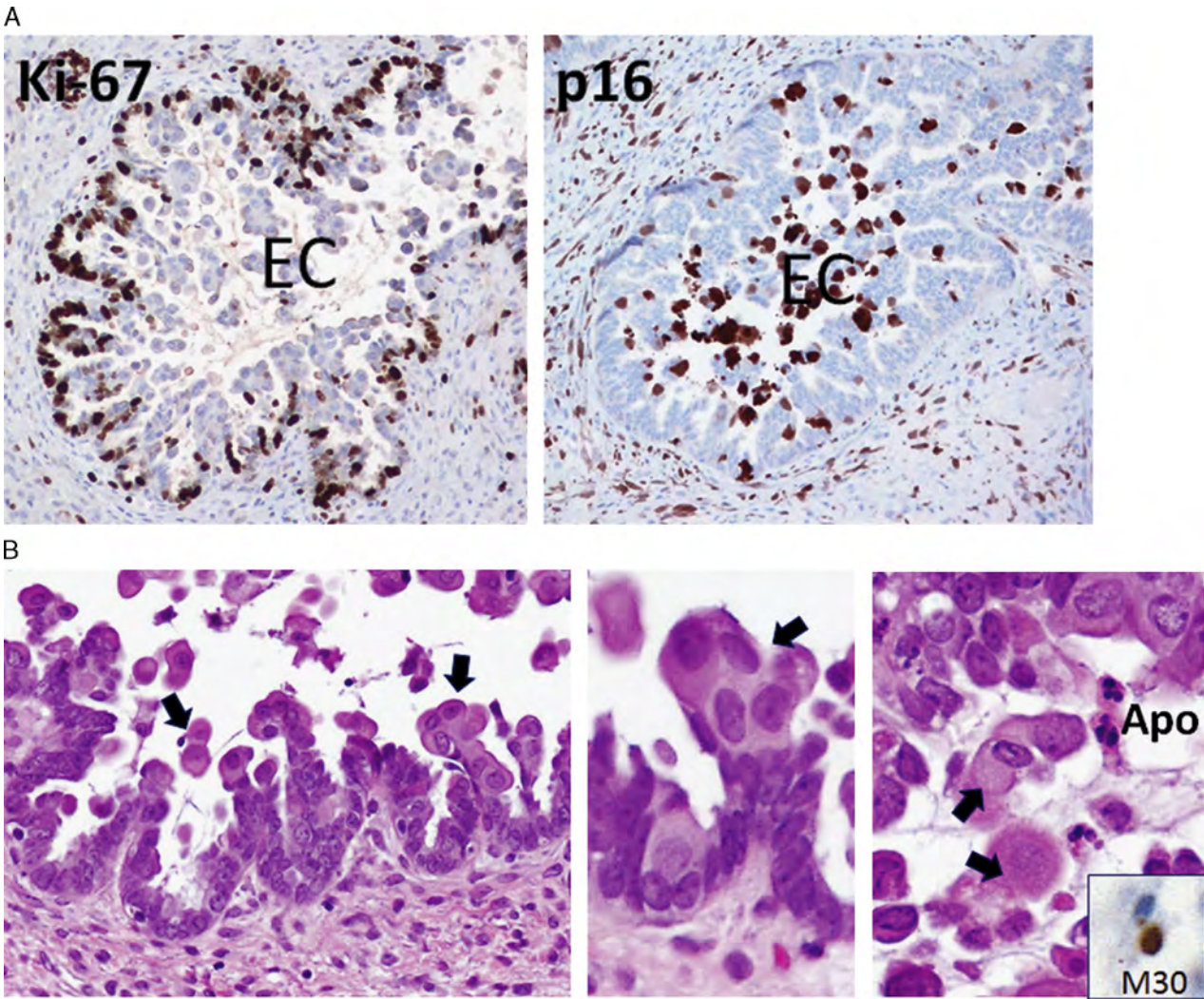


**FIGURE 2.** An APST harboring mutant *BRAF*<sup>V600</sup> showing expression of Ki-67 and p16 A, EC cells tend to be Ki-67 negative and strongly and diffusely p16 positive. B, EC cells (arrows) showing senescent features characterized by nuclei with washed out indistinct chromatin (arrows). Apoptotic cells (Apo) are positive for an apoptotic marker, M30 (see inset).



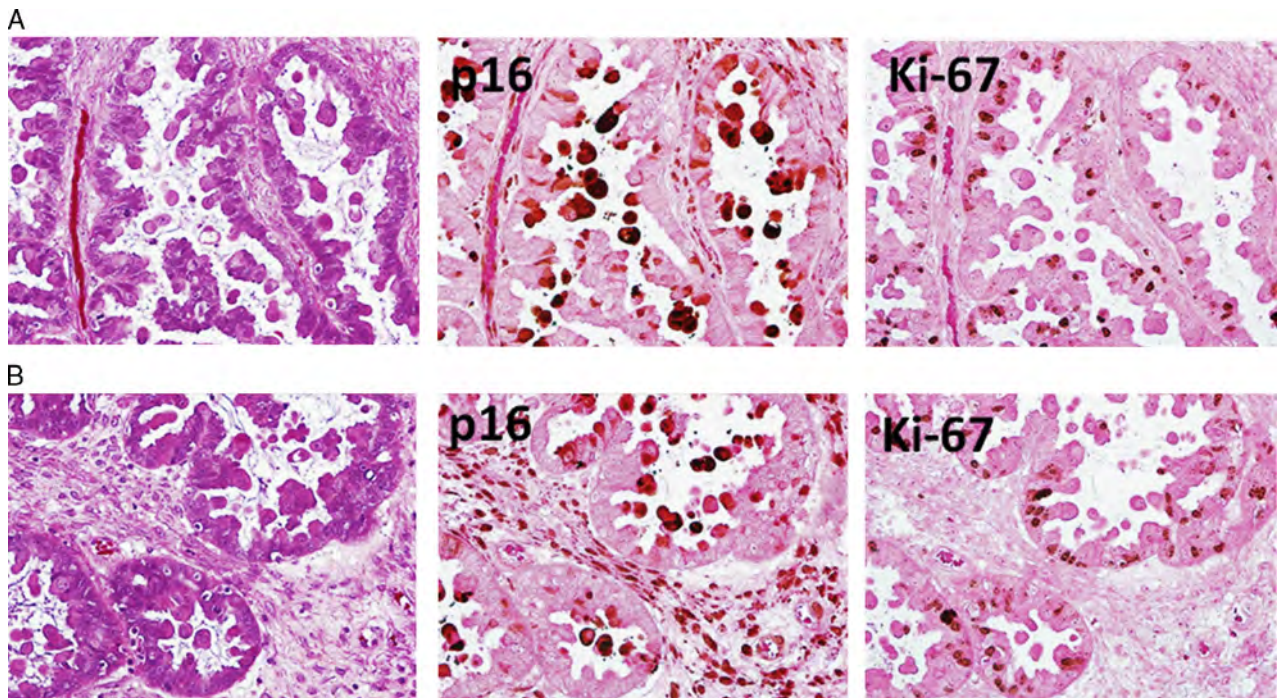


**FIGURE 3.** Immunostaining pattern of p16 and Ki-67 in an APST. EC cells that are positive for p16 and are devoid of Ki-67 immunoreactivity. A and B represent 2 different areas from the same case, and the slides were counterstained with eosin only to reveal the abundant cytoplasm in EC cells.

the epithelial layer of the tumor and in 1 case in the underlying stroma of the tumor, so-called “microinvasion.” Using  $>1\%$  EC cells as a cutoff point, it was found that they were present in all 25 APSTs harboring mutant *BRAF*, in 4 (14%) of 29 APSTs with *KRAS* mutation, and in 1 (6%) of 17 APSTs with wild-type *KRAS* and *BRAF* (Table 1). The mutation status of APST according to clinical stages is summarized in Table 2. Because mutations of *KRAS* and *BRAF* are mutually exclusive, we combined the mutant *KRAS* and wild-type *KRAS/BRAF* groups into 1 group, designated the “*BRAF* wild-type” group, and observed that EC cells were significantly more often present in the *BRAF*-mutated than the wild-type group ( $P < 0.0001$ , Fisher’s exact test, 2-tailed).

Immunohistochemical staining revealed that the EC cells in contrast to the adjacent cuboidal/columnar cells were intensely stained for both nuclear and cytoplasmic p16, a senescence-associated marker,<sup>21,22</sup> and were essentially negative for Ki-67, a proliferative marker (Figs. 2, 3). EC cells had a significantly lower Ki-67 index than the cuboidal/columnar cells ( $P = 0.02$ , paired 2-tailed *t*-test). Occasional apoptotic cells adjacent to EC cells were also observed (Fig. 2B). They were positive for M30 staining, an apoptotic marker.

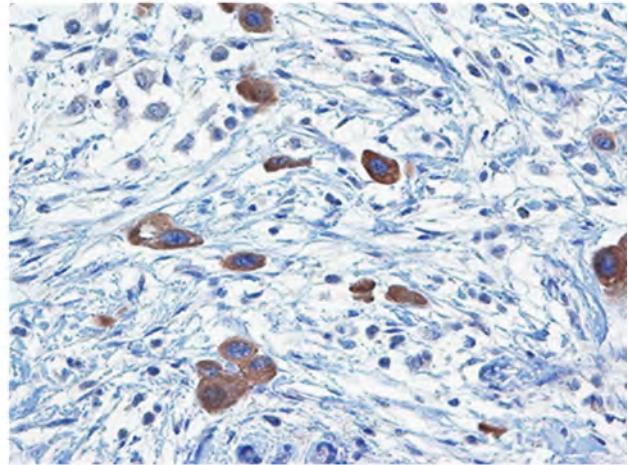
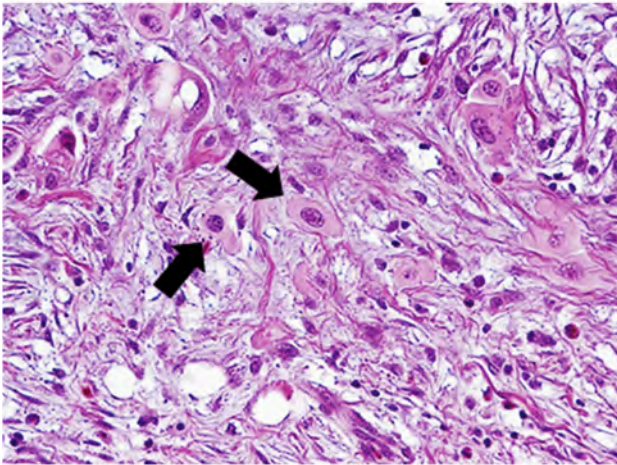
In our previous study, almost all primary APSTs and their concurrent implants were found to have the same mutation status of *KRAS* and *BRAF*.<sup>12</sup> In this study, there were 40 APSTs with at least 1 concurrent peritoneal implant that were available for study. Among them, 37 (92.5%) showed the same morphologic features

in the primary tumor and implant in terms of the presence or absence of EC cells. Similar concordance of EC cells was observed in 10 (91%) of 11 bilateral APSTs. Two implants, one with many EC cells positive for VE1 and another without EC cells negative for VE1 are shown in Figure 4. Interestingly, the cases in which there was discordance of EC cells between the primary tumors and implants occurred only in tumors and implants with mutant *KRAS* (3 of 23 cases). Those discordant cases include 2 with EC cells in the primary tumors but not in the implants and 1 case in which the primary tumor lacked EC cells, but they were present in the implants. All the cases with mutant *BRAF* and wild-type *KRAS* and *BRAF* showed concordant morphologic features in both the primary tumor and implants (17 of 17 cases), that is, the presence of EC cells in mutant *BRAF* cases and absent EC cells in both primary tumor and corresponding implant(s) in cases wild-type for *KRAS* and *BRAF*.

The above findings suggest that mutant *BRAF* protein may induce changes resulting in the development of EC cells that we interpreted on morphologic grounds as evidence of cellular senescence. To test this hypothesis, we ectopically expressed mutant *BRAF*<sup>V600E</sup> in human ovarian surface epithelial HOSE cells (Fig. 5). HOSE cells expressing *BRAF*<sup>V600E</sup> had a greater percentage of cells that were positive for SA- $\beta$ -gal stain, a conventional marker of cellular senescence, than the control cells (27% vs. 3%). Immunofluorescent staining also demonstrated that as compared with control cells HOSE cells expressing *BRAF*<sup>V600E</sup> had a much greater number of cells positive



A



B

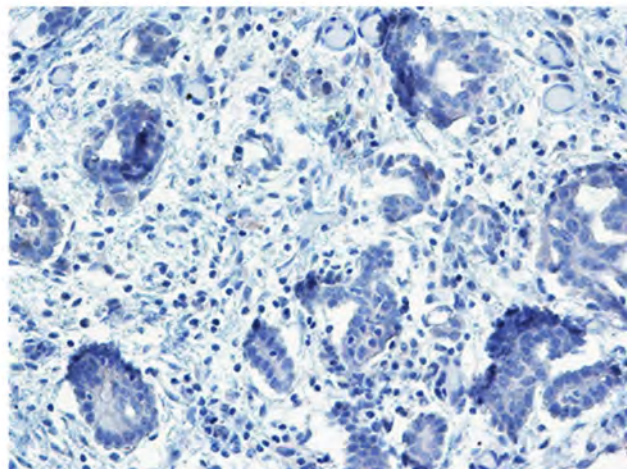
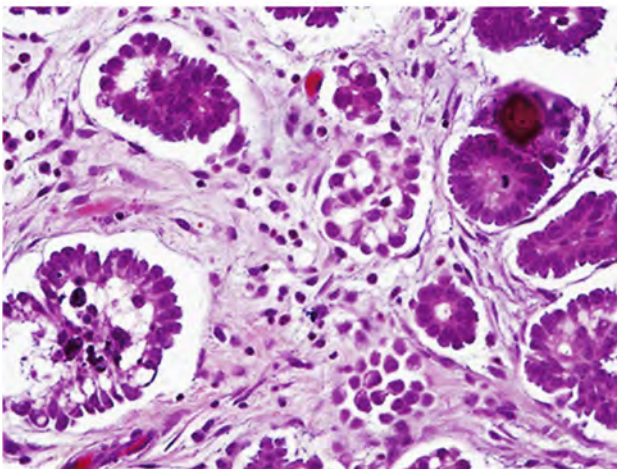


**FIGURE 4.** A, VE1-positive desmoplastic noninvasive implant contains many EC cells, identical to the EC cells in foci of “microinvasion” (arrows). B, VE1-negative implant does not contain EC cells.

for p16 and p21 that are upregulated during cellular senescence. In contrast, in a BrdU incorporation study *BRAF*<sup>V600E</sup> transfected cells showed a decrease in DNA synthesis as compared with control cells (Fig. 5).

## DISCUSSION

Cellular senescence is a fundamental biological phenomenon involved in embryogenesis, tissue development, and various pathobiological conditions.<sup>23</sup> Although it has been extensively studied in cell culture, microscopic characterization of senescence in tissue sections has not been well described. In this study, we identified a population of epithelial cells in APSTs characterized by abundant EC, distinct cell borders, nuclei with faintly staining chromatin, strong expression of p16, and loss of proliferative activity as evidenced by essentially no Ki-67 immunoreactivity. These features are commonly seen in senescent cells in vitro. The EC cells, along with cuboidal and columnar cells, comprise the cellular population that lines

the papillae of the APSTs. The latter 2 cell types have relatively scant cytoplasm, bland, round to oval nuclei, and are frequently ciliated. The EC cells tend to be rounder, less frequently ciliated, and are closely apposed to the cuboidal and columnar cells. When there is cellular stratification they tend to be at a slightly higher level than the cuboidal/columnar cells, approaching the surface of the papillae and then detaching, acquiring more abundant EC and losing their cilia in the process. As a consequence they appear to “float” above the papillae and occasionally are present in the underlying stroma, so-called “microinvasion.” Mitotic figures are present only in the cuboidal and columnar cells. Occasional apoptotic cells adjacent to the EC cells are also evident. The entire process appears to reflect senescence manifested by transformation of cuboidal and columnar cells to EC cells. This interpretation is supported by a previous study in which we demonstrated that compared with the cuboidal and columnar cells, the EC cells showed a significant decrease in ER, PR, WT1, and Ki-67 labeling index.<sup>14</sup> In the present

study, we found that the EC cells are specifically associated with *BRAF* mutations, as they were detected in 100% of APSTs with *BRAF* mutations but in only 10% of APSTs with wild-type *BRAF* and *KRAS* or *KRAS* mutations, suggesting that they are a morphologic marker of *BRAF* mutation in these tumors. The above finding was confirmed by our in vitro cell culture studies showing that mutant *BRAF* leads to the development of senescent cells with similar morphologic features. Expression of p16 and absence of Ki-67 labeling has been previously reported in senescent cells in colorectal adenomatous polyps with *BRAF* mutations.<sup>22</sup>

The findings in this study are reminiscent of “oncogene-induced senescence,” a well-established mechanism that impedes cancer development in humans<sup>24,25</sup> in which oncogenic stress induced by an oncogenic protein such as mutant *BRAF* protein leads to DNA double-strand breaks in nontransformed epithelial cells. This activates the DNA damage response that is responsible for growth inhibition and induction of senescence through activation of p53-p21 and p16 pathways.<sup>21,26–29</sup> As *TP53* mutations are

exceptionally rare in APSTs, the intact p53 protein may serve as the upstream checkpoint control that triggers the senescence pathway in *BRAF*-mutated APSTs.

Our study raises a number of intriguing questions. First, if *BRAF* mutations result in cellular senescence in APSTs, why is this genotype clonally selected in many of them? We postulate that *BRAF* mutation, like *KRAS* mutation, is required for tumor initiation, because mutations in both genes have multiple tumor-promoting effects including upregulation of glucose transporter-1 (GLUT1), an essential surface protein that results in an increase in glucose metabolism required for tumor transformation.<sup>27</sup> Once an APST develops, the epithelial cells may initiate a mechanism to restrain tumor progression as occurs in many benign human neoplasms, including colorectal adenomatous polyps and melanocytic nevi.<sup>30–32</sup> This may account for why *BRAF*-mutated advanced-stage LGSCs are much less common than *BRAF*-mutated advanced-stage APSTs.<sup>12,33–35</sup>

Second, how do tumors that progress to LGSC overcome the senescence induced by *BRAF* mutations?

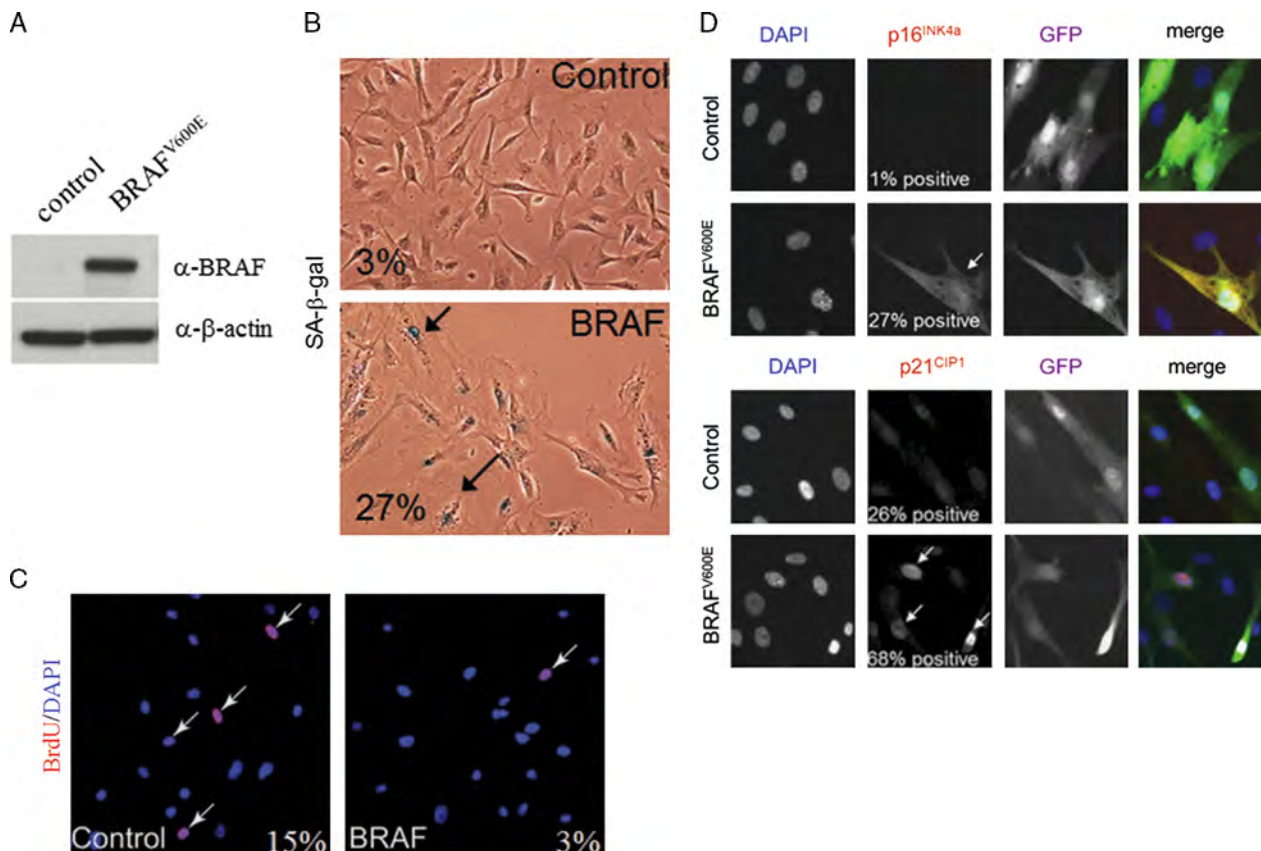


**FIGURE 5.** A, Western blot analysis shows expression of mutant *BRAF* protein in primary HOSE cells transduced with the *BRAF*<sup>V600E</sup> expressing construct. B, SA-β-gal activity in primary HOSE cells expressing *BRAF*<sup>V600E</sup>. Arrows point to large, flat SA-β-gal-positive senescent cells. C, BrdU incorporation is decreased in primary HOSE cells expressing *BRAF*<sup>V600E</sup> as compared with control non-transduced cells. Arrows point to BrdU-positive cells (BrdU in red and cell nuclei counterstained with DAPI in blue). D, Expression of *BRAF*<sup>V600E</sup> in HOSE cells in culture results in an increase in p16 and p21. Arrows indicate p16 and p21 positive cells, respectively. Cells were engineered to coexpress nuclear GFP when they were transfected with the expression plasmids. The fluorescence images were merged in the rightmost panel.



We suspect that, as with the progression of precursor lesions to frankly malignant tumors, for example, as occurs in melanoma and lung cancer,<sup>36,37</sup> additional molecular genetic alterations occur during progression from an APST to an LGSC, which abolish the checkpoint control by the p53-p21 and p16 pathways. We have previously analyzed the genome-wide copy number alterations in ovarian low-grade serous neoplasms and reported that hemizygous ch1p36 deletion and ch9p21 homozygous or hemizygous deletions are much more common in ovarian LGSCs than in APSTs.<sup>8</sup> The ch1p36 region contains several candidate tumor suppressors including miR-34a, which is required for DNA damage response and is the direct p53 target that mediates its tumor-suppressor functions.<sup>38,39</sup> Likewise, the ch9p21 region corresponding to the *CDKN2A/B* locus encodes 3 well-known tumor-suppressor proteins, p14 (Arf), p16, and p15 that inhibit cyclin-dependent kinase. Thus, deletions or silencing of miR-34a and *CDKN2A/B* loci may abrogate the p53 checkpoint on *BRAF* mutations and permit APSTs to escape senescence and progress to LGSC. In this regard, it has been reported that p16 expression levels are significantly decreased in LGSCs as compared with APSTs.<sup>40</sup>

Finally, why are EC cells more commonly detected in *BRAF*-mutated than in *KRAS*-mutated APSTs? It has been demonstrated that *KRAS* and *BRAF* kinases may form their own unique signaling networks in addition to the shared function in activating MEK signaling.<sup>41–43</sup> Therefore, in APSTs it is likely that, although mutations of *KRAS* and *BRAF* contribute equally to tumor initiation, they may have different functions after the tumor has developed. Tumors with mutant *BRAF* undergo senescence, characterized by the presence of EC cells, whereas APSTs with mutant *KRAS* or wild-type *BRAF* and *KRAS* are less likely to undergo senescence and therefore do not express the EC phenotype. Furthermore, after cytoreductive surgery occult implants harboring mutant *BRAF* are likely to undergo cellular senescence and have a reduced risk for recurrence and progression. In conclusion, this study provides new evidence that mutation of *BRAF* appears to have a paradoxical effect, acting as a driver mutation for initiation of an APST while also apparently inhibiting progression to LGSC. This finding sheds light on the pathogenesis of this unique group of ovarian tumors, which has perplexed pathologists and gynecologists for over half a century. The study also has important clinical implications by correlating a specific morphologic phenotype, namely, EC cells with *BRAF* mutation, thereby providing pathologists with the ability to identify a group of APSTs that are likely to behave in a benign manner from those that are more likely to progress to LGSC. This would allow gynecologists to target a group of patients for close surveillance and possibly further treatment while sparing another group of patients from additional and potentially harmful treatment. Although highly provocative, our conclusions must be validated by larger clinicopathologic studies.

## REFERENCES

- Shih IeM, Kurman RJ. Molecular pathogenesis of ovarian borderline tumors: new insights and old challenges. *Clin Cancer Res*. 2005;11:7273–7279.
- Cho KR, Shih IM. Ovarian cancer. *Annu Rev Pathol*. 2009;4:287–313.
- Shih IeM, Chen L, Wang CC, et al. Distinct DNA methylation profiles in ovarian serous neoplasms and their implications in ovarian carcinogenesis. *Am J Obstet Gynecol*. 2010;203:e1–22.
- Fader AN, Java J, Krivak TC, et al. The prognostic significance of pre- and post-treatment CA-125 in grade 1 serous ovarian carcinoma: a Gynecologic Oncology Group study. *Gynecol Oncol*. 2013;132:560–565.
- May T, Shoni M, Crum CP, et al. Low-grade and high-grade serous Mullerian carcinoma: review and analysis of publicly available gene expression profiles. *Gynecol Oncol*. 2013;128:488–492.
- Fader AN, Java J, Ueda S, et al. Survival in women with grade 1 serous ovarian carcinoma. *Obstet Gynecol*. 2013;122:225–232.
- Seidman JD, Bell DA, Crum CP, et al. Tumors of the ovary—Serous borderline tumor/atypical proliferative serous tumor. In: Kurman RJ, Carcangiu ML, Herrington S, Young RH, eds. *WHO Classification of Tumors of Female Reproductive Organs*. Lyon: IARC; 2014:17–24.
- Kuo KT, Guan B, Feng Y, et al. Analysis of DNA copy number alterations in ovarian serous tumors identifies new molecular genetic changes in low-Grade and high-grade carcinomas. *Cancer Res*. 2009;69:4036–4042.
- Kuhn E, Wu RC, Guan B, et al. Identification of molecular pathway aberrations in uterine serous carcinoma by genome-wide analyses. *J Natl Cancer Inst*. 2012;104:1503–1513.
- Singer G, Oldt R III, Cohen Y, et al. Mutations in *BRAF* and *KRAS* characterize the development of low-grade ovarian serous carcinoma. *J Natl Cancer Inst*. 2003;95:484–486.
- Jones S, Wang TL, Kurman RJ, et al. Low-grade serous carcinomas of the ovary contain very few point mutations. *J Pathol*. 2012;226:413–420.
- Ardighieri L, Zeppernick F, Hannibal CG, et al. Mutational analysis of *BRAF* and *KRAS* in ovarian atypical proliferative serous (borderline) tumors and associated peritoneal implants. *J Pathol*. 2014;232:19–22.
- Pohl G, Ho CL, Kurman RJ, et al. Inactivation of the mitogen-activated protein kinase pathway as a potential target-based therapy in ovarian serous tumors with *KRAS* or *BRAF* mutations. *Cancer Res*. 2005;65:1994–2000.
- Maniar KP, Wang Y, Visvanathan K, et al. Evaluation of microinvasion and lymph node involvement in ovarian serous borderline/atypical proliferative serous tumors: a morphologic and immunohistochemical analysis of 37 cases. *Am J Surg Pathol*. 2014;38:743–755.
- Dyck HG, Hamilton TC, Godwin AK, et al. Autonomy of the epithelial phenotype in human ovarian surface epithelium: changes with neoplastic progression and with a family history of ovarian cancer. *Int J Cancer*. 1996;69:429–436.
- Bitler BG, Nicodemus JP, Li H, et al. Wnt5a suppresses epithelial ovarian cancer by promoting cellular senescence. *Cancer Res*. 2011;71:6184–6194.
- Zhang R, Poustovoitov MV, Ye X, et al. Formation of MacroH2A-containing senescence-associated heterochromatin foci and senescence driven by ASF1a and HIRA. *Dev Cell*. 2005;8:19–30.
- Aird KM, Zhang G, Li H, et al. Suppression of nucleotide metabolism underlies the establishment and maintenance of oncogene-induced senescence. *Cell Rep*. 2013;3:1252–1265.
- Zhang R, Chen W, Adams PD. Molecular dissection of formation of senescence-associated heterochromatin foci. *Mol Cell Biol*. 2007;27:2343–2358.
- Dimri GP, Lee X, Basile G, et al. A biomarker that identifies senescent human cells in culture and in aging skin in vivo. *Proc Natl Acad Sci USA*. 1995;92:9363–9367.
- Michaloglou C, Vredeveld LC, Soengas MS, et al. BRAF600-associated senescence-like cell cycle arrest of human naevi. *Nature*. 2005;436:720–724.

22. Kriegl L, Neumann J, Vieth M, et al. Up and downregulation of p16(Ink4a) expression in BRAF-mutated polyps/adenomas indicates a senescence barrier in the serrated route to colon cancer. *Mod Pathol*. 2011;24:1015–1022.
23. Hayflick L, Moorhead PS. The serial cultivation of human diploid cell strains. *Exp Cell Res*. 1961;25:585–621.
24. Collado M, Gil J, Efeyan A, et al. Tumour biology: senescence in premalignant tumours. *Nature*. 2005;436:642.
25. Collado M, Serrano M. Senescence in tumours: evidence from mice and humans. *Nat Rev Cancer*. 2010;10:51–57.
26. Haffner MC, De Marzo AM, Meeker AK, et al. Transcription-induced DNA double strand breaks: both oncogenic force and potential therapeutic target? *Clin Cancer Res*. 2011;17:3858–3864.
27. Sheu JJ, Guan B, Tsai FJ, et al. Mutant BRAF induces DNA strand breaks, activates DNA damage response pathway, and up-regulates glucose transporter-1 in nontransformed epithelial cells. *Am J Pathol*. 2012;180:1179–1188.
28. Sagun KC, Carcamo JM, Golde DW. Antioxidants prevent oxidative DNA damage and cellular transformation elicited by the over-expression of c-MYC. *Mutat Res*. 2006;593:64–79.
29. Vogelstein B, Lane D, Levine AJ. Surfing the p53 network. *Nature*. 2000;408:307–310.
30. Bartkova J, Horejsi Z, Koed K, et al. DNA damage response as a candidate anti-cancer barrier in early human tumorigenesis. *Nature*. 2005;434:864–870.
31. Bartkova J, Rezaei N, Liontos M, et al. Oncogene-induced senescence is part of the tumorigenesis barrier imposed by DNA damage checkpoints. *Nature*. 2006;444:633–637.
32. Gorgoulis VG, Vassiliou LV, Karakaidos P, et al. Activation of the DNA damage checkpoint and genomic instability in human precancerous lesions. *Nature*. 2005;434:907–913.
33. Grisham RN, Iyer G, Garg K, et al. BRAF mutation is associated with early stage disease and improved outcome in patients with low-grade serous ovarian cancer. *Cancer*. 2013;119:548–554.
34. Wong KK, Tsang YT, Deavers MT, et al. BRAF mutation is rare in advanced-stage low-grade ovarian serous carcinomas. *Am J pathol*. 2010;177:1611–1617.
35. Farley J, Brady WE, Vathipadiekal V, et al. Selumetinib in women with recurrent low-grade serous carcinoma of the ovary or peritoneum: an open-label, single-arm, phase 2 study. *Lancet Oncol*. 2013;14:134–140.
36. Dankort D, Filenova E, Collado M, et al. A new mouse model to explore the initiation, progression, and therapy of BRAFV600E-induced lung tumors. *Genes Dev*. 2007;21:379–384.
37. Dankort D, Curley DP, Carlidge RA, et al. Braf(V600E) cooperates with Pten loss to induce metastatic melanoma. *Nat Genet*. 2009;41:544–552.
38. Kato M, Paranjape T, Muller RU, et al. The mir-34 microRNA is required for the DNA damage response in vivo in *C. elegans* and in vitro in human breast cancer cells. *Oncogene*. 2009;28:2419–2424.
39. He L, He X, Lim LP, et al. A microRNA component of the p53 tumour suppressor network. *Nature*. 2007;447:1130–1134.
40. Schlosshauer PW, Deligdisch L, Penault-Llorca F, et al. Loss of p16INK4A expression in low-grade ovarian serous carcinomas. *Int J Gynecol Pathol*. 2011;30:22–29.
41. Downward J. Targeting RAS signalling pathways in cancer therapy. *Nat Rev Cancer*. 2003;3:11–22.
42. Blasco RB, Francoz S, Santamaria D, et al. c-Raf, but not B-Raf, is essential for development of K-Ras oncogene-driven non-small cell lung carcinoma. *Cancer Cell*. 2011;19:652–663.
43. Chapman MS, Miner JN. Novel mitogen-activated protein kinase kinase inhibitors. *Exp Opin Investig Drug*. 2011;20:209–220.





## Metabolic alterations accompanying oncogene-induced senescence

Katherine M Aird & Rugang Zhang

To cite this article: Katherine M Aird & Rugang Zhang (2014) Metabolic alterations accompanying oncogene-induced senescence, Molecular & Cellular Oncology, 1:3, e963481, DOI: [10.4161/23723548.2014.963481](https://doi.org/10.4161/23723548.2014.963481)

To link to this article: <http://dx.doi.org/10.4161/23723548.2014.963481>



© 2014 The Author(s). 2014 Taylor & Francis Group, LLC



Published online: 23 Dec 2014.



Submit your article to this journal [↗](#)



Article views: 219



View related articles [↗](#)



View Crossmark data [↗](#)

# Metabolic alterations accompanying oncogene-induced senescence

Katherine M Aird\* and Rugang Zhang

The Wistar Institute; Gene Expression and Regulation; Philadelphia, PA, 19104, USA

**Keywords:** autophagy, lipogenesis, metabolism, oncogene-induced senescence, oxidative phosphorylation, RRM2, glycolysis, TCA cycle, The Warburg Effect

**Abbreviations:** 3-AP, 3-aminopyridine-2-carboxaldehyde thiosemicarbazone; ACC, acetyl-CoA carboxylase; ACLY, ATP-dependent citrate lyase; CPT1, carnitine-palmitoyl transferase I; dNDP, deoxyribonucleoside diphosphate; dNTP, deoxyribonucleotide triphosphate; FASN, fatty acid synthase; GPC, L- $\alpha$ -glycerophosphocholine; MDH, malate dehydrogenase; ME, malic enzyme; NAD, nicotinamide adenine dinucleotide; NDP, ribonucleoside diphosphate; NTP, ribonucleoside triphosphate; OIS, oncogene-induced senescence; PC, phosphocholine; PDH, pyruvate dehydrogenase kinase; PDK, pyruvate dehydrogenase kinase; PDP2, pyruvate dehydrogenase phosphatase 2; PKM2, pyruvate kinase M2; PML, promyelocytic leukemia; PPAR, peroxisome proliferator-activated receptor; PPP, pentose phosphate pathway; SA-B-Gal, senescence-associated  $\beta$ -galactosidase; RISP, Rieske iron sulfur protein; RNR, ribonucleotide reductase; ROS, reactive oxygen species; RRM1, ribonucleotide reductase subunit M1; RRM2, ribonucleotide reductase subunit M2; RRM2B/p53R2, ribonucleotide reductase subunit M2B; SASP, senescence-associated secretory phenotype; SDHA, succinate dehydrogenase; TCA, tricarboxylic acid.

Senescence is defined as a stable cell growth arrest. Oncogene-induced senescence (OIS) occurs in normal primary human cells after activation of an oncogene in the absence of other cooperating oncogenic stimuli. OIS is therefore considered a *bona fide* tumor suppression mechanism *in vivo*. Indeed, overcoming OIS-associated stable cell growth arrest can lead to tumorigenesis. Although cells that have undergone OIS do not replicate their DNA, they remain metabolically active. A number of recent studies report significant changes in cellular metabolism during OIS, including alterations in nucleotide, glucose, and mitochondrial metabolism and autophagy. These alterations may be necessary for stable senescence-associated cell growth arrest, and overcoming these shifts in metabolism may lead to tumorigenesis. This review highlights what is currently known about alterations in cellular metabolism during OIS and the implication of OIS-associated metabolic changes in cellular transformation and the development of cancer therapeutic strategies.

## Introduction

### Senescence

Senescence was first described in 1961 by Leonard Hayflick and Paul Moorhead while working at The Wistar Institute in

Philadelphia.<sup>1</sup> Specifically, these scientists found that normal cells in culture could only double a limited number of times, after which the cells would exit the cell cycle (termed “senescence”). In the decades since this discovery, a number of other stimuli have been shown to induce senescence, including oncogene activation, DNA damage, oxidative damage, and certain chemotherapeutic agents.<sup>2</sup> Although the cells do not continue to replicate their DNA, it is well appreciated that senescent cells remain metabolically active, and that these metabolic changes play a role in both senescence-associated cell growth arrest and human disease.

### Oncogene-induced senescence

Oncogene-induced senescence (OIS) occurs when an oncogene (such as RAS, BRAF, MYC, etc.) becomes activated in a normal diploid cell.<sup>3</sup> This leads to a paradoxical stable cell cycle exit, which arrests cell growth.<sup>4</sup> Therefore, OIS is considered a *bona fide* tumor suppressor mechanism *in vivo*.<sup>4,5</sup> For instance, benign nevi, which are often characterized by mutations in BRAF and NRAS, have been shown to be senescent lesions.<sup>4</sup>

OIS is characterized by a number of phenotypic and molecular alterations. Phenotypically, cells that have undergone OIS exhibit a large, flat morphology and are positive for increased  $\beta$ -galactosidase activity (termed senescence-associated  $\beta$ -galactosidase [SA- $\beta$ -Gal]).<sup>6</sup> Additionally, OIS is often accompanied by accumulation of DNA damage, in particular DNA double strand breaks, and a robust DNA damage response.<sup>7–10</sup> This damage is largely due to the aberrant DNA replication observed during OIS.<sup>9,11</sup> Further, OIS is characterized by upregulation of the p53/p21 and pRb/p16 pathways,<sup>12</sup> which both play a role in inhibition of cell cycle progression. Many recent reports demonstrate that cells undergoing OIS secrete a number of inflammatory mediators, including cytokines and chemokines, termed the senescence-associated secretory phenotype (SASP).<sup>13</sup> The SASP

\*Correspondence to: Katherine M Aird, Ph.D; E-mail: kaird@wistar.org  
Submitted: 07/11/2014; Revised: 08/06/2014; Accepted: 08/12/2014  
<http://dx.doi.org/10.4161/23723548.2014.963481>

This is an Open Access article distributed under the terms of the Creative Commons Attribution-Non-Commercial License (<http://creativecommons.org/licenses/by-nc/3.0/>), which permits unrestricted non-commercial use, distribution, and reproduction in any medium, provided the original work is properly cited. The moral rights of the named author(s) have been asserted.

is thought to play a role in both the establishment and maintenance of the senescence-associated cell growth arrest.<sup>14</sup> Taken together, cells undergoing OIS activate a number of cellular signaling pathways to ensure a stable cell growth arrest.

Although senescent cells do not replicate their DNA, they remain metabolically active.<sup>2,15</sup> It is now known that a number of changes in cellular metabolism occur during OIS.<sup>16</sup> This review will focus on the changes in cellular metabolism that accompany OIS, including changes in nucleotide, glucose, mitochondrial, and lipid metabolism and autophagy. We will also discuss how these pathways may be circumvented during transformation and tumorigenesis.

## Metabolic Changes During OIS

### Nucleotide metabolism is decreased during OIS

Deoxyribonucleotide triphosphates (dNTPs) are necessary for both nuclear and mitochondrial DNA replication and repair.<sup>17,18</sup> Alterations in dNTP levels are known to play a pathogenic role in a number of human diseases, including cancer.<sup>9,11</sup> dNTPs can be synthesized through the *de novo* pathway or the salvage pathway.<sup>19</sup> The rate-limiting step in the synthesis of dNTPs during the *de novo* pathway is reduction of ribonucleoside di- or tri- phosphates (NDPs/NTPs) to deoxyribonucleotide di- or tri- phosphates (dNDPs/dNTPS) by ribonucleotide reductase (RNR).<sup>17,18</sup> RNR is a tetrameric complex comprised of 2 large catalytic subunits (R1: ribonucleotide reductase M1 [RRM1]) and 2 small regulatory subunits (R2: ribonucleotide reductase M2 [RRM2] or RRM2B/p53R2). Although RRM1 is expressed during all phases of the cell cycle, RRM2 and p53R2 are cell-cycle regulated.<sup>20</sup> RRM2 is expressed during S phase, when dNTPs are needed for DNA replication,<sup>20</sup> whereas p53R2 is expressed during G0/G1 and is important for DNA repair and mitochondrial DNA synthesis.<sup>21</sup> Changes in the expression or activity of RNR can therefore lead to altered DNA synthesis and repair.

Our group and others have shown that the levels of all 4 dNTPs are significantly decreased during OIS.<sup>9,11,22</sup> We found that this is specifically due to a decrease in expression of RRM2 (Fig. 1), but not RRM1 or p53R2.<sup>9</sup> Interestingly, the decrease in dNTP levels via suppression of RRM2 is a driver, not a consequence, of the cell cycle exit.<sup>9</sup> Increasing dNTP levels by ectopic expression of RRM2 or addition of exogenous nucleosides in oncogene-expressing normal diploid cells is able to overcome the aberrant DNA replication, DNA damage accumulation, and senescence-associated stable cell growth arrest induced by oncogenic RAS or BRAF.<sup>9,22</sup> Additionally, decreasing nucleotide metabolism using short hairpin RNA-mediated specific knockdown of RRM2 expression can induce the senescence-associated stable cell growth arrest via aberrant DNA replication and DNA damage accumulation.<sup>9</sup> These results demonstrate that nucleotide metabolism is decreased during OIS and is a key driver of the OIS phenotype.

We recently reported that RRM2, and therefore nucleotide metabolism, is decreased in human benign nevi with mutations in BRAF or NRAS.<sup>9</sup> Decreased RRM2 expression was significantly correlated with increased p16 expression, suggesting that these cells have undergone OIS. Additionally, melanoma cell

lines and primary melanoma samples with mutations in BRAF or NRAS display a marked increase in RRM2 expression. This suggests that overcoming the suppression of nucleotide metabolism that occurs during OIS may allow cells to re-enter the cell cycle, gain additional mutagenic hits, and become transformed. Indeed addition of exogenous nucleosides or ectopic RRM2 could overcome full senescence induced by RAS.<sup>9</sup> Additionally, supraphysiological levels of RRM2 or dNTPs can lead to DNA damage and genomic instability,<sup>9,23</sup> which is a hallmark of cancer cells.<sup>24,25</sup> RRM2 is transcriptionally regulated by E2F1 (Fig. 1).<sup>9,26,27</sup> E2F1 is negatively regulated by pRb (Fig. 1),<sup>28,29</sup> which is an important effector of the senescence phenotype.<sup>12</sup> In some contexts, loss of pRb can suppress the OIS phenotype.<sup>12</sup> When pRb is lost, E2F1 is no longer repressed and can induce transcription of a number of genes that regulate metabolism, including RRM2.<sup>30</sup> Additionally, loss of p53 can suppress OIS and can overcome OIS in cells with low p16 expression.<sup>10,31,32</sup> Interestingly, a repressive E2F, E2F7, is a p53 target gene.<sup>33</sup> E2F7 cooperates with pRb to promote senescence, thus coupling the p53 and pRb pathways. We have previously shown that E2F7 replaces E2F1 on the RRM2 promoter during OIS to suppress RRM2 transcription (Fig. 1).<sup>9</sup> This suggests that p53 and pRb act in concert to suppress nucleotide metabolism during OIS, and loss of these tumor suppressors may overcome OIS due to an increase in nucleotide metabolism, thereby leading to cancer formation.

### Glucose metabolism is altered during OIS

Glucose is one of the main cellular nutrients and is used in a variety of cellular metabolic processes such as the pentose phosphate pathway (PPP) and the tricarboxylic acid (TCA) cycle.<sup>34,35</sup> Glucose metabolites are necessary for nucleotide, amino acid, and lipid biogenesis. Under normal conditions, cells take up glucose through glucose transporters. Intracellular glucose is then metabolized during a process called glycolysis, which has an end product of pyruvate and produces 2 ATP molecules. The pyruvate can then be further metabolized. In normal cells under anaerobic conditions, pyruvate is generally metabolized into lactate (fermentation), during which reduced nicotinamide adenine dinucleotide (NAD<sup>+</sup>) is produced. This NAD<sup>+</sup> is important for cells to continue glycolysis. Under aerobic conditions, pyruvate dehydrogenase (PDH) metabolizes pyruvate into Acetyl Co-A to be further used in the TCA cycle and oxidative phosphorylation to produce 36 ATP molecules.

Cancer cells preferentially use glycolysis and subsequent fermentation to produce ATP even under aerobic conditions.<sup>24,34,36</sup> First observed by Otto Warburg in 1924,<sup>37</sup> this is now known as the Warburg effect. Although glycolysis is a much less efficient way of producing ATP, cancer cells have a high demand for biomass to continue proliferation.<sup>36</sup> To keep up with both the bioenergetic and biomass needs of a highly proliferative state, tumor cells increase their glucose uptake and metabolism through a variety of mechanisms, including increased expression of glucose transporters and glycolytic enzymes.<sup>34,35</sup> This allows for the high rate of growth and proliferation that is a hallmark of cancer cells.<sup>24</sup>

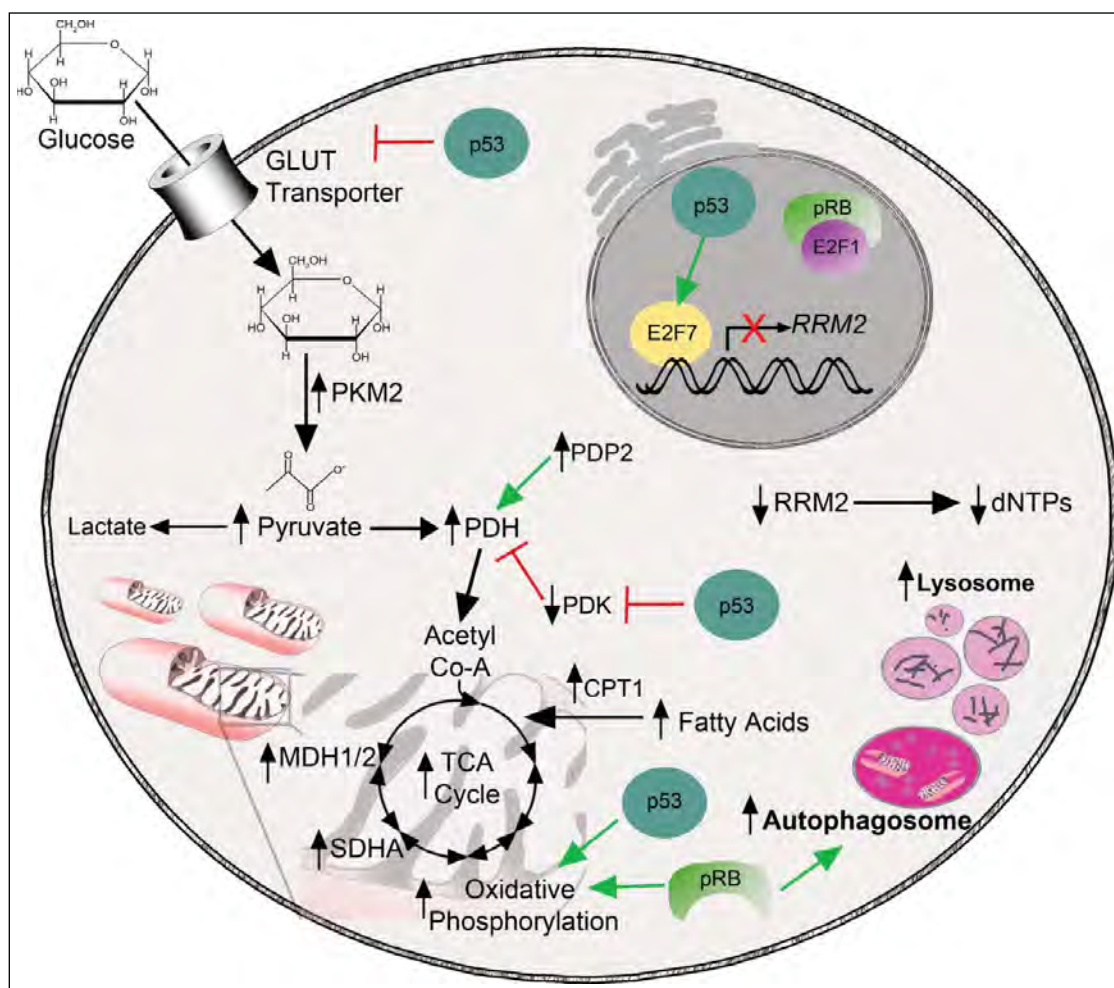


**Figure 1.** Alterations in metabolic pathways during oncogene-induced senescence. Glucose enters the cell through glucose transporters. p53 inhibits glucose uptake via negative regulation of glucose transporters.<sup>45</sup> During glycolysis, glucose is metabolized into pyruvate. One glycolytic enzyme, PKM2, is significantly upregulated during OIS.<sup>40</sup> Additionally, pyruvate levels are higher in cells that have undergone OIS.<sup>40</sup> The pyruvate produced by metabolism of glucose can be shunted into multiple pathways including fermentation, which leads to lactate production, or into the TCA cycle after further processing by PDH. PDH and its positive regulator PDP2 are upregulated during OIS, whereas the negative regulator of PDH (PDK1) is downregulated,<sup>42,43</sup> possibly in part through inhibition mediated by p53.<sup>53</sup> This suggests that pyruvate is preferentially shunted into the TCA cycle and away from fermentation. Levels of TCA cycle metabolites are increased during OIS, as are a number of TCA cycle enzymes, including SDHA and MDH1/2.<sup>43</sup> Oxidative phosphorylation is also increased during OIS through increased expression of all complexes in the electron transport chain.<sup>43</sup> p53 and pRb also positively regulate oxidative phosphorylation.<sup>30,53,54</sup> Nucleotide metabolism is decreased in cells that have undergone OIS as a result of suppression of E2F1-mediated transcription of RRM2 and increased repression by the p53 target E2F7.<sup>9</sup> Free fatty acid levels are increased in cells undergoing OIS, most likely due to an increase in fatty acid oxidation.<sup>52</sup> Finally, both autophagy and lysosomal activity are increased during OIS,<sup>68,75,76</sup> which may be in part occur via positive regulation through pRb.<sup>79</sup>

A number of recent studies have indicated that glucose metabolism is altered during OIS but with conflicting findings. Some studies have indicated an increase in glucose uptake during OIS.<sup>38–40</sup> However, a number of other studies have observed either no change or a significant decrease in glucose uptake.<sup>41–43</sup> The basis for the discrepancy among these studies remains to be determined, although it may be due to differences in cell type, oncogenes, or timing. Regardless, all of these studies have shown changes in glucose metabolism when cells undergo OIS.

Two reports have demonstrated that cells undergoing OIS have increased pyruvate levels,<sup>40,42</sup> demonstrating an increase in

glycolysis. This is most likely due to increased expression of a number of enzymes involved in pyruvate synthesis, such as pyruvate kinase (PKM2),<sup>40</sup> and pyruvate metabolism, including the gatekeeper enzyme pyruvate dehydrogenase (PDH) (Fig. 1).<sup>42,43</sup> Because PDH expression is increased, the pyruvate that is produced during glycolysis is shunted into the TCA cycle, thereby decreasing shunting into the fermentation arm that leads to lactate production. Taken together, these studies reveal an overall shift in glucose metabolism in cells undergoing OIS toward the mitochondrial TCA cycle and away from fermentation and the Warburg effect. This is consistent with the fact that OIS is a tumor suppression mechanism.



It is thought that the Warburg effect is a consequence of increased cellular proliferation during tumorigenesis, and not necessarily a cause of transformation itself.<sup>44</sup> However, a number of important senescence effectors are known to play an important role in metabolism. For instance, loss of p53 can suppress OIS in some contexts.<sup>10,31,32</sup> p53 is known to transcriptionally repress glucose transporters (GLUT-1, GLUT-3, GLUT-4) and a number of glycolytic enzymes.<sup>45</sup> Additionally, p53 positively regulates oxidative phosphorylation (Fig. 1),<sup>46</sup> thus loss of p53 can lead to a switch from oxidative phosphorylation to increased aerobic glycolysis.<sup>46</sup> Therefore, suppressing OIS could lead to a change in glucose metabolism that primes cells to become cancerous.

### Mitochondrial metabolism is altered during OIS

Mitochondria are the cell's powerhouses. Under normal oxygen conditions, glucose is broken down into pyruvate, which is then shunted through the TCA cycle. The TCA cycle starts when pyruvate dehydrogenase metabolizes pyruvate into acetyl-CoA.<sup>47</sup> Acetyl-CoA can also be produced from fatty acid oxidation (discussed below).<sup>48</sup> A series of enzymatic reactions then occurs to produce 3 molecules of NADH, which can then fuel oxidative phosphorylation (oxphos). Oxphos occurs in the inner mitochondrial membrane through 5 enzyme complexes<sup>49</sup> and is the most efficient way for a cell to produce ATP as it generates 36 ATP molecules for each glucose molecule.<sup>36</sup>

A number of recent studies have indicated a significant shift in mitochondrial metabolism in OIS cells. Firstly, a number of studies have demonstrated that cells undergoing OIS display mitochondrial dysfunction. Studies of RAS- or HER2-induced senescence reveal that cells undergoing OIS have decreased mitochondrial membrane potential,<sup>39,50</sup> indicating mitochondrial dysfunction. Interestingly, these studies report conflicting results in terms of mitochondrial mass and mitochondrial DNA content, likely due to differences in cell type and the oncogene used. Cadenas et al. reported that mitochondrial mass is decreased and that mitochondria are found in vacuole-rich areas, likely demonstrating that these dysfunctional mitochondria are targeted for degradation.<sup>50</sup> In contrast, Moiseeva et al. found that mitochondrial mass and DNA content is increased in cells undergoing OIS.<sup>39</sup> These authors also observed a marked increase in mitochondrial superoxides, indicating a significant change in mitochondrial metabolism. Indeed, senescence can be directly induced by interference with normal mitochondrial metabolism using specific knockdown of the important mitochondrial protein Rieske iron sulfur protein (RISP) or the pharmacologic inhibitors rotenone and oligomycin.<sup>39</sup> Although studies have shown some conflicting results, it is clear that mitochondrial metabolism is markedly changed during OIS and may regulate senescence.

In addition to changes in mitochondria themselves, flux through the mitochondrial TCA cycle is increased in cells undergoing OIS. One study has demonstrated a significant increase in TCA cycle metabolites in OIS cells (Fig. 1).<sup>42</sup> This is likely due to both an increase in the mitochondrial pyruvate gatekeeper enzyme PDH<sup>42,43</sup> and an increase in enzymes in the TCA cycle such as malate dehydrogenase (MDH1/2) and succinate

dehydrogenase (SDHA).<sup>43</sup> Increased PDH activity results from decreased expression of the PDH suppressive pyruvate dehydrogenase kinase 1 (PDK1) and increased expression of the PDH activating pyruvate dehydrogenase phosphatase 2 (PDP2) (Fig. 1).<sup>42,51</sup>

Oxidative phosphorylation is one of the most important biological processes of the mitochondrion.<sup>47</sup> A number of studies have shown that oxphos is increased during OIS, leading to an increase in oxygen consumption (Fig. 1).<sup>38,42,52</sup> This is likely due to increased TCA cycle metabolites and enzyme expression<sup>42,43</sup> in addition to increased expression of all complexes of the electron transport chain.<sup>43</sup> Increased oxygen consumption and oxphos complex enzyme expression should lead to an increase in ATP levels. However, a number of studies have shown a decrease in ATP levels in cells undergoing OIS.<sup>39-41</sup> This may be due to an increased usage of ATP by senescent cells for other highly energetic metabolic processes.

As discussed above, cancer cells show a marked decrease in TCA cycle and oxidative phosphorylation compared to normal cells. However, this is not due to mitochondrial defects in tumor cells,<sup>35</sup> but instead is most likely due to an increase in glucose uptake and glycolytic enzymes in addition to an increase in the PDH inhibitory PDK enzymes.<sup>34,44</sup> This leads to hyperactivation of aerobic glycolysis and less pyruvate entering the TCA cycle. As discussed above, loss of p53 can suppress OIS,<sup>10,32</sup> and p53 is known to be important for mitochondrial respiration and as a negative transcriptional regulator of aerobic glycolysis (Fig. 1). In part, this occurs through negative regulation of PDK2 (Fig. 1).<sup>53</sup> Loss of p53 thereby leads to an increase in PDK2, which in turn reduces the amount of pyruvate entering the mitochondria for the TCA cycle.<sup>44</sup> Additionally, loss of pRB, which can suppress OIS,<sup>12</sup> leads to decreased mitochondrial oxidative phosphorylation.<sup>30,54</sup> This indicates that suppression of OIS through loss of p53 and/or pRB can switch metabolism from the mitochondria to a more Warburg effect type of phenotype.

### Lipid metabolism is altered during OIS

Lipids are important for a number of cellular processes, including energy storage and signaling, and as components of cellular membranes.<sup>55</sup> Lipids can be grouped into 8 different categories including 2 lipids that will be discussed below: fatty acids and phospholipids. Importantly, fatty acids can be used as a major source of energy during a process called fatty acid oxidation (or  $\beta$ -oxidation) in which these lipids are catabolized into acetyl-CoA to be used in the TCA cycle. During  $\beta$ -oxidation, fatty acids are transported across the outer mitochondrial membrane by carnitine-palmitoyl transferase I (CPT1), which is rate-limiting for this process.<sup>56</sup> Although phospholipids are generally thought to be most important as a major component of cellular membranes, they can also be signaling messengers. Phospholipids are generated from fatty acids and can have different head groups; in particular, choline is the head group of phosphatidylcholine, which is the main constituent of cell membranes.<sup>57</sup> These phospholipids can be catabolized into free fatty acids to generate ATP under periods of cell stress.<sup>55</sup>

Recent studies have shown a change in lipid metabolism in cells undergoing OIS. Quijano et al. recently demonstrated that senescent cells display an elevation in free fatty acid levels (Fig. 1).<sup>52</sup> However, this is not due to an increase in lipid metabolism because these authors showed a decrease in acetyl-CoA carboxylase (ACC), the rate-limiting enzyme in lipid metabolism, in cells undergoing OIS. Instead, an increase in fatty acid oxidation was found to be the dominant factor in the increase in oxygen consumption in these cells. This may be another reason why senescent cells display an increase in oxygen consumption but no appreciable increase in ATP levels. The mechanism by which increased fatty acid levels are increased in OIS cells is unclear but may be due to promyelocytic leukemia (PML) activation of the fatty acid oxidation pathway through peroxisome proliferator-activated receptor (PPAR) signaling.<sup>58</sup> PML and PML nuclear bodies are known to play a major role during OIS.<sup>59,60</sup> Increased levels of fatty acids and their subsequent degradation, leading to increased NADPH levels, may occur because of an increased need for antioxidants to combat the high levels of reactive oxygen species (ROS) observed during OIS.<sup>39,61</sup> Interestingly, changes in fatty acid oxidation were shown to play a role in the senescence-associated secretory phenotype (SASP). Knockdown of CPT1, the rate-limiting enzyme in fatty acid oxidation, decreased the SASP during OIS.<sup>52</sup> This suggests that fatty acid oxidation is necessary for SASP expression during OIS. Another recent study also indicates an alteration in lipid metabolism during OIS. Gey et al. found a specific decrease in phosphocholine (PC) and an increase in L- $\alpha$ -glycerophosphocholine (GPC), suggesting catabolism of phospholipids via phospholipase A1 and/or A2 and lysophospholipase.<sup>62</sup> Indeed, another study showed alterations specifically in mitochondrial phospholipids,<sup>50</sup> which may play a role in the mitochondrial dysfunction observed during OIS. These studies suggest that the changes in lipid metabolism observed during OIS may play a specific role in the senescence phenotype, especially the SASP.

It has become apparent in recent years that lipid biogenesis is altered in cancer cells.<sup>48</sup> In contrast to cells that have undergone OIS, which display increased fatty acid catabolism, many cancer cells show a significant increase in *de novo* fatty acid synthesis.<sup>48</sup> This is likely due to increased expression of key enzymes in this pathway, including ATP-dependent citrate lyase (ACLY), acetyl-CoA carboxylase (ACC), and fatty acid synthase (FASN).<sup>34,48</sup> A number of the fatty acid pathway enzymes are regulated by AKT.<sup>63</sup> Interestingly, activation of AKT or suppression of PTEN in cells that have undergone OIS can overcome the cell growth arrest.<sup>64,65</sup> Although AKT/PTEN is involved in a number of different pathways, these data suggest that overcoming OIS through upregulation of these pathways may be in part due to a change in lipid biogenesis.

#### Autophagy and lysosomal activity is increased during OIS

Autophagy is literally the process by which a cell eats itself.<sup>66</sup> Macroautophagy, which is the process discussed in this review, delivers cytoplasmic materials to an autolysosome via an autophagosome. Therefore, autophagy and the lysosomal compartment are intimately linked. Under nutrient-rich conditions, the

mTORC1 complex generally inhibits autophagy.<sup>67</sup> Under nutrient-poor conditions, mTORC1 is inhibited, leading to upregulation of a number of autophagy-related genes (Atg genes) and initiation of the phagophore. Autophagy is thought to be a cell survival mechanism and has been implicated in several human diseases including cancer.<sup>66</sup>

A number of studies have indicated that autophagy is upregulated during OIS. LC-III, a marker of autophagy, and the number of autophagic vesicles are both significantly increased in cells undergoing OIS (Fig. 1).<sup>68</sup> Indeed, long-lived proteins are degraded at an increased rate in OIS cells compared to proliferating cells. Autophagy is likely increased during OIS as a result of repression of the mTORC1 and mTORC2 complexes through a negative feedback loop.<sup>69</sup> Furthermore, induction of autophagy was found to be necessary for OIS as knockdown of key autophagic proteins such as ATG5 or ATG7 bypassed senescence induced by RAS, BRAF, or the KSHV v-cyclin A protein.<sup>68,70-73</sup> It is known that senescent cells display an increase in protein content.<sup>43,74</sup> Therefore, during senescence, autophagy is probably activated to increase the amino acid content in order to cope with the higher rate of protein translation.<sup>75</sup>

Similar to the increase in autophagy, a number of studies have observed an increase in lysosomal activity in cells undergoing OIS. This is likely because autophagy and lysosomes go hand-in-hand to quickly degrade proteins and other biomolecules within the cell. Young et al. observed a significant increase in lysosomal genes in cells undergoing OIS.<sup>68</sup> These authors also observed an increased lysosomal compartment using LysoTracker and electron microscopy (Fig. 1). The increase in lysosomal gene expression directly correlates with the timing of the increase in autophagy genes, indicating coordinated upregulation of both cellular processes during OIS. A more recent study further identified the mechanism of upregulation of lysosomal genes. Urbanelli et al. demonstrated a significant increase in the transcription factor TFEB that leads to upregulation of HEXA and HEXB, which encode lysosomal glycohydrolase  $\beta$ -hexosaminidase.<sup>76</sup> Taken together, these studies indicate an increase in both autophagy and lysosomal activity in cells undergoing OIS.

Subversion of the autophagic process can overcome OIS<sup>68</sup> and potentially lead to transformation of cells. Indeed, autophagy is thought to be a tumor suppressive mechanism.<sup>66</sup> Autophagy is negatively regulated by mTOR,<sup>77</sup> which is induced during AKT signaling.<sup>78</sup> As discussed above, increased AKT signaling through activated AKT or inactivated PTEN can overcome the OIS-associated cell growth arrest.<sup>64,65</sup> In addition to the role of this pathway in other metabolic processes, this may also be due to inhibition of autophagy. Autophagy is also positively regulated by pRb (Fig. 1),<sup>79</sup> and loss of pRb can suppress OIS,<sup>68</sup> which may in part be due to a decrease in autophagy. Together, these studies suggest that overcoming OIS through suppression of autophagy could lead to transformation and tumorigenesis.

#### Targeting the metabolome as a pro-senescence cancer therapeutic strategy

Senescence is now thought to be a viable outcome for cancer therapy.<sup>80</sup> Additionally, targeting the altered metabolome in

cancer cells has attracted great interest in recent years.<sup>47,81,82</sup> Numerous compounds that have been developed to target different metabolic pathways are reviewed elsewhere.<sup>47,81,82</sup> Here, we will review recent studies that have shown that shifting metabolism toward that seen during OIS could be a viable strategy to induce cancer cell senescence and/or regression of tumors.

#### Targeting nucleotide metabolism as a pro-senescence cancer therapy

Cells that have undergone OIS show a marked decrease in dNTP levels and the rate-limiting enzyme RRM2.<sup>9,22</sup> Overcoming the decrease in nucleotide metabolism can lead to re-entry of fully senescent cells into the cell cycle.<sup>9</sup> To sustain a high level of proliferation, cancer cells require elevated levels of dNTPs.<sup>24</sup> It is possible to exploit this need by targeting this pathway to induce cancer cell senescence. A number of inhibitors of the nucleotide metabolic pathway are currently being used in the clinic.<sup>11,81</sup> Studies from our laboratory have shown that inhibition of nucleotide metabolism through specific knockdown or inhibition of RRM2 using 3-aminopyridine-2-carboxaldehyde thiosemicarbazone (3-AP)<sup>83</sup> can induce senescence in multiple cancer cell models with oncogenic signaling activation.<sup>9,84</sup> Notably, senescence induced by RRM2 inhibition is independent of p53 and p16 and correlates with the DNA damage response.<sup>9,84</sup> This supports the premise that inhibition of this pathway in cancer cells is a viable pro-senescence therapeutic strategy. The dNTP metabolic pathway has been exploited for cancer treatment for decades. New insights suggest that it remains an important target for the development of novel cancer therapeutic strategies using senescence as a primary tumor suppression mechanism.

#### Targeting glucose metabolism as a pro-senescence cancer therapy

During OIS, cells display a significant shift in glucose metabolism toward the mitochondrial TCA and oxidative phosphorylation pathways and away from the Warburg effect and fermentation (discussed above). Increased aerobic glycolysis and fermentation are hallmarks of cancer cells.<sup>24</sup> Therefore, suppression of OIS may alter glucose metabolism to a more Warburg effect-like phenotype. Because aerobic glycolysis is not observed in normal cells, targeting this pathway has been of major interest in recent years; indeed, a number of agents are being developed to target this pathway for cancer therapy.<sup>81,82</sup> For example, a small molecule of the GLUT1 transporter (WZB117) induces senescence and inhibits tumor growth *in vivo*.<sup>85</sup> Although a number of other inhibitors of glycolysis have been developed, most have not moved past Phase I/II clinical trials and their development has been discontinued.<sup>82</sup> This is most often due to unacceptable toxicities.<sup>81</sup> Future inhibitors will need to be more specific to limit off-target effects. Nevertheless, these data support the hypothesis that shifting metabolism away from the Warburg effect is a viable pro-senescence cancer therapeutic strategy.

#### Targeting mitochondrial metabolism

OIS cells display a significant increase in TCA cycle intermediates and oxidative phosphorylation (discussed above).

Although cancer cells have functional mitochondria,<sup>35</sup> most of their ATP is produced through glycolysis.<sup>36</sup> Therefore, drugs that shift metabolism toward the mitochondria may induce senescence of cancer cells. For instance, upregulation of PDH by knockdown of PDK1, which would shunt pyruvate into the TCA cycle,<sup>44</sup> can cause regression of melanoma tumors with oncogenic BRAF mutations.<sup>42</sup> In addition, knockdown of malic enzymes (ME1/2) can induce senescence of tumor cells.<sup>86</sup> ME1/2 metabolize malate into pyruvate, thereby producing NADPH, which is necessary for a number of metabolic processes including nucleic acid synthesis.<sup>44</sup> Thus, targeting the mitochondrial pathways can exert an effect on other metabolic pathways known to play a role in senescence.

### Concluding Remarks

In recent years, it has becoming increasingly clear that OIS is accompanied by a significant alteration in cellular metabolism. Given that OIS is a tumor suppressor mechanism,<sup>4,5</sup> the changes in cellular metabolism are mostly opposite to those observed during tumorigenesis. For example, during OIS glucose metabolites are mainly shunted toward the TCA cycle and oxidative phosphorylation. This is in contrast to tumor metabolism, which shunts glucose either to fermentation to produce lactate or the PPP, thereby increasing the level of nucleotides and other necessary biomolecules for proliferation. This indicates that these pathways play a role in the tumor suppressive phenotype of OIS. Understanding these alterations in the metabolome may give researchers further insight into how cells are able to circumvent the OIS phenotype to become cancerous. Indeed, a number of key senescence effectors such as p53 and pRb also play major roles in metabolism.<sup>30,34,44,46,53,54,79</sup> This underscores the importance of further understanding these pathways to potentially prevent the bypass of OIS. Additionally, this knowledge may allow us to exploit cancer cells' metabolic weaknesses as a therapeutic strategy. Interestingly, a recent study found that exploiting metabolic changes during therapy-induced senescence of cancer cells could induce a synthetic lethality.<sup>38</sup> This suggests that these changes can be targeted in cancer patients to improve cancer therapy. Further studies are therefore warranted to fully understand the metabolic alterations accompanying OIS and how these are changed when cells overcome the OIS-associated cell cycle exit.

#### Disclosure of Potential Conflicts of Interest

No potential conflicts of interest were disclosed.

#### Funding

This work was supported by a NIH/NCI grant (R01CA160331 to R.Z.), a DoD Ovarian Cancer Academy Award (OC093420 to R.Z.) and an NIH/NCI training grant (T32CA9171–35 to K.M.A.). Support of Core Facilities used in this study was provided by Cancer Center Support Grant (CCSG) CA010815 to The Wistar Institute.



## References

- Hayflick L, Moorhead PS. The serial cultivation of human diploid cell strains. *Exp Cell Res* 1961; 25:585-621; PMID:13905658; [http://dx.doi.org/10.1016/0014-4827\(61\)90192-6](http://dx.doi.org/10.1016/0014-4827(61)90192-6)
- Campisi J, d'Adda di Fagagna F. Cellular senescence: when bad things happen to good cells. *Nat Rev Mol Cell Biol* 2007; 8:729-40; PMID:17667954; <http://dx.doi.org/10.1038/nrm2233>
- Yaswen P, Campisi J. Oncogene-induced senescence pathways weave an intricate tapestry. *Cell* 2007; 128:233-4; PMID:17254959; <http://dx.doi.org/10.1016/j.cell.2007.01.005>
- Mooi WJ, Peeper DS. Oncogene-induced cell senescence—halting on the road to cancer. *N Engl J Med* 2006; 355:1037-46; PMID:16957149; <http://dx.doi.org/10.1056/NEJMr062285>
- Braig M, Lee S, Lodenkemper C, Rudolph C, Peters AH, Schlegelberger B, Stein H, Dorken B, Jenuwein T, Schmitt CA. Oncogene-induced senescence as an initial barrier in lymphoma development. *Nature* 2005; 436:660-5; PMID:16079837; <http://dx.doi.org/10.1038/nature03841>
- Dimri GP, Lee X, Basile G, Acosta M, Scott G, Roskelley C, Medrano EE, Linskens M, Rubelj I, Pereira-Smith O, et al. A biomarker that identifies senescent human cells in culture and in aging skin in vivo. *Proc Natl Acad Sci U S A* 1995; 92:9363-7; PMID:7568133; <http://dx.doi.org/10.1073/pnas.92.20.9363>
- Bartek J, Bartkova J, Lukas J. DNA damage signalling guards against activated oncogenes and tumour progression. *Oncogene* 2007; 26:7773-9; PMID:18066090; <http://dx.doi.org/10.1038/sj.onc.1210881>
- Bartkova J, Rezaei N, Liontos M, Karakaidos P, Kletsas D, Issaeva N, Vassiliou LV, Kolettas E, Niforou K, Zoumpourlis VC, et al. Oncogene-induced senescence is part of the tumorigenesis barrier imposed by DNA damage checkpoints. *Nature* 2006; 444:633-7; PMID:17136093; <http://dx.doi.org/10.1038/nature05268>
- Aird KM, Zhang G, Li H, Tu Z, Bitler BG, Garipov A, Wu H, Wei Z, Wagner SN, Herlyn M, et al. Suppression of nucleotide metabolism underlies the establishment and maintenance of oncogene-induced senescence. *Cell Rep* 2013; 3:1252-65; PMID:23562156; <http://dx.doi.org/10.1016/j.celrep.2013.03.004>
- Di Micco R, Fumagalli M, Cicalese A, Piccinin S, Gasparini P, Luise C, Schurra C, Garre M, Nuciforo PG, Bensimon A, et al. Oncogene-induced senescence is a DNA damage response triggered by DNA hyper-replication. *Nature* 2006; 444:638-42; PMID:17136094; <http://dx.doi.org/10.1038/nature05327>
- Aird KM, Zhang R. Nucleotide metabolism, oncogene-induced senescence and cancer. *Cancer Lett* 2014; PMID:24486217
- Serrano M, Lin AW, McCurrach ME, Beach D, Lowe SW. Oncogenic ras provokes premature cell senescence associated with accumulation of p53 and p16INK4a. *Cell* 1997; 88:593-602; PMID:9054499; [http://dx.doi.org/10.1016/S0092-8674\(00\)81902-9](http://dx.doi.org/10.1016/S0092-8674(00)81902-9)
- Coppe JP, Desprez PY, Krtolica A, Campisi J. The senescence-associated secretory phenotype: the dark side of tumor suppression. *Annu Rev Pathol* 2010; 5:99-118; PMID:20078217; <http://dx.doi.org/10.1146/annurev-pathol-121808-102144>
- Kuilman T, Michaloglou C, Vredeveld LC, Douma S, van Doorn R, Desmet CJ, Aarden LA, Mooi WJ, Peeper DS. Oncogene-induced senescence relayed by an interleukin-dependent inflammatory network. *Cell* 2008; 133:1019-31; PMID:18555778; <http://dx.doi.org/10.1016/j.cell.2008.03.039>
- Collado M, Serrano M. Senescence in tumours: evidence from mice and humans. *Nat Rev Cancer* 2010; 10:51-7; PMID:20029423; <http://dx.doi.org/10.1038/nrc2772>
- Salama R, Sadaie M, Hoare M, Narita M. Cellular senescence and its effector programs. *Genes Dev* 2014; 28:99-114; PMID:24449267; <http://dx.doi.org/10.1101/gad.235184.113>
- Reichard P. Interactions between deoxyribonucleotide and DNA synthesis. *Annu Rev Biochem* 1988; 57:349-74; PMID:3052277; <http://dx.doi.org/10.1146/annurev.bi.57.070188.002025>
- Nordlund P, Reichard P. Ribonucleotide reductases. *Annu Rev Biochem* 2006; 75:681-706; PMID:16756507; <http://dx.doi.org/10.1146/annurev.biochem.75.103004.142443>
- Blakley RL, Vitols E. The control of nucleotide biosynthesis. *Annu Rev Biochem* 1968; 37:201-24; PMID:4875716; <http://dx.doi.org/10.1146/annurev.bi.37.070168.001221>
- Engstrom Y, Eriksson S, Jildevik I, Skog S, Thelander L, Tribukait B. Cell cycle-dependent expression of mammalian ribonucleotide reductase. Differential regulation of the two subunits. *J Biol Chem* 1985; 260:9114-6; PMID:3894352
- Hakansson P, Hofer A, Thelander L. Regulation of mammalian ribonucleotide reduction and dNTP pools after DNA damage and in resting cells. *J Biol Chem* 2006; 281:7834-41; PMID:16436374; <http://dx.doi.org/10.1074/jbc.M512894200>
- Mannava S, Moparthy KC, Wheeler LJ, Natarajan V, Zucker SN, Fink EE, Im M, Flanagan S, Burhans WC, Zeitouni NC, et al. Depletion of deoxyribonucleotide pools is an endogenous source of DNA damage in cells undergoing oncogene-induced senescence. *Am J Pathol* 2013; 182:142-51; PMID:23245831; <http://dx.doi.org/10.1016/j.ajpath.2012.09.011>
- D'Angiolella V, Donato V, Forrester FM, Jeong YT, Pellacani C, Kudo Y, Saraf A, Florens L, Washburn MP, Pagano M. Cyclin F-mediated degradation of ribonucleotide reductase M2 controls genome integrity and DNA repair. *Cell* 2012; 149:1023-34; PMID:22632967; <http://dx.doi.org/10.1016/j.cell.2012.03.043>
- Hanahan D, Weinberg RA. Hallmarks of cancer: the next generation. *Cell* 2011; 144:646-74; PMID:21376230; <http://dx.doi.org/10.1016/j.cell.2011.02.013>
- Negrini S, Gorgoulis VG, Halazonetis TD. Genomic instability—an evolving hallmark of cancer. *Nat Rev Mol Cell Biol* 2010; 11:220-8; PMID:20177397; <http://dx.doi.org/10.1038/nrm2858>
- Chabes AL, Bjorklund S, Thelander L. S Phase-specific transcription of the mouse ribonucleotide reductase R2 gene requires both a proximal repressive E2F-binding site and an upstream promoter activating region. *J Biol Chem* 2004; 279:10796-807; PMID:14688249; <http://dx.doi.org/10.1074/jbc.M312482200>
- DeGregori J, Kowalik T, Nevins JR. Cellular targets for activation by the E2F1 transcription factor include DNA synthesis- and G1/S-regulatory genes. *Mol Cell Biol* 1995; 15:4215-24; PMID:7623816
- Flemington EK, Speck SH, Kaelin WG Jr. E2F-1-mediated transactivation is inhibited by complex formation with the retinoblastoma susceptibility gene product. *Proc Natl Acad Sci U S A* 1993; 90:6914-8; PMID:8346196; <http://dx.doi.org/10.1073/pnas.90.15.6914>
- Helin K, Harlow E, Fattaey A. Inhibition of E2F-1 transactivation by direct binding of the retinoblastoma protein. *Mol Cell Biol* 1993; 13:6501-8; PMID:8413249
- Nicolay BN, Dyson NJ. The multiple connections between pRB and cell metabolism. *Curr Opin Cell Biol* 2013; 25:735-40; PMID:23916769; <http://dx.doi.org/10.1016/j.ccb.2013.07.012>
- Coppe JP, Patil CK, Rodier F, Sun Y, Munoz DP, Goldstein J, Nelson PS, Desprez PY, Campisi J. Senescence-associated secretory phenotypes reveal cell-non-autonomous functions of oncogenic RAS and the p53 tumor suppressor. *PLoS Biol* 2008; 6:2853-68; PMID:19053174; <http://dx.doi.org/10.1371/journal.pbio.0060301>
- Di Micco R, Sulli G, Dobrev M, Liontos M, Botrugno OA, Gargiulo G, Dal Zuffo R, Matti V, d'Ario G, Montani E, et al. Interplay between oncogene-induced DNA damage response and heterochromatin in senescence and cancer. *Nat Cell Biol* 2011; 13:292-302; PMID:21336312; <http://dx.doi.org/10.1038/ncb2170>
- Aksoy O, Chicas A, Zeng T, Zhao Z, McCurrach M, Wang X, Lowe SW. The atypical E2F family member E2F7 couples the p53 and RB pathways during cellular senescence. *Genes Dev* 2012; 26:1546-57; PMID:22802529; <http://dx.doi.org/10.1101/gad.196238.112>
- Romero-Garcia S, Lopez-Gonzalez JS, Baez-Viveros JL, Aguilar-Cazares D, Prado-Garcia H. Tumor cell metabolism: an integral view. *Cancer Biol Ther* 2011; 12:939-48; PMID:22057267; <http://dx.doi.org/10.4161/cbt.12.11.18140>
- Ward PS, Thompson CB. Metabolic reprogramming: a cancer hallmark even warburg did not anticipate. *Cancer Cell* 2012; 21:297-308; PMID:22439925; <http://dx.doi.org/10.1016/j.ccr.2012.02.014>
- Vander Heiden MG, Cantley LC, Thompson CB. Understanding the Warburg effect: the metabolic requirements of cell proliferation. *Science* 2009; 324:1029-33; PMID:19460998; <http://dx.doi.org/10.1126/science.1160809>
- Warburg O. On the origin of cancer cells. *Science* 1956; 123:309-14; PMID:13298683; <http://dx.doi.org/10.1126/science.123.3191.309>
- Dorr JR, Yu Y, Milanovic M, Beuster G, Zasada C, Dabritz JH, Liscic J, Lenze D, Gerhardt A, Schleicher K, et al. Synthetic lethal metabolic targeting of cellular senescence in cancer therapy. *Nature* 2013; 501:421-5; PMID:23945590; <http://dx.doi.org/10.1038/nature12437>
- Moiseeva O, Bourdeau V, Roux A, Deschenes-Simard X, Ferbeyre G. Mitochondrial dysfunction contributes to oncogene-induced senescence. *Mol Cell Biol* 2009; 29:4495-507; PMID:19528227; <http://dx.doi.org/10.1128/MCB.01868-08>
- Mazurek S, Zwierschke W, Jansen-Durr P, Eigenbrodt E. Metabolic cooperation between different oncogenes during cell transformation: interaction between activated ras and HPV-16 E7. *Oncogene* 2001; 20:6891-8; PMID:11687968; <http://dx.doi.org/10.1038/sj.onc.1204792>
- Gitenay D, Wiel C, Lallet-Daher H, Vindrieux D, Aubert S, Payen L, Simonnet H, Bernard D. Glucose metabolism and hexosamine pathway regulate oncogene-induced senescence. *Cell Death Disease* 2014; 5:e1089; PMID:24577087; <http://dx.doi.org/10.1038/cddis.2014.63>
- Kaplon J, Zheng L, Meissl K, Chaneton B, Selivanov VA, Mackay G, van der Burg SH, Verdegem EM, Cascante M, Shlomi T, et al. A key role for mitochondrial gatekeeper pyruvate dehydrogenase in oncogene-induced senescence. *Nature* 2013; 498:109-12; PMID:23685455; <http://dx.doi.org/10.1038/nature12154>
- Li M, Durbin KR, Sweet SM, Tipton JD, Zheng Y, Kelleher NL. Oncogene-induced cellular senescence elicits an anti-Warburg effect. *Proteomics* 2013; 13:2585-96; PMID:23798001; <http://dx.doi.org/10.1002/pmic.201200298>
- Cairns RA, Harris IS, Mak TW. Regulation of cancer cell metabolism. *Nat Rev Cancer* 2011; 11:85-95; PMID:21258394; <http://dx.doi.org/10.1038/nrc2981>
- Chen JQ, Russo J. Dysregulation of glucose transport, glycolysis, TCA cycle and glutaminolysis by oncogenes and tumor suppressors in cancer cells. *Biochim Biophys Acta* 2012; 1826:370-84; PMID:22750268



46. Matoba S, Kang JG, Patino WD, Wragg A, Boehm M, Gavrilova O, Hurley PJ, Bunz F, Hwang PM. p53 regulates mitochondrial respiration. *Science* 2006; 312:1650-3; PMID:16728594; <http://dx.doi.org/10.1126/science.1126863>
47. Jones NP, Schulze A. Targeting cancer metabolism—aiming at a tumour's sweet-spot. *Drug Discov Today* 2012; 17:232-41; PMID:22207221; <http://dx.doi.org/10.1016/j.drudis.2011.12.017>
48. Santos CR, Schulze A. Lipid metabolism in cancer. *FEBS J* 2012; 279:2610-23; PMID:22621751; <http://dx.doi.org/10.1111/j.1742-4658.2012.08644.x>
49. Papa S, Martino PL, Capitanio G, Gaballo A, De Rasio D, Signorile A, Petruzzella V. The oxidative phosphorylation system in mammalian mitochondria. *Adv Exp Med Biol* 2012; 942:3-37; PMID:22399416; [http://dx.doi.org/10.1007/978-94-007-2869-1\\_1](http://dx.doi.org/10.1007/978-94-007-2869-1_1)
50. Cadenas C, Vosbeck S, Hein EM, Hellwig B, Langer A, Hayen H, Franckenstein D, Buttner B, Hammad S, Marchan R, et al. Glycerophospholipid profile in oncogene-induced senescence. *Biochim Biophys Acta* 2012; 1821:1256-68; PMID:22178194; <http://dx.doi.org/10.1016/j.bbalip.2011.11.008>
51. Olenchok BA, Vander Heiden MG. Pyruvate as a pivot point for oncogene-induced senescence. *Cell* 2013; 153:1429-30; PMID:23791173; <http://dx.doi.org/10.1016/j.cell.2013.06.001>
52. Quijano C, Cao L, Fergusson MM, Romero H, Liu J, Gutkind S, Rovira II, Mohney RP, Karoly ED, Finkel T. Oncogene-induced senescence results in marked metabolic and bioenergetic alterations. *Cell Cycle* 2012; 11:1383-92; PMID:22421146; <http://dx.doi.org/10.4161/cc.19800>
53. Contractor T, Harris CR. p53 negatively regulates transcription of the pyruvate dehydrogenase kinase Pdk2. *Cancer Res* 2012; 72:560-7; PMID:22123926; <http://dx.doi.org/10.1158/0008-5472.CAN-11-1215>
54. Sankaran VG, Orkin SH, Walkley CR. Rb intrinsically promotes erythropoiesis by coupling cell cycle exit with mitochondrial biogenesis. *Genes Dev* 2008; 22:463-75; PMID:18258751; <http://dx.doi.org/10.1101/gad.1627208>
55. Ameer F, Scanduzzi L, Hasnain S, Kalbacher H, Zaidi N. De novo lipogenesis in health and disease. *Metabolism* 2014; 63:895-902; PMID:24814684; <http://dx.doi.org/10.1016/j.metabol.2014.04.003>
56. Deberardinis RJ, Lum JJ, Thompson CB. Phosphatidylinositol 3-kinase-dependent modulation of carnitine palmitoyltransferase 1A expression regulates lipid metabolism during hematopoietic cell growth. *J Biol Chem* 2006; 281:37372-80; PMID:17030509; <http://dx.doi.org/10.1074/jbc.M608372200>
57. Gibellini F, Smith TK. The Kennedy pathway—De novo synthesis of phosphatidylethanolamine and phosphatidylcholine. *IUBMB Life* 2010; 62:414-28; PMID:20503434; <http://dx.doi.org/10.1002/iub.354>
58. Carracedo A, Weiss D, Leliart AK, Bhasin M, de Boer VC, Laurent G, Adams AC, Sundvall M, Song SJ, Ito K, et al. A metabolic prosurvival role for PML in breast cancer. *J Clin Invest* 2012; 122:3088-100; PMID:22886304; <http://dx.doi.org/10.1172/JCI62129>
59. Pearson M, Carbone R, Sebastiani C, Cioce M, Fagioli M, Saito S, Higashimoto Y, Appella E, Minucci S, Pandolfi PP, et al. PML regulates p53 acetylation and premature senescence induced by oncogenic Ras. *Nature* 2000; 406:207-10; PMID:10910364; <http://dx.doi.org/10.1038/35021000>
60. Ferbeyre G, de Stanchina E, Querido E, Baptiste N, Prives C, Lowe SW. PML is induced by oncogenic ras and promotes premature senescence. *Genes Dev* 2000; 14:2015-27; PMID:10950866
61. Lee AC, Fenster BE, Ito H, Takeda K, Bae NS, Hirai T, Yu ZX, Ferrans VJ, Howard BH, Finkel T. Ras proteins induce senescence by altering the intracellular levels of reactive oxygen species. *J Biol Chem* 1999; 274:7936-40; PMID:10075689; <http://dx.doi.org/10.1074/jbc.274.12.7936>
62. Gey C, Seeger K. Metabolic changes during cellular senescence investigated by proton NMR-spectroscopy. *Mech Ageing Dev* 2013; 134:130-8; PMID:23416267; <http://dx.doi.org/10.1016/j.mad.2013.02.002>
63. Porstmann T, Griffiths B, Chung YL, Delpuech O, Griffiths JR, Downward J, Schulze A. PKB/Akt induces transcription of enzymes involved in cholesterol and fatty acid biosynthesis via activation of SREBP. *Oncogene* 2005; 24:6465-81; PMID:16007182
64. Vredevelde LC, Possik PA, Smit MA, Meissl K, Michaloglou C, Horlings HM, Ajouaou A, Kortman PC, Dankort D, McMahon M, et al. Abrogation of BRAFV600E-induced senescence by PI3K pathway activation contributes to melanomagenesis. *Genes Dev* 2012; 26:1055-69; PMID:22549727; <http://dx.doi.org/10.1101/gad.187252.112>
65. Kennedy AL, Morton JP, Manoharan I, Nelson DM, Jamieson NB, Pawlikowski JS, McBryan T, Doyle B, McKay C, Oien KA, et al. Activation of the PI3K/AKT pathway suppresses senescence induced by an activated RAS oncogene to promote tumorigenesis. *Mol Cell* 2011; 42:36-49; PMID:21474066; <http://dx.doi.org/10.1016/j.molcel.2011.02.020>
66. Kondo Y, Kanzawa T, Sawaya R, Kondo S. The role of autophagy in cancer development and response to therapy. *Nat Rev Cancer* 2005; 5:726-34; PMID:16148885; <http://dx.doi.org/10.1038/nrc1692>
67. Mizushima N, Komatsu M. Autophagy: renovation of cells and tissues. *Cell* 2011; 147:728-41; PMID:22078875; <http://dx.doi.org/10.1016/j.cell.2011.10.026>
68. Young AR, Narita M, Ferreira M, Kirschner K, Sadaie M, Darot JF, Tavares S, Arakawa S, Shimizu S, Watt FM, et al. Autophagy mediates the mitotic senescence transition. *Genes Dev* 2009; 23:798-803; PMID:19279323; <http://dx.doi.org/10.1101/gad.519709>
69. Courtois-Cox S, Genther Williams SM, Reczek EE, Johnson BW, McGillicuddy LT, Johannessen CM, Hollstein PE, MacCollin M, Cichowski K. A negative feedback signaling network underlies oncogene-induced senescence. *Cancer Cell* 2006; 10:459-72; PMID:17157787; <http://dx.doi.org/10.1016/j.ccr.2006.10.003>
70. Leidal AM, Cyr DP, Hill RJ, Lee PW, McCormick C. Subversion of autophagy by Kaposi's sarcoma-associated herpesvirus impairs oncogene-induced senescence. *Cell Host Microbe* 2012; 11:167-80; PMID:22341465; <http://dx.doi.org/10.1016/j.chom.2012.01.005>
71. Leidal AM, Lee PW, McCormick C. Viral subversion of autophagy impairs oncogene-induced senescence. *Autophagy* 2012; 8:1138-40; PMID:22735194; <http://dx.doi.org/10.4161/auto.20340>
72. Liu H, He Z, Simon HU. Autophagy suppresses melanoma tumorigenesis by inducing senescence. *Autophagy* 2014; 10:372-3; PMID:24300435; <http://dx.doi.org/10.4161/auto.27163>
73. Liu H, He Z, von Rutte T, Yousefi S, Hunger RE, Simon HU. Down-regulation of autophagy-related protein 5 (ATG5) contributes to the pathogenesis of early-stage cutaneous melanoma. *Sci Transl Med* 2013; 5:202ra123; PMID:24027027; <http://dx.doi.org/10.1126/scitranslmed.3005864>
74. De Cecco M, Jeyapalan J, Zhao X, Tamamori-Adachi M, Sedivy JM. Nuclear protein accumulation in cellular senescence and organismal aging revealed with a novel single-cell resolution fluorescence microscopy assay. *Aging (Albany NY)* 2011; 3:955-67; PMID:22006542
75. Narita M, Young AR, Narita M. Autophagy facilitates oncogene-induced senescence. *Autophagy* 2009; 5:1046-7; PMID:19652542; <http://dx.doi.org/10.4161/auto.5.7.9444>
76. Urbanelli L, Magini A, Ercolani L, Sagini K, Polchi A, Tancini B, Brozzi A, Armeni T, Principato G, Emiliani C. Oncogenic H-Ras up-regulates acid beta-hexosaminidase by a mechanism dependent on the autophagy regulator TFEB. *PLoS One* 2014; 9:e89485; PMID:24586816; <http://dx.doi.org/10.1371/journal.pone.0089485>
77. Yu L, McPhee CK, Zheng L, Mardones GA, Rong Y, Peng J, Mi N, Zhao Y, Liu Z, Wan F, et al. Termination of autophagy and reformation of lysosomes regulated by mTOR. *Nature* 2010; 465:942-6; PMID:20526321; <http://dx.doi.org/10.1038/nature09076>
78. Schmelzle T, Hall MN. TOR, a central controller of cell growth. *Cell* 2000; 103:253-62; PMID:11057898; [http://dx.doi.org/10.1016/S0092-8674\(00\)00117-3](http://dx.doi.org/10.1016/S0092-8674(00)00117-3)
79. Jiang H, Martin V, Gomez-Manzano C, Johnson DG, Alonso M, White E, Xu J, McDonnell TJ, Shinjima N, Fucyo J. The RB-E2F1 pathway regulates autophagy. *Cancer Res* 2010; 70:7882-93; PMID:20807803; <http://dx.doi.org/10.1158/0008-5472.CAN-10-1604>
80. Nardella C, Clohessy JG, Alimonti A, Pandolfi PP. Pro-senescence therapy for cancer treatment. *Nat Rev Cancer* 2011; 11:503-11; PMID:21701512; <http://dx.doi.org/10.1038/nrc3057>
81. Vander Heiden MG. Targeting cancer metabolism: a therapeutic window opens. *Nat Rev Drug Discov* 2011; 10:671-84; PMID:21878982; <http://dx.doi.org/10.1038/nrd3504>
82. Galluzzi L, Kepp O, Vander Heiden MG, Kroemer G. Metabolic targets for cancer therapy. *Nat Rev Drug Discov* 2013; 12:829-46; PMID:24113830; <http://dx.doi.org/10.1038/nrd4145>
83. Finch RA, Liu MC, Cory AH, Cory JG, Sartorelli AC. Triapine (3-aminopyridine-2-carboxaldehyde thiosemicarbazone; 3-AP): an inhibitor of ribonucleotide reductase with antineoplastic activity. *Adv Enzyme Regul* 1999; 39:3-12; PMID:10470363; [http://dx.doi.org/10.1016/S0065-2571\(98\)00017-X](http://dx.doi.org/10.1016/S0065-2571(98)00017-X)
84. Aird KM, Li H, Xin F, Constantinopoulos PA, Zhang R. Identification of ribonucleotide reductase M2 as a potential target for pro-senescence therapy in epithelial ovarian cancer. *Cell Cycle* 2014; 13:199-207; PMID:24200970; <http://dx.doi.org/10.4161/cc.26953>
85. Liu Y, Cao Y, Zhang W, Bergmeier S, Qian Y, Akbar H, Colvin R, Ding J, Tong L, Wu S, et al. A small-molecule inhibitor of glucose transporter 1 downregulates glycolysis, induces cell-cycle arrest, and inhibits cancer cell growth in vitro and in vivo. *Mol Cancer Ther* 2012; 11:1672-82; PMID:22689530; <http://dx.doi.org/10.1158/1535-7163.MCT-12-0131>
86. Jiang P, Du W, Mancuso A, Wellen KE, Yang X. Reciprocal regulation of p53 and malic enzymes modulates metabolism and senescence. *Nature* 2013; 493:689-93; PMID:23334421; <http://dx.doi.org/10.1038/nature11776>



Contents lists available at ScienceDirect

## Cancer Letters

journal homepage: [www.elsevier.com/locate/canlet](http://www.elsevier.com/locate/canlet)

## Mini-review

## Nucleotide metabolism, oncogene-induced senescence and cancer

Katherine M. Aird, Rugang Zhang\*

Gene Expression and Regulation Program, The Wistar Institute Cancer Center, The Wistar Institute, Philadelphia, PA 19104, United States

## ARTICLE INFO

## Article history:

Available online xxxxx

## Keywords:

Nucleotide metabolism  
Cancer  
Oncogene-induced senescence  
DNA damage response  
Replication stress  
Cancer therapy

## ABSTRACT

Senescence is defined as a stable cell growth arrest. Oncogene-induced senescence (OIS) occurs when an activated oncogene is expressed in a normal cell. OIS acts as a bona fide tumor suppressor mechanism by driving stable growth arrest of cancer progenitor cells harboring the initial oncogenic hit. OIS is often characterized by aberrant DNA replication and the associated DNA damage response. Nucleotides, in particular deoxyribonucleotide triphosphates (dNTPs), are necessary for both DNA replication and repair. Imbalanced dNTP pools play a role in a number of human diseases, including during the early stages of cancer development. This review will highlight what is currently known about the role of decreased nucleotide metabolism in OIS, how nucleotide metabolism leads to transformation and tumor progression, and how this pathway can be targeted as a cancer therapeutic by inducing senescence of cancer cells.

© 2014 Elsevier Ireland Ltd. All rights reserved.

## 1. Introduction

Nucleotides are necessary for a variety of cellular processes. It has been well characterized that imbalances in nucleotide levels lead to a variety of human diseases, including cancer [1–4], immunodeficiency [5,6], aging [7,8], kidney diseases [9,10], gout [6], and a number of mitochondrial pathologies [11,12].

**Abbreviations:** 3-AP, 3-aminopyridine-2-carboxaldehyde thiosemicarbazone; ATM, ataxia telangiectasia mutated; ATR, ataxia telangiectasia and Rad3-related protein; AMP/ADP/ATP, adenosine mono-, di-, and tri-phosphate; BLM, Bloom syndrome RecQ helicase-like; BRAF, V-raf murine sarcoma viral oncogene homolog B; BRCA1/2, Breast Cancer 1/2, Early Onset; CDK, cyclin-dependent kinase; CMP/CDP/CTP, cytidine mono-, di-, and tri-phosphate; c-myc, v-myc avian myelocytomatosis viral oncogene homolog; DNA, deoxyribonucleic acid; DDR, DNA damage response; dNDP, deoxyribonucleotide diphosphate; dNTP, deoxyribonucleotide triphosphate; E2F1, E2F transcription factor 1; E2F7, E2F transcription factor 7; EOC, epithelial ovarian cancer; GMP/GDP/GTP, guanosine mono-, di-, and tri-phosphate; HRAS, Harvey Rat Sarcoma Viral Oncogene Homolog; HU, hydroxyurea; IMP, inosine monophosphate; NADPH, Nicotinamide adenine dinucleotide phosphate; NDP, ribonucleoside diphosphate; NRAS, neuroblastoma RAS viral (V-Ras) oncogene homolog; NTP, ribonucleoside triphosphate; OIS, oncogene-induced senescence; p53R2/RRM2B, Ribonucleotide Reductase M2 B (TP53 Inducible); pRb, retinoblastoma protein; R1, ribonucleotide reductase subunit 1; R1/RRM1, ribonucleotide reductase M1; R2, ribonucleotide reductase subunit 2; Rad51, Rad51 recombinase; RAS, rat sarcoma oncogene; RECQL4, RecQ Protein-Like 4; RNR, ribonucleotide reductase; RRM2, ribonucleotide reductase M2; SA-B-Gal, senescence-associated beta-galactosidase; shRNA, short hairpin RNA; TS, thymidylate synthase; TTP, thymidine triphosphate; UDP, uridine diphosphate; UMP, uridine monophosphate; WRN, Werner syndrome ATP-dependent helicase.

\* Corresponding author. Address: Room 307B, The Wistar Institute, 3601 Spruce Street, Philadelphia, PA 19104, United States. Tel.: +1 215 495 6840.

E-mail address: [rzhang@wistar.org](mailto:rzhang@wistar.org) (R. Zhang).

## 1.1. Synthesis of nucleotides: The de novo pathway

Nucleotides can be synthesized through either the de novo pathway or the salvage pathway [13]. In the de novo pathway, glucose and glutamine are the main nutrients needed to synthesize nucleotides [14]. Glucose is converted to ribose-5-phosphate during the pentose phosphate pathway, which is used for both purine and pyrimidine synthesis [15]. Glutamine is necessary for supplying nitrogen [16]. Purines and pyrimidines are synthesized in two distinct ways [13,15,17]. Purines are made by directly assembling the atoms that comprise the purine ring onto ribose-5-phosphate through 11 steps. This yields inosine monophosphate (IMP), which is further modified to produce adenosine monophosphate (AMP) and guanosine monophosphate (GMP). In contrast, during pyrimidine synthesis, the pyrimidine ring is completed before addition of the ribose-5-phosphate moiety. Pyrimidines are made through a 6-step process, which produces uridine monophosphate (UMP). UMP can then be converted into cytidine triphosphate (CTP). Thymine nucleotides are synthesized after uridine diphosphate (UDP) and cytidine diphosphate (CDP) are reduced, and thymidylate synthase (TS) is necessary for dTTP synthesis [17].

## 1.2. Synthesis of nucleotides: The salvage pathway

In addition to the de novo pathway, a salvage pathway exists for both purine and pyrimidines [13,17,18]. Normal cells undergo turnover and degradation of cellular materials, leading to release of free purines or substrates that compose the pyrimidine ring [17]. These can be converted back into dNTPs by a variety of en-

<http://dx.doi.org/10.1016/j.canlet.2014.01.017>

0304-3835/© 2014 Elsevier Ireland Ltd. All rights reserved.

zymes in both the cytosol and mitochondria [17,18]. Interestingly, pyrimidine salvage is more efficient than purine salvage [17].

### 1.3. Synthesis of deoxyribonucleotides

One particular type of nucleotide, 2'-deoxyribonucleoside 5'-triphosphates (dNTPs), is necessary for both DNA replication and repair [17,19]. Without the correct levels of dNTPs, cells cannot faithfully replicate either nuclear or mitochondrial DNA, and DNA damage cannot be repaired [7,20]. The rate-limiting step in dNTP synthesis is reduction of ribonucleoside di- or tri- phosphates (NDPs/NTPs) at the 2' position of ribose sugar to deoxyribonucleotide-di- or tri- phosphates (dNDPs/dNTPS) by ribonucleotide reductase (RNR) [17,19]. During reduction of ribonucleosides, RNR is oxidized and then reduced by either thioredoxin or glutathione [19]. Nicotinamide adenine dinucleotide phosphate (NADPH) is the ultimate source of the electrons. RNR reduces all four rNDPs/rNTPs (i.e., ADP/ATP, GDP/GTP, UDP/UTP, and CDP/CTP) [17]. RNR activity is tightly regulated by allosteric regulation and enzyme specificity [19]. RNR is a tetrameric complex consisting of two large catalytic subunits (R1: ribonucleotide reductase M1, RRM1) and two small regulatory subunits (R2: ribonucleotide reductase M2, RRM2; or p53R2/RRM2B) [17,19]. RRM1 contains both the catalytic site and the allosteric regulatory sites [19]. RRM1 is expressed throughout all phases of the cell cycle [21]. The R2 subunit contains the tyrosyl radical, the site necessary for the reduction reaction [19]. RRM2 is the R2 subunit that controls reduction during S phase of the cell cycle when dNTPs are needed for DNA replication [21]. Therefore, RRM2 expression is rate-limiting for RNR activity [19]. In contrast, p53R2 is involved in supplying dNTPs for DNA repair and mitochondrial DNA synthesis in the G0/G1 phase of the cell cycle [22].

### 1.4. Senescence

First described in 1961 by Leonard Hayflick and Paul Moorhead, cellular senescence is defined as a stable cell growth arrest [23]. Senescence can be induced by a number of different stimuli, including critically shortened telomeres, activated oncogenes, DNA damage, and some cancer therapeutics [24]. Senescent cells have unique morphological and molecular characteristics [25]. Phenotypically, they are characterized by a large, flat morphology and increased activity of  $\beta$ -galactosidase (termed senescence-associated  $\beta$ -galactosidase or SA- $\beta$ -gal) [26].

### 1.5. Oncogene-induced senescence

Oncogene-induced senescence (OIS) occurs when an oncogene (such as RAS or BRAF) becomes activated in a primary (normal) mammalian cell [27]. Paradoxically, expression of an activated oncogene leads to a cell cycle exit and sustained growth arrest [28]. OIS is therefore considered a bona fide tumor suppressor mechanism *in vivo* [24,29]. The hallmarks of OIS include DNA replication stress leading to a sustained DNA damage response (DDR) [30,31] and upregulation of the p53/p21 and p16/pRb pathways (Fig. 1), which contribute to the stable growth arrest [32].

This review will focus on the role of nucleotide metabolism as a newly identified pathway in OIS. In addition, we will discuss how changes in nucleotide metabolism can overcome OIS and transform cells. Finally, we will briefly outline how nucleotide metabolism is a diagnostic and prognostic biomarker for cancer and how this pathway could be targeted as a cancer therapeutic by inducing senescence of cancer cells.

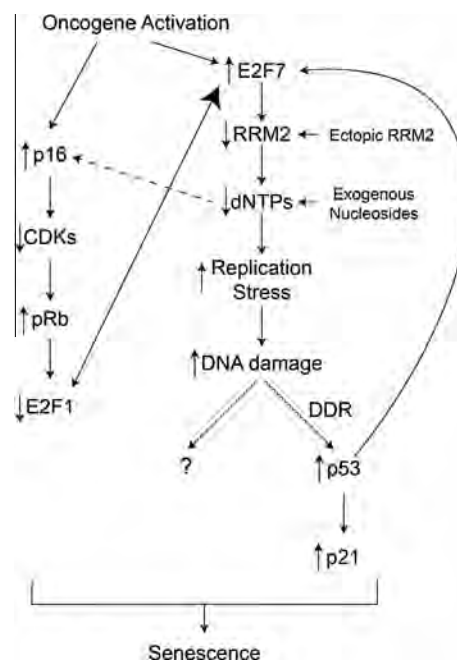


**Fig. 1.** Overview of the oncogene-induced senescence pathway. Oncogene-induced senescence begins with activation of an oncogene in a primary (normal) mammalian cell. This upregulates the repressive E2F7, which inhibits transcription of the RRM2 gene. Inhibition of RRM2 leads to a significant decrease in dNTP levels. This leads to two outcomes: (1) replication stress and accumulation of DNA damage; and (2) upregulation of p16 through an unknown mechanism. Replication stress and DNA damage accumulation activates the DNA damage response (DDR), in particular p53. p53 activation positively feeds back by further increasing E2F7 activity. Sustained activation of p53 induces high expression of p21, which helps facilitate cell cycle arrest. DNA damage can also lead to cell cycle arrest independent of p53 and p21 status. Upregulation of p16 inhibits cyclin-dependent kinases (CDKs), which relieves their inhibition of pRb. pRb can then repress E2F1 activity, which leads to more E2F7 binding to repress RRM2 transcription. Decreased E2F1 also leads to a cell cycle exit through a decrease in transcription of numerous cell cycle-related genes. These pathways all act in concert to establish and maintain the stable senescence-associated cell cycle exit.

## 2. Role of nucleotide metabolism in oncogene-induced senescence

Nucleotide metabolism and imbalances in dNTP pools have long been known to play a role in a variety of human pathologies [1–4]. However, until recently, there was no specific research to demonstrate that nucleotide metabolism plays a role in OIS. The following sections will review what is currently known about the role of dNTP pools in OIS, including their role in replication stress, the DNA damage response, and execution of senescence pathways after oncogene activation.

### 2.1. Role of decreased dNTP pools in replication stress during OIS

Senescence induced by activated oncogenes such as RAS is characterized by accumulation of cells in S-phase of the cell cycle [30]. This is due to the induction of replication stress leading to stalled and collapsed replication forks, thereby arresting cells in S-phase [30,31]. The replication stress leads to activation of either ataxia telangiectasia and Rad3-related protein (ATR) (stalled forks) or ataxia telangiectasia mutated (ATM) (collapsed forks), which effectively activates an intra-S phase checkpoint [33,34]. Indeed, suppression of S-phase progression is sufficient to block RAS-induced senescence [35]. Early studies showed that a decrease in dNTP pools by hydroxyurea (HU) leads to an S-phase arrest [36,37]. Recent evidence from our lab suggests that the replication



stress observed during OIS is specifically due to a decrease in dNTP levels (Fig. 1) [38]. Specifically, we showed a transcriptional decrease in RRM2, whose expression is rate-limiting for rNDP/rNTP reduction to dNDPs/dNTPs [19]. Indeed, ectopic expression of RRM2, which is sufficient to restore cellular dNTP levels, or supplementation with exogenous nucleosides is able to overcome the replication stress observed during OIS (Fig. 1) [38]. Interestingly, replication stress due to decreased dNTP pools has also been shown to play a role in longevity in yeast [39]. Additionally, patients with mutations in replication regulators such as the RecQ helicases [e.g., Werner syndrome ATP-dependent helicase (WRN), (Bloom syndrome RecQ helicase-like (BLM), and RecQ Protein-Like 4 (RECQL4)] display replication stress, genomic instability, and accelerated aging phenotypes [40,41]. Given that cellular senescence is thought to contribute to tissue aging, these data suggest that dNTP pools play a larger role in replication stress during senescence.

## 2.2. Role of decreased dNTP pools in the activation of the DNA damage response during OIS

In addition to replication stress, accumulation of DNA damage and activation of the DDR are hallmarks of OIS (Fig. 1) [30,31,42]. Until recently, it was unclear whether replication stress or oxidative stress was the cause of the DNA damage and DDR during OIS. Results from our lab indicate that replication stress induced by a decrease in dNTP pools plays a major role in the accumulation of DNA damage observed during OIS (Fig. 1) [38]. Specifically, we show that restoration of cellular dNTP levels by either addition of exogenous nucleosides or ectopic RRM2 expression is sufficient to suppress the DDR. This correlates with rescue of the oncogene-induced DNA replication stress [38]. Another report has corroborated our finding that decreased dNTP levels are the cause of the DNA damage during senescence induced by either oncogenic RAS [43] or c-myc [44]. These authors also found that thymidylate synthase (TS) and the large subunit RRM1 were also downregulated during OIS [43], suggesting a global decrease in the nucleotide metabolic pathway during OIS. However, data from our lab demonstrates that RRM2 downregulation, but not other regulators of the nucleotide metabolic pathway such as p53R2 or RRM1, occurs before the cell cycle exit [38]. This indicates that RRM2 downregulation drives the suppression of nucleotide metabolism observed during OIS, and downregulation of other regulators of the nucleotide metabolic pathway may be simply a consequence of OIS-associated cell growth arrest.

## 2.3. The role of decreased dNTP pools in the execution of the OIS-associated cell cycle exit

Senescence was initially defined as an irreversible cell cycle exit [45]. In contrast to what has been observed with the reversible effects of HU on the cell cycle [36,37], cells cannot re-enter the cell cycle after a decrease in dNTP pools due to decreased RRM2 (Fig. 1) [38]. Therefore, the consequence of decreased dNTP pools must go beyond replication stress and the associated DDR. It is known that numerous signaling pathways are activated during OIS, in particular the p53/p21 and p16/pRb pathways (Fig. 1) [32]. Indeed, as discussed above, the decrease in dNTP pools leads to accumulation of DNA damage and a sustained induction of the DDR [38]. Additionally, the decrease in dNTP pools also leads to elevated expression of the cell cycle regulators p21 and p16 [38], which are both upregulated during OIS [32]. p16 phosphorylates cyclin-dependent kinases (CDKs), which relieves the inhibition of pRb (Fig. 1) [46]. pRb inhibits activating E2Fs such as E2F1 [47–50]. Under normal growth conditions, E2F1 contributes to transcription of RRM2 [51]. Interestingly, RRM2 downregulation occurs

at the transcriptional level through replacement of the transcriptional activator E2F1 with the transcriptionally repressive E2F7 at the promoter of RRM2 gene (Fig. 1) [38]. This reinforces the decrease in dNTP pools and therefore the OIS-associated cell cycle exit. This is consistent with results from a previous report demonstrating a positive feedback loop between p53 and E2F7 [52]. Downregulation of RRM2 activates p53 [38], which then enhances E2F7 expression [52]. In addition, pRb decreases E2F1 activity [49,50], which may allow for enhanced binding of the repressive E2F7 to the RRM2 promoter. This suggests that these pathways act in concert to maintain the stable cell growth arrest. Interestingly, the decrease in RRM2 seems to be one of the first signals in this feedback loop as it occurs while cells maintain proliferation [38]. Moreover, in RAS-infected cells, ectopic RRM2 or supplementation with exogenous nucleosides can override the activation of p53 (Fig. 1). These data all point to the presence of a feedback loop whereby the decrease in RRM2 leads to a further decrease in RRM2 through activation of the p53/E2F7 pathway and pRb pathway. Interestingly, senescence of cancer cells such as melanoma and ovarian cancer cells induced by RRM2 inhibition is independent of both p53 and pRb pathway [38,53]. However, this correlates with activation of the DDR. This suggests senescence induced by RRM2 inhibition depends upon DNA damage and the associated pathway (Fig. 1). Indeed, exogenous nucleosides suppress the DDR and also inhibit senescence induced by RRM2 inhibition. Future studies are warranted to elucidate the downstream pathways activated by DNA damage that mediate senescence and the associated cell growth arrest induced by suppression of nucleotide metabolism.

## 3. Nucleotide metabolism in cancer

OIS is considered to be a tumor suppressor mechanism *in vivo* [29]. However, cells that have undergone OIS can accumulate additional oncogenic hits over time, which may lead to senescence bypass and transformation. For instance, benign nevi (moles) that have undergone OIS due to expression of oncogenic BRAF or NRAS can eventually become melanomas [54]. It is important to understand how cells can bypass senescence and become transformed. These observations may allow for better preventative measures or novel cancer therapeutics. The following sections will discuss the role of nucleotide metabolism in transformation, cancer progression, and cancer therapeutics.

### 3.1. Role of nucleotide metabolism in genomic integrity, senescence bypass, and transformation

We have already discussed the role of decreased dNTP pools in replication stress and the DDR (Sections 2.1 and 2.2). It is well known that replication stress can lead to genomic instability [7], which is a hallmark of cancer cells [55,56]. Indeed, patients with mutations in proteins necessary for genomic integrity (i.e., BRCA1/2, Rad51, etc...) are prone to cancer [57]. Notably, early studies in yeast models demonstrated that decreased dNTP levels lead to increased mutagenesis through an increase in genomic instability [58]. A number of recent publications have attempted to elucidate the mechanism of OIS bypass and transformation. Our lab demonstrated that melanocytes expressing oncogenic BRAF or NRAS can bypass senescence when exogenous nucleosides are supplemented into the cell culture medium (Fig. 1) [38]. These data have been corroborated in fibroblasts expressing HRAS [38,43]. Additionally, we found that either ectopic expression of RRM2 or exogenous nucleoside supplementation could overcome the cell cycle exit in fully senescent fibroblasts [38]. Because these cells maintain oncogene expression, it is easy to surmise that these



senescent bypassed cells could become transformed. Indeed, one report demonstrates that decreased dNTP pools in E6/E7 cells is what causes transformation of these cells [59]. Although E6/E7 expression does not induce senescence, this study clearly indicates that low dNTP pools may play a role in the early phases of tumorigenesis.

Interestingly, overexpression of RRM2 or p53R2 is tumorigenic by itself (Fig. 2) [60]. Increased RRM2 or p53R2 expression is mutagenic *in vitro* and leads to lung neoplasms *in vivo*. Notably, RRM2 overexpression induces a higher mutation frequency *in vitro* compared to p53R2 overexpression. In addition, RRM2 transgenic mice have larger and more malignant lung neoplasms compared to p53R2 transgenic mice. These results indicate that RRM2 may be a more potent oncogene than p53R2. Additionally, another nucleotide metabolic enzyme TS can independently transform cells and lead to tumor formation *in vivo* [61–63]. In contrast, expression of RRM1 is thought to be tumor suppressive (Fig. 2). Indeed, in both *in vitro* and *in vivo* models, overexpression of RRM1 can reduce tumor formation, migration, and metastasis [64–66]. These studies indicate that nucleotide metabolism plays an important role in senescence bypass, tumor formation, and progression.

### 3.2. Role of nucleotide metabolism as a cancer biomarker

It is clear that changes in nucleotide metabolism can lead to transformation and tumorigenesis (discussed in Section 3.1). Therefore, many studies have sought to determine whether components of the nucleotide metabolic pathway are either prognostic or diagnostic biomarkers in a variety of cancers.

A number of studies have shown that RRM2 is both a prognostic and diagnostic biomarker. RRM2 has been shown to be a diagnostic biomarker in colon, breast and pancreas [67–69]. Recent studies from our lab have shown that RRM2 expression is both a prognos-

tic and diagnostic biomarker for melanomas with oncogenic BRAF or NRAS [38] and epithelial ovarian cancer (EOC) [53]. In EOC, RRM2 expression positively correlates with the cell proliferation marker Ki67, tumor grade, and stage [53]. We also observed that high RRM2 expression independently predicts a shorter overall survival in both EOC and melanoma patients [53,38]. Interestingly, in the same cohort of melanoma patients, RRM1 did not correlate with survival [38]. This underscores the importance of RRM2 in cancer progression.

The role of the other R2 subunit, p53R2, as a biomarker is not as clear. p53R2 has been shown to be diagnostic biomarker for a variety of cancer types, including melanoma [70], non-small cell lung cancer [71], and squamous cell carcinoma [72]. In addition, high p53R2 expression is also a poor prognostic biomarker in non-small cell lung cancer [71] and squamous cell carcinoma [73]. However, some studies have indicated that high p53R2 leads to a better prognosis [74,75]. Future studies will need to be done on larger patient cohorts to truly determine whether p53R2 expression predicts better or worse patient outcome.

The role of RRM1 in the diagnosis and prognosis of cancer is also unclear. Studies have indicated that RRM1 is a tumor suppressor (Fig. 2) [65]; therefore, high RRM1 expression is a predictor of better survival [76–78]. In contrast, other studies have found that high RRM1 expression leads to poor survival [78,79]. In fact, one study found that depending on what treatment patients received, high RRM1 expression was inconclusive for patient prognosis [80]. Our study in melanoma compared RRM1 and RRM2 expression. We found that RRM2, but not RRM1, predicted better survival in patients with BRAF or NRAS positive tumors [38]. The conflicting results between studies make it hard to fully distinguish whether RRM1 expression is important for the diagnosis and prognosis of cancer patients.

Other enzymes further upstream in the nucleotide biosynthetic pathway have also been shown as important cancer biomarkers. For instance, high expression of thymidylate synthase, which is necessary for dTTP synthesis [17], is a predictor of poor survival in different cancer types [81,82].

Taken together, these studies demonstrate that nucleotide pool imbalances, and in particular dNTP pool imbalances, are both diagnostic and prognostic biomarkers for a large variety of human cancers.

### 3.3. Inhibiting nucleotide metabolism for cancer therapeutics

Since nucleotide metabolism plays a role in transformation and tumor progression (discussed in Sections 3.1 and 3.2), inhibition of this pathway has long been considered a therapeutic strategy for cancer. As tumor cells have a higher need for dNTPs [55,56], many of the anti-tumor therapeutics affecting nucleotide metabolism are aimed at RNR [83–87]. The first class of drugs that were found to inhibit nucleotide metabolism are free radical scavengers, including hydroxyurea [88] and trimidox (Fig. 2) [89]. Because these compounds are free radical scavengers, they can inhibit RNR by inactivating the tyrosyl radical on R2 necessary for its reductive capacity [89–94]. Although hydroxyurea was initially found to be a potent anti-neoplastic agent, it has many limitations, including low affinity for RNR and a very short half-life [95,96]. These limitations have led to a decrease in the use of hydroxyurea in the clinic.

More recently, iron chelators have been used as a way to target RNR [97] because iron is necessary for formation of the tyrosyl radical center [19]. 3-aminopyridine-2-carboxaldehyde thiosemicarbazone (3-AP, Triapine) is the best studied iron chelator that inhibits RNR activity (Fig. 2) [98]. It is 100-fold more potent than hydroxyurea in both enzyme inhibition and cancer cell growth inhibition. It can inhibit the activity of both RRM2 and p53R2 [98,99], which disallows for compensation by the other R2 subunit.

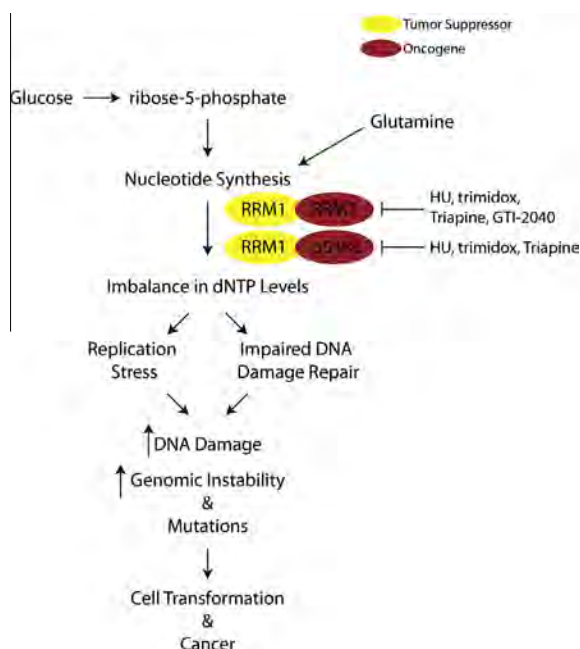


**Fig. 2.** Overview of nucleotide metabolic pathway in cancer. Synthesis of nucleotides begins with formation of ribose-5-phosphate from glucose. Along with glutamine, which donates the necessary nitrogen, a number of modifications lead to formation of nucleotides. A change in RRM1, RRM2, or p53R2 expression can lead to dNTP pool imbalances. Ultimately, this imbalance leads to replication stress and impaired DNA damage repair, which consequently increases DNA damage, genomic instability, and mutations. This ultimately contributes to cell transformation and cancer. Numerous inhibitors have been developed to inhibit RRM2 and p53R2, including HU (hydroxyurea), trimidox, Triapine (3-AP), and GTI-2040.

Triapine as a single agent has generally not been effective as a therapeutic for cancer patients [100,101]. However, in combination with DNA damage agents such as cisplatin or radiation, Triapine shows some synergistic activity [102,103], and many clinical trials are still underway (clinicaltrials.gov). One of the main issues with Triapine is the number of side effects, including dyspnea and methemoglobinemia [97,103,104], which limits the use of this drug.

Data from both hydroxyurea and Triapine demonstrate that more specific RNR inhibitors are needed to minimize toxic side effects. With the identification of antisense, more recent work has gone into specifically targeting RNR subunits. Currently, an antisense oligonucleotide to RRM2 (GTI-2040) is in clinical trials (clinicaltrials.gov) (Fig. 2). Phase II clinical trials with published results have shown little added benefit with GTI-2040 [105–107]. It is possible that p53R2 could compensate for RRM2 when it is inhibited. Additionally, the effect of GTI-2040 has not been fully examined in combination with cisplatin or radiation. This may lead to a synergistic effect similar to combination therapy with Triapine (discussed above). Results from our lab using a short hairpin RNA (shRNA) specific for RRM2 indicate that these cells undergo senescence [38,53] and not cell death. Senescent cells remain metabolically active [24], which may allow for cellular changes that could overcome senescence. Therefore, finding combination strategies that would kill these senescent cells will be important for future targeting of RNR.

#### 4. Concluding remarks

dNTPs are necessary for both DNA replication and repair. The rate-limiting step in dNTP synthesis is the reduction of rNDPs to dNDPs by RNR. Over the past year, it has become clear that the small subunit of RNR, RRM2, plays a major role in the senescence tumor suppression mechanism. Without downregulation of RRM2, cells with activated oncogenes can bypass senescence, which may ultimately lead to cell transformation and tumorigenesis (Fig. 1). Because this enzyme is so important in the establishment of uncontrolled growth in cancer and the maintenance of proliferation, anti-tumor drugs have been developed that target this specific part of the nucleotide metabolic pathway (Fig. 2). More work needs to be done to explore new combination strategies by targeting RNR to drive senescence of cancer cells treated with chemotherapeutics or targeted therapies that only induce a transient cell growth arrest. Further, it will be interesting to investigate ways to eliminate senescent cells induced by RNR inhibition via promoting apoptosis. Together, these approaches may ultimately lead to a sustained, long-term response to therapeutics in cancer and enhance survival of cancer patients.

#### Conflict of Interest

There is no conflicts of interest to be declared.

#### Acknowledgements

This work was supported by a NIH/NCI grant (R01CA160331 to R.Z.), a DoD Ovarian Cancer Academy Award (OC093420 to R.Z.) and an NIH/NCI training grant (T32CA9171–35 to K.M.A.). Support of Core Facilities used in this study was provided by Cancer Center Support Grant (CCSG) CA010815 to The Wistar Institute.

#### References

- [1] M. Meuth, The molecular basis of mutations induced by deoxyribonucleoside triphosphate pool imbalances in mammalian cells, *Exp. Cell Res.* 181 (1989) 305–316.
- [2] G. Weinberg, B. Ullman, D.W. Martin Jr., Mutator phenotypes in mammalian cell mutants with distinct biochemical defects and abnormal deoxyribonucleoside triphosphate pools, *Proc. Natl. Acad. Sci. USA* 78 (1981) 2447–2451.
- [3] P. Chabosseau, G. Buhagiar-Labarchede, R. Onclercq-Delic, S. Lambert, M. Debatisse, O. Brison, M. Amor-Gueret, Pyrimidine pool imbalance induced by BLM helicase deficiency contributes to genetic instability in Bloom syndrome, *Nat. Commun.* 2 (2011) 368.
- [4] L. Chang, R. Guo, Q. Huang, Y. Yen, Chromosomal instability triggered by Rrm2b loss leads to IL-6 secretion and plasmacytic neoplasms, *Cell Rep.* 3 (2013) 1389–1397.
- [5] A.J. Ammann, Purine nucleotide imbalance in immunodeficiency disorders, *Basic Life Sci.* 31 (1985) 487–502.
- [6] G.R. Boss, J.E. Seegmiller, Genetic defects in human purine and pyrimidine metabolism, *Annu. Rev. Genet.* 16 (1982) 297–328.
- [7] W.C. Burhans, M. Weinberger, DNA replication stress, genome instability and aging, *Nucleic Acids Res.* 35 (2007) 7545–7556.
- [8] C.K. Mathews, DNA precursor metabolism and genomic stability, *Faseb J.* 20 (2006) 1300–1314.
- [9] T. Kimura, S. Takeda, Y. Sagiya, M. Gotoh, Y. Nakamura, H. Arakawa, Impaired function of p53R2 in Rrm2b-null mice causes severe renal failure through attenuation of dNTP pools, *Nat. Genet.* 34 (2003) 440–445.
- [10] V.N. Dobrovolsky, T. Bucci, R.H. Hefflich, J. Desjardins, F.C. Richardson, Mice deficient for cytosolic thymidine kinase gene develop fatal kidney disease, *Mol. Genet. Metab.* 78 (2003) 1–10.
- [11] A.W. El-Hattab, F. Scaglia, Mitochondrial DNA depletion syndromes: review and updates of genetic basis, manifestations, and therapeutic options, *Neurotherapeutics* 10 (2013) 186–198.
- [12] R.D. Pitceathly, C. Smith, C. Fratter, C.L. Alston, L. He, K. Craig, E.L. Blakely, J.C. Evans, J. Taylor, Z. Shabbir, M. Deschauer, U. Pohl, M.E. Roberts, M.C. Jackson, C.A. Halfpenny, P.D. Turnpenny, P.W. Lunt, M.G. Hanna, A.M. Schaefer, R. McFarland, R. Horvath, P.F. Chinnery, D.M. Turnbull, J. Poulton, R.W. Taylor, G.S. Gorman, Adults with RRM2B-related mitochondrial disease have distinct clinical and molecular characteristics, *Brain* 135 (2012) 3392–3403.
- [13] R.L. Blakley, E. Vitols, The control of nucleotide biosynthesis, *Annu. Rev. Biochem.* 37 (1968) 201–224.
- [14] C.V. Dang, Links between metabolism and cancer, *Genes. Dev.* 26 (2012) 877–890.
- [15] S.C. Hartman, J.M. Buchanan, Nucleic acids, purines, pyrimidines (nucleotide synthesis), *Annu. Rev. Biochem.* 28 (1959) 365–410.
- [16] P. Newsholme, J. Procopio, M.M. Lima, T.C. Pithon-Curi, R. Curi, Glutamine and glutamate—their central role in cell metabolism and function, *Cell Biochem. Funct.* 21 (2003) 1–9.
- [17] P. Reichard, Interactions between deoxyribonucleotide and DNA synthesis, *Annu. Rev. Biochem.* 57 (1988) 349–374.
- [18] A.W. Murray, The biological significance of purine salvage, *Annu. Rev. Biochem.* 40 (1971) 811–826.
- [19] P. Nordlund, P. Reichard, Ribonucleotide reductases, *Annu. Rev. Biochem.* 75 (2006) 681–706.
- [20] M. Anglana, F. Apiou, A. Bensimon, M. Debatisse, Dynamics of DNA replication in mammalian somatic cells: nucleotide pool modulates origin choice and interorigin spacing, *Cell* 114 (2003) 385–394.
- [21] Y. Engstrom, S. Eriksson, I. Jildevik, S. Skog, L. Thelander, B. Tribukait, Cell cycle-dependent expression of mammalian ribonucleotide reductase. Differential regulation of the two subunits, *J. Biol. Chem.* 260 (1985) 9114–9116.
- [22] P. Hakansson, A. Hofer, L. Thelander, Regulation of mammalian ribonucleotide reduction and dNTP pools after DNA damage and in resting cells, *J. Biol. Chem.* 281 (2006) 7834–7841.
- [23] L. Hayflick, P.S. Moorhead, The serial cultivation of human diploid cell strains, *Exp. Cell Res.* 25 (1961) 585–621.
- [24] J. Campisi, F. d'Adda di Fagagna, Cellular senescence: when bad things happen to good cells, *Nat. Rev. Mol. Cell Biol.* 8 (2007) 729–740.
- [25] F. Rodier, J. Campisi, Four faces of cellular senescence, *J. Cell Biol.* 192 (2011) 547–556.
- [26] G.P. Dimri, X. Lee, G. Basile, M. Acosta, G. Scott, C. Roskelley, E.E. Medrano, M. Linskens, I. Rubelj, O. Pereira-Smith, et al., A biomarker that identifies senescent human cells in culture and in aging skin in vivo, *Proc. Natl. Acad. Sci. USA* 92 (1995) 9363–9367.
- [27] P. Yaswen, J. Campisi, Oncogene-induced senescence pathways weave an intricate tapestry, *Cell* 128 (2007) 233–234.
- [28] W.J. Mooi, D.S. Peeper, Oncogene-induced cell senescence—halting on the road to cancer, *N Engl. J. Med.* 355 (2006) 1037–1046.
- [29] M. Braig, S. Lee, C. Lodenkemper, C. Rudolph, A.H. Peters, B. Schlegelberger, H. Stein, B. Dorken, T. Jenuwein, C.A. Schmitt, Oncogene-induced senescence as an initial barrier in lymphoma development, *Nature* 436 (2005) 660–665.
- [30] R. Di Micco, M. Fumagalli, A. Cicalese, S. Piccinin, P. Gasparini, C. Luise, C. Schurra, M. Garre, P.G. Nucifora, A. Bensimon, R. Maestro, P.G. Pelicci, F. d'Adda di Fagagna, Oncogene-induced senescence is a DNA damage response triggered by DNA hyper-replication, *Nature* 444 (2006) 638–642.
- [31] J. Bartkova, N. Rezaei, M. Liontos, P. Karakaidos, D. Kletsas, N. Issaeva, L.V. Vassiliou, E. Kolettas, K. Niforou, V.C. Zoumpourlis, M. Takaoka, H. Nakagawa, F. Tort, K. Fugger, F. Johansson, M. Sehested, C.L. Andersen, L. Dyrskjot, T. Orntoft, J. Lukas, C. Kittas, T. Helleday, T.D. Halazonetis, J. Bartek, V.G. Gorgoulis, Oncogene-induced senescence is part of the tumorigenesis barrier imposed by DNA damage checkpoints, *Nature* 444 (2006) 633–637.

- [32] M. Serrano, A.W. Lin, M.E. McCurrach, D. Beach, S.W. Lowe, Oncogenic ras provokes premature cell senescence associated with accumulation of p53 and p16INK4a, *Cell* 88 (1997) 593–602.
- [33] A.J. Osborn, S.J. Elledge, L. Zou, Checking on the fork: the DNA-replication stress-response pathway, *Trends Cell Biol.* 12 (2002) 509–516.
- [34] K.A. Cimprich, D. Cortez, ATR: an essential regulator of genome integrity, *Nat. Rev. Mol. Cell Biol.* 9 (2008) 616–627.
- [35] A. Alimonti, C. Nardella, Z. Chen, J.G. Clohessy, A. Carracedo, L.C. Trotman, K. Cheng, S. Varmeh, S.C. Kozma, G. Thomas, E. Rosivatz, R. Woscholski, F. Cognetti, H.I. Scher, P.P. Pandolfi, A novel type of cellular senescence that can be enhanced in mouse models and human tumor xenografts to suppress prostate tumorigenesis, *J. Clin. Invest.* 120 (2010) 681–693.
- [36] V. Bianchi, E. Pontis, P. Reichard, Changes of deoxyribonucleoside triphosphate pools induced by hydroxyurea and their relation to DNA synthesis, *J. Biol. Chem.* 261 (1986) 16037–16042.
- [37] M. Matsumoto, D.A. Rey, J.G. Cory, Effects of cytosine arabinoside and hydroxyurea on the synthesis of deoxyribonucleotides and DNA replication in L1210 cells, *Adv. Enzyme. Regul.* 30 (1990) 47–59.
- [38] K.M. Aird, G. Zhang, H. Li, Z. Tu, B.G. Bitler, A. Garipov, H. Wu, Z. Wei, S.N. Wagner, M. Herlyn, R. Zhang, Suppression of Nucleotide Metabolism Underlies the Establishment and Maintenance of Oncogene-Induced Senescence, *Cell Rep.* (2013).
- [39] M. Weinberger, L. Feng, A. Paul, D.L. Smith Jr., R.D. Hontz, J.S. Smith, M. Vujcic, K.K. Singh, J.A. Huberman, W.C. Burhans, DNA replication stress is a determinant of chronological lifespan in budding yeast, *PLoS ONE* 2 (2007) e748.
- [40] C.Z. Bahrati, I.D. Hickson, RecQ helicases: suppressors of tumorigenesis and premature aging, *Biochem. J.* 374 (2003) 577–606.
- [41] L. Larizza, I. Magnani, G. Roversi, Rothmund-Thomson syndrome and RECQL4 defect: splitting and lumping, *Cancer Lett.* 232 (2006) 107–120.
- [42] F.A. Mallette, M.F. Gaumont-Leclerc, G. Ferbeyre, The DNA damage signaling pathway is a critical mediator of oncogene-induced senescence, *Genes. Dev.* 21 (2007) 43–48.
- [43] S. Mannava, K.C. Moparthy, L.J. Wheeler, V. Natarajan, S.N. Zucker, E.E. Fink, M. Im, S. Flanagan, W.C. Burhans, N.C. Zeitouni, D.S. Shewach, C.K. Mathews, M.A. Nikiforov, Depletion of deoxyribonucleotide pools is an endogenous source of DNA damage in cells undergoing oncogene-induced senescence, *Am. J. Pathol.* 182 (2013) 142–151.
- [44] S. Mannava, K.C. Moparthy, L.J. Wheeler, K.I. Leonova, J.A. Wawrzyniak, A. Bianchi-Smiraglia, A.E. Berman, S. Flanagan, D.S. Shewach, N.C. Zeitouni, A.V. Gudkov, C.K. Mathews, M.A. Nikiforov, Ribonucleotide reductase and thymidylate synthase or exogenous deoxyribonucleosides reduce DNA damage and senescence caused by C-MYC depletion, *Aging (Albany NY)* 4 (2012) 917–922.
- [45] J. Campisi, Senescent cells, tumor suppression, and organismal aging: good citizens, bad neighbors, *Cell* 120 (2005) 513–522.
- [46] M. Serrano, G.J. Hannon, D. Beach, A new regulatory motif in cell-cycle control causing specific inhibition of cyclin D/CDK4, *Nature* 366 (1993) 704–707.
- [47] S.W. Hiebert, S.P. Chellappan, J.M. Horowitz, J.R. Nevins, The interaction of RB with E2F coincides with an inhibition of the transcriptional activity of E2F, *Genes. Dev.* 6 (1992) 177–185.
- [48] N. Dyson, The regulation of E2F by pRB-family proteins, *Genes. Dev.* 12 (1998) 2245–2262.
- [49] K. Helin, E. Harlow, A. Fattaey, Inhibition of E2F-1 transactivation by direct binding of the retinoblastoma protein, *Mol. Cell Biol.* 13 (1993) 6501–6508.
- [50] E.K. Flemington, S.H. Speck, W.G. Kaelin Jr., E2F-1-mediated transactivation is inhibited by complex formation with the retinoblastoma susceptibility gene product, *Proc. Natl. Acad. Sci. USA* 90 (1993) 6914–6918.
- [51] Y.W. Zhang, T.L. Jones, S.E. Martin, N.J. Caplen, Y. Pommier, Implication of checkpoint kinase-dependent up-regulation of ribonucleotide reductase R2 in DNA damage response, *J. Biol. Chem.* 284 (2009) 18085–18095.
- [52] O. Aksoy, A. Chicas, T. Zeng, Z. Zhao, M. McCurrach, X. Wang, S.W. Lowe, The atypical E2F family member E2F7 couples the p53 and RB pathways during cellular senescence, *Genes. Dev.* 26 (2012) 1546–1557.
- [53] K.M. Aird, H. Li, F. Xin, P.A. Konstantinopoulos, R. Zhang, Identification of ribonucleotide reductase M2 as a potential target for pro-senescence therapy in epithelial ovarian cancer, *Cell Cycle* 13 (2014).
- [54] L.C. Vredevelde, P.A. Possik, M.A. Smit, C. Meissl, C. Michaloglou, H.M. Horlings, A. Ajouaou, P.C. Kortman, D. Dankort, M. McMahon, W.J. Mooi, D.S. Peeper, Abrogation of BRAFV600E-induced senescence by PI3K pathway activation contributes to melanomagenesis, *Genes. Dev.* 26 (2012) 1055–1069.
- [55] D. Hanahan, R.A. Weinberg, The hallmarks of cancer, *Cell* 100 (2000) 57–70.
- [56] D. Hanahan, R.A. Weinberg, Hallmarks of cancer: the next generation, *Cell* 144 (2011) 646–674.
- [57] K.W. Kinzler, B. Vogelstein, Cancer-susceptibility genes. Gatekeepers and caretakers, *Nature* 386 (1997) 761–763.
- [58] C. Holmberg, O. Fleck, H.A. Hansen, C. Liu, R. Slaaby, A.M. Carr, O. Nielsen, Ddb1 controls genome stability and meiosis in fission yeast, *Genes. Dev.* 19 (2005) 853–862.
- [59] A.C. Bester, M. Roniger, Y.S. Oren, M.M. Im, D. Sarni, M. Chaoat, A. Bensimon, G. Zamir, D.S. Shewach, B. Kerem, Nucleotide deficiency promotes genomic instability in early stages of cancer development, *Cell* 145 (2011) 435–446.
- [60] X. Xu, J.L. Page, J.A. Surtees, H. Liu, S. Lagedrost, Y. Lu, R. Bronson, E. Alani, A.Y. Nikitin, R.S. Weiss, Broad overexpression of ribonucleotide reductase genes in mice specifically induces lung neoplasms, *Cancer Res.* 68 (2008) 2652–2660.
- [61] M. Chen, L. Rahman, D. Voeller, E. Kastanos, S.X. Yang, L. Feigenbaum, C. Allegra, F.J. Kaye, P. Steeg, M. Zajac-Kaye, Transgenic expression of human thymidylate synthase accelerates the development of hyperplasia and tumors in the endocrine pancreas, *Oncogene* 26 (2007) 4817–4824.
- [62] L. Rahman, D. Voeller, M. Rahman, S. Lipkowitz, C. Allegra, J.C. Barrett, F.J. Kaye, M. Zajac-Kaye, Thymidylate synthase as an oncogene: a novel role for an essential DNA synthesis enzyme, *Cancer Cell* 5 (2004) 341–351.
- [63] D. Voeller, L. Rahman, M. Zajac-Kaye, Elevated levels of thymidylate synthase linked to neoplastic transformation of mammalian cells, *Cell Cycle* 3 (2004) 1005–1007.
- [64] H. Fan, A. Huang, C. Villegas, J.A. Wright, The R1 component of mammalian ribonucleotide reductase has malignancy-suppressing activity as demonstrated by gene transfer experiments, *Proc. Natl. Acad. Sci. USA* 94 (1997) 13181–13186.
- [65] A. Gautam, G. Bepler, Suppression of lung tumor formation by the regulatory subunit of ribonucleotide reductase, *Cancer Res.* 66 (2006) 6497–6502.
- [66] A. Gautam, Z.R. Li, G. Bepler, RRM1-induced metastasis suppression through PTEN-regulated pathways, *Oncogene* 22 (2003) 2135–2142.
- [67] X. Liu, H. Zhang, L. Lai, X. Wang, S. Loera, L. Xue, H. He, K. Zhang, S. Hu, Y. Huang, R.A. Nelson, B. Zhou, L. Zhou, P. Chu, S. Zhang, S. Zheng, Y. Yen, Ribonucleotide reductase small subunit M2 serves as a prognostic biomarker and predicts poor survival of colorectal cancers, *Clin. Sci. (Lond)* 124 (2013) 567–578.
- [68] H. Fujita, K. Ohuchida, K. Mizumoto, S. Itaba, T. Ito, K. Nakata, J. Yu, T. Kayashima, R. Souza, T. Tajiri, T. Manabe, T. Ohtsuka, M. Tanaka, Gene expression levels as predictive markers of outcome in pancreatic cancer after gemcitabine-based adjuvant chemotherapy, *Neoplasia* 12 (2010) 807–817.
- [69] D.T. Jones, T. Lechertier, R. Mitter, J.M. Herbert, R. Bicknell, J.L. Jones, J.L. Li, F. Buffa, A.L. Harris, K. Hodiola-Dilke, Gene expression analysis in human breast cancer associated blood vessels, *PLoS ONE* 7 (2012) e44294.
- [70] S. Matsushita, R. Ikeda, T. Fukushige, Y. Tajitsu, K. Gunshin, H. Okumura, M. Ushiyama, S. Akiyama, K. Kawai, Y. Takeda, K. Yamada, T. Kanekura, P53R2 is a prognostic factor of melanoma and regulates proliferation and chemosensitivity of melanoma cells, *J. Dermatol. Sci.* 68 (2012) 19–24.
- [71] H. Uramoto, K. Sugio, T. Oyama, T. Hanagiri, K. Yasumoto, P53R2, p53 inducible ribonucleotide reductase gene, correlated with tumor progression of non-small cell lung cancer, *Anticancer Res.* 26 (2006) 983–988.
- [72] S. Yanamoto, G. Kawasaki, I. Yoshitomi, A. Mizuno, Expression of p53R2, newly p53 target in oral normal epithelium, epithelial dysplasia and squamous cell carcinoma, *Cancer Lett.* 190 (2003) 233–243.
- [73] H. Okumura, S. Natsugoe, N. Yokomakura, Y. Kita, M. Matsumoto, Y. Uchikado, T. Setoyama, T. Owaki, S. Ishigami, T. Aikou, Expression of p53R2 is related to prognosis in patients with esophageal squamous cell carcinoma, *Clin. Cancer Res.* 12 (2006) 3740–3745.
- [74] N.Y. Hsu, J.Y. Wu, X. Liu, Y. Yen, C.Y. Chen, M.C. Chou, H. Lee, Y.W. Cheng, P53R2 expression as a prognostic biomarker in early stage non-small cell lung cancer, *Oncol. Lett.* 1 (2010) 609–613.
- [75] X. Liu, L. Lai, X. Wang, L. Xue, S. Loera, J. Wu, S. Hu, K. Zhang, M.L. Kuo, L. Zhou, H. Zhang, Y. Wang, B. Zhou, R.A. Nelson, S. Zheng, S. Zhang, P. Chu, Y. Yen, Ribonucleotide reductase small subunit M2B prognoses better survival in colorectal cancer, *Cancer Res.* 71 (2011) 3202–3213.
- [76] G. Bepler, S. Sharma, A. Cantor, A. Gautam, E. Haura, G. Simon, A. Sharma, E. Sommers, L. Robinson, RRM1 and PTEN as prognostic parameters for overall and disease-free survival in patients with non-small-cell lung cancer, *J. Clin. Oncol.* 22 (2004) 1878–1885.
- [77] M. Pesta, V. Kulda, O. Fiala, J. Safranek, O. Topolcan, G. Krakorova, R. Cerny, M. Pesek, Prognostic significance of ERCC1, RRM1 and BRCA1 in surgically-treated patients with non-small cell lung cancer, *Anticancer Res.* 32 (2012) 5003–5010.
- [78] L.P. Jordeheim, P. Seve, O. Tredan, C. Dumontet, The ribonucleotide reductase large subunit (RRM1) as a predictive factor in patients with cancer, *Lancet Oncol.* 12 (2011) 693–702.
- [79] Q. Wang, X. Liu, J. Zhou, Y. Huang, S. Zhang, J. Shen, S. Loera, X. Yuan, W. Chen, M. Jin, S. Shibata, Y. Liu, P. Chu, L. Wang, Y. Yen, Ribonucleotide reductase large subunit M1 predicts poor survival due to modulation of proliferative and invasive ability of gastric cancer, *PLoS ONE* 8 (2013) e70191.
- [80] H. Xie, W. Jiang, J. Jiang, Y. Wang, R. Kim, X. Liu, Predictive and prognostic roles of ribonucleotide reductase M1 in resectable pancreatic adenocarcinoma, *Cancer* 119 (2012) 173–181.
- [81] B.C. Pestalozzi, H.F. Peterson, R.D. Gelber, A. Goldhirsch, B.A. Gusterson, H. Trihadi, J. Lindtner, H. Cortes-Funes, E. Simoncini, M.J. Byrne, R. Golouh, C.M. Rudenstam, M. Castiglione-Gertsch, C.J. Allegra, P.G. Johnston, Prognostic importance of thymidylate synthase expression in early breast cancer, *J. Clin. Oncol.* 15 (1997) 1923–1931.
- [82] C.J. Allegra, S. Paik, L.H. Colangelo, A.L. Parr, I. Kirsch, G. Kim, P. Klein, P.G. Johnston, N. Wolmark, H.S. Wieand, Prognostic value of thymidylate synthase, Ki-67, and p53 in patients with Dukes' B and C colon cancer: a National Cancer Institute-National Surgical Adjuvant Breast and Bowel Project collaborative study, *J. Clin. Oncol.* 21 (2003) 241–250.
- [83] G. Nocentini, Ribonucleotide reductase inhibitors: new strategies for cancer chemotherapy, *Crit. Rev. Oncol. Hematol.* 22 (1996) 89–126.
- [84] N.M. Cerqueira, P.A. Fernandes, M.J. Ramos, Ribonucleotide reductase: a critical enzyme for cancer chemotherapy and antiviral agents, *Recent Pat. Anticancer Drug. Discov.* 2 (2007) 11–29.



- [85] N.M. Cerqueira, S. Pereira, P.A. Fernandes, M.J. Ramos, Overview of ribonucleotide reductase inhibitors: an appealing target in anti-tumour therapy, *Curr. Med. Chem.* 12 (2005) 1283–1294.
- [86] J.G. Cory, Ribonucleotide reductase as a chemotherapeutic target, *Adv. Enzyme Regul.* 27 (1988) 437–455.
- [87] J. Shao, B. Zhou, B. Chu, Y. Yen, Ribonucleotide reductase inhibitors and future drug design, *Curr. Cancer Drug. Targets* 6 (2006) 409–431.
- [88] K. Madaan, D. Kaushik, T. Verma, Hydroxyurea: a key player in cancer chemotherapy, *Expert Rev. Anticancer Ther.* 12 (2011) 19–29.
- [89] T. Szekeres, K. Gharehbaghi, M. Fritzer, M. Woody, A. Srivastava, B. van't Riet, H.N. Jayaram, H.L. Elford, Biochemical and antitumor activity of trimidox, a new inhibitor of ribonucleotide reductase, *Cancer Chemother Pharmacol.* 34 (1994) 63–66.
- [90] G. Lassmann, L. Thelander, A. Graslund, EPR stopped-flow studies of the reaction of the tyrosyl radical of protein R2 from ribonucleotide reductase with hydroxyurea, *Biochem. Biophys. Res. Commun.* 188 (1992) 879–887.
- [91] B. Nigovic, N. Kujundzic, K. Sankovic, Electron transfer in N-hydroxyurea complexes with iron(III), *Eur. J. Med. Chem.* 40 (2005) 51–55.
- [92] H.L. Elford, Functional regulation of mammalian ribonucleotide reductase, *Adv. Enzyme Regul.* 10 (1972) 19–38.
- [93] H.L. Elford, B. Van't Riet, G.L. Wampler, A.L. Lin, R.M. Elford, Regulation of ribonucleotide reductase in mammalian cells by chemotherapeutic agents, *Adv. Enzyme Regul.* 19 (1980) 151–168.
- [94] H.L. Elford, G.L. Wampler, B. van't Riet, New ribonucleotide reductase inhibitors with antineoplastic activity, *Cancer Res.* 39 (1979) 844–851.
- [95] G.L. Beckloff, H.J. Lerner, D. Frost, F.M. Russo-Alesi, S. Gitomer, Hydroxyurea (NSC-32065) in biologic fluids: dose-concentration relationship, *Cancer Chemother Rep.* 48 (1965) 57–58.
- [96] P.R. Gwilt, W.G. Tracewell, Pharmacokinetics and pharmacodynamics of hydroxyurea, *Clin. Pharmacokinet* 34 (1998) 347–358.
- [97] Y. Yu, E. Gutierrez, Z. Kovacevic, F. Saletta, P. Obeidy, Y. Suryo Rahmanto, D.R. Richardson, Iron chelators for the treatment of cancer, *Curr. Med. Chem.* 19 (2012) 2689–2702.
- [98] R.A. Finch, M.C. Liu, A.H. Cory, J.G. Cory, A.C. Sartorelli, Triapine (3-aminopyridine-2-carboxaldehyde thiosemicarbazone; 3-AP): an inhibitor of ribonucleotide reductase with antineoplastic activity, *Adv. Enzyme Regul.* 39 (1999) 3–12.
- [99] R.A. Finch, M. Liu, S.P. Grill, W.C. Rose, R. Loomis, K.M. Vasquez, Y. Cheng, A.C. Sartorelli, Triapine (3-aminopyridine-2-carboxaldehyde-thiosemicarbazone): a potent inhibitor of ribonucleotide reductase activity with broad spectrum antitumor activity, *Biochem. Pharmacol.* 59 (2000) 983–991.
- [100] C.M. Nutting, C.M. van Herpen, A.B. Miah, S.A. Bhide, J.P. Machiels, J. Buter, C. Kelly, D. de Raucourt, K.J. Harrington, Phase II study of 3-AP Triapine in patients with recurrent or metastatic head and neck squamous cell carcinoma, *Ann. Oncol.* 20 (2009) 1275–1279.
- [101] S. Attia, J. Kolesar, M.R. Mahoney, H.C. Pitot, D. Laheru, J. Heun, W. Huang, J. Eickhoff, C. Erlichman, K.D. Holen, A phase 2 consortium (P2C) trial of 3-aminopyridine-2-carboxaldehyde thiosemicarbazone (3-AP) for advanced adenocarcinoma of the pancreas, *Invest. New Drugs* 26 (2008) 369–379.
- [102] C.A. Kunos, T. Radivoyevitch, S. Waggoner, R. Debernardo, K. Zanotti, K. Resnick, N. Fusco, R. Adams, R. Redline, P. Faulhaber, A. Dowlati, Radiochemotherapy plus 3-aminopyridine-2-carboxaldehyde thiosemicarbazone (3-AP, NSC #663249) in advanced-stage cervical and vaginal cancers, *Gynecol. Oncol.* 130 (2013) 75–80.
- [103] C. Kunos, T. Radivoyevitch, F.W. Abdul-Karim, J. Fanning, O. Abulafia, A.J. Bonebrake, L. Usha, Ribonucleotide reductase inhibition restores platinum-sensitivity in platinum-resistant ovarian cancer: a Gynecologic Oncology Group Study, *J. Trans. Med.* 10 (2012) 79.
- [104] C.A. Kunos, T. Radivoyevitch, S.T. Ingalls, C.L. Hoppel, Management of 3-aminopyridine-2-carboxaldehyde thiosemicarbazone-induced methemoglobinemia, *Future Oncol.* 8 (2012) 145–150.
- [105] N.B. Leighl, S.A. Laurie, X.E. Chen, P. Ellis, F.A. Shepherd, J.J. Knox, G. Goss, R.L. Burkes, G.R. Pond, C. Dick, Y. Yen, J.A. Zwiebel, M.J. Moore, A phase I/II study of GTI-2040 plus docetaxel as second-line treatment in advanced non-small cell lung cancer: a study of the PMH phase II consortium, *J. Thorac. Oncol.* 4 (2009) 1163–1169.
- [106] S.S. Sridhar, C.M. Canil, K.N. Chi, S.J. Hotte, S. Ernst, L. Wang, E.X. Chen, A. Juhasz, Y. Yen, P. Murray, J.A. Zwiebel, M.J. Moore, A phase II study of the antisense oligonucleotide GTI-2040 plus docetaxel and prednisone as first-line treatment in castration-resistant prostate cancer, *Cancer Chemother Pharmacol.* 67 (2010) 927–933.
- [107] W.M. Stadler, A.A. Desai, D.I. Quinn, R. Bukowski, B. Poiesz, C.G. Kardinal, N. Lewis, A. Makalinalao, P. Murray, F.M. Torti, A Phase I/II study of GTI-2040 and capecitabine in patients with renal cell carcinoma, *Cancer Chemother Pharmacol.* 61 (2008) 689–694.



# Identification of ribonucleotide reductase M2 as a potential target for pro-senescence therapy in epithelial ovarian cancer

Katherine M Aird<sup>1</sup>, Hua Li<sup>1</sup>, Frances Xin<sup>2</sup>, Panagiotis A Konstantinopoulos<sup>3,\*</sup>, and Rugang Zhang<sup>1,\*</sup>

<sup>1</sup>Gene Expression and Regulation Program; The Wistar Institute Cancer Center; The Wistar Institute; Philadelphia, PA USA; <sup>2</sup>Cell and Molecular Biology Graduate Program; School of Medicine; The University of Pennsylvania; Philadelphia, PA USA; <sup>3</sup>Medical Gynecological Oncology Program; Dana Farber Cancer Institute; Harvard Medical School; Harvard University; Boston, MA USA

**Keywords:** epithelial ovarian cancer, cellular senescence, ribonucleotide reductase M2 (RRM2), DNA damage response, cell proliferation

**Abbreviations:** dNTPs, 2'-deoxyribonucleoside 5'-triphosphates; EOC, epithelial ovarian cancer; IHC, immunohistochemical; RNR, ribonucleotide reductase; RRM2, ribonucleotide reductase M2; SA- $\beta$ -gal, senescence-associated  $\beta$ -galactosidase; shRRM2, short hairpin RNA to the human *RRM2* gene

Epithelial ovarian cancer (EOC) is the leading cause of gynecological-related cancer deaths in the United States. There is, therefore, an urgent need to develop novel therapeutic strategies for this devastating disease. Cellular senescence is a state of stable cell growth arrest that acts as an important tumor suppression mechanism. Ribonucleotide reductase M2 (RRM2) plays a key role in regulating the senescence-associated cell growth arrest by controlling biogenesis of 2'-deoxyribonucleoside 5'-triphosphates (dNTPs). The role of RRM2 in EOC remains poorly understood. Here we show that RRM2 is expressed at higher levels in EOCs compared with either normal ovarian surface epithelium ( $P < 0.001$ ) or fallopian tube epithelium ( $P < 0.001$ ). RRM2 expression significantly correlates with the expression of Ki67, a marker of cell proliferation ( $P < 0.001$ ). Moreover, RRM2 expression positively correlates with tumor grade and stage, and high RRM2 expression independently predicts a shorter overall survival in EOC patients ( $P < 0.001$ ). To delineate the functional role of RRM2 in EOC, we knocked down RRM2 expression in a panel of EOC cell lines. Knockdown of RRM2 expression inhibits the growth of human EOC cells. Mechanistically, RRM2 knockdown triggers cellular senescence in these cells. Notably, this correlates with the induction of the DNA damage response, a known mediator of cellular senescence. These data suggest that targeting RRM2 in EOCs by suppressing its activity is a novel pro-senescence therapeutic strategy that has the potential to improve survival of EOC patients.

## Introduction

Ovarian cancer is the most lethal gynecological malignancy and the fifth leading cancer-related cause of death among women in the United States.<sup>1</sup> The vast majority of ovarian cancers (>85%) are categorized as epithelial ovarian cancer (EOC).<sup>2</sup> EOCs are classified into distinct histological types including serous, mucinous, endometrioid, and clear cell.<sup>2</sup> The most common histology of EOC is serous (~60% of all cancers), and less common histologies include endometrioid, clear cell, and mucinous.<sup>3</sup> Recently, an alternative classification has been proposed, in which EOC is broadly divided into 2 types.<sup>4</sup> Type I EOC includes mucinous, low-grade serous, low-grade endometrioid, and clear cell carcinomas, and type II EOC includes high-grade serous and high-grade endometrioid carcinomas.<sup>4</sup> Although significant advances have occurred in the field of therapeutics for solid tumors, cancer

mortality in women with ovarian cancer has remained at the same level for over 2 decades.<sup>5</sup> Unfortunately, the molecular etiology of ovarian cancer remains to be fully elucidated.<sup>5</sup> Therefore, there is a great need to identify molecular factors that are predictive of clinical outcome and, more importantly, explore the feasibility of targeting these newly identified factors to develop urgently needed EOC therapies.

Ribonucleotide reductase (RNR) catalyzes the conversion of ribonucleoside 5'-diphosphates into their corresponding 2'-deoxyribonucleoside 5'-triphosphates (dNTPs), the building blocks of DNA that are necessary for both DNA replication and repair.<sup>6</sup> Ribonucleotide reductase M2 (RRM2) is the regulatory subunit of RNR that is necessary for dNTP biogenesis during the S phase of the cell cycle when DNA replication occurs.<sup>7</sup> Tumor cells are characterized by an uncontrolled proliferation, and synthesis of DNA is necessary for this process. Consistently, RRM2

\*Correspondence to: Rugang Zhang; Email: rzhang@wistar.org; Panagiotis A Konstantinopoulos; Email: panagiotisa\_konstantinopoulos@dfci.harvard.edu  
Submitted: 08/30/2013; Revised: 10/09/2013; Accepted: 10/24/2013  
<http://dx.doi.org/10.4161/cc.26953>

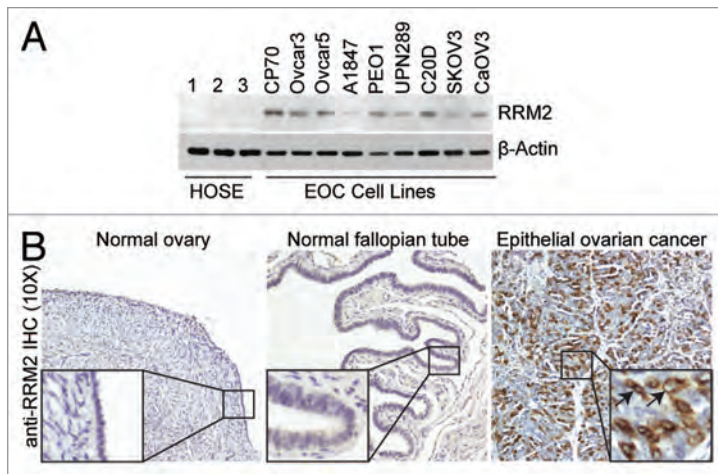


**Figure 1.** RRM2 is upregulated in EOC cells and tumor specimens. **(A)** Expression of RRM2 protein in 3 individual isolations of normal human ovarian surface epithelial (HOSE) cells and the indicated human EOC cell lines by immunoblotting.  $\beta$ -actin was used as a loading control. **(B)** Immunohistochemical staining of RRM2 protein expression in normal ovary, normal fallopian tube, and human EOC tissue specimens. Shown is an example of a high-grade serous EOC tissue specimen. Arrows point to the RRM2 positively stained EOC cells.

is known to play an active role during tumorigenesis<sup>8</sup> and has been suggested as a potential target for developing cancer therapeutics.<sup>9</sup> In addition, RRM2 is implicated in mediating resistance to cancer chemotherapy.<sup>10</sup> RRM2 is a known prognostic biomarker for several cancer types such as colon, breast, and pancreas.<sup>11-13</sup> Indeed, several inhibitors of RRM2 have entered clinical trials for these cancer types.<sup>9,14,15</sup> However, the role of RRM2 in EOC remains poorly understood.

Cellular senescence is a state of stable cell growth arrest that can be induced by a variety of triggers, including critically shortened telomeres, activated oncogenes, DNA damage, and certain cancer therapeutics such as cisplatin.<sup>16</sup> Senescent cells have unique morphological and molecular characteristics, including a large, flat morphology and increased activity of  $\beta$ -galactosidase (termed senescence-associated  $\beta$ -galactosidase or SA- $\beta$ -gal).<sup>17</sup> Importantly, reactivation of the senescence-promoting pathways, such as p53 in murine cancer models, leads to senescence of cancer cells and associated tumor regression.<sup>18-20</sup> Therefore, induction of senescence represents a novel mechanism for developing cancer therapeutics.<sup>21,22</sup> Notably, RRM2 plays a critical role in establishing and maintaining the senescence-associated cell growth arrest induced by activated oncogenes.<sup>23</sup> RRM2 is suppressed during senescence, and its overexpression is sufficient to overcome senescence. This correlates with the changes in DNA damage response during senescence.<sup>23-26</sup> Interestingly, senescence induced by C-MYC depletion in melanoma cells suppresses RRM2 expression and the subsequent depletion of dNTP pools.<sup>24</sup> This raises the possibility that RRM2 is a bona fide target for driving cancer cells to undergo senescence and the associated stable cell growth arrest and, thus, represents a target for the development of pro-senescence therapies. However, this has never been tested in EOCs.

In this study, we determined that RRM2 protein expression is higher in EOC cancer cell lines compared with normal human

ovarian surface epithelial cells. Likewise, RRM2 is significantly upregulated in EOC specimens compared with either normal human ovarian surface epithelium or fallopian tube epithelium. RRM2 expression in EOC significantly correlates with an increase in the expression of Ki67, a marker of cell proliferation. Using an independent data set, we validated that RRM2 is expressed at a higher level in EOCs compared with normal human ovarian surface epithelial cells. In addition, RRM2 expression positively correlates with tumor stage and grade in EOC patients. Importantly, there was a significant reverse correlation between RRM2 expression and overall survival in EOC patients. Functionally, suppression of RRM2 activity by knocking down its expression in EOC cells inhibited the proliferation of these cells. Mechanistically, RRM2 knockdown induces senescence of EOC cells, which correlates with an increase of DNA damage in these cells, a known trigger of senescence. These data show that RRM2 expression is an independent prognostic factor for EOC patients and suggest that targeting RRM2 represents a novel strategy for developing urgently needed EOC therapy by inducing EOC cells to undergo senescence.

## Results

### RRM2 is often upregulated in EOCs compared with either normal human ovarian surface epithelium or fallopian tube epithelium

To determine whether RRM2 is upregulated in EOC cell lines, we examined the protein expression level of RRM2 in 3 individual isolations of normal human ovarian epithelial (HOSE) cells and 9 different human EOC cell lines by immunoblotting. RRM2 protein levels were higher in all examined human EOC cell lines compared with the HOSE cells (Fig. 1A). The RRM2 antibody is specific, because only 1 band appears in immunoblotting analysis, and a short hairpin RNA to the human *RRM2* gene (shRRM2) that efficiently knocks down RRM2 expression decreases the intensity of the single band detected by the anti-RRM2 antibody (Fig. S1A). Next, we sought to determine whether RRM2 upregulation also occurs in human EOC specimens. Toward this goal, we examined the expression of RRM2 by immunohistochemical (IHC) staining analysis in 105 cases of EOCs and 35 normal human ovary specimens. Recent evidence suggests that a proportion of EOCs may arise from the distal fallopian tube epithelial cells.<sup>27,28</sup> Thus, we also included 36 normal human fallopian tube specimens in our study. The cytoplasm of EOC cells was positive for RRM2 IHC staining (Fig. 1B). In contrast, RRM2 staining in normal human ovarian surface epithelial cells or fallopian tube epithelial cells was nearly negative (Fig. 1B). The anti-RRM2 antibody-staining signal was specific, because blocking anti-RRM2 antibody binding with a specific blocking peptide significantly decreased the IHC signal (Fig. S1B). RRM2 expression was scored as high (H score  $\geq 50$ ) or low (H score  $< 50$ ) based on a histological score as previously described,<sup>29,30</sup> which considers both percentage and intensity of the staining signal. RRM2 was scored as high in 43.8% (46/105) of human EOCs. In contrast, RRM2 was scored high in 0%

**Table 1.** RRM2 protein expression; correlation between RRM2 expression and Ki67 cell proliferation marker or clinicopathological variables

| Patient characteristics          | low (n) | high (n) | total (n) | high (%) | P        |
|----------------------------------|---------|----------|-----------|----------|----------|
| <b>Normal epithelial tissue</b>  |         |          |           |          |          |
| Normal ovary                     | 35      | 0        | 35        | 0.0%     | <0.001*  |
| Normal fallopian tube            | 35      | 1        | 36        | 2.8%     | <0.001** |
| <b>Epithelial ovarian cancer</b> | 59      | 46       | 105       | 43.8%    |          |
| <b>Type I</b>                    | 14      | 5        | 19        | 26.3%    |          |
| Low-grade serous                 | 5       | 0        | 5         |          |          |
| Mucinous                         | 3       | 0        | 3         |          |          |
| Low-grade endometrioid           | 2       | 1        | 3         |          |          |
| Clear cell                       | 4       | 4        | 8         |          |          |
| <b>Type II</b>                   | 45      | 41       | 86        | 47.7%    |          |
| High-grade serous                | 41      | 34       | 75        |          |          |
| High-grade endometrioid          | 4       | 7        | 11        |          |          |
| <b>Age</b>                       |         |          |           |          |          |
| ≤55                              | 20      | 20       | 40        | 50.0%    |          |
| >55                              | 39      | 26       | 65        | 40.0%    | 0.316    |
| <b>Ki67<sup>a</sup></b>          |         |          |           |          |          |
| 0–10%                            | 15      | 1        | 16        | 6.3%     |          |
| 10–40%                           | 14      | 5        | 19        | 26.3%    |          |
| 40–100%                          | 27      | 40       | 67        | 59.7%    | <0.001   |
| Undetermined                     | 3       | 0        | 3         |          |          |

\*Compared with epithelial ovarian cancer,  $P < 0.001$ ; \*\*Compared with high grade serous epithelial ovarian cancer,  $P < 0.001$ ; <sup>a</sup>Spearman Rank Order Correlation also showed Ki67 positively correlated with RRM2 ( $P < 0.001$ ,  $r_s = 0.551$ ).

(0/35) and 2.8% (1/36) of normal human ovarian surface epithelium and fallopian tube epithelium, respectively (Table 1). Statistical analysis revealed that RRM2 was expressed at significantly higher levels in human EOCs compared with either normal human ovarian surface epithelium ( $P < 0.001$ ) or fallopian tube epithelium ( $P < 0.001$ ) (Table 1). We conclude that RRM2 is expressed at significantly higher levels in EOCs compared with either normal human ovarian surface epithelium or fallopian tube epithelium.

Since RRM2 expression regulates dNTP biogenesis, which is necessary for DNA replication during cell proliferation,<sup>6</sup> we sought to determine whether RRM2 expression correlates with cell proliferation in EOC specimens. Toward this goal, we stained the same set of EOC specimens with an antibody against Ki67, a marker of cell proliferation. Indeed, there is a significant correlation between expression of RRM2 and Ki67 in EOC specimens (Table 1), inferring a role for RRM2 in promoting the proliferation of EOC cells. Thus, we conclude that the RRM2 expression

positively correlates with the cell proliferation marker Ki67 in EOCs.

#### High RRM2 expression positively correlates with tumor stage and grade and independently predicts a shorter overall survival in EOC patients

Next, we wanted to validate our findings in an independent data set. Toward this goal, we analyzed 2 published independent EOC gene expression profile microarray data sets with clinical annotations.<sup>31,32</sup> The first data set included 99 individual EOC specimens (37 endometrioid, 41 serous, 13 mucinous, and 8 clear cell histosubtypes) and 4 individual normal ovary samples, while the second data set included 285 EOC specimens (18 borderline tumors and 267 EOC specimens of various grades and stages). Corroborating with our IHC results (Table 1), RRM2 was significantly upregulated in EOC specimens compared with normal tissue (Fig. 2A). There was also a significant increase in RRM2 expression in EOC specimens compared with non-invasive ovarian tumors of low malignant potential (i.e., borderline

tumors) (Fig. 2B). Additionally, RRM2 expression was significantly increased in advanced compared with early stage EOCs (Fig. 2C). Further, RRM2 expression significantly increased with tumor grade of EOCs (Fig. 2D). Finally, RRM2 expression was significantly increased in all 4 major EOC histotypes compared with normal controls (Fig. 2E).

We also evaluated RRM2 expression among the 6 molecular subtypes of EOCs as previously defined by Tothill et al. based on gene expression profiling.<sup>32</sup> We found that subtypes C3 and C6 had significantly lower RRM2 expression compared with

the other subtypes (Fig. 2F). Notably, C3 and C6 molecular subtypes predominantly consist of serous borderline and low-grade and early-stage endometrioid tumors, respectively.<sup>32</sup> In contrast, the vast majority of type II high-grade serous and high-grade endometrioid EOCs segregate with C1, C2, C4, and C5 molecular subtypes.<sup>32</sup> Consistent with our finding that RRM2 expression correlates with the expression of the cell proliferation marker Ki67 (Table 1), RRM2 low-expressing C3 and C6 molecular subtypes are characterized by low expression of cell proliferation markers.<sup>32</sup> Together, these data validate the

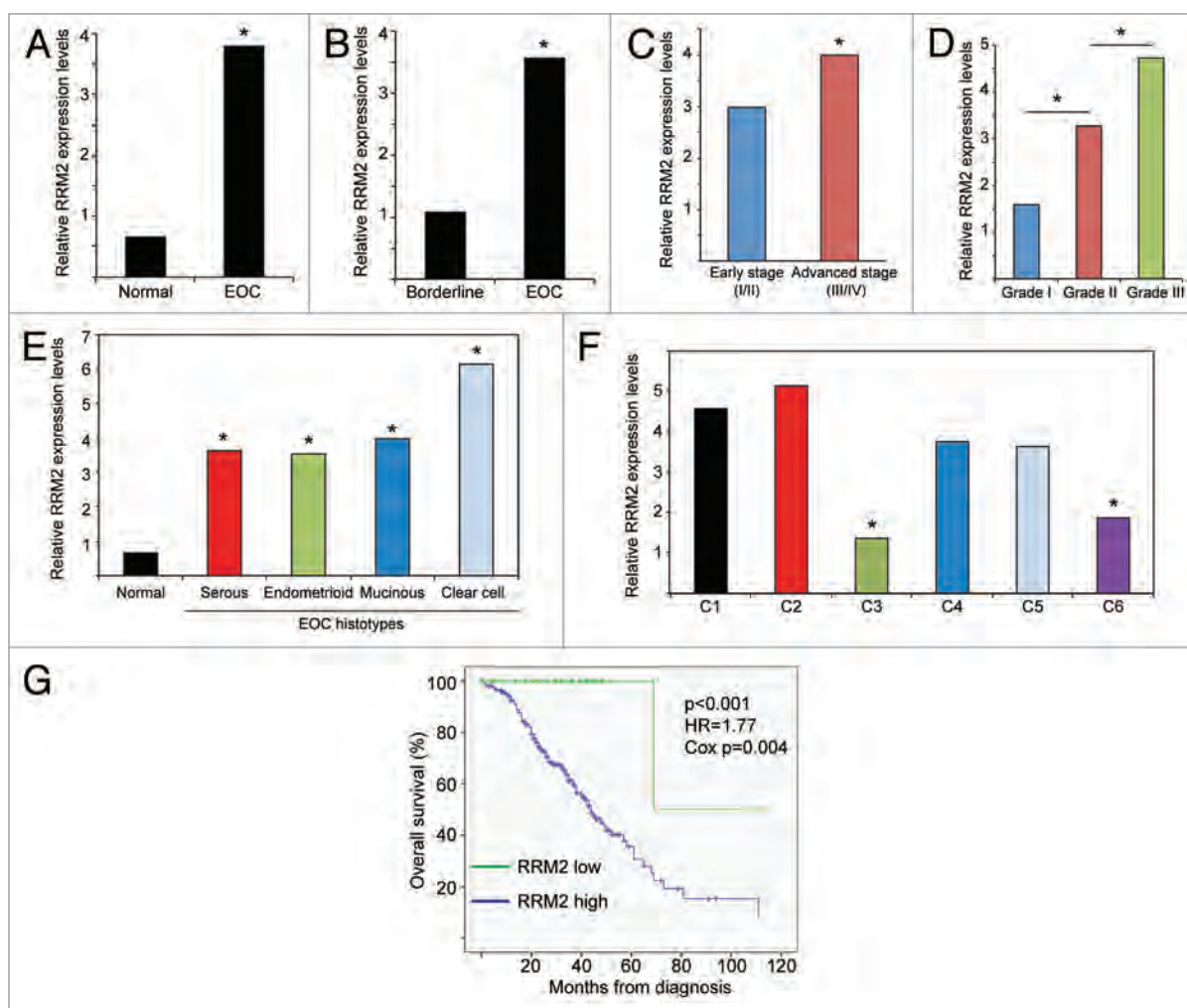


**Figure 2.** RRM2 expression correlates with tumor grade and stage and is a poor prognostic marker in EOC patients. (A) RRM2 is upregulated in EOC specimens (n = 99) compared with normal ovarian surface epithelium samples (n = 4).<sup>31</sup> \* $P < 1 \times 10^{-7}$ , false discovery rate (FDR)  $< 1 \times 10^{-7}$ . (B) RRM2 is upregulated in invasive serous EOC specimens (n = 246) compared with non-invasive, borderline serous tumors of low malignant potential (n = 18).<sup>32</sup> \* $P < 1 \times 10^{-7}$ , FDR  $< 1 \times 10^{-7}$ . (C) RRM2 is upregulated in advanced stage (stage 3 and 4) EOC specimens (n = 239) compared with early stage (stage 1 and 2) EOC specimens (n = 42).<sup>32</sup> \* $P = 0.0199$ , FDR = 0.0199. (D) RRM2 is upregulated in grade 2 EOCs (n = 97) compared with grade 1 EOCs (n = 19) and in grade 3 EOCs (n = 164) compared with grade 1 or grade 2 EOCs.<sup>32</sup> \* $P < 0.001$ . Grade 1 vs. grade 2:  $P = 0.0003$ , FDR = 0.0006. Grade 1 vs. grade 3:  $P < 1 \times 10^{-7}$ , FDR  $< 1 \times 10^{-7}$ . Grade 2 vs. grade 3:  $P = 3.04 \times 10^{-5}$ , FDR =  $3.04 \times 10^{-5}$ . (E) RRM2 is upregulated in serous (41 samples), endometrioid (n = 37), mucinous (n = 13), and clear cell (n = 8) histotypes of EOCs compared with normal human ovarian surface epithelium (n = 4).<sup>31</sup> \* $P < 0.0002$ . Endometrioid vs. normal  $P = 2.3 \times 10^{-6}$ , FDR =  $4.6 \times 10^{-6}$ . Serous vs. normal  $P = 4.4 \times 10^{-6}$ , FDR =  $8.8 \times 10^{-6}$ . Mucinous vs. normal  $P = 0.00013$ , FDR = 0.0003. Clear cell vs. normal  $P = 8.4 \times 10^{-5}$ , FDR = 0.00017. (F) RRM2 is higher in C1 (n = 83), C2 (n = 50), C4 (n = 46), and C5 (n = 36) EOC molecular subtypes compared with C3 (n = 28), and C6 (n = 8).<sup>32</sup> \* $P < 1 \times 10^{-7}$ , FDR  $< 1 \times 10^{-7}$ . C3 vs. C1, C3 vs. C2, C3 vs. C4, and C3 vs. C5: all are statistically significant at the level of  $P < 0.01$  and FDR  $< 0.01$ . C6 vs. C1, C6 vs. C2, C6 vs. C4, and C6 vs. C5: all are statistically significant at the level of  $P < 0.01$  and FDR  $< 0.01$ . (G) High RRM2 expression predicts a shorter overall survival in EOC patients. Kaplan-Meier curves of overall survival for EOC patients with high RRM2 expression (C1, C2, C4, and C5 EOC molecular subtypes) or low RRM2 expression (C3 and C6 molecular subtypes). Median overall survival 44 mo for high RRM2 vs. 69 mo for low RRM2 in EOC patients.<sup>32</sup> Log rank  $P < 0.001$ , Cox  $P = 0.004$  and hazard ratio (HR) for high RRM2 EOC patients = 1.77. Adjusted Cox  $P = 0.02$  and HR = 1.58.



finding that RRM2 is often upregulated in EOC and show that RRM2 expression positively correlates with tumor grade and stage in EOC specimens.

Next, we sought to determine whether there is an association between RRM2 expression and the survival of EOC patients. Toward this goal, we compared the overall survival of EOC patients with low RRM2 expression (C3 and C6 molecular subtypes) to the patients with high RRM2 expression (C1, C2, C4, and C5 molecular subtypes). EOC patients with high RRM2 expression ( $n = 215$ ) had significantly worse overall survival compared with those with low RRM2 expression ( $n = 36$ ) (Fig. 2G, median overall survival 44 vs. 69 m, log rank  $P < 0.001$ ). Of note, multivariate analysis showed that the association of high RRM2 expression with worse survival was independent of stage and grade (adjusted HR = 1.58, Cox  $P = 0.02$ ). Thus, we conclude that high RRM2 expression independently predicts a shorter overall survival in EOC patients.

#### Knockdown of RRM2 inhibits the growth of EOC cells

Our data indicate that RRM2 is often upregulated in EOC, and its expression correlates with the expression of Ki67, a cell proliferation marker (Table 1). Next, we sought to determine the effects of knockdown of RRM2 in EOC cells on the proliferation of these cells. Toward this goal, we developed 2 individual shRRM2s. The knockdown efficacy of shRRM2s was confirmed by immunoblotting in SKOV3 EOC cells (Fig. 3A). Notably, RRM2 knockdown significantly decreased BrdU incorporation, which identifies actively proliferating cells in the S phase of the cell cycle, in SKOV3 cells (Fig. 3B and C). Consistently, the growth of SKOV3 cells was notably inhibited by knockdown of RRM2 as evidenced by cell growth curve analysis (Fig. 3D). Additionally, a decreased ability to form colonies in both anchorage-dependent and anchorage-independent experiments was observed in shRRM2-expressing cells compared with controls (Fig. 3E–G). The growth inhibition was observed in cells expressing 2 individual shRRM2s, and there is a correlation between the efficacy of knockdown and the rate of growth inhibition (Fig. 3). This suggests that the observed phenotypes are not due to potential off-target effects. In addition, similar results were observed in OVCAR5 and PEO1 EOC cells (Fig. S2), showing that this is not a cell line-specific

phenomenon. Taken together, we conclude that knockdown of RRM2 expression inhibits the growth of human EOC cells.

#### Knockdown of RRM2 induces senescence of EOC cells, which correlates with an increase in DNA damage

Next, we sought to determine the mechanism by which RRM2 knockdown suppresses the growth of human EOC cells. Notably, markers of apoptosis such as cleaved caspase 3, cleaved Lamin A, and cleaved PARP p85 were not induced by RRM2 knockdown in human EOC cells (Fig. S3A). RRM2 plays a key role in regulating the establishment and maintenance of senescence and the associated cell growth arrest.<sup>23</sup> Thus, we sought to determine whether RRM2 knockdown induces senescence of human EOC cells. Toward this goal, we examined the expression of SA- $\beta$ -gal activity, a universal marker of cellular senescence,<sup>17</sup> in control and RRM2 knocking down EOC cells. Indeed, knockdown of RRM2 in SKOV3 EOC cells significantly increased SA- $\beta$ -gal activity compared with control cells (Fig. 4A and B). It has been shown that RRM2 expression regulates senescence through affecting the DNA damage response due to its role in dNTP biogenesis, which is necessary for both DNA replication and repair.<sup>23</sup>

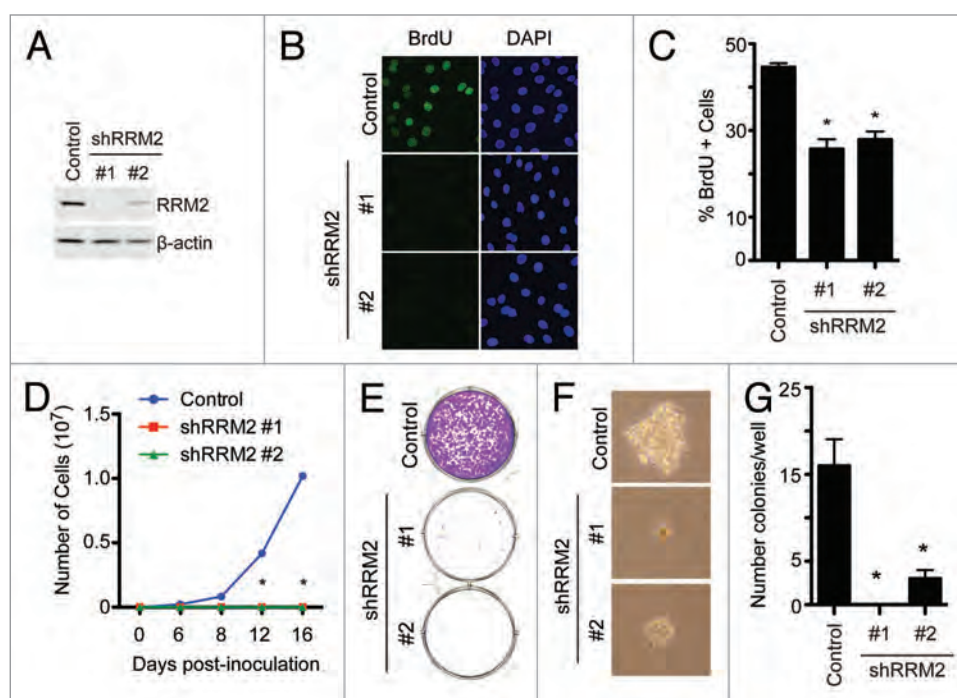


**Figure 3.** Knockdown of RRM2 inhibits cell growth and proliferation of EOC cells. (A) SKOV3 EOC cells were infected with control or 2 individual shRRM2-encoding lentivirus and selected with 3  $\mu$ g/ml puromycin. The expression of RRM2 was determined in drug-selected cells by immunoblotting.  $\beta$ -actin was used as a loading control. (B) Same as (A) but labeled with 10  $\mu$ M BrdU for 30 min to identify the cells that are actively undergoing DNA replication, and the incorporated BrdU was visualized by immunofluorescence staining. DAPI counterstaining was used to visualize cell nuclei. (C) Quantification of (B) 200 cells from each of the indicated groups were examined for BrdU incorporation. Mean of 3 independent experiments with SEM  $*P < 0.01$  compared with controls. (D) Same as (A) but an equal number of cells (3000 cells/well) were seeded in 6-well plates, and the number of cells was counted at the indicated time points. Mean of 3 independent experiments with SD  $*P < 0.05$  compared with controls. (E) Same as (D), but after 2 weeks of culture the plates were stained with 0.05% crystal violet in PBS to visualize focus formation. Shown are representative images of 3 independent experiments. (F) Same as (D), but cells were seeded into soft agar, and 2 weeks later, the colonies were visualized with bright field fluorescence. Shown are representative images of 3 independent experiments. (G) Quantification of (F). Colonies were stained with 1% crystal violet and counted. Mean of 3 independent experiments with SEM  $*P < 0.05$  compared with controls.

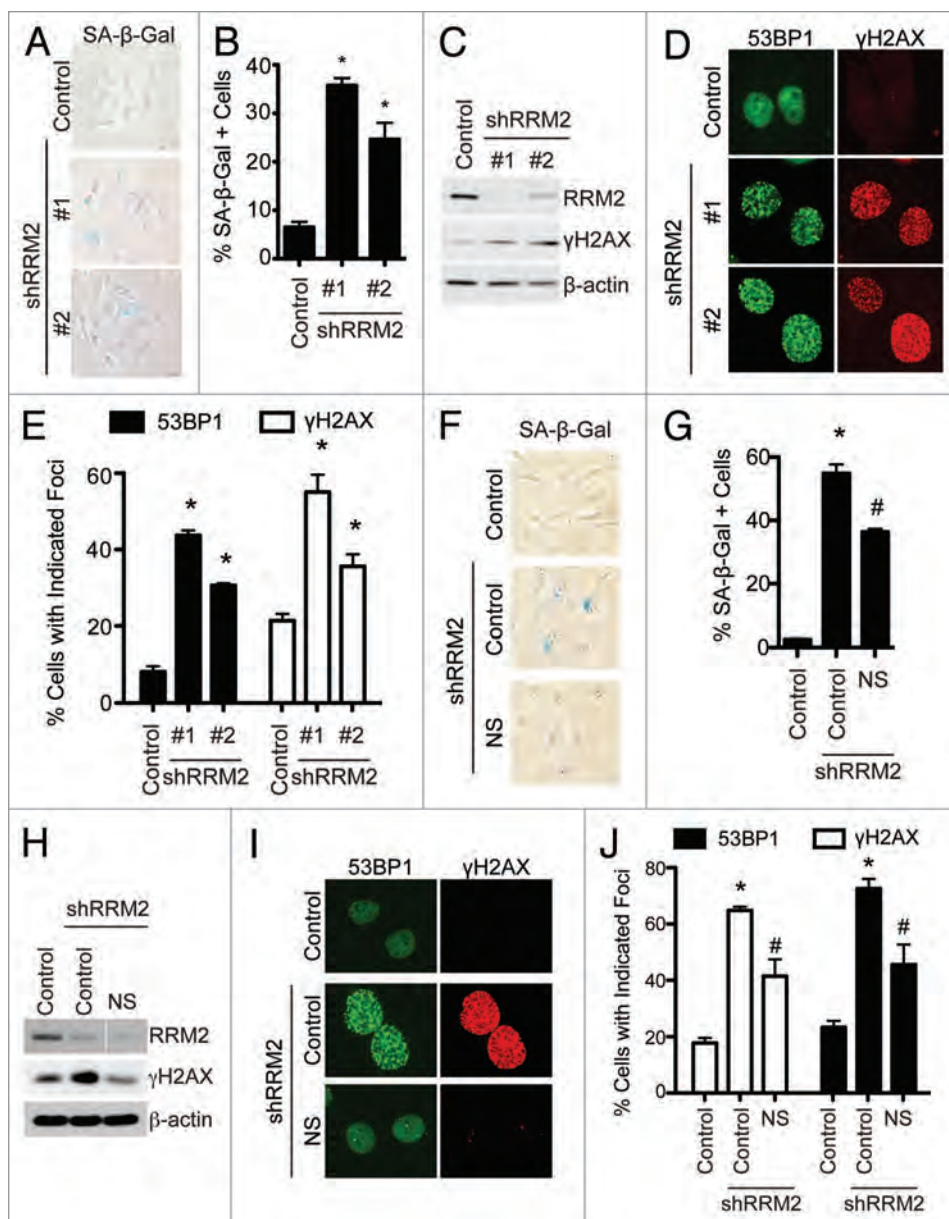


**Figure 4.** Knockdown of RRM2 induces senescence of EOC cells, which correlates with an increase in DNA damage. (A) SKOV3 cells were infected with control or 2 individual shRRM2-encoding lentivirus and selected with 3  $\mu$ g/ml puromycin. After 7 d in culture, cells were stained for SA- $\beta$ -gal activity. (B) Quantification of (A). Two hundred cells from each of the indicated groups were examined for SA- $\beta$ -gal activity. Mean of 3 independent experiments with SEM \**P* < 0.05 compared with controls. (C) Same as (A), but RRM2 and  $\gamma$ H2AX expression were determined by immunoblotting.  $\beta$ -actin was used as a loading control. (D) Same as (A), but  $\gamma$ H2AX and 53BP1 foci formation were determined by immunofluorescence. (E) Quantification of (D). Two hundred cells from each of the indicated groups were examined for  $\gamma$ H2AX and 53BP1 foci. Mean of 3 independent experiments with SEM \**P* < 0.05 compared with controls. (F) SKOV3 cells were infected with control or an shRRM2-encoding lentivirus with or without addition of 250 nM of exogenous nucleosides and selected with 3  $\mu$ g/ml puromycin. After 7 d in culture, cells were stained for SA- $\beta$ -gal activity. (G) Quantification of (F). Two hundred cells from each of the indicated groups were examined for SA- $\beta$ -gal activity. Mean of 3 independent experiments with SEM. \**P* < 0.05 compared with controls. #*P* < 0.05 compared with shRRM2 alone cells. (H) Same as (F) but  $\gamma$ H2AX and RRM2 protein expression was determined by immunoblotting.  $\beta$ -actin was used as a loading control. (I) Same as (F) but  $\gamma$ H2AX and 53BP1 foci formation were determined by immunofluorescence. (J) Quantification of (I). Two hundred cells from each of the indicated groups were examined for  $\gamma$ H2AX and 53BP1 foci. Mean of 3 independent experiments with SEM \**P* < 0.05 compared with controls. #*P* < 0.05 compared with shRRM2 alone cells.

In addition, it has been demonstrated that the DNA damage is a trigger for cellular senescence.<sup>22</sup> Thus, we sought to determine whether senescence induced by RRM2 knockdown is due to an increase in DNA damage. Toward this goal, we examined the expression of markers of DNA damage such as protein expression of  $\gamma$ H2AX and  $\gamma$ H2AX and 53BP1 foci formation in RRM2-knockdown cells. Compared with controls, there was a significant increase in  $\gamma$ H2AX protein expression and  $\gamma$ H2AX and 53BP1 foci formation in RRM2-knockdown cells (Fig. 4C–E). Similar results were observed in multiple EOC cell lines such as OVCAR5 and PEO1 cells (Fig. S3B–G), suggesting that the observed effects are not cell line-specific. We next sought to determine whether inhibition of RRM2 activity mimics RRM2 knockdown in inducing senescence and the DNA damage response in EOC cells. Indeed, treatment of EOC cells with 3-AP, a known inhibitor of RRM2 activity,<sup>33,34</sup> also induced a significant increase in expression of markers of senescence and DNA damage in EOC cells (Fig. S3H–L). These data indicate that knockdown or inhibition of RRM2 activity induces senescence through an increase in DNA damage. Finally, we wanted to determine whether addition of exogenous nucleosides suppresses the senescence phenotype induced by RRM2 knockdown. Toward this goal, we supplemented the media with exogenous nucleosides in RRM2-knockdown cells. Exogenous nucleosides significantly decreased the SA- $\beta$ -gal activity in RRM2-knockdown cells (Fig. 4F–G). Additionally, exogenous nucleosides significantly decreased the DNA damage observed in RRM2-knockdown cells (Fig. 4H–J). This was not due to an increase in RRM2 levels, because addition of nucleosides had no effect on RRM2 knockdown (Fig. 4H). These results support the idea that senescence and DNA damage induced by RRM2 knockdown is mediated by a decrease in dNTP levels. Taken together, these results



demonstrate that knockdown or inhibition of RRM2 activity suppresses the growth of human EOC cells by triggering the DNA damage response and, ultimately, inducing cellular senescence.

## Discussion

In this study, we found that RRM2 is often upregulated in EOC cell lines and in EOC specimens compared with normal controls, which positively correlates with expression of the cell proliferation marker Ki67 and independently predicts a shorter overall survival in EOC patients. We also found that knockdown of RRM2 in EOC cells inhibits the proliferation and growth of these cells. Mechanistically, we found that knockdown of RRM2 induces a DNA damage response, which ultimately causes the EOC cells to senesce. Taken together, these data indicate that RRM2 is a poor prognostic factor for EOC, and inhibiting its activity represents a novel strategy for developing urgently needed EOC therapeutics by driving EOC cells to undergo senescence.

We found that RRM2 is significantly upregulated in EOC compared with normal tissue or borderline ovarian tumors in 3 independent cohorts (Figs. 1 and 2; Table 1), which corroborates with data from recent studies that show RRM2 is overexpressed in EOCs.<sup>35,36</sup> RRM2 upregulation is sufficient to overcome the senescence-associated cell growth arrest tumor suppression mechanism,<sup>23-26</sup> implying that RRM2 may drive proliferation of transformed cells. Indeed, we observed that RRM2 expression positively correlates with the expression of the cell proliferation marker Ki67 (Table 1). Consistently, RRM2 knockdown or activity inhibition using 3-AP in human EOC cells suppresses the proliferation of these cells by triggering cellular senescence (Fig. 4; Fig. S3). Together, these data indicate that the elevated levels of RRM2 observed in human EOC cells promote the proliferation of these cells by inhibiting the cellular senescence tumor-suppressing mechanism. Inducing cancer cells to undergo senescence has recently been described as a potential therapeutic strategy.<sup>21,22</sup> Indeed, recent studies from our lab and others have shown that induction of senescence pathways in tumor cells can cause tumor growth inhibition or regression.<sup>19,20,37</sup> The current study establishes that RRM2 is a potential target for developing pro-senescence therapy for EOC.

Here, we found that there was a significant increase in RRM2 expression in invasive EOCs compared with borderline ovarian tumors (Fig. 2B). Additionally, RRM2 expression increased with increasing tumor stage and grade (Fig. 2C and D) and in more invasive molecular subtypes (Fig. 2F), suggesting that RRM2 expression could delineate early vs. late-stage and aggressive tumors. Consistently, there was a significant inverse correlation between RRM2 expression and the overall survival of EOC patients (Fig. 2G). However, the association between RRM2 and overall survival is independent of tumor stage and grade (adjusted HR = 1.58, Cox  $P$  = 0.02). This indicates that RRM2 expression correlates with disease progression and could be used as a novel independent prognostic biomarker for EOC patients.

The p53 and pRB tumor-suppressor pathways are key senescence effectors.<sup>16,38,39</sup> Notably, p53 is null in both the OVCAR5

and SKOV3 cell lines and is mutated in the PEO1 cell line.<sup>37,40</sup> In addition, p16 is deleted in all 3 EOC cell lines used.<sup>41</sup> As knockdown of RRM2 in these cells was able to induce senescence (Fig. 4; Fig. S3), it must be independent of both p53 and p16. This indicates that human cancer cells that lack functional p53 and p16 retain the capacity to undergo senescence through suppressing RRM2. These data suggest that RRM2 is a bona fide target for driving EOC cells to undergo senescence. Several drugs, such as hydroxyurea, gemcitabine, and triapine, are thought to inhibit RRM2 activity; however, none of them is specific, which results in adverse side effects.<sup>9</sup> Indeed, nonspecific toxicities associated with these drugs hamper their clinical applications. Therefore, more specific RRM2 inhibitors will need to be tested to determine whether specific RRM2 inhibition is sufficient to drive the senescence of EOC cells.

Interestingly, an increase in DNA damage was observed in human EOC cells with RRM2 knockdown (Fig. 4; Fig. S3) or treated with the RRM2 inhibitor 3-AP (Fig. S3J–L). This phenotype was rescued by addition of exogenous nucleosides (Fig. 4H–J), supporting the notion that RRM2 regulates senescence through its role in dNTP biosynthesis. This suggests that senescence induced by RRM2 knockdown is mediated by the DNA damage response, one of the hallmarks of senescence and a known inducer of senescence.<sup>16,22,42</sup> These results are consistent with previous reports from our lab and others.<sup>23-26</sup> Cisplatin, which is the primary front-line chemotherapy used for EOC,<sup>5</sup> also induces DNA damage.<sup>43</sup> Therefore, it is interesting to speculate whether there might be synergism between RRM2 inhibition and cisplatin treatment to increase the DNA damage to a threshold beyond which senescence would occur. This may lead to the conversion of transient growth arrest induced by a low dose of cisplatin to a stable senescence-associated cell growth, which may have less side effects and a better clinical outcome.<sup>22</sup> Furthermore, in patients with BRCA1 or BRCA2 mutations, poly ADP ribose polymerase (PARP) inhibitors have shown promise due to synthetic lethality after DNA damage.<sup>44</sup> It will be interesting to test whether RRM2 inhibition in combination with PARP inhibitors could lead to synthetic lethality in cells with mutated BRCA1/BRCA2.

In conclusion, the present study showed that RRM2 is often upregulated in EOC, and high RRM2 expression independently predicts poor prognosis for EOC patients. We also found that suppressing RRM2 activity leads to growth inhibition through a cellular senescence mechanism via the DNA damage response. Together, our data suggest that inhibition of RRM2 to induce senescence of human EOC cells is a potential novel EOC therapeutic strategy.

## Materials and Methods

### Cells and culture conditions

Primary human ovarian surface epithelial (HOSE) cells were isolated and cultured as described previously.<sup>45</sup> Human EOC cell lines were cultured in RPMI-1640 medium supplemented with 10% FBS according to ATCC and as previously described.<sup>45</sup> Nucleosides were purchased from Sigma-Aldrich and used at a

concentration of 250 nM. 3-AP (Sigma) was used at a concentration of 1  $\mu$ M.

#### Human ovarian specimens and immunohistochemistry

The protocol to evaluate de-identified human tissue specimens was approved by the institutional review board. Ovarian tumor microarray and normal human ovary and fallopian tube specimens were obtained from the Fox Chase Cancer Center Biosample Repository Core Facility (BRCCF). Histopathology of the selected specimens was provided by BRCCF. Immunohistochemistry (IHC) was conducted by using goat anti-RRM2 polyclonal antibody (Santa Cruz Biotechnology) and mouse anti-Ki67 (Dako) with a Dako EnVision System and the Peroxidase (DAB) kit following the manufacturer's instructions and as previously described.<sup>17</sup> The RRM2 blocking peptide used to raise the anti-RRM2 antibody was purchased from Santa Cruz Biotechnologies and used undiluted to block the binding of the antibody.

#### Plasmids and antibodies

pLKO.1-shRRM2 plasmids were obtained from Open Biosystems (Waltham, MA). The following antibodies were obtained from the indicated suppliers: goat anti-RRM2 (Santa Cruz Biotechnology), mouse anti- $\gamma$ H2AX (Millipore), rabbit anti-53BP1 (Bethyl), mouse anti-BrdU FITC (BD Biosciences), rabbit anti-PARP p85 fragment (Promega), rabbit anti-cleaved caspase 3 (Cell Signaling), and mouse anti- $\beta$ -actin (Sigma-Aldrich).

#### Lentivirus infections

Lentivirus was packaged using the Virapower Kit from Invitrogen following the manufacturer's instructions as described previously.<sup>45-47</sup> Cells infected with viruses encoding the puromycin-resistance gene were selected in 1  $\mu$ g/ml puromycin.

#### Immunofluorescence, BrdU labeling, and SA- $\beta$ -gal staining

Immunofluorescence staining and BrdU labeling for cultured cells was performed as described previously using antibodies described above.<sup>47-50</sup> SA- $\beta$ -Gal staining was performed as previously described.<sup>17</sup>

#### Colony formation assay, soft agar assay, and growth curve analysis

Growth curves were generated by plating an equal amount of cells (20 000 cells/well) and counting the cell number at the indicated time points. For colony formation, equal number of cells (3000 cells/well) was inoculated in 6-well plates and cultured for additional 2 wk. The colony formation was visualized by staining

the plates with 0.05% crystal violet as previously described.<sup>47</sup> Soft agar assays were performed as previously described.<sup>45</sup>

#### Data sets and statistical analysis

Raw gene expression data (Affymetrix CEL files) were retrieved from 2 previously reported clinically annotated microarray data sets<sup>31,32</sup> from different institutions (University of Michigan<sup>31</sup> and Peter MacCallum Cancer Center in Australia<sup>32</sup>). Both data sets are publicly available in Gene Expression Omnibus (GSE6008 and GSE9891, respectively) and were profiled on Affymetrix HG\_U133A arrays (University of Michigan) and Affymetrix Human Genome U133 Plus 2.0 Array. Raw data were imported in BRB-ArrayTools Version: 4.2.0 (Biometrics Research Branch, National Cancer Institute) and were processed using Robust Multi-Array (RMA) analysis. The first data set included 99 individual epithelial ovarian tumors (37 endometrioid, 41 serous, 13 mucinous, and 8 clear cell carcinomas) and 4 individual normal ovary samples. The second data set included 285 epithelial ovarian cancers (18 borderline tumors and 267 invasive tumors) of various grades and stages.

Comparison of RRM2 expression levels between different classes (i.e., grades, histologies, stages, etc.) was performed using the class Comparison Between Groups of Arrays Tool of BRB-ArrayTools. Parametric *t* test or *F* test *P* values were reported for 2 or more classes, respectively. Overall survival curves were generated by the Kaplan–Meier method, and differences between survival curves were assessed for statistical significance with the log-rank test. SPSS (version 16; SPSS Inc) package was used for the survival analysis. The *P* values of all statistical tests were 2-sided.

#### Disclosure of Potential Conflicts of Interest

No potential conflicts of interest were disclosed.

#### Grant Support

NIH/NCI grants (R01CA160331 and R01CA163377 to RZ), a DoD Ovarian Cancer Academy Award (OC093420 to RZ), and a NIH/NCI training grant (T32CA9171-35 to KMA). Support of Core Facilities used in this study was provided by Cancer Center Support Grant (CCSG) CA010815 to The Wistar Institute.

#### Supplemental Materials

Supplemental materials may be found here:  
[www.landesbioscience.com/journals/cc/article/26953](http://www.landesbioscience.com/journals/cc/article/26953)

#### References

1. Siegel R, Naishadham D, Jemal A. Cancer statistics, 2013. *CA Cancer J Clin* 2013; 63:11-30; PMID:23335087; <http://dx.doi.org/10.3322/caac.21166>
2. Arulkumaran S, Regan L, Farquharson DIM. *Obstetrics and gynaecology*. Oxford: Oxford University Press, 2011
3. Farley J, Ozbun LL, Birrer MJ. Genomic analysis of epithelial ovarian cancer. *Cell Res* 2008; 18:538-48; PMID:18427574; <http://dx.doi.org/10.1038/cr.2008.52>
4. Shih IM, Kurman RJ. Ovarian tumorigenesis: a proposed model based on morphological and molecular genetic analysis. *Am J Pathol* 2004; 164:1511-8; PMID:15111296; [http://dx.doi.org/10.1016/S0002-9440\(10\)63708-X](http://dx.doi.org/10.1016/S0002-9440(10)63708-X)
5. Vaughan S, Coward JI, Bast RC Jr., Berchuck A, Berek JS, Brenton JD, Coukos G, Crum CC, Drapkin R, Etemadmoghadam D, et al. Rethinking ovarian cancer: recommendations for improving outcomes. *Nat Rev Cancer* 2011; 11:719-25; PMID:21941283; <http://dx.doi.org/10.1038/nrc3144>
6. Nordlund P, Reichard P. Ribonucleotide reductases. *Annu Rev Biochem* 2006; 75:681-706; PMID:16756507; <http://dx.doi.org/10.1146/annurev.biochem.75.103004.142443>
7. Engström Y, Eriksson S, Jildevik I, Skog S, Thelander L, Tribukait B. Cell cycle-dependent expression of mammalian ribonucleotide reductase. Differential regulation of the two subunits. *J Biol Chem* 1985; 260:9114-6; PMID:3894352
8. Furuta E, Okuda H, Kobayashi A, Watabe K. Metabolic genes in cancer: their roles in tumor progression and clinical implications. *Biochim Biophys Acta* 2010; 1805:141-52; PMID:20122995
9. Shao J, Zhou B, Chu B, Yen Y. Ribonucleotide reductase inhibitors and future drug design. *Curr Cancer Drug Targets* 2006; 6:409-31; PMID:16918309; <http://dx.doi.org/10.2174/15680090677723949>



10. Lin ZP, Belcourt MF, Cory JG, Sartorelli AC. Stable suppression of the R2 subunit of ribonucleotide reductase by R2-targeted short interference RNA sensitizes p53(-/-) HCT-116 colon cancer cells to DNA-damaging agents and ribonucleotide reductase inhibitors. *J Biol Chem* 2004; 279:27030-8; PMID:15096505; <http://dx.doi.org/10.1074/jbc.M402056200>
11. Liu X, Zhang H, Lai L, Wang X, Loera S, Xue L, He H, Zhang K, Hu S, Huang Y, et al. Ribonucleotide reductase small subunit M2 serves as a prognostic biomarker and predicts poor survival of colorectal cancers. *Clin Sci (Lond)* 2013; 124:567-78; PMID:23113760; <http://dx.doi.org/10.1042/CS20120240>
12. Fujita H, Ohuchida K, Mizumoto K, Itaba S, Ito T, Nakata K, Yu J, Kayashima T, Souzaki R, Tajiri T, et al. Gene expression levels as predictive markers of outcome in pancreatic cancer after gemcitabine-based adjuvant chemotherapy. *Neoplasia* 2010; 12:807-17; PMID:20927319
13. Jones DT, Lechertier T, Mitter R, Herbert JM, Bicknell R, Jones JL, Li JL, Buffa F, Harris AL, Hodiava-Dilke K. Gene expression analysis in human breast cancer associated blood vessels. *PLoS One* 2012; 7:e44294; PMID:23056178; <http://dx.doi.org/10.1371/journal.pone.0044294>
14. Wadler S, Makower D, Clairmont C, Lambert P, Fehn K, Szoln M. Phase I and pharmacokinetic study of the ribonucleotide reductase inhibitor, 3-aminopyridine-2-carboxaldehyde thiosemicarbazone, administered by 96-hour intravenous continuous infusion. *J Clin Oncol* 2004; 22:1553-63; PMID:15119798; <http://dx.doi.org/10.1200/JCO.2004.07.158>
15. Chao J, Synold TW, Morgan RJ Jr., Kunos C, Longmate J, Lenz HJ, Lim D, Shibata S, Chung V, Stoller RG, et al. A phase I and pharmacokinetic study of oral 3-aminopyridine-2-carboxaldehyde thiosemicarbazone (3-AP, NSC #663249) in the treatment of advanced-stage solid cancers: a California Cancer Consortium Study. *Cancer Chemother Pharmacol* 2012; 69:835-43; PMID:22105720; <http://dx.doi.org/10.1007/s00280-011-1779-5>
16. Campisi J, d'Adda di Fagagna F. Cellular senescence: when bad things happen to good cells. *Nat Rev Mol Cell Biol* 2007; 8:729-40; PMID:17667954; <http://dx.doi.org/10.1038/nrm2233>
17. Dimri GP, Lee X, Basile G, Acosta M, Scott G, Roskelley C, Medrano EE, Linskens M, Rubelj I, Pereira-Smith O, et al. A biomarker that identifies senescent human cells in culture and in aging skin in vivo. *Proc Natl Acad Sci U S A* 1995; 92:9363-7; PMID:7568133; <http://dx.doi.org/10.1073/pnas.92.20.9363>
18. Alimonti A, Nardella C, Chen Z, Clohessy JG, Carracedo A, Trotman LC, Cheng K, Varmeh S, Kozma SC, Thomas G, et al. A novel type of cellular senescence that can be enhanced in mouse models and human tumor xenografts to suppress prostate tumorigenesis. *J Clin Invest* 2010; 120:681-93; PMID:20197621; <http://dx.doi.org/10.1172/JCI40535>
19. Ventura A, Kirsch DG, McLaughlin ME, Tuveson DA, Grimm J, Lintault L, Newman J, Reczek EE, Weissleder R, Jacks T. Restoration of p53 function leads to tumour regression in vivo. *Nature* 2007; 445:661-5; PMID:17251932; <http://dx.doi.org/10.1038/nature05541>
20. Xue W, Zender L, Miething C, Dickens RA, Hernandez E, Krizhanovsky V, Cordon-Cardo C, Lowe SW. Senescence and tumour clearance is triggered by p53 restoration in murine liver carcinomas. *Nature* 2007; 445:656-60; PMID:17251933; <http://dx.doi.org/10.1038/nature05529>
21. Nardella C, Clohessy JG, Alimonti A, Pandolfi PP. Pro-senescence therapy for cancer treatment. *Nat Rev Cancer* 2011; 11:503-11; PMID:21701512; <http://dx.doi.org/10.1038/nrc3057>
22. Ewald JA, Desotelle JA, Wilding G, Jarrard DF. Therapy-induced senescence in cancer. *J Natl Cancer Inst* 2010; 102:1536-46; PMID:20858887; <http://dx.doi.org/10.1093/jnci/djq364>
23. Aird KM, Zhang G, Li H, Tu Z, Bitler BG, Garipov A, et al. Suppression of Nucleotide Metabolism Underlies the Establishment and Maintenance of Oncogene-Induced Senescence. *Cell Rep* 2013.
24. Mannava S, Moparthy KC, Wheeler LJ, Leonova KI, Wawrzyniak JA, Bianchi-Smiraglia A, Berman AE, Flanagan S, Shewach DS, Zeitouni NC, et al. Ribonucleotide reductase and thymidylate synthase or exogenous deoxyribonucleosides reduce DNA damage and senescence caused by C-MYC depletion. *Aging (Albany NY)* 2012; 4:917-22; PMID:23249808
25. Mannava S, Moparthy KC, Wheeler LJ, Natarajan V, Zucker SN, Fink EE, Im M, Flanagan S, Burhans WC, Zeitouni NC, et al. Depletion of deoxyribonucleotide pools is an endogenous source of DNA damage in cells undergoing oncogene-induced senescence. *Am J Pathol* 2013; 182:142-51; PMID:23245831; <http://dx.doi.org/10.1016/j.ajpath.2012.09.011>
26. Darzynkiewicz Z. Perturbation of nucleotide metabolism--the driving force of oncogene-induced senescence. *Oncotarget* 2013; 4:649-50; PMID:23660114
27. Kurman RJ, Shih IeM. The origin and pathogenesis of epithelial ovarian cancer: a proposed unifying theory. *Am J Surg Pathol* 2010; 34:433-43; PMID:20154587; <http://dx.doi.org/10.1097/PAS.0b013e3181cf3d79>
28. Levanon K, Crum C, Drapkin R. New insights into the pathogenesis of serous ovarian cancer and its clinical impact. *J Clin Oncol* 2008; 26:5284-93; PMID:18854563; <http://dx.doi.org/10.1200/JCO.2008.18.1107>
29. McCarty KS Jr., Szabo E, Flowers JL, Cox EB, Leight GS, Miller L, Konrath J, Soper JT, Budwit DA, Creasman WT, et al. Use of a monoclonal anti-estrogen receptor antibody in the immunohistochemical evaluation of human tumors. *Cancer Res* 1986; 46(Suppl):4244s-8s; PMID:3524805
30. McCarty KS Jr., Miller LS, Cox EB, Konrath J, McCarty KS Sr. Estrogen receptor analyses. Correlation of biochemical and immunohistochemical methods using monoclonal anti-receptor antibodies. *Arch Pathol Lab Med* 1985; 109:716-21; PMID:3893381
31. Hendrix ND, Wu R, Kuick R, Schwartz DR, Fearon ER, Cho KR. Fibroblast growth factor 9 has oncogenic activity and is a downstream target of Wnt signaling in ovarian endometrioid adenocarcinomas. *Cancer Res* 2006; 66:1354-62; PMID:16452189; <http://dx.doi.org/10.1158/0008-5472.CAN-05-3694>
32. Tothill RW, Tinker AV, George J, Brown R, Fox SB, Lade S, Johnson DS, Trivett MK, Etemadmoghadam D, Locandro B, et al. Australian Ovarian Cancer Study Group. Novel molecular subtypes of serous and endometrioid ovarian cancer linked to clinical outcome. *Clin Cancer Res* 2008; 14:5198-208; PMID:18698038; <http://dx.doi.org/10.1158/1078-0432.CCR-08-0196>
33. Cory JG, Cory AH, Rappa G, Lorico A, Liu MC, Lin TS, Sartorelli AC. Inhibitors of ribonucleotide reductase. Comparative effects of amino- and hydroxy-substituted pyridine-2-carboxaldehyde thiosemicarbazones. *Biochem Pharmacol* 1994; 48:335-44; PMID:8053929; [http://dx.doi.org/10.1016/0006-2952\(94\)90105-8](http://dx.doi.org/10.1016/0006-2952(94)90105-8)
34. Finch RA, Liu MC, Cory AH, Cory JG, Sartorelli AC. Triapine (3-aminopyridine-2-carboxaldehyde thiosemicarbazone; 3-AP): an inhibitor of ribonucleotide reductase with antineoplastic activity. *Adv Enzyme Regul* 1999; 39:3-12; PMID:10470363; [http://dx.doi.org/10.1016/S0065-2571\(98\)00017-X](http://dx.doi.org/10.1016/S0065-2571(98)00017-X)
35. Wang LM, Lu FF, Zhang SY, Yao RY, Xing XM, Wei ZM. Overexpression of catalytic subunit M2 in patients with ovarian cancer. *Chin Med J (Engl)* 2012; 125:2151-6; PMID:22884145
36. Zhang M, Wang J, Yao R, Wang L. Small interfering RNA (siRNA)-mediated silencing of the M2 subunit of ribonucleotide reductase: a novel therapeutic strategy in ovarian cancer. *Int J Gynecol Cancer* 2013; 23:659-66; PMID:23466567; <http://dx.doi.org/10.1097/IGC.0b013e318287e2b3>
37. Bitler BG, Nicodemus JP, Li H, Cai Q, Wu H, Hua X, Li T, Birrer MJ, Godwin AK, Cairns P, et al. Wnt5a suppresses epithelial ovarian cancer by promoting cellular senescence. *Cancer Res* 2011; 71:6184-94; PMID:21816908; <http://dx.doi.org/10.1158/0008-5472.CAN-11-1341>
38. Courtis-Cox S, Jones SL, Cichowski K. Many roads lead to oncogene-induced senescence. *Oncogene* 2008; 27:2801-9; PMID:18193093; <http://dx.doi.org/10.1038/sj.onc.1210950>
39. Kuilman T, Michaloglou C, Mooi WJ, Peeper DS. The essence of senescence. *Genes Dev* 2010; 24:2463-79; PMID:21078816; <http://dx.doi.org/10.1101/gad.1971610>
40. Yaginuma Y, Westphal H. Abnormal structure and expression of the p53 gene in human ovarian carcinoma cell lines. *Cancer Res* 1992; 52:4196-9; PMID:1638534
41. Watson JE, Gabra H, Taylor KJ, Rabiasz GJ, Morrison H, Perry P, Smyth JE, Porteous DJ. Identification and characterization of a homozygous deletion found in ovarian ascites by representational difference analysis. *Genome Res* 1999; 9:226-33; PMID:10077528
42. Halicka HD, Zhao H, Li J, Lee YS, Hsieh TC, Wu JM, Darzynkiewicz Z. Potential anti-aging agents suppress the level of constitutive mTOR- and DNA damage- signaling. *Aging (Albany NY)* 2012; 4:952-65; PMID:23363784
43. Siddik ZH. Cisplatin: mode of cytotoxic action and molecular basis of resistance. *Oncogene* 2003; 22:7265-79; PMID:14576837; <http://dx.doi.org/10.1038/sj.onc.1206933>
44. Banerjee S, Kaye SB, Ashworth A. Making the best of PARP inhibitors in ovarian cancer. *Nat Rev Clin Oncol* 2010; 7:508-19; PMID:20700108; <http://dx.doi.org/10.1038/nrclinonc.2010.116>
45. Li H, Cai Q, Godwin AK, Zhang R. Enhancer of zeste homolog 2 promotes the proliferation and invasion of epithelial ovarian cancer cells. *Mol Cancer Res* 2010; 8:1610-8; PMID:21115743; <http://dx.doi.org/10.1158/1541-7786.MCR-10-0398>
46. Ye X, Zerlanko B, Kennedy A, Banumathy G, Zhang R, Adams PD. Downregulation of Wnt signaling is a trigger for formation of facultative heterochromatin and onset of cell senescence in primary human cells. *Mol Cell Biol* 2007; 27:183-96; PMID:17643369; <http://dx.doi.org/10.1016/j.molcel.2007.05.034>
47. Wainstock DH. A decade of Developmental Cell. *Dev Cell* 2011; 21:1; PMID:21763596; <http://dx.doi.org/10.1016/j.devcel.2011.07.002>
48. Zhang R, Pousovoitov MV, Ye X, Santos HA, Chen W, Daganzo SM, Erzberger JP, Serebriiskii IG, Canutescu AA, Dunbrack RL, et al. Formation of MacroH2A-containing senescence-associated heterochromatin foci and senescence driven by ASF1a and HIRA. *Dev Cell* 2005; 8:19-30; PMID:15621527; <http://dx.doi.org/10.1016/j.devcel.2004.10.019>
49. Zhang R, Chen W, Adams PD. Molecular dissection of formation of senescence-associated heterochromatin foci. *Mol Cell Biol* 2007; 27:2343-58; PMID:17242207; <http://dx.doi.org/10.1128/MCB.02019-06>
50. Zhang R, Liu ST, Chen W, Bonner M, Pehrson J, Yen TJ, Adams PD. HP1 proteins are essential for a dynamic nuclear response that rescues the function of perturbed heterochromatin in primary human cells. *Mol Cell Biol* 2007; 27:949-62; PMID:17101789; <http://dx.doi.org/10.1128/MCB.01639-06>

# Chromatin remodeling, BRCA1, SAHF and cellular senescence

Zhigang Tu, Katherine M. Aird and Rugang Zhang\*

Gene Expression and Regulation Program; The Wistar Institute; Philadelphia, PA USA

Cellular senescence is a state of stable cell growth arrest. Activation of oncogenes in primary mammalian cells typically triggers cellular senescence. Oncogene-induced senescence is an important tumor suppression mechanism, driving stable growth arrest of cancer progenitor cells harboring the initial oncogenic hit. Chromatin in the nuclei of senescent human cells is often reorganized to form specialized domains of facultative heterochromatin, known as senescence-associated heterochromatin foci (SAHF).<sup>1</sup> SAHF contribute to senescence-associated cell growth arrest by sequestering and silencing proliferation-promoting genes such as the E2F target gene cyclin A.<sup>1</sup> Notably, SAHF are different from constitutive heterochromatin, such as pericentromeres, which are largely excluded from SAHF.<sup>1</sup>

BRCA1 has been implicated in regulating chromatin structure. For example, oncogene-induced BRCA1 chromatin dissociation is known to regulate SAHF formation during senescence.<sup>2</sup> Consistently, it has been demonstrated that BRCA1 causes large-scale chromatin de-condensation.<sup>3</sup> In contrast, BRCA1 is implicated in regulating pericentromeric heterochromatin by silencing the repetitive satellite transcripts through ubiquitination of histone H2A.<sup>4</sup> This suggests that BRCA1 may function to antagonize or promote heterochromatin formation in a genomic locus-specific manner.

BRCA1 interacts with BRG1 in transformed cells. BRG1 is the catalytic subunit of the SWI/SNF chromatin-remodeling complex. BRG1 is known to regulate heterochromatin structure. For example, similar to the effects of BRCA1 loss on pericentromeres, it has been previously

demonstrated that BRG1 deletion results in dissolution of pericentromeric heterochromatin.<sup>5</sup> These findings support the notion that the BRCA1 and BRG1 complex is critical for constitutive heterochromatin structure at pericentromeres. It will be interesting to investigate whether the BRCA1 and BRG1 complex remains at pericentromeres to maintain the silencing of the satellite repeats in senescent cells.

Activation of oncogenes such as RAS dissociates BRCA1 from chromatin.<sup>2</sup> Interestingly, the interaction between BRCA1 and BRG1 is disrupted in cells undergoing senescence.<sup>6</sup> This correlates with an increase in the level of BRG1 in the chromatin fraction.<sup>6</sup> Indeed, ectopic BRG1 is sufficient to drive SAHF formation. Further, BRCA1 chromatin dissociation and the disruption of the interaction between BRCA1 and BRG1 correlate with SAHF formation during senescence.<sup>6</sup> This suggests that BRCA1 antagonizes SAHF formation in the euchromatic genomic loci that encode for proliferation-promoting genes by sequestering BRG1 away from chromatin. Consequently, dissociation of BRCA1 from chromatin silences the expression of these genes through SAHF formation by BRG1. In addition, we discovered that the association of BRG1 with the promoters of the p21- and p16-encoding genes are enhanced during senescence.<sup>6</sup> However, there is no detectable change in BRCA1's association with the promoters of these genes.<sup>6</sup> These findings suggest that BRG1 promotes or silences the expression of its target genes in a context-dependent manner during senescence. Further studies using global profiling of the changes in the distribution of BRG1 and BRCA1 by chromatin immunoprecipitation followed by next

generation sequencing (ChIP-seq) in young and senescent cells will ultimately test these possibilities.

As discussed above, BRG1's association with the promoters of the p16- and p21-encoding genes are enhanced in senescent cells.<sup>6</sup> Upregulation of p16 and p21 by BRG1 depends upon its chromatin remodeling activity.<sup>6</sup> For example, a mutant BRG1 that is defective in its chromatin remodeling activity fails to upregulate p16 and p21 and is also impaired in SAHF formation.<sup>6</sup> This suggests that BRG1 may drive SAHF formation directly via its chromatin remodeling activity and/or indirectly through upregulating p16 and p21 expression.

BRG1 has been shown to interact with pRB,<sup>7</sup> a key regulator of SAHF formation.<sup>1</sup> Interestingly, the interaction between BRG1 and pRB is enhanced during senescence.<sup>6</sup> This correlates with an increased level of BRG1 in the chromatin fraction of senescent cells.<sup>6</sup> A similar increase in BRG1 in the chromatin fraction of senescent cells was also observed using non-biased proteomic analysis of young and senescent cells.<sup>8</sup> Consistent with the idea that the enhanced BRG1 and pRB complex drives SAHF formation, BRG1 overexpression drives SAHF formation, and its knockdown suppresses SAHF formation induced by oncogenic RAS or BRCA1 knockdown.<sup>6</sup> Significantly, BRG1's interaction with pRB is necessary for its ability to drive SAHF formation. For example, a mutant BRG1 that can no longer bind to pRB also fails to induce SAHF formation.<sup>6</sup> Interestingly, the mutant BRG1 remains capable of upregulating p16 and p21.<sup>6</sup> This finding suggests that the interaction between BRG1 and pRB is necessary for

\*Correspondence to: Rugang Zhang; Email: rzhang@wistar.org

Submitted: 04/02/13; Accepted: 04/17/13

<http://dx.doi.org/10.4161/cc.24986>

Comment on: Tu Z, et al. Mol Cell Biol 2013; 33:1819-29; PMID:23438604; <http://dx.doi.org/10.1128/MCB.01744-12>

SAHF formation and likely for silencing proliferation-promoting genes through SAHF formation. However, this interaction is dispensable for upregulating p16 and p21 by BRG1, which depends upon its chromatin remodeling activity.<sup>6</sup>

Oncogene-induced BRCA1 chromatin dissociation contributes to the accumulation of DNA damage in senescent cells due to impaired BRCA1-mediated DNA repair.<sup>2</sup> Interestingly, senescence and SAHF formation induced by ectopic BRG1 is independent of the DDR.<sup>6</sup> These findings suggest that BRG1 and the DDR function independently of each other downstream of BRCA1 chromatin dissociation to promote SAHF formation and senescence.

In summary, BRCA1 chromatin dissociation increases the level of BRG1 in the chromatin fraction of senescent cells. This correlates with an enhanced BRG1 and pRB interaction that drives SAHF formation by silencing proliferation-promoting genes, while upregulating p16 and p21 senescence-promoting factors via BRG1's chromatin remodeling activity in a pRB-independent manner.

#### References

1. Narita M, et al. *Cell* 2003; 113:703-16; PMID:12809602; [http://dx.doi.org/10.1016/S0092-8674\(03\)00401-X](http://dx.doi.org/10.1016/S0092-8674(03)00401-X)
2. Tu Z, et al. *Dev Cell* 2011; 21:1077-91; PMID:22137763; <http://dx.doi.org/10.1016/j.devcel.2011.10.010>
3. Ye Q, et al. *J Cell Biol* 2001; 155:911-21; PMID:11739404; <http://dx.doi.org/10.1083/jcb.200108049>
4. Zhu Q, et al. *Nature* 2011; 477:179-84; PMID:21901007; <http://dx.doi.org/10.1038/nature10371>
5. Bourgo RJ, et al. *Mol Biol Cell* 2009; 20:3192-9; PMID:19458193; <http://dx.doi.org/10.1091/mbc.E08-12-1224>
6. Tu Z, et al. *Mol Cell Biol* 2013; 33:1819-29; PMID:23438604; <http://dx.doi.org/10.1128/MCB.01744-12>
7. Dunaief JL, et al. *Cell* 1994; 79:119-30; PMID:7923370; [http://dx.doi.org/10.1016/0092-8674\(94\)90405-7](http://dx.doi.org/10.1016/0092-8674(94)90405-7)
8. Chicas A, et al. *Proc Natl Acad Sci USA* 2012; 109:8971-6; PMID:22615382; <http://dx.doi.org/10.1073/pnas.1119836109>



# Role of EZH2 in epithelial ovarian cancer: from biological insights to therapeutic target

Hua Li and Rugang Zhang\*

Gene Expression and Regulation Program, The Wistar Institute, Philadelphia, PA, USA

## Edited by:

Angeles Alvarez Secord, Duke University Medical Center, USA

## Reviewed by:

le-Ming Shih, Johns Hopkins Medical Institutions, USA

Reuven Reich, Hebrew University of Jerusalem, Israel

## \*Correspondence:

Rugang Zhang, Gene Expression and Regulation Program, The Wistar Institute, 3601 Spruce Street, Philadelphia, PA 19104, USA.  
e-mail: rzhang@wistar.org

EZH2 is the catalytic subunit of polycomb repressive complex 2 (PRC2), which generates a methylation epigenetic mark at lysine 27 residue of histone H3 (H3K27me3) to silence gene expression. EZH2 target genes are involved in a variety of biological processes such as stem cell pluripotency, cell proliferation, and oncogenic transformation. EZH2 is often over-expressed in epithelial ovarian cancer (EOC) cells and in ovarian cancer-associated stromal endothelial cells. Notably, EZH2 promotes cell proliferation, inhibits apoptosis and enhances angiogenesis in EOCs. In contrast to genetic alterations, which are typically non-reversible, epigenetic alterations are reversible. Thus, inhibiting EZH2/PRC2 activity represents an attractive strategy for developing ovarian cancer therapeutics by targeting both ovarian cancer cells and ovarian tumor microenvironment. Here we discuss the progress recently obtained in understanding how EZH2/PRC2 promotes malignant phenotypes of EOC. In addition, we focus on strategies for targeting EZH2/PRC2 to develop novel EOC epigenetic therapeutics.

**Keywords:** epithelial ovarian cancer, EZH2, PRC2, EZH2 inhibitors, epigenetic therapeutics

Epithelial ovarian cancer (EOC) accounts for more death than any other gynecological malignancies in the developed world (American Cancer Society, 2012). Thus, there is an urgent need to understand the etiology and biology of the disease to develop new therapeutics. EZH2 catalyzes lysine 27 methylation on histone H3 to epigenetically silence the expression of its target genes (Bracken et al., 2006). EZH2 by itself is catalytically inactive and has to complex with other components of polycomb repressive complex 2 (PRC2) to exert its enzymatic activity (Cao and Zhang, 2004; Ketel et al., 2005). At minimum, it requires SUZ12 and EED subunits, while RbAp48 subunit can further boost the methyltransferase activity of EZH2 (Cao and Zhang, 2004). PRC2/EZH2 target genes are highly enriched for pathways that regulate stem cell pluripotency, cell proliferation, and oncogenic transformation (Kleer et al., 2003; Ting et al., 2006; Jones and Baylin, 2007; Schwartz and Pirrotta, 2007; Jaenisch and Young, 2008; Li et al., 2012a). Not surprisingly, components of PRC2 are often over-expressed in human cancers and their expression often positively correlates with aggressiveness in these diseases (Varambally et al., 2002; Kleer et al., 2003; Li et al., 2010, 2012b). In addition, gain-of-function mutations in EZH2 have also been reported in certain hematopoietic malignancies (Ryan et al., 2011; Majer et al., 2012). Notably, it has been shown that EZH2 and other components of PRC2 play a key role in regulating proliferation, apoptosis, and invasion of human EOC cells (Li et al., 2010, 2012b; Lu et al., 2010). In addition, EZH2 regulates EOC microenvironment by enhancing angiogenesis (Lu et al., 2010). Significantly, highly specific small molecule inhibitors of EZH2 methyltransferase activity have recently been developed (Knutson et al., 2012; McCabe et al., 2012b; Qi et al., 2012). Here we will discuss latest advances in understanding the biological function and regulation of EZH2/PRC2 in EOC as well as the therapeutic targeting EZH2/PCR2 in this devastating disease.

## EXPRESSION AND REGULATION OF EZH2/PRC2

EZH2, when presents in PRC2, can add up to three methyl groups to the lysine 27 of histone H3 (H3K27Me3) via its SET domain methyltransferase (Bracken et al., 2006). EZH2 is often over-expressed in human EOC cells compared with normal human ovarian surface epithelial cell (Li et al., 2010). In addition, there is recent evidence to suggest that a proportion of high-grade serous EOC may arise from distal fallopian tube epithelial cells (Levanon et al., 2008; Kurman and Shih, 2010; Kuhn et al., 2012). Notably, compared with normal fallopian tube epithelium, EZH2 is over-expressed in high-grade serous EOC (Li et al., 2012b). Likewise, other components of PRC2 such as SUZ12 are also over-expressed in EOC compared with either normal human ovarian surface epithelial cells or fallopian tube epithelial cells (Li et al., 2012b). Indeed, the expression of EZH2 and SUZ12 positively correlates with each other in human EOCs, further supporting the idea that EZH2 functions within PRC2 in EOC (Li et al., 2012b).

Interestingly, although EZH2 upregulation correlates with an increased level of H3K27Me3 in EOC cell lines (Li et al., 2010), there is evidence to suggest that EZH2 levels do not correlate with H3K27Me3 levels in primary EOC specimens (Wei et al., 2008). There are a number of possible reasons for this phenomenon. First, although the core subunits of PRC2 such as EZH2, SUZ12, and EED are over-expressed in EOC cells (Li et al., 2010, 2012b), the expression of other PRC2 associated proteins such as RbAp48 and AEBP2 can also affect the methyltransferase activity of EZH2 and/or the recruitment of PRC2 to its target genes (Cao and Zhang, 2004). For example, *in vitro* histone methyltransferase assay showed that addition of RbAp48 to EZH2–EED–SUZ12 complex or AEBP2 to the EZH2–EED–SUZ12–RbAp48 complex significantly increased the methyltransferase activity of PRC2 (Cao and Zhang, 2004). In addition, it was recently found



that polycomb-like (PCL) family proteins such as PHF19 play a critical role in the recruitment of PRC2/EZH2 to its target genes (Ballare et al., 2012). Biochemically, C-terminal end of PHF19 binds to SUZ12 in the context of an intact PRC2 (Ballare et al., 2012). Knockdown of PHF19 did not affect the stability of the PRC2 complex, but the association of PRC2 with the promoters of target genes was substantially reduced and, consequently, vast majority of target genes lost their H3K27Me3 epigenetic mark (Ballare et al., 2012). Likewise, JARID2 is also important for the recruitment of PRC2 to its target genes (Landeira et al., 2010). Together, these findings demonstrated that a stable association of PRC2 at target genes is required for its gene silencing function and PRC2 associated proteins play a key role in regulating the recruitment of PRC2 to its target genes. Another class of regulators of PRC2's genomic localization is non-coding RNAs such as HOTAIR (Tsai et al., 2010), XIST (Zhao et al., 2008), and intronic RNAs (Guil et al., 2012). They bind directly to PRC2 to regulate its association with target genes. Finally, histone demethylases such as UTX and JMJD3 can decrease the levels of H3K27Me3 (Agger et al., 2007) and loss of function mutations in UTX have been reported in human cancers (Gui et al., 2011; Jankowska et al., 2011). Thus, it will be interesting to examine the correlation between expression of core subunits of PRC2 and expression of PRC2 associated proteins, non-coding RNAs and histone demethylases in EOC.

In addition to over-expression, gain-of-function EZH2 mutations have been reported in hematopoietic malignancies (Ryan et al., 2011; Majer et al., 2012). The most common mutations occur within the SET domain that confers methyltransferase activity. For example, Y641 mutations have been identified in ~20% of germinal-center diffuse large B-cell lymphomas and in ~7% of follicular lymphomas (Bodor et al., 2011). Interestingly, these mutations are always heterozygous and the resulting cells also carries a wild type copy of EZH2 (Morin et al., 2010; Sneeringer et al., 2010). Mechanistically, the mutant EZH2 exhibits little to no activity for H3K27Me0 substrate and a decreased activity for H3K27Me1 substrate, while display significantly increased activity for H3K27Me2 substrate (Sneeringer et al., 2010). Consequently, the wild type EZH2 retained in these cells accounts for the generation of H3K27Me1 and H2K27Me2, which led to a global increase in H3K27Me3 by the mutant EZH2 in these tumor cells. Notably, A677 mutations in the EZH2's SET domain also occur in human lymphoma albeit at much lower rate compared with Y641, which exhibits an increased enzymatic activity independent of H3K27 methylation status (McCabe et al., 2012a). This led to a global increase in H3K27Me3 levels (McCabe et al., 2012a). Regardless, EZH2 mutation has not been reported in EOC and there is no evidence of EZH2 mutation in EOCs based on the newly released The Cancer Genome Atlas (TCGA) EOC database.

In response to intrinsic and extrinsic cues, EZH2 activity is regulated by post-translation modification such as phosphorylation. For example, T350 residue of EZH2 is subject to cyclin-dependent kinases (CDK) 1 and 2 during S and G2/M phases of the cell cycle, respectively (Chen et al., 2010). T350 phosphorylation enhances PRC2/EZH2-mediated gene silencing through increasing the recruitment of PRC2 to its target genes, while has no effect on PRC2 complex assembly or EZH2 enzymatic activity (Chen et al., 2010). Thus, this mechanism links intrinsic cell cycle

progression to EZH2 function. In addition, extracellular cues can also affect EZH2 function by signaling activated kinases such as AKT (Cha et al., 2005) and p38 (Palacios et al., 2010). S21 residue of EZH2 can be phosphorylated by AKT, which decreases histone methylation by PRC2 (Cha et al., 2005). Interestingly, recent evidence suggests that phosphorylation of EZH2 by AKT at S21 site leads to PRC2-independent association of EZH2 with androgen receptor and activation of its target genes in prostate cancer cells (Xu et al., 2012). Given that AKT is often hyperactive in EOC (Altomare et al., 2004), it is possible that AKT directly regulates EZH2 in a PRC2-independent manner to activate certain genes in EOC. In addition, in skeletal muscle stem cells, stress response kinase p38 alpha phosphorylates T372 residue of EZH2 in response to exposure to TNF inflammatory cytokine (Palacios et al., 2010). This leads to an enhanced repression of PRC2 target skeletal muscle stem cell marker to promote cell differentiation. Notably, the relevance of these post-translation phosphorylation modifications in EOC remains to be determined.

### ROLE OF EZH2/PRC2 IN EOC

Components of PRC2 are often over-expressed in human EOC cells and their expression positively correlates with markers of cell proliferation such as Ki67 (Li et al., 2010, 2012b). Significantly, higher levels of EZH2 (Lu et al., 2010) or SUZ12 (Li et al., 2012b) expression predict shorter overall survival in EOC patients. Indeed, knockdown of EZH2 (Li et al., 2010) or SUZ12 (Li et al., 2012b) suppresses the growth of human EOC cells *in vitro* and *in vivo* in both subcutaneous and orthotopic xenograft EOC models in immunocompromised mice. This is due to induction of programmed cell death or apoptosis (Li et al., 2010, 2012b). In addition, knockdown of EZH2 suppresses the invasion of human EOC cells (Li et al., 2010; Lu et al., 2010; Rao et al., 2010), which correlates with a decrease in transforming growth factor-beta 1 (TGF  $\beta$ 1) expression and an increase in E-cadherin expression (Rao et al., 2010). These observed phenotypes correlate with a decrease in the levels of H3K27Me3 in these cells (Rao et al., 2010). Together, these findings are consistent with the notion that EZH2/PRC2 promotes EOC by suppressing cell apoptosis (Li et al., 2010, 2012b) and increasing their invasion potential (Li et al., 2010; Rao et al., 2010) by silencing its target genes through H3K27Me3 epigenetic mark.

Notably, EZH2 expression is upregulated in ovarian cancer stem cell-like cells enriched by chemotherapy (Rizzo et al., 2011) and knockdown of EZH2 leads to loss of stem cell-like properties in these cells (Rizzo et al., 2011), such as anchorage-independent growth and tumor growth in xenograft mouse model. Similarly, it has been demonstrated that compared with cisplatin sensitive parental EOC cells, EZH2 expression is upregulated in *in vitro* derived cisplatin-resistant EOC cells (Hu et al., 2010). Conversely, knockdown of EZH2 re-sensitized drug-resistant ovarian cancer cells to cisplatin (Hu et al., 2010). Together, these reports support the idea that EZH2 may contribute to chemoresistance by regulating stem-like cell population in EOCs.

Interestingly, EZH2 is also over-expressed in EOC-associated endothelial cells due to a direct paracrine VEGF stimulation (Lu et al., 2010) and EZH2 promotes angiogenesis by silencing vasohibin1 (VASH1) (Lu et al., 2010). Consistently, EZH2 knockdown

in the EOC-associated endothelial cells inhibits angiogenesis and reduces EOC growth, which is further enhanced by EZH2 knockdown in EOC cells (Lu et al., 2010). Thus, EZH2 also contributes to malignant behaviors of EOC by altering EOC-associated tumor microenvironment through promoting angiogenesis. Notably, recent anti-angiogenesis clinical trials by targeting VEGF demonstrated potential benefit when added to standard chemotherapy in the first-line treatment of ovarian cancer (Burger et al., 2011; Perren et al., 2011). Together, these observations suggest that EZH2 is a potential target for designing new anti-angiogenesis therapy in EOC.

Genome-wide chromatin immunoprecipitation followed by deep sequencing analysis and gene expression profile reveal that the number of genes upregulated upon EZH2 knockdown is significantly lower than the number of genes whose genomic loci are directly occupied by EZH2/H3K27Me3 (Li et al., 2012a). This is consistent with the observation that histone deacetylase (Van der Vlag and Otte, 1999) and DNA methylation (Nakamura et al., 2008) also regulate the expression of EZH2 target genes. In addition to VASH1, the cellular networks enriched by EZH2 target genes in EOC cells include cell death, growth and proliferation and reproductive system development, and cancer (Li et al., 2012a). These findings further support EZH2's proliferation-promoting and apoptosis-suppressing function. Notably, HRK, a proapoptotic gene, is subjected to H3K27Me3 mediated gene silencing in EOC cells and HRK plays a key role in regulating apoptosis induced by suppressing H3K27Me3 (Li et al., 2012b). HRK is also subjected to DNA methylation (Nakamura et al., 2008) mediated gene silencing, further suggesting possible cooperation between H3K27Me3 and DNA methylation mediated gene silencing.

### THERAPEUTIC TARGETING EZH2/PRC2 IN EOC

In contrast to genetic changes that are non-reversible, epigenetic alterations are reversible. This feature makes epigenetic alterations in cancer an ideal target for developing cancer therapeutics (Dawson and Kouzarides, 2012). Significantly, EZH2 is over-expressed in both EOC cells and EOC-associated endothelial cells and its knockdown suppresses EOC growth (Li et al., 2010; Lu et al., 2010). These observed effects correlate with a decrease in levels of H3K27Me3, the enzymatic product of EZH2 methyltransferase (Li et al., 2010; Lu et al., 2010). Together, these findings strongly suggest that EZH2's methyltransferase activity is a potential target for developing urgently needed EOC therapeutics.

The first reported inhibitor of EZH2's methyltransferase activity is DZNep, an inhibitor of S-adenosylhomocysteine (SAH) hydrolase (Tan et al., 2007). However, DZNep indirectly inhibits EZH2 activity by causing the degradation of components of PRC2 through increasing the cellular levels of SAH, the inhibitory byproduct of methyltransferase reaction (Tan et al., 2007). In addition, DZNep is non-specific with major effects on a number of other histone methyl marks and, consequently, has been shown to be very toxic (Miranda et al., 2009). In contrast, a number of new specific EZH2 methyltransferase inhibitors have been reported very recently including most notably GSK126 (McCabe et al., 2012b) and EPZ005687 (Knutson et al., 2012) and EI1 (Qi et al., 2012). These inhibitors act in a S-adenosylmethionine (SAM)

competitive manner with no effects on expression of components of PRC2 or other histone methyl marks. This characteristic of the newly developed inhibitors allows to distinguish the EZH2's methyltransferase-dependent and -independent function. In a panel of B-cell lymphoma cell lines, EZH2 methyltransferase specific inhibitors are particularly sensitive in cells harboring mutations in Y641 or A677 residue (McCabe et al., 2012b). Interestingly, the cell line with A677 mutation appears to be most sensitive, which correlates with the fact that A677 mutant efficiently catalyzes all three steps of H3K27 methylation while Y641 mutant preferentially enhance the reaction from di- to trimethylation (McCabe et al., 2012a). In addition, it appears that loss-of-function mutation in H3K27Me3 demethylase UTX may also confer sensitivity to EZH2 inhibitors (McCabe et al., 2012b). However, gain-of-function mutation is not sufficient to predict response to EZH2 inhibitors because certain cell lines with EZH2 mutation are not sensitive to EZH2 inhibitors (McCabe et al., 2012b). Significantly, EZH2 inhibitor GSK126 eradicated the growth of xenografted B-cell lymphoma cells with EZH2 mutations (McCabe et al., 2012b). Despite the fact that EZH2 is essential during development and is known to regulate normal tissue stem cell properties, mice tolerated GSK126 very well with no apparent toxicity (McCabe et al., 2012b). Together, these findings suggest that EZH2 inhibitors such as GSK126 are potential novel epigenetic intervention reagents for B-cell lymphoma harboring gain-of-function EZH2 mutations.

EZH2 inhibitors are equally effective in decreasing H3K27Me3 in cancer cell lines with wild type EZH2 compared with those with gain-of-function EZH2 mutations (Knutson et al., 2012; McCabe et al., 2012b). However, cell lines with wild type EZH2 are typically much less sensitive to GSK126 (McCabe et al., 2012b). This observation suggests that methyltransferase-independent function of EZH2 also contributes to the malignant phenotypes observed in EZH2 over-expressing cancer cells. Notably, EZH2 is over-expressed but not mutated in EOC. In addition, inhibition of PRC2 by knockdown EZH2 (Li et al., 2010) or SUZ12 (Li et al., 2012b) is effective in inhibiting the growth of EOC cells with over-expressed components of PRC2. Therefore, it will be critical to evaluate the effectiveness of EZH2 inhibitors in preclinical models for their effects on EOC cell growth as well as EOC-associated angiogenesis. In addition to inhibiting EZH2's methyltransferase activity, targeting the PRC2 complex formation, or the associated factors that affect PRC2 genome-wide distribution may represent an alternative strategy for targeting PRC2 in EOCs. Further, given the evidence that EZH2 target genes may also subject to other epigenetic silencing mechanisms (Van der Vlag and Otte, 1999; Nakamura et al., 2008), it will be interesting to examine whether there are synergies between EZH2 inhibitors and inhibitors of other epigenetic silencers such as HDAC and DNA methyltransferase inhibitors. Finally, given its potential role in conferring chemotherapy resistance (Knutson et al., 2012; McCabe et al., 2012b; Qi et al., 2012), it will be interesting to determine whether EZH2 inhibitors re-sensitize chemo-resistant EOC cells.

### CONCLUSION AND PERSPECTIVE

In summary, EZH2 and other components of PRC2 are often over-expressed in EOC cells (Li et al., 2010, 2012b) and EOC-associated endothelial cells (Lu et al., 2010). EZH2/PRC2

promotes proliferation, suppresses apoptosis and increases invasion potential of EOC cells (Li et al., 2010), and enhances angiogenesis of EOC-associated endothelial cells (Lu et al., 2010). The expression pattern and functional importance of EZH2/PRC2 establish it as an exciting target for developing new EOC therapeutics. Thus, it will very interesting to test the newly developed EZH2 inhibitors in relevant preclinical *in vitro* and *in vivo* models. In addition to H3K27 residue, EZH2 can also methylate other proteins. For example, EZH2 methylates an orphan nuclear receptor ROR $\alpha$  (Lee et al., 2012). Further, EZH2/PRC2 may also have methyltransferase-independent function. Indeed, EZH2 is present in both cytoplasm and nuclei and cytoplasmic EZH2 has been shown to regulate actin polymerization and cell signaling (Su

et al., 2005). Accordingly, a further understanding the mechanisms by which EZH2/PRC2 promote EOC will provide scientific rationale for developing inhibitors of EZH2/PRC2 as novel EOC therapeutics.

## ACKNOWLEDGMENTS

This work was supported by the National Cancer Institute of the National Institutes of Health (R01CA163377 to Rugang Zhang) and, in part, by a DOD ovarian cancer academy award (OC093420 to Rugang Zhang). Support of Core Facilities used in this study was provided by Cancer Center Support Grant (CCSG) CA010815 to The Wistar Institute. We thank Dr. Benjamin G. Bitler for critical reading of the manuscript.

## REFERENCES

- Agger, K., Cloos, P. A., Christensen, J., Pasini, D., Rose, S., Rappsilber, J., et al. (2007). UTX and JMJD3 are histone H3K27 demethylases involved in HOX gene regulation and development. *Nature* 449, 731–734.
- Altomare, D. A., Wang, H. Q., Skele, K. L., De Rienzo, A., Klein-Szanto, A. J., Godwin, A. K., et al. (2004). AKT and mTOR phosphorylation is frequently detected in ovarian cancer and can be targeted to disrupt ovarian tumor cell growth. *Oncogene* 23, 5853–5857.
- American Cancer Society. (2012). *Cancer Facts & Figures 2012*. Atlanta: American Cancer Society.
- Ballare, C., Lange, M., Lapinaite, A., Martin, G. M., Morey, L., Pascual, G., et al. (2012). Phf19 links methylated Lys36 of histone H3 to regulation of Polycomb activity. *Nat. Struct. Mol. Biol.* 19, 1257–1265.
- Bodor, C., O'Riain, C., Wrench, D., Matthews, J., Iyengar, S., Tayyib, H., et al. (2011). EZH2 Y641 mutations in follicular lymphoma. *Leukemia* 25, 726–729.
- Bracken, A. P., Dietrich, N., Pasini, D., Hansen, K. H., and Helin, K. (2006). Genome-wide mapping of Polycomb target genes unravels their roles in cell fate transitions. *Genes Dev.* 20, 1123–1136.
- Burger, R. A., Brady, M. F., Bookman, M. A., Fleming, G. F., Monk, B. J., Huang, H., et al. (2011). Incorporation of bevacizumab in the primary treatment of ovarian cancer. *N. Engl. J. Med.* 365, 2473–2483.
- Cao, R., and Zhang, Y. (2004). SUZ12 is required for both the histone methyltransferase activity and the silencing function of the EED-EZH2 complex. *Mol. Cell* 15, 57–67.
- Cha, T. L., Zhou, B. P., Xia, W., Wu, Y., Yang, C. C., Chen, C. T., et al. (2005). Akt-mediated phosphorylation of EZH2 suppresses methylation of lysine 27 in histone H3. *Science* 310, 306–310.
- Chen, S., Bohrer, L. R., Rai, A. N., Pan, Y., Gan, L., Zhou, X., et al. (2010). Cyclin-dependent kinases regulate epigenetic gene silencing through phosphorylation of EZH2. *Nat. Cell Biol.* 12, 1108–1114.
- Dawson, M. A., and Kouzarides, T. (2012). Cancer epigenetics: from mechanism to therapy. *Cell* 150, 12–27.
- Gui, Y., Guo, G., Huang, Y., Hu, X., Tang, A., Gao, S., et al. (2011). Frequent mutations of chromatin remodeling genes in transitional cell carcinoma of the bladder. *Nat. Genet.* 43, 875–878.
- Guil, S., Soler, M., Portela, A., Carriere, J., Fonalleras, E., Gomez, A., et al. (2012). Intronic RNAs mediate EZH2 regulation of epigenetic targets. *Nat. Struct. Mol. Biol.* 19, 664–670.
- Hu, S., Yu, L., Li, Z., Shen, Y., Wang, J., Cai, J., et al. (2010). Overexpression of EZH2 contributes to acquired cisplatin resistance in ovarian cancer cells in vitro and in vivo. *Cancer Biol. Ther.* 10, 788–795.
- Jaenisch, R., and Young, R. (2008). Stem cells, the molecular circuitry of pluripotency and nuclear reprogramming. *Cell* 132, 567–582.
- Jankowska, A. M., Makishima, H., Tiu, R. V., Szpurka, H., Huang, Y., Traina, F., et al. (2011). Mutational spectrum analysis of chronic myelomonocytic leukemia includes genes associated with epigenetic regulation: UTX, EZH2, and DNMT3A. *Blood* 118, 3932–3941.
- Jones, P. A., and Baylin, S. B. (2007). The epigenomics of cancer. *Cell* 128, 683–692.
- Ketel, C. S., Andersen, E. F., Vargas, M. L., Suh, J., Strome, S., and Simon, J. A. (2005). Subunit contributions to histone methyltransferase activities of fly and worm polycomb group complexes. *Mol. Cell Biol.* 25, 6857–6868.
- Kleer, C. G., Cao, Q., Varambally, S., Shen, R., Ota, I., Tomlins, S. A., et al. (2003). EZH2 is a marker of aggressive breast cancer and promotes neoplastic transformation of breast epithelial cells. *Proc. Natl. Acad. Sci. U.S.A.* 100, 11606–11611.
- Knutson, S. K., Wigle, T. J., Warholic, N. M., Sneeringer, C. J., Allain, C. J., Klaus, C. R., et al. (2012). A selective inhibitor of EZH2 blocks H3K27 methylation and kills mutant lymphoma cells. *Nat. Chem. Biol.* 8, 890–896.
- Kuhn, E., Kurman, R. J., and Shih, I. M. (2012). Ovarian cancer is an imported disease: fact or fiction? *Curr. Obstet. Gynecol. Rep.* 1, 1–9.
- Kurman, R. J., and Shih, I. M. (2010). The origin and pathogenesis of epithelial ovarian cancer: a proposed unifying theory. *Am. J. Surg. Pathol.* 34, 433–443.
- Landeira, D., Sauer, S., Poot, R., Dvorkina, M., Mazzarella, L., Jorgensen, H. F., et al. (2010). Jarid2 is a PRC2 component in embryonic stem cells required for multi-lineage differentiation and recruitment of PRC1 and RNA Polymerase II to developmental regulators. *Nat. Cell Biol.* 12, 618–624.
- Lee, J. M., Lee, J. S., Kim, H., Kim, K., Park, H., Kim, J. Y., et al. (2012). EZH2 generates a methyl degron that is recognized by the DCAF1/DBB1/CUL4 E3 ubiquitin ligase complex. *Mol. Cell* 48, 572–586.
- Levanon, K., Crum, C., and Drapkin, R. (2008). New insights into the pathogenesis of serous ovarian cancer and its clinical impact. *J. Clin. Oncol.* 26, 5284–5293.
- Li, H., Bitler, B. G., Vathipadiekal, V., Maradeo, M. E., Slifker, M., Creasy, C. L., et al. (2012a). ALDH1A1 is a novel EZH2 target gene in epithelial ovarian cancer identified by genome-wide approaches. *Cancer Prev. Res. (Phila.)* 5, 484–491.
- Li, H., Cai, Q., Wu, H., Vathipadiekal, V., Dobbin, Z. C., Li, T., et al. (2012b). SUZ12 promotes human epithelial ovarian cancer by suppressing apoptosis via silencing HRK. *Mol. Cancer Res.* 10, 1462–1472.
- Li, H., Cai, Q., Godwin, A. K., and Zhang, R. (2010). Enhancer of zeste homolog 2 promotes the proliferation and invasion of epithelial ovarian cancer cells. *Mol. Cancer Res.* 8, 1610–1618.
- Lu, C., Han, H. D., Mangala, L. S., Ali-Fehmi, R., Newton, C. S., Ozburn, L., et al. (2010). Regulation of tumor angiogenesis by EZH2. *Cancer Cell* 18, 185–197.
- Majer, C. R., Jin, L., Scott, M. P., Knutson, S. K., Kuntz, K. W., Keilhack, H., et al. (2012). A687V EZH2 is a gain-of-function mutation found in lymphoma patients. *FEBS Lett.* 586, 3448–3451.
- McCabe, M. T., Graves, A. P., Ganji, G., Diaz, E., Halsey, W. S., Jiang, Y., et al. (2012a). Mutation of A677 in histone methyltransferase EZH2 in human B-cell lymphoma promotes hypertrimethylation of histone H3 on lysine 27 (H3K27). *Proc. Natl. Acad. Sci. U.S.A.* 109, 2989–2994.
- McCabe, M. T., Ott, H. M., Ganji, G., Korenchuk, S., Thompson, C., Van Aller, G. S., et al. (2012b). EZH2 inhibition as a therapeutic strategy for lymphoma with EZH2-activating mutations. *Nature* 492, 108–112.
- Miranda, T. B., Cortez, C. C., Yoo, C. B., Liang, G., Abe, M., Kelly, T. K., et al. (2009). DZNep is a global histone methylation inhibitor that reactivates developmental genes not silenced by DNA methylation. *Mol. Cancer Ther.* 8, 1579–1588.
- Morin, R. D., Johnson, N. A., Severson, T. M., Mungall, A. J., An, J., Goya, R., et al. (2010). Somatic

- mutations altering EZH2 (Tyr641) in follicular and diffuse large B-cell lymphomas of germinal-center origin. *Nat. Genet.* 42, 181–185.
- Nakamura, M., Shimada, K., and Konishi, N. (2008). The role of HRK gene in human cancer. *Oncogene* 27(Suppl. 1), S105–S113.
- Palacios, D., Mozetta, C., Consalvi, S., Caretti, G., Saccone, V., Proserpio, V., et al. (2010). TNF/p38alpha/polycomb signaling to Pax7 locus in satellite cells links inflammation to the epigenetic control of muscle regeneration. *Cell Stem Cell* 7, 455–469.
- Perren, T. J., Swart, A. M., Pfisterer, J., Ledermann, J. A., Pujade-Lauraine, E., Kristensen, G., et al. (2011). A phase 3 trial of bevacizumab in ovarian cancer. *N. Engl. J. Med.* 365, 2484–2496.
- Qi, W., Chan, H., Teng, L., Li, L., Chuai, S., Zhang, R., et al. (2012). Selective inhibition of Ezh2 by a small molecule inhibitor blocks tumor cells proliferation. *Proc. Natl. Acad. Sci. U.S.A.* 109, 21360–21365.
- Rao, Z. Y., Cai, M. Y., Yang, G. F., He, L. R., Mai, S. J., Hua, W. F., et al. (2010). EZH2 supports ovarian carcinoma cell invasion and/or metastasis via regulation of TGF-beta1 and is a predictor of outcome in ovarian carcinoma patients. *Carcinogenesis* 31, 1576–1583.
- Rizzo, S., Hersey, J. M., Mellor, P., Dai, W., Santos-Silva, A., Liber, D., et al. (2011). Ovarian cancer stem cell-like side populations are enriched following chemotherapy and over-express EZH2. *Mol. Cancer Ther.* 10, 325–335.
- Ryan, R. J., Nitta, M., Borger, D., Zukerberg, L. R., Ferry, J. A., Harris, N. L., et al. (2011). EZH2 codon 641 mutations are common in BCL2-rearranged germinal center B cell lymphomas. *PLoS ONE* 6:e28585. doi:10.1371/journal.pone.0028585
- Schwartz, Y. B., and Pirrotta, V. (2007). Polycomb silencing mechanisms and the management of genomic programmes. *Nat. Rev. Genet.* 8, 9–22.
- Sneeringer, C. J., Scott, M. P., Kuntz, K. W., Knutson, S. K., Pollock, R. M., Richon, V. M., et al. (2010). Coordinated activities of wild-type plus mutant EZH2 drive tumor-associated hypertrimethylation of lysine 27 on histone H3 (H3K27) in human B-cell lymphomas. *Proc. Natl. Acad. Sci. U.S.A.* 107, 20980–20985.
- Su, I. H., Dobenecker, M. W., Dickinson, E., Oser, M., Basavaraj, A., Marqueron, R., et al. (2005). Polycomb group protein ezh2 controls actin polymerization and cell signaling. *Cell* 121, 425–436.
- Tan, J., Yang, X., Zhuang, L., Jiang, X., Chen, W., Lee, P. L., et al. (2007). Pharmacologic disruption of Polycomb-repressive complex 2-mediated gene repression selectively induces apoptosis in cancer cells. *Genes Dev.* 21, 1050–1063.
- Ting, A. H., McGarvey, K. M., and Baylin, S. B. (2006). The cancer epigenome – components and functional correlates. *Genes Dev.* 20, 3215–3231.
- Tsai, M. C., Manor, O., Wan, Y., Mosammamaparast, N., Wang, J. K., Lan, F., et al. (2010). Long non-coding RNA as modular scaffold of histone modification complexes. *Science* 329, 689–693.
- Van der Vlag, J., and Otte, A. P. (1999). Transcriptional repression mediated by the human polycomb-group protein EED involves histone deacetylation. *Nat. Genet.* 23, 474–478.
- Varambally, S., Dhanasekaran, S. M., Zhou, M., Barrette, T. R., Kumar-Sinha, C., Sanda, M. G., et al. (2002). The polycomb group protein EZH2 is involved in progression of prostate cancer. *Nature* 419, 624–629.
- Wei, Y., Xia, W., Zhang, Z., Liu, J., Wang, H., Adsay, N. V., et al. (2008). Loss of trimethylation at lysine 27 of histone H3 is a predictor of poor outcome in breast, ovarian, and pancreatic cancers. *Mol. Carcinog.* 47, 701–706.
- Xu, K., Wu, Z. J., Groner, A. C., and He, H. H. (2012). EZH2 oncogenic activity in castration-resistant prostate cancer cells is polycomb-independent. *Science* 338, 1465–1469.
- Zhao, J., Sun, B. K., Erwin, J. A., Song, J. J., and Lee, J. T. (2008). Polycomb proteins targeted by a short repeat RNA to the mouse X chromosome. *Science* 322, 750–756.

**Conflict of Interest Statement:** The authors declare that the research was conducted in the absence of any commercial or financial relationships that could be construed as a potential conflict of interest.

Received: 19 December 2012; paper pending published: 07 January 2013; accepted: 23 February 2013; published online: 13 March 2013.

Citation: Li H and Zhang R (2013) Role of EZH2 in epithelial ovarian cancer: from biological insights to therapeutic target. *Front. Oncol.* 3:47. doi: 10.3389/fonc.2013.00047

This article was submitted to *Frontiers in Women's Cancer*, a specialty of *Frontiers in Oncology*.

Copyright © 2013 Li and Zhang. This is an open-access article distributed under the terms of the Creative Commons Attribution License, which permits use, distribution and reproduction in other forums, provided the original authors and source are credited and subject to any copyright notices concerning any third-party graphics etc.



---

## A High-Content Screening Assay for Small-Molecule Modulators of Oncogene-Induced Senescence

Benjamin G. Bitler, Lauren S. Fink, Zhi Wei, Jeffrey R. Peterson and Rugang Zhang

*J Biomol Screen* 2013 18: 1054 originally published online 3 June 2013

DOI: 10.1177/1087057113491827

The online version of this article can be found at:

<http://jbx.sagepub.com/content/18/9/1054>

---

Published by:



<http://www.sagepublications.com>

On behalf of:



[Journal of Biomolecular Screening](#)

Additional services and information for *Journal of Biomolecular Screening* can be found at:

Email Alerts: <http://jbx.sagepub.com/cgi/alerts>

Subscriptions: <http://jbx.sagepub.com/subscriptions>

Reprints: <http://www.sagepub.com/journalsReprints.nav>


Permissions: <http://www.sagepub.com/journalsPermissions.nav>

>> [Version of Record](#) - Sep 23, 2013

[OnlineFirst Version of Record](#) - Jun 3, 2013

[What is This?](#)

# A High-Content Screening Assay for Small-Molecule Modulators of Oncogene-Induced Senescence

Journal of Biomolecular Screening  
18(9) 1054–1061  
© 2013 Society for Laboratory  
Automation and Screening  
DOI: 10.1177/1087057113491827  
jbx.sagepub.com  


Benjamin G. Bitler<sup>1</sup>, Lauren S. Fink<sup>2</sup>, Zhi Wei<sup>3</sup>,  
Jeffrey R. Peterson<sup>2</sup>, and Rugang Zhang<sup>1</sup>

## Abstract

Cellular senescence is a state of stable cell growth arrest. Activation of oncogenes such as RAS in mammalian cells typically triggers cellular senescence. Oncogene-induced senescence (OIS) is an important tumor suppression mechanism, and suppression of OIS contributes to cell transformation. Oncogenes trigger senescence through a multitude of incompletely understood downstream signaling events that frequently involve protein kinases. To identify target proteins required for RAS-induced senescence, we developed a small-molecule screen in primary human fibroblasts undergoing senescence induced by oncogenic RAS (H-Ras<sup>G12V</sup>). Using a high-content imaging system to monitor two hallmarks of senescence, senescence-associated  $\beta$ -galactosidase activity expression and inhibition of proliferation, we screened a library of known small-molecule kinase inhibitors for those that suppressed OIS. Identified compounds were subsequently validated and confirmed using a third marker of senescence, senescence-associated heterochromatin foci. In summary, we have established a novel high-content screening platform that may be useful for elucidating signaling pathways mediating OIS by targeting critical pathway components.

## Keywords

cancer and cancer drugs, cell-based assays, high-content screening, kinases

## Introduction

Aberrant oncogene activation is an important driver of cellular transformation; however, initial atypical oncogene activation that occurs in primary cells typically triggers cellular senescence, a state of stable cell growth arrest.<sup>1–3</sup> Oncogene-induced senescence (OIS) is an important tumor suppressive pathway, and suppression of OIS promotes tumorigenesis.<sup>4</sup> For example, oncogenic RAS or BRAF triggers senescence of melanocytes, which results in formation of benign nevi and thus suppresses melanoma development.<sup>5–7</sup> The RAS oncogene is mutated in a number of cancer types (reviewed in Schubert et al.<sup>8</sup>). Oncogenic RAS has been extensively studied in the context of OIS, where it triggers senescence by a cascade of kinases.<sup>3</sup>

Senescent cells exhibit several distinctive morphological characteristics and molecular markers, including a large, flat morphology; decrease in cell proliferation; and expression of senescence-associated  $\beta$ -galactosidase activity (SA- $\beta$ -gal)<sup>9</sup> (reviewed in Itahana et al.<sup>10</sup>). Expression of SA- $\beta$ -gal activity is considered a universal marker of senescent cells.<sup>11</sup> In addition, senescence induced by oncogenic RAS is also characterized by domains of transcriptionally silenced heterochromatin, known as senescence-associated heterochromatin foci (SAHF).<sup>12</sup> SAHF contribute to

senescence by silencing proliferation-promoting genes such as E2F target genes.<sup>13</sup>

Inactivation of tumor suppressors such as p53 and p16 inhibits OIS.<sup>3</sup> Due to the importance of OIS in tumor suppression, compounds that regulate OIS not only serve as useful tools in studying OIS but may also lead to the identification of new tumor suppressors. As a result, we have

<sup>1</sup>Gene Expression and Regulation Program, The Wistar Institute, Philadelphia, PA, USA

<sup>2</sup>Cancer Biology Program, Fox Chase Cancer Center, Philadelphia, PA, USA

<sup>3</sup>Department of Computer Science, New Jersey Institute of Technology, Newark, NJ, USA

Received Jan 30, 2013, and in revised form Apr 3, 2013. Accepted for publication May 7, 2013.

Supplementary material for this article is available on the *Journal of Biomolecular Screening* Web site at <http://jbx.sagepub.com/supplemental>.

## Corresponding Authors:

Rugang Zhang, PhD, Gene Expression and Regulation Program, The Wistar Institute, 3601 Spruce St, Philadelphia, PA 19104, USA.  
Email: rzhang@wistar.org

Jeffrey R. Peterson, PhD, Cancer Biology Program, Fox Chase Cancer Center, 333 Cottman Ave, Philadelphia, PA 19111, USA.  
Email: jeffrey.peterson@fccc.edu

developed a high-content screening assay to aid in the identification of novel OIS regulators. We used a kinase inhibitor library to determine compounds that inhibited OIS in the context of oncogenic RAS overexpression. In addition, the identified compounds could be studied further to help elucidate proteins involved in mediating OIS, which may lead to identification of novel tumor suppressors.

Previously, a screen for modulators of stress-induced senescence in prostate cancer has been described.<sup>14</sup> In this study, the authors used percentage of SA- $\beta$ -gal-positive cells as a senescence output, but the screen is limited due to the necessity of having to manually quantify SA- $\beta$ -gal-positive cells. In contrast, we report the development of a high-content imaging-based screen assay. In addition, using a library of 160 well-characterized kinase inhibitors, we performed a proof-of-principle screen for inhibitors of senescence induced by oncogenic RAS.

SA- $\beta$ -gal activity was used in a high-content screening assay in a 96-well platform as the primary measure of senescence. To eliminate artifactual hits due to decreased cell number in the absence of OIS inhibition, we quantified cell numbers using nuclear staining. Using this newly developed platform, we identified 17 kinase inhibitors as suppressors of oncogenic RAS-induced senescence. We further confirmed our findings by using SAHF staining as an additional marker of senescence. All 17 inhibitors were individually validated, and 15 of 17 these were confirmed. This study introduces a novel assay for screening of modulators of OIS, and we report the identification of several compounds as bona fide suppressors of OIS.

## Materials and Methods

### Tissue Culture

Primary diploid fibroblasts (IMR90) were cultured according to the American Type Culture Collection (ATCC, Manassas, VA). Experiments were performed with IMR90 that were between 25 and 36 population doublings (PD).

### Plasmids and Retrovirus

pBABE-H-Ras<sup>G12V</sup> was obtained from Addgene (Cambridge, MA). Retrovirus production and transduction previously have been described.<sup>15</sup> Phoenix cells were used to facilitate retroviral packaging (Dr. Gary Nolan, Stanford University, Stanford, CA).

### Screen Setup

Double infections of IMR90 cells in 100-mm dishes were performed using a retrovirus encoding for pBABE-H-Ras<sup>G12V</sup> (days -1 and 0, respectively). Cells were selected with puromycin (1  $\mu$ g/mL) for an additional 2 days and then plated into

a 96-well plate (1000 cells/well). The initial number of cells per well (1000) was optimized to avoid confluence-induced growth inhibition. At the end of day 2, cells were treated with kinase inhibitors (KIs) by pin transfer at ~250 nM. On day 9, cells were subjected to a quantitative SA- $\beta$ -gal assay (described below) and stained with DAPI to visualize nuclei, which allowed for quantification of cell number.

### Senescence Assay

The SA- $\beta$ -gal assay previously has been described.<sup>9</sup> Briefly, cells were fixed in 2% formaldehyde and 0.2% glutaraldehyde and washed with phosphate-buffered saline. Staining solution (40 mM Na<sub>2</sub>HPO<sub>4</sub>, 150 mM NaCl, 2 mM MgCl<sub>2</sub>, 5 mM K<sub>3</sub>Fe(CN)<sub>6</sub>, 5 mM K<sub>4</sub>Fe(CN)<sub>6</sub>, and 1 mg/mL X-gal) was added with a multichannel pipette, and cells were incubated for 24 h. Cells were stained with DAPI (0.15  $\mu$ g/mL) to visualize nuclei.

For the screen, four fluorescence and four phase-contrast images (individual image size = 2.9 megabytes) were acquired from each well of the 96-well plates with an ImageXpress Micro high-content imaging system (Molecular Devices, Sunnyvale, CA). Using a 10 $\times$  Pan-Fluor objective with a working distance of 15.2 mm, phase-contrast images were captured (exposure time = 5  $\mu$ s) to record SA- $\beta$ -gal staining. Fluorescence images were captured using a 10 $\times$  Pan-Fluor objective with a Semrock filter (300-W xenon lamp; excitation = 377/50 nm, emission = 447/60 nm, and exposure time = 55  $\mu$ s) to record DAPI staining of cell nuclei. Note that at 10 $\times$  magnification, SAHF are indistinguishable. In addition, objective and filter cube change together with image-based autofocus, allowing for simultaneous imaging of both channels. Images were analyzed using the MultiWavelength Scoring module in MetaXpress image analysis software (Molecular Devices). Briefly, based on preliminary experiments with control and RAS-expressing cells, a threshold was determined at which to define positive  $\beta$ -gal pixels. This threshold was applied to all of the phase-contrast images (**Fig. 1**, orange pixels), and the masked area for each image was systematically quantified. DAPI-positive nuclei were counted with MetaXpress image analysis software (version 3.1) by restricting counts to circular objects with a diameter greater than 1 micron. AcuityXpress software (version 2.02, Molecular Devices) was used for informatics processing and data visualization. The four images were quantified and the values for each SA- $\beta$ -gal area and nuclei number were averaged. Compared with counting the percentage of SA- $\beta$ -gal-positive cells manually, the current approach allows for a high-content screening assay to be developed. Overall, automatic image acquisition to quantification averaged 2 h per 96-well plate.

We determined the average number of cells ( $N_{\text{ctrl}}$ ) and SA- $\beta$ -gal area ( $BGPP_{\text{ctrl}}$ ) for IMR90s transduced with pBABE-H-Ras<sup>G12V</sup> treated with DMSO vehicle control, which served as a positive base value for comparison. The

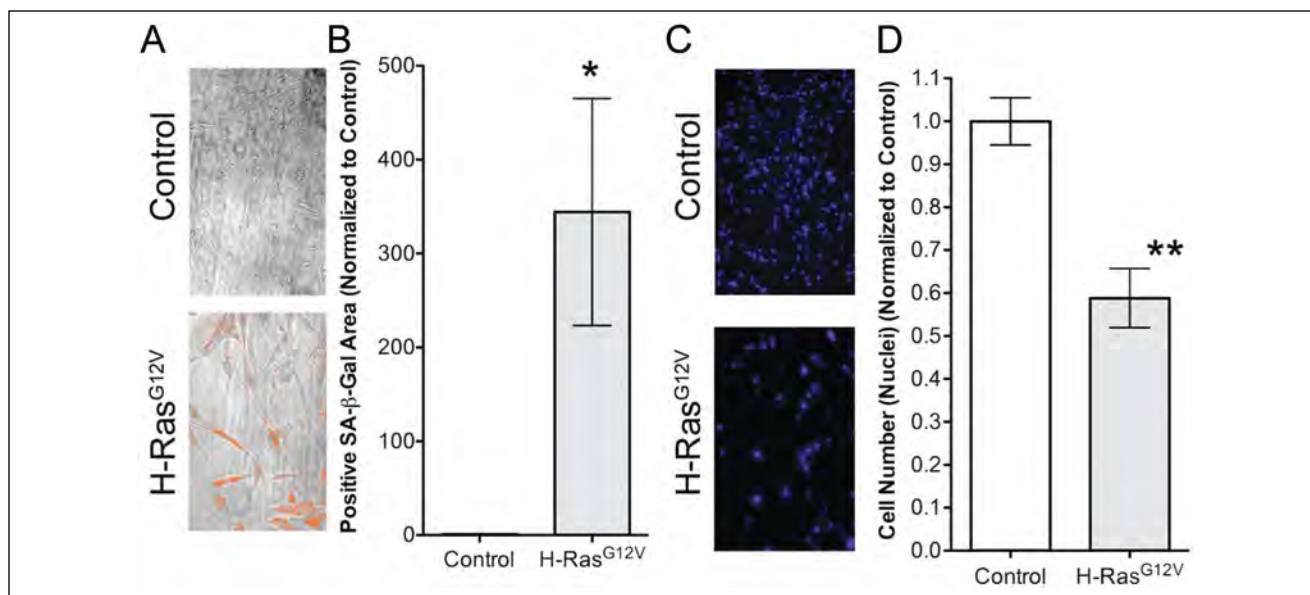


**Figure 1.** Screen output development. Using the ImageXpress Micro high-content imaging system, each well was systematically imaged eight times: four bright-field images and four fluorescence images. **(A)** Representative bright-field images from screen. Note the “mask” (orange pixels) applied to bright-field images indicating the quantified senescence-associated  $\beta$ -galactosidase activity (SA- $\beta$ -gal)-positive area. **(B)** Quantification of SA- $\beta$ -gal-positive area between control and H-Ras<sup>G12V</sup> cells (\* $p = .029$ ). **(C)** Representative fluorescence images from screen. **(D)** Quantification of nuclei between control and H-Ras<sup>G12V</sup> cells (\*\* $p = .0034$ ).

average number of nuclei and SA- $\beta$ -gal area from each of the 160 kinase inhibitors was normalized to DMSO. These normalized values were averaged between replicates. KIs that inhibited senescence were identified by the following equation: KIs prevented senescence if  $N_{Kix} > [N_{ctrl} + \text{standard deviation of } N_{ctrl}]$  and at the same time  $BGPP_{Kix} < [BGPP_{ctrl} - \text{standard deviation of } BGPP_{ctrl}]$ .

All 17 active compounds identified as hits in the screen, along with an inactive control compound (CAS 648449-76-7; PI3K $\gamma$  inhibitor II), were individually examined for SA- $\beta$ -gal activity and SAHF formation. Three hundred cells from each group were examined for  $\beta$ -galactosidase (blue) positivity within the cytosol. Using total cell number and  $\beta$ -galactosidase-positive cells, the positive percentage was calculated. Cells were stained with DAPI to visualize nuclei and SAHF. Three hundred cells from each group were examined for punctate DAPI-stained dense spots, where  $>10$  spots within the nuclear compartment were considered SAHF positive. Using total cell number and SAHF-positive cells, the positive percentage was calculated. Cells were imaged using a Nikon Eclipse Ni fluorescence microscope (Nikon, Tokyo, Japan) as previously described.<sup>16</sup> These experiments were performed in triplicate. Data from validation experiments are shown as a percentage of SA- $\beta$ -gal- or SAHF-positive cells.

### Statistical Analysis

Statistical significance was determined by  $t$  test using GraphPad statistical software, version 5.0b (GraphPad

Software, La Jolla, CA). Values were considered significant if  $p < .05$ . Z' score was calculated using Microsoft Excel (Microsoft Corp., Redmond, WA).

### Kinase Inhibitor Library

The kinase inhibitor library, which contained 160 well-characterized kinase inhibitors, was purchased from EMD Millipore (InhibitorSelect; Millipore, Billerica, MA). Compounds were maintained in 100% DMSO. Inhibitors were added to the growth medium of cells growing in 96-well microplates by pin transfer (Final DMSO % = 0.375%). Eight wells of cells in each plate treated with DMSO (vehicle control) were included as vehicle controls. To avoid plate location-specific effects, these DMSO wells were spread across the plate.

### Results

#### Development of a High-Content Screening Assay for Identifying Small-Molecule Suppressors of Senescence Induced by Oncogenic RAS

Ectopic expression of activated oncogenes such as RAS is a standard approach to induce cellular senescence in a synchronized manner in primary mammalian cells.<sup>3</sup> Thus, we ectopically expressed oncogenic H-RAS<sup>G12V</sup> by retroviral transduction in primary human fibroblasts (IMR90 cells) to induce senescence. Senescence phenotypes such as SA- $\beta$ -gal



activity typically take several days to develop.<sup>15</sup> SA- $\beta$ -gal activity in the cytoplasm is considered a universal marker of cellular senescence<sup>9</sup> and can be visualized by phase-contrast microscopy. In addition, a definitive marker of senescence is a decreased cell proliferation (reviewed in Hayflick<sup>17</sup>). We sought to develop a high-content assay for screening small-molecule modulators of senescence.

In an initial pilot experiment, using MetaXpress image analysis, a threshold of SA- $\beta$ -gal intensity was established to define a SA- $\beta$ -gal-positive pixel. This threshold was subsequently used in the large-scale screen to apply a “mask” to the four phase-contrast images, and the positive pixel area per image was determined (**Fig. 1A**, orange area). Importantly, we observed a significant and robust increase in SA- $\beta$ -gal area in RAS-infected cells compared with controls (**Fig. 1B**). We also observed a significant reduction in the number of nuclei in RAS-expressing cells compared with control cells (**Fig. 1C,D**). The average SA- $\beta$ -gal area and number of nuclei for the positive control (DMSO vehicle treated RAS-expressing cells) from the same screening plate were used as a baseline to compare with the KI-treated cells.

It is well established that a cascade of kinases plays a role in regulating oncogenic RAS-induced senescence.<sup>18</sup> We therefore applied our screening assay using a library of 160 well-characterized kinase inhibitors in a 96-well plate format.<sup>19</sup> The screen was performed by treating RAS-transduced cells with 250 nM of each of the 160 kinase inhibitors or vehicle control (DMSO) (**Fig. 2A**). This concentration was chosen based on typical concentrations at which these compounds are used in cell-based assays.<sup>19</sup> Furthermore, it is known that cell density affects SA- $\beta$ -gal activity. To limit the potential nonspecific effects of cell density on SA- $\beta$ -gal expression, a range of cell concentrations were tested during assay development to avoid cell confluence over the course of the assay. Typically, 1000 RAS-overexpressing cells were inoculated per well. We used a time point of 9 days following RAS transduction to assess OIS based on our previous work.<sup>15</sup> Eight wells of vehicle control were included in each plate as positive controls for comparison. In addition, control virus-infected cells were included as negative controls for comparison. Cells in the 96-well plates were fixed, and markers of senescence were examined at day 9 after RAS infection. Specifically, we stained the fixed cells for SA- $\beta$ -gal activity and with a fluorescent DNA dye (DAPI) to visualize nuclei, which was used as a surrogate for cell number. Four phase-contrast and fluorescence images were taken of each well and systematically quantified and averaged. This assay allows us to measure the expression of a senescence marker simultaneously with cell number to reflect changes in cell proliferation in the same population of cells. To ensure that the decrease in expression of SA- $\beta$ -gal activity was not due to a decrease in cell proliferation, we focused on kinase

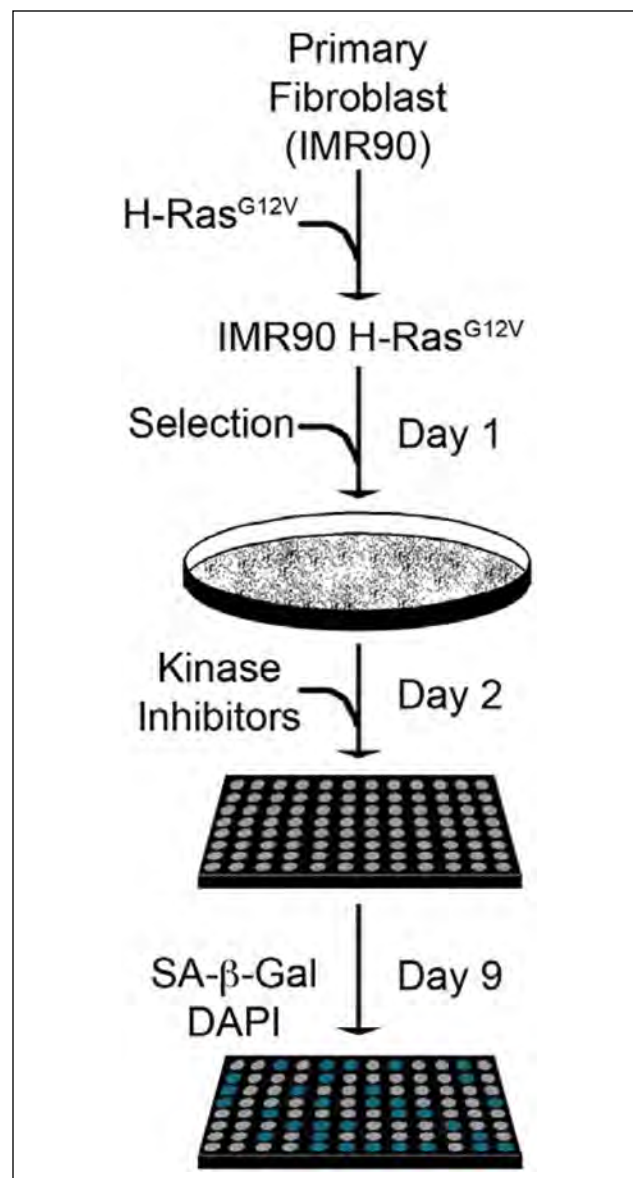


**Figure 2.** Senescence screen setup and analysis. Primary fibroblasts (IMR90s) were transduced with an H-Ras<sup>G12V</sup> encoding retrovirus over 2 days (days –1 and 0). Cells were then selected with puromycin (1  $\mu$ g/mL) for 2 days, plated into 96-well plates (1000 cells/well), and, at the end of the second day, treated with the kinase inhibitor library at a uniform concentration (250 nM). Cells were incubated for 7 additional days to allow for senescence and then fixed in a formaldehyde/glutaraldehyde solution. To visualize the senescence-associated  $\beta$ -galactosidase activity (SA- $\beta$ -gal) activity and determine cell number, fixed cells were incubated with X-gal and labeled with DAPI.

inhibitors that significantly suppressed SA- $\beta$ -gal activity but did not decrease cell proliferation.

Averages of SA- $\beta$ -gal area and nuclei number from biological replicate experiments were compiled and normalized to the mean of vehicle (DMSO) control wells. These data were graphed on a scatter plot (**Fig. 3**). Hits were

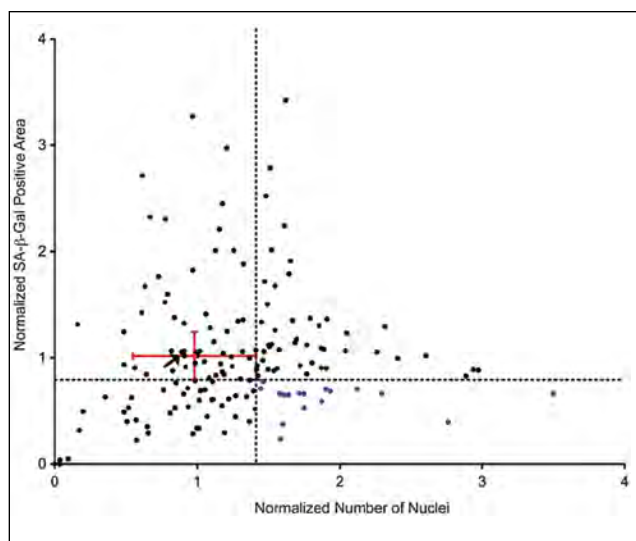


**Figure 3.** Identification of senescence-suppressing kinase inhibitors. Both the nuclei number and senescence-associated  $\beta$ -galactosidase activity (SA- $\beta$ -gal) area were normalized to DMSO-treated control wells (red dot). The normalized numbers of nuclei (a surrogate of cell number) and SA- $\beta$ -gal area were graphed. The delineation (dotted lines) separates the graph into quadrants, and placement of the lines was determined from the standard deviation of DMSO control wells (red error bars). The lower right quadrant indicates kinase inhibitors that have significantly more nuclei and less SA- $\beta$ -gal area (blue dots). Arrow indicates inhibitor used as negative control in subsequent validation experiments.

identified as compounds that reduced SA- $\beta$ -gal area by at least one standard deviation below the mean of DMSO control and conversely increased cell number (nuclei) above one standard deviation of the DMSO control mean (Fig. 3, bottom right quadrant, blue dots). According to these criteria, 17 of the 160 compounds tested significantly suppressed SA- $\beta$ -gal area while maintaining nuclei number in RAS-expressing cells (compounds are listed in Suppl. Table S1).

### Validation of Identified Compounds as Suppressors of Oncogene-Induced Senescence

Recapitulating the experimental design of the screen, we individually treated RAS-expressing cells with DMSO vehicle control or with 250 nM of the 17 identified inhibitors. As an additional control, RAS-expressing cells were also treated with a kinase inhibitor (CAS 648449-76-7; PI3K $\gamma$  inhibitor II) that had no effect on SA- $\beta$ -gal area or cell number based on initial screening (Fig. 3, arrow). These cells were then used in the SA- $\beta$ -gal assay to examine changes in expression of SA- $\beta$ -gal activity. Upon manual quantification of SA- $\beta$ -gal-positive cells, we discovered that 16 of 17 inhibitors significantly reduced the expression of SA- $\beta$ -gal activity in our validation experiments (Fig. 4A,B and Suppl. Table S2).

To further confirm senescence suppression by these compounds, we next assayed their effect using an independent marker of senescence, SAHF, which are domains of punctate DAPI stain in the nuclei of senescent cells (Fig. 5A, white arrowheads).<sup>12</sup> Toward this goal, RAS-expressing cells were treated with the 17 kinase inhibitors identified in the initial screen, a negative control inhibitor (CAS 648449-76-7; PI3K $\gamma$  inhibitor II), or DMSO. After 9 days of culture, we stained the cells with DAPI to visualize the formation of SAHF. In this independent validation, we discovered that 16 of 17 inhibitors significantly inhibited oncogenic RAS-induced SAHF formation. Interestingly, the inhibitor that failed to prevent SAHF formation (CAS 371935-74-9; PI-103) was not the same as the inhibitor that failed to reduce SA- $\beta$ -gal activity (CAS 612847-09-3; Akt inhibitor VIII) (Fig. 5A,B and Suppl. Table S2). The discrepancy was not unexpected as there is evidence that SAHF formation is not always necessary for cells to undergo senescence.<sup>20,21</sup> Thus, this compound confirms that SAHF formation can be uncoupled from SA- $\beta$ -gal activity and may represent a novel tool to understand this phenomenon. In addition, we also examined changes in cell number. Notably, one compound significantly decreased cell number compared with DMSO or negative control inhibitor (CAS 371935-74-9; PI-103; data not shown), while cell number was not suppressed by the other 16 compounds. Interestingly, the compound that decreased cell number was the same compound that failed to suppress SAHF (Fig. 5). These confirmation experiments reveal a false-positive rate of 11.7%. In summary, we validated 15 of the 17 compounds identified from the initial screening as bona fide suppressors of oncogenic RAS-induced senescence, demonstrating that this assay is a robust platform for identifying small-molecule regulators of OIS.

### Discussion

In the current study, we describe the assay development, identification, and validation of a high-content screening assay for small-molecule modulators of OIS. Using a kinase inhibitor library, we have identified a list of small-molecule compounds that suppress oncogenic RAS-induced senescence. We have previously demonstrated that most of these compounds target multiple kinases.<sup>19</sup> Thus, understanding the mechanism of suppression of OIS by these compounds will require further identification of the relevant kinase targets. Here our identification of 15 kinase inhibitors that suppress oncogenic RAS-induced senescence validates this assay for identifying such compounds. Significantly, we confirmed the activity of the identified inhibitors using the original screening assay (SA- $\beta$ -gal activity) and further validated the compounds using an independent senescence marker, SAHF. One of the inhibitors identified (AMPK Compound C, CAS 855405-64-3) has been reported to prevent senescence, further demonstrating the accuracy of this newly

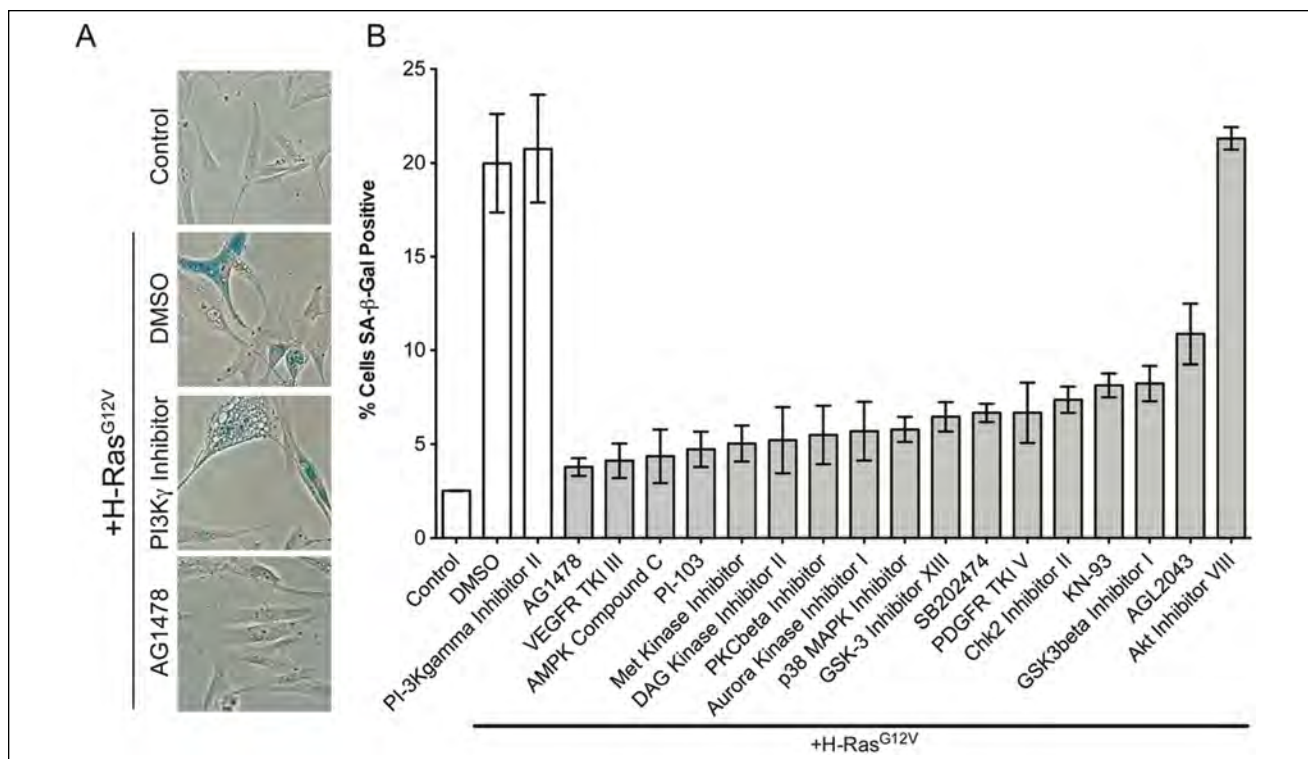


**Figure 4.** Validation of kinase inhibitors that significantly inhibit senescence-associated  $\beta$ -galactosidase activity (SA- $\beta$ -gal) activity. (A) Primary fibroblasts (IMR90s) were transduced with a control or H-Ras<sup>G12V</sup> encoding retrovirus. Cells were plated into six-well plates (15,000 cells/well), selected with puromycin (1  $\mu$ g/mL), for 2 days and at the end of the second day treated with 250 nM of kinase inhibitors. Cells were incubated for 7 additional days to allow for senescence and then fixed. SA- $\beta$ -gal activity was visualized and nuclei were labeled with DAPI. (B) Quantification of SA- $\beta$ -gal-positive cells (300 cells were counted for each condition). Gray bar = experimental conditions and white bars = controls. TKI, tyrosine kinase inhibitor. Average percentages and *p* values are in **Supplemental Table S2**. Experiments were performed in triplicate (error bars = standard error).

developed assay.<sup>22</sup> Notably, none of the other identified compounds has specifically been reported to alter senescence. Follow-up studies with these compounds will investigate the relationship between inhibition of a specific kinase and the OIS pathways, which will elucidate molecular mechanisms underlying RAS-induced OIS. In addition, dose-dependent effects of these compounds also will be examined. Taken together, these data establish high-content screening assays for suppressors of senescence and identify several compounds as suppressors of oncogene-induced senescence.

The high-content screening assay reported here is unique because of the simultaneous utilization of multiple criteria to identify potential hits. Conventional single-parameter screens often use two to three standard deviations to identify positive hits. Notably, only two compounds (CAS 866405-64-3; AMPK Compound C and CAS 120166-69-0; diacylglycerol kinase inhibitor I) were scored as hits if two standard deviations was used as the cutoff criterion for both SA- $\beta$ -gal and cell number screening parameters (2 of 160 compounds; hit rate = 1.25%). Both compounds were among the list of compounds confirmed in the follow-up validation assays. In addition, the identification of AMPK Compound C using two standard deviations again

demonstrates the accuracy of the screen. Importantly, we confirmed 15 of the 17 compounds identified using one standard deviation for both SA- $\beta$ -gal and cell number screening parameters as the cutoff. These findings support the use of the criteria described in the current assay. For single-parameter-based screening, *Z'* score is typically used to reflect the robustness of assay. Using SA- $\beta$ -gal as a single parameter, we explored *Z'* score (*Z'* score = 0.89) for our newly developed assay by comparing an example of compounds that do not suppress SA- $\beta$ -gal (i.e., CAS 212779-48-1; Cdc28p kinase inhibitor) with an example of compounds that efficiently suppress SA- $\beta$ -gal (i.e., CAS 3895-92-9; PKC inhibitor).<sup>23</sup> This further supports the robustness of this newly developed high-content screening assay.

Compared with genetic manipulation for loss-of-function studies, small-molecule inhibitors offer certain advantages in studying kinase function. For example, many kinases are known scaffold proteins that mediate formation of multiple protein large complexes. Genetic knockdown will lead to collapse of these protein complexes and consequently result in unintended nonspecific effects. In contrast, small-molecule inhibitors of these kinases offer a unique opportunity to study



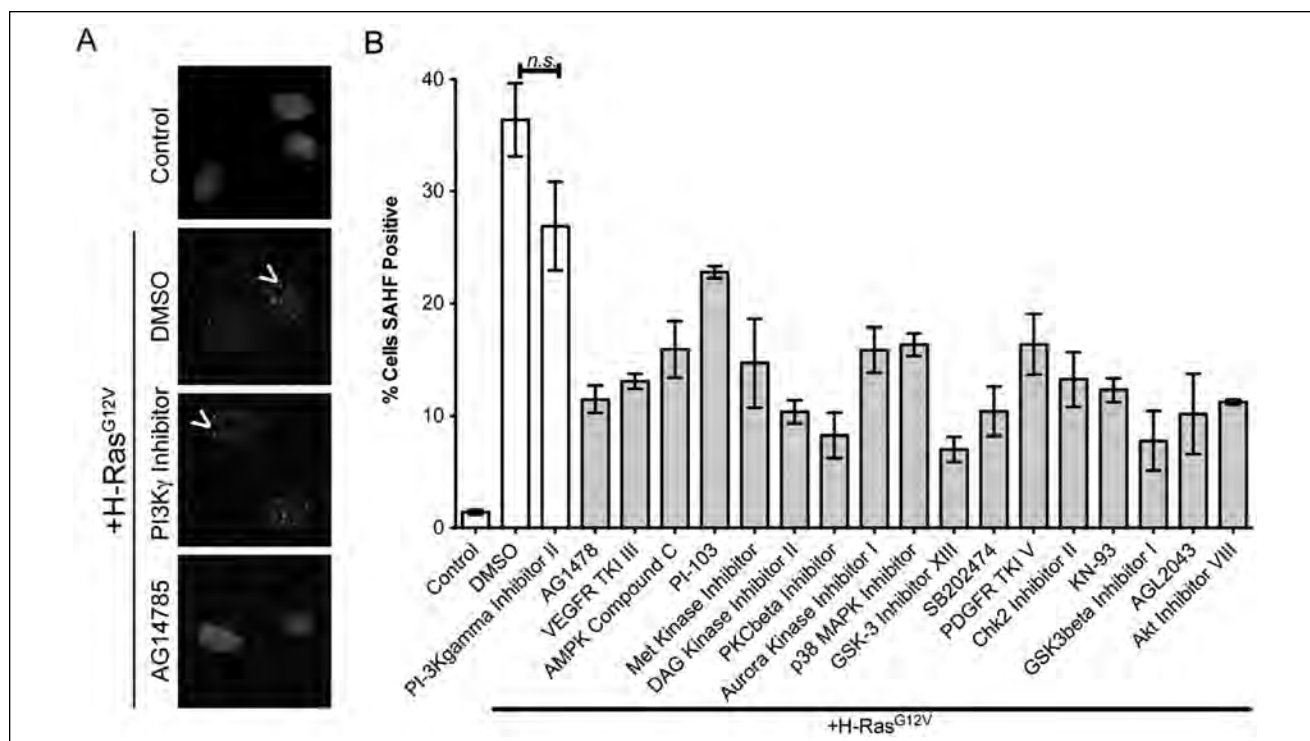


**Figure 5.** Senescence-suppressing compounds also inhibit senescence-associated heterochromatin foci (SAHF), an additional marker of senescence. **(A)** Primary fibroblasts (IMR90s) were transduced with a control or H-Ras<sup>G12V</sup> encoding retrovirus. Cells were plated into six-well plates (15,000 cells/well), selected with puromycin (1  $\mu$ g/mL) for 2 days, and, at the end of the second day, treated with 250 nM of kinase inhibitors. Cells were incubated for 7 additional days to allow for senescence and then fixed. Nuclei were labeled with DAPI, and nuclei containing punctate spots (arrows) were counted as SAHF positive. **(B)** Quantification of SAHF-positive cells (cells counted >300). Order of inhibitors, determined by senescence-associated  $\beta$ -galactosidase activity, is shown in **Figure 3**. Gray bars = experimental conditions and white bars = controls. TKI, tyrosine kinase inhibitor. Average percentages and *p* values are in **Supplemental Table S2**. Experiments were performed in triplicate (error bars = standard error).

kinase activity without affecting the interacting proteins. The inhibitors identified here will be invaluable tools in elucidating the role of these kinases in regulating OIS; however, a caveat to the use of small-molecule inhibitors is the potential for off-target effects. Therefore, future studies knocking down target kinases with short hairpin RNAs will be critical to confirm the kinases role in OIS.

The proof-of-principle kinase inhibitor screen described in this report identified compounds that suppressed senescence, which was determined by a decrease in SA- $\beta$ -gal activity. In validation studies, we observed a discrepancy between kinase inhibitors that prevented SA- $\beta$ -gal versus those that inhibited SAHF. Therefore, future versions of the screen will include measuring the percentage of SAHF following treatment, which, in conjunction with other markers, should increase reliability to identify senescent cells. In addition, the high-content screening approach used in this assay will also allow for future studies to examine enhancers of OIS. Taking advantage of the platform developed herein and using compounds beyond kinase inhibitors may yield a more comprehensive understanding of OIS.

Although senescence is known to be an important tumor suppression mechanism during tumor initiation and

progression, it may also be an important mechanism for developing cancer therapeutics. For example, reactivation of the tumor suppressor p53 in murine liver and sarcoma models triggers cellular senescence and the associated tumor regression due to activation of the innate immune response.<sup>24</sup> Likewise, we have also demonstrated that restoration of noncanonical Wnt signaling in ovarian cancer cells suppresses tumorigenesis by inducing cellular senescence.<sup>25</sup> Thus, small-molecule inhibitors that promote senescence of cancer cells could be developed as potential cancer therapeutics. Future studies will employ the high-content screening platform established in the current study to identify small molecules that promote senescence of human cancer cells such as melanoma cells, which can arise by overcoming the senescence tumor suppression mechanism.<sup>26,27</sup> These small molecular activators of senescence would, by definition, possess antiproliferative activity and may have value as potential anticancer agents.

In conclusion, we established a high-content screening platform for identifying small-molecule regulators of cellular senescence and identified a list of small-molecule compounds that are suppressors of senescence induced by oncogenic RAS.



## Acknowledgments

We thank Dr. Katherine Aird for critical reading of this manuscript, as well as Dr. Margret Einarson and Ms. Anna Pecherskaya at Fox Chase Cancer Center Translational Research Facility for technical assistance.

## Declaration of Conflicting Interests

The authors declared no potential conflicts of interest with respect to the research, authorship, and/or publication of this article.

## Funding

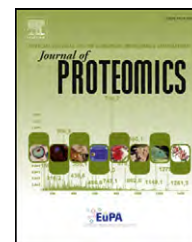
The authors received no financial support for the research, authorship, and/or publication of this article: This work was supported by a National Institutes of Health (NIH)/National Cancer Institute grant (R01CA160331 to R.Z.), a Department of Defense award (OC093420 to R.Z.), and an NIH/National Institute of General Medicine grant (R01GM083025 to J.R.P.). B.G.B. is an American Cancer Society Postdoctoral Fellow (PF-13-058-01-TBE). Support of core facilities used in this study was provided by a Cancer Center Support Grant (CA010815) to The Wistar Institute, and CA006927 to Fox Chase Cancer Center.

## References

- Chen, Z.; Trotman, L. C.; Shaffer, D.; et al. Crucial Role of p53-Dependent Cellular Senescence in Suppression of Pten-Deficient Tumorigenesis. *Nature* **2005**, *436*, 725–730.
- Lin, A. W.; Barradas, M.; Stone, J. C.; et al. Premature Senescence Involving p53 and p16 Is Activated in Response to Constitutive MEK/MAPK Mitogenic Signaling. *Genes Dev.* **1998**, *12*, 3008–3019.
- Serrano, M.; Lin, A. W.; McCurrach, M. E.; et al. Oncogenic Ras Provokes Premature Cell Senescence Associated with Accumulation of p53 and p16INK4a. *Cell* **1997**, *88*, 593–602.
- Kuilman, T.; Michaloglou, C.; Mooi, W. J.; et al. The Essence of Senescence. *Genes Dev.* **2010**, *24*, 2463–2479.
- Goel, V. K.; Ibrahim, N.; Jiang, G.; et al. Melanocytic Nevus-like Hyperplasia and Melanoma in Transgenic BRAFV600E Mice. *Oncogene* **2009**, *28*, 2289–2298.
- Bauer, J.; Curtin, J. A.; Pinkel, D.; et al. Congenital Melanocytic Nevi Frequently Harbor NRAS Mutations but No BRAF Mutations. *J. Invest. Dermatol.* **2007**, *127*, 179–182.
- Denoyelle, C.; Abou-Rjaily, G.; Bezrookove, V.; et al. Anti-oncogenic Role of the Endoplasmic Reticulum Differentially Activated by Mutations in the MAPK Pathway. *Nat. Cell Biol.* **2006**, *8*, 1053–1063.
- Schubbert, S.; Shannon, K.; Bollag, G. Hyperactive Ras in Developmental Disorders and Cancer. *Nat. Rev. Cancer* **2007**, *7*, 295–308.
- Dimri, G. P.; Lee, X.; Basile, G.; et al. A Biomarker That Identifies Senescent Human Cells in Culture and in Aging Skin In Vivo. *Proc. Natl. Acad. Sci. U. S. A.* **1995**, *92*, 9363–9367.
- Itahana, K.; Campisi, J.; Dimri, G. P. Methods to Detect Biomarkers of Cellular Senescence: The Senescence-Associated Beta-Galactosidase Assay. *Methods Mol. Biol.* **2007**, *371*, 21–31.
- Caldwell, M. E.; DeNicola, G. M.; Martins, C. P.; et al. Cellular Features of Senescence during the Evolution of Human and Murine Ductal Pancreatic Cancer. *Oncogene* **2012**, *31*, 1599–1608.
- Narita, M.; Nunez, S.; Heard, E.; et al. W. Rb-mediated Heterochromatin Formation and Silencing of E2F Target Genes during Cellular Senescence. *Cell* **2003**, *113*, 703–716.
- Zhang, R.; Chen, W.; Adams, P. D. Molecular Dissection of Formation of Senescence-Associated Heterochromatin Foci. *Mol. Cell. Biol.* **2007**, *27*, 2343–2358.
- Ewald, J. A.; Peters, N.; Desotelle, J. A.; et al. A High-Throughput Method to Identify Novel Senescence-Inducing Compounds. *J. Biomol. Screen.* **2009**, *14*, 853–858.
- Tu, Z.; Aird, K. M.; Bitler, B. G.; et al. Oncogenic RAS Regulates BRIP1 Expression to Induce Dissociation of BRCA1 from Chromatin, Inhibit DNA Repair, and Promote Senescence. *Dev. Cell* **2011**, *21*, 1077–1091.
- Zhang, R.; Poustovoitov, M. V.; Ye, X.; et al. Formation of MacroH2A-Containing Senescence-Associated Heterochromatin Foci and Senescence Driven by ASF1a and HIRA. *Dev. Cell* **2005**, *8*, 19–30.
- Hayflick, L. The Cell Biology of Aging. *Clin. Geriatr. Med.* **1985**, *1*, 15–27.
- Sun, P.; Yoshizuka, N.; New, L.; et al. PRAK Is Essential for Ras-Induced Senescence and Tumor Suppression. *Cell* **2007**, *128*, 295–308.
- Anastasiadis, T.; Deacon, S. W.; Devarajan, K.; et al. Comprehensive Assay of Kinase Catalytic Activity Reveals Features of Kinase Inhibitor Selectivity. *Nat. Biotechnol.* **2011**, *29*, 1039–1045.
- Kosar, M.; Bartkova, J.; Hubackova, S.; et al. Senescence-Associated Heterochromatin Foci Are Dispensable for Cellular Senescence, Occur in a Cell Type- and Insult-Dependent Manner and Follow Expression of p16(ink4a). *Cell Cycle* **2011**, *10*, 457–468.
- Di Micco, R.; Sulli, G.; Dobrev, M.; et al. Interplay between Oncogene-Induced DNA Damage Response and Heterochromatin in Senescence and Cancer. *Nat. Cell Biol.* **2011**, *13*, 292–302.
- Zu, Y.; Liu, L.; Lee, M. Y.; et al. SIRT1 Promotes Proliferation and Prevents Senescence through Targeting LKB1 in Primary Porcine Aortic Endothelial Cells. *Circ. Res.* **2010**, *106*, 1384–1393.
- Zhang, J. H.; Chung, T. D.; Oldenburg, K. R. A Simple Statistical Parameter for Use in Evaluation and Validation of High Throughput Screening Assays. *J. Biomol. Screen.* **1999**, *4*, 67–73.
- Xue, W.; Zender, L.; Miething, C.; et al. Senescence and Tumour Clearance Is Triggered by p53 Restoration in Murine Liver Carcinomas. *Nature* **2007**, *445*, 656–660.
- Bitler, B. G.; Nicodemus, J. P.; Li, H.; et al. Wnt5a Suppresses Epithelial Ovarian Cancer by Promoting Cellular Senescence. *Cancer Res.* **2011**, *71*, 6184–6194.
- Dhomen, N.; Reis-Filho, J. S.; da Rocha Dias, S.; et al. Oncogenic Braf Induces Melanocyte Senescence and Melanoma in Mice. *Cancer Cell* **2009**, *15*, 294–303.
- Michaloglou, C.; Vredeveld, L. C.; Soengas, M. S.; et al. BRAFV600-Associated Senescence-like Cell Cycle Arrest of Human Naevi. *Nature* **2005**, *436*, 720–724.

Available online at [www.sciencedirect.com](http://www.sciencedirect.com)

ScienceDirect

[www.elsevier.com/locate/jprot](http://www.elsevier.com/locate/jprot)

# Protein isoform-specific validation defines multiple chloride intracellular channel and tropomyosin isoforms as serological biomarkers of ovarian cancer

Hsin-Yao Tang<sup>a</sup>, Lynn A. Beer<sup>a</sup>, Janos L. Tanyi<sup>b</sup>, Rugang Zhang<sup>c</sup>, Qin Liu<sup>a</sup>, David W. Speicher<sup>a,\*</sup>

<sup>a</sup>Center for Systems and Computational Biology and Molecular and Cellular Oncogenesis Program, The Wistar Institute, Philadelphia, PA, USA

<sup>b</sup>Ovarian Cancer Research Center, University of Pennsylvania, Philadelphia, PA, USA

<sup>c</sup>Gene Expression and Regulation Program, The Wistar Institute, Philadelphia, PA, USA

## ARTICLE INFO

### Article history:

Received 22 January 2013

Accepted 10 June 2013

Available online 21 June 2013

### Keywords:

Biomarker validation

Biomarker isoforms

Protein families

Ovarian cancer biomarkers

Multiple reaction monitoring

Proteomics

## ABSTRACT

New serological biomarkers for early detection and clinical management of ovarian cancer are urgently needed, and many candidates have been reported. A major challenge frequently encountered when validating candidates in patients is establishing quantitative assays that distinguish between highly homologous proteins. The current study tested whether multiple members of two recently discovered ovarian cancer biomarker protein families, chloride intracellular channel (CLIC) proteins and tropomyosins (TPM), were detectable in ovarian cancer patient sera. A multiplexed, label-free multiple reaction monitoring (MRM) assay was established to target peptides specific to all detected CLIC and TPM family members, and their serum levels were quantitated for ovarian cancer patients and non-cancer controls. In addition to CLIC1 and TPM1, which were the proteins initially discovered in a xenograft mouse model, CLIC4, TPM2, TPM3, and TPM4 were present in ovarian cancer patient sera at significantly elevated levels compared with controls. Some of the additional biomarkers identified in this homolog-centric verification and validation approach may be superior to the previously identified biomarkers at discriminating between ovarian cancer and non-cancer patients. This demonstrates the importance of considering all potential protein homologs and using quantitative assays for cancer biomarker validation with well-defined isoform specificity.

### Biological significance

This manuscript addresses the importance of distinguishing between protein homologs and isoforms when identifying and validating cancer biomarkers in plasma or serum. Specifically, it describes the use of targeted in-depth LC-MS/MS analysis to determine the members of two protein families, chloride intracellular channel (CLIC) and tropomyosin (TPM) proteins that are detectable in sera of ovarian cancer patients. It then establishes a multiplexed isoform- and homology-specific MRM assay to quantify all observed gene products in these two protein families as well as many of the closely related tropomyosin isoforms. Using this assay, levels of all detected CLICs and TPMs were quantified in ovarian cancer patient and control subject sera. These results demonstrate that in addition to the previously known CLIC1, multiple tropomyosins and CLIC4 are promising new ovarian

\* Corresponding author at: The Wistar Institute, 3601 Spruce St., Room 272A, Philadelphia, PA 19104, USA. Tel.: +1 215 898 3972; fax: +1 215 495 6915.

E-mail address: [speicher@wistar.org](mailto:speicher@wistar.org) (D.W. Speicher).

1874-3919/\$ – see front matter © 2013 Elsevier B.V. All rights reserved.

<http://dx.doi.org/10.1016/j.jprot.2013.06.016>

cancer biomarkers. Based on these initial validation studies, these new ovarian cancer biomarkers appear to be superior to most previously known ovarian cancer biomarkers.

© 2013 Elsevier B.V. All rights reserved.

## 1. Introduction

Epithelial ovarian cancer (EOC) is the most lethal gynecological cancer in the United States, with an estimated 22,280 new cases detected and 15,500 deaths in 2012 [1]. When diagnosed early (Stages I/II), treatment is generally successful, with a five-year survival rate of up to 90%; but unfortunately, most cases are not detected until after the cancer has spread, resulting in a dismal five-year survival rate of 30% or less [2,3]. There are currently no effective screening tests for EOC early detection, and existing clinical tests using protein biomarkers, such as cancer antigen 125 (CA-125), human epididymis protein-4 (HE4), or multivariate OVA1, are only approved for monitoring disease recurrence, therapeutic response, or for use in managing women with an ovarian adnexal mass [4–7]. The most commonly used EOC biomarker, CA125, is recognized as a poor biomarker for early detection due to its high false-positive rate and poor sensitivity and specificity [8,9]. Better biomarkers or, more likely, panels of markers are urgently needed to diagnose early-stage EOC with high sensitivity and specificity, and for clinical management of the disease after initial diagnosis.

We and others have leveraged proteomics to discover new EOC biomarkers. Diverse experimental systems, including cancer cell cultures, tissue specimens, ascites fluid, secretomes, and mouse models, have been investigated using numerous proteomics strategies in attempts to identify better EOC biomarkers [10–21]. Using an in-depth 4D analysis of serum from severe combined immunodeficiency (SCID) mice containing a human endometrial ovarian cancer tumor, we recently identified 106 candidate human proteins with at least two peptides [21]. In that study, we performed a pilot validation on candidate biomarkers in the 20–55 kDa region of 1D SDS gels and found that nearly half the proteins discovered in the xenograft mouse model could be detected in human serum using multiple reaction monitoring analysis. Two of the tested candidates, chloride intracellular channel 1 (CLIC1) and cathepsin D 30 kDa fragment (CTSD-30 kDa), showed significantly elevated serum levels in cancer patients compared with non-cancer controls [21].

A major advantage of xenograft mouse models is that proteins shed by human tumors into mouse blood can be unambiguously distinguished by exploiting species differences in peptide sequences identified by liquid chromatography–tandem mass spectrometry (LC–MS/MS). However, the capacity to distinguish species differences diminishes as the sequence homology between the two species for specific proteins increases, especially with lower-abundance proteins where sequence coverage is typically low. Similarly, the capacity to distinguish between homologous human members of protein families during the discovery phase is often limited by low sequence coverage of candidate biomarkers.

The high number of candidates identified using current proteomics methods, coupled with the lack of well-characterized immunoassays for most of the new candidates, necessitates the use of alternative quantitative techniques

capable of screening candidates in patient serum or plasma. MRM has recently emerged as the most effective targeted quantitative technique for biomarker verification due to its high selectivity and multiplexing capability [22,23]. Despite the recent wide use of MRM as a quantitative tool in proteomics, concerns have been raised regarding its specificity and selectivity [24,25]. One of the major concerns is the specificity of peptide signals chosen for MRM quantitation, especially in a complex proteome background. In addition, the use of proteolytic fragmentation in discovery experiments creates a fundamental problem of protein inference [26]. In complex proteomes such as serum or plasma, it is often not trivial to reconnect peptides to a precise protein of origin due to the presence of shared tryptic peptides from protein isoforms (alternatively splicing forms from a single gene) and members of a protein family (proteins produced by homologous genes). Although the term “protein isoform” has been variably defined, in this study, protein isoform will be used to indicate related protein sequences from a single gene. These isoforms may be produced by alternative splicing, proteolytic processing, or other posttranslational modifications. Homologs or homologous proteins will be used to refer to members of a protein family produced by different genes.

The protein inference problem is further aggravated by substantial redundancy in the database caused by completely or nearly completely redundant entries, partial sequences, polymorphisms, sequencing errors, etc. In order to prevent inflation of protein counts in discovery experiments, a common practice is to use the parsimony principle or the Occam’s razor constraint to report a minimal list of proteins that can account for all observed peptides [26]. This often results in multiple protein entries being assigned to a set of peptides due to homologous proteins and redundancy in the database, and the actual protein(s) present in the sample can be ambiguous.

Importantly, the failure to detect peptides unique to an isoform does not prove that the isoform is not present in the sample. This is particularly critical in biomarker studies, as the correct or best biomarker may be a protein family member or isoform that was not explicitly identified in the discovery phase. It is important to differentiate isoforms and homologous family members because these related proteins are often associated with distinct structural or functional roles [27–29]. This is particularly important in cancer biomarker validation studies, because only the specific members of a protein family that are shed by the tumor into the blood should ideally be quantified. In this regard, any assay, including sandwich ELISA assays, could give misleading results if the isoform and family member specificity is unknown or if multiple related proteins are quantitated as a group. MRM has been used successfully to quantitate specific protein isoforms or mutant proteins especially from cell extracts [30–32]. However, targeted serological quantitation of serum biomarkers using MRM methods is a relatively new approach, and little is known about how the accuracy of protein quantitation is affected by the isoform and family member specificity of the peptides chosen.

We have developed a gel-based, label-free MRM quantitation approach (GeLC-MRM) as a rapid, first-level biomarker verification strategy using human plasma or serum samples [21,33,34]. This approach consists of major protein depletion, 1-D gel separation, in-gel trypsin digestion, and reversed-phase nanoLC-MRM analysis [33]. We previously demonstrated the reproducibility of the entire GeLC-MRM workflow and showed that it was capable of providing accurate relative quantitation of candidate biomarkers in the low ng/mL range from less than 100  $\mu$ L of serum or plasma [33,35]. It also has the added capability of distinguishing various molecular weight-forms of proteins that often are not distinguished using alternative proteome fractionation strategies and may not be distinguished by some immunoassays. We have successfully applied the GeLC-MRM strategy to validate a number of ectopic pregnancy and ovarian cancer candidate biomarkers, and subsequently confirmed one of the ectopic pregnancy low-abundant candidates using higher throughput immunoassays on a larger patient sample set [21,33–35]. In the current study, we used in-depth GeLC-MS/MS analysis of patient serum pools and isoform-specific MRM assays to identify and quantitate additional EOC biomarkers related to CLIC1 and tropomyosin 1 (TPM1) in individual patient sera. Additional members in both protein families were detected which significantly distinguished between cancer and control patients, and some of the newly identified biomarkers may be superior to the previously identified homologs.

## 2. Materials and methods

### 2.1. Reagents and chemicals

Dithiothreitol (DTT) was obtained from GE Healthcare (Piscataway, NJ). Iodoacetamide and 200 proof molecular biology grade ethanol were purchased from Sigma-Aldrich (St. Louis, MO). HPLC-grade acetonitrile was purchased from Thomas Scientific (Swedesboro, NJ). Sequencing-grade modified trypsin was purchased from Promega (Madison, WI).

### 2.2. Human serum collection and processing

All research in this study involving human specimens was conducted under The Wistar Institute Institutional Review Board-approved protocols #2109171, #EX2110012, and #260221. All human samples were derived from subjects with informed written consent. Data were analyzed anonymously. Serum samples were processed for MS analysis either individually or as pools, as previously described [21]. Characteristics of each ovarian cancer patient and non-cancer control are shown in Supplemental Table 3.

### 2.3. Immunoaffinity depletion and SDS-PAGE

Samples were depleted of 20 abundant serum proteins using a ProteoPrep20 Immunodepletion Column (Sigma-Aldrich) as previously described [21,36]. Briefly, 30–60  $\mu$ L of serum was filtered through a 0.22  $\mu$ m microcentrifuge filter and injected onto the column. The unbound proteins were collected, pooled, and precipitated with nine volumes of 200 proof ethanol

prechilled to  $-20^{\circ}\text{C}$ . Ethanol supernatants were carefully removed and protein pellets were dried, frozen and stored at  $-20^{\circ}\text{C}$  until further use. Frozen protein pellets were thawed, resuspended in 1% SDS, 50 mM Tris-HCl pH 8, reduced and alkylated prior to SDS-PAGE. For all samples, an equivalent of 10  $\mu$ L of original serum was loaded into three adjacent lanes, separated for 4 cm, and stained with Colloidal Blue (Invitrogen). All stained gels did not show any major differences in total gel lane intensities. Each gel lane was sliced into uniform 1 mm slices, and adjacent lane slices were combined and digested with modified trypsin (Promega, Madison, WI) as previously described [36].

### 2.4. LC-MS/MS of patient sample pools

To identify CLIC and TPM isoforms and family members that could be detected in ovarian cancer patient sera, label-free comparisons of pooled sera were performed. One pool of serum from patients with benign ovarian masses and three pools of advanced ovarian cancer patient serum samples were made. Serum pools were immunodepleted, separated on a 1-D SDS gel for 4 cm, sliced into 40 fractions, and digested with trypsin as described above. Eight microliter of tryptic digests were analyzed using an LTQ Orbitrap XL mass spectrometer (Thermo Scientific, Waltham, MA) connected to a NanoACQUITY UPLC system (Waters, Milford, MA). Peptides were eluted at 200 nL/min using a 229-min discovery gradient consisting of 5–28% B over 168 min, 28–50% B over 51.5 min, 50–80% B over 5 min, and 80% B for 4.5 min, before returning to 5% B over 0.5 min. A short blank gradient was run before injecting the next sample. The mass spectrometer was set to scan  $m/z$  from 400 to 2000. The full MS scan was collected at 60,000 resolution in the Orbitrap in profile mode followed by data-dependant MS/MS scans on the six-most-abundant ions exceeding a minimum threshold of 1000 collected in the linear trap. Monoisotopic precursor selection was enabled and charge-state screening was enabled to reject  $z = 1$  ions. Ions subjected to MS/MS were excluded from repeated analysis for 60 s.

### 2.5. Data processing

MS/MS spectra were extracted and searched using the SEQUEST algorithm (v. 28, rev. 13, University of Washington, Seattle, WA) in Bioworks (v. 3.3.1, Thermo Scientific) against the human UniRef100 protein sequence database (v. June 2011) plus common contaminants, and decoy sequences. The decoy database was produced by reversing the sequence of each database entry, and the entire reversed database was appended in front of the forward database. Spectra were searched with a partial tryptic constraint with up to two missed cleavages, 100 ppm precursor mass tolerance, 1 Da fragment ion mass tolerance, static modification of cys (+57.0215 Da), and variable modification of methionine (+15.9949 Da). Consensus protein lists were created using DTASelect (v. 2.0, licensed from Scripps Research Institute, La Jolla, CA) and the following filters were applied: remove proteins that are subsets of others, full tryptic constraint, a minimum of two peptides, mass accuracy  $\leq 10$  ppm, and  $\Delta\text{Cn} \geq 0.05$ . We previously showed that this database search and filtering strategy enhanced high-confidence detection of



low-abundance blood proteins compared with commonly used alternative strategies [37]. The peptide false discovery rate (FDR), calculated based on decoy count, was less than 1% based on redundant peptide count (spectra count). The peptide FDR was 1% based on non-redundant peptide count. Quantitative comparisons of all detected CLIC and TPM family members across serum pools were performed using Rosetta Elucidator software to compare peptide signal intensities in full MS scans. Retention time alignment, feature identification (discrete ion signals), feature extraction, and protein identifications were performed by the Elucidator system as previously described [21,33,34].

## 2.6. Label-free GeLC-MRM analysis

Serum samples were depleted of 20 abundant serum proteins, separated on a 1-D SDS gel for 4 cm, sliced into 40 fractions, and digested with trypsin as described above [21]. We had previously showed good reproducibility of the overall analytical pipeline, including major protein depletions, gels, trypsin digests, and the MRM analyses with consistent recovery of proteins in technical replicates [33]. MRM experiments were performed on a 5500 QTRAP hybrid triple quadrupole/linear ion trap mass spectrometer (AB SCIEX, Foster City, CA) interfaced with a NanoACQUITY UPLC system. Eight microliter of tryptic digests were injected using the partial loop injection mode onto a UPLC Symmetry trap column (180  $\mu\text{m}$  i.d.  $\times$  2 cm packed with 5  $\mu\text{m}$  C18 resin; Waters) and then separated by RP-HPLC on a BEH C18 nanocapillary analytical column (75  $\mu\text{m}$  i.d.  $\times$  25 cm, 1.7  $\mu\text{m}$  particle size; Waters) at 45 °C. Chromatography was performed with Solvent A (Milli-Q water with 0.1% formic acid) and Solvent B (acetonitrile with 0.1% formic acid). Peptides were eluted using a 27-min MRM gradient at 400 nL/min for 5–35% B over 24 min, and 35% B for 3 min before returning to 5% B in 0.5 min. To minimize sample carryover, a fast blank gradient was run between each sample. MRM data were acquired at unit resolution in both Q1 and Q3 with a spray voltage of 3300 V, curtain gas of 20 p.s.i., nebulizer gas of 10 p.s.i., interface heater temperature of 150 °C, and a pause time of 3 ms. To monitor system performance, a reference enolase digest sample was interspersed between experimental samples, at approximately every 18 samples. We previously demonstrated the long-term reproducibility of label-free MRM quantitation, where the majority of the enolase peptides were found to have a coefficient of variation (CV) of <16% [33]. In addition, MRM transitions for 4 trypsin self-digestion peptides (VATVSLPR, LSSPATLNSR, LGHNIDVLEGNQFINAAK and IITHPNFNGNTLDNDIMLIK) were also monitored in each sample to ensure retention time reproducibility of the LC system.

In MRM assay development, peptide candidates for targeted proteins were selected from the Orbitrap LC-MS/MS analysis described above. In some cases, peptide candidates were derived from prior human plasma/serum LC-MS/MS proteomic analyses. Initially, 4 or more transitions per peptides, including the most dominant y-ions observed from Orbitrap LC-MS/MS, were targeted in advanced ovarian cancer patient pooled samples known to contain the proteins of interest using the 229-min discovery gradient described above. Correct peptide MRM traces were selected based on overlapping MRM

transitions at the retention time that correspond to the peptide retention time observed in the Orbitrap LC-MS/MS analysis. MRM-initiated detection and sequencing (MIDAS) was also used to generate MS/MS data to confirm peptide identities. Subsequently, three to four most intense MRM transitions were selected for each peptide, and samples containing the targeted proteins were re-analyzed using the shorter 27-min MRM gradient to determine the correct peptide retention times. In addition to the proteins described in this study, a number of other proteins were also monitored. A total of 172 transitions were monitored in the final method. Scheduled MRM was used to reduce the number of concurrent transitions and maximize the dwell time for each transition. The detection window was set at 3 min, and the target scan time was set at 1.8 s. With these parameters, the maximum concurrent transitions were 53, and with the expected peak width of ~22 s, a minimum of 10 data points per chromatographic peak was expected. Data analyses were performed using MultiQuant version 2.1 software (AB SCIEX). Correct peptide MRM transitions have the expected retention times and consistent ratios of overlapping transitions. The most abundant interference-free transition for each peptide was used for quantitation.

Protein levels across samples were determined as previously described [33]. First, each peptide amount was determined by summing the peptide's peak area across all gel slices analyzed. The summed peptide area for each sample was then normalized by dividing it by the average value for that peptide in the advanced cancer samples. Finally, the protein amount in each sample was determined by taking the average of the normalized peptide values (normalized area).

## 2.7. Statistical analyses

Serum levels of candidate biomarkers were compared across sample groups using the Mann-Whitney test, and Bonferroni-adjusted P-values were reported in scatter plots. Results were considered statistically significant if the Bonferroni-adjusted P-value of the test was less than 0.05. Spearman's correlation coefficients were calculated to examine correlations among all tested tropomyosin peptides. For each candidate biomarker, a receiver operator characteristic (ROC) curve was generated and the area under the curve was calculated to reflect biomarker-specific potential sensitivity and specificity for distinguishing non-cancer controls vs. cancer patients.

# 3. Result and discussion

## 3.1. Ambiguities in identification of EOC candidate biomarker isoforms from analysis of xenograft mouse serum

We previously identified 106 human proteins with at least two peptides from the serum of a xenograft mouse model of human ovarian endometrioid cancer (TOV-112D tumors) using a gel-based, multidimensional protein profiling strategy [21]. In that study, GeLC-MRM quantitation of candidate biomarkers in the 20–55 kDa region showed that CLIC1 and the mature form of CTSD were significantly elevated in ovarian cancer patients compared with non-cancer individuals. An interesting candidate biomarker that was not included in that initial validation

experiment was TPM1 isoform 6. This protein was initially identified as a human protein in the xenograft mouse serum based upon the detection of two human-specific peptides and four peptides common to human and mouse (Supplemental Table 1). But in the course of setting up assays for the current validation study, we observed that the two apparently human-specific peptides based upon use of the UniRef100 v. 2007 database were now shared with new mouse sequences in the UniProtKB 2011 database (Supplemental Fig. 1). This meant that if the newer database had been used in the original xenograft mouse discovery experiment, TPM1 would not have been identified as a human protein but would have been categorized

**Table 1 – Peptides identified in TOV-112D xenograft mouse serum and human serum pools.**

| Sequence <sup>a</sup>                                    | Number of unique database entries | Gene                   |
|--|-----------------------------------|------------------------|
| <i>TPM1 peptides identified in xenograft mouse serum</i> |                                   |                        |
| ETAEDVASLN <sup>b</sup>                                  | 6                                 | TPM1                   |
| SLQEQAADAEER <sup>b</sup>                                | 7                                 | TPM1                   |
| (K)LVIIISDLER <sup>b</sup>                               | 18                                | TPM1                   |
| MEIQEIQLK  | 38                                | TPM1, TPM3             |
| IQLVEEELDR <sup>b</sup>                                  | 43                                | TPM1, TPM2, TPM3, TPM4 |
| <i>TPM1 peptides detected in patient serum pools</i>     |                                   |                        |
| ETAEDVASLN <sup>b</sup>                                  | 6                                 | TPM1                   |
| SLQEQAADAEER <sup>b</sup>                                | 7                                 | TPM1                   |
| (K)LVIIISDLER <sup>b</sup>                               | 18                                | TPM1                   |
| MEIQEIQLK  | 38                                | TPM1, TPM3             |
| (R)IQLVEEELDR <sup>b</sup>                               | 43                                | TPM1, TPM2, TPM3, TPM4 |
| AELSEGQVR <sup>b</sup>                                   | 10                                | TPM1                   |
| YEEEEK <sup>c</sup>                                      | 57                                | TPM1, TPM2, TPM3, TPM4 |
| ATDAEADVASLN <sup>c,d</sup>                              | 19                                | TPM1, TPM2             |
| <i>TPM2 peptides detected in patient serum pools</i>     |                                   |                        |
| (K)LVILEGELER <sup>b</sup>                               | 11                                | TPM2, TPM4             |
| (R)IQLVEEELDR <sup>b</sup>                               | 43                                | TPM1, TPM2, TPM3, TPM4 |
| ATDAEADVASLN <sup>c</sup>                                | 19                                | TPM1, TPM2             |
| MELQEMQLK  | 8                                 | TPM2                   |
| SLMASEEYSTK  | 3                                 | TPM2                   |
| YEEEEK <sup>c</sup>                                      | 57                                | TPM1, TPM2, TPM3, TPM4 |
| EDKYEEEEK  | 31                                | TPM2, TPM3, TPM4       |
| CGDLEELK <sup>c</sup>                                    | 6                                 | TPM2, TPM4             |
| <i>TPM3 peptides detected in patient serum pools</i>     |                                   |                        |
| (K)IQLVQQQADAEER <sup>b</sup>                            | 16                                | TPM3                   |
| (R)IQLVEEELDR <sup>b</sup>                               | 43                                | TPM1, TPM2, TPM3, TPM4 |
| MELQEIQLK  | 38                                | TPM1, TPM3             |
| (K)LVIIISDLER  | 19                                | TPM3                   |
| HIAEEADR   | 22                                | TPM3, TPM4             |
| MLDQTLDDLNM  | 12                                | TPM3                   |
| YEEEEK <sup>c</sup>                                      | 57                                | TPM1, TPM2, TPM3, TPM4 |
| EDKYEEEEK  | 31                                | TPM2, TPM3, TPM4       |
| CLSAAEEK   | 14                                | TPM3                   |
| AADAEVVASLN  | 1                                 | TPM3                   |

**Table 1 (continued)**

| Sequence <sup>a</sup>                                | Number of unique database entries | Gene                   |
|--|-----------------------------------|------------------------|
| <i>TPM4 peptides detected in patient serum pools</i> |                                   |                        |
| (K)IQALQQQADEAEDR <sup>b</sup>                       | 3                                 | TPM4                   |
| (K)LVILEGELER <sup>b</sup>                           | 11                                | TPM2, TPM4             |
| EENVGLHQTLDQTLNELNCI                                 | 4                                 | TPM4                   |
| AEGDVAALNR <sup>b</sup>                              | 4                                 | TPM4                   |
| MEIQEMQLK  | 2                                 | TPM4                   |
| YSEKEDKYEEEEK  | 4                                 | TPM4                   |
| CGDLEELK <sup>c</sup>                                | 6                                 | TPM2, TPM4             |
| (R)IQLVEEELDR <sup>b</sup>                           | 43                                | TPM1, TPM2, TPM3, TPM4 |
| HIAEEADR   | 22                                | TPM3, TPM4             |
| EKAEGDVAALNR   | 3                                 | TPM4                   |
| YEEEEK <sup>c</sup>                                  | 57                                | TPM1, TPM2, TPM3, TPM4 |
| EDKYEEEEK  | 31                                | TPM2, TPM3, TPM4       |
| TIDDLK   | 4                                 | TPM4                   |
| ASDAEGDVAALNR  | 1                                 | TPM4                   |

<sup>a</sup> Detected peptides shared by multiple gene products are listed under all matching proteins. Underlined sequences were identified as human in the UniProtKB 2007 database, but also matched a mouse homolog in a later database (see text).

<sup>b</sup> Peptide targeted for MRM. Successful quantitation.

<sup>c</sup> Peptide targeted for MRM. Unsuccessful quantitation.

<sup>d</sup> This peptide is not present in the group of TPM1 isoforms (Fig. 2) defined by peptides identified from the xenograft mouse serum.

as “species indistinguishable”, as all identified peptides would be common to human and mouse. This change in species categorization due to database updates was not a widespread problem, because re-examination of the species specificity of our previously identified putative human peptides revealed that only seven peptides (approximately 1%) were identical to new mouse entries in the 2011 database.

As discussed above, inferring the correct peptide–protein association is often confounded by the presence of shared peptides from homologous proteins, alternative splice variants, or nearly identical database entries [26]. But for MRM quantitation of cancer biomarkers, it is important to accurately determine the peptide–protein relationship to ensure that the correct family member and protein isoform is being quantitated. In order to determine all potential peptide–protein associations for the observed TPM peptides, each peptide identified in the xenograft mouse was searched against the human UniProtKB database (February, 2012) using the BLAST algorithm. All database entries containing the peptide sequence were identified and redundant entries were manually removed. When available, gene names associated with each database entry were extracted (Table 1). These peptides show a great degree of ambiguity in peptide–protein association due to the large number of known TPM isoforms and the very high homology between TPM genes. Tropomyosin is encoded by four genes (TPM1 to TPM4), and each gene can further generate multiple isoforms by the use of alternative promoters and/or alternative RNA splicing. More than 40 distinct TPM sequences have been reported in vertebrates [38,39]. The TPM1 peptides identified from the xenograft model were initially assigned to TPM1 isoform 6

(Q7Z6L8) using the parsimony principle to explain all the identified peptides (Supplemental Table 1). While BLAST indicates that TPM1 is present, the exact TPM1 isoform is ambiguous. Furthermore, the presence of TPM2, TPM3, or TPM4 cannot be excluded and needs to be considered.

### 3.2. Protein homologs detectable in patient serum pools that correlate with EOC

To determine which TPM isoform(s) are detectable in ovarian cancer patient serum, we used an ovarian patient serum protein dataset from in-depth GeLC-MS/MS analysis of the 20–55 kDa region of one benign control and three different late-stage ovarian cancer patient immunoaffinity-depleted serum pools. In addition to TPM isoforms, we searched for additional isoforms and closely related homologs of CLIC1, Peroxiredoxin-6 (PRDX6), and CTSD, as these proteins were previously validated as promising EOC biomarkers from the TOV-112D xenograft model [21]. Results are summarized in Supplemental Table 2. No homologs for PRDX6 or CTSD were identified that had greater than 25% sequence identity, but CLIC4, a CLIC1 homolog, was identified in the ovarian cancer patient sera. Analysis of gel fractions beyond the 20–55 kDa region did not identify additional members of CLIC or TPM protein families. The amounts of all CLIC and TPM proteins identified in the patient sera were quantitated by summing MS intensities for all peptides unique to a specific gene product (Fig. 1). There was evidence of protein products for all four TPM genes, and all gene products showed elevated levels in EOC. However, the different TPM gene products did not show consistent abundance level patterns across all cancer pools,

indicating that these gene products were not coordinately shed into the blood of cancer patients.

In the case of TPM1, one new TPM1-specific peptide and two shared peptides were discovered in the patient serum in addition to all previously identified TPM1 isoform 6 peptides from the xenograft mouse serum (Fig. 2, Table 1, Supplemental Table 2). Based on the newly identified AELSEGQVR peptide, all observed peptides were contained within two TPM1 isoforms, TPM1 variant 6 (Q1ZYL5) or B7Z596. These two sequences share 80% identity and differ from each other at the C-terminus. Distinguishing between these isoforms was not feasible in this study due to the inability to detect any isoform-specific C-terminal peptides. Although no other TPM1 isoforms were conclusively identified in human serum, their presence cannot be ruled out. But the failure to detect any unique peptides to other TPM1 isoforms suggests they are either not present or are present in much lower abundance in human serum.

CLIC1 was confirmed to be both detected and elevated in ovarian cancer patient serum compared to the benign control. Also, CLIC4 was detected by nine specific peptides and showed elevated levels in ovarian cancer patient sera, suggesting that it was an additional EOC candidate biomarker. But, similar to the TPMs, the CLIC gene products did not show consistent abundance level patterns across all cancer pools (Fig. 1).

The detection of CLIC4 in ovarian cancer patient sera by nine specific peptides raised the question as to why only human CLIC1 had been previously identified in the xenograft mouse serum [21]. Examination of the xenograft mouse data showed that CLIC4 had been identified by four peptides; however, all peptides were identical to mouse sequences so this protein was identified as species indistinguishable

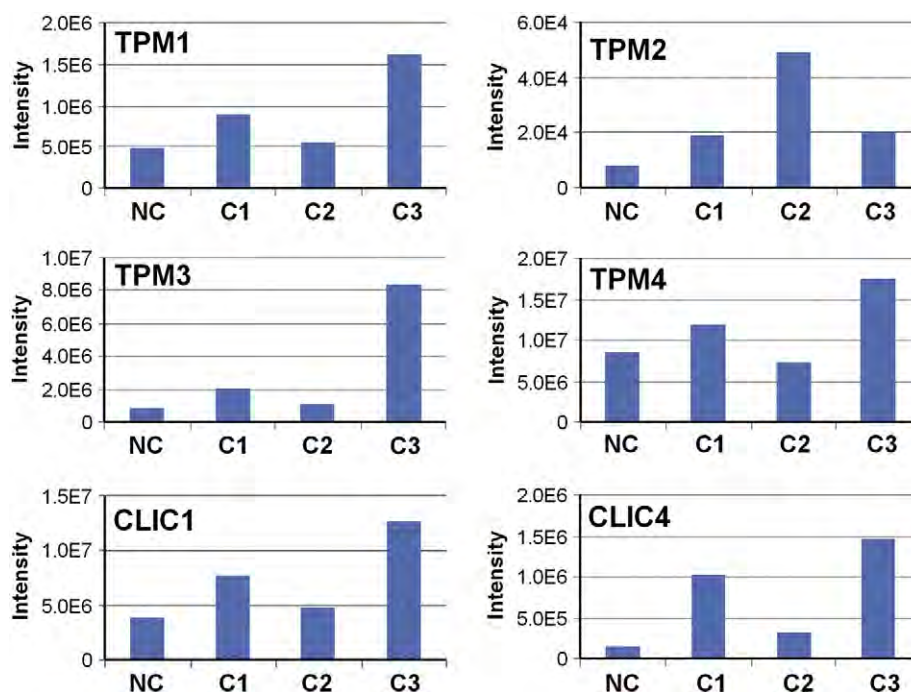


**Fig. 1 – Quantitative comparisons of TPM and CLIC isoforms using label-free discovery mode, GeLC-MS/MS analysis of patient serum pools.** LC-MS chromatograms were aligned and quantitatively compared using the Elucidator software. Intensities of all identified peptides unique to the indicated protein isoform were summed for each of four serum pools (NC — non-cancer; C1, C2, C3 — three different advanced ovarian cancer pools).



|                         |   |
|-------------------------|---|
| SP P09493-5 isoform 5   | -----MA 2   |
| TR D9YZV7 isoform 6     | -----MA 2   |
| TR Q59GR8 variant       | GGRDFTAPGRRGRRRTERPGRGGPALGSQDSRGSRRRAAGLSHCSPPARLPFGAMA 60       |
| TR B7Z722 isoform CRA_i | -----MA 2   |
| TR Q1ZYLS variant 6     | -----MA 2   |
| TR B7Z596 cDNA FLJ55130 | -----MA 2   |
|                         | **  |
| SP P09493-5 isoform 5   | GSSSLEAVRRKIRSLQEQAADAEERAGTLQRELDHERKLRETAADVASLNRIQLVEEE 62     |
| TR D9YZV7 isoform 6     | GSSSLEAVRRKIRSLQEQAADAEERAGTLQRELDHERKLRETAADVASLNRIQLVEEE 62     |
| TR Q59GR8 variant       | GSSSLEAVRRKIRSLQEQAADAEERAGTLQRELDHERKLRETAADVASLNRIQLVEEE 120    |
| TR B7Z722 isoform CRA_i | GSSSLEAVRRKIRSLQEQAADAEERAGTLQRELDHERKLRETAADVASLNRIQLVEEE 62     |
| TR Q1ZYLS variant 6     | GSSSLEAVRRKIRSLQEQAADAEERAGTLQRELDHERKLRETAADVASLNRIQLVEEE 62     |
| TR B7Z596 cDNA FLJ55130 | GSSSLEAVRRKIRSLQEQAADAEERAGTLQRELDHERKLRETAADVASLNRIQLVEEE 62     |
|                         | *****   |
| SP P09493-5 isoform 5   | LDRAQERLATALQKLEAEKKADESERGMKVIESRAQKDEEKMEIQEIQLKEAKHIAEDA 122   |
| TR D9YZV7 isoform 6     | LDRAQERLATALQKLEAEKKADESERGMKVIESRAQKDEEKMEIQEIQLKEAKHIAEDA 122   |
| TR Q59GR8 variant       | LDRAQERLATALQKLEAEKKADESERGMKVIESRAQKDEEKMEIQEIQLKEAKHIAEDA 180   |
| TR B7Z722 isoform CRA_i | LDRAQERLATALQKLEAEKKADESERGMKVIESRAQKDEEKMEIQEIQLKEAKHIAEDA 122   |
| TR Q1ZYLS variant 6     | LDRAQERLATALQKLEAEKKADESERGMKVIESRAQKDEEKMEIQEIQLKEAKHIAEDA 122   |
| TR B7Z596 cDNA FLJ55130 | LDRAQERLATALQKLEAEKKADESERGMKVIESRAQKDEEKMEIQEIQLKEAKHIAEDA 122   |
|                         | *****   |
| SP P09493-5 isoform 5   | DRKYEAVARKLVIIIESDLERAEERAEELSEGKCAELEELKTVTNNLSLEAQAEKYSQKE 182  |
| TR D9YZV7 isoform 6     | DRKYEAVARKLVIIIESDLERAEERAEELSEGKCAELEELKTVTNNLSLEAQAEKYSQKE 182  |
| TR Q59GR8 variant       | DRKYEAVARKLVIIIESDLERAEERAEELSEGKCAELEELKTVTNNLSLEAQAEKYSQKE 240  |
| TR B7Z722 isoform CRA_i | DRKYEAVARKLVIIIESDLERAEERAEELSEGKCAELEELKTVTNNLSLEAQAEKYSQKE 182  |
| TR Q1ZYLS variant 6     | DRKYEAVARKLVIIIESDLERAEERAEELSEGQVRLQEEQLRIMDQTLKALMAAEKYSQKE 182 |
| TR B7Z596 cDNA FLJ55130 | DRKYEAVARKLVIIIESDLERAEERAEELSEGQVRLQEEQLRIMDQTLKALMAAEKYSQKE 182 |
|                         | *****   |
| SP P09493-5 isoform 5   | DRYEEIKVLSDKLKEAETRAEFAERSVTKLEKSIDDLEDQLYQQLEQNRLTN-ELKLA 241    |
| TR D9YZV7 isoform 6     | DRYEEIKVLSDKLKEAETRAEFAERSVTKLEKSIDDLEDQLYQQLEQNRLTN-ELKLA 241    |
| TR Q59GR8 variant       | DRYEEIKVLSDKLKEAETRAEFAERSVTKLEKSIDDLEDQLYQQLEQNRLTN-ELKLA 299    |
| TR B7Z722 isoform CRA_i | DRYEEIKVLSDKLKEAETRAEFAERSVTKLEKSIDDLEEKVAHAKEENLSMHQ-MLDQT 241   |
| TR Q1ZYLS variant 6     | DRYEEIKVLSDKPKEAETRAEFAERSVTKLEKSIDDLEDQLYQQLEQNRLTN-ELKLA 241    |
| TR B7Z596 cDNA FLJ55130 | DRYEEIKVLSDKLKEAETRAEFAERSVTKLEKSIDDLEGLSSVFSILIMVEYQPGKT 242     |
|                         | *****   |
| SP P09493-5 isoform 5   | LNED----- 245   |
| TR D9YZV7 isoform 6     | LNED----- 245   |
| TR Q59GR8 variant       | LNED----- 303   |
| TR B7Z722 isoform CRA_i | LLELNNM----- 248  |
| TR Q1ZYLS variant 6     | LNED----- 245   |
| TR B7Z596 cDNA FLJ55130 | IFQFKGIHIDTLLCTCTFFLCVLWGFSLWLLNS 275                             |
|                         | :   |

**Fig. 2 – Sequence alignment of selected TPM1 Isoforms.** TPM1 isoforms that contain all five xenograft-identified peptides (green highlight) were aligned using the Clustal algorithm. Two additional peptides (gray highlight) were subsequently identified in analyses of ovarian cancer patient sample pools. Inclusion of these peptides suggests the presence of TPM1 Q1ZYLS or B7Z596. The database type (SP, Swiss-Prot entry; TR, TrEMBL entry), identifier, and brief description are indicated for each sequence. Tryptic sites (K or R) are indicated in red. Boxed sequences — peptides used for MRM quantitation.

(Supplemental Table 1). This is not surprising, as the human and mouse CLIC4 sequences are 99% identical (Fig. 3A). While distinguishing between mouse and human CLIC4 is very difficult, distinguishing the different CLIC gene products in human serum is more straightforward, as the four CLIC genes with similar molecular weights exhibit only moderate sequence homology (Fig. 3B). Specifically, the two isoforms, detected in ovarian cancer patient sera, CLIC1 and CLIC4, share 67% identity. Hence, most CLIC peptides observed in the xenograft mouse serum and in patient serum pools were unique to either CLIC1 or CLIC4.

### 3.3. Development of MRM assays for quantitation of CLIC4 and TPM isoforms

CLIC and TPM isoform levels in individual serum samples that included 15 non-cancer control serum samples and 18 late-stage cancer samples were determined using GeLC-MRM. Peptides were selected based on their isoform specificity and

signal intensity in MRM analysis using a 5500 QTRAP mass spectrometer. Peptide candidates for MRM were derived from a combination of the LC-MS/MS analyses reported above and all prior human plasma/serum LC-MS/MS proteomic analyses. In the case of CLIC4, selection of MRM peptides was relatively straightforward because no major homolog issues were encountered with the identified peptides (Fig. 3B). Inclusion of peptides identified from other serum proteome analyses allowed selection of peptides with the strongest MRM signal. For example, the CLIC4 peptide, YLTNAYSRL, was found to produce a stronger MRM signal than some of the peptides discovered in the above analysis of patient serum pools and was therefore used for MRM quantitation (Supplemental Table 3).

Selecting appropriate peptides for MRM quantitation of TPM isoforms in general, and TPM1 specifically, was more complicated due to the large number of TPM isoforms. While TPM1 variant 6 (or isoform B7Z596) was clearly identified in the human serum samples, other TPM1 isoforms also could be present (Fig. 2). Therefore, AELSEQQVR, which was specific



**Fig. 3 – Sequence alignments of CLIC sequences. (A)** Alignment of the 99% identical human (Q9Y696) and mouse (Q9QYB1) CLIC4 sequences. **(B)** Alignment of the four human CLIC gene products that are of similar size and hence could be present in the 25–50 kDa region of serum that was analyzed in this study (CLIC1 – O00299; CLIC2 – O015247; CLIC3 – O95833; CLIC4 – Q9Y696). Database identifiers are from the Swiss-Prot database. Tryptic sites (K or R) are indicated in red. Yellow highlight – peptides identified in the xenograft mouse serum. Gray highlight – peptides identified only in the patient serum pools. Green highlight – peptides identified in both the xenograft mouse and patient serum. Boxed sequences – peptides used for MRM quantitation.

The levels of TPM and CLIC isoforms in individual patient samples were quantitated using GeLC-MRM. As in the case for ELISA assays commonly used to quantitate blood proteins, equal volumes of serum from each patient were processed in the same manner for MRM quantitation. We have previously demonstrated the accuracy, sensitivity, reproducibility, and linearity of peptide calibration curves of the label-free GeLC-MRM approach [33]. Specifically, we showed that the overall analytical pipeline, including duplicate immunodepletions

and technical replicates were reproducible with most peptides displaying CVs of less than 15% [33]. Reproducibility of major protein depletions and trypsin digestions has also been demonstrated by others [22,40]. GeLC-MRM quantitation of the CLIC and TPM peptides and normalized protein values (see [Materials and methods](#)) for individual patient samples are summarized in Supplemental Table 3. TPM peptide

amounts were graphically compared across all serum samples as a first-level test of potential differences across patients in peptides specific for certain isoforms and those shared by multiple isoforms both within the TPM1 isoform group and across gene products (Supplemental Fig. 2). Similarly, the protein levels (normalized and averaged peptide values) across patient samples were compared as shown in Fig. 4A. All the

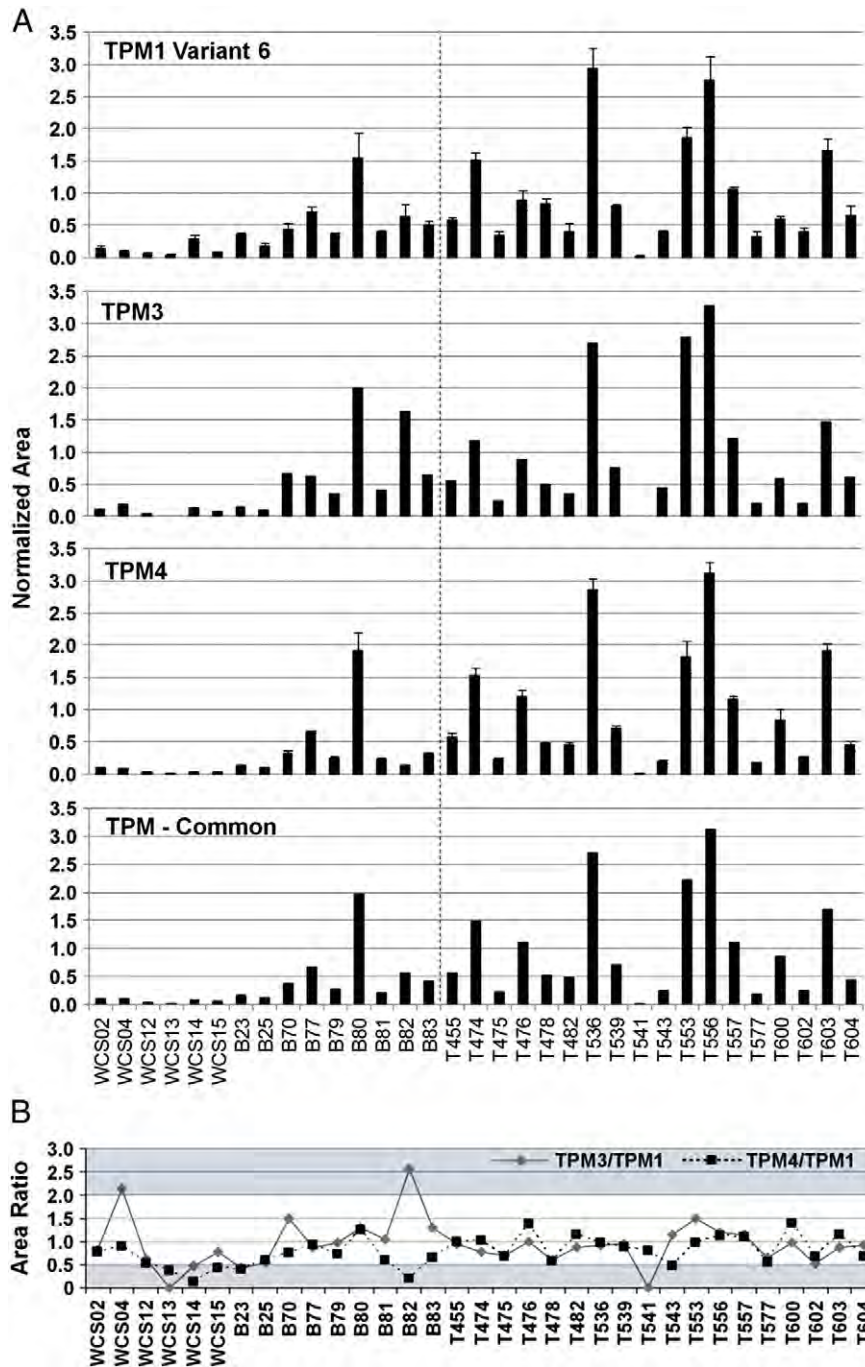


**Fig. 4 – (A)** GeLC-MRM quantitation of tropomyosin proteins in non-cancer individuals (WCS and B series) and individuals with late-stage (T) ovarian cancer. The following peptides were assigned to isoforms: TPM1 variant 6 (ETAADVSLNR, SLQEQADAAEER, LVIHESDLR, AELSEGQVR); TPM3 (IQVLQQQADDAEER); TPM4 (AEGDVAALNR, IQALQQQADEADR, [K] LVILEGELER) and TPM-Common (all family members) ([R]IQLVEELDR). Error bars are standard deviations determined from normalized individual peptide levels for each protein. Individual peptide levels across samples are shown in Supplemental Fig. 2. **(B)** Normalized area ratio plots of TPM3/TPM1 and TPM4/TPM1 to visualize differences in protein levels across samples.

TPM peptides and TPM family members displayed similar quantitative profiles across serum samples (Supplemental Fig. 2, Fig. 4A). However, a substantial number of the individual samples showed substantial differences in pairwise ratios of TPMs (Fig. 4B), suggesting that different TPMs may have differing capacities to distinguish ovarian cancer patients from non-cancer cases. Nevertheless, Spearman's rank correlation coefficient analysis showed that all tropomyosin peptides analyzed here are highly correlated within each patient group with P-values <0.001 (data not shown), indicating a lack of evidence that specific tropomyosins differ from other isoforms in being able to distinguish between ovarian cancer and non-cancer control. Also, if alternative TPM isoforms are present that were not considered in this study and they share some of the quantified peptides, their contribution is either minor or they track with the isoforms quantitated here. Finally, factor analysis shows that all the tropomyosin isoforms analyzed here are measuring the same factor (data not shown), which is consistent with the similar quantitative profiles shown in Fig. 4A. Since the distribution of all tropomyosin peptides is similar, the peptide (K)LVILEGELER that is shared between TPM2 and TPM4 was assigned to TPM4 for the purpose of calculating the TPM4 protein level.

These data show that multiple TPMs that can be detected in human ovarian cancer patient sera in the present cohort appear to fluctuate in abundance levels in concert, although some variations in ratios of family members were observed in individual samples. To determine whether specific TPM family members or combinations of TPMs are superior ovarian cancer biomarkers than TPM1 alone will require testing of additional, larger patient cohorts. Furthermore, specific TPM family members may be more selective for specific clinical applications such as monitoring responses to de-bulking surgery, therapeutic response, or disease reoccurrence. Supporting this possibility, preliminary comparisons of biomarkers in patients with low CA125 levels pre- and post-surgery suggest that TPM3 may be a superior biomarker for this application (data not shown). Tropomyosin is also known to be modified by post-translational modifications such as acetylation and phosphorylation, and the influence of post-translationally modified forms in ovarian cancer diagnosis also could be tested.

GeLC-MRM quantitative results for CLIC1 and CLIC4 protein levels also are shown in Fig. 5, and individual peptide levels are shown in Supplemental Figs. 3 and 4. Similar to TPM isoforms, the normalized area ratio plots between the two CLIC proteins show considerable variations for some of the samples. As

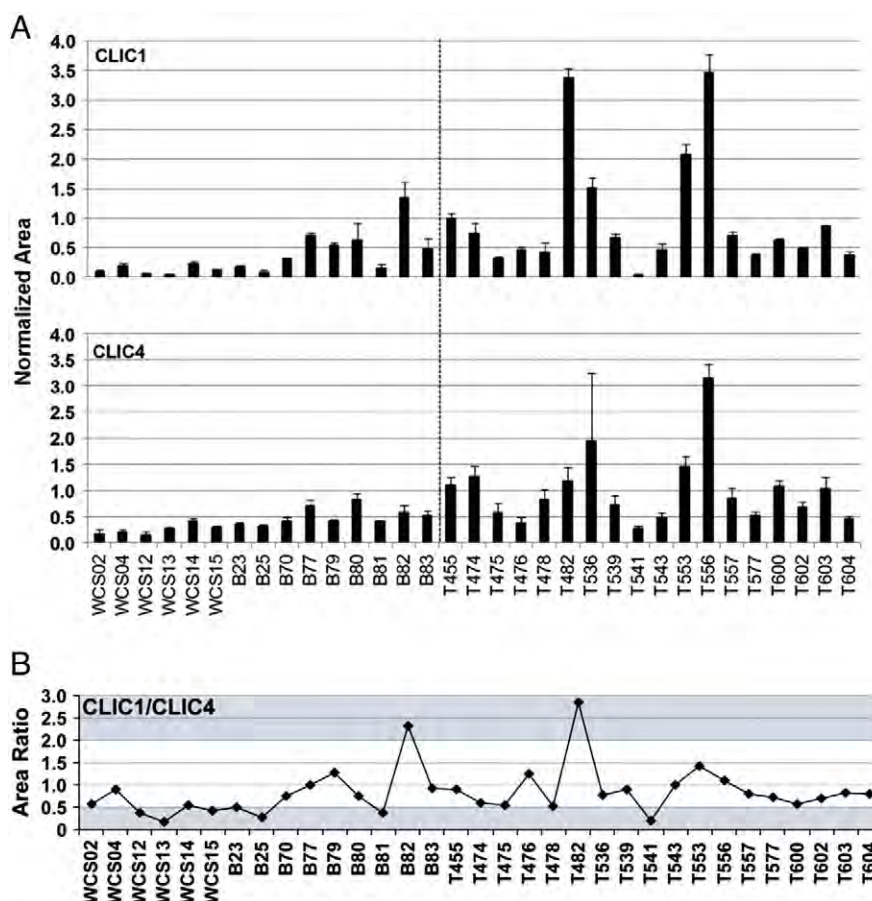


**Fig. 5 – (A)** GeLC-MRM quantitation of CLIC1 and CLIC4 proteins in non-cancer individuals (WCS and B series) and individuals with late-stage (T) ovarian cancer. Peptides used for quantitation are GVTFNVTTVDTK, LAALNPESNTAGLDIFAK and NSNPALNDNLEK for CLIC1, and NSRPEANEALER, YLTNAYSR and EVEIAYSVDVAK for CLIC4. Individual peptide levels across samples are shown in Supplemental Figs. 3 (CLIC1) and 4 (CLIC4). Error bars are standard deviations determined from normalized individual peptide levels for each protein. **(B)** Normalized area ratio plots of CLIC1/CLIC4 to visualize differences in protein levels across samples.



expected, since the same patient samples were used, CLIC1 results were similar to previously reported results for this protein [21]. The moderate differences observed between the two sets of label-free measurements are expected, since the assays were performed at different times and on different instruments. That is, previous analyses were performed on an AB SCIEX 4000 QTRAP and the current results were from a more sensitive AB SCIEX 5500 QTRAP instrument. The CLIC1 measurements were repeated here to provide a direct comparison to CLIC4. For both CLIC proteins, all peptides from the same protein showed similar distributions among the individual patient samples (Supplemental Figs. 3 and 4), indicating that the MRM signals used for quantitation were derived from the same protein and quantitation was not appreciably affected by interfering signals.

### 3.5. CLIC and TPM isoforms can distinguish EOC from non-cancer cases

The capacities of the CLIC and TPM isoforms to distinguish EOC cases were assessed using the GeLC-MRM quantitation data (Supplemental Table 3). A two-way comparison between the non-cancer and cancer groups using scatter plots and the

Mann-Whitney test showed that all isoforms could significantly distinguish ( $P < 0.05$ ) between cancer and non-cancer (Fig. 6). Based on the  $P$ -value, CLIC4 appeared to be the best candidate in distinguishing cancer from non-cancer and TPM3 was the weakest, although this relative ranking could easily change as additional patients are tested. Future analysis of larger cohorts will allow us to more definitively identify which proteins in these two protein families can most reliably distinguish non-cancer from ovarian cancer.

To evaluate the potential diagnostic efficacy for each of these proteins, receiver operating characteristic (ROC) curve analyses were performed on the non-cancer and cancer groups (Fig. 7). Consistent with the Mann-Whitney test, CLIC4 showed the largest area under the curve (AUC) and TPM3 showed the lowest area. In future studies of larger patient cohorts, we plan to test these CLIC and TPM homologs in parallel with other biomarkers to identify optimal biomarker combinations that may outperform any single biomarker for detection and clinical monitoring of EOC.

To our knowledge, the plasma levels of CLIC4 and products of different TPM genes have not been reported previously in serum from ovarian cancer patients. CLIC4 is an interesting multifunctional protein that has been shown to be highly

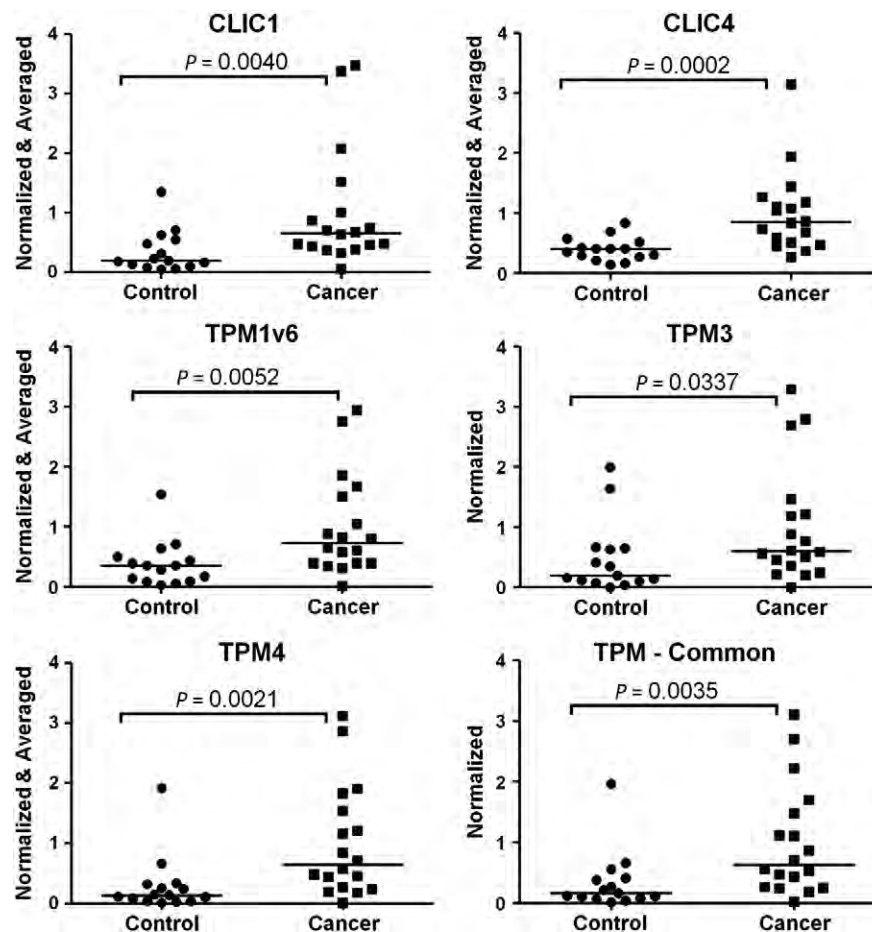
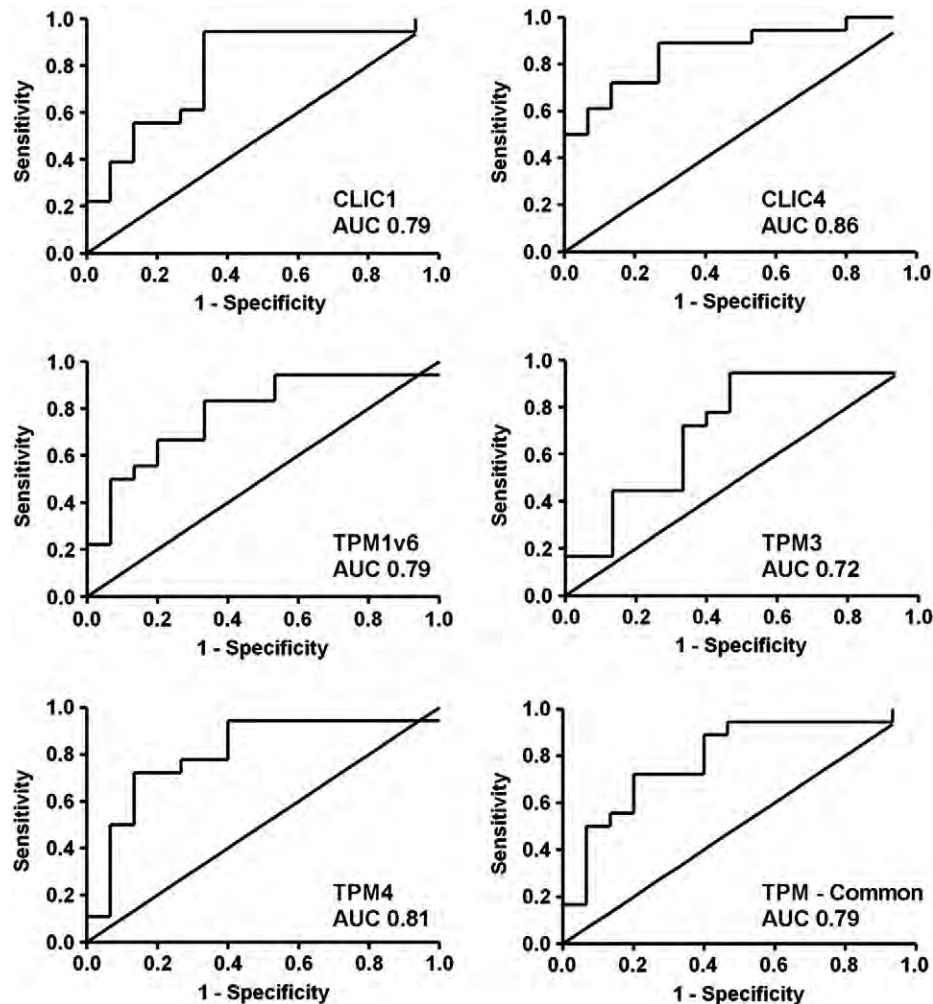


Fig. 6 – Scatter plots showing GeLC-MRM quantitation of the CLIC and TPM isoforms in non-cancer controls ( $n = 15$ ), and ovarian cancer patients ( $n = 18$ ).  $P$ -values were calculated using the Mann-Whitney test with Bonferroni adjustment. Horizontal bars in each group indicate the median serum level of the protein. Peptides associated with each tropomyosin isoform are shown in Fig. 4.





**Fig. 7 – ROC curves of the CLIC and TPM isoforms.** ROC curves were generated from non-cancer controls and ovarian cancer patients' datasets. The area under the ROC curve is indicated for each candidate. The peptides associated with each tropomyosin isoform are shown in Fig. 4.

expressed in ovarian cancer stroma and may play an important role in cancer development [41,42]. Since CLIC4 has the highest AUC of any of the biomarkers reported here or in our previous xenograft mouse biomarker validation study [21], it may be the best biomarker within this group, but this must be confirmed in further studies. The tropomyosins are a family of actin filament-binding proteins that have a well-defined central role in regulating muscle contraction and cytoskeletal organization in non-muscle cells. Decreased expression of specific TPMs has been commonly associated with the transformed phenotype and has been reported for cancer cells and tissues, including EOC [43–45]. The serological levels of TPMs have not been well studied, although high plasma levels of TPM4 have been associated with asbestos exposure [46] and increased levels of TPM serum antibodies were observed in colorectal cancer patients [47].

Although these proteins show substantial promise as EOC biomarkers, the performance of these markers for early detection and/or clinical management of disease after initial diagnosis must be determined in larger cohorts collected from different sites, longitudinal prediagnostic

blood specimens, and specimens collected throughout the therapeutic treatment.

#### 4. Conclusions

In the current study, we assessed the potential utility of multiple CLIC and TPM family members as serological biomarkers of ovarian cancer. We demonstrated that quantitative MRM assays could be set up to distinguish between all gene products in these families that were detectable in pools of ovarian cancer patient sera. Although in the case of very complex protein families with many highly homologous gene products and isoforms, the presence of additional highly homologous isoforms could not be ruled out. Nonetheless, by using a combination of unique and shared peptides together with correlation and factor analysis, we determined that any unidentified isoforms either do not occur at a significant level or change in parallel with the isoforms explicitly defined by unique peptides. In summary, we found that in addition to the previously identified CLIC1, CLIC4 and all four TPM gene

products (TPM1, TPM2, TPM3, and TPM4) are significantly elevated in ovarian cancer patients compared with non-cancer controls. Further testing of larger patient cohorts is needed to determine whether the multiple CLIC and TPM family members consistently correlate with each other. The differing ratios of family member pairs indicate incomplete correlation and suggest that specific family members may be superior for specific biomarker applications.

## Acknowledgments

This work was supported by National Institutes of Health grant CA131582 to D.W.S., an institutional grant to The Wistar Institute (NCI Cancer Core Grant CA010815), and the Reproductive Scientist Development Program (NIH grant 5K12HD00849). We gratefully acknowledge the use of the Wistar Institute Proteomics Core Facility and Dr. Dionyssios Katsaros, University of Turin, Turin, Italy, for providing patient serum specimens. We gratefully acknowledge the administrative assistance of Mea Fuller.

## Appendix A. Supplementary data

Supplementary data to this article can be found online at <http://dx.doi.org/10.1016/j.jprot.2013.06.016>.

## REFERENCES

- [1] Siegel R, Naishadham D, Jemal A. Cancer statistics, 2012. *CA Cancer J Clin* 2012;62:10–29.
- [2] Cannistra SA. Cancer of the ovary. *N Engl J Med* 2004;351:2519–29.
- [3] Mutch DG. Surgical management of ovarian cancer. *Semin Oncol* 2002;29:3–8.
- [4] Klug TL, Bast Jr RC, Niloff JM, Knapp RC, Zurawski Jr VR. Monoclonal antibody immunoradiometric assay for an antigenic determinant (CA 125) associated with human epithelial ovarian carcinomas. *Cancer Res* 1984;44:1048–53.
- [5] Anastasi E, Marchei GG, Viggiani V, Gennarini G, Frati L, Reale MG. HE4: a new potential early biomarker for the recurrence of ovarian cancer. *Tumour Biol* 2010;31:113–9.
- [6] Zhang Z, Bast Jr RC, Yu Y, Li J, Sokoll LJ, Rai AJ, et al. Three biomarkers identified from serum proteomic analysis for the detection of early stage ovarian cancer. *Cancer Res* 2004;64:5882–90.
- [7] Moore RG, Jabre-Raughley M, Brown AK, Robison KM, Miller MC, Allard WJ, et al. Comparison of a novel multiple marker assay vs the Risk of Malignancy Index for the prediction of epithelial ovarian cancer in patients with a pelvic mass. *Am J Obstet Gynecol* 2010;203:228.e1–6.
- [8] Moss EL, Hollingworth J, Reynolds TM. The role of CA125 in clinical practice. *J Clin Pathol* 2005;58:308–12.
- [9] Nick AM, Sood AK. The ROC 'n' role of the multiplex assay for early detection of ovarian cancer. *Nat Clin Pract Oncol* 2008;5:568–9.
- [10] Gagne JP, Gagne P, Hunter JM, Bonicalzi ME, Lemay JF, Kelly I, et al. Proteome profiling of human epithelial ovarian cancer cell line TOV-112D. *Mol Cell Biochem* 2005;275:25–55.
- [11] Dai L, Li C, Shedden KA, Misek DE, Lubman DM. Comparative proteomic study of two closely related ovarian endometrioid adenocarcinoma cell lines using cIEF fractionation and pathway analysis. *Electrophoresis* 2009;30:1119–31.
- [12] Zhu Y, Wu R, Sangha N, Yoo C, Cho KR, Shedden KA, et al. Classifications of ovarian cancer tissues by proteomic patterns. *Proteomics* 2006;6:5846–56.
- [13] Bengtsson S, Krogh M, Szigyarto CA, Uhlen M, Schedvins K, Silfversward C, et al. Large-scale proteomics analysis of human ovarian cancer for biomarkers. *J Proteome Res* 2007;6:1440–50.
- [14] Gortzak-Uzan L, Ignatchenko A, Evangelou AI, Agochiya M, Brown KA, St Onge P, et al. A proteome resource of ovarian cancer ascites: integrated proteomic and bioinformatic analyses to identify putative biomarkers. *J Proteome Res* 2008;7:339–51.
- [15] Kuk C, Kulasingam V, Gunawardana CG, Smith CR, Batruch I, Diamandis EP. Mining the ovarian cancer ascites proteome for potential ovarian cancer biomarkers. *Mol Cell Proteomics* 2009;8:661–9.
- [16] Faca VM, Ventura AP, Fitzgibbon MP, Pereira-Faca SR, Pitteri SJ, Green AE, et al. Proteomic analysis of ovarian cancer cells reveals dynamic processes of protein secretion and shedding of extra-cellular domains. *PLoS One* 2008;3:e2425.
- [17] Gunawardana CG, Kuk C, Smith CR, Batruch I, Soosaipillai A, Diamandis EP. Comprehensive analysis of conditioned media from ovarian cancer cell lines identifies novel candidate markers of epithelial ovarian cancer. *J Proteome Res* 2009;8:4705–13.
- [18] Wei BR, Hoover SB, Ross MM, Zhou W, Meani F, Edwards JB, et al. Serum S100A6 concentration predicts peritoneal tumor burden in mice with epithelial ovarian cancer and is associated with advanced stage in patients. *PLoS One* 2009;4:e7670.
- [19] Pitteri SJ, JeBailey L, Faca VM, Thorpe JD, Silva MA, Ireton RC, et al. Integrated proteomic analysis of human cancer cells and plasma from tumor bearing mice for ovarian cancer biomarker discovery. *PLoS One* 2009;4:e7916.
- [20] He Y, Wu X, Liu X, Yan G, Xu C. LC-MS/MS analysis of ovarian cancer metastasis-related proteins using a nude mouse model: 14-3-3 zeta as a candidate biomarker. *J Proteome Res* 2010;9:6180–90.
- [21] Tang HY, Beer LA, Chang-Wong T, Hammond R, Gimotty P, Coukos G, et al. A xenograft mouse model coupled with in-depth plasma proteome analysis facilitates identification of novel serum biomarkers for human ovarian cancer. *J Proteome Res* 2012;11:678–91.
- [22] Anderson L, Hunter CL. Quantitative mass spectrometric multiple reaction monitoring assays for major plasma proteins. *Mol Cell Proteomics* 2006;5:573–88.
- [23] Dorn B, Aebersold R. Options and considerations when selecting a quantitative proteomics strategy. *Nat Biotechnol* 2010;28:710–21.
- [24] Sherman J, McKay MJ, Ashman K, Molloy MP. How specific is my SRM?: the issue of precursor and product ion redundancy. *Proteomics* 2009;9:1120–3.
- [25] Duncan MW, Yergey AL, Patterson SD. Quantifying proteins by mass spectrometry: the selectivity of SRM is only part of the problem. *Proteomics* 2009;9:1124–7.
- [26] Nesvizhskii AI, Aebersold R. Interpretation of shotgun proteomic data: the protein inference problem. *Mol Cell Proteomics* 2005;4:1419–40.
- [27] Rodriguez-Pineiro AM, de la Cadena MP, Lopez-Saco A, Rodriguez-Berrocá FJ. Differential expression of serum clusterin isoforms in colorectal cancer. *Mol Cell Proteomics* 2006;5:1647–57.
- [28] Kriventseva EV, Koch I, Apweiler R, Vingron M, Bork P, Gelfand MS, et al. Increase of functional diversity by alternative splicing. *Trends Genet* 2003;19:124–8.
- [29] Garcia-Blanco MA, Baraniak AP, Lasda EL. Alternative splicing in disease and therapy. *Nat Biotechnol* 2004;22:535–46.

- [30] Costenoble R, Picotti P, Reiter L, Stallmach R, Heinemann M, Sauer U, et al. Comprehensive quantitative analysis of central carbon and amino-acid metabolism in *Saccharomyces cerevisiae* under multiple conditions by targeted proteomics. *Mol Syst Biol* 2011;7:464.
- [31] Zulak KG, Lippert DN, Kuzyk MA, Domanski D, Chou T, Borchers CH, et al. Targeted proteomics using selected reaction monitoring reveals the induction of specific terpene synthases in a multi-level study of methyl jasmonate-treated Norway spruce (*Picea abies*). *Plant J* 2009;60:1015–30.
- [32] Wang Q, Chaerkady R, Wu J, Hwang HJ, Papadopoulos N, Kopelovich L, et al. Mutant proteins as cancer-specific biomarkers. *Proc Natl Acad Sci U S A* 2011;108:2444–9.
- [33] Tang HY, Beer LA, Barnhart KT, Speicher DW. Rapid verification of candidate serological biomarkers using gel-based, label-free multiple reaction monitoring. *J Proteome Res* 2011;10:4005–17.
- [34] Beer LA, Tang HY, Sriswasdi S, Barnhart KT, Speicher DW. Systematic discovery of ectopic pregnancy serum biomarkers using 3-D protein profiling coupled with label-free quantitation. *J Proteome Res* 2011;10:1126–38.
- [35] Rausch ME, Beer L, Sammel MD, Takacs P, Chung K, Shaunik A, et al. A disintegrin and metalloprotease protein-12 as a novel marker for the diagnosis of ectopic pregnancy. *Fertil Steril* 2011;95:1373–8.
- [36] Beer LA, Tang HY, Barnhart KT, Speicher DW. Plasma biomarker discovery using 3D protein profiling coupled with label-free quantitation. *Methods Mol Biol* 2011;728:3–27.
- [37] Wang H, Tang HY, Tan GC, Speicher DW. Data analysis strategy for maximizing high-confidence protein identifications in complex proteomes such as human tumor secretomes and human serum. *J Proteome Res* 2011;10:4993–5005.
- [38] Gunning PW, Schevzov G, Kee AJ, Hardeman EC. Tropomyosin isoforms: divining rods for actin cytoskeleton function. *Trends Cell Biol* 2005;15:333–41.
- [39] Choi C, Kim D, Kim S, Jeong S, Song E, Helfman DM. From skeletal muscle to cancer: insights learned elucidating the function of tropomyosin. *J Struct Biol* 2012;177:63–9.
- [40] Liu T, Qian WJ, Mottaz HM, Gritsenko MA, Norbeck AD, Moore RJ, et al. Evaluation of multiprotein immunoaffinity subtraction for plasma proteomics and candidate biomarker discovery using mass spectrometry. *Mol Cell Proteomics* 2006;5:2167–74.
- [41] Yao Q, Qu X, Yang Q, Wei M, Kong B. CLIC4 mediates TGF-beta1-induced fibroblast-to-myofibroblast transdifferentiation in ovarian cancer. *Oncol Rep* 2009;22:541–8.
- [42] Shukla A, Yuspa SH. CLIC4 and Schnurri-2: a dynamic duo in TGF-beta signaling with broader implications in cellular homeostasis and disease. *Nucleus* 2010;1:144–9.
- [43] Helfman DM, Flynn P, Khan P, Saeed A. Tropomyosin as a regulator of cancer cell transformation. *Adv Exp Med Biol* 2008;644:124–31.
- [44] Raval GN, Bharadwaj S, Levine EA, Willingham MC, Geary RL, Kute T, et al. Loss of expression of tropomyosin-1, a novel class II tumor suppressor that induces anoikis, in primary breast tumors. *Oncogene* 2003;22:6194–203.
- [45] Chow SN, Chen RJ, Chen CH, Chang TC, Chen LC, Lee WJ, et al. Analysis of protein profiles in human epithelial ovarian cancer tissues by proteomic technology. *Eur J Gynaecol Oncol* 2010;31:55–62.
- [46] Rostila A, Puustinen A, Toljamo T, Vuopala K, Lindstrom I, Nyman TA, et al. Peroxiredoxins and tropomyosins as plasma biomarkers for lung cancer and asbestos exposure. *Lung Cancer* 2012;77:450–9.
- [47] Lu H, Goodell V, Disis ML. Targeting serum antibody for cancer diagnosis: a focus on colorectal cancer. *Expert Opin Ther Targets* 2007;11:235–44.

# Three-dimensional culture sensitizes epithelial ovarian cancer cells to EZH2 methyltransferase inhibition

Michael D. Amatangelo,<sup>1,†</sup> Azat Garipov,<sup>1,4,†</sup> Hua Li,<sup>1</sup> Jose R. Conejo-Garcia,<sup>2</sup> David W. Speicher<sup>3</sup> and Rugang Zhang<sup>1,\*</sup>

<sup>1</sup>Gene Expression and Regulation Program; The Wistar Institute; Philadelphia, PA USA; <sup>2</sup>Tumor Microenvironment and Metastasis Program; The Wistar Institute; Philadelphia, PA USA; <sup>3</sup>Molecular and Cellular Oncogenesis Program; The Wistar Institute; Philadelphia, PA USA; <sup>4</sup>Kazan Federal University; Kazan, Russia

<sup>†</sup>These authors contributed equally to this work.

**Keywords:** epithelial ovarian cancer, EZH2, EZH2 inhibitor GSK343, 3D culture, apoptosis

**Abbreviations:** 2D, two-dimensional culture; 3D, three-dimensional culture; DLBCL, diffuse large B cell lymphoma; ECM, extracellular matrix; EOC, epithelial ovarian cancer; EZH2, enhancer of zeste homolog 2; H3K27Me3, lysine 27 tri-methylated histone H3; HOSE, human ovarian surface epithelial cells; PRC2, polycomb repressive complex 2

Inhibitors of EZH2 methyltransferase activity have been demonstrated to selectively suppress the growth of diffused large B cell lymphoma (DLBCL) cells with gain-of-function mutations in EZH2, while exhibiting very limited effects on the growth of DLBCL cells with wild-type EZH2. Given that EZH2 is often overexpressed but not mutated in solid tumors, it is important to investigate the determinants of sensitivity of solid tumor cells to EZH2 inhibitors. In the current study, we show that three-dimensional (3D) culture of epithelial ovarian cancer (EOC) cells that overexpress EZH2 sensitizes these cells to EZH2 methyltransferase inhibition. Treatment of EOC cells with GSK343, a specific inhibitor of EZH2 methyltransferase, decreases the level of H3K27Me3, the product of EZH2's enzymatic activity. However, GSK343 exhibited limited effects on the growth of EOC cells in conventional two-dimensional (2D) culture. In contrast, GSK343 significantly suppressed the growth of EOC cells cultured in 3D matrigel extracellular matrix (ECM), which more closely mimics the tumor microenvironment in vivo. Notably, GSK343 induces apoptosis of EOC cells in 3D but not 2D culture. In addition, GSK343 significantly inhibited the invasion of EOC cells. In summary, we show that the 3D ECM sensitizes EOC cells to EZH2 methyltransferase inhibition, which suppresses cell growth, induces apoptosis and inhibits invasion. Our findings imply that in EZH2 wild-type solid tumors, the ECM tumor microenvironment plays an important role in determining sensitivity to EZH2 inhibition and suggest that targeting the ECM represents a novel strategy for enhancing EZH2 inhibitor efficacy.

## Introduction

Enhancer of zeste homolog 2 (EZH2) is the catalytic subunit of polycomb repressive complex 2 (PRC2), which plays an important role in epigenetic gene silencing.<sup>1,2</sup> PRC2 functions to silence gene expression by tri-methylating the lysine 27 residue of histone H3 (H3K27) associated with target genes.<sup>1,2</sup> EZH2 has been shown to target genes involved in a variety of biological processes, such as cell proliferation and apoptosis.<sup>3</sup> Epithelial ovarian cancer (EOC) is currently the deadliest of all gynecological cancers,<sup>4</sup> highlighting the urgent need to identify new targets for developing therapeutics for EOC. EOCs are classified into distinct histological types, including serous, mucinous, endometrioid and clear cell. The most common histology of EOC is serous (~60% of all cancers).<sup>5</sup> Recently, an alternative classification has been proposed, in which EOC is broadly divided into two types.<sup>6</sup> Type

I EOC includes mucinous, low-grade serous, low-grade endometrioid and clear cell carcinomas, and type II EOC includes high-grade serous carcinomas, which is the most lethal histosubtype.<sup>6</sup> EZH2 is often overexpressed in all histosubtypes of EOCs, and its expression promotes cell proliferation and invasion, inhibits apoptosis and enhances angiogenesis in EOCs.<sup>7,8</sup> Therefore, inhibiting EZH2/PRC2 activity might represent an attractive strategy for developing urgently needed EOC therapeutics.<sup>9</sup>

Normal epithelial tissues exist as well-organized polarized single cell layers regulated by the surrounding microenvironment and extracellular matrix (ECM).<sup>10-12</sup> During cancer progression this organization is disrupted as cancer cells proliferate and invade into the ECM.<sup>12,13</sup> Significantly, this process is not well replicated in the conventional two-dimensional (2D) tissue culture environment that is often used to assay potential therapeutics. It has been shown that non-transformed epithelial cells cultured with

\*Correspondence to: Rugang Zhang; Email: rzhang@wistar.org  
Submitted: 04/16/13; Revised: 05/20/13; Accepted: 05/24/13  
<http://dx.doi.org/10.4161/cc.25163>



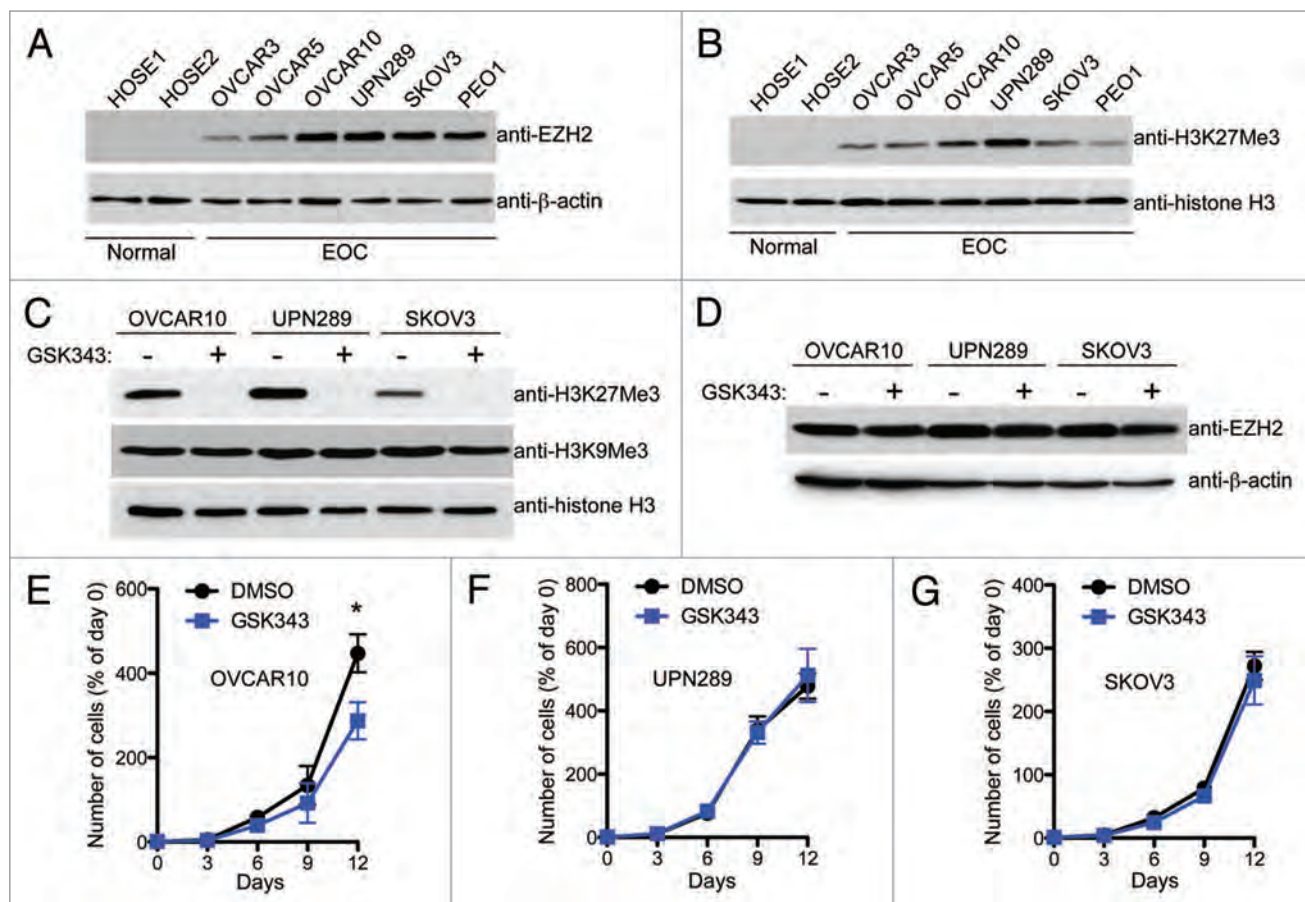


**Figure 1.** The EZH2 inhibitor GSK343 exhibits limited effects on the growth of human EOC cells under conventional 2D monolayer culture. (A) Expression of EZH2 and  $\beta$ -actin in two individual batches of normal human ovarian surface epithelial (HOSE) cells and indicated human EOC cell lines was determined by immunoblotting. (B) Same as (A) but for H3K27Me3 and histone H3 expression determined by immunoblotting. (C) Expression of H3K27Me3, H3K9Me3 and histone H3 was determined in the indicated EOC cell lines by immunoblotting after 3 d of treatment with GSK343 (1  $\mu$ M) or vehicle control (0.1% DMSO). (D) Same as (C) but for EZH2 and  $\beta$ -actin expression determined by immunoblotting. (E–G) Cell growth curves for OVCAR10, UPN289 and SKOV3 cell lines treated with GSK343 (1  $\mu$ M) or vehicle control (0.1% DMSO) over 12 d. Media was changed and cells counted every 3 d, time points represent the mean of three independent experiments with SD, \* $p < 0.05$ .

reconstituted basement membrane form hollow, growth-arrested, polarized three-dimensional (3D) structures that have many features of epithelial cells grown *in vivo*.<sup>12,14</sup> Tumorigenic cells cultured in the same way often form large, solid, proliferating and invasive structures characteristic of *in vivo* tumors.<sup>12</sup> These 3D models have led to powerful insights into tumor growth, behavior and drug responses that would not be possible in conventional 2D monolayer cultures.<sup>11</sup>

GSK343 is a cofactor S-(S'-adenosyl)-L-methionine competitive EZH2 methyltransferase inhibitor.<sup>15</sup> Notably, GSK343 is highly selective for EZH2 over a number of other methyltransferases such as SUV39H1 and G9a, with selectivity greater than 1,000-fold.<sup>15</sup> Here we examined the effects of GSK343 on the growth and invasion of human EOC cells. Interestingly, our data indicates that EZH2 inhibition is significantly more potent in suppressing the growth of EOC cells in 3D, which more closely mimics the tumor microenvironment *in vivo* compared with conventional 2D monolayer culture.<sup>11</sup> In addition, we show that this correlates with induction of apoptosis of human EOC cells in 3D but not 2D cultures. Further, we show that GSK343 suppresses

the invasion of human EOC cells. These data establish that 3D ECM plays an important role in determining the sensitivity of EOC cells to EZH2 inhibitors and imply that EZH2 methyltransferase activity promotes aberrant 3D phenotypes in EOC cells.

## Results

**EZH2 inhibitor exhibited limited effects on the growth of human EOC cells under conventional 2D monolayer culture.** Compared with normal human ovarian surface epithelial (HOSE) cells, EZH2 is expressed at a higher level in EOC cell lines (Fig. 1A). Consistently, the levels of H3K27Me3, the product of EZH2 methyltransferase enzymatic activity,<sup>1</sup> are also higher in EOC cells compared with HOSE cells (Fig. 1B). We sought to determine the effects of GSK343 on the malignant phenotypes of EOC cells. Toward this goal, we titrated GSK343 concentration in two EOC cell lines that express high levels of EZH2, OVCAR10 and SKOV3 (Fig. S1A and B). We observed a dose-dependent decrease in the level of H3K27Me3 in cells treated

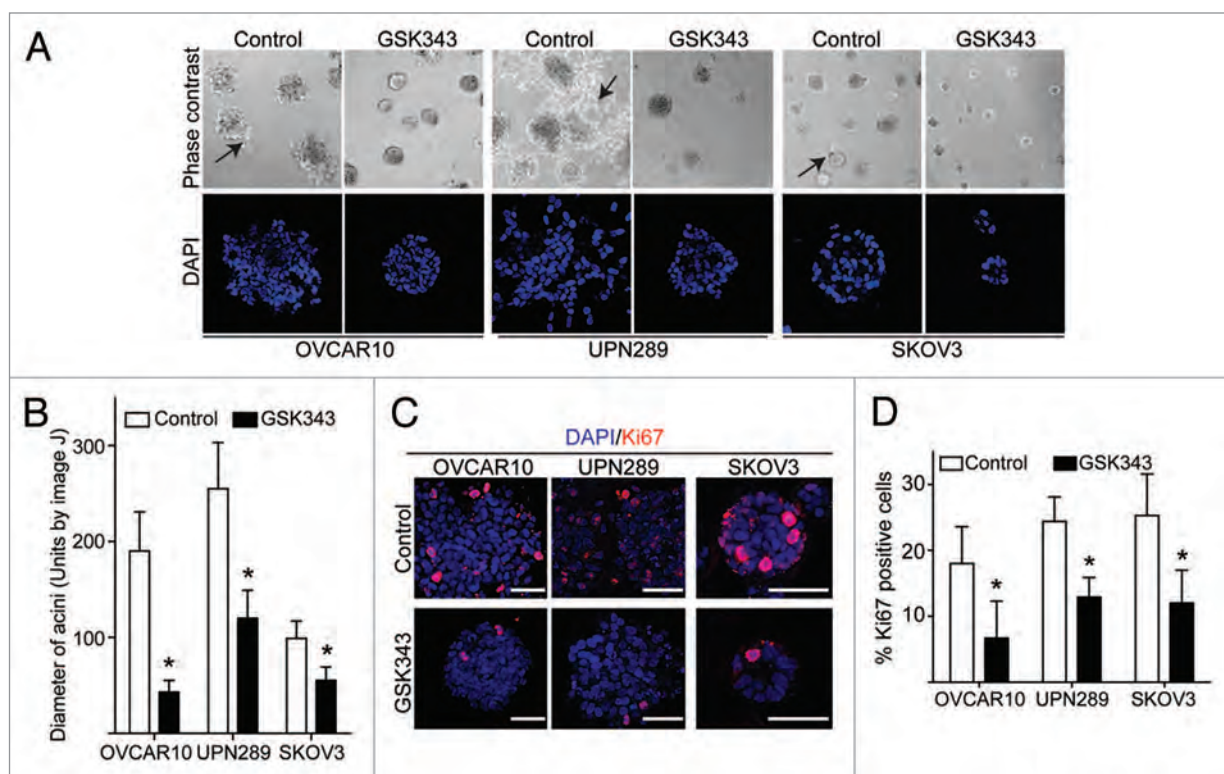


**Figure 2.** The EZH2 inhibitor GSK343 significantly suppresses the growth of human EOC cells in 3D cultures. **(A)** Indicated EOC cells were cultured in 3D Matrigel and treated with GSK343 (1  $\mu$ M) or vehicle control (0.1% DMSO) for 12 d. 3D acini were examined by phase contrast (top) or stained with the nuclei fluorescence dye DAPI (bottom). Note differences in acini size and shape. Arrows indicate examples of invasive structures observed in EOC 3D cultures. **(B)** Quantification of acini size formed by the indicated EOC cells treated with GSK343 (1  $\mu$ M) or vehicle control (0.1% DMSO) after 12 d of growth in Matrigel. Mean of three independent experiments with SD, \* $p < 0.05$ . **(C)** Same as **(A)** but stained for Ki-67 expression. Bar = 40  $\mu$ m. **(D)** Quantification of **(C)**. Ki-67 positive staining cells in the indicated EOC cells treated with GSK343 (1  $\mu$ M) or vehicle control (0.1% DMSO) after 12 d of growth in Matrigel. Numbers represent mean number of cells counted in 5 acini for each condition. Mean of three independent experiments with SD, \* $p < 0.05$ .

with GSK343 and a > 90% reduction in the level of H3K27Me3 in EOC cells treated with 1  $\mu$ M GSK343 for 72 h (Fig. 1C; Fig. S1A and B). In contrast, levels of H3K9Me3, which are generated by different histone methyltransferases such as SUV39H1 and SETDB1<sup>16</sup> were not affected by GSK343 (Fig. 1C). This further demonstrates the specificity of GSK343 as an EZH2 methyltransferase inhibitor. Notably, GSK343 treatment had no appreciable effect on EZH2 expression (Fig. 1D; Fig. S1A and B), suggesting that the effects observed in GSK343 treated cells are not due to loss of EZH2 expression. Together, we conclude that the EZH2 inhibitor GSK343 efficiently decreases the level of H3K27Me3 in EOC cells.

Expression of EZH2 positively correlates with markers of cellular proliferation in primary EOC specimens, and its knock-down suppresses the growth of human EOC cells.<sup>7</sup> Thus, we sought to determine the effects of GSK343 on growth of EOC cells with high EZH2 expression, such as OVCAR10, UPN289 and SKOV3, under conventional 2D monolayer cultures. We treated these EOC cells with 1  $\mu$ M GSK343 for a period of 12 d, with fresh treatment every 3 d, because we observed a > 90% reduction of H3K27Me3 levels in these cells after 3 d of GSK343 treatment (Fig. 1C; Fig. S1A and B). Interestingly, although treatment with GSK343 resulted in a minor but statistically significant decrease in growth of OVCAR10 cells over

12 d, GSK343 had minimal to no effects on the growth of UPN289 and SKOV3 cells (Fig. 1E–G). Similarly, we observed that GSK343 has no statistically significant effects on the growth of EOC cells with relatively low EZH2 expression, such as OVCAR3, OVCAR5 and PEO1 (Fig. S1C–E), despite efficient reduction of H3K27Me3 levels (Fig. S1F). This suggests that the inability of GSK343 to suppress the growth of EOC cells is not due to variations in the levels of EZH2 expression. Based on these results, we conclude that EZH2 inhibitor has limited effects on the growth of human EOC cells under conventional 2D monolayer culture.

**EZH2 inhibitor significantly suppresses the growth of human EOC cells in 3D cultures.** It is well established that the tumor microenvironment and ECM play an important role in regulating tumor phenotypes, in part through epigenetic mechanisms.<sup>17</sup> Accordingly, 3D culture utilizing ECM components is often used to mimic the in vivo tumor microenvironment.<sup>10</sup> We hypothesized that cellular interactions with the ECM might regulate the effects that EZH2 inhibition has on EOC cells. Thus, we sought to determine the effects of GSK343 on the growth of EOC cells in 3D cultures using a Matrigel basement membrane ECM. Significantly, we observed that GSK343 suppressed the size of acini formed by EOC cell lines (Fig. 2A and B). In addition, we observed that treatment of EOC cells with GSK343 resulted



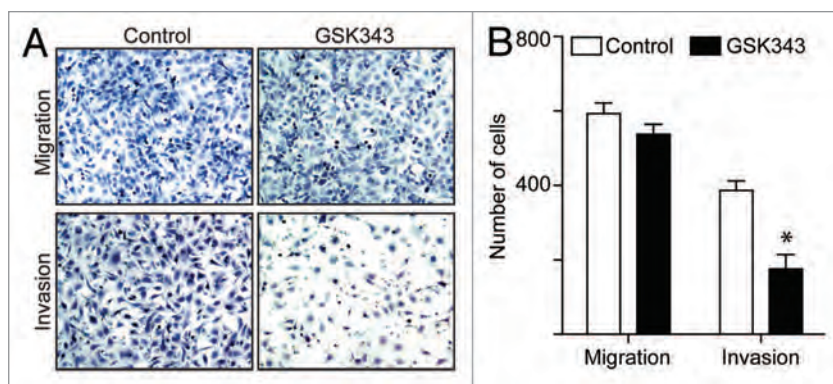


**Figure 3.** The EZH2 inhibitor GSK343 suppresses invasion of human EOC cells. (A) Equal number of SKOV3 cells treated with 1  $\mu$ M GSK343 or vehicle control (0.1% DMSO) were assayed for migration through uncoated control membrane or invasion through Matrigel-coated membrane. The cells migrated through control membrane or invaded through Matrigel-coated membrane were stained with 1% crystal violet in PBS. (B) Quantification of (A). Number of SKOV3 cells migrated through control membrane or invaded through Matrigel-coated membrane. Numbers represent mean of three independent experiments. \* $p < 0.05$ .

in a more compact acini structure that is characteristic of normal epithelial cells with decreased appearance of invasive characteristics (Fig. 2A). Furthermore, when acini were stained for Ki-67, a marker of cell proliferation, we observed a significant decrease in Ki-67-positive cells in GSK343-treated cells compared with controls (Fig. 2C and D). Indeed, cell number was also decreased by GSK343 in 3D cultures (Fig. S2). Similar observations were made using multiple EOC cell lines (Fig. 2), suggesting that the observed effects are not cell line-specific. Together, we conclude that EZH2 inhibition suppresses the growth of human EOC cells in 3D culture conditions.

**EZH2 inhibitor suppresses the invasion of human EOC cells.** Since we observed a decrease in the appearance of invasive characteristics in GSK343-treated EOC cells under 3D culture conditions (Fig. 2A), we next sought to directly determine the effects of GSK343 on the invasion of human EOC cells. Indeed, GSK343 significantly inhibited the invasion of SKOV3 EOC cells as determined by a Boyden chamber assay (Fig. 3A and B). Interestingly, while GSK343 inhibited the invasion of SKOV3 EOC cells, it does not statistically affect the migration of SKOV3 cells (Fig. 3A and B). This is consistent with the report that EZH2 knockdown suppresses the invasion of human EOC cells while having no effects on the migration of these cells.<sup>7</sup> Notably, GSK343 has no appreciable effects on the growth of human SKOV3 cells in 2D (Fig. 1), suggesting that the observed effects are not due to a decrease in the proliferation of these cells. Inhibition of invasion was also observed in UPN289 and OVCAR10 EOC cells (Fig. S3), suggesting that these effects are not cell line-specific. Based on these results, we conclude that EZH2 inhibition suppresses the invasion of human EOC cells.

**EZH2 inhibitor induces apoptosis of EOC cells in 3D but not 2D culture conditions.** We next sought to determine the mechanism by which GSK343 inhibits the growth of human EOC cells in 3D but not 2D culture conditions. Toward this goal, we performed cell cycle distribution analysis on cells grown

in 2D vs. 3D conditions using flow cytometry. Consistent with the idea that GSK343 induces apoptosis of EOC cells in 3D culture, we observed a significant increase of sub- $G_1$  phase population in GSK343-treated SKOV3 cells compared with controls (Fig. 4A–C). In contrast, there were no effects of GSK343 on sub- $G_1$  population of EOC cells cultured in 2D conditions (Fig. 4A–C). Indeed, the percentage of Annexin V-positive cells was increased by GSK343 treatment compared with controls (Fig. 4D and E). This further supports the notion that GSK343 induces apoptosis of EOC cells cultured in 3D. In contrast, GSK343 failed to increase the percentage of Annexin V positivity in EOC cells cultured in 2D (Fig. 4D and E). In addition, we observed that there was a significant decrease in  $G_2/M$  phase of the cell cycle in EOC cells treated with GSK343 compared with controls in 3D but not 2D culture conditions (Fig. 4A–C). This is consistent with our observation that expression of cell

proliferation marker Ki-67 is decreased by GSK343 in 3D cultures (Fig. 2C and D). In contrast, a decrease in  $G_2/M$  phase of the cell cycle is not observed in conventional 2D cultures treated with GSK343 (Fig. 4A–C). Similarly, we observed an increase in sub- $G_1$  phase and a decrease in  $G_2/M$  phase of the cell cycle in GSK343-treated OVCAR10 and UPN289 EOC cells cultured in 3D conditions (Fig. S3), suggesting that the observed effects are not cell line-specific. Interestingly, GSK343 significantly decreases the S phase population of the cells in OVCAR10 cells in 2D cultures (Fig. S4). This is consistent with the observed minor suppression of growth by GSK343 in OVCAR10 cells in 2D cultures (Fig. 1D). However, GSK343 has no significant effects on cell cycle distribution of UPN289 or SKOV3 cells in 2D cultures (Fig. 4; Fig. S4), which is consistent with the observation that GSK343 does not significantly affect the growth of these cells in 2D cultures (Fig. 1F and G). Taken together, we conclude that EZH2 inhibition induces apoptosis and decreases the  $G_2/M$  phase population of EOC cells in 3D, but not 2D cultures. These results suggest that cell interactions with the ECM in the tumor microenvironment play an important role in determining the efficacy of EZH2 inhibitors.

We next sought to determine the effects of GSK343 on the expression of PRC2/H3K27Me3 target genes in human EOC cells. It has previously been established that *HRK*, a pro-apoptotic PRC2/H3K27Me3 target gene, plays a key role in regulating apoptosis of EOC cells induced by decreasing H3K27Me3 levels in these cells.<sup>18</sup> Thus, we determined the effects of GSK343 on the expression of *HRK* in 2D vs. 3D cultures. Indeed, we observed a significant upregulation of *HRK* in EOC cells treated with GSK343 in 3D cultures but not in 2D cultures (Fig. 4F and G). Notably, upregulation of *HRK* by GSK343 was observed in multiple EOC cell lines (Fig. 4F and G), suggesting that this is not a cell line-specific effect. From these results, we conclude that EZH2 inhibition upregulates the pro-apoptotic H3K27Me3 target gene *HRK* in 3D cultures.

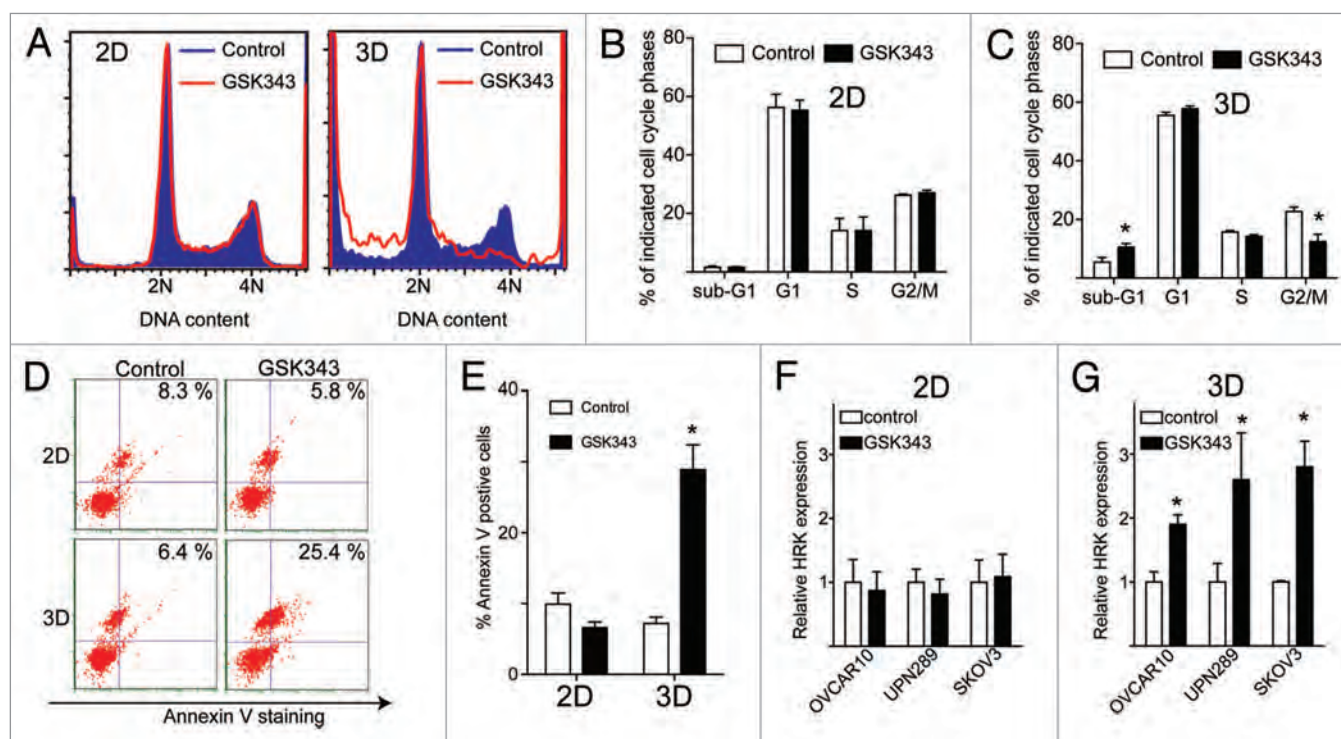


**Figure 4.** The EZH2 inhibitor GSK343 induces apoptosis and decreases the G<sub>2</sub>/M phase population of EOC cells cultured in 3D conditions. (A) Representative cell-cycle distribution as determined by FACS analysis for SKOV3 cells treated with 1  $\mu$ M GSK343 (red) or 0.1% DMSO vehicle control (blue) after 4 d of growth on tissue culture plastic (left) or in Matrigel (right). (B) Quantitation of (A). The percentage of sub-G<sub>1</sub>, G<sub>1</sub>, S and G<sub>2</sub>/M of SKOV3 cells treated with 1  $\mu$ M GSK343 (black bars) or 0.1% DMSO vehicle control (white bars) after 4 d of growth in 2D monolayer culture. Mean of three independent experiments with SD. (C) Same as (B) but for cells cultured in 3D in Matrigel. Mean of three independent experiments with \*p < 0.05. (D) Same as (B and C) but stained for Annexin V, a marker of apoptosis. Percentage of Annexin V positive cells was indicated. (E) Quantification of (D). Mean of three independent experiments with SD, \*p < 0.05. (F and G) Same as (B and C) but examined for relative HRK expression in the indicated EOC cells treated with 1  $\mu$ M GSK343 (black bars) or 0.1% DMSO vehicle control (white bars) after 4 d of growth in 3D in Matrigel as determined by q-RT PCR. Numbers represent expression relative to  $\beta$ -2-microglobulin (B2M) expression. Mean of three independent experiments with SD, \*p < 0.05.

## Discussion

There is no evidence of EZH2 mutation in EOCs based on the recently released The Cancer Genome Atlas (TCGA) ovarian cancer database (<http://tcga-data.nci.nih.gov/>).<sup>19</sup> In addition, based on the TCGA ovarian database, *EZH2* gene amplification (> 4 copy) is rare (~2%) in EOC.<sup>19</sup> However, EZH2 is often overexpressed in EOCs.<sup>7,8,18</sup> In this study, we found that inhibition of EZH2 methyltransferase activity by GSK343 had little effect on the growth of human EOC cells in conventional 2D cultures (Fig. 1). This is consistent with the multiple reports in diffuse large B cell lymphoma (DLBCL), where, although EZH2 inhibitors are similarly effective in decreasing H3K27Me3 levels in both EZH2 wild-type overexpressed and mutant DLBCL cells, EZH2 mutant DLBCL cells are selectively growth-inhibited by EZH2 inhibitors.<sup>20-22</sup> Significantly, we show that growth of human EOC cells in 3D Matrigel ECM significantly sensitizes them to the effects of EZH2 inhibition (Fig. 2). In the context of solid tumors, our present study suggests that the ECM in the tumor microenvironment plays an important role in determining the sensitivity of cancer cells to EZH2 inhibitors. Interestingly, EZH2 has been shown to play an active role in ECM remodeling by repressing the expression of ECM-regulating enzymes in

prostate cancer cells.<sup>23,24</sup> The ECM is known to play a critical role in regulating cell growth, therefore it is plausible that EZH2 inhibitors restrain the growth of tumor cells in 3D by repressing their ability to remodel the ECM.<sup>25,26</sup> In addition, integrins are cell-surface receptors that regulate adhesion of tumor cells to the ECM, and certain integrin genes, whose expression is known to suppress cell proliferation, are regulated by EZH2.<sup>27</sup> Thus, it is also possible that EZH2 inhibition may alter the interaction between tumor cells and ECM to restrain the proliferation of tumor cells. Regardless, it is likely that EZH2 methyltransferase activity regulates the way cells interact with ECM, which is responsible for the efficacy of EZH2 inhibitors like GSK343 observed in 3D culture.

It has previously been demonstrated that GSK343 displays high clearance rate in pharmacokinetic studies,<sup>15</sup> which prevented us from testing its effects in vivo in an animal model. Here we utilized an in vitro 3D model for tumor growth that bridges the gap between animal models and traditional monolayer cultures that lack important determinants of cell growth and treatment response such as the ECM tumor microenvironment.<sup>10</sup> In addition, similar effects are also observed using another EZH2 inhibitor, namely GSK926 (data not shown),<sup>15</sup> suggesting that the observed effects are not unique to GSK343. Together, these



findings suggest that strategies to alter ECM in tumor microenvironment may enhance the tumor-suppressive activity of EZH2 inhibitors. Notably, previous studies have demonstrated that 2D vs. 3D culture conditions lead to different sensitivity of cancer cells to cytotoxic drugs such as PI3K inhibitor LY294002, where cancer cells are more sensitive to cytotoxic drugs in 2D compared with 3D culture conditions.<sup>28</sup>

Notably, EZH2 inhibition decreases the invasive characteristics of human EOC cells in 3D cultures (Fig. 2A) and in the classical Boyden chamber assay, while it has no significant effects on the migration of these cells (Fig. 3). Consistently, it has previously been demonstrated that EZH2 knockdown suppresses the invasion of human EOC cells, while having no effects on the migration of human EOC cells.<sup>7</sup> Together, these data are consistent with the idea that EZH2 plays an important function in regulating how tumor cells interact with the surrounding ECM to promote the invasion of human EOC cells. Thus EZH2 inhibitors may represent a potential therapeutic tool to reverse this phenotype.

EZH2 knockdown will have global effects on a cell in many biological processes. For example, EZH2 knockdown by short hairpin RNA is known to inhibit cell growth, induce apoptosis and suppress invasion of human EOC cells under conventional 2D cultures.<sup>7,8</sup> This correlates with a decrease in the level of H3K27Me3 in these cells.<sup>7,8</sup> However, we found that EZH2 inhibitor exhibited very limited effects on cell growth and apoptosis of EOC cells in 2D monolayer cultures (Fig. 1; Fig. S1). This suggests that additional methyltransferase-independent function of EZH2 may account for the knockdown phenotype observed under 2D cultures. Significantly, we show that growth in a 3D Matrigel ECM model sensitizes human EOC cells to EZH2 inhibition to induce growth inhibition and apoptosis (Figs. 2 and 4). These results suggest that cancer therapeutics which show little efficacy in conventional 2D models may still have therapeutic benefit within the ECM tumor microenvironment. Together, these findings show that EZH2 methyltransferase activity is required to promote cell growth and suppress apoptosis in the context of the solid tumor microenvironment. Furthermore, they suggest that targeting the ECM in the tumor microenvironment is a novel strategy to enhance the tumor-suppressive effects of EZH2 inhibition. They also imply that EZH2 inhibitors have the potential to be developed as a novel EOC therapeutics, which are urgently needed. Toward this goal, our future studies will investigate how the ECM tumor microenvironment enhances the tumor-suppressive effects of EZH2 inhibitors in EOC. In addition, it will be important to profile the changes in gene expression and, in particular, changes in the expression of direct EZH2 target genes in EOC cells cultured in 2D vs. 3D conditions induced by EZH2 inhibitors. The expression pattern of these genes could serve as potential biomarkers for predicting the response of solid tumors, such as EOC to EZH2 inhibitors.

## Materials and Methods

**EZH2 inhibitor, antibodies and cell culture.** EZH2 methyltransferase inhibitor GSK343 was obtained through the

Structure Genomics Consortium (SGC Toronto, M5G1L7). GSK343 was dissolved in DMSO at a stock concentration of 5 mM. Human EOC cell lines OVCAR3, OVCAR5, OVCAR10, UPN 289, SKOV3 and PEO1 cells were described previously<sup>7</sup> and were maintained in RPMI-1640 medium, supplemented with 10% fetal bovine serum, penicillin (100 units/mL) and streptomycin (100 µg/mL). The following antibodies from the indicated suppliers were used: anti-EZH2 (BD Biosciences), anti-histone H3 (Millipore), anti-H3K9Me3 (AbCam), anti-H3K27Me3 (Cell Signaling), anti-β-actin (Sigma-Aldrich), anti-Ki-67 (Dako).

**Cell proliferation assay.**  $1 \times 10^3$  cells were plated in triplicate per well in a 12-well plate. Cells were treated the next day, day 0, with RPMI-1640 media supplemented with 10% FBS with either vehicle control (DMSO) or 1 µM of GSK343. Every 3 d for 12 d total, cells were trypsinized and counted using a hemocytometer. At the end of the experiments, the control cells reach ~90% of confluence.

**Matrigel invasion assay.** BD BioCoat™ Matrigel™ Invasion Chamber was used to measure cell invasion according to manufacturer's instruction and described previously.<sup>7</sup> Briefly, EOC cells were treated with either vehicle control (DMSO) or 1 µM GSK343 for 48 h. Cells were allowed to invade for 48 h toward 5% FBS and 2 ng/ml EGF (Invitrogen) and were subsequently fixed with 4% formaldehyde and stained with 0.05% crystal violet in PBS. The number of cells that migrated across control membrane or invaded through Matrigel-coated membrane was determined in four fields in rectangle across each membrane.

**3D cell culture and immunofluorescence staining.** 3D culture of EOCs was adapted from previously published methods for breast epithelial cell lines.<sup>14</sup> Briefly, 40 µL of growth factor reduced-Matrigel (GFR-Matrigel™; BD Biosciences) was pipetted into each well of an 8-well chamber slide (BD Biosciences). Single-cell suspensions of each cell lines ( $400 \mu\text{L}$  of  $1 \times 10^4$  cells/mL) in RPMI-1640 supplemented with 5% FBS, 2 ng/ml of EGF (Invitrogen), 3% Matrigel and either vehicle control (DMSO) or drug was pipetted into each pre-coated well. Matrigel media with either vehicle control (DMSO) or drug was changed every 3 d and cells were grown for 12 d total. Immunofluorescence was performed on day 12 by fixing samples in 2% paraformaldehyde, permeabilizing in 2% paraformaldehyde with 0.5% Triton-X. Samples were incubated with primary antibodies for 2 h at room temperature, highly cross absorbed secondary antibodies (Invitrogen) for 1 h at room temperature and mounted with prolong anti-fade reagent (Invitrogen).

**Flow cytometry.** Briefly,  $1 \times 10^5$  cells were either plated directly into each well of a 12-well plate and treated with either vehicle control (DMSO) or 1 µM GSK343 (for 2D), or plated into a well of a 12-well plate that was pre-coated with 120 µL of Matrigel and treated either vehicle control (DMSO), or 1 µM GSK343 (for 3D). Cells were grown in RPMI-1640 supplemented with 5% FBS, 2 ng/ml of EGF (Invitrogen), cells in 3D were also supplemented with 3% Matrigel. Cells were analyzed on day 4. To release cells from 3D cultures, cells were treated with ice-cold trypsin for 10 min, and Matrigel was disrupted

with a wide orifice pipette. For cell cycle analysis, cells were pelleted by centrifugation at 200 g at 4°C for 5 min, washed with ice cold PBS and fixed in 1 ml of ice-cold 70% ethanol for 60 min. The cells were then centrifuged, washed in 1 ml PBS and resuspended in 0.5 ml propidium iodide solution with RNase (Sigma) and incubated for 30 min at 37°C. Cells were then analyzed for DNA content using a BD LSR14 Flow Cytometer. For Annexin-V analysis, cells were pelleted by centrifugation at 200 g at 4°C for 5 min, washed and resuspended at  $2 \times 10^6$  cells/ml in fresh media. One hundred  $\mu$ l of cells were then added to three wells of a 96-well plate. Cells were incubated with 100  $\mu$ l of Guava Nexin Reagent for 20 min at RT and analyzed on the Guava system.

**RNA isolation and qRT-PCR.** RNA was isolated using Trizol (Invitrogen) according to manufacturer's instruction. For quantitative real-time PCR (qRT-PCR), Trizol-isolated RNA was further purified using an RNeasy kit (Qiagen) following manufacturer's instruction. The primers for *HRK* genes used for qRT-PCR are: forward: 5'-GCAACAGGTT GGTGAAAACC CT-3' and reverse: 5'-ATTGGGGTGT CTGTTTCTGC AGC-3'.

Expression of the housekeeping gene  $\beta$ -2-microglobulin was used to normalize mRNA expression.

#### Disclosure of Potential Conflicts of Interest

No potential conflicts of interest were disclosed.

#### Aknoweldgements

We thank Structure Genomics Consortium for GSK343 and Dr Caretha Creasy at GlaxoSmithKline Pharmaceuticals for critical reading of the manuscript. R.Z. is an Ovarian Cancer Research Fund (OCRF) Liz Tilberis Scholar. This work was supported by the National Cancer Institute of the National Institutes of Health (R01CA163377 to R.Z.) and in part by a DOD ovarian cancer academy award (OC093420 to R.Z.). Support of Core Facilities used in this study was provided by Cancer Center Support Grant (CCSG) CA010815 to The Wistar Institute.

#### Supplemental Materials

Supplemental materials may be found here: [www.landesbioscience.com/journals/cc/article/25163](http://www.landesbioscience.com/journals/cc/article/25163)

#### References

- Cao R, Wang L, Wang H, Xia L, Erdjument-Bromage H, Tempst P, et al. Role of histone H3 lysine 27 methylation in Polycomb-group silencing. *Science* 2002; 298:1039-43; PMID:12351676; <http://dx.doi.org/10.1126/science.1076997>
- Czermin B, Melfi R, McCabe D, Seitz V, Imhof A, Pirrotta V. Drosophila enhancer of Zeste/ESC complexes have a histone H3 methyltransferase activity that marks chromosomal Polycomb sites. *Cell* 2002; 111:185-96; PMID:12408863; [http://dx.doi.org/10.1016/S0092-8674\(02\)00975-3](http://dx.doi.org/10.1016/S0092-8674(02)00975-3)
- Simon JA, Lange CA. Roles of the EZH2 histone methyltransferase in cancer epigenetics. *Mutat Res* 2008; 647:21-9; PMID:18723033; <http://dx.doi.org/10.1016/j.mrfmmm.2008.07.010>
- Cancer Facts & Figures. Atlanta: American Cancer Society 2012
- Arulkumaran S, Regan L, Farquharson DIM. Obstetrics and gynaecology. Oxford: Oxford University Press, 2011
- Shih IeM, Kurman RJ. Ovarian tumorigenesis: a proposed model based on morphological and molecular genetic analysis. *Am J Pathol* 2004; 164:1511-8; PMID:15111296; [http://dx.doi.org/10.1016/S0002-9440\(10\)63708-X](http://dx.doi.org/10.1016/S0002-9440(10)63708-X)
- Li H, Cai Q, Godwin AK, Zhang R. Enhancer of zeste homolog 2 promotes the proliferation and invasion of epithelial ovarian cancer cells. *Mol Cancer Res* 2010; 8:1610-8; PMID:21115743; <http://dx.doi.org/10.1158/1541-7786.MCR-10-0398>
- Lu C, Han HD, Mangala LS, Ali-Fehmi R, Newton CS, Ozburn L, et al. Regulation of tumor angiogenesis by EZH2. *Cancer Cell* 2010; 18:185-97; PMID:20708159; <http://dx.doi.org/10.1016/j.ccr.2010.06.016>
- Li H, Zhang R. Role of EZH2 in Epithelial Ovarian Cancer: From Biological Insights to Therapeutic Target. *Front Oncol* 2013; 3:47; PMID:23494175; <http://dx.doi.org/10.3389/fonc.2013.00047>
- Yamada KM, Cukierman E. Modeling tissue morphogenesis and cancer in 3D. *Cell* 2007; 130:601-10; PMID:17719539; <http://dx.doi.org/10.1016/j.cell.2007.08.006>
- Griffith LG, Swartz MA. Capturing complex 3D tissue physiology in vitro. *Nat Rev Mol Cell Biol* 2006; 7:211-24; PMID:16496023; <http://dx.doi.org/10.1038/nrm1858>
- Debnath J, Brugge JS. Modelling glandular epithelial cancers in three-dimensional cultures. *Nat Rev Cancer* 2005; 5:675-88; PMID:16148884; <http://dx.doi.org/10.1038/nrc1695>
- Cukierman E, Pankov R, Stevens DR, Yamada KM. Taking cell-matrix adhesions to the third dimension. *Science* 2001; 294:1708-12; PMID:11721053; <http://dx.doi.org/10.1126/science.1064829>
- Debnath J, Muthuswamy SK, Brugge JS. Morphogenesis and oncogenesis of MCF-10A mammary epithelial acini grown in three-dimensional basement membrane cultures. *Methods* 2003; 30:256-68; PMID:12798140; [http://dx.doi.org/10.1016/S1046-2023\(03\)00032-X](http://dx.doi.org/10.1016/S1046-2023(03)00032-X)
- Verma SK, Tian XR, LaFrance LV, Duquenne C, Suarez DP, Newlander KA, et al. Identification of Potent, Selective, Cell-Active Inhibitors of the Histone Lysine Methyltransferase EZH2. *ACS Med Chem Lett* 2012; 3:1091-6; <http://dx.doi.org/10.1021/ml3003346>
- Jenuwein T. The epigenetic magic of histone lysine methylation. *FEBS J* 2006; 273:3121-35; PMID:16857008; <http://dx.doi.org/10.1111/j.1742-4658.2006.05343.x>
- Weaver VM, Gilbert P. Watch thy neighbor: cancer is a communal affair. *J Cell Sci* 2004; 117:1287-90; PMID:15020668; <http://dx.doi.org/10.1242/jcs.01137>
- Li H, Cai Q, Wu H, Vathipadiekal V, Dobbin ZC, Li T, et al. SUZ12 promotes human epithelial ovarian cancer by suppressing apoptosis via silencing HRK. *Mol Cancer Res* 2012; 10:1462-72; PMID:22964433; <http://dx.doi.org/10.1158/1541-7786.MCR-12-0335>
- Cancer Genome Atlas Research Network. Integrated genomic analyses of ovarian carcinoma. *Nature* 2011; 474:609-15; PMID:21720365; <http://dx.doi.org/10.1038/nature10166>
- Knutson SK, Wigle TJ, Warholik NM, Sneideringer CJ, Allain CJ, Klaus CR, et al. A selective inhibitor of EZH2 blocks H3K27 methylation and kills mutant lymphoma cells. *Nat Chem Biol* 2012; 8:890-6; PMID:23023262
- McCabe MT, Otr HM, Ganji G, Korenchuk S, Thompson C, Van Aller GS, et al. EZH2 inhibition as a therapeutic strategy for lymphoma with EZH2-activating mutations. *Nature* 2012; 492:108-12; PMID:23051747; <http://dx.doi.org/10.1038/nature11606>
- Qi W, Chan H, Teng L, Li L, Chuai S, Zhang R, et al. Selective inhibition of Ezh2 by a small molecule inhibitor blocks tumor cells proliferation. *Proc Natl Acad Sci USA* 2012; 109:21360-5; PMID:23236167; <http://dx.doi.org/10.1073/pnas.1210371110>
- Shin YJ, Kim JH. The role of EZH2 in the regulation of the activity of matrix metalloproteinases in prostate cancer cells. *PLoS One* 2012; 7:e30393; PMID:22272343; <http://dx.doi.org/10.1371/journal.pone.0030393>
- Varambally S, Dhanasekaran SM, Zhou M, Barrette TR, Kumar-Sinha C, Sanda MG, et al. The polycomb group protein EZH2 is involved in progression of prostate cancer. *Nature* 2002; 419:624-9; PMID:12374981; <http://dx.doi.org/10.1038/nature01075>
- Ulrich TA, de Juan Pardo EM, Kumar S. The mechanical rigidity of the extracellular matrix regulates the structure, motility, and proliferation of glioma cells. *Cancer Res* 2009; 69:4167-74; PMID:19435897; <http://dx.doi.org/10.1158/0008-5472.CAN-08-4859>
- Wozniak MA, Desai R, Solski PA, Der CJ, Keely PJ. ROCK-generated contractility regulates breast epithelial cell differentiation in response to the physical properties of a three-dimensional collagen matrix. *J Cell Biol* 2003; 163:583-95; PMID:14610060; <http://dx.doi.org/10.1083/jcb.200305010>
- Ferraro A, Mourtoukou D, Kosmidou V, Avlonitis S, Kontogeorgos G, Zografos G, et al. EZH2 is regulated by ERK/AKT and targets integrin alpha2 gene to control Epithelial-Mesenchymal Transition and anoikis in colon cancer cells. *Int J Biochem Cell Biol* 2013; 45:243-54; PMID:23116973; <http://dx.doi.org/10.1016/j.biocel.2012.10.009>
- Fischbach C, Chen R, Matsumoto T, Schmelzle T, Brugge JS, Polverini PJ, et al. Engineering tumors with 3D scaffolds. *Nat Methods* 2007; 4:855-60; PMID:17767164; <http://dx.doi.org/10.1038/nmeth1085>

# Suppression of Nucleotide Metabolism Underlies the Establishment and Maintenance of Oncogene-Induced Senescence

Katherine M. Aird,<sup>1</sup> Gao Zhang,<sup>2</sup> Hua Li,<sup>1</sup> Zhigang Tu,<sup>1</sup> Benjamin G. Bitler,<sup>1</sup> Azat Garipov,<sup>1</sup> Hong Wu,<sup>3</sup> Zhi Wei,<sup>4</sup> Stephan N. Wagner,<sup>5,6</sup> Meenhard Herlyn,<sup>2</sup> and Rugang Zhang<sup>1,\*</sup>

<sup>1</sup>Gene Expression and Regulation Program

<sup>2</sup>Tumor Microenvironment and Metastasis Program

The Wistar Institute Cancer Center, The Wistar Institute, Philadelphia, PA 19104, USA

<sup>3</sup>Department of Pathology, Fox Chase Cancer Center, Philadelphia, PA 19111, USA

<sup>4</sup>Department of Computer Science, New Jersey Institute of Technology, Newark, NJ 07102, USA

<sup>5</sup>Division of Immunology, Allergy and Infectious Diseases, Department of Dermatology, Medical University of Vienna, Waehringer Guertel 18-20, 1090 Vienna, Austria

<sup>6</sup>CeMM Research Center for Molecular Medicine of the Austrian Academy of Sciences, Lazarettgasse 14, 1090 Vienna, Austria

\*Correspondence: [rzhang@wistar.org](mailto:rzhang@wistar.org)

<http://dx.doi.org/10.1016/j.celrep.2013.03.004>

## SUMMARY

Oncogene-induced senescence is characterized by a stable cell growth arrest, thus providing a tumor suppression mechanism. However, the underlying mechanisms for this phenomenon remain unknown. Here, we show that a decrease in deoxyribonucleotide triphosphate (dNTP) levels underlies oncogene-induced stable senescence-associated cell growth arrest. The decrease in dNTP levels is caused by oncogene-induced repression of ribonucleotide reductase subunit M2 (RRM2), a rate-limiting protein in dNTP synthesis. This precedes the senescence-associated cell-cycle exit and coincides with the DNA damage response. Consistently, RRM2 down-regulation is both necessary and sufficient for senescence. Strikingly, suppression of nucleotide metabolism by RRM2 repression is also necessary for maintenance of the stable senescence-associated cell growth arrest. Furthermore, RRM2 repression correlates with senescence status in benign nevi and melanoma, and its knockdown drives senescence of melanoma cells. These data reveal the molecular basis whereby the stable growth arrest of oncogene-induced senescence is established and maintained through suppression of nucleotide metabolism.

## INTRODUCTION

Cellular senescence is defined as a state of stable cell growth arrest (Campisi, 2005). Activation of oncogenes, such as RAS, in normal mammalian cells typically triggers oncogene-induced senescence (OIS) (Yaswen and Campisi, 2007), which is a bona fide tumor suppressor mechanism in vivo (Campisi and

d'Adda di Fagagna, 2007). For example, benign nevi formed by human melanocytes that have undergone OIS are thought to suppress melanomagenesis (Mooi and Peeper, 2006). Although known to be important for tumor suppression, to date, the molecular mechanism underlying the stable OIS-associated cell growth arrest remains unknown.

Oncogenic signaling triggers cellular senescence via various senescence effectors. In particular, senescence induced by activated oncogenes such as RAS is characterized by a sustained DNA damage response (DDR) triggered by aberrant DNA replication during the S phase of the cell cycle (Bartkova et al., 2006; Di Micco et al., 2006). This ultimately activates the p53/p21 and p16/pRB pathways (Serrano et al., 1997). Activation of these signaling pathways cultivates the expression of markers of senescence such as senescence-associated heterochromatin foci (SAHF), which are specialized domains of facultative heterochromatin that contribute to senescence by silencing proliferation-promoting genes (Narita et al., 2003; Zhang et al., 2007a), and increased senescence-associated  $\beta$ -galactosidase (SA- $\beta$ -gal) activity (Dimri et al., 1995).

Cellular deoxyribonucleotide triphosphate (dNTP) levels play a key role in regulating DNA replication and, consequently, cell proliferation (Reichard, 1988). However, whether changes in the nucleotide metabolic pathway play a role in regulating OIS-associated stable cell growth arrest has never been investigated. Ribonucleotide reductase (RNR) plays a key role in dNTP biogenesis (Nordlund and Reichard, 2006). RNR is a tetrameric complex consisting of two large catalytic subunits (termed RRM1) and two small regulatory subunits (RRM2 or p53R2) (Nordlund and Reichard, 2006). Notably, RRM2 is the regulatory subunit that controls dNTP synthesis during the S phase of the cell cycle, whereas RRM1 is present throughout the cell cycle (Engström et al., 1985). Importantly, RRM2 expression is rate-limiting for RNR activity (Nordlund and Reichard, 2006). In contrast, p53R2 is involved in supplying dNTPs for DNA repair and mitochondrial DNA synthesis in the G0/G1 phase of the cell cycle (Håkansson et al., 2006). Whether RRM2 plays a role in



regulating OIS, which is characterized by aberrant DNA replication, the DDR, and a stable cell growth arrest, has never been investigated.

Here, we report that a decrease in dNTP levels underlies the establishment and maintenance of the stable OIS-associated cell growth arrest. We show that addition of exogenous nucleosides is sufficient to overcome OIS-associated cell growth arrest, which correlates with suppressing aberrant DNA replication and inhibiting the DDR. Mechanistically, we discovered that the decrease in dNTP levels is caused by oncogene-induced suppression of RRM2 expression. This correlates with the recruitment of E2F7, an atypical E2F transcriptional repressor, to its promoter. Indeed, we show that RRM2 downregulation is both necessary and sufficient for the establishment and maintenance of the stable senescence-associated cell growth arrest. Further underscoring the importance of this pathway in regulating senescence in human cancers, we show that RRM2 expression inversely correlates with senescence status in human nevi and melanoma specimens harboring oncogenic BRAF or NRAS. Additionally, high RRM2 expression correlates with poor overall survival in patients with melanoma with oncogenic BRAF or NRAS. Finally, knockdown of RRM2 drives senescence of melanoma cells harboring these activated oncogenes. Taken together, our results reveal the mechanistic basis whereby an activated oncogene establishes and maintains the stable senescence-associated cell growth arrest by suppressing nucleotide metabolism.

## RESULTS

### Exogenous Nucleosides Suppress OIS and Its Associated Cell Growth Arrest

Senescent cells are characterized by a stable cell growth arrest (Campisi, 2005), and nucleotide metabolism plays a critical role in regulating cell growth (Reichard, 1988). To test the hypothesis that nucleotide metabolism regulates OIS, IMR90 primary human fibroblasts were infected with RAS-encoding retrovirus to induce senescence (Figure S1A), and exogenous nucleosides were added at the time of infection. Compared with controls, addition of exogenous nucleosides significantly suppressed the expression of markers of senescence such as SAHF formation (Figures 1A and 1B), SA- $\beta$ -gal activity (Figures 1A and 1B), and the upregulation of p16, p21, and p53 (Figure 1C). In addition, senescence induced by oncogenic RAS is characterized by the DDR (Bartkova et al., 2006; Di Micco et al., 2006). Thus, we examined markers of the DDR such as formation of  $\gamma$ H2AX foci in these cells. Compared with controls, addition of exogenous nucleosides significantly decreased  $\gamma$ H2AX foci formation (Figures 1D and 1E). Next, we determined the effects of exogenous nucleosides on the senescence-associated cell-cycle exit by bromodeoxyuridine (BrdU) incorporation. Exogenous nucleosides significantly increased BrdU incorporation in RAS-infected cells compared with controls (Figures 1F and 1G). Finally, we sought to determine the effects of exogenous nucleosides on the OIS-associated cell growth arrest by colony-formation and cell growth curve assays. Compared with RAS-alone controls, there was a significant increase in colony formation (Figure 1H) and cell growth (Figure 1I) in exogenous nucleoside-supple-

mented cells. Interestingly, senescence induced by DNA damage reagents such as doxorubicin or etoposide was not affected by addition of exogenous nucleosides (Figures S1B–S1I), suggesting that the observed effects are not merely a consequence of DNA damage. Based on these results, we conclude that exogenous nucleosides added at the time of infection are sufficient to suppress OIS and its associated cell growth arrest.

### Exogenous Nucleosides Are Sufficient to Overcome the OIS-Associated Cell Growth Arrest in Established Senescent Cells

We next wanted to determine the effects of exogenous nucleosides on the stable OIS-associated cell growth arrest in established senescent cells. To do so, stable senescence-associated cell growth arrest was established by culturing RAS-infected cells for 6 days, as evidenced by the minimal BrdU incorporation in these cells compared with controls as well as no appreciable cell growth during the experimental period (Figures S2A–S2C). Then FACS was performed with C<sub>12</sub>FDG, a fluorogenic substrate for SA- $\beta$ -gal activity in live cells (Debacq-Chainiaux et al., 2009) (Figure 2A). FACS-sorted senescent cells were further cultured with or without exogenous nucleosides. We then examined the expression of markers of senescence and proliferation in these cells. Compared with controls, markers of senescence such as SA- $\beta$ -gal activity and p16 and p21 expression were all suppressed by exogenous nucleosides (Figures 2B–2D). In contrast, markers of cell proliferation, such as BrdU incorporation, were increased in the established senescent cells exposed to exogenous nucleosides (Figure 2E). Strikingly, addition of exogenous nucleosides to these cells reversed the oncogene-induced stable senescence-associated cell growth arrest, as evidenced by marked growth of these cells (Figure 2F). Notably, these observations were not due to a loss of RAS expression because RAS was expressed at similar levels in these cells compared to those without exposure to exogenous nucleosides (Figure S2D). Similar observations were also made when RAS cells were allowed to senesce for a longer period of time (e.g., exogenous nucleosides added at day 12; Figures S2E–S2G). Likewise, we also observed similar effects of exogenous nucleosides in another primary human fibroblast cell line, WI38 (Figures S2H–S2J), demonstrating that this is not a cell line-specific phenomenon. Interestingly, withdrawal of nucleosides from these cells was sufficient for the cells to senesce again, as shown by an increase in SA- $\beta$ -gal activity (Figures 2G and 2H) and p21 and p16 expression (Figure 2I), and a decrease in both cyclin A expression (Figure 2I) and cell growth (Figure 2J). Taken together, these data indicate that addition of exogenous nucleosides is sufficient to overcome the stable OIS-associated cell growth arrest in established senescent cells.

### A Decrease in dNTP Levels Occurs Prior to the OIS-Associated Cell-Cycle Exit

Because addition of exogenous nucleosides suppresses senescence (Figures 1 and 2), we next sought to determine whether changes in dNTP levels occur during OIS. Toward this goal, we measured dNTP levels in control and RAS-infected IMR90 cells. To limit the potential effects of cell cycle and cell proliferation status on dNTP levels, we performed a detailed time course



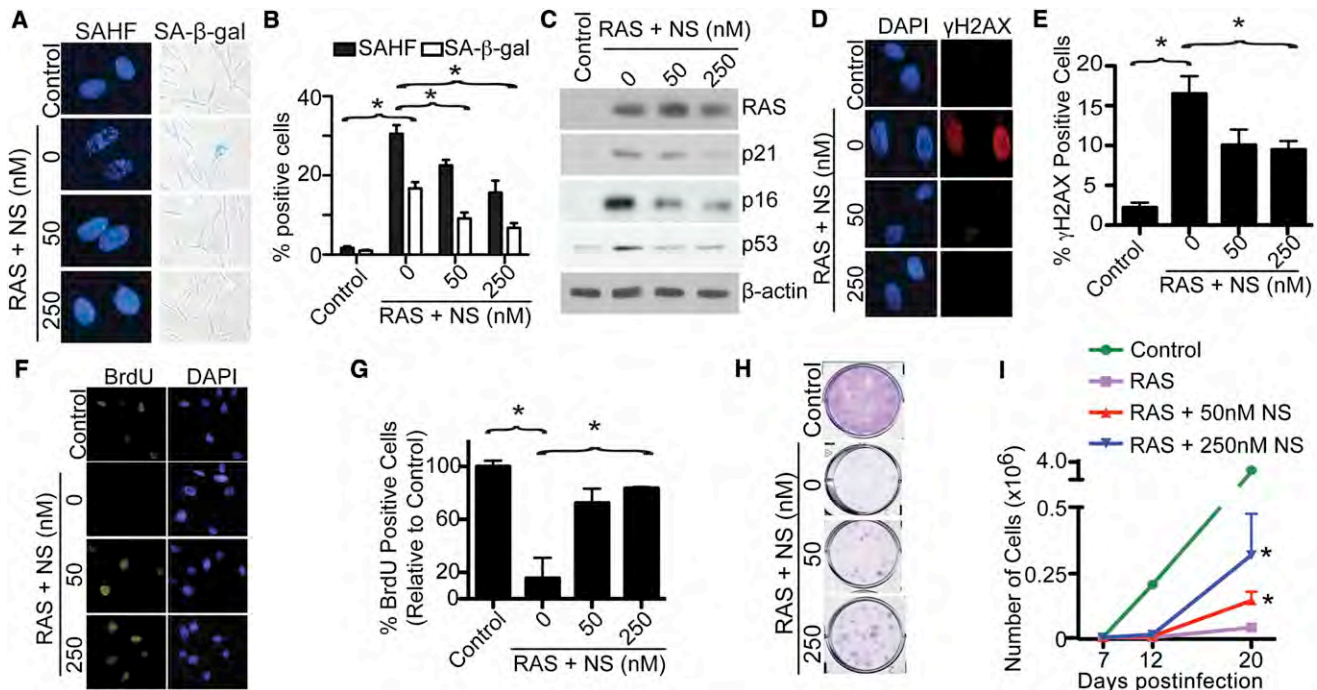


**Figure 1. Exogenous Nucleosides Suppress OIS and Its Associated Cell Growth Arrest**

(A) IMR90 cells were infected with control or RAS-encoding retrovirus with or without addition of the indicated concentration of nucleosides (NS) at the time of infection. On day 6, drug-selected cells were examined for SAHF formation and SA-β-gal activity.

(B) Quantification of (A). Mean of three independent experiments with SEM is shown. \* $p < 0.05$ .

(C) Same as (A) but examined for expression of RAS, p21, p16, p53, and β-actin by immunoblotting.

(D) Same as (A) but stained for γH2AX foci formation. DAPI counterstaining was used to visualize nuclei.

(E) Quantification of (D). Mean of three independent experiments with SEM is shown. \* $p < 0.05$ .

(F) Same as (A) but labeled with BrdU for 1 hr. The incorporated BrdU was visualized by immunofluorescence. DAPI counterstaining was used to visualize nuclei.

(G) Quantification of (F). Mean of three independent experiments with SEM is shown. \* $p < 0.01$ .

(H) Same as (A), but an equal number of cells were inoculated in 6-well plates. After 2 weeks, the plates were stained with 0.05% crystal violet in PBS to visualize colony formation. Shown are representative images of three independent experiments.

(I) Same as (A), but an equal number of cells were seeded in 6-well plates. The number of cells was counted at the indicated time points after infection. Mean of three independent experiments with SEM is shown. \* $p < 0.05$  compared with RAS-alone cells.

See also Figure S1.

analysis for cell-cycle distribution using FACS analysis, markers of cell proliferation such as serine 10 phosphorylated histone H3 (pS10H3), and markers of senescence such as p21 and p16 (Figures S3A and S3B). Based on the time course analysis, we determined the dNTP levels on day 2, which is prior to the cell-cycle exit, as further demonstrated by comparable BrdU incorporation and cyclin A expression in RAS-infected cells compared to controls (Figures S3C–S3E). Strikingly, the levels of all four dNTPs were significantly decreased in RAS-infected cells compared with controls at this time point (Figure 3A). Together, these data support the idea that there is a decrease in dNTP levels, which occurs prior to the OIS-associated cell-cycle exit.

Addition of exogenous nucleosides suppresses OIS-associated DDR (Figures 1C–1E), which is triggered by aberrant DNA replication (Bartkova et al., 2006; Di Micco et al., 2006). Moreover, RAS significantly decreases dNTP levels prior to the senescence-associated cell-cycle exit (Figure 3A). Thus, we sought to determine whether the decrease in dNTP levels plays a role in regulating aberrant DNA replication induced by oncogenic RAS. Toward this goal, we determined the changes in the

dynamics of DNA replication in control and RAS-infected cells with or without exogenous nucleosides using the DNA-combing analysis (Figures S3F and S3G). This allows for observation of single-stranded DNA (ssDNA) to determine DNA replication fork dynamics (namely elongating, terminated, and newly fired, as illustrated in Figure S3G). Indeed, addition of exogenous nucleosides significantly rescued the aberrant DNA replication observed during RAS-induced senescence (Figure 3B). Notably, this correlates with a significant restoration of dNTP levels in RAS-infected cells supplemented with exogenous nucleosides (Figure 3C). This result is consistent with the idea that the observed effects are due to restoration of dNTP levels. Together, these results support the premise that a decrease in dNTP levels contributes to the aberrant DNA replication observed during RAS-induced senescence.

#### Oncogene-Induced Repression of RRM2 Occurs Prior to the Senescence-Associated Cell-Cycle Exit

We next wanted to determine the molecular mechanism whereby dNTP levels decrease during OIS. RNR is a key enzyme

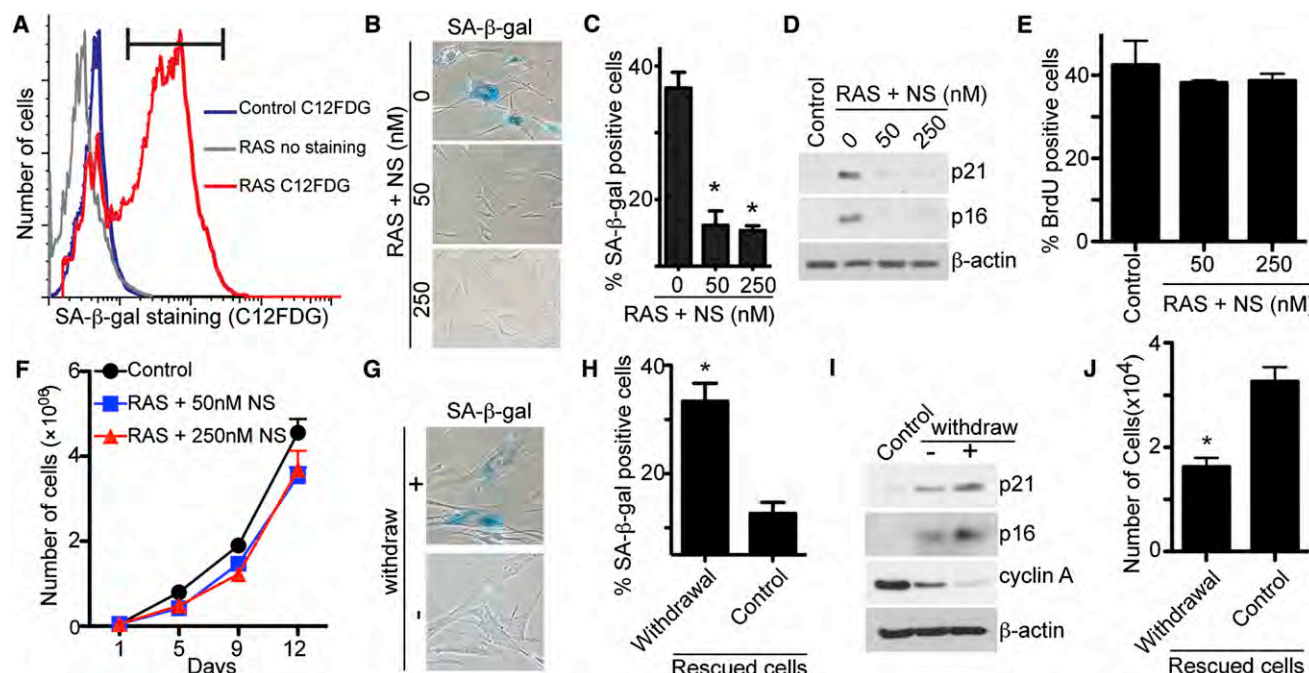


**Figure 2. Exogenous Nucleosides Are Sufficient to Overcome the Stable OIS-Associated Cell Growth Arrest in Established Senescent Cells**

(A) IMR90 cells were infected with RAS-encoding retrovirus. On day 6, drug-selected cells were subjected to flow cytometric sorting (FACS) of SA-β-gal-positive cells using C<sub>12</sub>FDG as a substrate. Black bar indicates the gate used for sorting.

(B) FACS-sorted senescent cells were cultured without or with indicated concentrations of nucleosides for an additional 14 days. The cells were then stained for SA-β-gal activity.

(C) Quantification of (B). Mean of three independent experiments with SEM is shown. \*p < 0.001.

(D) Same as (B) but examined for p16, p21, and β-actin expression by immunoblotting.

(E) Same as (B) but labeled with BrdU for 1 hr. Mean of three independent experiments with SEM is shown.

(F) Same as (B), but an equal number of cells that overcome senescence or control (parental) cells were inoculated in 6-well plates, and the number of cells was counted at the indicated time points. Mean of three independent experiments with SEM is shown.

(G) Cells that overcome senescence in the presence of exogenous nucleosides (50 nM) isolated from (B) (rescued cells) were continually cultured in the presence of NS (control) or withdrawn from NS exposure for an additional 17 days and stained for SA-β-gal activity.

(H) Quantification of (G). Mean of three independent experiments with SEM is shown. \*p < 0.01.

(I) Same as (G) but examined for p21, p16, cyclin A, and β-actin expression by immunoblotting.

(J) Same as (G), but an equal number of cells were inoculated in 6-well plates after withdrawal, and the number of cells was counted 4 days later. Mean of three independent experiments with SEM is shown. \*p < 0.05.

See also Figure S2.

in dNTP biosynthesis, and RRM2, the regulatory subunit of RNR, is rate-limiting for this process (Nordlund and Reichard, 2006). Thus, we sought to determine whether RRM2 expression is regulated during OIS. To do so, we examined the protein levels of RRM2 in control and RAS-infected cells in a detailed time course study comparing the kinetics of RRM2 expression with the expression of markers of cell proliferation such as cyclin A and pS10H3. Strikingly, as early as day 1, when RAS cells are still proliferating based on the expression of cyclin A and pS10H3 (Figures 4A and S3B), RRM2 protein expression was already decreased in RAS-infected cells compared to controls (Figure 4A). At this time point, expression of other regulators of dNTP metabolism, namely RRM1 and p53R2, was not decreased (Figure S4A), demonstrating that this is specific to RRM2. We next sought to determine the changes in RRM2 expression in cycling cells by staining for the RRM2 protein in BrdU-positive cells (transiently labeled for 1 hr). The RRM2-

staining signal was specific because knockdown of RRM2 protein decreased the immunofluorescent signal (Figure S4B). Indeed, RRM2 protein expression was decreased even in BrdU-positive RAS-infected cells (Figure 4B). Notably, RRM2 downregulation coincided with the DDR as evidenced by the accumulation of γH2AX (Figure 4A), suggesting that downregulation of RRM2 may contribute to the DDR observed during OIS. However, RRM2 downregulation was not a consequence of the DDR because ionizing radiation, which induces DNA damage, failed to suppress RRM2 expression (Figure S4C). Together, these results indicate that RRM2 is downregulated prior to the OIS-associated cell-cycle exit and coincides with activation of the DDR during senescence.

We next sought to determine the molecular mechanism underlying downregulation of RRM2 during OIS. First, we asked whether RRM2 is downregulated at the transcriptional level. Accordingly, quantitative RT-PCR (qRT-PCR) was performed in

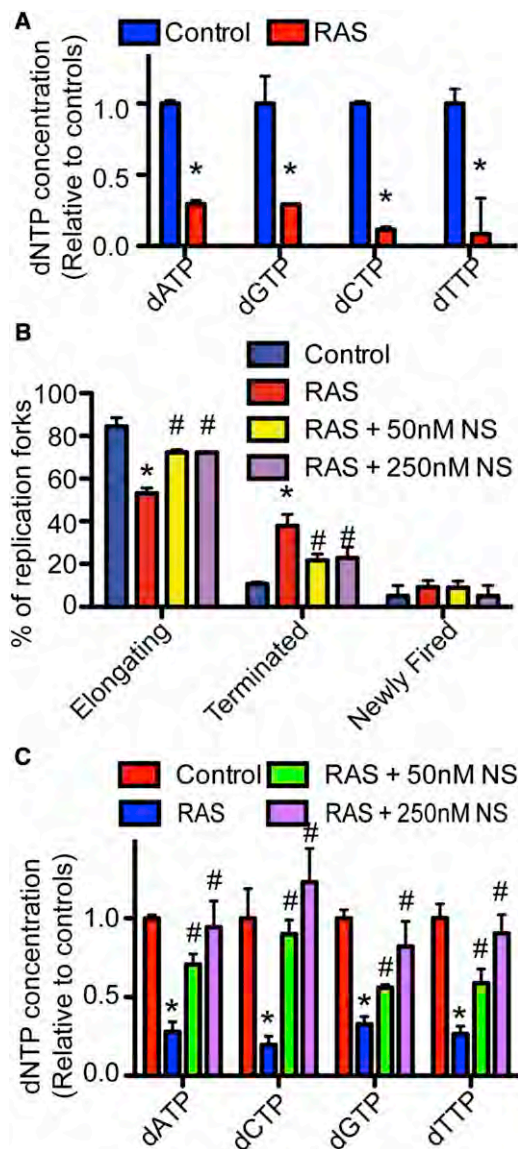


**Figure 3. A Decrease in dNTP Levels Occurs Prior to the OIS-Associated Cell-Cycle Exit**

(A) IMR90 cells were infected with control or RAS-encoding retrovirus. On day 2, cellular dNTP levels were measured. Mean of three independent experiments with SEM is shown. \* $p < 0.05$ .

(B) Same as (A), but RAS-infected cells were supplemented with or without the indicated concentration of nucleosides at the time of infection. Mean of three independent experiments with SEM is shown. \* $p < 0.05$  control versus RAS; # $p < 0.05$  RAS versus RAS plus 50 or 250 nM NS.

(C) Same as (B), but cellular dNTP levels were measured. Mean of three independent experiments with SEM is shown. \* $p < 0.05$  versus control; # $p < 0.05$  versus RAS alone.

See also Figure S3.

control and RAS-infected cells. Similar to RRM2 protein expression, *RRM2* mRNA expression was significantly decreased after RAS infection but prior to the senescence-associated cell-cycle exit (i.e., at day 1; Figure 4C). Consistent with the idea that decreased *RRM2* mRNA expression is due to decreased tran-

scription, there was a significant decrease in the activity of the cloned human *RRM2* gene proximal promoter (−1,071 to +76) in the RAS-infected cells compared with controls (Figures 4D and S4D). Together, we conclude that RRM2 is downregulated at the transcriptional level, and this occurs before the senescence-associated cell-cycle exit.

To identify the transcription factor that contributes to RRM2 repression during senescence, systematic promoter mapping was performed. Notably, an E2F binding site within the proximal promoter (−998 to −991) was identified to contribute to the suppression of *RRM2* transcription in response to RAS (Figure 4D; data not shown). Deletion of the E2F binding site in the *RRM2* promoter significantly restored promoter activity in RAS-infected cells (Figure 4D). Chromatin immunoprecipitation (ChIP) experiments using an E2F1 antibody demonstrated that the binding of transcriptional activator E2F1 to the human *RRM2* gene promoter was significantly reduced in RAS-infected cells compared with controls (Figure 4E). Interestingly, RRM2 is downregulated, whereas the cells are highly proliferative, and other E2F1 target genes such as cyclin A remain highly expressed (e.g., Figure 4A). These results suggest that the RRM2 downregulation observed during OIS is context dependent. To further determine the mechanism of RRM2 downregulation, we performed ChIP analysis using antibodies to the repressive E2F transcriptional factors E2F4 and E2F7 (Chen et al., 2009). These data demonstrate that binding of the atypical transcriptional repressor E2F7 to the human *RRM2* gene promoter was significantly enhanced in RAS-infected cells compared to controls (Figure 4E), whereas there was no change in E2F4 binding (data not shown). Indeed, a detailed time course study revealed that downregulation of RRM2 coincides with upregulation of E2F7 during RAS-induced senescence (Figure 4F). These results indicate that an enhanced association of the atypical transcriptional repressor E2F7 with the *RRM2* gene promoter and a simultaneous decrease in binding of transcriptional activator E2F1 to the *RRM2* gene promoter contribute to downregulation of RRM2 prior to the OIS-associated cell-cycle exit.

### Knockdown of RRM2 Induces Senescence in Primary Human Fibroblasts

We next wanted to determine whether RRM2 downregulation is sufficient to induce senescence. To do so, we infected cells with lentivirus encoding small hairpin RNAs to the human *RRM2* gene (shRRM2). The knockdown efficacy of shRRM2 was confirmed by qRT-PCR and immunoblotting (Figures 5A and S5A). Consistent with the hypothesis that RRM2 downregulation decreases the dNTP levels observed during senescence, we determined that knockdown of RRM2 caused a significant decrease in dNTP levels (Figure S5B). In addition, we determined that knockdown of RRM2 triggers aberrant DNA replication (Figures 5B and S5C). Furthermore, DDR markers such as formation of 53BP1 and  $\gamma$ H2AX foci were significantly induced by shRRM2 (Figures 5C, 5D, S5D, and S5E). Likewise,  $\gamma$ H2AX and p53 protein expression was upregulated in shRRM2-expressing cells compared to controls (Figures 5E and S5F). Together, these results support the idea that a decrease in dNTP levels caused by RRM2 downregulation drives aberrant DNA replication and consequently the DDR observed during OIS.



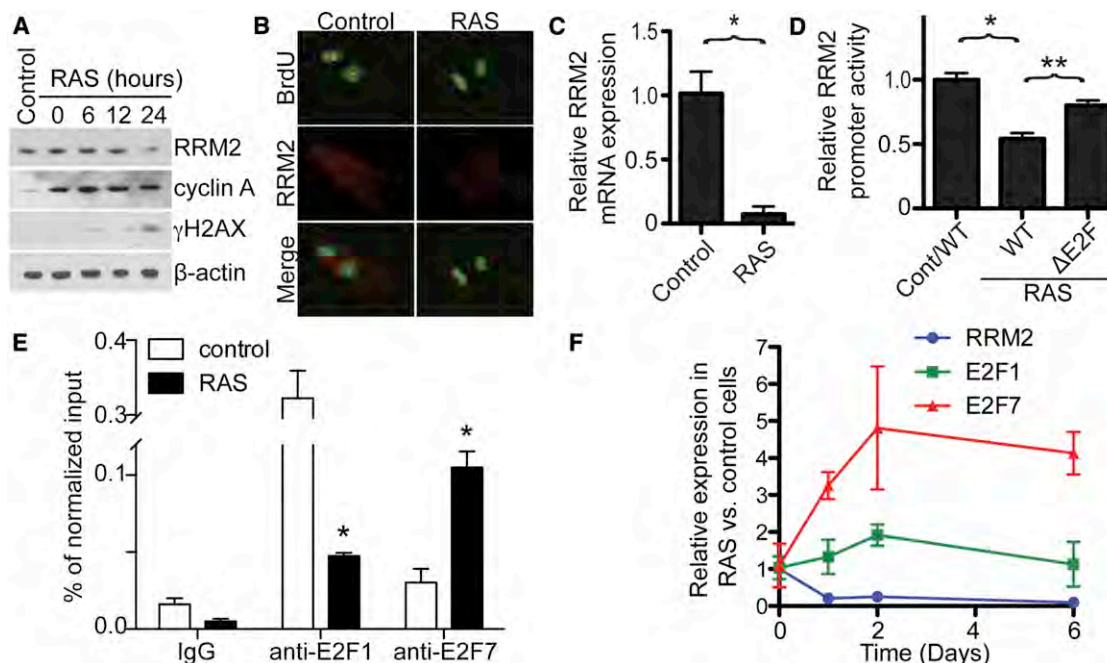


**Figure 4. Oncogene-Induced Repression of RRM2 Occurs Prior to the OIS-Associated Cell-Cycle Exit**

(A) IMR90 cells were infected with control or RAS-encoding retrovirus. The expression of RRM2, cyclin A,  $\gamma$ H2AX, and  $\beta$ -actin was determined by immunoblotting at the indicated time points after completing RAS infection.

(B) IMR90 cells were infected with control or RAS-encoding retrovirus. On day 1, the infected cells were labeled with BrdU for 1 hr, and the expression of RRM2 in BrdU-incorporated cells was visualized by immunofluorescence.

(C) Same as (A), but cells were examined for RRM2 mRNA expression by qRT-PCR on day 1. Mean of three independent experiments with SEM is shown. \* $p < 0.01$ .

(D) On day 2, drug-selected control or RAS-infected cells were electroporated with a luciferase reporter driven by a WT or E2F binding site-deleted ( $\Delta$ E2F) mutant human proximal *RRM2* gene promoter. A luminescent  $\beta$ -gal reporter was used as an internal control to normalize the transfection efficacy. Mean of three independent experiments with SEM is shown. \* $p < 0.001$  Control/WT versus RAS/WT; \*\* $p < 0.05$  WT versus  $\Delta$ E2F.

(E) Same as (C), but cells were examined for E2F1 and E2F7 binding to the *RRM2* promoter by ChIP using an E2F1 or E2F7 antibody. An isotype-matched IgG was used as a control. Mean of three independent experiments with SEM is shown. \* $p < 0.001$ .

(F) IMR90 cells were infected with control or RAS-encoding retrovirus. Expression of RRM2, E2F1, and E2F7 mRNA was determined by qRT-PCR at the indicated time points. Mean of three independent experiments with SEM is shown.

See also Figure S4.

We next determined whether knockdown of RRM2 is sufficient to induce senescence and the associated cell-cycle exit. Compared with controls, markers of senescence such as SA- $\beta$ -gal activity (Figures 5F, 5G, S5G, and S5H) were induced by RRM2 knockdown. Consistently, markers of cell proliferation, including expression of cyclin A and pS10H3 (Figures 5H and S5I) and BrdU incorporation (Figures 5I, 5J, S5J, and S5K), were lower in shRRM2-expressing cells. Indeed, senescence-associated cell growth arrest was evident in RRM2 knockdown cells, as demonstrated by assays such as colony formation (Figures 5K and S5L) and cell growth curves (Figure 5L). Together, we conclude that knockdown of RRM2 induces cellular senescence in primary human fibroblasts.

To limit the potential off-target effects of shRNAs, we performed rescue experiments by infecting cells with a retrovirus encoding a wild-type (WT) RRM2 cDNA together with a lentivirus encoding an shRRM2 that targets the 5' UTR of the human *RRM2* gene. Knockdown of endogenous RRM2 was confirmed by downregulation of RRM2 mRNA measured by

qRT-PCR using primers targeting the 5' UTR (Figure 5A), whereas expression of ectopic RRM2 was confirmed by expression of RRM2 mRNA measured by qRT-PCR using primers targeting the open reading frame (ORF) region and immunoblotting (Figures 5A and 5E). Indeed, compared with cells expressing shRRM2 alone, ectopic RRM2 expression rescued the aberrant DNA replication induced by shRRM2 (Figure 5B). Additionally, the DDR induced by shRRM2 was also suppressed by ectopic RRM2. Formation of  $\gamma$ H2AX and 53BP1 foci (Figures 5C and 5D) and  $\gamma$ H2AX and p53 expression (Figure 5E) were significantly lower in cells expressing both shRRM2 and ectopic RRM2 compared with shRRM2 alone. Furthermore, expression of markers of senescence such as SA- $\beta$ -gal activity (Figures 5F and 5G) and upregulation of p21 (Figure 5H) was inhibited by ectopic RRM2 in the shRRM2-expressing cells. Moreover, ectopic RRM2 was sufficient to rescue the senescence-associated cell-cycle exit induced by RRM2 knockdown, as demonstrated by upregulation of cyclin A and pS10H3 (Figure 5H), increased BrdU incorporation



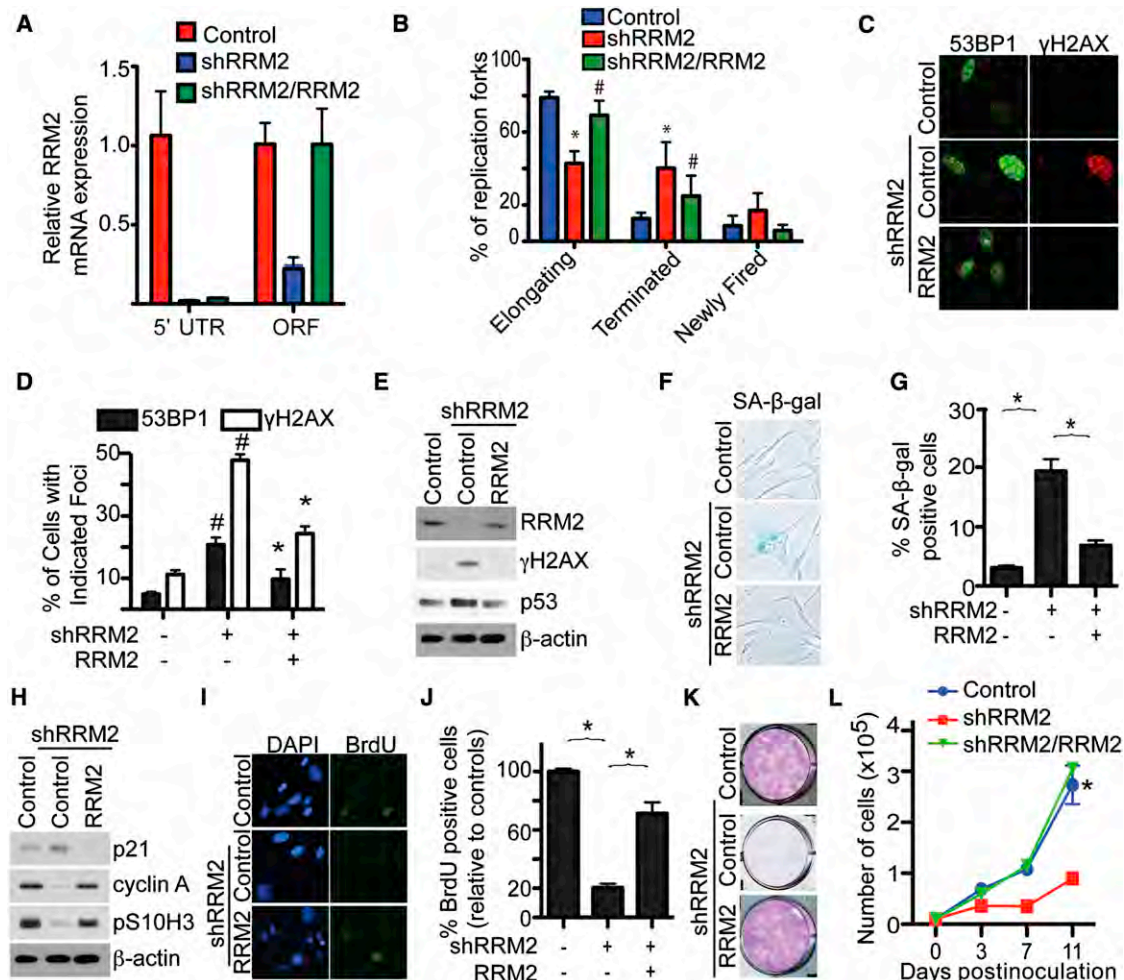


**Figure 5. Knockdown of RRM2 Decreases dNTP Levels and Induces Senescence of Primary Human Fibroblasts**

(A) IMR90 cells were infected with a lentivirus-encoding shRRM2 that targets the 5' UTR of the human *RRM2* gene together with a retrovirus encoding a control or WT RRM2. On day 6, expression of RRM2 mRNA was determined by qRT-PCR using primers designed to its 5' UTR (only amplifies endogenous but not ectopic RRM2 mRNA) or its ORF (amplifies both endogenous and ectopic RRM2 mRNA). Mean of three independent experiments with SEM is shown.

(B) Same as (A) but examined for DNA replication dynamics using the DNA-combing technique on day 2. Mean of three independent experiments with SEM is shown. \* $p < 0.05$  control versus shRRM2; # $p < 0.05$  shRRM2 alone versus shRRM2/RRM2.

(C) Same as (A) but examined for formation of 53BP1 and  $\gamma$ H2AX foci by immunofluorescence at day 6.

(D) Quantification of (C). Mean of three independent experiments with SEM is shown. # $p < 0.001$  versus vector controls; \* $p < 0.001$  versus shRRM2-only cells.

(E) Same as (A) but examined for RRM2,  $\gamma$ H2AX, p53, and  $\beta$ -actin expression by immunoblotting.

(F) Same as (A) but stained for SA- $\beta$ -gal activity.

(G) Quantification of (F). Mean of three independent experiments with SEM is shown. \* $p < 0.001$ .

(H) Same as (A) but examined for p21, cyclin A, pS10H3, and  $\beta$ -actin by immunoblotting.

(I) Same as (A) but labeled with BrdU for 1 hr, and the incorporated BrdU was visualized by immunofluorescence. DAPI counterstaining was used to visualize nuclei.

(J) Quantification of (I). The relative percentage of BrdU-positive cells was calculated against vector controls. Mean of three independent experiments with SEM is shown. \* $p < 0.001$ .

(K) Same as (A), but an equal number of the indicated cells were seeded in 6-well plates. After 2 weeks, the plates were stained with 0.05% crystal violet in PBS to visualize colony formation. Shown are representative images from three independent experiments.

(L) Same as (K), but the number of cells was counted at the indicated time points. Mean of three independent experiments with SEM is shown. \* $p < 0.001$  compared with cells expressing shRRM2 alone.

See also Figure S5.

(Figures 5I and 5J), colony formation (Figure 5K), and cell growth (Figure 5L) compared to shRRM2 alone. Notably, the ectopically expressed RRM2 levels were comparable to its

endogenous level (Figures 5A and 5E), suggesting that the observed effects are not due to supraphysiological levels of RRM2 expression. Together, we conclude that knockdown of

RRM2 is sufficient to trigger aberrant DNA replication, the DDR, and senescence in primary human cells.

### Ectopic RRM2 Expression Is Sufficient to Overcome the Stable OIS-Associated Cell Growth Arrest

We next sought to determine whether downregulation of RRM2 is necessary for the OIS-associated cell growth arrest. Toward this goal, we ectopically expressed RRM2 in RAS-infected cells. Compared with controls, ectopic RRM2 suppressed markers of senescence such as SA- $\beta$ -gal activity and SAHF formation (Figures 6A and 6B) and upregulation of p16 and p21 (Figure 6C). Indeed, ectopic RRM2 suppressed the OIS-associated cell-cycle exit, as evidenced by the significant increase in cyclin A and pS10H3 expression (Figure 6C) and BrdU incorporation (Figures 6D and 6E). Ectopic RRM2 significantly suppressed the OIS-associated growth arrest as determined by colony-formation assays (Figure 6F) and cell growth curves (Figure 6G). Of note, to limit the effects of supraphysiological levels of RRM2 expression, we expressed the ectopic RRM2 at a level lower than that of control cells (Figure 6C). Importantly, the observed effects correlated with the rescue of dNTP levels by ectopic RRM2 in these cells (Figure 6H), further supporting the idea that RRM2 downregulation plays a major role in decreasing dNTP levels during OIS. In addition, ectopic RRM2 significantly suppressed the aberrant DNA replication observed during RAS-induced senescence (Figure 6I). This result suggests that RRM2 suppresses aberrant DNA replication by rescuing the decrease in dNTP levels. Likewise, the DDR was also suppressed by ectopic RRM2, as demonstrated by a decrease in the formation of 53BP1 and  $\gamma$ H2AX foci (Figures 6J and 6K) as well as a decrease in p53 and  $\gamma$ H2AX protein expression (Figure 6L). Based on these data, we conclude that RRM2 downregulation is necessary for senescence, and restoration of dNTP levels by ectopic RRM2 expression suppresses senescence.

We found that exogenous nucleosides are sufficient to overcome the OIS-associated cell growth arrest in established senescent cells (Figure 2). Because ectopic RRM2 is sufficient to rescue the decrease in dNTP levels during senescence (Figure 6H), we next sought to determine whether ectopic RRM2 expression is sufficient to overcome the stable OIS-associated cell growth arrest in established senescent cells. To do so, stably arrested senescent cells induced by RAS were infected with a lentivirus encoding RRM2 (which can infect growth-arrested, nondividing cells), and markers of senescence and cell cycle were examined. Compared with controls, markers of senescence such as SA- $\beta$ -gal activity and p16 expression were suppressed by the lentivirus-mediated RRM2 expression (Figures 6M–6O). Significantly, expression of RRM2 was able to overcome the stable OIS-associated arrest, as evidenced by both increased pS10H3 expression and marked cell growth (Figures 6O and 6P). These observations were not due to a loss of RAS expression because RAS was expressed at similar levels in both control and RRM2-expressing cells (Figure 6O). Together, these data indicate that RRM2 repression is necessary for maintenance of the stable senescence-associated cell growth arrest in established senescent cells.

### RRM2 Repression Correlates with Senescence Status in Human Nevi and Malignant Melanoma Harboring Oncogenic BRAF or NRAS

We next sought to determine the importance of our findings in a pathologically relevant model. Benign human nevi harboring activated oncogenes are comprised of oncogene-induced senescent melanocytes (Michaloglou et al., 2005). In addition, there is evidence to suggest that the progression of benign nevi with oncogenic BRAF or NRAS into malignant melanoma correlates with OIS bypass (Dankort et al., 2007; Dhomen et al., 2009; Kuilman et al., 2010). Thus, we sought to validate our findings by examining RRM2 expression in human benign nevi and malignant melanoma specimens. First, we determined whether RRM2 is downregulated during oncogenic BRAF or NRAS-induced senescence of primary human melanocytes. Indeed, RRM2 expression was significantly inhibited during senescence of melanocytes induced by oncogenic BRAF or NRAS (Figures 7A–7C and S6A–S6C). Similar to what we observed in primary human fibroblasts (Figure 1), exogenous nucleosides were able to suppress senescence induced by oncogenic BRAF in primary human melanocytes (Figures S6D–S6F). These results suggest that RRM2 expression may promote melanoma by suppressing oncogenic BRAF or NRAS-induced senescence.

We also determined that RRM2 expression was significantly increased in human melanoma cells harboring oncogenic BRAF or NRAS compared to normal human melanocytes (Figure 7D). Notably, it has previously been demonstrated that supraphysiological levels of RRM2 promote tumorigenesis by causing genomic instability and the DDR (D'Angiolella et al., 2012; Xu et al., 2008). Consistently, we observed that physiological levels of RRM2 suppress oncogenic RAS-induced DDR (Figure 6), whereas DDR markers such as  $\gamma$ H2AX remain high in RAS-infected cells expressing supraphysiological levels of RRM2 (Figures S6G and S6H).

We next compared expression of RRM2, the senescence marker p16, and the cell proliferation marker Ki67 in a cohort of human benign nevi and melanoma specimens harboring oncogenic BRAF or NRAS (Table S1). Strikingly, RRM2 expression was nearly negative in human nevi with oncogenic BRAF or NRAS, whereas the expression of RRM2 was significantly higher in the melanoma specimens with oncogenic BRAF or NRAS (Figures 7E and 7F). Consistently, expression of p16 was significantly higher in benign human nevi compared to malignant melanomas (Figures 7E and S6I). In contrast, expression of Ki67 was negative in benign human nevi and significantly higher in melanoma specimens (Figures 7E and S6J). These results are consistent with the idea that the supraphysiological levels of RRM2 observed in melanoma specimens contribute to melanoma by suppressing oncogenic BRAF or NRAS-induced senescence. We next determined whether RRM2 expression negatively correlates with survival in patients with melanoma harboring oncogenic BRAF or NRAS. Indeed, high RRM2 expression significantly correlates with poor overall survival in these patients with melanoma (Figure 7G). In contrast, expression of RRM1 does not correlate with the survival of patients with melanoma harboring oncogenic BRAF or NRAS (Figure S6K). We conclude that RRM2 repression correlates with

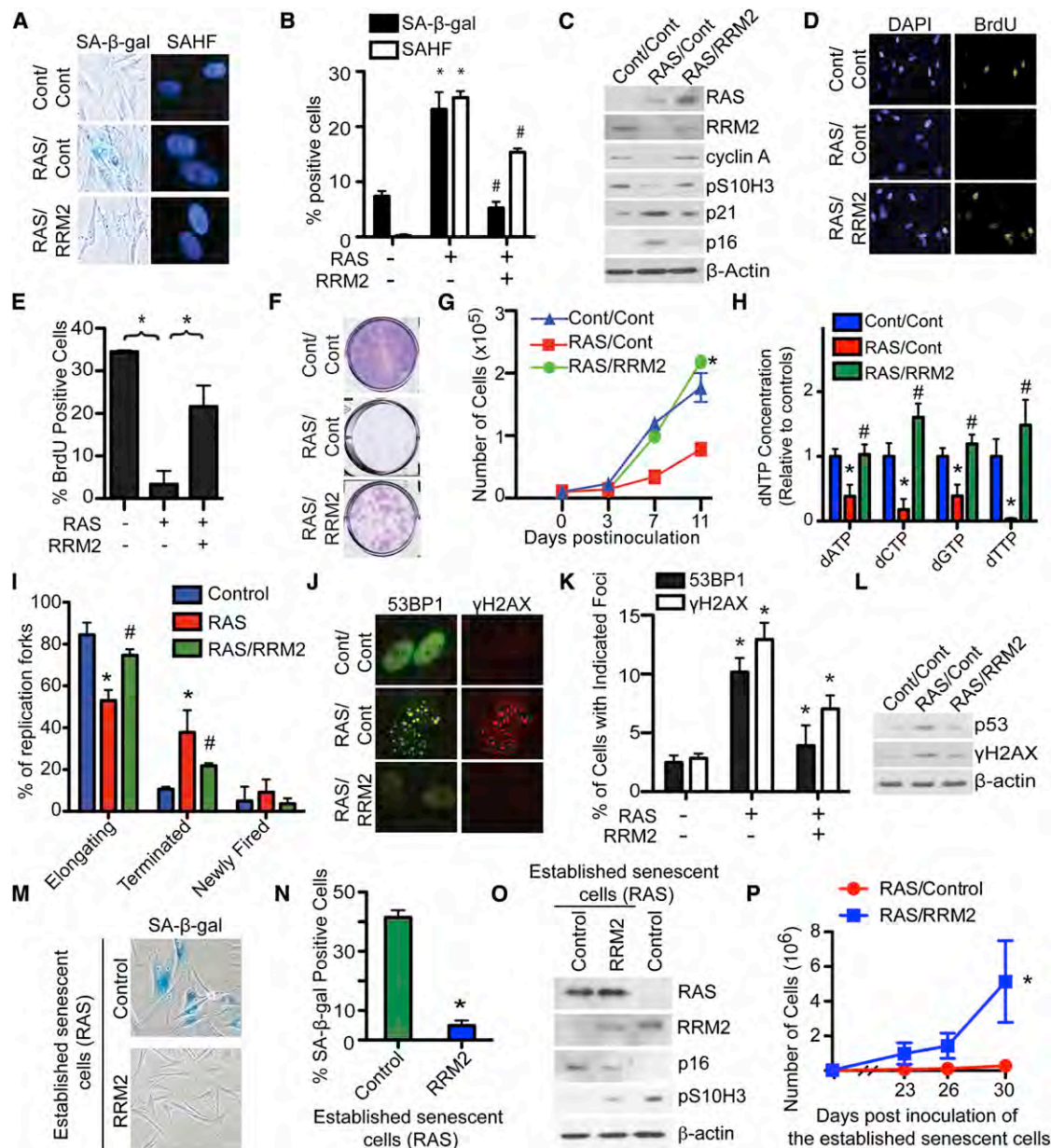


**Figure 6. Ectopic RRM2 Expression Suppresses Senescence and Is Sufficient to Overcome the Stable OIS-Associated Cell Growth Arrest**

(A) IMR90 cells were coinfecting with retrovirus-encoding control or RAS together with or without RRM2. Cells were examined for SA-β-gal activity or SAHF expression on day 6.

(B) Quantification of (A). Mean of three independent experiments with SEM is shown. \* $p < 0.05$  control versus RAS; # $p < 0.05$  RAS alone versus RAS/RRM2.

(C) Same as (A) but examined for RAS, RRM2, cyclin A, pS10H3, p21, p16, and β-actin expression by immunoblotting.

(D) Same as (A), but the cells were labeled with BrdU for 1 hr, and the BrdU incorporation was visualized by immunofluorescence. DAPI counterstaining was used to visualize nuclei.

(E) Quantification of (D). Mean of three independent experiments with SEM is shown. \* $p < 0.01$ .

(F) Same as (A), but an equal number of the indicated cells were seeded in 6-well plates. After 2 weeks, the plates were stained with 0.05% crystal violet in PBS to visualize colony formation. Shown are representative images from three independent experiments.

(G) Same as (F), but the number of cells was counted at the indicated time points. Mean of three independent experiments with SEM is shown. \* $p < 0.01$ .

(H) Same as (A), but on day 2, the concentrations of all four dNTPs were examined.  $p < 0.05$  control versus RAS (\*) and  $p < 0.05$  RAS alone versus RAS/RRM2 (#). Mean of three independent experiments with SEM is shown.

(I) Same as (H) but examined for DNA replication dynamics using the DNA-combing technique on day 2. Mean of three independent experiments with SEM is shown. \* $p < 0.05$  control versus RAS; # $p < 0.05$  RAS alone versus RAS/RRM2.

(J) Same as (A) but examined for the formation of 53BP1 and γH2AX foci by immunofluorescence at day 6.

(K) Quantification of (J). Mean of three independent experiments with SEM is shown. \* $p < 0.05$ .

(legend continued on next page)



the senescence status of human benign nevi and melanoma specimens, and high RRM2 expression significantly correlates with worse overall survival in patients with melanoma.

Finally, we wanted to determine whether melanoma cells harboring activated oncogenes can be driven to undergo senescence by knockdown of RRM2. To do this, UACC-62 human melanoma cells were infected with two individual shRRM2s. The knockdown efficacy of shRRM2s in UACC-62 cells was confirmed by immunoblotting (Figure 7H). The growth of UACC-62 cells was notably inhibited by knockdown of RRM2, as determined by cell growth curves (Figure 7I) and colony formation (Figure 7J). Interestingly, the DDR marker  $\gamma$ H2AX was upregulated by RRM2 knockdown (Figure 7H). To determine whether these cells were undergoing senescence, SA- $\beta$ -gal activity was assessed. Indeed, UACC-62 cells infected with shRRM2 had significantly increased SA- $\beta$ -gal activity compared to controls (Figures 7K and 7L). Similar results were also obtained with another melanoma cell line, WM164 (Figures S6L–S6P), suggesting that the observed effects are not cell line specific. These results demonstrate that knockdown of RRM2 in melanoma cells suppresses the growth of these cells by triggering cellular senescence.

## DISCUSSION

In this study, we demonstrate that a decrease in dNTP levels underlies the establishment and maintenance of the stable OIS-associated cell growth arrest. Mechanistically, we discovered that the decrease in dNTP levels is due to the transcriptional repression of the *RRM2* gene through recruitment of E2F7 prior to the senescence-associated cell-cycle exit. This correlates with aberrant DNA replication and coincides with the DDR during OIS. Notably, RRM2 downregulation is both necessary and sufficient for senescence, which correlates with its effects on the changes in cellular dNTP levels. Significantly, we demonstrated that suppression of nucleotide metabolism through RRM2 repression is necessary for maintenance of the stable OIS-associated cell growth arrest because established senescent cells can reenter the cell cycle after expression of ectopic RRM2. Underscoring the physiological relevance of the current discovery, we showed that RRM2 repression positively correlates with the senescence status of melanocytes in human benign nevi and melanoma specimens harboring oncogenic BRAF or NRAS. Additionally, high RRM2 expression correlates with poor overall survival in patients with melanoma harboring oncogenic BRAF or NRAS. Knockdown of RRM2 in human melanoma cells with activated oncogenes drives senescence of these cells, supporting the hypothesis that RRM2 promotes melanoma by suppressing the senescence tumor suppression mechanism.

We show that addition of exogenous nucleosides in established senescent cells is able to overcome the senescence-associated cell growth arrest (Figure 2). In addition, knockdown of RRM2 expression drives senescence and the associated cell growth arrest (Figures 5 and S5). Conversely, ectopic RRM2 is sufficient to overcome the stable senescence-associated cell growth arrest (Figure 6). These observed effects correlate with the changes in dNTP levels in these cells (Figures 5, 6, and S5). Significantly, RRM2 repression, which drives the decrease in dNTP levels, occurs prior to the senescence-associated cell-cycle exit (Figures 4A and 4B), demonstrating that the observed effects are not a consequence of senescence or its associated cell growth arrest. These results support the premise that the decrease in dNTP levels induced by RRM2 repression is necessary and sufficient for establishing and maintaining the stable senescence-associated cell growth arrest induced by activated oncogenes.

OIS is characterized by aberrant DNA replication during the S phase of the cell cycle, which triggers the DDR (Bartkova et al., 2006; Di Micco et al., 2006). Here, we show that dNTP levels are decreased prior to the OIS-associated cell-cycle exit (Figure 3A), and addition of exogenous nucleosides significantly rescues the aberrant DNA replication and DDR during OIS (Figures 1D, 1E, 3B, and 3C). These data indicate that there is a correlation between the decrease in dNTP pools and aberrant DNA replication and DDR during OIS. However, the effect of nucleosides on OIS is not a consequence of DDR because senescence induced by DNA-damaging agents such as doxorubicin and etoposide is not affected by exogenous nucleosides (Figures S1B–S1I). This further supports the premise that the decrease in dNTP levels is specifically linked to aberrant DNA replication during OIS. Indeed, RRM2 knockdown decreases dNTP levels and triggers aberrant DNA replication and the DDR (Figures 5B–5D and S5C–S5E). Conversely, ectopic RRM2 rescues the decrease in dNTP levels and suppresses the aberrant DNA replication and DDR induced by activated oncogenes (Figures 6H–6K). Together, these data support a model whereby oncogene-induced repression of RRM2 decreases the dNTP levels, which triggers aberrant DNA replication and the DDR and, ultimately, OIS-associated cell growth arrest. It is possible that the DDR triggered by aberrant DNA replication is irreparable in the context of oncogene activation because of the lack of dNTPs due to RRM2 repression. This causes persistent DDR observed in established senescent cells (Rodier et al., 2009) and underlies the stable OIS-associated cell growth arrest.

One of the classical examples of OIS as a tumor suppression mechanism is melanocytic nevi arising from oncogenic BRAF or NRAS (Kuilman et al., 2010). The stable growth arrest observed in these lesions is thought to prevent transformation of these cells into malignant melanoma (Mooi and Peeper, 2006). Here,

(L) Same as (A) but examined for p53,  $\gamma$ H2AX, and  $\beta$ -actin expression by immunoblotting.

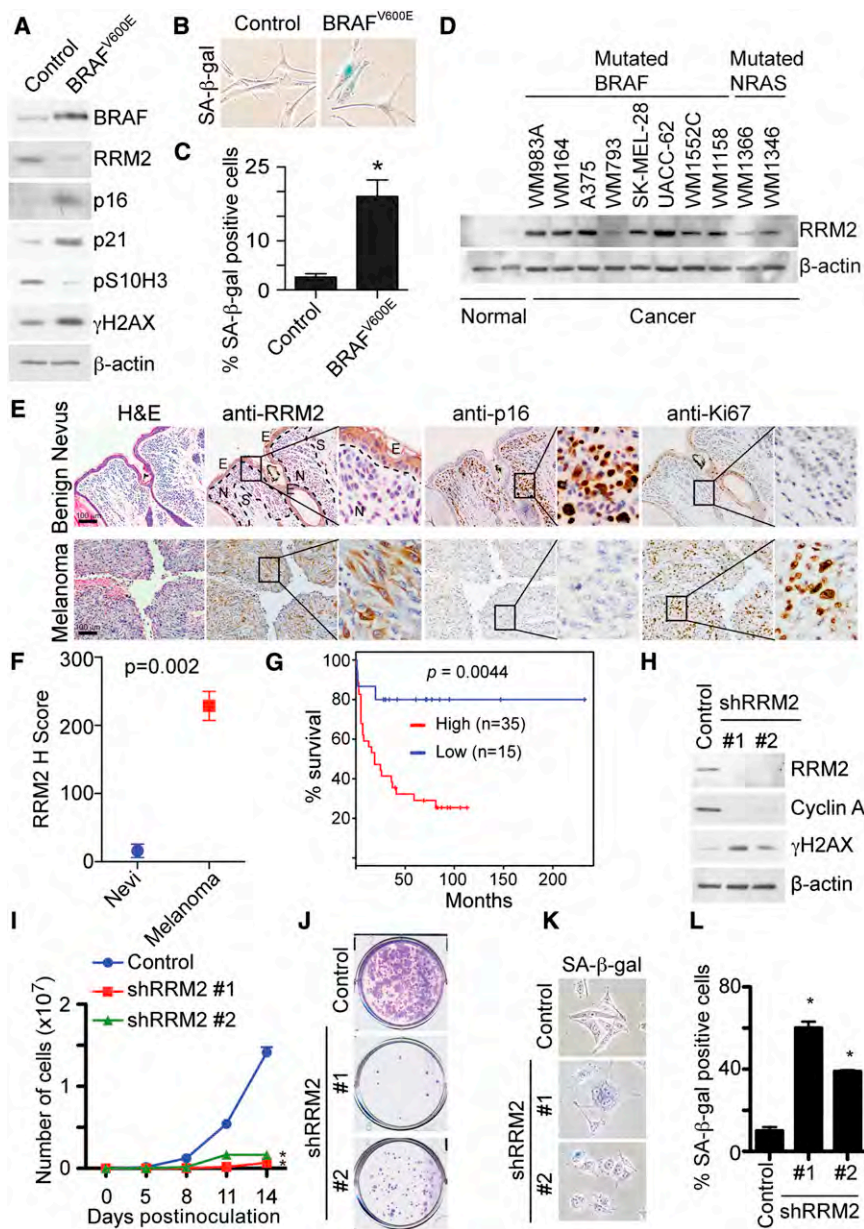
(M) IMR90 cells were infected with RAS-encoding retrovirus. On day 6, established senescent cells were infected with a lentivirus encoding RRM2 or an empty vector control. After an additional 14 days, the cells were stained for SA- $\beta$ -gal activity.

(N) Quantification of (M). Mean of three independent experiments with SEM is shown. \* $p < 0.001$ .

(O) Same as (M) but examined for RAS, RRM2, p16, pS10H3, and  $\beta$ -actin expression by immunoblotting.

(P) Same as (M), but an equal number of cells were inoculated in 6-well plates, and the number of cells was counted at the indicated time points. Mean of three independent experiments with SEM is shown. \* $p < 0.05$ .





plates were stained with 0.05% crystal violet in PBS to visualize colony formation. Shown are representative images of three independent experiments. (K) Same as (H) but stained for SA-β-gal activity. (L) Quantification of (K). Mean of three independent experiments with SEM is shown. \* $p < 0.05$  compared with controls. See also Figure S6 and Table S1.

we found that RRM2 repression correlates with senescence status in human melanocytic nevi and melanoma specimens harboring oncogenic BRAF or NRAS (Figure 7). Interestingly, as previously reported by Michaloglou et al. (2005), expression of the senescence marker p16 in melanocytic nevi is heterogeneous with a proportion of negative expression cells (Figure 7E). In contrast, RRM2 repression occurs in nearly all melanocytes within the benign nevi (Figures 7E and 7F). This suggests that suppression of nucleotide metabolism plays a broader role in maintaining the OIS-associated stable cell growth

arrest, such as the one observed in melanocytic nevi, compared to p16. Together, these findings are consistent with the idea that RRM2 repression is necessary for the stable cell growth arrest observed in OIS-associated benign lesions such as melanocytic nevi.

Cellular dNTP levels play a role in regulating cell proliferation by controlling DNA synthesis (Reichard, 1988). Here, we show that activation of oncogenes decreases dNTP levels in primary human cells prior to OIS-associated cell growth arrest due to oncogene-induced RRM2 downregulation (Figures 3 and 6H).

### Figure 7. RRM2 Is Repressed in Human Benign Nevi, whereas Overexpressed in Melanoma; Knockdown of RRM2 Drives Senescence of Melanoma Cells

(A) Melanocytes were infected with a lentivirus encoding control or BRAF<sup>V600E</sup>. At 21 days after infection, cells were examined for BRAF, RRM2, p16, p21, pS10H3, γH2AX, and β-actin expression by immunoblotting.

(B) Same as (A) but examined for SA-β-gal activity.

(C) Quantification of (B). Mean of two independent experiments with SEM is shown. \* $p < 0.01$ .

(D) RRM2 and β-actin expression in two individual isolations of normal human melanocytes and the indicated human melanoma cell lines by immunoblotting is shown. Mutation status of BRAF and NRAS of the selected cell lines is indicated.

(E) Immunohistochemical staining of RRM2, p16, and Ki67 in benign human nevus (N) and human melanoma tissue specimens harboring oncogenic BRAF or NRAS. Shown are examples of a benign human nevus and a human melanoma tissue harboring oncogenic BRAF<sup>V600E</sup>. S, stroma; E, epidermal compartments.

(F) Quantification of RRM2 staining in (E). Expression of RRM2 in benign human nevi ( $n = 5$ ) and melanoma tissue specimens ( $n = 7$ ) was quantified using the histological score. Mean of three independent experiments with SEM is shown.

(G) A high level of RRM2 expression correlates with shorter overall survival in human patients with melanoma harboring oncogenic BRAF or NRAS. The univariate overall survival curve (Kaplan-Meier method) for patients with melanoma ( $n = 50$ ) with high or low RRM2 expression is detailed in Experimental Procedures.

(H) UACC-62 human melanoma cells were infected with control or two individual shRRM2s encoding lentivirus. RRM2, cyclin A, γH2AX, and β-actin expression was determined by immunoblotting.

(I) Same as (H), but an equal number of cells were seeded in 6-well plates, and the number of cells was counted at the indicated time points. Mean of three independent experiments with SEM is shown. \* $p < 0.05$  compared with controls.

(J) Same as (I), but after 2 additional weeks, the

This suggests that RRM2 downregulation leads to an uncoordinated cell proliferation and dNTP supply, which ultimately leads to senescence and the associated cease of proliferation. Consistently, changes in nucleotide metabolism have been implicated in the early stages of cancer development. For example, the viral oncogenic protein HPV16 E6/7 induces genomic instability by suppressing dNTP synthesis (Bester et al., 2011). Furthermore, we show that RRM2 repression correlates with senescence status in human nevi or melanoma specimens harboring oncogenic BRAF or NRAS (Figures 7 and S6). Consistently, knockdown of RRM2 drives the senescence of melanoma cells harboring activated oncogenes (Figures 7H–7L and S6L–S6P). These data are consistent with a model whereby RRM2 expression regulates the OIS-associated cell growth arrest by acting as a key switch for the coordinated cell proliferation and dNTP supply.

We show that RRM2 is downregulated at the transcriptional level during OIS (Figures 4C and 4D). In addition, we show that RRM2 transcriptional repression correlates with an enhanced association with E2F7, a transcriptional repressor, with the promoter of the *RRM2* gene (Figure 4E). This correlates with a simultaneous decrease in binding of transcriptional activator E2F1 to the *RRM2* gene promoter. Indeed, E2F7 upregulation demonstrated the same kinetics as RRM2 downregulation during OIS (Figure 4F). Consistent with our observation, E2F7 has recently been shown to be upregulated during the early stages of senescence (Aksoy et al., 2012). In addition, RRM2 has also been shown to be regulated by c-Myc (Liu et al., 2008), a key regulator of the nucleotide biosynthetic pathway (Dang, 1999, 2011). Thus, it is plausible that c-Myc may cooperate indirectly with E2F7 and E2F1 in regulating RRM2 transcription prior to the senescence-associated cell-cycle exit.

We found that RRM2 is significantly overexpressed in melanoma cells (Figures 7D–7F). Notably, supraphysiological levels of RRM2 can lead to genomic instability, DNA damage, and tumorigenesis by causing an imbalance in dNTP pools (D'Angiolla et al., 2012; Xu et al., 2008). Here, we show that supraphysiological levels of RRM2 observed in melanoma cells correlate with loss of expression of markers of senescence in melanoma specimens (Figure 7). In addition, we found that markers of the DDR remain high in RAS-infected primary human fibroblasts expressing supraphysiological levels of RRM2 (Figures S6G and S6H). These data support the notion that supraphysiological levels of RRM2 suppress OIS and simultaneously promote genomic instability by allowing error-prone replication due to an imbalance in dNTP pools, which ultimately drives tumorigenesis. These data also demonstrate the important role of RRM2 in cancer development by controlling dNTP pools. Indeed, RRM2 knockdown in human melanoma cells harboring oncogenic BRAF suppressed the proliferation of these cells by triggering senescence (Figures 7H–7L and S6L–S6P). The p53 and pRB tumor suppressor pathways are key senescence effectors (Campisi and d'Adda di Fagnana, 2007; Courtois-Cox et al., 2008; Kuilman et al., 2010). Notably, p53 is mutated in the WM164 cell line (Weiss et al., 1993). In addition, p16 is deleted in the UACC-62 cell line (Ikediobi et al., 2006) and mutated in the WM164 cell line (Ohta et al., 1994). However, knockdown of RRM2 in these cells was able to induce senescence (Figures 7H–7L and S6L–S6P). Therefore, senescence induced by

RRM2 inhibition in melanoma cells is independent of both p53 and p16. This indicates that human cancer cells that lack functional p53 and p16 retain the capacity to undergo senescence through suppressing RRM2. These data suggest that inhibition of the nucleotide biosynthetic pathway by suppressing RRM2 represents a bona fide target for driving cancer cells to undergo senescence.

In summary, suppression of nucleotide metabolism via RRM2 repression underlies the establishment and maintenance of the stable cell growth arrest, the hallmark that characterizes OIS as an important tumor suppression mechanism. These data place altered nucleotide metabolism at the heart of OIS regulation and provide the molecular basis by which the stable OIS-associated cell growth arrest is established and maintained.

## EXPERIMENTAL PROCEDURES

### Retrovirus and Lentivirus Infections

Retrovirus production and transduction were performed as described previously (Tu et al., 2011; Ye et al., 2007; Zhang et al., 2005) using Phoenix cells to package the infection viruses (Dr. Gary Nolan, Stanford University). Lentivirus was packaged using the ViraPower Kit (Invitrogen, Carlsbad, CA, USA) following the manufacturer's instructions and as described previously (Li et al., 2010; Tu et al., 2011; Ye et al., 2007). Cells infected with viruses encoding the puromycin-resistance gene were selected in 3  $\mu$ g/ml puromycin.

### FACS for C<sub>12</sub>FDG Expression

Cells were incubated with 33  $\mu$ M C<sub>12</sub>FDG (Invitrogen) for 1 hr as described previously by Debacq-Chainiaux et al. (2009). After rinsing with PBS, C<sub>12</sub>FDG-positive cells were sorted using a FACS ARIAll (BD Biosciences, San Jose, CA, USA).

### DNA-Combing Analysis

Cells were pulse labeled for 10 min with medium containing 2 mM of BrdU (Sigma-Aldrich), washed twice with PBS, incubated in regular medium for 20 min, and then chased for 20 min with medium containing 2 mM iododeoxyuridine (IdU; Sigma-Aldrich). Harvesting and spreading of DNA fibers were performed as previously described by Merrick et al. (2004). The DNA fibers were stained with antibodies to BrdU (Abcam) and IdU (Fitzgerald Industries, Acton, MA, USA), and the staining was visualized using secondary antibodies labeled with FITC and Cy3, respectively. DNA fibers were counterstained with a primary antibody to ssDNA (Millipore) and were visualized with a secondary antibody labeled with Alexa Fluor 350 (Invitrogen), allowing the exclusion of any broken or tangled fibers. DNA replication forks were scored as elongating, terminated, or newly fired, as previously described by Bartkova et al. (2006).

### Measurement of dNTP Concentrations in Cells

Briefly,  $5 \times 10^6$  cells were harvested and resuspended in 80% methanol. Cells were vortexed and stored at  $-20^\circ\text{C}$  overnight. Next, cells were boiled for 3 min and centrifuged at  $4^\circ\text{C}$  at  $17,000 \times g$  for 20 min. Supernatants were harvested and dried using a vacuum centrifuge. Pellets were resuspended in nuclease-free water and stored at  $-20^\circ\text{C}$  until use. dNTP concentration was measured as previously described by Wilson et al. (2011).

### ChIP Analysis

ChIP in control and RAS-infected IMR90 cells was performed at day 2 as previously described (Zhang et al., 2007b) using antibodies against E2F1 (Santa Cruz Biotechnology), E2F7 (Santa Cruz Biotechnology), or an isotype-matched IgG control. Immunoprecipitated DNA was analyzed using SYBR Green qPCR Mastermix (SA Biosciences, Valencia, CA, USA) against the human *RRM2* gene promoter region containing the E2F1/E2F7 binding site using the following primers: forward, 5'-CTCCAGCTCCTGGCCTCAA-3', and reverse, 5'-RCCGCGTGGACTGTTAATGC-3'.

### Immunofluorescence, BrdU Labeling, and SA- $\beta$ -Gal Staining

Immunofluorescence staining and BrdU labeling were performed as described previously using antibodies described above (Tu et al., 2011; Zhang et al., 2005, 2007a, 2007b). SA- $\beta$ -gal staining was performed as previously described (Dimri et al., 1995). For quantification, a minimum of 200 cells from each group was examined.

Please see the [Extended Experimental Procedures](#) for further details.

### SUPPLEMENTAL INFORMATION

Supplemental Information includes six figures, one table, and Extended Experimental Procedures and can be found with this article online at <http://dx.doi.org/10.1016/j.celrep.2013.03.004>.

### LICENSING INFORMATION

This is an open-access article distributed under the terms of the Creative Commons Attribution-NonCommercial-No Derivative Works License, which permits non-commercial use, distribution, and reproduction in any medium, provided the original author and source are credited.

### ACKNOWLEDGMENTS

We thank Drs. Dario Altieri, Maureen Murphy, and Ronen Marmorstein for comments. We would also like to thank Dr. Greg Enders for the p16 antibody. We thank Jeffery Faust, David Ambrose, and Scott Weiss in the Wistar Institute Flow Cytometry facility for technical help. R.Z. is an Ovarian Cancer Research Fund Liz Tilberis Scholar. This work was supported by a NIH/NCI grant (R01CA160331 to R.Z.), a DoD Ovarian Cancer Academy Award (OC093420 to R.Z.), by the FWF-Austrian Science Fund (L590-B12 to S.N.W.), and an NIH/NCI training grant (T32CA9171-35 to K.M.A.). Support of core facilities used in this study was provided by Cancer Center Support Grant CA010815 to The Wistar Institute.

Received: October 31, 2012

Revised: January 28, 2013

Accepted: March 1, 2013

Published: April 4, 2013

### REFERENCES

Aksoy, O., Chicas, A., Zeng, T., Zhao, Z., McCurrach, M., Wang, X., and Lowe, S.W. (2012). The atypical E2F family member E2F7 couples the p53 and RB pathways during cellular senescence. *Genes Dev.* 26, 1546–1557.

Bartkova, J., Rezaei, N., Liontos, M., Karakaidos, P., Kletsas, D., Issaeva, N., Vassiliou, L.V., Kolettas, E., Niforou, K., Zoumpouris, V.C., et al. (2006). Oncogene-induced senescence is part of the tumorigenesis barrier imposed by DNA damage checkpoints. *Nature* 444, 633–637.

Bester, A.C., Roniger, M., Oren, Y.S., Im, M.M., Sami, D., Chaoat, M., Bensimon, A., Zamir, G., Shewach, D.S., and Kerem, B. (2011). Nucleotide deficiency promotes genomic instability in early stages of cancer development. *Cell* 145, 435–446.

Campisi, J. (2005). Senescent cells, tumor suppression, and organismal aging: good citizens, bad neighbors. *Cell* 120, 513–522.

Campisi, J., and d'Adda di Fagagna, F. (2007). Cellular senescence: when bad things happen to good cells. *Nat. Rev. Mol. Cell Biol.* 8, 729–740.

Chen, H.Z., Tsai, S.Y., and Leone, G. (2009). Emerging roles of E2Fs in cancer: an exit from cell cycle control. *Nat. Rev. Cancer* 9, 785–797.

Courtois-Cox, S., Jones, S.L., and Cichowski, K. (2008). Many roads lead to oncogene-induced senescence. *Oncogene* 27, 2801–2809.

Dang, C.V. (1999). c-Myc target genes involved in cell growth, apoptosis, and metabolism. *Mol. Cell Biol.* 19, 1–11.

Dang, C.V. (2011). Therapeutic targeting of Myc-reprogrammed cancer cell metabolism. *Cold Spring Harb. Symp. Quant. Biol.* 76, 369–374.

D'Angiolella, V., Donato, V., Forrester, F.M., Jeong, Y.T., Pellacani, C., Kudo, Y., Saraf, A., Florens, L., Washburn, M.P., and Pagano, M. (2012). Cyclin F-mediated degradation of ribonucleotide reductase M2 controls genome integrity and DNA repair. *Cell* 149, 1023–1034.

Dankort, D., Filenova, E., Collado, M., Serrano, M., Jones, K., and McMahon, M. (2007). A new mouse model to explore the initiation, progression, and therapy of BRAFV600E-induced lung tumors. *Genes Dev.* 21, 379–384.

Debacq-Chainiaux, F., Erusalimsky, J.D., Campisi, J., and Toussaint, O. (2009). Protocols to detect senescence-associated beta-galactosidase (SA-beta-gal) activity, a biomarker of senescent cells in culture and in vivo. *Nat. Protoc.* 4, 1798–1806.

Dhomen, N., Reis-Filho, J.S., da Rocha Dias, S., Hayward, R., Savage, K., Delmas, V., Larue, L., Pritchard, C., and Marais, R. (2009). Oncogenic Braf induces melanocyte senescence and melanoma in mice. *Cancer Cell* 15, 294–303.

Di Micco, R., Fumagalli, M., Cicalese, A., Piccinin, S., Gasparini, P., Luise, C., Schurra, C., Garre', M., Nuciforo, P.G., Bensimon, A., et al. (2006). Oncogene-induced senescence is a DNA damage response triggered by DNA hyper-replication. *Nature* 444, 638–642.

Dimri, G.P., Lee, X., Basile, G., Acosta, M., Scott, G., Roskelley, C., Medrano, E.E., Linskens, M., Rubelj, I., Pereira-Smith, O., et al. (1995). A biomarker that identifies senescent human cells in culture and in aging skin in vivo. *Proc. Natl. Acad. Sci. USA* 92, 9363–9367.

Engström, Y., Eriksson, S., Jildevik, I., Skog, S., Thelander, L., and Tribukait, B. (1985). Cell cycle-dependent expression of mammalian ribonucleotide reductase. Differential regulation of the two subunits. *J. Biol. Chem.* 260, 9114–9116.

Håkansson, P., Hofer, A., and Thelander, L. (2006). Regulation of mammalian ribonucleotide reduction and dNTP pools after DNA damage and in resting cells. *J. Biol. Chem.* 281, 7834–7841.

Ikedobi, O.N., Davies, H., Bignell, G., Edkins, S., Stevens, C., O'Meara, S., Santarius, T., Avis, T., Barthorpe, S., Brackenbury, L., et al. (2006). Mutation analysis of 24 known cancer genes in the NCI-60 cell line set. *Mol. Cancer Ther.* 5, 2606–2612.

Kuilman, T., Michaloglou, C., Mooi, W.J., and Peeper, D.S. (2010). The essence of senescence. *Genes Dev.* 24, 2463–2479.

Li, H., Cai, Q., Godwin, A.K., and Zhang, R. (2010). Enhancer of zeste homolog 2 promotes the proliferation and invasion of epithelial ovarian cancer cells. *Mol. Cancer Res.* 8, 1610–1618.

Liu, Y.C., Li, F., Handler, J., Huang, C.R., Xiang, Y., Neretti, N., Sedivy, J.M., Zeller, K.I., and Dang, C.V. (2008). Global regulation of nucleotide biosynthetic genes by c-Myc. *PLoS One* 3, e2722.

Merrick, C.J., Jackson, D., and Diffley, J.F. (2004). Visualization of altered replication dynamics after DNA damage in human cells. *J. Biol. Chem.* 279, 20067–20075.

Michaloglou, C., Vredeveld, L.C., Soengas, M.S., Denoyelle, C., Kuilman, T., van der Horst, C.M., Majoor, D.M., Shay, J.W., Mooi, W.J., and Peeper, D.S. (2005). BRAFE600-associated senescence-like cell cycle arrest of human naevi. *Nature* 436, 720–724.

Mooi, W.J., and Peeper, D.S. (2006). Oncogene-induced cell senescence—halting on the road to cancer. *N. Engl. J. Med.* 355, 1037–1046.

Narita, M., Nunez, S., Heard, E., Narita, M., Lin, A.W., Hearn, S.A., Spector, D.L., Hannon, G.J., and Lowe, S.W. (2003). Rb-mediated heterochromatin formation and silencing of E2F target genes during cellular senescence. *Cell* 113, 703–716.

Nordlund, P., and Reichard, P. (2006). Ribonucleotide reductases. *Annu. Rev. Biochem.* 75, 681–706.

Ohta, M., Nagai, H., Shimizu, M., Rasio, D., Berd, D., Mastrangelo, M., Singh, A.D., Shields, J.A., Shields, C.L., Croce, C.M., et al. (1994). Rarity of somatic and germline mutations of the cyclin-dependent kinase 4 inhibitor gene, CDK4I, in melanoma. *Cancer Res.* 54, 5269–5272.

Reichard, P. (1988). Interactions between deoxyribonucleotide and DNA synthesis. *Annu. Rev. Biochem.* 57, 349–374.

Rodier, F., Coppé, J.P., Patil, C.K., Hoeijmakers, W.A., Muñoz, D.P., Raza, S.R., Freund, A., Campeau, E., Davalos, A.R., and Campisi, J. (2009).

- Persistent DNA damage signalling triggers senescence-associated inflammatory cytokine secretion. *Nat. Cell Biol.* 11, 973–979.
- Serrano, M., Lin, A.W., McCurrach, M.E., Beach, D., and Lowe, S.W. (1997). Oncogenic ras provokes premature cell senescence associated with accumulation of p53 and p16INK4a. *Cell* 88, 593–602.
- Tu, Z., Aird, K.M., Bitler, B.G., Nicodemus, J.P., Beeharry, N., Zia, B., Yen, T.J., and Zhang, R. (2011). Oncogenic Ras regulates BRIP1 expression to induce dissociation of BRCA1 from chromatin, inhibit DNA repair, and promote senescence. *Dev. Cell* 21, 1077–1091.
- Weiss, J., Schwechheimer, K., Cavenee, W.K., Herlyn, M., and Arden, K.C. (1993). Mutation and expression of the p53 gene in malignant melanoma cell lines. *Int. J. Cancer* 54, 693–699.
- Wilson, P.M., Labonte, M.J., Russell, J., Louie, S., Ghobrial, A.A., and Ladner, R.D. (2011). A novel fluorescence-based assay for the rapid detection and quantification of cellular deoxyribonucleoside triphosphates. *Nucleic Acids Res.* 39, e112.
- Xu, X., Page, J.L., Surtees, J.A., Liu, H., Lagedrost, S., Lu, Y., Bronson, R., Alani, E., Nikitin, A.Y., and Weiss, R.S. (2008). Broad overexpression of ribonucleotide reductase genes in mice specifically induces lung neoplasms. *Cancer Res.* 68, 2652–2660.
- Yaswen, P., and Campisi, J. (2007). Oncogene-induced senescence pathways weave an intricate tapestry. *Cell* 128, 233–234.
- Ye, X., Zerlanko, B., Kennedy, A., Banumathy, G., Zhang, R., and Adams, P.D. (2007). Downregulation of Wnt signaling is a trigger for formation of facultative heterochromatin and onset of cell senescence in primary human cells. *Mol. Cell* 27, 183–196.
- Zhang, R., Poustovoitov, M.V., Ye, X., Santos, H.A., Chen, W., Daganzo, S.M., Erzberger, J.P., Serebriiskii, I.G., Canutescu, A.A., Dunbrack, R.L., et al. (2005). Formation of MacroH2A-containing senescence-associated heterochromatin foci and senescence driven by ASF1a and HIRA. *Dev. Cell* 8, 19–30.
- Zhang, R., Chen, W., and Adams, P.D. (2007a). Molecular dissection of formation of senescence-associated heterochromatin foci. *Mol. Cell. Biol.* 27, 2343–2358.
- Zhang, R., Liu, S.T., Chen, W., Bonner, M., Pehrson, J., Yen, T.J., and Adams, P.D. (2007b). HP1 proteins are essential for a dynamic nuclear response that rescues the function of perturbed heterochromatin in primary human cells. *Mol. Cell. Biol.* 27, 949–962.



## BRG1 Is Required for Formation of Senescence-Associated Heterochromatin Foci Induced by Oncogenic RAS or BRCA1 Loss

Zhigang Tu, Xinying Zhuang, Yong-Gang Yao and Rugang Zhang

*Mol. Cell. Biol.* 2013, 33(9):1819. DOI: 10.1128/MCB.01744-12.

Published Ahead of Print 25 February 2013.

---

Updated information and services can be found at:  
<http://mcb.asm.org/content/33/9/1819>

---

### SUPPLEMENTAL MATERIAL

*These include:*

[Supplemental material](#)

### REFERENCES

This article cites 39 articles, 17 of which can be accessed free at: <http://mcb.asm.org/content/33/9/1819#ref-list-1>

### CONTENT ALERTS

Receive: RSS Feeds, eTOCs, free email alerts (when new articles cite this article), [more»](#)

---

---

Information about commercial reprint orders: <http://journals.asm.org/site/misc/reprints.xhtml>  
To subscribe to to another ASM Journal go to: <http://journals.asm.org/site/subscriptions/>

---

Journals.ASM.org

# BRG1 Is Required for Formation of Senescence-Associated Heterochromatin Foci Induced by Oncogenic RAS or BRCA1 Loss

Zhigang Tu,<sup>a</sup> Xinying Zhuang,<sup>b</sup> Yong-Gang Yao,<sup>b</sup> Rugang Zhang<sup>a</sup>

Gene Expression and Regulation Program, The Wistar Institute, Philadelphia, Pennsylvania, USA<sup>a</sup>; Key Laboratory of Animal Models and Human Disease Mechanisms of the Chinese Academy of Sciences, Kunming Institute of Zoology, Kunming, Yunnan, China<sup>b</sup>

Cellular senescence is an important tumor suppression mechanism. We have previously reported that both oncogene-induced dissociation of BRCA1 from chromatin and BRCA1 knockdown itself drive senescence by promoting formation of senescence-associated heterochromatin foci (SAHF). However, the molecular mechanism by which BRCA1 regulates SAHF formation and senescence is unclear. BRG1 is a chromatin-remodeling factor that interacts with BRCA1 and pRB. Here we show that BRG1 is required for SAHF formation and senescence induced by oncogenic RAS or BRCA1 loss. The interaction between BRG1 and BRCA1 is disrupted during senescence. This correlates with an increased level of chromatin-associated BRG1 in senescent cells. BRG1 knockdown suppresses the formation of SAHF and senescence, while it has no effect on BRCA1 chromatin dissociation induced by oncogenic RAS, indicating that BRG1 functions downstream of BRCA1 chromatin dissociation. Furthermore, BRG1 knockdown inhibits SAHF formation and senescence induced by BRCA1 knockdown. Conversely, BRG1 overexpression drives SAHF formation and senescence in a DNA damage-independent manner. This effect depends upon BRG1's chromatin-remodeling activity as well as the interaction between BRG1 and pRB. Indeed, the interaction between BRG1 and pRB is enhanced during senescence. Chromatin immunoprecipitation analysis revealed that BRG1's association with the human *CDKN2A* and *CDKN1A* gene promoters was enhanced during senescence induced by oncogenic RAS or BRCA1 knockdown. Consistently, knockdown of pRB, p21<sup>CIP1</sup>, and p16<sup>INK4a</sup>, but not p53, suppressed SAHF formation induced by BRG1. Together, these studies reveal the molecular underpinning by which BRG1 acts downstream of BRCA1 to promote SAHF formation and senescence.

Activation of oncogenes (such as RAS) in primary mammalian cells typically triggers cellular senescence, a state of irreversible cell growth arrest (1, 2). Oncogene-induced senescence is an important tumor suppression mechanism *in vivo* (1). Senescent cells display several morphological and molecular characteristics. For instance, they are positive for senescence-associated  $\beta$ -galactosidase (SA- $\beta$ -gal) activity (3). In addition, chromatin in the nuclei of senescent human cells typically reorganizes to form specialized domains of facultative heterochromatin called senescence-associated heterochromatin foci (SAHF) (4–8). SAHF are enriched in markers of heterochromatin such as histone H2A variant macroH2A (mH2A), di- or trimethylated lysine 9 histone H3 (H3K9Me2/3), and heterochromatin protein 1 (HP1) proteins (5, 7). SAHF formation contributes to the senescence-associated cell cycle exit by directly sequestering and silencing proliferation-promoting genes (4, 7). The p53 and pRB tumor suppressor pathways are the key regulators of senescence (1). Indeed, p16<sup>INK4a</sup>, an upstream regulator of pRB, and p21<sup>CIP1</sup>, a downstream target of p53, promote SAHF formation (7, 9). In addition, senescence induced by oncogenic RAS is characterized by a DNA damage response (10) and is accompanied by the accumulation of markers of DNA damage such as upregulation of  $\gamma$ H2AX protein expression and increased formation of  $\gamma$ H2AX DNA damage foci (10, 11).

BRCA1 plays an important role in DNA damage repair (12, 13). Germ line mutations in the *BRCA1* gene predispose women to breast and ovarian cancer (12). We have previously demonstrated that BRCA1 becomes dissociated from chromatin in response to activation of oncogenes such as RAS (14). This promotes senescence by driving SAHF formation (14). In addition, BRCA1 chromatin dissociation contributes to the accumulation of DNA damage by impairing the BRCA1-mediated DNA repair response (14). Similarly, we showed that BRCA1 knockdown

drives SAHF formation and senescence and triggers the DNA damage response (14). It has also been shown that cells from the *BRCA1* exon 11 knockout mouse exhibit signs of premature senescence (15, 16). However, the molecular mechanism by which BRCA1 regulates SAHF formation and senescence remains to be determined. In addition, it is unclear whether SAHF formation induced by BRCA1 chromatin dissociation or BRCA1 knockdown is independent of the DNA damage response.

BRCA1 has also been implicated in regulating high-order chromatin structure. For example, targeting BRCA1 to an amplified *lac* operator-containing chromosome region in the mammalian genome results in large-scale chromatin unfolding (17). This suggests that BRCA1 antagonizes heterochromatin formation. Notably, BRCA1 also interacts with the BRG1 subunit of the ATP-dependent SWI/SNF chromatin-remodeling complex (18). BRG1 acts as an activator or repressor of gene expression in a context-dependent manner (19). Loss of BRG1 function is associated with malignant transformation (19), and BRG1 heterozygous deletion results in spontaneous tumor development in mouse models, indicating its role as a tumor suppressor (20, 21). Notably, BRG1 interacts with pRB (22), a key regulator of SAHF formation and

Received 27 December 2012 Returned for modification 19 January 2013

Accepted 19 February 2013

Published ahead of print 25 February 2013

Address correspondence to Rugang Zhang, rzhang@wistar.org.

Supplemental material for this article may be found at <http://dx.doi.org/10.1128/MCB.01744-12>.

Copyright © 2013, American Society for Microbiology. All Rights Reserved.

doi:10.1128/MCB.01744-12

senescence (4, 7, 23). BRG1 also plays a role in promoting cell growth arrest and senescence phenotypes (22, 24–27). However, whether the interaction between BRG1 and BRCA1 or pRB is regulated during senescence is unknown. In addition, whether BRG1 contributes to SAHF formation induced by oncogenic RAS or BRCA1 knockdown has never been investigated.

Here we show that the interaction between BRCA1 and BRG1 is disrupted in cells undergoing senescence. This correlates with an increased level of chromatin-associated BRG1 in senescent cells. BRG1 is required for SAHF formation and senescence induced by BRCA1 chromatin dissociation or BRCA1 knockdown. Conversely, ectopic BRG1 drives SAHF formation and senescence, which requires its chromatin-remodeling activity to up-regulate p16<sup>INK4a</sup> and p21<sup>CIP1</sup>. Indeed, the association of BRG1 with the promoters of the SAHF-regulating genes *CDKN2A* (encoding p16<sup>INK4a</sup>) and *CDKN1A* (encoding p21<sup>CIP1</sup>) was enhanced during senescence induced by oncogene activation or BRCA1 knockdown. Interestingly, BRG1 promotes SAHF and senescence in a DNA damage response-independent manner. Further, we show that the interaction between BRG1 and pRB is enhanced during senescence and that SAHF formation induced by ectopic BRG1 requires its interaction with pRB. Finally, we found that knockdown of pRB, p16<sup>INK4a</sup>, and p21<sup>CIP1</sup>, but not p53, impairs SAHF formation induced by BRG1.

## MATERIALS AND METHODS

**Cell culture.** IMR90 cells were cultured according to the ATCC and as previously described (5, 23). Experiments were performed on IMR90 cells between population doublings 25 and 35.

**Plasmids, antibodies, and immunoblotting.** pBABE-puro, pBABE-puro-H-RAS<sup>G12V</sup>, pBABE-puro-BRG1, and pBABE-puro-BRG1 (K798R) were obtained from Addgene. The BRCA1 short hairpin RNAs (shRNAs) were described previously (14). pBABE-puro-BRG1 delRB with a deletion of amino acids (aa) 1357 to 1361 (BRG1  $\Delta$ RB) was generated using standard molecular cloning techniques. Lentivirus-encoded shRNAs were purchased from Open Biosystems. The sense strand sequences for the BRG1 shRNAs are 5'-CCCGTGGACTTCAAGAAGAT A-3' and 5'-CGGCAGACACTGTGATCATTT-3'. The sense strand sequences for the p16<sup>INK4a</sup> shRNAs are 5'-CATGGAGCCTTCGGCTGAC T-3' and 5'-GCGCTGCCCAACGCACGAAT-3'. The sense strand sequences for the p21<sup>CIP1</sup> shRNAs are 5'-CGCTCTACATCTTCTGCCT TA-3' and 5'-GACAGATTTCTACCACTCCAA-3'. The sense strand sequences for the pRB shRNAs are 5'-CCACATTATTTCTAGTCCAAA-3' and 5'-CAGAGATCGTGATTGAGATT-3'. The sense strand sequences for the p53 shRNAs are 5'-GAGGGATGTTTGGGAGATGTA-3' and 5'-GTCCAGATGAAGCTCCCAGAA-3'. The following antibodies were obtained from the indicated suppliers: rabbit anti-BRCA1 (Upstate), mouse anti-BRCA1 (Calbiochem) for immunofluorescence staining, rabbit anti-BRG1 (Santa Cruz), mouse anti-p21<sup>CIP1</sup> (Santa Cruz), mouse anti-p16<sup>INK4a</sup> (Santa Cruz), mouse anti- $\beta$ -actin (Sigma), mouse anti-RAS (BD Bioscience), mouse anti-p53 (Calbiochem), rabbit anti-serine 15-phosphorylated p53 (Cell Signaling), rabbit anti-FLAG (Cell Signaling), mouse anti-pRB (Cell Signaling), rabbit anti-histone H3 (Millipore), and mouse anti-H3K9me2 (Abcam). Rabbit anti-mH2A1.2 was described previously (4, 28). Immunoblotting was performed using standard protocols with the antibodies indicated above.

**Retrovirus and lentivirus infections.** Retrovirus production and transduction were performed as described previously (5, 29) using Phoenix cells to package the infection viruses (Gary Nolan, Stanford University). Lentivirus was packaged using a Virapower kit from Invitrogen by following the manufacturer's instructions and as described previously (29, 30). Cells infected with viruses carrying a gene conferring resistance

to puromycin or neomycin were selected in 1  $\mu$ g/ml puromycin or 500  $\mu$ g/ml neomycin (G418), respectively.

**Co-IP analysis.** Cells were washed twice with phosphate-buffered saline (PBS) and lysed using a buffer containing 50 mM Tris-HCl (pH 8.0), 1 mM EDTA, 0.5% NP-40, and 150 mM NaCl with the proteinase inhibitors. The supernatant was collected by centrifuging the cell lysates at 12,000  $\times$  g for 10 min at 4°C. One milligram of total protein supernatant was subjected to immunoprecipitation (IP) using 2  $\mu$ g anti-FLAG antibody (Sigma), anti-BRG1 antibody (Santa Cruz), or an isotype-matched IgG control by incubating the antibodies with supernatant for 2 h at 4°C. The IP products were separated on an SDS-PAGE gel and immunoblotted with anti-pRB, anti-BRCA1, or anti-BRG1 antibodies to visualize the immunoprecipitated proteins.

**Chromatin isolation and chromatin immunoprecipitation (ChIP) analysis.** Chromatin was prepared according to previously published methods (6, 31). Chromatin-bound proteins in the chromatin fraction were detected by immunoblotting using antibodies against BRCA1, BRG1, and histone H3 as indicated above.

ChIP analysis in control, RAS-infected, or BRCA1 knockdown IMR90 cells was performed at day 4 post-drug selection as previously described (14) using a polyclonal anti-BRG1 antibody (Santa Cruz), an anti-BRCA1 antibody (Millipore), or an isotype-matched IgG control. Immunoprecipitated DNA was analyzed by PCR or SYBR green-based quantitative PCR (Qiagen). Primers against the human *CDKN2A* gene promoter region are 5'-TGATTTCGATTCTCGGTGGG-3' and 5'-GGGTGTTGGT GTCATAGGG-3'. Primers against the human *CDKN1A* gene promoter region are 5'-TTCAGGAGACAGACAACCTCACTC-3' and 5'-GACACC CCAACAAAGCATCTTG-3'.

**Immunofluorescence and SA- $\beta$ -gal staining.** Immunofluorescence staining was performed as described previously using the antibodies described above (4, 5, 28). SA- $\beta$ -gal staining was performed as previously described (3).

**Comet assay.** A comet assay was performed with a CometAssay (Trevigen) kit following the manufacturer's instruction. DNA damage was measured in artificial Olive Moment units using Cometscore software. A *t* test for significance was performed using Graph Prism software.

## RESULTS

**The interaction between BRCA1 and BRG1 is disrupted in cells undergoing senescence, which correlates with an increased level of chromatin-associated BRG1 and an enhanced interaction between BRG1 and pRB.** We have previously shown that oncogenic RAS dissociates BRCA1 from chromatin, which contributes to formation of SAHF and the senescence phenotype (14). Notably, BRCA1 chromatin dissociation is not a consequence of G<sub>1</sub> phase accumulation in the fully established senescence cells (14), because BRCA1 becomes dissociated from chromatin prior to G<sub>1</sub> phase accumulation in RAS-infected cells compared with controls (see Fig. S1 in the supplemental material). Likewise, knockdown of BRCA1 in primary human cells induces formation of SAHF and senescence (14). Given the role of p16<sup>INK4a</sup> and p21<sup>CIP1</sup> in promoting SAHF formation and senescence (2), we first examined changes in the expression of p16<sup>INK4a</sup> and p21<sup>CIP1</sup> in IMR90 normal human fibroblasts expressing shRNAs corresponding to the human *BRCA1* gene (shBRCA1) that efficiently knock down BRCA1 protein expression (Fig. 1A). Compared with controls, the expression of both p16<sup>INK4a</sup> and p21<sup>CIP1</sup> was upregulated in BRCA1 knockdown cells (Fig. 1B). Notably, similar results were obtained by multiple shBRCA1s (Fig. 1A and B), suggesting that the observed phenotype was not due to off-target effects.

It has been demonstrated that BRCA1 interacts with BRG1, an ATP-dependent chromatin-remodeling factor, in transformed cancer cells (18). In addition, the *CDKN2A* and *CDKN1A* genes,

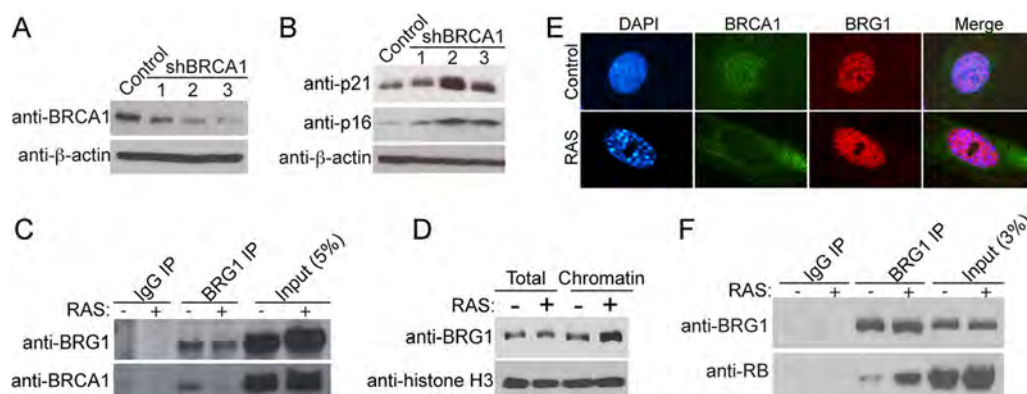


**FIG 1** The interaction between BRG1 and BRCA1 is disrupted during senescence, which correlates with an increased level of chromatin-associated BRG1. (A) IMR90 normal human fibroblasts were infected with lentivirus encoding the indicated shBRCA1 or the control. Drug-selected cells were examined for the expression of BRCA1 and  $\beta$ -actin by immunoblotting. (B) Same as described for panel A except that cells were examined for the expression of p21<sup>CIP1</sup> and p16<sup>INK4a</sup> by immunoblotting. (C) IMR90 cells were infected with retrovirus encoding control or oncogenic H-RAS<sup>G12V</sup>. Drug-selected cells were subjected to coimmunoprecipitation experiments using an anti-BRG1 antibody. An isotype-matched IgG was used as a negative control. Levels of immunoprecipitated BRG1 and BRCA1 were determined by immunoblotting using the indicated antibodies. (D) Same as described for panel C except that the cells were subjected to fractionation to prepare chromatin and the expression of BRG1 and histone H3 in the chromatin fraction of the indicated cells was examined by immunoblotting. (E) Same as described for panel C except that the cells were subjected to immunofluorescence staining using anti-BRCA1 and anti-BRG1 antibodies. DAPI, 4',6'-diamidino-2-phenylindole. (F) Same as described for panel C except that the cells were subjected to coimmunoprecipitation experiments using an anti-BRG1 antibody. An isotype-matched IgG was used as a negative control. Levels of immunoprecipitated BRG1 and pRB were determined by immunoblotting using the indicated antibodies.

which respectively encode p16<sup>INK4a</sup> and p21<sup>CIP1</sup> proteins, are known BRG1 target genes (24, 32). Thus, we sought to determine whether the interaction between BRCA1 and BRG1 is regulated during senescence of IMR90 fibroblasts induced by oncogenic RAS. Toward this goal, IMR90 cells expressing oncogenic RAS to induce senescence or control were subjected to co-immunoprecipitation (co-IP) using an anti-BRG1 antibody. An isotype-matched IgG was used as a negative control. Consistent with the previous observations in cancer cells (18), we found that BRG1 is associated with BRCA1 in control proliferating cells by co-IP analysis (Fig. 1C). Interestingly, we found that this association was lost in RAS-infected cells (Fig. 1C). This was not due to a decrease of either BRCA1 or BRG1 expression level, as the input levels of BRCA1 and BRG1 are comparable between control and RAS-infected cells at this time point (Fig. 1C). Notably, the co-IP demonstrated a high stoichiometry of BRG1 and BRCA1 complex formation, as pulling down BRG1 brought down a similar fraction of BRCA1 (Fig. 1C). Since BRCA1 became dissociated from chromatin (14) and the interaction between BRG1 and BRCA1 was disrupted during senescence (Fig. 1C), we examined the changes in the levels of BRG1 in chromatin fractions during senescence. In contrast to BRCA1's chromatin dissociation (14), BRG1 levels in the chromatin fraction were increased in RAS-infected cells compared with controls (Fig. 1D). This was not due to an increase in total BRG1 levels in RAS-infected cells compared to controls (Fig. 1D). Consistently, immunofluorescence staining of BRCA1 and BRG1 showed that the colocalization between BRCA1 and BRG1 was decreased in the nuclei of RAS-induced senescent cells compared with controls (Fig. 1E). Based on this result, we conclude that the interaction between BRCA1 and BRG1 is disrupted and chromatin-associated BRG1 levels are increased in cells undergoing senescence.

BRG1 interacts with pRB, a known regulator of SAHF formation and senescence (7, 22, 23). Thus, we sought to determine whether the interaction between BRG1 and pRB is regulated dur-

ing senescence. To do so, we performed co-IP using an anti-BRG1 antibody in control and RAS-infected cells. An isotype-matched IgG was used as a control. Interestingly, the interaction between BRG1 and pRB was enhanced in cells undergoing senescence (Fig. 1F).

**Ectopic BRG1 drives SAHF formation and senescence.** Knockout of BRG1 results in the dissolution of pericentromeric heterochromatin (33), suggesting that BRG1 plays a role in regulating heterochromatin structure. Therefore, we next sought to determine whether ectopic BRG1 is sufficient to drive SAHF formation. Toward this goal, we ectopically expressed wild-type BRG1 in IMR90 normal human fibroblasts (Fig. 2A). Indeed, there was a significant increase in SAHF formation in cells ectopically expressing BRG1 compared with controls (Fig. 2B and C). Consistently, other markers of SAHF such as formation of H3K9Me2 and mH2A1.2 foci were also induced by the ectopically expressed wild-type BRG1 (Fig. 2B and C). Expression of SA- $\beta$ -gal activity, a hallmark of cellular senescence (3), was also induced by wild-type BRG1 expression (Fig. 2D and E). Thus, we conclude that ectopic expression of wild-type BRG1 drives SAHF formation and senescence.

We next sought to determine whether BRG1's ability to drive SAHF formation is dependent upon its chromatin-remodeling activity. To do so, we obtained a mutant BRG1 with a single amino acid substitution at amino acid residue 798 (BRG1 K798R), which has previously been demonstrated to be deficient in chromatin-remodeling activity (34). Compared with wild-type controls, the mutant BRG1 that is deficient in chromatin-remodeling activity was also severely impaired in its ability to drive SAHF formation and the expression of SA- $\beta$ -gal activity (Fig. 2A to E). Since p16<sup>INK4a</sup> and p21<sup>CIP1</sup> are key regulators of SAHF formation and are known BRG1 target genes (7, 9, 24, 32), we next examined the expression of p16<sup>INK4a</sup> and p21<sup>CIP1</sup> in cells expressing the control, wild-type BRG1, and the mutant BRG1. Compared with controls, the expression of both p16<sup>INK4a</sup> and p21<sup>CIP1</sup> was upregulated by



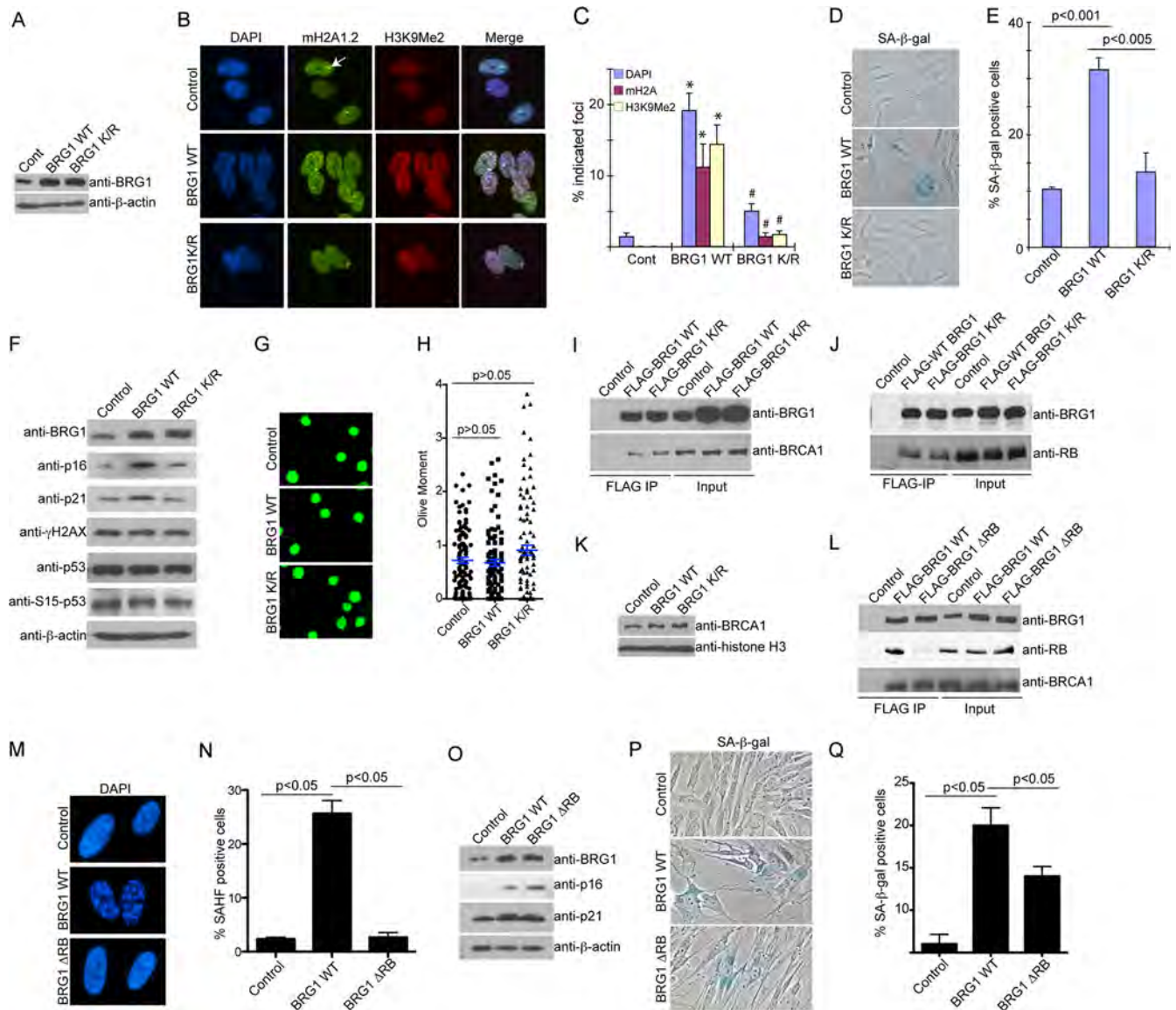


**FIG 2** Ectopic expression of BRG1 drives SAHF formation and senescence, which is dependent upon its chromatin-remodeling activity. (A) IMR90 cells were infected with retrovirus encoding a wild-type BRG (BRG WT), a K798R mutant BRG1 that is defective in chromatin-remodeling activity (BRG1 K/R), or the control (Cont). Expression of BRG1 was examined by immunoblotting in the drug-selected cells. Expression of  $\beta$ -actin was used as a loading control. (B) Same as described for panel A except that cells were stained with DAPI and the indicated antibodies to visualize SAHF. The arrow points to an example of inactivated X chromosome stained by mH2A1.2 antibody in control IMR90 cells. (C) Quantitation of the results shown in panel B. A total of 200 cells from each of the indicated groups were examined for the expression of the indicated markers. Data represent the means of the results of three independent experiments with standard deviations (SD). \*,  $P < 0.05$  (compared with controls); #,  $P < 0.05$  (compared with wild-type BRG1). (D) Same as described for panel A except that cells were stained for SA- $\beta$ -gal activity. (E) Quantitation of the results shown in panel D. A total of 200 cells from each of the indicated groups were examined for expression of SA- $\beta$ -gal activity. Data represent the means of the results of three independent experiments with SD. (F) Same as described for panel A except that cells were examined for expression of BRG1, p16<sup>INK4a</sup>, p21<sup>CIP1</sup>, p53, serine 15-phosphorylated p53 (S15-p53), and  $\gamma$ H2AX by immunoblotting. Expression of  $\beta$ -actin was used as a loading control. (G) Same as described for panel A except that cells were measured for the extent of DNA damage using the comet assay. Note that these experiments were performed at the same time as those shown in Fig. 4I, where shBRCA1-expressing cells were used as positive controls. (H) Quantitation of the results shown in panel G. The extent of DNA damage measured by the comet assay was calculated as artificial Olive Moment units as described in Materials and Methods. Olive Moment levels in 100 cells from each group were measured. Means of the data representing Olive Moment units with standard errors of the means (SEM) are shown in blue. (I) IMR90 cells were infected with retrovirus encoding FLAG-tagged wild-type BRG1, the BRG1 K/R mutant, or the control. Drug-selected cells were subjected to coimmunoprecipitation experiments using an anti-FLAG antibody. An isotype-matched IgG was used as a negative control. Levels of immunoprecipitated BRG1 and BRCA1 were determined by immunoblotting using the indicated antibodies. (J) Same as described for panel I except that cells were examined for the levels of immunoprecipitated BRG1 and pRB. (K) Same as described for panel A except that cells were subjected to fractionation to prepare chromatin and the expression of BRCA1 and histone H3 in the chromatin fraction of the indicated cells was examined by immunoblotting. (L) IMR90 cells were infected with retrovirus encoding FLAG-tagged wild-type BRG1 (BRG1 WT), BRG1 with aa 1357 to 1361 deleted (BRG1  $\Delta$ RB), or the control. Drug-selected cells were subjected to coimmunoprecipitation experiments using an anti-FLAG antibody. An isotype-matched IgG was used as a negative control. Levels of immunoprecipitated BRG1, pRB, and BRCA1 were determined by immunoblotting using the indicated antibodies. (M) Same as described for panel L except that cells were stained with DAPI to visualize SAHF formation. (N) Quantitation of the results shown in panel M. A total of 200 cells from each of the indicated groups were examined for SAHF formation. Data represent the means of the results of three independent experiments with SD. (O) Same as described for panel L except that cells were examined for BRG1, p21<sup>CIP1</sup>, p16<sup>INK4a</sup>, and  $\beta$ -actin expression by immunoblotting using the indicated antibodies. (P) Same as described for panel L except that cells were stained for SA- $\beta$ -gal activity. (Q) Quantitation of the results shown in panel P. A total of 200 cells from each of the indicated groups were examined for SA- $\beta$ -gal activity. Data represent the means of the results of three independent experiments with SD.

wild-type BRG1 but not mutant BRG1 that is deficient in chromatin-remodeling activity (Fig. 2F). Together, we conclude that the chromatin-remodeling activity of BRG1 is required for SAHF formation and senescence, which correlates with the upregulation of p16<sup>INK4a</sup> and p21<sup>CIP1</sup> in these cells.

Since formation of SAHF and senescence induced by BRCA1 knockdown or oncogenic RAS is accompanied by the accumulation of DNA damage (see Fig. S1C in the supplemental material) (14), we next examined the expression of  $\gamma$ H2AX, a marker of DNA damage, in cells expressing wild-type BRG1 or mutant BRG1 (BRG1 K798R). Interestingly, the expression of  $\gamma$ H2AX was not upregulated by the expression of wild-type or mutant BRG1 compared with controls (Fig. 2F). Likewise, the formation of  $\gamma$ H2AX foci was not significantly induced by wild-type BRG1 (see Fig. S2 in the supplemental material). Further, the expression of p53 or serine 15 phosphorylated p53 was not upregulated by the expression of either wild-type or mutant BRG1 (Fig. 2F). We next directly measured the extent of DNA damage in these cells using the comet assay. Compared with controls, the extent of DNA damage was not significantly affected by either wild-type or mutant BRG1 (Fig. 2G and H). Interestingly, both wild-type BRG1 and the BRG1 K798R mutant were able to interact with BRCA1 (Fig. 2I), suggesting that the inability of the BRG1 K798R mutant to induce SAHF formation and senescence was not due to an impaired interaction with BRCA1. In addition, the interaction between BRG1 and pRB was not disrupted by the BRG1 K798R mutant, suggesting that the observed effects were not due to a complete misfolding of the mutant protein (Fig. 2J). Notably, ectopically expressed BRG1 did not dissociate BRCA1 from chromatin (Fig. 2K), suggesting that BRG1 acts downstream of BRCA1 chromatin dissociation. We previously showed that oncogene-induced BRCA1 chromatin dissociation contributes to both SAHF formation and DNA damage accumulation (14). Likewise, BRCA1 knockdown triggers SAHF formation and DNA damage response (14). Here we showed that ectopic BRG1 drove SAHF formation but not the DNA damage response and that BRG1 did not dissociate BRCA1 from chromatin (Fig. 2B, C, F to H, and K). Together, these data support the premise that BRG1 acts downstream of BRCA1 chromatin dissociation to promote SAHF formation during senescence.

Next, we sought to determine the importance of the interaction between BRG1 and pRB in formation of SAHF induced by BRG1. Toward this goal, we generated a mutant BRG1 that no longer binds to pRB (deletion of aa 1357 to 1361; BRG1  $\Delta$ RB) (22, 35, 36) and confirmed the disruption of the interaction between BRG1  $\Delta$ RB and pRB by co-IP analysis (Fig. 2L). Notably, the BRG1  $\Delta$ RB mutant retained its ability to interact with BRCA1 (Fig. 2L). This result suggests that the effects observed in the BRG1  $\Delta$ RB mutant were not due to a complete misfolding of the protein. Indeed, compared with wild-type BRG1, the BRG1  $\Delta$ RB mutant was significantly impaired in its ability to drive SAHF formation (Fig. 2M and N). Interestingly, compared with wild-type BRG1, there was no overt difference in induction of p16<sup>INK4a</sup> and p21<sup>CIP1</sup> by the BRG1  $\Delta$ RB mutant (Fig. 2O). Given that the BRG1 chromatin-remodeling-activity-deficient mutant (BRG1 K798R) failed to upregulate p16<sup>INK4a</sup> and p21<sup>CIP1</sup> (Fig. 2F), this result suggests that upregulation of p16<sup>INK4a</sup> and p21<sup>CIP1</sup> expression induced by BRG1 functions upstream of pRB, which is independent of the interaction between BRG1 and pRB and dependent on BRG1's chromatin-remodeling activity. Consistently, compared

with wild-type BRG1, levels of other markers of senescence such as SA- $\beta$ -gal activity were decreased in BRG1  $\Delta$ RB mutant-expressing cells, albeit to a much lesser extent than that seen SAHF formation in wild-type BRG1-expressing cells (Fig. 2P and Q). Based on these results, we conclude that the interaction between BRG1 and pRB is enhanced in cells undergoing senescence and that SAHF formation induced by BRG1 requires its interaction with pRB.

**Knockdown of BRG1 suppresses SAHF formation and senescence induced by oncogenic RAS.** We next sought to determine whether BRG1 is required for the SAHF formation and senescence that is associated with BRCA1 chromatin dissociation induced by oncogenic RAS. To do so, we obtained two individual shRNAs corresponding to the human *BRG1* gene (shBRG1) that can efficiently knock down BRG1 expression (e.g., see Fig. 3D). We infected IMR90 cells with oncogenic RAS to induce BRCA1 chromatin dissociation, SAHF formation, and senescence together with shBRG1 or the control. Compared with RAS-alone cells, knockdown of BRG1 significantly suppressed the RAS-induced SA- $\beta$ -gal activity and SAHF formation (Fig. 3A to C). However, BRG1 knockdown itself had no effects on expression of markers of senescence such as SA- $\beta$ -gal activity or SAHF formation (see Fig. S3 in the supplemental material). Interestingly, BRG1 knockdown in mesenchymal stem cells induces the senescence phenotype (27). The discrepancy may be explained by differences in the experimental systems. Notably, the expression of both p16<sup>INK4a</sup> and p21<sup>CIP1</sup> was significantly downregulated by shBRG1 compared with RAS-alone controls (Fig. 3D). This was not due to a lower level of RAS expression in BRG1 knockdown cells, as the RAS expression was comparable (Fig. 3D). Interestingly, BRG1 knockdown had no effects on BRCA1 chromatin dissociation induced by oncogenic RAS (Fig. 3E). This result further supports the premise that BRG1 functions downstream of RAS-induced BRCA1 chromatin dissociation. Consistently, BRG1 knockdown did not overtly affect RAS-induced DNA damage accumulation. For example, RAS-induced upregulation of  $\gamma$ H2AX expression or formation of  $\gamma$ H2AX foci was not significantly affected by shBRG1 compared with controls (Fig. 3F; see also Fig. S4 in the supplemental material). Based on these results, we conclude that knockdown of BRG1 suppresses RAS-induced SAHF formation and senescence, which is independent of the DNA damage response.

Our results suggest that BRG1 contributes to SAHF formation and senescence induced by oncogenic RAS by promoting p16<sup>INK4a</sup> and p21<sup>CIP1</sup> expression, which depends upon BRG1's chromatin-remodeling activity (Fig. 2). Thus, we examined the association of BRG1 with the promoters of the *CDKN2A* (encoding p16<sup>INK4a</sup>) and *CDKN1A* (encoding p21<sup>CIP1</sup>) genes in IMR90 cells infected with oncogenic RAS by ChIP using an anti-BRG1 antibody. An isotype-matched IgG was used as a negative control for ChIP analysis. Compared with controls, BRG1's association with the promoters of both *CDKN2A* and *CDKN1A* genes was significantly enhanced in RAS-infected cells (Fig. 3G to J). In contrast, compared with controls, there was no overt change in BRCA1's association with the promoters of either the *CDKN2A* or *CDKN1A* gene in RAS-infected cells (see Fig. S5 in the supplemental material).

**BRG1 enhances senescence induced by BRCA1 knockdown, and knockdown of BRG1 suppresses SAHF formation and senescence induced by BRCA1 knockdown.** We next sought to determine whether ectopic expression of BRG1 enhances the senescence phenotype induced by BRCA1 knockdown. Toward this

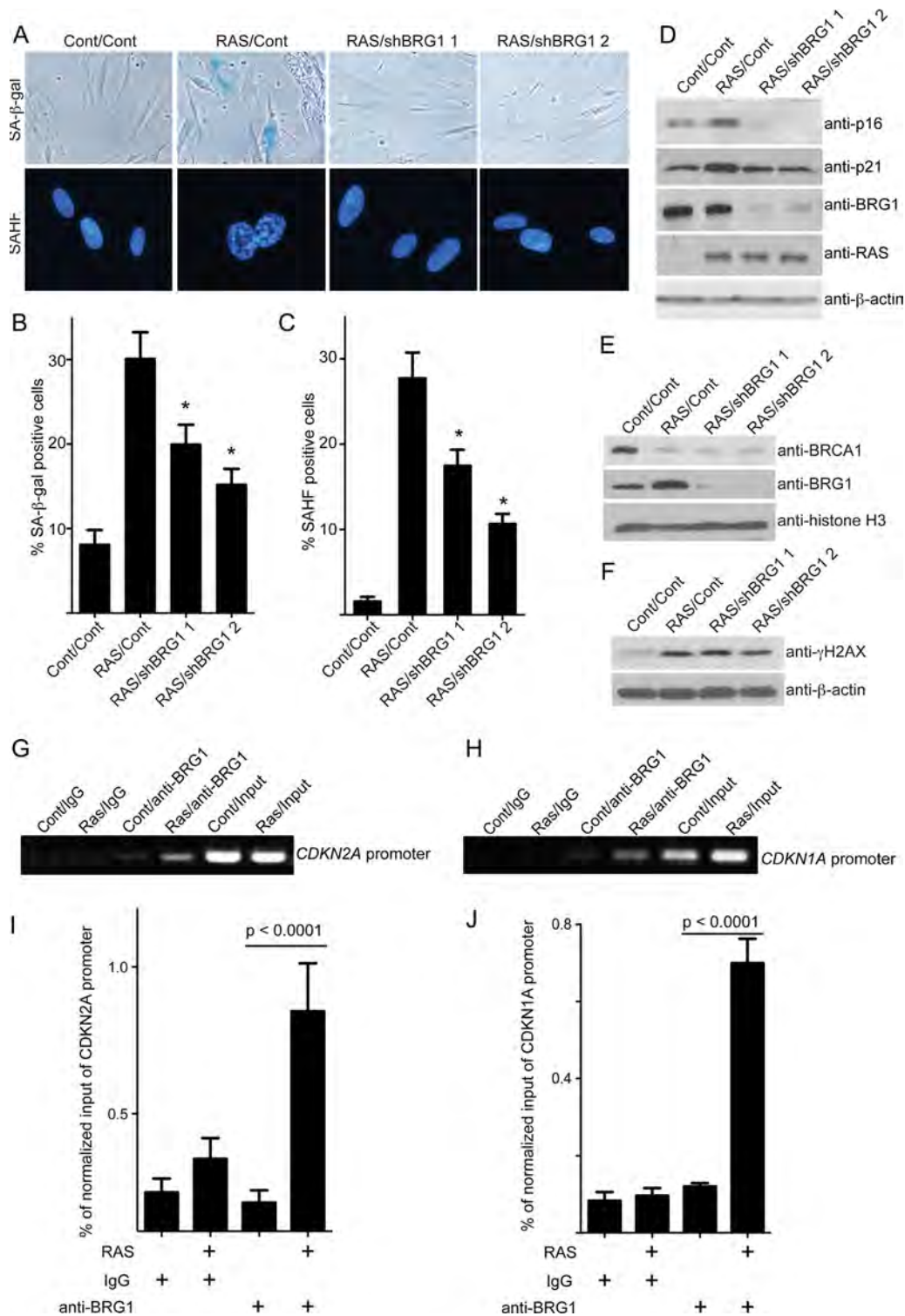


**FIG 3** Knockdown of BRG1 suppresses SAHF formation and senescence induced by oncogenic RAS. (A) IMR90 cells were infected with retrovirus encoding oncogenic H-RAS<sup>G12V</sup> together with lentivirus encoding the indicated shBRG1 or the control. Drug-selected cells were stained for SA-β-gal activity or DAPI to visualize SAHF formation. (B and C) Quantitation of the results shown in panel A. A total of 200 cells from each of the indicated group were examined for SA-β-gal activity or SAHF formation. Data represent the means of the results of three independent experiments with SD. \*,  $P < 0.05$  (compared with cells with RAS alone). (D) Same as described for panel A except that cells were examined for expression of p16<sup>INK4a</sup>, p21<sup>CIP1</sup>, BRG1, and RAS by immunoblotting. Expression of β-actin was used as a loading control. (E) Same as described for panel A except that the cells were subjected to fractionation to prepare chromatin and the expression of BRCA1 and BRG1 in the chromatin fraction of the indicated cells was examined by immunoblotting. Expression of histone H3 was used as a loading control. (F) Same as described for panel A except that cells were examined for expression of γH2AX by immunoblotting. Expression of β-actin was used as a loading control. (G) IMR90 cells were infected with retrovirus encoding oncogenic H-RAS<sup>G12V</sup> or the control. Drug-selected cells were used to perform chromatin immunoprecipitation (ChIP) using an anti-BRG1 antibody. An isotype-matched IgG was used as a negative control for ChIP analysis. The immunoprecipitated DNA was subjected to PCR analysis using primers that amplify the promoter region of the human *CDKN2A* gene. (H) Same as described for panel G except that the immunoprecipitated DNA was subjected to quantitative PCR analysis. Data represent the means of the results of three independent experiments with SD. (I and J) Same as described for panels H and G except that the human *CDKN1A* gene promoter was analyzed.



goal, we infected IMR90 fibroblasts with a lentivirus encoding shBRCA1 together with a retrovirus encoding the wild type or the chromatin-remodeling-activity-deficient BRG1 mutant (BRG1 K798R). Compared with shBRCA1-alone cells, expression of wild-type BRG1 but not mutant BRG1 induced a more pronounced senescence phenotype, as indicated by a significant increase in SAHF formation and expression of SA- $\beta$ -gal activity (Fig. 4A to C). Notably, this correlated with an increased induction of p16<sup>INK4a</sup> and p21<sup>CIP1</sup> but not  $\gamma$ H2AX expression (Fig. 4D). Based on these results, we conclude that ectopic BRG1 enhances the senescence phenotype induced by BRCA1 knockdown, which correlates with enhanced expression of p16<sup>INK4a</sup> and p21<sup>CIP1</sup>.

Our evidence supports the hypothesis that BRG1 acts downstream of BRCA1 chromatin dissociation to promote SAHF formation during RAS-induced senescence. We next wanted to directly test the effects of BRG1 knockdown on SAHF formation and senescence induced by BRCA1 knockdown. To do this, we infected IMR90 cells with a lentivirus encoding shBRCA1 together with a lentivirus encoding shBRG1 or the control. Compared with shBRCA1-alone cells, BRG1 knockdown significantly suppressed the expression of SA- $\beta$ -gal activity and SAHF formation induced by BRCA1 knockdown (Fig. 4E to G). This was accompanied by a notable downregulation of p16<sup>INK4a</sup> and p21<sup>CIP1</sup> in shBRCA1/shBRG1-expressing cells compared with shBRCA1-alone cells (Fig. 4H). Taken together, these data indicate that BRG1 contributes to SAHF formation and senescence induced by BRCA1 knockdown and that this correlates with its effects on the expression of p16<sup>INK4a</sup> and p21<sup>CIP1</sup>.

We next sought to determine the effects of BRG1 knockdown on the DNA damage induced by BRCA1 knockdown by examining  $\gamma$ H2AX expression and directly measuring the extent of DNA damage in these cells using the comet assay. Notably, BRG1 knockdown did not overtly affect BRCA1 knockdown-induced  $\gamma$ H2AX expression (Fig. 4H). Likewise, BRG1 knockdown did not significantly affect the extent of DNA damage induced by BRCA1 knockdown as measured by the comet assay (Fig. 4I and J). Taking these results together, we conclude that BRG1 knockdown does not suppress the DNA damage response induced by BRCA1 knockdown.

Notably, chromatin-associated BRG1 levels were increased in BRCA1 knockdown cells (Fig. 4K), further supporting the notion that BRCA1 functions upstream of BRG1. This was not due to an increase in the total BRG1 protein level in BRCA1 knockdown cells (Fig. 4K). Since BRCA1 knockdown induces the expression of p21<sup>CIP1</sup> and p16<sup>INK4a</sup>, we next examined the association of BRG1 with the promoters of *CDKN2A* and *CDKN1A* genes in BRCA1 knockdown cells. Similar to what we observed in cells expressing oncogenic RAS, which induces dissociation of BRCA1 from chromatin, we observed that BRG1's association with the promoters of *CDKN2A* and *CDKN1A* genes was significantly enhanced in BRCA1 knockdown cells compared with controls (Fig. 4L to O). Together, these results further support the premise that BRG1 contributes to SAHF formation and senescence induced by BRCA1 chromatin dissociation or BRCA1 knockdown through promoting p16<sup>INK4a</sup> and p21<sup>CIP1</sup> expression.

**Knockdown of pRB, p16<sup>INK4a</sup>, and p21<sup>CIP1</sup>, but not p53, inhibits SAHF formation induced by ectopic BRG1 expression.** We showed that p16<sup>INK4a</sup> and p21<sup>CIP1</sup> expression is induced by BRG1 (Fig. 2F). In addition, a mutant BRG1 (BRG1 K798R) that is deficient in chromatin-remodeling activity is also impaired in

SAHF formation (Fig. 2B and C). Further, we showed that the interaction between BRG1 and pRB is required for SAHF formation induced by BRG1 (Fig. 2M and N). However, we failed to observe an increase in p53 expression in BRG1-expressing cells (Fig. 2F). We next sought to directly determine the effects of knockdown of pRB, p16<sup>INK4a</sup>, p21<sup>CIP1</sup>, or p53 on SAHF formation induced by ectopic BRG1. To do so, we developed two individual shRNAs corresponding to the human *CDKN2A*, *CDKN1A*, *pRB*, or *p53* gene. The knockdown efficacy of these shRNAs was confirmed by immunoblotting using antibodies specific to pRB, p16<sup>INK4a</sup>, p21<sup>CIP1</sup>, and p53 (Fig. 5A to D). Interestingly, knockdown of pRB, p16<sup>INK4a</sup>, or p21<sup>CIP1</sup> inhibited SAHF formation induced by ectopic BRG1 expression (Fig. 5E and F). In contrast, knockdown of p53 had no significant effects on SAHF formation induced by ectopic BRG1 expression (Fig. 5E and F). Based on these results, we conclude that knockdown of pRB, p16<sup>INK4a</sup>, or p21<sup>CIP1</sup>, but not p53, inhibits SAHF formation induced by ectopic BRG1 expression.

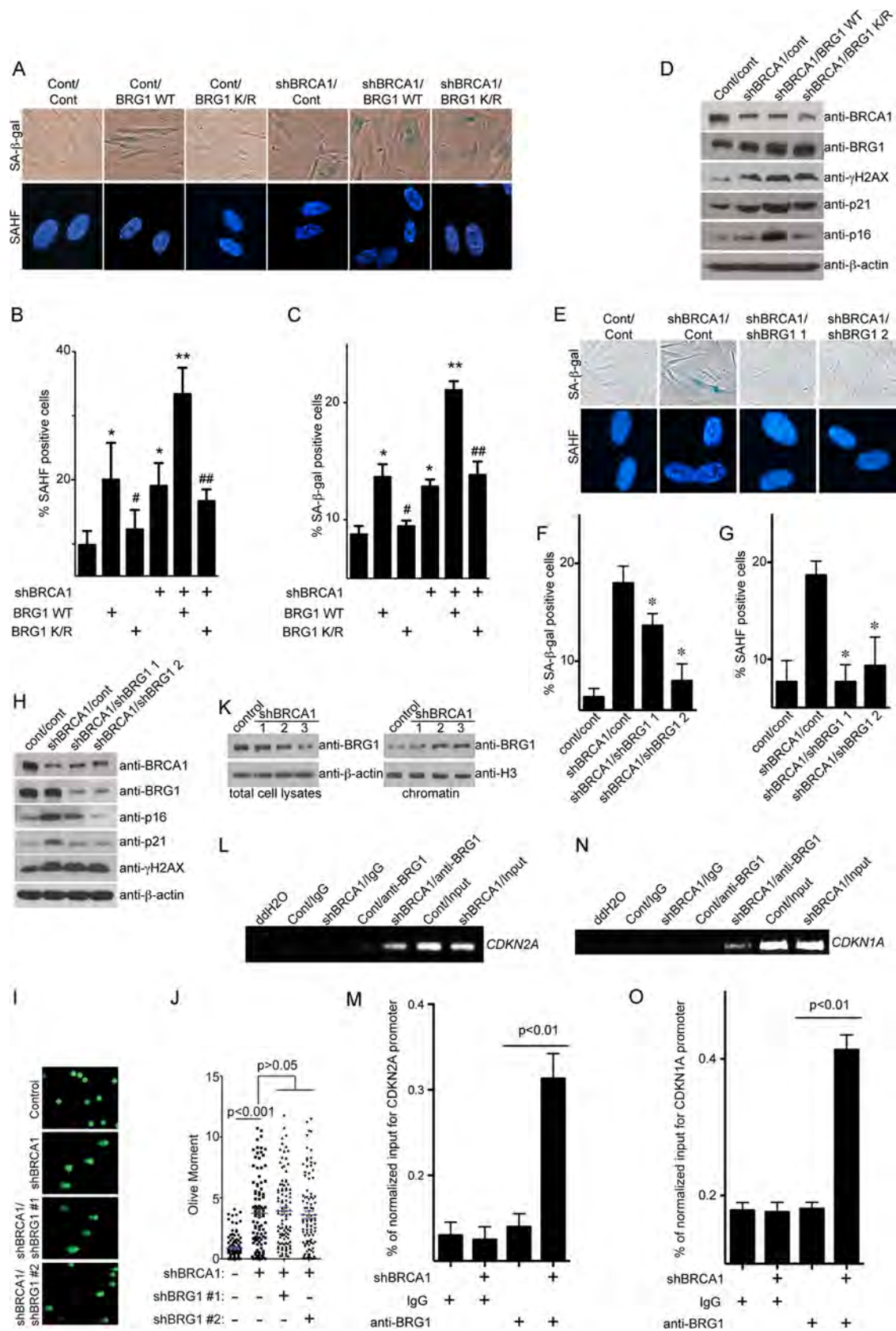
BRCA1 knockdown induces both SAHF formation and the DNA damage response (14), and suppression of the DNA damage response impairs SAHF formation (37). We next sought to determine the effects of knockdown of pRB, p16<sup>INK4a</sup>, p21<sup>CIP1</sup>, or p53 on SAHF formation induced by BRCA1 knockdown. Notably, knockdown of pRB, p16<sup>INK4a</sup>, p21<sup>CIP1</sup>, or p53 inhibited SAHF formation (Fig. 5G to I). Since knockdown of p53 suppresses SAHF formation induced by knockdown of BRCA1 but not ectopic BRG1 (Fig. 5), these data further support the premise that BRG1 functions downstream of BRCA1 knockdown to drive SAHF formation.

## DISCUSSION

**The role of BRG1 in SAHF formation induced by BRCA1 knockdown or BRCA1 chromatin dissociation.** Here we demonstrated that the interaction between BRG1 and BRCA1 was regulated during RAS-induced senescence (Fig. 1C and D). In addition, chromatin-associated BRG1 levels were increased in cells undergoing senescence induced by oncogenic RAS or BRCA1 knockdown (Fig. 1D and 4K). Consistently, ectopic BRG1 expression drove formation of SAHF and senescence (Fig. 2). Conversely, knockdown of BRG1 inhibited the formation of SAHF induced by oncogenic RAS or BRCA1 knockdown (Fig. 3 and 4). Further, we demonstrated that ectopic BRG1 enhanced SAHF formation induced by BRCA1 knockdown, which resulted in a more pronounced senescence phenotype (Fig. 4). However, BRG1 did not dissociate BRCA1 from chromatin (Fig. 2). Interestingly, BRG1's role in promoting SAHF formation is independent of the DNA damage response (Fig. 2F to H, 3F, and 4D to F; see also Fig. S2 and S4 in the supplemental material), while BRCA1 chromatin dissociation or knockdown induces both SAHF formation and DNA damage response (14). Consistently, knockdown of p53 inhibited SAHF formation induced by BRCA1 knockdown but not by ectopic BRG1 (Fig. 5). Together, these results support the premise that BRG1 acts downstream of BRCA1 to promote SAHF formation during senescence (Fig. 6). In addition, they suggest that oncogene-induced BRCA1 chromatin dissociation contributes to the accumulation of DNA damage observed in senescent cells through BRG1-independent mechanisms (Fig. 6). In agreement with this conclusion, we have previously shown that BRCA1-mediated DNA repair is impaired during RAS-induced senescence (14).

We show that the interaction between BRCA1 and BRG1 is





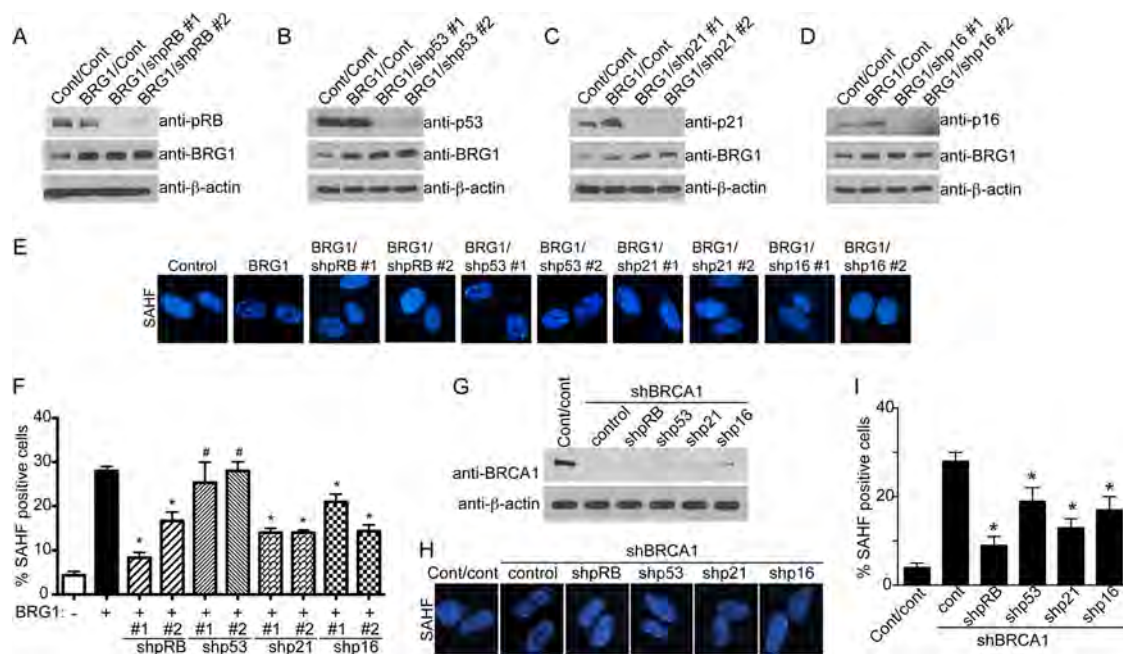


**FIG 5** Knockdown of pRB, p21<sup>CIP1</sup>, or p16<sup>INK4a</sup>, but not p53, inhibits SAHF formation induced by ectopic BRG1 expression. (A) IMR90 cells were infected with retrovirus encoding BRG1 together with lentivirus encoding the indicated shpRB or the control. Drug-selected cells were examined for expression of pRB, BRG1, and  $\beta$ -actin by immunoblotting using the indicated antibodies. (B) Same as described for panel A except that cells were examined for expression of shp53. (C) Same as described for panel A except that cells were examined for expression of shp21. (D) Same as described for panel A except that cells were examined for expression of shp16. (E) Same as described for panels A to D except that cells were stained with DAPI to visualize SAHF formation. (F) Quantification of the results shown in panel E. A total of 200 cells from each of the indicated groups were examined for SAHF formation. Data represent the means of the results of three independent experiments with SD. \*,  $P < 0.05$  (compared with BRG1-expressing cells); #,  $P > 0.05$  (compared with BRG1-expressing cells). (G) IMR90 cells were infected with lentivirus encoding shBRCA1 (#3) together with lentivirus encoding the indicated shpRB (#1), shp53 (#2), shp21 (#1), shp16 (#2), or the control. Drug-selected cells were examined for expression of BRCA1 and  $\beta$ -actin by immunoblotting using the indicated antibodies. Please see panel A for the knockdown efficacy of the indicated shRNAs. (H) Same as described for panel G except that cells were stained with DAPI to visualize SAHF formation. (I) Quantification of the results shown in panel H. A total of 200 cells from each of the indicated groups were examined for SAHF formation. Data represent the means of the results of three independent experiments with SD. \*,  $P < 0.05$  (compared with cells expressing only shBRCA1).

disrupted during senescence, which correlates with the dissociation of BRCA1 from chromatin and an enhanced association of BRG1 with chromatin (Fig. 1). Consistently, the colocalization between BRG1 and BRCA1 was decreased in the nuclei of senescent cells (Fig. 1E). BRCA1 knockdown, which mimics BRCA1

chromatin dissociation and the disruption of the interaction between BRCA1 and BRG1, increased the levels of chromatin-associated BRG1 (Fig. 4K). In contrast, BRG1 overexpression did not affect BRCA1 chromatin association (Fig. 2K). Together, these results suggest that BRCA1 chromatin dissociation and disruption

**FIG 4** Knockdown of BRG1 suppresses SAHF formation and senescence induced by BRCA1 knockdown. (A) IMR90 cells were infected with lentivirus encoding shBRCA1 (#3) together with retrovirus encoding wild-type BRG1 (BRG1 WT) or a mutant BRG1 that is defective in chromatin remodeling (BRG1 K/R). Drug-selected cells were stained for SA- $\beta$ -gal activity or with DAPI to visualize SAHF formation. (B and C) Quantitation of the results shown in panel A. A total of 200 cells from each of the indicated groups were examined for SA- $\beta$ -gal activity or SAHF formation. Data represent the means of the results of three independent experiments with SD. \*,  $P < 0.05$  (compared with controls); #,  $P > 0.05$  (compared with controls); \*\*,  $P < 0.05$  (compared with either shBRCA1 alone or BRG1 WT alone); ##,  $P > 0.05$  (compared with shBRCA1 alone). (D) Same as described for panel A but examined for expression of BRCA1, BRG1,  $\gamma$ H2AX, p21<sup>CIP1</sup>, and p16<sup>INK4a</sup> by immunoblotting. Expression of  $\beta$ -actin was used as a loading control. (E) IMR90 cells were infected with retrovirus encoding shBRCA1 (#3) together with indicated shBRG1 or the control. Drug-selected cells were stained for SA- $\beta$ -gal activity or with DAPI to visualize SAHF formation. (F and G) Quantitation of the results shown in panel E. A total of 200 cells from each of the indicated groups were examined for SA- $\beta$ -gal activity or SAHF formation. Data represent the means of the results of three independent experiments with SD. \*,  $P < 0.05$  (compared with shBRCA1-alone cells). (H) Same as described for panel E except that cells were examined for expression of BRCA1, BRG1,  $\gamma$ H2AX, p16<sup>INK4a</sup>, and p21<sup>CIP1</sup> by immunoblotting. Expression of  $\beta$ -actin was used as a loading control. (I) Same as described for panel E except that measurements to determine the extent of DNA damage were performed using the comet assay. (J) Quantitation of the results shown in panel I. The extent of DNA damage measured by the comet assay was calculated in artificial Olive Moment units as described in Materials and Methods. Olive Moment levels in 100 cells from each group were measured. Means of the data representing Olive Moment units with standard errors of the means (SEM) are shown in blue. (K) IMR90 cells were infected with lentivirus encoding the indicated shBRCA1 or the control. Drug-selected cells were subjected to fractionation to prepare chromatin, and the expression of BRG1 in the total cell lysates and the chromatin fraction of the indicated cells was examined by immunoblotting. Expression of  $\beta$ -actin and histone H3 was used as a loading control. Please see Fig. 1A for the shBRCA1 knockdown efficacy. (L) IMR90 cells were infected with lentivirus encoding shBRCA1 (#3) or the control. Drug-selected cells were used to perform ChIP analysis using an anti-BRG1 antibody. An isotype-matched IgG was used as a negative control for ChIP analysis. The immunoprecipitated DNA was subjected to PCR analysis using primers that amplify the promoter region of the human *CDKN2A* gene. (M) Same as described for panel L except that the immunoprecipitated DNA was subjected to quantitative PCR analysis. Data represent the means of the results of three independent experiments with SD. (N and O) Same as described for panels L and M except that the human *CDKN1A* gene promoter was analyzed.

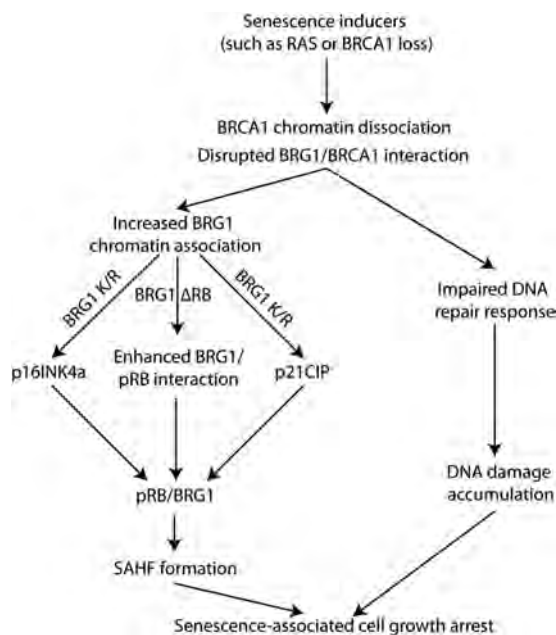


**FIG 6** A model for the role of BRG1 in regulating SAHF formation and senescence downstream of BRCA1 loss or oncogenic RAS, which triggers BRCA1 chromatin dissociation.

of the BRCA1 and BRG1 interaction, which act upstream of BRG1 during senescence, are associated (Fig. 6). Our data also show that the interaction between BRCA1 and BRG1 was present in the soluble fractions (Fig. 1C). These data are consistent with a model whereby soluble BRCA1 sequesters BRG1 away from chromatin and disruption of the interaction between BRCA1 and BRG1 causes an enhanced association of BRG1 with chromatin during senescence.

**Molecular mechanisms by which BRG1 promote SAHF formation.** BRG1 is known to regulate heterochromatin structure. Indeed, BRG1 interacts with pRB, which is known to play a key role in regulating SAHF formation (7, 22). Here we show that the interaction between BRG1 and pRB was enhanced during senescence and that formation of SAHF induced by ectopic BRG1 required its interaction with pRB (Fig. 1F and 2L to N). Consistently, knockdown of pRB suppressed SAHF formation induced by ectopic BRG1 expression (Fig. 5). However, the BRG1  $\Delta$ RB mutant did not affect upregulation of p16<sup>INK4a</sup> and p21<sup>CIP1</sup> (Fig. 2O). In contrast, a chromatin-remodeling-activity-deficient BRG1 mutant (BRG1 K798R) that failed to induce p16<sup>INK4a</sup> and p21<sup>CIP1</sup> expression was unable to drive SAHF formation (Fig. 2B and C). These data suggest that the BRG1 and pRB complex acts downstream of p16<sup>INK4a</sup> and p21<sup>CIP1</sup>, whose expression requires BRG1's chromatin-remodeling activity (Fig. 6). Indeed, both p16<sup>INK4a</sup> and p21<sup>CIP1</sup> are known regulators of pRB (38). Together, these data support the notion that the complex of BRG1 and pRB functions downstream of p16<sup>INK4a</sup> and p21<sup>CIP1</sup> to promote SAHF formation (Fig. 6).

It has been demonstrated that p16<sup>INK4a</sup> and pRB are necessary for SAHF formation during senescence induced by oncogenic RAS (7). However, p53 and p21<sup>CIP1</sup> are not necessary for SAHF formation in this context (7). In contrast, both p53 and p21<sup>CIP1</sup> are required for SAHF formation induced by knockdown of adenovirus E1A-associated p400 protein (9). Here we show that ec-

topic BRG1 induced the expression of p21<sup>CIP1</sup> and p16<sup>INK4a</sup> but had no effects on p53 expression (Fig. 2F). This is consistent with a previous report showing that BRG1-induced upregulation of p21<sup>CIP1</sup> is independent of p53 (24). Notably, the association of BRG1 with the promoters of the *CDKN2A* and *CDKN1A* genes, which encode pRB regulators p16<sup>INK4a</sup> and p21<sup>CIP1</sup>, was enhanced during senescence induced by oncogenic RAS or BRCA1 knockdown (Fig. 3G to J and 4L to O). In addition, we demonstrated that knockdown of BRG1 suppressed SAHF formation, which correlates with suppression of expression of both p16<sup>INK4a</sup> and p21<sup>CIP1</sup> induced by BRCA1 knockdown or oncogenic RAS (Fig. 3 and 4). Further, knockdown of p16<sup>INK4a</sup>, p21<sup>CIP1</sup>, or pRB, but not p53, inhibited SAHF formation induced by ectopic BRG1 expression (Fig. 5). Together, these data support a model whereby BRG1 promotes SAHF formation via its interaction with pRB, which is regulated by the upregulation of p16<sup>INK4a</sup> and p21<sup>CIP1</sup> through its chromatin-remodeling activity (Fig. 6).

**BRG1, DNA damage, and SAHF.** Here we showed that ectopic BRG1 drives SAHF formation and that this is independent of the DNA damage response by multiple markers (Fig. 2F to H; see also Fig. S2 in the supplemental material). These DNA damage markers include expression of  $\gamma$ H2AX, p53, and serine 15-phosphorylated p53 (Fig. 2F). Consistently, BRG1 did not affect the extent of DNA damage in these cells, as measured by the comet assay (Fig. 2G and H). Conversely, knockdown of BRG1 inhibited SAHF formation induced by oncogenic RAS or BRCA1 knockdown with no overt effects on the DNA damage response (Fig. 3F and 4H to J; see also Fig. S4 in the supplemental material). Interestingly, previous evidence suggests that formation of SAHF limits the extent of DNA damage induced by oncogenic RAS (37). Likewise, it has been demonstrated that ectopic p16<sup>INK4a</sup> drives SAHF formation. However, p16<sup>INK4a</sup>-induced senescence displays little DNA damage response (39). Together, our data suggest that DNA damage is not necessary for SAHF formation.

In summary, we showed that the interaction between BRG1 and BRCA1 is regulated during senescence. BRG1 is required for SAHF formation and senescence induced by BRCA1 knockdown or oncogenic RAS, which triggers BRCA1 chromatin dissociation. This correlates with an increase in chromatin-associated BRG1 levels. The association of BRG1 with the promoters of *CDKN2A* and *CDKN1A* genes is enhanced during senescence and correlates with the upregulation of p16<sup>INK4a</sup> and p21<sup>CIP1</sup> in a chromatin-remodeling-activity-dependent manner. In addition, the interaction between BRG1 and pRB is enhanced during senescence and SAHF formation induced by ectopic BRG1 requires its interaction with pRB. Further, p16<sup>INK4a</sup> and p21<sup>CIP1</sup> act upstream of pRB to mediate SAHF formation induced by ectopic BRG1 (Fig. 6). Thus, our current report sheds new light on how BRG1 regulates SAHF formation and senescence downstream of BRCA1 loss or oncogenic RAS that triggers BRCA1 chromatin dissociation.

## ACKNOWLEDGMENTS

We thank Katherine Aird, Benjamin Bitler, and Michael Amatangelo for critical reading of the manuscript and other members of the laboratory for discussions and suggestions.

This work was supported by a NIH/NCI grant (R01CA160331 to R.Z.) and, in part, by a DOD award (OC093420 to R.Z.). Support of core facilities used in this study was provided by Cancer Center Support Grant CA010815 to The Wistar Institute.



## REFERENCES

- Campisi J. 2005. Senescent cells, tumor suppression, and organismal aging: good citizens, bad neighbors. *Cell* 120:513–522.
- Adams PD. 2009. Healing and hurting: molecular mechanisms, functions, and pathologies of cellular senescence. *Mol. Cell* 36:2–14.
- Dimri GP, Lee X, Basile G, Acosta M, Scott G, Roskelley C, Medrano EE, Linskens M, Rubelj I, Pereira-Smith O, Peacocke M, Campisi J. 1995. A biomarker that identifies senescent human cells in culture and in aging skin in vivo. *Proc. Natl. Acad. Sci. U. S. A.* 92:9363–9367.
- Zhang R, Chen W, Adams PD. 2007. Molecular dissection of formation of senescence-associated heterochromatin foci. *Mol. Cell. Biol.* 27:2343–2358.
- Zhang R, Poustovoitov MV, Ye X, Santos HA, Chen W, Daganzo SM, Erzberger JP, Serebriiskii IG, Canutescu AA, Dunbrack RL, Pehrson JR, Berger JM, Kaufman PD, Adams PD. 2005. Formation of MacroH2A-containing senescence-associated heterochromatin foci and senescence driven by ASF1a and HIRA. *Dev. Cell* 8:19–30.
- Narita M, Krizhanovsky V, Nunez S, Chicas A, Hearn SA, Myers MP, Lowe SW. 2006. A novel role for high-mobility group proteins in cellular senescence and heterochromatin formation. *Cell* 126:503–514.
- Narita M, Nunez S, Heard E, Lin AW, Hearn SA, Spector DL, Hannon GJ, Lowe SW. 2003. Rb-mediated heterochromatin formation and silencing of E2F target genes during cellular senescence. *Cell* 113:703–716.
- Braig M, Lee S, Loddemkemper C, Rudolph C, Peters AH, Schlegelberger B, Stein H, Dorken B, Jenuwein T, Schmitt CA. 2005. Oncogene-induced senescence as an initial barrier in lymphoma development. *Nature* 436:660–665.
- Chan HM, Narita M, Lowe SW, Livingston DM. 2005. The p400 E1A-associated protein is a novel component of the p53 → p21 senescence pathway. *Genes Dev.* 19:196–201.
- Di Micco R, Fumagalli M, Cicalese A, Piccinin S, Gasparini P, Luise C, Schurra C, Garre M, Nuciforo PG, Bensimon A, Maestro R, Pelicci PG, d'Adda di Fagnana F. 2006. Oncogene-induced senescence is a DNA damage response triggered by DNA hyper-replication. *Nature* 444:638–642.
- Bartkova J, Rezaei N, Liontos M, Karakaidos P, Kletsas D, Issaeva N, Vassiliou LV, Kolettas E, Niforou K, Zoumpouris VC, Takaoka M, Nakagawa H, Tort F, Fugger K, Johansson F, Sehested M, Andersen CL, Dyrskjot L, Orntoft T, Lukas J, Kittas C, Helleday T, Halazonetis TD, Bartek J, Gorgoulis VG. 2006. Oncogene-induced senescence is part of the tumorigenesis barrier imposed by DNA damage checkpoints. *Nature* 444:633–637.
- Scully R, Livingston DM. 2000. In search of the tumour-suppressor functions of BRCA1 and BRCA2. *Nature* 408:429–432.
- Gudmundsdottir K, Ashworth A. 2006. The roles of BRCA1 and BRCA2 and associated proteins in the maintenance of genomic stability. *Oncogene* 25:5864–5874.
- Tu Z, Aird KM, Bitler BG, Nicodemus JP, Beechey N, Zia B, Yen TJ, Zhang R. 2011. Oncogenic Ras regulates BRIP1 expression to induce dissociation of BRCA1 from chromatin, inhibit DNA repair, and promote senescence. *Dev. Cell* 21:1077–1091.
- Cao L, Li W, Kim S, Brodie SG, Deng CX. 2003. Senescence, aging, and malignant transformation mediated by p53 in mice lacking the Brca1 full-length isoform. *Genes Dev.* 17:201–213.
- Cao L, Kim S, Xiao C, Wang RH, Coumoul X, Wang X, Li WM, Xu XL, De Soto JA, Takai H, Mai S, Elledge SJ, Motoyama N, Deng CX. 2006. ATM-Chk2-p53 activation prevents tumorigenesis at an expense of organ homeostasis upon Brca1 deficiency. *EMBO J.* 25:2167–2177.
- Ye Q, Hu YF, Zhong H, Nye AC, Belmont AS, Li R. 2001. BRCA1-induced large-scale chromatin unfolding and allele-specific effects of cancer-predisposing mutations. *J. Cell Biol.* 155:911–921.
- Bochar DA, Wang L, Beniya H, Kinev A, Xue Y, Lane WS, Wang W, Kashanchi F, Shiekhattar R. 2000. BRCA1 is associated with a human SWI/SNF-related complex: linking chromatin remodeling to breast cancer. *Cell* 102:257–265.
- Reisman D, Glaros S, Thompson EA. 2009. The SWI/SNF complex and cancer. *Oncogene* 28:1653–1668.
- Bultman S, Gebuhr T, Yee D, La Mantia C, Nicholson J, Gilliam A, Randazzo F, Metzger D, Chambon P, Crabtree G, Magnuson T. 2000. A Brg1 null mutation in the mouse reveals functional differences among mammalian SWI/SNF complexes. *Mol. Cell* 6:1287–1295.
- Bultman SJ, Herschkowitz JI, Godfrey V, Gebuhr TC, Yaniv M, Perou CM, Magnuson T. 2008. Characterization of mammary tumors from Brg1 heterozygous mice. *Oncogene* 27:460–468.
- Dunaief JL, Strober BE, Guha S, Khavari PA, Alin K, Luban J, Bege-mann M, Crabtree GR, Goff SP. 1994. The retinoblastoma protein and BRG1 form a complex and cooperate to induce cell cycle arrest. *Cell* 79:119–130.
- Ye X, Zerlanko B, Zhang R, Somaiah N, Lipinski M, Salomoni P, Adams PD. 2007. Definition of pRB- and p53-dependent and -independent steps in HIRA/ASF1a-mediated formation of senescence-associated heterochromatin foci. *Mol. Cell. Biol.* 27:2452–2465.
- Hendricks KB, Shanahan F, Lees E. 2004. Role for BRG1 in cell cycle control and tumor suppression. *Mol. Cell. Biol.* 24:362–376.
- Trouche D, Le Chalony C, Muchardt C, Yaniv M, Kouzarides T. 1997. RB and hbrm cooperate to repress the activation functions of E2F1. *Proc. Natl. Acad. Sci. U. S. A.* 94:11268–11273.
- Napolitano MA, Cipollaro M, Cascino A, Melone MA, Giordano A, Galderisi U. 2007. Brg1 chromatin remodeling factor is involved in cell growth arrest, apoptosis and senescence of rat mesenchymal stem cells. *J. Cell Sci.* 120:2904–2911.
- Naidu SR, Love IM, Imbalzano AN, Grossman SR, Androphy EJ. 2009. The SWI/SNF chromatin remodeling subunit BRG1 is a critical regulator of p53 necessary for proliferation of malignant cells. *Oncogene* 28:2492–2501.
- Zhang R, Liu ST, Chen W, Bonner M, Pehrson J, Yen TJ, Adams PD. 2007. HP1 proteins are essential for a dynamic nuclear response that rescues the function of perturbed heterochromatin in primary human cells. *Mol. Cell. Biol.* 27:949–962.
- Ye X, Zerlanko B, Kennedy A, Banumathy G, Zhang R, Adams PD. 2007. Downregulation of Wnt signaling is a trigger for formation of facultative heterochromatin and onset of cell senescence in primary human cells. *Mol. Cell* 27:183–196.
- Li H, Cai Q, Godwin AK, Zhang R. 2010. Enhancer of zeste homolog 2 promotes the proliferation and invasion of epithelial ovarian cancer cells. *Mol. Cancer Res.* 8:1610–1618.
- Méndez J, Stillman B. 2000. Chromatin association of human origin recognition complex, cdc6, and minichromosome maintenance proteins during the cell cycle: assembly of prereplication complexes in late mitosis. *Mol. Cell. Biol.* 20:8602–8612.
- Kia SK, Gorski MM, Giannakopoulos S, Verrijzer CP. 2008. SWI/SNF mediates polycomb eviction and epigenetic reprogramming of the INK4b-ARF-INK4a locus. *Mol. Cell. Biol.* 28:3457–3464.
- Bourgo RJ, Siddiqui H, Fox S, Solomon D, Sansam CG, Yaniv M, Muchardt C, Metzger D, Chambon P, Roberts CW, Knudsen ES. 2009. SWI/SNF deficiency results in aberrant chromatin organization, mitotic failure, and diminished proliferative capacity. *Mol. Biol. Cell* 20:3192–3199.
- Sif S, Saurin AJ, Imbalzano AN, Kingston RE. 2001. Purification and characterization of mSin3A-containing Brg1 and hBrm chromatin remodeling complexes. *Genes Dev.* 15:603–618.
- Strober BE, Dunaief JL, Guha S, Goff SP. 1996. Functional interactions between the hBRM/hBRG1 transcriptional activators and the pRB family of proteins. *Mol. Cell. Biol.* 16:1576–1583.
- Kang H, Cui K, Zhao K. 2004. BRG1 controls the activity of the retinoblastoma protein via regulation of p21CIP1/WAF1/SDI. *Mol. Cell. Biol.* 24:1188–1199.
- Di Micco R, Sulli G, Dobrev M, Liontos M, Botrugno OA, Gargiulo G, Dal Zuffo R, Matti V, d'Ario G, Montani E, Mercurio C, Hahn WC, Gorgoulis V, Minucci S, d'Adda di Fagnana F. 2011. Interplay between oncogene-induced DNA damage response and heterochromatin in senescence and cancer. *Nat. Cell Biol.* 13:292–302.
- Ortega S, Malumbres M, Barbacid M. 2002. Cyclin D-dependent kinases, INK4 inhibitors and cancer. *Biochim. Biophys. Acta* 1602:73–87.
- Rodier F, Coppe JP, Patil CK, Hoeijmakers WA, Munoz DP, Raza SR, Freund A, Campeau E, Davalos AR, Campisi J. 2009. Persistent DNA damage signalling triggers senescence-associated inflammatory cytokine secretion. *Nat. Cell Biol.* 11:973–979.



# Molecular Cancer Research



## NF-YA Underlies EZH2 Upregulation and Is Essential for Proliferation of Human Epithelial Ovarian Cancer Cells

Azat Garipov, Hua Li, Benjamin G. Bitler, et al.

*Mol Cancer Res* 2013;11:360-369. Published OnlineFirst January 29, 2013.

|                               |   |
|-------------------------------|---|
| <b>Updated version</b>        | Access the most recent version of this article at:<br>doi: <a href="https://doi.org/10.1158/1541-7786.MCR-12-0661">10.1158/1541-7786.MCR-12-0661</a>  |
| <b>Supplementary Material</b> | Access the most recent supplemental material at:<br><a href="http://mcr.aacrjournals.org/content/suppl/2013/01/29/1541-7786.MCR-12-0661.DC1.html">http://mcr.aacrjournals.org/content/suppl/2013/01/29/1541-7786.MCR-12-0661.DC1.html</a> |

|                       |   |
|-----------------------|---|
| <b>Cited Articles</b> | This article cites by 34 articles, 17 of which you can access for free at:<br><a href="http://mcr.aacrjournals.org/content/11/4/360.full.html#ref-list-1">http://mcr.aacrjournals.org/content/11/4/360.full.html#ref-list-1</a> |
|-----------------------|---|

|                                   |   |
|-----------------------------------|---|
| <b>E-mail alerts</b>              | <a href="#">Sign up to receive free email-alerts</a> related to this article or journal.  |
| <b>Reprints and Subscriptions</b> | To order reprints of this article or to subscribe to the journal, contact the AACR Publications Department at <a href="mailto:pubs@aacr.org">pubs@aacr.org</a> .          |
| <b>Permissions</b>                | To request permission to re-use all or part of this article, contact the AACR Publications Department at <a href="mailto:permissions@aacr.org">permissions@aacr.org</a> . |

## NF-YA Underlies EZH2 Upregulation and Is Essential for Proliferation of Human Epithelial Ovarian Cancer Cells

Azat Garipov<sup>1,4</sup>, Hua Li<sup>1</sup>, Benjamin G. Bitler<sup>1</sup>, Roshan J. Thapa<sup>2</sup>, Siddharth Balachandran<sup>2</sup>, and Rugang Zhang<sup>1,3</sup>

### Abstract

Epithelial ovarian cancer (EOC) accounts for the most gynecologic malignancy-associated deaths in the United States. Enhancer of zeste homolog 2 (EZH2), which silences gene expression through generating trimethylation on lysine 27 residue of histone H3 (H3K27Me3), is often overexpressed in EOCs and has been suggested as a therapeutic target. However, the mechanism underlying EZH2 overexpression in EOCs is unknown. Here, we show that EZH2 is upregulated at the transcription level, and two CCAAT boxes in the proximal regions of the human *EZH2* gene promoter are critical for its transcription in EOC cells. Indeed, NF-YA, the regulatory subunit of the CCAAT-binding transcription factor NF-Y, is expressed at higher levels in human EOCs than in primary human ovarian surface epithelial (HOSE) cells. In addition, there is a positive correlation between expression of NF-YA and EZH2 in EOCs. Notably, high NF-YA expression predicts shorter overall survival in patients with EOCs. The association of NF-YA with the promoter of the human *EZH2* gene is enhanced in human EOC cells compared with primary HOSE cells. Significantly, knockdown of NF-YA downregulates EZH2, decreases H3K27Me3 levels, and suppresses the growth of human EOC cells both *in vitro* and in a xenograft mouse model. Notably, NF-YA knockdown induces apoptosis of EOC cells and ectopic EZH2 expression partially rescues apoptosis induced by NF-YA knockdown. Together, these data reveal that NF-Y is a key regulator of EZH2 expression and is required for EOC cell proliferation, thus representing a novel target for developing EOC therapeutics. *Mol Cancer Res*; 11(4); 360–9. ©2013 AACR.

### Introduction

Epithelial ovarian cancer (EOC) accounts for more deaths than any other gynecologic malignancy in the United States (1). EOCs are classified into distinct histologic types including serous, mucinous, endometrioid, and clear cell. The most common histology of EOC is serous (~60% of all cancers; ref. 2). Recently, an alternative classification has been proposed, in which EOC is broadly divided into 2 types (3). Type I EOC includes mucinous, low-grade serous, low-grade endometrioid, and clear cell carcinomas, and type II EOC includes high-grade serous carcinomas, which is the most lethal histosubtype (3).

Enhancer of zeste homolog 2 (EZH2) is a histone methyltransferase that mediates gene silencing by catalyzing trimethylation of lysine 27 residue of histone H3 (H3K27Me3;

ref. 4). EZH2 is often expressed at higher levels in human EOCs, and its expression positively correlates with cell proliferation (5). Further underscoring the importance of EZH2 in EOCs, EZH2 knockdown triggers apoptosis of human EOC cells (5). These findings identify EZH2 as a putative target for developing EOC therapeutics. Thus, it is important to elucidate the mechanism underlying EZH2 upregulation in EOCs to gain insights into the biology of the disease.

Gene amplification contributes to EZH2 upregulation in several types of cancers, including malignancies of the breast and prostate (6). However, on the basis of the newly released the cancer genome atlas (TCGA) ovarian database (<http://tcga-data.nci.nih.gov/>; ref. 7), *EZH2* gene amplification (>4 copy) is rare (~2%) in EOCs, suggesting that additional mechanisms make more significant contributions to EZH2 upregulation in EOC cells.

NF-Y is a transcription factor that specifically binds to the CCAAT consensus site (8). NF-Y is a heterotrimer, consisting of 3 subunits NF-YA, NF-YB, and NF-YC. NF-YA is the regulatory subunit that is differentially expressed, whereas NF-YB and NF-YC are constitutively expressed (9–11). As a result of differential splicing, NF-YA has 2 isoforms, namely short and long (12). Both isoforms bind DNA and are equivalently active in transcriptional activation (9). NF-Y acts as a transcriptional activator by recruiting p300 histone acetyltransferase, which promotes gene expression by generating acetylation epigenetic marker on histone H3

**Authors' Affiliations:** <sup>1</sup>Gene Expression and Regulation Program, The Wistar Institute; <sup>2</sup>Immune Cell Development and Host Defense Program, <sup>3</sup>Women's Cancer Program, Fox Chase Cancer Center, Philadelphia, Pennsylvania; and <sup>4</sup>Kazan Federal University, Kazan, Russia

**Note:** Supplementary data for this article are available at Molecular Cancer Research Online (<http://mcr.aacrjournals.org/>).

**Corresponding Author:** Rugang Zhang, The Wistar Institute, Room 308, 3601 Spruce Street, Philadelphia, PA 19104. Phone: 215-495-6840; Fax: 215-495-6840; E-mail: rzhang@wistar.org

doi: 10.1158/1541-7786.MCR-12-0661

©2013 American Association for Cancer Research.

(13, 14). Clinically, upregulated NF-Y target genes convey a poor prognosis in multiple cancers including those of the breast and lung (15). However, the role of NF-Y in EOCs has never been investigated.

Here, we show that EZH2 is upregulated at the transcriptional level, and 2 CCAAT sites at the proximal region of the human *EZH2* gene promoter play a key role in regulating its transcription. NF-YA, the regulatory subunit of NF-Y transcription factor that binds to CCAAT sites, is upregulated in human EOCs compared with normal human ovarian surface epithelial (HOSE) cells. In addition, ectopic NF-YA upregulates EZH2 in normal HOSE cells. Importantly, there is a positive correlation between expression of NF-YA and EZH2 in human EOCs, and a high level of NF-YA predicts poor overall survival in patients with EOCs. Chromatin immunoprecipitation (ChIP) analysis revealed that the interaction between NF-YA and the promoter of human *EZH2* gene is enhanced in human EOC cells compared with normal HOSE cells. Knockdown of NF-YA downregulates EZH2, decreases the levels of H3K27Me3, and suppresses the growth of human EOC cells both *in vitro* and in a xenograft mouse model. Mechanistically, we find that NF-YA knockdown triggers apoptosis of human EOC cells and ectopic EZH2 expression partially rescues the apoptosis induced by NF-YA knockdown. Together, these data show that NF-Y plays a key role in regulating EZH2 transcription and is essential for proliferation of human EOC cells.

## Material and Methods

### Cell culture

Normal HOSE cells were cultured as previously described (5). Human EOC cell lines (PEO1, SKOV3, and OVCAR5) were cultured according to American Type Culture Collection in RPMI-1640 media supplemented with 10% FBS and as previously described (5). EOC cell line identification was further confirmed by DNA Diagnostic Center (Fairfield, OH).

### Quantitative reverse transcriptase polymerase chain reaction (qRT-PCR) and immunoblotting

RNA from cultured normal HOSE cells or human EOC cell lines was isolated using TRIzol (Invitrogen) according to the manufacturer's instructions. For qRT-PCR, TRIzol-isolated RNA was further purified using the RNeasy Kit (Qiagen) following the manufacturer's instructions. Primers used for qRT-PCR were purchased from Applied Biosystems. Expression of the housekeeping gene  $\beta$ 2-microglobulin mRNA was used to normalize mRNA expression. The antibodies used for immunoblotting analysis were from the indicated suppliers as following: anti-NF-YA (Santa Cruz), anti-EZH2 (BD Bioscience), anti-H3K27Me3 (Cell Signaling), anti-H3K9Me3 (Abcam), anti-cleaved PARP p85 fragment (Promega), anti-cleaved caspase-3 (Cell signaling), and anti-histone H3 (Millipore).

### Luciferase promoter activity and mutagenesis analysis

Indicated fragments of the proximal human *EZH2* promoter were generated by PCR and cloned into the pGL2

basic luciferase reporter plasmid (Promega) following standard molecular cloning protocols. The NF-YA-binding site single basepair substitution mutant was generated by PCR using standard molecular cloning protocols. Luciferase reporter plasmids were transfected into SKOV3, PEO1, and OVCAR5 EOC cells or normal HOSE cells using Lipofectamine2000 (Invitrogen) following the manufacturer's instructions. A luminescent  $\beta$ -galactosidase plasmid (Clontech) was included as an internal control to normalize the variation in transfection efficiency.

### Chromatin immunoprecipitation (ChIP) analysis

ChIP was conducted using a kit from Millipore following the manufacturer's instructions. Briefly, SKOV3, PEO1, OVCAR5 EOC cells, and normal HOSE cells were fixed with 1% formaldehyde. After cell lysis, gDNA was sheared into 300 to 500 bp fragments by sonication. Sheared chromatin was incubated with anti-NF-YA (Santa Cruz), anti-p300 (Santa Cruz), anti-histone H3 (Millipore), or anti-acetylated histone H3 (Millipore) antibodies overnight at 4°C. After reversing the cross-link, DNA was extracted using the phenol-chloroform method. The immunoprecipitated DNA was then amplified by PCR. The primers used for PCR amplification were: for distal *EZH2* gene promoter: forward primer: 5'-GTCGGGAGTTCGAGAC-3' and reverse primer: 5'-GTCGGCTCAGCTGTG-3'; and for proximal *EZH2* gene promoter: forward primer: 5'-CTGTGATTGGACGGGC-3' and reverse primer: 5'-ACTCGCGTTGTTCCC-3'.

### Inducible EZH2 overexpression, short hairpin RNA, lentivirus packaging, and infection

Inducible EZH2 expression was achieved by using the Retro-X Tet-On Advanced Inducible Expression System (Invitrogen) following the manufacturer's instructions. Lentivirus packaging was conducted using the Virapower Kit (Invitrogen) according to the manufacturer's instructions. Briefly, cells at 40% to 50% confluence were infected with lentivirus-expressing short hairpin RNA (shRNA) to the human *NF-YA* gene (shNF-YA) or vector control. The infected cells were drug-selected with 3  $\mu$ g/mL puromycin. The mature sense sequences of the 3 individual shNF-YA are: 5'-CCATCATGCAAGTACCTGTTT-3', 5'-TTCTGTCCTGTAGTAAAGGGC-3', and 5'-CGAGCTAACTAGAGGCAGAA-3'. pLV-CMV-H4-puro lentiviral vector (kindly provided by Dr. Alexey Ivanov, West Virginia University, Morgantown, WV) was used to produce the lentivirus-expressing NF-YA.

### Anchorage-independent soft agar assay

Soft agar assays were conducted as previously described (5). Briefly, 2,500 cells were resuspended in 0.35% low melting point agarose dissolved in RPMI-1640 medium supplemented with 10% FBS and inoculated on top of 0.6% low melting point agarose base in 6-well plates. After 2 weeks in culture, the plates were stained with 0.005% crystal violet, and the number of colonies was counted.

### Annexin V staining for detecting apoptotic cells (Guava assay)

Phosphatidylserine externalization was detected using an Annexin V staining kit (Millipore) following the manufacturer's instructions. Annexin V-positive cells were detected using the Guava System and analyzed with the Guava Nexin software Module (Millipore).

### Xenograft tumorigenesis assay

The protocol was approved by the Institutional Animal Care and Use Committee (IACUC). A total of  $6 \times 10^5$  cells in PBS (pH 7.3) were injected subcutaneously into 6-week-old female nude athymic mice. The mice were sacrificed 30 days postinoculation. Tumor size was measured, and the tumor volume ( $\text{mm}^3$ ) was calculated using the following formula: tumor volume ( $\text{mm}^3$ ) =  $a^2 \times b/2$ , where  $a$  is the smaller diameter and  $b$  is the larger diameter.

### Data sets

Gene expression microarray data sets for 53 cases of laser capture and microdissected high-grade serous EOCs and 10 individual isolations of normal HOSE cells were obtained from Gene Expression Omnibus (GEO; <http://www.ncbi.nlm.nih.gov/geo/>; GEO accession number: GSE18521). Gene expression data from 24 cases of laser capture microdissected primary nonmalignant fallopian tube epithelium and 13 cases of high-grade serous EOCs (GEO accession number: GSE10971) is also used in our analysis.

### Statistical analysis

Quantitative data are expressed as mean  $\pm$  SD unless otherwise stated. ANOVA with Fisher least significant difference (LSD) was used to identify significant differences in multiple comparisons. Spearman test was used to measure statistical dependence between *EZH2* mRNA levels and *NF-YA* mRNA levels. For all statistical analyses, the level of significance was set at 0.05.

## Results

### *EZH2* is upregulated at the transcriptional level, and two CCAAT sites in the proximal region of the human *EZH2* gene promoter are critical for its transcription in human EOC cells

It has been shown that *EZH2* protein is overexpressed in EOC cells (5). To determine whether the upregulation occurs at the transcriptional level, we examined the mRNA level of *EZH2* in human EOC cell lines and in normal HOSE cells by qRT-PCR. Compared with normal HOSE cells, the *EZH2* mRNA level was significantly higher in human EOC cell lines (Fig. 1A). This suggests that *EZH2* is upregulated at the transcriptional level in human EOC cells. In agreement, a luciferase reporter driven by a 1,152 bp (−1,011 to +141 bp) proximal fragment of the human *EZH2* gene promoter was highly active in human EOC cell lines than in normal HOSE cells (Supplementary Fig. S1A). E2F transcriptional factor is known to play a role in regulating the transcription of the human *EZH2* gene in human

EOC cells (6). In addition, Elk-1 transcription factor has also been implicated in regulating *EZH2* gene transcription (16). Notably, deletion of both E2F- and Elk-1-binding sites only caused an approximate 2-fold decrease in *EZH2* gene promoter activity in human EOC cells (Fig. 1B and Supplementary Fig. S1B and S1C). However, the *EZH2* mRNA levels are 30 to 50 times higher in human EOC cell lines than in normal HOSE cells (Fig. 1A), and the *EZH2* gene promoter activity shows the similar fold changes in these cells (Supplementary Fig. S1A). These data suggest that mechanisms in addition to E2F and Elk-1 play a more important role in regulating the transcription of the human *EZH2* gene in EOC cells.

Systematic promoter serial deletion analysis revealed that 2 CCAAT sites in the proximal promoter of the human *EZH2* gene are critical for its promoter activity (Fig. 1B). We observed similar effects in multiple human EOC cell lines (Fig. 1B and Supplementary Fig. S1B and S1C), showing that this is not a cell line-specific effect. Strikingly, a single basepair change in each of the CCAAT-binding sites (changed to CCAAC) severely impaired the activity of the *EZH2* gene promoter in human EOC cells (Fig. 1C and D). On the basis of these findings, we conclude that 2 CCAAT sites in the proximal region of the human *EZH2* gene promoter play a key role in regulating the transcriptional activity of the human *EZH2* gene in EOC cells.

### NF-YA is expressed at higher levels in human EOC cells and ectopic NF-YA expression drives *EZH2* expression in normal HOSE cells

NF-Y is a transcription factor that binds specifically to the CCAAT consensus site (17). We thus sought to determine whether NF-YA, the regulatory subunit of NF-Y (8), is upregulated in human EOC cells. Indeed, NF-YA is expressed at higher levels in human EOC cells than in normal HOSE cells (Fig. 2A and Supplementary Fig. S2). The anti-NF-YA antibody we used here can recognize both short and long isoforms of the NF-YA (Fig. 2A and Supplementary Fig. S2). Consistently, both *EZH2* and H3K27Me3 are expressed at higher levels in human EOC cells than in normal HOSE cells (Fig. 2A). However, NF-YA upregulation is not a consequence of cell transformation, as NF-YA is not upregulated in normal HOSE cells expressing hTERT, SV40 early region (s/L antigen) and oncogenic H-RAS<sup>G12V</sup> (Supplementary Fig. S3), which has previously been shown to be sufficient for transforming normal HOSE cells (18). We next sought to determine whether NF-YA is sufficient to upregulate *EZH2* in normal HOSE cells. Toward this goal, 2 independent isolates of normal HOSE cells were infected with a lentivirus encoding NF-YA, and *EZH2* expression was examined by immunoblotting analysis. Indeed, ectopic NF-YA expression induced *EZH2* expression in normal HOSE cells (Fig. 2B). On the basis of these results, we conclude that NF-YA is expressed at higher levels in human EOC cells than in normal HOSE cells, and ectopic NF-YA is sufficient to upregulate *EZH2* in normal HOSE cells.



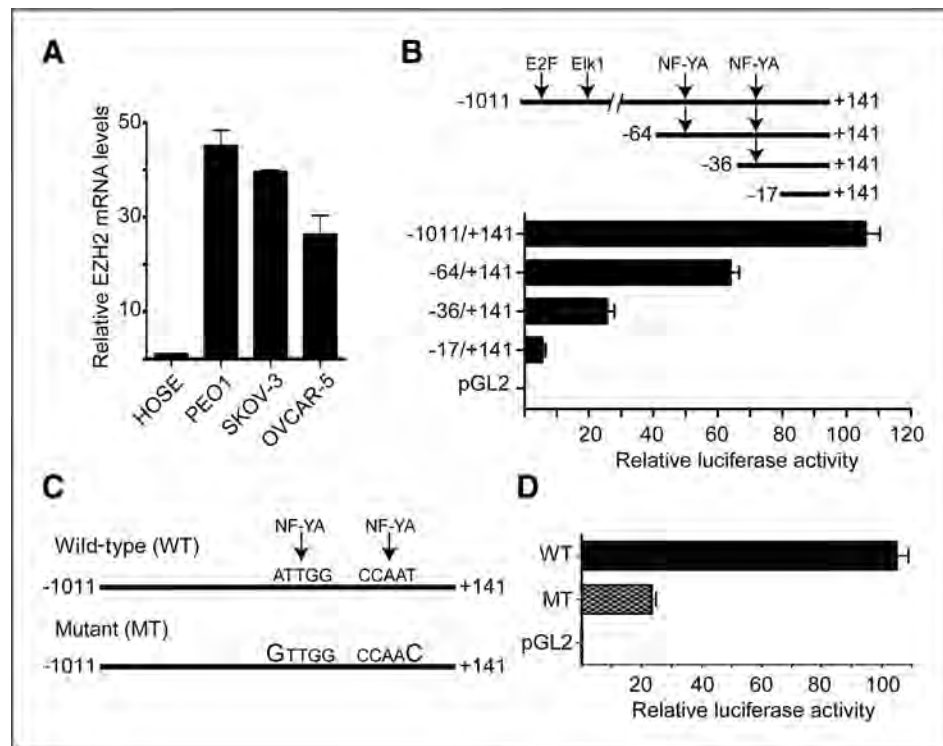


**Figure 1.** EZH2 is upregulated at the transcriptional level, and 2 CCAAT sites within proximal region of the human *EZH2* gene promoter are critical for its transcriptional activation in EOC cells. A, *EZH2* mRNA level was determined by qRT-PCR in normal HOSE cells and indicated EOC cell lines. Mean of 3 independent experiments with SD. B, SKOV3 EOC cells were transfected with a luciferase reporter driven by the indicated proximal promoter fragment of the human *EZH2* gene. Twelve hours posttransfection, luciferase reporter activity was determined. A luminescent  $\beta$ -gal reporter (Clontech) was used to normalize the transfection efficacy. Mean of 3 independent experiments with SD. C, two CCAAT sites in proximal region of the human *EZH2* gene promoter were mutated to CCAAC, which is known to be sufficient to inhibit the binding of the CCAAT-binding transcription factor, NF-Y (36). Note that the first CCAAT site is inverted. D, luciferase activity of wild-type *EZH2* (WT) gene promoter compared with CCAAT sites mutated *EZH2* (MT) gene promoter as diagrammed in (C). Mean of 3 independent experiments with SD.

#### NF-YA expression positively correlates with the expression of EZH2 in human EOC cells and a high level of NF-YA predicts shorter overall survival in EOC patients

We next examined whether expression of NF-YA and EZH2 is positively correlated in human EOCs. In addition to EOC cells, EZH2 is also upregulated in ovarian tumor-associated stromal cells such as endothelial cells (19). To limit the confounding effects of EOC-associated stromal cells, we sought to correlate the expression of NF-YA and EZH2 in specimens from laser capture and microdissected (LCM) high-grade serous tumors, which account for a majority of EOC-associated mortalities (3). Toward this goal, we examined the expression of NF-YA and EZH2 in a published microarray database, which compares the gene expression profile in 53 cases of LCM high-grade serous EOC and 10 individual isolations of normal HOSE cells (20). Notably, NF-YA expression is significantly higher in human EOCs than in normal HOSE cells (Fig. 2C). Consistent with previous reports (5, 19), EZH2 was expressed at significantly higher levels in human EOCs than in normal HOSE cells (Fig. 2D). Indeed, there was a significant positive correlation between expression of NF-

YA and EZH2 in a Spearman statistical analysis of the cases including EOC alone or both EOC and primary HOSE cells (Fig. 2E,  $P < 0.001$ ). Next, we determined whether there is an association between NF-YA expression and the survival of patients with EOCs. Upon dividing EOC cases into NF-YA high or low based on the median NF-YA expression, we found that a high level of NF-YA expression was significantly associated with shorter overall survival (Fig. 2F,  $P = 0.0388$ ). Notably, there is recent evidence to suggest that a proportion of serous histosubtype EOCs may arise from distant fallopian tube epithelium (21, 22). Using a published microarray analysis (23), we found that NF-YA is also expressed at higher levels in serous ovarian carcinomas than in primary nonmalignant fallopian tube epithelial cells (Fig. 2G,  $P < 0.001$ ). Together, we conclude that NF-YA is expressed at higher levels in human EOC cells than in normal HOSE cells or nonmalignant fallopian tube epithelial cells, and ectopic NF-YA is sufficient to drive EZH2 expression in normal HOSE cells. Significantly, expression of NF-YA positively correlates with expression of EZH2 in high-grade serous EOCs, and high levels of NF-YA predict shorter overall survival in patients with EOCs.

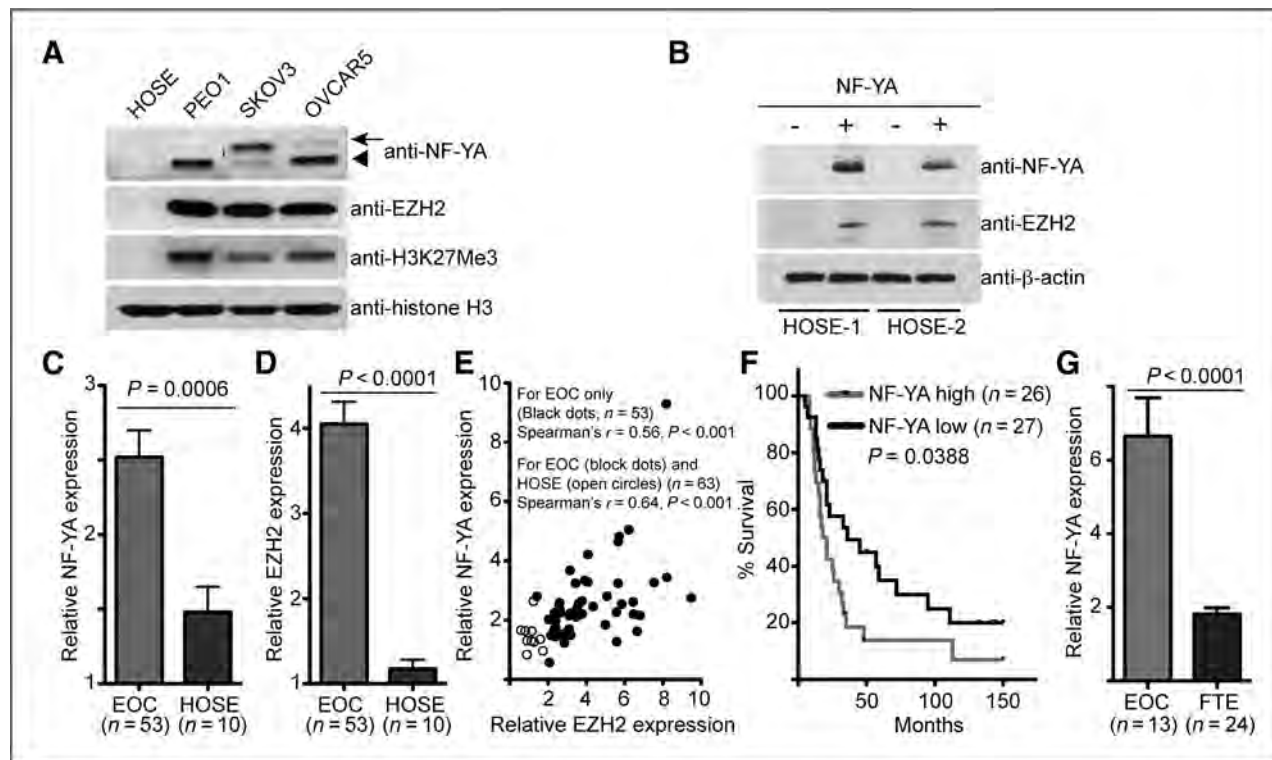


**Figure 2.** NF-YA expression positively correlates with EZH2 expression in human EOC cells, and a high level of NF-YA predicts shorter overall survival in patients with EOCs. A, expression of NF-YA, EZH2, H3K27Me3, and histone H3 in indicated human EOC cell lines and normal HOSE cells determined by immunoblotting. Note that the arrow points to the long NF-YA isoform and the arrowhead points to the short NF-YA isoform. B, normal HOSE cells were infected with a lentivirus encoding NF-YA or control. Drug-selected cells were examined for expression of NF-YA, EZH2, and  $\beta$ -actin by immunoblotting. C, NF-YA is expressed at higher levels in human EOCs than in normal HOSE cells. Relative expression of NF-YA mRNA in LCM high-grade serous EOC ( $n = 53$ ) and normal HOSE cells ( $n = 10$ ). D, same as (C) but for expression of EZH2 mRNA. E, NF-YA expression positively correlates with EZH2 expression. Correlation between expression of NF-YA and EZH2 was determined by Spearman statistical analysis. F, high NF-YA expression predicts a shorter overall survival in patients with EOCs. Kaplan–Meier survival curve for patients with EOCs with low or high NF-YA expression. G, NF-YA is expressed at higher levels in human EOCs than in primary nonmalignant human fallopian tube epithelial (FTE) cells. Relative expression of NF-YA mRNA in high-grade serous EOC ( $n = 13$ ) and LCM primary nonmalignant FTE cells ( $n = 24$ ).

### The association of NF-YA with the proximal promoter of the human *EZH2* gene is enhanced in human EOC cells

Next, we determined whether the association of NF-YA with the human *EZH2* gene promoter is enhanced in human EOC cells compared with normal HOSE cells by ChIP analysis using an anti-NF-YA antibody. An isotype-matched IgG was used as a negative control and an antibody to the core histone H3 was used as a positive control in ChIP analysis. To further limit potential nonspecific effects, we chose a distal region of the human *EZH2* gene promoter that does not have NF-YA-binding sites as a genomic region negative control (Fig. 3A). There is evidence to suggest that NF-YA activates its target gene expression by recruiting p300 histone acetyltransferase (24, 25). Thus, we also examined the association of p300 with the human *EZH2* gene promoter using an anti-p300 antibody. Indeed, both NF-YA and p300 showed an enhanced association with the proximal region of the human *EZH2* gene promoter in human EOC cells compared with normal HOSE cells (Fig. 3B). In contrast, NF-YA and p300 did not associate with the distal region of the human *EZH2* promoter that lacks NF-YA-binding sites (Fig. 3B). Notably, NF-YA is associated with a known NF-YA target gene

*CCNA2* that has NF-YA-binding sites (CCAAT) in its promoter but not with negative control genes such as  *$\alpha$ -tubulin*, *RPS19*, and *YBL1* that do not have NF-YA-binding sites in their promoters, showing the specificity of NF-YA antibody in ChIP analysis (Supplementary Fig. S4; refs. 26–28). It has previously been reported that p300 binds NF-Y target gene promoters to promote the expression of these genes by generating acetylation epigenetic marker on histone H3 (25, 29, 30). Indeed, there was an increase in acetylated histone H3 in the proximal promoter of the human *EZH2* gene where NF-YA and p300 bind in human EOC cells compared with normal HOSE cells (Fig. 3C). On the basis of these results, we conclude that there is an association of NF-YA and p300 with the proximal promoter of the human *EZH2* gene in human EOC cells, and this association correlates with increased levels of acetylated histone H3.

### NF-YA knockdown suppresses EZH2 expression and inhibits the growth of human EOC cells *in vitro* and in a xenograft EOC model

We next sought to determine the effects of NF-YA knockdown on expression of EZH2 in human EOC cells.

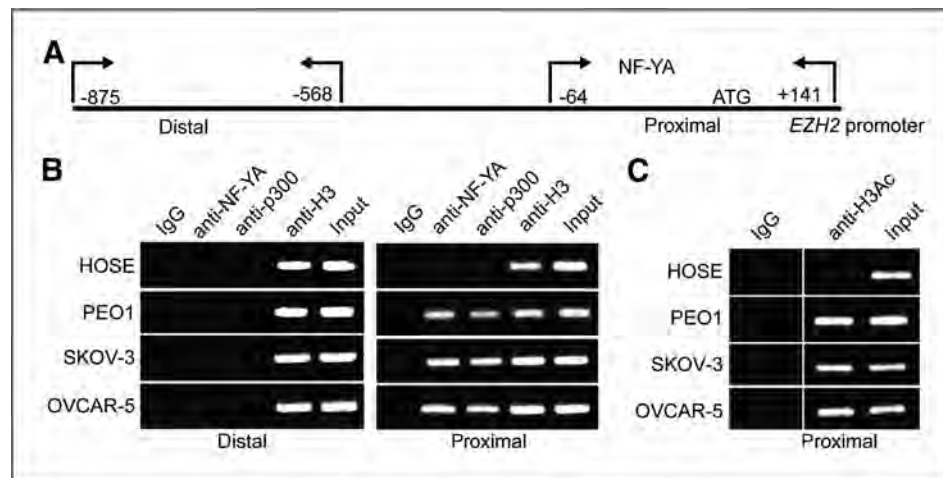


**Figure 3.** The association of NF-YA and its co-activator p300 with the human *EZH2* gene promoter is enhanced in human EOC cells compared with normal HOSE cells. A, diagram of the human *EZH2* gene promoter with indicated positions of primers used for proximal (–64/+141) and distal (–875/–568) regions of the human *EZH2* gene promoter in ChIP analysis. B, normal HOSE cells or indicated EOC cell lines were subjected to ChIP analysis using antibodies specific to NF-YA or p300, respectively. An isotype-matched IgG was used as a negative control, and antibody against core histone H3 was used as a positive control. After ChIP analysis, the distal and proximal regions of the human *EZH2* gene promoter were subjected to PCR amplification using primers detailed in materials and methods and as diagramed in (A). C, same as (B) but using an antibody against acetylated histone H3.

To this end, we used 3 individual shRNAs to the human *NF-YA* gene (shNF-YA). The knockdown efficacy of shNF-YAs was examined by immunoblotting (Fig. 4A and Supplementary Fig. S2A and S2B) and two shNF-YAs (#1 and #2) were found to efficiently reduce NF-YA levels, whereas a third (#3) was largely ineffective and used as a non-silencing negative control. Notably, shNF-YA that efficiently knocked down NF-YA also suppressed the expression of *EZH2* (Fig. 4A and Supplementary Fig. S2A and S2B). Consistently, the levels of H3K27Me<sub>3</sub>, the product of *EZH2*'s methyltransferase activity, were also decreased by shNF-YA that knocks down NF-YA (Fig. 4A and Supplementary Fig. S5 and S6A–B). In addition, similar observations were made in lung cancer cell line H1299 and breast cancer cell line MCF7, suggesting that this is not unique in EOC cells (Supplementary Fig. S5). We observed the same effects using 2 individual shNF-YAs (Fig. 4A and Supplementary Fig. S5 and S6A–B), suggesting that this is not due to off-target effects. In contrast, levels of H3K9Me<sub>3</sub>, which are generated by different histone methyltransferases such as Suv39H1 and SETDB1 (31), were not affected by NF-YA knockdown (Fig. 4A). As a negative control, the shNF-YA #3 that does not efficiently knockdown NF-YA also failed to overtly decrease the *EZH2* and H3K27Me<sub>3</sub> levels in human EOC cells (Fig. 4A).

Expression of *EZH2* positively correlates with expression of markers of cell proliferation (5), and NF-YA knockdown suppresses the expression of *EZH2* (Fig. 4A). Thus, we wanted to determine the effects of NF-YA knockdown on the growth of human EOC cells. Compared with controls, 2 individual shNF-YAs that efficiently knocked down NF-YA suppressed both the anchorage-dependent and -independent growth of human EOC cells (Fig. 4B and C). In contrast, one shNF-YA (#3) that does not efficiently knockdown NF-YA failed to suppress the growth of human EOC cells

(Fig. 4B and C). Similar effects of NF-YA knockdown on cell growth were observed in multiple EOC cells (Fig. 4 and Supplementary Fig. S6), showing that this is not cell line-specific. On the basis of these results, we conclude that NF-YA knockdown suppresses the growth of human EOC cells *in vitro* in both an anchorage-dependent and -independent conditions.

Next, we examined the effects of NF-YA knockdown on the growth of human EOC cells *in vivo* in a xenograft mouse model. We subcutaneously injected control or shNF-YA-expressing human EOC cells into the immunocompromised (athymic nude) mice. Consistent with our *in vitro* findings, we found that compared with controls, shNF-YAs that efficiently knocked down NF-YA expression suppressed the growth of xenografted human EOC cells (Fig. 4D and E). In contrast, the shNF-YA #3 that does not efficiently knockdown NF-YA also failed to significantly suppress the growth of implanted human EOC cells (Fig. 4D and E). Thus, we conclude that NF-YA knockdown suppresses the growth of human EOC cells *in vivo* in a xenograft EOC mouse model.

### NF-YA knockdown triggers apoptosis of human EOC cells

We next determined the mechanism by which NF-YA knockdown suppresses the growth of human EOC cells. As NF-YA regulates *EZH2* expression (Fig. 2) and knockdown of *EZH2* induces apoptosis of EOC cells (5), we examined the effects of NF-YA on apoptosis of human EOC cells. We observed a significant increase of apoptosis markers in NF-YA knockdown cells. These markers include an increase in Annexin V detection as measured by the Guava Nexin assay (Fig. 5A and B) and an increase of cleaved caspase-3 and cleaved PARP p85 (Fig. 5C). *HRK*, a pro-apoptotic gene, has recently been shown as an H3K27Me<sub>3</sub> target gene and plays



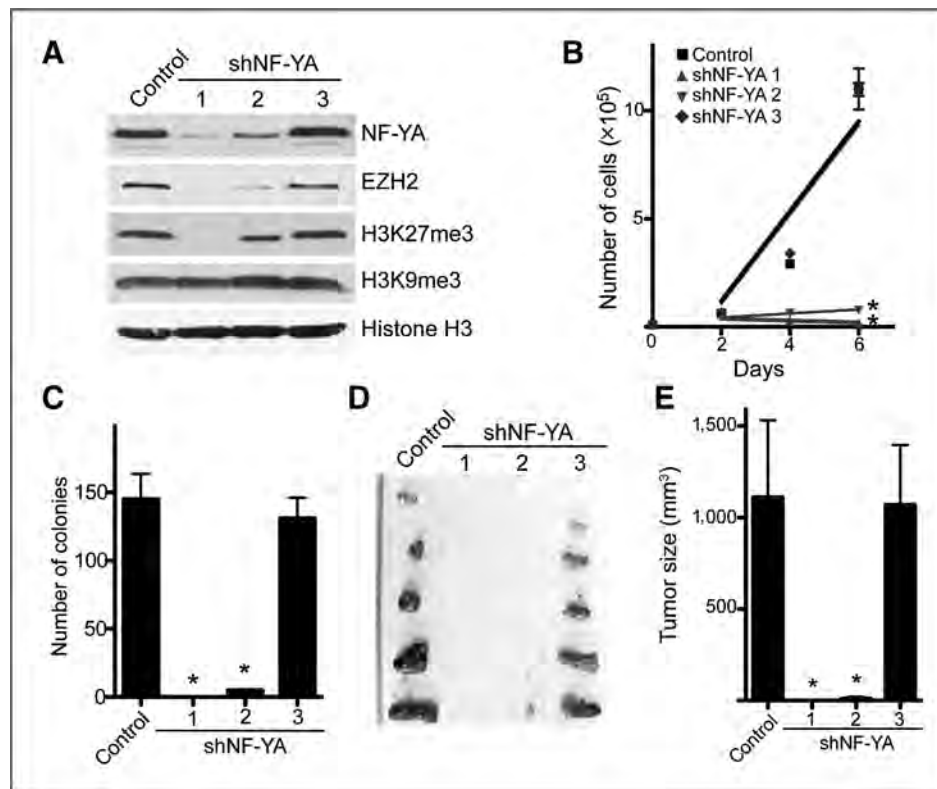


**Figure 4.** NF-YA knockdown suppresses the expression of EZH2 and inhibits the growth of human EOC cells *in vitro* and in a xenograft EOC mouse model. A, SKOV3 EOC cells were infected with lentivirus encoding the indicated shNF-YAs or control. Drug-selected cells were examined for expression of NF-YA, EZH2, H3K27Me3, and H3K9Me3 by immunoblotting. Expression of core histone H3 was used as a loading control. B, same as (A), but equal number of drug-selected cells was seeded and counted at indicated time points. \*,  $P < 0.05$  compared with either control or shNF-YA #3. Mean of 3 independent experiments with SD and linear regression. C, same as (A), but equal number of drug-selected cells were assayed for anchorage-independent growth in soft agar. Mean of 3 independent experiments with SD. \*,  $P < 0.05$  compared with either control or shNF-YA #3. D, same as (A), but equal number of the indicated cells were subcutaneously injected in immunocompromised nude mice ( $n = 5$ ). Four weeks postinjection, tumors were removed from mice. E, quantification of (D), the size of tumors was measured. Error bars represent SD. \*,  $P < 0.05$  compared with either control or shNF-YA #3.

a key role in mediating apoptosis induced by decreasing H3K27Me3 levels (32). As NF-YA knockdown suppresses EZH2 expression and decreasing H3K27Me3 levels, we sought to determine the effects of NF-YA knockdown on the expression of HRK. Indeed, HRK expression is significantly upregulated in NF-YA knockdown cells (Fig. 5D). Together, we conclude that NF-YA knockdown induces apoptosis of human EOC cells.

As NF-YA knockdown suppresses the expression of EZH2, we examined whether downregulation of EZH2 contributes to apoptosis induced by NF-YA knockdown. Toward this goal, we ectopically expressed an inducible EZH2 in EOC cells. We examined the expression of markers of apoptosis in cells expressing shNF-YA with or without inducible EZH2 expression. Compared with shNF-YA only cells, in which EZH2 is downregulated, ectopic EZH2 induction partially rescued the apoptosis induced by NF-YA knockdown as evidenced by decreased levels of apoptotic markers such as cleaved PARP p85 and cleaved caspase-3 (Fig. 5E). Together, we conclude that apoptosis induced by NF-YA knockdown is, at least in part, due to suppression of EZH2 expression.

## Discussion

We showed that ectopic NF-YA expression is sufficient to drive EZH2 upregulation in normal HOSE cells (Fig. 2B). Interestingly, we observed cell death in normal HOSE cells with NF-YA ectopic expression (data not shown), which prevented us from further analyzing these cells. Consistent with our observation, a previous report showed that ectopic NF-YA promotes p53-mediated apoptosis in normal mouse embryonic fibroblasts and inactivation of p53 partially suppresses the apoptosis induced by NF-YA expression (33). Indeed, we also found that p53 is activated upon NF-YA expression in normal HOSE cells (data not shown). These data suggest that p53 inactivation is necessary for the survival of NF-YA-expressing cells. Notably, p53 is often inactivated in EOCs. For example, p53 is inactivated in virtually all high-grade serous EOCs (7). Thus, it is possible that inactivation of p53 may cooperate with NF-YA in EOC cells. In addition, recent evidence suggests that a proportion of high-grade serous EOCs may arise from the distal fallopian tube epithelial cells (21, 22). Thus, it will be interesting to examine whether ectopic NF-YA expression is sufficient to



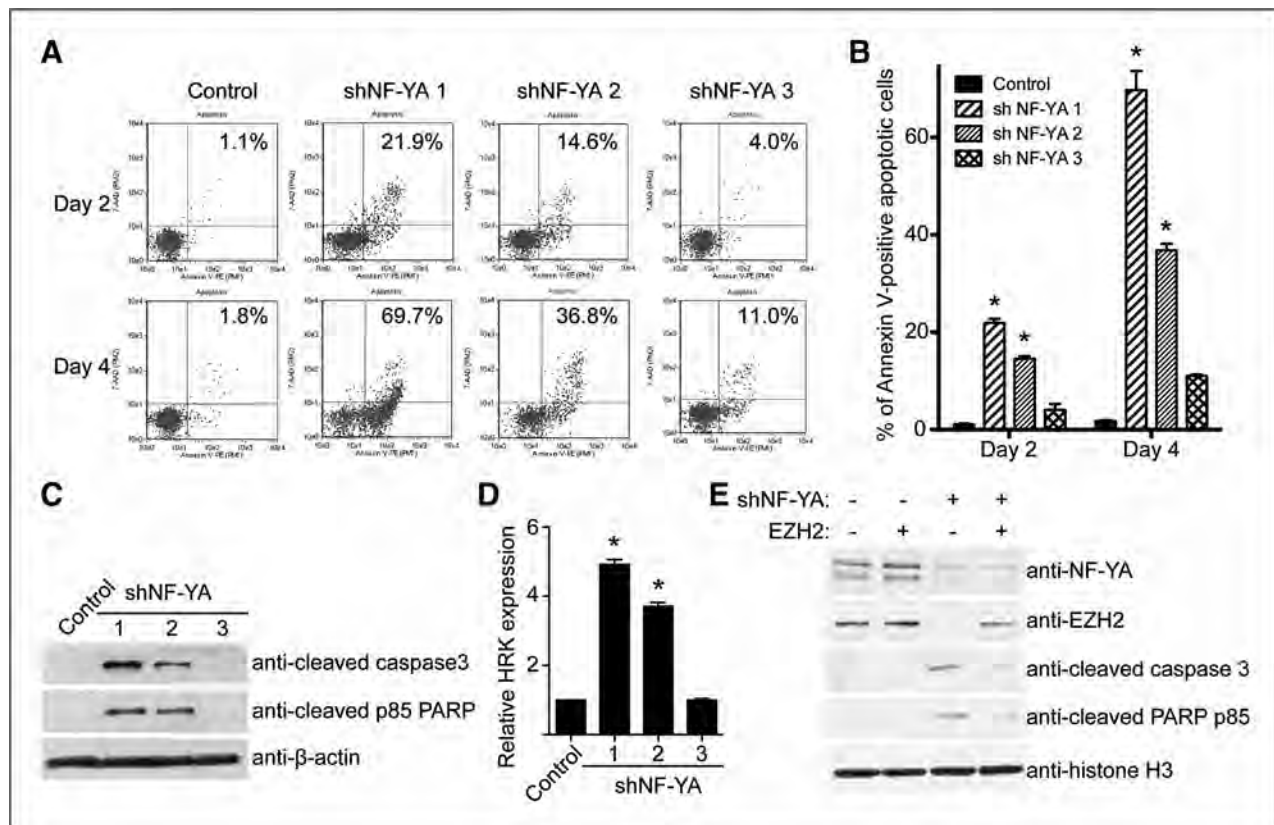


**Figure 5.** NF-YA knockdown induces apoptosis of human EOC cells. A, SKOV3 EOC cells were infected with lentivirus encoding the indicated shNF-YAs or control. Guava Nexin assay was conducted at the indicated time points. B, quantification of (A). Mean of 3 independent experiments with SD. \*,  $P < 0.05$  compared with either control or shNF-YA #3. C, same as (A) but examined for expression of apoptosis markers, cleaved caspase-3, and cleaved PARP p85 by immunoblotting. D, same as (A) but examined for *HRK* gene expression by qRT-PCR. \*,  $P < 0.05$  compared with either control or shNF-YA #3. E, SKOV3 EOC cells were engineered to express a Tet-inducible EZH2. These cells were infected with a lentivirus shNF-YA with or without simultaneous induction of EZH2 expression. Drug-selected cells were examined for expression of NF-YA, EZH2 and indicated apoptosis markers by immunoblotting. Expression of core histone H3 was used as a loading control.

drive EZH2 expression in fallopian tube epithelial cells once these cells become more accessible.

We showed that NF-YA is upregulated in EOCs. However, TCGA gene copy number analysis indicates that NF-YA gene (6p21.3) amplification occurs rare in EOCs (~1% specimens show >4 copy of NF-YA gene; <http://cancergenome.nih.gov/>). This suggests that additional mechanisms contribute to NF-YA upregulation in human EOCs. In the future, we will elucidate additional mechanisms that contribute to NF-YA upregulation in EOCs. In addition, it will be critical to further validate the correlation between NF-YA expression and survival of patients with EOCs in independent cohorts.

We discovered that the expression of NF-YA and EZH2 positively correlates in human EOCs (Fig. 2C–E), further supporting the premise that NF-YA plays a key role in regulating EZH2 expression. However, the Spearman coefficient  $r$  was 0.56 for EOC only and 0.64 for EOCs plus normal HOSE cells (Fig. 2E). This result is consistent with the idea that other factors, such as E2F and Elk-1 (Fig. 1B; refs. 6, 16), also play a role in the expression of EZH2.

We showed that EZH2 is a direct NF-YA target gene (Fig. 3). EZH2 knockdown induces apoptosis in human EOC cells (5). Consistently, knockdown of NF-YA also triggers apoptosis of human EOC cells (Fig. 5). However, ectopic EZH2 expression can only partially rescue the apoptosis induced by NF-YA knockdown and these cells will ultimately undergo apoptosis (Fig. 5E and data not shown). These results suggest that other NF-YA target genes also contribute to the apoptosis induced by NF-YA knockdown. Indeed, the anti-apoptotic genes such as *Bcl-xl* and *Bcl2* are also directly controlled by NF-Y transcription factor (34). Further studies are warranted to identify additional NF-YA target genes that contribute to the apoptosis of human EOC cells induced by NF-YA knockdown. In addition, these findings indicate that inhibiting NF-YA could be an alternative strategy for suppressing EZH2 in EOC cells and NF-YA represents a putative target for developing novel EOC therapeutics. Thus, it will be interesting to examine inhibitors of NF-YA transcription factor such as GWL-78 (35) on the malignant phenotypes of human EOC cells.

In summary, we show that 2 NF-Y-binding CCAAT sites within the proximal region of the human *EZH2* gene promoter play a key role in regulating *EZH2* expression in human EOC cells. NF-YA, the regulatory subunit of NF-Y transcription factor, is upregulated in human EOC cells compared with normal HOSE cells. In addition, ectopic NF-YA drives *EZH2* expression in normal HOSE cells. The expression of NF-YA positively correlates with the expression of *EZH2* in primary EOCs, and a high level of NF-YA expression predicts shorter overall survival in patients with EOCs. Consistently, NF-YA knockdown suppresses *EZH2* expression and inhibits the growth of human EOC cells *in vitro* and in a xenograft mouse model. NF-YA knockdown triggers apoptosis of human EOC cells, and downregulation of *EZH2*, at least in part, contributes to apoptosis induced by NF-YA knockdown in these cells. These results establish that NF-YA underlies *EZH2* upregulation and is essential for proliferation of human EOC cells. We believe that these studies provided important insights into the biology of EOC and identified NF-YA as a potential target for intervention of EOCs.

## References

- American Cancer Society. Cancer facts & figures 2012. Atlanta, GA: American Cancer Society. 2012.
- Arulkumaran S, Regan L, Farquharson DIM. Obstetrics and gynaecology. Oxford, UK: Oxford University Press; 2011.
- Shih le M, Kurman RJ. Ovarian tumorigenesis: a proposed model based on morphological and molecular genetic analysis. *Am J Pathol* 2004;164:1511–8.
- Cao R, Wang L, Wang H, Xia L, Erdjument-Bromage H, Tempst P, et al. Role of histone H3 lysine 27 methylation in Polycomb-group silencing. *Science* 2002;298:1039–43.
- Li H, Cai Q, Godwin AK, Zhang R. Enhancer of zeste homolog 2 promotes the proliferation and invasion of epithelial ovarian cancer cells. *Mol Cancer Res* 2010;8:1610–8.
- Bracken AP, Pasini D, Capra M, Prosperini E, Colli E, Helin K. *EZH2* is downstream of the pRB-E2F pathway, essential for proliferation and amplified in cancer. *EMBO J* 2003;22:5323–35.
- The Cancer Genome Atlas Research Network. Integrated genomic analyses of ovarian carcinoma. *Nature* 2011;474:609–15.
- Mantovani R. The molecular biology of the CCAAT-binding factor NF-Y. *Gene* 1999;239:15–27.
- Marziali G, Perrotti E, Ilari R, Coccia EM, Mantovani R, Testa U, et al. The activity of the CCAAT-box binding factor NF-Y is modulated through the regulated expression of its A subunit during monocyte to macrophage differentiation: regulation of tissue-specific genes through a ubiquitous transcription factor. *Blood* 1999;93:519–26.
- Farina A, Manni I, Fontemaggi G, Tiainen M, Cenciarelli C, Bellorini M, et al. Down-regulation of cyclin B1 gene transcription in terminally differentiated skeletal muscle cells is associated with loss of functional CCAAT-binding NF-Y complex. *Oncogene* 1999;18:2818–27.
- Bolognese F, Wasner M, Dohna CL, Gurtner A, Ronchi A, Muller H, et al. The cyclin B2 promoter depends on NF-Y, a trimer whose CCAAT-binding activity is cell-cycle regulated. *Oncogene* 1999;18:1845–53.
- Li XY, Hooft van Huijsduijnen R, Mantovani R, Benoist C, Mathis D. Intron-exon organization of the NF-Y genes. Tissue-specific splicing modifies an activation domain. *J Biol Chem* 1992;267:8984–90.
- Gurtner A, Fuschi P, Magi F, Colussi C, Gaetano C, Dobbelsstein M, et al. NF-Y dependent epigenetic modifications discriminate between proliferating and postmitotic tissue. *PLoS ONE* 2008;3:e2047.
- Li Q, Herler M, Landsberger N, Kaludov N, Ogryzko VV, Nakatani Y, et al. Xenopus NF-Y pre-sets chromatin to potentiate p300 and acetylation-responsive transcription from the Xenopus hsp70 promoter *in vivo*. *EMBO J* 1998;17:6300–15.
- Yamanaka K, Mizuarai S, Eguchi T, Itadani H, Hirai H, Kotani H. Expression levels of NF-Y target genes changed by CDKN1B correlate with clinical prognosis in multiple cancers. *Genomics* 2009;94:219–27.
- Fujii S, Tokita K, Wada N, Ito K, Yamauchi C, Ito Y, et al. MEK-ERK pathway regulates *EZH2* overexpression in association with aggressive breast cancer subtypes. *Oncogene* 2011;30:4118–28.
- Mantovani R. A survey of 178 NF-Y binding CCAAT boxes. *Nucleic Acids Res* 1998;26:1135–43.
- Liu J, Yang G, Thompson-Lanza JA, Glassman A, Hayes K, Patterson A, et al. A genetically defined model for human ovarian cancer. *Cancer Res* 2004;64:1655–63.
- Lu C, Han HD, Mangala LS, Ali-Fehmi R, Newton CS, Ozbun L, et al. Regulation of tumor angiogenesis by *EZH2*. *Cancer Cell* 2010;18:185–97.
- Mok SC, Bonome T, Vathipadiekal V, Bell A, Johnson ME, Wong KK, et al. A gene signature predictive for outcome in advanced ovarian cancer identifies a survival factor: microfibril-associated glycoprotein 2. *Cancer Cell* 2009;16:521–32.
- Kurman RJ, Shih le M. The origin and pathogenesis of epithelial ovarian cancer: a proposed unifying theory. *Am J Surg Pathol* 2010;34:433–43.
- Levanon K, Crum C, Drapkin R. New insights into the pathogenesis of serous ovarian cancer and its clinical impact. *J Clin Oncol* 2008;26:5284–93.
- Tone AA, Begley H, Sharma M, Murphy J, Rosen B, Brown TJ, et al. Gene expression profiles of luteal phase fallopian tube epithelium from BRCA mutation carriers resemble high-grade serous carcinoma. *Clin Cancer Res* 2008;14:4067–78.
- Hughes R, Kristiansen M, Lassot I, Desagher S, Mantovani R, Ham J. NF-Y is essential for expression of the proapoptotic *bim* gene in sympathetic neurons. *Cell Death Differ* 2011;18:937–47.
- Salsi V, Caretti G, Wasner M, Reinhard W, Haugwitz U, Engeland K, et al. Interactions between p300 and multiple NF-Y trimers govern cyclin B2 promoter function. *J Biol Chem* 2003;278:6642–50.
- Kramer A, Carstens CP, Wasserman WW, Fahl WE. CBP/cycA, a CCAAT-binding protein necessary for adhesion-dependent cyclin A

## Disclosure of Potential Conflict of Interest

No potential conflicts of interest were disclosed.

## Authors' Contributions

**Conception and design:** A. Garipov, R.J. Thapa, R. Zhang  
**Development of methodology:** A. Garipov, R.J. Thapa  
**Acquisition of data (provided animals, acquired and managed patients, provided facilities, etc.):** A. Garipov, B.G. Bitler, R.J. Thapa, S. Balachandran  
**Analysis and interpretation of data (e.g., statistical analysis, biostatistics, computational analysis):** A. Garipov, H. Li, S. Balachandran, R. Zhang  
**Writing, review, and/or revision of the manuscript:** A. Garipov, B.G. Bitler, S. Balachandran, R. Zhang  
**Administrative, technical, or material support (i.e., reporting or organizing data, constructing databases):** A. Garipov  
**Study supervision:** A. Garipov, S. Balachandran, R. Zhang

## Grant Support

This work was supported by the National Cancer Institute of the NIH (R01CA163377 to R. Zhang) and, in part, by a DOD ovarian cancer academy award (OC093420 to R. Zhang). Support of Core Facilities used in this study was provided by Cancer Center Support Grant (CCSG) CA010815 to The Wistar Institute.

The costs of publication of this article were defrayed in part by the payment of page charges. This article must therefore be hereby marked *advertisement* in accordance with 18 U.S.C. Section 1734 solely to indicate this fact.

Received November 28, 2012; revised January 10, 2013; accepted January 14, 2013; published OnlineFirst January 29, 2013.

- transcription, consists of NF-Y and a novel Mr 115,000 subunit. *Cancer Res* 1997;57:5117–21.
27. Kramer A, Carstens CP, Fahl WE. A novel CCAAT-binding protein necessary for adhesion-dependent cyclin A transcription at the G1/S boundary is sequestered by a retinoblastoma-like protein in G0. *J Biol Chem* 1996;271:6579–82.
  28. Testa A, Donati G, Yan P, Romani F, Huang TH, Vigano MA, et al. Chromatin immunoprecipitation (ChIP) on chip experiments uncover a widespread distribution of NF-Y binding CCAAT sites outside of core promoters. *J Biol Chem* 2005;280:13606–15.
  29. Di Agostino S, Strano S, Emiliozzi V, Zerbini V, Mottolese M, Sacchi A, et al. Gain of function of mutant p53: the mutant p53/NF-Y protein complex reveals an aberrant transcriptional mechanism of cell cycle regulation. *Cancer Cell* 2006;10:191–202.
  30. Caretti G, Salsi V, Vecchi C, Imbriano C, Mantovani R. Dynamic recruitment of NF-Y and histone acetyltransferases on cell-cycle promoters. *J Biol Chem* 2003;278:30435–40.
  31. Jenuwein T. The epigenetic magic of histone lysine methylation. *FEBS J* 2006;273:3121–35.
  32. Li H, Cai Q, Wu H, Vathipadiekal V, Dobbin ZC, Li T, et al. SUZ12 promotes human epithelial ovarian cancer by suppressing apoptosis via silencing HRK. *Mol Cancer Res* 2012;10:462–72.
  33. Gurtner A, Fuschi P, Martelli F, Manni I, Artuso S, Simonte G, et al. Transcription factor NF-Y induces apoptosis in cells expressing wild-type p53 through E2F1 upregulation and p53 activation. *Cancer Res* 2010;70:9711–20.
  34. Benatti P, Basile V, Merico D, Fantoni LI, Tagliafico E, Imbriano C. A balance between NF-Y and p53 governs the pro- and anti-apoptotic transcriptional response. *Nucleic Acids Res* 2008;36:1415–28.
  35. Kotecha M, Kluza J, Wells G, O'Hare CC, Forni C, Mantovani R, et al. Inhibition of DNA binding of the NF-Y transcription factor by the pyrrolobenzodiazepine-polyamide conjugate GWL-78. *Mol Cancer Ther* 2008;7:1319–28.
  36. Hu Q, Bhattacharya C, Maity SN. CCAAT binding factor (CBF) binding mediates cell cycle activation of topoisomerase IIalpha. Conventional CBF activation domains are not required. *J Biol Chem* 2002;277:37191–200.

# Identification of Multiple Novel Protein Biomarkers Shed by Human Serous Ovarian Tumors into the Blood of Immunocompromised Mice and Verified in Patient Sera

Lynn A. Beer<sup>1</sup>, Huan Wang<sup>1</sup>, Hsin-Yao Tang<sup>1</sup>, Zhijun Cao<sup>1‡</sup>, Tony Chang-Wong<sup>1</sup>, Janos L. Tanyi<sup>2</sup>, Rugang Zhang<sup>3</sup>, Qin Liu<sup>1</sup>, David W. Speicher<sup>1\*</sup>

**1** Center for Systems and Computational Biology, and Molecular and Cellular Oncogenesis Program, The Wistar Institute, Philadelphia, Pennsylvania, United States of America, **2** Ovarian Cancer Research Center, The University of Pennsylvania, Philadelphia, Pennsylvania, United States of America, **3** Gene Expression and Regulation Program, The Wistar Institute, Philadelphia, Pennsylvania, United States of America

## Abstract

The most cancer-specific biomarkers in blood are likely to be proteins shed directly by the tumor rather than less specific inflammatory or other host responses. The use of xenograft mouse models together with in-depth proteome analysis for identification of human proteins in the mouse blood is an under-utilized strategy that can clearly identify proteins shed by the tumor. In the current study, 268 human proteins shed into mouse blood from human OVCAR-3 serous tumors were identified based upon human vs. mouse species differences using a four-dimensional plasma proteome fractionation strategy. A multi-step prioritization and verification strategy was subsequently developed to efficiently select some of the most promising biomarkers from this large number of candidates. A key step was parallel analysis of human proteins detected in the tumor supernatant, because substantially greater sequence coverage for many of the human proteins initially detected in the xenograft mouse plasma confirmed assignments as tumor-derived human proteins. Verification of candidate biomarkers in patient sera was facilitated by in-depth, label-free quantitative comparisons of serum pools from patients with ovarian cancer and benign ovarian tumors. The only proteins that advanced to multiple reaction monitoring (MRM) assay development were those that exhibited increases in ovarian cancer patients compared with benign tumor controls. MRM assays were readily developed for all 11 novel biomarker candidates selected by this process and analysis of larger pools of patient sera suggested that all 11 proteins are promising candidate biomarkers that should be further evaluated on individual patient blood samples.

**Citation:** Beer LA, Wang H, Tang H-Y, Cao Z, Chang-Wong T, et al. (2013) Identification of Multiple Novel Protein Biomarkers Shed by Human Serous Ovarian Tumors into the Blood of Immunocompromised Mice and Verified in Patient Sera. PLoS ONE 8(3): e60129. doi:10.1371/journal.pone.0060129

**Editor:** Shannon M. Hawkins, Baylor College of Medicine, United States of America

**Received:** November 9, 2012; **Accepted:** February 22, 2013; **Published:** March 27, 2013

**Copyright:** © 2013 Beer et al. This is an open-access article distributed under the terms of the Creative Commons Attribution License, which permits unrestricted use, distribution, and reproduction in any medium, provided the original author and source are credited.

**Funding:** This work was supported by National Institutes of Health (NIH) grant CA131582 to DWS and an institutional grant to The Wistar Institute, National Cancer Institute (NCI) Cancer Core Grant CA010813, and by the Reproductive Scientist Development Program, NIH grant 5K12HD00849 to JLT (www.nih.gov). The funders had no role in the study design, data collection and analysis, decision to publish, or preparation of the manuscript.

**Competing Interests:** The authors have declared that no competing interests exist.

\* E-mail: speicher@wistar.org

‡ Current address: The National Center for Toxicological Research, U.S. Food and Drug Administration, Jefferson, Arizona, United States of America

## Introduction

Epithelial ovarian cancer (EOC) is the fifth-leading cause of cancer-related deaths in women, with a higher fatality-to-case ratio than any other gynecologic malignancy in the United States. [1,2,3] A major problem is that greater than two-thirds of EOC cases are diagnosed at advanced stages (Stages 3 or 4), when five-year survival is about 33%. In contrast, when the disease is diagnosed at Stage 1, five-year survival is approximately 90%. [2] CA125 is the best known EOC biomarker; however, 50–60% of early-stage EOC does not express CA125. In addition, while greater than 80% of advanced EOC has elevated CA125, this is not a sufficient diagnosis, as CA125 levels are also elevated in a number of other conditions. [1,4,5,6] Due to the low incidence of ovarian cancer in the general population, the specificity and sensitivity requirements for early screening are quite high, and achieving suitable performance is likely to require a panel of biomarkers superior to most existing biomarkers. [2,7,8,9]

Additional biomarkers, either instead of or in conjunction with CA125, are needed for predicting clinical outcome, stratifying therapeutic options, monitoring response to therapy, and detecting recurrence of the disease.

Although proteomic technologies have improved dramatically, discovering novel blood biomarkers for cancers remains formidable due to the vast complexity of the plasma proteome and the likelihood that any tumor-specific proteins will be present at very low abundance. In addition, comparison of patient and control serum or plasma to discover biomarkers is complicated by the fact that cancers and other conditions induce inflammatory responses involving changes in abundance of multiple blood proteins, and these changes are not very specific to a single disease. [10] Identifying cancer-specific changes in the context of this great complexity and inflammation-induced variability is very difficult when patient serum samples are directly analyzed to discover new biomarkers using proteomics. For this reason, many investigators have turned to alternative strategies for initial discovery of



candidate biomarkers, including proteome analysis of: EOC cell lines, cell surface proteins in EOC cell lines, proteins shed by these cells into the media (the secretome), and patient ascites. [11,12,13,14,15,16] While all of these methods identify many proteins associated with EOC, a critical missing factor is that it is not apparent which of these proteins will migrate into the blood and be potential EOC serum/plasma biomarkers. Furthermore, changes in abundance levels of a protein in the tumor tissue do not necessarily correlate with their abundance levels in the blood.

The primary experimental systems where migration into the blood is assured are mouse models. Hence, one approach is to identify quantitative differences in plasma or serum of genetically engineered mice bearing murine ovarian tumors compared with appropriate controls. [17] While this model provides more consistent genetic and environmental backgrounds compared with patients, the complication of sorting protein changes caused by inflammatory host responses from proteins shed by the tumor persists. An important under-utilized alternative that circumvents the host response problem is xenograft mouse models, where in-depth proteome analysis can identify human proteins shed by the tumor into the murine blood based upon species differences in peptide sequences found in serum or plasma. Another advantage of the xenograft mouse model system, like genetically engineered mice, is a higher tumor-to-blood-volume ratio compared with patients, as well as homogeneous genetic backgrounds, environment, and diet to minimize confounding factors.

We recently identified 106 human proteins shed by a human endometrial ovarian cancer cell line (TOV-112D) into the blood of SCID mice using an in-depth 4D proteome analysis of this xenografted mouse serum. Specifically, serum was depleted of the three most abundant serum proteins followed by microscale solution isoelectrofocusing (MicroSol IEF), SDS-PAGE, and LC-MS/MS. [18] Furthermore, pilot validation of selected candidate biomarkers demonstrated that some of these proteins could be detected in human serum using multiple reaction monitoring (MRM) analysis—and three tested biomarkers were shown to be significantly elevated in cancer patients compared with normal donors. [18] Although that study identified several new biomarkers, the verification and initial validation steps were not very efficient. The success rate of establishing MRM assays for targeted candidate biomarkers using advanced EOC patient serum pools was less than 50%, and only about half of the proteins quantified using these MRM assays exhibited elevated levels in pilot analyses of advanced EOC patients using pools of patient sera ( [18] and data not shown). Hence, overall, only about 20% of the TOV-112D candidate biomarkers selected for verification and initial validation in patients resulted in successful MRM assays that exhibited elevated levels in EOC in a small pilot analysis.

The current study was designed to improve ovarian cancer biomarker discovery using the xenograft mouse model system, improve the efficiency of MRM assay development and preliminary verification of biomarker candidates, and identify candidates that may include biomarkers with some degree of specificity for the serous ovarian cancer subtype. High grade serous ovarian cancers are very aggressive and account for most deaths from EOC, although they only constitute approximately half of EOC cases. Plasma from SCID mice bearing OVCAR-3 serous ovarian tumors was analyzed using an optimized 4-D plasma proteome analysis method, which resulted in identification of 268 human proteins based on two or more peptides. Parallel analysis of supernatants from the serous tumor excised from the SCID mice and incubated briefly in cell culture media increased the sequence coverage for many of the human proteins, thereby both confirming these proteins were human and providing more

proteotypic peptides for MRM assay development. Selected high-priority candidate biomarkers were then compared to a dataset from a label-free quantitative comparison of serum pools from cancer patients with advanced-stage EOC and benign controls. Finally, candidate biomarkers observed to be elevated in pooled sera from advanced EOC cancer patients in the label-free analysis were selected for multiplexed assay development using targeted mass spectrometry analysis with the multiple reaction monitoring (MRM) method. MRM analysis is an alternative mass spectrometry approach utilizing the discriminating power of triple quadrupole mass spectrometers, or their equivalent, to select and quantify a series of specific analytes and associated fragment ions. MRM enables rapid, quantitative measures of proteins in complex mixtures such as plasma and serum, without a dependency on the generation of antibodies or immunoassays. [19,20] Overall, the strategy used in this study proved to be highly efficient, as 100% of the proteins selected for MRM assay development resulted in successful assay development and showed elevated levels in serum pools of advanced EOC patients compared with an approximately 20% success rate in earlier studies that attempted to quantify and verify TOV-112D candidate biomarkers.

## Materials and Methods

### Reagents

Molecular-biology-grade ethanol (200 proof); LC-MS-grade formic acid; sodium phosphate monobasic; *N,N*-dimethylacrylamide (DMA), ammonium bicarbonate; and iodoacetamide were purchased from Sigma-Aldrich (St. Louis, MO). Sodium dodecyl sulfate (SDS), 2-mercaptoethanol, and Tris were purchased from Bio-Rad (Hercules, CA). ZOOM focusing buffers and thiourea were obtained from Invitrogen (Carlsbad, CA). PlusOne reagents dithiothreitol (DTT), 3-[[3-cholamidopropyl]dimethylammonio]-1-propanesulfonate (CHAPS), and urea were purchased from GE Healthcare (Piscataway, NJ). HPLC-grade acetonitrile was purchased from Thomas Scientific (Swedesboro, NJ). Tris(2-carboxyethyl)phosphine (TCEP) was obtained from Pierce (Rockford, IL), and sequencing-grade modified trypsin was purchased from Promega (Madison, WI).

### Cell Culture

The human EOC serous cell line OVCAR-3 was obtained from the American Type Culture Collection (ATCC, Manassas, VA). The cells were maintained in a 37°C incubator with a 5% CO<sub>2</sub>–95% air atmosphere in RPMI-1640 medium (ATCC) supplemented with 10% fetal calf serum.

### Ovarian Cancer Growth *in vivo*

This study was carried out in accordance with the recommendations in the Guide for the Care and use of Laboratory Animals of the National Institutes of Health under protocol #111959 using severe combined immunodeficiency (SCID) mice. The study protocol was reviewed and approved by The Wistar Institute's Institutional Animal Care and Use Committee (IACUC). All efforts were made to minimize suffering.

Nine SCID mice were injected subcutaneously in the flank with 50 µL of OVCAR-3 cells ( $2 \times 10^6$ ) mixed 1:1 with 50 µL Matrigel (BD Biosciences, San Jose, CA). Tumors were allowed to grow until final tumor size was estimated to be at least 1 cm<sup>3</sup> using calipers, but less than 10% of body weight. Blood was collected, mice were euthanized, and tumors were removed at 12 weeks post-injection. Necrosis of tumor tissue was assessed by microscopic inspection of hematoxylin and eosin (H&E) stained, paraffin-embedded sections (5 µm).

### SCID Mouse Plasma

Blood was collected from SCID mice containing visible OVCAR-3 tumors (see above section) by cardiac puncture under anesthesia into Microtainer 0.5 mL K<sub>2</sub> EDTA Blood Collection Tubes (Becton Dickinson, Franklin Lakes, NJ). The tubes were centrifuged for 3 min at room temperature, and aliquots of plasma from individual mice were snap-frozen and stored at  $-80^{\circ}\text{C}$ . Plasma from the four mice that contained the largest, minimally neurotic tumors were subsequently thawed and pooled to average variations among individual mice. The pooled plasma was re-aliquoted, snap-frozen, and stored at  $-80^{\circ}\text{C}$  until analysis using the 4-D fractionation method (immunoaffinity depletion/MicroSol IEF/SDS gel and trypsin digestion/LC-MS/MS). Total protein concentration of the pooled plasma was measured using a BCA Protein Assay (Pierce).

### Tumor Supernatant Isolation

Immediately after removing tumors from eight of the nine SCID mice bearing the largest OVCAR-3 tumors, a section of fresh ovarian tumor tissue from each mouse was cut into small pieces ( $2\text{--}3\text{ mm}^3$ ), placed in the upper chamber of a  $5\text{ }\mu\text{m}$  PVDF microcentrifuge filter (Millipore, Billerica, MA), and washed three times with  $400\text{ }\mu\text{L}$  of PBS for 1 min each. The tissue sections were then transferred to the upper chamber of a  $0.22\text{ }\mu\text{m}$  PVDF microcentrifuge filter and incubated in  $400\text{ }\mu\text{L}$  of serum-free RPMI-1640 medium for 2 h in 5% CO<sub>2</sub>, 95% air at  $37^{\circ}\text{C}$ . After incubation, the supernatant (conditioned media) was recovered by centrifugation, then frozen and stored at  $-80^{\circ}\text{C}$  until needed. For tumor supernatant analysis,  $500\text{ }\mu\text{L}$  aliquots of conditioned media from tumors from four mice were thawed, pooled, and concentrated to  $\sim 30\text{ }\mu\text{L}$  by ultrafiltration using a 10 K MWCO concentration unit. Membrane rinses using 1% SDS, 50 mM Tris, pH 8.5 were combined with the concentrated sample to maximize protein recovery.

### Human Serum

Human sera from normal subjects and patients with benign ovarian tumors, early-stage ovarian cancer, and late-stage ovarian cancer were collected before clinical treatment at approximately the time of diagnosis and prior to surgery as previously described. [18] Descriptions of the patients, healthy controls, and pooling strategies are summarized in **Table S2**. All research in this study involving human specimens was conducted under The Wistar Institute's Institutional Review Board (IRB) approved protocols, #2109171, #EX2110012, and #2602221 and in accordance with Health Insurance Portability and Accountability Act (HIPAA) requirements. All human samples were derived from subjects with informed written consent. Data were analyzed anonymously.

### Immunoaffinity Removal of Major Blood Proteins

The pooled mouse plasma was depleted using a  $4.6\times 100\text{ mm}$  MARS Mouse-3 HPLC column (Agilent Technologies, Wilmington, DE), essentially as previously described, [18] with the exception that a total of  $400\text{ }\mu\text{L}$  of pooled plasma was diluted five-fold with equilibration buffer, filtered through a  $0.22\text{ }\mu\text{m}$  microcentrifuge filter, and applied to the antibody column in eight serial injections of  $250\text{ }\mu\text{L}$  per depletion.

Human serum samples (typically  $30\text{--}60\text{ }\mu\text{L}$ ) were depleted of the 20-most-abundant serum proteins using a ProteoPrep20 Immunodepletion Column (Sigma), as described previously. [21].

### MicroSol IEF Fractionation

Immunodepleted and concentrated mouse plasma ( $2.2\text{ mg}$ ) was fractionated by MicroSol IEF as previously described, [18,22,23] using a ZOOM-IEF fractionator (Invitrogen) where the separation chambers were defined by immobilized gel membranes having pH values of 3.0, 4.6, 5.4, 6.2, and 12.0, respectively.

### SDS-PAGE/in-gel Trypsin Digestion

After evaluation of the MicroSol IEF separation on analytical SDS gels, concentrated samples were loaded onto multiple lanes of pre-cast 12% Bis-Tris NuPAGE gels (Invitrogen) and separated for discrete distances (1 or 4 cm). The concentrated tumor supernatants from both pools were loaded onto multiple lanes of pre-cast 12% Bis-Tris NuPAGE gels (Invitrogen) and separated for 6 cm. Gels were stained with Colloidal Blue (Invitrogen), each gel lane was sliced into uniform 1 mm slices, and corresponding slices from triplicate lanes were combined in a single well of a 96-well pierced digestion plate (Bio-Machines, Inc., Carrboro, NC) and digested overnight with  $0.02\text{ }\mu\text{g}/\mu\text{L}$  of modified trypsin, as previously described. [21,24].

### LC-MS/MS

Tryptic digests were analyzed using an LTQ-Orbitrap XL mass spectrometer (Thermo Scientific, Waltham, MA) interfaced with a Nano-ACQUITY UPLC system (Waters, Milford, MA), as described previously. [21] For each tryptic digest,  $8\text{ }\mu\text{L}$  was injected onto a UPLC Symmetry trap column ( $180\text{ }\mu\text{m}$  i.d.  $\times$  2 cm packed with  $5\text{ }\mu\text{m}$  C18 resin; Waters), and tryptic peptides were separated by RP-HPLC on a BEH C18 nanocapillary analytical column ( $75\text{ }\mu\text{m}$  i.d.  $\times$  25 cm,  $1.7\text{ }\mu\text{m}$  particle size; Waters). The mass spectrometer was set to scan  $m/z$  from 400 to 2000. The full MS scan was collected at 60,000 resolution in the Orbitrap in profile mode followed by data-dependant MS/MS scans on the six most abundant ions exceeding a minimum threshold of 1000 collected in the linear trap. Monoisotopic precursor selection was enabled and charge-state screening was enabled to reject  $z=1$  ions. Ions subjected to MS/MS were excluded from repeated analysis for 60 s.

### Data Processing

MS/MS spectra were extracted and searched using the SEQUEST algorithm (v. 28, rev. 13, University of Washington, Seattle, WA) in Bioworks (v. 3.3.1, Thermo Scientific) against a combined human and mouse UniRef100 protein sequence database (v. June 20,2011) to which commonly observed "contaminants" (trypsin, keratins, etc.) were added. A decoy database was produced by reversing the protein sequence of each database entry, and the entire reversed database was appended in front of the forward human and mouse databases, respectively. Spectra were searched with a partial tryptic constraint of up to two missed cleavages, 100 ppm precursor mass tolerance, 1 Da fragment ion mass tolerance, static modification of cys (+99.06840 for samples alkylated with DMA or +57.0215 Da for samples alkylated with IAM), and variable modification of methionine (+15.9949). The use of a partial tryptic constraint and 100 ppm precursor tolerance for the database search had recently been shown to enhance depth of analysis for serum and plasma proteomes. [25] Consensus protein lists were created using DTASelect (v. 2.0, licensed from Scripps Research Institute, La Jolla, CA) and the following filters were applied: full tryptic constraint, mass accuracy  $\leq 10\text{ ppm}$ , and  $\Delta\text{Cn} \geq 0.05$ . [25] FDR was estimated from the ratio of unique peptides matching reverse sequences to the number of unique peptides matching forward

sequences. Non-redundant peptide totals derived from DTASelect and used for FDR calculations include variable modifications and different charge states as separate peptides. Different charge states and variable modifications of methionine oxidation were collapsed into a single unique peptide count, and peptides shared among multiple proteins were assigned to the protein having the highest sequence coverage, as previously described. [18].

Proteins identified in the database search were sorted into “human,” “mouse,” or “indistinguishable” based upon their species-specific sequences, as previously described. [18] To confirm species-specific assignments, putative uniquely human and mouse sequences were searched against the mouse and human UniRef100 databases (v. 6/20/11), respectively, using BLAST. Keratins and other presumed contaminants were removed from the entire dataset.

### Label-free Quantitation of Patient Serum Pools

To determine whether candidate biomarkers could be detected in ovarian cancer patient sera, in-depth discovery mode analyses of patient serum pools were conducted followed by global label-free quantitative comparisons. One pool of serum from benign patients and three pools of advanced ovarian cancer patient serum samples were made as described in **Table S2**. Pools were immunodepleted and separated on a 1 D SDS gel, each serum proteome was separated into 40 fractions, and each slice was digested with trypsin and analyzed by LC-MS/MS using a 4 h gradient at 200 nL/min consisting of 5–28% B over 168 min, 28–50% B over 51.5 min, 50–80% B over 5 min, and 80% B for 4.5 min, before returning to 5% B over 0.5 min. A short blank gradient was run in between samples to minimize carryover. Full-MS and LC-MS/MS data from fractions 17–32, which encompassed the 8–50 kDa region of the gel, were analyzed using Rosetta Elucidator software (version 3.3, Rosetta Biosoftware, Seattle, WA) to compare peptide signal intensities in full MS scans. Based on peptide elution profiles and ion signal density, data for this label-free comparison was trimmed to 16–200 min. Retention time (RT) alignment, feature identification (discrete ion signals), feature extraction, and protein identifications were performed by the Elucidator system as previously described. [21,26].

### Label-free Multiple Reaction Monitoring

MRM experiments were performed on a 5500 QTRAP hybrid triple quadrupole/linear ion trap mass spectrometer (AB Sciex, Foster City, CA) interfaced with a Nano-ACQUITY UPLC system with the column heater maintained at 45°C. Tryptic digests were injected using the partial loop injection mode onto a UPLC Symmetry trap column (180  $\mu$ m i.d.  $\times$  2 cm packed with 5  $\mu$ m C18 resin), and then separated by RP-HPLC on a BEH C18 nanocapillary analytical column (75 mm i.d.  $\times$  25 cm, 1.7 mm particle size; Waters). Chromatography was performed with solvent A, consisting of Milli-Q water with 0.1% formic acid, and solvent B, as acetonitrile with 0.1% formic acid. Peptides and transitions used for quantitation were selected from discovery results (typically the mouse tumor supernatant) and further verified by MRM-initiated detection and sequencing (MIDAS) using the 5500 QTRAP mass spectrometer. MIDAS experiments were performed at 200 nL/min with a 77-min gradient consisting of 5–28% B over 42 min, 28–50% B over 25.5 min, 50–80% B over 5 min, and 80% B for 4.5 min, before returning to 5% B over 0.5 min. To increase throughput, after optimal peptides and transitions were established, label-free MRM assays were performed with a 41-min gradient, in which peptides were eluted at 400 nL/min for 5–35% B over 38 min and 35% B for 3 min, before returning to 5% B over 0.5 min.

MRM data were acquired with a spray voltage of 3300 V, curtain gas of 20 p.s.i., nebulizer gas of 10 p.s.i., interface heater temperature of 150°C, and a pause time of 3 ms. Multiple MRM transitions were monitored per peptide at unit resolution in both Q1 and Q3 quadrupoles to maximize specificity. Scheduled MRM was used to reduce the number of concurrent transitions and maximize the dwell time for each transition. The detection window was set at 2 min, and the target scan time was set at 1.8 s. Data analysis was performed using Skyline v.1.2. [27] The transition with the strongest signal for each peptide was used for quantification unless interference from the matrix was observed. In these cases, another transition free of interference was chosen for quantification.

## Results and Discussion

### Overview of Discovery, Prioritization and Verification of EOC Biomarkers Using a Xenograft Serous EOC Mouse Model

The strategies used to improve ovarian cancer biomarker discovery using the xenograft mouse model system, select high priority candidate biomarkers, and improve the efficiency of MRM assay development and biomarker verification are outlined in **Figure 1**. In the discovery phase, OVCAR-3, an established human serous cell line, was grown in SCID mice. Xenograft mouse plasma pooled from four mice with the largest tumors was subjected to extensive fractionation (180 fractions) using a 4 D plasma proteome separation method developed in our laboratory which consists of immunoaffinity depletion of major serum proteins, MicroSol IEF, 1D SDS-PAGE, and LC-MS/MS. [24] Representative analytical and preparative 1D SDS gels showing MicroSol IEF fractions prior to LC-MS/MS analysis can be found in **Figure S1 B and C**, respectively. Human proteins identified in the plasma by at least two peptides, at least one of which was uniquely human, were prioritized and verified as illustrated and described in further detail below. Although this biomarker candidate discovery study used a cell line representative of a late stage tumor, our working hypothesis is that the best cancer biomarkers will be shed by the tumor into the blood and will correlate with tumor size. These biomarkers will ideally be detectable in serum or plasma at higher levels than in control subjects, even when the tumors are small, and the levels of these biomarkers will increase as the tumor grows. By utilizing the xenograft mouse model and identifying human proteins, we are assured that the candidate biomarkers are derived from the tumor and shed into the blood, at least in this model system.

### Analyses of the Xenograft Mouse Plasma Proteome and Corresponding Tumor Supernatants

Plasma from four mice containing OVCAR-3 tumors that were at least 1 cm<sup>3</sup> was pooled and analyzed using the 4D method described above. Fractionation using MicroSol IEF and 1D SDS gels yielded 180 fractions and subsequent analysis of these fractions by LC-MS/MS produced more than 1.1 million spectra, which were searched against a combined human and mouse database. A total of 3647 non-redundant human and mouse proteins were initially identified by 22,890 peptides at a peptide FDR of 5.7% for all proteins, and a 0.5% FDR for protein identifications with two or more peptides. After species classification, 268 human proteins were identified by two or more peptides and an additional 550 by a single peptide (**Figure 2**). Because the FDR was considerably lower for proteins with  $\geq 2$  peptides in both the plasma and tumor supernatant samples, we only considered

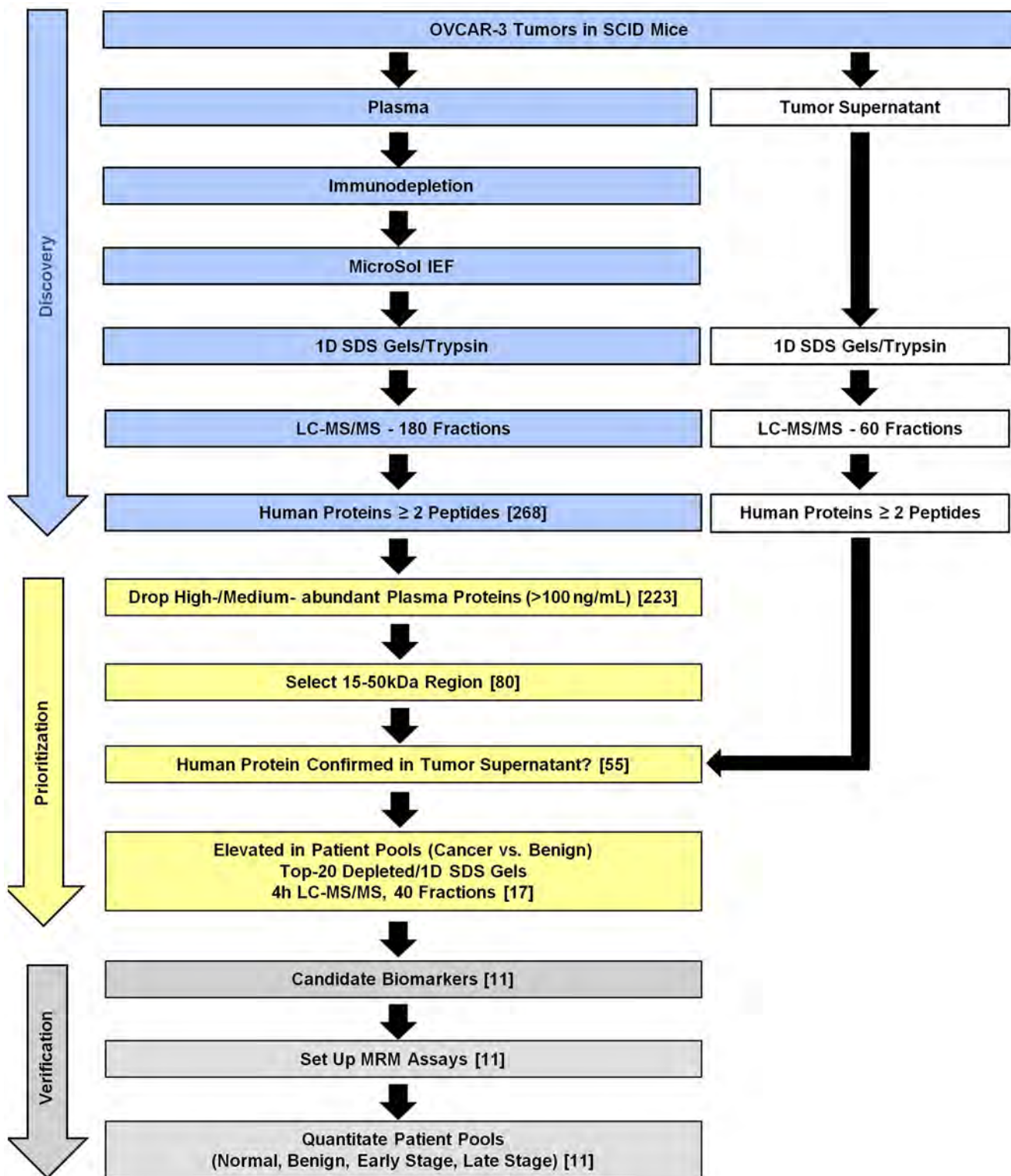


**Figure 1. Scheme for ovarian cancer biomarker discovery and efficient verification using a xenograft mouse model.** Candidate biomarkers were discovered in the xenograft mouse plasma using a 4D plasma proteome profiling method. Parallel analysis of the tumor supernatant was used to confirm human protein identifications and expand sequence coverage. A multi-step prioritization method ensured that only those proteins detectable in advanced EOC patient sera at elevated levels advanced to MRM assay development and verification in larger pools of patient sera.

doi:10.1371/journal.pone.0060129.g001



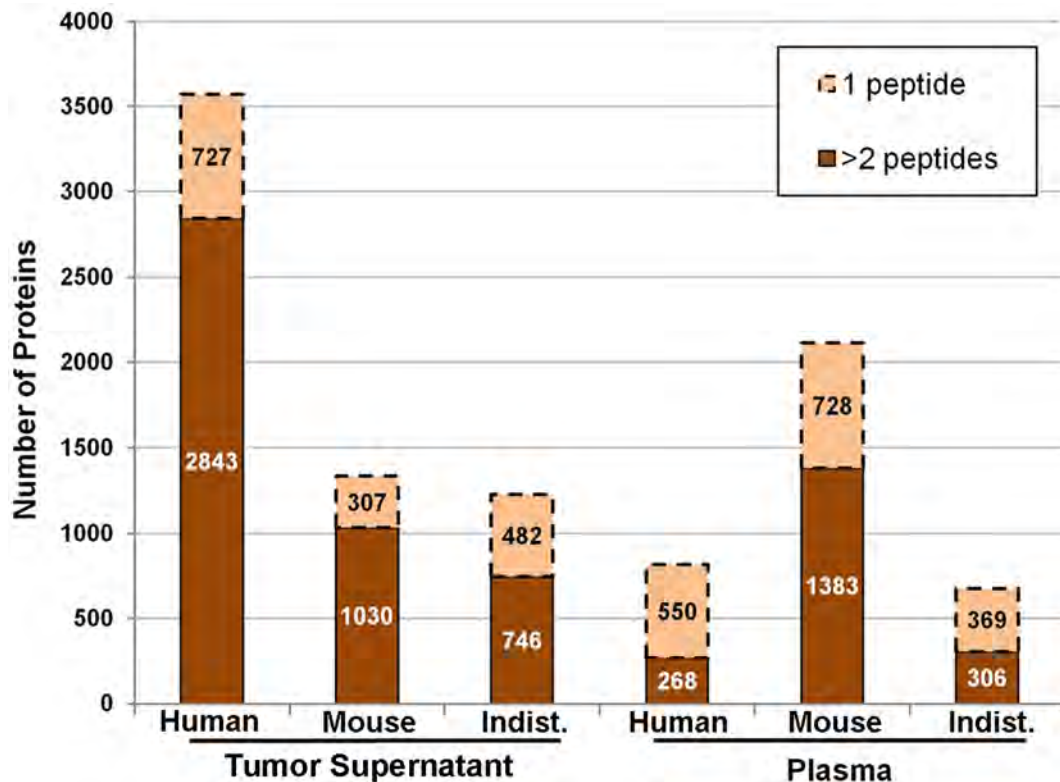


**Figure 2. Proteins identified in the xenograft plasma and tumor supernatant.** The numbers of unique (nonredundant) proteins identified in the OVCAR-3 xenograft tumor supernatant and mouse plasma are shown after sorting proteins based on species classification where at least one peptide was uniquely human, uniquely mouse, or indistinguishable (Indist.), that is, all detected peptides were common to human and mouse homologs.

doi:10.1371/journal.pone.0060129.g002

proteins having two or more peptide identifications for downstream analyses.

Due to the difficulty of detecting low abundance human proteins in the mouse plasma, tumor supernatants from the same batch of SCID mice with OVCAR-3 tumors were analyzed to attempt to achieve more extensive sequence coverage of human proteins detected in the mouse plasma. Concentrated tumor supernatants were separated on 1D SDS gels, each lane was sliced into 60 uniform fractions (**Figure S1A**), and each sample was digested with trypsin followed by LC-MS/MS analysis resulting in 487,076 MS/MS spectra, which were searched against a combined mouse and human database. A total of 6066 unique proteins were identified from 46,111 peptides at a peptide FDR of 0.9%. Eliminating single peptide proteins resulted in 4619 unique protein entries, with a peptide FDR of 0.03%. This list of high-confidence proteins ( $\geq 2$  peptides) identified from the combined human and mouse dataset is listed in **Table S1**. This complete dataset was divided into “human” and “mouse” based upon the presence of at least one peptide unique to that species, while “indistinguishable” proteins contained only peptides common to both species. A total of 2843 human proteins were identified by two or more peptides, and an additional 727 human proteins were identified by single peptides (**Figure 2**).

Interestingly, the tumor supernatant dataset provided a much greater depth of analysis both in terms of total proteins identified and sequence coverage of most proteins, despite the less extensive fractionation used. Also, the proportion of total identified proteins that could be assigned as human was far higher in the tumor supernatant. In part, this was expected because the plasma analysis

was dominated by detection of high and medium abundance mouse plasma proteins. However, it also indicates that the contribution of mouse cells in the tumor, including fibroblasts and vascular cells, was relatively minor compared to shedding of proteins by the human tumor cells.

### The Tumor Supernatant Increases Sequence Coverage of Human Proteins Detected in the Xenograft Mouse Plasma

Over 2800 human proteins from the tumor were identified in the supernatant and this dataset is a possible source of additional plasma biomarkers for ovarian cancer. However, unless the proteins were also detected in the mouse plasma, there is no assurance that proteins observed in the supernatant would be shed into and be detectable in the blood. Furthermore, the plasma analysis had already identified nearly 300 human proteins, which exceeds the number of proteins that could be feasibly tested in human serum. Hence, in this study, the larger tumor supernatant dataset was only used to confirm the “human” assignment of proteins identified in the mouse plasma, although this large dataset almost certainly contains additional potential plasma biomarkers that could be explored in future studies. Confirmation of apparent human proteins in the mouse plasma is important because many proteins were assigned as human based upon the detection of one human peptide and one or more peptides with sequences common to both species. A few of these apparent human proteins may be false positives while others could represent unreported mouse polymorphisms, mouse sequences not reported in the database, etc. Also, some identified proteins represent a protein family but

the peptides identified in the plasma do not unambiguously define a unique isoform. Therefore, for most of the human proteins identified in the plasma, the tumor supernatant dataset improved the confidence of species assignment and in some cases more clearly defined family member(s) present in the xenograft plasma samples by confirming the original peptide and protein identifications and, in most cases, providing more extensive peptide coverage.

Examples of using the tumor supernatant data to expand the utility of data from the xenograft plasma are shown in **Figure 3**. PSMA1 (**Figure 3A**) was identified by a total of 10 peptides in the mouse plasma, but only a single one of these was a uniquely human peptide. This protein could have been de-prioritized because of its high homology to a mouse counterpart and the possibility that the single uniquely human peptide in the plasma might have been a false positive identification or unknown mouse sequence variant. However, the tumor supernatant identified an additional five peptides that were uniquely human, thus increasing the confidence of the species assignment for the original plasma identification. **Figure 3B** shows PSME2, a protein identified by two uniquely human peptides in the plasma dataset, and therefore the species assignment as human is well supported. But, the tumor supernatant analysis identified six additional human peptides, thereby providing more proteotypic peptides for setting up MRM assays.

The tumor supernatant and plasma datasets were compared to a study by Pitteri *et al.* that identified candidate biomarkers by comparing a genetically engineered mouse model and secretomes

of ovarian cancer cells. [17] That study validated eight proteins found to be at higher abundance levels in ovarian cancer patients' plasma, and they also described identification of an additional nine proteins previously identified as ovarian cancer plasma biomarkers. Of the 17 candidate markers described by Pitteri *et al.*, we identified eight proteins (CTSB, FASN, IGFBP2, LCN2, MIF, THBS1, WFDC2, and NRCAM) in our tumor supernatant analysis, and three proteins (FASN, IGFBP2, and LCN1) in the high-confidence xenograft plasma dataset.

We also compared the results from the current study using OVCAR-3 cells, a serous EOC cell line to an earlier xenograft mouse study using an endometrioid EOC cell line (TOV-112D) where we identified three new biomarkers of ovarian cancer that could distinguish cancer patients from normal individuals. [18] These three biomarkers, CLIC1, CTSD, and PRDX6, were all identified in the current study.

Overall, these comparisons show that different biomarker discovery strategies result in detection of overlapping, but non-identical sets of biomarkers. These data also demonstrate that analysis of the tumor supernatant in parallel with xenograft mouse plasma is useful for confirming candidate biomarkers detected in xenograft mouse plasma.

### Prioritization and Selection of Candidate Biomarkers for Verification Using Patient Sera

Efficient methods for selecting the best candidate biomarkers and economically verifying them in serum or plasma of EOC patients are needed because, some, but not all proteins shed by

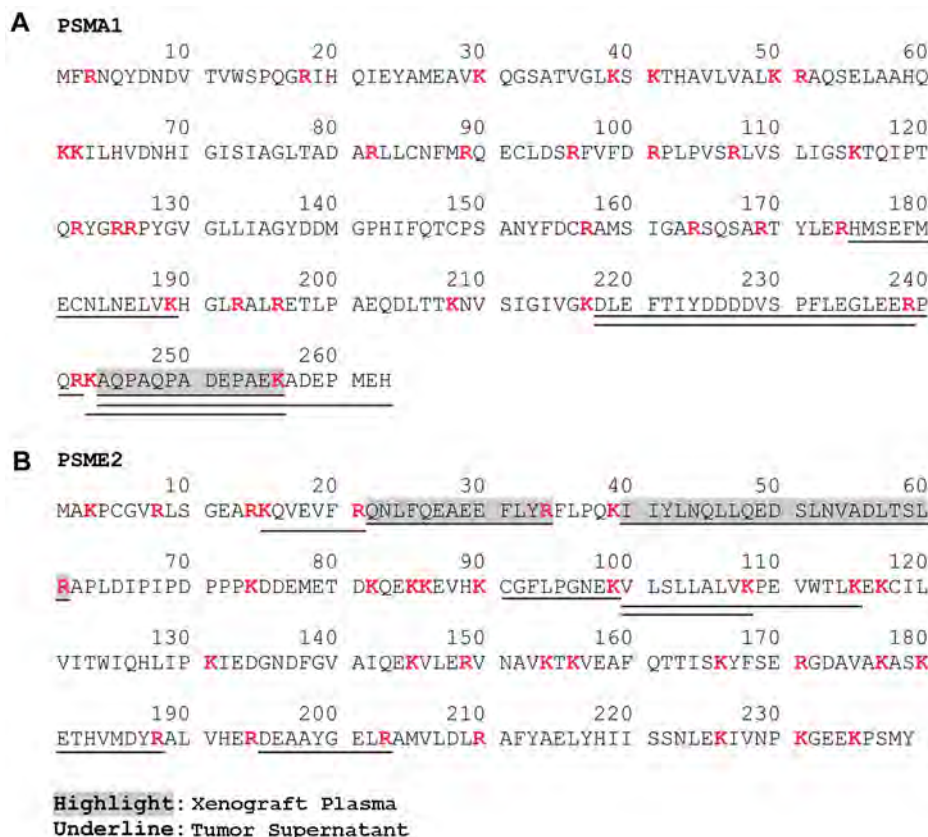
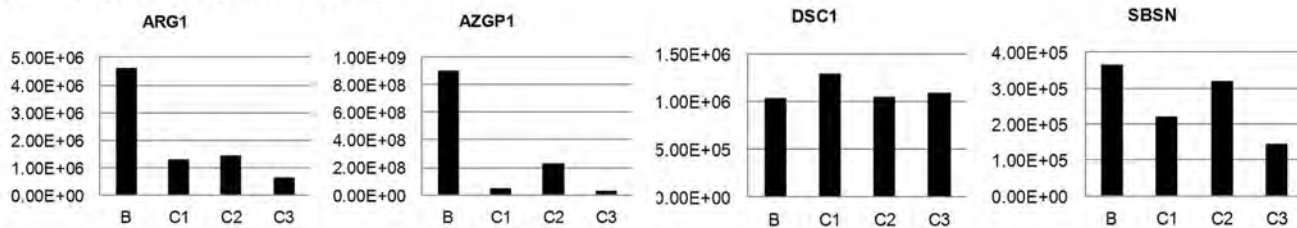
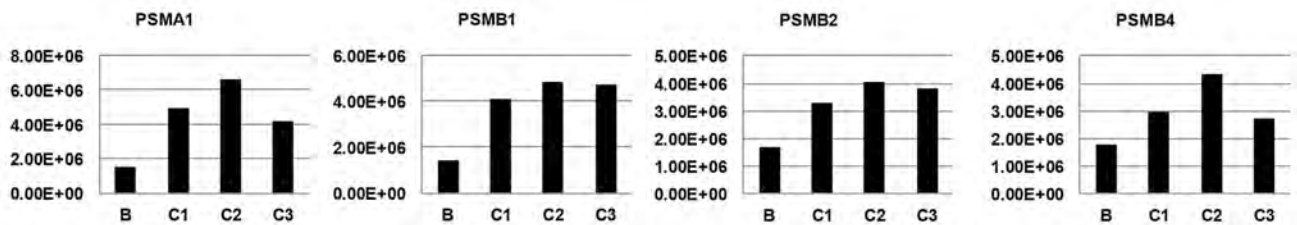


**Figure 3. Sequence coverage for selected human proteins from the xenograft plasma and tumor supernatants.** Examples of candidate biomarkers, PSMA1 and PSME2, where increased sequence coverage is obtained from analysis of the tumor supernatant (underlined peptides) compared to the xenograft plasma (grey highlight). Tryptic sites (K or R) are indicated in red.  
doi:10.1371/journal.pone.0060129.g003

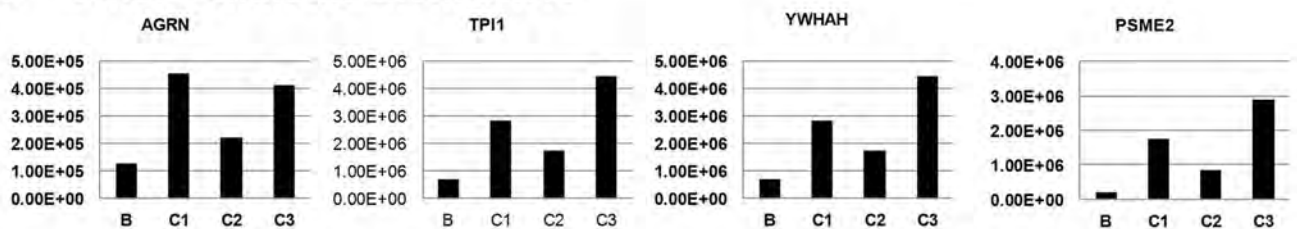
## A Failed Candidates



## B Candidate Proteasome Proteins



## C Other Candidate Biomarkers



## D Previously Known Biomarkers

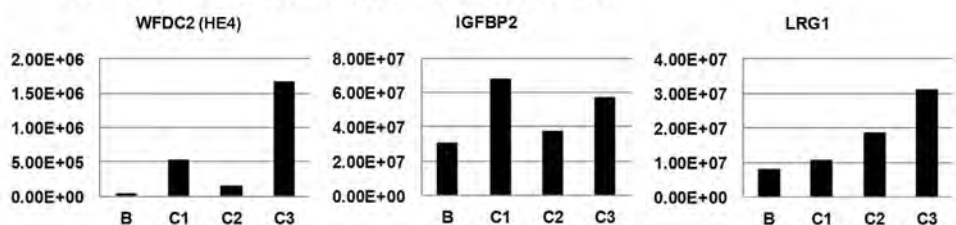


**Figure 4. Quantitative comparisons of candidate biomarkers using label-free discovery mode LC-MS/MS analysis of patient serum pools.** Summed protein intensities from a Rosetta Elucidator label-free analysis are shown for benign (B, n = 9) and three different late-stage ovarian cancer pools (C1, n = 9; C2, n = 9; C3, n = 5). (A) Representative proteins that failed this screen because intensities were lower or showed no difference in cancer pools compared with benign disease. (B) Four different isoforms of the proteasome complex selected for further validation because they showed elevated levels in all cancer pools compared with benign sera. (C) Additional representative proteins selected for further validation because they showed elevated levels in all cancer pools compared with benign sera. (D) Three biomarkers previously reported by others and re-discovered in the current study (see **Table 1**).

doi:10.1371/journal.pone.0060129.g004

EOC tumors into blood are expected to be good biomarkers of the disease. Furthermore, some proteins detected in the xenograft mouse model may not be detectable in human blood using current methods either because the concentration in human blood is below detection limits of available assays or because in some cases the shedding may be unique to the mouse model. As noted above, when we evaluated a panel of candidate biomarkers from the TOV-112D xenograft mice tumors, the overall success in setting up MRM assays and demonstrating elevated levels of the targeted biomarker in EOC patient sera was only about 20%. Hence, an important challenge is to develop appropriate methods for more efficient triaging of candidate biomarkers and evaluating them in serum of EOC patients.

The xenograft plasma proteome was prioritized starting with the 268 human proteins identified by two or more peptides (**Figure 2**). This dataset was further refined by removing a few trypsin and keratin contaminants that were missed at the initial contaminant-removal step due to ambiguous protein descriptions or isoform differences. In addition, proteins known to be in normal human plasma at medium- to high-abundant levels ( $>100$  ng/mL [28,29]) and hemoglobins were removed. Such proteins were not considered to be viable candidate biomarkers because the contribution of shedding from a small tumor is unlikely to be discernible above the normal variation of that protein in the general population. For example, if a protein is normally in the plasma of unaffected individuals in the 1–5  $\mu$ g/mL range and the protein is also shed by a typical ovarian tumor, which contributes

**Table 1.** Candidate biomarkers for validation in patient serum pools.

| Gene Name   | Protein Description                                 | # Peptides <sup>a</sup><br>(Supernatant) | # Peptides <sup>a</sup><br>(Plasma) |
|---|---|--|-------------------------------------|
| <b>B. Previously reported biomarkers re-identified in this study</b>                                |   |  |                                     |
| IGFBP2  | Insulin-like growth factor-binding protein 2 [38]   | 9/5                                      | 5/4                                 |
| WFDC2 (HE4)   | WAP four-disulfide core domain protein 2 [39]       | 2/0                                      | 0                                   |
| LRG1  | Leucine-rich alpha-2-glycoprotein [40]              | 0  | 1/1                                 |
| <b>A. Novel candidates identified from xenograft mouse plasma and verified in tumor supernatant</b> |   |  |                                     |
| AGRN  | Agrin and agrin fragments                           | 61/9                                     | 5/1                                 |
| PSME2   | Proteasome activator complex subunit 2              | 8/11                                     | 2/8                                 |
| TPI1  | Triosephosphate isomerase                           | 7/18                                     | 4/10                                |
| DDAH2   | N(G),N(G)-dimethylarginine dimethylaminohydrolase 2 | 7/8                                      | 1/4                                 |
| GM2A  | GM2 ganglioside activator protein (GM2A), mRNA      | 3/0                                      | 3/0                                 |
| YWHAB   | 14-3-3 protein beta/alpha                           | 2/8                                      | 1/12                                |
| YWHAH   | 14-3-3 protein eta                                  | 2/9                                      | 1/7                                 |
| PSMA1   | Proteasome subunit alpha type-1                     | 6/14                                     | 1/10                                |
| PSMB1   | Proteasome subunit beta type-1                      | 3/9                                      | 1/6                                 |
| PSMB2   | Proteasome subunit beta type-2                      | 1/10                                     | 1/6                                 |
| PSMB4   | Proteasome subunit beta type-4                      | 3/5                                      | 2/5                                 |

<sup>a</sup>Number of peptides that are uniquely human/number of peptides common to mouse and human homolog.  
doi:10.1371/journal.pone.0060129.t001

another 50 ng/mL of that protein into the plasma, the contribution from the tumor is not detectable above normal variation.

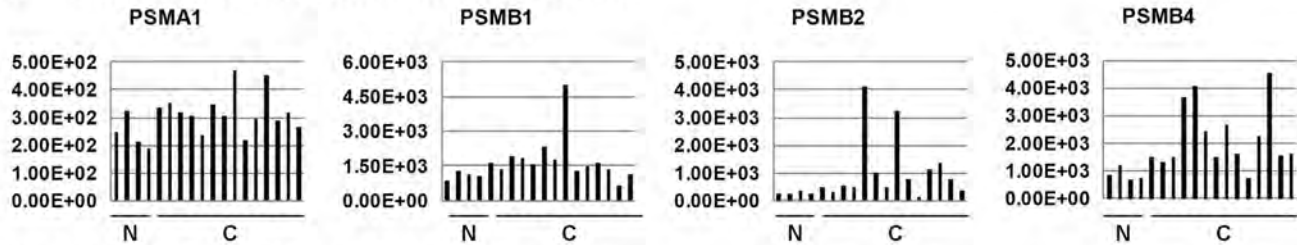
### Verification of Candidate Biomarkers in the 15–50 kDa Region Using the Tumor Supernatant and Label-free Discovery Proteomics Analysis of Patient Pools

Candidate biomarkers in the 15–50 kDa region of the gel were selected for further prioritization and verification because this was the region of the gel that contained the largest density of human proteins in the xenograft plasma analysis. By focusing on a discrete region of the gel we could increase the subsequent throughput of MRM assays by minimizing the number of fractions that need to be analyzed to quantitate the targeted group of candidate biomarkers. Candidates in this region that were identified with at least the same number of peptides in the tumor supernatant were considered further (**Figure 1** and **Table 1**). These candidate biomarkers were then compared to data from an in-depth label-free quantitative comparison of pools of patient sera using a 4 h gradient for the LC-MS/MS runs. One serum pool from patients with benign tumors (pool B, n = 9), was compared to three serum pools from patients with advanced ovarian cancer (pool C1: stage 3, n = 9; pool C2: stage 3, n = 9; pool C3: stage 4, n = 5). Descriptions of the patients and the sample pooling strategy are provided in **Table S2**. Acquisition of full MS and data-dependent MS/MS scans were identical to those described for the xenograft proteome analyses, with the exception that ions subjected to MS/MS were excluded from repeated analysis for 180 s. Xenograft plasma candidate biomarkers that could be detected in these human serum pools were quantitatively compared across pools using peptide ion signal intensities from the Rosetta Elucidator System's peptide report results. Peptides were grouped into consensus proteins by protein description and peptide intensities were summed for each protein. The criteria for selecting candidates for further validation were proteins that showed increases in all three cancer pools compared with the benign serum, and where the average intensity of the three cancer pools

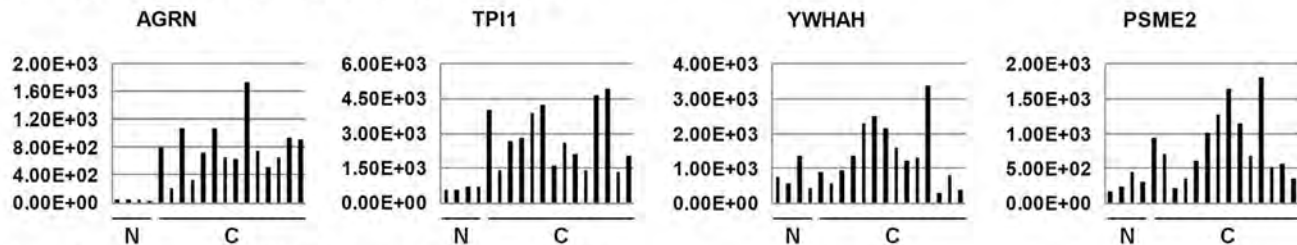
was at least 1.7 times that of the benign serum pool (**Figure 4**). Candidates whose protein intensities did not increase in cancer were not considered to be good biomarkers (**Figure 4A**). For example, ARG1 and AZGP1 failed because they showed decreases in cancer relative to benign disease—a trend that does not correlate with cancer burden, and DSC1 and SBSN were not further considered because the benign and cancer pools exhibited similar levels of these proteins. **Figure 4B** shows a number of proteasome subunits that exhibited increases in ovarian cancer. The proteasome complex is responsible for degradation of proteins crucial to cell cycle regulation and apoptosis and has been recognized as a potential target for cancer therapy. [30] Specific proteasome subunits, including PSMB2 and PSMB4, have been identified as upregulated in gene expression profiles of ovarian carcinomas. [31,32] Interestingly, circulating intact proteasomes have recently been reported to correlate with EOC, [33] but the assay used in that study did not distinguish specific isoforms or quantify subunits that may not have been in intact proteasomes. **Figure 4C** shows representative additional promising candidates. One candidate, AGRN, is a 215 kDa protein previously identified as being upregulated in ovarian cancer tissue samples compared with normal and non-ovarian tissue samples, [34] but it has not previously been reported to be a serum biomarker for EOC. In this study, it was identified by SDS-PAGE as both the intact 215 kDa protein and as a 43 kDa fragment from the C-terminal region of the protein in the tumor supernatant. In contrast, only the 43 kDa fragment which is presumably a proteolytic fragment produced by proteolysis either in the tumor or in the blood was detected in the xenograft plasma. The peptides quantitated in **Figure 4C** belong to the fragment and correlate with ovarian cancer in this experiment. Additionally, six proteins, including ANXA1, FABP5, PSMB3, PSMB6, PSMB8, and PSMB9 were deprioritized because they were either closely related to other selected biomarkers, or based on biology were considered unlikely to be specific to ovarian cancer. Finally, three biomarkers previously reported by others were detected in either the xenograft



## A Candidate Proteasome Proteins



## B Other Candidate Biomarkers



## C Previously Known Biomarkers

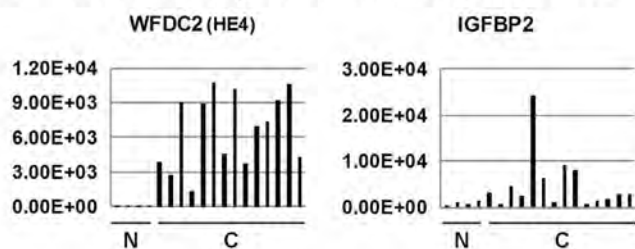


**Figure 5. Gene expression of candidate biomarkers in ovarian tissues.** Gene expression levels for normal ovary tissue (N; n = 4) and papillary serous ovarian carcinoma primary tumor samples (C, n = 14) are shown. (A) Representative candidate proteasome proteins. (B) Representative novel proteins identified in the xenograft mouse plasma. (C) Two previously reported ovarian cancer biomarkers that were identified in the current dataset. Microarray hybridization data were processed and scaled as previously described. [36,37] Data were extracted from [www.BioGPS.org](http://www.BioGPS.org). doi:10.1371/journal.pone.0060129.g005

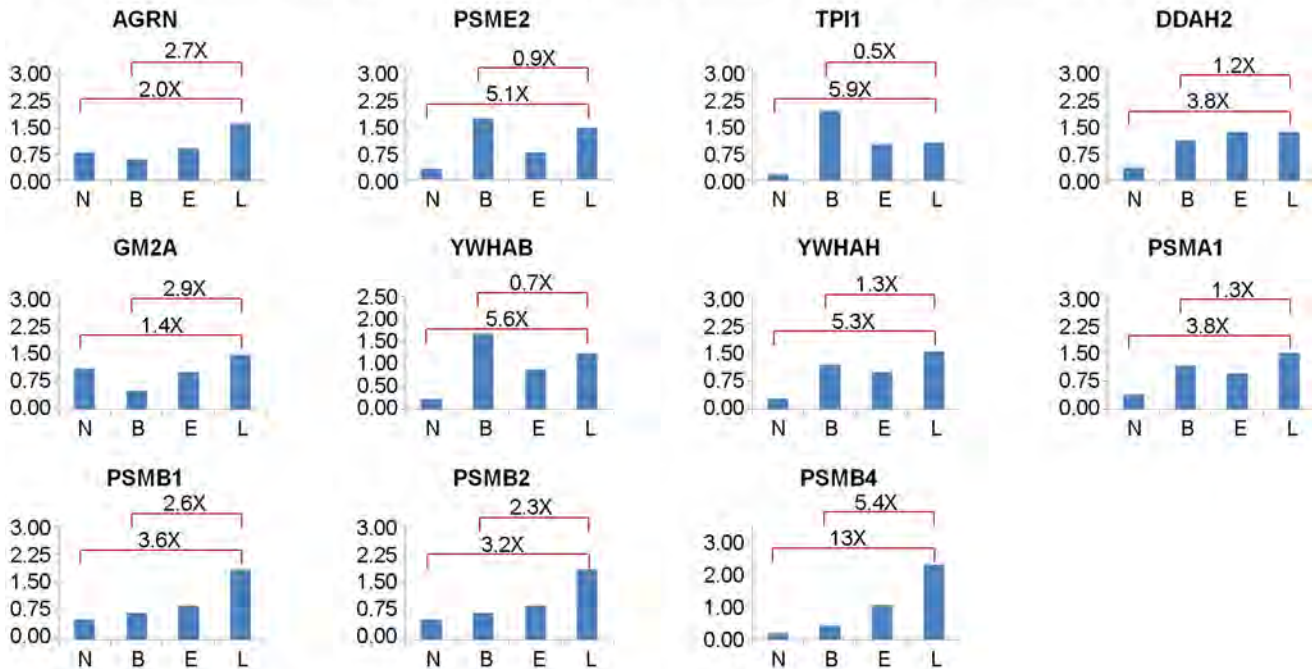
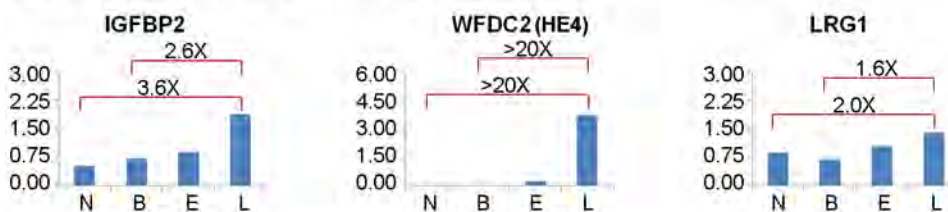
mouse plasma or tumor supernatant or both (**Table 1**) and were within the targeted 15–50 kDa region of the gel. These known biomarkers, which included HE4 (WFDC2) one of the two FDA approved ovarian cancer biomarkers, were included in our prioritization and verification analyses as known biomarker references. As expected, these three proteins exhibited increased levels in the cancer pools compared with the benign pool (**Figure 4D**). CA125 was not identified in the xenograft plasma, presumably due to its extensive glycosylation and low concentration as well as the high complexity of plasma; however, it was identified in the tumor supernatant by its alternative protein name ‘Mucin-16’ (**Table S2**).

### Potential Correlation of Biomarkers with Gene Expression

To evaluate whether gene expression in ovarian tumor tissues could be a useful indicator of whether a protein is promising serum biomarker, we queried our candidate biomarkers from **Table 1** against published microarray hybridization data using BioGPS, a centralized gene portal of combined gene annotation resources. [35] Specifically, gene expression levels for normal ovarian tissue (n = 4) and papillary serous ovarian carcinoma primary tumor samples (n = 14) [36,37] were extracted for each of the candidate markers listed in **Table 1**. **Figure 5** shows examples of gene expression patterns for some of our novel and two known ovarian cancer biomarkers. These gene expression levels can be compared

with the observed levels of these same proteins in the benign and EOC patient serum pools (**Figure 4**). Some proteins show similar trends; that is, elevated levels in both the serum and tumor tissue levels for EOC, including AGRN, TPI1, and HE4. However, other proteins do not exhibit much similarity between tissue expression and serum levels. For proteins such as YWHAH and PSME2, gene expression levels overlap extensively between normal and cancer tissue, but the serum levels of these proteins show similar patterns to those for AGRN and TPI1. Also, PSMA1 exhibits similar expression levels between normal and EOC tumor samples but much higher levels in the serum of EOC patients compared with benign tumor controls. Interestingly, at the gene expression level, each of the four illustrated proteasome subunits exhibits differing expression patterns at the cancer tissue level but all four subunits show elevated serum levels in all cancer patient pools compared with the benign sera.

Overall, these comparisons suggest that gene expression levels are not reliable indicators of blood levels of a given protein, and use of gene expression levels to predict blood biomarkers is likely to be of limited value. This is not surprising because: 1) gene expression levels do not always correlate with protein abundance within cells; 2) shedding of proteins into the extracellular space and, more specifically, into the vascular system, does not necessarily depend upon the tissue levels of that protein; and 3) changes in proteolytic processing, PTM levels, or other processing

**A. Novel candidates identified from xenograft mouse plasma and verified in tumor supernatant****B. Previously reported biomarkers**

**Figure 6. Verification of promising candidate biomarkers using a label-free MRM assay.** Normalized relative protein amounts are shown for serum pools of normal (N; n = 9), benign (B; n = 10), early-stage ovarian cancer (E; stages 1 and 2; n = 18), and late-stage ovarian cancer (L; stage 3; n = 29). Ratios of late-stage cancer to benign disease and normal donors are shown above the histograms. (A) The 11 novel high priority biomarkers from the 15–50 kDa region of the gel. (B) Three previously reported biomarkers included as references and analyzed in parallel with the novel biomarkers.

doi:10.1371/journal.pone.0060129.g006

of proteins that might affect their blood concentration may differ between normal and cancer states.

### MRM Assays and Quantitation of Normal, Benign, Early Stage EOC and Late Stage EOC Serum Pools

We subsequently attempted to set up MRM assays for the 11 novel and three known biomarkers shown in **Table 1** as described in Methods. MRM assays achieve high selectivity by monitoring the combination of the specific mass/charge of a parent ion and a unique fragment ion produced after collision to quantify the targeted peptide in a complex mixture. MRM assays targeting at least two peptides per protein were successfully established for all targeted proteins. The methods were integrated into a single multiplexed MRM assay that was subsequently used to quantitate the levels of these proteins in four serum pools, including: a normal serum pool (pool N; n = 9), a benign ovarian tumor pool (pool B, n = 10), an early-stage ovarian cancer pool (pool E: stage 1 and 2, n = 18), and a late-stage cancer pool (pool L: stage 3, n = 29). The cancer pools included serum from patients with different EOC histotypes, although the majority of tumors were the serous

subtype as is typically the case in groups of EOC patients. Details of the patients and samples used to prepare these pools are summarized in **Table S2**. The peptides and transitions used in the integrated multiplex MRM assay, as well as the resulting relative quantitative data for the four pools, are shown in **Table S3**. Resulting relative protein quantities for the four pools are summarized in **Figure 6A** for the 11 novel candidates. The levels in the same serum pools of the three previously reported biomarkers are shown for reference in **Figure 6B**.

These results confirm that quantitative MRM assays were established for all 11 targeted proteins and that all targeted proteins showed elevated levels in initial analysis of sera from advanced EOC. This 100% success using these two criteria is dramatically better than the 20% success rate achieved for setting up MRM assays for TOV-112D derived candidate biomarkers showing elevated levels in initial screens of sera from advanced EOC. This more efficient selection of candidate biomarkers was achieved because the current strategy utilized additional criteria prior to attempting to set up MRM assays. The key advantages of the current approach include analysis of the tumor supernatant to extend sequence coverage for putative human plasma proteins in

the xenograft mouse plasma and comparison of remaining high priority candidate biomarkers to an in-depth discovery mode quantitative comparison of serum pools from benign and advanced EOC patients. This latter analysis identified those proteins detectable in patient serum as well as those proteins exhibiting elevated levels in EOC patient sera. Interestingly, approximately two-thirds of the high priority candidates from the xenograft mouse plasma both expected to be in the 15–50 kDa region and verified in the tumor supernatant, were detected in the patient pools and half of these met the criteria used above for elevated levels in EOC serum. This 20% success rate is very similar to that obtained with the TOV-112D candidate biomarkers. The major difference in the current study is that time and expenses were not invested in attempting to set up MRM assays for the 75–80% of biomarkers that would ultimately fail to be detected in patient plasma or that would not show elevated levels in advanced EOC patient serum. Although substantial mass spectrometer and analysis time was invested in conducting the in-depth discovery mode quantitative comparison of serum pools from benign and advanced EOC patients, these analyses do not need to be repeated as the same dataset can be used to screen future candidate biomarkers. Additionally, this study includes pools of mixed histotypes that approximate the mixtures of cancer subtypes typically seen clinically because the numbers of available samples and the assay throughput were too low to distinguish potential subtype specific biomarkers. One goal of future studies using higher throughput assays such as sandwich ELISA will be to carefully evaluate potential relationships between EOC subtypes and these biomarker candidates.

## Conclusions

In the current study, improved strategies for both discovery and triaging novel blood biomarkers for EOC have been developed. The utility of analyzing xenograft mouse plasma and the corresponding tumor supernatant in parallel was demonstrated. The presence of human proteins in the plasma demonstrated these proteins were produced by the tumor and shed into the blood, but many of these assignments were based upon only a few peptides. Analysis of the tumor supernatant produced far more extensive sequence coverage for human proteins and confirmed many of the proteins identified in the plasma as human. In most cases an increased sequence coverage provided additional peptide candidates for potential MRM assays. A second key step in the prioritization and verification strategy was to compare candidate plasma biomarkers to an in-depth, label-free comparison of benign disease and advanced cancer patient serum pools to prescreen candidate biomarkers prior to setting up MRM assays. By extending reverse-phase gradients for the discovery mode analysis of these samples to four hours, the detection sensitivity is similar to that of MRM assays using shorter gradients. That is, if a protein cannot be detected in this dataset, it will probably not be feasible to set up an MRM assay and, therefore, effort is not wasted in assay development. Furthermore, by comparing candidate biomarker levels in the benign and advanced cancer patient pools, only those proteins showing elevated levels in the cancer sera advance to MRM assay development. This new approach reduces the effort invested in setting up MRM assays by about four-fold relative to the biomarkers detected in advanced EOC patient sera

at elevated levels. Based upon initial screening of large pools of normal, benign, early, and advanced ovarian cancer sera, all of the biomarkers selected for MRM assay development in the current study should move forward and be further evaluated using serum or plasma from individual patients and controls. Although the fold changes observed in the pooled samples for most of these candidate biomarkers are not as large as HE4, the ranges of values for these biomarkers in individual EOC and control sera need to be determined in order to compare their diagnostic capacities to HE4 and CA125. While it is unlikely that most individual biomarkers will prove to be superior to HE4 or CA125, it is more likely that combinations with each other or with CA125 and HE4 could outperform the use CA125 or HE4 alone. Finally, the strategies developed in this study demonstrate that in-depth analysis of xenograft mouse plasma with efficient pilot verification using multiplexed assays can efficiently identify multiple promising candidate EOC biomarkers. This approach can be readily applied to further in-depth analysis of the OVCAR-3 cell line, as well as other EOC cell lines to identify additional EOC plasma biomarkers.

## Supporting Information

**Figure S1** Analysis of OVCAR-3 xenograft plasma and tumor supernatant. (A) SDS-PAGE of concentrated media from the OVCAR-3 tumor supernatant. The sample was separated for 6 cm, the gel lane was sliced into 60 uniform fractions, digested with trypsin and analyzed by LC-MS/MS. (B) Analytical SDS-PAGE of unfractionated, depleted mouse plasma (DP), and MicroSol IEF fractions (F1–F4) and membrane extractions (M1–M5). (C) Representative preparative SDS-PAGE of the samples shown in panel B. Distances samples were separated are indicated and gel lanes were cut into 1 mm slices for trypsin digestion and subsequent LC-MS/MS analysis. (PDF)

**Table S1** Proteins identified in the OVCAR-3 tumor supernatant by two or more unique peptides. (PDF)

**Table S2** Sample classification for ovarian cancer patient sera. (PDF)

**Table S3** Peptide transitions monitored by MRM. (PDF)

## Acknowledgments

We gratefully acknowledge Dr. Dionyssios Katsaros, University of Turin, Turin, Italy, for providing benign and ovarian cancer sera. We gratefully acknowledge the Proteomics Core, the Histotechnology Core, and the Animal Facility of the Wistar Institute for their assistance in this project. The administrative assistance of Mea Fuller is gratefully acknowledged.

## Author Contributions

Advice and critical evaluation of manuscript: RZ. Conceived and designed the experiments: LAB HYT DWS. Performed the experiments: LAB HW HYT ZC TCW. Analyzed the data: LAB HYT ZC QL DWS. Contributed reagents/materials/analysis tools: JLT. Wrote the paper: LAB HYT DWS.

## References

1. Jemal A, Siegel R, Ward E, Hao Y, Xu J, et al. (2008) Cancer statistics, 2008. *CA Cancer J Clin* 58: 71–96.
2. Clarke-Pearson DL (2009) Clinical practice. Screening for ovarian cancer. *N Engl J Med* 361: 170–177.
3. Cannistra SA (2004) Cancer of the ovary. *N Engl J Med* 351: 2519–2529.
4. Jacobs I, Bast RC (1989) The CA125 tumour-associated antigen: a review of the literature. *Hum Reprod* 4: 1–12.

5. Woolas RP, Xu FJ, Jacobs IJ, Yu YH, Daly L, et al. (1993) Elevation of multiple serum markers in patients with stage I ovarian cancer. *J Natl Cancer Inst* 85: 1748–1751.
6. Bast RC Jr, Klug TL, St John E, Jenison E, Niloff JM, et al. (1983) A radioimmunoassay using a monoclonal antibody to monitor the course of epithelial ovarian cancer. *N Engl J Med* 309: 883–887.
7. Sasaroli D, Coukos G, Scholler N (2009) Beyond CA125: the coming of age of ovarian cancer biomarkers. Are we there yet? *Biomark Med* 3: 275–288.
8. Cramer DW, Bast RC Jr, Berg CD, Diamandis EP, Godwin AK, et al. (2011) Ovarian cancer biomarker performance in prostate, lung, colorectal, and ovarian cancer screening trial specimens. *Cancer Prev Res (Phila)* 4: 365–374.
9. Zhu CS, Pinsky PF, Cramer DW, Ransohoff DF, Hartge P, et al. (2011) A framework for evaluating biomarkers for early detection: validation of biomarker panels for ovarian cancer. *Cancer Prev Res (Phila)* 4: 375–383.
10. Hoffman SA, Joo WA, Echan LA, Speicher DW (2007) Higher dimensional (Hi-D) separation strategies dramatically improve the potential for cancer biomarker detection in serum and plasma. *J Chromatogr B Analyt Technol Biomed Life Sci* 849: 43–52.
11. Gortzak-Uzan L, Ignatchenko A, Evangelou AI, Agochiya M, Brown KA, et al. (2008) A proteome resource of ovarian cancer ascites: integrated proteomic and bioinformatic analyses to identify putative biomarkers. *J Proteome Res* 7: 339–351.
12. Faca VM, Ventura AP, Fitzgibbon MP, Pereira-Faca SR, Pitteri SJ, et al. (2008) Proteomic analysis of ovarian cancer cells reveals dynamic processes of protein secretion and shedding of extra-cellular domains. *PLoS One* 3: e2425.
13. Kuk C, Kulasingam V, Gunawardana CG, Smith CR, Batruch I, et al. (2009) Mining the ovarian cancer ascites proteome for potential ovarian cancer biomarkers. *Mol Cell Proteomics* 8: 661–669.
14. Amon LM, Law W, Fitzgibbon MP, Gross JA, O'Brian K, et al. (2010) Integrative proteomic analysis of serum and peritoneal fluids helps identify proteins that are up-regulated in serum of women with ovarian cancer. *PLoS One* 5: e11137.
15. Zhang Y, Xu B, Liu Y, Yao H, Lu N, et al. (2012) The ovarian cancer-derived secretory/releasing proteome: A repertoire of tumor markers. *Proteomics* 12: 1883–1891.
16. Faca VM, Hanash SM (2009) In-depth proteomics to define the cell surface and secretome of ovarian cancer cells and processes of protein shedding. *Cancer Res* 69: 728–730.
17. Pitteri SJ, JeBailey L, Faca VM, Thorpe JD, Silva MA, et al. (2009) Integrated proteomic analysis of human cancer cells and plasma from tumor bearing mice for ovarian cancer biomarker discovery. *PLoS One* 4: e7916.
18. Tang HY, Beer LA, Chang-Wong T, Hammond R, Gimotty P, et al. (2012) A xenograft mouse model coupled with in-depth plasma proteome analysis facilitates identification of novel serum biomarkers for human ovarian cancer. *J Proteome Res* 11: 678–691.
19. Kuhn E, Wu J, Karl J, Liao H, Zolg W, et al. (2004) Quantification of C-reactive protein in the serum of patients with rheumatoid arthritis using multiple reaction monitoring mass spectrometry and <sup>13</sup>C-labeled peptide standards. *Proteomics* 4: 1175–1186.
20. Anderson L, Hunter CL (2006) Quantitative mass spectrometric multiple reaction monitoring assays for major plasma proteins. *Mol Cell Proteomics* 5: 573–588.
21. Beer LA, Tang HY, Sriswasdi S, Barnhart KT, Speicher DW (2011) Systematic discovery of ectopic pregnancy serum biomarkers using 3-D protein profiling coupled with label-free quantitation. *J Proteome Res* 10: 1126–1138.
22. Zuo X, Echan L, Hembach P, Tang HY, Speicher KD, et al. (2001) Towards global analysis of mammalian proteomes using sample prefractionation prior to narrow pH range two-dimensional gels and using one-dimensional gels for insoluble and large proteins. *Electrophoresis* 22: 1603–1615.
23. Tang HY, Speicher DW (2005) Complex proteome prefractionation using microscale solution isoelectrofocusing. *Expert Rev Proteomics* 2: 295–306.
24. Tang HY, Ali-Khan N, Echan LA, Levenkova N, Rux JJ, et al. (2005) A novel four-dimensional strategy combining protein and peptide separation methods enables detection of low-abundance proteins in human plasma and serum proteomes. *Proteomics* 5: 3329–3342.
25. Wang H, Tang HY, Tan GC, Speicher DW (2011) Data analysis strategy for maximizing high-confidence protein identifications in complex proteomes such as human tumor secretomes and human serum. *J Proteome Res* 10: 4993–5005.
26. Liu Q, Tan G, Levenkova N, Li T, Pugh EN Jr, et al. (2007) The proteome of the mouse photoreceptor sensory cilium complex. *Mol Cell Proteomics* 6: 1299–1317.
27. MacLean B, Tomazela DM, Shulman N, Chambers M, Finney GL, et al. (2010) Skyline: an open source document editor for creating and analyzing targeted proteomics experiments. *Bioinformatics* 26: 966–968.
28. Anderson L (2005) Candidate-based proteomics in the search for biomarkers of cardiovascular disease. *J Physiol* 563: 23–60.
29. Polanski M, Anderson NL (2007) A list of candidate cancer biomarkers for targeted proteomics. *Biomark Insights* 1: 1–48.
30. Voorhees PM, Dees EC, O'Neil B, Orlowski RZ (2003) The proteasome as a target for cancer therapy. *Clin Cancer Res* 9: 6316–6325.
31. Yue W, Sun LY, Li CH, Zhang LX, Pei XT (2004) [Screening and identification of ovarian carcinomas related genes]. *Ai Zheng* 23: 141–145.
32. Nowee ME, Snijders AM, Rockx DA, de Wit RM, Kosma VM, et al. (2007) DNA profiling of primary serous ovarian and fallopian tube carcinomas with array comparative genomic hybridization and multiplex ligation-dependent probe amplification. *J Pathol* 213: 46–55.
33. Heubner M, Wimberger P, Dahlmann B, Kasimir-Bauer S, Kimmig R, et al. (2011) The prognostic impact of circulating proteasome concentrations in patients with epithelial ovarian cancer. *Gynecol Oncol* 120: 233–238.
34. Tchagang AB, Tewfik AH, DeRycke MS, Skubitz KM, Skubitz AP (2008) Early detection of ovarian cancer using group biomarkers. *Mol Cancer Ther* 7: 27–37.
35. Wu C, Orozco C, Boyer J, Leglise M, Goodale J, et al. (2009) BioGPS: an extensible and customizable portal for querying and organizing gene annotation resources. *Genome Biol* 10: R130.
36. Welsh JB, Zarrinkar PP, Sapinoso LM, Kern SG, Behling CA, et al. (2001) Analysis of gene expression profiles in normal and neoplastic ovarian tissue samples identifies candidate molecular markers of epithelial ovarian cancer. *Proc Natl Acad Sci U S A* 98: 1176–1181.
37. Su AI, Welsh JB, Sapinoso LM, Kern SG, Dimitrov P, et al. (2001) Molecular classification of human carcinomas by use of gene expression signatures. *Cancer Res* 61: 7388–7393.
38. Baron-Hay S, Boyle F, Ferrier A, Scott C (2004) Elevated serum insulin-like growth factor binding protein-2 as a prognostic marker in patients with ovarian cancer. *Clin Cancer Res* 10: 1796–1806.
39. Hellstrom I, Raycraft J, Hayden-Ledbetter M, Ledbetter JA, Schummer M, et al. (2003) The HE4 (WFDC2) protein is a biomarker for ovarian carcinoma. *Cancer Res* 63: 3695–3700.
40. Andersen JD, Boylan KL, Jemmerson R, Geller MA, Misemer B, et al. (2010) Leucine-rich alpha-2-glycoprotein-1 is upregulated in sera and tumors of ovarian cancer patients. *J Ovarian Res* 3: 21.



## Detection of Senescence-Associated Heterochromatin Foci (SAHF)

Katherine M. Aird and Rugang Zhang

### Abstract

One of the most prominent features of cellular senescence, a stress response that prevents the propagation of cells that have accumulated potentially oncogenic alterations, is a permanent loss of proliferative potential. Thus, at odds with quiescent cells, which resume proliferation when stimulated to do so, senescent cells cannot proceed through the cell cycle even in the presence of mitogenic factors. Here, we describe a set of cytofluorometric techniques for studying how chemical and/or physical stimuli alter the cell cycle in vitro, in both qualitative and quantitative terms. Taken together, these methods allow for the identification of *bona fide* cytostatic effects as well as for a refined characterization of cell cycle distributions, providing information on proliferation, DNA content, as well as the presence of cell cycle phase-specific markers. At the end of the chapter, a set of guidelines is offered to assist researchers that approach the study of the cell cycle with the interpretation of results.

**Key words:** Cancer, Cyclin B1, HCT 116, Histone H3, Mitosis

---

### 1. Introduction

Cellular senescence is a state of irreversible cell growth arrest. Cellular senescence can be triggered by a variety of stimuli such as critically shortened telomeres, which occur after extensive cell division, or activation of certain oncogenes (such as H-RAS<sup>G12V</sup> or BRAF<sup>V600E</sup>) (1–3). By definition, senescent cells are irreversibly growth arrested, and one of the necessary steps towards this irreversible cell cycle exit is the suppression of E2F target genes (4), which are mainly involved in promoting cell proliferation and S phase cell cycle progression (5). Promoters of E2F target genes typically acquire heterochromatic features during senescence (4). The heterochromatin associated with this process is specialized domains of facultative heterochromatin that often form in senescent human cells, senescence-associated heterochromatin foci (SAHF) (4, 6–12).

SAHF were first described in 2003 by Narita et al. who observed that the nuclei of senescent cells contain 30–50 bright, punctate DNA-stained dense foci that can be readily distinguished from chromatin in normal cells (4). Importantly, SAHF are not associated with cells undergoing quiescence, indicating that SAHF formation is not associated with reversible cell cycle exit (4). In addition, SAHF have also been shown to be distinct from constitutive heterochromatin because centromeres, telomeres, and other constitutive heterochromatin regions are not included in SAHF (4, 12, 13). Further, SAHF are also different from other facultative heterochromatin such as inactivated X chromosomes (Xi) in female human cells. For example, histone modifications such as lysine 27 trimethylated histone H3 (H3K27Me3) are associated with Xi but not SAHF (4).

SAHF play a role in sequestering proliferation-promoting genes (4), including E2F target genes such as cyclin A (12), which is required for the progression through S phase of the cell cycle (14). Indeed, SAHF do not contain any active transcription sites (4), demonstrating their role in contributing to the senescence-associated cell cycle exit. Significantly, disruption of SAHF formation can cause cell transformation (15), which infers that SAHF contribute to the tumor-suppressive function of senescence. Recently, there is evidence to suggest that SAHF may limit the extent of DNA damage signaling which may prevent senescent cells from undergoing apoptosis induced by high DNA damage signaling, thereby maintaining the viability of senescent cells (11). Finally, there is emerging evidence to suggest that SAHF may play a role in the senescence phenotype in vivo (16–19).

A number of different inducers of senescence cause the formation of SAHF, including activated oncogenes such as H-RAS<sup>G12V</sup> and BRAF<sup>V600E</sup> (4, 20, 21), extensive passaging (4), chemotherapeutics such as etoposide (4) and hydroxyurea (9), and bacterial toxins (9). However, SAHF formation and senescence are not always coupled. Indeed, a number of studies have shown that senescence can occur in the absence of SAHF formation. For instance, activation of AKT and knockdown of PTEN do not cause SAHF formation (22, 23). It is also important to note that SAHF formation is cell-line dependent (9). For example, senescence induced by extensive passaging in the primary human embryonic fibroblast cell lines IMR90 and WI38 cells is associated with SAHF, while senescence triggered by extensive passaging in BJ cells (primary human foreskin fibroblasts) is not associated with SAHF formation (4). The difference between these cell lines correlates with a variation in activation of the p16/pRb pathway after extensive passaging (9). Indeed, senescence induced by activated oncogenes (such as H-RAS<sup>G12V</sup> and BRAF<sup>V600E</sup>) in BJ cells triggers SAHF formation, which is associated with activation of the p16/

pRb pathway (24, 25). Notably, mouse cells do not form robust SAHF, although they do display a marked increase in staining of certain components of SAHF such as macroH2A (26).

To date, a number of molecular markers of SAHF have been described (reviewed in ref. 6, 10, 27) including macroH2A (8), a histone variant known to contribute to X chromosome inactivation and gene silencing (28); high mobility group A (HMGA) proteins, which coordinate with p16<sup>INK4a</sup> to induce SAHF formation and are required for maintaining SAHF (15); and di- or tri-methylated lysine 9 histone H3 (H3K9Me2/3) and bound HP1 proteins (4, 12), two common markers of heterochromatin (29). Together with DAPI, co-staining for these markers is a simple and reliable method to determine the presence of SAHF in senescent cells. Here, using oncogenic-RAS (H-RAS<sup>G12V</sup>) as an inducer of senescence and SAHF, we describe a method for the immunofluorescent detection of SAHF using DAPI and specific antibodies to components of SAHF such as macroH2A, H3K9Me2/3, and HP1 proteins.

---

## 2. Materials

### 2.1. Cell Culture for Expression of Oncogenic RAS

- pBABE-puro and pBABE-puro-H-RAS<sup>G12V</sup> constructs (Addgene) (see Note 1).
- 2.5 M CaCl<sub>2</sub>.
- 2×BBS:50mM *N,N*-bis(2-hydroxyethyl)-2-aminoethanesulfonic acid (BES), 280 mM NaCl, 1.5 mM Na<sub>2</sub>HPO<sub>4</sub>, pH 6.95 (see Note 2).
- Laemmli sample buffer: 50 mM Tris-HCl, 2% (w/v) sodium dodecyl sulfate (SDS), 100 mM dithiothreitol, 10% (v/v) glycerol, and 0.05% (w/v) bromophenol blue (pH 6.8).
- Equipment and reagents for SDS-polyacrylamide gel electrophoresis (PAGE).
- Bradford reagent (Bio-Rad) and 1 mg/mL bovine serum albumin (BSA) as standard.
- PVDF transfer membrane.
- Towbin transfer buffer: 170 mM glycine, 22 mM Tris-HCl, and 0.01% (w/v) SDS (pH 8.3).
- Anti-RAS antibody (BD Transduction Laboratories).
- 0.45 µm filter.
- Sterile-filtered ddH<sub>2</sub>O.
- Phoenix cells (a gift from Gary Nolan) growing in Dulbecco's modified Eagle's medium supplemented with 10% (v/v) fetal bovine serum, 1% (w/v) penicillin-streptomycin, and 1% (w/v)

L-glutamine in a humidified 37°C, 5% (v/v) CO<sub>2</sub> incubator (see Note 3).

- IMR90 cells (ATCC) growing in DMEM supplemented with 20% (v/v) FBS, 1% (w/v) L-glutamine, 1% (v/v) nonessential amino acid solution, 2% (v/v) essential amino acids, 1% (v/v) vitamins, and 1% (w/v) penicillin–streptomycin in a humidified 37°C, 5% (v/v) CO<sub>2</sub> incubator (see Notes 4 and 5).
- 0.25% (w/v) Trypsin + 1 mM EDTA.
- Sterile-filtered Dulbecco’s phosphate-buffered saline (PBS), pH 7.3.
- Sterile-filtered, 1 mg/mL puromycin in PBS, pH 7.3.
- Sterile-filtered, 8 mg/mL (w/v) polybrene in ddH<sub>2</sub>O (Sigma-Aldrich, St. Louis, MO, USA).
- 10-cm cell culture dishes and 6-well cell culture plates.
- Clean and sterile glass coverslips.

**2.2. Fluorescent Staining of SAHF and Microscopic Examination of SAHF**

- 4% (w/v) paraformaldehyde (see Note 6).
- PBS, pH 7.3.
- 0.2% (v/v) and 1% (v/v) Triton-X in PBS, pH 7.3.
- 3% (w/v) BSA in PBS, pH 7.3 (see Note 7).
- Primary antibodies to macroH2A, H3K9Me2, H3K9Me3, HP-1α, HP-1β, or HP-1γ (Table 1) (see Note 8).
- Appropriate secondary antibodies (Table 2) (see Note 9).
- 5 mg/mL 4',6-diamidino-2-phenylindole dihydrochloride (DAPI) in ddH<sub>2</sub>O.
- Clean microscope slides.

**Table 1**  
**Primary antibodies used to identify SAHF by immunofluorescence**

| Protein  | Source  | Dilution      | References |
|----------|---|---------------|------------|
| MacroH2A | Drs. Rugang Zhang (The Wistar Institute) and Peter D. Adams (University of Glasgow) | 1:2,000       | (7)        |
| HP-1α    | Dr. William Earnshaw (University of Edinburgh)                                      | 1:200         | (8)        |
| HP-1β    | Millipore (MAB3448)   | 1:20,000      | (9)        |
| HP-1γ    | Millipore (MAB3450)   | 1:2,000       | (7)        |
| H3K9Me3  | Abcam (ab8898)  | 1:500–1:1,000 | (9)        |
| H3K9Me2  | Abcam (ab7312)  | 1:500–1:1,000 | (9)        |



**Table 2**  
**Fluorescent secondary antibodies used to visualize SAHF components**

| Antibody              | Catalog numbers | Dilution |
|-----------------------|-----------------|----------|
| Cy3 goat anti-mouse   | 115-165-003     | 1:5,000  |
| FITC goat anti-rabbit | 111-095-003     | 1:1,000  |

- Anti-fade fluorescence mounting media: 0.25 g *p*-phenylenediamine (Sigma-Aldrich) dissolved in 25 mL 1× PBS (pH 9.0) mixed with 225 mL glycerol (see Note 10).
- Fluorescent microscope with the ability to view blue, green, and red channels (e.g., Nikon 80i).

### 3. Methods

#### 3.1. Cell Culture for Expression of Oncogenic RAS

The infectious retrovirus is generated by transfecting the plasmid DNA into a packaging cell line, for example, Phoenix cells ([http://www.stanford.edu/group/nolan/protocols/pro\\_helper\\_dep.html](http://www.stanford.edu/group/nolan/protocols/pro_helper_dep.html)). Transfection-quality DNA of the retrovirus plasmid is made using a Qiafilter Plasmid Maxi kit, according to the manufacturer's instructions. After transfection, the Phoenix cells reverse transcribe the plasmid DNA into an RNA that is packaged into infectious virus and expelled from the cells. Then, the tissue culture supernatant containing the virus is applied to the cells of interest to deliver the activated oncogenes (e.g., H-RAS<sup>G12V</sup>) to the target cells. The infected cells can be selected in puromycin to enrich for cells that have been infected. To assess the efficiency of puromycin to kill uninfected cells, perform a mock virus infection. To assess the efficiency of infection, infect one plate with a virus known to have a high titer (e.g., pBABE-puro vector, Addgene).

1. Split the Phoenix cells to  $5 \times 10^6$  cells per 10-cm dish in 10 mL medium 24 h before transfection (see Note 11). Culture in a 37°C, 5% (v/v) CO<sub>2</sub> incubator overnight.
2. Twenty-four hours later, and 4 h prior to transfection, change the medium to 9 mL of pre-warmed, fresh growth media.
3. Dilute the required amount of 2.5 M CaCl<sub>2</sub> to 250 mM in sterile ddH<sub>2</sub>O and aliquot 0.5 mL per transfection to separate, sterile 15 mL polystyrene tubes.
4. Add 30 µg of the supercoiled plasmid DNA of the intended virus to each tube.

5. Add 0.5 mL of 2× BBS by dripping slowly from a 1 mL pipette vertically down the center of the tube (1–2 drops per second). Do not mix. Incubate the mixture for 15 min. At this time, the precipitate should be barely visible to the naked eye.
6. Use a 1 mL pipette to blow air bubbles through the solution to mix the precipitate. Evenly distribute the mixture drop-wise into the medium of the plate of Phoenix cells.
7. Rock the plates back and forth very gently to mix the calcium phosphate precipitate and then place in a humidified 37°C incubator with 5% (v/v) CO<sub>2</sub> overnight.
8. Change the medium to 6 mL fresh, pre-warmed growth media approximately 24 h later (see Note 12).
9. On the same day as step 8, prepare the target IMR90 primary human embryonic fibroblast cells for infection. A confluent 10 cm dish of cells should be split 1:4 in regular growth media so that cells are 50–60% confluent on the next day (i.e., the first day of infection).
10. Twenty-four hours later, collect the supernatant from the Phoenix cells after step 8 and put through a 0.45 µm filter. Add 6 mL of fresh, pre-warmed growth media to the Phoenix cells (see Note 12).
11. Infect the target cells. Aspirate the IMR90 media from the dish. For a 10 cm dish of target cells, add 3 mL fresh media and 3 mL of virus-containing supernatant harvested from the Phoenix cells drop-wise onto the IMR90 cells.
12. Add 6 µL of 8 mg/mL (w/v) polybrene to make a final concentration of 8 µg/mL, and swirl the dishes to mix. Put the cell dish back into a 5% (v/v) CO<sub>2</sub>-containing incubator.
13. Culture the infected cells for 24 h. Repeat the infection (Subheading 3.1, steps 10–12) to increase efficiency.
14. Remove the medium from the IMR90 cells 24 h post infection and replace with 10 mL of fresh, pre-warmed IMR90 growth media that contains puromycin at a final concentration of 1 µg/mL.
15. Typically, 3 days after addition of puromycin, all of the noninfected cells should be dead. At this time, there should be no surviving cells left in the mock virus-infected dish.
16. At the desired time point (see Note 13), split the IMR90 cells into 6-well plates containing clean, sterile glass coverslips.
17. At the same time, harvest an aliquot of the infected cells for Western blot analysis (see Note 14).

### **3.2. Fluorescent Staining of SAHF**

To visualize SAHF, DAPI is used to stain for DNA, while specific antibodies to components of SAHF (e.g., macroH2A, H3K9Me2/3, and HP1 proteins) should be used for indirect immunofluorescence

staining. To assess the specificity of the antibody staining pattern, an isotype-matched control primary antibody and/or omission of the primary antibody should be included as negative controls for immunofluorescence staining. In addition, IMR90 cells infected with vector control-encoding retrovirus should be included as a negative control.

1. Gently wash the coverslips three times with PBS, pH 7.3 to remove all culture media (see Note 15).
2. Fix cells in freshly prepared 4% (w/v) paraformaldehyde for 10 min at room temperature (see Note 16).
3. Wash the coverslips three times with PBS, pH 7.3 to remove fixing solution (see Note 17).
4. Permeabilize the cells by incubating the coverslips in 0.2% (v/v) Triton X-100 in PBS (pH 7.3) for 5 min at room temperature.
5. Block the coverslips with 3% (w/v) BSA in PBS, pH 7.3 for 5 min at room temperature.
6. Incubate the coverslips with the primary antibodies diluted in 3% (w/v) BSA in PBS, pH 7.3 by inverting the coverslip onto 200  $\mu$ L of diluted antibody spotted on parafilm. Incubate for 1–2 h at room temperature.
7. Put the coverslips back into the 6-well plates with the cell side face up. Wash the coverslips three times with 1% (v/v) Triton X-100 in PBS, pH 7.3.
8. Dilute the appropriate secondary antibodies (Table 2) in 3% (w/v) BSA in PBS, pH 7.3. Incubate the coverslips with 2 mL secondary antibody solution in each well for 1 h at room temperature in the dark.
9. Stain SAHF by incubating the coverslips with 0.15  $\mu$ g/mL final concentration of DAPI diluted in 3% (w/v) BSA in PBS, pH 7.3 for 3 min at room temperature (see Note 18).
10. Wash the slide three times with PBS, pH 7.3.
11. Mount the inverted coverslips (cells facing the microscope slide) into one drop of mounting media (approximately 20  $\mu$ L). Aspirate the excess liquid, and seal the coverslips using nail polish (see Note 19).
12. After the slides have dried, observe SAHF using a fluorescent microscope (see Notes 20 and 21).

### **3.3. Microscopic Examination of SAHF**

1. After immunofluorescence staining, the processed slides can be examined under a fluorescent microscope.
2. DAPI staining should reveal punctate staining in oncogenic H-RAS<sup>G12V</sup>-infected cells, while vector control cells should display diffuse staining across the cell nuclei (Fig. 1).

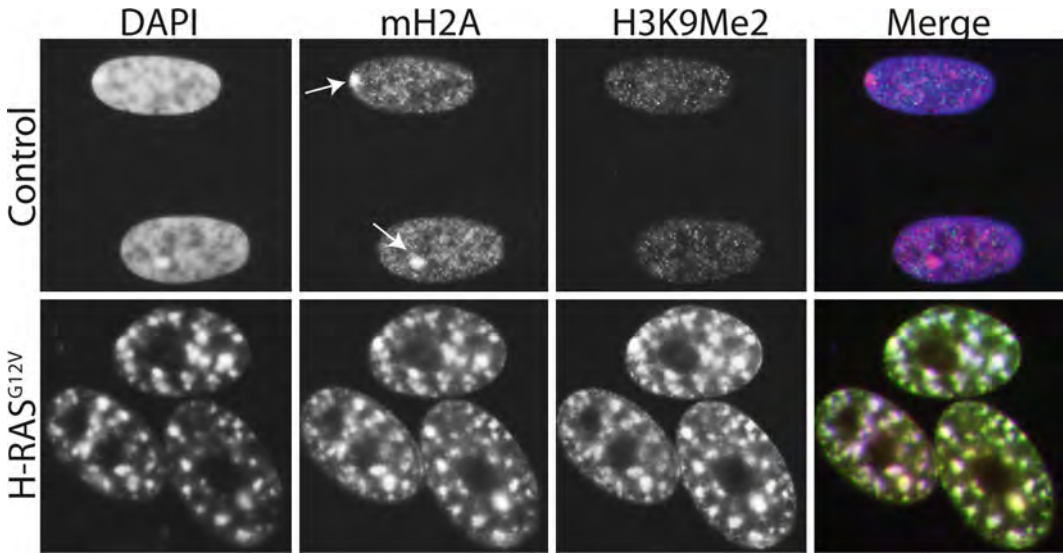


Fig. 1. IMR90 cells were infected with a puromycin-resistant retrovirus encoding oncogenic H-RAS<sup>G12V</sup> or vector control. Drug-selected cells were stained with antibodies to H3K9Me2 and histone H2A variant macroH2A. DAPI counterstaining was used to visualize SAHF. Note the robust punctate DAPI foci in the H-RAS<sup>G12V</sup>-infected cells, which co-localize with both macroH2A and H3K9Me2. Arrows point to inactivated X chromosome in control IMR90 female fibroblast cells. Chicken anti-macroH2A1.2 primary antibody was obtained from Dr. John R. Pehrson (University of Pennsylvania) (28). Rabbit anti-H3K9Me3 is from AbCam (ab8898) and was used at 1:500. Secondary antibodies were FITC-labeled goat anti-chicken (1:2,500) and Cy3-labeled goat anti-rabbit (1:5,000), which were both obtained from Jackson Immunolabs.

3. The number of cells with SAHF staining depends upon the duration of RAS expression. For example, ~50% of RAS-infected cells display SAHF by DAPI staining 7–9 days post drug selection.
4. Components of SAHF such as macroH2A, HP1 proteins, and H3K9Me2/3 form foci that co-localize with DAPI-stained SAHF in RAS-infected cells. In vector control cells, HP1 protein and H3K9Me2/3 staining is largely diffuse. MacroH2A staining marks the single foci in female mammalian cells (such as IMR90 and WI38 primary human fibroblast cells) that is the inactivated X chromosome (Fig. 1).
5. As negative controls, staining using isotype-matched IgG controls as the primary antibody or using the secondary antibody only (without the primary antibody) should not show foci that co-localize with DAPI-stained SAHF. The controls herein will obviously be specific to each component of SAHF.
6. Importantly, regardless of the specific components, not all cells with DAPI-stained SAHF-positive cells will display foci for components of SAHF. This is because relocalization of components of SAHF into DAPI-stained foci is typically a later event compared with formation of DAPI foci (8).



## 4. Notes

1. As discussed in the introduction, other oncogenes (BRAF/MEK/ERK) and other cellular stressors can cause the formation of SAHF. We recommend using H-RAS<sup>G12V</sup> as a positive control because activation of RAS induces distinct SAHF formation in a variety of cell types.
2. Correct pH of the 2× BBS solution is necessary for efficient plasmid transfection using this method.
3. Never let cells reach confluence as this may decrease transfection efficiency. Passage Phoenix cells in 300 µg/mL hygromycin (Roche) and 1 µg/mL diphtheria toxin (Sigma) for 1 week every month to maintain transfection efficiency. For more information, please visit Gary Nolan's Web site ([http://www.stanford.edu/group/nolan/retroviral\\_systems/retsys.html](http://www.stanford.edu/group/nolan/retroviral_systems/retsys.html)).
4. For oncogene-induced SAHF formation (or to study other types of stressors), low population doubling (PD) IMR90 cells should be used (PD < 35). However, if you wish to study replicative senescence-induced SAHF, high PD IMR90 cells (e.g., PD65) should be used instead.
5. Other cell lines and cell types form SAHF (9); however, this must be determined on a cell type-by-cell type basis. It is important to note that mouse cells do not form distinct SAHF structures that are visible by DAPI staining alone. Instead, macroH2A may serve as a marker for SAHF in senescent mouse cells (26).
6. To make 4% paraformaldehyde, weigh 2 g of paraformaldehyde (Sigma) and add 25 mL of ddH<sub>2</sub>O, 25 mL 2× PBS, pH 7.3, and 100 µL 1 N NaOH. Vortex and incubate this mixture at 65°C for 10–15 min to dissolve the paraformaldehyde (vortex the tube every 5 min). Cool the solution to room temperature before use.
7. Adding 0.02% (w/v) sodium azide to the 3% (w/v) BSA in PBS will decrease potential contamination and increase the shelf life.
8. Any of these markers can be used in addition to DAPI staining to identify SAHF. See Table 11 for antibody catalog numbers, dilutions, and references.
9. Secondary antibodies to the appropriate species can be purchased from Jackson Immunolabs. See Table 2 for details.
10. Mounting media should be aliquoted and stored at –80°C. Once the media changes to an orange color, replace with a fresh batch.
11. Although the Phoenix cells are easy to remove from the plate, use 0.25% (w/v) trypsin + 1 mM EDTA to fully separate the cells and avoid cell aggregation.

12. Be very gentle when adding fresh media as Phoenix cells do not adhere very well to the plate. It is typical that Phoenix cells change shape after changing them into fresh medium. They will fully recover after 6–8 h of culture in the newly changed medium.
13. SAHF should start to appear approximately 3–4 days after starting selection and typically reach the highest percentage with ~50% RAS-infected cells positive for DAPI-stained SAHF around 7–9 days after starting drug selection.
14. Protein lysates can be made by directly adding 1× Laemmli sample buffer followed by boiling for 5 min. Samples can be stored at –80°C. Ectopically expressed oncogenic-RAS should be confirmed by Western blotting. Cell extracts should be fractionated by SDS-PAGE, transferred to a PVDF membrane, and then Western blotted with antibody to RAS (BD Biosciences, 610001). An antibody to a housekeeping gene (e.g.,  $\beta$  actin) should be used as a loading control.
15. Senescent cells do not adhere very well to coverslips; therefore, rinsing coverslips with PBS before fixation should be done very carefully. In instances where rinsing coverslips with PBS may lead to loss of cells, this step can be skipped, and coverslips can be directly immersed in 4% (w/v) paraformaldehyde for 10 min.
16. At this step, soluble proteins can be removed to only retain tightly bound chromatin proteins. To do so, cells can be pre-extracted with 5 mM  $\text{MgCl}_2$  in 0.2% (v/v) Triton-X in PBS for 5 min to preserve SAHF while removing the soluble proteins. Extra care should be taken when performing pre-extraction and the following steps of washing and fixation as these pre-extracted cells can be easily washed off the coverslips.
17. After fixation, coverslips can be washed 3× with PBS and stored at 4°C for up to 2 weeks before processing.
18. Higher DAPI concentrations and longer incubation periods will make it harder to distinguish DAPI-stained SAHF.
19. Avoid air bubbles when mounting coverslips.
20. Slides can be stored at –20°C for up to a month. However, it is important to note that the fluorescent signal may fade over time.
21. The same methods can be applied to other cell lines/cell types to determine SAHF formation. As not all cell lines or all causes of cellular senescence induce SAHF formation (see Subheading 1 for details), we recommend the use of IMR90 cells expressing oncogenic H-RAS<sup>G12V</sup> as a positive control.

## Acknowledgments

This work was funded by a NIH/NCI grant (R01CA160331), a Liz Tilberis Scholar Award from the Ovarian Cancer Research Fund and the Department of Defense Ovarian Cancer Academy Award (OC093420). Support of Core Facilities used in this study was provided by Cancer Center Support Grant (CCSG) CA010815 to The Wistar Institute.

## References

1. Kuilman T, Michaloglou C, Mooi WJ, Peeper DS (2010) The essence of senescence. *Genes Dev* 24:2463–2479
2. Campisi J (2005) Senescent cells, tumor suppression, and organismal aging: good citizens, bad neighbors. *Cell* 120:513–522
3. Campisi J, d'Adda di Fagagna F (2007) Cellular senescence: when bad things happen to good cells. *Nat Rev Mol Cell Biol* 8:729–740
4. Narita M, Nunez S, Heard E, Narita M, Lin AW, Hearn SA, Spector DL, Hannon GJ, Lowe SW (2003) Rb-mediated heterochromatin formation and silencing of E2F target genes during cellular senescence. *Cell* 113:703–716
5. Ren B, Cam H, Takahashi Y, Volkert T, Terragni J, Young RA, Dynlacht BD (2002) E2F integrates cell cycle progression with DNA repair, replication, and G(2)/M checkpoints. *Genes Dev* 16:245–256
6. Zhang R, Adams PD (2007) Heterochromatin and its relationship to cell senescence and cancer therapy. *Cell Cycle* 6:784–789
7. Zhang R, Liu ST, Chen W, Bonner M, Pehrson J, Yen TJ, Adams PD (2007) HP1 proteins are essential for a dynamic nuclear response that rescues the function of perturbed heterochromatin in primary human cells. *Mol Cell Biol* 27:949–962
8. Zhang R, Poustovoitov MV, Ye X, Santos HA, Chen W, Daganzo SM, Erzberger JP, Serebriiskii IG, Canutescu AA, Dunbrack RL, Pehrson JR, Berger JM, Kaufman PD, Adams PD (2005) Formation of MacroH2A-containing senescence-associated heterochromatin foci and senescence driven by ASF1a and HIRA. *Dev Cell* 8:19–30
9. Kosar M, Bartkova J, Hubackova S, Hodny Z, Lukas J, Bartek J (2011) Senescence-associated heterochromatin foci are dispensable for cellular senescence, occur in a cell type- and insult-dependent manner and follow expression of p16(ink4a). *Cell Cycle* 10:457–468
10. Adams PD (2007) Remodeling of chromatin structure in senescent cells and its potential impact on tumor suppression and aging. *Gene* 397:84–93
11. Di Micco R, Sulli G, Dobrev M, Lontos M, Botrugno OA, Gargiulo G, dal Zuffo R, Matti V, d'Ario G, Montani E, Mercurio C, Hahn WC, Gorgoulis V, Minucci S, d'Adda di Fagagna F (2011) Interplay between oncogene-induced DNA damage response and heterochromatin in senescence and cancer. *Nat Cell Biol* 13:292–302
12. Zhang R, Chen W, Adams PD (2007) Molecular dissection of formation of senescence-associated heterochromatin foci. *Mol Cell Biol* 27:2343–2358
13. Funayama R, Saito M, Tanobe H, Ishikawa F (2006) Loss of linker histone H1 in cellular senescence. *J Cell Biol* 175:869–880
14. Pagano M, Pepperkok R, Verde F, Ansorge W, Draetta G (1992) Cyclin A is required at two points in the human cell cycle. *EMBO J* 11:961–971
15. Narita M, Narita M, Krizhanovsky V, Nunez S, Chicas A, Hearn SA, Myers MP, Lowe SW (2006) A novel role for high-mobility group a proteins in cellular senescence and heterochromatin formation. *Cell* 126:503–514
16. Collado M, Gil J, Efeyan A, Guerra C, Schuhmacher AJ, Barradas M, Benguria A, Zaballos A, Flores JM, Barbacid M, Beach D, Serrano M (2005) Tumour biology: senescence in premalignant tumours. *Nature* 436:642
17. Herbig U, Ferreira M, Condel L, Carey D, Sedivy JM (2006) Cellular senescence in aging primates. *Science* 311:1257
18. Kreiling JA, Tamamori-Adachi M, Sexton AN, Jeyapalan JC, Munoz-Najar U, Peterson AL, Manivannan J, Rogers ES, Pchelintsev NA, Adams PD, Sedivy JM (2011) Age-associated increase in heterochromatic marks in murine and primate tissues. *Aging Cell* 10:292–304

19. Collado M, Serrano M (2010) Senescence in tumours: evidence from mice and humans. *Nat Rev Cancer* 10:51–57
20. Martin C, Chen S, Heilos D, Sauer G, Hunt J, Shaw AG, Sims PF, Jackson DA, Lovric J (2010) Changed genome heterochromatinization upon prolonged activation of the Raf/ERK signaling pathway. *PLoS One* 5:e13322
21. Michaloglou C, Vredeveld LC, Soengas MS, Denoyelle C, Kuilman T, van der Horst CM, Majoor DM, Shay JW, Mooi WJ, Peeper DS (2005) BRAFE600-associated senescence-like cell cycle arrest of human naevi. *Nature* 436:720–724
22. Kennedy AL, Morton JP, Manoharan I, Nelson DM, Jamieson NB, Pawlikowski JS, McBryan T, Doyle B, McKay C, Oien KA, Enders GH, Zhang R, Sansom OJ, Adams PD (2011) Activation of the PIK3CA/AKT pathway suppresses senescence induced by an activated RAS oncogene to promote tumorigenesis. *Mol Cell* 42:36–49
23. Tu Z, Aird KM, Bitler BG, Nicodemus JP, Beechary N, Xia B, Yen TJ, Zhang R (2011) Oncogenic RAS regulates BRIP1 expression to induce dissociation of BRCA1 from chromatin, inhibit DNA repair, and promote senescence. *Dev Cell* 21:1077–1091
24. Deng Q, Liao R, Wu BL, Sun P (2004) High intensity ras signaling induces premature senescence by activating p38 pathway in primary human fibroblasts. *J Biol Chem* 279:1050–1059
25. Ye X, Zerlanko B, Zhang R, Somaiah N, Lipinski M, Salomoni P, Adams PD (2007) Definition of pRB- and p53-dependent and -independent steps in HIRA/ASF1a-mediated formation of senescence-associated heterochromatin foci. *Mol Cell Biol* 27:2452–2465
26. Kennedy AL, McBryan T, Enders GH, Johnson FB, Zhang R, Adams PD (2010) Senescent mouse cells fail to overtly regulate the HIRA histone chaperone and do not form robust senescence associated heterochromatin foci. *Cell Div* 5:16
27. Funayama R, Ishikawa F (2007) Cellular senescence and chromatin structure. *Chromosoma* 116:431–440
28. Costanzi C, Pehrson JR (1998) Histone macroH2A1 is concentrated in the inactive X chromosome of female mammals. *Nature* 393:599–601
29. Trojer P, Reinberg D (2007) Facultative heterochromatin: is there a distinctive molecular signature? *Mol Cell* 28:1–13



## SUZ12 Promotes Human Epithelial Ovarian Cancer by Suppressing Apoptosis via Silencing HRK

Hua Li<sup>1</sup>, Qi Cai<sup>2</sup>, Hong Wu<sup>3</sup>, Vinod Vathipadiekal<sup>7</sup>, Zachary C. Dobbin<sup>8</sup>, Tianyu Li<sup>4</sup>, Xiang Hua<sup>5</sup>, Charles N. Landen<sup>8</sup>, Michael J. Birrer<sup>7</sup>, Margarita Sánchez-Beato<sup>9</sup>, and Rugang Zhang<sup>1,6</sup>

### Abstract

Epithelial ovarian cancer (EOC) ranks first as the cause of death for gynecological cancers in the United States. SUZ12 is a component of the polycomb repressive complex 2 (PRC2) and is essential for PRC2-mediated gene silencing by generating trimethylation on lysine 27 residue of histone H3 (H3K27Me3). The role of SUZ12 in EOC has never been investigated. Here, we show that SUZ12 is expressed at significantly higher levels in human EOC ( $n = 117$ ) compared with either normal human ovarian surface epithelium ( $n = 35$ ,  $P < 0.001$ ) or fallopian tube epithelium ( $n = 15$ ,  $P < 0.001$ ). There is a positive correlation between expression of SUZ12 and EZH2 in human EOC ( $P < 0.001$ ). In addition, expression of SUZ12 positively correlates with Ki67, a marker of cell proliferation ( $P < 0.001$ ), and predicts shorter overall survival ( $P = 0.0078$ ). Notably, knockdown of SUZ12 suppresses the growth of human EOC cells *in vitro* and *in vivo* in both orthotopic and subcutaneous xenograft EOC models. In addition, SUZ12 knockdown decreases the levels of H3K27Me3 and triggers apoptosis of human EOC cells. Mechanistically, we identified Harakiri (HRK), a proapoptotic gene, as a novel SUZ12 target gene, and showed that HRK upregulation mediates apoptosis induced by SUZ12 knockdown in human EOC cells. In summary, we show that SUZ12 promotes the proliferation of human EOC cells by inhibiting apoptosis and HRK is a novel SUZ12 target gene whose upregulation contributes to apoptosis induced by SUZ12 knockdown. *Mol Cancer Res*; 10(11); 1462–72. ©2012 AACR.

### Introduction

More than 85% of ovarian cancers are of epithelial origin (1). Epithelial ovarian cancers (EOC) are classified into distinct histologic types including serous, mucinous, endometrioid, and clear cell (1). The most common histology of EOC is serous (~60% of all cancers) and less common histologies include endometrioid, clear cell, and mucinous (2). Recently, an alternative classification has been proposed, in which EOC is broadly divided into 2 types (3). Type I EOC includes mucinous, low-grade serous, low-grade endometrioid, and clear cell carcinomas, and type II EOC includes high-grade serous and high-grade endometrioid

carcinomas (3). EOC remains the most lethal gynecological malignancy in the United States (4). Thus, there is an urgent need to better understand the etiology of EOC to develop novel therapeutics for this disease.

SUZ12 is essential for polycomb repressive complex 2 (PRC2)-mediated gene silencing (5–8). In addition to SUZ12, PRC2 also contains the catalytic subunit EZH2 (9). PRC2 epigenetically silences gene transcription by generating trimethylation on lysine 27 residue of histone H3 (H3K27Me3). EZH2 lacks methyltransferase enzyme activity on its own, and has to complex with SUZ12 to attain histone methyltransferase activity (9, 10).

EZH2 is overexpressed in several types of cancers, including prostate and breast cancers (11–15). Its overexpression correlates with the aggressiveness and poor prognosis in breast and prostate cancers (11–13). Indeed, EZH2 is often overexpressed in human EOC and its knockdown triggers apoptosis of human EOC cells (16, 17). In contrast, the role of SUZ12 in EOC remains poorly understood.

Here, we examined the expression of SUZ12 in human EOC specimens and discovered that SUZ12 is expressed at significantly higher levels in human EOCs compared with either normal human ovarian surface epithelium or fallopian tube epithelium. In addition, we showed that SUZ12 expression positively correlates with expression of EZH2 and Ki67, a cell proliferation marker. Conversely, SUZ12 knockdown suppresses the growth of human EOC cells *in vitro* and *in vivo* in xenograft EOC models. Consistently,

**Authors' Affiliations:** <sup>1</sup>Gene Expression and Regulation Program, The Wistar Institute; <sup>2</sup>Histopathology Facility; <sup>3</sup>Department of Pathology; <sup>4</sup>Bio-statistics and Bioinformatics Facility; <sup>5</sup>Transgenic Facility; <sup>6</sup>Women's Cancer Program, Fox Chase Cancer Center, Philadelphia, Pennsylvania; <sup>7</sup>Massachusetts General Hospital Cancer Center, Harvard Medical School, Boston, Massachusetts; <sup>8</sup>Department of Obstetrics and Gynecology, University of Alabama at Birmingham, Birmingham, Alabama; and <sup>9</sup>Human Genetics Programme, Spanish National Cancer Research Centre (CNIO) and Hospital Universitario Puerta de Hierro-Majadahonda, Madrid, Spain

**Note:** Supplementary data for this article are available at Molecular Cancer Research Online (<http://mcr.aacrjournals.org/>).

**Corresponding Author:** Rugang Zhang, Room 308, The Wistar Institute, 3601 Spruce Street, Philadelphia, PA 19104. Phone: 215-495-6840; Fax: 215-898-3792; Email: rzhang@wistar.org

doi: 10.1158/1541-7786.MCR-12-0335

©2012 American Association for Cancer Research.

SUZ12 knockdown induces apoptosis of human EOC cells. Mechanistically, we identified Harakiri (HRK), a proapoptotic gene, as a novel SUZ12 target gene whose upregulation contributes to apoptosis induced by SUZ12 knockdown in human EOC cells.

## Materials and Methods

### Cell culture

Human EOC cell lines SKOV3, PEO1, and OVCAR10 were cultured according to American Type Culture Collection and as we have previously described (16, 18). The cell line identification was confirmed by DNA Diagnostic Center (www.dnacenter.com).

### FACS, immunofluorescence staining, and immunoblot analysis

Fluorescence-activated cell sorting (FACS) and indirect immunofluorescence staining were conducted as described previously (19). The following antibodies were used for immunofluorescence: rabbit anti-H3K27Me3 (Cell Signaling, 1:1,000), and rabbit anti-H3K9Me2 (Abcam, 1:500). The antibodies used for immunoblot were from indicated suppliers: rabbit anti-H3K27Me3 (Cell signaling, 1:1,000), rabbit anti-H3K9Me3 (Abcam, 1:2,000), mouse antihistone H3 (Millipore, 1:10,000), mouse anti-glyceraldehyde-3-phosphate dehydrogenase (GAPDH; Millipore, 1:10,000), rabbit anti-PARP p85 fragment (Promega, 1:1,000), rabbit anti-cleaved caspase 3 (Cell Signaling, 1:1,000), and rabbit anti-cleaved Lamin A (Cell signaling, 1:1,000), and mouse anti-HA (Cell signaling, 1:1,000). Mouse anti-SUZ12 (220A) was as described previously (20).

### siRNA, shRNA, lentivirus packaging, and infection

The sense sequences of 2 individual short hairpin RNA (shRNA) to the human *SUZ12* gene (shSUZ12) are: 5'-GCTTACGTTTACTGGTTTCTT-3' and 5'-CGGAATCTCATAGACCAATA-3', respectively. Lentivirus packaging was conducted using virapower system (Invitrogen) according to manufacturer's instruction. PEO1 and SKOV3 at 40% to 50% confluence were infected with lentivirus expressing shSUZ12 or vector control. The infected cells were selected with 1 µg/mL (for PEO1) or 3 µg/mL (for SKOV3) of puromycin, respectively. siHRK was purchased from Dharmacon (Cat: L-008216-00-0005) and transfection was conducted following the manufacturer's instruction. A siRNA to luciferase (siGL2) was used as a negative control.

### Inducible expression of shRNA resistant SUZ12

To generate shRNA resistant SUZ12 expression construct that do not affect the protein sequence, but resistant to the shSUZ12 #1, 3 rounds of mutagenesis were carried out to mutate every third base of the coding region in *SUZ12* open reading frame (ORF) targeted by shSUZ12 #1 using Quikchange II XL Site-Directed Mutagenesis kit (Stratagene, Cat. No: 200521). Mutagenic primers are as the following: Round 1: forward: 5'-GTCAGCTCATTTGCAACTCA-

CATTACACGGGTTTCTTCCAC-3' and reverse: 5'-GTGGAAGAAACCCGTGAATGTGAGTTGCAAATGAGCTGAC-3'; Round 2 forward: 5'-CTCACATTTCACGGGCTTTTCCACAAAAATGATAAGC-3' and reverse: 5'-GCTTATCATTTTTGTGGAAAAAGCCCGTGAATGTGAG-3'; and Round 3 forward: 5'-GTCAGCTCATTTGCAATTGACATTACACGGGCTTTTCC-3' and reverse: 5'-GGAAAAAGCCCGTGAATGTC-AATTGCAATGAGCTGAC-3'. The shRNA resistant SUZ12 was then subcloned into an inducible retroviral vector pRetroXTight-Pur (Retro-X Tet-On, Invitrogen) and the inducible SUZ12 SKOV3 cell line was generated following manufacturer's instruction. Twenty-four hours after infection with shSUZ12 #1 virus, shRNA resistant SUZ12 was induced by DOX (Clontech, 500 ng/mL) following manufacturer's instruction.

### Human ovarian tissue microarrays and specimens

Tissue microarrays, including core samples from 117 primary human EOCs, 35 cases of normal ovary tissues and 15 cases of fallopian tube tissues were obtained from FCCC Biosample Repository Core Facility. Use of these human specimens was approved by the Institutional Review Board.

### Immunohistochemical staining and scoring

The expression of SUZ12 was detected using avidin-biotin-peroxidase methods and as previously described (18). Briefly, tissue sections were subjected to antigen retrieval by steaming in 0.01 mol/L of sodium citrate buffer (pH 6.0) for 30 minutes. After quenching endogenous peroxidase activity with 3% hydrogen peroxide and blocking nonspecific protein binding with 1% bovine serum albumin, sections were incubated overnight with primary monoclonal SUZ12 antibody (220A 1:40) at 4°C, followed by biotinylated goat anti-mouse IgG (DAKO, 1:400) for 1 hour, detecting the antibody complexes with the labeled streptavidin-biotin system, and visualizing them with the chromogen 3,3'-diaminobenzidine. Sections were lightly counterstained with hematoxylin. In addition, anti-EZH2 (Millipore; 1:100) and anti-Ki67 (Dako, 1:100) antibodies were used on consecutive sections as we have previously described (16).

### RNA isolation, qRT-PCR, and PCR array

RNA was isolated using Trizol (Invitrogen) according to manufacturer's instruction. For quantitative real-time PCR (qRT-PCR), Trizol-isolated RNA was further purified using an RNeasy kit (Qiagen) following manufacture's instruction. The primers for *HRK* genes used for qRT-PCR are: forward: 5'-GCAACAGGTTGGTGAACCCCT-3' and reverse: 5'-ATTGGGGTGTCTGTTTCTGCAGC-3'. Expression of the housekeeping gene  $\beta$ -2-microglobulin was used to normalize mRNA expression. Apoptosis genes PCR array was purchased from SABiosciences (Cat: PAHS-012A) and the analysis was conducted following the manufacturer's instruction. The RT-PCR data was analyzed by using RT2 Profiler PCR Array Data Analysis version 3.4. For survival analysis, RNA was isolated and amplified from

microdissected high-grade serous primary ovarian tumor specimens as described previously (21). All specimens and their corresponding clinical information were obtained under Institutional Review Board-approved protocols. qRT-PCR for *SUZ12* was conducted using the following primers: forward: 5'-CCGAGCACTGTGGTTGAGTA-3'; and reverse: 5'-AACTGCATCTGATGGTGGTG-3' using a SYBR Green 1-Step qRT-PCR kit accordingly to the manufacturer's instructions (Invitrogen). Expression of the housekeeping gene *GAPDH* was used to normalize mRNA expression.

#### Soft agar colony formation assay

A total of 5,000 cells were inoculated in a 6-well plate in 1.5 mL of RPMI 1640 medium supplemented with 10% FBS and 0.35% agar on a base layer of 1.5 mL of the same medium containing 0.6% agar as previously described. Three weeks after plating, the cells were stained with 0.005% crystal violet (Sigma) in PBS to visualize the colonies.

#### Annexin V staining for detecting apoptotic cells

Phosphatidylserine externalization was detected using an Annexin V staining kit (Millipore) following manufacture's instruction. Annexin V positive cells were detected by Guava system and analyzed with Guava Nexin software Module (Millipore).

#### In vivo tumorigenicity assay

The protocol was approved by Institutional Animal Care and Use Committee. For orthotopic transplantation, SKOV3 cells were infected with a luciferase encoding retrovirus (hygro-pWZL-Luciferase) and infected cells were selected with 50 µg/mL hygromycin as previously described (18). Drug-selected cells were then infected with control or shSUZ12 encoding lentivirus and subsequently selected with 3 µg/mL puromycin and 50 µg/mL hygromycin.  $3 \times 10^5$  drug-selected cells were unilaterally injected into ovarian bursa sac of immunocompromised mice with 9 mice in each group. From week 2 postinfection, tumors were visualized by injecting luciferin (i.p.; 4 mg/mice) resuspended in PBS and imaged with an IVIS Spectrum imaging system every 2 weeks until week 8. Images were analyzed using Live Imaging 4.0 software. At week 8, tumors were surgically dissected and fixed in 10% formalin. For subcutaneous (s.c.) transplantation, SKOV3 cells were infected with control or shSUZ12 encoding lentivirus and subsequently selected with 3 µg/mL puromycin.  $1 \times 10^6$  drug-selected cells were subcutaneously injected into flank of immunocompromised mice with 5 mice in each group (16). Tumor growth was monitored every 2 weeks. Tumor volume was calculated by the equation  $V(\text{mm}^3) = (axb^2)/2$ , where  $a$  is the largest diameter and  $b$  is the perpendicular diameter. At week 5, tumors were surgically dissected and fixed in 10% formalin.

#### Chromatin Immunoprecipitation (ChIP)

SKOV3 cells were fixed with 1% formaldehyde for 15 min and quenched with 0.125 M glycine at room temperature as

we have previously described (22). Chromatin was isolated by adding cell lysis buffer (1% SDS, 10 mmol/L EDTA, 50 mmol/L Tris-HCl, pH 8.1, 1 mmol/L phenylmethylsulfonylfluoride) followed by sonication to shear the DNA to an average length of 300–500 bp. Lysates were precleared with Salmon Sperm DNA/Protein A Agarose (Millipore, Cat. No:16–157) for 1 to 2 hours. The following antibodies were used to conduct chromatin Immunoprecipitation (ChIP): anti-H3K27Me3 (C36B11, Cell signaling), anti-histone H3 (05–928, Millipore), or anti-SUZ12 (220A). An isotype matched IgG was used as a negative control. ChIP DNA was purified by phenol-chloroform extraction and ethanol precipitation and analyzed with PCR against the genomic locus of the human *HRK* gene (forward: 5'-GAA ACA AAA ACC CAA GAC TAA G-3' and reverse: 5'-TGA CTA CCT TGG GAA AGA ATG ATA G-3'). PCR products were visualized on a 2% agarose gel.

#### Statistical analysis

Quantitative data were expressed as mean  $\pm$  SD, unless otherwise stated. ANOVA with Fisher's Least Significant Difference was used to identify significant differences in multiple comparisons. The  $\chi^2$  test was used to analyze the relationship between categorical variables. Overall survival was defined as the time elapsed from the date of diagnosis and the date of death from ovarian cancer, otherwise were considered as censored observations. Kaplan–Meier survival plots were generated and comparisons made using the log-rank statistic. For all statistical analyses, the level of significance was set at 0.05.

## Results

### SUZ12 is expressed at significantly higher levels in human EOCs compared with either normal human ovarian surface epithelium or fallopian tube epithelium

We sought to determine the expression of SUZ12 protein in human EOCs by immunohistochemistry (IHC). The specificity of the anti-SUZ12 antibody was confirmed in our study. A single band at the predicted molecular weight (~83 kDa) was detected in human SKOV3 cells and was absent after expression of a shRNA to the human *SUZ12* gene (shSUZ12) that effectively knocked down SUZ12 mRNA expression (Supplementary Fig. S1A and data not shown). In addition, SUZ12 staining was lost when primary anti-SUZ12 antibody was replaced with an isotype-matched IgG control (Supplementary Fig. S1B).

We next examined SUZ12 expression in 117 cases of human EOCs and 35 cases of normal human ovary with surface epithelium. Notably, there is recent evidence to suggest that a proportion of EOC may arise from distant fallopian tube epithelium (23, 24). Thus, we also included 15 cases of normal human fallopian tube specimens in our study. As shown in Fig. 1A and Supplementary Fig. S1C, in all 4 major histosubtypes of human EOCs, the nuclei was positive for SUZ12 IHC staining. In contrast, SUZ12 staining in normal human ovarian surface epithelial cells or fallopian tube epithelial cells was markedly weaker (Fig. 1A).



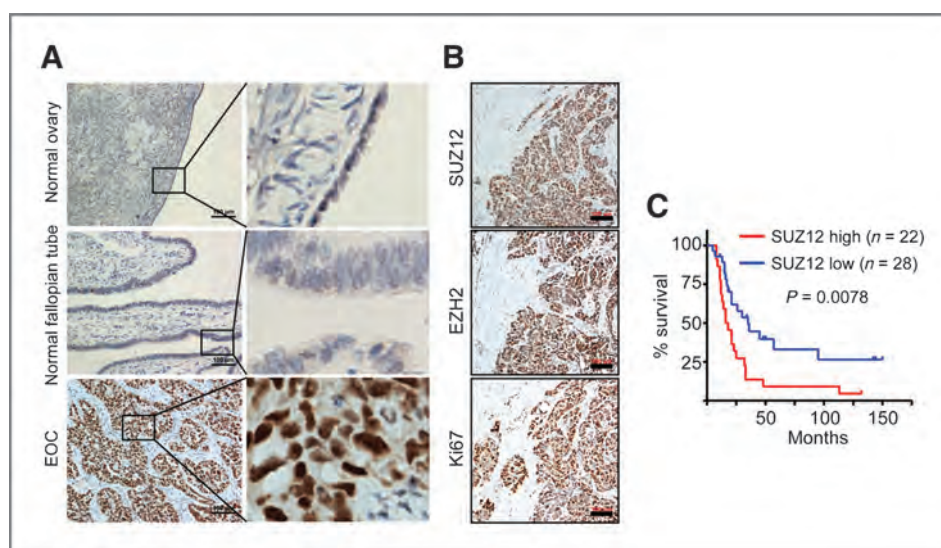


**Figure 1.** SUZ12 is expressed at significantly higher levels in human EOCs compared with normal human ovarian surface epithelium or fallopian tube epithelium, and predicts poor overall survival in EOC patients. A, examples of SUZ12 IHC staining in normal human ovarian surface epithelium, fallopian tube epithelium, and human EOC (shown is an example of high-grade serous histosubtype EOC specimen). Bar = 100  $\mu$ m. B, representative images from consecutive, serial sections of the same EOC specimen depicting the positive correlation between expression of SUZ12 and expression of EZH2 and Ki67, a cell proliferation marker. Bar = 100  $\mu$ m. C, a higher SUZ12 expression correlates with a shorter overall survival in EOC patients. The univariate overall survival curve (Kaplan–Meier method) for EOC patients with high ( $n = 22$ ) or low ( $n = 28$ ) SUZ12 expression based on median levels of mRNA expression determined by qRT-PCR in a cohort of 50 EOC patients ( $P = 0.0078$ ). The  $p$  value was calculated based on Log-rank (Mantel-Cox) test using GraphPad Prism version 5.0 software.

We scored expression of SUZ12 as high ( $H$  score  $\geq 50$ ) or low ( $H$  score  $< 50$ ) based on a histologic score as previously described (25, 26). SUZ12 was scored as high in 76.9% (90/117) of human EOCs. In contrast, SUZ12 was scored high in 20% (7/35) and 13.3% (2/15) of normal human ovarian surface epithelium and fallopian tube epithelium, respectively (Table 1). Statistical analysis revealed that SUZ12 was expressed at significantly higher levels in human EOCs compared with either normal human ovarian surface epithelium ( $P < 0.001$ ) or fallopian tube epithelium ( $P < 0.001$ ; Table 1). Consistently, SUZ12 was expressed at higher levels in human EOC cell lines compared with normal human ovarian surface epithelial cells (Supplementary Fig. S1D). On the basis of these studies, we conclude that SUZ12 is expressed at significantly higher level in human EOCs compared with either normal human ovarian surface epithelium or fallopian tube epithelium.

#### **SUZ12 expression positively correlates with expression of EZH2 and Ki67, and predicts shorter overall survival**

We next sought to determine the correlation between expression of SUZ12 and EZH2, or Ki67, a marker of cell proliferation. We examined the expression of EZH2 and Ki67 by IHC in the same set of human EOC specimens (Fig. 1B and Table 1). There was a significant, positive correlation between expression of SUZ12 and EZH2 ( $P < 0.001$ ) or Ki67 ( $P < 0.001$ ; Table 1). We next examined the correlation between SUZ12 expression and clinical and pathological features of human EOCs. There is a trend toward significance between expression of SUZ12 and tumor stage ( $P = 0.122$ ; Table 1). Notably, the majority

of the examined EOC cases are type II high-grade serous subtypes that are typically of stage III/IV (Table 1). Furthermore, we assessed the correlation between SUZ12 expression and prognosis of EOC patients ( $n = 50$ ), for which long-term follow-up data were available. There was a significant correlation between expression of SUZ12 and overall survival in EOC patients ( $P = 0.0078$ ; Fig. 1C). On the basis of these results, we conclude that SUZ12 expression positively correlates with expression of EZH2 and Ki67, and predicts poor overall survival in EOC patients.

#### **SUZ12 knockdown suppresses the growth of human EOC cells *in vitro* and *in vivo***

As SUZ12 expression correlates with expression of a cell proliferation marker Ki67, we sought to determine the effects of SUZ12 knockdown on proliferation of human EOC cells. Toward this goal, we used 2 individual shRNAs to the human *SUZ12* gene (shSUZ12). The knockdown efficacy of shSUZ12 in SKOV3 human cells was confirmed by immunoblot (Fig. 2A). Notably, the level of H3K27Me3 was significantly reduced in shSUZ12 expressing SKOV3 cells as determined by both immunoblot and immunofluorescence staining (Fig. 2A and B). In contrast, shSUZ12 has no effects on the level of trimethylated lysine 9 histone H3 (H3K9Me3) that is generated by the histone methyltransferases such as Suv39H1, Suv39H2, and SETDB1 (Fig. 2A and B; ref. 27). Together, these data support the premise that SUZ12 is necessary for H3K27Me3 epigenetic modification in human EOC cells.

Compared with controls, SUZ12 knockdown significantly inhibited both anchorage-dependent and independent



**Table 1.** SUZ12 expression in human EOCs and its correlation with clinicopathological variables or expression of EZH2 and Ki67

| Patient characteristics         | SUZ12 protein expression |          |           |          | p                   |
|---------------------------------|--------------------------|----------|-----------|----------|---------------------|
|                                 | Low (n)                  | High (n) | Total (n) | High (%) |                     |
| Normal tissue                   |                          |          |           |          |                     |
| Normal ovary epithelial         | 28                       | 7        | 35        | 20.0%    | <0.001 <sup>a</sup> |
| Fallopian tube                  | 13                       | 2        | 15        | 13.3%    | <0.001 <sup>b</sup> |
| Epithelial ovarian cancer       | 27                       | 90       | 117       | 76.9%    |                     |
| Type I                          | 7                        | 17       | 24        | 70.8%    |                     |
| Low-grade serous                | 4                        | 1        | 5         |          |                     |
| Mucinous                        | 1                        | 2        | 3         |          |                     |
| Low grade Endometrioid          | 2                        | 5        | 7         |          |                     |
| Clear cell                      | 0                        | 8        | 8         |          |                     |
| Other                           | 0                        | 1        | 1         |          |                     |
| Type II                         | 20                       | 73       | 93        | 78.5%    |                     |
| High-grade serous               | 16                       | 71       | 87        |          |                     |
| Other (high-grade endometrioid) | 4                        | 2        | 6         |          |                     |
| Age                             |                          |          |           |          |                     |
| ≤55                             | 11                       | 33       | 44        | 75.0%    | 0.701               |
| >55                             | 16                       | 57       | 73        | 78.1%    |                     |
| Laterality                      |                          |          |           |          |                     |
| Left                            | 8                        | 25       | 33        | 75.8%    | 0.988               |
| Right                           | 5                        | 17       | 22        | 77.3%    |                     |
| Bilaterality                    | 14                       | 47       | 61        | 77.1%    |                     |
| Undetermined                    | 0                        | 1        | 1         |          |                     |
| Ki67 <sup>c</sup>               |                          |          |           |          |                     |
| 0%–10%                          | 16                       | 9        | 25        | 36.0%    | <0.001              |
| 10%–40%                         | 6                        | 18       | 24        | 75.0%    |                     |
| 40%–100%                        | 5                        | 63       | 68        | 92.7%    |                     |
| EZH2 expression <sup>d</sup>    |                          |          |           |          |                     |
| Low                             | 19                       | 22       | 41        | 53.7%    | <0.001              |
| High                            | 8                        | 68       | 76        | 89.5%    |                     |
| Tumor stage                     |                          |          |           |          |                     |
| Stage 1/2                       | 10                       | 20       | 30        | 66.7%    | 0.122               |
| Stage 3/4                       | 17                       | 70       | 87        | 80.5%    |                     |

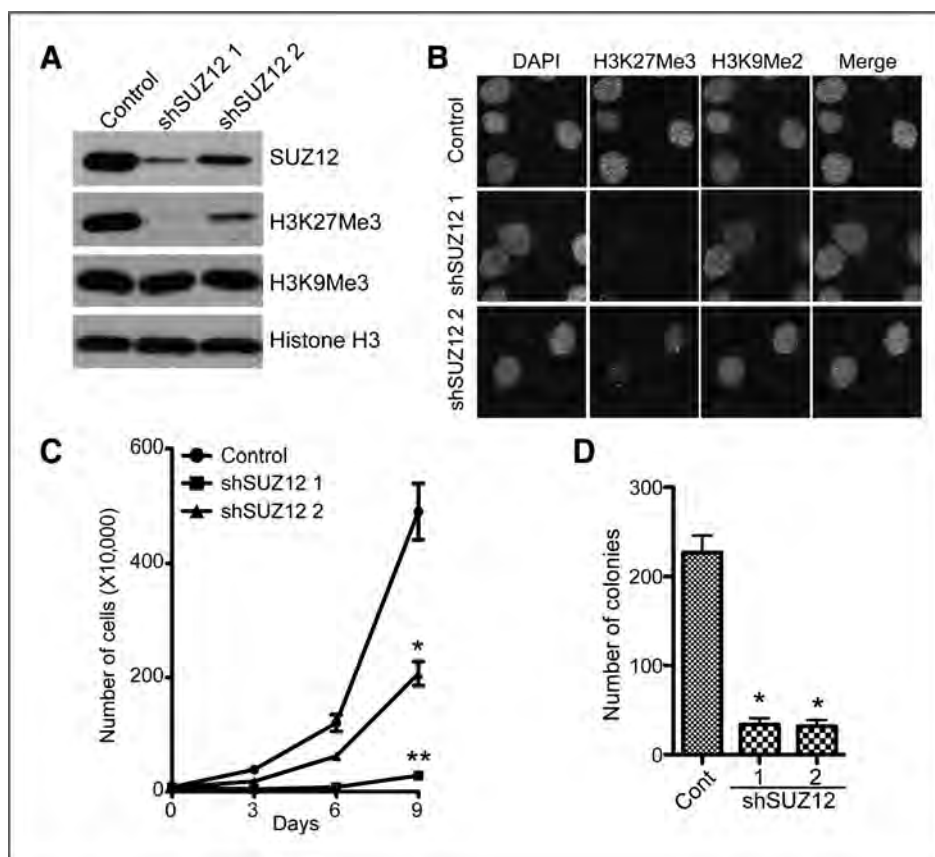
<sup>a</sup>Compared with epithelial ovarian cancer,  $P < 0.001$ .<sup>b</sup>Compared with serous epithelial ovarian cancer,  $P < 0.001$ .<sup>c</sup>Spearman's Rank Order Correlation also showed SUZ12 positively correlated with Ki67 ( $P < 0.001$ ), and  $r_s$  is 0.465.<sup>d</sup>Spearman's Rank Order Correlation also showed SUZ12 positively correlated with EZH2 ( $P < 0.001$ ), and  $r_s$  is 0.515.

growth in soft agar in SKOV3 cells ( $P < 0.001$ ; ref. Fig. 2C and D). In addition, SUZ12 knockdown also decreased the expression levels of H3K27Me3 and suppressed both anchorage-dependent and independent growth in PEO1 cells (Supplementary Fig. S2), suggesting that the observed growth inhibitory effects are not cell line specific.

We next sought to determine the effects of SUZ12 knockdown on the growth of SKOV3 cells *in vivo* in immunocompromised mice. Toward this goal, a luciferase gene was retrovirally transduced into control or shSUZ12-expressing SKOV3 cells to monitor the cell growth *in vivo* via noninvasive imaging as previously described (18). These cells were injected unilaterally into the bursa sac covering the

ovary in female immunocompromised mice ( $n = 9$  for each of the groups). Tumor growth was monitored by measuring luciferase activity every 2 weeks starting at week 2 after injection, and the tumor growth was followed for a total of 8 weeks. Indeed, SUZ12 knockdown significantly suppressed the orthotopically xenografted SKOV3 human EOC cells compared with controls (Fig. 3A and B). In addition, we also examined the growth of control and shSUZ12-expressing SKOV3 cells in a s.c. xenograft model in immunocompromised mice. The same growth inhibitory effects of shSUZ12 were also observed in the s.c. xenograft EOC model (Fig. 3C and D). SUZ12 knockdown in the surgically dissected xenografted tumors was confirmed by IHC staining (Fig.

**Figure 2.** SUZ12 knockdown inhibits the growth of human EOC cells *in vitro*. A, SKOV3 cells were infected with 2 individual lentivirus encoded shSUZ12 or control. Three days post drug selection, cells were examined for expression of SUZ12, H3K27Me3, H3K9Me3, and histone H3 by immunoblot. B, same as A, but examined for expression of H3K27Me3 and H3K9Me2 by immunofluorescence staining. 4', 6-diamidino-2-phenylindole counterstaining was used to visualize the cell nuclei. C, same as A, but equal number of drug-selected cells were seeded and counted at indicated time points using trypan blue exclusion assay that only counts for the viable cells. In addition, the cells were ensured to be in log phase throughout the experiments by splitting them before they reached confluence. Mean of 3 independent experiments with SD. \*,  $P = 0.001$  and \*\*,  $P < 0.001$  compared with controls. D, same as A, 5,000 drug-selected cells were seeded in soft agar and the number of colonies were counted after 3 weeks of culture. Mean of 3 independent experiments with SD. \*,  $P < 0.001$  compared with controls.



3E). On the basis of these results, we conclude that SUZ12 knockdown suppresses the growth of human EOC cells *in vivo* in both orthotopic and s.c. xenograft EOC models.

### SUZ12 knockdown triggers apoptosis of human EOC cells

Next, we sought to determine the cellular mechanism by which SUZ12 knockdown inhibits the growth of human EOC cells. DNA content analysis determined by FACS showed that there was an increase in the percentage of the sub-G<sub>1</sub> phase in SUZ12 knockdown cells compared with controls (Fig. 4A and B), suggesting that these cells may undergo apoptosis. Indeed, markers of apoptosis were significantly induced in SUZ12 knockdown cells compared with controls. Those markers include increased percentage of Annexin V positively stained cells as measured by Guava Nexin assay and upregulation of cleaved Lamin A, PARP p85, and caspase 3 as determined by immunoblot (Fig. 4C–E). The degree of apoptosis induced by shSUZ12 correlated with the level of SUZ12 knockdown by 2 individual shSUZ12 (Fig. 4), suggesting that the observed apoptosis in SUZ12 knockdown EOC cells was not because of off-target effects.

To further limit the potential off-target effect, we conducted the rescue experiments. Toward this goal, we generated a shSUZ12 #1 resistant HA-tagged SUZ12-expressing construct that expresses the wild-type protein. Expression of

shSUZ12 efficiently knocked down the expression of endogenous SUZ12 mRNA as reflected by semiquantitative RT-PCR using primers targeting the 3' end untranslated region (UTR; Fig. 5A). The expression of shSUZ12 #1 resistant HA-tagged SUZ12 was confirmed at both the mRNA level by semiquantitative RT-PCR using primers targeting the ORF and at the protein level by immunoblot using an anti-HA antibody (Fig. 5A and B). Indeed, expression of HA-tagged shSUZ12-resistant wild-type SUZ12 protein partially rescued the decrease of H3K27Me3 level and suppressed the expression of markers of apoptosis such as expression of cleaved Lamin A, PARP p85, and caspase 3 in SUZ12 knockdown SKOV3 cells (Fig. 5B). Notably, the ectopic HA-tagged shSUZ12 #1 resistant wild-type SUZ12 protein is expressed at a level lower than the endogenous SUZ12 level observed in SKOV3 cells (Fig. 5A and B), suggesting that the observed effects are not because of supraphysiologic levels of ectopic SUZ12 expression.

### HRK is a SUZ12 target gene that contributes to apoptosis induced by SUZ12 knockdown

Next, we sought to determine the molecular mechanism by which SUZ12 knockdown induces apoptosis of human EOC cells. Toward this goal, we sought to identify the direct SUZ12 target genes that are implicated in promoting apoptosis observed in SUZ12 knockdown EOC cells. We compared the expression of apoptosis-regulating genes

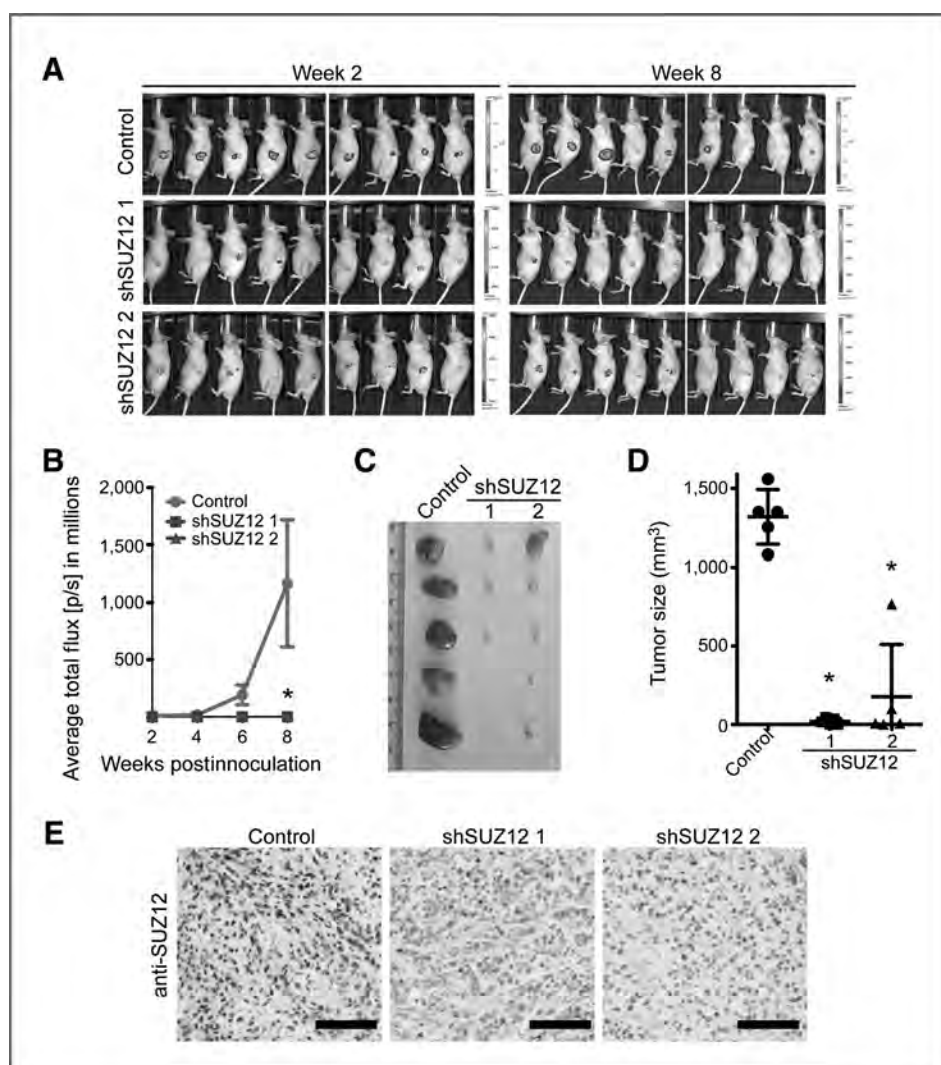


**Figure 3.** SUZ12 knockdown inhibits the growth of human EOC cells *in vivo*. **A**, SKOV3 cells were transduced with luciferase-encoding hygromycin-resistant retrovirus together with a puromycin-resistant shSUZ12 encoding lentivirus or control.  $3 \times 10^5$  drug-selected cells were unilaterally injected into the periovarian bursa sac of the female immunocompromised mice ( $n = 9$  for each of the groups). The radiance of luciferase bioluminescence, an indicator of the rate of tumor growth, was measured every other week from week 2 until week 8 by using the IVIS imaging system. Shown are images taken at week 2 and week 8, respectively. **B**, quantification of tumor growth from the indicated cells. \*,  $P = 0.009$  compared with controls. **C**,  $1 \times 10^5$  drug-selected control and indicated shSUZ12-expressing SKOV3 cells were injected subcutaneously into immunocompromised mice ( $n = 5$  for each of the groups). 5 weeks postinjection, tumors were surgically removed from mice. **D**, quantitation of **C**, the size of tumors was measured. Mean of tumor sizes with SEM.  $P < 0.001$  compared with controls. **E**, xenografted tumors formed by control or indicated shSUZ12-expressing SKOV3 cells were sectioned and stained for SUZ12 expression. Bar = 100  $\mu$ m.

between control and SUZ12 knockdown SKOV3 cells using a qRT-PCR array that consists of 84 apoptosis-regulating genes (Supplementary Table S1 and Fig. S3). We hypothesized that apoptosis-promoting genes are epigenetically silenced by SUZ12 in EOC cells via H3K27Me3 and SUZ12 knockdown induces apoptosis of EOC cells by upregulating the expression of these genes. Thus, we cross-examined the apoptosis-regulating qRT-PCR array data in SKOV3 cells with a H3K27Me3 ChIP followed by next generation sequencing (ChIP-seq) dataset in SKOV3 cells (28). This analysis revealed 2 H3K27Me3 direct target genes that are upregulated more than 2-fold in SUZ12 knockdown SKOV3 cells, namely, *HRK* and *TNFRSF9*.

BH3-only Bcl-2 family member *HRK* is a proapoptotic gene (29). Notably, *HRK* has been implicated in regulating apoptosis of human ovarian cancer cells and murine ovarian reserve (30, 31). Thus, we tested the role of *HRK* in mediating apoptosis induced by SUZ12 knockdown. We confirmed the upregulation of *HRK* in SUZ12 knockdown

SKOV3 cells by qRT-PCR (Fig. 6A). Significantly, we showed that SUZ12 directly binds to the *HRK* genomic locus by ChIP analysis (Fig. 6B). Likewise, we showed that H3K27Me3 epigenetic marker is present in the *HRK* genomic locus (Fig. 6B). Importantly, knockdown of SUZ12 severely diminished the association of SUZ12 and H3K27Me3 with the *HRK* genomic locus (Fig. 6B). This result suggests that the presence of H3K27Me3 in *HRK* genomic locus is dependent upon SUZ12 and the association of SUZ12 to the *HRK* genomic locus is specific. It has previously been shown that DNA methylation contributes to *HRK* downregulation in certain types of cancers such as prostate (32). Thus, we treated EOC cells with 5-azacytidine (5-AzaC), a DNA demethylation drug (33), and examined the expression of *HRK* in these cells. 5-AzaC failed to upregulate *HRK* expression in EOC cells (Supplementary Fig. S4). This result suggests that *HRK* expression is not regulated by DNA methylation in human EOC cells. Consistent with our findings, based on the newly released the Cancer Genome Atlas (TCGA) ovarian cancer database



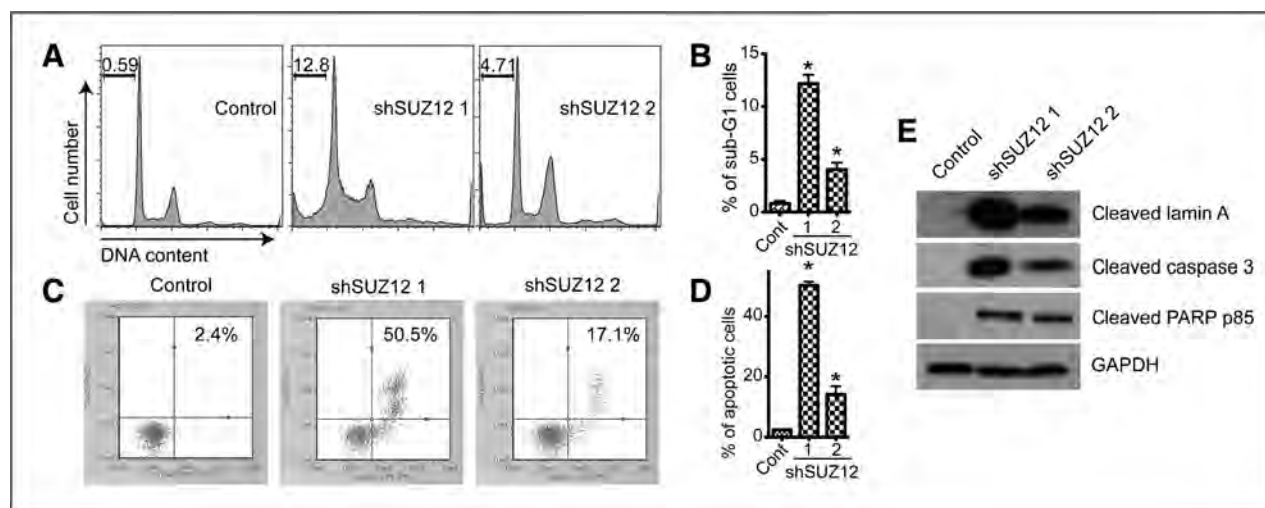


**Figure 4.** SUZ12 knockdown triggers apoptosis of human EOC cells. A, control and shSUZ12 expressing SKOV3 cells were examined for cell-cycle distribution by FACS. The percentage of sub-G<sub>1</sub> cells was indicated. B, quantitation of A. Mean of 3 independent experiments with SD. \*,  $P < 0.001$  compared with controls. C, control and indicated shSUZ12-expressing SKOV3 cells were stained for Annexin V, a cell surface marker of apoptosis. Annexin V-positive cells were measured by Guava Nexin assay. The percentage of Annexin V positive cells was indicated. D, quantitation of C. Mean of 3 independent experiments with SD. \*,  $P < 0.001$  compared with controls. E, same as A and C, but examined for expression of cleaved lamin A, caspase 3 and PARP p85, in control and indicated shEZH2-expressing cells.

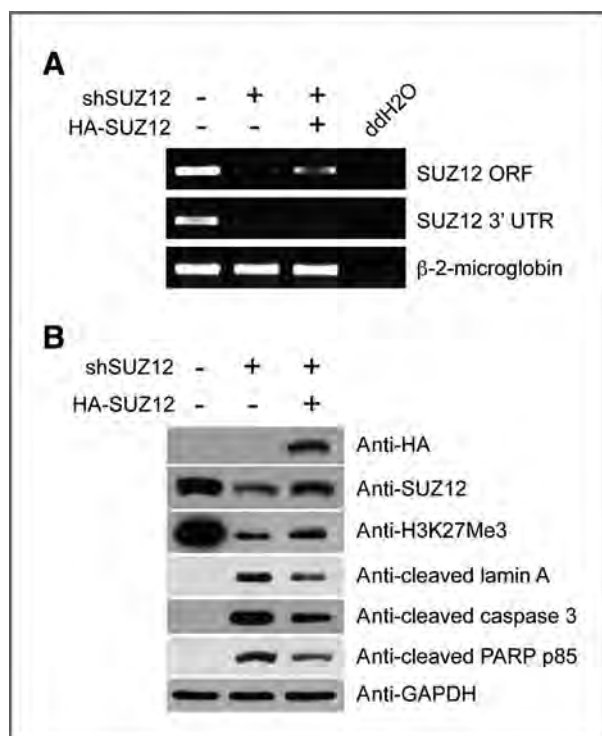


**Figure 5.** shSUZ12 resistant HA-tagged SUZ12 rescues apoptosis induced by SUZ12 knockdown. A, SKOV3 cells were infected with a lentivirus encoding shSUZ12 (#1) together with control or an shSUZ12 resistant SUZ12 that expresses wild type SUZ12 protein. Expression of SUZ12 mRNA was determined by RT-PCR using primers designed to its 3' UTR (only amplifies endogenous but not ectopic SUZ12 mRNA) or its ORF, amplifies both endogenous and ectopic SUZ12 mRNA). B, same as A, but examined for expression of HA, SUZ12, H3K27Me3, GAPDH, and markers of apoptosis including cleaved lamin A, caspase 3, and PARP p85.

(34), *HRK* gene promoter methylation is very rare in human ovarian cancer (<1% cases show >50% of promoter methylation in human *HRK* gene promoter; <http://cancergenome.nih.gov/>; ref. 34).

Next, we sought to determine whether apoptosis induced by SUZ12 knockdown is mediated, in part, by upregulation of *HRK*. Toward this goal, we knocked down the *HRK* expression in SUZ12 knockdown cells. *HRK* knockdown was confirmed by qRT-PCR (Supplementary Fig. S5). Indeed, *HRK* knockdown notably suppressed the expression of markers of apoptosis such as the percentage of sub-G<sub>1</sub> phase cells and expression of cleaved lamin A, PARP p85, and caspase 3, in SUZ12 knockdown cells (Fig. 6C and D and Supplementary Fig. S6). Similar results were also obtained in OVCAR10 human EOC cell line (Supplementary Fig. S7), showing that the observed effects are not cell line specific. On the basis of these results, we conclude that *HRK* is a novel SUZ12 target gene whose upregulation contributes to apoptosis induced by SUZ12 knockdown in human EOC cells.

## Discussion

Herein, we showed that SUZ12 is expressed at significantly higher levels in human EOCs compared with either normal human ovarian surface epithelium or fallopian tube epithelium. SUZ12 is located at 17q21 and gene amplification has been shown to contribute to SUZ12 upregulation in a number of cancer types (20). However, based on the newly released TCGA ovarian cancer database (34), *SUZ12* gene amplification is very rare in human ovarian cancer (<1% cases show >3 copy of *SUZ12* gene; <http://cancergenome.nih.gov/>), suggesting that gene amplification is not a major mechanism that underlies SUZ12 upregulation in human EOCs. Recently, microRNA has also been



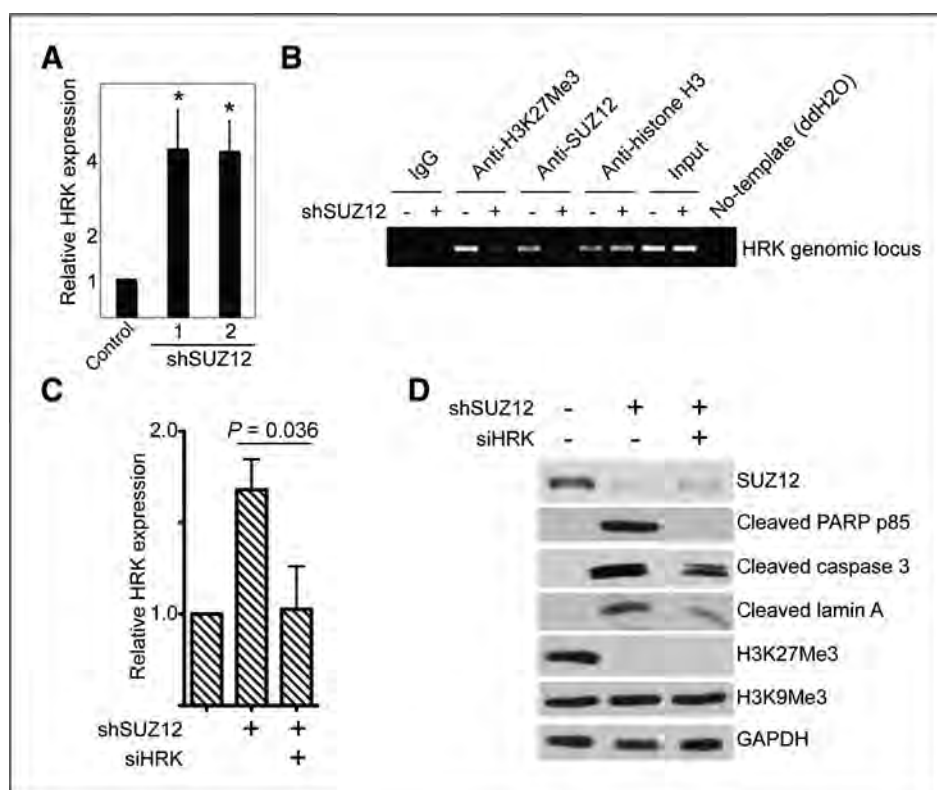


**Figure 6.** *HRK* is a novel SUZ12 target gene whose upregulation contributes to apoptosis induced by SUZ12 knockdown. A, *HRK* mRNA expression was determined in SKOV3 cells expressing indicated shSUZ12 or control by qRT-PCR. Expression of the housekeeping gene  $\beta$ -2-microglobulin was used to normalize mRNA expression. \*,  $P < 0.001$  compared with controls. B, SKOV3 cells expressing shSUZ12 (#1) or control were subjected to ChIP analysis using antibodies against H3K27Me3 or SUZ12 using primers targeted to *HRK* genomic locus. A isotype matched IgG was used as a negative control and an anti-*HRK* core histone H3 antibody was used as a positive control for ChIP analysis. C, SKOV3 cells express shSUZ12 (#1) with or without transfection with siRNA to the human *HRK* gene (siHRK). Expression of *HRK* mRNA in the indicated cells was determined by qRT-PCR. Expression of the housekeeping gene  $\beta$ -2-microglobulin was used to normalize mRNA expression. D, same as A, but examined for expression of SUZ12, H3K27Me3, H3K9Me3, GAPDH, and markers of apoptosis including cleaved lamin A, caspase 3, and PARP p85.

implicated in regulating the expression of SUZ12 (35). Nevertheless, future studies are warranted to elucidate the mechanisms by which SUZ12 is upregulated in human EOCs.

We showed that SUZ12 expression positively correlates with expression of EZH2 in human EOCs (Fig. 1B and Table 1). However, we cannot rule out the possibility that SUZ12 may also have additional EZH2-independent functions in EOC cells. Interestingly, it has previously been reported that H3K27Me3 levels do not correlate with the EZH2 levels in human EOC specimens (36). It is possible that additional factors such as H3K27Me3 demethylase JMJD3 and UTX may also regulate H3K27Me3 levels in EOC cells (37). In addition, SUZ12 expression correlates with expression of a cell proliferation marker, Ki67 (Fig. 1B and Table 1). EZH2 has been shown as a poor prognosis marker in a number of cancer types (38). Similarly, we found that a higher level of SUZ12 expression positively correlates with a poor overall survival in human EOC patients. Collectively, PRC2 could serve as independent prognosis biomarkers for EOCs.

The proapoptotic *HRK* gene is located at 12q13.1 and is transcriptionally regulated in several cancer cell types

(29, 39, 40). Interestingly, we discovered that *HRK* is a novel target of SUZ12-mediated gene silencing via H3K27Me3, and showed that its upregulation contributes to apoptosis induced by SUZ12 knockdown in human EOC cells (Fig. 6). Notably, SUZ12 knockdown severely diminished the H3K27Me3 level (Fig. 2A). Thus, inhibition of SUZ12 by shRNA might affect pathways in addition to *HRK* in these cells. Consistently, it has been shown that SUZ12 also regulates the expression of genes implicated in cell-cycle progression and DNA damage and repair (20). In the future, it will be interesting to investigate additional SUZ12 target genes that contribute to growth inhibition observed in SUZ12 knockdown EOC cells.

We showed that knockdown of SUZ12 is sufficient to decrease the levels of H3K27Me3 in human EOC cells (Fig. 2). This is consistent with the premise that SUZ12 is required for PRC2 complex-mediated gene silencing via H3K27Me3 epigenetic modification. Indeed, SUZ12 expression positively correlates with the expression of EZH2 (Fig. 1B and Table 1). These results suggest that the interaction between SUZ12 and EZH2 may be an alternative target for inactivating PRC2 in addition to the methyltransferase activity of EZH2. Consistently with this idea,

phosphorylation of EZH2 by CDK1 kinase at Thr487 is thought to decrease H3K27Me3 levels by disrupting the interaction between SUZ12 and EZH2 (41).

In summary, the data reported here show that SUZ12 is often overexpressed in human EOCs and its expression positively correlates with EZH2, a high proliferation index, and a poor overall survival in EOC patients. Knockdown of SUZ12 suppresses the growth of human EOC cells *in vitro* and *in vivo* in both orthotopic and s.c xenograft EOC models. Indeed, knockdown of SUZ12 triggers apoptosis of human EOC cells. Furthermore, these observed effects correlate with a decrease in H3K27Me3 level, suggesting that SUZ12 functions via PRC2 to suppress apoptosis of human EOC cells. Mechanistically, we identified the proapoptotic HRK gene as a novel SUZ12 target gene whose upregulation contributes to apoptosis induced by SUZ12 knockdown in human EOC cells.

### Disclosure of Potential Conflict of Interest

No potential conflicts of interest were disclosed.

### References

- Arulkumar S, Regan L, Farquharson DIM. Obstetrics and gynaecology. Oxford: Oxford University Press; 2011.
- Farley J, Ozbun LL, Birrer MJ. Genomic analysis of epithelial ovarian cancer. *Cell Res* 2008;18:538–48.
- Shih Ie M, Kurman RJ. Ovarian tumorigenesis: a proposed model based on morphological and molecular genetic analysis. *Am J Pathol* 2004;164:1511–8.
- Ozols RF, Bookman MA, Connolly DC, Daly MB, Godwin AK, Schilder RJ, et al. Focus on epithelial ovarian cancer. *Cancer Cell* 2004;5:19–24.
- Cao R, Wang L, Wang H, Xia L, Erdjument-Bromage H, Tempst P, et al. Role of histone H3 lysine 27 methylation in Polycomb-group silencing. *Science* 2002;298:1039–43.
- Czermin B, Melfi R, McCabe D, Seitz V, Imhof A, Pirrotta V. Drosophila enhancer of Zeste/ESC complexes have a histone H3 methyltransferase activity that marks chromosomal Polycomb sites. *Cell* 2002;111:185–96.
- Kuzmichev A, Nishioka K, Erdjument-Bromage H, Tempst P, Reinberg D. Histone methyltransferase activity associated with a human multiprotein complex containing the Enhancer of Zeste protein. *Genes Dev* 2002;16:2893–905.
- Muller J, Hart CM, Francis NJ, Vargas ML, Sengupta A, Wild B, et al. Histone methyltransferase activity of a Drosophila Polycomb group repressor complex. *Cell* 2002;111:197–208.
- Cao R, Zhang Y. SUZ12 is required for both the histone methyltransferase activity and the silencing function of the EED-EZH2 complex. *Mol Cell* 2004;15:57–67.
- Ketel CS, Andersen EF, Vargas ML, Suh J, Strome S, Simon JA. Subunit contributions to histone methyltransferase activities of fly and worm polycomb group complexes. *Mol Cell Biol* 2005;25:6857–68.
- Kleer CG, Cao Q, Varambally S, Shen R, Ota I, Tomlins SA, et al. EZH2 is a marker of aggressive breast cancer and promotes neoplastic transformation of breast epithelial cells. *Proc Natl Acad Sci U S A* 2003;100:11606–11.
- Bachmann IM, Halvorsen OJ, Collett K, Stefansson IM, Straume O, Haukaas SA, et al. EZH2 expression is associated with high proliferation rate and aggressive tumor subgroups in cutaneous melanoma and cancers of the endometrium, prostate, and breast. *J Clin Oncol* 2006;24:268–73.
- Varambally S, Dhanasekaran SM, Zhou M, Barrette TR, Kumar-Sinha C, Sanda MG, et al. The polycomb group protein EZH2 is involved in progression of prostate cancer. *Nature* 2002;419:624–9.
- Saramaki OR, Tammela TL, Martikainen PM, Vessella RL, Visakorpi T. The gene for polycomb group protein enhancer of zeste homolog 2 (EZH2) is amplified in late-stage prostate cancer. *Genes Chromosomes Cancer* 2006;45:639–45.
- Bryant RJ, Cross NA, Eaton CL, Hamdy FC, Cunliffe VT. EZH2 promotes proliferation and invasiveness of prostate cancer cells. *Prostate* 2007;67:547–56.
- Li H, Cai Q, Godwin AK, Zhang R. Enhancer of zeste homolog 2 promotes the proliferation and invasion of epithelial ovarian cancer cells. *Mol Cancer Res* 2010;8:1610–8.
- Lu C, Han HD, Mangala LS, Ali-Fehmi R, Newton CS, Ozbun L, et al. Regulation of tumor angiogenesis by EZH2. *Cancer Cell* 2010;18:185–97.
- Bitler BG, Nicodemus JP, Li H, Cai Q, Wu H, Hua X, et al. Wnt5a suppresses epithelial ovarian cancer by promoting cellular senescence. *Cancer Res* 2011;71:6184–94.
- Nicoletti I, Migliorati G, Pagliacci MC, Grignani F, Riccardi C. A rapid and simple method for measuring thymocyte apoptosis by propidium iodide staining and flow cytometry. *J Immunol Methods* 1991;139:271–9.
- Martin-Perez D, Sanchez E, Maestre L, Suela J, Vargiu P, Di Lisio L, et al. Deregulated expression of the polycomb-group protein SUZ12 target genes characterizes mantle cell lymphoma. *Am J Pathol* 2010;177:930–42.
- Ventura A, Kirsch DG, McLaughlin ME, Tuveson DA, Grimm J, Lintault L, et al. Restoration of p53 function leads to tumour regression *in vivo*. *Nature* 2007;445:661–5.
- Tu Z, Aird KM, Bitler BG, Nicodemus JP, Beeharry N, Xia B, et al. Oncogenic RAS regulates BRIP1 expression to induce dissociation of BRCA1 from chromatin, inhibit DNA repair, and promote senescence. *Dev Cell* 2011;21:1077–91.
- Kurman RJ, Shih Ie M. The origin and pathogenesis of epithelial ovarian cancer: a proposed unifying theory. *Am J Surg Pathol* 2010;34:433–43.
- Levanon K, Crum C, Drapkin R. New insights into the pathogenesis of serous ovarian cancer and its clinical impact. *J Clin Oncol* 2008;26:5284–93.
- McCarty KS Jr, Szabo E, Flowers JL, Cox EB, Leight GS, Miller L, et al. Use of a monoclonal anti-estrogen receptor antibody in the immunohistochemical evaluation of human tumors. *Cancer Res* 1986;46:4244s–8s.
- McCarty KS Jr., Miller LS, Cox EB, Konrath J, McCarty KS Sr. Estrogen receptor analyses. Correlation of biochemical and immunohistochem-

### Authors' Contributions

**Conception and design:** H. Li, R. Zhang  
**Development of methodology:** H. Li, Q. Cai, X. Hua, C.N. Landen,  
**Acquisition of data (provided animals, acquired and managed patients, provided facilities, etc.):** Q. Cai, H. Wu, V. Vathipadiekal, Z.C. Dobbin, X. Hua, C.N. Landen, M.J. Birrer,  
**Analysis and interpretation of data (e.g., statistical analysis, biostatistics, computational analysis):** H. Li, Q. Cai, H. Wu, V. Vathipadiekal, T. Li, C.N. Landen, M.J. Birrer,  
**Writing, review, and/or revision of the manuscript:** H. Li, M.J. Birrer, R. Zhang  
**Administrative, technical, or material support (i.e., reporting or organizing data, constructing databases):** X. Hua, C.N. Landen,  
**Study supervision:** R. Zhang  
**Other:** Contribute fundamental materials for research, M. Sanchez-Beato

### Grant Support

R. Zhang is an Ovarian Cancer Research Fund (OCRF) Liz Tilberis Scholar. This work was supported by an NIH/NCI R01 CA163377 in part by a DOD ovarian cancer academy award (OC093420 to R. Zhang). Support of Core Facilities used in this study was provided by Cancer Center Support Grant (CCSG) CA010815 to The Wistar Institute.

The costs of publication of this article were defrayed in part by the payment of page charges. This article must therefore be hereby marked *advertisement* in accordance with 18 U.S.C. Section 1734 solely to indicate this fact.

Received June 4, 2012; revised August 2, 2012; accepted August 17, 2012; published OnlineFirst September 10, 2012.

- ical methods using monoclonal antireceptor antibodies. *Arch Pathol Lab Med* 1985;109:716–21.
27. Jenuwein T. The epigenetic magic of histone lysine methylation. *FEBS J* 2006;273:3121–35.
  28. Li H, Bitler BG, Maradeo ME, Slifker M, Vathipadiekal V, Creasy CL, et al. Aldh1a1 is a novel EZH2 target gene in epithelial ovarian cancer identified by genome-wide approaches. *Cancer Prev Res (Phila)* 2012;5:484–91.
  29. Inohara N, Ding L, Chen S, Nunez G. harakiri, a novel regulator of cell death, encodes a protein that activates apoptosis and interacts selectively with survival-promoting proteins Bcl-2 and Bcl-X(L). *EMBO J* 1997;16:1686–94.
  30. Lin J, Page C, Jin X, Sethi AO, Patel R, Nunez G. Suppression activity of pro-apoptotic gene products in cancer cells, a potential application for cancer gene therapy. *Anticancer Res* 2001;21:831–9.
  31. Jurisicova A, Taniuchi A, Li H, Shang Y, Antenos M, Detmar J, et al. Maternal exposure to polycyclic aromatic hydrocarbons diminishes murine ovarian reserve via induction of Harakiri. *J Clin Invest* 2007;117:3971–8.
  32. Nakamura M, Shimada K, Konishi N. The role of HRK gene in human cancer. *Oncogene* 2008;27 Suppl 1:S105–13.
  33. Baylin SB, Herman JG, Graff JR, Vertino PM, Issa JP. Alterations in DNA methylation: a fundamental aspect of neoplasia. *Adv Cancer Res* 1998;72:141–96.
  34. Integrated genomic analyses of ovarian carcinoma. *Nature* 2011;474:609–15.
  35. Iliopoulos D, Lindahl-Allen M, Polytharchou C, Hirsch HA, Tsiachlis PN, Struhl K. Loss of miR-200 inhibition of Suz12 leads to polycomb-mediated repression required for the formation and maintenance of cancer stem cells. *Mol Cell* 2010;39:761–72.
  36. Wei Y, Xia W, Zhang Z, Liu J, Wang H, Adsay NV, et al. Loss of trimethylation at lysine 27 of histone H3 is a predictor of poor outcome in breast, ovarian, and pancreatic cancers. *Mol Carcinog* 2008;47:701–6.
  37. Swigut T, Wysocka J. H3K27 demethylases, at long last. *Cell* 2007;131:29–32.
  38. Simon JA, Lange CA. Roles of the EZH2 histone methyltransferase in cancer epigenetics. *Mutat Res* 2008;647:21–9.
  39. Imaizumi K, Morihara T, Mori Y, Katayama T, Tsuda M, Furuyama T, et al. The cell death-promoting gene DP5, which interacts with the BCL2 family, is induced during neuronal apoptosis following exposure to amyloid beta protein. *J Biol Chem* 1999;274:7975–81.
  40. Sanz C, Benito A, Inohara N, Ekhterae D, Nunez G, Fernandez-Luna JL. Specific and rapid induction of the proapoptotic protein Hrk after growth factor withdrawal in hematopoietic progenitor cells. *Blood* 2000;95:2742–7.
  41. Wei Y, Chen YH, Li LY, Lang J, Yeh SP, Shi B, et al. CDK1-dependent phosphorylation of EZH2 suppresses methylation of H3K27 and promotes osteogenic differentiation of human mesenchymal stem cells. *Nat Cell Biol* 2011;13:87–94.

# RAS, cellular senescence and transformation

## The BRCA1 DNA repair pathway at the crossroads

Zhigang Tu, Katherine M. Aird and Rugang Zhang<sup>†,\*</sup>

Women's Cancer Program and Epigenetics and Progenitor Cell Keystone Program; Fox Chase Cancer Center; Philadelphia, PA USA

<sup>†</sup>Current affiliation: Gene Expression and Regulation Program; The Wistar Institute; Philadelphia, PA USA

**Keywords:** oncogene, RAS, cellular senescence, cell transformation, DNA damage, BRCA1, BRIP1, B-Myb

**Abbreviations:** PI3K, phosphatidylinositol-3-kinase; shB-Myb, short hairpins RNA to the human B-Myb gene; SA- $\beta$ -gal, senescence-associated beta-galactosidase activity

Submitted: 02/08/12

Accepted: 03/02/12

<http://dx.doi.org/10.4161/sgtp.19884>

\*Correspondence to: Rugang Zhang;  
Email: rzhang@wistar.org

Commentary to: Tu Z, Aird KM, Bitler BG, Nicodemus JP, Beeharry N, Xia B, et al. Oncogenic RAS regulates BRIP1 expression to induce dissociation of BRCA1 from chromatin, inhibit DNA repair, and promote senescence. *Dev Cell* 2011; 21:1077-91; PMID: 22137763.

The definition of an oncogene is a gene that actively promotes tumorigenesis. For example, activation of RAS oncogene promotes cell transformation and cancer. Paradoxically, in primary mammalian cells, oncogenic RAS typically triggers cellular senescence, a state of irreversible cell growth arrest. Oncogene-induced senescence is an important tumor suppression mechanism *in vivo*. Here, we discuss our recent evidence that RAS-induced suppression of DNA repair response via dissociation of BRCA1 from chromatin promotes senescence while predisposing cells to senescence bypass and transformation by allowing for secondary hits. The molecular mechanism we uncovered helps reconcile the tumor-promoting nature of oncogenic RAS with the tumor-suppressing role of oncogene-induced senescence.

Oncogenic mutations in the RAS gene are present in ~30% of human cancers.<sup>1</sup> Oncogenic RAS proteins promote cell transformation through the engagement of downstream pathways such as phosphatidylinositol-3-kinase (PI3K)/AKT and the RAF family of serine/threonine kinases such as BRAF.<sup>2-4</sup> Paradoxically, activation of the RAS oncogene in primary mammalian cells typically induces a status of irreversible cell growth arrest, known as cellular senescence.<sup>5</sup> By driving irreversible growth arrest of cancer progenitor cells harboring the initial oncogenic hit, oncogene-induced senescence is an important tumor suppression mechanism *in vivo*.<sup>5</sup> Further underscoring the importance of senescence

in tumor suppression, reactivation of tumor suppressors such as p53 triggers cellular senescence and associated tumor regression due to activation of the innate immune response in mouse models.<sup>6</sup> Recently, the senescence-associated secretory phenotype has been proposed to be a cell non-autonomous mechanism by which senescent cells promote transformation of neighboring premalignant cells.<sup>5,7</sup> Here, we discuss our recent discovery of a novel cell-intrinsic mechanism by which oncogenic RAS drives cellular senescence while predisposing cells to secondary hits, which ultimately promotes senescence bypass in RAS-expressing primary human cells.<sup>8</sup>

Downstream effectors of RAS such as BRAF and AKT all possess the ability to induce senescence on their own in primary mammalian cells.<sup>9,10</sup> Likewise, inactivation of PTEN, a negative regulator of AKT, also triggers senescence in primary mammalian cells.<sup>11</sup> Notably, there are differences in the senescence induced by different oncogenes. For example, it has been demonstrated that the senescence induced by RAS or BRAF is associated with activation of the DNA damage response.<sup>12</sup> However, senescence induced by AKT or loss of PTEN is independent of the DNA damage response.<sup>13,14</sup> Accordingly, it has been proposed that DNA damage-independent senescence could be utilized as a novel mechanism for developing cancer therapeutics.<sup>13,15</sup> Aberrant DNA replication is thought to be the trigger of the DNA damage response during senescence induced by oncogenic RAS mutants.<sup>12</sup> Consistently, RAS-induced senescence is



dependent upon S phase progression, and inhibition of S phase progression by treating cells with Aphidicolin or contact inhibition blocks RAS-induced senescence.<sup>13</sup> In contrast, senescence induced by loss of PTEN is independent of S phase progression and can occur in quiescent cells.<sup>13</sup> Thus, the difference in DNA damage response observed in senescence induced by different oncogenes is likely due to their ability to trigger aberrant DNA replication.

Aberrant DNA replication induced by oncogenic RAS is transient and occurs only at the very early stages of senescence.<sup>12</sup> However, DNA damage accumulates in fully senescent cells days after aberrant DNA replication in primary human cells, which supposedly have intact DNA repair machinery.<sup>12,14</sup> This evidence suggests that the impairment of DNA repair might contribute to the accumulation of DNA damage during RAS-induced senescence. In support of this idea, we discovered that BRCA1 becomes dissociated from chromatin in RAS-infected primary human cells, and BRCA1-mediated DNA repair response is impaired in these cells.<sup>8</sup> This observation is unique in that other markers of DNA damage that have been reported in the literature, such as ATM, ATR, Chk1, Chk2,  $\gamma$ H2A and 53BP1, are all activated during senescence induced by oncogenic RAS.<sup>12,16</sup> Importantly, BRCA1 chromatin dissociation occurs well before the RAS-induced cell cycle exit,<sup>8</sup> suggesting that this is not a consequence of the senescence-associated cell cycle exit. Moreover, senescence induced by AKT or loss of PTEN is not associated with BRCA1 chromatin dissociation, correlating with a lack in DNA damage response in these cells.<sup>8</sup> This observation further supports the hypothesis that BRCA1 chromatin dissociation is not merely a consequence of senescence. Additionally, BRCA1 chromatin dissociation displays the same kinetics as DNA damage accumulation, and suppression of BRCA1 chromatin dissociation is sufficient to inhibit DNA damage accumulation.<sup>8</sup> Further, BRCA1 knockdown triggers DNA damage and senescence in primary human cells.<sup>8</sup> Together, these findings further support the premise that BRCA1 chromatin dissociation contributes to the

accumulation of DNA damage during RAS-induced senescence.

It is important to note that the levels of activated RAS oncogene determine the outcome of RAS expression. For example, in an inducible H-RAS<sup>G12V</sup> transgenic mouse model, low levels of oncogenic RAS promote cell proliferation, while high levels of oncogenic RAS drive cell senescence.<sup>17</sup> Interestingly, tumorigenesis is associated with enrichment of high RAS induction, senescence and senescence bypass.<sup>17</sup> Notably, the levels of oncogenic H-RAS<sup>G12V</sup> observed in T24, a human bladder cancer cell line, is sufficient to trigger BRCA1 chromatin dissociation in primary human cells.<sup>8</sup> This suggests that physiological level of RAS observed in human cancer cells is sufficient to trigger BRCA1 chromatin dissociation.

As stated previously, oncogene-induced BRCA1 chromatin dissociation well precedes the cell cycle exit during senescence. In addition, oncogenic RAS impairs BRCA1-mediated DNA repair response in cycling RAS-infected cells at a very early stage of senescence.<sup>8</sup> Together, a large time window is created for cells to accumulate secondary oncogenic hits prior to the senescence-associated cell cycle exit, which ultimately leads to senescence bypass in a minority of cells while the vast majority of cells eventually exit from the cell cycle and become senescent. Consistent with this model, RAS-expressing cells accumulate significantly greater DNA damage after IR treatment, and IR treatment promotes senescence bypass in RAS-infected cells.<sup>8</sup> In mouse models, activated oncogenes (such as RAS or BRAF) have been shown to initially induce senescence and formation of benign lesions. However, these lesions ultimately lead to the development of invasive cancer.<sup>17-19</sup> This is consistent with our model whereby oncogenic RAS induces senescence in the vast majority of cells while promoting senescence bypass in a minority of cells, which ultimately outgrow the majority of senescent cells and become transformed.

Interestingly, cells from BRCA1 exon 11 knockout mice display signs of cellular senescence.<sup>20</sup> Exon 11 of the mouse BRCA1 gene encodes for the two BRCT repeats of the BRCA1 protein. Recently, it has been demonstrated that BRCT repeats

are essential for the tumor suppressive function of BRCA1.<sup>21</sup> Notably, we discovered that the C-terminus of BRCA1, which contains two BRCT repeats, is sufficient to be dissociated from chromatin in response to oncogenic RAS.<sup>8</sup> BRCT repeats of BRCA1 bind to phosphorylated partners such as BRIP1, Abbarax/RAP80 and CtIP to form three distinct complexes in a mutually exclusive manner.<sup>22</sup> These distinct complexes regulate activation of checkpoints in response to DNA damage.<sup>22</sup> We found that BRIP1, but not RAP80 or CtIP, is downregulated prior to BRCA1 chromatin dissociation. In addition, BRIP1 knockdown dissociates BRCA1 from chromatin, induces the DNA damage response and triggers cellular senescence. Conversely, ectopic BRIP1 suppresses BRCA1 chromatin dissociation, the DNA damage response and cellular senescence induced by oncogenic RAS.<sup>8</sup> Together, these findings suggest a key role of BRIP1 in regulating RAS-induced senescence.

BRIP1 was first described as a member of the DEAH helicase family that binds to the BRCT repeats of BRCA1.<sup>23</sup> The interaction between BRIP1 and BRCA1 depends upon the phosphorylation of BRIP1 at residue serine 990, which is regulated in a cell cycle-dependent manner.<sup>24</sup> The BRIP1-containing BRCA1 complex is implicated in regulating activation of S phase checkpoint.<sup>25</sup> For example, it has been demonstrated that BRIP1 is required for timely S phase progression.<sup>25</sup> In addition, BRIP1 and BRCA1 facilitate DNA replication during the S phase of the cell cycle by mediating the loading of CDC45L, the replication-licensing factor.<sup>26</sup> Thus, RAS-induced suppression of BRIP1 may promote senescence by driving aberrant DNA replication and activating S phase checkpoints during RAS-induced senescence.

The interaction between BRIP1 and BRCA1 suggests that BRIP1 might be linked to increased cancer risk. Indeed, it has been shown that germline mutations that alter its helicase function or disrupt its interaction with BRCA1 are associated with early-onset breast cancer.<sup>27,28</sup> Counter intuitively, the levels of BRIP1 are elevated in breast carcinoma, and higher levels of BRIP1 are associated with higher tumor

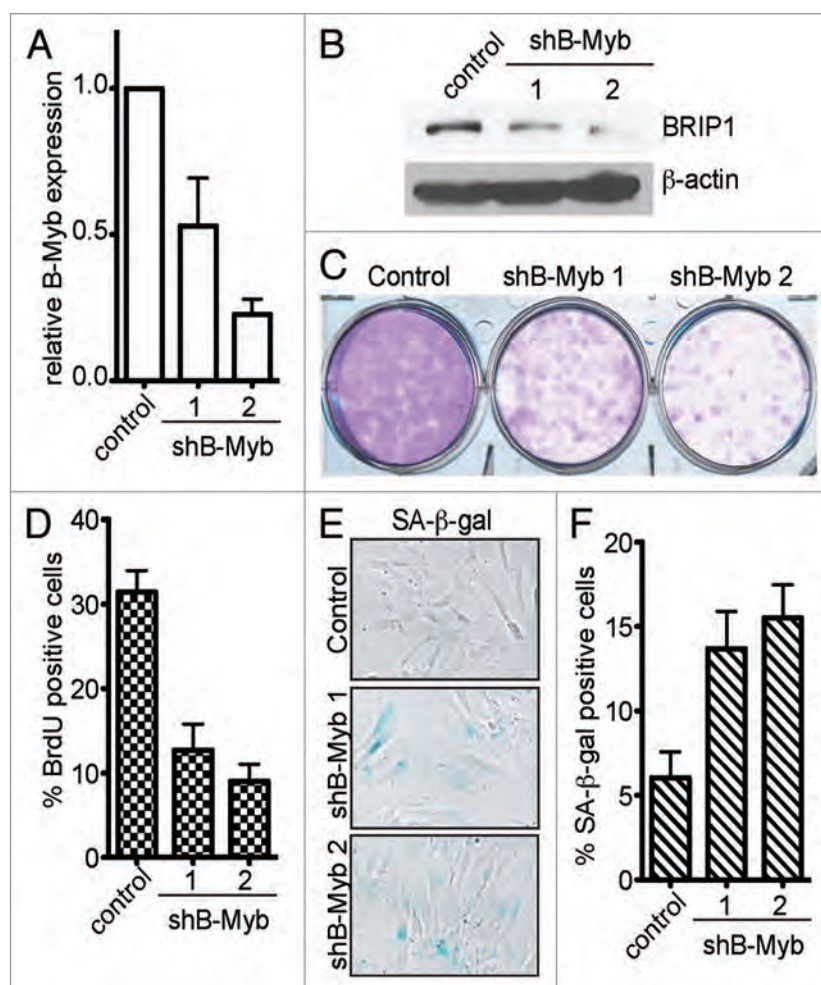


**Figure 1.** B-Myb knockdown suppresses the expression of BRIP1 and induces senescence. (A) IMR90 primary human fibroblasts were infected with lentivirus encoding two individual short hairpin RNAs to the human *B-Myb* gene (shB-Myb) or a control. The sense sequences for the shB-Myb are: 5'-GCT AAC AAC AAA GTT CCA CTT-3' and 5'-CCC AGA TCA GAA GTA CTC CAT-3'. Expression of B-Myb mRNA in the drug-selected cells was determined by qRT-PCR. (B) Same as (A), but examined for BRIP1 and  $\beta$ -actin expression by immunoblot. (C) Same as (A), but equal number of cells ( $1 \times 10^4$ ) were loaded in 6-well plates for 12 d and stained with 0.05% crystal violet for colony formation. (D) Same as (A), but labeled for 1 h with 10  $\mu$ M BrdU, and the percentage of the BrdU positive cells was quantified by immunofluorescence staining. (E) Same as (A), but stained for SA- $\beta$ -gal activity, a marker of cellular senescence. (F) Quantitation of (D). 100 cells from each of the indicated groups were examined for SA- $\beta$ -gal activity. Mean of three independent experiments with SD.

grade.<sup>29</sup> In addition, high levels of BRIP1 positively correlate with HER2 status and expression of Ki67, a marker of cell proliferation.<sup>29</sup> It has been demonstrated that HER2 overexpression drives senescence in primary human mammary epithelial cells.<sup>30</sup> Thus, overexpression of BRIP1 may contribute to breast cancer by promoting proliferation of mammary epithelial cells through suppressing senescence induced by HER2 overexpression.

As discussed above, IR-treatment in RAS-infected cells promotes senescence bypass.<sup>8</sup> In IR-treatment-induced senescence bypassed cells, we show that BRIP1 remains downregulated and BRCA1

remains dissociated from chromatin.<sup>8</sup> This is likely due to selection pressure imposed by exogenous DNA damage treatment. In addition, we observed the accumulation of DNA damage in these senescence-bypassed cells compared with controls.<sup>8</sup> This suggests that DNA repair remains impaired in these RAS-expressing senescence-bypassed cells induced by IR-treatment. Consistently, it has previously been demonstrated that the DNA damage response is attenuated in RAS-expressing transformed cells.<sup>31</sup>

Interestingly, we observed rare colonies that bypassed RAS-induced senescence after extended culture without exogenous

DNA damage treatment.<sup>8</sup> The formation of these colonies may reflect the rare senescence-bypassed cells that are associated with endogenous DNA damage triggered by oncogenic RAS. Thus, it will be interesting to examine the levels of BRIP1 expression and chromatin-associated BRCA1 levels in these cells. Because restoration of BRIP1 expression and suppression of BRCA1 chromatin dissociation inhibits RAS-induced senescence,<sup>8</sup> it is plausible that the senescence bypass observed in these rare colonies is due to restoration of BRIP1 expression and, consequently, rescuing BRCA1 chromatin dissociation. Our model would predict

that these senescence-bypassed cells with restored BRIP1 expression and chromatin-associated BRCA1 levels would be independent of the DNA damage response. Likewise, it will be interesting to determine the levels of DNA damage in HER2 positive breast carcinoma specimens with elevated levels of BRIP1.<sup>29</sup>

RAS-induced BRIP1 downregulation that triggers BRCA1 chromatin dissociation was due to suppression of B-Myb expression,<sup>8</sup> a known regulator of RAS-induced senescence. For example, ectopic B-Myb suppresses senescence of primary mouse embryonic fibroblasts induced by oncogenic RAS.<sup>32</sup> Similar to BRIP1, B-Myb expression is required for S phase entry and acts as a crucial factor for DNA replication during S phase.<sup>33</sup> Depletion of B-Myb triggers aberrant DNA replication and the DNA damage response.<sup>33</sup> Given its role in S phase entry and progression, it is not surprising that gene amplification or overexpression of B-Myb occurs in several types of cancer.<sup>34,35</sup>

B-Myb directly regulates BRIP1 by binding to the proximal promoter region of the human BRIP1 gene.<sup>8</sup> However, it remains to be determined whether B-Myb downregulation is sufficient to induce BRCA1 downregulation and senescence. To address this question, we developed two individual short hairpins RNA to the human *B-Myb* gene (shB-Myb). The efficacy of B-Myb knockdown by the shB-Mybs was confirmed by qRT-PCR (Fig. 1A). Indeed, BRIP1 expression was downregulated in B-Myb knockdown cells (Fig. 1B). Further, B-Myb knockdown suppressed the proliferation of primary human fibroblasts as determined by decreased colony formation and BrdU incorporation (Fig. 1C and D). Consistent with the idea that growth inhibition induced by B-Myb knockdown is due to senescence, expression of SA- $\beta$ -gal, a marker of cellular senescence,<sup>36</sup> was induced in B-Myb knockdown cells (Fig. 1E and F). Together, these data further support that premise that B-Myb is a key regulator of BRIP1 during senescence.

In summary, a very early stage of RAS-induced cellular senescence involves suppression of BRIP1 expression to dissociate BRCA1 from chromatin and thereby impair the BRCA1-mediated DNA repair.

This promotes cellular senescence and senescence-associated accumulation of DNA damage while also allowing for subsequent secondary hits that may predispose rare clones of cells to escape senescence and ultimately contribute to cell transformation. Therefore, this newly discovered cell-intrinsic pathway reconciles the tumor-promoting nature of oncogenic RAS with the tumor-suppressing role of RAS-induced senescence.

#### Acknowledgments

R.Z. is an Ovarian Cancer Research Fund (OCRF) Liz Tilberis Scholar. This work was supported in part by an NCI FCCC-UPenn ovarian cancer SPORE (P50 CA083638) pilot project and SPORE career development award (to R.Z.), a DOD ovarian cancer academy award (OC093420 to R.Z.), a NIH/NCI grant (R01CA160331 to R.Z.), and an OCRF program project (to R.Z.).

#### References

- Bos JL. ras oncogenes in human cancer: a review. *Cancer Res* 1989; 49:4682-9; PMID:2547513.
- Rodriguez-Viciano P, Warne PH, Dhand R, Vanhaesebroeck B, Gout I, Fry MJ, et al. Phosphatidylinositol-3-OH kinase as a direct target of Ras. *Nature* 1994; 370:527-32; PMID:8052307; <http://dx.doi.org/10.1038/370527a0>.
- Warne PH, Viciano PR, Downward J. Direct interaction of Ras and the amino-terminal region of Raf-1 in vitro. *Nature* 1993; 364:352-5; PMID:8332195; <http://dx.doi.org/10.1038/364352a0>.
- Han M, Golden A, Han Y, Sternberg PW. *C. elegans* lin-45 raf gene participates in let-60 ras-stimulated vulval differentiation. *Nature* 1993; 363:133-40; PMID:8483497; <http://dx.doi.org/10.1038/363133a0>.
- Campisi J. Senescent cells, tumor suppression and organismal aging: good citizens, bad neighbors. *Cell* 2005; 120:513-22; PMID:15734683; <http://dx.doi.org/10.1016/j.cell.2005.02.003>.
- Xue W, Zender L, Miething C, Dickins RA, Hernandez E, Krizhanovsky V, et al. Senescence and tumour clearance is triggered by p53 restoration in murine liver carcinomas. *Nature* 2007; 445:656-60; PMID:17251933; <http://dx.doi.org/10.1038/nature05529>.
- Campisi J, d'Adda di Fagnano F. Cellular senescence: when bad things happen to good cells. *Nat Rev Mol Cell Biol* 2007; 8:729-40; PMID:17667954; <http://dx.doi.org/10.1038/nrm2233>.
- Tu Z, Aird KM, Bitler BG, Nicodemus JP, Beeharry N, Xia B, et al. Oncogenic RAS regulates BRIP1 expression to induce dissociation of BRCA1 from chromatin, inhibit DNA repair and promote senescence. *Dev Cell* 2011; 21:1077-91; PMID:22137763; <http://dx.doi.org/10.1016/j.devcel.2011.10.010>.
- Michaloglou C, Vredevelde LC, Soengas MS, Denoyelle C, Kuilman T, van der Horst CM, et al. BRAFE600-associated senescence-like cell cycle arrest of human naevi. *Nature* 2005; 436:720-4; PMID:16079850; <http://dx.doi.org/10.1038/nature03890>.
- Krizhanovsky V, Xue W, Zender L, Yon M, Hernandez E, Lowe SW. Implications of cellular senescence in tissue damage response, tumor suppression and stem cell biology. *Cold Spring Harb Symp Quant Biol* 2008; 73:513-22; PMID:19150958; <http://dx.doi.org/10.1101/sqb.2008.73.048>.
- Chen Z, Trotman LC, Shaffer D, Lin HK, Dotan ZA, Niki M, et al. Crucial role of p53-dependent cellular senescence in suppression of Pten-deficient tumorigenesis. *Nature* 2005; 436:725-30; PMID:16079851; <http://dx.doi.org/10.1038/nature03918>.
- Di Micco R, Fumagalli M, Cicalese A, Piccinin S, Gasparini P, Luise C, et al. Oncogene-induced senescence is a DNA damage response triggered by DNA hyper-replication. *Nature* 2006; 444:638-42; PMID:17136094; <http://dx.doi.org/10.1038/nature05327>.
- Alimonti A, Nardella C, Chen Z, Ciohesy JG, Carracedo A, Trotman LC, et al. A novel type of cellular senescence that can be enhanced in mouse models and human tumor xenografts to suppress prostate tumorigenesis. *J Clin Invest* 2010; 120:681-93; PMID:20197621; <http://dx.doi.org/10.1172/JCI40535>.
- Kennedy AL, Morton JP, Manoharan I, Nelson DM, Jamieson NB, Pawlikowski JS, et al. Activation of the PIK3CA/AKT pathway suppresses senescence induced by an activated RAS oncogene to promote tumorigenesis. *Mol Cell* 2011; 42:36-49; PMID:21474066; <http://dx.doi.org/10.1016/j.molcel.2011.02.020>.
- Nardella C, Ciohesy JG, Alimonti A, Pandolfi PP. Pro-senescence therapy for cancer treatment. *Nat Rev Cancer* 2011; 11:503-11; PMID:21701512; <http://dx.doi.org/10.1038/nrc3057>.
- Di Micco R, Sulli G, Dobrev M, Lontos M, Bottrugno OA, Gargiulo G, et al. Interplay between oncogene-induced DNA damage response and heterochromatin in senescence and cancer. *Nat Cell Biol* 2011; 13:292-302; PMID:21363612; <http://dx.doi.org/10.1038/ncb2170>.
- Sarkisian CJ, Keister BA, Stairs DB, Boxer RB, Moody SE, Chodosh LA. Dose-dependent oncogene-induced senescence in vivo and its evasion during mammary tumorigenesis. *Nat Cell Biol* 2007; 9:493-505; PMID:17450133; <http://dx.doi.org/10.1038/ncb1567>.
- Dankort D, Filenova E, Collado M, Serrano M, Jones K, McMahon M. A new mouse model to explore the initiation, progression and therapy of BRAF<sup>V600E</sup>-induced lung tumors. *Genes Dev* 2007; 21:379-84; PMID:17299132; <http://dx.doi.org/10.1101/gad.1516407>.
- Dhomen N, Reis-Filho JS, da Rocha Dias S, Hayward R, Savage K, Delmas V, et al. Oncogenic Braf induces melanocyte senescence and melanoma in mice. *Cancer Cell* 2009; 15:294-303; PMID:19345328; <http://dx.doi.org/10.1016/j.ccr.2009.02.022>.
- Cao L, Li W, Kim S, Brodie SG, Deng CX. Senescence, aging and malignant transformation mediated by p53 in mice lacking the Brca1 full-length isoform. *Genes Dev* 2003; 17:201-13; PMID:12533509; <http://dx.doi.org/10.1101/gad.1050003>.
- Shakya R, Reid LJ, Reczek CR, Cole F, Egli D, Lin CS, et al. BRCA1 tumor suppression depends on BRCT phosphoprotein binding, but not its E3 ligase activity. *Science* 2011; 334:525-8; PMID:22034435; <http://dx.doi.org/10.1126/science.1209909>.
- Huen MS, Sy SM, Chen J. BRCA1 and its toolbox for the maintenance of genome integrity. *Nat Rev Mol Cell Biol* 2010; 11:138-48; PMID:20029420; <http://dx.doi.org/10.1038/nrm2831>.
- Cantor SB, Bell DW, Ganesan S, Kass EM, Drapkin R, Grossman S, et al. BACH1, a novel helicase-like protein, interacts directly with BRCA1 and contributes to its DNA repair function. *Cell* 2001; 105:149-60; PMID:11301010; [http://dx.doi.org/10.1016/S0092-8674\(01\)00304-X](http://dx.doi.org/10.1016/S0092-8674(01)00304-X).

24. Yu X, Chini CC, He M, Mer G, Chen J. The BRCT domain is a phospho-protein binding domain. *Science* 2003; 302:639-42; PMID:14576433; <http://dx.doi.org/10.1126/science.1088753>.
25. Kumaraswamy E, Shiekhattar R. Activation of BRCA1/BRCA2-associated helicase BACH1 is required for timely progression through S phase. *Mol Cell Biol* 2007; 27:6733-41; PMID:17664283; <http://dx.doi.org/10.1128/MCB.00961-07>.
26. Greenberg RA, Sobhian B, Pathania S, Cantor SB, Nakatani Y, Livingston DM. Multifactorial contributions to an acute DNA damage response by BRCA1/BARD1-containing complexes. *Genes Dev* 2006; 20:34-46; PMID:16391231; <http://dx.doi.org/10.1101/gad.1381306>.
27. Cantor S, Drapkin R, Zhang F, Lin Y, Han J, Pamidi S, et al. The BRCA1-associated protein BACH1 is a DNA helicase targeted by clinically relevant inactivating mutations. *Proc Natl Acad Sci USA* 2004; 101:2357-62; PMID:14983014; <http://dx.doi.org/10.1073/pnas.0308717101>.
28. De Nicolo A, Tancredi M, Lombardi G, Flemma CC, Barbuti S, Di Cristofano C, et al. A novel breast cancer-associated BRIP1 (FANCJ/BACH1) germ-line mutation impairs protein stability and function. *Clin Cancer Res* 2008; 14:4672-80; PMID:18628483; <http://dx.doi.org/10.1158/1078-0432.CCR-08-0087>.
29. Eelen G, Vanden Bempt I, Verlinden L, Drijckoningen M, Smeets A, Neven P, et al. Expression of the BRCA1-interacting protein Brip1/BACH1/FANCJ is driven by E2F and correlates with human breast cancer malignancy. *Oncogene* 2008; 27:4233-41; PMID:18345034; <http://dx.doi.org/10.1038/onc.2008.51>.
30. Ansicau S, Bastid J, Doreau A, Morel AP, Bouchet BP, Thomas C, et al. Induction of EMT by twist proteins as a collateral effect of tumor-promoting inactivation of premature senescence. *Cancer Cell* 2008; 14:79-89; PMID:18598946; <http://dx.doi.org/10.1016/j.ccr.2008.06.005>.
31. Abulaiti A, Fikaris AJ, Tsygankova OM, Meinkoth JL. Ras induces chromosome instability and abrogation of the DNA damage response. *Cancer Res* 2006; 66:10505-12; PMID:17079472; <http://dx.doi.org/10.1158/0008-5472.CAN-06-2351>.
32. Masselink H, Vastenhout N, Bernards R. B-myb rescues ras-induced premature senescence, which requires its transactivation domain. *Cancer Lett* 2001; 171:87-101; PMID:11485831; [http://dx.doi.org/10.1016/S0304-3835\(01\)00631-0](http://dx.doi.org/10.1016/S0304-3835(01)00631-0).
33. Lorvellec M, Dumon S, Maya-Mendoza A, Jackson D, Frampton J, García P. B-Myb is critical for proper DNA duplication during an unperturbed S phase in mouse embryonic stem cells. *Stem Cells* 2010; 28:1751-9; PMID:20715180; <http://dx.doi.org/10.1002/stem.496>.
34. Bar-Shira A, Pinthus JH, Rozovsky U, Goldstein M, Sellers WR, Yaron Y, et al. Multiple genes in human 20q13 chromosomal region are involved in an advanced prostate cancer xenograft. *Cancer Res* 2002; 62:6803-7; PMID:12460888.
35. Thorner AR, Hoadley KA, Parker JS, Winkel S, Millikan RC, Perou CM. In vitro and in vivo analysis of B-Myb in basal-like breast cancer. *Oncogene* 2009; 28:742-51; PMID:19043454; <http://dx.doi.org/10.1038/onc.2008.430>.
36. Dimri GP, Lee X, Basile G, Acosta M, Scott G, Roskelley C, et al. A biomarker that identifies senescent human cells in culture and in aging skin in vivo. *Proc Natl Acad Sci USA* 1995; 92:9363-7; PMID:7568133; <http://dx.doi.org/10.1073/pnas.92.20.9363>.



# Oncogenic Ras Regulates BRIP1 Expression to Induce Dissociation of BRCA1 from Chromatin, Inhibit DNA Repair, and Promote Senescence

Zhigang Tu,<sup>1</sup> Katherine M. Aird,<sup>1</sup> Benjamin G. Bitler,<sup>1</sup> Jasmine P. Nicodemus,<sup>1</sup> Neil Beeharry,<sup>2</sup> Bing Xia,<sup>3</sup> Tim J. Yen,<sup>2</sup> and Rugang Zhang<sup>1,2,\*</sup>

<sup>1</sup>Women's Cancer Program

<sup>2</sup>Epigenetics and Progenitor Cells Keystone Program

Fox Chase Cancer Center, 333 Cottman Avenue, Philadelphia, PA 19111, USA

<sup>3</sup>The Cancer Institute of New Jersey, University of Medicine & Dentistry of New Jersey, Robert Wood Johnson Medical School, New Brunswick, NJ 08901, USA

\*Correspondence: [rugang.zhang@fccc.edu](mailto:rugang.zhang@fccc.edu)

DOI 10.1016/j.devcel.2011.10.010

## SUMMARY

Here, we report a cell-intrinsic mechanism by which oncogenic RAS promotes senescence while predisposing cells to senescence bypass by allowing for secondary hits. We show that oncogenic RAS inactivates the BRCA1 DNA repair complex by dissociating BRCA1 from chromatin. This event precedes senescence-associated cell cycle exit and coincides with the accumulation of DNA damage. Downregulation of BRIP1, a physiological partner of BRCA1 in the DNA repair pathway, triggers BRCA1 chromatin dissociation. Conversely, ectopic BRIP1 rescues BRCA1 chromatin dissociation and suppresses RAS-induced senescence and the DNA damage response. Significantly, cells undergoing senescence do not exhibit a BRCA1-dependent DNA repair response when exposed to DNA damage. Overall, our study provides a molecular basis by which oncogenic RAS promotes senescence. Because DNA damage has the potential to produce additional “hits” that promote senescence bypass, our findings may also suggest one way a small minority of cells might bypass senescence and contribute to cancer development.

## INTRODUCTION

Activation of oncogenes (such as RAS) in primary mammalian cells typically triggers a cascade of molecular and cellular events, which ultimately culminates in a state of irreversible cell growth arrest (Campisi, 2005). This process is termed oncogene-induced senescence and is an important tumor suppression mechanism in vivo (Campisi, 2005). Paradoxically, the definition of an oncogene is a gene that actively promotes tumorigenesis. The mechanism underlying this paradox remains poorly understood.

Senescent cells display several hallmark morphological and molecular characteristics. These cells are positive for senescence-associated  $\beta$ -galactosidase (SA- $\beta$ -gal) activity (Dimri et al., 1995). In addition, chromatin in the nuclei of senescent human cells often reorganizes to form specialized domains of facultative heterochromatin called senescence-associated heterochromatin foci (SAHF) (Braig et al., 2005; Narita et al., 2003, 2006; Zhang et al., 2005, 2007a). SAHF contain markers of heterochromatin, including di- and tri-methylated lysine 9 histone H3 (H3K9Me2/H3K9Me3), histone H2A variant mH2A, and HMGA (Narita et al., 2003, 2006; Zhang et al., 2005). SAHF formation contributes to senescence-induced cell cycle exit by directly sequestering and silencing proliferation-promoting genes (Narita et al., 2003; Zhang et al., 2007a).

Oncogene-induced senescence is often characterized by the accumulation of DNA damage; in particular, DNA double-strand breaks (DSBs) (Bartkova et al., 2006; Di Micco et al., 2006). For example, oncogenic RAS mutants induce DNA damage by triggering aberrant DNA replication (Di Micco et al., 2006). However, it remains to be determined whether impaired DNA repair contributes to the accumulation of DNA damage observed during oncogene-induced senescence.

BRCA1 plays an important role in DNA DSB repair (Scully and Livingston, 2000). Germline mutations in the *BRCA1* gene predispose women to breast and ovarian cancer (Scully and Livingston, 2000), and inactivation of BRCA1 contributes to cancer development by causing genomic instability (Turner et al., 2004). BRCA1 interacts with various DNA damage repair proteins through its two C terminus BRCA1 C-terminal (BRCT) repeats. The BRCT repeats of BRCA1 recognize cognate partners by binding to their phosphoserine residues (Manke et al., 2003; Yu et al., 2003), and their binding partners include BRCA1-interacting protein 1 (BRIP1), CtIP, and RAP80/Abraxas (Wang et al., 2007; Yu et al., 1998, 2003). In addition, BRCA1 interacts with partner and localizer of BRCA2 (PALB2), which is necessary for localization of BRCA2 to DNA DSBs (Xia et al., 2006). Functional BRCA1 is required for localizing/sustaining PALB2 at sites of DNA DSBs and error-free homologous recombination repair (Livingston, 2009; Sy et al., 2009; Zhang et al., 2009). A role for BRCA1 in senescence is implied by findings from the *BRCA1* exon 11 knockout mouse whose cells exhibit

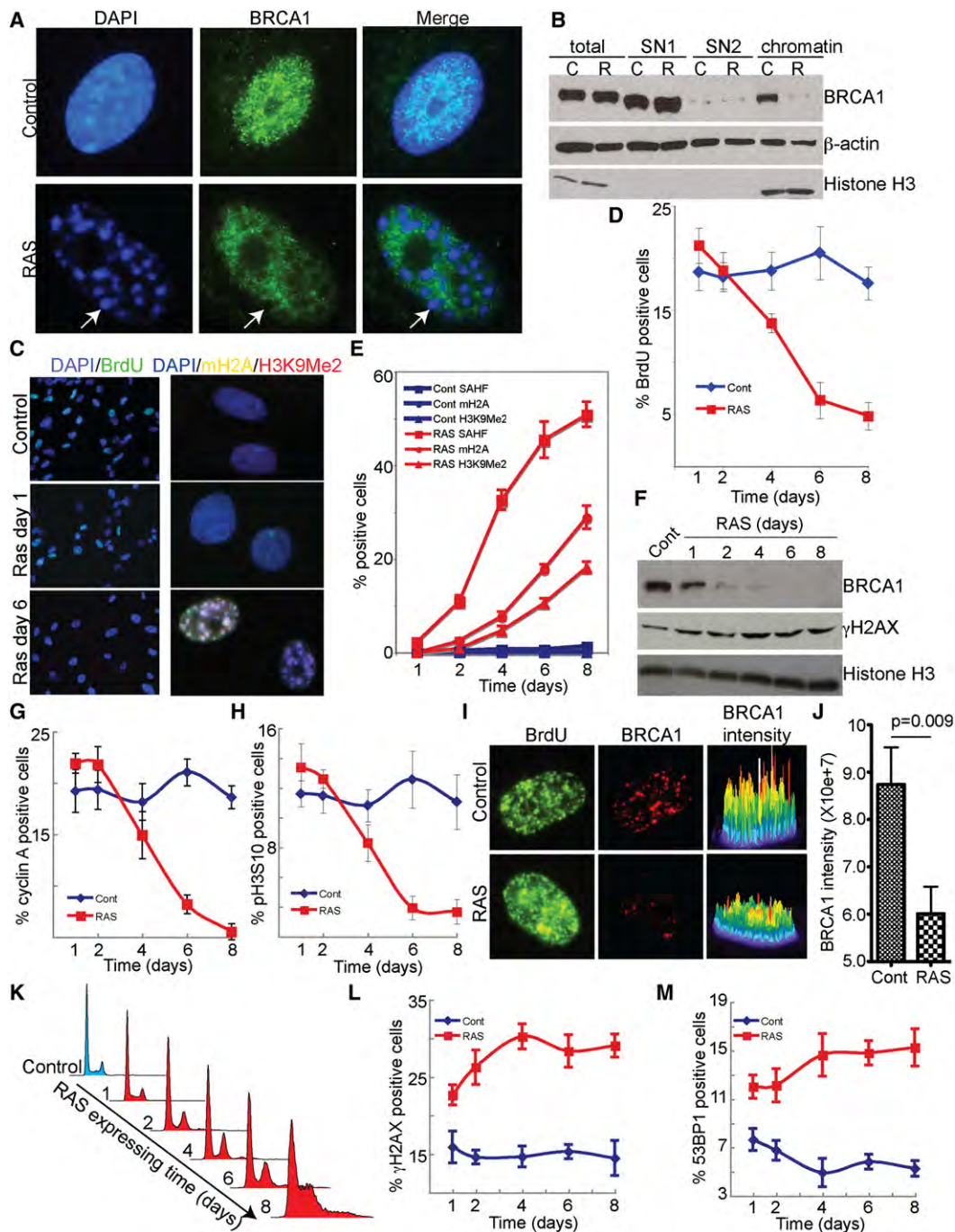


**Figure 1. Oncogene-Induced Dissociation of BRCA1 from Chromatin Occurs prior to the Oncogene-Induced Cell Cycle Exit and Coincides with the Accumulation of DNA Damage during Senescence**

(A) IMR90 cells were infected with retrovirus-encoding control or oncogenic RAS to induce senescence. Drug-selected cells were stained with DAPI to visualize SAHF and an anti-BRCA1 antibody at day 5. Arrows point to an example of BRCA1-excluded SAHF in senescent IMR90 cells.

(B) Same as (A) but examined for expression of BRCA1,  $\beta$ -actin, and histone H3 in soluble (cytoplasmic soluble fraction SN1 and nuclear soluble fraction SN2) and chromatin fractions of control (C) or RAS (R)-infected IMR90 cells by western blot. Note that equal amounts of total proteins were loaded for total cell lysates, SN1, SN2, and chromatin fractions.

(C) Same as (A). At days 1 and 6, control and RAS-infected cells were labeled with BrdU for 1 hr (left) or stained with DAPI to visualize SAHF and antibodies against mH2A and H3K9Me2 that form foci that colocalize with SAHF in senescent human cells (right).

(D and E) Time course of BrdU labeling (D) and formation of SAHF, mH2A, and H3K9Me2 foci (E) in control and RAS-infected IMR90 cells. Mean of three independent experiments with SD.

(F) Same as (D) but examined for expression of BRCA1,  $\gamma$ H2AX, and histone H3 in the chromatin fractions of control and RAS-infected cells at the indicated time points by western blot.

signs of senescence (Cao et al., 2003). These observations suggest that senescence and tumorigenesis pathways may converge on BRCA1-associated DNA damage responses.

Here, we report a cell-intrinsic mechanism by which oncogenic RAS promotes senescence but at the same time predisposes cells to secondary hits, which ultimately leads to senescence bypass.

## RESULTS

### BRCA1 Becomes Dissociated from Chromatin during Oncogenic RAS-Induced Senescence

Senescent cells are characterized by the accumulation of DNA DSBs (Bartkova et al., 2006; Di Micco et al., 2006; Halazonetis et al., 2008), and one of the critical players in DSB repair is BRCA1 (Scully and Livingston, 2000). To test the hypothesis that changes in BRCA1 function occur during oncogene-induced senescence, we first examined changes in the subcellular distribution of BRCA1 during RAS-induced senescence of IMR90 primary human fibroblasts (see Figure S1A available online). BRCA1 immunofluorescence (IF) staining was performed in proliferating (control) and senescent IMR90 primary human fibroblasts induced by RAS. Notably, BRCA1 was excluded from SAHF in senescent cells (Figure 1A). In addition, similar results were obtained using multiple anti-BRCA1 antibodies (one rabbit polyclonal and two individual mouse monoclonal antibodies) (data not shown). We next fractionated protein from proliferating (control) and senescent IMR90 cells into soluble and chromatin fractions (Méndez and Stillman, 2000; Narita et al., 2006) and tested each for the presence of BRCA1. Compared with control cells, BRCA1 levels were dramatically decreased in the chromatin fractions of senescent IMR90 cells (Figure 1B; Figure S1B).

We next sought to exclude the possibility that BRCA1 chromatin dissociation was caused by supra-physiological levels of RAS. To do so, we titrated RAS expression in IMR90 cells to levels lower than those in the classic bladder cancer cell line T24 that harbors an oncogenic RAS mutation (H-RAS<sup>G12V</sup>, the same RAS mutant used in the current study) (Hurlin et al., 1989) (Figure S1C). Importantly, we observed a decrease in BRCA1 levels in the chromatin fractions of RAS-infected IMR90 cells with lower RAS expression than the T24 cells (Figure S1C). Interestingly, BRCA1 levels in the chromatin fractions of T24 cells were also notably lower when compared to IMR90 cells, albeit similar levels of total BRCA1 levels were observed (Figure S1C). Together, our data show that the physiological levels of oncogenic RAS observed in cancerous cells are sufficient to dissociate BRCA1 from chromatin in primary cells.

Next, we asked whether BRCA1 chromatin dissociation is unique to IMR90 cells induced to senesce by RAS. To answer

this question, primary WI38 and BJ human fibroblasts, which both senesce after oncogenic RAS is expressed (Ye et al., 2007; Zhang et al., 2005) (data not shown), were infected with control or RAS-encoding retrovirus. Compared with controls, BRCA1 levels were dramatically decreased in the chromatin fractions of RAS-infected WI38 and BJ cells (Figure S1D). Taken together, these data demonstrate that BRCA1 becomes dissociated from chromatin during RAS-induced senescence.

### BRCA1 Chromatin Dissociation Precedes the Cell Cycle Exit during RAS-Induced Senescence

We next sought to determine whether BRCA1 chromatin dissociation occurs early or late during RAS-induced senescence. Toward this goal, we conducted a detailed time course analysis of chromatin-associated BRCA1, senescence-associated cell cycle exit (determined by BrdU incorporation or expression of cyclin A or serine 10 phosphorylated histone H3 [pH3S10]), and other markers of senescence (such as formation of SAHF, mH2A foci, and H3K9Me2 foci) in control and RAS-infected IMR90 cells (Figures 1C–1H). Strikingly, as early as day 1 (Figure S1A), BRCA1 was largely dissociated from chromatin (Figure 1F; Figure S1K), which is well before the senescence-associated cell cycle exit and accumulation of markers of senescence (Figures 1C–1H).

BRCA1 forms discrete nuclear foci during the S/G2 phases of the cell cycle in normal cycling cells (Durant and Nickoloff, 2005; Scully et al., 1997a; Xu et al., 2001). Therefore, we sought to determine whether RAS expression impairs BRCA1 foci formation in cycling cells. Toward this goal, at day 2, control and RAS-infected IMR90 cells were labeled with BrdU to identify S phase cells. We next pre-extracted soluble proteins from control and RAS-infected cells and stained these cells with antibodies against BRCA1 and BrdU. Indeed, the intensity of BRCA1 foci in BrdU-positive cells was significantly weaker in RAS-infected IMR90 cells compared with controls ( $p = 0.009$ ) (Figures 1I and 1J). This is not simply a consequence of DNA damage because this did not occur in ionizing radiation (IR)-treated cells (Figures S1E and S1F). Furthermore, control and RAS-infected IMR90 cells were stained with antibodies against BRCA1 and cyclin A, a marker of the S/G2 phases of the cell cycle (Erlandsson et al., 2000; Sartori et al., 2007). Consistently, BRCA1 foci were either negative or notably weaker in cyclin A-positive RAS-infected cells compared with controls (Figures S1G and S1H). Finally, FACS analysis revealed that RAS-infected cells accumulated at the S and G2/M phases of the cell cycle compared with controls at this stage (day 2) (Figure 1K; Figures S1I and S1J). From these results, we conclude that oncogene-induced dissociation of BRCA1 from chromatin precedes the oncogene-induced cell cycle exit during senescence.

(G and H) Same as (D) but stained for cyclin A expression (using a mouse anti-cyclin A antibody) (G) or pH3S10 (H) by IF at the indicated time points.

(I and J) At day 2, control and RAS-infected cells were labeled with BrdU for 1 hr, and soluble proteins were pre-extracted (see Experimental Procedures for details). Pre-extracted cells were stained with antibodies against BRCA1 and BrdU. The intensity of BRCA1 staining in BrdU-positive control and RAS-infected cells was quantified using MetaMorph software (J) ( $n = 30$ ).

(K) Same as (D) but examined for cell cycle distribution by flow cytometry.

(L and M) Same as (D) but examined for expression of  $\gamma$ H2AX (L) or 53BP1 (M) expression by IF staining. A total of 200 cells from each of the indicated groups were examined for formation of  $\gamma$ H2AX or 53BP1 foci. Mean of three independent experiments with SD.

See also Figure S1.



### BRCA1 Chromatin Dissociation Coincides with the Accumulation of DNA Damage

We next asked whether BRCA1 chromatin dissociation plays a role in the DNA damage accumulation observed during RAS-induced senescence. Strikingly, accumulation of markers of DNA damage, including formation of  $\gamma$ H2AX and 53BP1 foci, accumulation of  $\gamma$ H2AX in chromatin fractions, and upregulation of p53 displayed the identical kinetics as dissociation of BRCA1 from chromatin in RAS-infected IMR90 cells (Figures 1F, 1L, 1M; Figures S1K–S1O). For example, as early as day 1,  $\gamma$ H2AX had already accumulated in chromatin fractions (Figure 1F; Figure S1K),  $\gamma$ H2AX and 53BP1 foci were increased, and the p53 expression levels were upregulated in RAS-infected IMR90 cells compared with controls (Figures 1L and 1M; Figures S1L–S1O). We conclude that RAS expression results in concomitant BRCA1 chromatin dissociation and DNA damage accumulation.

To determine whether BRCA1 chromatin dissociation is a RAS-specific effect, IMR90 cells were infected with control, RAS, BRAF, or myristylated AKT1 (myr-AKT1)-encoding retrovirus. Ectopic expression of RAS, BRAF, and myr-AKT1 was confirmed by western blot (data not shown). Notably, expression of RAS, BRAF, and myr-AKT1 all induced expression of markers of senescence in IMR90 cells (Figure S2A) (Krizhanovsky et al., 2008; Michaloglou et al., 2005; Xue et al., 2007; Zhang et al., 2005). Next, we examined BRCA1 protein levels in total cell lysates and chromatin fractions of control, RAS, BRAF, and myr-AKT1-infected IMR90 cells by western blot. Strikingly, compared with controls, BRCA1 levels decreased dramatically in the chromatin fractions of RAS and BRAF-infected IMR90 cells, but not in myr-AKT1-infected IMR90 cells (Figure 2A). These results suggest that BRCA1 chromatin dissociation is dependent upon specific oncogenic pathways and is not simply a consequence of senescence.

We next sought to determine whether BRCA1 chromatin dissociation coincides with DNA damage accumulation or is associated with SAHF formation. Toward this goal, control, RAS, BRAF, and myr-AKT1-infected IMR90 cells were stained with DAPI to visualize SAHF and with an antibody to mH2A, which is a component of SAHF (Zhang et al., 2005). Both RAS and BRAF, but not myr-AKT1, induced formation of SAHF and mH2A foci (Figure 2B). Additionally, compared with controls, both RAS and BRAF expression induced formation of  $\gamma$ H2AX and 53BP1 foci and increased levels of chromatin-associated  $\gamma$ H2AX and 53BP1 (Figures 2C–2E). In contrast, myr-AKT1, which did not induce BRCA1 chromatin dissociation, failed to induce formation of  $\gamma$ H2AX and 53BP1 foci or increase the levels of chromatin-associated  $\gamma$ H2AX and 53BP1 (Figures 2C–2E). Consistently, it has been recently reported that cell senescence induced by myr-AKT1 is not associated with SAHF formation or the DNA damage response (Kennedy et al., 2011). Similarly, PTEN knockdown induced expression of markers of senescence but had no effects on BRCA1 chromatin association and also failed to trigger formation of  $\gamma$ H2AX foci or SAHF (Figures S2B–S2G). Likewise, it has been previously shown that senescence induced by loss of PTEN is not associated with the accumulation of DNA damage (Alimonti et al., 2010). The lack of both DNA damage and BRCA1 chromatin dissociation in the PTEN knockdown cells is consistent with the idea that BRCA1 chromatin dissociation contributes to DNA damage accumulation.

We next directly measured the extent of DNA damage in control, RAS, BRAF, and myr-AKT1-infected IMR90 cells using the comet assay. Compared with controls, there was a significant increase in DNA damage in RAS and BRAF-infected IMR90 cells ( $p < 0.05$ ), whereas the difference between control and myr-AKT1-infected IMR90 cells was not significant ( $p > 0.05$ ) (Figures 2F and 2G). The combined data suggest that dissociation of BRCA1 from chromatin coincides with DNA damage accumulation, correlates with SAHF formation, and is independent of PI3K/AKT signaling.

### BRCA1 Knockdown Induces Senescence

We next sought to test whether BRCA1 knockdown is sufficient to drive SAHF formation and senescence in IMR90 cells. Toward this goal, three individual short hairpin RNA to the human *BRCA1* (shBRCA1) genes with different degrees of BRCA1 knockdown efficacy were utilized. BRCA1 knockdown efficiency was confirmed by IF staining and western blot (Figures 3A and 3B). Two individual shBRCA1s (#2 and #3), which efficiently knocked down BRCA1, induced SAHF formation and expression of SA- $\beta$ -gal activity (Figures 3C–3F). Notably, an shBRCA1 (#1) that knocked down BRCA1 with  $\sim 40\%$  efficacy at the total protein level had no effect on SAHF formation or expression of SA- $\beta$ -gal activity (Figures 3A–3F). Interestingly, similar to the hyperproliferation observed in RAS-infected IMR90 cells prior to cell cycle exit (e.g., Figures 1G and 1H; Figure S5) (Di Micco et al., 2006), knockdown of BRCA1 in IMR90 cells also triggers a minor but statistically significant hyperproliferation prior to the cell cycle exit as demonstrated by increased BrdU incorporation (Figure S3A). Consistent with a previous report (Krum et al., 2010), we observed an increase in expression of  $\gamma$ H2AX as well as formation of  $\gamma$ H2AX foci following BRCA1 knockdown (Figures S3B and S3C). We conclude that knockdown of BRCA1 is sufficient to drive senescence.

### Downregulation of BRIP1 Expression Triggers BRCA1 Chromatin Dissociation

Next, we investigated the molecular mechanism underlying BRCA1 chromatin dissociation. Notably, a fragment of the C terminus of BRCA1 (aa 1314–1863) containing two BRCT repeats was sufficient to be dissociated from chromatin in IMR90 cells infected with RAS (Figure S4A), suggesting that factors that interact with the BRCT repeats of BRCA1 may trigger BRCA1 chromatin dissociation.

BRCT repeats of BRCA1 bind to BRIP1, CtIP, and RAP80/Abraxas (Wang et al., 2007; Yu et al., 1998, 2003). Compared with controls, BRIP1 levels in both total cell lysates and the chromatin fractions of RAS-infected cells were dramatically decreased (Figures 4A and 4B; Figure S4B). In contrast, expression levels of CtIP and RAP80 did not overtly change in RAS-infected cells at the same time (Figure 4A). Notably, RAS-induced downregulation of BRIP1 occurred prior to the cell cycle exit, as reflected by the kinetics of cyclin A and pH3S10 expression (Figure 4B). Together, these results suggest that downregulation of BRIP1 may trigger BRCA1 chromatin dissociation in RAS-infected cells.

BRIP1 was first identified as a BRCA1 physiological binding partner (Cantor et al., 2001). We next sought to determine whether BRIP1 is downregulated at the mRNA level in



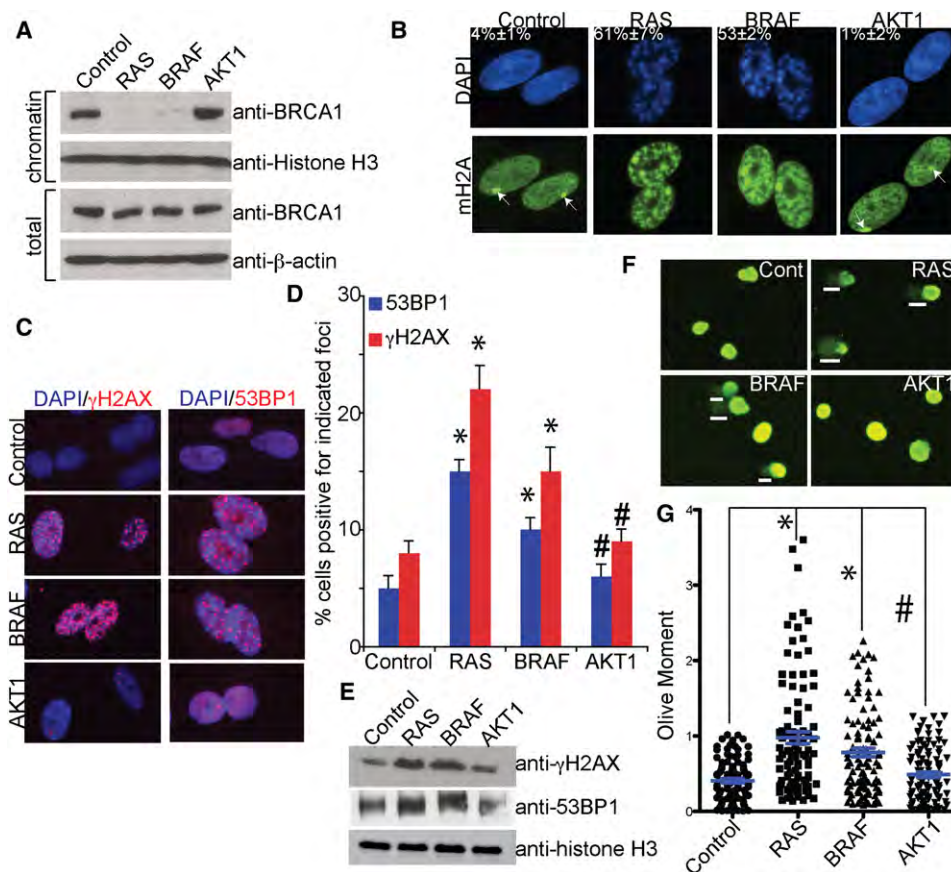


**Figure 2. Oncogene-Induced BRCA1 Chromatin Dissociation Correlates with DNA Damage Accumulation and SAHF Formation**

(A) IMR90 cells were infected with control or the indicated activated oncogene-encoding retrovirus. Expression of BRCA1, histone H3, and  $\beta$ -actin in the chromatin fractions and total cell lysates of indicated cells was assayed by western blot at day 4.

(B) Same as (A) but stained with DAPI and an antibody to mH2A, which is a component of SAHF. Percentage of SAHF-positive cells is indicated. Mean of three independent experiments with SD. Arrows point to mH2A-stained inactivated X chromosome (Costanzi and Pehrson, 1998).

(C) Same as (A) but stained with DAPI or antibodies against  $\gamma$ H2AX or 53BP1.

(D) Quantitation of (C). A total of 200 cells were examined for formation of  $\gamma$ H2AX foci and 53BP1 foci. Cells with more than five nuclear foci for  $\gamma$ H2AX or 53BP1 were counted as positive. Mean of three independent experiments with SD. \* $p < 0.05$  and # $p > 0.05$  as compared to controls.

(E) Expression of  $\gamma$ H2AX, 53BP1, and histone H3 in the chromatin fractions of IMR90 cells infected with vector control or indicated activated oncogenes as determined by western blot.

(F) Same as (A). At day 2, drug-selected indicated cells were assayed for DNA damage by the comet assay. White bars indicate the examples of comet tails that resulted from damaged DNA.

(G) Quantitation of (F). DNA damage from the comet assay is calculated as artificial Olive Moment unit as described in Experimental Procedures. The Olive Moment in 100 cells from each group was measured. Mean of Olive Moment with SEM is shown in blue. \* $p < 0.05$  and # $p > 0.05$  as compared to control.

See also Figure S2.

RAS-infected IMR90 cells. Expression of BRIP1 and BRCA1 mRNA in control and RAS-infected IMR90 cells was examined by quantitative reverse transcriptase-polymerase chain reaction (qRT-PCR). Compared with controls, BRIP1 mRNA levels were significantly decreased as early as day 1 in RAS-infected cells (Figure 4C). However, the BRCA1 mRNA expression level did not statistically change at the same time (Figure 4C). This is consistent with the idea that RAS-induced BRIP1 repression triggers BRCA1 chromatin dissociation prior to RAS-induced cell cycle exit.

We next sought to determine the mechanism underlying BRIP1 downregulation in RAS-infected cells. BRIP1 mRNA expression is downregulated in RAS-infected cells (Figure 4C),

but the stability of BRIP1 mRNA is not decreased by RAS expression (data not shown), suggesting that BRIP1 may be regulated at the transcriptional level. Consistently, the activity of a 400 bp (–300 bp – +100 bp) fragment of the proximal human *BRIP1* gene promoter was significantly suppressed in RAS-infected cells (Figure S4C). Notably, deletion of a critical B-Myb binding site from the *BRIP1* promoter blocked the RAS-mediated suppression of promoter activity, suggesting that B-Myb plays a critical role in suppressing BRIP1 expression in response to RAS (Figure S4C). Interestingly, it has previously been demonstrated that B-Myb suppresses oncogenic RAS induced senescence (Masselink et al., 2001). Consistently, we observed downregulation of B-Myb in RAS-infected cells prior

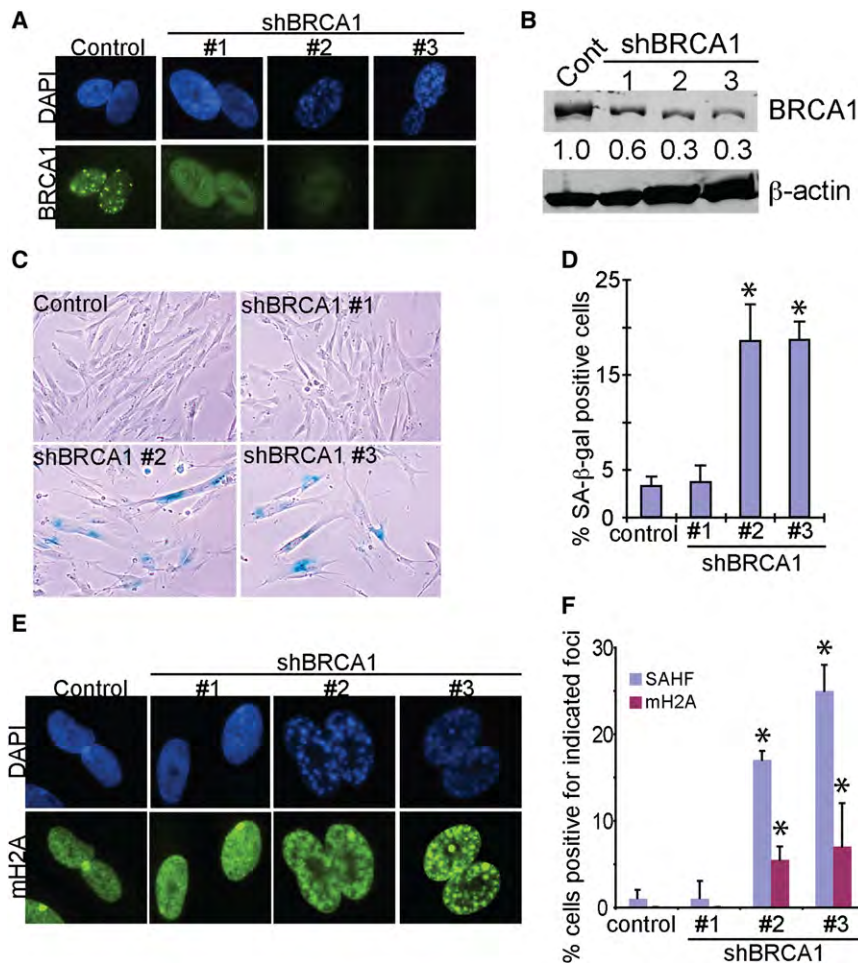


**Figure 3. BRCA1 Knockdown Induces Senescence**

(A) IMR90 cells were infected with lentivirus encoding three individual shRNAs to the human BRCA1 gene or a vector control and stained with an anti-BRCA1 antibody. Note that the BRCA1 nuclear foci in control cells are associated with the S/G2 phases of the cell cycle (Scully et al., 1997b), indicating that the BRCA1 staining is specific.

(B) Same as (A) but assayed for BRCA1 and β-actin expression by western blot. The levels of BRCA1 expression were quantified using the LI-COR Odyssey imaging system (normalized using β-actin as a loading control). Cont, control.

(C) Same as (A) but stained for SA-β-gal activity at day 5.

(D) Quantitation of (C). A total of 100 cells were examined for expression of SA-β-gal activity. Mean of three independent experiments with SD. \*p < 0.03.

(E) Same as (C) but stained with DAPI to visualize SAHF and an antibody against mH2A.

(F) Quantitation of (E). A total of 100 cells were examined for SAHF and mH2A foci formation. Mean of three independent experiments with SD. \*p < 0.02.

See also Figure S3.

to the RAS-induced cells cycle exit (i.e., as early as 12 hr) compared with controls (Figure S4D). Significantly, using an anti-B-Myb antibody, chromatin immunoprecipitation studies demonstrated that the binding of B-Myb to the promoter of the human *BRIP1* gene was significantly reduced in RAS-infected cells compared with controls (Figure 4D). Additionally, it has recently been demonstrated that B-Myb expression is suppressed by upregulation of microRNA 29 (mir29) during senescence (Lafferty-Whyte et al., 2009; Martinez et al., 2011). Consistently, expression of mir29 was upregulated in RAS-infected cells as early as 6 hr compared with controls (Figure S4E). We conclude that RAS-mediated inhibition of B-Myb contributes to the downregulation of BRIP1 during RAS-induced senescence.

Next, we asked whether knockdown of BRIP1 drives BRCA1 chromatin dissociation and senescence. Three individual shRNAs to the human *BRIP1* gene (shBRIP1) were developed, and the efficacy of BRIP1 knockdown was confirmed by western blot (Figure 4E). BRCA1 levels in the chromatin fractions of shBRIP1-expressing cells were greatly reduced when compared to controls (Figure 4E). In addition, we observed an increase in expression of γH2AX in shBRIP1-expressing cells (Figure S4F). Notably, BRIP1 knockdown induced expression of markers of senescence, including SA-β-gal activity and SAHF formation (Figures 4F and 4G). Consistent with this, BRIP1 knockdown

expression of an shBRIP1-resistant wild-type BRIP1 significantly reduced the expression of markers of senescence induced by shBRIP1 (Figures 4H–4J), indicating the specificity of the senescence phenotype induced by BRIP1 knockdown. We conclude that BRIP1 knockdown is sufficient to dissociate BRCA1 from chromatin and induce senescence.

The interaction between BRIP1 and the BRCT repeats of BRCA1 depends on phosphorylation of BRIP1 at serine 990 (S990) (Yu et al., 2003). Thus, we determined whether rescuing of senescence by BRIP1 depends on the phosphorylation of BRIP1 at S990. For this purpose, we made a serine to alanine mutant (S990A) that mimics the nonphosphorylated state of BRIP1 (Yu et al., 2003). Compared with wild-type BRIP1, BRIP1 S990A failed to rescue the senescence induced by BRIP1 knockdown (Figures 4H–4J). This result suggests that the interaction between BRCA1 and BRIP1 plays a critical role in regulating senescence.

#### Ectopic BRIP1 Rescues BRCA1 Chromatin Dissociation and Suppresses RAS-Induced Senescence

We next asked whether ectopic BRIP1 might rescue BRCA1 chromatin dissociation and suppress oncogene-induced senescence. Toward this goal, IMR90 cells were cotransduced with a retrovirus encoding RAS to induce senescence and a retrovirus



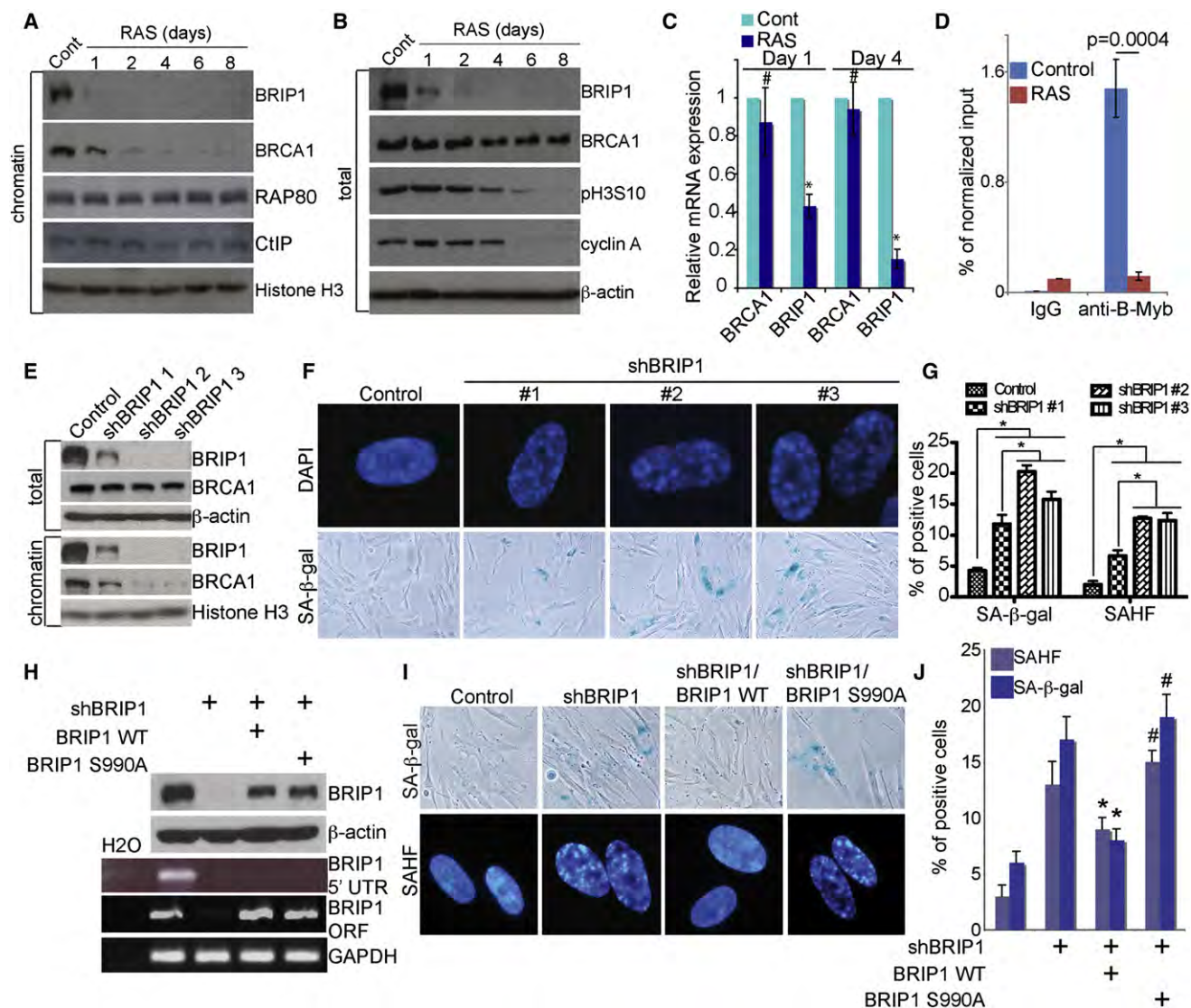


**Figure 4. BRIP1 Repression Triggers BRCA1 Chromatin Dissociation**

(A) IMR90 cells were infected with control (Cont) or RAS-encoding retrovirus. Expression of BRIP1, BRCA1, RAP80, CtIP, and histone H3 in the chromatin fractions of control and RAS-infected IMR90 cells was determined by western blot at the indicated time points.

(B) Same as (A). Expression of BRIP1, BRCA1, pH3S10, cyclin A, and  $\beta$ -actin was determined by western blot at the indicated time points in total cell lysates of control and RAS-infected IMR90 cells.

(C) Same as (A). Expression of BRCA1 and BRIP1 mRNA was determined by qRT-PCR at indicated time points in control and RAS-infected IMR90 cells. Mean of three independent experiments with SD. # $p > 0.05$  and \* $p < 0.01$  versus controls.

(D) Same as (A). Control and RAS-infected cells were subjected to chromatin immunoprecipitation using an anti-B-Myb antibody as detailed in [Experimental Procedures](#). The immunoprecipitated DNA was subjected to quantitative PCR analysis using primers that cover the B-Myb binding site in the promoter of human *BRIP1* gene.

(E) IMR90 cells were infected with lentivirus-encoding shBRIP1 or control. Expression of BRIP1, BRCA1, histone H3, and  $\beta$ -actin in total cell lysates and in chromatin fractions was determined by western blot.

(F) Same as (E) but stained for SA- $\beta$ -gal activity or with DAPI to visualize SAHF.

(G) Quantitation of (F). Mean of four independent experiments with SEM. \* $p < 0.05$ .

(H) IMR90 cells were infected with a lentivirus-encoding shBRIP1 (#3) together with control, an shBRIP1-resistant wild-type BRIP1 (BRIP1 WT), or an shBRIP1-resistant S990A mutant as detailed in the [Experimental Procedures](#). Expression of BRIP1 and  $\beta$ -actin in drug-selected cells was determined by western blot (top). In addition, expression of *BRIP1* mRNA was determined by RT-PCR using primers designed to its 5' UTR region (only amplifies endogenous but not ectopic *BRIP1* mRNA) or its open reading frame (amplifies both endogenous and ectopic *BRIP1* mRNA) (bottom).

(I) Same as (H) but stained for SA- $\beta$ -gal activity or with DAPI to visualize SAHF.

(J) Quantitation of (I). Mean of three independent experiments with SD. \* $p < 0.05$  and # $p > 0.05$  compared with only shBRIP1-expressing cells.

See also [Figure S4](#).

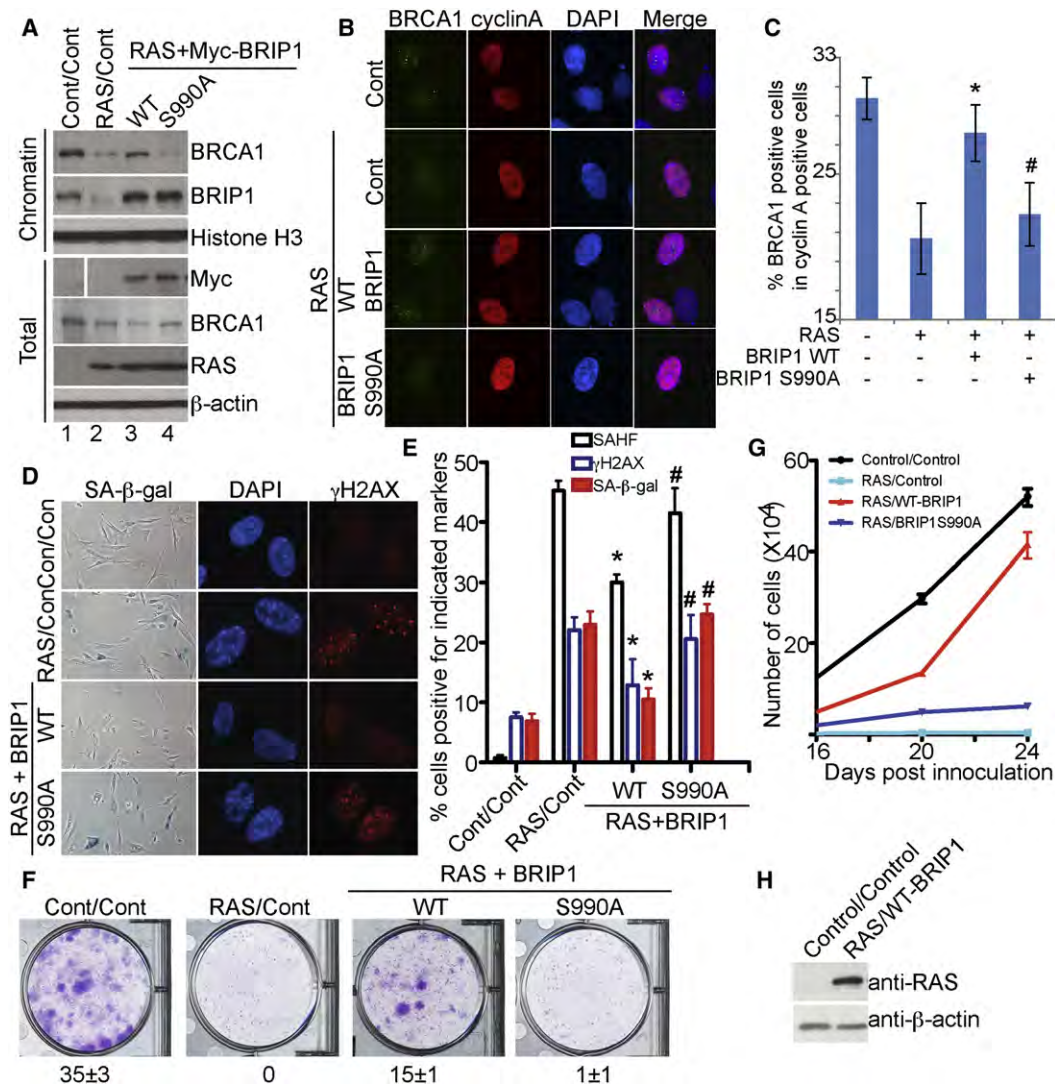


**Figure 5. Ectopic BRIP1 Rescues BRCA1 Chromatin Dissociation and Suppresses Oncogene-Induced Senescence and DNA Damage Response**

(A) IMR90 cells were infected with retroviruses encoding RAS together with control (Cont), Myc-tagged wild type (WT) BRIP1, or BRIP1 S990A mutant. At day 4, drug-selected cells were examined for expression of BRCA1, BRIP1, and histone H3 in the chromatin fractions and for expression of Myc-tagged ectopic BRIP1, BRCA1, RAS, and  $\beta$ -actin in total cell lysates.

(B) Same as (A) but stained with antibodies against BRCA1 and cyclin A.

(C) Quantitation of (B). A total of 100 cyclin A-positive cells were examined for BRCA1 foci formation. Mean of three independent experiments with SD. \* $p < 0.05$  and # $p > 0.05$  compared with RAS-infected controls.

(D) Same as (A) but stained for SA- $\beta$ -gal activity or DAPI to visualize SAHF or an antibody against  $\gamma$ H2AX to detect DNA damage.

(E) Quantitation of (D). Mean of four independent experiments with SD. \* $p < 0.015$  and # $p > 0.12$  versus RAS-infected control cells.

(F) Same as (A) but equal numbers of cells ( $3 \times 10^3$  cells/well) were plated in 6-well plates in triplicate for focus formation assays. After 2 weeks in culture, the plates were stained with 0.05% crystal violet in PBS to visualize foci. Shown are representative images of four independent experiments. Number of foci is indicated as mean with SD.

(G) Same as (F), but the number of cells was counted at indicated time points. Mean of three independent experiments with SD.

(H) Control and the senescence-bypassed cells isolated from (G) were examined for RAS and  $\beta$ -actin expression by western blot.

See also Figure S5.

encoding a Myc-tagged wild-type BRIP1 or control. Compared with controls, BRIP1 expression notably rescued the levels of BRCA1 in the chromatin fractions of RAS-infected cells (Figure 5A, lane 2 versus lane 3). This was not due to a lower RAS expression level because RAS was expressed at a higher level in ectopic

BRIP1-expressing cells compared to controls (Figure 5A, lane 2 versus lane 3). In addition, the total BRCA1 protein level was not increased by ectopic BRIP1 (Figure 5A, lane 2 versus lane 3), implying that the increased level of chromatin-associated BRCA1 was not due to increased levels of total BRCA1.



Notably, ectopic BRIP1 restored BRCA1 foci formation in cyclin A-positive RAS-infected cells (Figures 5B and 5C). Interestingly, ectopic BRIP1 did not affect RAS-induced hyperproliferation (Figure S5), a trigger of the DNA damage response (Di Micco et al., 2006), suggesting that ectopic BRIP1 may instead affect DNA repair. In addition, expression of ectopic BRIP1 in RAS-infected cells suppressed expression of markers of senescence including SA- $\beta$ -gal activity, SAHF formation, and senescence-induced cell growth arrest, and inhibited DNA damage response revealed by decreased  $\gamma$ H2AX foci formation when compared to controls (Figures 5D–5H). These data further support the conclusion that BRIP1 plays a major role in BRCA1 chromatin association during RAS-induced senescence.

We next sought to determine whether suppression of BRCA1 chromatin dissociation by BRIP1 depends on the phosphorylation of BRIP1 at S990. Compared with wild-type BRIP1, the BRIP1 S990A mutant failed to rescue BRCA1 chromatin dissociation in RAS-infected cells (Figure 5A, lane 3 versus lane 4) and was also impaired in restoring BRCA1 foci in cyclin A-positive RAS-infected cells (Figures 5B and 5C). These results imply that the interaction between BRIP1 and BRCA1 is necessary for suppression of BRCA1 chromatin dissociation by BRIP1. Notably, the BRIP1 S990A mutant failed to suppress senescence and its associated DNA damage accumulation in RAS-infected IMR90 cells (Figures 5D–5G). We conclude that suppression of senescence by ectopic BRIP1 is dependent on its interaction with BRCA1.

#### Oncogenic RAS Impairs the BRCA1-Mediated DNA Repair Response prior to RAS-Induced Cell Cycle Exit during Senescence

We next asked whether oncogene-induced BRCA1 chromatin dissociation inactivates the BRCA1-mediated DNA repair response. Upon DNA damage BRCA1 foci largely disappear in normal cycling cells, although new damage-induced foci form hours after DNA damage during the S/G2 phase of the cell cycle (Chen et al., 1998; Durant and Nickoloff, 2005; Scully et al., 1997a; Xu et al., 2001). To determine the effects of oncogenic RAS expression on the BRCA1-mediated DNA repair response, at day 2, control and RAS-infected IMR90 cells were treated with 2 Gy of IR to induce DNA DSBs. Notably, IR did not prevent BRCA1 chromatin dissociation in RAS-infected cells (Figure 6A). This was not due to a lack of DNA damage induction by IR in RAS-infected cells because nearly 100% of both control and RAS-infected cells were positive for  $\gamma$ H2AX foci (Figure 6B). We next examined formation of damage-induced BRCA1 foci in the S/G2 phases of cycling cells by costaining cells with antibodies against BRCA1 and cyclin A 5 hr after IR treatment (Peng et al., 2006; Zhang et al., 2009). As expected, BRCA1 foci were significantly induced upon IR treatment in controls (Figures 6C and 6D). However, formation of damage-induced BRCA1 foci was severely impaired in RAS-infected IMR90 cells when exposed to IR (Figures 6C and 6D).

Functional BRCA1 is required for relocating/sustaining BRCA2 and its partner protein PALB2 at damage-induced foci (Sy et al., 2009; Zhang et al., 2009), which are critical for BRCA1-mediated DNA DSB repair (Huen et al., 2010). Consistently, formation of damage-induced BRCA2 and PALB2 foci was also significantly

impaired in RAS-infected cells upon IR treatment compared to controls (Figures 6E–6G). Based on these results, we conclude that oncogenic RAS impairs the BRCA1-mediated DNA repair response prior to the RAS-induced cell cycle exit during senescence.

#### DNA Damage Promotes Senescence Bypass in RAS-Infected Cells

The impaired ability of BRCA1 to repair DNA damage promotes genomic instability, facilitates acquisition of oncogenic alterations, and ultimately drives tumorigenesis (Turner et al., 2004). Thus, we anticipated that impaired BRCA1-mediated DNA repair might lead to DNA damage accumulation and allow for accumulation of secondary hits that might promote senescence bypass. Consistently, we reproducibly observed rare foci of senescence-bypassed cells in RAS-infected IMR90 cells (Figure S6A). RAS remains overexpressed in those cells (Figure S6B), suggesting that senescence bypass is not due to loss of ectopic RAS expression. To directly test our hypothesis, control and RAS-infected IMR90 cells were treated with 2 Gy IR at day 2, and the extent of DNA damage was measured by the comet assay. At this time point, BRCA1 was largely dissociated from chromatin in RAS-infected proliferative cells (Figure 1F). There was increased DNA damage in IR-treated RAS-infected cells, which was significantly greater than either IR-treated control cells or RAS-infected cells without IR treatment ( $p < 0.05$ ) (Figures 7A and 7B). Notably, ectopic expression of wild-type BRIP1, but not the BRIP1 S990A mutant, suppressed the DNA damage accumulation in IR-treated RAS-infected cells (Figures 7C and 7D).

We next sought to determine whether this decreased ability to repair DNA might lead to senescence bypass. We tested this by focus formation and cell growth assays. Indeed, IR treatment consistently induced senescence bypass as evidenced by both focus formation and apparent cell growth in IR-treated cells compared to controls (Figures 7E and 7F). Notably, senescence-bypassed cells formed colonies under anchorage-independent growth condition in soft agar (Figures 7G and 7H). As a negative control, IR did not promote the proliferation of control cells (Figure 7E; Figures S6D and S6E). To eliminate the possibility that senescence bypass observed in IR-treated cells was due to loss of ectopic RAS, these cells were isolated and analyzed by western blot for exogenous RAS expression. Compared with controls, RAS remained greatly overexpressed in the senescence-bypassed cells (Figure 7I). In addition, pRB was hyperphosphorylated, and p53 expression was reduced in the senescence-bypassed cells (Figure 7J), suggesting that inactivation of the key senescence-promoting pRB and p53 pathways contributes to the senescence bypass induced by IR treatment. Notably, IR treatment has no effect on senescence-associated cell growth arrest once RAS-infected cells have exited from cell cycle (e.g., at day 7) (Figures S6C–S6E). This result suggests that the senescence bypass observed in IR-treated RAS-infected cells is not due to the preexistence of senescence-resistant cells. Ectopic BRIP1 suppresses senescence (Figures 5D–5H), which prevented us from determining whether rescuing BRCA1 chromatin dissociation by ectopic BRIP1 inhibits IR treatment-induced senescence bypass in RAS-infected cells.

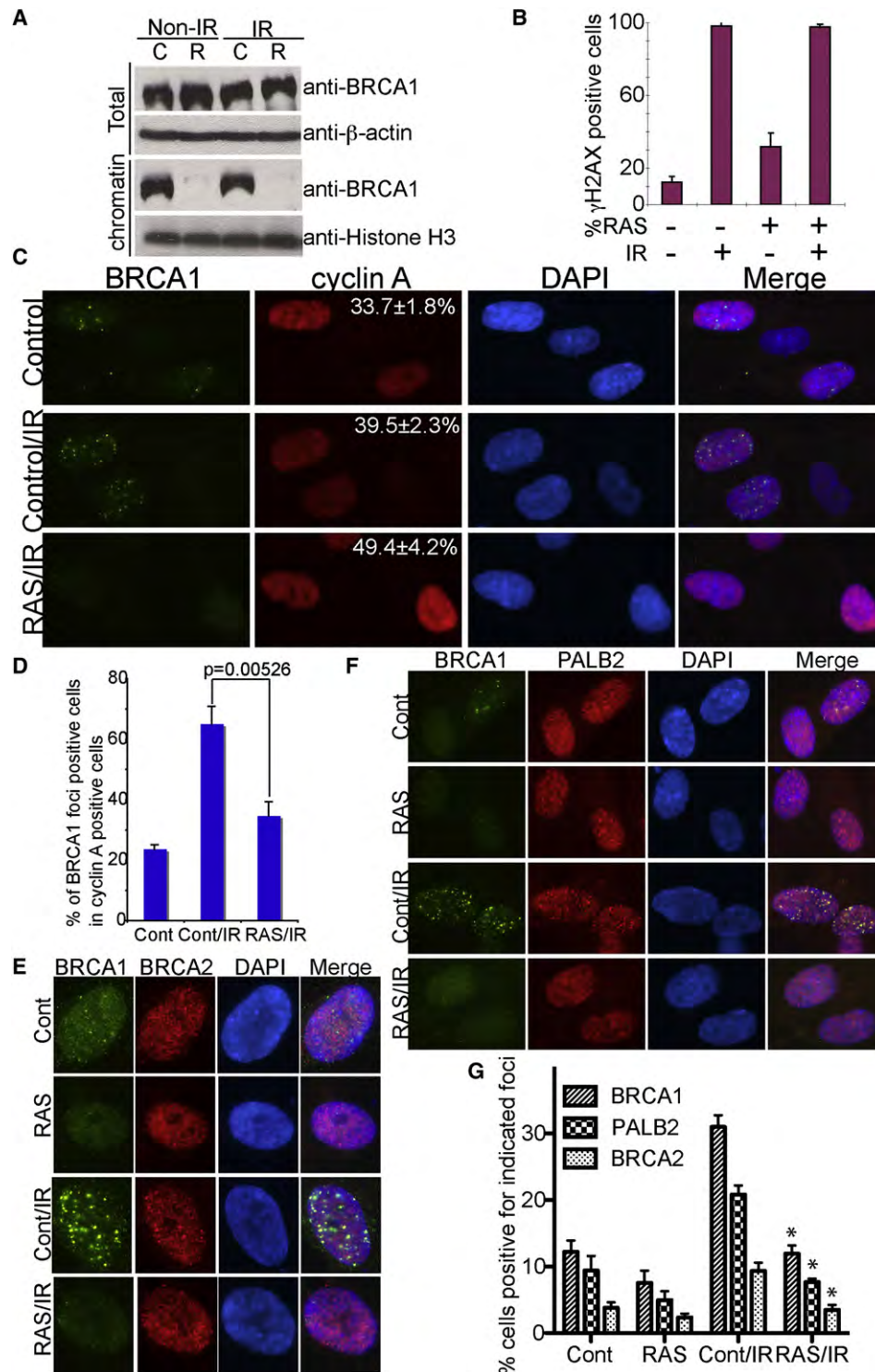


**Figure 6. BRCA1-Mediated DNA Repair Response Is Impaired prior to the Oncogene-Induced Cell Cycle Exit**

(A) IMR90 cells were infected with control (C) or RAS (R)-encoding retrovirus. At day 2, drug-selected cells were treated with or without 2 Gy IR. After 5 hr of recovery, expression of BRCA1, histone H3, and  $\beta$ -actin in total cell lysates and in the chromatin fractions was determined by western blot.

(B) Same as (A) but quantified for  $\gamma$ H2AX foci formation in the indicated groups. Mean of three independent experiments with SD.

(C) Same as (A) but stained with antibodies against BRCA1 and cyclin A (using a rabbit anti-cyclin A antibody). Percentage of cyclin A-positive cells is indicated as mean of three independent experiments with SD.

(D) Quantitation of (C). A total of 100 cyclin A-positive cells from each of the indicated groups were examined for BRCA1 foci formation. Mean of three independent experiments with SD.

If senescence bypass in IR-treated cells is achieved through accumulation of DNA damage and acquisition of secondary hits due to BRCA1 chromatin dissociation induced by BRIP1 repression, we anticipated that BRIP1 might remain downregulated, and BRCA1 might remain dissociated from chromatin in the senescence-bypassed cells. Indeed, compared with controls, BRIP1 remained downregulated, and BRCA1 remained dissociated from chromatin in the senescence-bypassed cells (Figure 7K). These results further support the idea that BRCA1 chromatin dissociation is not merely a consequence of senescence-associated cell cycle exit because the senescence-bypassed cells are highly proliferative. In addition, markers of DNA damage (such as  $\gamma$ H2AX and 53BP1 foci) were expressed at higher levels in the senescence-bypassed cells compared to controls (Figures 7L–7N). This is consistent with the idea that BRCA1 chromatin dissociation contributes to DNA damage accumulation in those cells. Together, these results suggest that the loss of BRCA1-mediated DNA repair may also allow for subsequent hits that ultimately enable a small fraction of Ras-induced cells to bypass senescence.

## DISCUSSION

Our study reveals that oncogenic RAS induces dissociation of BRCA1 from chromatin prior to the cell cycle exit during RAS-induced senescence. This dissociation of BRCA1 from chromatin coincides with DNA damage accumulation. Downregulation of BRIP1, a BRCA1-binding partner, contributes to BRCA1 chromatin dissociation. Conversely, ectopic BRIP1 rescues BRCA1 chromatin dissociation and suppresses RAS-induced senescence. Significantly, the BRCA1-mediated DNA repair response is impaired prior to the RAS-induced cell cycle exit, which renders cells susceptible to the accumulation of secondary hits. In some instances this may ultimately allow for senescence bypass.

### The Role of BRCA1 Chromatin Dissociation during Oncogene-Induced Senescence

DNA damage persists in senescent cells (Rodier et al., 2009), suggesting that defects in DNA repair may contribute to the accumulation of DNA damage observed during senescence. Our data reveal that BRCA1 chromatin dissociation coincides with DNA damage accumulation, which occurs as early as the hyperproliferation phase in RAS-infected cells (Figures 1F–1H, 1L, and 1M). A previous report by Di Micco et al. (2006) showed that the accumulation of DNA damage closely follows the hyperproliferation phase in RAS-infected cells during senescence. The basis for this minor discrepancy between these two reports remains to be determined. It could be due to quantitative approaches used in the current study, which make it easier to reveal subtle differences at early stages (Figures 1L and 1M). We showed that BRCA1 chromatin dissociation correlates with the DNA damage response in both RAS and BRAF-infected cells

(Figure 2). Furthermore, BRCA1 knockdown in primary human cells triggers the DNA damage response and induces senescence (Figure 3; Figure S3B and S3C). Finally, suppression of BRCA1 chromatin dissociation by ectopic BRIP1 suppresses the DNA damage induced by oncogenic RAS (Figures 5B–5E). Together, these results support the notion that BRCA1 chromatin dissociation contributes to the accumulation of DNA damage during oncogene-induced senescence.

Herein, we demonstrated that RAS-induced dissociation of BRCA1 from chromatin precedes SAHF formation (Figures 1C–1F), and BRCA1 knockdown drives SAHF formation (Figure 3). Furthermore, BRCA1 chromatin dissociation correlates with SAHF formation in IMR90 cells expressing RAS and BRAF oncogenes (Figures 2A and 2B). Consistent with this idea that BRCA1 antagonizes heterochromatin formation and/or maintenance, it has been previously demonstrated that targeting BRCA1 to an amplified lac operator-containing chromosome region in the mammalian genome results in large-scale chromatin unfolding (Ye et al., 2001). We were unable to ectopically express wild-type BRCA1 in primary human cells (data not shown), which prevented us from determining whether ectopically expressed BRCA1 might suppress SAHF formation. However, ectopic BRIP1 was able to rescue BRCA1 chromatin dissociation and suppress SAHF formation (Figures 5D and 5E). Together, these findings support the idea that BRCA1 chromatin dissociation promotes senescence by contributing to SAHF formation.

Suppression of the DNA damage response by ectopic BRIP1 inhibits SAHF formation (Figures 5B–5E). Conversely, knockdown of BRCA1, which induces DNA damage, drives SAHF formation (Figure 3; Figure S3). In addition, AKT or shPTEN, neither of which dissociates BRCA1 from chromatin, also fails to induce a DNA damage response or SAHF formation (Figure 2; Figure S2). Together, these data suggest that DNA damage response triggered by BRCA1 chromatin dissociation is required for SAHF formation. Indeed, there is evidence to suggest that formation of SAHF limits the degree of DNA damage response during oncogene-induced senescence (Di Micco et al., 2011). However, the DNA damage response is not sufficient for SAHF formation, which also requires activation of p16/pRB and HIRA/PML pathways (Narita et al., 2003; Ye et al., 2007; Zhang et al., 2005, 2007a). Overall, these results support the notion that DNA damage is necessary but not sufficient for SAHF formation.

### The Role of BRIP1 Repression during Oncogene-Induced Senescence

Stable BRIP1 knockdown reduces damage-induced BRCA1 foci formation, and BRIP1-deficient cells demonstrate defects in the number and intensity of BRCA1 foci (Peng et al., 2006). This suggests that BRIP1 plays an important role in BRCA1-mediated DNA repair. BRIP1 has been shown to be significantly downregulated in response to RAS expression in primary human fibroblasts based on gene expression microarray analysis, while

(E) Same as (C) but stained with antibodies against BRCA1 and BRCA2.

(F) Same as (C) but stained with antibodies against BRCA1 and PALB2.

(G) Quantitation of results from (E) and (F). A total of 100 cells from each of the indicated group were examined for BRCA1, BRCA2, and PALB2 foci formation. Mean of three independent experiments with SD. \* $p < 0.02$  versus control IR-treated cells. Cont, control.



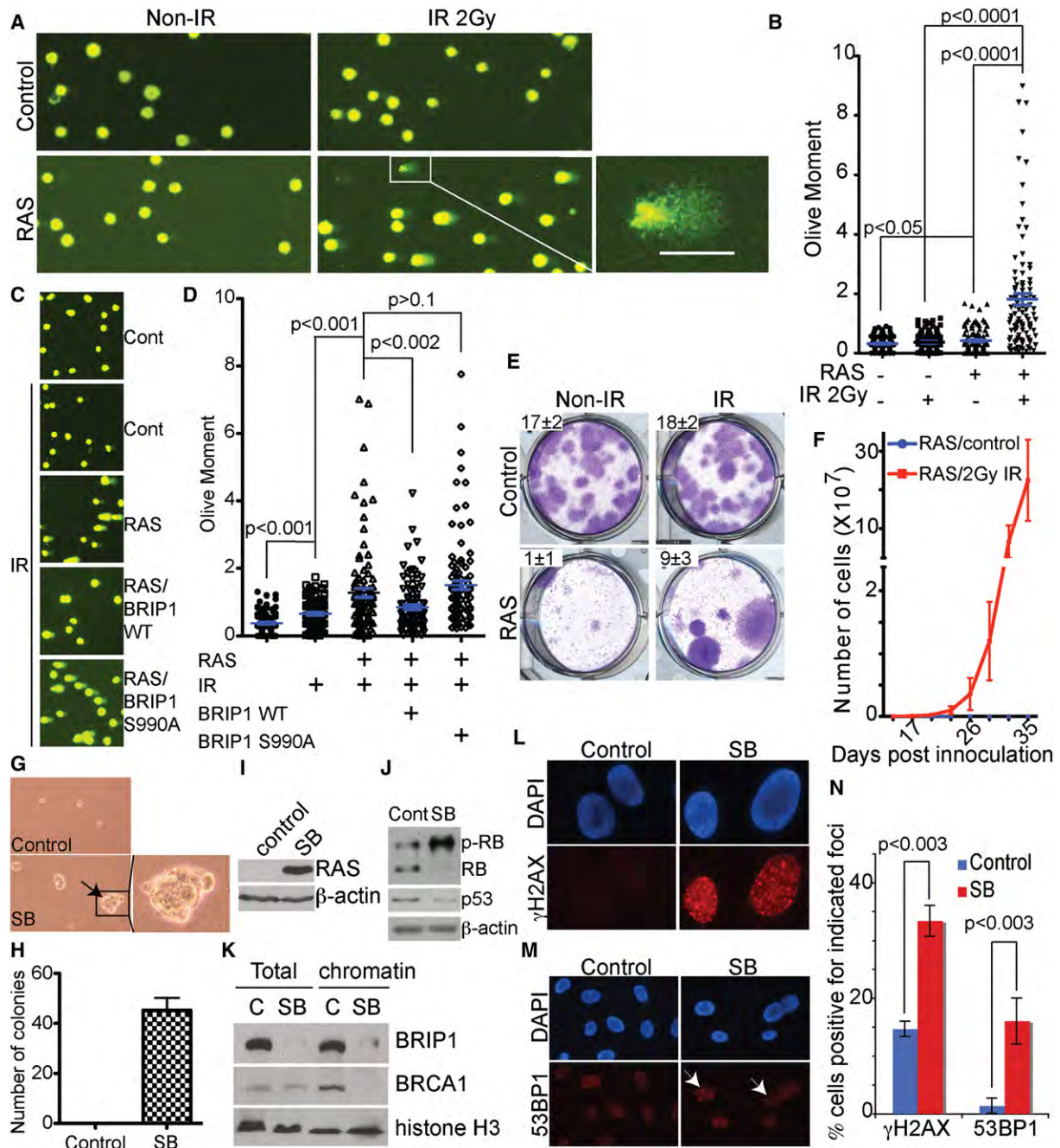


**Figure 7. DNA Damage Promotes Senescence Bypass**

(A) IMR90 cells were infected with control or RAS-encoding retrovirus, and drug-selected cells were treated with or without 2 Gy IR at day 2. After 5 hr of recovery, comet assays were performed to detect DNA damage. Shown are representative images of six independent experiments. The white bar indicates an example of the comet tails that reflect the extent of DNA damage. Note that a shorter exposure time was used here compared with Figure 2F to avoid saturation of comet tail signal in IR-treated RAS-infected cells.

(B) Quantitation of results from (A). A total of 120 cells from each of the indicated groups were measured for Olive Moment. Means of Olive Moment with SEM are indicated in blue. Note that there was a significant increase in DNA damage in RAS-infected cells without IR treatment compared with controls ( $p < 0.05$ ).

(C) Same as (A). Comet assays were performed to detect DNA damage in the indicated cells. Shown are representative images of three independent experiments. Cont, control.

(D) Quantitation of results from (C). A total of 100 cells from each of the indicated groups were measured for Olive Moment. Means of Olive Moment with SEM are indicated in blue.

(E) At day 2, control and RAS-infected BJ-hTERT cells were treated with or without 2 Gy IR. Equal numbers of the indicated cells ( $3 \times 10^3$  cells/well) were plated in 6-well plates for focus formation assays. After 2 weeks of culture, the plates were stained with 0.05% crystal violet in PBS to visualize foci. Shown are representative images of four independent experiments. The number of foci is indicated as mean with SD.



CtIP and RAP80 are not among the list of genes whose expression is significantly changed in the same analysis (Mason et al., 2004). Interestingly, BRIP1, but not CtIP or RAP80/Abraxas, regulates DNA replication and is required for timely S phase progression (Huen et al., 2010; Kumaraswamy and Shiekhhattar, 2007), implying that the BRCA1/BRIP1 complex may regulate senescence by altering DNA replication. In support of this idea, RAS-induced senescence is characterized as a DNA damage response triggered by aberrant DNA replication (Di Micco et al., 2006). Furthermore, B-Myb, a key regulator of BRIP1 expression (Figure 4D; Figures S4C and S4D), is critical for proper DNA replication and regulates the DNA damage response (Ahlbory et al., 2005; Lorvellec et al., 2010). Notably, BRIP1 is expressed at higher levels in advanced breast carcinomas, and its overexpression correlates with a higher cell proliferation index (Eelen et al., 2008), supporting the notion that high levels of BRIP1 may contribute to cell proliferation by suppressing senescence (Figure 5). Taken together, these data imply a key role for BRIP1 in accumulation of DNA damage during oncogene-induced senescence.

### The Role of BRCA1 Chromatin Dissociation in Senescence Bypass

Oncogene-induced BRCA1 chromatin dissociation precedes the cell cycle exit during senescence (Figure 1). Significantly, oncogenic RAS impairs BRCA1-mediated DNA repair response prior to the cell cycle exit during senescence (Figures 6 and 7). This allows for the creation of a large time window for cells to accumulate secondary oncogenic hits prior to the senescence-associated cell cycle exit, which ultimately leads to senescence bypass in a minority of cells while the vast majority of cells eventually exit from the cell cycle and become senescent. Consistent with this model, RAS-expressing cells accumulate significantly greater DNA damage after IR treatment, and IR treatment promotes senescence bypass in RAS-infected cells (Figure 7). The mechanism we uncovered here may help explain the paradox of why activation of oncogenes (such as RAS) promotes senescence but at the same time predisposes cells to transformation.

## EXPERIMENTAL PROCEDURES

### Chromatin Isolation and Chromatin Immunoprecipitation

Chromatin was prepared according to published methods (Méndez and Stillman, 2000; Narita et al., 2006). Soluble proteins in supernatant 1 (SN1, cytoplasmic) and 2 (SN2, nuclear) and chromatin-bound proteins in the chromatin fraction were detected by western blot.

Chromatin immunoprecipitation in control and RAS-infected IMR90 cells was performed at day 6 as previously described (Zhang et al., 2007b) using a monoclonal anti-B-Myb antibody (Santa Cruz Biotechnology) or an isotype-matched IgG control. Immunoprecipitated DNA was analyzed using SYBR Green quantitative PCR (SABiosciences) against the human *BRIP1* gene promoter region containing the B-Myb binding site using the following primers: forward, 5'-ATAAAGCGGAGCCCTGGAAGAGAA-3'; reverse, 5'-ATTCGTCTCGGGTTGTGTG-GTTGA-3'.

### Comet Assay

The comet assay was performed with the CometAssay (Trevigen) kit following the manufacturer's instructions. DNA damage was measured as the artificial Olive Moment using CometScore software downloaded from <http://www.tritekcorp.com>. To determine significance, the t test was performed using GraphPad Prism software (<http://www.graphpad.com>).

### Anchorage-Independent Growth in Soft Agar and Focus Formation Assay

Anchorage-independent growth in soft agar was performed as previously described (Li et al., 2010). For focus formation, 4 days after initial infection, control or oncogenic H-RAS<sup>G12V</sup>-encoding retrovirus-infected BJ-hTERT cells were treated with 2 Gy IR. Cells were cultured for 6 days to eliminate the apoptotic cells induced by IR. Then, control and H-RAS<sup>G12V</sup>-expressing cells with or without IR treatment were seeded into 6-well plates at a density of 3000 cells/well in triplicate. Two weeks later, the plates were stained with 0.05% crystal violet in PBS (Kuilman et al., 2008).

### Retrovirus and Lentivirus Infections

Retrovirus production and transduction were performed as described previously (Ye et al., 2007; Zhang et al., 2005) using Phoenix cells to package the infection viruses (Dr. Gary Nolan, Stanford University). Lentivirus was packaged using the ViraPower Kit from Invitrogen following the manufacturer's instructions and as described previously (Li et al., 2010; Ye et al., 2007). Cells infected with viruses encoding a drug-resistant gene to puromycin or neomycin were selected in 1 and 500  $\mu$ g/ml, respectively, of the corresponding agent.

### Immunofluorescence, BrdU Labeling, FACS, and SA- $\beta$ -gal Staining

Immunofluorescence staining and BrdU labeling for cultured cells were performed as described previously using antibodies described above (Zhang et al., 2005, 2007a, 2007b). Soluble protein pre-extraction with detergent was carried out as described previously (Taddei et al., 2001). Briefly, cells were incubated with PBS supplemented with 0.5% Triton X-100 for 5 min at room temperature, followed by fixation in 4% paraformaldehyde (Sigma-Aldrich) for 10 min. Fixed cells were incubated with a rabbit anti-BRCA1 antibody for 1 hr at room temperature and visualized by incubating the cells with goat anti-rabbit Cy3 (Jackson ImmunoResearch; 1:5000) secondary antibody followed by detection of BrdU using a FITC-labeled anti-BrdU antibody (BD Biosciences). FACS was performed as previously described (Ye et al., 2007), and FlowJo software was used to analyze cell cycle distribution. SA- $\beta$ -gal staining was performed as previously described (Dimri et al., 1995).

For additional information about cell culture methods, RT-PCR, and luciferase assays, as well as antibodies and plasmids used in this study, please see the Supplemental Experimental Procedures.

(F) Same as (E), but an equal number ( $1 \times 10^4$ ) of indicated cells were inoculated and cultured. The number of cells from each group was counted at indicated time points. Mean of three independent experiments with SD.

(G) Equal numbers of parental and senescence-bypassed cells were grown under anchorage-independent conditions in soft agar. Arrow points to an example of colonies formed by the senescence-bypassed cells.

(H) Quantitation of (G). Mean of three independent experiments with SD.

(I) Expression of RAS and  $\beta$ -actin in control (C) and the senescence-bypassed (SB) cells isolated from (F) was determined by western blot.

(J) Same as (I) but assayed for pRB, p53, and  $\beta$ -actin expression by western blot.

(K) Same as (I) but examined for expression of BRIP1, BRCA1, and histone H3 in total cell lysates and in the chromatin fractions by western blot.

(L) Same as (I) but stained with an anti- $\gamma$ -H2AX antibody.

(M) Same as (L) but stained with an anti-53BP1 antibody. Arrows point to examples of 53BP1 foci-positive cells.

(N) Quantitation of (L) and (M). A total of 100 cells from each indicated group were examined for  $\gamma$ -H2AX and 53BP1 foci formation. Mean of three independent experiments with SD.

See also Figure S6.

## SUPPLEMENTAL INFORMATION

Supplemental Information includes six figures and Supplemental Experimental Procedures and can be found with this article online at doi:10.1016/j.devcel.2011.10.010.

## ACKNOWLEDGMENTS

We thank Dr. Kathy Wilson and Igor Makhlin for reagents, other laboratory members for critical discussion, and Dr. Xinying Zhuang for technical assistance. We thank Drs. Hua-Ying Fan, Erica Golemis, and Maureen Murphy for critical reading of the manuscript. Z.T. performed most of the experiments, designed the experiments, and drafted the manuscript. K.M.A. contributed to Figure 4H and Figures S2C, S2D, S2F, S2G, and S4C. B.G.B. contributed to Figure 4D. J.P.N. contributed to initial observations that led to Figure 1A. N.B., B.X., and T.J.Y. provided critical materials and/or reagents. R.Z. conceived the study, designed experiments, and wrote the manuscript. R.Z. is an Ovarian Cancer Research Fund (OCRF) Liz Tilberis Scholar. This work was supported in part by an NCI FCCC-UPenn ovarian cancer SPORE (P50 CA083638) pilot project and SPORE career development award (to R.Z.), a DOD ovarian cancer academy award (OC093420 to R.Z.), and an OCRF program project (to R.Z.). B.G.B. is supported by an NCI postdoctoral training grant (CA-009035-35). We would like to acknowledge Anna Pecherskaya and Margret Einarson for help with quantitative image analysis and Emmanuelle Nicolas for help with microRNA qRT-PCR analysis.

Received: October 7, 2010

Revised: June 29, 2011

Accepted: October 11, 2011

Published online: December 1, 2011

## REFERENCES

- Ahlborg, D., Appl, H., Lang, D., and Klempnauer, K.H. (2005). Disruption of B-myb in DT40 cells reveals novel function for B-Myb in the response to DNA-damage. *Oncogene* 24, 7127–7134.
- Alimonti, A., Nardella, C., Chen, Z., Clohessy, J.G., Carracedo, A., Trotman, L.C., Cheng, K., Varmeh, S., Kozma, S.C., Thomas, G., et al. (2010). A novel type of cellular senescence that can be enhanced in mouse models and human tumor xenografts to suppress prostate tumorigenesis. *J. Clin. Invest.* 120, 681–693.
- Bartkova, J., Rezaei, N., Lontos, M., Karakaidos, P., Kletsas, D., Issaeva, N., Vassiliou, L.V., Kolettas, E., Niforou, K., Zoumpourlis, V.C., et al. (2006). Oncogene-induced senescence is part of the tumorigenesis barrier imposed by DNA damage checkpoints. *Nature* 444, 633–637.
- Braig, M., Lee, S., Loddenkemper, C., Rudolph, C., Peters, A.H., Schlegelberger, B., Stein, H., Dörken, B., Jenuwein, T., and Schmitt, C.A. (2005). Oncogene-induced senescence as an initial barrier in lymphoma development. *Nature* 436, 660–665.
- Campisi, J. (2005). Senescent cells, tumor suppression, and organismal aging: good citizens, bad neighbors. *Cell* 120, 513–522.
- Cantor, S.B., Bell, D.W., Ganesan, S., Kass, E.M., Drapkin, R., Grossman, S., Wahner, D.C., Sgroi, D.C., Lane, W.S., Haber, D.A., and Livingston, D.M. (2001). BACH1, a novel helicase-like protein, interacts directly with BRCA1 and contributes to its DNA repair function. *Cell* 105, 149–160.
- Cao, L., Li, W., Kim, S., Brodie, S.G., and Deng, C.X. (2003). Senescence, aging, and malignant transformation mediated by p53 in mice lacking the Brca1 full-length isoform. *Genes Dev.* 17, 201–213.
- Chen, J., Silver, D.P., Walpita, D., Cantor, S.B., Gazdar, A.F., Tomlinson, G., Couch, F.J., Weber, B.L., Ashley, T., Livingston, D.M., and Scully, R. (1998). Stable interaction between the products of the BRCA1 and BRCA2 tumor suppressor genes in mitotic and meiotic cells. *Mol. Cell* 2, 317–328.
- Costanzi, C., and Pehrson, J.R. (1998). Histone macroH2A1 is concentrated in the inactive X chromosome of female mammals. *Nature* 393, 599–601.
- Di Micco, R., Fumagalli, M., Cicalese, A., Piccinin, S., Gasparini, P., Luise, C., Schurra, C., Garre', M., Nuciforo, P.G., Bensimon, A., et al. (2006). Oncogene-induced senescence is a DNA damage response triggered by DNA hyper-replication. *Nature* 444, 638–642.
- Di Micco, R., Sulli, G., Dobrev, M., Lontos, M., Botrugno, O.A., Gargiulo, G., dal Zuffo, R., Matti, V., d'Ario, G., Montani, E., et al. (2011). Interplay between oncogene-induced DNA damage response and heterochromatin in senescence and cancer. *Nat. Cell Biol.* 13, 292–302.
- Dimri, G.P., Lee, X., Basile, G., Acosta, M., Scott, G., Roskelley, C., Medrano, E.E., Linskens, M., Rubelj, I., Pereira-Smith, O., et al. (1995). A biomarker that identifies senescent human cells in culture and in aging skin in vivo. *Proc. Natl. Acad. Sci. USA* 92, 9363–9367.
- Durant, S.T., and Nickoloff, J.A. (2005). Good timing in the cell cycle for precise DNA repair by BRCA1. *Cell Cycle* 4, 1216–1222.
- Eelen, G., Vanden Bempt, I., Verlinden, L., Drijckoningen, M., Smeets, A., Neven, P., Christiaens, M.R., Marchal, K., Bouillon, R., and Verstuyf, A. (2008). Expression of the BRCA1-interacting protein Brip1/BACH1/FANCD1 is driven by E2F and correlates with human breast cancer malignancy. *Oncogene* 27, 4233–4241.
- Erlundsson, F., Linnman, C., Ekholm, S., Bengtsson, E., and Zetterberg, A. (2000). A detailed analysis of cyclin A accumulation at the G(1)/S border in normal and transformed cells. *Exp. Cell Res.* 259, 86–95.
- Halazonetis, T.D., Gorgoulis, V.G., and Bartek, J. (2008). An oncogene-induced DNA damage model for cancer development. *Science* 319, 1352–1355.
- Huen, M.S., Sy, S.M., and Chen, J. (2010). BRCA1 and its toolbox for the maintenance of genome integrity. *Nat. Rev. Mol. Cell Biol.* 11, 138–148.
- Hurlin, P.J., Maher, V.M., and McCormick, J.J. (1989). Malignant transformation of human fibroblasts caused by expression of a transfected T24 HRAS oncogene. *Proc. Natl. Acad. Sci. USA* 86, 187–191.
- Kennedy, A.L., Morton, J.P., Manoharan, I., Nelson, D.M., Jamieson, N.B., Pawlikowski, J.S., McBryan, T., Doyle, B., McKay, C., Oien, K.A., et al. (2011). Activation of the PIK3CA/AKT pathway suppresses senescence induced by an activated RAS oncogene to promote tumorigenesis. *Mol. Cell* 42, 36–49.
- Krizhanovskiy, V., Xue, W., Zender, L., Yon, M., Hernando, E., and Lowe, S.W. (2008). Implications of cellular senescence in tissue damage response, tumor suppression, and stem cell biology. *Cold Spring Harb. Symp. Quant. Biol.* 73, 513–522.
- Krum, S.A., la Rosa Dalugdugan, E., Miranda-Carboni, G.A., and Lane, T.F. (2010). BRCA1 forms a functional complex with  $\gamma$ -H2AX as a late response to genotoxic stress. *J. Nucleic Acids* 2010, 801594.
- Kuilman, T., Michaloglou, C., Vredeveld, L.C., Douma, S., van Doorn, R., Desmet, C.J., Aarden, L.A., Mooi, W.J., and Peepers, D.S. (2008). Oncogene-induced senescence relayed by an interleukin-dependent inflammatory network. *Cell* 133, 1019–1031.
- Kumaraswamy, E., and Shiekhattar, R. (2007). Activation of BRCA1/BRCA2-associated helicase BACH1 is required for timely progression through S phase. *Mol. Cell. Biol.* 27, 6733–6741.
- Lafferty-Whyte, K., Cairney, C.J., Jamieson, N.B., Oien, K.A., and Keith, W.N. (2009). Pathway analysis of senescence-associated miRNA targets reveals common processes to different senescence induction mechanisms. *Biochim. Biophys. Acta* 1792, 341–352.
- Li, H., Cai, Q., Godwin, A.K., and Zhang, R. (2010). Enhancer of zeste homolog 2 promotes the proliferation and invasion of epithelial ovarian cancer cells. *Mol. Cancer Res.* 8, 1610–1618.
- Livingston, D.M. (2009). Cancer. Complicated supercomplexes. *Science* 324, 602–603.
- Lorvellec, M., Dumon, S., Maya-Mendoza, A., Jackson, D., Frampton, J., and García, P. (2010). B-Myb is critical for proper DNA duplication during an unperturbed S phase in mouse embryonic stem cells. *Stem Cells* 28, 1751–1759.
- Manke, I.A., Lowery, D.M., Nguyen, A., and Yaffe, M.B. (2003). BRCT repeats as phosphopeptide-binding modules involved in protein targeting. *Science* 302, 636–639.

- Martinez, I., Cazalla, D., Almstead, L.L., Steitz, J.A., and DiMaio, D. (2011). miR-29 and miR-30 regulate B-Myb expression during cellular senescence. *Proc. Natl. Acad. Sci. USA* 108, 522–527.
- Mason, D.X., Jackson, T.J., and Lin, A.W. (2004). Molecular signature of oncogenic ras-induced senescence. *Oncogene* 23, 9238–9246.
- Masselink, H., Vastenhouw, N., and Bernards, R. (2001). B-myb rescues ras-induced premature senescence, which requires its transactivation domain. *Cancer Lett.* 171, 87–101.
- Méndez, J., and Stillman, B. (2000). Chromatin association of human origin recognition complex, cdc6, and minichromosome maintenance proteins during the cell cycle: assembly of prereplication complexes in late mitosis. *Mol. Cell. Biol.* 20, 8602–8612.
- Michaloglou, C., Vredevelde, L.C., Soengas, M.S., Denoyelle, C., Kuilman, T., van der Horst, C.M., Majoor, D.M., Shay, J.W., Mooi, W.J., and Peepers, D.S. (2005). BRAFE600-associated senescence-like cell cycle arrest of human naevi. *Nature* 436, 720–724.
- Narita, M., Nunez, S., Heard, E., Narita, M., Lin, A.W., Hearn, S.A., Spector, D.L., Hannon, G.J., and Lowe, S.W. (2003). Rb-mediated heterochromatin formation and silencing of E2F target genes during cellular senescence. *Cell* 113, 703–716.
- Narita, M., Narita, M., Krizhanovskiy, V., Nunez, S., Chicas, A., Hearn, S.A., Myers, M.P., and Lowe, S.W. (2006). A novel role for high-mobility group proteins in cellular senescence and heterochromatin formation. *Cell* 126, 503–514.
- Peng, M., Litman, R., Jin, Z., Fong, G., and Cantor, S.B. (2006). BACH1 is a DNA repair protein supporting BRCA1 damage response. *Oncogene* 25, 2245–2253.
- Rodier, F., Coppé, J.P., Patil, C.K., Hoeijmakers, W.A., Muñoz, D.P., Raza, S.R., Freund, A., Campeau, E., Davalos, A.R., and Campisi, J. (2009). Persistent DNA damage signalling triggers senescence-associated inflammatory cytokine secretion. *Nat. Cell Biol.* 11, 973–979.
- Sartori, A.A., Lukas, C., Coates, J., Mistrik, M., Fu, S., Bartek, J., Baer, R., Lukas, J., and Jackson, S.P. (2007). Human CtIP promotes DNA end resection. *Nature* 450, 509–514.
- Scully, R., and Livingston, D.M. (2000). In search of the tumour-suppressor functions of BRCA1 and BRCA2. *Nature* 408, 429–432.
- Scully, R., Chen, J., Ochs, R.L., Keegan, K., Hoekstra, M., Feunteun, J., and Livingston, D.M. (1997a). Dynamic changes of BRCA1 subnuclear location and phosphorylation state are initiated by DNA damage. *Cell* 90, 425–435.
- Scully, R., Chen, J., Plug, A., Xiao, Y., Weaver, D., Feunteun, J., Ashley, T., and Livingston, D.M. (1997b). Association of BRCA1 with Rad51 in mitotic and meiotic cells. *Cell* 88, 265–275.
- Sy, S.M., Huen, M.S., and Chen, J. (2009). PALB2 is an integral component of the BRCA complex required for homologous recombination repair. *Proc. Natl. Acad. Sci. USA* 106, 7155–7160.
- Taddei, A., Maison, C., Roche, D., and Almouzni, G. (2001). Reversible disruption of pericentric heterochromatin and centromere function by inhibiting deacetylases. *Nat. Cell Biol.* 3, 114–120.
- Turner, N., Tutt, A., and Ashworth, A. (2004). Hallmarks of ‘BRCAness’ in sporadic cancers. *Nat. Rev. Cancer* 4, 814–819.
- Wang, B., Matsuo, S., Ballif, B.A., Zhang, D., Smogorzewska, A., Gygi, S.P., and Elledge, S.J. (2007). Abraxas and RAP80 form a BRCA1 protein complex required for the DNA damage response. *Science* 316, 1194–1198.
- Xia, B., Sheng, Q., Nakanishi, K., Ohashi, A., Wu, J., Christ, N., Liu, X., Jasin, M., Couch, F.J., and Livingston, D.M. (2006). Control of BRCA2 cellular and clinical functions by a nuclear partner, PALB2. *Mol. Cell* 22, 719–729.
- Xu, B., Kim, S.T., and Kastan, M.B. (2001). Involvement of Brca1 in S-phase and G(2)-phase checkpoints after ionizing irradiation. *Mol. Cell. Biol.* 21, 3445–3450.
- Xue, W., Zender, L., Miething, C., Dickins, R.A., Hernando, E., Krizhanovskiy, V., Cordon-Cardo, C., and Lowe, S.W. (2007). Senescence and tumour clearance is triggered by p53 restoration in murine liver carcinomas. *Nature* 445, 656–660.
- Ye, Q., Hu, Y.F., Zhong, H., Nye, A.C., Belmont, A.S., and Li, R. (2001). BRCA1-induced large-scale chromatin unfolding and allele-specific effects of cancer-predisposing mutations. *J. Cell Biol.* 155, 911–921.
- Ye, X., Zerlanko, B., Zhang, R., Somaiah, N., Lipinski, M., Salomoni, P., and Adams, P.D. (2007). Definition of pRB- and p53-dependent and -independent steps in HIRA/ASF1a-mediated formation of senescence-associated heterochromatin foci. *Mol. Cell. Biol.* 27, 2452–2465.
- Yu, X., Wu, L.C., Bowcock, A.M., Aronheim, A., and Baer, R. (1998). The C-terminal (BRCT) domains of BRCA1 interact in vivo with CtIP, a protein implicated in the CtBP pathway of transcriptional repression. *J. Biol. Chem.* 273, 25388–25392.
- Yu, X., Chini, C.C., He, M., Mer, G., and Chen, J. (2003). The BRCT domain is a phospho-protein binding domain. *Science* 302, 639–642.
- Zhang, R., Poustovoitov, M.V., Ye, X., Santos, H.A., Chen, W., Daganzo, S.M., Erzberger, J.P., Serebriiskii, I.G., Canutescu, A.A., Dunbrack, R.L., et al. (2005). Formation of MacroH2A-containing senescence-associated heterochromatin foci and senescence driven by ASF1a and HIRA. *Dev. Cell* 8, 19–30.
- Zhang, R., Chen, W., and Adams, P.D. (2007a). Molecular dissection of formation of senescence-associated heterochromatin foci. *Mol. Cell. Biol.* 27, 2343–2358.
- Zhang, R., Liu, S.T., Chen, W., Bonner, M., Pehrson, J., Yen, T.J., and Adams, P.D. (2007b). HP1 proteins are essential for a dynamic nuclear response that rescues the function of perturbed heterochromatin in primary human cells. *Mol. Cell. Biol.* 27, 949–962.
- Zhang, F., Ma, J., Wu, J., Ye, L., Cai, H., Xia, B., and Yu, X. (2009). PALB2 links BRCA1 and BRCA2 in the DNA-damage response. *Curr. Biol.* 19, 524–529.

# Cancer Prevention Research



## ALDH1A1 Is a Novel EZH2 Target Gene in Epithelial Ovarian Cancer Identified by Genome-Wide Approaches

Hua Li, Benjamin G. Bitler, Vinod Vathipadiekal, et al.

*Cancer Prev Res* 2012;5:484-491. Published OnlineFirst December 5, 2011.

### Updated Version

Access the most recent version of this article at:  
doi:[10.1158/1940-6207.CAPR-11-0414](https://doi.org/10.1158/1940-6207.CAPR-11-0414)

### Supplementary Material

Access the most recent supplemental material at:  
<http://cancerpreventionresearch.aacrjournals.org/content/suppl/2011/12/04/1940-6207.CAPR-11-0414.DC1.html>

### Cited Articles

This article cites 37 articles, 15 of which you can access for free at:  
<http://cancerpreventionresearch.aacrjournals.org/content/5/3/484.full.html#ref-list-1>

### E-mail alerts

[Sign up to receive free email-alerts](#) related to this article or journal.

### Reprints and Subscriptions

To order reprints of this article or to subscribe to the journal, contact the AACR Publications Department at [pubs@aacr.org](mailto:pubs@aacr.org).

### Permissions

To request permission to re-use all or part of this article, contact the AACR Publications Department at [permissions@aacr.org](mailto:permissions@aacr.org).



## Research Article

## ALDH1A1 Is a Novel EZH2 Target Gene in Epithelial Ovarian Cancer Identified by Genome-Wide Approaches

Hua Li<sup>1</sup>, Benjamin G. Bitler<sup>1</sup>, Vinod Vathipadiekal<sup>4</sup>, Marie E. Maradeo<sup>2</sup>, Michael Slifker<sup>3</sup>, Caretha L. Creasy<sup>5</sup>, Peter J. Tummino<sup>5</sup>, Paul Cairns<sup>2</sup>, Michael J. Birrer<sup>4</sup>, and Rugang Zhang<sup>1</sup>

## Abstract

Epithelial ovarian cancer (EOC) remains the most lethal gynecologic malignancy in the United States. EZH2 silences gene expression through trimethylating lysine 27 on histone H3 (H3K27Me3). EZH2 is often overexpressed in EOC and has been suggested as a target for EOC intervention. However, EZH2 target genes in EOC remain poorly understood. Here, we mapped the genomic loci occupied by EZH2/H3K27Me3 using chromatin immunoprecipitation followed by next-generation sequencing (ChIP-seq) and globally profiled gene expression in EZH2-knockdown EOC cells. Cross-examination of gene expression and ChIP-seq revealed a list of 60 EZH2 direct target genes whose expression was upregulated more than 1.5-fold upon EZH2 knockdown. For three selected genes (*ALDH1A1*, *SSTR1*, and *DACT3*), we validated their upregulation upon EZH2 knockdown and confirmed the binding of EZH2/H3K27Me3 to their genomic loci. Furthermore, the presence of H3K27Me3 at the genomic loci of these EZH2 target genes was dependent upon EZH2. Interestingly, expression of *ALDH1A1*, a putative marker for EOC stem cells, was significantly downregulated in high-grade serous EOC ( $n = 53$ ) compared with ovarian surface epithelial cells ( $n = 10$ ,  $P < 0.001$ ). Notably, expression of *ALDH1A1* negatively correlated with expression of EZH2 ( $n = 63$ , Spearman  $r = -0.41$ ,  $P < 0.001$ ). Thus, we identified a list of 60 EZH2 target genes and established that *ALDH1A1* is a novel EZH2 target gene in EOC cells. Our results suggest a role for EZH2 in regulating EOC stem cell equilibrium via regulation of *ALDH1A1* expression. *Cancer Prev Res*; 5(3); 484–91. ©2011 AACR.

## Introduction

Epithelial ovarian cancer (EOC) accounts for more deaths than any other gynecologic malignancy in the United States. EOCs are classified into distinct histologic types including serous, mucinous, endometrioid, and clear cell (1). The most common histology of EOC is serous (~60% of all cancers) and less common histologies include endometrioid, clear cell, and mucinous (1). Recently, an alternative classification has been proposed, in which EOC is broadly divided into 2 types (2). Type I EOC includes mucinous, low-grade serous, low-grade endometrioid, and clear cell carcinomas, and type II EOC includes high-grade serous carcinomas, which is the most lethal histosubtype (2).

Enhancer of zeste homology 2 (EZH2) is a histone methyltransferase that mediates gene silencing by catalyzing the trimethylation on lysine 27 of histone H3 (H3K27Me3; ref. 3). EZH2 is often expressed at higher levels in human EOC cells, and its expression positively correlates with cell proliferation in these cells (4). Further underscoring the importance of EZH2 in EOC, EZH2 knockdown triggers apoptosis and inhibits the invasion of human EOC cells (4). In addition, EZH2 is overexpressed in ovarian tumor-associated endothelial cells, which promotes angiogenesis (5). Finally, there is evidence to suggest that EZH2 is overexpressed in ovarian cancer stem cell-like populations enriched by chemotherapy (6). Accordingly, EZH2 has been suggested as a putative target for developing EOC therapeutics. Thus, it is important to identify EZH2 target genes in EOC to gain insights into the biology of the disease and to facilitate translational EOC research related to EZH2. Although a number of EZH2 target genes have been characterized in a few cancer types, including prostate and breast, using chromatin immunoprecipitation (ChIP)-on-chip analysis (7, 8), studies that aim to globally identify EZH2 target genes in EOC cells have yet to be conducted.

Here, we report the identification of direct EZH2 target genes in human EOC cells using a combination of genome-wide approaches. Specifically, we identified the genomic loci occupied by EZH2/H3K27Me3 using ChIP followed by next-generation sequencing (ChIP-seq). In addition, we discovered a list of genes whose expression was upregulated

**Authors' Affiliations:** <sup>1</sup>Women's Cancer Program and Epigenetics and Progenitor Cell Keystone Program, <sup>2</sup>Cancer Biology Program, <sup>3</sup>Biostatistics and Bioinformatics Facility, Fox Chase Cancer Center, Philadelphia, Pennsylvania; <sup>4</sup>Massachusetts General Hospital Cancer Center and Harvard Medical School, Boston, Massachusetts; and <sup>5</sup>Cancer Epigenetics Discovery Performance Unit, Oncology R&D, GlaxoSmithKline Pharmaceuticals, Inc., Collegeville, Pennsylvania

**Note:** Supplementary data for this article are available at Cancer Prevention Research Online (<http://cancerprevres.aacrjournals.org/>).

**Corresponding Author:** Rugang Zhang, Fox Chase Cancer Center, W446, 333 Cottman Avenue, Philadelphia, PA 19111. Phone: 215-728-7108; Fax: 215-728-3616; E-mail: [rugang.zhang@fccc.edu](mailto:rugang.zhang@fccc.edu)

doi: 10.1158/1940-6207.CAPR-11-0414

©2011 American Association for Cancer Research.

more than 1.5-fold in EZH2-knockdown EOC cells compared with controls using gene expression microarray analysis. Cross-examination of gene expression profiling and ChIP-seq analysis revealed a list of 60 genes that are direct EZH2/H3K27Me3 target genes, including 56 novel putative EZH2 target genes. For validation, we selected 3 genes that are implicated in regulating stem cells, apoptosis, cell growth, or invasion. We validated their upregulation upon EZH2 knockdown in EOC cells and confirmed the binding of EZH2/H3K27Me3 by ChIP analysis. Interestingly, expression of ALDH1A1, a putative marker for EOC stem cells (9–11), was expressed at significantly lower levels in high-grade serous EOC than in normal human ovarian surface epithelial (HOSE) cells and negatively correlated with expression of EZH2.

## Materials and Methods

### Cell culture, short hairpin RNA, lentivirus packaging and infection

The SKOV3 human EOC cell line was cultured according to the American Type Culture Collection and as previously described (4, 12). SKOV3 cell line identification was further confirmed by DNA Diagnostic Center. The sense sequences of 2 individual short hairpin RNAs (shRNA) to the human *EZH2* genes are as we have previously published (4). Lentivirus packaging was conducted using ViraPower system (Invitrogen) according to the manufacturer's instruction and as previously described (4). Briefly, SKOV3 cells at 40% to 50% confluency were infected with lentivirus expressing shRNA to EZH2 or vector control. The infected cells were drug selected with 3  $\mu$ g/mL of puromycin to eliminate noninfected cells.

### Antibodies, Western blot analysis, RNA isolation, and quantitative reverse-transcriptase PCR

The following antibodies were used for Western blot analysis: mouse anti-EZH2 (1:2,500; BD Bioscience), rabbit anti-H3K27Me3 (1:1,000; Cell Signaling), and mouse anti-GAPDH (1:10,000; Millipore). RNA from cultured human SKOV3 EOC cells was isolated using TRIzol (Invitrogen) according to the manufacturer's instruction. For quantitative reverse-transcriptase PCR (qRT-PCR), TRIzol-isolated RNA was further purified using an RNeasy kit (Qiagen) following the manufacturer's instruction. The primers for *ALDH1A1*, *SSTR1*, and *DACT3* genes used for qRT-PCR were purchased from Applied Biosystems. Expression of the housekeeping gene  $\beta$ -2-microglobulin was used to normalize mRNA expression.

### ChIP-seq analysis and ChIP validation for selected EZH2 target genes

Briefly, SKOV3 cells were fixed with 1% formaldehyde for 15 minutes and quenched with 0.125 mol/L glycine. Chromatin was isolated by adding lysis buffer (1% SDS, 10 mmol/L EDTA, 50 mmol/L Tris-HCl, pH 8.1, 1 mmol/L phenylmethylsulfonyl fluoride) followed by disruption with a Dounce homogenizer. Lysates were sonicated using

a Misonix Sonicator 3000 to shear the DNA to an average length of 300 to 500 bp. Lysates were cleared by centrifugation to collect chromatin suspensions. Prior to their use in the ChIP protocol, protein A agarose beads (Invitrogen) were preblocked using blocking proteins and nucleic acids for 3 hours. For each ChIP reaction, an aliquot of chromatin (20–30  $\mu$ g) was precleared with 30  $\mu$ L preblocked protein A agarose beads for 1 to 2 hours. ChIP reactions were set up using precleared chromatin and antibody (anti-H3K27Me3, Millipore 07-449; anti-EZH2, Millipore 07-689) and incubated overnight at 4°C. Preblocked protein A agarose beads were added and incubation at 4°C was continued for another 3 hours. Agarose beads containing the immune complexes were washed, and the immune complexes eluted from the beads were subjected to RNase treatment at 37°C for 20 minutes and proteinase K treatment at 37°C for 3 hours. Cross-links were reversed, and ChIP DNAs were purified by phenol–chloroform extraction and ethanol precipitation.

ChIP DNA was amplified using the Illumina ChIP-Seq DNA Sample Prep Kit. In brief, DNA was resonicated and ends were polished and 5'-phosphorylated using T4 DNA polymerase, Klenow polymerase, and T4 polynucleotide kinase. After addition of 3'-A to the ends using Klenow fragment (3'-5' exo minus), Illumina genomic adapters were ligated and the sample was size-fractionated (300–400 bp) on a 2% agarose gel. After a final PCR amplification step (18 cycles, Phusion polymerase), the resulting DNA libraries were quantified and tested by qPCR at the same specific genomic regions as the original ChIP DNA to assess quality of the amplification reactions. DNA libraries were sequenced on a Genome Analyzer II. Sequences (36-nucleotide reads) were aligned to the human genome (NCBI Build 37.1/hg19) using Eland software (Illumina). Aligned sequences were extended *in silico* at their 3'-ends to a length of 240 bp, which is the average genomic fragment length in the size-selected library, and assigned to 32-nucleotide bins along the genome. The resulting histograms were stored in BAR (Binary Analysis Results) files. Peak locations were determined using the MACS algorithm.

For validation of binding of EZH2/H3K27Me3 to the genomic loci of the selected EZH2/H3K27Me3 target genes, SKOV3 EOC cells were transduced with lentivirus encoding control or shEZH2. Drug-selected cells were subjected to ChIP analysis as previously described (13, 14). The following antibodies were used to conduct ChIP: anti-EZH2 (C11, BD Biosciences), anti-H3K27Me3 (C36B11, Cell Signaling), and anti-histone H3 (05-928, Millipore). An isotype-matched IgG was used as a negative control. Immunoprecipitated DNA was analyzed with PCR against the genomic regions of *ALDH1A1* (forward: 5'-TGGCACTGGTTATT-CAACGTGGTC-3' and reverse: 5'-GAGGGTGAAGCTCTTGTTAGTTT-3'), *DACT3* (forward: 5'-CACACACACACACAAACAGTGCCT-3' and reverse: 5'-TTCCTCCAAC-TAGGCTGGCAGTTT-3') and *SSTR1* (forward: 5'-TAGCC-TAAGCTGCCTGCTGTGTTA-3' and reverse: 5'-AAAGTG-CATGTGCGGTCTGTTAGC-3'). PCR products were visualized on a 2% agarose gel.

For gene expression microarray analysis in SKOV3 cells, 500 ng of total RNA was amplified and labeled using Agilent QuickAmp labeling kit following the manufacturer's protocol. A total of 1.65  $\mu$ g of Cy-3-labeled cRNA targets were hybridized onto Agilent 4  $\times$  44 k whole genome arrays for 17 hours at 65°C and washed according to procedure described by Agilent. The hybridized slides were scanned at 5- $\mu$ m resolution on an Agilent scanner (Agilent), and fluorescent intensities of hybridization signals are extracted using Agilent Feature Extraction software.

Gene expression microarray data sets for 53 cases of laser capture and microdissected (LCM) high-grade serous EOC and 10 individual isolations of normal HOSE cells were obtained from Gene Expression Omnibus (GEO; <http://www.ncbi.nlm.nih.gov/geo/>; GEO accession number: GSE18521).

Quantitative data are expressed as mean  $\pm$  SD unless otherwise stated. ANOVA with Fisher least significant difference (LSD) was used to identify significant differences in multiple comparisons. Spearman test was used to measure statistical dependence between EZH2 mRNA levels and ALDH1A1 mRNA levels. For all statistical analyses, the level of significance was set at 0.05.

### Genome-wide mapping of EZH2/H3K27Me3 direct target genes in human EOC cells

To identify genes whose expression was suppressed by EZH2, we conducted gene expression microarray analysis in control and EZH2-knockdown SKOV3 human EOC cells. Two individual shRNAs to the human *EZH2* gene (shEZH2) were used to limit potential off-target effects. Knockdown efficacy was confirmed by immunoblotting analysis (Fig. 1A). EZH2 knockdown notably decreased the levels of H3K27Me3, which is consistent with the idea that EZH2 plays a major role in regulating the levels of H3K27Me3 in human EOC cells (Fig. 1A). A list of 148 genes and 501 genes were upregulated more than 1.5-fold by shEZH2#1 and shEZH2#2, respectively, whereas 128 genes overlapped between the 2 different shEZH2s (Fig. 1B). Further data can be found at GEO database upon publication (GEO access number: GSE31433). The difference in the number of the genes altered by 2 individual shEZH2s may be due to different degrees of EZH2 knockdown. Consistent with this possibility, shEZH2#2, which decreases EZH2 levels with better efficacy than shEZH2#1, resulted in a greater number of upregulated genes (Fig. 1A and B). Alternatively, the differences in gene upregulation observed with individual EZH2 shRNAs may be due to off-target effects. To avoid this potential issue, we chose to analyze the genes that are upregulated by both shEZH2s. Of note, some of the known EZH2 target genes were approaching the 1.5-fold upregula-

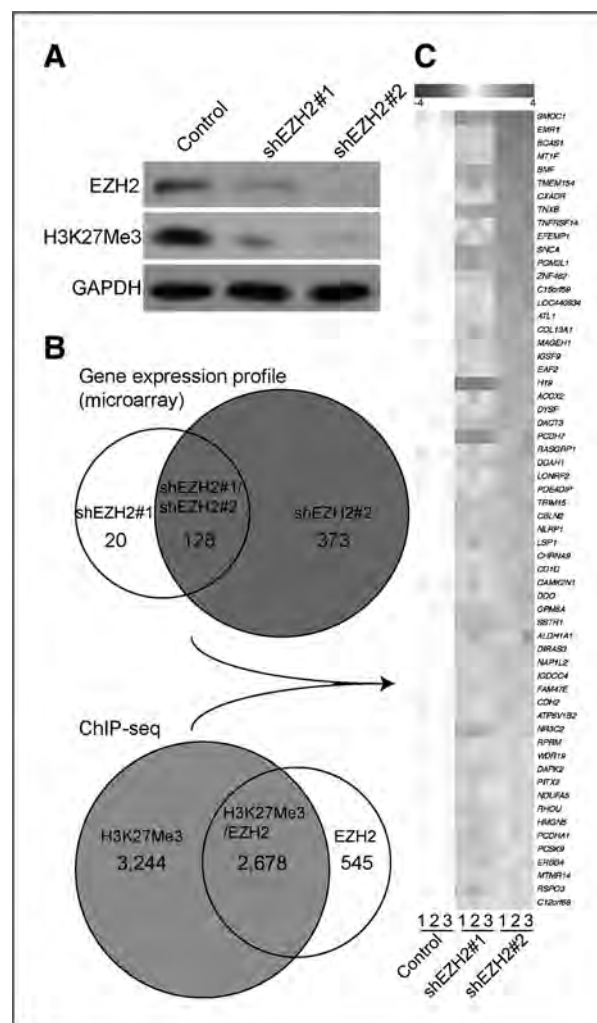


**Figure 1.** Identification of EZH2 target genes in human SKOV3 EOC cells. A, SKOV3 cells were infected with indicated lentivirus encoding shEZH2 or control. Drug-selected cells were examined for expression of EZH2, H3K27Me3, and GAPDH by immunoblotting analysis using indicated antibodies. B, schematic of experimental strategies used to identify EZH2 target genes. Genes whose expression was upregulated more than 1.5-fold upon EZH2 knockdown by 2 individual shEZH2 were identified by global gene expression microarray analysis. Genomic loci occupied by EZH2/H3K27Me3 were profiled by ChIP-seq analysis. C, cross-examination of gene expression profiling and ChIP-seq analysis as illustrated in (B) revealed a list of 60 putative EZH2 target genes in human SKOV3 EOC cells. GAPDH, glyceraldehyde-3-phosphate dehydrogenase.

tion cutoff point but were not included in further analysis, including *VASH1* (5) and *E-cadherin* (ref. 15; data not shown). Although the conservative approach we implemented may lead to missing certain EZH2 target genes, we felt these rigorous methods allowed us to minimize false-positive EZH2 target genes in human EOCs.

We next sought to identify genomic loci that are directly bound by EZH2/H3K27Me3. Toward this goal, we conducted ChIP-seq analysis in SKOV3 human EOC cells using antibodies specific to EZH2 or H3K27Me3. EZH2 and H3K27Me3 occupancy was mapped to the genomic loci of



3,223 and 5,922 genes, respectively, and 2,678 genes were associated with both EZH2 and H3K27Me3 (Fig. 1B and Supplementary Table S1). The difference between the number of genes whose locus was occupied by EZH2 and H3K27Me3 may reflect the difference in affinity of the antibodies used for ChIP. Alternatively, for methylated sites not bound by EZH2, it is possible that other epigenetic regulators in addition to EZH2 can also generate H3K27Me3. Consistently, EZH1, a homolog of EZH2 in human cells, is also capable of catalyzing H3K27Me3 epigenetic modifications, albeit at a lower rate than EZH2 (16). Furthermore, genes bound by EZH2, but not H3K27Me3, may reflect an H3K27Me3-independent function for EZH2 as previous reports have suggested (for example, see ref. 17).

To identify the genes that are directly silenced by EZH2, we cross-examined the gene expression and ChIP-seq data. As a result, we identified a list of 60 EZH2/H3K27Me3 target genes whose expression was upregulated more than 1.5-fold upon EZH2 knockdown in SKOV3 human EOC cells (Fig. 1C). Further confirming our approach, 4 of the 60 identified genes have previously been shown as EZH2/H3K27Me3 target genes, namely, *SNAC* (18), *H19* (19), *DIRAS3* (20), and *DACT3* (21). Notably, Ingenuity networks analysis revealed that the networks enriched by the identified genes included (i) cell death, growth, and proliferation (e.g., *BMF*, *DAPK2*, *NLRP1*, and *DIRAS3*) and (ii) reproductive system development and cancer (e.g., *EAF2*, *ALDH1A1*, *SSTR1*, and *MAGEH1*; data not shown). This is consistent with the proliferation-promoting and apoptosis-suppressing function of EZH2, which we have previously reported in human EOC cells (4).

Interestingly, the number of genes upregulated more than 1.5-fold upon EZH2 knockdown is notably lower than the number of genes whose genomic loci are directly occupied by EZH2/H3K27Me3 (Fig. 1B). This result suggests that additional mechanisms may cooperate with EZH2/H3K27Me3 in silencing or reactivating EZH2 target genes. Consistent with this idea, previous reports have shown that EZH2 target genes are also subject to epigenetic silencing by H3K9Me3 (22) or histone deacetylase (23). This implies that to achieve maximum reactivation of EZH2/H3K27Me3-silenced target genes in human EOC cells, additional epigenetic gene silencing mechanisms may be considered for simultaneous targeting together with EZH2

inhibition. Alternatively, this result may be due to the bivalent modification (i.e., H3K27Me3 and H3K4Me3) at the genomic loci of those upregulated genes, which primes those genes for activation while keeping them silenced (24). Further studies are warranted to differentiate these possibilities.

#### Validation of the selected EZH2 target genes in human EOC cells

The list of upregulated genes was prioritized for validation by examining their expression in the newly released the Cancer Genomics Atlas (TCGA) ovarian database (25). We first chose those genes whose expression was downregulated more than 2-fold in more than 75% of EOC cases in TCGA ovarian database. In addition, known imprinted genes such as *H19* (19) and *DIRAS3* (20) or poorly annotated genes were excluded. Given that EZH2 promotes proliferation and invasion, suppresses apoptosis, and regulates stem cell-like population in human EOCs (4, 6), we selected 3 identified EZH2/H3K27Me3 target genes with one or more of these roles for validation studies. Those genes are *ALDH1A1* (11), *SSTR1* (26), and *DACT3* (ref. 21; Table 1).

We first validated the upregulation of the selected 3 genes in EZH2-knockdown SKOV3 human EOC cells by qRT-PCR. Indeed, all 3 selected genes were significantly upregulated in shEZH2-expressing SKOV3 cells compared with controls (Fig. 2,  $P < 0.05$  vs. controls.). In addition, all 3 genes were upregulated by both shEZH2s, and there was a correlation between the degree of EZH2 knockdown and the levels of upregulation of these genes (Figs. 1A and 2). We conclude that EZH2 knockdown upregulates the expression of *ALDH1A1*, *SSTR1*, and *DACT3* in SKOV3 human EOC cells.

Next, we sought to validate the binding of EZH2/H3K27Me3 to the genomic loci of the selected genes. Toward this goal, we conducted ChIP analysis using antibodies specific to EZH2 or H3K27Me3, respectively. An isotype-matched IgG was used as a negative control, and an antibody to the core histone H3 was used as a positive control for ChIP analysis. Indeed, we observed the binding of both EZH2 and H3K27Me3 to the genomic loci of the selected EZH2 target genes in SKOV3 human EOC cells as determined by ChIP analysis (Fig. 3).

**Table 1.** Three putative EZH2 target genes identified by genome-wide approaches selected for further validation

| Gene name         | Location | Function   | % TCGA cases downregulated >2-fold |
|-------------------|----------|--|------------------------------------|
| NM_000689 ALDH1A1 | 9q21.13  | Cancer stem cell marker                              | 96                                 |
| NM_001049 SSTR1   | 14q13    | Proliferation and invasion inhibitor, cell signaling | 95                                 |
| NM_145056 DACT3   | 19q13.32 | Apoptosis inducer, Wnt signaling antagonist          | 76                                 |



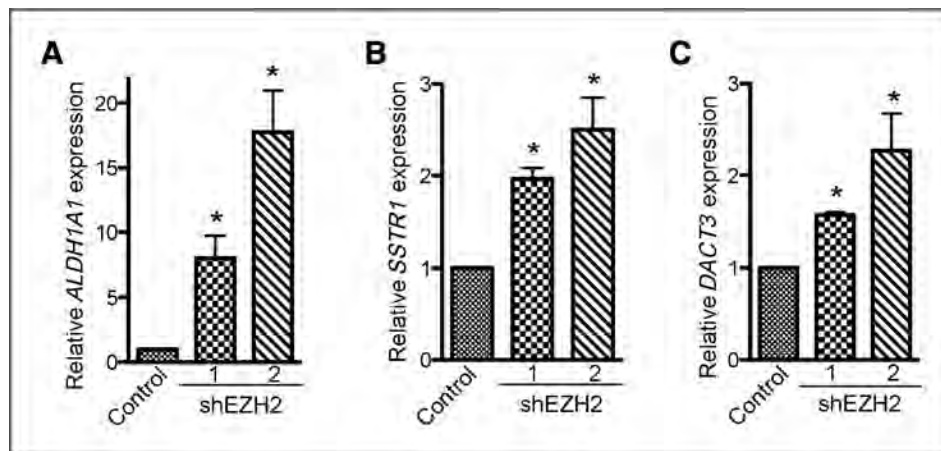


Figure 2. Validation of upregulation of the selected EZH2-silenced target genes in SKOV3 human EOC cells upon EZH2 knockdown by qRT-PCR. SKOV3 cells were infected with lentivirus encoding the indicated shEZH2s or control. After drug selection, mRNA was extracted and examined for expression of (A) *ALDH1A1* mRNA, (B) *SSTR1* mRNA, and (C) *DACT3* mRNA by qRT-PCR. Expression of  $\beta$ -2-microglobulin was used to normalize the expression of *ALDH1A1*, *SSTR1* and *DACT3* mRNA. \*,  $P < 0.05$  compared with controls.

We next sought to determine whether the occupancy of H3K27Me3 on the genomic loci of EZH2 target genes depends upon EZH2. Toward this goal, we conducted the ChIP analysis in EZH2-knockdown SKOV3 EOC cells. Indeed, knockdown of EZH2 severely weakened the association of both EZH2 and H3K27Me3 to the genomic loci of the selected EZH2 target genes (Fig. 3). This result suggests that EZH2 plays a major role in regulating H3K27Me3 modification on the genomic loci of these genes in human EOC cells. This result also implies that the binding of EZH2/H3K27Me3 to the genomic loci of these genes we observed here is specific.

#### Expression of EZH2 inversely correlates with expression of *ALDH1A1*

We next sought to determine whether there is an inverse correlation between expression of EZH2 and expression of the EZH2 target genes that we have identified and validated in this study. In addition to EOC cells, EZH2 is upregulated

in ovarian tumor-associated endothelial cells (5). To limit the confounding effects of EOC-associated stromal cells (including EOC-associated endothelial cells), we chose to analyze the correlation between expression of EZH2 and its target genes in specimens from LCM high-grade serous subtype EOC, which accounts for the majority of EOC-associated mortalities (27).

EZH2 is expressed at higher levels in human EOC cells than in normal HOSE cells (4). Therefore, we hypothesized that EZH2 target genes that are silenced by EZH2 would be expressed at lower levels in human EOC cells. Toward testing this hypothesis, we examined the expression of EZH2 and the 3 validated EZH2 target genes in a published microarray database, which compares the gene expression profile in 53 cases of LCM high-grade serous EOCs and 10 individual isolations of primary HOSE cells (28). Consistent with our previous report (4), EZH2 was expressed at significantly higher levels in human EOCs than in primary HOSE cells ( $P < 0.001$ ; Fig. 4A and B). Notably, the EZH2 target gene *ALDH1A1* was expressed at significantly lower levels in human EOCs than in normal HOSE cells ( $P < 0.001$ ; Fig. 4C and D). Indeed, there was a negative correlation between expression of EZH2 and its target gene *ALDH1A1* in a Spearman statistical analysis of the cases including both EOC and primary HOSE cells ( $P < 0.001$  and  $r = -0.41$ ; Fig. 4E, including both open circles and solid dots). However, the coefficient Spearman  $r$  is 0.41. This result indicates that other factors may also play a role in the expression relation. Consistently, there is evidence to suggest that Notch signaling also regulates *ALDH1A1* expression (29). In addition, the correlation between expression of EZH2 and *ALDH1A1* is not significant among EOC cases ( $P = 0.81$ ; Fig. 4E, solid dots only). This may be due to the fact the *ALDH1A1* is expressed at very low levels in the vast majority of EOC cases, and thus, the variation in expression may simply be a reflection of experimental variations.

Comparing EOCs with normal HOSE cells, *ALDH1A1* showed a high fold change in expression (>8-fold), whereas *SSTR1* (~3.5-fold) or *DACT3* (<1.5-fold) only showed a moderate to minimal fold change in expression (Fig. 4D and Supplementary Fig. S1). It is possible that EZH2 is the

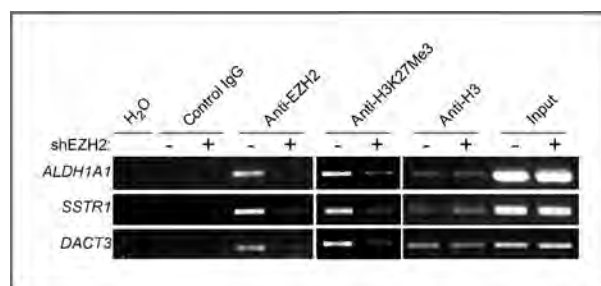


Figure 3. Validation of occupancy of the genomic loci of the selected EZH2 target genes by EZH2 and H3K27Me3 in SKOV3 human EOC cells using ChIP analysis. Control and shEZH2#2-expressing SKOV3 cells were subjected to ChIP analysis using antibodies specific to EZH2 or H3K27Me3, respectively. An isotype-matched IgG was used as a negative control, and an antibody specific to core histone H3 was used as a positive control. After ChIP analysis, the genomic loci of the indicated genes were subjected to PCR amplification using primers detailed in Materials and Methods. Please see Fig. 1A for shEZH2 knockdown efficacy. Shown are representative images of 3 independent experiments. Note that for H3K27Me3 ChIP, a low number of PCR cycles were used compared with EZH2 or histone H3 ChIP to avoid oversaturation of signals.

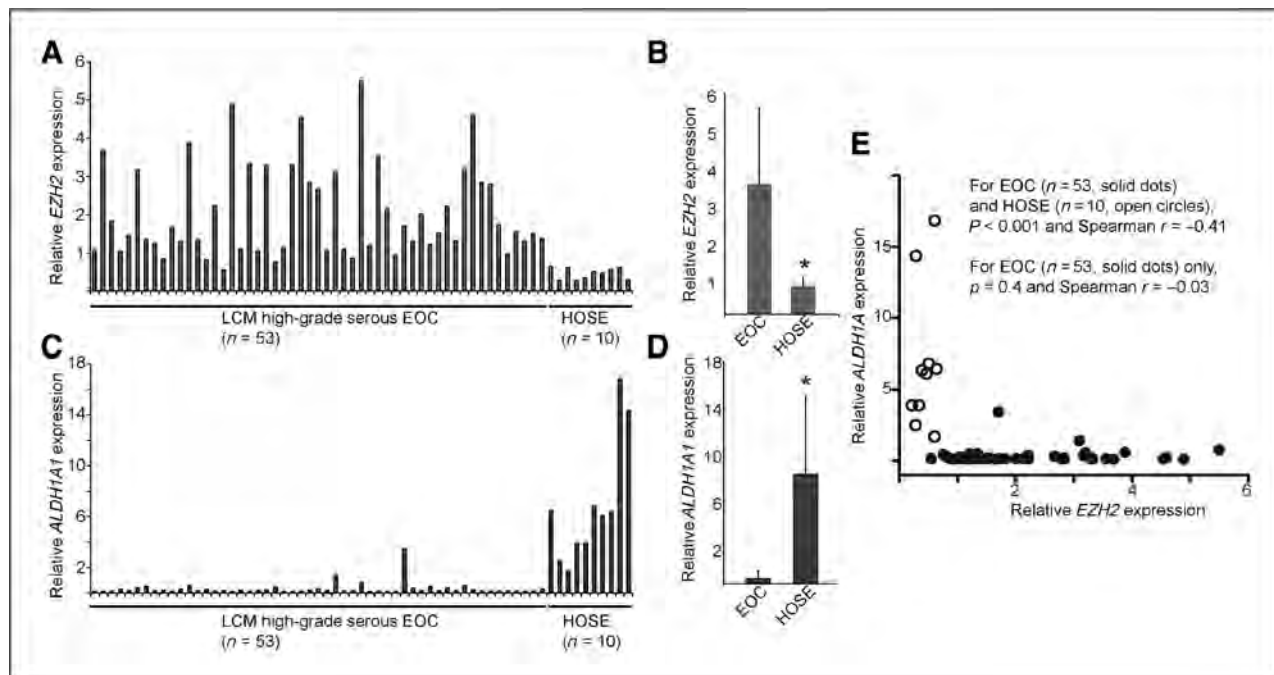


Figure 4. EZH2 targets ALDH1A1 in high-grade serous subtype EOC. A, relative expression of *EZH2* mRNA in 53 cases of LCM high-grade serous EOC and 10 individual isolations of normal HOSE cells. B, quantitation of (A). \*,  $P < 0.001$  compared with high-grade serous EOC. C, same as (A), but for relative expression of *ALDH1A1* mRNA. D, quantitation of (C). \*,  $P < 0.001$  compared with high-grade serous EOC. E, correlation between expression of *ALDH1A1* and *EZH2* as determined by Spearman statistical analysis using GraphPad Prism version 5.0 software.

major epigenetic regulator of ALDH1A1, whereas additional epigenetic silencing mechanisms may contribute to suppression of the other 2 validated EZH2 target genes. In support of this possibility, EZH2 knockdown induced much greater levels of upregulation for ALDH1A1 (up to 22-fold) than the other 2 EZH2 target genes (Fig. 2).

Next, we sought to examine the correlation between expression of EZH2 or ALDH1A1 and survival of patients with high-grade serous EOC. Consistent with our previous report (4), the difference in overall survival between high and low EZH2 expression in patients with high-grade serous EOC was not significant ( $P = 0.1684$ ; Supplementary Fig. S2). In addition, the difference in survival between low ALDH1A1 expression group and high ALDH1A1 group was not significant ( $P = 0.7789$ ; Supplementary Fig. S2). In contrast to our results, high ALDH1A1 has previously been reported to be associated with poor prognosis in patients with EOC (10, 30). The basis for this discrepancy remains to be determined. However, the discrepancy could be due to different methods that were used in this study (microarray) versus the other 2 studies (immunohistochemical staining).

ALDH1A1 has been reported as a marker of cancer stem cells in certain types of cancers including breast and ovarian (10, 29, 31–33). Likewise, EZH2 plays an important role in stem cell biology (34). Our data suggest that EZH2 directly regulates the levels of ALDH1A1 in EOC cells, implying that EZH2 may regulate the EOC stem cell population by controlling the levels of ALDH1A1 expression. Similarly, it has been shown that EZH2 directly regulates the epigenetic status of Nanog, an important factor for both embryonic

stem cell and induced pluripotent stem cells, to balance the equilibrium between self-renewal and differentiation of stem cells (35). Similarly, other putative markers of cancer stem cells [such as CD133 (ref. 36) and TACSTD2 (ref. 37)] have been also reported to be hypermethylated in cancerous cells. While the expression in stem cells will be masked by the vastly more abundant non-stem cell population in our or any similar analysis, it is nevertheless intriguing that differential expression of ALDH1A1 has been described as a marker of stemness in cancer, including in EOC (10, 33). Together, our data suggest that EZH2 may regulate the EOC stem cell population by controlling the levels of ALDH1A1 expression. Our future work will test this hypothesis.

In the present study, using a combination of global gene expression profiling and genome-wide ChIP-seq analysis, we identified a list of 60 EZH2 direct target genes, whose expression was upregulated more than 1.5-fold upon EZH2 knockdown in human EOC cells. These genes include 56 novel putative EZH2 target genes and 4 known EZH2 target genes. We validated 3 selected EZH2 target genes that are implicated in regulating cancer stem cells, cell proliferation, apoptosis, and cell invasion. We showed that ALDH1A1, a putative marker of EOC stem cells (11), was expressed at lower levels in high-grade serous EOCs than in normal HOSE cells, and there was a negative correlation between expression of EZH2 and expression of ALDH1A1. Further studies are warranted to mine the data presented here as well as functional characterization of the identified EZH2 target genes. These studies should provide important insights

into the biology of EOC development and the identification of potential candidate targets for prevention and intervention of EOC.

#### Disclosure of Potential Conflicts of Interest

C.L. Creasy and P.J. Tummino are employees and stockholders of GlaxoSmithKline Pharmaceuticals. No potential conflicts of interests were disclosed by other authors.

#### Acknowledgments

The authors thank Dr. Katherine Aird for critical reading of the manuscript, members of laboratory of R. Zhang for discussion, and Dr. Yue-Sheng Li at the genomics facility of Fox Chase Cancer Center for technical assistance.

#### Grant Support

This work was supported in part by a NCI FCCC-UPenn ovarian cancer SPOR (P50 CA083638) pilot project and SPOR career development award (to R. Zhang) and a DOD ovarian cancer academy award (OC093420 to R. Zhang). B.G. Bitler is supported by an NCI postdoctoral training grant (CA-009035-35). R. Zhang is an Ovarian Cancer Research Fund (OCRF) Liz Tilberis Scholar.

The costs of publication of this article were defrayed in part by the payment of page charges. This article must therefore be hereby marked *advertisement* in accordance with 18 U.S.C. Section 1734 solely to indicate this fact.

Received August 24, 2011; revised November 10, 2011; accepted November 14, 2011; published OnlineFirst December 5, 2011.

#### References

- Farley J, Ozbun LL, Birrer MJ. Genomic analysis of epithelial ovarian cancer. *Cell Res* 2008;18:538–48.
- Shih Ie M, Kurman RJ. Ovarian tumorigenesis: a proposed model based on morphological and molecular genetic analysis. *Am J Pathol* 2004;164:1511–8.
- Cao R, Wang L, Wang H, Xia L, Erdjument-Bromage H, Tempst P, et al. Role of histone H3 lysine 27 methylation in Polycomb-group silencing. *Science* 2002;298:1039–43.
- Li H, Cai Q, Godwin AK, Zhang R. Enhancer of zeste homolog 2 promotes the proliferation and invasion of epithelial ovarian cancer cells. *Mol Cancer Res* 2010;8:1610–8.
- Lu C, Han HD, Mangala LS, Ali-Fehmi R, Newton CS, Ozbun L, et al. Regulation of tumor angiogenesis by EZH2. *Cancer Cell* 2010;18:185–97.
- Rizzo S, Hersey JM, Mellor P, Dai W, Santos-Silva A, Liber D, et al. Ovarian cancer stem cell like side populations are enriched following chemotherapy and overexpress EZH2. *Mol Cancer Ther* 2011;10:325–35.
- Kondo S, Shen L, Cheng AS, Ahmed S, Bumber Y, Charo C, et al. Gene silencing in cancer by histone H3 lysine 27 trimethylation independent of promoter DNA methylation. *Nat Genet* 2008;40:741–50.
- Tan J, Yang X, Zhuang L, Jiang X, Chen W, Lee PL, et al. Pharmacologic disruption of Polycomb-repressive complex 2-mediated gene repression selectively induces apoptosis in cancer cells. *Genes Dev* 2007;21:1050–63.
- Kryczek I, Liu S, Roh M, Vatan L, Szeliga W, Wei S, et al. Expression of aldehyde dehydrogenase and CD133 defines ovarian cancer stem cells. *Int J Cancer* 2012;130:29–39.
- Landen CN Jr, Goodman B, Katre AA, Steg AD, Nick AM, Stone RL, et al. Targeting aldehyde dehydrogenase cancer stem cells in ovarian cancer. *Mol Cancer Ther* 2010;9:3186–99.
- Silva IA, Bai S, McLean K, Yang K, Griffith K, Thomas D, et al. Aldehyde dehydrogenase in combination with CD133 defines angiogenic ovarian cancer stem cells that portend poor patient survival. *Cancer Res* 2011;71:3991–4001.
- Bitler BG, Nicodemus JP, Li H, Cai Q, Wu H, Hua X, et al. Wnt5a suppresses epithelial ovarian cancer by promoting cellular senescence. *Cancer Res* 2011;71:6184–94.
- Zhang R, Chen W, Adams PD. Molecular dissection of formation of senescence-associated heterochromatin foci. *Mol Cell Biol* 2007;27:2343–58.
- Tu Z, Aird KM, Bitler BG, Nicodemus JP, Beeharry N, Xia B, et al. Oncogenic RAS regulates BRIP1 expression to induce dissociation of BRCA1 from chromatin, inhibit DNA repair, and promote senescence. *Dev Cell* 2011;21:1077–91.
- Cao Q, Yu J, Dhanasekaran SM, Kim JH, Mani RS, Tomlins SA, et al. Repression of E-cadherin by the polycomb group protein EZH2 in cancer. *Oncogene* 2008;27:7274–84.
- Margueron R, Li G, Sarma K, Blais A, Zavadil J, Woodcock CL, et al. Ezh1 and Ezh2 maintain repressive chromatin through different mechanisms. *Mol Cell* 2008;32:503–18.
- Shi B, Liang J, Yang X, Wang Y, Zhao Y, Wu H, et al. Integration of estrogen and Wnt signaling circuits by the polycomb group protein EZH2 in breast cancer cells. *Mol Cell Biol* 2007;27:5105–19.
- Yu J, Rhodes DR, Tomlins SA, Cao X, Chen G, Mehra R, et al. A polycomb repression signature in metastatic prostate cancer predicts cancer outcome. *Cancer Res* 2007;67:10657–63.
- Pasini D, Bracken AP, Hansen JB, Capillo M, Helin K. The polycomb group protein Suz12 is required for embryonic stem cell differentiation. *Mol Cell Biol* 2007;27:3769–79.
- Lu Z, Luo RZ, Lu Y, Zhang X, Yu Q, Khare S, et al. The tumor suppressor gene ARH1 regulates autophagy and tumor dormancy in human ovarian cancer cells. *J Clin Invest* 2008;118:3917–29.
- Jiang X, Tan J, Li J, Kivimäe S, Yang X, Zhuang L, et al. DACT3 is an epigenetic regulator of Wnt/beta-catenin signaling in colorectal cancer and is a therapeutic target of histone modifications. *Cancer Cell* 2008;13:529–41.
- Hawkins RD, Hon GC, Lee LK, Ngo Q, Lister R, Pelizzola M, et al. Distinct epigenomic landscapes of pluripotent and lineage-committed human cells. *Cell Stem Cell* 2010;6:479–91.
- van der Vlag J, Otte AP. Transcriptional repression mediated by the human polycomb-group protein EED involves histone deacetylation. *Nat Genet* 1999;23:474–8.
- Bernstein BE, Mikkelsen TS, Xie X, Kamal M, Huebert DJ, Cuff J, et al. A bivalent chromatin structure marks key developmental genes in embryonic stem cells. *Cell* 2006;125:315–26.
- Cancer Genome Atlas Research Network. Integrated genomic analyses of ovarian carcinoma. *Nature* 2011;474:609–15.
- Pyronnet S, Bousquet C, Najib S, Azar R, Laklai H, Susini C. Antitumor effects of somatostatin. *Mol Cell Endocrinol* 2008;286:230–7.
- Kurman RJ, Shih Ie M. The origin and pathogenesis of epithelial ovarian cancer: a proposed unifying theory. *Am J Surg Pathol* 2010;34:433–43.
- Mok SC, Bonome T, Vathipadiekal V, Bell A, Johnson ME, Wong KK, et al. A gene signature predictive for outcome in advanced ovarian cancer identifies a survival factor: microfibril-associated glycoprotein 2. *Cancer Cell* 2009;16:521–32.
- Sullivan JP, Spinola M, Dodge M, Raso MG, Behrens C, Gao B, et al. Aldehyde dehydrogenase activity selects for lung adenocarcinoma stem cells dependent on notch signaling. *Cancer Res* 2010;70:9937–48.
- Deng S, Yang X, Lassus H, Liang S, Kaur S, Ye Q, et al. Distinct expression levels and patterns of stem cell marker, aldehyde dehydrogenase isoform 1 (ALDH1), in human epithelial cancers. *PLoS One* 2010;5:e10277.
- Tanner B, Hengstler JG, Dietrich B, Henrich M, Steinberg P, Weikel W, et al. Glutathione, glutathione S-transferase alpha and pi, and aldehyde dehydrogenase content in relationship to drug resistance in ovarian cancer. *Gynecol Oncol* 1997;65:54–62.
- Ginestier C, Hur MH, Charafe-Jauffret E, Monville F, Dutcher J, Brown M, et al. ALDH1 is a marker of normal and malignant human mammary

- stem cells and a predictor of poor clinical outcome. *Cell Stem Cell* 2007;1:555–67.
33. Yang X, Lin X, Zhong X, Kaur S, Li N, Liang S, et al. Double-negative feedback loop between reprogramming factor LIN28 and microRNA let-7 regulates aldehyde dehydrogenase 1-positive cancer stem cells. *Cancer Res* 2010;70:9463–72.
  34. Margueron R, Reinberg D. The Polycomb complex PRC2 and its mark in life. *Nature* 2011;469:343–9.
  35. Villasante A, Piazzolla D, Li H, Gomez-Lopez G, Djabali M, Serrano M. Epigenetic regulation of Nanog expression by Ezh2 in pluripotent stem cells. *Cell Cycle* 2011;10:1488–98.
  36. Yi JM, Tsai HC, Glockner SC, Lin S, Ohm JE, Easwaran H, et al. Abnormal DNA methylation of CD133 in colorectal and glioblastoma tumors. *Cancer Res* 2008;68:8094–103.
  37. Ibragimova I, Ibanez de Caceres I, Hoffman AM, Potapova A, Dulaimi E, Al-Saleem T, et al. Global reactivation of epigenetically silenced genes in prostate cancer. *Cancer Prev Res* 2010;3:1084–92.





# Cancer Research

## Wnt5a Suppresses Epithelial Ovarian Cancer by Promoting Cellular Senescence

Benjamin G. Bitler, Jasmine P. Nicodemus, Hua Li, et al.

*Cancer Res* 2011;71:6184-6194. Published OnlineFirst August 4, 2011.

|                               |   |
|-------------------------------|---|
| <b>Updated Version</b>        | Access the most recent version of this article at:<br>doi: <a href="https://doi.org/10.1158/0008-5472.CAN-11-1341">10.1158/0008-5472.CAN-11-1341</a>  |
| <b>Supplementary Material</b> | Access the most recent supplemental material at:<br><a href="http://cancerres.aacrjournals.org/content/suppl/2011/08/04/0008-5472.CAN-11-1341.DC1.html">http://cancerres.aacrjournals.org/content/suppl/2011/08/04/0008-5472.CAN-11-1341.DC1.html</a> |

|                        |   |
|------------------------|---|
| <b>Cited Articles</b>  | This article cites 50 articles, 18 of which you can access for free at:<br><a href="http://cancerres.aacrjournals.org/content/71/19/6184.full.html#ref-list-1">http://cancerres.aacrjournals.org/content/71/19/6184.full.html#ref-list-1</a>                |
| <b>Citing Articles</b> | This article has been cited by 1 HighWire-hosted articles. Access the articles at:<br><a href="http://cancerres.aacrjournals.org/content/71/19/6184.full.html#related-urls">http://cancerres.aacrjournals.org/content/71/19/6184.full.html#related-urls</a> |

|                                   |   |
|-----------------------------------|---|
| <b>E-mail alerts</b>              | <a href="#">Sign up to receive free email-alerts</a> related to this article or journal.  |
| <b>Reprints and Subscriptions</b> | To order reprints of this article or to subscribe to the journal, contact the AACR Publications Department at <a href="mailto:pubs@aacr.org">pubs@aacr.org</a> .          |
| <b>Permissions</b>                | To request permission to re-use all or part of this article, contact the AACR Publications Department at <a href="mailto:permissions@aacr.org">permissions@aacr.org</a> . |

## Wnt5a Suppresses Epithelial Ovarian Cancer by Promoting Cellular Senescence

Benjamin G. Bitler<sup>1</sup>, Jasmine P. Nicodemus<sup>1</sup>, Hua Li<sup>1</sup>, Qi Cai<sup>2</sup>, Hong Wu<sup>3</sup>, Xiang Hua<sup>4</sup>, Tianyu Li<sup>5</sup>, Michael J. Birrer<sup>7</sup>, Andrew K. Godwin<sup>8</sup>, Paul Cairns<sup>6</sup>, and Rugang Zhang<sup>1</sup>

### Abstract

Epithelial ovarian cancer (EOC) remains the most lethal gynecologic malignancy in the United States. Thus, there is an urgent need to develop novel therapeutics for this disease. Cellular senescence is an important tumor suppression mechanism that has recently been suggested as a novel mechanism to target for developing cancer therapeutics. Wnt5a is a noncanonical Wnt ligand that plays a context-dependent role in human cancers. Here, we investigate the role of Wnt5a in regulating senescence of EOC cells. We show that Wnt5a is expressed at significantly lower levels in human EOC cell lines and in primary human EOCs ( $n = 130$ ) compared with either normal ovarian surface epithelium ( $n = 31$ ;  $P = 0.039$ ) or fallopian tube epithelium ( $n = 28$ ;  $P < 0.001$ ). Notably, a lower level of Wnt5a expression correlates with tumor stage ( $P = 0.003$ ) and predicts shorter overall survival in EOC patients ( $P = 0.003$ ). Significantly, restoration of Wnt5a expression inhibits the proliferation of human EOC cells both *in vitro* and *in vivo* in an orthotopic EOC mouse model. Mechanistically, Wnt5a antagonizes canonical Wnt/ $\beta$ -catenin signaling and induces cellular senescence by activating the histone repressor A/promyelocytic leukemia senescence pathway. In summary, we show that loss of Wnt5a predicts poor outcome in EOC patients and Wnt5a suppresses the growth of EOC cells by triggering cellular senescence. We suggest that strategies to drive senescence in EOC cells by reconstituting Wnt5a signaling may offer an effective new strategy for EOC therapy. *Cancer Res*; 71(19); 6184–94. ©2011 AACR.

### Introduction

Cellular senescence is an important tumor suppression mechanism *in vivo* (1). In primary mammalian cells, cellular senescence can be triggered by various inducers including critically shortened telomeres and activated oncogenes (such as oncogenic *RAS*; ref. 1). Senescent cells are viable but non-dividing (2). Senescent cells also exhibit several distinctive morphologic characteristics and molecular markers, including a large flat cellular morphology and expression of senescence-associated  $\beta$ -galactosidase (SA- $\beta$ -gal) activity (3). In murine liver carcinoma and sarcoma models, reactivation of the tumor suppressor p53 induces senescence and is associated with tumor regression (4, 5). Hence, driving cancer cells to undergo

cellular senescence represents a novel mechanism for developing cancer therapeutics (6, 7).

More than 85% of ovarian cancers are of epithelial origin (8). Epithelial ovarian cancers (EOC) are classified into distinct histologic types including serous, mucinous, endometrioid, and clear cell (9). The most common histology of EOC is serous (~60% of all cancers) and less common histologies include endometrioid, clear cell, and mucinous (9). Recently, an alternative classification has been proposed, in which EOC is broadly divided into 2 types (10). Type I EOC includes endometrioid, mucinous, low-grade serous, and clear-cell carcinomas, and type II EOC includes high-grade serous carcinomas (10). EOC remains the most lethal gynecologic malignancy in the United States (8). Thus, there is an urgent need to better understand the etiology of EOC to develop novel therapeutics for this devastating disease.

Wnt signaling is initiated by binding of the Wnt ligand to its cognate frizzled receptor (11). Canonical Wnt signaling results in stabilization of the key transcription factor  $\beta$ -catenin, which then translocates into the nucleus and drives expression of its target genes, such as *CCND1* (*cyclin D1*), *FOSL1*, and *c-MYC* (12, 13). Canonical Wnt signaling is active in the putative somatic stem/progenitor cells of the coelomic epithelium of the mouse ovary (14). Underscoring the importance of Wnt signaling in EOC, in a murine ovarian cancer model, activation of canonical Wnt signaling cooperates with inactivation of the tumor suppressor PTEN in driving ovarian carcinogenesis (15). However, the role of Wnt signaling in EOC is not fully understood.

**Authors' Affiliations:** <sup>1</sup>Women's Cancer Program, <sup>2</sup>Biosample Repository Facility, <sup>3</sup>Department of Pathology, <sup>4</sup>Transgenic Facility, <sup>5</sup>Department of Bioinformatics and Biostatistics, and <sup>6</sup>Department of Surgical Oncology, Fox Chase Cancer Center, Philadelphia, Pennsylvania; <sup>7</sup>Massachusetts General Hospital Cancer Center, Boston, Massachusetts; and <sup>8</sup>University of Kansas Medical Center, Kansas City, Kansas

**Note:** Supplementary data for this article are available at Cancer Research Online (<http://cancerres.aacrjournals.org/>).

**Corresponding Author:** Rugang Zhang, W446, Fox Chase Cancer Center, 333 Cottman Avenue, Philadelphia, PA 19111. Phone: 215-728-7108; Fax: 215-728-3616; E-mail: [rugang.zhang@fccc.edu](mailto:rugang.zhang@fccc.edu)

doi: 10.1158/0008-5472.CAN-11-1341

©2011 American Association for Cancer Research.

Wnt5a is a noncanonical Wnt ligand that plays opposing roles in different types of cancer and has variable expression dependent on the cancer context (16). Specifically, in EOC the role of Wnt5a remains unclear. Thus, in this study, we investigated Wnt5a expression and its potential function in human EOC cells. We discovered that Wnt5a was expressed at significantly lower levels in primary human EOC compared with either primary human ovarian surface epithelium or fallopian tube epithelium. Notably, loss of Wnt5a expression was associated with tumor stage and predicted shorter overall survival in EOC patients. Significantly, Wnt5a reconstitution inhibited the growth of EOC cells both *in vitro* and *in vivo* in an orthotopic EOC mouse model by promoting cellular senescence. These studies show, for the first time, a functional role of the noncanonical Wnt ligand, Wnt5a, in promoting senescence. Importantly, they also suggest that promoting EOC cells to undergo senescence represents a potential novel strategy for developing urgently needed EOC therapeutics.

## Materials and Methods

### Cells and culture conditions

Primary human ovarian surface epithelial (HOSE) cells were isolated and cultured as previously described (17). Human EOC cell lines were obtained from American Type Culture Collection (ATCC) and were passaged for less than 6 months. EOC cell line identification was further confirmed by DNA Diagnostic Center (www.dnacenter.com). EOC cell lines were cultured according to ATCC in RPMI-1640 medium supplemented with 10% FBS. 5-Aza-cytidine (Aza-C; Sigma) was used at working concentration of 5  $\mu$ mol/L (18).

### Human ovarian specimens and immunohistochemistry

The protocol to evaluate deidentified human tissue specimens was approved by Fox Chase Cancer Center (FCCC) institutional review board. Ovarian tumor microarray and normal human ovary and fallopian tube specimens were obtained from the FCCC Biosample Repository Core Facility (BRCF). Histopathology of the selected specimens on the tumor microarrays was provided by BRCF. Immunohistochemistry (IHC) was conducted by using goat anti-Wnt5a polyclonal antibody (R&D Systems) and mouse anti-Ki-67 (Dako) with a DAKO EnVision System and the Peroxidase (DAB) kit (DAKO Corporation) following the manufacturer's instructions and as previously described (17). Wnt5a staining was scored in a double-blinded manner by Dr. Qi Cai at the BRCF, and a proportion of the cases were independently confirmed by Dr. Hong Wu, a board-certified pathologist, at the FCCC Department of Pathology.

### Anchorage-independent soft agar colony formation assay

Soft agar assay were carried out as previously described (17). Briefly, 3,500 cells were resuspended in 0.35% low melt agarose dissolved in RPMI-1640 medium supplemented with 10% FBS and inoculated on top of 0.6% low melt agarose base in 6-well plates. After 2 weeks in culture, the plates were stained with

0.005% crystal violet, and the number of colonies was counted by using a dissecting microscope.

### Retrovirus production, infection, and drug selection

The following retrovirus constructs were used: pBABE-puro was obtained from Addgene, hygro-pWZL-luciferase was a kind gift of Dr. Denise Connolly, and pBABE-Wnt5a was generated by using standard cloning protocol. Retrovirus packaging was done as previously described by using Phoenix packaging cells (19, 20). To increase infection efficacy, double virus infection was carried out. For drug selection, 3  $\mu$ g/mL of puromycin was used for the OVCAR5 human EOC cell line.

### Reverse transcriptase PCR, quantitative reverse transcriptase PCR, and immunoblotting

RNA from cultured primary HOSE cells or human EOC cell lines was isolated by using TRIzol (Invitrogen) according to manufacturer's instruction. For quantitative reverse transcriptase PCR (qRT-PCR), TRIzol-isolated RNA was further purified by using an RNeasy kit (QIAGEN) following manufacture's instruction. The *Wnt5a*, *CCND1*, *FOSL1*, and *c-MYC* primers used for qRT-PCR were purchased from SABiosciences. mRNA expression of the housekeeping gene  $\beta$ -2-microglobulin (B2M) was used to normalize mRNA expression. Soluble  $\beta$ -catenin was extracted, using a buffer that consisting of 10 mmol/L Tris-HCl (pH 7.5), 0.05% NP-40, 10 mmol/L NaCl, 3 mmol/L  $MgCl_2$ , 1 mmol/L EDTA, and protease inhibitors (Roche) as previously described (21, 22). The following antibodies were used for immunoblotting from the indicated suppliers, goat anti-Wnt5a (R&D Systems), mouse  $\beta$ -actin (Sigma), mouse anti-GAPDH (Millipore), mouse anti- $\beta$ -catenin, mouse anti-Rb (BD Biosciences), and rabbit anti-pRBpS780 (Cell Signaling).

### Immunofluorescence and SA- $\beta$ -gal staining

Indirect immunofluorescence staining was carried out as previously described (19, 20, 22). The following antibodies were used for immunofluorescence: a cocktail of mouse anti-HIRA monoclonal antibodies (WC19, WC117, and WC119; 1:10; ref. 20) and a rabbit anti-PML antibody (Chemicon, 1:5,000). Images were captured by a DS-QiImc camera on a Nikon Eclipse 80i microscope and processed by NIS-Elements BR3.0 software (Nikon). SA- $\beta$ -gal staining was carried out as described previously (3, 23). For SA- $\beta$ -gal staining in sections from xenografted tumors, 8 separate fields were examined from 2 individual tumors for each of the groups.

### *In vivo* orthotopic xenograft tumorigenesis study

The protocol was approved by the FCCC Institutional Animal Care and Use Committee. OVCAR5 cells were infected with a luciferase-encoding retrovirus (hygro-pWZL-luciferase) and infected cells were selected with 50  $\mu$ g/mL hygromycin. Drug-selected cells were then infected with control or Wnt5a-encoding retrovirus and subsequently selected with 3  $\mu$ g/mL puromycin and 50  $\mu$ g/mL hygromycin. A total of  $3 \times 10^6$  drug-selected cells were unilaterally injected into the ovarian bursa sac of immunocompromised mice (6 mice per group; ref. 24). From day 10 postinfection, tumors were visualized by injecting luciferin (intraperitoneal, 4 mg/mice) resuspended in PBS and

imaged with an IVIS Spectrum imaging system every 5 days until day 30. Images were analyzed by Live Imaging 4.0 software. At day 30, tumors were surgically dissected and either fixed in 10% formalin or fresh-frozen in Optimal Cutting Temperature compound (Tissue-Tek). Sections of the dissected tumors were processed by the FCCC Histopathology Core Facility.

### Statistical analysis

Quantitative data are expressed as mean  $\pm$  SD, unless otherwise indicated. ANOVA with Student's *t* test was used to identify significant differences in multiple comparisons. The Pearson  $\chi^2$  test was used to analyze the relationship between categorical variables. Overall survival was defined as the time elapsed from the date of diagnosis and the date of death from any cause or the date of last follow-up. Kaplan–Meier survival plots were generated and comparisons were made by using the log-rank sum statistic. For all statistical analyses, the level of significance was set at 0.05.

## Results

### Wnt5a is expressed at significantly lower levels in human EOC cell lines and primary human EOCs compared with normal human ovarian surface epithelium or fallopian tube epithelium

To determine Wnt5a expression in human EOC cell lines and primary HOSE cells, we examined the relative Wnt5a mRNA levels by carrying out semiquantitative RT-PCR. We observed that Wnt5a mRNA levels were greatly diminished in human EOC cell lines compared with primary HOSE cells (Fig. 1A). This finding was further confirmed through qRT-PCR analysis of Wnt5a mRNA in multiple isolations of primary HOSE cells and human EOC cell lines, showing that the levels of Wnt5a mRNA were significantly lower in human EOC cell lines compared with primary HOSE cells (Fig. 1B;  $P = 0.008$ ). Consistently, we observed that Wnt5a protein levels were also lower in human EOC cell lines compared with primary HOSE cells as determined by immunoblotting (Fig. 1C). On the basis of these results, we conclude that Wnt5a is expressed at lower levels in human EOC cell lines compared with primary HOSE cells.

We next determined whether the loss of Wnt5a expression found in human EOC cell lines was also observed in primary human EOCs. We examined Wnt5a expression in 130 cases of primary human EOC specimens and 31 cases of normal human ovary with surface epithelium by IHC, using an antibody against Wnt5a (Table 1). In addition, there is recent evidence to suggest that a proportion of high-grade serous EOC may arise from distant fallopian tube epithelium (25). Thus, we also included 28 cases of normal human fallopian tube specimens in our IHC analysis (Table 1). The specificity of the anti-Wnt5a antibody was confirmed in our study (Supplementary Fig. S1). A single band at predicted molecular weight ( $\sim 42$  kDa) was detected in OVCAR5 cells with ectopically expressed Wnt5a and was absent after expression of a short hairpin RNA to the human Wnt5a gene (shWnt5a), which effectively knocked down Wnt5a mRNA expression (Supplementary Fig. S1A and data not shown). In addition, Wnt5a staining was lost when

primary anti-Wnt5a antibody was replaced with an isotype-matched IgG control (Supplementary Fig. S1B).

As shown in Figure 1D, in normal human ovarian surface epithelial cells and fallopian tube epithelial cells, both cytoplasm and cell membrane were positive for Wnt5a IHC staining (black arrows, Fig. 1D). In contrast, Wnt5a staining in EOC cells was dramatically decreased (Fig. 1D). We scored expression of Wnt5a as high ( $H$ -score  $\geq 30$ ) or low ( $H$ -score  $< 30$ ) on the basis of a histological score ( $H$ -score; 26), which considers both intensity of staining and percentage of positively stained cells, as previously described (17). Wnt5a expression was scored as high in 58.1% (18/31) cases of normal human ovarian surface epithelium and 82.1% (23/28) cases of normal human fallopian tube epithelium (Table 1). In contrast, Wnt5a expression was scored as high in 37.7% (49/130) cases of primary human EOCs (Table 1). Statistical analysis revealed that Wnt5a was expressed at significantly lower levels in primary human EOCs compared with either normal human ovarian surface epithelium ( $P = 0.039$ ) or normal human fallopian tube epithelium ( $P < 0.001$ ; Table 1). On the basis of these studies, we conclude that Wnt5a is expressed at significantly lower levels in primary human EOCs compared with either normal human ovarian surface epithelium or fallopian tube epithelium.

### Wnt5a expression negatively correlates with tumor stage and lower Wnt5a expression predicts shorter overall survival

We next examined the correlation between Wnt5a expression and clinical and pathologic features of human EOCs. Significantly, there was a negative correlation between Wnt5a expression and tumor stage ( $P = 0.003$ ; Table 1). Notably, the majority of examined cases are high-grade serous subtypes that are usually of stage 3/4. In addition, we examined the correlation between expression of Wnt5a and a marker of cell proliferation, Ki-67 (ref. 27; Fig. 1E). There was a significant negative correlation between Wnt5a expression and Ki-67 ( $P = 0.038$ ; Table 1). We next assessed whether Wnt5a expression based on  $H$  score might predict prognosis of EOC patients (High,  $H$ -score  $\geq 30$ ; Low,  $H$ -score  $< 30$ ;  $n = 123$ ), for which long-term follow-up data were available. Significantly, lower Wnt5a expression correlated with shorter overall survival in the examined EOC patients ( $P = 0.003$ ; Fig. 1F). Together, we conclude that a lower level of Wnt5a expression correlates with tumor stage and predicts shorter overall survival in human EOC patients.

### Wnt5a gene promoter hypermethylation contributes to its downregulation in human EOC cells

Wnt5a gene promoter hypermethylation has been implicated as a mechanism underlying its silencing in several types of human cancers (16). Consistently, we also observed Wnt5a gene promoter hypermethylation in a number of human EOC cell lines (Fig. 2A; Supplementary Table S1). Further supporting a role of promoter hypermethylation in suppression of Wnt5a expression, treatment with a DNA demethylation drug, Aza-C (28), in PEO1 EOC cells resulted in a significant increase in levels of both Wnt5a mRNA and protein (Fig. 2B and C). We



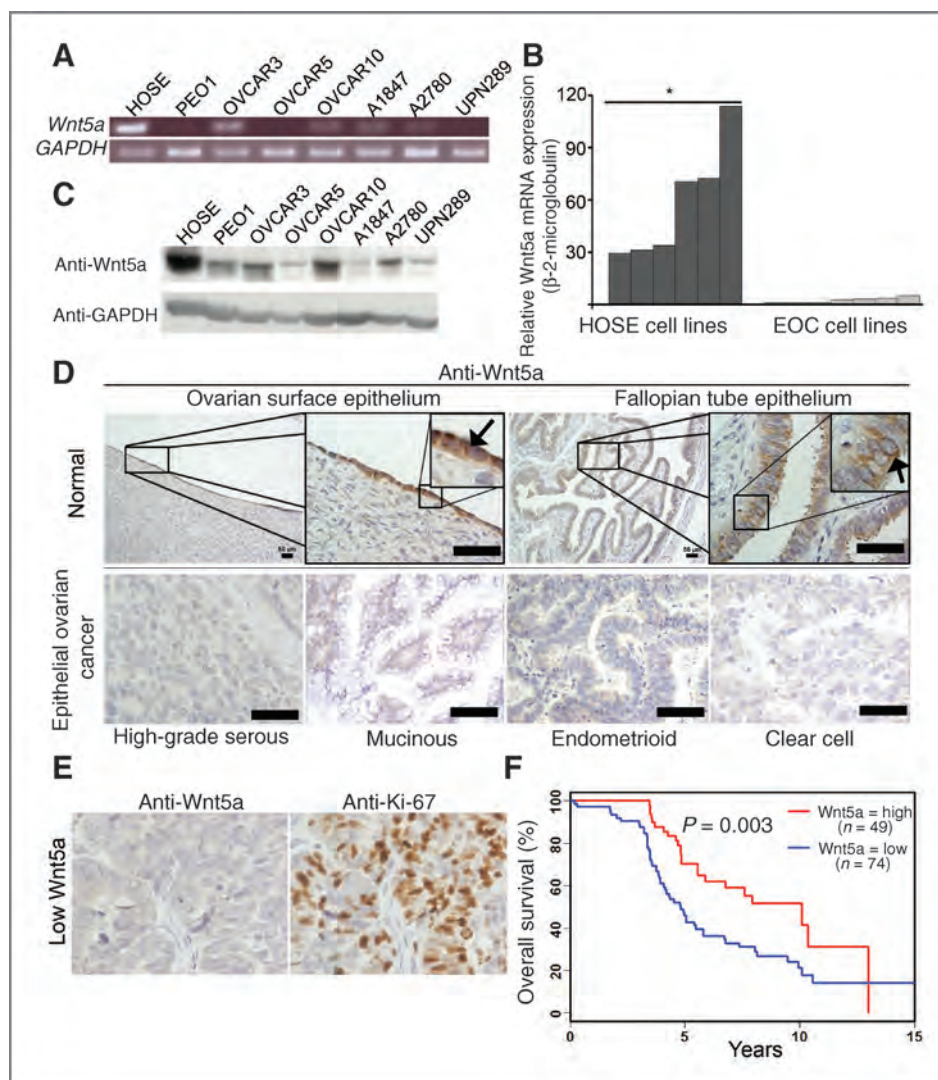


**Figure 1.** Wnt5a is expressed at significantly lower levels in human EOC cells compared with normal human ovarian surface or fallopian tube epithelial cells, and a lower level of Wnt5a expression predicts shorter overall survival in human EOC patients. **A**, expression of Wnt5a mRNA in primary HOSE cells and the indicated human EOC cell lines was determined by semiquantitative RT-PCR. Expression of glyceraldehyde 3-phosphate dehydrogenase (GAPDH) mRNA was used as a loading control. **B**, Wnt5a mRNA levels were quantified by qRT-PCR in 6 individual isolations of primary HOSE cells and 7 different EOC cell lines. Expression of  $\beta$ -2-microglobulin was used to normalize Wnt5a mRNA expression. \*,  $P = 0.008$  compared with human EOC cells. **C**, same as **A**, but examined for Wnt5a and GAPDH protein expression by immunoblotting. **D**, examples of Wnt5a IHC staining in normal human ovarian surface epithelium, fallopian tube epithelium, and EOC of indicated histologic subtypes. Bar, 50  $\mu$ m. Arrows point to examples of positively stained human ovarian surface epithelial cells and fallopian tube epithelial cells. **E**, representative images from tissue microarray depicting low Wnt5a expression correlated with high Ki-67, a cell proliferation marker. **F**, loss of Wnt5a expression is an independent poor prognosis marker in human EOC patients. A lower level of Wnt5a expression correlates with shorter overall survival in human EOC patients. The univariate overall survival curve (Kaplan–Meier method) for EOC patients ( $n = 123$ ) with high- or low-Wnt5a expression as determined by immunohistochemical analysis.

conclude that *Wnt5a* gene promoter hypermethylation contributes to its downregulation in human EOC cells.

#### Wnt5a restoration inhibits the growth of human EOC cells by antagonizing the canonical Wnt/ $\beta$ -catenin signaling

We next sought to determine the effects of Wnt5a reconstitution in human EOC cells. Wnt5a expression was reconstituted in the OVCAR5 EOC cell line via retroviral transduction. Ectopically expressed Wnt5a was confirmed by

both qRT-PCR and immunoblotting in OVCAR5 cells stably expressing Wnt5a or a vector control (Fig. 3A and B). Of note, the levels of ectopically expressed Wnt5a in OVCAR5 cells are comparable with the levels observed in primary HOSE cells (Fig. 3B). Interestingly, Wnt5a reconstitution in OVCAR5 human EOC cells significantly inhibited both anchorage-dependent and anchorage-independent growth in soft agar compared with vector controls (Fig. 3C and D). In addition, similar growth inhibition by Wnt5a reconstitution was also observed in the PEO1 human EOC cell line

**Table 1.** Wnt5a expression in primary human EOCs and correlation of its expression with clinicopathologic variables

| Patient characteristics           | Wnt5a protein expression |          |           |          | P                  |
|-----------------------------------|--------------------------|----------|-----------|----------|--------------------|
|                                   | Low (n)                  | High (n) | Total (n) | High (%) |                    |
| <i>Age (23–85 y; mean 59.2 y)</i> |                          |          |           |          |                    |
| ≤55                               | 24                       | 16       | 40        | 40.0     | 0.900              |
| >55                               | 52                       | 33       | 85        | 38.8     |                    |
| Unknown                           | 5                        | 0        | 5         |          |                    |
| <i>Laterality</i>                 |                          |          |           |          |                    |
| Left                              | 22                       | 14       | 36        | 38.9     | 0.957              |
| Right                             | 12                       | 9        | 21        | 42.9     |                    |
| Bilaterality                      | 35                       | 24       | 59        | 40.7     |                    |
| Undetermined                      | 12                       | 2        | 14        |          |                    |
| <i>Histotype</i>                  |                          |          |           |          |                    |
| EOC                               | 81                       | 49       | 130       | 37.7     | 0.005 <sup>a</sup> |
| Type I                            | 16                       | 21       | 37        | 56.8     |                    |
| Low-grade serous                  | 1                        | 1        | 2         | 50.0     |                    |
| Endometrioid                      | 4                        | 9        | 13        | 69.2     |                    |
| Mucinous                          | 2                        | 3        | 5         | 60.0     |                    |
| Clear cell                        | 5                        | 4        | 9         | 44.4     |                    |
| Others                            | 4                        | 4        | 8         | 50.0     |                    |
| Type II                           |                          |          |           |          |                    |
| High-grade serous                 | 65                       | 28       | 93        | 30.1     |                    |
| Normal epithelium                 |                          |          |           |          |                    |
| Ovarian surface                   | 13                       | 18       | 31        | 58.1     |                    |
| Fallopian tube                    | 5                        | 23       | 28        | 82.1     |                    |
| <i>Ki-67</i>                      |                          |          |           |          |                    |
| Low                               | 22                       | 23       | 44        | 52.3     | 0.038              |
| High                              | 51                       | 24       | 75        | 32.0     |                    |
| Undetermined                      | 7                        | 3        | 11        |          |                    |
| <i>Tumor grade</i>                |                          |          |           |          |                    |
| 1                                 | 3                        | 7        | 10        | 70.0     | 0.003 <sup>c</sup> |
| 2                                 | 12                       | 8        | 20        | 40.0     |                    |
| 3                                 | 64                       | 31       | 95        | 32.6     |                    |
| Undetermined                      | 2                        | 3        | 5         |          |                    |
| <i>Tumor stage</i>                |                          |          |           |          |                    |
| Stage 1/2                         | 12                       | 18       | 30        | 60.0     | 0.003 <sup>c</sup> |
| Stage 3/4                         | 67                       | 29       | 96        | 30.2     |                    |
| Undetermined                      | 2                        | 2        | 4         |          |                    |

<sup>a</sup>Compared with type I EOC.<sup>b</sup>Compared with EOC.<sup>c</sup>Compared with stage 1/2.

(Supplementary Fig. S2A–C) suggesting that this effect is not cell line specific. On the basis of these results, we conclude that Wnt5a reconstitution inhibits the growth of human EOC cells *in vitro*.

Canonical Wnt signaling promotes cell proliferation and Wnt5a has been shown to antagonize the canonical Wnt/β-catenin signaling in certain cell contexts (16, 29–31). Because Wnt5a expression inversely correlated with expression of Ki-67 (Fig. 1E; Table 1), a cell proliferation marker, we hypothesized that Wnt5a would suppress the growth of human EOC cells by

antagonizing canonical Wnt/β-catenin signaling. To test our hypothesis, we examined the effect of Wnt5a reconstitution on expression of markers of active Wnt/β-catenin signaling in human EOC cells, namely the levels of "active" soluble β-catenin (21, 22, 32) and expression of β-catenin target genes such as *CCND1*, *c-MYC*, and *FOSL1* (12, 13). Indeed, we observed a decrease in soluble β-catenin in Wnt5a-reconstituted OVCAR5 cells compared with vector controls (Fig. 3E). Consistently, we also observed a significant decrease in the levels of β-catenin target genes in these cells, namely *CCND1*

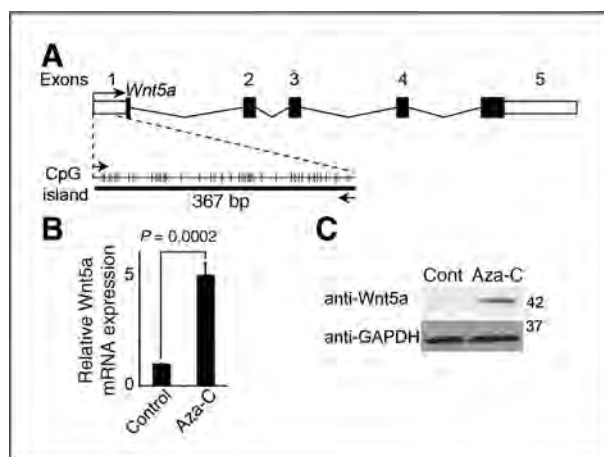


**Figure 2.** Promoter DNA CpG island hypermethylation contributes to Wnt5a downregulation in human EOC cells. **A**, schematic structure of the human *Wnt5a* gene transcript and its promoter CpG islands. Locations of exon 1 (open rectangle), CpG sites (vertical lines) and coding exons (filled rectangle), and the transcription start site (curved arrow) are indicated. Flat arrows indicate the positions of primers used for PCR amplification, and the size of PCR product is also indicated. **B**, PEO1 cells were treated with 5  $\mu$ mol/L Aza-C for 4 days, and mRNA was isolated from control- and Aza-C-treated cells and examined for *Wnt5a* mRNA expression by qRT-PCR. Mean of 3 independent experiments with SD. **C**, same as (**B**) but examined for Wnt5a protein expression by immunoblotting.

( $P = 0.0095$ ), *FOSL1* ( $P = 0.0012$ ), and *c-MYC* ( $P = 0.0286$ ; Fig. 3F). Similar effects of Wnt5a reconstitution on expression of markers of active Wnt/ $\beta$ -catenin signaling (such as decreased levels of soluble  $\beta$ -catenin) were also observed in PEO1 human EOC cells (Supplementary Fig. S2D), suggesting that this is not cell line specific. On the basis of these results, we conclude that Wnt5a suppresses the growth of human EOC cells by antagonizing canonical Wnt/ $\beta$ -catenin signaling in human EOC cells.

#### Wnt5a reconstitution drives cellular senescence in human EOC cells

Next, we sought to determine the cellular mechanism whereby Wnt5a inhibits the growth of human EOC cells. We have previously shown that suppression of canonical Wnt signaling promotes cellular senescence in primary human fibroblasts by activating the senescence-promoting histone repressor A (HIRA)/promyelocytic leukemia (PML) pathway (22). PML bodies are 20 to 30 dot-like structures in the nucleus of virtually all human cells. PML bodies are sites of poorly defined tumor suppressor activity and are disrupted in acute PML (33). PML has been implicated in regulating cellular senescence. For example, the foci number and size of PML bodies increase during senescence (33, 34) and inactivation of PML suppresses senescence (35). Activation of the HIRA/PML pathway is reflected by the recruitment of HIRA into PML bodies (36).

To determine whether Wnt5a reconstitution activates the HIRA/PML senescence pathway and induces senescence in EOC cells, we first sought to determine whether the HIRA/PML pathway is conserved in human ovarian epithelial cells. Ectop-

ically expressing activated oncogenes (such as oncogenic *RAS*) is a standard approach for inducing senescence in a synchronized manner in primary human cells (1, 2, 19, 20). Indeed, ectopic expression of oncogenic *H-RAS*<sup>G12V</sup> induced senescence of primary HOSE cells, as evident by an increase in SA- $\beta$ -gal activity, a universal marker of cellular senescence (Supplementary Fig. S3A and B). Notably, the HIRA/PML pathway was activated during senescence of primary HOSE cells induced by oncogenic *RAS*, as evident by the relocalization of HIRA into PML bodies (Supplementary Fig. S3C and D). This result shows that the senescence-promoting HIRA/PML pathway is conserved in human ovarian epithelial cells. In addition, primary HOSE cells with HIRA foci displayed a marked decrease in BrdU incorporation, a marker of cell proliferation, compared with HIRA foci-negative cells (Supplementary Fig. S3E and F). This result is consistent with the idea that activation of the HIRA/PML pathway is directly correlated with senescence-associated cell growth arrest (37).

We next asked whether Wnt5a expression is regulated during natural senescence of primary HOSE cells. Indeed, we observed an increase in the levels of Wnt5a mRNA in senescent primary HOSE cells compared with young cells (Fig. 4A–C). In addition, we found that ectopic Wnt5a induces senescence of primary HOSE cells (Fig. 4D–F). Together, we conclude that Wnt5a plays a role in regulating senescence of primary HOSE cells.

As Wnt5a antagonizes canonical Wnt signaling in human EOC cells (Fig. 3E and F), we sought to determine whether Wnt5a restoration might activate the senescence-promoting HIRA/PML pathway and induce senescence in human EOC cells. Toward this goal, we examined the localization of HIRA in OVCAR5 EOC cells reconstituted with Wnt5a or vector control. Notably, there was a significant increase in the percentage of cells with HIRA localized to PML bodies in Wnt5a restored human EOC cells compared with controls (Fig. 5A and B;  $P = 0.004$ ). In addition, we also observed an increase in the number and size of PML bodies in the Wnt5a restored OVCAR5 EOC cells (Fig. 5A), which are also established markers of cellular senescence (35, 38). Similarly, we observed activation of the HIRA/PML pathway by Wnt5a restoration in PEO1 human EOC cells (Supplementary Fig. S4A and B), suggesting that the observed effects are not cell line specific. Together, we conclude that Wnt5a reconstitution activates the HIRA/PML senescence pathway.

The p53 and pRB tumor suppressor pathways play a key role in regulating senescence (1). Thus, we sought to determine whether activation of the HIRA/PML pathway depends on the p53 and pRB pathways. Interestingly, p16<sup>INK4a</sup>, the upstream repressor of pRB, is deleted in OVCAR5 human EOC cell line (39). In addition, the levels of total phosphorylated pRB were not decreased by Wnt5a, whereas the levels of cyclin D1/CKD4-mediated Serine 780 phosphorylation on pRB (pRBpS780) were decreased by Wnt5a (ref. 40; Fig. 5C and D). Furthermore, p53 is null in OVCAR5 cells (41). We conclude that activation of the HIRA/PML pathway is independent of the p53 and p16<sup>INK4a</sup>.

We next sought to determine whether Wnt5a restoration induces SA- $\beta$ -gal activity, a universal marker of cellular senescence (1). Indeed, SA- $\beta$ -gal activity was notably induced by



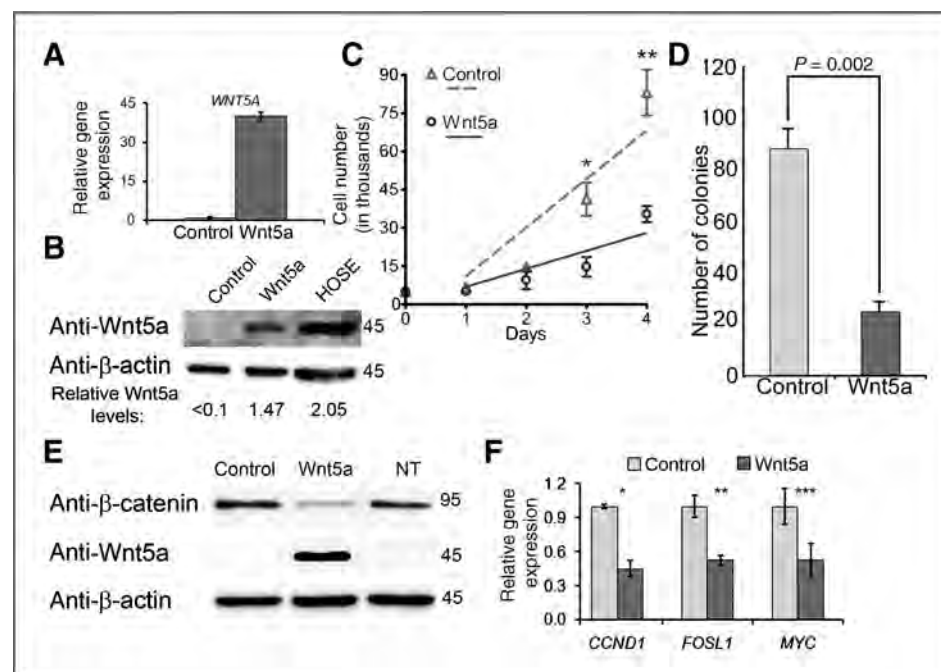


**Figure 3.** Wnt5a restoration inhibits the growth of human EOC cells by antagonizing canonical Wnt/β-catenin signaling. **A**, OVCAR5 cells were transduced with a control or Wnt5a-encoding puromycin-resistant retrovirus. The infected cells were drug-selected with 3 μg/mL puromycin. Expression of Wnt5a mRNA in drug-selected cells was determined by qRT-PCR. **B**, same as **A**, but examined for expression of Wnt5a and β-actin in control or Wnt5a-infected OVCAR5 and primary HOSE cells by immunoblotting. Relative levels of Wnt5a expression was indicated on the basis of the densitometric analysis, using NIH ImageJ software. **C**, same as **A**, but equal number (5,000) of drug-selected control (open triangles and dotted line) or Wnt5a-infected cells (open circles and solid line) were cultured on plastic plates for 4 days, and the number of cells was counted [control ± SD or Wnt5a ± SD ( $n = 3$ ); Student's *t* test was used for calculating *P* value] at day 1 ( $6,666 \pm 1,258$  vs.  $5,000 \pm 1,000$ ;  $P = 0.1469$ ), day 2 ( $14,583 \pm 954$  vs.  $9,583 \pm 3,463$ ;  $P = 0.084$ ), day 3 ( $41,250 \pm 6,538$  vs.  $14,750 \pm 2,787$ ; \*,  $P = 0.0038$ ), and day 4 ( $83,055 \pm 8,978$  vs.  $35,416 \pm 2,055$ ; \*\*,  $P = 0.001$ ). Mean of 3 independent experiments with SD and linear regression. **D**, same as **C**, but grown under anchorage-independent condition in soft agar. The number of colonies was counted 2 weeks after initial inoculation. Mean of 3 independent experiments with SD. **E**, same as **A**, but examined for the levels of soluble β-catenin and β-actin expression by immunoblotting. NT, nontreated. **F**, same as **A**, but examined for expression of indicated β-catenin target genes by qRT-PCR. Expression of β-2-microglobulin was used to normalize the expression of indicated genes. \*,  $P = 0.0095$ ; \*\*,  $P = 0.0012$ ; and \*\*\*,  $P = 0.0286$  compared with controls.

Wnt5a reconstitution in both OVCAR5 and PEO1 human EOC cells compared with controls (Fig. 5E and F; Supplementary Fig. S4C and D, respectively). On the basis of these results, we concluded that Wnt5a restoration induced senescence of human EOC cells by activating the HIRA/PML senescence pathway.

#### Wnt5a inhibits the growth of human EOC cells *in vivo* by inducing cellular senescence

We next sought to determine whether Wnt5a would mediate growth inhibition and induce senescence *in vivo* in an orthotopic EOC model in immunocompromised mice. A luciferase gene was retrovirally transduced into control or Wnt5a-reconstituted OVCAR5 cells to monitor the cell growth *in vivo* via noninvasive imaging. These cells were injected unilaterally into the bursa sac covering the ovary in female immunocompromised mice ( $n = 6$  for each of the groups; Supplementary Fig. S5). Tumor growth was monitored every 5 days starting at day 10 postinjection by measuring luciferase activity, and the growth of the tumor was followed for a total of 30 days (Fig. 6A). Wnt5a significantly suppressed the growth of xenografted OVCAR5 human EOC cells compared with controls (Fig. 6B;  $P < 0.03$ ). Consistently, following general pathologic examination during surgical dissection at day 30, we observed that tumor

sizes were notably smaller from mice injected with Wnt5a-reconstituted OVCAR5 cells compared with controls (data not shown). The expression of ectopic Wnt5a was confirmed by IHC staining in sections from dissected tumors (Fig. 6C).

We next sought to determine whether cell proliferation was suppressed by Wnt5a reconstitution in dissected tumors. Toward this goal, we examined the expression of Ki-67 by IHC. We observed, there was a significant decrease in the number of Ki-67-positive cells in tumors formed by Wnt5a-reconstituted OVCAR5 cells compared with controls (Fig. 6D and E). In addition, intensity of Ki-67 staining was also notably weaker in Ki-67-positive Wnt5a-reconstituted OVCAR5 cells than in control Ki-67-positive cells (Fig. 6D). On the basis of these results, we conclude that Wnt5a reconstitution inhibits the proliferation of human EOC cells *in vivo* in an orthotopic xenograft EOC model.

We next investigated whether the growth inhibition observed by Wnt5a reconstitution *in vivo* was due to induction of cellular senescence. Toward this goal, we examined the expression of SA-β-gal activity in fresh sections of dissected tumors formed by OVCAR5 cells reconstituted with Wnt5a or control cells. Indeed, we observed a significant increase in the number of cells positive for SA-β-gal activity in OVCAR5 cells reconstituted with Wnt5a compared with control tumors



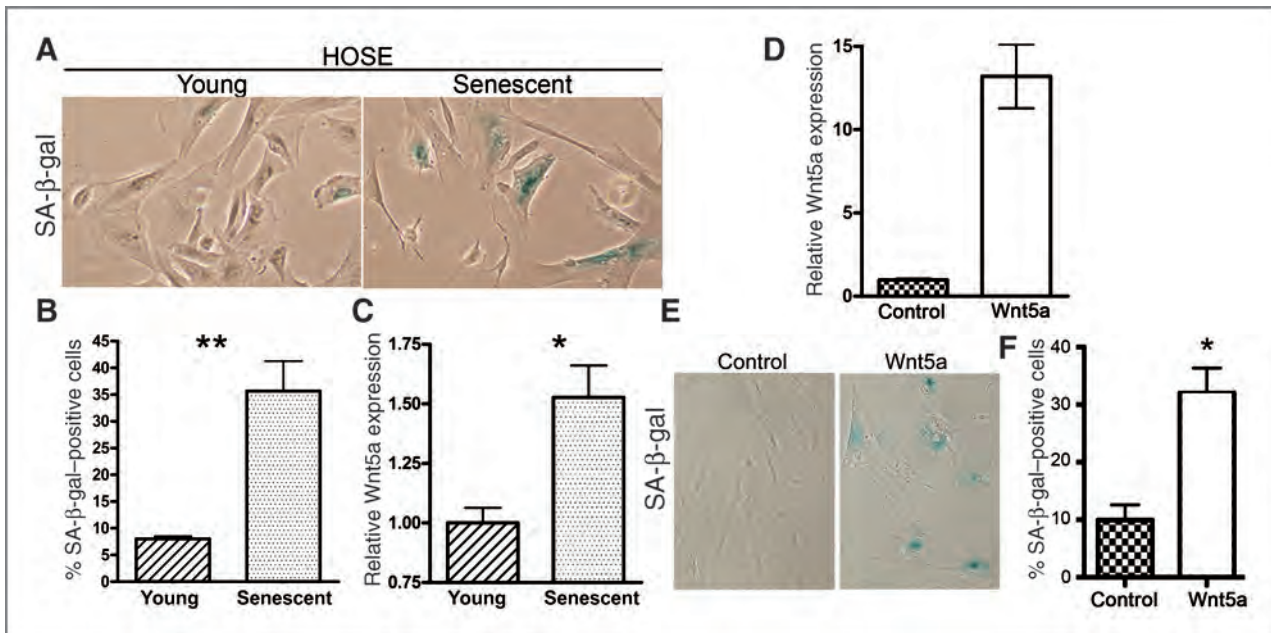


**Figure 4.** Wnt5a promotes senescence of primary HOSE cells. A, young proliferating primary HOSE cells were passaged to senescence (after 7 population doublings). Expression of SA-β-gal activity was measured in young and naturally senescent primary HOSE cells. B, same as (A). Quantitation of SA-β-gal-positive cells. \*\*,  $P < 0.001$ . C, same as (A), but mRNA was isolated and examined for *Wnt5a* expression by qRT-PCR. Expression of B2M was used as a control. \*,  $P = 0.003$ . D, young primary HOSE cells were transduced with retrovirus encoding human *Wnt5a* gene or a control. Expression of Wnt5a in indicated cells was determined by qRT-PCR. Expression of B2M was used as a control. E, same as (D), but stained for expression of SA-β-gal activity in drug-selected cells. F, quantitation of (E). Mean of 3 independent experiments with SD. \*,  $P < 0.05$ .

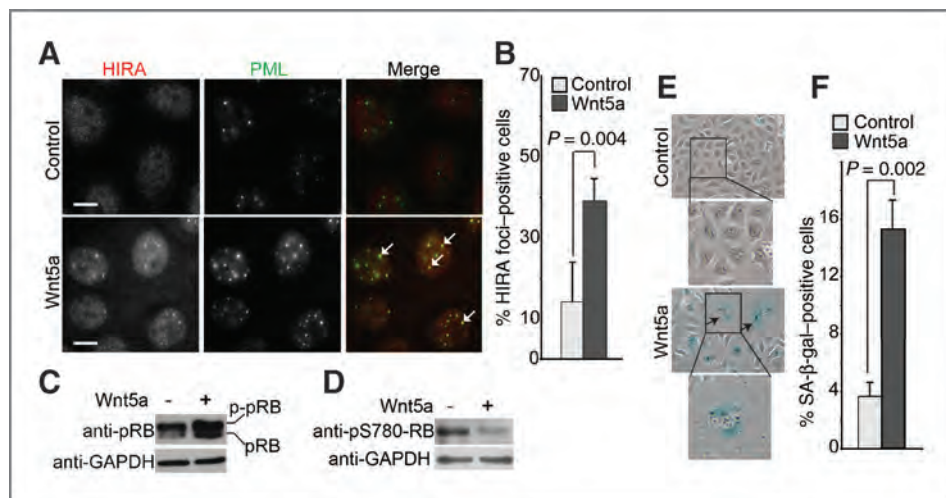
(Fig. 6F and G;  $P = 0.003$ ). Together, we conclude that Wnt5a reconstitution inhibits the growth of human EOC cells *in vivo* by inducing cellular senescence.

## Discussion

Driving cancer cells to undergo cellular senescence has recently been proposed to be a novel mechanism to target for developing cancer therapeutics (1, 6). For example, pharmacologic inhibitor of *PTEN* drives senescence and, consequently, inhibits tumorigenesis *in vivo* in xenograft models of *PTEN*

heterozygous prostate cancer cells (42, 43). Compared with apoptosis, therapeutics that drive cellular senescence are proposed to have less cytotoxic side effects (6), which makes pro-senescence therapy attractive. Herein, we describe that restoration of Wnt5a signaling drives senescence of human EOC cells both *in vitro* and *in vivo* in an orthotopic mouse model of EOC (Figs. 5 and 6). Restoring gene expression by gene therapy has had limited success. Therefore, restoring Wnt5a signaling via exogenous ligand could prove to be an alternative approach. Interestingly, it has been previously reported that a Wnt5a-derived hexapeptide is sufficient to restore Wnt5a

**Figure 5.** Wnt5a restoration triggers cellular senescence in human EOC cells. A, control and Wnt5a-expressing OVCAR5 EOC cells were stained with antibodies to HIRA and PML. Arrows point to examples of colocalized HIRA and PML bodies. Bar, 10 μm. B, quantitation of (A). A total of 200 cells from control and Wnt5a-expressing cells were examined for HIRA and PML colocalization. Mean of 3 independent experiments with SD. C, same as (A), but examined for pRB and GAPDH expression. D, same as (C), but examined for pRBpS780 and GAPDH expression. E, same as (A), but examined for SA-β-gal activity. F, quantitation of (E). Mean of 3 independent experiments with SD.



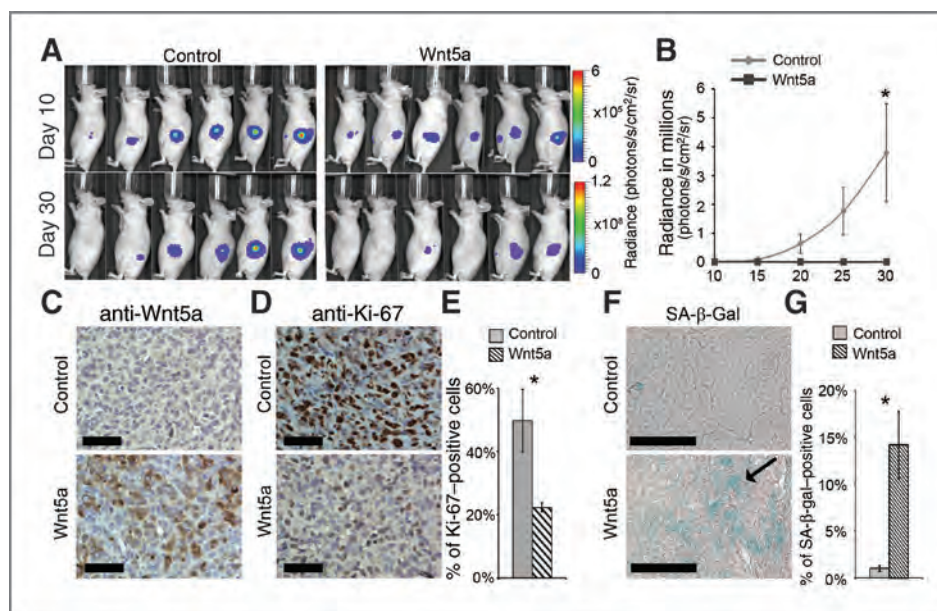


**Figure 6.** Wnt5a restoration inhibits tumor growth and promotes senescence of human EOC cells *in vivo*. **A**, OVCAR5 cells were transduced with luciferase-encoding hygromycin-resistant retrovirus together with a control or Wnt5a-encoding puromycin-resistant retrovirus. Drug-selected cells were unilaterally injected into the periovarian bursa sac of the female immunocompromised mice ( $n = 6$  for each of the groups). The radiance of luciferase bioluminescence, an indicator of the rate for tumor growth, was measured every 5 days from day 10 until day 30 by using the IVIS imaging system. Shown are images taken at day 10 and day 30, respectively. **B**, quantitation of tumor growth from injected OVCAR5 cells expressing Wnt5a or control at indicated time points. \*,  $P = 0.038$  compared with controls. **C**, following tumor dissection, expression of Wnt5a in tumors formed by control or Wnt5a-expressing OVCAR5 EOC cells was determined by immunohistochemical staining against Wnt5a (magnification, 40 $\times$ ). Bar, 50  $\mu$ m. **D**, same as (C), but examined for expression of Ki-67, a marker of cell proliferation (magnification, 40 $\times$ ). Bar, 50  $\mu$ m. **E**, quantitation of (D). \*,  $P = 0.008$  compared with controls. **F**, expression of SA- $\beta$ -gal activity was examined on sections of fresh-frozen tumors formed by OVCAR5 cells expressing control or Wnt5a (magnification, 40 $\times$ ). Bar, 100  $\mu$ m. **G**, quantitation of (F). \*,  $P = 0.003$  compared with controls. Arrow points to an example of SA- $\beta$ -gal positive cells.

signaling both *in vitro* and *in vivo* in xenograft models of breast cancer (44). It would be interesting to test whether the Wnt5a-derived hexapeptide will be sufficient to reconstitute Wnt5a signaling and drive senescence of EOC cells. Our data suggest that cellular senescence is a potential target for developing EOC therapeutics. In addition, these data imply that restoration of Wnt5a signaling represents a potential novel strategy to drive senescence of EOC cells.

This study is the first to show a role for Wnt5a in regulating senescence. We showed that Wnt5a activated the senescence-promoting HIRA/PML pathway in human EOC cells (Fig. 5A; Supplementary Fig. S4A). In primary human cells, activation of HIRA/PML pathway is sufficient to drive senescence by facilitating epigenetic silencing of proliferation-promoting genes (such as E2F target genes; ref. 19). Herein, we reported for the first time that the key HIRA/PML senescence pathway can be reactivated to drive senescence of human cancer cells. Further studies are warranted to elucidate the molecular basis by which Wnt5a restoration and activation of HIRA/PML pathway drive cellular senescence in human EOC cells.

Interestingly, senescence induced by Wnt5a restoration in human EOC cells was independent of both the p53 and p16<sup>INK4a</sup> tumor suppressors, which implies that EOC cells that lack p53 and p16<sup>INK4a</sup> retain the capacity to undergo senescence via HIRA/PML pathway through suppressing the canonical Wnt signaling. This is consistent with previous reports showing that cancer cells that lack p53 and pRB retain the

capacity to undergo senescence when treated with anticancer agents or ionizing radiation (6). Notably, although the levels of total phosphorylated pRB were not decreased by Wnt5a, we observed a decrease in the levels of pRBpS780 that is mediated by cyclin D1/CDK4 (Fig. 5C and D). Future studies will determine whether the decrease in pRBpS780 levels plays a role in regulating senescence of human EOC cells.

Expression of Wnt5a is altered in many types of cancers (45). For example, in melanoma, Wnt5a overexpression correlates with cancer progression and a higher tumor stage (16). However, in colorectal and esophageal squamous cell carcinomas, Wnt5a has been described to be a tumor suppressor and was frequently silenced by promoter hypermethylation (16, 46). Consistently, we also observed Wnt5a promoter hypermethylation in a number of human EOC cell lines in which Wnt5a is downregulated (Fig. 2; Supplementary Table S1). This result is consistent with the idea that Wnt5a promoter hypermethylation contributes to Wnt5a downregulation in human EOC cells.

Wnt5a function is highly dependent on cellular context (45). For example, the cellular Wnt receptor/coreceptor context dictates the downstream signaling pathways upon the binding of Wnt5a, which include activating noncanonical Wnt signaling or antagonizing canonical Wnt/ $\beta$ -catenin signaling (47). These reports illustrate that Wnt5a expression and its resulting activity are cell type and context dependent. The Wnt receptor/coreceptor profile in EOC cells is currently unknown, and our future studies will elucidate the mechanism by which Wnt5a

antagonizes Wnt/ $\beta$ -catenin signaling in human EOC cells. Regardless, our data show that Wnt5a downregulation is an independent predictor for overall survival in EOC patients. In contrast, 2 other studies showed that higher Wnt5a expression predicts poor survival in EOC patients (48, 49). The basis for this discrepancy remains to be elucidated. An explanation may be that our study included more cases than the other 2 studies (130 EOC cases in our study vs. 38 cases in the study by Badiglian and colleagues or 63 cases in the study by Peng and colleagues). It may also be due to the difference in the composition of type I and type II cases in this study compared with the other 2 studies. The vast majority of EOC cases in this study are of type II high-grade serous subtypes. Consistently, our data showed that there is a difference in Wnt5a expression between type I and type II EOC ( $P = 0.005$ ; Table 1). Furthermore, it has been shown in microarray analysis that Wnt5a is expressed at lower levels in laser capture and microdissected high-grade serous EOC compared with normal primary HOSE cells (50).

In summary, the data reported here show that Wnt5a is often expressed at lower levels in human EOCs compared with either normal human ovarian surface epithelium or fallopian tube epithelium. A lower level of Wnt5a expression correlates with tumor stage and predicts shorter overall survival in EOC patients. Reconstitution of Wnt5a signaling inhibits the growth of human EOC cells both *in vitro* and *in vivo*. In addition, Wnt5a reconstitution suppresses the proliferation-promoting canonical Wnt/ $\beta$ -catenin signaling in human EOC cells. Significantly, Wnt5a reconstitution drives cellular senescence in human EOC

cells and this correlates with activation of the senescence-promoting HIRA/PML pathway. Together, our data imply that reconstitution of Wnt5a signaling to drive senescence of human EOC cells is a potential novel strategy for developing EOC therapeutics.

### Disclosure of Potential Conflicts of Interest

No potential conflicts of interest were disclosed.

### Acknowledgments

The authors thank Dr. Denise Connolly for reagent, Dr. Harvey Hensley for technical assistance, and Drs. Katherine Aird and Maureen Murphy for critical reading of the manuscript.

### Grant Support

R. Zhang is an Ovarian Cancer Research Fund (OCRF) Liz Tilberis Scholar. This work was supported in part by a NCI FCCC-UPenn ovarian cancer SPORE (P50 CA083638) pilot project and SPORE career development award (to R. Zhang), a DOD ovarian cancer academy award (OC093420 to R. Zhang), an OCRF program project (to R. Zhang, M.J. Birrer, and A.K. Godwin), and a generous gift from Catherine and Peter Getchell. B.G. Bitler is supported by a NCI postdoctoral training grant (CA-009035-35).

The costs of publication of this article were defrayed in part by the payment of page charges. This article must therefore be hereby marked *advertisement* in accordance with 18 U.S.C. Section 1734 solely to indicate this fact.

Received April 18, 2011; revised July 28, 2011; accepted July 29, 2011; published OnlineFirst August 4, 2011.

### References

- Kuilman T, Michaloglou C, Mooi WJ, Peeper DS. The essence of senescence. *Genes Dev* 2010;24:2463–79.
- Adams PD. Healing and hurting: molecular mechanisms, functions, and pathologies of cellular senescence. *Mol Cell* 2009;36:2–14.
- Dimri GP, Lee X, Basile G, Acosta M, Scott G, Roskelley C, et al. A biomarker that identifies senescent human cells in culture and in aging skin *in vivo*. *Proc Natl Acad Sci U S A* 1995;92:9363–7.
- Ventura A, Kirsch DG, McLaughlin ME, Tuveson DA, Grimm J, Lintault L, et al. Restoration of p53 function leads to tumour regression *in vivo*. *Nature* 2007;445:661–5.
- Xue W, Zender L, Miething C, Dickins RA, Hernando E, Krizhanovskiy V, et al. Senescence and tumour clearance is triggered by p53 restoration in murine liver carcinomas. *Nature* 2007;445:656–60.
- Ewald JA, Desotelle JA, Wilding G, Jarrard DF. Therapy-induced senescence in cancer. *J Natl Cancer Inst* 2010;102:1536–46.
- Peeper DS. PICS-ure this: pro-senescence therapy? *Cancer Cell* 2010;17:219–20.
- Ozols RF, Bookman MA, Connolly DC, Daly MB, Godwin AK, Schilder RJ, et al. Focus on epithelial ovarian cancer. *Cancer Cell* 2004;5:19–24.
- Farley J, Ozbun LL, Birrer MJ. Genomic analysis of epithelial ovarian cancer. *Cell Res* 2008;18:538–48.
- Shih Ie M, Kurman RJ. Ovarian tumorigenesis: a proposed model based on morphological and molecular genetic analysis. *Am J Pathol* 2004;164:1511–8.
- Moon RT, Kohn AD, De Ferrari GV, Kaykas A. WNT and beta-catenin signalling: diseases and therapies. *Nat Rev Genet* 2004;5:691–701.
- Kato M. WNT signaling pathway and stem cell signaling network. *Clin Cancer Res* 2007;13:4042–5.
- Mann B, Gelos M, Siedow A, Hanski ML, Gratchev A, Ilyas M, et al. Target genes of beta-catenin-T cell-factor/lymphoid-enhancer-factor signaling in human colorectal carcinomas. *Proc Natl Acad Sci U S A* 1999;96:1603–8.
- Szotek PP, Chang HL, Brennan K, Fujino A, Pieretti-Vanmarcke R, Lo Celso C, et al. Normal ovarian surface epithelial label-retaining cells exhibit stem/progenitor cell characteristics. *Proc Natl Acad Sci U S A* 2008;105:12469–73.
- Wu R, Hendrix-Lucas N, Quirk R, Zhai Y, Schwartz DR, Akyol A, et al. Mouse model of human ovarian endometrioid adenocarcinoma based on somatic defects in the Wnt/beta-catenin and PI3K/Pten signaling pathways. *Cancer Cell* 2007;11:321–33.
- McDonald SL, Silver A. The opposing roles of Wnt-5a in cancer. *Br J Cancer* 2009;101:209–14.
- Li H, Cai Q, Godwin AK, Zhang R. Enhancer of zeste homolog 2 promotes the proliferation and invasion of epithelial ovarian cancer cells. *Mol Cancer Res* 2010;8:1610–8.
- Ibanez de Caceres I, Dulaimi E, Hoffman AM, Al-Saleem T, Uzzo RG, Cairns P. Identification of novel target genes by an epigenetic reactivation screen of renal cancer. *Cancer Res* 2006;66:5021–8.
- Zhang R, Chen W, Adams PD. Molecular dissection of formation of senescence-associated heterochromatin foci. *Mol Cell Biol* 2007;27:2343–58.
- Zhang R, Poustovoitov MV, Ye X, Santos HA, Chen W, Daganzo SM, et al. Formation of MacroH2A-containing senescence-associated heterochromatin foci and senescence driven by ASF1a and HIRA. *Dev Cell* 2005;8:19–30.
- Cheyette BN, Waxman JS, Miller JR, Takemaru K, Sheldahl LC, Khlebtsova N, et al. Dapper, a Dishevelled-associated antagonist of beta-catenin and JNK signaling, is required for notochord formation. *Dev Cell* 2002;2:449–61.
- Ye X, Zerlanko B, Kennedy A, Banumathy G, Zhang R, Adams PD. Downregulation of Wnt signaling is a trigger for formation of facultative heterochromatin and onset of cell senescence in primary human cells. *Mol Cell* 2007;27:183–96.



23. Itahana K, Campisi J, Dimri GP. Methods to detect biomarkers of cellular senescence: the senescence-associated beta-galactosidase assay. *Methods Mol Biol* 2007;371:21–31.
24. Connolly DC, Hensley HH. Xenograft and transgenic mouse models of epithelial ovarian cancer and non invasive imaging modalities to monitor ovarian tumor growth *in situ* - applications in evaluating novel therapeutic agents. *Curr Protoc Pharmacol* 2009;45:14.12.1–26.
25. Kurman RJ, Shih Ie M. The origin and pathogenesis of epithelial ovarian cancer: a proposed unifying theory. *Am J Surg Pathol* 2010;34:433–43.
26. McCarty KS Jr, Szabo E, Flowers JL, Cox EB, Leight GS, Miller L, et al. Use of a monoclonal anti-estrogen receptor antibody in the immunohistochemical evaluation of human tumors. *Cancer Res* 1986;46:4244s–8s.
27. Gerdes J, Lemke H, Baisch H, Wacker HH, Schwab U, Stein H. Cell cycle analysis of a cell proliferation-associated human nuclear antigen defined by the monoclonal antibody Ki-67. *J Immunol* 1984;133:1710–5.
28. Baylin SB, Herman JG, Graff JR, Vertino PM, Issa JP. Alterations in DNA methylation: a fundamental aspect of neoplasia. *Adv Cancer Res* 1998;72:141–96.
29. Liang H, Chen Q, Coles AH, Anderson SJ, Pihan G, Bradley A, et al. Wnt5a inhibits B cell proliferation and functions as a tumor suppressor in hematopoietic tissue. *Cancer Cell* 2003;4:349–60.
30. Mikels AJ, Nusse R. Purified Wnt5a protein activates or inhibits beta-catenin-TCF signaling depending on receptor context. *PLoS Biol* 2006;4:e115.
31. Topol L, Jiang X, Choi H, Garrett-Beal L, Carolan PJ, Yang Y. Wnt-5a inhibits the canonical Wnt pathway by promoting GSK-3-independent beta-catenin degradation. *J Cell Biol* 2003;162:899–908.
32. Reya T, Clevers H. Wnt signalling in stem cells and cancer. *Nature* 2005;434:843–50.
33. Bernardi R, Pandolfi PP. Structure, dynamics and functions of promyelocytic leukaemia nuclear bodies. *Nat Rev Mol Cell Biol* 2007;8:1006–16.
34. Mallette FA, Goumard S, Gaumont-Leclerc MF, Moiseeva O, Ferbeyre G. Human fibroblasts require the Rb family of tumor suppressors, but not p53, for PML-induced senescence. *Oncogene* 2004;23:91–9.
35. Ferbeyre G, de Stanchina E, Querido E, Baptiste N, Prives C, Lowe SW. PML is induced by oncogenic *ras* and promotes premature senescence. *Genes Dev* 2000;14:2015–27.
36. Salomoni P, Pandolfi PP. The role of PML in tumor suppression. *Cell* 2002;108:165–70.
37. Ye X, Zerlanko B, Zhang R, Somaiah N, Lipinski M, Salomoni P, et al. Definition of pRB- and p53-dependent and -independent steps in HIRA/ASF1a-mediated formation of senescence-associated heterochromatin foci. *Mol Cell Biol* 2007;27:2452–65.
38. Pearson M, Carbone R, Sebastiani C, Cioce M, Fagioli M, Saito S, et al. PML regulates p53 acetylation and premature senescence induced by oncogenic *Ras*. *Nature* 2000;406:207–10.
39. Watson JE, Gabra H, Taylor KJ, Rabiasz GJ, Morrison H, Perry P, et al. Identification and characterization of a homozygous deletion found in ovarian ascites by representational difference analysis. *Genome Res* 1999;9:226–33.
40. Lundberg AS, Weinberg RA. Functional inactivation of the retinoblastoma protein requires sequential modification by at least two distinct cyclin-cdk complexes. *Mol Cell Biol* 1998;18:753–61.
41. Yaginuma Y, Westphal H. Abnormal structure and expression of the p53 gene in human ovarian carcinoma cell lines. *Cancer Res* 1992;52:4196–9.
42. Alimonti A, Nardella C, Chen Z, Clohessy JG, Carracedo A, Trotman LC, et al. A novel type of cellular senescence that can be enhanced in mouse models and human tumor xenografts to suppress prostate tumorigenesis. *J Clin Invest* 2010;120:681–93.
43. Collado M. Exploring a 'pro-senescence' approach for prostate cancer therapy by targeting PTEN. *Future Oncol* 2010;6:687–9.
44. Saffholm A, Tuomela J, Rosenkvist J, Dejmeck J, Harkonen P, Andersson T. The Wnt-5a-derived hexapeptide Foxy-5 inhibits breast cancer metastasis *in vivo* by targeting cell motility. *Clin Cancer Res* 2008;14:6556–63.
45. Pukrop T, Binder C. The complex pathways of Wnt 5a in cancer progression. *J Mol Med* 2008;86:259–66.
46. Li J, Ying J, Fan Y, Wu L, Ying Y, Chan AT, et al. WNT5A antagonizes WNT/beta-catenin signaling and is frequently silenced by promoter CpG methylation in esophageal squamous cell carcinoma. *Cancer Biol Ther* 2007;10:617–24.
47. Nishita M, Enomoto M, Yamagata K, Minami Y. Cell/tissue-tropic functions of Wnt5a signaling in normal and cancer cells. *Trends Cell Biol* 2010;20:346–54.
48. Badiglian Filho L, Oshima CT, De Oliveira Lima F, De Oliveira Costa H, De Sousa Damiao R, Gomes TS, et al. Canonical and noncanonical Wnt pathway: a comparison among normal ovary, benign ovarian tumor and ovarian cancer. *Oncol Rep* 2009;21:313–20.
49. Peng C, Zhang X, Yu H, Wu D, Zheng J. Wnt5a as a predictor in poor clinical outcome of patients and a mediator in chemoresistance of ovarian cancer. *Int J Gynecol Cancer* 2011;21:280–8.
50. Mok SC, Bonome T, Vathipadiekal V, Bell A, Johnson ME, Wong KK, et al. A gene signature predictive for outcome in advanced ovarian cancer identifies a survival factor: microfibril-associated glycoprotein 2. *Cancer Cell* 2009;16:521–32.



# Molecular Cancer Research



## Enhancer of Zeste Homolog 2 Promotes the Proliferation and Invasion of Epithelial Ovarian Cancer Cells

Hua Li, Qi Cai, Andrew K. Godwin, et al.

*Mol Cancer Res* 2010;8:1610-1618. Published OnlineFirst November 29, 2010.

**Updated Version** Access the most recent version of this article at:  
doi:[10.1158/1541-7786.MCR-10-0398](https://doi.org/10.1158/1541-7786.MCR-10-0398)

**Cited Articles** This article cites 50 articles, 16 of which you can access for free at:  
<http://mcr.aacrjournals.org/content/8/12/1610.full.html#ref-list-1>

**Citing Articles** This article has been cited by 2 HighWire-hosted articles. Access the articles at:  
<http://mcr.aacrjournals.org/content/8/12/1610.full.html#related-urls>

**E-mail alerts** [Sign up to receive free email-alerts](#) related to this article or journal.

**Reprints and Subscriptions** To order reprints of this article or to subscribe to the journal, contact the AACR Publications Department at [pubs@aacr.org](mailto:pubs@aacr.org).

**Permissions** To request permission to re-use all or part of this article, contact the AACR Publications Department at [permissions@aacr.org](mailto:permissions@aacr.org).

# Enhancer of Zeste Homolog 2 Promotes the Proliferation and Invasion of Epithelial Ovarian Cancer Cells

Hua Li<sup>1</sup>, Qi Cai<sup>2</sup>, Andrew K. Godwin<sup>1</sup>, and Rugang Zhang<sup>1,3</sup>

## Abstract

Enhancer of zeste homolog 2 (EZH2) is the catalytic subunit of the polycomb repressive complex 2 (PRC2) that includes noncatalytic subunits suppressor of zeste 12 (SUZ12) and embryonic ectoderm development (EED). When present in PRC2, EZH2 catalyzes trimethylation on lysine 27 residue of histone H3 (H3K27Me3), resulting in epigenetic silencing of gene expression. Here, we investigated the expression and function of EZH2 in epithelial ovarian cancer (EOC). When compared with primary human ovarian surface epithelial (pHOSE) cells, EZH2, SUZ12, and EED were expressed at higher levels in all 8 human EOC cell lines tested. Consistently, H3K27Me3 was also overexpressed in human EOC cell lines compared with pHOSE cells. EZH2 was significantly overexpressed in primary human EOCs ( $n = 134$ ) when compared with normal ovarian surface epithelium ( $n = 46$ ;  $P < 0.001$ ). EZH2 expression positively correlated with expression of Ki67 ( $P < 0.001$ ; a marker of cell proliferation) and tumor grade ( $P = 0.034$ ) but not tumor stage ( $P = 0.908$ ) in EOC. There was no correlation of EZH2 expression with overall ( $P = 0.3$ ) or disease-free survival ( $P = 0.2$ ) in high-grade serous histotype EOC patients ( $n = 98$ ). Knockdown of EZH2 expression reduced the level of H3K27Me3 and suppressed the growth of human EOC cells both *in vitro* and *in vivo* in xenograft models. EZH2 knockdown induced apoptosis of human EOC cells. Finally, we showed that EZH2 knockdown suppressed the invasion of human EOC cells. Together, these data demonstrate that EZH2 is frequently overexpressed in human EOC cells and its overexpression promotes the proliferation and invasion of human EOC cells, suggesting that EZH2 is a potential target for developing EOC therapeutics. *Mol Cancer Res*; 8(12); 1610–8. ©2010 AACR.

## Introduction

Enhancer of zeste homolog 2 (EZH2) is the catalytic subunit of polycomb repressive complex 2 (PRC2; refs. 1–4). In addition to EZH2, PRC2 also contains the noncatalytic subunits embryonic ectoderm development (EED) and suppressor of zeste 12 (SUZ12; ref. 5). PRC2 plays an important role in epigenetic gene silencing via methylation of lysine 27 residue of histone H3 (H3K27) and can add up to 3 methyl groups to the lysine side chain. EZH2 lacks enzyme activity on its own, and has to complex with EED

and SUZ12 to attain robust histone methyltransferase activity (5, 6). The trimethylated form of H3K27 (H3K27Me3) is thought to be the main form that confers transcriptional silencing function (7–10).

EZH2 is overexpressed in several types of cancers (11–15) and is correlated with aggressiveness and poor prognosis in breast and prostate cancers (11–13). In breast epithelial cells, EZH2 overexpression causes anchorage-independent growth and increases cell invasiveness *in vitro* (11). In prostate cancer cells, inhibition of EZH2 blocked the growth of prostate cancer cells (13, 15). In addition, SUZ12 is also upregulated in certain types of cancer, including colon, breast, and liver (16–18).

More than 85% of ovarian cancers are of epithelial origin (19). Epithelial ovarian cancers (EOC) are classified into distinct histologic subtypes including serous, mucinous, endometrioid, and clear cell (19). The most common histology of EOC is serous (50%–60% of all EOCs), approximately, 75% of which is high-grade and 25% is low-grade (20–22). Less common histologies include endometrioid (25%), clear cell (4%), and mucinous (4%; ref. 20, 21). Recently, an alternative classification has gained traction, in which EOC is broadly divided into 2 types (22). Type I EOC includes endometrioid, mucinous, low-grade serous, and clear cell carcinomas, and type II EOC includes high-grade serous carcinomas (22). EOC remains the most

**Authors' Affiliations:** <sup>1</sup>Women's Cancer Program, <sup>2</sup>Biosample Repository Facility, and <sup>3</sup>Epigenetics and Progenitor Cells Keystone Program, Fox Chase Cancer Center, Philadelphia, Pennsylvania

**Note:** Supplementary data for this article are available at Molecular Cancer Research Online (<http://mcr.aacrjournals.org/>).

**Authors' Contributions:** H. Li performed all the experiments and drafted the manuscript. Q. Cai and A.K. Godwin reviewed and provided primary human ovarian carcinoma and normal ovary specimens. R. Zhang conceived the study, designed the experiments and wrote the manuscript.

**Corresponding Author:** Rugang Zhang, Women's Cancer Program, Fox Chase Cancer Center, W446, 333 Cottman Avenue, Philadelphia, PA 19111. Phone: 215-728-7108; Fax: 215-728-3616. E-mail: rugang.zhang@fccc.edu

doi: 10.1158/1541-7786.MCR-10-0398

©2010 American Association for Cancer Research.

lethal gynecologic malignancy in the Western world (19). Thus, there is an urgent need to identify new targets for developing novel therapeutics for EOC. Although EZH2 is overexpressed in tumor-associated endothelial cells in invasive EOC (23) and regulates tumor angiogenesis in EOC (24), its role in pathogenesis of EOC remains poorly understood. Here, we examined the expression of the subunits of PRC2 and H3K27Me3 in human EOC cell lines. In addition, we determined EZH2 expression in primary human EOCs of different histologic subtypes by immunohistochemistry (IHC). Further, we investigated the effects of EZH2 knockdown by short hairpin RNA (shRNA) on H3K27Me3 expression, cell growth, and invasion of human EOC cells.

## Material and Methods

### Cell culture

Primary human ovarian surface epithelial (pHOSE) cells were isolated and cultured as previously described (25). The protocol was approved by Fox Chase Cancer Center (FCCC) institutional review board. Human EOC cell lines A1847, A2780, OVCAR3, OVCAR5, OVCAR10, PEO1, SKOV3, and UPN289 were kindly provided by Drs. Thomas Hamilton and Steve Williams at FCCC and were maintained in 1640 medium, supplemented with 10% FBS, 2 mmol/L of L-glutamine, penicillin (100 units/mL), and streptomycin (100 µg/mL).

### shRNA, lentivirus packaging, and infection

The sense sequences of 2 individual shRNA EZH2 are: 5'-CCAACACAAGTCATCCCATT-3' and 5'-CGGAAATCTTAAACCAAGAAT-3', respectively. Lentivirus packaging was performed using virapower system (Invitrogen) according to manufacturer's instruction. PEO1 and SKOV3 at 40% to 50% confluence were infected with lentivirus expressing shRNA to the human *EZH2* gene or vector control. The infected cells were drug-selected with 1 µg/mL (for PEO1) or 3 µg/mL (for SKOV3) of puromycin, respectively.

### Human ovarian tissue microarrays

Tissue microarrays, including core samples from 134 primary human EOCs and 46 cases of normal ovary tissues were obtained from FCCC Biosample Repository Core Facility. Use of these human specimens was approved by the Institutional Review Board.

### Immunohistochemical staining and scoring

The expression of EZH2 and Ki67 proteins was detected using avidin-biotin-peroxidase methods. Briefly, tissue sections were subjected to antigen retrieval by steaming in 0.01 mol/L of sodium citrate buffer (pH 6.0) for 30 minutes. After quenching endogenous peroxidase activity with 3% hydrogen peroxide and blocking nonspecific protein binding with 1% bovine serum albumin, sections were incubated overnight with primary monoclonal antibody (anti-EZH2: Millipore, 1:100; anti-Ki67: DAKO,

1:100) at 4°C, followed by biotinylated goat anti-mouse IgG (DAKO, 1:400) for 1 hour, detecting the antibody complexes with the labeled streptavidin-biotin system (DAKO), and visualizing them with the chromogen 3,3'-diaminobenzidine. Sections were lightly counterstained with hematoxylin. Tissues in which nuclei were stained for EZH2 or Ki67 protein were considered positive. Two 1-mm cores were examined in each specimen on the tissue microarray and cells were counted in at least 5 high-power fields, with approximately 200 cells analyzed per high-power field.

### FACS, immunofluorescence staining, and Western blot analysis

FACS and indirect immunofluorescence (IF) staining were performed as described previously (26–28). The following antibodies were used for IF: rabbit anti-H3K27Me3 (Cell Signaling, 1:1,000), and rabbit anti-H3K9Me3 (Abcam, 1:500). The antibodies used for Western blotting were from indicated suppliers: mouse anti-EZH2 (Millipore; 1:2,500), rabbit anti-H3K27Me3 (Cell signaling, 1:1,000), rabbit anti-H3K9Me3 (Abcam, 1:2,000), mouse anti-histone H3 (Millipore, 1:10,000), mouse anti-GAPDH (Millipore, 1:10,000), rabbit anti-PARP p85 fragment (Promega, 1:1,000), rabbit anti-cleaved caspase 3 (Cell Signaling, 1:1,000), and rabbit anti-cleaved Lamin A (Cell signaling, 1:1,000).

### Soft agar colony formation assay

A total of  $1 \times 10^4$  cells per well were inoculated in a 6-well plate in 1.5 mL of RPMI 1640 medium supplemented with 10% FBS and 0.35% agar on a base layer of 1.5 mL of the same medium containing 0.6% agar. Three weeks after plating, the cells were stained with 1% crystal violet (Sigma) in PBS to visualize the colonies. Number of colonies that were larger than 50 µm (approximately 100 cells) in diameter in each well was counted.

### Matrigel invasion assay

BD BioCoat Matrigel Invasion Chamber was used to measure cell invasion according to manufacturer's instruction. Cells ( $1 \times 10^5$  cells per well) suspended in 0.5 ml RPMI 1640 medium were added to the upper compartment of 24-well matrigel-coated or noncoated 8 µm membrane, and RPMI 1640 medium supplemented with 10% FBS was applied to the lower compartment. After incubating 22 hours at 37°C, 5% CO<sub>2</sub>, the cells were fixed with 4% formaldehyde and stained with 1% crystal violet in PBS. The number of cells that migrated across control membrane or invaded through Matrigel-coated membrane was determined in 9 fields across the center and the periphery of the membrane.

### Annexin V staining for detecting apoptotic cells

Phosphatidylserine externalization was detected using an Annexin V staining kit (Millipore) following manufacture's instruction. Annexin V positive cells were detected by

Guava system and analyzed with Guava Nexin software Module (Millipore).

### *In vivo* tumorigenicity assay

A total of  $5 \times 10^6$  cells in PBS (pH 7.3) per mouse were injected subcutaneously into the flank of 6-week-old female nude athymic mice. The mice were sacrificed 4 weeks post-inoculation. Width and length of tumor size were measured and the tumor volume ( $\text{mm}^3$ ) was calculated using the following formula: tumor volume ( $\text{in mm}^3$ ) = length  $\times$  width<sup>2</sup>  $\times$  0.52.

### Statistical analysis

Quantitative data were expressed as mean  $\pm$  SD, unless otherwise stated. analysis of variance (ANOVA) with Student's *t* test was used to identify significant differences in multiple comparisons. The  $\chi^2$  test was used to analyze the relationship between categorical variables. Overall survival was defined as the time elapsed from the date of diagnosis and the date of death from any cause or the date of last follow-up. Disease-free survival was defined as the time elapsed from the date of surgery and the date of the first recurrence. Kaplan–Meier survival plots were generated and comparisons made using the log-rank statistic. For all statistical analyses, the level of significance was set at 0.05.

## Results

### The catalytic and noncatalytic subunits of PRC2 complex and H3K27Me3 are expressed at higher levels in human EOC cell lines compared with pHOSE cells

Expression of EZH2, EED, and SUZ12 was examined by Western blotting in cultures of pHOSE cells isolated from 5 different individuals and 8 human EOC cell lines. When compared with pHOSE cells, EZH2, EED, and SUZ12 were expressed at higher levels in all human EOC cell lines tested (Fig. 1A). Consistently, the levels of H3K27Me3, the product of EZH2 histone H3 lysine 27 methyltransferase activity, was also increased in human EOC cell lines compared with pHOSE cells (Fig. 1A). On the basis of these results, we conclude that the catalytic and noncatalytic subunits of PRC2 and H3K27Me3 are expressed at higher levels in human EOC cell lines compared with pHOSE cells.

### EZH2 is overexpressed in primary human EOCs and its expression positively correlates with expression of Ki67, a cell proliferation marker

We next sought to examine the expression of EZH2, the catalytic subunit of PRC complex, in 134 primary human EOCs and 46 normal ovary tissue specimens by IHC staining (Table 1; Fig. 1B; Supplementary Fig. S1). The specificity of the EZH2 antibody used for IHC staining was confirmed by the following (Supplementary Fig. S1A and B). First, a single band at right molecule weight ( $\sim 95\text{KD}$ ) was obtained in Western blotting of human EOC cell line SKOV3 using the EZH2 antibody, and this band was absent after expression of shRNA to the human *EZH2* gene (shEZH2) that effectively knocked down EZH2

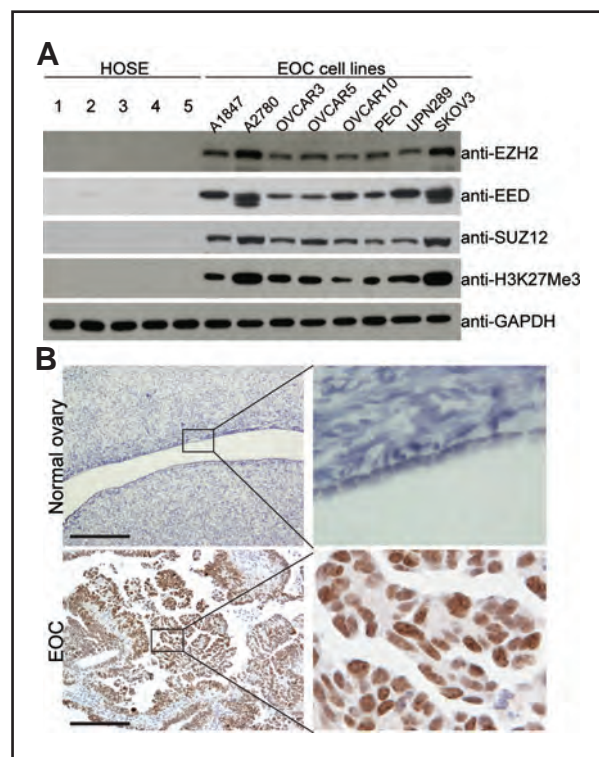


**Figure 1.** EZH2 is expressed at higher levels in human EOC cell lines and primary human EOCs compared with normal ovarian surface epithelium. A, expression of EZH2, EED, SUZ12, H3K27Me3, and GAPDH in 5 individual batches of pHOSE cell cultures and indicated human EOC cell lines was determined by Western blotting. B, examples of EZH2 immunohistochemical staining in normal ovary and primary human EOC (shown is an example of high-grade serous histotype EOC). Bar = 50  $\mu\text{m}$ .

mRNA expression (Supplementary Fig. S1A and data not shown). In addition, EZH2 staining signal was lost when primary anti-EZH2 was replaced with an isotype-matched IgG control (Supplementary Fig. S1B). Importantly, the nuclei of human EOC cells were strongly stained by the anti-EZH2 antibody (Fig. 1B; Supplementary Fig. S1C). By contrast, ovarian surface epithelial cells were negative for EZH2 staining (Fig. 1B).

We scored expression of EZH2 as low (H-score  $\leq 100$ ) or high (H-score  $> 100$ ) based on the histochemical score (29, 30), which considers both the intensity of staining and the percentage of positively stained cells. EZH2 expression in the surface epithelium of all 46 normal ovaries was scored as low (in fact, negative EZH2 staining). EZH2 was scored as low in 34% (46 of 134) and high in 66% (88 of 134) of primary EOCs tested, respectively. When compared with normal ovarian surface epithelium, EZH2 was expressed at significantly higher levels in primary human EOCs ( $P < 0.001$ ). Because EZH2 has been implicated in promoting cell proliferation (12), we stained the same set of primary human EOC specimens with Ki67, a cell proliferation marker, and compared the expression of EZH2 and Ki67 expression in consecutive sections. There



**Table 1.** Correlation between EZH2 expression and tumor cell proliferation (Ki67) or clinicopathologic variables

| Patient characteristics    | EZH2 protein expression |          |           |          | P                  |
|----------------------------|-------------------------|----------|-----------|----------|--------------------|
|                            | Low (n)                 | High (n) | Total (n) | High (%) |                    |
| Age (23–85 y, mean 59.6 y) |                         |          |           |          |                    |
| ≤55                        | 17                      | 31       | 48        | 64.58    | 0.843              |
| >55                        | 29                      | 57       | 86        | 66.28    |                    |
| Laterality                 |                         |          |           |          |                    |
| Left                       | 12                      | 25       | 37        | 67.57    | 0.764              |
| Right                      | 7                       | 18       | 25        | 72.00    |                    |
| Bilaterality               | 22                      | 39       | 61        | 63.93    |                    |
| Undetermined               | 5                       | 6        | 11        | 54.55    |                    |
| Histotype                  |                         |          |           |          |                    |
| Epithelial ovarian cancer  | 46                      | 88       | 134       | 65.67    | 0.577 <sup>a</sup> |
| Type I                     | 11                      | 25       | 36        | 69.44    |                    |
| Low-grade serous           | 2                       | 0        | 2         |          |                    |
| Endometrioid               | 5                       | 8        | 13        |          |                    |
| Mucinous                   | 1                       | 4        | 5         |          |                    |
| Clear cell                 | 2                       | 6        | 8         |          |                    |
| Others                     | 1                       | 7        | 8         |          |                    |
| Type II                    | 35                      | 63       | 98        | 64.29    |                    |
| High-grade serous          | 35                      | 63       | 98        | 64.29    |                    |
| Normal ovarian epithelium  | 46                      | 0        | 46        | 0.00     |                    |
| Ki67                       |                         |          |           |          |                    |
| 0%–10%                     | 27                      | 2        | 29        | 6.90     | <0.001             |
| 10%–40%                    | 10                      | 17       | 27        | 62.96    |                    |
| 40%–100%                   | 9                       | 69       | 78        | 88.46    |                    |
| Tumor grade                |                         |          |           |          |                    |
| Well differentiation       | 6                       | 3        | 9         | 33.33    | 0.034              |
| Moderate differentiation   | 10                      | 12       | 22        | 54.55    |                    |
| Poor differentiation       | 29                      | 70       | 99        | 70.71    |                    |
| Undetermined               | 1                       | 3        | 4         | 75.00    |                    |
| Tumor stage                |                         |          |           |          |                    |
| Stage 1/2                  | 12                      | 21       | 33        | 63.64    | 0.908              |
| Stage 3/4                  | 33                      | 55       | 88        | 62.50    |                    |
| Undetermined               | 1                       | 12       | 13        | 92.31    |                    |

<sup>a</sup>Compared with type I,  $P = 0.577$ .<sup>b</sup>Compared with epithelial ovarian cancer,  $P < 0.001$ .

was a significant correlation between EZH2 expression and Ki67 expression ( $P < 0.001$ ; Table 1). Together, we conclude that EZH2 is significantly overexpressed in primary human EOCs compared with normal ovarian surface epithelium and its expression correlates with a high proliferation index revealed by Ki67 staining.

#### EZH2 expression is positively correlated with tumor grade but not tumor stage, or overall or disease-free survival

We next sought to determine the correlation between EZH2 expression and clinical and pathologic features of human EOCs. There was a significantly positive correlation between EZH2 expression and tumor grade ( $P = 0.034$ ;

Table 1). However, EZH2 expression was not associated with tumor stage ( $P = 0.908$ ; Table 1). Next, we sought to determine whether EZH2 expression correlates with prognosis of type II high-grade serous histotype EOC patients for which long-term follow-up data were available ( $n = 98$ ). The difference in overall ( $P = 0.3$ ) or disease-free ( $P = 0.2$ ) survival between low EZH2 expression group ( $n = 35$ ) and high EZH2 expression group ( $n = 63$ ) was not significant (Fig. 2).

#### EZH2 knockdown inhibits the growth of human EOC cells *in vitro* and *in vivo*

Because EZH2 expression positively correlates with Ki67 expression (Table 1), we sought to determine the effects of EZH2 knockdown on proliferation of human EOC cells. To

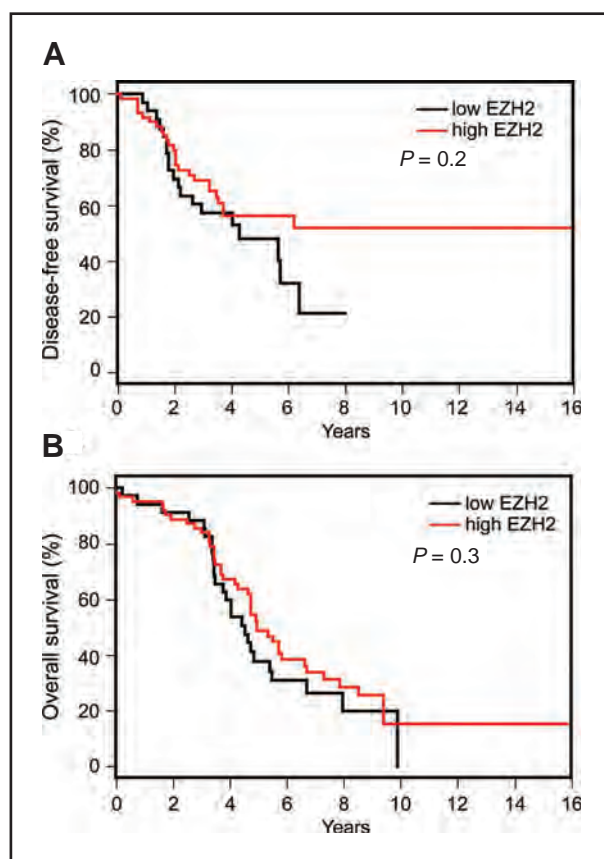


**Figure 2.** EZH2 expression does not correlate with disease-free or overall survival in high-grade serous histotype EOC patients. The univariate disease-free (A) and overall survival (B) curves (Kaplan–Meier method) for high-grade serous histotype EOC patients with low or high EZH2 protein levels as assessed by immunohistochemistry analysis.

knockdown EZH2 expression in SKOV3 cells, we developed 2 individual lentivirus encoded shEZH2. The knockdown efficacy of shEZH2 in SKOV3 cells was confirmed by Western blotting (Fig. 3A). Consistently, the level of H3K27Me3 level was significantly reduced by shEZH2 expression in SKOV3 cells as determined by both Western blotting and IF staining (Fig. 3B and C). As a negative control, shEZH2 expression has no effects on the level of trimethylated lysine 9 histone H3 (H3K9Me3) that is generated by histone methyltransferase Suv39H (ref. 31; Fig. 3B and C). Compared with controls, EZH2 knockdown significantly reduced both anchorage-dependent and -independent growth in soft agar in SKOV3 cells ( $P < 0.001$ ; Fig. 3D and E). The degree of growth inhibition by shEZH2 correlated with the level of EZH2 knockdown in SKOV3 cells by 2 individual shEZH2 (Fig. 3), suggesting that the observed growth inhibition by shEZH2 was not because of off-target effects. In addition, EZH2 knockdown in PEO1 cells has same effects on the expression of H3K27Me3 and also suppressed both anchorage-dependent and -independent cell growth (Supplementary Fig. S2), suggesting that the observed growth inhibition is not cell line specific.

We next sought to determine the effects of EZH2 knockdown on the growth of SKOV3 cells *in vivo* in immuno-compromised nude mice. Control and shEZH2 expressing SKOV3 cells were injected subcutaneously into nude mice with  $5 \times 10^6$  cells per mice and 5 mice in each group. Four weeks after injection, the sizes of xenografted tumors were compared between control and shEZH2 expressing cells (Fig. 4A and B). EZH2 knockdown by shEZH2 in the xenograft tumors was confirmed by IHC staining (Fig. 4C). shEZH2 expression significantly inhibited the growth of xenografted SKOV3 cells (Fig. 4A and B).

### EZH2 knockdown inhibits the invasion of human EOC cells

EZH2 has been implicated in regulating cell invasion in several types of cancer cells (11, 15, 32, 33). Thus, we sought to determine the effects of EZH2 knockdown on invasion of human EOC cells. Toward this goal, control and shEZH2 expressing SKOV3 cells were tested for their ability to migrate through uncoated control membrane or invade through matrigel-coated membrane. Compared with controls, EZH2 knockdown significantly inhibited the invasion of SKOV3 cells as revealed by a decreased invasion index that is calculated as the ratio between the number of cells invaded through matrigel-coated membrane and the number of cells migrated through control membrane (Fig. 5). Inhibition of invasion was observed by 2 individual shEZH2 in SKOV3 cells (Fig. 5). In addition, the degree of invasion inhibition correlated with the degree of EZH2 knockdown (Figs. 3 and 5), suggesting that this is not because of off-targets effects. On the basis of these results, we conclude that EZH2 knockdown inhibits the invasion of human EOC cells.

### EZH2 knockdown triggers apoptosis in human EOC cells

We next sought to determine the mechanisms by which EZH2 knockdown inhibits the growth of human EOC cells. DNA content analysis determined by FACS showed that there was no statistical difference in cell-cycle distribution between control and shEZH2 expressing cells (Supplementary Fig. S3). We next examined the markers of apoptosis in control and shEZH2 expressing SKOV3 cells. When compared with controls, markers of apoptosis were significantly induced by shEZH2 expression (Fig. 6). Those apoptotic markers include increased percentage of cells at sub-G1 phase as measured by FACS analysis (Fig. 6A), increased percentage of Annexin V positively stained cells as measured by Guava Nexin assay (Fig. 6B), upregulation of cleaved Lamin A, PARP p85, and caspase 3 (Fig. 6C; ref. 34). Together, we conclude that EZH2 knockdown induces apoptosis of human EOC cells.

### Discussion

Consistent with our findings, EZH2 mRNA expression was upregulated 2-fold or more in more than 80% of high-grade serous human EOC specimens in the newly released

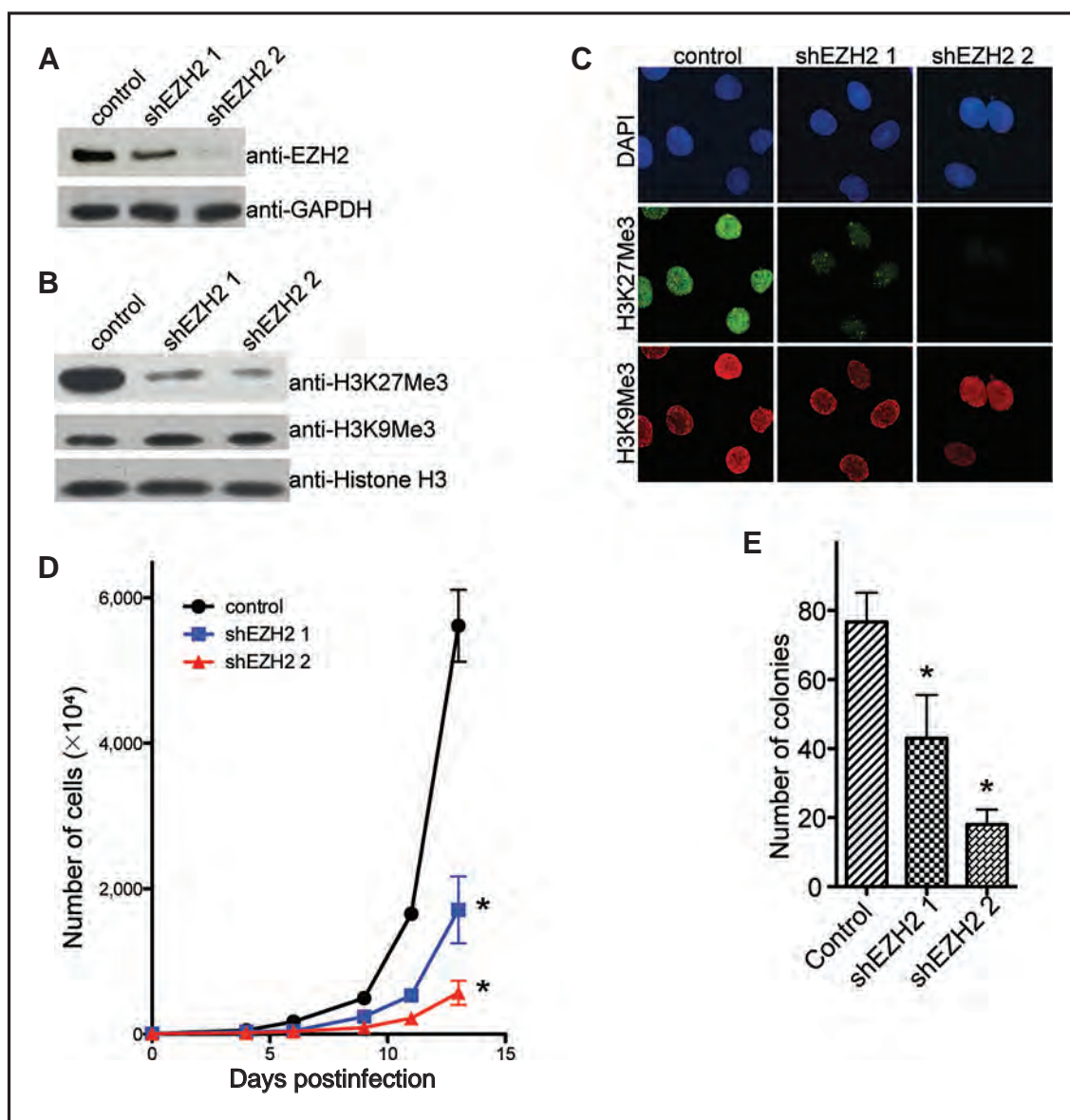


**Figure 3.** EZH2 knockdown inhibits the growth of SKOV3 cells *in vitro*. A, SKOV3 cells were infected with 2 individual lentivirus encoded shEZH2 or control. Drug-selected cells were examined for expression of EZH2 and GAPDH by Western blotting. B, same as A, but examined for expression of H3K27Me3 and H3K9Me3 by Western blotting. C, same as A, but examined for expression of H3K27Me3 and H3K9Me3 by immunofluorescence staining. DAPI counterstaining was used to visualize the cell nuclei. D, same as A, but equal number of drug-selected cells were seeded and counted at indicated time points. Mean of 3 independent experiments with SD. \*,  $P < 0.001$ . E, same as A,  $1 \times 10^4$  cells were seeded in soft agar and the number of colonies were counted after 3 weeks of culture. Mean of 3 independent experiments with SD. \*,  $P < 0.001$ .

the Cancer Genomics Atlas (TCGA) serous ovarian cystadenocarcinoma gene expression database (<http://cancergenome.nih.gov/>). *EZH2* gene is located at chromosome 7q36.1. Gene amplification contributes to EZH2 overexpression in several types of cancer (14, 35). However, TCGA gene copy-number analysis indicates that *EZH2* gene amplification occurs only in a very small percentage of EOCs (<10% specimens show >4 copy of *EZH2* gene; <http://cancergenome.nih.gov/>), suggesting that gene amplification is not a major mechanism that leads to EZH2

upregulation in human EOCs. EZH2 is an E2F target gene (35). A very recent study showed that VEGF stimulates EZH2 expression in human EOC cells via E2F family members, E2F1 and E2F3 (24). However, VEGF only stimulates the expression of EZH2 mRNA up to 3-fold (24), which is far below the level of increase in EZH2 mRNA or protein in human EOC cells compared with cultured pHOSE cells (Fig. 1 and data not shown), suggesting additional mechanisms contribute to EZH2 upregulation in human EOC cells. In the future, we will elucidate



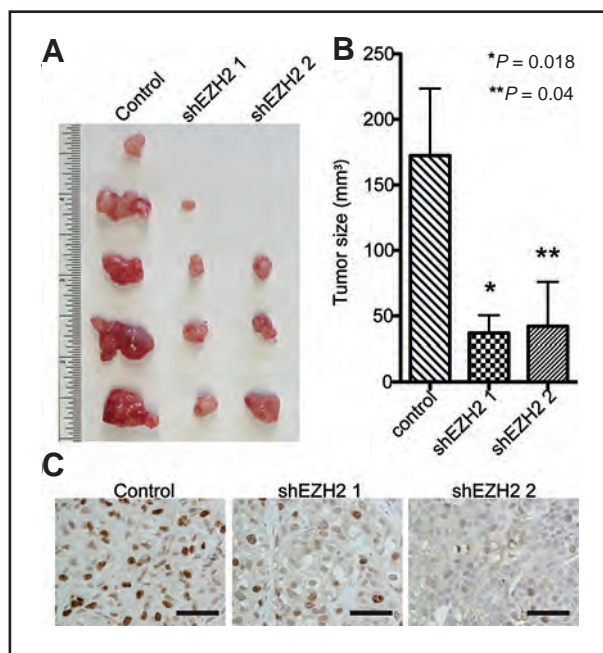


**Figure 4.** EZH2 knockdown suppresses the growth of SKOV3 cells *in vivo* in immunocompromised mice. A,  $5 \times 10^6$  control or shEZH2 expressing SKOV3 cells were injected subcutaneously into immunocompromised nude mice ( $n = 5$ ). Four weeks postinjection, tumors were removed from mice. B, quantitation of A, the size of tumors was measured. Mean of tumor sizes with SEM. C, xenografted tumors formed by control or shEZH2 expressing SKOV3 cells were sectioned and stained for EZH2 expression. Bar = 50  $\mu$ m.

additional mechanisms that contribute to EZH2 upregulation in human EOCs.

EZH2 has been demonstrated as a prognostic marker for breast and prostate cancers and positively correlates with disease-free survival and overall survival in those patient populations (11–13). In addition, EZH2 overexpression correlates with more advanced disease stages of breast and prostate cancers (11, 13). However, EZH2 expression was not a prognostic marker in other types of cancers including renal clear cell carcinoma and hepatocellular carcinomas (33, 36). We showed that there was no significant correlation between EZH2 expression and disease-free or overall survival in high-grade serous EOC patients (Fig. 2). Consistent with our findings, low expression of H3K27Me3 has been demonstrated to be a poor prognostic marker in EOC (37). In contrast, a very recent study showed that EZH2 expression in either EOC cells or ovarian tumor vasculature is predictive of poor clinical outcome (24). The basis for the discrepancy between our study and that of Lu et al.'s is unclear. A possible reason may be that we correlated EZH2 expression with overall or disease-free survival only in high-grade serous histotype EOCs (Fig. 2), whereas the study by Lu et al. includes additional histotypes of EOCs (24).

We showed that EZH2 expression positively correlated with Ki67 expression in EOCs (Table 1). There are conflicting results regarding the prognostic value of Ki67 in ovarian carcinoma (38–42). A recent study by Kobel et al.

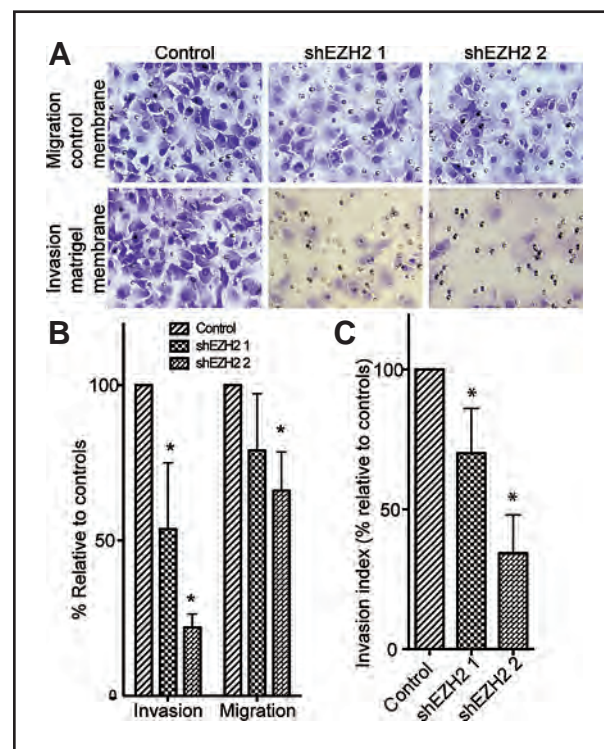


**Figure 5.** EZH2 knockdown suppresses the invasion of SKOV3 cells. A, equal number of control and shEZH2 expressing SKOV3 cells were assayed for migration through uncoated control membrane or invasion through matrigel-coated membrane. The cells migrated through control membrane or invaded through matrigel-coated membrane were stained with 1% crystal violet in PBS. B, quantitation of A. Relative percentage of shEZH2 expressing cells migrated through control membrane or invaded through matrigel-coated membrane compared with controls was indicated. Mean of 3 independent experiments with SD. \*,  $P < 0.05$ . C, invasion index of shEZH2 expressing SKOV3 cells compared with controls. Invasion index is the ratio between cells invaded through matrigel-coated membrane and cells migrated through control membrane. Mean of 3 independent experiments with SD. \*,  $P < 0.05$ .

(43) suggests that differences in Ki67 index among different subtypes of EOCs confound the Ki67 survival analysis because nearly all high-grade serous EOCs have a high Ki67 index. In analysis of each individual subtypes, Ki67 is no longer a prognostic marker. Consistent with this, although EZH2 correlates with Ki67 expression (Table 1), EZH2 expression was not a prognostic indicator for either overall or disease-free survival in the tested high-grade serous histotype EOC patients (Fig. 2).

Interestingly, when compared with normal ovarian surface epithelium, EZH2 expression is significantly upregulated (up to 23-fold) in ovarian epithelial inclusion cysts (44), which are thought to be the precursor lesion of a subset of EOC (45). This suggests that EZH2 overexpression is an early event during EOC development. Although ovarian surface epithelium is thought to be the cell origin of EOC (46), there are still several histopathology-based theories that differ in their explanations about the origins of EOC (46–48). Notably, recent evidence suggests that a proportion of high-grade serous EOC may arise from distal fallopian tube



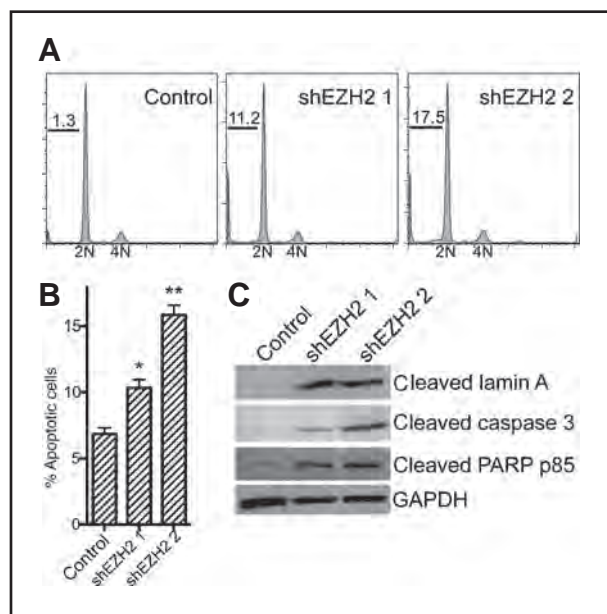


**Figure 6.** EZH2 knockdown induces apoptosis of SKOV3 cells. A, control and shEZH2 expressing SKOV3 cells were examined for cell-cycle distribution by FACS. The percentage of sub-G1 cells was indicated. B, control and shEZH2 expressing cells were stained for Annexin V, a cell surface marker of apoptosis. Annexin V-positive cells were measured by Guava Nexin assay. Mean of 3 independent experiments with SD. \*,  $P = 0.019$  and \*\*,  $P < 0.001$  compared with controls. C, same as B, but examined for expression of cleaved Lamin A, PARP p85, and caspase 3, all markers of apoptosis in control and shEZH2 expressing cells.

(48). Therefore, it will be interesting to examine EZH2 expression in normal fallopian tube epithelium.

Multiple genes have been implicated in EZH2 inhibition-induced apoptosis. For example, FBXO32 contributes to EZH2 inhibition induced-apoptosis in breast cancer cells (45), and Bim expression has been demonstrated to mediate EZH2 inhibition-induced apoptosis in prostate cancer cells (49). Likewise, E-cadherin, DAB2IP, and SLIT2 have all been implicated in mediating increased invasiveness conferred by high levels of EZH2 expression (32, 50–52).

## References

- Cao R, Wang L, Wang H, Xia L, Erdjument-Bromage H, Tempst P, et al. Role of histone H3 lysine 27 methylation in Polycomb-group silencing. *Science* 2002;298:1039–43.
- Czermin B, Melfi R, McCabe D, Seitz V, Imhof A, Pirrotta V. Drosophila enhancer of Zeste/ESC complexes have a histone H3 methyltransferase activity that marks chromosomal Polycomb sites. *Cell* 2002;111:185–96.
- Kuzmichev A, Nishioka K, Erdjument-Bromage H, Tempst P, Reinberg D. Histone methyltransferase activity associated with a human multiprotein complex containing the Enhancer of Zeste protein. *Genes Dev* 2002;16:2893–905.
- Muller J, Hart CM, Francis NJ, Vargas ML, Sengupta A, Wild B, et al. Histone methyltransferase activity of a Drosophila Polycomb group repressor complex. *Cell* 2002;111:197–208.
- Cao R, Zhang Y. SUZ12 is required for both the histone methyltransferase activity and the silencing function of the EED-EZH2 complex. *Mol Cell* 2004;15:57–67.
- Ketel CS, Andersen EF, Vargas ML, Suh J, Strome S, Simon JA. Subunit contributions to histone methyltransferase activities of fly and worm polycomb group complexes. *Mol Cell Biol* 2005;25:6857–68.
- Schwartz YB, Kahn TG, Nix DA, Li XY, Bourgon R, Biggin M, et al. Genome-wide analysis of Polycomb targets in Drosophila melanogaster. *Nat Genet* 2006;38:700–5.
- Schuettengruber B, Ganapathi M, Leblanc B, Portoso M, Jaschek R, Tolhuis B, et al. Functional anatomy of polycomb and trithorax chromatin landscapes in Drosophila embryos. *PLoS Biol* 2009;7:e13.
- Boyer LA, Plath K, Zeitlinger J, Brambrink T, Medeiros LA, Lee TI, et al. Polycomb complexes repress developmental regulators in murine embryonic stem cells. *Nature* 2006;441:349–53.
- Lee TI, Jenner RG, Boyer LA, Guenther MG, Levine SS, Kumar RM, et al. Control of developmental regulators by Polycomb in human embryonic stem cells. *Cell* 2006;125:301–13.
- Kleer CG, Cao Q, Varambally S, Shen R, Ota I, Tomlins SA, et al. EZH2 is a marker of aggressive breast cancer and promotes neoplastic

Further studies are warranted to delineate the molecular mechanisms by which EZH2 overexpression promotes proliferation and invasion of human EOC cells.

In summary, the data reported here show that EZH2 is overexpressed in approximately 66% of primary human EOCs and its overexpression correlates with a high proliferation index and tumor grade in EOCs. Knockdown of EZH2 inhibits the growth of human EOC cells *in vitro* and *in vivo*. EZH2 knockdown induces apoptosis of human EOC cells. In addition, EZH2 knockdown suppresses the invasion of human EOC cells. Further, inhibition of the growth and invasion of human EOC cells induced by EZH2 knockdown correlates with a decrease in the levels of H3K27Me3, suggesting that EZH2 histone methyltransferase activity is critical for its function in human EOC cells. Together, our data imply that EZH2 is a potential target for developing epigenetic modifying therapeutics for EOC.

## Disclosure of Potential Conflicts of Interest

No potential conflicts of interest were declared.

## Acknowledgments

We thank Drs. Thomas Hamilton and Steve Williams at Fox Chase Cancer Center for human epithelial ovarian cancer cell lines, Tianyu Li at Fox Chase Cancer Center Biostatistics and Bioinformatics facility for statistical analysis, and JoEllen Weaver at Fox Chase Cancer Center Biosample Repository facility for technical support, and Dr. Denise Connolly for critical reading of the manuscript.

## Grant Support

R. Zhang is an Ovarian Cancer Research Fund (OCRF) Liz Tilberis Scholar. This work was supported, in part, by a NCI FCCC-UPenn ovarian cancer SPOR (P50 CA083638) pilot project and career development award (R. Zhang), a Department of Defense Ovarian Cancer Academy award OC093420 (R. Zhang) and an OCRF program project (A. K. Godwin and R. Zhang).

The costs of publication of this article were defrayed in part by the payment of page charges. This article must therefore be hereby marked *advertisement* in accordance with 18 U.S.C. Section 1734 solely to indicate this fact.

Received 08/30/2010; revised 09/30/2010; accepted 10/08/2010; published OnlineFirst 11/29/2010.

- transformation of breast epithelial cells. *Proc Natl Acad Sci USA* 2003;100:11606–11.
12. Bachmann IM, Halvorsen OJ, Collett K, Stefansson IM, Straume O, Haukaas SA, et al. EZH2 expression is associated with high proliferation rate and aggressive tumor subgroups in cutaneous melanoma and cancers of the endometrium, prostate, and breast. *J Clin Oncol*. 2006;24:268–73.
  13. Varambally S, Dhanasekaran SM, Zhou M, Barrette TR, Kumar-Sinha C, Sanda MG, et al. The polycomb group protein EZH2 is involved in progression of prostate cancer. *Nature* 2002;419:624–9.
  14. Saramaki OR, Tammela TL, Martikainen PM, Vessella RL, Visakorpi T. The gene for polycomb group protein enhancer of zeste homolog 2 (EZH2) is amplified in late-stage prostate cancer. *Genes Chromosomes Cancer* 2006;45:639–45.
  15. Bryant RJ, Cross NA, Eaton CL, Hamdy FC, Cunliffe VT. EZH2 promotes proliferation and invasiveness of prostate cancer cells. *Prostate* 2007;67:547–56.
  16. Kuzmichev A, Margueron R, Vaquero A, Preissner TS, Scher M, Kirmizis A, et al. Composition and histone substrates of polycomb repressive group complexes change during cellular differentiation. *Proc Natl Acad Sci USA* 2005;102:1859–64.
  17. Kirmizis A, Bartley SM, Kuzmichev A, Margueron R, Reinberg D, Green R, et al. Silencing of human polycomb target genes is associated with methylation of histone H3 Lys 27. *Genes Dev* 2004;18:1592–605.
  18. Kirmizis A, Bartley SM, Farnham PJ. Identification of the polycomb group protein SU(Z)12 as a potential molecular target for human cancer therapy. *Mol Cancer Ther* 2003;2:113–21.
  19. Ozols RF, Bookman MA, Connolly DC, Daly MB, Godwin AK, Schilder RJ, et al. Focus on epithelial ovarian cancer. *Cancer Cells* 2004;5:19–24.
  20. Farley J, Ozbun LL, Birrer MJ. Genomic analysis of epithelial ovarian cancer. *Cell Res* 2008;18:538–48.
  21. Stany MP, Bonome T, Wamunyokoli F, Zorn K, Ozbun L, Park DC, et al. Classification of ovarian cancer: a genomic analysis. *Adv Exp Med Biol* 2008;622:23–33.
  22. Shih Ie M, Kurman RJ. Ovarian tumorigenesis: a proposed model based on morphological and molecular genetic analysis. *Am J Pathol* 2004;164:1511–8.
  23. Lu C, Bonome T, Li Y, Kamat AA, Han LY, Schmandt R, et al. Gene alterations identified by expression profiling in tumor-associated endothelial cells from invasive ovarian carcinoma. *Cancer Res* 2007;67:1757–68.
  24. Lu C, Han HD, Mangala LS, Ali-Fehmi R, Newton CS, Ozbun L, et al. Regulation of tumor angiogenesis by EZH2. *Cancer Cell* 2010;18:185–97.
  25. Bellacosa A, Godwin AK, Peri S, Devarajan K, Caretti E, Vanderveer L, et al. Altered gene expression in morphologically normal epithelial cells from heterozygous carriers of BRCA1 or BRCA2 mutations. *Cancer Prev Res (Phila)*. 2010;3:48–61.
  26. Zhang R, Chen W, Adams PD. Molecular dissection of formation of senescence-associated heterochromatin foci. *Mol Cell Biol* 2007;27:2343–58.
  27. Zhang R, Liu ST, Chen W, Bonner M, Pehrson J, Yen TJ, et al. HP1 proteins are essential for a dynamic nuclear response that rescues the function of perturbed heterochromatin in primary human cells. *Mol Cell Biol* 2007;27:949–62.
  28. Zhang R, Poustovoitov MV, Ye X, Santos HA, Chen W, Daganzo SM, et al. Formation of MacroH2A-containing senescence-associated heterochromatin foci and senescence driven by ASF1a and HIRA. *Dev Cell* 2005;8:19–30.
  29. McCarty KS, Jr/surname>, Miller LS, Cox EB, Konrath J, McCarty KS, Sr. Estrogen receptor analyses. Correlation of biochemical and immunohistochemical methods using monoclonal anti-receptor antibodies. *Arch Pathol Lab Med* 1985;109:716–21.
  30. McCarty KS Jr., Szabo E, Flowers JL, Cox EB, Leight GS, Miller L, et al. Use of a monoclonal anti-estrogen receptor antibody in the immunohistochemical evaluation of human tumors. *Cancer Res*. 1986;46:4244s–8s.
  31. Jenuwein T. The epigenetic magic of histone lysine methylation. *FEBS J*. 2006;273:3121–35.
  32. Cao Q, Yu J, Dhanasekaran SM, Kim JH, Mani RS, Tomlins SA, et al. Repression of E-cadherin by the polycomb group protein EZH2 in cancer. *Oncogene*. 2008;27:7274–84.
  33. Sudo T, Utsunomiya T, Mimori K, Nagahara H, Ogawa K, Inoue H, et al. Clinicopathological significance of EZH2 mRNA expression in patients with hepatocellular carcinoma. *Br J Cancer*. 2005;92:1754–8.
  34. Nicholson DW, Thornberry NA. Caspases: killer proteases. *Trends Biochem Sci*. 1997;22:299–306.
  35. Bracken AP, Pasini D, Capra M, Prosperini E, Colli E, Helin K. EZH2 is downstream of the pRB-E2F pathway, essential for proliferation and amplified in cancer. *EMBO J*. 2003;22:5323–35.
  36. Hinz S, Weikert S, Magheli A, Hoffmann M, Engers R, Miller K, et al. Expression profile of the polycomb group protein enhancer of Zeste homologue 2 and its prognostic relevance in renal cell carcinoma. *J Urol* 2009;182:2920–5.
  37. Wei Y, Xia W, Zhang Z, Liu J, Wang H, Adsay NV, et al. Loss of trimethylation at lysine 27 of histone H3 is a predictor of poor outcome in breast, ovarian, and pancreatic cancers. *Mol Carcinog* 2008;47:701–6.
  38. Munstedt K, von Georgi R, Franke FE. Correlation between MIB1-determined tumor growth fraction and incidence of tumor recurrence in early ovarian carcinomas. *Cancer Invest* 2004;22:185–94.
  39. Khouja MH, Baekelandt M, Nesland JM, Holm R. The clinical importance of Ki-67, p16, p14, and p57 expression in patients with advanced ovarian carcinoma. *Int J Gynecol Pathol* 2007;26:418–25.
  40. Korkolopoulou P, Vassilopoulos I, Konstantinidou AE, Zorzos H, Patsouris E, Agapitos E, et al. The combined evaluation of p27Kip1 and Ki-67 expression provides independent information on overall survival of ovarian carcinoma patients. *Gynecol Oncol* 2002;85:404–14.
  41. Green JA, Berns EM, Coens C, van Luijk I, Thompson-Hehir J, van Diest P, et al. Alterations in the p53 pathway and prognosis in advanced ovarian cancer: a multi-factorial analysis of the EORTC Gynaecological Cancer group (study 55865). *Eur J Cancer* 2006;42:2539–48.
  42. Anttila M, Kosma VM, Ji H, Wei-Ling X, Puolakka J, Juhola M, et al. Clinical significance of alpha-catenin, collagen IV, and Ki-67 expression in epithelial ovarian cancer. *J Clin Oncol* 1998;16:2591–600.
  43. Kobel M, Kalloger SE, Boyd N, McKinney S, Mehl E, Palmer C, et al. Ovarian carcinoma subtypes are different diseases: implications for biomarker studies. *PLoS Med*. 2008;5:e232.
  44. Pothuri B, Leitao MM, Levine DA, Viale A, Olshen AB, Arroyo C, et al. Genetic analysis of the early natural history of epithelial ovarian carcinoma. *PLoS One* 2010;5:e10358.
  45. Salazar H, Godwin AK, Daly MB, Laub PB, Hogan WM, Rosenblum N, et al. Microscopic benign and invasive malignant neoplasms and a cancer-prone phenotype in prophylactic oophorectomies. *J Natl Cancer Inst* 1996;88:1810–20.
  46. Kurman RJ, Shih Ie M. The origin and pathogenesis of epithelial ovarian cancer: a proposed unifying theory. *Am J Surg Pathol* 34:433–43.
  47. Dubeau L. The cell of origin of ovarian epithelial tumours. *Lancet Oncol* 2008;9:1191–7.
  48. Levanon K, Crum C, Drapkin R. New insights into the pathogenesis of serous ovarian cancer and its clinical impact. *J Clin Oncol* 2008;26:5284–93.
  49. Wu ZL, Zheng SS, Li ZM, Qiao YY, Aau MY, Yu Q. Polycomb protein EZH2 regulates E2F1-dependent apoptosis through epigenetically modulating Bim expression. *Cell Death Differ* 2010;17:801–10.
  50. Herranz N, Pasini D, Diaz VM, Franci C, Gutierrez A, Dave N, et al. Polycomb complex 2 is required for E-cadherin repression by the Snail1 transcription factor. *Mol Cell Biol* 2008;28:4772–81.
  51. Min J, Zaslavsky A, Fedele G, McLaughlin SK, Reczek EE, De Raedt T, et al. An oncogene-tumor suppressor cascade drives metastatic prostate cancer by coordinately activating Ras and nuclear factor-kappaB. *Nat Med* 2010;16:286–94.
  52. Chen H, Tu SW, Hsieh JT. Down-regulation of human DAB2IP gene expression mediated by polycomb Ezh2 complex and histone deacetylase in prostate cancer. *J Biol Chem* 2005;280:22437–44.

**Wnt5a-dependent induction of senescence suppresses epithelial ovarian cancer.**

Benjamin G. Bitler<sup>1</sup>, Jasmine P. Nicodemus<sup>1</sup>, Hua Li<sup>1</sup>, Qi Cai<sup>2</sup>, Keri Soring<sup>3</sup>, Michael J. Birrer<sup>6</sup>, Denise C. Connolly<sup>1</sup>, Andrew K. Godwin<sup>2</sup>, Paul Cairns<sup>3</sup>, Hong Wu<sup>4</sup>, Rugang Zhang<sup>1,5</sup>

<sup>1</sup> Women's Cancer Program, <sup>2</sup> Biosample Repository Facility, <sup>3</sup> Department of Surgical Oncology, <sup>4</sup> Department of Pathology, <sup>5</sup> Epigenetic and Progenitor Cell Keystone Program, Fox Chase Cancer Center; <sup>6</sup> Massachusetts General Hospital Cancer Center, Harvard Medical School.

Epithelial Ovarian Cancer (EOC) remains the most lethal gynecological malignancy in US and is the fifth leading cause of cancer deaths among American women. Thus, there is an urgent need to understand the etiology of EOC to develop novel therapies for this disease. Here, we demonstrated that a non-canonical Wnt ligand, Wnt5a, is expressed at significantly lower levels in human EOC cell lines and in primary human EOC compared with either normal ovarian surface epithelial cells or fallopian tube epithelial cells. Importantly, expression of Wnt5a in primary human EOC inversely correlates with tumor stage but not tumor grade. Interestingly, Wnt5a expression is significantly lower in Type II high-grade serous EOC compared to Type I EOC that includes low-grade serous, mucinous, clear cell and endometrioid subtypes of EOC. In addition, we discovered that hypermethylation of promoter CpG island contributes to Wnt5a downregulation in human EOC cells. Significantly, restoration of Wnt5a expression in human EOC cells promoted senescence of EOC cells and resulted in a dramatic decrease in cell proliferation both *in vitro* and *in vivo* in an orthotopic model of EOC in the ovary of SCID mice. Mechanistically, Wnt5a inhibited canonical Wnt/ $\beta$ -catenin signaling and resulted in the activation of senescence-promoting histone repressor A/PML pathway. In summary, we show that Wnt5a is often expressed at lower levels in primary human EOC and Wnt5a expression suppresses the growth of EOC cells by triggering senescence through antagonizing canonical Wnt signaling. These results also suggest that loss of Wnt5a expression is a putative marker of EOC and that non-canonical Wnt signaling is a potent target for developing novel EOC therapeutics.

An abstract presented at the 3<sup>rd</sup> International Symposium on Ovarian Cancer

## **Wnt Signaling, Cellular Senescence and Ovarian Cancer Therapy**

Rugang Zhang, Ph.D.

Program in Gene Expression and Regulation, The Wistar Institute, Philadelphia, PA 19104.

Epithelial ovarian cancer (EOC) remains the most lethal gynecological malignancy in the US. Thus, there is an urgent need to develop novel therapeutics for this disease. Cellular senescence is a tumor suppression mechanism that has been suggested as a novel mechanism for developing cancer therapeutics. Wnt5a is a non-canonical Wnt ligand that plays a context-dependent role in human cancers. Recently, we discovered a lower level of Wnt5a expression predicted shorter overall survival in EOC patients. Significantly, Wnt5a restoration inhibited proliferation of EOC cells both *in vitro* and *in vivo* in an orthotopic mouse model. Mechanistically, Wnt5a antagonizes Wnt/ $\beta$ -catenin signaling and induces cellular senescence by activating the epigenetic histone repressor A (HIRA)/promyelocytic leukemia (PML) senescence pathway. These data suggest that promoting cells to undergo senescence by reconstituting Wnt5a signaling represents a novel strategy for developing urgently needed EOC therapeutics. Here we performed preliminary experiments with a Wnt5a-mimetic hexapeptide, Foxy5. In EOC cell lines, Foxy5 significantly inhibits the proliferation of EOC cells by downregulating  $\beta$ -catenin and its transcriptional target, *CCND1* (cyclin D1). In addition, Foxy5 inhibits EOC cell migration in a classical wound-healing assay. In summary, we show that loss of Wnt5a predicts poor outcome in EOC patients and Wnt5a suppresses the growth of EOC cells by triggering cellular senescence. We suggest that strategies to drive senescence in EOC cells by reconstituting Wnt5a signaling via using Foxy5 may offer an effective new strategy for EOC therapy.